Lecture Notes in Networks and Systems 415

Jagdev Singh · George A. Anastassiou · Dumitru Baleanu · Carlo Cattani · Devendra Kumar *Editors*

Advances in Mathematical Modelling, Applied Analysis and Computation

Proceedings of ICMMAAC 2021

Springer

Lecture Notes in Networks and Systems

Volume 415

The series "Lecture Notes in Networks and Systems" publishes the latest developments in Networks and Systems—quickly, informally and with high quality. Original research reported in proceedings and post-proceedings represents the core of LNNS.

Volumes published in LNNS embrace all aspects and subfields of, as well as new challenges in, Networks and Systems.

The series contains proceedings and edited volumes in systems and networks, spanning the areas of Cyber-Physical Systems, Autonomous Systems, Sensor Networks, Control Systems, Energy Systems, Automotive Systems, Biological Systems, Vehicular Networking and Connected Vehicles, Aerospace Systems, Automation, Manufacturing, Smart Grids, Nonlinear Systems, Power Systems, Robotics, Social Systems, Economic Systems and other. Of particular value to both the contributors and the readership are the short publication timeframe and the world-wide distribution and exposure which enable both a wide and rapid dissemination of research output.

The series covers the theory, applications, and perspectives on the state of the art and future developments relevant to systems and networks, decision making, control, complex processes and related areas, as embedded in the fields of interdisciplinary and applied sciences, engineering, computer science, physics, economics, social, and life sciences, as well as the paradigms and methodologies behind them.

Indexed by SCOPUS, INSPEC, WTI Frankfurt eG, zbMATH, SCImago.

All books published in the series are submitted for consideration in Web of Science.

For proposals from Asia please contact Aninda Bose (aninda.bose@springer.com).

Jagdev Singh · George A. Anastassiou ·
Dumitru Baleanu · Carlo Cattani · Devendra Kumar
Editors

Advances in Mathematical Modelling, Applied Analysis and Computation

Proceedings of ICMMAAC 2021

Springer

Editors
Jagdev Singh
Department of Mathematics
JECRC University
Jaipur, India

Dumitru Baleanu
Department of Mathematics
Cankaya University
Ankara, Turkey

Devendra Kumar
Department of Mathematics
University of Rajasthan
Jaipur, India

George A. Anastassiou
Department of Mathematics
University of Memphis
Tennessee, TN, USA

Carlo Cattani
Engineering School, DEIM
University of Tuscia
Viterbo, Italy

ISSN 2367-3370 ISSN 2367-3389 (electronic)
Lecture Notes in Networks and Systems
ISBN 978-981-19-0178-2 ISBN 978-981-19-0179-9 (eBook)
https://doi.org/10.1007/978-981-19-0179-9

This Springer imprint is published by the registered company Springer Nature Singapore Pte Ltd.
The registered company address is: 152 Beach Road, #21-01/04 Gateway East, Singapore 189721, Singapore

Preface

This book is based around the 4th International Conference on "Mathematical Modelling, Applied Analysis and Computation (ICMMAAC 21)" held in JECRC University, Jaipur on 5–7 August 2021. The book contains several recent advanced and important topics in mathematical modelling, applicable analysis and numerical simulations having uses in science, engineering and finance. The book is very useful for the graduate and post-graduate students, researchers and educators working in different directions of research in applied mathematics and related fields. The general readers interested in mathematical theories and techniques having practical applications in solving real-world problems should also find the book very interesting and useful. The book contains 36 chapters which are organized as follows:

Chapter "A Collection of Hilfer Fractional Opial Inequalities" presents a collection of Hilfer fractional left and right side Opial type inequalities. These cover forward, reverse and extreme cases, and contain one, two and several functions of distinct non-integer orders at different powers. The estimates are very general covering several distinct settings.

Chapter "On a Non-linear Diffusion Model of Wood Impregnation: Analysis, Approximate Solutions, and Experiments with Relaxing Boundary Conditions" establishes approximate integral-balance solutions of nonlinear diffusion model for wood impregnation by methacrylate in two cases, namely, Dirichlet boundary condition considering instantaneous saturation of the wood surface contacting with the liquid bath and relaxing Dirichlet boundary conditions accounting the fact that instantaneous saturation is unphysical and takes some time to be developed.

Chapter "Algorithmic Complexity-Based Fractional-Order Derivatives in Computational Biology" presents a novel mathematical informed framework and multi-staged integrative technique concerning algorithmic complexity. This chapter aims at investigating a robust and accurate model reliant on the mixture of fractional-order derivative and artificial neural network for the diagnostic and differentiability predictive purposes for the disease which may reveal several and transient biological characteristic. Another objective of this chapter is benefitting from the concept of algorithmic complexity to attain the non-integer order derivative with the least complexity in order that it would be possible to achieve the optimized solution.

Chapter "Case Study of Non-singular Kernel Model for MHD Boundary Layer Flow of a Rate Type Fluid over an Oscillating Plate" presents the MHD boundary layer flow of rate type fluid over an oscillating inclined infinite plate along with Newtonian heating and slip at the boundary. The model is established by applying the Atangana-Baleanu time-fractional derivative operator. Temperature and velocity fields for the fractional-order model are calculated. The physical significance of the parameters like relaxation time, fractional-order parameter, Grashof number, and inclination of the plate is investigated and their control on the velocity of the fluid is examined graphically.

Chapter "Multilayer Perceptron Artificial Neural Network Approach to Solve Sixth-Order Two-Point Boundary Value Problems" presents a multilayer perceptron artificial neural network technique for solving the sixth-order boundary value problems that arise in various branches of engineering and physics such as hydrodynamics, fluid dynamics, astrophysics, beam theory and so on. The obtained solutions of these boundary value problems by applied method are optimal as compared to other existing approximation techniques. In order to decide the performance of the proposed technique some models are analysed. The numerical outcomes show that the suggested strategy is very effective for higher order boundary value problems and required low memory space and less computational time.

Chapter "Wavelet Transform on Generalized Quotient Spaces and Its Applications" presents the theory of generalized quotients which is a generalization of Schwartz distributions. The general construction of generalized quotients is discussed, which is employed to several function spaces in order to attain various generalized quotient spaces. The wavelet transform is extended to these spaces to obtain some generalized outcomes. The idea of convolution related to wavelet is employed to obtain operational properties for quotient of sequences. The wavelet transform of periodic quotient of sequences is expressed and a uniqueness theorem is defined for the wavelet transform of analytic functions. Some fundamental concepts of the theory of generalized quotients are discussed and then some of its applications such as extending the wavelet transform on a space of generalized quotients on the torus are explained.

Chapter "Certain Image Formulae of the Incomplete I-Function Under the Conformable and Pathway Fractional Integral and Derivative Operators" studies several interesting image formulae of the incomplete I-function under the conformable and pathway fractional operators. Since both the incomplete I-function and the conformable fractional operators are very general among special functions as well as fractional integral and derivative operators, the principal outcomes discussed in this chapter can give a number of specific identities, some of which are explicitly shown in the corollaries.

Chapter "Explicit Exact Solutions and Conservation Laws of Modified Alpha Equation" investigates the invariant solutions of generalized modified alpha equation which are derived by utilizing the Lie classical symmetry scheme. The obtained solutions are in terms of trigonometric functions and hyperbolic functions. This equation can be used in solidifying and nucleation problem. The conservation laws are obtained by employing the multiplier approach. The graphical representations

are also demonstrated for some of the obtained solutions. Some new solutions of those equations are found that have been considered earlier in literature, as well as some of the previous solutions can also be recovered by considering special values.

Chapter "Some Approximation Results on Durrmeyer Modification of Generalized Szász–Mirakjan Operators" deals with the approximation features of the summation-integral-type operators defined by Mishra et al. It consists of the local outcomes and convergence theorem of the defined operators. The asymptotic nature of the operators and the quantitative means of Voronovskaja-type theorem are presented. The Grüss Voronovskaja-type theorem is discussed. To support the approximation results of the operators, the graphical representation is presented.

Chapter "Fuzzy Approach to Solve General De-Novo Programming Problem" introduces a modified fuzzy approach to solve GDNPP by means of reflection of decision-maker's choice. It is observed that flexibility in decision-maker's choice to some extent could be studied in multi-objective linear programming problem utilizing meta-goal programming technique. This flexibility in decision process can also be effectively considered by applying fuzzy scheme for solving GDNPP, which is obtained by introducing novel constraints as per requirement of the problem. The proposed technique of solution has been shown by a numerical illustration. The obtained solutions have been compared with those of other existing techniques of solving GDNPP.

Chapter "Comparative Study of Eight Classification Models for Diagnosis and Prediction of Breast Cancer" deals with eight models such as Logistic Regression, K-Nearest Neighbourhood, Decision Tree, Random Forest, Artificial Neural Network, Gaussian Naïve Bayes, Support Vector Machine and AdaBoost classifier which are utilized for predicting two classes, i.e. benign and malignant. To select the best fit classification model for prediction, a confusion matrix is used for evaluating the performance of each model. Further, parameters, for example, precision, accuracy, recall, specificity, F-measure and Matthews correlation coefficient, are investigated for each model. The Wisconsin breast cancer diagnosis dataset and Coimbra breast cancer dataset are applied for experimental outcomes.

Chapter "Mathematical Model for Demonetization" investigates a demonetization effect on a population by using a compartmental mathematical model. Mathematical analysis of the model presents that there is an existence of demonetization–free equilibrium and demonetization existence equilibrium. The numerical results of the model are obtained and the outcomes reveal that demonetization effect persist in the system.

Chapter "An Inflationary Demand Scheme with Pareto Deterioration in Two Warehouses" deals with a two storage inventory model (one of them is Own Warehouse (OW) and another is Rented Warehouse (RW)) with exponentially time-varying demand considering partial backlogging. The capacity of own warehouse is fixed (U units), to store more units than the limited range of OW, the supplier has to rent another warehouse (RW) at higher holding cost. Two warehouse policies with linear holding cost and Pareto–type decay in an inflationary environment are studied. The sensitivity investigation has been investigated to show the effects of diverse parameters of the inventory system.

Chapter "Exact Solitary Wave Solutions of the (3+1)-Dimensional Generalised Kadomtsev-Petviashvili Benjamin-Bona-Mahony Equation" studies the (3+1)-dimensional generalized Kadomtsev-Petviashvili Benjamin-Bona-Mahony equation. By applying the modified hyperbolic function expansion method, the exact solitary wave solutions of the nonlinear partial differential equation have been derived. The required basic information for the technique of modified hyperbolic expansion has been provided. Two numerical examples have been demonstrated and the exact solutions obtained are described with the help of two–dimensional and three–dimensional graphs.

Chapter "Effect of Oblique Magnetic and Electric Fields on the Kelvin-Helmholtz Instability at the Interface Between Porous and Fluid Layers" deals with the effect of inclined magnetic and electric field on the growth rate of the Kelvin-Helmholtz instability of a flow in porous layer. The base flow is considered to be fully developed and the linear theories along with normal modes are applied to understand the stability of the flow over the interface between the fluid saturated porous layer and clear fluid layer of large extent. The effect of inclined magnetic and electric fields on the growth rate of instability is examined in terms of non-dimensional parameters. The numerical and graphical outcomes demonstrated and validated for wide range of non-dimensional parameters.

Chapter "Heat Transfer for MHD Flow in an Inclined Channel with Heat Generation/Absorption" deals with the motion of an incompressible viscous fluid in an inclined channel. A uniform magnetic field is employed normal to the channel, considering heat absorption, heat generation and viscous dissipation into account. The non-dimensional partial differential equations are transformed into ordinary differential equations (ODEs) and the perturbation technique is applied for solving ODEs. The velocity and temperature properties have been analysed through graphs.

Chapter "Volterra Equation with Constant Fractional Order and Variable Order Fractal Dimension" studies a general Volterra equation with the new differential and integral operators. The condition is presented under which the uniqueness and existence of the exact solutions can be obtained for three cases involving power law, exponential decay law and the generalized Mittag-Leffler function. Numerical solutions and error analysis are presented for each case.

Chapter "On the Parabolic Instability Region for Kuo Problem" demonstrates Kuo problem which deals with incompressible, inviscid, parallel zonal flows. For this Kuo problem, a parabolic instability region without any restriction which intersects with Howard semi-circle under some condition is derived. A novel upper bound for the growth rate of an unstable mode is obtained.

Chapter "Font Design Through RQT Bézier Curve Using Shape Parameters" deals with RQT Bézier curve utilizing two shape parameters. These new curves are more adaptable due to the existence of shape parameters and geometric characteristics. To confirm whether the studied curve satisfied the convex hull characteristic or not, limitations on shape, weight and declared end-pointed curvatures have been used. This curve is applied for smooth curve compositions by generating piecewise rational trigonometric curves that are adjacent in parametric and geometric Hermite continuity criteria.

Chapter "Effect of Partial Slip on Peristaltic Transport of MHD-Carreau Fluid in a Flexible Channel with Non-uniform Heat Source and Sink" studies the effect of magnetic field, partial slip flow and irregular heat generation and absorption of Carreau liquid in peristaltic movement through flexible channel. By using suitable non–dimensional parameters the governing equations are reduced to standard nonlinear partial differential equations. By employing multi-step differential transformation method solutions of emerging equations are obtained. The role of influential factors on velocity, concentration and temperature is demonstrated via graphs.

Chapter "Invariant Preserving Schemes for Multi-symplectic Integrator of Two Long Waves' Interactions" reports the idea of discrete conservation of symplecticity to discretization's for two long wave's interactions. This characteristic is endemic and it is explained that it also leads to exact discrete conservation of momentum and energy for propagation two long wave's interactions. Multi-symplectic integrators are examined for propagation two long waves' interactions and analysed the conservation aspect for multi-symplectic integrator. The numerical simulations are also shown.

Chapter "Study of Effect of Overlapping Stenosis on Flow Field Considering Non-Newtonian Reiner Rivlin Blood Flow in Artery" presents the impact of overlapping stenosis associate to symmetric stenosis for distinct shape parameters on parameters of flow field. By considering Reiner–Rivlin stress and strain constitutive relations appropriate for blood rheology the governing conservation equations are derived. To reveal shear thinning, shear thickening and dilatancy effect, the suitability of generalized Reiner–Rivlin constitutive relation is reported from the literature. The solution for flow field is founded for steady axi-symmetric case for both overlapping stenosis and axially symmetric for several shape parameters. To discuss the effect of overlapping stenosis associate to symmetric stenosis the flow fields for symmetric and overlapping stenosis are compared.

Chapter "Pathway Fractional Integral Formulae Involving Extended Bessel-Maitland Function in the Kernel" deals with two composition formulae of pathway fractional integral operators associated with altered modifications of the Bessel-Maitland function. Pertinent connections of certain special cases of key results with known outcomes have been investigated.

Chapter "Analytical Approximate Approach to the Helmholtz-Duffing Oscillator" studies a new analytical approximation for the period and periodic solutions for the Helmholtz-Duffing oscillator. The key aim of this work is to approximate the integration in exact analytical period of equation by applying a well-known quadrature rules. Comparison of the outcomes attained employing this scheme with the exact one and existing outcomes shows simplicity, accuracy and efficiency of the proposed method for the whole range of initial amplitudes and the equation parameter in a variety of cases. The approach can be easily modified to other existing strongly nonlinear oscillators.

Chapter "Haar Wavelet Series Method for Solving Simultaneous Proportional Delay Differential Equations" reports a novel numerical technique to find the approximate solution of simultaneous proportional delay differential equations (SPDDEs). To transform the SPDDEs into a system of algebraic matrix equations with unknown coefficients matrices, the discussed method uses delayed Haar wavelet series and collocation points. By applying suitable solver, the values of these unknown row

matrices can be found. By applying these coefficients the solution in forms of collocated Haar wavelet series is found.

Chapter "Fractional Reaction–DiffusionModel: An Efficient Computational Technique for Nonlinear Time-Fractional Schnakenberg Model" studies the q-homotopy analysis transform method (q-HATM) to obtain the solutions for the nonlinear fractional-order reaction-diffusion systems, for example, the fractional Schnakenberg model. For modelling of morphogen in developmental biology, study of these models is well known. In this chapter, study of Schnakenberg models is considered with exciting results. The obtained results show that the studied technique is very interesting and resolves the complex nonlinear issues that arise in the field of science and technology.

Chapter "Existence of Salvage Value in a Memory Dependent EOQ Model in Absence of Deteriorating Items" deals with an inventory model by considering the effect of the past experience. By applying concept of fractional calculus, the inclusion of memory effect in the inventory system has been investigated. The existence of salvage value in the memory dependent inventory system in absence of deteriorating items has been studied. At last, sensitivity analysis is discussed to analyse the crucial parameters of the system for the market studies so that it would be given care seriously.

Chapter "A Fuzzy Decomposable Approach for Posfust Reliability Evaluation of a Repairable Substation Automation System" represents a new technique to study the posfust reliability of a substation automated system. The fuzzy failure and fuzzy repair rates in the aspect of possibility have been discussed. In this scheme, a decomposition technique is used to a normal and convex fuzzy set. The complete process is compared with the existing method and applied method with the aid of numerical example.

Chapter "Solution of Fingering Phenomenon Arising in Porous Media in Horizontal Direction by Combination of Elzaki Transform and Adomian Decomposition Method" studies the solution of fingering aspect appearing in fluid flow via porous media in horizontal direction. This idea has a crucial role in oil recovery process. Mathematical construction of the fingering aspect has been obtained and it is represented by nonlinear partial differential equation. To compute the solution for the studied model, Elzaki Adomian decomposition scheme has been applied. The applied technique provides the solution in a convergent series. To analyse the accuracy of the discussed method, the applied technique is compared with variational iteration method.

Chapter "Numerical Study of Melting Impact on MHD Non-Newtonian Casson Fluid Flow Ran on a Stretching Sheet in a Porous Medium with Radiation and Dissipation Effect" reports the aspects of melting heat transference in the porous medium of MHD Casson fluid affected by thermal radiation and viscous dissipation in addition with heat source/sink effect. The nonlinear problem is handled by using the Runge-Kutta-Fehlberg method by reducing the governing equations into ordinary differential equations. By utilizing MATLAB software along with shooting method the graphical representation has been shown. The effect of Nusselt number and skin-friction coefficient has been illustrated. The results of the present study are related

with the convenient works in particular conditions and more contracts have been identified.

Chapter "Impact of Hall Current and Rotation on Unsteady MHD Oscillatory Dusty Fluid Flow Through Horizontal Porous Plates" studies the effect of Hall current on unsteady MHD oscillatory dusty fluid flow through the horizontal rotating porous plates. The momentum and energy equations on the basis of certain restrictions have been obtained. The governing equations have been simplified and solved by analytical approach. For velocity and temperature, the closed analytical solutions have been found. To reveal the key aspects of several physical parameters on the fluid flow, the numerical simulations are shown graphically. The outcomes found in this chapter are compared and authenticated with the existing results in the literature.

Chapter "Study of Aligned MHD Casson Fluid Past a Shrinking Sheet with Viscous Dissipation" studies the effect of viscous dissipation on aligned MHD flow in a Casson fluid with heat and flow transfer over shrinking sheet. The effects of several parameters have been investigated on different profiles. By employing similarity transformations the governing partial differential equations are converted to ordinary differential equations. By applying Runge-Kutta-Fehlberg technique with the aid of shooting scheme, the scientific outcomes have been discussed.

Chapter "Spin Coating of Non-Newtonian Nanofluid with Silver and Copper as Nanoparticle" investigates the characteristics of the flow and film thickness variation of non-Newtonian nanofluid during spin coating process. In case of non-newtonian fluid the viscosity is not a constant term. In case of non-Newtonian fluid, the viscosity and solvent diffusivity are dependent on polymer concentration. The silver and copper are taken as a nanoparticle and sodium alginate is taken as a non-Newtonian base fluid. The nature of the film thickness for the distinct parameters, for example, initial film thickness, angular velocity of the rotating disc and volume fraction of the nanoparticles has been studied.

Chapter "Analysis of Soret and Dufour Effect on MHD Fluid Flow Over a Slanted Stretching Sheet with Chemical Reaction, Heat Source and Radiation" investigates the MHD laminar flow with heat flux, mass flux and magnetic flux, buoyancy ratio, thermal conduction, and radiation with convective boundary condition for suction and injection of an electromagnetic fluid. The similarity transformations are employed to get the coupled ODEs from coupled partial differential equation and then these ODEs are handled by using RK-4 scheme. The impacts of different physical quantities are demonstrated numerically graphically on different profiles.

Chapter "Entropy Generation in Fourth-Grade Fluid Flow with Variable Thermal Conductivity" presents a numerical examination of thermo-fluidic configuration confronting entropy generation in the fourth grade fluid flow via a parallel plate channel with temperature-dependent thermal conductivity. The problem is formulated in terms of boundary value problem and examined by using RK-4-order scheme along with shooting technique. Thermodynamic irreversibility analysis is studied through quantification of entropy generation and Bejan numbers.

Chapter "Solution of Nonlinear Fractional Differential Equation Using New Integral Transform Method" presents the solution of fractional-order nonlinear partial differential equations by utilizing the Elzaki decomposition technique. The method

is a powerful scheme for solving fractional differential equation. Some numerical cases are illustrated to examine the efficiency of the proposed scheme.

The editors are thankful to the contributors for submitting their valuable research articles. The editors are grateful to the reviewers for their sincere efforts in evaluating the papers in a timely manner. We are also thankful to our colleagues and friends for their constant support and help during execution of task for bringing out this volume.

Jaipur, India — Jagdev Singh
Tennessee, USA — George A. Anastassiou
Ankara, Turkey — Dumitru Baleanu
Viterbo, Italy — Carlo Cattani
Jaipur, India — Devendra Kumar
September 2022

Contents

Editors and Contributors

About the Editors

Jagdev Singh is Professor and Head in the Department of Mathematics at JECRC University, Rajasthan, India. He did his Master of Science (M.Sc.) and Ph.D. in Mathematics from University of Rajasthan, India. His fields of research include Mathematical Modelling, Special Functions, Fractional Calculus, Fluid Dynamics, Analytical and Numerical Methods. He has published four books, viz. Fractional Calculus in Medical and Health Science (2020), Engineering Mathematics-I (2008), Engineering Mathematics-II (2013), and Advanced Engineering Mathematics-IV (2008). He has to his credit over 244 research papers published in various journals of repute, and his h-index is 53. He has attended a number of national and international conferences and presented several research papers. He is on the Editorial Board of various journals and reviewer of several journals. He is on the Clarivate Analytics list of highly cited researchers in 2020 and 2021. He won the Riemann Award for Young Scientists in Testimony of the High Regard of Achievements in the area of Fractional Calculus and its Applications in the First International Conference on Modern Fractional Calculus and Its Applications at Biruni University, Istanbul, Turkey, December 4–6, 2020. He won the International Obada Prize in 2021 for Young Distinguished Researcher.

George A. Anastassiou was born in Athens, Greece, in 1952. He received his B.Sc. degree in Mathematics from Athens University, Greece, in 1975. He received his Diploma in Operations Research from Southampton University, UK, in 1976. He also received his MA in Mathematics from University of Rochester, USA, in 1981. He was awarded his Ph.D. in Mathematics from University of Rochester, USA, in 1984. During 1984–86, he served as Visiting Assistant Professor at the University of Rhode Island, USA. Since 1986 till now 2020, he is Faculty Member at the University of Memphis, USA. He is currently Full Professor of Mathematics since 1994. His research area is "Computational Analysis" in the very broad sense. He has published

over 550 research articles in international mathematical journals and over 43 monographs, proceedings, and textbooks in well-known publishing houses. Several awards have been awarded to him. In 2007, he received the Honorary Doctoral Degree from University of Oradea, Romania. He is Associate Editor over 70 international mathematical journals and Editor in Chief in three journals, most notably in the well-known "Journal of Computational Analysis and Applications."

Dumitru Baleanu is Professor at the Institute of Space Sciences, Magurele–Bucharest, Romania, and Visiting Staff Member at the Department of Mathematics, Cankaya University, Ankara, Turkey. His research interests include fractional dynamics and its applications, fractional differential equations, dynamic systems on time scales, and Lie symmetries. He has published more than 1000 papers indexed in SCI. He is one of the editors of five books published by Springer and one published by AIP Conference Proceedings. He is Editorial Board Member of the journals indexed in SCI, viz. Mathematical Methods in Applied Sciences, Applied Numerical Mathematics, Mathematics, Journal of Computational and Nonlinear Dynamics, Symmetry and Fractional Calculus and Applied Analysis. He has received more than 15000 citations in journals covered by SCI, and his Hirsch index is 65. He was on the Thompson Reuter list of highly cited researchers in 2015, 2016, 2017, 2018, 2019, 2020 and 2021. He won the International Obada Prize in 2019.

Carlo Cattani is Professor (Habil. Full Professor) of Mathematical Physics at the Department of Economics, Engineering, Society and Enterprise of Tuscia University, Italy, since 2015. He has been previously appointed at the University of Rome "La Sapienza" (1980–2004) and University of Salerno (2004–2015). He is Research Fellow at the Italian Council of Research (1978–1980) and Visiting Research Fellow at the Physics Institute of the Stockholm University (1987–1988). His main research interests are focusing on numerical and computational mathematical models and methods. Author of more than 270 scientific papers and several books, he has given significant contributions to fundamental topics such as numerical methods, fractional calculus, fractals, wavelets, and nonlinear waves. He has been awarded as Honorary Professor at the Azerbaijan University (2019), at the BSP University, Ufa-Russia (2009), and (in 2018) as Adjunct Professor at the Ton Duc Thang University—HCMC Vietnam.

Devendra Kumar is Assistant Professor in the Department of Mathematics, University of Rajasthan, Rajasthan, India. He did his Master of Science (M.Sc.) and Ph.D. in Mathematics from University of Rajasthan, India. His areas of interest are Mathematical Modelling, Special Functions, Fractional Calculus, Applied Functional Analysis, Nonlinear Dynamics, Analytical and Numerical Methods. He has published four books, viz. Engineering Mathematics-I (2008), Engineering Mathematics-II (2013), Fractional Calculus in Medical and Health Science (2020), and Methods of Mathematical Modelling: Fractional Differential Equations (2020). He has to his credit over 250 research papers published in various journals of repute, and his h-index is 53. He has attended a number of national and international conferences and presented

several research papers. He is on the Editorial Board of several Journals of Mathematics. He is also a reviewer of various journals. He is on the Clarivate Analytics list of highly cited researchers in 2020 and 2021. He won the Bertram Ross Award in Testimony of the High Regard of Achievements in the area of Fractional Calculus and its Applications in the First International Conference on Modern Fractional Calculus and Its Applications at Biruni University, Istanbul, Turkey, December 4–6, 2020.

Contributors

Afroz Afroz MANUU, Hyderabad, India

Amsalu Hafte Department of Physics, Wollo University, Dessie, Ethiopia

Anastassiou George A. Department of Mathematical Sciences, University of Memphis, Memphis, U.S.A.

Asgir Maryam Department of Mathematics, Government College University Lahore, Lahore, Pakistan

Asha S. K. Department of Studies and Research in Mathematics, Karnatak University, Dharwad, India

Atangana Abdon Faculty of Natural and Agricultural Science, Institute for Groundwater Studied, University of Free State, Bloemfontein, South Africa;
Department of Medical Research, China Medical University Hospital, China Medical University, Taichung, Taiwan

Baleanu Dumitru Department of Mathematics, Çankaya University, Balgat, Ankara, Turkey;
Institute of Space Sciences, Magurele–Bucharest, Romania

Bansal Manish Kumar Department of Mathematics, Jaypee Institute of Information Technology, Noida, Uttar Pradesh, India

Beleri Joonabi Department of Studies and Research in Mathematics, Karnatak University, Dharwad, India

Bhattacharya Debasish NIT Agartala, Jirania, India

Bohra M. Department of Mathematics, Government Mahila Engineering College, Ajmer, India

Bonyah Ebenezer Department of Mathematics Education, Akenten Appiah Menka University of Skills Training and Entrepreneurial Development, Kumasi, Ghana

Chakraborty Sayanta NIT Agartala, Jirania, India

Champati Santilata Department of Mathematics, Siksha 'O' Anusandhandhan (Deemed to Be University), Bhubaneswar, India

Chandra Shekara Guruva Reddy Assistant Professor, Department of Mathematics, BMS College of Engineering, Bangalore, India

Choi Junesang Department of Mathematics, Dongguk University, Gyeongju, Republic of Korea

Dash Nibedita Department of Mathematics, School of Physical Sciences, Doon University, Dehradun, India

Devi Renu Department of Mathematics, SOES, GD Goenka University, Gurugram, Haryana, India

Dubay Ravi Shanker Department of Mathematics, AMITY School of Engineering and Technology, AMITY University, Jaipur, Rajasthan, India

Dube Mridula Department of Mathematics and Computer Science, R. D. University, Jabalpur, MP, India

Ganesh V. Department of Engineering, University of Technology and Applied Sciences, Muscat, Sultanate of Oman

Gaur Pradip Kumar Department of Mathematics, JECRC University, Jaipur, Rajasthan, India

Ghanbari B. Department of Basic Science, Kermanshah University of Technology, Kermanshah, Iran

Gill Vinod Department of Mathematics, Government college, Haryana, India

Govindarajan A. Department of Mathematics, SRM Institute of Science and Technology, Chennai, India

Gupta Nishi Department of Mathematics and Computer Science, R. D. University, Jabalpur, MP, India

Hristov Jordan Department of Chemical Engineering, University of Chemical Technology and Metallurgy, Sofia, Bulgaria

Hussain Basharat MANUU, Hyderabad, India

Jain Ruchi Department of Mathematics & Statistics, Manipal University Jaipur, Jaipur, Rajasthan, India

Jangid Sanju Department of Mathematics & Statistics, Manipal University Jaipur, Jaipur, Rajasthan, India

Jha Abhay Kumar Department of Mathematics, Motihari College of Engineering, Bihar, India

Jyoti Divya Department of Mathematics and Statistics, School of Basic and Applied Sciences, Central University of Punjab, Bathinda, Punjab, India

Karaca Yeliz University of Massachusetts Medical School (UMASS), Worcester, MA, USA

Kumar Devendra Department of Mathematics, University of Rajasthan, Jaipur, Rajasthan, India

Kumar Ganesh Department of Mathematics, University of Rajasthan, Jaipur, Rajasthan, India

Kumar Manoj Department of Mathematics, Motilal Nehru National Institute of Technology Allahabad, Prayagraj, U.P., India

Kumar Sachin Department of Mathematics and Statistics, School of Basic and Applied Sciences, Central University of Punjab, Bathinda, Punjab, India

Lavanya S. Department of Mathematics, Koneru Lakshmaiah Education Foundation, Vaddeswaram, India

Maity Susanta National Institute of Technology, Arunachal Pradesh Yupia, Dist. Papum Pare, Arunachal Pradesh, India

Malagi Naveen S. Department of Studies in Mathematics, Davangere University, Shivagangothri, India

Mallick Biswajit Department of Mathematics, School of Applied Sciences, KIIT Deemed to be University, Bhubaneswar, Odisha, India

Meher Ramakanta Department of Mathematics and Humanites, Sardar Vallabhbhai National Institute of Technology Surat, Surat, Gujarat, India

Mehta Ruchika Department of Mathematics & Statistics, Manipal University Jaipur, Jaipur, Rajasthan, India

Mehta Tripti Department of Mathematics, S. S. Jain Subodh P. G. College, Jaipur, Rajasthan, India

Mishra Lakshmi Narayan Department of Mathematics, School of Advanced Sciences, Vellore Institute of Technology, Tamil Nadu, Vellore, India

Mishra Vishnu Narayan Department of Mathematics, Indira Gandhi National Tribal University, Lalpur, Amarkantak, Anuppur, Madhya Pradesh, India

Mohanty Hemangini Department of Centre for Applied Mathematics and Computing, Siksha 'O' Anusandhandhan (Deemed to Be University), Bhubaneswar, India

Nag Swatilekha Pandit Deendayal Upadhaya Adarsha Mahavidyalaya, Behali, Assam, India

Osalusi Oluwasoji John Department of Mathematics, Government College University Lahore, Lahore, Pakistan

Pakhira Rituparna Department of Engineering Science and Humanities, Academy Of Technology, Adisaptagram, West Bengal, India

Pankaj Ram Dayal Department of Mathematics, J.N.V. University, Jodhpur, Rajasthan, India

Poply Vikas Department of Mathematics, KLP College, Rewari, Haryana, India

Prakasha D. G. Department of Studies in Mathematics, Davangere University, Shivagangothri, India

Prasannakumara B. C. Department of Studies in Mathematics, Davangere University, Shivagangothri, India

Purohit S. D. Department of HEAS (Mathematics), Rajasthan Technical University, Kota, India

Rathore Himanshu Department of Mechanical Engineering, Arya College of Engineering & I.T, Jaipur, Rajasthan, India

Rathour Laxmi Anuppur, Madhya Pradesh, India

Rawat Aparna Department of Mathematics and Statistics, Banasthali Vidyapith, Banasthali, India

Riaz Muhammad Bilal Department of Automation, Biomechanics and Mechatronics, Lodz University of Technology, Lodz, Poland;
Department of Mathematics, University of Management and Technology Lahore, Lahore, Pakistan;
Institute for Groundwater Studies, University of the Free State, Bloemfontein, South Africa

Sahu Prakash Kumar Department of Mathematics, School of Applied Sciences, KIIT Deemed to be University, Bhubaneswar, Odisha, India

Selvakumaran K. A. Department of Mathematics, R.M.K. College of Engineering and Technology, Puduvoyal, Tamil Nadu, India

Shafiq Anum School of Mathematics and Statistics, Nanjing University of Information Science and Technology, Nanjing, China

Sharma M. K. Department of Mathematics, C.C.S. University, Meerut, India

Singh Abhishek Department of Mathematics and Statistics, Banasthali Vidyapith, Banasthali, India

Singh Jagdev Department of Mathematics, JECRC University, Jaipur, Rajasthan, India

Singh Sarita Department of Mathematics, School of Physical Sciences, Doon University, Dehradun, India

Singh Twinkle Applied Mathematics and Humanities Department, Sardar Vallabhbhai National Institute of Technology, Gujarat, India

Sunita Department of Mathematics, University of Rajasthan, Jaipur, Rajasthan, India

Suthar D. L. Department of Mathematics, Wollo University, Dessie, Ethiopia

Tailor Gomatiben Department of Mathematics, AMITY School of Engineering and Technology, AMITY University, Jaipur, Rajasthan, India

Thiripura Sundari B. Department of Mathematics, SRM Institute of Science and Technology, Chennai, India

Varsoliwala Archana Applied Mathematics and Humanities Department, Sardar Vallabhbhai National Institute of Technology, Gujarat, India

Veeresha P. Center for Mathematical Needs, Department of Mathematics, CHRIST (Deemed to Be University), Bengaluru-560029, India

Venkata Ramana Reddy G. Department of Mathematics, Koneru Lakshmaiah Education Foundation, Vaddeswaram, India

Verma Akanksha Department of Mathematics, Motilal Nehru National Institute of Technology Allahabad, Prayagraj, U.P., India

Vijayalakshmi R. Department of Mathematics, SRM Institute of Science and Technology, Chennai, India

Vinita Makkar Department of Mathematics, SoBAS, GD Goenka University, Gurugram, Haryana, India

Vyas Paresh Department of Mathematics, University of Rajasthan, Jaipur, India

Yadav Harendra Department of Mathematics, C.C.S. University, Meerut, India

Yadav Kusum Department of Mathematics, University of Rajasthan, Jaipur, India

Yadav Rishikesh Department of Mathematics and Humanites, Sardar Vallabhbhai National Institute of Technology Surat, Surat, Gujarat, India;
Namur Institute for Complex Systems (naXys) and Department of Mathematics, University of Namur, Namur, Belgium

Yusuf Amidu African Institute for Mathematical Sciences, Accra, Ghana

Zafar Azhar Ali Department of Mathematics, Government College University Lahore, Lahore, Pakistan

A Collection of Hilfer Fractional Opial Inequalities

George A. Anastassiou

Abstract Here we present a detailed collection of the Hilfer fractional left and right side Opial-type inequalities. These cover forward, reverse, and extreme cases and involve one, two, and several functions of various non-integer orders at various powers. Our estimates are very general covering many different settings.

Keywords Hilfer fractional derivative · Opial inequality · Fractional integral inequalities

1 Background

The original Opial inequality [16] (see also [15], p. 114) states the following:

Theorem 1 *If* $f \in C^1([0,a])$ *with* $f(0) = f(a) = 0$ *and* $f(x) > 0$ *on* $(0,a)$, *then*

$$\int_0^a \left| f(x) f'(x) \right| dx \leq \frac{a}{4} \int_0^a \left(f'(x) \right)^2 dx. \tag{1}$$

The constant $\frac{a}{4}$ *is the best possible constant.*

This result for classical derivatives has been generalized in several directions (see, for instance, [1, 2]).

The author was the first to extend (1) for fractional derivatives, see [3], in 2000. For a complete treatment, see his monograph [11] of 2009.

Here we present a complete collection of left and right side fractional Opial-type inequalities involving the left and right side Hilfer fractional derivatives.

Let $-\infty < a < b < \infty$, the left and right Riemann–Liouville fractional integrals of order $\alpha \in \mathbb{C}$ $(\mathcal{R}(\alpha) > 0)$ are defined by

G. A. Anastassiou (✉)
Department of Mathematical Sciences, University of Memphis, Memphis 38152, U.S.A.
e-mail: ganastss@memphis.edu

J. Singh et al. (eds.), *Advances in Mathematical Modelling, Applied Analysis and Computation*, Lecture Notes in Networks and Systems 415,
https://doi.org/10.1007/978-981-19-0179-9_1

$$\left(I_{a+}^{\alpha} f\right)(x) = \frac{1}{\Gamma(\alpha)} \int_a^x (x-t)^{\alpha-1} f(t)\, dt, \tag{2}$$

$x > a$; where Γ stands for the gamma function, and

$$\left(I_{b-}^{\alpha} f\right)(x) = \frac{1}{\Gamma(\alpha)} \int_x^b (t-x)^{\alpha-1} f(t)\, dt, \tag{3}$$

$x < b$.

The Riemann–Liouville left and right fractional derivatives of order $\alpha \in \mathbb{C}$ $(\mathcal{R}(\alpha) \geq 0)$ are defined by

$$\left(\Delta_{a+}^{\alpha} y\right)(x) = \left(\frac{d}{dx}\right)^n \left(I_{a+}^{n-\alpha} y\right)(x) = \frac{1}{\Gamma(n-\alpha)} \left(\frac{d}{dx}\right)^n \int_a^x (x-t)^{n-\alpha-1} y(t)\, dt \tag{4}$$

($n = \lceil \mathcal{R}(\alpha) \rceil$, $\lceil \cdot \rceil$ means ceilling of the number; $x > a$)

$$\left(\Delta_{b-}^{\alpha} y\right)(x) = (-1)^n \left(\frac{d}{dx}\right)^n \left(I_{b-}^{n-\alpha} y\right)(x) =$$

$$\frac{(-1)^n}{\Gamma(n-\alpha)} \left(\frac{d}{dx}\right)^n \int_x^b (t-x)^{n-\alpha-1} y(t)\, dt \tag{5}$$

($n = \lceil \mathcal{R}(\alpha) \rceil$; $x < b$), respectively; where $\mathcal{R}(\alpha)$ is the real part of α.

In particular, when $\alpha = n \in \mathbb{Z}_+$, then

$$\left(\Delta_{a+}^{0} y\right)(x) = \left(\Delta_{b-}^{0} y\right)(x) = y(x);$$

$$\left(\Delta_{a+}^{n} y\right)(x) = y^{(n)}(x), \text{ and } \left(\Delta_{b-}^{n} y\right)(x) = (-1)^n y^{(n)}(x), \quad n \in \mathbb{N},$$

see [17].

We need to mention the left and right side Hilfer fractional derivatives.

Definition 1 *([18])* Let $\nu > 0$, $\nu \notin \mathbb{N}$, $\lceil \nu \rceil = n \in \mathbb{N}$, $f \in C([a,b])$. The Hilfer fractional derivative (left-sided and right-sided) ${}^{H}\mathbb{D}_{a+(b-)}^{\nu,\beta} f$ of order ν and type $0 \leq \beta \leq 1$ are defined by

$${}^{H}\mathbb{D}_{a+}^{\nu,\beta} f(x) = I_{a+}^{\beta(n-\nu)} \left(\frac{d}{dx}\right)^n I_{a+}^{(1-\beta)(n-\nu)} f(x), \tag{6}$$

and

$${}^{H}\mathbb{D}_{b-}^{\nu,\beta} f(x) = I_{b-}^{\beta(n-\nu)} \left(-\frac{d}{dx}\right)^n I_{b-}^{(1-\beta)(n-\nu)} f(x), \tag{7}$$

$x \in [a,b]$.

We make

Remark 1 When $\beta = 0$, we get the Riemann–Liouville fractional derivatives, while when $\beta = 1$, we obtain the Caputo-type fractional derivatives as follows (with $f \in C^n([a,b])$):

$$D_{a+}^{\nu} f(x) = \frac{1}{\Gamma(n-\nu)} \int_a^x (x-t)^{n-\nu-1} f^{(n)}(t)\, dt, \tag{8}$$

and

$$D_{b-}^{\nu} f(x) = \frac{(-1)^n}{\Gamma(n-\nu)} \int_x^b (t-x)^{n-\nu-1} f^{(n)}(t)\, dt, \tag{9}$$

$\forall\, x \in [a,b]$.

We define $\delta := \nu + \beta(n-\nu)$. We notice that $n-1 < \nu \leq \nu + \beta(n-\nu) \leq \nu + n - \nu = n$, hence $\lceil \delta \rceil = n$. We can easily write that

$$^{H}\mathbb{D}_{a+}^{\nu,\beta} f(x) = I_{a+}^{\delta-\nu} \Delta_{a+}^{\delta} f(x), \tag{10}$$

and

$$^{H}\mathbb{D}_{b-}^{\nu,\beta} f(x) = I_{b-}^{\delta-\nu} \Delta_{b-}^{\delta} f(x), \tag{11}$$

$x \in [a,b]$.

We have that

$$\Delta_{a+}^{\delta} f(x) = \left(\frac{d}{dx}\right)^n I_{a+}^{(1-\beta)(n-\nu)} f(x), \tag{12}$$

and

$$\Delta_{b-}^{\delta} f(x) = \left(-\frac{d}{dx}\right)^n I_{b-}^{(1-\beta)(n-\nu)} f(x), \tag{13}$$

$x \in [a,b]$.

In particular, when $0 < \nu < 1$ and $0 \leq \beta \leq 1$; $\delta = \nu + \beta(1-\nu)$, we have that

$$^{H}\mathbb{D}_{a+}^{\nu,\beta} f(x) = \frac{1}{\Gamma(\delta-\nu)} \int_a^x (x-t)^{\delta-\nu-1} \Delta_{a+}^{\delta} f(t)\, dt, \tag{14}$$

and

$$^{H}\mathbb{D}_{b-}^{\nu,\beta} f(x) = \frac{1}{\Gamma(\delta-\nu)} \int_x^b (t-x)^{\delta-\nu-1} \Delta_{b-}^{\delta} f(t)\, dt, \tag{15}$$

$x \in [a,b]$.

Next we mention some Hilfer fractional representation formulae:

Theorem 2 *([12]) Let $\nu > 0$, $\nu \notin \mathbb{N}$, $\lceil \nu \rceil = n$, $0 < \beta < 1$; $f \in C([a,b])$, $[a,b] \subset \mathbb{R}$; and set $\delta = \nu + \beta(n-\nu)$. Assume further that $\Delta_{a+}^{\delta} f \in C([a,b])$: $\Delta_{a+}^{\delta-j} f(a) =$*

0, *for* $j = 1, ..., n$. *Let also* $\gamma > 0 : \lceil \gamma \rceil = m$, *with* $\varepsilon = \gamma + \beta (m - \gamma)$, *and assume that* $\nu > \gamma$ *and* $\delta > \varepsilon$. *Then*

$$ {}^{H}\mathbb{D}_{a+}^{\gamma,\beta} f(x) = \frac{1}{\Gamma(\nu - \gamma)} \int_a^x (x - t)^{\nu-\gamma-1} \, {}^{H}\mathbb{D}_{a+}^{\nu,\beta} f(t) \, dt, \tag{16} $$

$x \in [a, b]$; *furthermore,* ${}^{H}\mathbb{D}_{a+}^{\gamma,\beta} f \in AC([a, b])$ *(absolutely continuous functions) if* $\nu - \gamma \geq 1$, *and* ${}^{H}\mathbb{D}_{a+}^{\gamma,\beta} f \in C([a, b])$ *if* $\nu - \gamma \in (0, 1)$.

We also mention

Theorem 3 *([12]) Let* $\nu > 0$, $\nu \notin \mathbb{N}$, $\lceil \nu \rceil = n$, $0 < \beta < 1$; $f \in C([a, b])$, $[a, b] \subset \mathbb{R}$; *and set* $\delta = \nu + \beta (n - \nu)$. *Assume further that* $\Delta_{b-}^{\delta} f \in C([a, b]) : \Delta_{b-}^{\delta-j} f(b) = 0$, *for* $j = 1, ..., n$. *Let also* $\gamma > 0 : \lceil \gamma \rceil = m$, *with* $\varepsilon = \gamma + \beta (m - \gamma)$, *and assume that* $\nu > \gamma$ *and* $\delta > \varepsilon$. *Then*

$$ {}^{H}\mathbb{D}_{b-}^{\gamma,\beta} f(x) = \frac{1}{\Gamma(\nu - \gamma)} \int_x^b (t - x)^{\nu-\gamma-1} \, {}^{H}\mathbb{D}_{b-}^{\nu,\beta} f(t) \, dt, \tag{17} $$

$x \in [a, b]$; *furthermore,* ${}^{H}\mathbb{D}_{b-}^{\gamma,\beta} f \in AC([a, b])$ *if* $\nu - \gamma \geq 1$, *and* ${}^{H}\mathbb{D}_{b-}^{\gamma,\beta} f \in C([a, b])$ *if* $\nu - \gamma \in (0, 1)$.

We continue with two extreme cases.

Theorem 4 *([12]) When* $\beta = 0$, *Theorems 2 and 3 are still valid. That is*

$$ \Delta_{a+}^{\gamma} f(x) = I_{a+}^{\nu-\gamma} \Delta_{a+}^{\nu} f(x), \tag{18} $$

and

$$ \Delta_{b-}^{\gamma} f(x) = I_{b-}^{\nu-\gamma} \Delta_{b-}^{\nu} f(x), \tag{19} $$

all $x \in [a, b]$, *respectively.*

The case of $\beta = 1$ collapses to Caputo-type fractional derivatives and related representation formulae (see [12]), already treated extensively in [11].

So, here we treat only $0 \leq \beta < 1$ case.

To motivate our work, we mention the Opial-type left side Hilfer fractional inequality:

Theorem 5 *([12]) All as in Theorem 2,* $0 \leq \beta < 1$. *Let also* $p, q > 1 : \frac{1}{p} + \frac{1}{q} = 1$, *and assume that* $\nu - \gamma > \frac{1}{q}$. *Then*

$$ \int_a^x \left| {}^{H}\mathbb{D}_{a+}^{\gamma,\beta} f(w) \right| \left| {}^{H}\mathbb{D}_{a+}^{\nu,\beta} f(w) \right| dw \leq $$

$$\frac{2^{-\frac{1}{q}}(x-a)^{(\nu-\gamma)+\left(\frac{1}{p}-\frac{1}{q}\right)}}{\Gamma(\nu-\gamma)\left[(p(\nu-\gamma-1)+1)(p(\nu-\gamma-1)+2)\right]^{\frac{1}{p}}}\left(\int_a^x\left|{}^H\mathbb{D}_{a+}^{\nu,\beta}f(w)\right|^q dw\right)^{\frac{2}{q}}, \tag{20}$$

$\forall\, x\in[a,b]$.

The corresponding Opial-type right side Hilfer fractional inequality follows:

Theorem 6 *([12]) All as in Theorem 3,* $0\le\beta<1$. *Let also* $p,q>1:\frac{1}{p}+\frac{1}{q}=1$, *and assume that* $\nu-\gamma>\frac{1}{q}$. *Then*

$$\int_x^b\left|{}^H\mathbb{D}_{b-}^{\gamma,\beta}f(w)\right|\left|{}^H\mathbb{D}_{b-}^{\nu,\beta}f(w)\right|dw\le$$

$$\frac{2^{-\frac{1}{q}}(b-x)^{(\nu-\gamma)+\left(\frac{1}{p}-\frac{1}{q}\right)}}{\Gamma(\nu-\gamma)\left[(p(\nu-\gamma-1)+1)(p(\nu-\gamma-1)+2)\right]^{\frac{1}{p}}}\left(\int_x^b\left|{}^H\mathbb{D}_{b-}^{\nu,\beta}f(w)\right|^q dw\right)^{\frac{2}{q}}, \tag{21}$$

$\forall\, x\in[a,b]$.

2 Main Results

Next comes a complete collection of left and right side fractional Opial-type inequalities engaging the left and right side Hilfer fractional derivatives.

2.1 Results Involving One Function

We start with a left side one:

Theorem 7 *Here all as in Theorem 2,* $0\le\beta<1$. *Then*

$$\int_a^x\left|{}^H\mathbb{D}_{a+}^{\gamma,\beta}f(w)\right|\left|{}^H\mathbb{D}_{a+}^{\nu,\beta}f(w)\right|dw\le\frac{(x-a)^{(\nu-\gamma+1)}}{\Gamma(\nu-\gamma+2)}\left(\left\|{}^H\mathbb{D}_{a+}^{\nu,\beta}f\right\|_\infty\right)^2, \tag{22}$$

$x\in[a,b]$.

Proof Similar to Proposition 25.1, [4], p. 547.

The right side one follows:

Theorem 8 *Here all as in Theorem 3,* $0\le\beta<1$. *Then*

$$\int_x^b\left|{}^H\mathbb{D}_{b-}^{\gamma,\beta}f(w)\right|\left|{}^H\mathbb{D}_{b-}^{\nu,\beta}f(w)\right|dw\le\frac{(b-x)^{\nu-\gamma+1}}{\Gamma(\nu-\gamma+2)}\left(\left\|{}^H\mathbb{D}_{b-}^{\nu,\beta}f\right\|_\infty\right)^2, \tag{23}$$

$x \in [a,b]$.

Proof Similar to (22).

We continue with converse results:

Theorem 9 *All as in Theorem 2,* $0 \leq \beta < 1$. *Suppose that* ${}^{H}\mathbb{D}_{a+}^{\nu,\beta} f(w) \not\equiv 0$ *and of fixed sign over* $[a,b]$. *Let* p, q *such that* $0 < p < 1$ *and* $\frac{1}{p} + \frac{1}{q} = 1$. *Then*

$$\int_a^x \left| {}^{H}\mathbb{D}_{a+}^{\gamma,\beta} f(w) \right| \left| {}^{H}\mathbb{D}_{a+}^{\nu,\beta} f(w) \right| dw \geq$$

$$\frac{2^{-\frac{1}{q}} (x-a)^{(\nu-\gamma)+\left(\frac{1}{p}-\frac{1}{q}\right)}}{\Gamma(\nu-\gamma)\left[(p(\nu-\gamma-1)+1)(p(\nu-\gamma-1)+2)\right]^{\frac{1}{p}}} \left(\int_a^x \left| {}^{H}\mathbb{D}_{a+}^{\nu,\beta} f(w) \right|^q dw \right)^{\frac{2}{q}}, \tag{24}$$

$\forall\, x \in [a,b]$.

Proof Similar to Theorem 25.3, [4], p. 547.

Theorem 10 *All as in Theorem 3,* $0 \leq \beta < 1$. *Suppose that* ${}^{H}\mathbb{D}_{b-}^{\nu,\beta} f(w) \not\equiv 0$ *and of fixed sign over* $[a,b]$. *Let* p, q *such that* $0 < p < 1$ *and* $\frac{1}{p} + \frac{1}{q} = 1$. *Then*

$$\int_x^b \left| {}^{H}\mathbb{D}_{b-}^{\gamma,\beta} f(w) \right| \left| {}^{H}\mathbb{D}_{b-}^{\nu,\beta} f(w) \right| dw \geq$$

$$\frac{2^{-\frac{1}{q}} (b-x)^{(\nu-\gamma)+\left(\frac{1}{p}-\frac{1}{q}\right)}}{\Gamma(\nu-\gamma)\left[(p(\nu-\gamma-1)+1)(p(\nu-\gamma-1)+2)\right]^{\frac{1}{p}}} \left(\int_x^b \left| {}^{H}\mathbb{D}_{b-}^{\nu,\beta} f(w) \right|^q dw \right)^{\frac{2}{q}}, \tag{25}$$

$\forall\, x \in [a,b]$.

Proof Similar to (24).

We continue with

Theorem 11 *All as in Theorem 2,* $0 \leq \beta < 1$. *Additionally, let* $k > 0 : \lceil k \rceil = m_1$, *with* $\varepsilon_1 = k + \beta(m_1 - k)$, *and assume* $\delta > \varepsilon_1$. *Assume further that* $\nu - k > 1$ *and* $\gamma = k + 1$. *Let* $p, q > 1 : \frac{1}{p} + \frac{1}{q} = 1$. *Then*

$$\int_a^x \left| \left({}^{H}\mathbb{D}_{a+}^{k,\beta} f \right)(w) \right| \left| \left({}^{H}\mathbb{D}_{a+}^{\gamma,\beta} f \right)(w) \right| dw \leq$$

$$\frac{(x-a)^{\frac{2(p(\nu-k-1)+1)}{p}}}{2\left(\Gamma(\nu-k)\right)^2 (p(\nu-k-1)+1)^{\frac{2}{p}}} \left(\int_a^x \left| \left({}^{H}\mathbb{D}_{a+}^{\nu,\beta} f \right)(w) \right|^q dw \right)^{\frac{2}{q}}, \tag{26}$$

$\forall\, x \in [a,b]$.

Proof Similar to Theorem 25.4, [4], p. 549.

Theorem 12 *All as in Theorem 3, and the rest as in Theorem 11. Then*

$$\int_x^b \left|\left({}^H\mathbb{D}_{b-}^{k,\beta} f\right)(w)\right| \left|\left({}^H\mathbb{D}_{b-}^{\gamma,\beta} f\right)(w)\right| dw \leq$$

$$\frac{(b-x)^{\frac{2(p(\nu-k-1)+1)}{p}}}{2\left(\Gamma(\nu-k)\right)^2 \left(p(\nu-k-1)+1\right)^{\frac{2}{p}}} \left(\int_x^b \left|\left({}^H\mathbb{D}_{b-}^{\nu,\beta} f\right)(w)\right|^q dw\right)^{\frac{2}{q}}, \tag{27}$$

$\forall\, x \in [a,b]$.

Proof Similar to (26).

We continue with extreme cases:

Theorem 13 *All as in Theorem 11, with $p = 1$, $q = \infty$. Then*

$$\int_a^x \left|\left({}^H\mathbb{D}_{a+}^{k,\beta} f\right)(w)\right| \left|\left({}^H\mathbb{D}_{a+}^{k+1,\beta} f\right)(w)\right| dw \leq$$

$$\frac{(x-a)^{2(\nu-k)} \left(\left\|{}^H\mathbb{D}_{a+}^{\nu,\beta} f\right\|_{\infty,(a,x)}\right)^2}{2\left(\Gamma(\nu-k+1)\right)^2}, \tag{28}$$

$\forall\, x \in [a,b]$.

Proof Similar to Proposition 25.2, [4], p. 551.

Theorem 14 *All as in Theorem 12; $p = 1$, $q = \infty$. Then*

$$\int_x^b \left|\left({}^H\mathbb{D}_{b-}^{k,\beta} f\right)(w)\right| \left|\left({}^H\mathbb{D}_{b-}^{k+1,\beta} f\right)(w)\right| dw \leq$$

$$\frac{(b-x)^{2(\nu-k)} \left(\left\|{}^H\mathbb{D}_{b-}^{\nu,\beta} f\right\|_{\infty,(x,b)}\right)^2}{2\left(\Gamma(\nu-k+1)\right)^2}, \tag{29}$$

$\forall\, x \in [a,b]$.

Proof Similar to (28).

We continue with reverse inequalities:

Theorem 15 *All as in Theorem 11. Here $\left({}^H\mathbb{D}_{a+}^{\nu,\beta} f\right)(w) \not\equiv 0$ and of fixed sign over $[a,b]$; furthermore, let $p, q : 0 < p < 1$ and $\frac{1}{p} + \frac{1}{q} = 1$. Then*

$$\int_a^x \left|{}^H\mathbb{D}_{a+}^{k,\beta} f(w)\right| \left|{}^H\mathbb{D}_{a+}^{\gamma,\beta} f(w)\right| dw \geq$$

$$\frac{(x-a)^{\frac{2(p(\nu-k-1)+1)}{p}}}{2\left(\Gamma(\nu-\gamma)\right)^2 \left(p(\nu-k-1)+1\right)^{\frac{2}{p}}} \left(\int_a^x \left|\left({}^H\mathbb{D}_{a+}^{\nu,\beta} f\right)(w)\right|^q dw\right)^{\frac{2}{q}}, \tag{30}$$

$\forall\, x \in [a,b]$.

Proof Similar to Theorem 25.5, [4], p. 553.

Theorem 16 *All as in Theorem 12. Here* $\left({}^H\mathbb{D}_{b-}^{\nu,\beta} f\right)(w) \not\equiv 0$ *and of fixed sign over* $[a,b]$*; furthermore, let* $p, q : 0 < p < 1$ *and* $\frac{1}{p} + \frac{1}{q} = 1$. *Then*

$$\int_x^b \left|{}^H\mathbb{D}_{b-}^{k,\beta} f(w)\right| \left|{}^H\mathbb{D}_{b-}^{\gamma,\beta} f(w)\right| dw \geq$$

$$\frac{(b-x)^{\frac{2(p(\nu-k-1)+1)}{p}}}{2\left(\Gamma(\nu-k)\right)^2 \left(p(\nu-k-1)+1\right)^{\frac{2}{p}}} \left(\int_x^b \left|\left({}^H\mathbb{D}_{b-}^{\nu,\beta} f\right)(w)\right|^q dw\right)^{\frac{2}{q}}, \tag{31}$$

$\forall\, x \in [a,b]$.

Proof Similar to (30).

Next we present

Theorem 17 *Let* $\nu > 0$, $\nu \notin \mathbb{N}$, $\lceil \nu \rceil = n$, $0 \leq \beta < 1$; $f \in C([a,b])$*; and set* $\delta = \nu + \beta(n-\nu)$. *Assume further that* $\Delta_{a+}^{\delta} f \in C([a,b]) : \Delta_{a+}^{\delta-j} f(a) = 0$, $j = 1, \ldots, n$. *Let also* $\gamma_i > 0 : \lceil \gamma_i \rceil = m_i$*;* $\nu - \gamma_i \geq 1$, *with* $\varepsilon_i = \gamma_i + \beta(m_i - \gamma_i)$, *and assume that* $\nu > \gamma_i$ *and* $\delta > \varepsilon_i$, $i = 1, \ldots, l$.

Here $a \leq x \leq b$; $q_1(x), q_2(x)$ *continuous functions on* $[a,b]$ *such that* $q_1(x) \geq 0$, $q_2(x) > 0$ *on* $[a,b]$, *and* $r_i > 0 : \sum_{i=1}^{l} r_i = r$. *Let* $s_1, s_1' > 1 : \frac{1}{s_1} + \frac{1}{s_1'} = 1$ *and* $s_2, s_2' > 1 : \frac{1}{s_2} + \frac{1}{s_2'} = 1$, *and* $p > s_2$.

Denote by

$$Q_1(x) := \left(\int_a^x (q_1(\omega))^{s_1'} d\omega\right)^{\frac{1}{s_1'}} \tag{32}$$

and

$$Q_2(x) := \left(\int_a^x (q_2(\omega))^{-\frac{s_2'}{p}} d\omega\right)^{\frac{r}{s_2'}}, \tag{33}$$

$$\sigma := \frac{p - s_2}{p s_2}.$$

Then

$$\int_a^x q_1(w) \prod_{i=1}^{l} \left| {}^{H}\mathbb{D}_{a+}^{\gamma_i,\beta} f(\omega) \right|^{r_i} d\omega \le Q_1(x)\, Q_2(x)$$

$$\prod_{i=1}^{l} \left\{ \frac{\sigma^{r_i\sigma}}{(\Gamma(\nu-\gamma_i))^{r_i} (\nu-\gamma_i-1+\sigma)^{r_i\sigma}} \right\} \tag{34}$$

$$\frac{(x-a)^{\left(\sum_{i=1}^{l}(\nu-\gamma_i-1)r_i+\sigma r+\frac{1}{s_1}\right)}}{\left(\left(\sum_{i=1}^{l}(\nu-\gamma_i-1)\, r_i s_1\right)+rs_1\sigma+1\right)^{\frac{1}{s_1}}} \left(\int_a^x q_2(w) \left| {}^{H}\mathbb{D}_{a+}^{\nu,\beta} f(\omega) \right|^{p} d\omega\right)^{\frac{r}{p}},$$

$\forall\, x \in [a,b]$.

Proof Similar to Theorem 26.1, p. 567 of [4].

Next we also present

Theorem 18 *Let $\nu > 0$, $\nu \notin \mathbb{N}$, $\lceil \nu \rceil = n$, $0 \le \beta < 1$; $f \in C([a,b])$; and set $\delta = \nu + \beta(n-\nu)$. Assume further that $\Delta_{b-}^{\delta} f \in C([a,b]) : \Delta_{b-}^{\delta-j} f(b) = 0$, $j = 1, ..., n$. Let also $\gamma_i > 0 : \lceil \gamma_i \rceil = m_i$; $\nu - \gamma_i \ge 1$, with $\varepsilon_i = \gamma_i + \beta(m_i - \gamma_i)$, and assume that $\nu > \gamma_i$ and $\delta > \varepsilon_i$, $i = 1, ..., l$.*

Here $a \le x \le b$; $q_1(x), q_2(x)$ continuous functions on $[a,b]$ such that $q_1(x) \ge 0$, $q_2(x) > 0$ on $[a,b]$, and $r_i > 0 : \sum_{i=1}^{l} r_i = r$. Let $s_1, s_1' > 1 : \frac{1}{s_1} + \frac{1}{s_1'} = 1$ and $s_2, s_2' > 1 : \frac{1}{s_2} + \frac{1}{s_2'} = 1$, and $p > s_2$.

Denote by

$$\overline{Q}_1(x) := \left(\int_x^b (q_1(\omega))^{s_1'} d\omega\right)^{\frac{1}{s_1'}} \tag{35}$$

and

$$\overline{Q}_2(x) := \left(\int_x^b (q_2(\omega))^{-\frac{s_2'}{p}} d\omega\right)^{\frac{r}{s_2'}}, \tag{36}$$

$$\sigma := \frac{p - s_2}{p s_2}.$$

Then

$$\int_x^b q_1(w) \prod_{i=1}^{l} \left| {}^{H}\mathbb{D}_{b-}^{\gamma_i,\beta} f(\omega) \right|^{r_i} d\omega \le \overline{Q}_1(x)\, \overline{Q}_2(x)$$

$$\prod_{i=1}^{l} \left\{ \frac{\sigma^{r_i\sigma}}{(\Gamma(\nu-\gamma_i))^{r_i} (\nu-\gamma_i-1+\sigma)^{r_i\sigma}} \right\} \tag{37}$$

$$\frac{(b-x)^{\left(\sum_{i=1}^{l}(\nu-\gamma_i-1)r_i+\sigma r+\frac{1}{s_1}\right)}}{\left(\left(\sum_{i=1}^{l}(\nu-\gamma_i-1)\,r_i s_1\right)+rs_1\sigma+1\right)^{\frac{1}{s_1}}}\left(\int_x^b q_2(w)\left|{}^{H}\mathbb{D}_{b-}^{\nu,\beta}f(\omega)\right|^p d\omega\right)^{\frac{r}{p}},$$

$\forall\, x\in[a,b]$.

Proof Similar to Theorem 26.1, p. 567 of [4].

Converse theorems follow:

Theorem 19 *Let $\nu>0$, $\nu\notin\mathbb{N}$, $\lceil\nu\rceil=n$, $0\le\beta<1$; $f\in C([a,b])$; and set $\delta=\nu+\beta(n-\nu)$. Assume further that $\Delta_{a+}^{\delta}f\in C([a,b])$: $\Delta_{a+}^{\delta-j}f(a)=0$, $j=1,...,n$. Let also $\gamma_i>0:\lceil\gamma_i\rceil=m_i$; $\nu-\gamma_i\ge1$, with $\varepsilon_i=\gamma_i+\beta(m_i-\gamma_i)$, and assume that $\nu>\gamma_i$ and $\delta>\varepsilon_i$, $i=1,...,l$; along with ${}^{H}\mathbb{D}_{a+}^{\nu,\beta}f>0$.*

Here $a\le x\le b$; $q_1(x),q_2(x)>0$ are continuous functions on $[a,b]$ and $r_i>0:\sum_{i=1}^{l}r_i=r$. Let $0<s_1,s_2<1$ and $s_1',s_2'<0$ such that $\frac{1}{s_1}+\frac{1}{s_1'}=1$, $\frac{1}{s_2}+\frac{1}{s_2'}=1$.

Denote by

$$Q_1(x):=\left(\int_a^x(q_1(\omega))^{s_1'}d\omega\right)^{\frac{1}{s_1'}}\tag{38}$$

and

$$Q_2(x):=\left(\int_a^x(q_2(\omega))^{-s_2'}d\omega\right)^{\frac{r}{s_2'}}.\tag{39}$$

Set

$$\lambda:=\frac{s_1s_2}{s_1s_2-1}.$$

Then

$$\int_a^x q_1(\omega)\left(\prod_{i=1}^{l}\left|{}^{H}\mathbb{D}_{a+}^{\gamma_i,\beta}f(\omega)\right|^{r_i}\right)d\omega\ge$$

$$\frac{Q_1(x)\,Q_2(x)}{\prod_{i=1}^{l}\{(\Gamma(\nu-\gamma_i))^{r_i}\left((\nu-\gamma_i-1)\,s_2^2s_1+1\right)^{\left(\frac{r_i}{s_2^2s_1}\right)}\}}\tag{40}$$

$$\frac{(x-a)^{\frac{\left\{\left(\sum_{i=1}^{l}r_i\left((\nu-\gamma_i-1)s_1+s_2^{-2}\right)\right)+1\right\}}{s_1}}}{\left\{\left(\sum_{i=1}^{l}r_i\left((\nu-\gamma_i-1)\,s_1+s_2^{-2}\right)\right)+1\right\}^{\frac{1}{s_1}}}\left(\int_a^x q_2^{\lambda s_2}(\omega)\left|{}^{H}\mathbb{D}_{a+}^{\nu,\beta}f(\omega)\right|^{\lambda s_2}d\omega\right)^{\frac{r}{\lambda s_2}},$$

$\forall\, x\in[a,b]$.

Proof Similar to Theorem 26.2, p. 570 of [4].

Theorem 20 *Let* $\nu > 0$, $\nu \notin \mathbb{N}$, $\lceil \nu \rceil = n$, $0 \leq \beta < 1$; $f \in C([a,b])$; *and set* $\delta = \nu + \beta(n-\nu)$. *Assume further that* $\Delta_{b-}^{\delta} f \in C([a,b]) : \Delta_{b-}^{\delta-j} f(b) = 0$, $j = 1, ..., n$. *Let also* $\gamma_i > 0 : \lceil \gamma_i \rceil = m_i$; $\nu - \gamma_i \geq 1$, *with* $\varepsilon_i = \gamma_i + \beta(m_i - \gamma_i)$, *and assume that* $\nu > \gamma_i$ *and* $\delta > \varepsilon_i$, $i = 1, ..., l$; *along with* ${}^{H}\mathbb{D}_{b-}^{\nu,\beta} f > 0$. *Here* $a \leq x \leq b$; $q_1(x), q_2(x) > 0$ *are continuous functions on* $[a,b]$ *and* $r_i > 0 : \sum_{i=1}^{l} r_i = r$. *Let* $0 < s_1, s_2 < 1$ *and* $s_1', s_2' < 0$ *such that* $\frac{1}{s_1} + \frac{1}{s_1'} = 1$, $\frac{1}{s_2} + \frac{1}{s_2'} = 1$. *Denote by*

$$\overline{Q}_1(x) := \left(\int_x^b (q_1(\omega))^{s_1'} d\omega \right)^{\frac{1}{s_1'}} \tag{41}$$

and

$$\overline{Q}_2(x) := \left(\int_x^b (q_2(\omega))^{-s_2'} d\omega \right)^{\frac{r}{s_2'}}. \tag{42}$$

Set

$$\lambda := \frac{s_1 s_2}{s_1 s_2 - 1}.$$

Then

$$\int_x^b q_1(w) \prod_{i=1}^{l} \left| {}^{H}\mathbb{D}_{b-}^{\gamma_i,\beta} f(\omega) \right|^{r_i} d\omega \geq$$

$$\frac{\overline{Q}_1(x)\, \overline{Q}_2(x)}{\prod_{i=1}^{l} \{(\Gamma(\nu-\gamma_i))^{r_i} ((\nu-\gamma_i-1) s_2^2 s_1 + 1)^{\left(\frac{r_i}{s_2^2 s_1}\right)}\}} \tag{43}$$

$$\frac{(b-x)^{\frac{\left\{\left(\sum_{i=1}^{l} r_i \left((\nu-\gamma_i-1)s_1 + s_2^{-2}\right)\right)+1\right\}}{s_1}}}{\left\{\left(\sum_{i=1}^{l} r_i \left((\nu-\gamma_i-1)s_1 + s_2^{-2}\right)\right)+1\right\}^{\frac{1}{s_1}}} \left(\int_x^b q_2^{\lambda s_2}(\omega) \left| {}^{H}\mathbb{D}_{b-}^{\nu,\beta} f(\omega) \right|^{\lambda s_2} d\omega \right)^{\frac{r}{\lambda s_2}},$$

$\forall\, x \in [a,b]$.

Proof Similar to Theorem 26.2, p. 570 of [4].

Extreme cases follow when $p = 1$ and $q = \infty$.

Theorem 21 *Let* $\nu > 0$, $\nu \notin \mathbb{N}$, $\lceil \nu \rceil = n$, $0 \leq \beta < 1$; $f \in C([a,b])$; *and set* $\delta = \nu + \beta(n-\nu)$. *Assume further that* $\Delta_{a+}^{\delta} f \in C([a,b]) : \Delta_{a+}^{\delta-j} f(a) = 0$, $j = 1, ..., n$. *Let also* $\gamma_i > 0 : \lceil \gamma_i \rceil = m_i$; $\nu - \gamma_i \geq 1$, *with* $\varepsilon_i = \gamma_i + \beta(m_i - \gamma_i)$, *and assume*

that $\nu > \gamma_i$ *and* $\delta > \varepsilon_i$, $i = 1, ..., l$. *Here* $a \le x \le b$, $0 \le \overline{q} \in C([a, b])$ *and* $r_i > 0 : \sum_{i=1}^{l} r_i = r$. *Then*

$$\int_a^x \overline{q}(w) \prod_{i=1}^{l} \left| {}^{H}\mathbb{D}_{a+}^{\gamma_i,\beta} f(w) \right|^{r_i} d\omega \le \tag{44}$$

$$\left\{ \frac{\|\overline{q}\|_{\infty,(a,x)} \left(\left\| {}^{H}\mathbb{D}_{a+}^{\nu,\beta} f \right\|_{\infty,(a,x)} \right)^{r}}{\prod_{i=1}^{l} (\Gamma(\nu - \gamma_i + 1))^{r_i}} \right\} \left\{ \frac{(x-a)^{r\nu - \sum_{i=1}^{l} r_i \gamma_i + 1}}{\left(r\nu - \sum_{i=1}^{l} r_i \gamma_i + 1 \right)} \right\}.$$

Proof Similar to Proposition 26.1 of [4], p. 573.

Theorem 22 *All as in Theorem 21, with now* $\Delta_{b-}^{\delta} f \in C([a, b]) : \Delta_{b-}^{\delta-j} f(b) = 0$, $j = 1, ..., n$. *Then*

$$\int_x^b \overline{q}(w) \prod_{i=1}^{l} \left| {}^{H}\mathbb{D}_{b-}^{\gamma_i,\beta} f(w) \right|^{r_i} dw \le \tag{45}$$

$$\left\{ \frac{\|\overline{q}\|_{\infty,(x,b)} \left(\left\| {}^{H}\mathbb{D}_{b-}^{\nu,\beta} f \right\|_{\infty,(x,b)} \right)^{r}}{\prod_{i=1}^{l} (\Gamma(\nu - \gamma_i + 1))^{r_i}} \right\} \left\{ \frac{(b-x)^{r\nu - \sum_{i=1}^{l} r_i \gamma_i + 1}}{\left(r\nu - \sum_{i=1}^{l} r_i \gamma_i + 1 \right)} \right\},$$

$\forall\, x \in [a, b]$.

Proof Similar to (44).

From now on, we present only left side inequalities as the right side ones follow easily.

2.2 Results Involving Two Functions

We present

Theorem 23 *Let* $\nu > 0$, $\nu \notin \mathbb{N}$, $\lceil \nu \rceil = n$, $0 \le \beta < 1$; $f_1, f_2 \in C([a, b])$; *and set* $\delta = \nu + \beta(n - \nu)$. *Assume further that* $\Delta_{a+}^{\delta} f_{j^*} \in C([a, b]) : \Delta_{a+}^{\delta-j} f_{j^*}(a) = 0$, $j = 1, ..., n$; $j^* = 1, 2$. *Let also* $\gamma_i > 0 : \lceil \gamma_i \rceil = m_i$; $\nu - \gamma_i \ge 1$, *with* $\varepsilon_i = \gamma_i + \beta(m_i - \gamma_i)$, *and assume that* $\nu > \gamma_i$ *and* $\delta > \varepsilon_i$, $i = 1, 2$; $a \le x \le b$. *Consider* $p(t) > 0$ *and* $q(t) \ge 0$, *with all* $p(t), \frac{1}{p(t)}, q(t) \in L_\infty(a, b)$. *Let* $\lambda_\nu > 0$ *and* $\lambda_\alpha, \lambda_{\overline{\beta}} \ge 0 : \lambda_\nu < p$, *where* $p > 1$. *Set*

$$P_k(\omega) := \int_a^\omega (\omega - t)^{\frac{(\nu - \gamma_k - 1)p}{(p-1)}} (p(t))^{-\frac{1}{(p-1)}} dt, \tag{46}$$

$k = 1, 2$, $a \le x \le b$;

$$A(\omega) := \frac{q(\omega)\left(P_1(\omega)\right)^{\lambda_\alpha\left(\frac{p-1}{p}\right)}\left(P_2(\omega)\right)^{\lambda_{\overline{\beta}}\left(\frac{p-1}{p}\right)}\left(p(\omega)\right)^{-\frac{\lambda_\nu}{p}}}{\left(\Gamma(\nu-\gamma_1)\right)^{\lambda_\alpha}\left(\Gamma(\nu-\gamma_2)\right)^{\lambda_{\overline{\beta}}}}, \tag{47}$$

$$A_0(x) := \left(\int_a^x \left(A(\omega)\right)^{\frac{p}{p-\lambda_\nu}} d\omega\right)^{\frac{p-\lambda_\nu}{p}}, \tag{48}$$

and

$$\delta_1 := \begin{cases} 2^{1-\left(\frac{\lambda_\alpha+\lambda_\nu}{p}\right)}, & \text{if } \lambda_\alpha+\lambda_\nu \le p, \\ 1, & \text{if } \lambda_\alpha+\lambda_\nu \ge p. \end{cases} \tag{49}$$

If $\lambda_{\overline{\beta}} = 0$, *we obtain that*

$$\int_a^x q(w)\left[\left|{}^H\mathbb{D}_{a+}^{\gamma_1,\beta} f_1(\omega)\right|^{\lambda_\alpha}\left|{}^H\mathbb{D}_{a+}^{\nu,\beta} f_1(\omega)\right|^{\lambda_\nu} + \left|{}^H\mathbb{D}_{a+}^{\gamma_1,\beta} f_2(\omega)\right|^{\lambda_\alpha}\left|{}^H\mathbb{D}_{a+}^{\nu,\beta} f_2(\omega)\right|^{\lambda_\nu}\right] d\omega \le \tag{50}$$

$$\left(A_0(x)\,|_{\lambda_{\overline{\beta}}=0}\right)\left(\frac{\lambda_\nu}{\lambda_\alpha+\lambda_\nu}\right)^{\frac{\lambda_\nu}{p}}\delta_1$$

$$\left[\int_a^x p(\omega)\left[\left|{}^H\mathbb{D}_{a+}^{\nu,\beta} f_1(\omega)\right|^p + \left|{}^H\mathbb{D}_{a+}^{\nu,\beta} f_2(\omega)\right|^p\right] d\omega\right]^{\frac{(\lambda_\alpha+\lambda_\nu)}{p}}.$$

Proof Similar toTheorem 2 of [5] and Theorem 4 of [9].

The counterpart of the last theorem follows.

Theorem 24 *All here are as in Theorem 23. Denote*

$$\delta_3 := \begin{cases} 2^{\frac{\lambda_{\overline{\beta}}}{\lambda_\nu}} - 1, & \text{if } \lambda_{\overline{\beta}} \ge \lambda_\nu, \\ 1, & \text{if } \lambda_{\overline{\beta}} \le \lambda_\nu. \end{cases} \tag{51}$$

If $\lambda_\alpha = 0$, *then*

$$\int_a^x q(w)\left[\left|{}^H\mathbb{D}_{a+}^{\gamma_2,\beta} f_2(\omega)\right|^{\lambda_{\overline{\beta}}}\left|{}^H\mathbb{D}_{a+}^{\nu,\beta} f_1(\omega)\right|^{\lambda_\nu} + \left|{}^H\mathbb{D}_{a+}^{\gamma_2,\beta} f_1(\omega)\right|^{\lambda_{\overline{\beta}}}\left|{}^H\mathbb{D}_{a+}^{\nu,\beta} f_2(\omega)\right|^{\lambda_\nu}\right] d\omega \le \tag{52}$$

$$\left(A_0\left(x\right)|_{\lambda_\alpha=0}\right)2^{p-\frac{\lambda_\nu}{p}}\left(\frac{\lambda_\nu}{\lambda_{\overline{\beta}}+\lambda_\nu}\right)^{\frac{\lambda_\nu}{p}}\delta_3^{\frac{\lambda_\nu}{p}}$$

$$\left[\int_a^x p\left(\omega\right)\left[\left|{}^H\mathbb{D}_{a+}^{\nu,\beta}f_1\left(\omega\right)\right|^p+\left|{}^H\mathbb{D}_{a+}^{\nu,\beta}f_2\left(\omega\right)\right|^p\right]d\omega\right]^{\frac{\left(\lambda_\nu+\lambda_{\overline{\beta}}\right)}{p}},$$

all $a\le x\le b$.

Proof Similar toTheorem 3 of [5] and Theorem 5 of [9].

The complete case $\lambda_\alpha,\lambda_{\overline{\beta}}\neq 0$ follows.

Theorem 25 *All here are as in Theorem 23. Denote*

$$\overline{\gamma}_1:=\begin{cases}2^{\frac{\lambda_\alpha+\lambda_{\overline{\beta}}}{\lambda_\nu}}-1, & \text{if } \lambda_\alpha+\lambda_{\overline{\beta}}\ge\lambda_\nu,\\ 1, & \text{if } \lambda_\alpha+\lambda_{\overline{\beta}}\le\lambda_\nu,\end{cases}\tag{53}$$

and

$$\overline{\gamma}_2:=\begin{cases}1, & \text{if } \lambda_\alpha+\lambda_{\overline{\beta}}+\lambda_\nu\ge p,\\ 2^{1-\left(\frac{\lambda_\alpha+\lambda_{\overline{\beta}}+\lambda_\nu}{p}\right)}, & \text{if } \lambda_\alpha+\lambda_{\overline{\beta}}+\lambda_\nu\le p.\end{cases}\tag{54}$$

Then

$$\int_a^x q\left(w\right)\left[\left|{}^H\mathbb{D}_{a+}^{\gamma_1,\beta}f_1\left(\omega\right)\right|^{\lambda_\alpha}\left|{}^H\mathbb{D}_{a+}^{\gamma_2,\beta}f_2\left(\omega\right)\right|^{\lambda_{\overline{\beta}}}\left|{}^H\mathbb{D}_{a+}^{\nu,\beta}f_1\left(\omega\right)\right|^{\lambda_\nu}+\right.\tag{55}$$

$$\left.\left|{}^H\mathbb{D}_{a+}^{\gamma_2,\beta}f_1\left(\omega\right)\right|^{\lambda_{\overline{\beta}}}\left|{}^H\mathbb{D}_{a+}^{\gamma_1,\beta}f_2\left(\omega\right)\right|^{\lambda_\alpha}\left|{}^H\mathbb{D}_{a+}^{\nu,\beta}f_2\left(\omega\right)\right|^{\lambda_\nu}\right]d\omega\le$$

$$A_0\left(x\right)\left(\frac{\lambda_\nu}{\left(\lambda_\alpha+\lambda_{\overline{\beta}}\right)\left(\lambda_\alpha+\lambda_{\overline{\beta}}+\lambda_\nu\right)}\right)^{\frac{\lambda_\nu}{p}}\left[\lambda_\alpha^{\frac{\lambda_\nu}{p}}\overline{\gamma}_2+2^{p-\frac{\lambda_\nu}{p}}\left(\overline{\gamma}_1\lambda_{\overline{\beta}}\right)^{\frac{\lambda_\nu}{p}}\right]$$

$$\left(\int_a^x p\left(\omega\right)\left[\left|{}^H\mathbb{D}_{a+}^{\nu,\beta}f_1\left(\omega\right)\right|^p+\left|{}^H\mathbb{D}_{a+}^{\nu,\beta}f_2\left(\omega\right)\right|^p\right]d\omega\right)^{\frac{\left(\lambda_\alpha+\lambda_{\overline{\beta}}+\lambda_\nu\right)}{p}},$$

all $a\le x\le b$.

Proof As for Theorem 4 of [5] and Theorem 6 of [9].

We continue with a special important case.

Theorem 26 *Let* $\nu>0$, $\nu\notin\mathbb{N}$, $\lceil\nu\rceil=n$, $0\le\beta<1$; $f_1,f_2\in C\left([a,b]\right)$; *and set* $\delta=\nu+\beta\left(n-\nu\right)$. *Assume further that* $\Delta_{a+}^{\delta}f_{j^*}\in C\left([a,b]\right):\Delta_{a+}^{\delta-j}f_{j^*}\left(a\right)=0$, $j=1,...,n$; $j^*=1,2$. *Let also* $\gamma_i>0:\lceil\gamma_i\rceil=m_i$; $\nu-\gamma_i\ge 1$, *with* $\varepsilon_i=\gamma_i+\beta$

$(m_i - \gamma_i)$, and assume that $\nu > \gamma_i$ and $\delta > \varepsilon_i$, $i = 1, 2$; but here it is $\gamma_2 = \gamma_1 + 1$; $a \le x \le b$. Consider $p(t) > 0$ and $q(t) \ge 0$, with all $p(t)$, $\frac{1}{p(t)}$, $q(t) \in L_\infty(a, b)$. Let $\lambda_\alpha \ge 0$, $0 < \lambda_{\alpha+1} < 1$, and $p > 1$. Denote

$$\theta_3 := \begin{cases} 2^{\frac{\lambda_\alpha}{\lambda_{\alpha+1}}} - 1, & \text{if } \lambda_\alpha \ge \lambda_{\alpha+1}, \\ 1, & \text{if } \lambda_\alpha \le \lambda_{\alpha+1}, \end{cases} \tag{56}$$

$$L(x) := \left(2\int_a^x (q(\omega))^{\frac{1}{1-\lambda_{\alpha+1}}} d\omega\right)^{1-\lambda_{\alpha+1}} \left(\frac{\theta_3 \lambda_{\alpha+1}}{\lambda_\alpha + \lambda_{\alpha+1}}\right)^{\lambda_{\alpha+1}}, \tag{57}$$

and

$$P_1(x) := \int_a^x (x-t)^{\frac{(\nu-\gamma_1-1)p}{p-1}} (p(t))^{-\frac{1}{p-1}} dt, \tag{58}$$

$$T(x) := L(x) \left(\frac{P_1(x)^{\frac{p-1}{p}}}{\Gamma(\nu-\gamma_1)}\right)^{\lambda_\alpha+\lambda_{\alpha+1}}, \tag{59}$$

$$\omega_1 := 2^{\frac{p-1}{p}(\lambda_\alpha+\lambda_{\alpha+1})}, \tag{60}$$

and

$$\Phi(x) := T(x)\,\omega_1. \tag{61}$$

Then

$$\int_a^x q(\omega) \left[\left| {}^H\mathbb{D}_{a+}^{\gamma_1,\beta} f_1(\omega) \right|^{\lambda_\alpha} \left| {}^H\mathbb{D}_{a+}^{\gamma_1+1,\beta} f_2(\omega) \right|^{\lambda_{\alpha+1}} + \left| {}^H\mathbb{D}_{a+}^{\gamma_1,\beta} f_2(\omega) \right|^{\lambda_\alpha} \left| {}^H\mathbb{D}_{a+}^{\gamma_1+1,\beta} f_1(\omega) \right|^{\lambda_{\alpha+1}} \right] d\omega \le \tag{62}$$

$$\Phi(x) \left[\int_a^x p(\omega) \left(\left| {}^H\mathbb{D}_{a+}^{\nu,\beta} f_1(\omega) \right|^p + \left| {}^H\mathbb{D}_{a+}^{\nu,\beta} f_2(\omega) \right|^p \right) d\omega \right]^{\frac{\lambda_\alpha+\lambda_{\alpha+1}}{p}},$$

all $a \le x \le b$.

Proof As in Theorem 5 of [5] and Theorem 8 of [9].

We give

Corollary 1 *All here are as in Theorem 23, with $\lambda_{\overline{\beta}} = 0$, $p(t) = q(t) = 1$. Then*

$$\int_a^x \left[\left| {}^H\mathbb{D}_{a+}^{\gamma_1,\beta} f_1(\omega) \right|^{\lambda_\alpha} \left| {}^H\mathbb{D}_{a+}^{\nu,\beta} f_1(\omega) \right|^{\lambda_\nu} + \left| {}^H\mathbb{D}_{a+}^{\gamma_1,\beta} f_2(\omega) \right|^{\lambda_\alpha} \left| {}^H\mathbb{D}_{a+}^{\nu,\beta} f_2(\omega) \right|^{\lambda_\nu} \right] d\omega \le \tag{63}$$

$$C_1(x)\left(\int_a^x\left(\left|{}^H\mathbb{D}_{a+}^{\nu,\beta}f_1(\omega)\right|^p+\left|{}^H\mathbb{D}_{a+}^{\nu,\beta}f_2(\omega)\right|^p\right)d\omega\right)^{\frac{(\lambda_\alpha+\lambda_\nu)}{p}},$$

all $a\le x\le b$, *where*

$$C_1(x):=\left(A_0(x)\,|_{\lambda_{\overline{\beta}}=0}\right)\left(\frac{\lambda_\nu}{\lambda_\alpha+\lambda_\nu}\right)^{\frac{\lambda_\nu}{p}}\delta_1, \tag{64}$$

$$\delta_1:=\begin{cases}2^{1-\frac{\lambda_\alpha+\lambda_\nu}{p}}, & \text{if } \lambda_\alpha+\lambda_\nu\le p,\\ 1, & \text{if } \lambda_\alpha+\lambda_\nu\ge p.\end{cases} \tag{65}$$

We find that

$$\left(A_0(x)\,|_{\lambda_{\overline{\beta}}=0}\right)=\left\{\left(\frac{(p-1)^{\frac{\lambda_\alpha p-\lambda_\alpha}{p}}}{(\Gamma(\nu-\gamma_1))^{\lambda_\alpha}(\nu p-\gamma_1 p-1)^{\frac{\lambda_\alpha p-\lambda_\alpha}{p}}}\right)\cdot\right.$$

$$\left.\left(\frac{(p-\lambda_\nu)^{\frac{p-\lambda_\nu}{p}}}{(\lambda_\alpha\nu p-\lambda_\alpha\gamma_1 p-\lambda_\alpha+p-\lambda_\nu)^{\frac{p-\lambda_\nu}{p}}}\right)\right\}(x-a)^{\frac{\lambda_\alpha\nu p-\lambda_\alpha\gamma_1 p-\lambda_\alpha+p-\lambda_\nu}{p}}. \tag{66}$$

Proof As for Corollary 1 of [5] and Corollary 10 of [9].

We continue with a related result regarding $\|\cdot\|_\infty$.

Theorem 27 *Let* $\nu>0$, $\nu\notin\mathbb{N}$, $\lceil\nu\rceil=n$, $0\le\beta<1$; $f_1,f_2\in C([a,b])$ *and set* $\delta=\nu+\beta(n-\nu)$. *Assume further that* $\Delta_{a+}^{\delta}f_{j^*}\in C([a,b]):\Delta_{a+}^{\delta-j}f_{j^*}(a)=0$, $j=1,\ldots,n$; $j^*=1,2$. *Let also* $\gamma_i>0:\lceil\gamma_i\rceil=m_i$; $\nu-\gamma_i\ge1$, *with* $\varepsilon_i=\gamma_i+\beta(m_i-\gamma_i)$ *and assume that* $\nu>\gamma_i$ *and* $\delta>\varepsilon_i$, $i=1,2$; $a\le x\le b$. *Consider* $p(x)\ge0$ *and* $p(x)\in L_\infty(a,b)$. *Let* $\lambda_\alpha,\lambda_{\overline{\beta}},\lambda_\nu\ge0$. *Set*

$$T(x):=\frac{(x-a)^{\left(\nu\lambda_\alpha-\gamma_1\lambda_\alpha+\nu\lambda_{\overline{\beta}}-\gamma_2\lambda_{\overline{\beta}}+1\right)}}{\left(\nu\lambda_\alpha-\gamma_1\lambda_\alpha+\nu\lambda_{\overline{\beta}}-\gamma_2\lambda_{\overline{\beta}}+1\right)}\cdot \tag{67}$$

$$\frac{\|p(s)\|_{\infty,(a,x)}}{(\Gamma(\nu-\gamma_1+1))^{\lambda_\alpha}(\Gamma(\nu-\gamma_2+1))^{\lambda_{\overline{\beta}}}}.$$

Then

$$\int_a^x p(w)\left[\left|{}^H\mathbb{D}_{a+}^{\gamma_1,\beta}f_1(\omega)\right|^{\lambda_\alpha}\left|{}^H\mathbb{D}_{a+}^{\gamma_2,\beta}f_2(\omega)\right|^{\lambda_{\overline{\beta}}}\left|{}^H\mathbb{D}_{a+}^{\nu,\beta}f_1(\omega)\right|^{\lambda_\nu}+\right.$$

$$\left.\left|{}^H\mathbb{D}_{a+}^{\gamma_2,\beta}f_1(\omega)\right|^{\lambda_{\overline{\beta}}}\left|{}^H\mathbb{D}_{a+}^{\gamma_1,\beta}f_2(\omega)\right|^{\lambda_\alpha}\left|{}^H\mathbb{D}_{a+}^{\nu,\beta}f_2(\omega)\right|^{\lambda_\nu}\right]d\omega\le \tag{68}$$

$$\frac{T(x)}{2}\left[\left\|{}^H\mathbb{D}_{a+}^{\nu,\beta}f_1\right\|_{\infty,(a,x)}^{2(\lambda_\alpha+\lambda_\nu)}+\left\|{}^H\mathbb{D}_{a+}^{\nu,\beta}f_1\right\|_{\infty,(a,x)}^{2\lambda_{\overline{\beta}}}+\right.$$

$$\left\| {}^{H}\mathbb{D}_{a+}^{\nu,\beta} f_2 \right\|_{\infty,(a,x)}^{2\lambda_{\overline{\beta}}} + \left\| {}^{H}\mathbb{D}_{a+}^{\nu,\beta} f_2 \right\|_{\infty,(a,x)}^{2(\lambda_\alpha+\lambda_\nu)} \Bigg],$$

all $a \le x \le b$.

Proof Similar to Theorem 7 of [5] and Theorem 18 of [9].

Next we give converse results involving two functions.

Theorem 28 *Let* $\nu > 0$, $\nu \notin \mathbb{N}$, $\lceil \nu \rceil = n$, $0 \le \beta < 1$; $f_1, f_2 \in C([a,b])$*; and set* $\delta = \nu + \beta(n-\nu)$. *Assume further that* $\Delta_{a+}^{\delta} f_{j^*} \in C([a,b]) : \Delta_{a+}^{\delta-j} f_{j^*}(a) = 0$, $j = 1, ..., n$; $j^* = 1, 2$. *Let also* $\gamma_i > 0 : \lceil \gamma_i \rceil = m_i$; $0 < p < 1$, $\frac{1}{p} > \nu - \gamma_i \ge 1$, *with* $\varepsilon_i = \gamma_i + \beta(m_i - \gamma_i)$, *and assume that* $\nu > \gamma_i$ *and* $\delta > \varepsilon_i$, $i = 1, 2$; $a \le x \le b$. *Consider* $p(t) > 0$ *and* $q(t) \ge 0$, *with all* $p(t), \frac{1}{p(t)}, q(t) \in L_\infty(a,b)$. *Further assume that* ${}^{H}\mathbb{D}_{a+}^{\nu,\beta} f_i$, $i = 1, 2$, *is of fixed sign a.e. on* $[a,b]$. *Let* $\lambda_\nu > 0$ *and* $\lambda_\alpha, \lambda_{\overline{\beta}} \ge 0$ *such that* $\lambda_\nu > p$. *Here* $P_k(\omega)$, $A(\omega)$, $A_0(x)$ *are as in (46), (47), and (48), respectively.*

Set

$$\delta_1 := 2^{1-\frac{(\lambda_\alpha+\lambda_\nu)}{p}}. \tag{69}$$

If $\lambda_{\overline{\beta}} = 0$, *then*

$$\int_a^x q(w) \Bigg[\left| {}^{H}\mathbb{D}_{a+}^{\gamma_1,\beta} f_1(\omega) \right|^{\lambda_\alpha} \left| {}^{H}\mathbb{D}_{a+}^{\nu,\beta} f_1(\omega) \right|^{\lambda_\nu} + \tag{70}$$

$$\left| {}^{H}\mathbb{D}_{a+}^{\gamma_1,\beta} f_2(\omega) \right|^{\lambda_\alpha} \left| {}^{H}\mathbb{D}_{a+}^{\nu,\beta} f_2(\omega) \right|^{\lambda_\nu} \Bigg] d\omega \ge$$

$$\left(A_0(x)\,|_{\lambda_{\overline{\beta}}=0} \right) \left(\frac{\lambda_\nu}{\lambda_\alpha + \lambda_\nu} \right)^{\frac{\lambda_\nu}{p}} \delta_1$$

$$\left[\int_a^x p(\omega) \left[\left| {}^{H}\mathbb{D}_{a+}^{\nu,\beta} f_1(\omega) \right|^p + \left| {}^{H}\mathbb{D}_{a+}^{\nu,\beta} f_2(\omega) \right|^p \right] d\omega \right]^{\frac{(\lambda_\alpha+\lambda_\nu)}{p}}.$$

Proof Similar toTheorem 5 of [10] and Theorem 4 of [8].

We continue with

Theorem 29 *All here are as in Theorem 28. Further assume* $\lambda_{\overline{\beta}} \ge \lambda_\nu$. *Denote*

$$\begin{aligned} \delta_2 &:= 2^{1-\frac{\lambda_{\overline{\beta}}}{\lambda_\nu}}, \\ \delta_3 &:= (\delta_2 - 1)\, 2^{-\frac{\lambda_{\overline{\beta}}}{\lambda_\nu}}. \end{aligned} \tag{71}$$

If $\lambda_\alpha = 0$, *then*

$$\int_a^x q(w)\left[\left|{}^{H}\mathbb{D}_{a+}^{\gamma_2,\beta} f_2(\omega)\right|^{\lambda_{\overline{\beta}}}\left|{}^{H}\mathbb{D}_{a+}^{\nu,\beta} f_1(\omega)\right|^{\lambda_\nu}+\left|{}^{H}\mathbb{D}_{a+}^{\gamma_2,\beta} f_1(\omega)\right|^{\lambda_{\overline{\beta}}}\left|{}^{H}\mathbb{D}_{a+}^{\nu,\beta} f_2(\omega)\right|^{\lambda_\nu}\right]d\omega \geq \tag{72}$$

$$\left(A_0(x)|_{\lambda_\alpha=0}\right)2^{p-\frac{\lambda_\nu}{p}}\left(\frac{\lambda_\nu}{\lambda_{\overline{\beta}}+\lambda_\nu}\right)^{\frac{\lambda_\nu}{p}}\delta_3^{\frac{\lambda_\nu}{p}}$$

$$\left(\int_a^x p(\omega)\left[\left|{}^{H}\mathbb{D}_{a+}^{\nu,\beta} f_1(\omega)\right|^p+\left|{}^{H}\mathbb{D}_{a+}^{\nu,\beta} f_2(\omega)\right|^p\right]d\omega\right)^{\frac{\left(\lambda_\alpha+\lambda_{\overline{\beta}}\right)}{p}},$$

all $a \leq x \leq b$.

Proof Similar toTheorem 6 of [10] and Theorem 5 of [8].

Next we give a particular converse result involving two functions.

Theorem 30 *Let* $\nu > 0$, $\nu \notin \mathbb{N}$, $\lceil \nu \rceil = n$, $0 \leq \beta < 1$; $f_1, f_2 \in C([a,b])$*; and set* $\delta = \nu + \beta(n-\nu)$. *Assume further that* $\Delta_{a+}^{\delta} f_{j^*} \in C([a,b]) : \Delta_{a+}^{\delta-j} f_{j^*}(a) = 0$, $j = 1, ..., n$; $j^* = 1, 2$. *Let also* $\gamma_i > 0 : \lceil \gamma_i \rceil = m_i$; $0 < p < 1$, $\frac{1}{p} > \nu - \gamma_i \geq 1$, *with* $\varepsilon_i = \gamma_i + \beta(m_i - \gamma_i)$, *and assume that* $\nu > \gamma_i$ *and* $\delta > \varepsilon_i$, $i = 1, 2$; $\gamma_2 = \gamma_1 + 1$; $a \leq x \leq b$. *Consider* $p(t) > 0$ *and* $q(t) \geq 0$, *with all* $p(t), \frac{1}{p(t)}, q(t), \frac{1}{q(t)} \in L_\infty(a,b)$. *Further assume that* ${}^{H}\mathbb{D}_{a+}^{\nu,\beta} f_i$, $i = 1, 2$, *is of fixed sign a.e. on* $[a,b]$. *Let* $\lambda_\alpha \geq \lambda_{\alpha+1} > 1$.

Denote

$$\theta_3 := \left(2^{1-\frac{\lambda_\alpha}{\lambda_{\alpha+1}}}-1\right)2^{-\frac{\lambda_\alpha}{\lambda_{\alpha+1}}}, \tag{73}$$

$L(x)$ *is as in (57),* $P_1(x)$ *as in (58),* $T(x)$ *as in (59),* ω_1 *as in (60), and* Φ *as in (61). Then*

$$\int_a^x q(\omega)\left[\left|{}^{H}\mathbb{D}_{a+}^{\gamma_1,\beta} f_1(\omega)\right|^{\lambda_\alpha}\left|{}^{H}\mathbb{D}_{a+}^{\gamma_1+1,\beta} f_2(\omega)\right|^{\lambda_{\alpha+1}}+\left|{}^{H}\mathbb{D}_{a+}^{\gamma_1,\beta} f_2(\omega)\right|^{\lambda_\alpha}\left|{}^{H}\mathbb{D}_{a+}^{\gamma_1+1,\beta} f_1(\omega)\right|^{\lambda_{\alpha+1}}\right]d\omega \geq \tag{74}$$

$$\Phi(x)\left[\int_a^x p(\omega)\left(\left|{}^{H}\mathbb{D}_{a+}^{\nu,\beta} f_1(\omega)\right|^p+\left|{}^{H}\mathbb{D}_{a+}^{\nu,\beta} f_2(\omega)\right|^p\right)d\omega\right]^{\frac{\lambda_\alpha+\lambda_{\alpha+1}}{p}},$$

all $a \leq x \leq b$.

Proof Similar to Theorem 7 of [10] and Theorem 7 of [8].

2.3 Results Involving Several Functions

We present

Theorem 31 *Here all notations, terms, and assumptions are as in Theorem 23, but for $f_j \in C([a,b])$, with $j = 1, ..., M \in \mathbb{N}$. Instead of δ_1 there, we define here*

$$\delta_1^* := \begin{cases} M^{1-\frac{\lambda_\alpha+\lambda_\nu}{p}}, & \text{if } \lambda_\alpha + \lambda_\nu \le p, \\ 2^{\frac{\lambda_\alpha+\lambda_\nu}{p}-1}, & \text{if } \lambda_\alpha + \lambda_\nu \ge p. \end{cases} \tag{75}$$

Call

$$\varphi_1(x) := \left(A_0(x)\,|_{\lambda_{\overline{\beta}}=0}\right)\left(\frac{\lambda_\nu}{\lambda_\alpha+\lambda_\nu}\right)^{\frac{\lambda_\nu}{p}}. \tag{76}$$

If $\lambda_{\overline{\beta}} = 0$, then

$$\int_a^x q(w)\left(\sum_{j=1}^M \left|{}^H\mathbb{D}_{a+}^{\gamma_1,\beta} f_j(\omega)\right|^{\lambda_\alpha}\left|{}^H\mathbb{D}_{a+}^{\nu,\beta} f_j(\omega)\right|^{\lambda_\nu}\right)d\omega \le$$

$$\delta_1^*\varphi_1(x)\left[\int_a^x p(\omega)\left(\sum_{j=1}^M \left|{}^H\mathbb{D}_{a+}^{\nu,\beta} f_j(\omega)\right|^{p}\right)d\omega\right]^{\frac{(\lambda_\alpha+\lambda_\nu)}{p}}, \tag{77}$$

all $a \le x \le b$.

Proof As in Theorem 2 of [6] and Theorem 4 of [7].

We continue with

Theorem 32 *All here are as in Theorem 31. Denote*

$$\delta_3 := \begin{cases} 2^{\frac{\lambda_{\overline{\beta}}}{\lambda_\nu}} - 1, & \text{if } \lambda_{\overline{\beta}} \ge \lambda_\nu, \\ 1, & \text{if } \lambda_{\overline{\beta}} \le \lambda_\nu, \end{cases} \tag{78}$$

$$\varepsilon_2 := \begin{cases} 1, & \text{if } \lambda_\nu + \lambda_{\overline{\beta}} \ge p, \\ M^{1-\frac{\lambda_\nu+\lambda_{\overline{\beta}}}{p}}, & \text{if } \lambda_\nu + \lambda_{\overline{\beta}} \le p, \end{cases} \tag{79}$$

and

$$\varphi_2(x) := \left(A_0(x)\,|_{\lambda_\alpha=0}\right)2^{\frac{p-\lambda_\nu}{p}}\left(\frac{\lambda_\nu}{\lambda_{\overline{\beta}}+\lambda_\nu}\right)^{\frac{\lambda_\nu}{p}}\delta_3^{\frac{\lambda_\nu}{p}}. \tag{80}$$

If $\lambda_\alpha = 0$, then

$$\int_a^x q(w)\left\{\left\{\sum_{j=1}^{M-1}\left[\left|{}^{H}\mathbb{D}_{a+}^{\gamma_2,\beta}f_{j+1}(\omega)\right|^{\lambda_{\overline{\beta}}}\left|{}^{H}\mathbb{D}_{a+}^{\nu,\beta}f_j(\omega)\right|^{\lambda_\nu}+\right.\right.\right.$$

$$\left.\left.\left.\left|{}^{H}\mathbb{D}_{a+}^{\gamma_2,\beta}f_j(\omega)\right|^{\lambda_{\overline{\beta}}}\left|{}^{H}\mathbb{D}_{a+}^{\nu,\beta}f_{j+1}(\omega)\right|^{\lambda_\nu}\right]\right\}+$$

$$\left.\left[\left|{}^{H}\mathbb{D}_{a+}^{\gamma_2,\beta}f_M(\omega)\right|^{\lambda_{\overline{\beta}}}\left|{}^{H}\mathbb{D}_{a+}^{\nu,\beta}f_1(\omega)\right|^{\lambda_\nu}+\left|{}^{H}\mathbb{D}_{a+}^{\gamma_2,\beta}f_1(\omega)\right|^{\lambda_{\overline{\beta}}}\left|{}^{H}\mathbb{D}_{a+}^{\nu,\beta}f_M(\omega)\right|^{\lambda_\nu}\right]\right\}d\omega$$

$$\leq 2^{\frac{\lambda_\nu+\lambda_{\overline{\beta}}}{p}}\varepsilon_2\varphi_2(x)\left\{\int_a^x p(\omega)\left[\sum_{j=1}^{M}\left|{}^{H}\mathbb{D}_{a+}^{\nu,\beta}f_j(\omega)\right|^p\right]d\omega\right\}^{\frac{\lambda_\nu+\lambda_{\overline{\beta}}}{p}},\qquad(81)$$

all $a\leq x\leq b$.

Proof As for Theorem 3 of [6] and Theorem 5 of [7].

We give the general case.

Theorem 33 *All are as in Theorem 31. Denote*

$$\overline{\gamma}_1:=\begin{cases}2^{\frac{\lambda_\alpha+\lambda_{\overline{\beta}}}{\lambda_\nu}}-1, & \text{if } \lambda_\alpha+\lambda_{\overline{\beta}}\geq\lambda_\nu,\\ 1, & \text{if } \lambda_\alpha+\lambda_{\overline{\beta}}\leq\lambda_\nu,\end{cases}\qquad(82)$$

and

$$\overline{\gamma}_2:=\begin{cases}1, & \text{if } \lambda_\alpha+\lambda_{\overline{\beta}}+\lambda_\nu\geq p,\\ 2^{1-\left(\frac{\lambda_\alpha+\lambda_{\overline{\beta}}+\lambda_\nu}{p}\right)}, & \text{if } \lambda_\alpha+\lambda_{\overline{\beta}}+\lambda_\nu\leq p.\end{cases}\qquad(83)$$

Set

$$\varphi_3(x):=A_0(x)\left(\frac{\lambda_\nu}{\left(\lambda_\alpha+\lambda_{\overline{\beta}}\right)\left(\lambda_\alpha+\lambda_{\overline{\beta}}+\lambda_\nu\right)}\right)^{\frac{\lambda_\nu}{p}}\left[\lambda_\alpha^{\frac{\lambda_\nu}{p}}\overline{\gamma}_2+2^{\frac{p-\lambda_\nu}{p}}\left(\overline{\gamma}_1\lambda_{\overline{\beta}}\right)^{\frac{\lambda_\nu}{p}}\right],\qquad(84)$$

and

$$\varepsilon_3:=\begin{cases}1, & \text{if } \lambda_\alpha+\lambda_{\overline{\beta}}+\lambda_\nu\geq p,\\ M^{1-\left(\frac{\lambda_\alpha+\lambda_{\overline{\beta}}+\lambda_\nu}{p}\right)}, & \text{if } \lambda_\alpha+\lambda_{\overline{\beta}}+\lambda_\nu\leq p.\end{cases}\qquad(85)$$

Then

$$\int_a^x q(w)\left[\sum_{j=1}^{M-1}\left[\left|{}^{H}\mathbb{D}_{a+}^{\gamma_1,\beta}f_j(\omega)\right|^{\lambda_\alpha}\left|{}^{H}\mathbb{D}_{a+}^{\gamma_2,\beta}f_{j+1}(\omega)\right|^{\lambda_{\overline{\beta}}}\left|{}^{H}\mathbb{D}_{a+}^{\nu,\beta}f_j(\omega)\right|^{\lambda_\nu}+\right.\right.$$

$$\left|{}^{H}\mathbb{D}_{a+}^{\gamma_2,\beta} f_j(\omega)\right|^{\lambda_{\overline{\beta}}} \left|{}^{H}\mathbb{D}_{a+}^{\gamma_1,\beta} f_{j+1}(\omega)\right|^{\lambda_\alpha} \left|{}^{H}\mathbb{D}_{a+}^{\nu,\beta} f_{j+1}(\omega)\right|^{\lambda_\nu}\Bigg] +$$

$$\Bigg[\left|{}^{H}\mathbb{D}_{a+}^{\gamma_1,\beta} f_1(\omega)\right|^{\lambda_\alpha} \left|{}^{H}\mathbb{D}_{a+}^{\gamma_2,\beta} f_M(\omega)\right|^{\lambda_{\overline{\beta}}} \left|{}^{H}\mathbb{D}_{a+}^{\nu,\beta} f_1(\omega)\right|^{\lambda_\nu} +$$

$$\left|{}^{H}\mathbb{D}_{a+}^{\gamma_2,\beta} f_1(\omega)\right|^{\lambda_{\overline{\beta}}} \left|{}^{H}\mathbb{D}_{a+}^{\gamma_1,\beta} f_M(\omega)\right|^{\lambda_\alpha} \left|{}^{H}\mathbb{D}_{a+}^{\nu,\beta} f_M(\omega)\right|^{\lambda_\nu}\Bigg]\Bigg] d\omega \leq$$

$$2^{\frac{\lambda_\alpha+\lambda_{\overline{\beta}}+\lambda_\nu}{p}} \varepsilon_3 \varphi_3(x) \left\{\int_a^x p(\omega) \left[\sum_{j=1}^{M} \left|{}^{H}\mathbb{D}_{a+}^{\nu,\beta} f_j(\omega)\right|^p\right] d\omega\right\}^{\frac{\left(\lambda_\alpha+\lambda_{\overline{\beta}}+\lambda_\nu\right)}{p}}, \tag{86}$$

all $a \leq x \leq b$.

Proof As for Theorem 4 of [6] and Theorem 6 of [7].

We give

Theorem 34 *All here are as in Theorem 26, but for* $f_j \in C([a,b])$, $j = 1, ..., M \in \mathbb{N}$. *Also put*

$$\varepsilon_4 := \begin{cases} 1, & \text{if } \lambda_\alpha + \lambda_{\alpha+1} \geq p, \\ M^{1-\left(\frac{\lambda_\alpha+\lambda_{\alpha+1}}{p}\right)}, & \text{if } \lambda_\alpha + \lambda_{\alpha+1} \leq p. \end{cases} \tag{87}$$

Then

$$\int_a^x q(w) \Bigg\{\{\sum_{j=1}^{M-1} \Bigg[\left|{}^{H}\mathbb{D}_{a+}^{\gamma_1,\beta} f_j(\omega)\right|^{\lambda_\alpha} \left|{}^{H}\mathbb{D}_{a+}^{\gamma_1+1,\beta} f_{j+1}(\omega)\right|^{\lambda_{\alpha+1}} +$$

$$\left|{}^{H}\mathbb{D}_{a+}^{\gamma_1,\beta} f_{j+1}(\omega)\right|^{\lambda_\alpha} \left|{}^{H}\mathbb{D}_{a+}^{\gamma_1+1,\beta} f_j(\omega)\right|^{\lambda_{\alpha+1}}\Bigg]\} + \Bigg[\left|{}^{H}\mathbb{D}_{a+}^{\gamma_1,\beta} f_1(\omega)\right|^{\lambda_\alpha} \left|{}^{H}\mathbb{D}_{a+}^{\gamma_1+1,\beta} f_M(\omega)\right|^{\lambda_{\alpha+1}} +$$

$$\left|{}^{H}\mathbb{D}_{a+}^{\gamma_1,\beta} f_M(\omega)\right|^{\lambda_\alpha} \left|{}^{H}\mathbb{D}_{a+}^{\gamma_1+1,\beta} f_1(\omega)\right|^{\lambda_{\alpha+1}}\Bigg]\Bigg\} d\omega \leq$$

$$2^{\frac{\lambda_\alpha+\lambda_{\alpha+1}}{p}} \varepsilon_4 \Phi(x) \left\{\int_a^x p(\omega) \left[\sum_{j=1}^{M} \left|{}^{H}\mathbb{D}_{a+}^{\nu,\beta} f_j(\omega)\right|^p\right] d\omega\right\}^{\frac{(\lambda_\alpha+\lambda_{\alpha+1})}{p}}, \tag{88}$$

all $a \leq x \leq b$.

Proof As for Theorem 5 of [6] and Theorem 7 of [7].

We continue with results regarding $\|\cdot\|_\infty$.

Theorem 35 *All are as in Theorem 27, but for* $f_j \in C([a,b])$, $j = 1, ..., M \in \mathbb{N}$. *Then*

$$\int_a^x p(w) \left\{ \left[\sum_{j=1}^{M-1} [\left| {}^H\mathbb{D}_{a+}^{\gamma_1,\beta} f_j(\omega) \right|^{\lambda_\alpha} \left| {}^H\mathbb{D}_{a+}^{\gamma_2,\beta} f_{j+1}(\omega) \right|^{\lambda_{\overline{\beta}}} \left| {}^H\mathbb{D}_{a+}^{\nu,\beta} f_j(\omega) \right|^{\lambda_\nu} + \right.\right.$$

$$\left. \left| {}^H\mathbb{D}_{a+}^{\gamma_2,\beta} f_j(\omega) \right|^{\lambda_{\overline{\beta}}} \left| {}^H\mathbb{D}_{a+}^{\gamma_1,\beta} f_{j+1}(\omega) \right|^{\lambda_\alpha} \left| {}^H\mathbb{D}_{a+}^{\nu,\beta} f_{j+1}(\omega) \right|^{\lambda_\nu}] \right] +$$

$$\left[\left| {}^H\mathbb{D}_{a+}^{\gamma_1,\beta} f_1(\omega) \right|^{\lambda_\alpha} \left| {}^H\mathbb{D}_{a+}^{\gamma_2,\beta} f_M(\omega) \right|^{\lambda_{\overline{\beta}}} \left| {}^H\mathbb{D}_{a+}^{\nu,\beta} f_1(\omega) \right|^{\lambda_\nu} + \right.$$

$$\left. \left. \left| {}^H\mathbb{D}_{a+}^{\gamma_2,\beta} f_1(\omega) \right|^{\lambda_{\overline{\beta}}} \left| {}^H\mathbb{D}_{a+}^{\gamma_1,\beta} f_M(\omega) \right|^{\lambda_\alpha} \left| {}^H\mathbb{D}_{a+}^{\nu,\beta} f_M(\omega) \right|^{\lambda_\nu} \right] \right\} d\omega \leq \tag{89}$$

$$T(x) \left\{ \sum_{j=1}^{M} \left[\left\| {}^H\mathbb{D}_{a+}^{\nu,\beta} f_j \right\|_{\infty,(a,x)}^{2(\lambda_\alpha+\lambda_\nu)} + \left\| {}^H\mathbb{D}_{a+}^{\nu,\beta} f_j \right\|_{\infty,(a,x)}^{2\lambda_{\overline{\beta}}} \right] \right\},$$

all $a \leq x \leq b$.

Proof Based on Theorem 27.

One based on Sect. 2.2 can write down converse results for several functions and also write down right side inequalities for two or several functions and cover interesting specific examples.

All these results can have great applications to related fractional differential equations proving the uniqueness of solutions or giving upper bounds to their solutions. The reader is referred to the author's monograph of 2009, [11], to continue such studies. We choose to stop here.

References

1. Agarwal RP (1995) Sharp Opial-type inequalities involving r-derivatives and their applications. Tohoku Math J 47:567–593
2. Agarwal RP, Pang PYH (1995) Opial inequalities with applications in differential and difference equations. Kluwer Academic Publishers, Dordrecht, Boston, London
3. Anastassiou GA (2000) Opial type inequalities involving functions and their ordinary and fractional derivatives. Comm Appl Anal 4(4):547–560
4. Anastassiou GA (2001) Quantitative approximation. Chapman & Hall/CRC, Boca Rarton, New York
5. Anastassiou GA (2004) Opial type inequalities involving fractional derivatives of two functions and applications. Comput Math Appl 48:1701–1731
6. Anastassiou GA (2005) Fractional Opial inequalities for several functions with applications. J Comput Anal Appl 7(3):233–259

7. Anastassiou GA (2008) Riemann–Liouville fractional Opial inequalities for several functions with applications. Commun Appl Anal 12(4):377–398
8. Anastassiou GA (2008) Reverse Riemann–Liouville fractional Opial inequalities for several functions. Complex Var Elliptic Equ 53(6):523–544
9. Anastassiou GA (2008) Opial type inequalities involving Riemann–Liouville fractional derivatives of two functions with applications. Math Comput Model 48:344–374
10. Anastassiou GA (2008) Converse fractional Opial inequalities for several functions. CUBO 10(1):117–142
11. Anastassiou GA (2009) Fractional differentiation inequalities. Springer, Heidelberg, New York
12. Anastassiou G (2021) Advancements on ψ-Hilfer fractional calculus and fractional integral inequalities. Nonlinear Complex accepted, Discontin
13. Anastassiou GA, Koliha J, Pecaric J (2001) Opial inequalities for fractional derivatives. Dyn Syst Appl 10:395–406
14. Anastassiou GA, Koliha J, Pecaric J (2002) Opial type L_p-inequalities for fractional derivatives. Intern J Math & Math Sci 31(2):85–95
15. Mitrinovic DS, Pecaric JE, Fink AM (1993) Classical and new inequalities in analysis. Kluwer Academic Publishers, Dordrecht
16. Opial Z (1960) Sur une inégalité. Ann Polon Math 8:29–32
17. Samko SG, Kilbas AA, Marichev OI (1993) Fractional integrals and derivatives: theory and applications. Gordon and Breach Science Publishers, Switzerland
18. Tomovski Ž, Hilfer R, Srivastava HM (2010) Fractional and operational calculus with generalized fractional derivative operators and Mittag-Leffler type functions. Integral Transf Spec Funct 21(11):797–814

On a Non-linear Diffusion Model of Wood Impregnation: Analysis, Approximate Solutions, and Experiments with Relaxing Boundary Conditions

Jordan Hristov

Abstract Analysis and approximate integral-balance solutions of a non-linear diffusion model of wood impregnation by methacrylate have been developed in two cases: (i) Dirichlet boundary condition assuming instantaneous saturation of the wood surface contacting the liquid bath and (ii) Relaxing Dirichlet boundary conditions accounting for the fact that instantaneous saturation is unphysical and takes some time to be established.

Keywords Diffusion · Wood impregnation · Non-linear diffusivity · Approximate solutions · Relaxing boundary conditions

1 Introduction

The liquid penetration into wood chips is an important technological operation related to the development of new building and insulation materials, materials for work under severe climatic conditions, as well as new materials for everyday use with increased and specific properties. Many approaches both experimental and theoretical have been developed to understand the main mechanisms and underlying phenomena of liquid penetration into the complex structures of woods [1–3]. In general, the forced penetration of liquids into wood's capillaries happens due to a pressure gradient which can be considered as a difference between the sum of external, hydrostatic and capillary pressure and the total gaseous and water vapour pressure in the wood chip internal space, that is,

$$\Delta P = \left(P_{external} + P_{hydrostatic} + P_{Capillary}\right) - P_{Gas+Vapours} \tag{1}$$

J. Hristov (✉)
Department of Chemical Engineering, University of Chemical Technology and Metallurgy, 8 Kliment Ohridsky Blvd, 1756 Sofia, Bulgaria
e-mail: jordan.hristov@mail.bg

J. Singh et al. (eds.), *Advances in Mathematical Modelling, Applied Analysis and Computation*, Lecture Notes in Networks and Systems 415,
https://doi.org/10.1007/978-981-19-0179-9_2

In general, from a theoretical point of view different, different types of liquid flows may occur in the porous structure of wood [2]. However, it is generally accepted by the convention that the flow is strongly non-linear including also molecular slip at the porous walls and kinetic energy loss when the fluid enters the pit openings [4–6]. Upon the assumption of pure viscous liquid flow inside the wood porous structure, the process can be modelled by the Darcy model

$$Q = \frac{K}{\mu} A \frac{\Delta P}{L} \tag{2}$$

where K is the permeability [m^2] and $\mu[Pa \cdot s]$ is the fluid dynamic viscosity.

Alternatively, the Poiseuille flow equation through N parallel capillaries of radius r

$$Q = N \frac{\pi}{8\mu} r^4 \frac{\Delta P}{L} \tag{3}$$

can be applied. In such cases, the capillary pressure may be presented by the capillary rise h and surface tension σ as

$$h = \sqrt{\frac{r\sigma}{2\mu} t} \tag{4}$$

1.1 Wood Impregnation: Main Factors Affecting the Process

The most important factor in the process of fluid penetration into the wood capillaries is the geometry which varies and depends on the type of wood nature. However, the longitudinal flow is dominant in woods and the most critical dimension is the length of the sample (wood chip). In this context, permeability is strongly affected by moisture and air contents. The viscosity of the penetrating fluid and its surface tension are the principal fluid characteristics when there are no chemical reactions during the impregnation process. But if a chemical reaction takes place, this may change the internal wood structure and affect the fluid flow through the capillaries. With increase in the temperature of the penetration liquid, below the boiling point, when the process is driven by constant outside pressure, the result is an increasing penetration rate, because of the reduction in the fluid viscosity. In this context, upon all conditions remaining unchanged, the increase in the pressure gradient also increases the penetration rate.

Thus, we may consider two types of fluid penetration (impregnation) regimes: (i) Upon a constant external pressure when the concentration in the bath surrounding the wood chip is not so important, and (ii) Penetration of fluid into the wood sample only due to capillary pressure in *a calm bath* with *concentration unchangeable during the entire impregnation process*. In both cases, the sample saturation S should be considered. In general, the concentration of saturation in a porous medium is defined as $C_\infty = \frac{M_\infty - M_0}{M_0}$, where M_0 is the initial amount (at $t = 0$). In wood impregnation Processing, the fluid saturation S (dimensionless quantity) is defined as

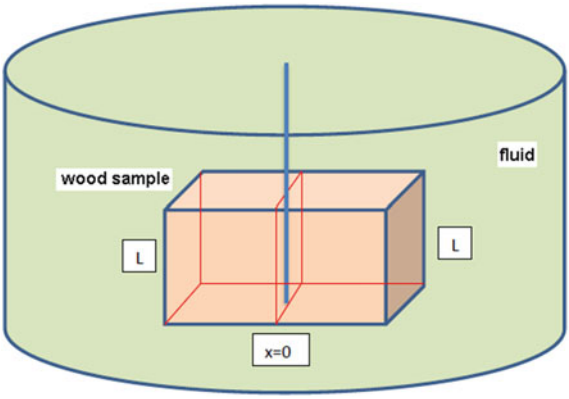

Fig. 1 Wood penetration in a stagnant fluid by the mechanism of capillary suction

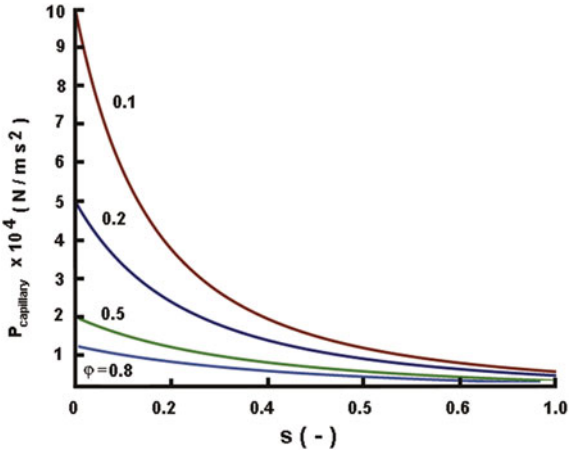

Fig. 2 Capillary pressure as a function of the wood saturation S at various porosities φ in accordance with Eq. (6) with $m = 2$

$$S = \frac{1}{\varphi}\left(\frac{\rho_f}{\rho_{rf}}\right) = \frac{\theta}{\varphi}\left(\frac{\rho_s}{\rho_{rf}}\right), \quad \theta = \frac{\rho_f}{\rho_{rf}} \tag{5}$$

where ρ_s is the bulk mass density of the dry wood [kg/m^3], ρ_f is the bulk mass density of the fluid inside the pores [kg/m^3], ρ_{rf} is the real mass density of the fluid [kg/m^3], φ is the wood porosity (dimensionless) and $0 < \varphi < 1$. If a capillary rise mechanism of liquid is only considered as a driving force, as in the present study, then the correlation between the saturation S and the porosity is well presented by the approximate reciprocal relation [2] of a typical shape presented in Fig. 1.

$$p_{cap} \equiv \frac{1}{\left(S + \sqrt{\varphi}\right)^m}, \quad 0 < S < 1 \tag{6}$$

where m depends on the accuracy of data approximation procedure (Fig. 1).

1.2 Kowalski's Model

Kowalski et al. [7], concerning diffusion of methacrylate in wood (impregnation) with the saturation $S = C/C_\infty$ (C_∞ is the saturation concentration corresponding to $S = 1$ as a dependent variable, formulated the following model:

$$\frac{\partial S}{\partial t} = \Lambda \rho_f \frac{\partial}{\partial x}\left[\frac{1}{\left(S+\sqrt{\varphi}\right)^2}\frac{\partial S}{\partial x}\right], \quad 0 \le S \le 1, \quad S\left(t=0\right) = 0 \tag{7}$$

with a boundary condition at the solid-fluid interface

$$\underbrace{-\Lambda \rho_f \frac{1}{\left(S+\sqrt{\varphi}\right)^2}\frac{\partial S}{\partial x}}_{inside\ the\ porous\ solid,\ at\ x\to 0} = \underbrace{\alpha_m\left(1-S\right)}_{outside\ the\ porous\ body\ ,\ at\ x\to 0} \tag{8}$$

This model assumes only capillary pressure (see the relationship (6)) as the driving force of the impregnation process. It is worth noting that in the formulation of the boundary condition (8), both sides consider the same value of S without taking into account that both sides of this relationship are constituted for different media separated by the fluid-solid interface at $x = 0$. This is a wrong formulation of a boundary condition, common for mass transfer processes, which has to be formulated as an equilibrium relationship, namely

$$q_{x=0}|_{fluid} = \alpha_m\left(C_{x=0} - C_\infty\right) \tag{9}$$

where $C_{x=0}$ is the concentration of the fluid at the interface, while α_m is the mass transfer coefficient at the same point from the side of the liquid bath where the wood sample is immersed.

The interface concentration can be easily converted to saturation S through the relationship (5) but we have to mention one important fact, precisely, the samples are in an infinite liquid bath with unchangeable concentration due to the part of fluid absorbed by the body. Therefore, two options might be considered concerning the correct formulation of this boundary condition, namely

(i) Instantaneous establishment of the equilibrium (saturation) at the body surface, that means $S_{x=0} = 1$, thus formulating Dirichlet boundary condition, and
(ii) A relaxing in time boundary condition taking into account that establishment of the equilibrium (complete saturation) at the solid-fluid interface needs some portion of time, that is, we need a formulation of the so-called viscoelastic boundary condition.

To close these comments, the main conclusion is that the boundary condition (8) is incorrectly formulated and physically unsound (see further Sect. 1.3). From a mathematical point of view, this boundary condition is challenging, as we will see in

the next section commenting on the Fokas' solution, but the results of these solutions are physically questionable.

1.3 Kowalski's Model: Some Comments

In the work of Kowalski et al. [7] from where the model considered in this work comes, the saturation flux j_s is defined as

$$j_s = -\Lambda \frac{1}{\left(S + \sqrt{\varphi}\right)^2} \frac{\partial S}{\partial x} \tag{10}$$

Here, Λ is a general constant depending on the process Parameter, and we may consider it as diffusivity in the sense of the diffusion process modelled by Eq. (7). Precisely, the relationship (10) can be presented more correctly as

$$j_s = -D(S) \frac{\partial S}{\partial x} \tag{11}$$

with a non-linear saturation-depended diffusivity expressed as

$$D\left(S\right) = \frac{D_0}{(S+b)^m}, \quad m = 2 \tag{12}$$

and related to the so-called Fujita's non-linear diffusivities [11–13].

It is worth noting to mention that Kowalski's model is a particular case of the general non-linear diffusion model with moving boundary formulated by Broadbridge (in a CSIRO preprint as quoted by [14] and also discussed in [15]) in a semi-infinite heterogeneous medium $0 < x < X\left(t\right)$, namely

$$\frac{\partial u}{\partial t} = \frac{\partial}{\partial x}\left[\frac{1+cx}{(a+bu)^2}\frac{\partial u}{\partial x} + \frac{c}{2b\left(a+bu\right)}\right], \quad 0 < x < X\left(t\right) \tag{13}$$

with fluxes at the boundaries

$$\frac{1+cx}{(a+bu)^2}\frac{\partial u}{\partial x} = U\left(t\right), \quad x = 0, \quad t > 0 \tag{14}$$

$$\frac{c}{2b\left(a+bu\right)}\frac{\partial u}{\partial x} = \alpha \dot{X}\left(t\right), \quad x = \dot{X}\left(t\right), \quad X\left(t=0\right) = 0 \tag{15}$$

For $c = 0$, corresponding to the homogenous case, i.e. when the diffusivity is spatially independent, we get

$$\frac{\partial u}{\partial t} = \frac{\partial}{\partial x}\left[\frac{1}{(a+bu)^2}\frac{\partial u}{\partial x}\right], \quad 0 < x < X(t) \tag{16}$$

which is the non-linear diffusion equation considered by Storm [16].

This equation, related to heat conduction in solid hydrogen, has been also studied by Rosen [17]. In the literature available, the main solution approaches address reciprocal transformations [8, 14, 18] (explained next in this text through Fokas' solution) and Backlund transformation [19].

1.4 Fokas' Solution Approach

Fokas et al. [8] considered the model (7)–(8) with a formulation considering a half part of the body (see Fig. 1) with an impermeable condition at the symmetry axis $x = 0$ as $(dS/dx)_{x=0} = 0$ and a fluid-solid interaction at the interface $x = L$ (the boundary condition—Eq. (8)). The main approach of Fokas is to linearize the model equation (due to the non-linear diffusion coefficient) and move the non-linearity to the boundary condition. This was done by applying the reciprocal transformation [8, 9] with a new variable $S^* = S + \sqrt{\varphi}$, namely

$$\frac{\partial S^*}{\partial t} = \frac{\partial}{\partial x}\left[\frac{1}{S^{*2}}\frac{\partial S^*}{\partial x}\right], 0 < x < L \tag{17}$$

and boundary conditions

$$\frac{\partial S^*}{\partial x} = 0, \quad x = 0 \tag{18}$$

$$-\frac{1}{S^{*2}}\frac{\partial S^*}{\partial x} = \alpha\left[1 + \sqrt{\varphi} - S^*\right], \quad \alpha = \frac{\alpha_m}{\Lambda\rho_f} \tag{19}$$

Then, applying the following reciprocal transformation to the model (17)–(19)

$$dx' = S^* dx + \frac{1}{S^{*2}}\frac{\partial S^*}{\partial x}dx, \quad dt' = dt, \quad S' = \frac{1}{S^*}, \quad 0 < \left|S^*\right| < \infty \tag{20}$$

the result is a linearized equation with a non-linear boundary condition (23), namely

$$\frac{\partial S'}{\partial t'} = \frac{\partial^2 S'}{\partial x'^2} \tag{21}$$

$$\frac{\partial S'}{\partial x'} = 0, \quad x' = x'\big|_{x=0} \tag{22}$$

$$\frac{\partial S'}{\partial x'} = \alpha\left[S'\left(1 + \sqrt{\varphi}\right) - 1\right], \quad x' = x'\big|_{x=L} \tag{23}$$

However, this linearization of the main equation needs a definition of the so-called reciprocal boundaries defined as follows:

At the symmetry axis

$$x'(0,t) = 0 \tag{24}$$

At the solid-fluid interface $(x = L)$

$$x'(L,t) = \sqrt{\varphi}L - \alpha\left(1+\sqrt{\varphi}\right)t + \alpha\int_0^t S^*(L,\tau)\,d\tau \tag{25}$$

Finally, the modified model becomes

$$\frac{\partial S'}{\partial t'} = \frac{\partial^2 S'}{\partial x'^2}, \quad 0 < x' < X'\left(t'\right) \tag{26}$$

$$\frac{\partial S'}{\partial x'} = 0, \quad x' = 0 \tag{27}$$

$$\frac{\partial S'}{\partial x'} = \alpha\left[S'\left(1+\sqrt{\varphi}\right) - 1\right], \quad x' = X'\left(t'\right), S' = \frac{1}{\sqrt{\varphi}}, \quad t' = 0 \tag{28}$$

$$X'\left(t'\right) = L\sqrt{\varphi} - \alpha\left(1+\sqrt{\varphi}\right)t' + \alpha\int_0^{t'} \frac{d\tau}{S'\left(X'(\tau),\tau\right)} \tag{29}$$

1.5 Some Comments and Aim

The main idea is to develop an approximate and physically adequate solution rather than mathematically correct but difficult to handle results. These two approaches are not in conflict but mainly demonstrate alternatives in the problem solution. Furthermore, there is a reformulation of the boundary condition at the fluid-porous medium interface stressing the attention on the fact that it should relate functional relationship on both sides of the solid-fluid interface which is not taken into account in Kowalski's model. In addition, *relaxing* Dirichlet boundary conditions account for the fact that *there is no instantaneous* surface (at the fluid-solid interface) saturation.

1.6 Chapter Organization

In the sequel, the following interrelated steps towards the new approach of the problem solution are developed: Sect. 2 presents the basic techniques of the integral-balance method (with an assumed parabolic profile 2.1.4) and the basic steps in the transformation of the non-linear diffusion term 2.1.3. The approximate solutions in Sect. 3 consider two principal directions: Solutions with the classical Dirichlet boundary condition (assuming instantaneous saturation of the fluid-sample interface) in 3.1 and experiments with relaxing Dirichlet boundary conditions allowing also to develop integral-balance solutions in 3.2. Numerical tests with both types of boundary conditions are presented in 3.1.4 and 3.3.4.

2 Integral-Balance Solutions and Related Model Transformations

The approximate solutions developed in this chapter are based on the integral-balance approach which transforms the initial diffusion model into an integral relation which has to be satisfied by an assumed profile (as a function of the dimensionless variable $\eta = x/\delta$) and obeying the so-called Goodman' boundary conditions [22, 23]

$$u\left(\delta\right) = \frac{\partial\left(\delta\right)}{\partial x} = 0 \tag{30}$$

This approach introduces *a finite penetration depth* $\delta\left(t\right)$ of the diffusion substance (absorbed fluid or heat) depending on the nature of diffusion process modelled. The motion of this front in time has a finite speed thus correcting the infinite speed of the original model which can be presented as

$$\frac{\partial\Theta}{\partial t} = \frac{\partial}{\partial x}\left[D_0\Theta^{-m}\frac{\partial\Theta}{\partial x}\right], \Theta = \left(S + \sqrt{\varphi}\right)^{-m} \tag{31}$$

where in the present case $m = 2$. Equation (31) is from the class of the *fast diffusion processes* [19] in contrast to the *slow diffusion processes* [24–26] where with $D\left(\Theta\right) = D_0\Theta^m$ $(m > 1)$ the solutions as *sharp fronts* propagate with *finite speeds* [25, 26].

The problem considered in this study is a transient process of fluid penetration into a porous medium, within a diffusion layer bounded within the range $0 < x < \delta$, up to the moment when the symmetric centre of the slab will be reached (when $\delta\left(t\right) = L$—see Fig. 3).

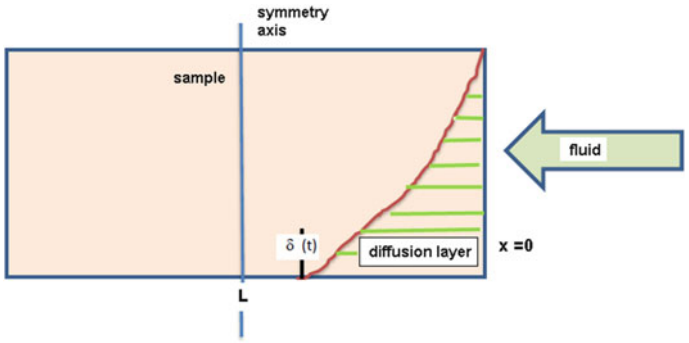

Fig. 3 One-dimensional physical model of fluid impregnation of a porous wood slab with a finite diffusion layer defining the penetration front $\delta(t)$

2.1 Integration Techniques

The integral-balance method employs mainly two principal integration techniques: (i) Single-integration method and (ii) Double-integration method. For the sake of clarity of explanations, these integration techniques will be briefly presented next.

2.1.1 Single-Integration method

The single integration over the penetration depth δ, known as the heat-balance integral method of Goodman [22], yields

$$\int_0^{\delta} \frac{\partial u\,(x,t)}{\partial t} dx = \int_0^{\delta} D_0 \frac{\partial^2 u\,(x,t)}{\partial x^2} dx \Rightarrow \frac{d}{dt} \int_0^{\delta} u\,(x,t)\,dx = -D_0 \frac{\partial u\,(0,t)}{\partial x} \quad (32)$$

This is a simple mass balance relation of the mass absorbed $m(t) = \int_0^{\delta} u dx$ whose time evolution $dm(t)/dt$ is controlled by the mass flux at the interface $x = 0$. On the right-hand side of (32), the gradient $\partial u\,(0,t)/\partial x$ should be defined through the assumed approximation of $u\,(x,t)$.

2.1.2 Double-Integration method

This approach has two consequent integration steps over different domains along the penetration depth, namely [26, 27] (1) integration from x to δ and consequently (2) integration from 0 to δ.

$$\int_0^{\delta}\int_x^{\delta}\frac{\partial u\,(x,t)}{\partial t}dxdx=\int_0^{\delta}\int_x^{\delta}D_0\frac{\partial^2 u\,(x,t)}{\partial x^2}dxd\Rightarrow\frac{d}{dt}\int_0^{\delta}\int_x^{\delta}u\,(x,t)dxdx=D_0u\,(0,t) \tag{33}$$

The result is that now the right-hand side of the new integral relationship depends on the boundary condition at $x=0$ only, i.e. *it is independent of the type of the assumed profile*. Moreover, this is a mass balance relationship in an integral form over the diffusion layer (penetration depth), expressed through the time evolution of the first moment of the absorbed mass of the fluid which at any time is balanced by the mass load (concentration) at the interface $x=0$.

2.1.3 Transform of the Non-linear Diffusivity

The method applied in this chapter does not utilize either the commonly encountered approach [28, 29] applying the similarity variable $\xi=x/\sqrt{D_0t}$ to the original model thus allowing to solve a non-linear ordinary differential equation [30] or the reciprocal technique commented earlier. The principal step is oriented towards a transformation of the diffusion term on the right-hand side of the original model allowing easily the application of the integral method (see such an example in [32]). Precisely, for the sake of simplicity and generalization of the applied technique, replacing S by u and $\sqrt{\varphi}$ by a, we have

$$\frac{D_0}{(a+bu)^2}\frac{\partial u}{\partial x}=-\frac{D_0}{b}\frac{\partial}{\partial x}\left[\frac{1}{(a+bu)}\right] \tag{34}$$

and therefore

$$\frac{\partial u}{\partial t}=-\frac{D_0}{b}\frac{\partial^2}{\partial x^2}\left[\frac{1}{(a+bu)}\right] \tag{35}$$

where, with $a=\sqrt{\varphi}$ and $b=1$, in the original notations we have

$$\frac{\partial u}{\partial\, t}=-D_0\frac{\partial^2}{\partial x^2}\left[\frac{1}{\left(\sqrt{\varphi}+S\right)}\right] \tag{36}$$

Equation (36) is the principle equation used in the solutions developed next. How this transformation affects the result of the integration techniques will be demonstrated next.

Single-integration method: Integrating the model equation in its general form (35) from 0 to δ, the result is

$$\int_0^{\delta}\frac{\partial u}{\partial\, t}dx=\int_0^{\delta}\frac{\partial}{\partial x}\left[\frac{-D_0}{(a+bu)^2}\frac{\partial u}{\partial x}\right]dx\Rightarrow\frac{d}{du}\int_0^{\delta}udx=\left[\frac{-D_0}{(a+bu)^2}\frac{\partial u}{\partial x}\right]_{x=0} \tag{37}$$

Therefore, the time evolution of the absorbed mass at any time is balanced by the mass flux at the interface $x = 0$ as it was commented earlier in the text. In terms of the liquid absorbed evolving in time, this means that the rate of mass uptake, i.e. $dm/dt = {}^{d}/_{dt} \int_0^{\delta} u dx$. Now, replacing the function $u(x,t)$ in (37) by an assumed profile u_a, expressed as a function of dimensionless space variable $\eta = x/\delta$ (see the next section), obeying the Goodman's conditions (30), we get

$$\frac{d}{dt} \int_0^{\delta} u_a(x,t) dx = \frac{D_0}{a + b u_a(0,t)} \frac{\partial u_a(0,t)}{\partial x} \tag{38}$$

where $u_a(0,t) = 1$ (Dirichlet problem, for instance) and $u_a(\delta,t) = u_a(\delta,t)/dx = 0$.

This integral relationship becomes a differential equation about $\delta(t)$ when u_a is replaced by the assumed profile (43).

Double-integration method: Following the DIM integration technology, we have

$$\int_0^{\delta} \int_x^{\delta} \frac{\partial u}{\partial t} dx dx = \int_0^{\delta} \int_x^{\delta} \frac{\partial}{\partial x} \left[\frac{D_0}{(a+bu)^2} \frac{\partial u}{\partial x} \right] dx dx \tag{39}$$

The first step in (39), in dimensionless fixed (non-moving) coordinates (see the comments in the next point), results in

$$\int_{\eta}^{1} \frac{-D_0}{b} \frac{\partial^2}{\partial \eta^2} \left[\frac{1}{(a+bu)} \right] d\eta = -D_0 \frac{\partial}{\partial \eta} \left[\frac{1}{(a+bu)} \right] \Bigg|_{\eta}^{1} = -D_0 \frac{\partial}{\partial \eta} \left[\frac{1}{a} - \frac{1}{(a+bu)} \right]_{\eta} \tag{40}$$

The second integration yields

$$\int_0^{1} \frac{-D_0}{b} \frac{\partial^2}{\partial \eta^2} \left[\frac{1}{(a+bu)} \right] d\eta = D_0 \frac{b u_0}{a(a+bu_0)} = D_0 \frac{b}{a(a+b)} \tag{41}$$

Taking into account that $a = cont.$ the result of the second integration is

$$\int_0^{\delta} \int_x^{\delta} \frac{\partial}{\partial x} \left[\frac{D_0}{(a+bu)^2} \frac{\partial u}{\partial x} \right] dx dx = D_0 \frac{b}{a(a+b)} \tag{42}$$

which depends only on the boundary condition (in this case $u_0 = u_s = 1$) at $x = 0$ (Dirichlet problem).

2.1.4 Assumed Profile

The solution developed further uses an assumed parabolic profile with an unspecified exponent n expressed as a function of the dimensionless variable (distance) $\eta = x/\delta$ [23], namely

$$u_a = u_0\left(1 - \frac{x}{\delta}\right)^n \Rightarrow S_a = S_0(1-\eta)^n \tag{43}$$

This assumed profile has been analysed in [31, 32] when the diffusion coefficient is constant as well as when it is concentration dependent [26]. Defining a dimensionless variable $\eta = x/\delta$, we have $0 \leq \eta \leq 1$ and consequently $S_a = S_s(1-\eta)^n$. At the boundaries of the penetration layer, we have $S(\eta = 0) = 1$ and $S(\eta = 1) = 0$, that is, it satisfies the boundary conditions (30). The introduction of the dimensionless variable $\eta = x/\delta$ allows the moving boundary problem (with a moving front $\delta(t)$) to be transformed into a fixed boundary problem.

3 Approximate Solutions

3.1 Dirichlet Boundary Condition

With the Dirichlet boundary condition, the approximate profile takes the form

$$S_a = S_0\left(1 - \frac{x}{\delta}\right)^n \tag{44}$$

Physically, this means instantaneous saturation of the solid-fluid interface at $x = 0$, that is, $S_0 = 1$ since by definition $0 < S < 1$. Now, we will see how upon such boundary condition the integration techniques of the integral method work and define the penetration depth $\delta(t)$.

3.1.1 Penetration Depth: Single Integration

From the integral relation of the single-integration approach (38) and applying the Leibniz rule to the left side, we get

$$\frac{d}{dt}\int_0^{\delta}\left(1 - \frac{x}{\delta}\right)^n dx = \frac{-D_0}{a + bS_a(0,t)}\frac{\partial S_a(0,t)}{\partial x} \tag{45}$$

With $S_a(0,t) = 1$ and $\frac{\partial S_a(0,t)}{\partial x} = -\frac{n}{\delta}$ in (45), we get

$$\frac{d}{dt}\int_0^{\delta}\left(1-\frac{x}{\delta}\right)^n dx = \frac{-D_0}{a+b}\left(-\frac{n}{\delta}\right) \Rightarrow \frac{1}{2}\frac{d\delta^2}{dt} = \frac{D_0}{a+b}n\,(n+1) \tag{46}$$

The integration of the final result in (46) with $a = \sqrt{\varphi}$ and $b = 1$, yields the penetration depth defined as

$$\delta_{HBIM} = \sqrt{D_0 t}\frac{\sqrt{2n\,(n+1)}}{\sqrt{1+\sqrt{\varphi}}} \tag{47}$$

or in a dimensionless form as

$$\frac{\delta_{HBIM}}{\sqrt{D_0 t}} = \frac{\sqrt{2n\,(n+1)}}{\sqrt{1+\sqrt{\varphi}}} \tag{48}$$

This result resembles the integral-balance solution of the classical diffusion equation where $\delta_{HBIM} = \sqrt{D_0 t}\sqrt{2n\,(n+1)}$ which can be obtained from (47) setting $\varphi = 0$, which refers to solid media without voids such as in heat conduction in solids (where this integral-balance solution is mainly applied); this extreme case is not considered in the development of the wood impregnation model discussed here.

3.1.2 Penetration Depth: Double Integration

With the result (40), then from the DIM integral relation (39) and the result (39) with the assumed profile (43), we get

$$\frac{1}{(n+1)\,(n+2)}\frac{d\delta^2}{dt} = D_0\frac{b}{a\,(a+b)} \Rightarrow \delta = \sqrt{D_0 t}\sqrt{(n+1)\,(n+2)}\sqrt{\frac{b}{a\,(a+b)}} \tag{49}$$

With $a = \sqrt{\varphi}$ and $b = 1$, the penetration depth is

$$\delta_{DIM} = \sqrt{D_0 t}\sqrt{(n+1)\,(n+2)}\Phi\,(\varphi)\,, \quad \Phi\,(\varphi) = \sqrt{\frac{1}{\sqrt{\varphi}\left(1+\sqrt{\varphi}\right)}} \tag{50}$$

or in a dimensionless form as

$$\frac{\delta_{DIM}}{\sqrt{D_0 t}} = \sqrt{(n+1)\,(n+2)}\Phi\,(\varphi) \tag{51}$$

The final functional relationship $\Phi\,(\varphi) = f\left(\sqrt{\varphi}\right)$ excludes the extreme cases of $\varphi = 0$ (a complete solid without voids) and $\varphi = 1$ (free space Fickian diffusion). For example, only to the physical adequacy of (50) with $\varphi = 0.5 \Rightarrow \sqrt{\varphi} \approx 0.707$, we get $\Phi\,(0.5) \approx 0.910$; also for $\varphi = 0.1$ (low-porosity solids), this function gets a

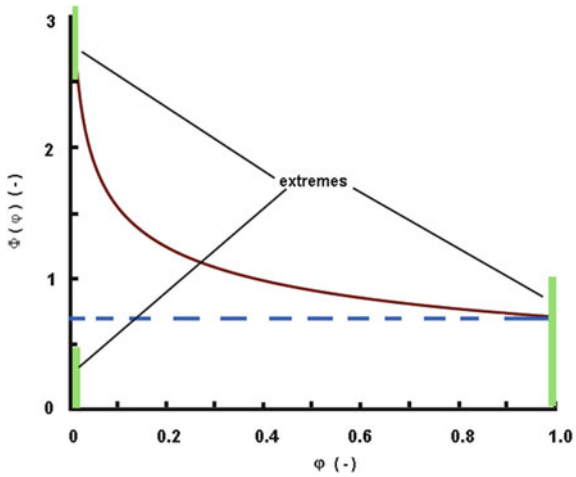

Fig. 4 Porosity function $\Phi(\varphi)$ controlling the depth of the diffusion layer

value $\Phi(0.5) \approx 1.550$; more illustrative is the plot in Fig. 4. In general, the increase in φ makes the penetration depth shorter and this is not in conflict with the physics since the saturation of the medium is inverse to its porosity because the capillary pressure (see (45)) increases with reduction in the medium porosity and therefore the flux defined by (10) increases too. In other words, the diffusivity defined by this relationship increases as the porosity is decreased upon conditions keeping equal level of the saturation S.

3.1.3 Approximate Saturation Profiles

With the results (47) and (50) about the penetration depth, we may now construct the approximate solution through the assumed profile (43) as follows.

Single integration (HBIM)

$$S_{HBIM} = \left[1 - \frac{x}{\sqrt{D_0 t}\frac{\sqrt{2n(n+1)}}{\sqrt{1+\sqrt{\varphi}}}}\right]^n = [1 - \eta N_1(n,\varphi)]^n, \quad N_1(n,\varphi) = \frac{\sqrt{1+\sqrt{\varphi}}}{\sqrt{2n(n+1)}} \tag{52}$$

Double integration (DIM)

$$S_{DIM} = \left[1 - \frac{x}{\sqrt{D_0 t}\sqrt{(n+1)(n+2)}\Phi(\varphi)}\right]^n = [1 - \eta N_2(n,\varphi)]^n \tag{53}$$

$$N_2(n,\varphi) = \sqrt{(n+1)(n+2)}\Phi(\varphi) = \sqrt{\frac{(n+1)(n+2)}{\sqrt{\varphi}\left(1+\sqrt{\varphi}\right)}} \tag{54}$$

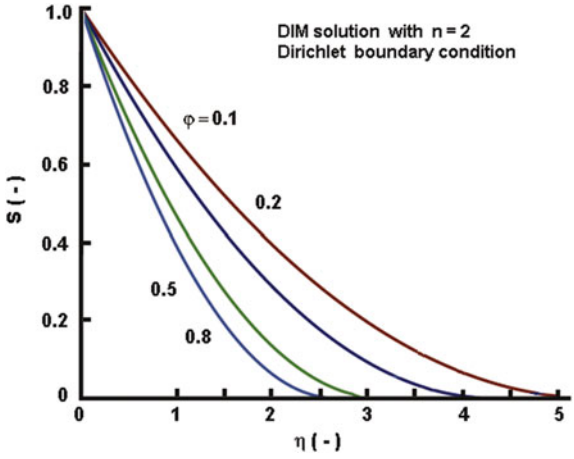

Fig. 5 Approximate profile generated by DIM solution and Dirichlet boundary condition for various sample porosities. The crossing points of the profiles and the horizontal axis mark the penetration depths

Both solutions (HBIM and DIM) generate the Boltzmann similarity variable $\eta = x/\sqrt{D_0 t}$ as an indicator that despite the non-linearity in the model equation the behaviour of the saturation spreading into the depth of the impregnated solids is Fickian.

The functions $N_1(n, \varphi)$ and $N_2(n, \varphi)$ accumulate effects of both the assumed profile and the physical initial condition of the medium *via* the porosity (assuming isotropic porous media without swelling or shrinking). Moreover, it represents implicitly the effect of the wood porosity and capillary pressure on the penetration depth.

3.1.4 Approximate Solutions: Numerical Tests

Qualitative numerical simulations of the approximate solutions with stipulate values of the exponent n ($n = 2$ and $n = 3$) are presented in Fig. 5. The behaviour of these profiles should be related to the effect of the sample porosity on the capillary pressure (see Fig. 2), that is, the lower wood porosity, the higher capillary pressure. As a consequence, the higher the capillary pressure, the longer the penetration depth. In general, since this a *fast diffusion* equation (see the comments related to Eq. (31)), the solutions are concave profiles which is a well-known fact [37, 38].

3.2 Relaxing Dirichlet Boundary Conditions

The problem developed in this section refers to the physical fact that all natural phenomena have their relaxation times up to establishments of equilibria. The Dirichlet boundary condition is classic in the parabolic diffusion problem, but its formula-

tion neglects the relaxation time of the surface concentration establishment, that is, it considers instantaneous surface equilibrium between the porous medium and the surrounding fluid. Since the main model is also parabolic and mainly valid for long times, now we formulate a relaxing boundary condition that should obey the following conditions:

$$S_0(t) = 0, \quad t = 0 \tag{55}$$

$$S_0(t) = 1, \quad t \to \infty \tag{56}$$

The second condition in (56) actually means the Dirichlet boundary condition to be reached at large acceptable technological time. From this point of view, we suggest three functions obeying the above conditions, namely

(a) Exponential relaxing boundary condition

$$S_0(t) = 1 - e^{-kt} \tag{57}$$

where the rate constant k controls the time needed by the equilibrium $S_0(t) = 1$ to be attained. This relaxing function can be considered as a solution of the kinetic equation

$$\frac{dS_0}{dt} = ke^{-kt}, \quad S_0(t = 0) = 0 \tag{58}$$

With this formulation, the assumed profile becomes

$$S(t) = \left(1 - e^{-kt}\right)\left(1 - \frac{x}{\delta}\right)^n \tag{59}$$

satisfying Goodman's boundary conditions.

(b) Relaxing boundary condition utilizing the Gaussian error function

$$S_0(t) = erf(kt) \tag{60}$$

with a rate constant k which is a solution of

$$\frac{dS_0}{dt} = \frac{2k}{\sqrt{\pi}}e^{-k^2t^2}, \quad S_0(t = 0) = 0 \tag{61}$$

leading to an assumed profile

$$S(t) = erf(kt)\left(1 - \frac{x}{\delta}\right)^n \tag{62}$$

(c) Relaxing boundary condition utilizing the Verhulst logistic function

$$S_0(t) = \frac{1}{1 + e^{-kt}} \tag{63}$$

widely used to simulate the Heaviside step function. The simple sigmoid function is a solution of the logistic differential equation (considered also as a special case of the Bernoulli equation)

$$\frac{dS_0}{dt} = kS_0\left(1 - \frac{S_0}{S_{sat}}\right), \quad S_0(0) = \frac{1}{2}, \quad S_{sat} = 1 \tag{64}$$

In this case, the first condition of (55) is not obeyed but this will not affect the solution developed next since an additional condition $\delta(t = 0) = 0$ should be satisfied. We apply only this simple sigmoid function since the task here is to see what is the integral-balance solution when the physical background needs the fluid-surface equilibrium to be modelled as a time-dependent process, but there is no restriction on other functions obeying the conditions (55) to be obeyed. In such a case, the assumed profile is

$$S_3(t) = \frac{1}{1 + e^{-kt}}\left(1 - \frac{x}{\delta}\right)^n \tag{65}$$

The behaviours of the relaxing functions considered are illustrated in Fig. 6 for various values of the rate constant k.

3.3 Penetration Depth and Applicability of the Selected Relaxing Functions

Now, we have to see what the results, when applying the selected relaxing boundary functions to the stages where the penetration depth should be determined, are. Here, we apply directly the DIM techniques since in this case, the right-hand side of the integral relation depends only on the boundary condition at $x = 0$.

3.3.1 Exponential Relaxation Function

With the exponential relaxing function (57), we have (see the formulation (49))

$$\int_0^{\delta}\int_x^{\delta}\left(1 - e^{-kt}\right)\left(1 - \frac{x}{\delta}\right)^n dxdx = D_0\frac{b}{a(a+b)}\left(1 - e^{-kt}\right) \tag{66}$$

which leads to

$$\frac{d}{dt}\left[\left(1 - e^{-kt}\right)\frac{\delta^2}{(n+1)(n+2)}\right] = D_0\frac{b}{a(a+b)}\left(1 - e^{-kt}\right) \tag{67}$$

The integration in (67) yields

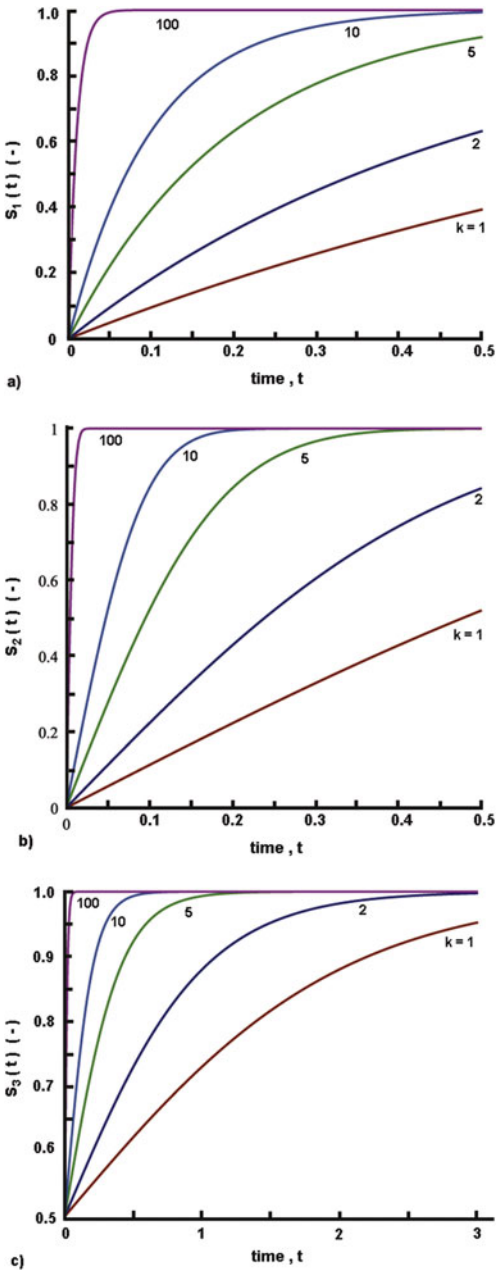

Fig. 6 Behaviour of the functions used to simulate the time-dependent saturation of the solid-fluid interface, for various values of the rate constant k: **a** S_1—exponential function; **b** S_2—error function; **c** S_3—logistic function

$$\delta^2 = D_0 \frac{b}{a\,(a+b)}\,(n+1)\,(n+2)\,\frac{1}{\left(1-e^{-kt}\right)}\left(t+\frac{e^{-kt}}{k}\right)+C_1 \tag{68}$$

With $C1 = 0$, we get

$$\delta = \sqrt{D_0 \frac{b}{a\,(a+b)}\,(n+1)\,(n+2)\,R_{exponential}(t)} \tag{69}$$

where

$$R_{exponential}(t) = \sqrt{\frac{1}{\left(1-e^{-kt}\right)}\left(t+\frac{e^{-kt}}{k}\right)} \tag{70}$$

The physical condition $\delta\,(t=0)=0$ cannot be obeyed since the first term on the right-hand side of (68) is singular at $t = 0$, but we can see that for large times we get $\delta^2 \equiv t$ which corresponds to the solution with already established Dirichlet boundary condition.

3.3.2 Error Function as a Relaxing Boundary Condition

With the error function as a boundary relaxing function and DIM, we get

$$\int_0^{\delta}\int_x^{\delta} erf\,(kt)\left(1-\frac{x}{\delta}\right)^n dxdx = D_0 \frac{b}{a\,(a+b)} erf\,(kt) \tag{71}$$

From (71), we have

$$\delta^2 = D_0 \frac{b}{a\,(a+b)}\,(n+1)\,(n+2)\left[t+\frac{1}{k\sqrt{\pi}erf\,(kt)\,e^{k^2t^2}}\right] \tag{72}$$

or in the manner of the classical solutions with the integral-balance method, we get

$$\delta = \sqrt{D_0 t}\sqrt{(n+1)\,(n+2)}\sqrt{\frac{b}{a\,(a+b)}}\left[1+\frac{1}{t\left[k\sqrt{\pi}erf\,(kt)\,e^{k^2t^2}\right]}\right]^{1/2} \tag{73}$$

In these functional relationships ((72) and (73)), the second terms in the brackets are also singular at $t = 0$, but we can easily see that for large times these terms become negligible and we get the classical result $\delta^2 \equiv t$.

Note 1: Both relaxing functions ((57) and (59)) lead to relationships for δ which are singular for $t = 0$ but behave physically correct for large times. They are illustrated in Fig. 7a, c, respectively The singularity at $t = 0$ can be, to some extent, and mainly from practical reasons, neglected since for $t > 0$ the solutions (in both cases)

behave physically correct and approach the case with the classical Dirichlet boundary condition. It is worth noting that the introduction of relaxing Dirichlet boundary condition when the main equation is parabolic avoids the infinite speed of solution but in the present case of wood interface it is easily handled as a solution but unphysical. To this end is worth noting that in the integral-balance solutions have an inherent drawback since in the simple case $\delta \equiv \sqrt{D_0 t} \Rightarrow d\delta/dt \equiv D_0/2\sqrt{t}$ which is singular at $t = 0$ and yields an infinite speed of the diffusion front. Such unphysical result can be avoided if the constitutive equation about the flux contains a relaxing part (see more details in [33, 34]), for instance, applying the fading memory approach [35, 36].

Note 2: Regarding the relaxation terms of the penetration depths for long times, there are two distinct behaviours: (i) For the exponential and logistic relaxation functions, controlling the boundary saturation, the long time behaviours approach the square-root time dependence relevant to the Dirichlet boundary condition (Fig. 7a, c). In contrast to these two cases, the use of the error function results in a relaxation term of the penetration depth which for long times approaches unity (see Fig. 7b).

Note 3: To see what should be done in such a case, it is important to see what the ratio of the relaxation time $\lambda = 1/k$ to the observation time is since the parabolic model of the fluid penetration into the porous wood has no natural relaxation time if the medium is considered as a semi-infinite. The ratio $De = \frac{\lambda}{t} = \frac{1}{kt}$ can be defined as a surface Deborah number. From the above expressions, it is obvious that for large values of the product kt, i.e. small De the classical Dirichlet boundary condition is practically acceptable. On the other hand, with physical objects having finite dimensions such as the wood chips impregnated, the classical diffusion time scale $t_D = L^2/D_0$ can be used to define $\frac{\lambda}{t_D} = \frac{\lambda D_0}{L^2} = De_{bulk}$ as a Deborah number also. If $\frac{\lambda}{t_D} = \frac{\lambda D_0}{L^2} \ll 1$, then we can also accept the instantaneous surface saturation modelled by the Dirichlet boundary condition as an acceptable approximation. All these thoughts address further studies requiring experimental data to be fitted, but for now, such data about the kinetics of surface saturation are missing; this does not allow us to establish the magnitude of the rate constant k and the best relaxation function that should be used at the boundary condition.

3.3.3 Logistic Relaxation Function

After the two tests with relaxing boundary conditions, let us now see what is the outcome of the integral-balance solution when the logistic function is used. In such a case, the DIM integral relation is

$$\int_0^{\delta}\int_x^{\delta} \frac{1}{\left(1+e^{-kt}\right)}\left(1-\frac{x}{\delta}\right)^n dxdx = D_0 \frac{b}{a\,(a+b)}\frac{1}{\left(1+e^{-kt}\right)} \tag{74}$$

leading to

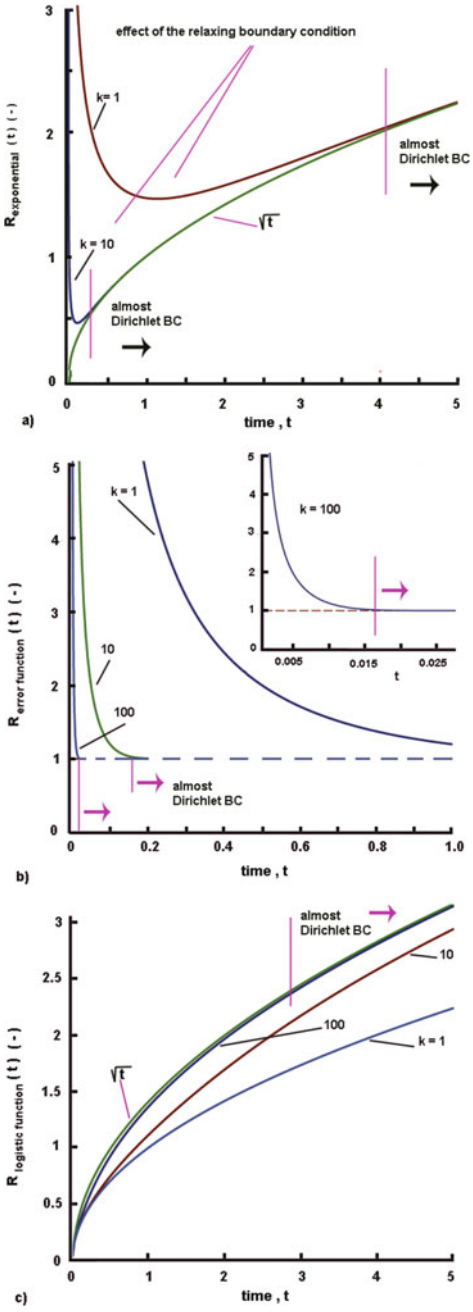

Fig. 7 Behaviour of the time-relaxing terms of the penetration depth with different relaxation functions at the boundary $x = 0$: **a** Exponential relaxation function; **b** Relaxing error function; **c** Logistic function at the boundary; **d** Relaxing term in Eq. (85). *Note* All calculations are performed starting from $t = 0.0001$ thus avoiding the numerical singularities

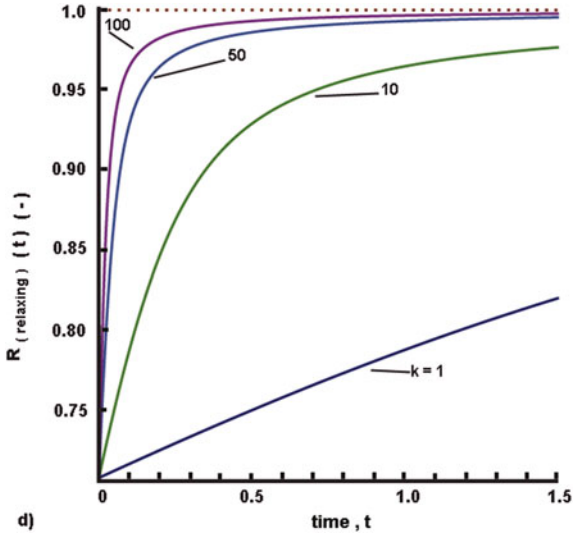

Fig. 8 Relaxing term (logistic function in the boundary condition) in Eq. (85)

$$\frac{d}{dt}\left[\frac{1}{\left(1+e^{-kt}\right)}\frac{\delta^2}{(n+1)(n+2)}\right]=D_0\frac{b}{a(a+b)}\frac{1}{\left(1+e^{-kt}\right)} \tag{75}$$

The integration in (75) yields

$$\delta^2=\left\{D_0\frac{b}{a(a+b)}\frac{1}{k}\left[\ln\frac{1+e^{-kt}}{e^{-kt}}\right]+C_3\right\}(n+1)(n+2)\left(1+e^{-kt}\right) \tag{76}$$

The condition $\delta^2(t=0)=0$ yields

$$0=2\left\{D_0\frac{b}{a(a+b)}\frac{1}{k}\ln(2)+C_3\right\}(n+1)(n+2)\Rightarrow C_3=-D_0\frac{b}{a(a+b)}\frac{1}{k}\ln(2) \tag{77}$$

Then,

$$\delta^2=D_0\frac{b}{a(a+b)}\frac{2}{k}\ln\left(\frac{1+e^{-kt}}{2e^{-kt}}\right)(n+1)(n+2) \tag{78}$$

and

$$\delta_3(t)=\sqrt{D_0}\sqrt{\frac{b}{a(a+b)}}\sqrt{(n+1)(n+2)}\sqrt{\frac{2}{k}}\sqrt{\ln\left(\frac{1+e^{-kt}}{2e^{-kt}}\right)} \tag{79}$$

which is valid for short times, as this approximation of the boundary condition suggested.

In the simplest case with large k and $t\to\infty$, the relaxation function approaches $\sqrt{t}$ because

$$\sqrt{\frac{2}{k}}\sqrt{\ln\left(\frac{1+e^{-kt}}{2e^{-kt}}\right)}=\sqrt{\frac{2}{k}}\sqrt{\ln\left(\frac{1+e^{kt}}{2}\right)} \tag{80}$$

then for $kt \to \infty$

$$\sqrt{\frac{2}{k}}\sqrt{\ln\left(\frac{1}{2}e^{kt}\right)}\approx\sqrt{\frac{2}{k}}\sqrt{\ln\left(e^{kt}\right)}\approx\sqrt{\frac{2}{k}}\sqrt{kt}\approx\sqrt{2}\sqrt{t} \tag{81}$$

thus providing the conventional DIM solution developed in the preceding section. It is demonstrated in Fig. 7c that for large values of the product kt, the relaxation terms behave as $\sqrt{t}$ corresponding to the solution developed with the unit step boundary (Dirichlet) condition. In addition, an alternative approach with the series expansion of the logarithmic term in the first expression of (78) yields

$$\ln\left(\frac{1+e^{-kt}}{2e^{-kt}}\right)\approx\frac{1}{2}t+\frac{1}{8}t^2-\frac{1}{198}t^4+O\left(t^6\right) \tag{82}$$

If only the linear term is accepted with $k = 1$, then from (79) we get the conventional DIM solution as a linear approximation

$$\delta_3(t)\approx\sqrt{D_0 t}\sqrt{\frac{b}{a\,(a+b)}}\sqrt{(n+1(n+2)} \tag{83}$$

Alternatively, we may express (79) in a more elegant way bearing in mind that $t = \ln\left(e^t\right)$ and $kt = \ln\left(e^{kt}\right)$. Then, multiplying and dividing the expression for $\delta_3\,(t)$ by $\sqrt{kt} = \sqrt{\ln\left(e^{kt}\right)}$ we get

$$\delta_3\,(t)=\sqrt{D_0 t}\sqrt{\frac{b}{a\,(a+b)}}\sqrt{(n+1)\,(n+2)}\sqrt{2}\sqrt{\frac{\ln\left(\frac{1+e^{-kt}}{2e^{-kt}}\right)}{kt}} \tag{84}$$

Rearranging (84), one obtains a more convenient result

$$\delta_3\,(t)=\sqrt{D_0 t}\sqrt{\frac{1}{\sqrt{\varphi}\left(1+\sqrt{\varphi}\right)}}\sqrt{(n+1)\,(n+2)}\sqrt{2}\sqrt{\frac{\ln\left(\frac{1+e^{-kt}}{2e^{-kt}}\right)}{kt}} \tag{85}$$

or in a dimensionless form as (bearing in mind that $a = \sqrt{\varphi}$ and $b = 1$)

$$\frac{\delta_3(t)}{\sqrt{D_0 t}} = \sqrt{\frac{1}{\sqrt{\varphi}\left(1+\sqrt{\varphi}\right)}}\sqrt{(n+1)(n+2)}\sqrt{2}\underbrace{\sqrt{\frac{\ln\left(\frac{1+e^{-kt}}{2e^{-kt}}\right)}{kt}}}_{R(relaxing)} \tag{86}$$

Now, we can see how for large times the dimensionless penetration depth approaches the solution developed with the unit step boundary (Dirichlet) condition. Obviously, at $t = 0$ it is singular, but as commented above, the singularity of penetration depth rate at $t = 0$ is an inherent property of the method when it is applied to parabolic models. The plots in Fig. 7d show the behaviour of the relaxation term in (85) and (86) for various values of the rate constant k.

3.3.4 Approximate Saturation Profiles with Relaxing Boundary Conditions

Finally, we have to construct the approximate solutions. We have discussed the problem related to the time development of the penetration depths, so in the sequel, we will stress attention only to the approximate solution with logistic function in the time-dependent boundary conditions. In this case, the approximate solution is

$$S_3(t) = \frac{1}{1+e^{-kt}}\left(1 - \frac{x}{\sqrt{D_0 t}}\frac{1}{\left[\sqrt{\frac{1}{\sqrt{\varphi}\left(1+\sqrt{\varphi}\right)}}\sqrt{(n+1)(n+2)}\sqrt{2}\sqrt{\frac{\ln\left(\frac{1+e^{-kt}}{2e^{-kt}}\right)}{kt}}\right]}\right)^n \tag{87}$$

or as

$$S_3(t) = \frac{1}{1+e^{-kt}}\left(1 - \frac{\eta}{\left[\sqrt{\frac{1}{\sqrt{\varphi}\left(1+\sqrt{\varphi}\right)}}\sqrt{(n+1)(n+2)}\sqrt{2}\sqrt{\frac{\ln\left(\frac{1+e^{-kt}}{2e^{-kt}}\right)}{kt}}\right]}\right)^n \tag{88}$$

We cannot express the solution only as a function of the Boltzmann similarity variable $\eta = \frac{x}{\sqrt{D_0 t}}$ since there are two time-dependent terms which both for large times approach unity. In such a case, only profiles in terms of the physical variables x and t are possible.

The plots in Figs. 8 and 9 show that the saturation profiles are concave in shape irrespective of the non-linearity of the problem solved. The normalized saturation profiles $S(t)/S_0(t)$ are similar irrespective of the relaxation function at the boundary $x = 0$. From these plots, we can see that the penetration depths for lower porosity (see Fig. 9a with $\varphi = 0.25$) are longer than when the medium porosity is higher

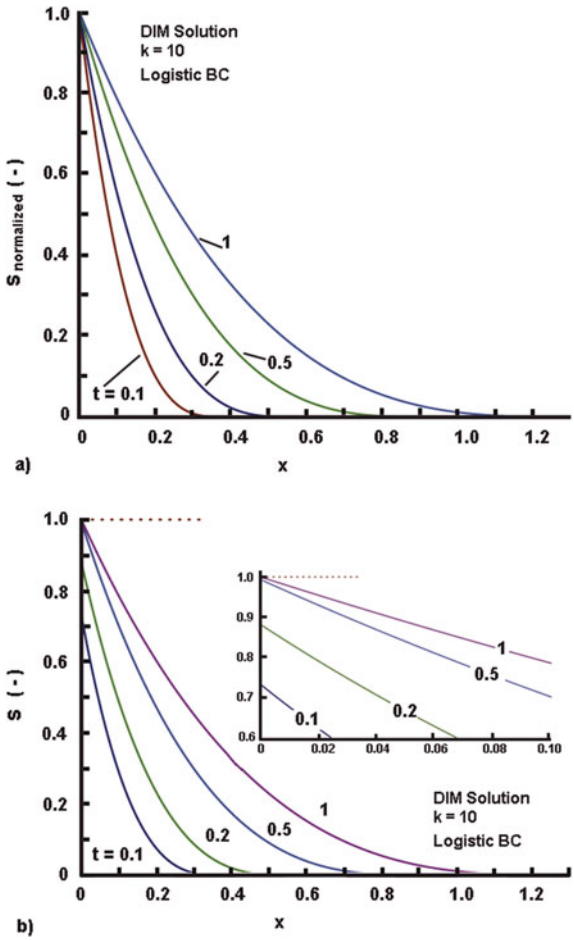

Fig. 9 Approximate solutions (saturation profiles) with a logistic function as a relaxing boundary condition along the x axis for various times: **a** Normalized profiles where $S_{normalized} = S(t)/S_{logistic}$; **b** Non-normalized profiles; Inset: the behaviours close to the interface showing the unsaturated solid (wood) surface at $x = 0$. *Note* Calculations performed with a porosity $\varphi = 0.5$, $D_0 = 1$ and $n = 3$

(see Fig. 9a with $\varphi = 0.5$).This fact has to be attributed to the reciprocal relationship between the capillary pressure and medium porosity (see Fig. 2 and the comments related to it). It is worth noting that the approach to relaxing boundary conditions adequately models (see Figs. 9b and 10b) the behaviour of real systems modelled as it is confirmed by the results of Kowalski et al. [7] which is shown schematically in Fig. 11.

It is obvious that surface saturation is a slow process needing hundreds of hours upon realistic circumstances. It is important to mention that the present work considers the diffusivity D_0 with dimension m^2/s which means the time is measured in seconds. This is correct, but we have to mention that the diffusivities of highly viscous fluids (such as the methacrylate used by Kowalski et al. [7] in low porous woods are extremely low and therefore it is more convenient to use a dimension m^2/h which leads to time measured in hours (as in Fig. 11). Kowalski's results strongly

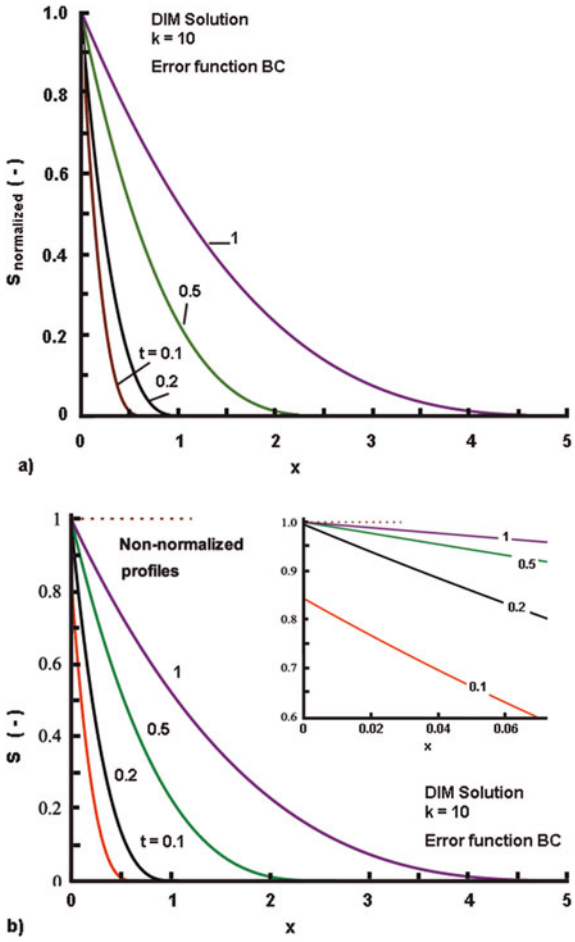

Fig. 10 Approximate solutions (saturation profiles) with error function as a relaxing boundary condition along the x axis for various times: **a** Normalized profiles where $S_{normalized} = S(t)/S_{errorfunction}$; **b** Non-normalized profiles; Inset: the behaviours close to the interface showing the unsaturated solid (wood) surface at $x = 0$. *Note* Calculations performed with a porosity $\varphi = 0.25$, $D_0 = 1$ and $n = 3$

indicate that even after 800 h (not presented here but available in Fig. 5a of [7]), the solid-surface interface remains unsaturated (i.e. with $S < 1$ at $x = L$ in Fig. 10). This once again confirms the adequacy of the approach with the relaxing Dirichlet boundary conditions (the term coined here) instead of the boundary condition (7) to cases when the penetration of the diffusant already reached the symmetry axis of the slab *while the solutions developed here consider only the initial stages of fluid diffusion process when* $\delta(t) < L$.

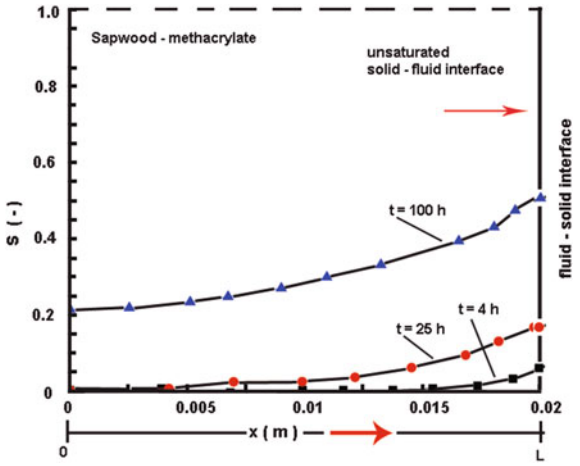

Fig. 11 Wood penetration in a stagnant fluid (methacrylate) by the mechanism of capillary suction: Results based on the solution of Kowalski et al. (Fig. 5a in [7]). *Note* The plot corresponds to the configuration shown in Fig. 1; the points correspond to the solution in [7] but the lines show only the tendency in the profile spatial development

4 Final Comments

This chapter addressed a non-linear diffusion model of a practically high relevant process of special wood treatment by liquids and polymers thus developing new wood-based materials achieving properties answering many new requirements in the modern technological world.

The starting point is the mode developed by Kowalski et al. [7] but, in general, this is a parabolic equation from the class of fast diffusion models with reciprocal diffusivities, or in other words with Fujita's concentration-depended diffusion coefficients. The model was analysed and the available solution [8] was analysed. Moreover, the boundary condition used was critically discussed from the point of view of its physical adequacy.

The approximate solutions developed here address the physical fact that the real processes of wood impregnation take place in infinite baths of fluids and therefore the Dirichlet boundary condition is more adequate rather than the flux boundary condition suggested in [7, 8]. However, taking into account the experimental results in [7] it was suggested that the classical Dirichlet boundary condition with a unit step of the saturation at the fluid-solid interface is also a mathematical approximation that conflicts with reality since there is no infinite speed of the wood surface saturation. This point of view resulted in the concept of time-relaxing Dirichlet boundary conditions. Precisely, this concept envisages a kinetic approach to the wood interface saturation where the complete Dirichlet boundary condition is attained for long times.

The approximate solutions developed reveal that when relaxing boundary conditions are employed, the final behaviour of the saturation profiles is more physically adequate and corresponds to the real observations in [7]. Moreover, the concept of relaxing boundary conditions approaching the unit steps at the solid-fluid interface is more general and allows formulating physically relevant boundary conditions not

only for the present case of wood impregnation but also for any other processes such as adsorption or absorption and surfactant adherence of surfactants on solid surfaces.

Last but not the least, it is important to mention that the calculations were performed with stipulated values of the exponent n. This makes the solutions qualitative, but highly informative because the next step addressing determining the optimal values of the profile exponent is a more complicated procedure that is beyond the scope of this study.

References

1. Rydholm SA (1965) Pulping processes. Interscience Publishers, New York
2. Siau JF (1984) Transport processes in wood. Springer, Berlin
3. Siau JF (1985) Nonisothermal moisture diffusion experiments analysed by four alternative equations. Wood Sci Technol 19:151–157
4. Sucoff EI, Chen PYS, Hossfeld RL (1965) Permeability of unseasoned xylem of northern white cedar. For Prod J 15:321–324
5. Kuroda N, Siau JF (1988) Evidence of nonlinear flow in softwoods from wood permeability measurements. Wood Fiber Sci 20:162–169
6. Siau JF, Petty JA (1979) Corrections for capillaries used in permeability measurements of wood. Wood Sci Technol 13:179–185
7. Kowalski SJ, Musielak G, Kyziol L (2002) Non-linear model for wood saturation. Transp Porous Media 46:77–89. https://doi.org/10.1023/A:1013875229939
8. Fokas AS, Rogers C, Schief WK (2005) Evolution of methacrylate distribution during wood saturation. Appl Math Lett 18:321–328. https://doi.org/10.1016/j.aml.2004.05.006
9. Rogers C (1985) Application of a reciprocal transformation to a two phase Stefan problem. J Phys A 18:L105–L109. https://doi.org/10.1088/0305-4470/18/3/002
10. Rogers C (1986) On a class of moving boundary problems in nonlinear heat conduction: application of a Backlund transformation. Int J Non-linear Mech 39:122–128. https://doi.org/10.1016/0020-7462(86)90032-6
11. Fujita H (1952) The exact pattern of a concentration-dependent diffusion in a semi-infinite medium. Part I. Text Res J 22:757–760. https://doi.org/10.1177/004051755202201106
12. Fujita H (1952) The exact pattern of a concentration-dependent diffusion in a semi-infinite medium. Part II. Text Res J 22:823–827. https://doi.org/10.1177/004051755202201209
13. Fujita H (1954) The exact pattern of a concentration-dependent diffusion in a semi-infinite medium. Part III. Text Res J 4:234–240. https://doi.org/10.1177/004051755402400304
14. Rogers C, Broadbridge P (1988) On a nonlinear moving boundary problem with heterogeneity: application of a reciprocal transformation. ZAMP 39:122–128. https://doi.org/10.1007/BF00945727
15. Broadbridge P (1988) Integrable forms of one-dimensional flow equation for unsaturated heterogeneous porous media. J Math Phys 29:622–627. https://doi.org/10.1063/1.528001
16. Storm ML (1951) Heat conduction in simple materials. J Appl Phys 22:940–951. https://doi.org/10.1063/1.1700076
17. Rosen G (1979) Nonlinear heat conduction in solid. Phys Rev B 19:2398–2399. https://doi.org/10.1103/PhysRevB.19.2398
18. Rosen G (1983) Reciprocal transformation for one-dimensional conservation equation. J Math Phys 24:793–794. https://doi.org/10.1063/1.525751
19. Bluman G, Kumei S (1980) On the remarkable nonlinear diffusion equation $(\partial/\partial x)\left[(u+b)^{-2}(\partial u/\partial x)\right]-(\partial/\partial t)=0$. J Math Phys 21:1019–1023. https://doi.org/10.1063/1.524550

20. Hristov J (2019) A new closed-form approximate solution to diffusion with quadratic Fujita's non-linearity: the case of diffusion controlled sorption kinetics relevant to rectangular adsorption isotherms. Heat Mass Transf 55:261–279. https://doi.org/10.1007/s00231-018-2408-1
21. Hristov J (2018) On the integral-balance solvability of the nonlinear Mullins model. In: Ghosh D, Giri D, Mohapatra R, Sakurai K, Savas E, Som T (eds) Mathematics and computing. ICMC 2018. Springer proceedings in mathematics and statistics, vol 253. Springer, Singapore, pp 53–66. https://doi.org/10.1007/978-981-13-2095-8
22. Goodman TR (1964) Application of integral methods to transient nonlinear heat transfer. In: Irvine TF, Hartnett JP (eds) Advances in heat transfer, vol 1. Academic Press, San Diego, CA, pp. 51–22. https://doi.org/10.1016/S0065-2717(08)70097-2
23. Hristov J (2009) The heat-balance integral method by a parabolic profile with unspecified exponent. Analysis and benchmark exercises. Thermal Sci 13:27–48. https://doi.org/10.2298/TSCI0902027H
24. Hill JM (1989) Similarity solutions for nonlinear diffusion—a new integration procedure. J Eng Math 23:141–155 (1989). https://doi.org/10.1007/BF00128865
25. Prasad SN, Salomon JB (2005) A new method for analytical solution of a degenerate diffusion equation. Adv Water Res 28:1091–1101. https://doi.org/10.1016/j.advwatres.2005.04.005
26. Hristov J (2016) Integral solutions to transient nonlinear heat (mass) diffusion with a power-law diffusivity. A semi-infinite medium with fixed boundary conditions. Heat Mass Transf 52:635–655. https://doi.org/10.1007/s00231-015-1579-2
27. Hristov J (2015) Approximate solutions to time-fractional models by integral balance approach. In: Cattani C, Srivastava HM, Yang X-J (eds) Fractional dynamics. De Gruyter Open, pp 78–109. https://doi.org/10.1515/9783110472097-006
28. Crank J, Park GS (1949) An evaluation of the diffusion coefficient for chloroform in polystyrene from simple absorption experiments. Trans Faraday Soc 45:240–249
29. Crank J, Park GS (1951) Diffusion in high polymers. Some anomalies and their significance. Trans Faraday Soc 47:1072–1084
30. Crank J (1979) The mathematics of diffusion, 2nd edn. Clarendon Press, Oxford , UK
31. Mitchell SL, Myers TG (2010) Application of standard and refined heat balance integral methods to one-dimensional Stefan problems. SIAM Rev 52:57–86.https://doi.org/10.1137/080733036
32. Hristov J (2019) A new closed-form approximate solution to diffusion with quadratic Fujita's non-linearity: the case of diffusion controlled sorption kinetics relevant to rectangular adsorption isotherms. Heat Mass Transf 55:261–279. https://doi.org/10.1007/s00231-018-2408-1
33. Hristov J (2013) A Note on the integral approach to non-linear heat conduction with Jeffrey's fading memory. Therm Sci 17:733–737. https://doi.org/10.2298/TSCI120826076H
34. Hristov J (2016) Transient heat diffusion with a non-singular fading memory: from the Cattaneo constitutive equation with Jeffrey's kernel to the Caputo-Fabrizio time-fractional derivative. Therm Sci 20:765–770. https://doi.org/10.2298/TSCI160112019H
35. Hristov J (2017) Derivation of fractional Dodson's equation and beyond: transient mass diffusion with a non-singular memory and exponentially fading-out diffusivity. Progr Fract Differ Appl 3:255–270.https://doi.org/10.18576/pfda/030402
36. Hristov J (2019) Bio-heat models revisited: concepts, derivations, nondimensalization and fractionalization approaches. Front Phys 2019. https://doi.org/10.3389/fphy.2019.001897:189
37. King JR, McCabe PM (2003) On the Fisher-KPP equation with fast nonlinear diffusion. Proc R Soc Lond A 459:2529–2546. https://doi.org/10.1098/rspa.2003.1134
38. Philip JR (1995) Fast diffusion with loss at infinity. J Austral Math Soc Ser B 36:438–459. https://doi.org/10.1017/S0334270000007487

Algorithmic Complexity-Based Fractional-Order Derivatives in Computational Biology

Yeliz Karaca and Dumitru Baleanu

Abstract Fractional calculus approach, providing novel models through the introduction of fractional-order calculus to optimization methods, is employed in machine learning algorithms. This scheme aims to attain optimized solutions by maximizing the accuracy of the model and minimizing the functions like the computational burden. Mathematical-informed frameworks are to be employed to enable reliable, accurate, and robust understanding of various complex biological processes that involve a variety of spatial and temporal scales. This complexity requires a holistic understanding of different biological processes through multi-stage integrative models that are capable of capturing the significant attributes on the related scales. Fractional-order differential and integral equations can provide the generalization of traditional integral and differential equations through the extension of the conceptions with respect to biological processes. In addition, algorithmic complexity (computational complexity), as a way of comparing the efficiency of an algorithm, can enable a better grasping and designing of efficient algorithms in computational biology as well as other related areas of science. It also enables the classification of the computational problems based on their algorithmic complexity, as defined according to the way the resources are required for the solution of the problem, including the execution time and scale with the problem size. Based on a novel mathematical informed framework and multi-staged integrative method concerning algorithmic complexity, this study aims at establishing a robust and accurate model reliant on the combination of fractional-order derivative and Artificial Neural Network (ANN) for the diagnostic and differentiability predictive purposes for the disease, (diabetes, as a metabolic disorder, in our case) which may display various and transient biological properties. Another aim of this study is benefitting from the concept of algorithmic complexity to obtain the fractional-order derivative with the least complexity in order that it would

Y. Karaca (✉)
University of Massachusetts Medical School (UMASS), Worcester, MA 01655, USA
e-mail: yeliz.karaca@ieee.org

D. Baleanu
Department of Mathematics, Çankaya University, 1406530 Balgat, Ankara, Turkey
e-mail: dumitru@cankaya.edu.tr

Institute of Space Sciences, Magurele–Bucharest R 76900, Romania

J. Singh et al. (eds.), *Advances in Mathematical Modelling, Applied Analysis and Computation*, Lecture Notes in Networks and Systems 415,
https://doi.org/10.1007/978-981-19-0179-9_3

be possible to achieve the optimized solution. To this end, the following steps were applied and integrated. Firstly, the Caputo fractional-order derivative with three-parametric Mittag-Leffler function ($\alpha,\ \beta,\ \gamma$) was applied to the diabetes dataset. Thus, new fractional models with varying degrees were established by ensuring data fitting through the fitting algorithm Mittag-Leffler function with three parameters ($\alpha,\ \beta,\ \gamma$) based on heavy-tailed distributions. Following this application, the new dataset, named the mfc_diabetes, was obtained. Secondly, classical derivative (calculus) was applied to the diabetes dataset, which yielded the cd_diabetes dataset. Subsequently, the performance of the new dataset as obtained from the first step and of the dataset obtained from the second step as well as of the diabetes dataset was compared through the application of the feed forward back propagation (FFBP) algorithm, which is one of the ANN algorithms. Next, the fractional order derivative model which would be the most optimal for the disease was generated. Finally, algorithmic complexity was employed to attain the Caputo fractional-order derivative with the least complexity, or to achieve the optimized solution. This approach through the application of fractional-order calculus to optimization methods and the experimental results have revealed the advantage of maximizing the model's accuracy and minimizing the cost functions like the computational costs, which points to the applicability of the method proposed in different domains characterized by complex, dynamic and transient components.

Keywords Computational complexity · Complex systems · Fractional calculus and complexity · Fractional-order derivatives · Caputo fractional-order derivative · Classical derivatives · Mittag-Leffler functions · Integer-order derivatives · Computational and nonlinear dynamics · Mathematical biology · Dynamic biological models · Data analysis · Data fitting · Uncertainty · Nonlinearity · Neural networks · Multilayer perceptron algorithm · Data-driven fractional biological modeling

1 Introduction

Complex systems, characterized by order and homogeneity, hierarchy of subsystems and different levels both in time and space, entail the observation of the interplay regarding various multiple biological elements including tissues, cells, molecules and human body. Given this complexity, it is not sufficient to identify and characterize the individual biological components in the system merely. Thus, in order to have a complete grasping of the multiple and emergent interactions between biological components and their respective pathways, mathematical modeling plays an important role for the solution of complex problems and the application to biological data so that the correlations between different observable phenomena can be revealed accurately. Besides such advantage to address the challenges like heterogeneity, being dynamic and having intricate characteristics, inherent in complex systems, mathematical models also allow researchers to explore the degree of com-

plexity related to processes and the way they are interconnected. Innovative thinking of modern science enables the interpretation of natural and physical phenomena via optimized models for the complex systems' analysis while exerting control for the related emergent and transient behaviors. Mathematical-informed frameworks are employed to provide researchers with accurate, reliable and robust understanding. At this point, fractional-order differential and integral equations procure the generalization of traditional integral and differential equations through the extension of the conceptions with respect to various biological phenomena. Hinting all non-integer numbers, which include irrational numbers, complex numbers as well as fractions, "fractional" shows and directs the "fractional view" to gain insights into natural phenomena [1, 2]. Proficiency in computational complexity provides a sophisticated, multifarious and integrative outlook to problems; that is the reason why applicable sets of ideas and implementations are put into real life to identify complex dynamic systems' subtle properties. One important aspect therein is to accept the varying degrees of problems so that the models can be constructed in a manner, which can adjust and fit the matter into the right data, which is another challenge in numerical and experimental analyses addressed in various domains including neuroscience [3], biology [4] and so forth.

Biological problems and phenomena, which are modeled by ordinary or partial differential equations with integer-order, can be described well by using ordinary and partial differential equations. At each time instance, the correct information can be measured through a non-integer order derivative; yet, one challenge might be related to the expression of the dynamics between two different points if the derivative is in the integer-order. Furthermore, due to having description of memory and also heredity-related properties, fractional derivatives display another difficulty. It is, therefore, acknowledged that compared to classical derivatives, fractional derivative may yield more useful information for the models related to biological diseases. Being the pillar of different systems in engineering and science, fractional differential equations are seen in a broad range of disciplines such as mathematical biology, physics, engineering, finance, biomechanics, control theory, circuit analysis, to name some. Any biological phenomenon is inherently characterized by uncertainty and nonlinearity; and thus, the variables, parameters, attributes, observation states as well as initial conditions in the model are required for computational purposes. When incomplete, imprecise or vague elements are existent with regard to parameters and variables, then errors are inevitably seen in observations, experiments, applications of different operating conditions or another case is maintenance-induced errors that are also uncertain in nature. The introduction of such uncertainties is conducted through fractional-order differential equations as defined in the Caputo sense to attain reliable, applicable and efficient techniques for the solution thereof.

Fractional Calculus (FC), a swiftly advancing discipline of mathematics with broad application domains (i.e. applied sciences, computer science, medical, ecological, physical, biological in addition to electricity [5–8]), refers to the calculus of derivatives and integrals of arbitrary complex order or real order. FC, therefore, provides the noteworthy and viable means to solve integral, differential and integro-differential equations [9, 10]. As a part of mathematics, fractional-order

calculus (FOC) addresses derivatives and integration of arbitrary order. For the solution of various fractional-order biological disease models in uncertain environments, there are different studies in the literature. Concerning the analytical investigation of fractional-order biological model, [11] addresses the implementation of iterative Laplace transform method for the solution of population models of non-integer order. The authors applied the Caputo operator to express the non-integer derivative of fractional order. The method suggested by the authors is stated to have a small volume of calculations, which allows its application to manage the various problems' solutions with fractional-order derivatives. Another study, namely [12], within the mathematical modeling of biological systems framework, explores the pathological behavior of HIV in fractional sense and the model proposed is investigated with three different fractional operators. Through the efficient numerical method proposed for the solutions of the related equations, the models presented are said to have the potential for the extraction of the new hidden features of biological systems. The new models provided on the basis of the three operators reveal asymptomatic behaviors, which do not seem during the modeling with integer-order derivatives; thus, the significance of fractional calculus is put forth due to its provision of more precise models of biological systems, allowing more realistic judgments concerning complex dynamics. Sajjadi et al. [13] is another study that handles chaos control and synchronization of a biological snap oscillator. By designing adaptive and optimal controllers, the authors attempted to overcome hyperchaotic behaviors, by compensating the undesirable hyperchaotic behaviors. The study introduces an adaptive control scheme for the synchronization of two identical snap oscillators. The development of a new fractional model is also presented in that study where efficient control strategies were employed in fractional sense to do controlling and synchronization effectively. Singh et al. [14] develop a fractional guava fruit model with memory effect and stability of the fractional model is discussed, besides the examination of existence and uniqueness of the solution by using Picard Lindelof approach. The study puts forth the importance of fractional operators through the consideration of a fractional guava fruit model that involves a non-local additionally non-singular fractional derivative regarding the interaction into guava pests and natural enemies. The approximate numerical solution of the fractional guava fruit problem is obtained by one numerical scheme suggested which is said to be efficient in terms of solving nonlinear fractional models of physical importance. With its peculiar complexity features, FOC reflects natural behavior relatively accurately in various areas (bioengineering [15], biology [16], electronics [17], image processing [18], control theory [19], robotics [20, 21] and signal processing [22], as well as viscoelasticity [23]).

Mittag-Leffler functions with one, two and three parameters due to the various applications in fractional calculus and fractional differential equations can be prone to modification on complex plane with the extension of certain fractional-calculus operators. In the literature, [24] provides the way Atangana-Baleanu and Prabhakar operators are applied to find fractional derivatives besides the functions' integrals concerning complex variables. Likely, differing numerical techniques are used along with the algorithms the Mittag-Leffler function's numerical evaluation,

$E_{\alpha,\beta}(z) = \sum_{k=0}^{\infty} \frac{z^k}{\Gamma(\beta+\alpha k)}$, $\alpha > 0,\ \beta \in R, z \in C$, and its derivative belonging to the parameters' each value $\alpha > 0,\ \beta \in R$ [25]. Dynamic models reflect a system's temporal aspects through a convenient memory function, resulting in the Mittag-Leffler waiting time renewal process and rendering the Mittag-Leffler function essential. Concerning data applications in the related scope, the study [26] addresses the characterization of anomalous diffusion and application of continuous time random walk (CTRW) theory to diffusion MRI. The authors introduced the CTRW parameters (α *and* β) and entropy as the biomarkers for diffusion in biological tissues. In the CTRW approach presented in the study, the Fourier transform generates a solution to the generalized diffusion equation which is to be expressed by the Mittag-Leffler function (MLF). While fitting the data to their model, the fractional-order parameters, α *and* β, along with the entropy measure, $H(q, \bar{\Delta})$, were found to provide good contrast between white and gray matter, with results yielded sensitive to the type of diffusion experiment conducted. Jose and Abraham [27] introduces a new generalized counting process with Mittag-Leffler inter-arrival time distribution. The model proposed is a generalization of the Poisson process and the authors overcome the computational intractability through the derivation of the Mittag-Leffler count model by employing polynomial expansion. Markov Chain Monte-Carlo (MCMC) methods, using Metropolis-Hastings algorithm, were utilized for the simulation new count model can be simulated. Another work [28] aims at the exploration a COVID-19 SEIR model that involves Atangana-Baleanu-Caputo type (ABC) fractional derivatives. Besides establishing existence, uniqueness, positivity as well as boundedness of the alternative model's solutions, the authors also present the stability results of the system proposed in their study. Furthermore, [25] is a study that investigates a new model based on COVID-19 with three compartments that involve susceptible, infected, and recovered class under the Mittag-Leffler type derivative. A scheme is also developed for the approximate solutions to the model considered through the application of a numerical technique named fractional Adams-Bashforth (AB) method. The study involves the use of some real data available and the authors conduct the numerical simulation that corresponds to different values of fractional order. Sher et al. [29] deals with COVID-19 through the consideration of a fractional-order epidemic model describing the disease's dynamics under non-singular kernel type of the fractional derivative. The fixed point theorem of Banach and Krasnoselskii's type is discussed, and the simulated results are compared with some of the real data reported for commutative class at classical order.

Making predictions based on mathematical models concerning biological processes and datasets necessitates the estimation of parameters step for the model's simulation. Thus, fitting parameters to experimental data is regarded as a challenge due to the fact that finding the model parameters' optimal values could require the exploration of a huge space while the model parameters' different values may display consistency with the data, known as identifiability problem accordingly, [30, 31] deal with the related problematic aspects in systems biology through different approaches. As for the algorithm, maintaining the best fit to the data as much as possible is important while eliminating the parameters from the model in a manner that will not impact the optimal fit, which means that there has to be a trade-off between goodness of

fit and model complexity as measured by the function of likelihood. Kiiveri [32], to illustrate, provides comparison with support vector machines and random forests. The advantage of variable selection and parameter estimation is at stake without any extra steps required to obtain a sparse model. Another important point regarding data fitting is that parameters may not have any biological meaning if the model selected is not informative. Concerning this point, [33] states that model parameters fit to biological processes have to be stable; whereas transferability of parameters is proposed by [34] for utility purposes with a high level and biological significance. To recap, goodness of fit and biologically meaningful parameters in model selection can ensure the identification of an effective model with a model selection process considering only the best fit. Adams et al. [34] point out this aspect in thermal optima and maxima, demonstrating that the biologically meaningful parameters have the facilitating function. Zhao et al. [35] also address the clustering challenge in big medical and biological datasets by developing a three-topic model-derived clustering methods, showing the application benefit of topic modeling as well as an analytic enhancement of the topic model-based methods. Albrecher et al. [36] define the class of matrix Mittag-Leffler distributions, studying some of its properties. The authors demonstrate that it can be interpreted as a specific case of an inhomogeneous phase-type distribution with random scaling factor and as the absorption time of a semi-Markov process with Mittag-Leffler distributed interarrival times. Both simulated data and a set of real-life data modeled differently in the previous times are used in the study.

Being credited as a natural mathematical model for power-law relations, fractional calculus, enables the observation of related links as accurate descriptors regarding natural phenomena. The application of fractional calculus to artificial neural networks (ANNs) provides significant advantages by providing the augmentation of a neural network (NN) through the implementation of differintegral operation based on fractional calculus to the data stream via each of the neurons in the neural network. It is, thus, possible to achieve achieved fitness, behavioral differences as well as related simulation-specific metrics through the related experimental processes. Fractional calculus approach to machine learning provides a novel method through the introduction of fractional-order calculus to optimization methods as employed in machine learning algorithms. It is, therefore, intended to maximize the model's accuracy and minimize the cost functions like the computational costs. Including ANNs, in all the machine learning algorithms, learning is a crucial step with respect to accuracy or convergence rate, obtained potentially by the use of fractional-order gradient in the area of data science. One of the related studies, [37], uses a model of a neural network with a new backpropagation rule employing a fractional-order derivative mechanism. The proposed scheme, by using the Grünwald–Letnikow definition of the discrete approximation of the fractional derivative, employs the fractional derivative mechanism to model the individual neurons' dynamics and to minimize the error function least. The network model proposed in the study is a new tool that could be utilized in the classification tasks of signals. One other study [38] has the aim of investigating the handling of the fractional vibration problem utilizing the multilayer artificial neural network (ANN) method. Fractional derivatives yield better models regarding the vibration systems in contrast with classical integer-order

models. The authors employed multilayer feed-forward neural architecture and error back-propagation algorithm with unsupervised learning to minimize error function as well as to modify the parameters (weights and biases). Kadam et al. [39] deal with ANN approximation of fractional derivative operators. The input-output data of Grünwald–Letnikov as well as Caputo fractional derivatives for a range of functions such as power law type, sinusoidal, ramp and Mittag-Leffler functions are used for the training of multilayer ANNs. Last but not least, based on the ANNs based on fractional calculus, [40, 41] propose a fractional-order deep backpropagation neural network model with L_2 regularization. The authors optimize the proposed network by the fractional gradient descent method with Caputo derivative while showing the required conditions for the convergence of the network proposed. The influence of L_2 regularization on the convergence is analyzed with the fractional-order variational method. The experiments performed on the dataset demonstrate that the proposed network is deterministically convergent and capable of avoiding overfitting in an effective way.

The conceptual aspects of algorithms and complexity become meaningful provided that they are defined in terms of formal computational models [42]. Computing is essential to address intensive data tasks and attain scalable solutions to complex problems. Therefore, it is important for researchers and developers to be cognizant of effects of computational complexity and its theory for better grasping and designing of efficient algorithms in computational biology. Given that, it is possible to classify the computational problems depending on their algorithmic complexity defined according to the way the resources required for the solution of the problem, including the execution time and scale with the problem size. Algorithmic complexity, called complexity or running time, is a way of comparing an algorithm's efficiency. For a particular task, an algorithm completing a task is regarded as more complex if more steps are involved. Varying in relation to the size of the input, complexity can be expressed with the Big O notation. Thus, complexity can be measured with regard to the time it takes for a program to run in relation to the size of the input, which is referred to as time complexity, or with regard to the memory it will take up, called space complexity. In computational biology, the investigation of algorithmic complexity provides guidance with regard to the application of efficient programs to process, model and analyze biological data [43]. Algorithmic complexity theory from the computer science perspective enables an individual to examine algorithms' properties to solve computational problems as well as the relationship between the size of an instance of the generic problem and the time needed for computation [44].

Based on a novel mathematical informed framework and multi-staged integrative method concerning algorithmic complexity, no earlier work exists equivalent to this study in the literature [32–44], as derived from such a holistic perspective with the methods proposed. The preliminary objective of this study is to establish a robust and accurate model based on the combination of fractional-order derivative and Artificial Neural Network (ANN) for the diagnostic and differentiability predictive purposes for the diseases (diabetes dataset in our case) which may display various and transient biological properties. In addition, we have also aimed to benefit from the concept of algorithmic complexity in order to obtain the fractional-order

derivative with the least complexity so that it could be possible to reach the optimized solution. To this end, we implemented the following steps: (i) The Caputo fractional derivative was applied with three-parametric Mittag-Leffler function to the diabetes dataset. In this way, new fractional models with varying degrees were established by ensuring data fitting through the Fitting algorithm Mittag-Leffler function with three parameters (α, β, γ) based on Heavy-tailed distributions. (By applying Algorithm 1 (Fitting algorithm Mittag-Leffler function with three parameters (α, β, γ) based on Heavy-tailed distributions.) to the diabetes dataset, in order to identify the optimized three-parametric ML function, ML (α, β, γ) parameters that fit the data were found with heavy-tailed distributions. Thus, the optimized ML (α, β, γ) functions were obtained. In other words, this application allowed us to find the best fitting Mittag-Leffler function with three parameters (α, β, γ) in the diabetes dataset). The reason and motivational aspect behind the choosing of the Mittag-Leffler function is that this function directs the distributions of broad application areas, which makes it possible to address irregular and heterogeneous environments for the dynamic problems' solution. Following this particular application, the new dataset, named mfc_diabetes, was obtained. (ii) Classical derivative (calculus) was applied to the diabetes dataset (namely the raw dataset); and accordingly, the cd_diabetes dataset was obtained. (iii) The performance of the new dataset as obtained from the Caputo fractional-order derivative with the three-parametric Mittag-Leffler function (based on step i), the dataset obtained from the classical derivative (calculus) application (based on step ii) and the diabetes dataset (ie: raw dataset) was compared through the application of the feed forward back propagation (FFBP) algorithm, which is among the ANN algorithms (along with accuracy rate, sensitivity, precision, specificity, F1 score, multiclass classification (MCC), ROC curve). Consequently, the fractional-order derivative model that would be the most optimal for the disease was generated, which makes up another motivational and novel aspect of the method proposed in our study. (iv) We benefited from the concept of algorithmic complexity to attain the Caputo fractional-order derivative with the least complexity, in other words, to achieve the optimized solution. This approach through the application of fractional-order calculus (FOC) to optimization methods has the advantage of maximizing the model's accuracy and minimizing the cost functions like the computational costs. Thus, algorithmic complexity was computed with the application of Caputo fractional-order derivative with three parametric Mittag-Leffler function and classical derivative (calculus) in a comparative way by identifying the complexity for each concerning the diabetes dataset. As a result, the derivatives with the highest and lowest level of complexity were identified with Big O. The experimental results obtained from our integrative and multi-stage approach corroborate the applicability of the scheme proposed through this study by revealing the Caputo fractional-order derivative with the least complexity yielded the best outcome based on the output derived from the ANN algorithm (FFBP).

The remainder parts of the study are outlined as follows. Section 2 is concerned with Biological Dataset and Methodology, with Sect. 2.1 on Diabetes Dataset and Sect. 2.2 methodology dealing with Mittag-Leffler Functions with Heavy-tailed distributions' Algorithm for Data Fitting Purposes, Caputo Fractional-order Deriva-

tives, Artificial Neural Networks Algorithm as well as Algorithmic (Computational) Complexity. Section 3 is entitled Experimental Results and Discussion. Finally, the last section, which is to say Sect. 4, presents the Conclusion, Outcomes and Future Directions of our study.

2 Biological Dataset and Methodology

2.1 Diabetes Dataset

The accurate interpretation of data is important for a complete understanding emerging properties resulting the interplay of multiple biological elements in complex biological systems. Therefore, it would not be adequate to characterize only the individual biological components in the system. Thus, accurate and appropriate mathematical modeling plays an important role to serve the investigation of problems since mathematical models enable us to explore how complexity processes and disruptions related to these processes influence the disease. This study addresses one biological dataset, diabetes, with dynamic, heterogeneous, and complex characteristics that are common diseases that need to be taken under meticulous control so that detrimental effects would not be the case for the future.

For the classification and prediction of diabetes disease, the variables of Underweight (18.5–), Healthy (18.5–25), Overweight (25–30) or Obese (30+) are taken into consideration on the body mass indices of the related individuals. As per this variable code interval, the insulin values ranging from 16 to 166 are accepted to be normal, whereas the values out of this interval are regarded as not normal. Moreover, the glucose values are taken as Low (70–), Normal (70–99), Secret (99–126) and High (126–200) for the classification (see Table 1 for the details of the diabetes dataset) [45].

2.2 Methodology

2.2.1 Mittag-Leffler Functions with Heavy-Tailed Distributions' Algorithm for Data Fitting Purposes

Mittag-Leffler functions with three parameters

Special function is one of the domains of mathematical analysis, associated with different topics like fractional calculus, differential equations and mathematical physics [44]. With its extensions, Mittag-Leffler function is among the noteworthy classes of special functions [45]. Due to the connections to fractional calculus, and fractional exponential functions, arising in solutions for the different fractional differential equations, they are known to be useful [46, 47].

Table 1 Diabetes dataset with attributes computed in unit

Diabetes classification	Attributes (units)
0 = Non-diabetes 1 = Diabetes	**Body mass index (BMI)** (weight in kg/(height in m)^2) **Age** (years) **Diastolic blood pressure** (mm Hg) **Skin thickness** Triceps skin fold thickness (mm) **Insulin** 2-h serum insulin (mu U/ml) **Number of pregnancy** **Diabetes pedigree function** (a function that calculates the probability that an individual may be afflicted with diabetes based on the genetic disposition) **Plasma glucose** (Concentration a 2-h interval in an oral glucose tolerance test)

* Dataset size: (768 × 9)

The original function of Mittag-Leffler $E_\alpha(z)$ depends on one single variable z nd one parameter α, described as per Eq. 1 [48].

$$E_\alpha(z) = \sum_{n=0}^{\infty} \frac{z^n}{\Gamma(n\alpha+1)'} \quad \alpha > 0, z \in C \tag{1}$$

Different ways are the case to extend this definition, the most known extensions are the functions. $E^{\gamma}_{\alpha,\beta}(z)$, being reliant upon variable z and three parameters with definitions as stated below [49, 50].

$$E^{\gamma}_{\alpha,\beta}(z) = \sum_{n=0}^{\infty} \binom{-\gamma}{n} \cdot \frac{(-z)^n}{\Gamma(n\alpha+\beta)} = \sum_{n=0}^{\infty} \frac{\Gamma(\gamma+n)}{\Gamma(\gamma)\Gamma(n\alpha+\beta)} \cdot \frac{z^n}{n!} \quad \alpha, \beta, \delta > 0, z \in C \tag{2}$$

Heavy-Tailed Distributions

Mittag-Leffler distribution

Denoted as $E_\alpha(y)$, Mittag-Leffler function was defined by Pillai [51], stating its dependence upon the distribution function or cumulative density function (cdf), indicated according to Eq. 3 [52].

$$f\,(x;\alpha) = 1 - E_{\alpha}\,(-y^{\alpha}) = \sum_{k=1}^{\infty} (-1)^{k-1} \frac{(k\alpha).x^{k\alpha-1}}{\Gamma(\alpha k+1)}, \quad \mathrm{x} > 0, 0 < \alpha \leq 1 \tag{3}$$

As a heavy-tailed distribution, Mittag-Leffler $\alpha = 1$, reduction to exponential distribution is conducted with mean 1. It is addressed as the exponential distribution's generalization. References [53–55] have addressed the varying characteristics of this distribution, proposing a class of discrete Mittag-Leffler distribution with the function of producing probability $(pgf)\ P\,(z) = E\,(X^{z}) = 1/\left[1 + c(1-z)^{\alpha}\right]$.

MLFD is a flexible distribution with different shapes, for example, those like non-increasing pattern with unique mode at, unimodal one with one or two non-zero modes. There also exist some different distributional properties, for instance, the recurrence relation with regard to probability distribution function (pdf), cdf, index of dispersion, classification, producing functions, formulae for different type of moments besides reliability properties as well as increasing failure rate, unimodality, survival and stochastic ordering.

Pareto distribution

As a random variable, Pareto distribution P_D [56] is followed by the Pareto distribution providing that it possesses the pattern of tail which is provided as follows [57]:

$$P_D\,(U) = \begin{cases} 1 - \frac{(b)}{U} & U \leq b \\ 0. & \mathrm{U} < \mathrm{b} \end{cases} \tag{4}$$

a and b denote the scale and shape parameters, in respective order, with 1 and 1 values.

Cauchy distribution

As a random variable, the Cauchy distribution [58] is followed with the tail formula formulated as per Eq. 5:

$$C_D\,(U) = \frac{1}{\pi} \arctan\left(\frac{2(U-\mu)}{\beta}\right) + \frac{1}{2} \tag{5}$$

b and u are the denotations of the scale and location parameters, in respective order with 1 and 0 values.

Weibull distribution

As a random variable, the Weibull (W_D) [59] is to follow the Weibull providing the tail formula is taken according to Eq. 6 [52–68].

$$W_D\,(U) = \exp^{(\frac{U}{k})^{\xi}} \tag{6}$$

k and ξ correspond to scale and shape parameters. With ξ having values, less than 1, the Weibull distribution is said to be heavy-tied. The k and ξ values are taken as 1 and 1 [51].

The comparison of the Mittag-Leffler distribution, Pareto distribution, Cauchy distribution and Weibull distribution has been done with respect to their performances,

through the utilization of the log likelihood value (MLE) and the Akaike Information Criterion (AIC). Their related definitions are as such.

$AIC = -21nL + 2k$, here k denotes the number of parameter(s) and L refers to the maximum log-likelihood concerning a specific dataset [19]. In addition, the applications of the following have also been performed: standard deviation (SD), mean absolute error (MAE), mean absolute percentage error (MAPE), sum of the square error (SSE), mean squared error (MSE) and root mean squared error (RMSE) (for theoretical aspects and other related details please see Refs. [60, 61].

Comparatively high (small) values of log likelihood (AIC) can suggest better fittings, which are outlined in Table 2 for Pareto distribution, Weibull distribution, Mittag-Leffler distribution and Cauchy distribution, respectively, yield, in an evident way, the best of the fit in the related order. Furthermore, the performance of the likelihood ratio test is also addressed so that MLFD Mittag-Leffler distribution, Cauchy distribution, Pareto distribution, Weibull distribution can be differentiated (see Table 2).

Mittag-Leffler function's numerical evaluation with the default accuracy set has the 10^{-4} the Matlab routine [62]. The function of Matlab $f = gml\_fun(a, b, c, x, eps0)$ addresses a generalized Mittag-Leffler function [63, 64].

Figure 3 is plotted for the functions, Pareto distribution, Weibull distribution, Mittag-Leffler distribution and Cauchy distribution, which have been computed by Matlab pattern of $[\ ] = gml\_fun(\ )$ which was made for the Mittag-Leffler function's evaluation [63, 64].

The fitting of the biological datasets in this study as based on the Mittag-Leffler function with two parameters (α, β, γ) relying on heavy-tailed distributions is a critical step in this process for the investigation of the complex attributes. The application steps for this investigation are presented in Algorithm 1 (for further related details, see [65]).

Algorithm 1: Fitting algorithm Mittag-Leffler function with three parameters (α, β, γ) based on Heavy-tailed distributions.

Step 1: Begin with a $\alpha = 1;\ \beta = 1\ and\ \gamma = 1\ mlf\ (1, 1, 1) = e^z$ as the most basic form of Mittag-Leffler function with three parameters.

Step 2: Fitting $mlf\ (1, 1, 1)$ in the following respective integer-order for: Mittag-Leffler distribution, Cauchy distribution, Pareto distribution, Weibull distribution.

Step 3: Do the calculation of the maximum likelihood estimation with MLE, AIC, SD, MAE, MAPE, SSE, MSE, RMSE.

Step 4: For $\beta = 1$ (constant), $\alpha = 0.1, 0.5, \ldots, 7, 10$ and $\gamma = 0.1, 0.5, \ldots, 7, 10$ the values are chosen accordingly for values of α; hence, the MLE, AIC, MLE, AIC, SD, MAE, MAPE, SSE, MSE and RMSE values are calculated as in Step 3 and the comparison of values is performed.

Step 5: For $\alpha = 1$ (constant), $\beta = 0.1, 0.5, \ldots, 7, 10$ and $\gamma = 0.1, 0.5, \ldots, 7, 10$ the values are chosen accordingly for values of β; hence, the MLE, AIC, MLE, AIC, SD, MAE, MAPE, SSE, MSE and RMSE values are calculated as in Step 3 and the comparison of values is performed.

Step 6: For $\gamma = 1$ (constant), $\alpha = 0.1, 0.5, \ldots, 7, 10$ and $\beta = 0.1, 0.5, \ldots, 7, 10$ the values are chosen accordingly for values of β; hence, the MLE, AIC, MLE, AIC,

SD, MAE, MAPE, SSE, MSE and RMSE values are calculated as in Step 3 and the comparison of values is performed.

Step 7: Based on the different values of α, β and γ as chosen, the best fit values are taken.

Step 8: Based on the procedure in Step 7, the calculations are performed distinctively and individually for all the heavy-tailed distributions (Mittag-Leffler Function distribution, Cauchy distribution, Pareto distribution, Weibull distribution) and comparative analyses are performed.

Through this algorithm (Fitting algorithm Mittag-Leffler function with three parameters (α, β, γ) based on Heavy-tailed distributions) applied to the diabetes dataset, in order to identify the optimized three-parametric ML function, ML (α, β, γ) parameters that fit the data were found with heavy-tailed distributions. The optimized ML (α, β, γ) functions were, thus, obtained. This application, in a way, allowed the finding of the best fitting Mittag-Leffler function with three parameters (α, β, γ) in the diabetes dataset.

Fractional-Order Derivatives

To comprehend the fractional calculus definitions and their uses, it is important that one is familiar with the particular mathematical explanations. Among these are the Gamma functions, Beta functions, Laplace transforms and Mittag-Leffler functions. Mittag-Leffler function is a critical function in mathematics with broad areas of application in fractional differential method. Mittag-Leffler function is also important in terms of differential equations theory depending on the exponential function as in integer-order.

The subsequent power series are employed for the definition of the Mittag-Leffler function, which is convergent in the entire complex plane [22]:

$$\begin{aligned} E^{\gamma}_{\alpha,\beta}(z) &= \sum_{n=0}^{\infty} \binom{-\gamma}{n} \cdot \frac{(-z)^n}{\Gamma(n\alpha+\beta)} \\ &= \sum_{n=0}^{\infty} \frac{\Gamma(\gamma+n)}{\Gamma(\gamma)\Gamma(n\alpha+\beta)} \cdot \frac{z^n}{n!} \quad \alpha, \beta, \delta > 0,\ z \in C \end{aligned} \tag{7}$$

As an entire function, it allows a simple generalization of the exponential function. It is reduced for $\alpha = 1$ and $\beta = 1$. About the convergence of power series in Eq. 8, the two parameters and possess the likelihood of being complex providing $\Re(\alpha) > 0$, $\Re(\beta) > 0$ and $\Re(\gamma) > 0$. The asymptomatic expansion of Mittag-Leffler is another interesting property signified as $z \to \infty$ in the different sectors of the complex plane [66].

Ordinary fractional differential equations are solved clearly through the Mittag-Leffler function, its generalized forms and relevant special functions. The role of the Mittag-Leffler function becomes more conspicuous in the solution of ordinary FDEs. The most expansively used definitions of fractional derivatives are Riemann, Liouville, Caputo and Grünwald-Letnikov. The two approaches are conducted for their introduction: the former one is dependent on the inversion of the generalization of the integer-order integral. The second approach is reliant on a more direct gen-

eralization of the limit of the difference quotients defining integer-order derivatives [67].

When a physical system is ruled by the fractional differential equation of Eq. 8 [60, 61],

$$a D_t^{\alpha} y(t) = f(t) \tag{8}$$

zero initial condition is under consideration and the Laplace transform specified in the aforementioned part provides the following Eq. 9:

$$G_1(s) = \frac{Y(s)}{U(s)} = \frac{1}{as^{\alpha}} \tag{9}$$

Equation 9's inverse Laplace transform yields another equation specified in Eq. 10.

$$g_1(t) = \frac{1}{a} \frac{t^{\alpha-1}}{\Gamma(\alpha)} \tag{10}$$

Equation 10's inverse Laplace transform yields another equation specified in Eq. 11.

$$g_1(t) = \frac{1}{a} \frac{t^{\alpha-1}}{\Gamma(\alpha)} \tag{11}$$

Equation 11 is regarded as the impulse response of the system's transfer function model $G_1(s)$. When one extends the concept for the two term differential equation, then the related structure will be according to Eq. 12 [66, 67]:

$$a D_t^{\alpha} y(t) + by(t) = f(t) \tag{12}$$

A similar Laplace operation with zero initial condition produces the system's transfer function based on Eq. 13.

$$G_2(s) = \frac{Y(s)}{U(s)} = \frac{1}{as^{\alpha} + b} = \frac{1}{a} . \frac{1}{s^{\alpha} + \frac{b}{a}} \tag{13}$$

The inverse Laplace of Eq. 13 lets the gaining of the following indication according to Eq. 14.

$$g_2(t) = \frac{1}{a} t^{\alpha-1} E_{\alpha,\alpha}\left(-\frac{b}{a} t^{\alpha}\right) \tag{14}$$

Caputo Fractional-Order Derivatives

Being preferred for the solution of differential equations, the Caputo definition is denoted according to Eq. 15 [22, 67]:

$$D_m^{\alpha} f(t) = \frac{1}{\Gamma(m-\alpha)} \int_0^t \frac{f^{(m)}(\tau)}{(t-\tau)^{\alpha+1-m}} d\tau, \tag{15}$$

That the Grünwald–Letnikov fractional derivative resembles Caputo fractional derivative is proven, with regard to the majority of the analytic functions. One slight different aspect is detected during the handling of the constant function. For a constant, the Caputo fractional derivative is zero; and yet, its Riemann-Liouville counterpart is not zero. Caputo fractional derivative is usually utilized for addressing the initial value fractional ordinary differential Equation 23.

The essential results on fractional integral and derivatives of the power function $(t-t_0)^{\beta}$ for, $\beta > -1$ are the case and for the Caputo's derivative, and in this regard, Eq. 16 is used as follows:

$$D_{t_0}^{\alpha}(t-t_0)^{\beta} = \begin{cases} 0 & \beta \in \{0, 1, \ldots, m-1\} \\ \frac{\Gamma(\beta+1)}{\Gamma(\beta-\alpha+1)}(t-t_0)^{\beta-\alpha} & \beta > m-1 \\ \text{nonexisting} & \text{otherwise} \end{cases} \tag{16}$$

When there is an absence of Caputo's derivative of $(t-t_0)^{\beta}$ for real $\beta < m-1$ with $\beta \notin \{0, 1, \ldots, m-1\}$ connected with the fact that when $m-th$ order derivative of $(t-t_0)^{\beta}$ is evaluated, the integer as per Eq. 17 is not integrable as with Eq. 16.

$$\begin{aligned} {}^{C}D_{t_0}^{\alpha} f(t) &:= J_{t_0}^{m} D^{m} f(t) \\ &= \frac{1}{\Gamma(m-\alpha)} \int_{t_0}^{t} (t-\tau)^{m-\alpha-1} f^{(m)}(\tau)\, d\tau, \quad t > t_0 \end{aligned} \tag{17}$$

D^m and $f^{(m)}$ denote the integer-order derivatives [68].

Unlike the Riemann-Liouville derivative, the Laplace transform for the Caputo's derivative is initialized with the standard initial values signified in terms of integer-order derivatives.

As a matter of fact, the definition of Caputo's derivative and Grünwald–Letnikov's derivative show consistency with the definition of Riemann-Liouville derivative, hinting that Grünwald–Letnikov positive non-integer order derivative definition is consistent with the Riemann-Liouville positive non-integer order derivative definition as an inference [57].

Artificial Neural Networks Algorithm

Neural networks are built depending on simple units that are connected with each other by a set of weighted connections. Generally speaking, such units own their structure and organization in the form of layers; and in that organization, each unit

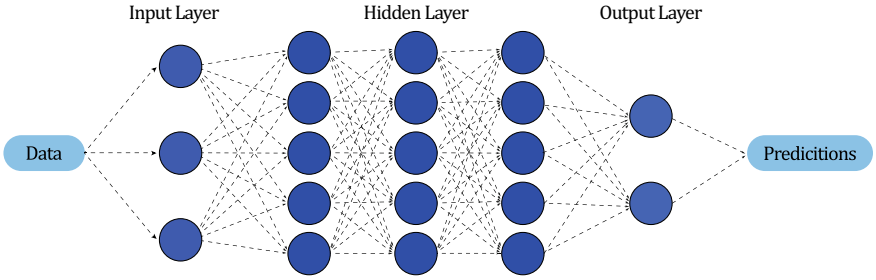

Fig. 1 The general network structure of the FFBP algorithm

of the first layer, in other words the input layer, signifies a feature of a pattern that will be considered for analyzing purposes. The units with respect to the last layer, which is to say, the output layer, generates a decision, subsequently, after the information propagation; so artificial neural networks (ANNs) are computational systems, which are inspired by biological neural networks that mimic the animals; brains. The procedure employed towards the learning process in a neural network is called the training algorithm. In this regard, Feed Forward Back Propagation algorithm is among the ANN algorithms [69].

Being among the most commonly utilized artificial neural networks, feedforward neural network is an artificial neural network with inter-unit connections that do not form a cycle [70]. With this aspect, it is different from the recurrent neural networks. The feedforward neural network is the first and simplest type of artificial neural network devised. Information moves only in one direction; and thus, no loops or cycles are existent in the network [70]. The network architecture of the algorithm is defined and the weights are involved [70, 71]. When the input examples with m-dimension are entered, $x_i = [x_1, x_2, \ldots, x_m]^T$ can be observed. Correspondingly, the output examples for n-dimension are noted by $d_k = [d_1, d_2, \ldots, d_n]^T$ (see Fig. 1). x_i values, the output values of the neurons in the ith layer (n), the total input that will correspond to a neuron in j layer is performed according to Eq. 18 [70–74] (see Fig. 1).

$$net_j = \sum_{i=i}^{m} w_{ij} X_i \tag{18}$$

The j neuron's output (namely transfer function input), which is in the hidden layer, is calculated as per Eq. 19 [70]

$$y_j = f_j\left(net_j\right) \quad j = 1, 2, \ldots, J \tag{19}$$

The total input corresponding to k neuron in the output layer is calculated as per Eq. 20:

$$net_k = \sum_{j=1}^{J} w_{kj}.y_j \tag{20}$$

The calculation of the non-linear output of a k neuron in the output layer is performed based on Eq. 21 [70, 74].

$$o_k = f_k\left(net_k\right), \quad k = 1, 2, \ldots, n \tag{21}$$

Based on the comparison of the output obtained from the network and actual output, the calculation of the e_k error is done according to Eq. 22 [70, 74].

$$e_k = (d_k - o_k) \tag{22}$$

D_k shows the target of any k neuron, which is in the output layer and O_k shows the outputs obtained from the network. The updating of the weights that are obtained from the output layer is also done, and the performance of the total square error calculation is conducted according to Eq. 23 for each of the examples:

$$E = \frac{1}{2}\sum_{k} (d_k - o_k)^2 \tag{23}$$

In this study, FFBP algorithm was applied to the diabetes dataset (768 × 9) for the diagnostic and predictive purposes of the disease classification.

Algorithmic (Computational) Complexity

Big-O notation, as a simple mathematical formula, provides the rough approximation or placing of an upper bound on the resource requirements for an algorithm depending on the size of the input-the *complexity* of the algorithm, refers to the algorithmic complexity. In technical aspects, algorithmic complexity is able to and supposed to apply to both space and time (storage and memory) resource requirements. What most are interested in is the running time of an algorithm [75, 76].

Algorithmic complexity is stated with the term of "*on the order of*", which indicates the rough or approximate cost of the algorithm in terms of resource requirements. "*on the order of*" is abbreviated as a capitalized "O", which provides the more known term which is the *Big-O* notation.

The form of *Big-O* notation is: O (formula)

In which, the *formula* is mathematical expression that is reliant on the input parameters or size of the input data for the algorithm. The input size is often denoted in the formula with a lower-case "n".

A brief presentation of the common forms of *Big-O notation*, in increasing order of cost and decreasing order of performance contain:

O(1) or O(k): Constant. Great, fastest, easy, simple, trivial,

O(log n): Logarithmic. Non-trivial yet really manageable.

O(n log n): Linearithmic. Not quite as good as linear, yet not that bad.

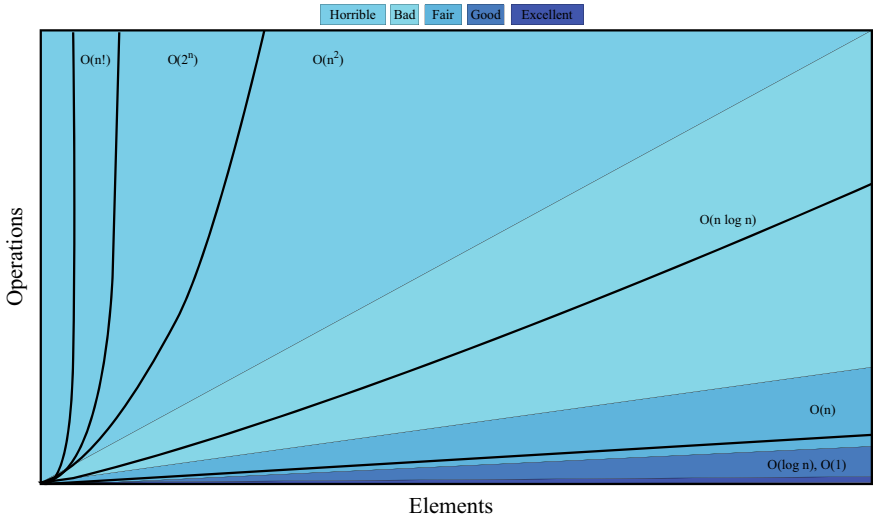

Fig. 2 The order of growth for algorithms as indicated in Big-O notation

$O(n^2)$: Quadratic. Approaching somewhat expensive, yet not terrible.

Big-O notation is a prominent notation used for the representation of algorithmic complexity. By providing an upper bound on complexity, it expresses the algorithm's worst-case performance in a way. Through this notation, it will be convenient to compare different algorithms since the notation yields apparently the expression of how the algorithm scales as the input size gets bigger, which is often termed as the order of growth (see Fig. 2) [76].

The Fast Fourier Transform (FFT)

The problem regarding the Fourier transform is due to its sine/cosine regression model form or its complex exponential form, which requires $O(n^2)$ operations for the computation of all the Fourier coefficients. Each frequency coefficient necessitates the multiplication of a summing a cosine or sine with all the data points. Regarding short-time series, this is not the case. However, for time series that are very long, this can be a costly computation even though they are to be conducted on the computers of the current era.

The Fast Fourier Transform (FFT), as a way to reduce the complexity of the Fourier transform computation from $O(n^2)$ to $O(nlogn)$, is an important improvement [77]. The primary version of the FFT is one with Cooley and Tukey. The basic idea is that:

Suppose, there is a time series $y_1, \ldots, y_n$ and one wishes to compute the complex Fourier coefficient z_1. Through the formula, this shall require the computing of:

$$z_0 = \sum_{t=0}^{n-1} y_t,$$

That is proportional to the mean of the data. If the data were de-meaned or de-trended, then this shall be zero. The next Fourier coefficient is, then,

$$z_1 = \sum_{t=0}^{n-1} y_1 \exp(-2\pi i.1.t/n)$$
$$= y_0 \exp(-2\pi i.1.0/n) + y_1 \exp(-2\pi i.1.1/n) + y_2 \exp(-2\pi i.2.1/n) + \cdots$$

At this point, assume that one wishes to compute the new coefficient z_1. Then, this would require the computing:

$$z_2 = y_0 \exp(-2\pi i.2.0/n) + y_1 \exp(-2\pi i.2.1/n) + \cdots$$

The exponential in the second term in the sum for is the same as the exponential in the third term in the sum for z_2, which are equal to $\exp(-2\pi i.1.2/n)$. There is not any need for the computation of this exponential quantity tow times, so it is possible to compute it for the first time, storing it in memory, then retrieving it when it is required to compute z_2 (assuming that retrieving from memory is faster than computing it from scratch). One can think of the FFT algorithm as an elaborate bookkeeping algorithm that keeps track of these symmetries in computing the Fourier coefficients.

3 Experimental Results and Discussion

Mathematical-informed modeling of complex systems by fractional order derivatives based on fractional calculus is important in order to be able to attain the related syntheses in an effective and robust way. In view of that, our study aims to establish a robust and accurate model based on the combination of fractional-order derivative and Artificial Neural Network (ANN) for the diagnostic and differentiability predictive purposes for the diseases which manifest various and transient biological properties. Moreover, another aim is to show the benefit of the concept of algorithmic complexity to obtain the fractional-order derivative with the least complexity in order that it would be conceivable to reach the optimized solution. To this end, the integrative multi-stage approach proposed in this study includes the steps outlined as follows:

(i) The Caputo fractional derivative was applied with three-parametric Mittag-Leffler function to the diabetes dataset. Thus, new fractional models with varying degrees were established by performing data fitting with the Fitting algorithm Mittag-Leffler function with three parameters (α, β, γ) based on Heavy-tailed distributions. (By applying Algorithm 1 (Fitting algorithm Mittag-Leffler function with three parameters (α, β, γ) based on heavy-tailed distributions.) to the diabetes dataset, to identify the optimized three-parametric ML function, ML (α, β, γ) parameters that fit the data were found with heavy-tailed distributions. In this way, the optimized ML (α, β, γ) functions were obtained. This application allowed the finding of the best fitting Mittag-Leffler function with three parameters (α, β, γ) in the dia-

betes dataset). After this particular application, the new dataset, mfc_diabetes, was obtained.

(ii) Classical derivative (calculus) was applied to the diabetes dataset (namely the raw dataset); and accordingly, the cd_diabetes dataset was obtained.

(iii) the performance of the new dataset, as obtained from the Caputo fractional-order derivative with the three-parametric Mittag-Leffler function (as per step i), the dataset obtained from the classical derivative (calculus) application (as per step ii) and the diabetes dataset (ie: raw dataset) was compared through the application of the feed forward back propagation (FFBP) algorithm, one of the ANN algorithms (along with accuracy rate, sensitivity, precision, specificity, F1 score, multiclass classification (MCC), ROC curve). As a result, the fractional-order derivative model, the most optimal one for the disease, was generated.

(iv) Algorithmic complexity was addressed to achieve the Caputo fractional-order derivative with the least complexity and with the optimized solution. Hence, algorithmic complexity was calculated with the application of Caputo fractional-order derivative with three parametric Mittag-Leffler function and classical derivative (calculus) in a comparative way by identifying the complexity for each concerning the diabetes dataset. The derivatives with the highest and lowest level of complexity were identified with *Big-O*. The experimental results obtained from our integrative and multi-stage approach demonstrate the applicability of the scheme proposed in this study by showing that the Caputo fractional-order derivative with the least complexity has yielded the best end result based on the output derived from FFBP.

All the analyses and results obtained as well as the visual depictions performed have been obtained by [78] and Phyton [79].

3.1 Application of Mittag-Leffler Functions with Heavy-Tailed Distributions' Algorithm for Data Fitting Purposes

By applying Algorithm 1 (Fitting algorithm Mittag-Leffler function with three parameters (α, β, γ) based on Heavy-tailed distributions.) to the diabetes dataset, in order to identify the optimized three-parametric ML function, ML (α, β, γ) parameters that fit the data were found with heavy-tailed distributions. Thus, the optimized ML (α, β, γ) functions were obtained. In other words, this application allowed us to find the best fitting Mittag-Leffler function with three parameters (α, β, γ) in the diabetes dataset.

Algorithm 1 Fitting algorithm Mittag-Leffler function based on heavy-tailed distributions has been applied to the diabetes dataset (768×9) for the nine attributes in units (number of pregnancy, plasma glucose, diastolic blood pressure, skin thickness, insulin, body mass index (BMI), diabetes pedigree function, age) (see Table 1 for further details).

Applications for Fitting Mittag-Leffler function based on heavy-tailed distributions to diabetes dataset (Number of pregnancy, plasma glucose, diastolic blood pressure, skin thickness, insulin, body mass index (BMI), diabetes pedigree function, age) were conducted concerning the related attributes. The log likelihood value and the Akaike Information Criterion (AIC) were computed as per the fitting to Mittag-Leffler distribution, Pareto distribution, Cauchy distribution and Weibull distributions (Step 2 carried out as per Algorithm 1) for all the attributes of diabetes dataset along with the different values of Mittag-Leffler function with three parameters (α, β, γ). Accordingly, Mittag Leffler functions were attained for all the significant attribute values (Step 3 carried out as per Algorithm 1).

Concerning the analyses, negative log likelihood: -log L was taken for the log likelihood value. By taking the log likelihood value, the maximum value, the distribution that is best fit is obtained. The best fit distribution is generated as retrieved from the Akaike Information Criterion (AIC) calculations. Negative log likelihood: in -log L gives the best fitting minimum value in the distribution, therefore, negative log likelihood was taken in the analyses. Hence, the lowest of the both values were taken and the best fitting distribution was achieved so that the ML functions which represent the data most suitably were obtained (Step 4 performed as per Algorithm 1). The lowest value was taken for each distribution; the computations were conducted for all the nine attributes. For the purpose of setting an example, presentations for one attribute, namely the body mass index (weight in kg/(height in m)^2, are indicated in Table 2). Thus, the lowest value obtained is indicated in bold in the related tables. The figure depictions as per the calculations obtained from the aforementioned attribute presented in the table show the distribution and also its peak points (see Fig. 3).

Table 2 provides the body mass index (weight in kg/(height in m)^2 attribute indicating the lowest value (indicated in bold) taken for each heavy-tailed distribution

The depictions as per the calculations obtained from the attributes presented in Table 2 for the Body mass index (weight in kg/(height in m)^2 attribute the heavy-tailed distributions (Mittag-Leffler distribution, Cauchy distribution, Pareto distribution, Weibull distribution) and its peak points are displayed in Fig. 3.

Two approaches exist regarding the handling of each diabetes dataset attribute to conduct the analysis mentioned above. The first approach is that for the results obtained from each distribution as per Algorithm 1 (based on the α, β and γ values), the most accurate distribution is achieved as per the results as have been obtained with the lowest value. The latter approach includes the addressing of the outcomes based on α, β and γ values according to the results generated by the four heavy-tailed distributions (namely Mittag-Leffler distribution, Cauchy distribution, Pareto distribution, Weibull distribution) in conjunction with MLE, AIC, SD, MAE, MAPE, SSE, MSE and RMSE) while at the same time making the comparison of the related attributes (see Table 3 for further details) between themselves; and additionally, the most accurate distribution is obtained as per the results attained with the minimum value. If there existed extreme points within the distribution, then those extreme values were not taken into account for the analyses performed in our study.

As per the applications in Algorithm 1, the diabetes dataset in line with the ML function, the best fit values are found to be as MLF(10,2,2).

Table 2 Body mass index (weight in kg/(height in m)^2 attribute computation based on the diabetes dataset for Mittag-Leffler function based on Heavy-tailed distributions

Distributions	α	β	γ	-log L	AC	SD	MAE	MAPE	SSE	MSE	RMSE
Mittag-Leffler dist.	0.5	0.5	0.5	<missing>	<missing>	<missing>	<missing>	<missing>	<missing>	<missing>	<missing>
Cauchy dist.	0.5	0.5	0.5	<missing>	<missing>	<missing>	<missing>	<missing>	<missing>	<missing>	<missing>
Pareto dist.	0.5	0.5	0.5	<missing>	<missing>	<missing>	<missing>	<missing>	<missing>	<missing>	<missing>
Weilbull dist.	0.5	0.5	0.5	<missing>	<missing>	<missing>	<missing>	<missing>	<missing>	<missing>	0.028959
Mittag-Leffler dist.	3	1	1	26598.571	53199.142	2.061189	0.003466	0.003466	0.644048	0.000839	0.020002
Cauchy dist.	3	1	1	4018.0837	8038.1674	2.061189	0.00781	0.003076	0.307272	0.0004	0.121285
Pareto dist.	3	1	1	3117.8201	6237.6401	2.061189	0.032074	0.016886	11.297328	0.01471	0.044071
Weilbull dist.	3	1	1	6104.8158	12211.632	2.061189	0.006318	0.005448	1.491643	0.001942	0.087339
Mittag-Leffler dist.	5	1	3	1967.1498	3936.2996	0.197894	0.081993	0.04835	5.858431	0.007628	0.077852
Cauchy dist.	5	1	3	1986.0064	3974.0128	0.197894	0.076484	0.044114	4.654852	0.006061	0.337281
Pareto dist.	5	1	3	894.22195	1790.4439	0.197894	0.322152	0.188561	87.36659	0.113759	0.172323
Weilbull dist.	5	1	3	1383.6363	2769.2725	0.197894	0.168421	0.097463	22.805815	0.029695	0.031756
Mittag-Leffler dist.	5	1	7	3961.3134	7924.6268	0.463599	0.012784	0.007145	0.774468	0.001008	0.040766
Cauchy dist.	5	1	7	2574.4379	5150.8757	0.463599	0.037056	0.014901	1.276306	0.001662	0.176273
Pareto dist.	5	1	7	1598.3795	3198.7591	0.463599	0.138224	0.059477	23.863365	0.031072	0.076839
Weilbull dist.	5	1	7	2207.7026	4417.4052	0.463599	0.063737	0.02687	4.534439	0.005904	0.241779
Mittag-Leffler dist.	7	2	1	1090.3544	2182.7089	0.000196	0.241779	0.241587	44.894942	0.058457	0.159029
Cauchy dist.	7	2	1	1412.099	2826.1979	0.000196	0.159029	0.158903	19.422822	0.02529	0.998415
Pareto dist.	7	2	1	1.218254	4.436507	0.000196	0.998415	0.997624	765.56759	0.996833	0.367588
Weilbull dist.	7	2	1	768.60938	1539.2188	0.000196	0.367588	0.367296	103.77269	0.135121	0.241587
Mittag-Leffler dist.	7	2	2	1090.9646	2183.9292	0.000391	0.241587	0.241204	44.823674	0.058364	0.158903
Cauchy dist.	7	2	2	1412.7084	2827.4167	0.000391	0.158903	0.158651	19.392028	0.02525	0.996834
Pareto dist.	7	2	2	2.435485	6.870969	0.000391	0.996834	0.995255	763.14538	0.993679	0.367296
Weilbull dist.	7	2	2	769.21877	1540.4375	0.000391	0.367296	0.366714	103.60817	0.134906	0.241203

(continued)

Table 2 (continued)

Distributions	α	β	γ	-log L	AC	SD	MAE	MAPE	SSE	MSE	RMSE
Mittag-Leffler dist.	7	2	4	1092.1864	2186.3729	0.000782	0.241203	0.24044	44.681318	0.058179	0.158651
Cauchy dist.	7	2	4	1413.9271	2829.8542	0.000782	0.158651	0.158149	19.330595	0.02517	0.993685
Pareto dist.	7	2	4	4.866886	11.733772	0.000782	0.993684	0.990542	758.33134	0.987411	0.366714
Weilbull dist.	7	2	4	770.43754	1542.8751	0.000782	0.366714	0.365554	103.27994	0.134479	0.240435
Mittag-Leffler dist.	7	2	8	1094.6363	2191.2726	0.001564	0.240435	0.238919	44.397331	0.057809	0.158148
Cauchy dist.	7	2	8	1416.3646	2834.7293	0.001564	0.158148	0.157151	19.20835	0.025011	0.987436
Pareto dist.	7	2	8	9.717495	21.43499	0.001564	0.987431	0.98121	748.82334	0.97503	0.365553
Weilbull dist.	7	2	8	772.87508	1547.7502	0.001564	0.365552	0.363248	102.6268	0.133629	0.24197
Mittag-Leffler dist.	**10**	**2**	**2**	**1089.746**	**2181.4921**	**0**	**0.24197**	**0.24197**	**44.966126**	**0.05855**	**0.159155**
Cauchy dist.	**10**	**2**	**2**	**1411.4908**	**2824.9816**	**0**	**0.159155**	**0.159154**	**19.453605**	**0.02533**	**0.999997**
Pareto dist.	**10**	**2**	**2**	**0.002462**	**2.004924**	**0**	**0.999997**	**0.999995**	**767.99508**	**0.999994**	**0.367879**
Weilbull dist.	**10**	**2**	**2**	**768.00123**	**1538.0025**	**0**	**0.367879**	**0.367878**	**103.93716**	**0.135335**	**0.24197**
Mittag-Leffler dist.	10	2	5	1089.7479	2181.4957	1.00E−06	0.24197	0.241969	44.96591	0.058549	0.159154
Cauchy dist.	10	2	5	1411.4927	2824.9853	1.00E−06	0.159154	0.159154	19.453511	0.02533	0.999992
Pareto dist.	10	2	5	0.006155	2.012311	1.00E−06	0.999992	0.999988	767.98769	0.999984	0.999992
Weilbull dist.	10	2	5	768.00308	1538.0062	1.00E−06	0.367878	0.367876	103.93666	0.135334	0.367878
Mittag-Leffler dist.	10	2	7	1089.7491	2181.4982	1.00E−06	0.241969	0.241968	44.965766	0.058549	0.241969
Cauchy dist.	10	2	7	1411.4939	2824.9878	1.00E−06	0.159154	0.159153	19.453449	0.02533	0.159154
Pareto dist.	10	2	7	0.008618	2.017235	1.00E−06	0.999989	0.999983	767.98277	0.999978	0.999989
Weilbull dist.	10	2	7	768.00431	1538.0086	1.00E−06	0.367877	0.367875	103.93633	0.135334	0.367877

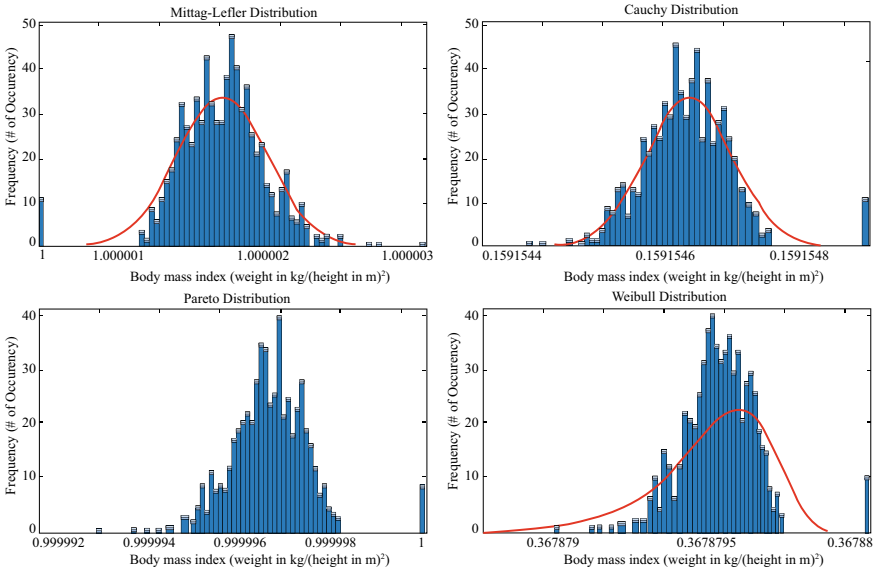

Fig. 3 The body mass index (weight in kg)/(height in m)^2 attribute computation based on diabetes dataset for Mittag-Leffler function based on Heavy-tailed distributions

3.2 Application of Caputo Fractional-Order Derivatives with Three Parametric Mittag-Leffler Functions to Diabetes Dataset

Algorithm 2 presents the application steps of fractional derivatives on datasets with non-integer orders accordingly for the diabetes dataset. Algorithm 2 serves the identification of the order degree, which identifies the most significant attribute. In this way, the fractional derivation function is formed.

Algorithm 2: Fractional derivatives application on dataset with non-integer orders.

Step 1: set non-integer orders (y = order = [0.1, 0.2, 0.3, 0.4, 0.5, 0.6, 0.7, 0.8, 0.9]).

Step 2: For the y order fractional derivatives that have been identified in Step 1, all the orders are applied to the attributes distinctly in the dataset. Consequently, z values are obtained.

Step 3: Print 3D graphs of three types of derivatives as grid and surface (x, y, z)=(for each attribute of the data u, α, derivative of all the data).

Algorithm 3 provides the application steps of Caputo fractional derivatives on the diabetes dataset (see Table 1). The most significant orders have been obtained as per the application of the procedures stated in Fig. 4, and for these orders, Caputo fractional-order derivative models have been identified, as elaborated with the results obtained accordingly.

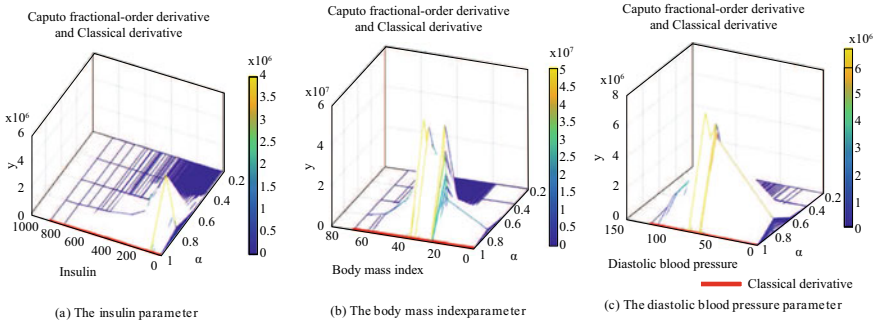

Fig. 4 Computational application of Caputo fractional-order derivatives and classical derivative, both with y = order = [0.1, 0.2, 0.3, 0.4, 0.5, 0.6, 0.7, 0.8, 0.9] for the three parameters. **a** The insulin parameter and CAD). **b** The body mass index parameter and **c** The body mass index parameter pertaining to the diabetes dataset

Algorithm 3: Caputo fractional derivatives application on diabetes dataset with non-integer orders:

Step 1: Set non-integer orders (y = order = [0.1, 0.2, 0.3, 0.4, 0.5, 0.6, 0.7, 0.8, 0.9]).

Step 2: For the y order Caputo fractional derivatives that have been identified in Step 1, all the orders are applied to the attributes distinctly in the dataset. As a result, values are obtained.

Step 3: Print graphs of types of derivatives as grid and surface $(x; y; z)$ = (for each attribute of the data u, α, derivative of all the data)

The computational application of Caputo fractional-order derivatives and classical derivative, both with y = order = [0.1, 0.2, 0.3, 0.4, 0.5, 0.6, 0.7, 0.8, 0.9], for all the parameters have been conducted (Table 1 for the diabetes dataset details) concerning the diabetes dataset. To set as an example and depict the computations in a clear way, we provide Fig. 4 for three parameters (the insulin parameter, the body mass index parameter and the body mass index parameter). Accordingly, Fig. 4 depicts the computational application of Caputo fractional-order derivatives and classical derivative, both with y = order = [0.1, 0.2, 0.3, 0.4, 0.5, 0.6, 0.7, 0.8, 0.9], for the three parameters concerning the diabetes dataset. For these orders, Caputo fractional-order derivative and classical derivative (calculus) models have been identified.

The computational application of Caputo fractional-order derivatives and classical derivative, both with y = order = [0.1, 0.2, 0.3, 0.4, 0.5, 0.6, 0.7, 0.8, 0.9], for all the parameters parameters have been performed (see Table 1 for the details) pertaining to the diabetes dataset. To set as an example and depict the computations in a clear way, we provide Fig. 4 for three parameters (parameters: The insulin parameter and CAD), the body mass index parameter and the body mass index parameter). Accordingly, Fig. 4 depicts the computational application of Caputo fractional-order derivatives and classical derivative, both with y = order = [0.1, 0.2, 0.3, 0.4, 0.5, 0.6, 0.7, 0.8, 0.9], for the three parameters (see Table 1 for the diabetes dataset details of all

the parameters involved) concerning the diabetes dataset. For these orders, Caputo fractional-order derivative and classical derivative models have been identified.

3.3 Application of ANN Algorithm to Diabetes Dataset and Results

The computational application of Caputo fractional-order derivatives and classical derivative obtained according to Fig. 5, with y = order = [0.1, 0.2, 0.3, 0.4, 0.5, 0.6, 0.7, 0.8, 0.9], for all the parameters (see Table 1) pertaining to the diabetes dataset yields the significant attributes in new datasets. For these orders based on the model, Caputo fractional-order derivative and classical derivative models have been identified. Table 3 provides the parameters of FFBP algorithm used in this study.

Figure 5 provides the application of Caputo fractional-order derivatives with Mittag-Leffer function parameters MLF (10, 2, 2) to the diabetes dataset, together with the new dataset (mfc_diabetes dataset), which was obtained from the significant attributes from the related application, with the FFBP algorithm application to the new dataset providing the orders' performance in terms of the disease's course and prediction.

Figure 6 provides the application of classical derivative to the diabetes dataset, along with the FFBP algorithm application to the new dataset (cd_diabetes dataset) providing the orders' performance in terms of the disease's course and prediction.

Table 4 provides the optimized results obtained from Caputo fractional-order derivatives with three parametric Mittag-Leffler function parameters' orders for the mfc_diabetes dataset and cd_diabetes dataset with the FFFBP algorithm application to the related dataset, besides the disease's diagnosis, course and prediction performances.

Table 3 The network parameters of the FFBP algorithm

Network properties	Values
Training properties	Levenberg-Marquardt ('trainlm')
Adoption learning function	Learngdm
Performance	Mean squared error (MSE)
Transfer function	Tansig
Epoch number	1000
Hidden layer number	1
Training dataset	(538×1)
Test	(115×1)
Validation dataset	(115×1)
Output	Diabetes

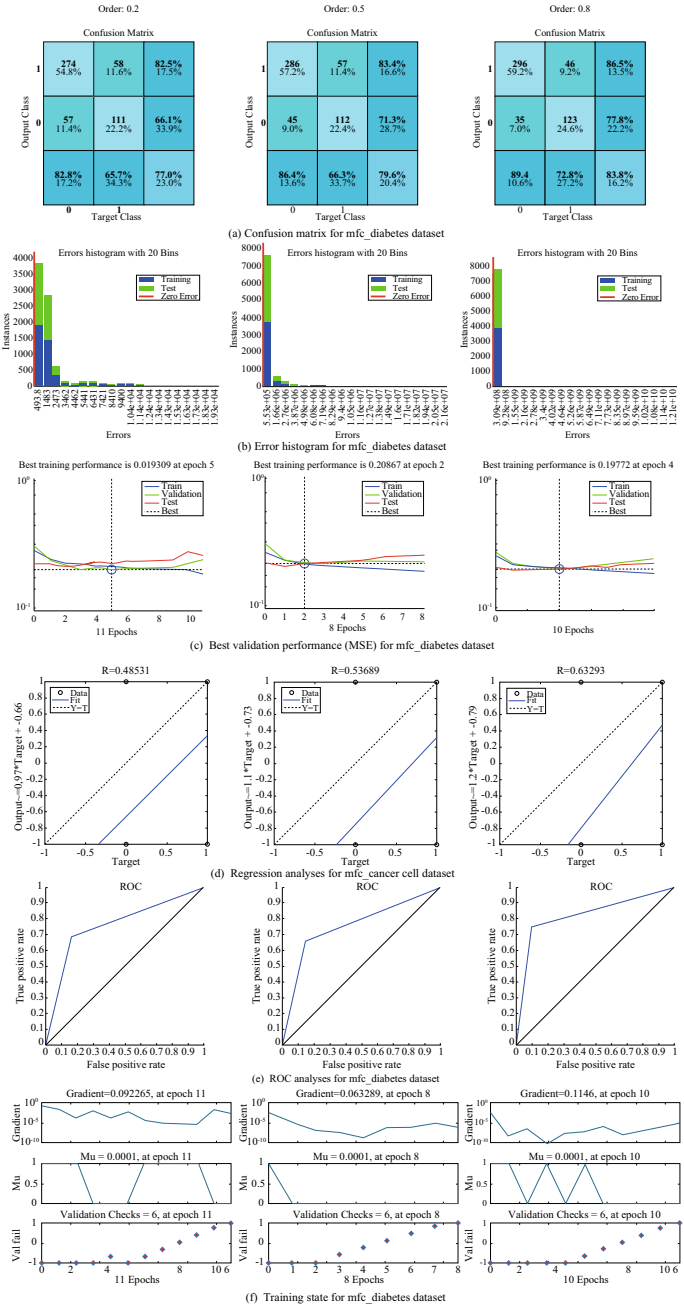

Fig. 5 The FFBP algorithm application to the mfc_diabetes dataset providing the orders' performance. **a** Confusion matrices. **b** Error Histograms with 20 Bins. **c** Best validation performance analyses. **d** Linear regression analyses. **e** ROC analyses and **f** Training state analyses

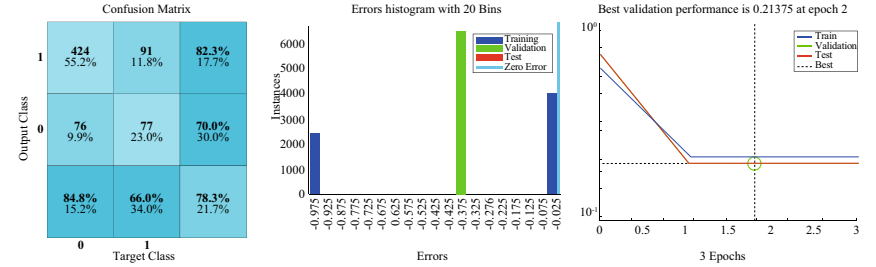

(a) Confusion matrix for cd_diabetes dataset (b) Error histogram for cd_diabetes dataset (c) Best validation performance (MSE)

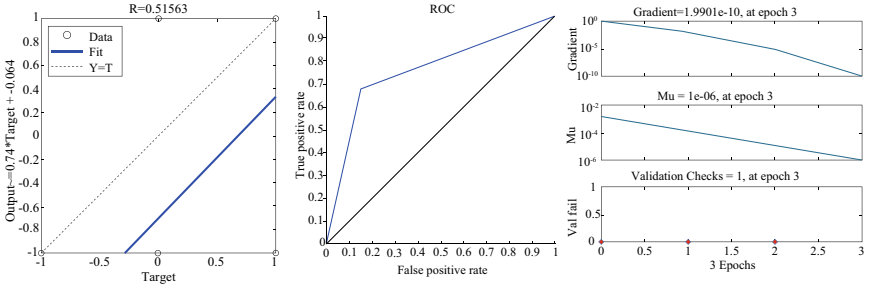

(d) Regression analyses for cd_diabetes dataset (e) ROC analyses for cd_diabetes dataset (f) Training state for cd_diabetes dataset

Fig. 6 The FFBP algorithm application to the cd_diabetes dataset providing the orders' performance. **a** Confusion matrices. **b** Error histograms with 20 Bins. **c** Best validation performance analyses. **d** Linear regression analyses. **e** ROC analyses and **f** Training state analyses

Table 4 The optimized results obtained from Caputo fractional-order derivatives with three parametric Mittag-Leffer function and classical derivative concerning the mfc_diabetes dataset and cd_diabetes dataset with FFBP algorithm

Fractional differential type/order	Percentage of correct classification (accuracy)	Sensitivity	Precision	Specificity	F1-score	Multiclass classification (MCC)	Area under ROC curve the (AUC)
Caputo/0.2	77.0000	65.6805	66.0714	82.7795	65.8754	0.48531	0.94345
Caputo/0.5	79.6000	66.2722	71.3376	86.4048	68.7117	0.53689	0.95495
Caputo/0.8	83.8000	72.7811	77.8481	89.4260	75.2294	0.63293	0.96152
Caputo/1	78.2552	66.0448	69.9605	84.8000	67.9463	0.51563	0.94981
Diabetes dataset	81.1198	99.6269	64.9635	71.2000	78.6451	0.67685	0.85654

Caputo fractional-order derivatives show the requirement of higher conditions of regularity for differentiability, and its derivative must initially be computed for the fractional derivative of a function in the Caputo sense.

Table 4 provides the results that have been obtained by Caputo fractional-order derivatives; and the classical derivative application is compared with the results of classical derivative presenting that Caputo fractionalorder derivative (with order 0.8)

generates better results. Table 4 presents the outcome that FFBP Algorithm application diabetes dataset based on Caputo fractional-order derivative and classical calculus yields the following best accuracy results for the respective orders: for order 0.2 (77.0000); for order 0.5 (79.6000%); for order 0.8 (83.8000%) and for order 1 (78.2552%). When the results obtained by Caputo fractional-order derivative application are observed, it apparently seems that Caputo fractional-order derivative with varying orders generates more accurate results. As a result, the Caputo fractional-order derivative for differentiable functions has yielded more robust accuracy rates. Therefore, the definition for Caputo fractional-order derivatives is performed for differentiable functions whereas functions that have no first-order derivative could have fractional derivatives with all orders which are less than one.

3.4 The Application of Algorithmic Complexity Based on Caputo Fractional-Order Derivative to the Diabetes Dataset

Algorithmic complexity, concerning the way the required resources are to be used for the solution of the problem, is employed for the classification of computational problems. Since some problems in computational biology are not feasible in the computational sense, the search for the optimal solution may be limiting in terms of practical aspects. As a result, it is sought that such problems are handled by approximations and heuristics to get over the computational necessities, which results in suboptimal solutions. However, when the underlying complexity of an algorithm is looked into, then efficiency of the algorithm can also be identified.

In view of that, while doing the complexity computations regarding Caputo fractional-order derivative with three parametric Mittag-Leffler function and classical derivative (cd), fast Fourier transform, gamma function, integration and mth derivative have been addressed in the form of Big O.

The application of the algorithmic complexity regarding three parametric Mittag-Leffler function is as per Eqs. 24 and 25.

$$E^{\gamma}_{\alpha,\beta}(x) = \sum_{n=0}^{\infty} \frac{\Gamma(\gamma+n)}{\Gamma(\gamma)\,\Gamma(n\alpha+\beta)} \cdot \frac{x^n}{n!} \quad \alpha, \beta, \delta > 0, \mathrm{x} \in N \tag{24}$$

$$\mathrm{O}(E^{\gamma}_{\alpha,\beta}(x)) = \mathrm{O}\left(\frac{\Gamma(\gamma+n)}{\Gamma(\gamma)\,\Gamma(n\alpha+\beta)} \cdot \frac{x^n}{n!}\right) \tag{25}$$

The application of the algorithmic complexity regarding Caputo fractional-order derivative (FOD) is as per Eqs. 26, 27 and 28.

Table 5 Results of the application of algorithmic complexity based on Caputo fractional-order with three parametric Mittag-Leffler function and classical derivatives to the diabetes dataset

	Order	Diabetes (N = 8)	
Caputo FOD with three parametric Mittag-Leffler function	0.2	$(N/\log(0.8))^2 * (\log(-18*N-4)/N)$	= 8.0288e + 02 + 5.0474e + 02i
	0.5	$(N/\log(0.5))^2 * (\log(-18*N-4)/N)$	= 83.2083 + 52.3105i
	0.8	$(N/\log(0.2))^2 * (\log(-18*N-4)/N)$	= 15.4337 + 9.7027i
cd	1	$(N/\log(0))^2 * (\log(-18*N-4)/N)$	= 0

$$O\left(D^{\alpha} f(t)\right) = O\left(\frac{1}{\Gamma(m-\alpha)} \int_0^t \frac{f^{(m)}(\tau)}{(t-\tau)^{\alpha+1-m}} d\tau\right) \tag{26}$$

$$O\left(D^{\alpha} f(t)\right) = O\left(\log(m-\alpha)^{-2}.N^2.O_{ML}(N)^m\right) \tag{27}$$

$$O\left(D^{\alpha} f(t)\right) = O\left(\log(1-\alpha)^{-2}.N^2.O_{ML}(N)\right) \tag{28}$$

The results of the application of algorithmic complexity based on Caputo fractional-order and classical derivatives to the diabetes dataset are provided in Table 5.

When Caputo fractional-order derivative with three parametric Mittag-Leffler function is $\alpha \leq 1$, α the value decreases, while the complexity increases logarithmically. When there is this condition, $\alpha = 1$, then it is trivial.

Based on the complexity results obtained for Caputo fractional-order derivative with three parametric Mittag-Leffler function concerning the algorithmic complexity obtained, as provided in Table 5, it is seen that the highest complexity is the case for order 0.2. The lowest complexity order is for 0.8.

The lowest order, which is 0.8, with the least complexity of Caputo fractional-order derivative, yields the best result as 83.8000% in the diagnosis and classification of the disease by the ANN algorithm.

4 Conclusions, Outcomes and Future Directions

Fractional calculus approach provides novel models by introducing fractional-order calculus to optimization methods, which is employed with regard to machine learning algorithms. This scheme aims at achieving optimized solutions by maximiz-

ing the accuracy of the model and minimizing the functions like computational costs. Mathematical-informed frameworks, in this structure, are utilized to allow accurate, reliable and robust understanding of various complex biological processes which include spatial and temporal scales. This complexity requires a comprehensive handling of different biological processes, capable of capturing the significant attributes on the temporal and spatial scales. The investigation of algorithmic complexity enables directions towards the application of efficient programs to process, model and analyze biological data in the field of computational biology. Furthermore, algorithmic complexity, as a way of comparing the efficiency of an algorithm, enables the examination of an algorithm's properties to solve computational problems along with the relationship between the size of an instance of the generic problem and the time needed for computation. Algorithmic complexity, moreover, allows the classification of the computational problems based on their algorithmic complexity, as defined according to the way the resources are required for the solution of the problem. Our aim in this study has been the diagnostic and differentiability predictive purposes for the disease, (diabetes, as a metabolic disorder, in our case) which might display various transient biological properties. Thus, we have aimed to establishing a robust and accurate model based on the combination of fractional-order derivative and Artificial Neural Network (ANN) and foreground the importance of algorithmic complexity in order to obtain the fractional-order derivative with the least complexity so that it would be possible to attain optimized solution. This sort of integrative multi-stage scheme based on mathematical-informed framework as proposed in our study has not been addressed in this manner in previous works in the literature [32–44]. Accordingly, the following steps have been applied to serve our aims: (i) The Caputo fractional derivative was applied with three-parametric Mittag-Leffler function (α, β, γ) to the diabetes dataset. Hence, new fractional models with varying degrees were established by ensuring data fitting through the Fitting algorithm Mittag-Leffler function with three parameters (α, β, γ) based on Heavy-tailed distributions. After this application, the new dataset (mfc_diabetes) was obtained. (ii) Classical derivative (calculus) was applied to the diabetes dataset, generating the cd_diabetes dataset. (iii) The performance of the new dataset as obtained from step (i) and the dataset obtained from step (ii) as well as the diabetes dataset was compared via the FFBP algorithm. The fractional-order derivative model which would be the most optimal for the disease was generated through this step. (iv) Algorithmic complexity was used to attain the Caputo fractional-order derivative with the least complexity, namely to achieve the optimized solution.

Considering these aspects and way of thinking proposed in our study, the following future directions can be stated:

– Computational biologists and researchers can benefit from algorithmic complexity to attain optimized solutions by managing the intensive data tasks through maximizing accuracy and minimizing computational costs; thus, to attain the most optimized results by providing directions to process, model and analyze the related data.

– Through the identification of the applicable models in advance by algorithmic complexity, it will be possible to attain efficiency in terms of resources when time needed to execute the algorithm and memory are considered.
– The use of factional-order derivative with the least complexity enables one to achieve the optimized scalable solutions to problems driven by complexity.
– The integration and application of multi-stage methods can assure a better understanding of complexity in computational biology algorithms and effective design of the concomitant high-performance computing.

The multi-stage integrative approach, including the application of fractional-order calculus to optimization methods, and the experimental results we obtained have revealed the benefit of maximizing the model's accuracy and minimizing the cost functions like the computational burden through algorithmic complexity, which elucidates the applicability of the method proposed in different domains characterized by complex, dynamic, variable and transient components.

References

1. Das S, Pan I (2012) Basics of fractional order signals and systems. Fractional order signal processing. Springer, Berlin, Heidelberg, pp 13–30
2. Karaca Y, Baleanu D, Computational fractional-order calculus and classical calculus AI for comparative differentiability prediction analyses of complex-systems-grounded paradigm. In: Multi-chaos, fractal and multi-fractional artificial intelligence of different complex systems. Elsevier
3. Singhal G, Aggarwal V, Acharya S, Aguayo J, He J, Thakor N (2010) Ensemble fractional sensitivity: a quantitative approach to neuron selection for decoding motor tasks. Comput Intell Neurosci
4. Magin RL (2010) Fractional calculus models of complex dynamics in biological tissues. Comput Math Appl 59(5):1586–1593
5. Mathai AM, Haubold HJ (2017) Fractional and multivariable calculus. In: Model building and optimization problems. Springer Optimization and its Applications, vol 122
6. Vosika ZB, Lazovic GM, Misevic GN, Simic-Krstic JB (2013) Fractional calculus model of electrical impedance applied to human skin. PloS one 8(4):59483
7. Gustafson K, del Castillo Negrete D, Dorland B (2006) Fractional calculus phenomenology in two-dimensional plasma models. In: APS division of plasma physics meeting abstracts, vol 48, pp 1–143
8. Aguilar JFG, Alvarado JJB, Garcia JJR, Fraga TC (2012) Modeling and simulation of equivalent circuits in description of biological systems-a fractional calculus approach. J Electr Bioimpedance 3(1):2–11
9. Baleanu D, Mohammadi H, Rezapour S (2020) A mathematical theoretical study of a particular system of Caputo Fabrizio fractional differential equations for the Rubella disease model. Adv Differ Eq 1:1–19
10. Khan MA, Hammouch Z, Baleanu D (2019) Modeling the dynamics of hepatitis E via the Caputo-Fabrizio derivative. Math Model Nat Phenom 14(3):311
11. Khan H, Khan A, Al Qurashi M, Baleanu D, Shah R (2020) An analytical investigation of fractional-order biological model using an innovative technique. Complexity
12. Jajarmi A, Baleanu D (2018) A new fractional analysis on the interaction of HIV with CD4+ T-cells. Chaos Solitons Fractals 113:221–229

13. Sajjadi SS, Baleanu D, Jajarmi A, Pirouz HM (2020) A new adaptive synchronization and hyperchaos control of a biological snap oscillator. Chaos Solitons Fractals 138:109919
14. Singh J, Ganbari B, Kumar D, Baleanu D (2021) Analysis of fractional model of guava for biological pest control with memory effect. J Adv Res 32:99–108
15. Sommacal L, Melchior P, Oustaloup A, Cabelguen J-M, Ijspeert AJ (2008) Fractional multi-models of the frog gastrocnemius muscle. J Vib Control 14(9–10):1415–1430
16. Toledo-Hernandez R, Rico-Ramirez V, Iglesias-Silva GA, Diwekar UM (2014) A fractional calculus approach to the dynamic optimization of biological reactive systems. Part I: fractional models for biological reactions. Chem Eng Sci 117:217–228
17. Krishna BT (2008) Reddy KVVS (2008) Active and passive realization of fractance device of order 1/2. Active Passive Electron Compon 5:369421
18. Debnath L (2003) Recent applications of fractional calculus to science and engineering. Int J Math Math Sci 54:3413–3442
19. Panda R, Dash M (2006) Fractional generalized splines and signal processing. Signal Process 86(9):2340–2350
20. Singh AP, Deb D, Agrawal H, Balas VE (2021) Modeling, stability and fractional control of single flexible link robotic manipulator. In: Fractional modeling and controller design of robotic manipulators. Springer, Cham pp 83–98
21. Liu Y, Zhang Z, Ma T (2021) Second-order leader-following consensus of fractional-order multi-agent systems. In: 2021 IEEE international conference on intelligence and safety for robotics (ISR). IEEE, pp 280–283
22. Gutierrez RE, Rosario JM, Tenreiro Machado J (2010) Fractional order calculus: basic concepts and engineering applications. Math Prob Eng
23. Garrappa R (2015) Numerical evaluation of two and three parameter Mittag-Leffler functions. SIAM J Numer Anal 53(3):1350–1369
24. Fernandez A, Husain I (2020) Modified Mittag-Leffler functions with applications in complex formulae for fractional calculus. Fractal Fractional 4(3):45
25. Bushnaq S, Shah K, Alrabaiah H (2020) On modeling of coronavirus-19 disease under Mittag-Leffler power law. Adv Differ Eq 1:1–16
26. Magin RL, Ingo C, Colon-Perez L, Triplett W, Mareci TH (2013) Characterization of anomalous diffusion in porous biological tissues using fractional order derivatives and entropy. Microporous Mesoporous Mater 178:39–43
27. Jose KK, Abraham B (2011) A count model based on Mittag-Leffler interarrival times. Statistica 71(4):501–514
28. Aghdaoui H, Tilioua M, Nisar KS, Khan I (2021) A fractional epidemic model with Mittag-Leffler kernel for COVID-19. Math Biol Bioinf 16(1):39–56
29. Sher M, Shah K, Khan ZA, Khan H, Khan A (2020) Computational and theoretical modeling of the transmission dynamics of novel COVID-19 under Mittag-Leffler power law. Alexandria Eng J 59(5):3133–3147
30. Slezak DF, Surez C, Cecchi GA, Marshall G, Stolovitzky G (2010) When the optimal is not the best: parameter estimation in complex biological models. PloS one 5(10):13283
31. Moles CG, Mendes P, Banga JR (2003) Parameter estimation in biochemical pathways: a comparison of global optimization methods. Genome Res 13(11):2467–2474
32. Kiiveri HT (2008) A general approach to simultaneous model fitting and variable elimination in response models for biological data with many more variables than observations. BMC Bioinf 9(1):1–9
33. Platt T, Denman KL, Jassby AD (1975) The mathematical representation and prediction of phytoplankton productivity. Technical report no 523. Tech Rep, Fisheries and Marine Service
34. Adams MP, Collier CJ, Uthicke S, Ow YX, Langlois L, O'Brien KR (2017) Model-t versus biological relevance: evaluating photosynthesis-temperature models for three tropical seagrass species. Sci Rep 7(1):1–12
35. Zhao W, Zou W, Chen JJ (2014) Topic modeling for cluster analysis of large biological and medical datasets. BMC Bioinf BioMed Central 15(11):1–11

36. Albrecher H, Bladt M, Bladt M (2020) Matrix Mittag-Leffler distributions and modeling heavy-tailed risks. Extremes 23:425–450
37. Gomolka Z (2018) Backpropagation algorithm with fractional derivatives. In: ITM web of conferences, vol 21. EDP Sciences
38. Mall S, Chakraverty S (2020) Artificial neural network based solution of fractional vibration model. Recent trends in wave mechanics and vibrations. Springer, Singapore, pp 393–406
39. Kadam P, Datkhile G, Vyawahare VA (2019) Artificial neural network approximation of fractional-order derivative operators: analysis and DSP implementation. Fractional calculus and fractional differential equations. Birkhuser, Singapore, pp 93–126
40. Yang G, Zhang B, Sang Z, Wang J, Chen H (2017) A Caputo-type fractional-order gradient descent learning of BP neural networks. International symposium on neural networks. Springer, Cham, pp 547–554
41. Bao C, Pu Y, Zhang Y (2018) Fractional-order deep backpropagation neural network. Comput Intell Neurosci
42. Du DZ, Ko KI (2011) Theory of computational complexity, vol 58. Wiley
43. Cirillo D, Valencia A (2018) Algorithmic complexity in computational biology. arXiv:1811.07312
44. Welch WJ (1982) Algorithmic complexity: three NP-hard problems in computational statistics. J Statist Comput Simul 15(1):17–25
45. UCI Irvine machine learning repository, 2021. https://archive.ics.uci.edu/ml/datasets/diabetes. Accessed 21 Feb 20
46. Camargo RF, de Oliveira EC, Vaz J (2020) On the generalized Mittag-Leffler function and its application in a fractional telegraph equation. Math Phy Anal Geom 15(82012):1–16
47. Kilbas AA, Srivastava HM, Trujillo JJ (2006) Theory and applications of fractional differential equations. Elsevier, Amsterdam, The Netherlands
48. Mittag-Leffler MG (1903) Sur la nouvelle function. Comptes Rendus l'Acadmie Sci 137:554–558
49. Prabhakar TR (1971) A singular integral equation with a generalized mittag leffler function in the kernel. Yokohama J Math 19:7–15
50. Gorenflo R, Kilbas AA, Mainardi F, Rogosin SV (2016) Mittag-Leffler functions, related topics and applications. Springer, Berlin, Germany
51. Pillai RN (1990) On Mittag-Leffler functions and related distributions. Ann Inst Istatist Math 42(1):157–161
52. Chakraborty S, Ong SH (2017) Mittag-Leffler function distribution-a new generalization of hyper-Poisson distribution. J Statist Distrib Appl 4(1):1–17
53. Mainardi F, Gorenflo R (2000) On Mittag-Leffler-type functions in fractional evolution processes. J Comput Appl Math 118:283–299
54. Mittag-Leffer MG (1902) Sur l'integrale de Laplace-Abel. CR Acad Sci Paris (Ser II) 136:937–939
55. Pillai RN, Jayakumar K (1995) Discrete Mittag-Leffler distributions. Statist Probab Lett 23:271–274
56. Arnold BC (2014) Pareto distribution. In: Wiley Stats Ref: Statistics Reference Online, pp 1–10
57. Ouyang Y, Wang W (2016) Comparison of definition of several fractional derivatives. In: 2016 international conference on education, management and computer science. Atlantis Press
58. Arnold BC, Beaver RJ (2000) The skew-cauchy distribution. Statist Probab Lett 49(3)
59. Kharazmi O (2016) Generalized weighted Weibull distribution. J Math Ext 10:89–118
60. D'Agostino RB (1986) Goodness-of-fit-techniques, vol 68. CRC Press
61. Fan J, Gijbels I (2018) Local polynomial modelling and its applications: monographs on statistics and applied probability 66. Routledge
62. Podlubny I, Kacenak M (2005) Mittag-Leffler function, mathworks, Inc. Matlab Central File Exchange. www.mathworks.com/matlabcentral/_leexchange/8738
63. Chen YQ (2008) Generalized Mittag-Leffler function, MathWorks, Inc. Matlab Central File Exchange. www.mathworks.com/matlabcentral/_leexchange, 20849

64. Petrs (2011) Fractional derivatives, fractional integrals, and fractional differential equations in Matlab, 9412
65. Baleanu D, Karaca Y, Mittag-Leffler functions with heavy-tailed distributions' algorithm based on different biology datasets to be fit for optimum mathematical models' strategies. Elsevier (published under)
66. Mainardi F (2014) On some properties of the Mittag-Leffler function $E_\alpha(-t^\alpha)$, completely monotone for $t > 0$ with $0 < \alpha < 1_0$. Discrete Continuous Dyn Syst-B 19(7):2267–2278
67. Mainardi F (2020) Why the Mittag-Leffler function can be considered the queen function of the fractional calculus? Entropy 22(12):1359
68. Garrappa R, Kaslik E, Popolizio M (2019) Evaluation of fractional integrals and derivatives of elementary functions: overview and tutorial. Mathematics 7(5):407
69. Karaca Y, Zhang YD, Muhammad K (2020) Characterizing complexity and self-similarity based on fractal and entropy analyses for stock market forecast modelling. Expert Syst Appl 144:113098
70. Karaca Y, Cattani C (2018) Computational methods for data analysis, vol 978. Berlin/Boston + co-pub, Walter de Gruyter GmbH, p 3110496352
71. Hagan MT, Menhaj MB (1994) Training feedforward networks with the Marquardt algorithm. IEEE Trans Neural Netw 5(6):989–993
72. Karaca Y, Cattani C (2019) A comparison of two hölder regularity functions to forecast stock indices by ANN algorithms. In: Misra S et al (eds) 19th international conference on computational science and its applications, vol 11620. Springer, Saint Petersburg, Russia, pp 270–284
73. Saeedi E, Hossain MS, Kong Y (2019) Feed-forward back-propagation neural networks in side-channel information characterization. J Circuits Syst Comput 28(1)
74. Karaca Y, Moonis M, Baleanu D (2020) Fractal and multifractional-based predictive optimization model for stroke subtypes' classification. Chaos Solitons Fractals 136:109820
75. Kong Q, Siauw T, Bayen AM (2021) Python programming and numerical methods, a guide for engineers and scientists
76. Chivers I, Sleightholme J (2015) An introduction to algorithms and the big O notation. Introduction to programming with Fortran. Springer, Cham, pp 359–364
77. Al Na'mneh R, Pan WD (2007) Five-step FFT algorithm with reduced computational complexity. Inf Process Lett 101(6):262–267
78. Mathworks The (2020) MATLAB r 2020b (2020) The MathWorks Inc. Natick, MA
79. Van Rossum G (1995) Python tutorial, technical report CS-R9526. Centrum voor Wiskunde en Informatica CWI, Amsterdam

Case Study of Non-singular Kernel Model for MHD Boundary Layer Flow of a Rate Type Fluid over an Oscillating Plate

Oluwasoji John Osalusi, Azhar Ali Zafar, Maryam Asgir, Dumitru Baleanu, and Muhammad Bilal Riaz

Abstract The magnetohydrodynamics boundary layer flow of rate type fluid over an oscillating inclined infinite plate along with Newtonian heating and slip at the boundary is investigated. The model is developed by using the Atangana-Baleanu time-fractional derivative operator. Temperature and velocity fields for the non-integer order derivative model are computed. From our general results, several results from the literature could be recovered, for example; the cases corresponding to the constant motion of the plate, as well as the analogous results for ordinary Maxwell fluid, the fractional viscous and ordinary viscous fluid could be recovered. Moreover, the physical significance of the parameters like relaxation time, fractional order parameter, Grashof number, and inclination of the plate is discussed and their control on the velocity of the fluid is analysed through graphical illustrations and useful conclusions are recorded.

Keywords MHD · Boundary layer · Newtonian heating · Fractional derivative · Slip effects

O. J. Osalusi (✉) · A. A. Zafar · M. Asgir
Department of Mathematics, Government College University Lahore, Lahore, Pakistan
e-mail: bilalsehole@gmail.com

D. Baleanu
Department of Mathematic, Cankay University, Ankara, Turkey

Institutes of Space Sciences, 077125 Magurele, Bucharest, Romania

M. B. Riaz
Department of Automation, Biomechanics and Mechatronics, Lodz University of Technology, 1/15 Stefanowskiego St., 90924 Lodz, Poland

Department of Mathematics, University of Management and Technology Lahore, Lahore, Pakistan

Institute for Groundwater Studies, University of the Free State, Bloemfontein, South Africa

J. Singh et al. (eds.), *Advances in Mathematical Modelling, Applied Analysis and Computation*, Lecture Notes in Networks and Systems 415,
https://doi.org/10.1007/978-981-19-0179-9_4

1 Introduction

Magnetohydrodynamics (MHD) boundary layer flow of fluids over an oscillating plate is the interest of many researchers because such models have lots of applications in the chemical and food industry [25]. MHD free and mixed convective flow, as well as the impacts of the flow of thermal energy and mass transference past an upright plate, have been extensively investigated in literary works [13, 18–20, 23, 27, 29]. Moreover, studies related to natural convective flow under the influence of magnetic parameters as well as with the flow of thermal energy and mass transmit over an inclined plate can be found in [1, 2, 8, 28].

In 2013, Mishra et al. [22] analysed the oscillatory suction and heat source influences on MHD fluid flow having the property of visco-elasticity passing across a permeable medium. The critical investigation of boundary layer flow over a permeable non-linearly elastic sheet with partial slip effect at the boundary was done by Mukhopadhyay [24]. Further investigations include MHD heat transference over a porous plate with slip effects [12], combined effects of partial slip and magnetic flux on diagonally prominent rheological fluid over an elastic surface [26], heat conductivity with emission consequences of slip flow of Casson fluid [30], mass transfer and radiation influences on MHD natural convective flow over an exponentially stimulated upright permeable plate [29], turbulent free convection in fluid over a vertical plate submerged in a permeable medium [35].

More recently, Gupta et al. examined the MHD flow of Williamson nanofluid confined by the stretching sheet with the variable thickness in [10]. Moreover, MHD three-dimensional boundary layer flow and heat transfer of water-driven nanoparticles are discussed in [11]. Furthermore, Imran et al. [14] investigated boundary layer flow of generalized MHD Maxwell fluid over an exponentially stimulated infinite perpendicular surface with Newtonian heating and slip effect at the bounds.

Due to fact that the complex behaviours of many materials can be explained with ease employing non-integer order derivative approach, that is the reason, the use of non-integer order derivatives in the modelling of dynamical systems is gaining much fame. Fractional order characterization inhered many physical phenomenon, hence, it is necessary to explain them. Non-integer order derivatives provide an excellent instrument for explaining the memory and hereditary characteristics of many materials and processes [6] that are clearly ignored while examining the model using classical integer- order derivative approaches. Clearly, classical integer-order models are inadequate to certify suitable correlation with experimental data. That is the very reason that, over the recent few years, researchers have renewed their investigations by using fractional order derivative to get accurate modelling and more insight of the dynamical systems, for example, we refer [6, 31, 32, 34] and the work cited in there. Nowadays, fractional calculus and its applications have caught the attention of many researchers. Many engineering, economics, and medical problems can easily be analysed and solved by models associated with fractional calculus In the literature, there are several definitions of the fractional derivative operators, which have their own advantages and disadvantages [3–5, 7]. In 2016, Atangana and

Baleanu [3] established fractional-order derivative with non-local and non-singular kernels having its implementation in heat transference models [4]. For some notable most recent studies using this new definition of fractional order derivative operator, we refer [15, 17].

Motivated by these investigations, we aim to explore the MHD boundary layer flow of rate-type fluid over a inclined plate that is oscillating in its plane. Furthermore, the flow is influenced by the slip effects and the Newtonian heating of the plate. The governing equations of the model are developed in the setting of fractional calculus employing the Atangana-Baleanu time-fractional derivative operator. Further, the control of the flow parameters on the dynamics of the fluid will be graphically analysed.

2 Problem Description

We shall examine an incompressible Maxwell fluid with unsteady boundary layer flow over an inclined plate along with Newtonian heating and slip at the boundary. The inclined plate makes an angle γ with ψ-axis and $0 < \gamma < \frac{\pi}{2}$. At t is zero, the plate and the fluid are static with constant temperature T_∞. Starting at $t > 0$, there will be a sinusoidal motion of the plate with a slip effect at the wall. The assumption as proposed by Makinde [21] was taken into account that the wall is subject to Newtonian heating. All the physical pertinent quantities are the function of ψ and t only as the plate is infinite. The influence of the magnetic flux is upright to the plate. The governing equations for Maxwell fluid flow problem associated with heat transfer and shear stress owing to a mix of heat emission and convection are elaborated in terms of partial differential equations (PDE) in a dimensionless form are [14, 21, 32].

$$\left(1+\lambda\frac{\partial}{\partial t}\right)\frac{\partial w(\psi,t)}{\partial t} = \frac{\partial^2 w(\psi,t)}{\partial \psi^2} + \left(1+\lambda\frac{\partial}{\partial t}\right) Gr\theta(\psi,t)\cos\gamma - M\left(1+\lambda\frac{\partial}{\partial t}\right) w(\psi,t) \tag{1}$$

$$\left(1+\lambda\frac{\partial}{\partial t}\right)\tau(\psi,t) = \frac{\partial w(\psi,t)}{\partial \psi} \tag{2}$$

$$\mathrm{Pr}_{eff}\frac{\partial\theta(\psi,t)}{\partial t} = \frac{\partial^2\theta(\psi,t)}{\partial\psi^2} \tag{3}$$

In the above relations $w(\psi,t)$ denotes the velocity of the fluid, $\tau(\psi,t)$ is the shear stress, $\theta(\psi,t) = \frac{T(\psi,t)-T_\infty}{T_w}$ temperature of the fluid. Moreover, λ, Gr, M and Pr_{eff} represent the relaxation time parameter, Grashof number, magnetic parameter and effective Prandtl number, respectively.

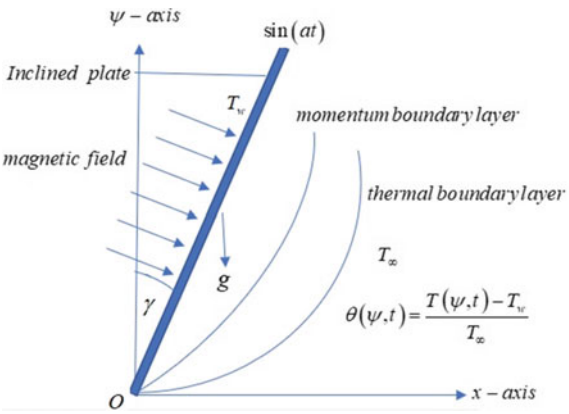

Fig. 1 Geometry of the problem

The imposed initial and boundary conditions are as follow:

$$w(\psi,0)=0,\quad \left.\frac{\partial w(\psi,t)}{\partial t}\right|_{t=0}=0,\quad \theta(\psi,0)=0, \tag{4}$$

$$w(0,t)-b\frac{\partial w(0,t)}{\partial y}=\sin(at),\quad \left.\frac{\partial\theta(\psi,t)}{\partial\psi}\right|_{\psi=0}=-[1+\theta(0,t)], \tag{5}$$

$$w(\psi,t)\to 0,\quad \theta(\psi,t)\to 0, as\quad \psi\to\infty. \tag{6}$$

where a is a constant and b describe the parameter of slip (Fig. 1).

Using Atangana-Baleanu time-fractional derivative operator of order $\alpha\in(0,1)$, Eqs. (1–3) become:

$$(1+\lambda^{ABC}D_t^{\alpha})\frac{\partial w(\psi,t)}{\partial t}=\frac{\partial^2 w(\psi,t)}{\partial\psi^2}+Gr(1+\lambda^{ABC}D_t^{\alpha})\theta(\psi,t)\cos\gamma - M(1+\lambda^{ABC}D_t^{\alpha})\,w(\psi,t), \tag{7}$$

$$\left(1+\lambda^{ABC}D_t^{\alpha}\right)\tau(\psi,t)=\frac{\partial w(\psi,t)}{\partial\psi},\quad Pr_{eff}{}^{ABC}D_t^{\alpha}\theta(\psi,t)=\frac{\partial^2\theta(\psi,t)}{\partial\psi^2}, \tag{8}$$

where time-fractional Atangana-Baleanu derivative is stated as [3]:

$${}^{ABC}D_t^{\alpha}(h(t))=\frac{1}{1-\alpha}\int_b^{\tau}h'(x)E_{\alpha}\left[-\alpha\frac{(\tau-x)^{\alpha}}{1-\alpha}\right]d\tau. \tag{9}$$

The Laplace transform (LT) of the time-fractional Atangana-Baleanu fractional derivative is

$$\mathcal{L}\left\{{}^{ABC}D_t^{\alpha}(w(\psi,t))\right\}(s) = \frac{s^{\alpha}\mathcal{L}\{w(\psi,s)\} - s^{\alpha-1}w(\psi,0)}{(1-\alpha)s^{\alpha}+\alpha}.$$

3 Investigation of the Solution of the Problem

3.1 Investigation of the Solution of the Temperature

For the solution of the temperature profile, we will solve the equation associated with temperature,

$$Pr_{eff}\frac{\partial\theta(\psi,t)}{\partial t} = \frac{\partial^2\theta(\psi,t)}{\partial y^2}, \tag{10}$$

subject to the conditions,

$$\theta(\psi,0) = 0, \tag{11}$$

$$\frac{\partial\theta(\psi,t)}{\partial\psi}|_{\psi=0} = -[1+\theta(0,t)], \tag{12}$$

$$\theta(\psi,t) \to 0, as \quad \psi \to \infty. \tag{13}$$

Applying the Laplace transform,

$$L\{\mathrm{Pr}_{eff}\,{}^{ABC}D_t^{\alpha}\theta(\psi,t)\} = L\left\{\frac{\partial^2\theta(\psi,t)}{\partial\psi^2}\right\}, \tag{14}$$

we get

$$\frac{\mathrm{Pr}_{eff}\,s^{\alpha}\bar{\theta}(\psi,s)}{(1-\alpha)s^{\alpha}+\alpha} = \frac{\partial^2\bar{\theta}(\psi,s)}{\partial\psi^2} \tag{15}$$

satisfying

$$\frac{\partial\bar{\theta}(0,s)}{\partial\psi} = -\left[\frac{1}{s}+\bar{\theta}(0,s)\right] \text{ and } \bar{\theta}(\psi,s)\to 0, \text{ as } \psi\to\infty. \tag{16}$$

Finally, solving (15) using $(16)_2$, we get

$$\bar{\theta}(\psi,s) = \frac{\sqrt{(1-\alpha)s^{\alpha}+\alpha}}{\sqrt{\mathrm{Pr}_{eff}\,s^{\alpha}}-\sqrt{(1-\alpha)s^{\alpha}+\alpha}}.\frac{e^{-\psi\sqrt{\frac{\mathrm{Pr}_{eff}s^{\alpha}}{(1-\alpha)s^{\alpha}+\alpha}}}}{s^{\alpha}} \tag{17}$$

or

$$\bar{\theta}(\psi,s) = \bar{\theta}_1(s)\times\bar{\theta}_2(\psi,s) \tag{18}$$

where

$$\bar{\theta_1}(s) = \frac{\sqrt{(1-\alpha)s^{\alpha}+\alpha}}{\sqrt{\mathrm{Pr}_{eff}\, s^{\alpha}} - \sqrt{(1-\alpha)s^{\alpha}+\alpha}}, \tag{19}$$

which can be written as

$$\begin{aligned}\bar{\theta_1}(s) = &\left\{\frac{(1-\alpha)s}{\mathrm{Pr}_{eff}+\alpha-1} + \frac{\mathrm{Pr}_{eff}\,\alpha}{(\mathrm{Pr}_{eff}+\alpha-1)^2} + \frac{\mathrm{Pr}_{eff}\,\alpha^2}{(\mathrm{Pr}_{eff}+\alpha-1)^3} \times \frac{1}{s-\frac{\alpha}{\mathrm{Pref}+\alpha-1}}\right\} \\ &\times \frac{\sqrt{\mathrm{Preff}}}{\sqrt{(1-\alpha)s^2+\alpha s}} \\ &+ \left\{\frac{(1-\alpha)}{\mathrm{Pr}_{eff}+\alpha-1} + \frac{\mathrm{Pr}_{eff}\,\alpha}{(\mathrm{Pr}_{eff}+\alpha-1)} + \frac{\mathrm{Pr}_{eff}\,\alpha}{(\mathrm{Pr}_{eff}+\alpha-1)^2} \times \frac{1}{s-\frac{\alpha}{\mathrm{Preff}}+\alpha-1}\right\},\end{aligned} \tag{20}$$

and

$$\bar{\theta_2}(\psi, s) = \frac{e^{-\psi\sqrt{\frac{\mathrm{Pr}_{eff}s^{\alpha}}{(1-\alpha)s^{\alpha}+\alpha}}}}{s^{\alpha}}. \tag{21}$$

Using the formulae

$$L^{-1}\left\{\frac{e^{-\psi\sqrt{\frac{\mathrm{Pr}_{eff}s^{\alpha}}{(1-\alpha)s^{\alpha}+\alpha}}}}{s^{\alpha}}\right\} = 1 - \frac{2\,\mathrm{Pr}_{eff}}{\pi}\int_0^{\infty}\frac{\sin(\frac{y}{\sqrt{1-\alpha}}x)}{x(\mathrm{Pr}_{eff}+x^2)}e^{(\frac{\psi}{1-x}\alpha^2)}dx, \tag{22}$$

$$L^{-1}\left\{\frac{a}{\sqrt{s^2+a^2}}\right\} = I_0(at) \text{ and } L^{-1}\left\{\frac{s}{\sqrt{s^2+a^2}}\right\} = \delta(t) + aI_1(at) \tag{23}$$

we get

$$\theta(\psi, t) = \int_0^t \theta_1(t-\tau)\theta_2(\psi, \tau)d\tau \tag{24}$$

where

$$\begin{aligned}\theta_1(t) = &a_1\sqrt{\frac{\mathrm{Pr}_{eff}}{1-\alpha}}e^{-bt}[\delta(t) + bI_1(bt)] + \sqrt{\frac{\mathrm{Pr}_{eff}}{1-\alpha}}(a_2 - ba_1)e^{-bt}I_o(bt) \\ &+ a_3\sqrt{\frac{\mathrm{Pr}_{eff}}{1-\alpha}}[e^{a_4t} + e^{-bt}I_o(bt)] + a_1\delta(t) + a_2e^{a_4t}\end{aligned} \tag{25}$$

and

$$\theta_2(\psi,t) = 1 - \frac{2\,\mathrm{Pr}_{eff}}{\pi}\int_0^{\infty} \frac{\sin(\frac{\psi}{\sqrt{1-\alpha}}x)}{x(\mathrm{Pr}_{eff}+x^2)} e^{(\frac{\psi}{1-x}\alpha^2)}dx \tag{26}$$

with $a_1 = \frac{1-\alpha}{\mathrm{Pr}_{eff}+\alpha-1}$, $a_2 = \frac{\mathrm{Pr}_{\mathrm{eff}}\,\alpha}{(\mathrm{Pr}_{eff}+\alpha-1)^2}$, $a_3 = \frac{\mathrm{Pr}_{\mathrm{eff}}\,\alpha^2}{(\mathrm{Pr}_{eff}+\alpha-1)^3}$, $a_4 = \frac{\alpha}{\mathrm{Pr}_{eff}+\alpha-1}$ and $b = \frac{\alpha}{2(1-\alpha)}$.

Moreover, the heat flow rate from plate to fluid is measured by Nusselt number: $Nu = \frac{\partial\theta(\psi,t)}{\partial\psi}\Big|_{\psi=0}$, so

$$Nu = \mathrm{Pr}_{eff}\, e^{a_4 t} - a_1\sqrt{\frac{\mathrm{Pr}_{eff}}{1-\alpha}}e^{-bt} I_o(bt) + a_2\sqrt{\frac{\mathrm{Pr}_{eff}}{1-\alpha}}\left[e^{a_4 t} + e^{-bt} I_o(bt)\right]. \tag{27}$$

By taking limit $\alpha \to 1$, we obtain the related results for the ordinary temperature field:

$$\theta(\psi,t) = e^{\left(-\psi+\frac{t}{\mathrm{Pr}_{eff}}\right)}\,\mathrm{erfc}\left(\frac{\psi\sqrt{\mathrm{Pr}_{eff}}}{2\sqrt{t}} - \sqrt{\frac{t}{\mathrm{Pr}_{eff}}}\right) - \mathrm{erfc}\left(\frac{\psi\sqrt{\mathrm{Pr}_{eff}}}{2\sqrt{t}}\right), \tag{28}$$

and the corresponding Nusselt number:

$$Nu = e^{\left(\frac{t}{Pr_{eff}}\right)}\left(2 - erfc\left(\sqrt{\frac{t}{\mathrm{Pr}_{eff}}}\right)\right). \tag{29}$$

3.2 *Investigation of the Solution of the Velocity*

Employing the LT on Eq. (7) considering the concerned initial condition, the velocity in transformed domain is obtained as follows:

$$\frac{[[s(1-\alpha)+\lambda]s^{\alpha}+s\alpha]\bar{w}(\psi,s)}{(1-\alpha)s^{\alpha}+\alpha}$$
$$= \frac{\partial^2\bar{w}(\psi,s)}{\partial\psi^2} + \left[\frac{[[s(1-\alpha)+\lambda]s^{\alpha}+s\alpha]}{(1-\alpha)s^{\alpha}+\alpha} Gr \frac{\sqrt{(1-\alpha)s+\alpha}}{\sqrt{\mathrm{Pr}_{eff}s^{\alpha}} - \sqrt{(1-\alpha)s^{\alpha}+\alpha}}\right]$$
$$\frac{e^{-y\sqrt{\mathrm{Pr}_{eff}s^{\alpha}/(1-\alpha)s^{\alpha}+\alpha}}}{s^{\alpha}}\cos\gamma - M[\frac{[s(1-\alpha)+\lambda]s^{\alpha}+s\alpha]}{(1-\alpha)s^{\alpha}+\alpha}]\bar{w}(\psi,s). \tag{30}$$

On simplification, we have:

$$\frac{\partial^2 \bar{u}(\psi, s)}{\partial \psi^2} - \left[\frac{[[s(1-\alpha)+\lambda]s^\alpha + s\alpha]}{(1-\alpha)s^\alpha + \alpha}(1+M) \right] \bar{w}(\psi, s)$$

$$= \left[\frac{[[s(1-\alpha)+\lambda]s^\alpha + s\alpha]}{(1-\alpha)s^\alpha + \alpha} Gr \frac{\sqrt{(1-\alpha)s+\alpha}}{\sqrt{\mathrm{Pr}_{eff} s^\alpha} - \sqrt{(1-\alpha)s^\alpha + \alpha}} \right]$$

$$\frac{e^{-\psi\sqrt{\mathrm{Pr}_{eff} s^\alpha/(1-\alpha)s^\alpha + \alpha}}}{s^\alpha} \cos\gamma.$$

Take $1-\alpha = \sigma$, $w = \frac{[[s\sigma+\lambda]s^\alpha + s\alpha]}{\sigma s^\alpha + \alpha}(1+M)$ and $A = \frac{[s\sigma+\lambda]s^\alpha + s\alpha}{s^\alpha(\sigma s^\alpha + \alpha)} \frac{\sqrt{\sigma s+\alpha} Gr \cos\gamma}{\sqrt{\mathrm{Pr}_{eff} s^\alpha - s^\alpha}\sqrt{\sigma s^\alpha + \alpha}}$, the last expression becomes

$$\frac{\partial^2 \bar{u}}{\partial \psi^2} - \omega \bar{w} = A e^{-\psi\sqrt{\frac{\mathrm{Pr}_{eff} s^\alpha}{\sigma s^\alpha + \alpha}}} \tag{31}$$

with boundary conditions $\bar{w}(0, s) - b\frac{\partial \bar{w}(0,s)}{\partial \psi} = \frac{a}{s^2+a^2}$ and $\bar{w}(\psi, s) \to 0$, as $\psi \to \infty$.

Equation (31) is a second-order non-homogenous differential equation. Its complimentary and particular solutions are of the form:

$$\bar{w}_c(\psi, s) = C_1 e^{\psi\sqrt{\omega}} + C_2 e^{-\psi\sqrt{\omega}}$$

$$\bar{w}_p(\psi, s) = \frac{A(\sigma s^\alpha + \alpha)e^{-\psi\sqrt{\frac{\mathrm{Pr}_{eff} s^\alpha}{s\sigma+\alpha}}}}{\mathrm{Pr}_{eff} s^\alpha - \omega^2(\sigma s^\alpha + \alpha)}$$

thus the general solution $\bar{w}(\psi, s) = \bar{w}_c(\psi, s) + \bar{w}_p(\psi, s)$ is

$$\bar{w}(\psi, s) = C_1 e^{\psi\sqrt{\omega}} + C_2 e^{-\psi\sqrt{\omega}} + \frac{A(\sigma s^\alpha + \alpha)e^{-\psi\sqrt{\frac{\mathrm{Pr}_{eff} s^\alpha}{s\sigma+\alpha}}}}{\mathrm{Pr}_{eff} s^\alpha - \omega^2(\sigma s^\alpha + \alpha)}. \tag{32}$$

In order to find C_1 and C_2, we use the conditions $\bar{w}(\psi, s) \to 0$, as $\psi \to \infty$ and $\bar{w}(0, s) - b\frac{\partial \bar{w}(0,s)}{\partial \psi} = \frac{a}{s^2+a^2}$, we have

$C_1 = 0$ and $C_2 = \frac{a - AK(s^2+a^2)(1+bD)}{(s^2+a^2)(1+b\sqrt{\omega})}$, where $K = \frac{\sigma s^\alpha + \alpha}{\mathrm{Pr}_{eff} s^\alpha - \omega^2(\sigma s^\alpha + \alpha)}$, and $D = \sqrt{\frac{\mathrm{Pr}_{eff} s^\alpha}{(\sigma s^\alpha + \alpha)}}$.

Finally,

$$\bar{w}(\psi, s) = \left[\frac{a}{(s^2+a^2)} + \left[\frac{((s\sigma+\lambda)s^{\alpha}+s\alpha)}{s^{\alpha}(\sigma s^{\alpha}+\alpha)}\frac{\sqrt{\sigma s+\alpha}Gr\cos\gamma}{\sqrt{\mathrm{Pr}_{eff}s^{\alpha}}-\sqrt{\sigma s^{\alpha}+\alpha}}\right]\right.$$
$$\times\left[\frac{\sigma s^{\alpha}+\alpha}{\mathrm{Pr}_{eff}s^{\alpha}-[\frac{[[s\sigma)+\lambda]s^{\alpha}+s\alpha]}{\sigma s^{\alpha}+\alpha}(1+M)]^2(\sigma s^{\alpha}+\alpha)}\left(1+b\sqrt{\frac{\mathrm{Pr}_{eff}s^{\alpha}}{\sigma s^{\alpha}+\alpha}}\right)\right]$$
$$\times\left[\left(\frac{1}{\left(1+b\sqrt{\frac{(1+M)(\sigma s^{\alpha}+\lambda)s^{\alpha}}{\sigma s^{\alpha}+\alpha}}\right)}\right)\right]e^{-\psi\sqrt{\frac{(s\sigma+\lambda)s^{\alpha}+s\alpha(1+M)}{\sigma s^{\alpha}+\alpha}}}$$
$$+\left[\left(\frac{(s\sigma+\lambda)s^{\alpha}+s\alpha}{s^{\alpha}(\sigma s^{\alpha}+\alpha)}\frac{\sqrt{\sigma s+\alpha}Gr\cos\gamma}{\sqrt{\mathrm{Pr}_{eff}s^{\alpha}}-\sqrt{\sigma s^{\alpha}+\alpha}}\right)\right.$$
$$\left.\left.\left(\frac{\sigma s^{\alpha}+\alpha}{\mathrm{Pr}_{eff}s^{\alpha}-[\frac{(s\sigma+\lambda)s^{\alpha}+s\alpha}{\sigma s^{\alpha}+\alpha}(1+M)]^2(\sigma s^{\alpha}+\alpha)}\right)\right]\times\left[e^{-\psi\sqrt{\frac{\mathrm{Pr}_{eff}s^{\alpha}}{\sigma s^{\alpha}+\alpha}}}\right]. \quad (33)$$

It is worth mentioning that inverse Laplace transform of Eq. (33) is somewhat tedious to obtain. In [29], Stehfest proposed a numerical algorithm for Laplace inversion. So, we will apply Stehfest's algorithm to obtain the solution for velocity in the original domain.

The Stehfest's algorithm is as follows [29];

$$\varphi(\Psi, t) = \frac{ln(2)}{t}\sum_{j=1}^{2q} d_j\bar{\varphi}(\Psi, j)\frac{ln(2)}{t}),$$

where q is the positive integer,

$$d_j = (-1)^{j+q}\sum_{i=[\frac{j+1}{2}]}^{min(j,q)}\frac{i^q(2i)!}{(q-i)!i!(i-1)!(j-i)!(2i-j)!},$$

and $[\frac{j+1}{2}]$ denote the integer part of the number $\frac{j+1}{2}$.

4 Limiting Solutions

In this part, using our general results, we will recover the results corresponding to the ordinary Maxwell and fractional/viscous fluids.

4.1 Ordinary Maxwell Model ($\alpha \to 1$)

Corresponding results for the case of ordinary Maxwell fluid can be recovered from our results by taking limit $\alpha \to 1$ in (33) and them applying Stehfest's algorithm to obtain the corresponding solution for velocity in the original domain Remember $1 - \alpha = \sigma$, as $\alpha \to 1, \sigma = 0$, so Eq. (33) becomes

$$\begin{aligned}\bar{w}(\psi, s) = &\left[\frac{a}{(s^2 + a^2)} + \frac{(\lambda + 1)Gr\cos\gamma}{\sqrt{\mathrm{Pr}_{eff}s} - 1}\left(\frac{1}{\mathrm{Pr}_{eff}s - \lambda^2 s^2}\right)\left(1 + b\sqrt{\mathrm{Pr}_{eff}s}\right)\right] \\ &\times \left(\frac{1}{(1 + b\sqrt{\lambda s(1 + M)})}\right) e^{-\psi\sqrt{(\lambda+1)s(1+M)}} \\ &+ \left[\left(\frac{(\lambda + 1)Gr}{\sqrt{\mathrm{Pr}_{eff}s} - 1}\right)\left(\frac{1}{\mathrm{Pr}_{eff}s - (\lambda + 1)s(1 + M)}\right)\right] e^{-\psi\sqrt{\mathrm{Pr}_{eff}s}}. \quad (34)\end{aligned}$$

4.2 Fractional Viscous Fluid ($\lambda = 0$)

Likewise, setting $\lambda = 0$ into Eq. (33), we get the corresponding results for fractional viscous fluid

$$\begin{aligned}\bar{w}(\psi, s) = &\left[\frac{a}{(s^2 + a^2)} + \left[\frac{(\sigma s^{\alpha+1} + s\alpha)}{s^\alpha(\sigma s^\alpha + \alpha)}\frac{\sqrt{\sigma s + \alpha}Gr\cos\gamma}{\sqrt{\mathrm{Pr}_{eff}s^\alpha} - \sqrt{\sigma s^\alpha + \alpha}}\right]\right. \\ &\times \left[\frac{\sigma s^\alpha + \alpha}{\mathrm{Pr}_{eff}s^\alpha - [\frac{[s\sigma\ s^{\alpha+1} + s\alpha]}{\sigma s^\alpha + \alpha}(1 + M)]^2(\sigma s^\alpha + \alpha)}\left(1 + b\sqrt{\frac{\mathrm{Pr}_{eff}s^\alpha}{\sigma s^\alpha + \alpha}}\right)\right] \\ &\times \left[\left(\frac{1}{\left(1 + b\sqrt{\frac{(1+M)\sigma s^{2\alpha}}{\sigma s^\alpha + \alpha}}\right)}\right)\right] e^{-\psi\sqrt{\frac{\sigma s^{\alpha+1} + s\alpha(1+M)}{\sigma s^\alpha + \alpha}}} \\ &+ \left[\left(\frac{\sigma s^{\alpha+1} + s\alpha}{s^\alpha(\sigma s^\alpha + \alpha)}\frac{\sqrt{\sigma s + \alpha}Gr\cos\gamma}{\sqrt{\mathrm{Pr}_{eff}s^\alpha} - \sqrt{\sigma s^\alpha + \alpha}}\right)\right. \\ &\left.\left.\left(\frac{\sigma s^\alpha + \alpha}{\mathrm{Pr}_{eff}s^\alpha - [\frac{\sigma s^{\alpha+1} + s\alpha}{\sigma s^\alpha + \alpha}(1 + M)]^2(\sigma s^\alpha + \alpha)}\right)\right] \times \left[e^{-\psi\sqrt{\frac{\mathrm{Pr}_{eff}s^\alpha}{\sigma s^\alpha + \alpha}}}\right]. \quad (35)\end{aligned}$$

4.3 Viscous Fluid ($\alpha \to 1$)

In order to recover the results for the case of viscous fluid apply limit $\alpha \to 1$ to Eq. (35), we get

$$\bar{w}(\psi, s) = \left[\frac{a}{(s^2 + a^2)} + \frac{Gr \cos\gamma}{\sqrt{\mathrm{Pr}_{eff} s} - 1} \frac{1 + b\sqrt{\mathrm{Pr}_{eff} s}}{\mathrm{Pr}_{eff} s - s^2(1+M)^2} \right] e^{-\psi\sqrt{s(1+M)}} + \frac{Gr \cos\gamma}{(\sqrt{\mathrm{Pr}_{eff} s} - 1)(\mathrm{Pr}_{eff} s - (s(1+M))^2)} e^{-\psi\sqrt{\mathrm{Pr}_{eff} s}} \tag{36}$$

5 Graphical Description and Discussion of the Results

In this section, we will discuss the influence of system parameters on fluid flow. Moreover, in pursuance of analysing the control of the physical pertinent parameters in particular Grashof number, relaxation time, magnetic field strength, fractional order parameter, and effect of the slip and non-slip boundary condition and inclination of the plane on the fluid flow behaviour. We have prepared the graphs of velocity versus ψ, corresponding to different values of parameters by using the computer software MATHCAD 15.

Figure 2 portrays the behaviour of the velocity curves for varying values of the fractional parameter with and without slip conditions. We have noticed that the fluid's velocity decreases as we increase the fractional parameter because the rise in the value of parameter α increases the viscosity of the fluid which results in a decline in the fluid's velocity. Also, it is observed that the velocity of the fluid without slip effect condition on the plate is larger than the velocity of the fluid with slip. The reason is that, for the case of no slip, the fluid elements are moving not only due to the temperature variations but also the shear stress provided by the motion of the plate.

The consequence of different values of Grashof number on the velocity curves with and without slip conditions is depicted in Fig. 3. It is reported that an add-up in the value of Grashof number, enhances the profiles of the velocity of the fluid. It is observed that the fluid with no-slip condition moves faster at different values of the Grashof number parameter as compared to the case when fluid slips on the wall.

Figure 4 illustrates velocity profiles versus ψ for varying values of relaxation time with and without slip. We have reported that any increase in relaxation time parameter results in depreciation in the velocity of the fluid for both cases, i.e. with and without slip conditions. Because, increase in relaxation time causes the thinning in shear stress, which results in fall in velocity.

The velocity curves against ψ for varying values of the magnetic parameter are plotted in Fig. 5. We have noticed that when magnetic strength grows there is depreciation in the fluid velocity curves. Because the Lorentz force that is induced by transverse magnetic field causes a drag force that resists the motion of the fluid.

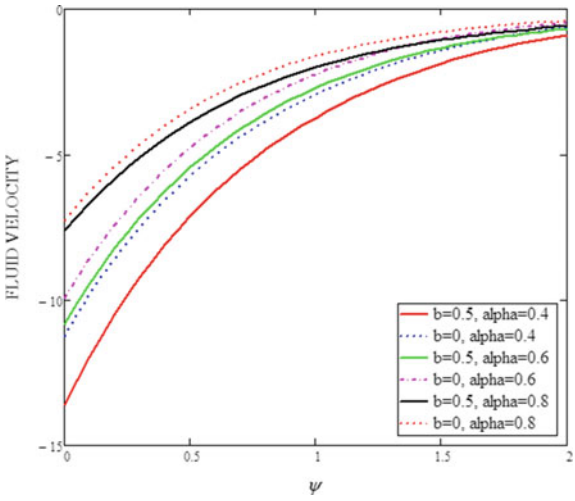

Fig. 2 Velocity description versus ψ for varying of fractional parameter with and without slip condition at t = 0.2

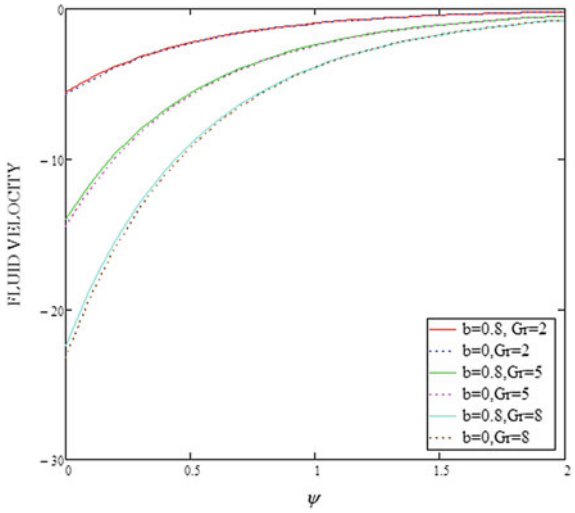

Fig. 3 Velocity description versus ψ for varying of Grashof number with and without slip condition at t = 0.2

Figure 6 shows the velocity curves against ψ for varying values of angle of inclination of the plate. It is noticed that elevation in inclination declines the velocity curves of the fluid.

In Figs. 7 and 8, we have compared the velocities of viscous (for $\lambda = 0$ in Eqs. (33) and (34)) and Maxwell (ordinary and fractional) fluid with and without slip condition. We have noticed that fractional and ordinary viscous fluid move faster than fractional and ordinary Maxwell fluids when there is a slip and no slip effect at the boundary. This is because Maxwell fluid contains both viscous and relaxation parameters, which reduce the velocity while viscous fluid contains only viscosity parameter.

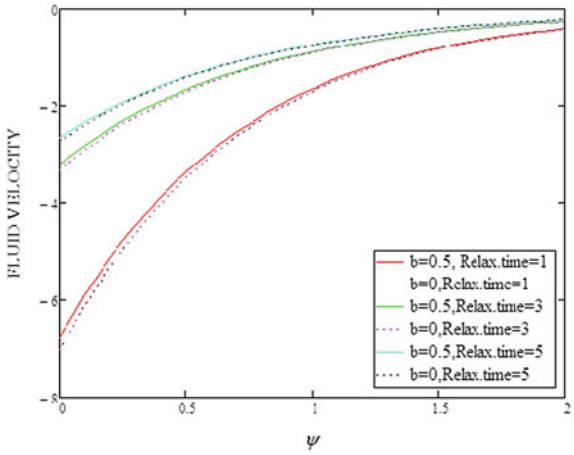

Fig. 4 Velocity description versus ψ for varying of relaxation time parameter with and without slip condition at t = 0.2

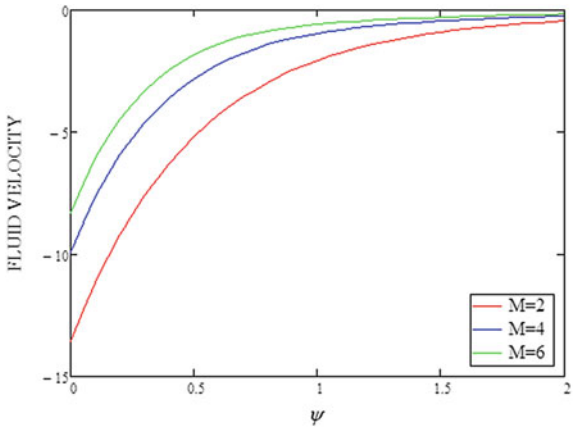

Fig. 5 Velocity description versus ψ for varying of Magnetic strength parameter at t = 0.2

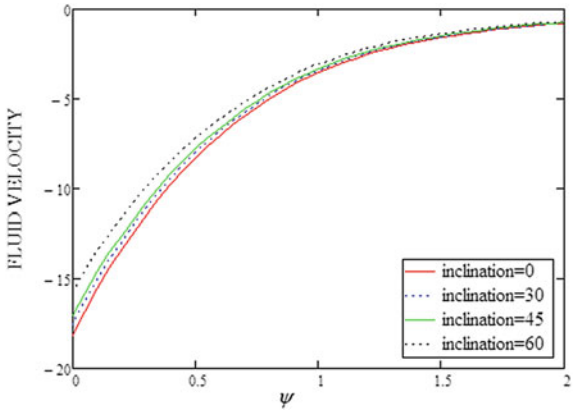

Fig. 6 Velocity description versus ψ for varying of angle of inclination at t = 0.2

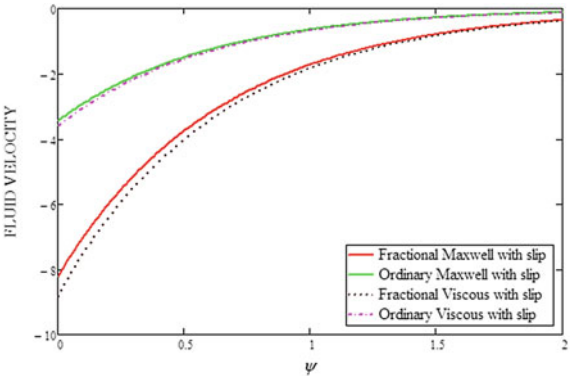

Fig. 7 Comparison betwixt Maxwell's fluid velocity (fractional and ordinary), and viscous fluid velocity (fractional and ordinary)

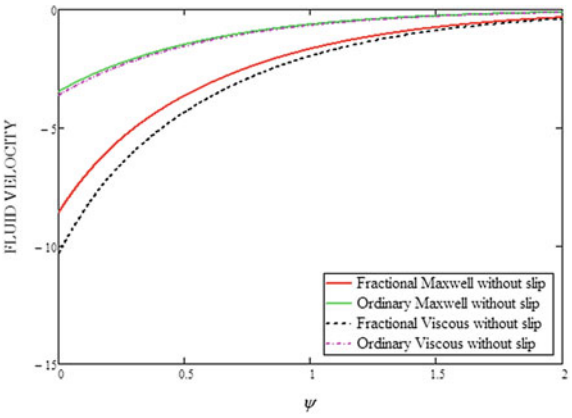

Fig. 8 Comparison betwixt Maxwell's fluid velocity (fractional and ordinary) and viscous fluid velocity (fractional and ordinary)

6 Final Remarks

Heat transfer magnetohydrodynamics boundary layer flow model of a rate type fluid over an inclined oscillating plate employing the recent definition of non-integer order derivative, i.e. Atangana-Baleanu time-fractional derivative operator in the sense of Caputo is developed. The fluid is flowing over an oscillating inclined plate with slip/no slip and Newtonian heating at the boundary. The governing equations for the description of the fluid flow phenomenon are used in dimensionless form and the Laplace transform method is employed to solve the problem. From our general results, several results from the literature could be recovered, for example; the cases corresponding to the constant motion of the plate (by setting frequency of oscillation of the plate equals to zero), as well as the analogous results for ordinary Maxwell fluid (by taking $\alpha = 1$), the fractional viscous (for $\lambda = 0$) and ordinary viscous fluid (for $\lambda = 0, \alpha = 0$) could be recovered. The important findings of the investigation are as under:

1. Increase in the value of fractional order parameter α, results depreciation in the velocity of the fluid, so α behaves as shear thickening parameter.
2. Velocity of fluid without slip effect is larger in comparison to the velocity of a fluid with slip.
3. Rise in the value of magnetic strength parameter M, decreases the fluid flow velocity.
4. Fluid velocity boosts up with the increase in Grashof number Gr.
5. The fluid flow depreciates with the increment in the value of relaxation time λ.
6. Influence of an increase in the angle of inclination of the plate results in decreases in the velocity of the fluid.
7. Viscous fluid flows faster than fractional/ ordinary Maxwell fluids for both the cases, i.e. with and without slip effect at the wall.

References

1. Alam MS, Rahman MM, Sattar MA (2006) MHD free convective heat and mass transfer flow past an inclined surface with heat generation. Thammasat Int J Sci Technol 11(4):1–8
2. Ali F, Khan I, Samiulhaq, Shafie S (2013) Conjugate effects of heat and mass transfer on MHD free convection flow over an inclined plate embedded in a porous medium. PLoS ONE 8(6):e65223. https://doi.org/10.1371/journal.pone.0065223
3. Atangana A, Baleanu D (2016) New fractional derivatives with nonlocal and non-singular kernel: theory and application to heat transfer model. Therm Sci 20(2):763–769. https://doi.org/10.2298/TSCI160111018A
4. Atangana A (2016) On the new fractional derivative and application to nonlinear Fisher's reaction-diffusion equation. Appl Math Comput 273:948–956
5. Atangana A, Nieto JJ (2015) Numerical solution for the model of RLC circuit via the fractional derivative without singular kernel. Adv Mech Eng 7(10):1–7
6. Caputo M, Mainardi F (1971) A new dissipation model based on memory mechanism. Pure Appl Geophys 91:134–147
7. Caputo M, Fabrizio M (2016) Applications of new time and spatial fractional derivatives with exponential kernels. Prog Fract Differ Appl 2(1):1–11
8. Chen CH (2004) Heat and mass transfer in MHD flow by natural convection from a permeable inclined surface with variable wall temperature and concentration. Acta Mechanica 172:219–235
9. Goswami A, Singh J, Kumar D, Sushilan (2019) An efficient analytical approach for fractional equal width equations describing hydro-magnetic waves in cold plasma. Phys A 524:563–575. https://doi.org/10.1016/j.physa.2019.04.058
10. Gupta S, Kumar D, Singh J (2019) MHD three dimensional boundary layer flow and heat transfer of Water driven copper and alumina nanoparticles induced by convective conditions. Int J Mod Phys B 33(26):1950307. https://doi.org/10.1142/S0217979219503077
11. Gupta S, Kumar D, Singh J (2020) Analytical study for MHD flow of Williamson nanofluid with the effects of variable thickness, nonlinear thermal radiation and improved Fourier's and Fick's Laws. SN Appl Sci 2:438. https://doi.org/10.1007/s42452-020-1995-x
12. Hayat T, Qasim M, Mesloub S (2011) MHD flow and heat transfer over permeable stretching sheet with slip conditions. Int J Numer Methods Fluids 66:963–975
13. Hussanan A, Anwar MI, Ali F, Khan I, Shafie S (2014) Natural convection flow past an oscillating plate with Newtonian heating. Heat Transf Res 45(2):119–137

14. Imran MA, Riaz MB, Shah NA, Zafar AA (2018) Boundary layer flow of MHD generalized Maxwell fluid over an exponentially accelerated infinite vertical surface with slip and Newtonian heating at the boundary. Results Phys 10:1061–1067
15. Khan H, Jarad F, Abdeljawad T, Khan A (2019) A singular ABC-fractional differential equation with p-Laplacian operator. Chaos Solitons Fractals 129:56–61
16. Khan A, Abdeljawad T, Gómez-Aguilar JF, Khan H (2020) Dynamical study of fractional order mutualism parasitism food web module. Chaos Solitons Fractals 134:109685
17. Khan H, Li Y, Khan A, Khan A (2019) Existence of solution for a fractional-order Lotka-Volterra reaction-diffusion model with Mittag-Leffler kernel. Math Methods Appl Sci 42(9):3377–3387
18. Kumar AGV, Varma SVK (2011) Radiation effects on MHD flow past an impulsively started exponentially accelerated vertical plate with variable temperature in the presence of heat generation. Int J Eng Sci Technol 3(14):2897–909
19. Makinde OD (2012) Heat and mass transfer by MHD mixed convection stagnation point flow toward a vertical plate embedded in a highly porous medium with radiation and internal heat generation. Meccanica 47:1173–1184
20. Makinde OD (2012) Chemically reacting hydromagnetic unsteady flow of a radiating fluid past a vertical plate with constant heat flux. Zeitschriftfr Naturforschung A 67a:239–247
21. Makinde OD (2012) Computational modelling of MHD unsteady flow and heat transfer over a flat plate with Navier slip and Newtonian heating. Braz J Chem Eng 29(1):159–166
22. Mishra SR, Dash GC, Acharya M (2013) Mass and heat transfer effect on MHD flow of a visco-elastic fluid through porous medium with oscillatory suction and heat source. Int J Heat Mass Transf 57:433–438
23. Muthucumaraswamy R, Kumar GS (2004) Thermal diffusion effects on moving infinite vertical plate in the presence of variable temperature and mass diffusion. Theor Appl Mech 31(1):35–46
24. Mukhopadhyay S (2013) Analysis of boundary layer flow over a porous nonlinearly stretching sheet with partial slip at the boundary. Alex Eng J 52:563–569
25. Nachtsheim PR, Swigert P (1965) Satisfaction of the asymptotic boundary conditions in numerical solution of the system of nonlinear equations of boundary layer type. NASA TND-3004
26. Nadeem S, Mehmood R, Akbar NS (2015) Combined effects of magnetic field and partial slip on obliquely striking rheological fluid over a stretching surface. J Magn Magn Mater 378:457–462
27. Ogulu A, Makinde OD (2009) Unsteady hydromagnetic free convection flow of a dissipative and radiating fluid past a vertical plate with constant heat flux. Chem Eng Commun 196(4):454–462
28. Palani G (2008) Convection effects on flow past an inclined plate with variable surface temperatures in water at 4 C. J Eng Ann 6(1):75–82
29. Pattnaik JR, Dash GC, Singh S (2012) Radiation and mass transfer effects on MHD free convection flow through porous medium past an exponentially accelerated vertical plate with variable temperature. J Eng Ann 10(3):175–182
30. Poornima T, Sreenivasulu P, Reddy NB (2014) Slip flow of Casson rheological fluid under variable thermal conductivity with radiation effects. Heat Transf Res 44:718–737
31. Podlubny I (1999) Fractional differential equations. Academic press, San Diego
32. Shah NA, Zafar AA, Akhtar S (2018) General solution for MHD-free convection flow over a vertical plate with ramped wall temperature and chemical reaction. Arab J Math 7:49–60. https://doi.org/10.10075/s40065-017-0187-z
33. Singh J, Kumar D, Purohit SD, Mishra AM, Bohra M (2021) An efficient numerical approach for fractional multi-dimensional diffusion equations with exponential memory. Numer Methods Partial Differ Equ 37(2):1631–1651. https://doi.org/10.1002/num.22601
34. Sun HG, Zhang Y, Baleanu D, Chen W, Chen YQ (2018) A new collection of real world applications of fractional calculus in science and engineering. Commun Nonlinear Sci Numer Simul 64:213–231. https://doi.org/10.1016/j.cnsns.2018.04.019
35. Uddin Z, Kumar M (2010) Unsteady free convection in a fluid past an inclined plate immersed in a porous medium. Comput Model New Technol 14(3):41–47

Multilayer Perceptron Artificial Neural Network Approach to Solve Sixth-Order Two-Point Boundary Value Problems

Akanksha Verma and Manoj Kumar

Abstract In this article, we have presented a multilayer perceptron artificial neural network (MLP ANN) method to solve the sixth-order boundary value problems that arise in several branches of engineering and physics such as fluid dynamics, hydrodynamics, beam theory, astrophysics and so on. The obtained solutions of these boundary value problems by our method are optimal as compared to other existing approximation methods. Furthermore, we have tested few models in order to decide the performance of the proposed technique. The numerical outcomes show that the proposed strategy is very effective for higher order boundary value problems and required low memory space and less computational time.

Keywords Sixth-order boundary value problem · Multilayer perceptron neural network · Quasi-Newton BFGS algorithm

AMS Subject Classification 65N20 · 65L10 · 68T07 · 68W50

1 Introduction

Boundary value problems (BVPs) play a vital role in the field of science and engineering and have attracted much attention. For instance, in the field of astronomy when a vast level layer of fluid is warmed under the action of rotation then instability occurs. If this instability is fixed as ordinary convection, then it is represented by sixth-order BVPs [1]. Other than this, the slender convecting layers encased by stable layers that are assumed to encircle A-type stars can be modeled by sixth-order BVPs [2, 3]. Glatzmaier [4] clarified that dynamo activity in certain stars can be demonstrated by

A. Verma (✉) · M. Kumar
Department of Mathematics, Motilal Nehru National Institute of Technology Allahabad, Prayagraj 211004, U.P., India
e-mail: rma1702@mnnit.ac.in

M. Kumar
e-mail: manoj@mnnit.ac.in

J. Singh et al. (eds.), *Advances in Mathematical Modelling, Applied Analysis and Computation*, Lecture Notes in Networks and Systems 415,
https://doi.org/10.1007/978-981-19-0179-9_5

sixth-order differential equations. Also, many authors have discussed the numerical behavior of sixth-order BVPs [5–7].

The literature of numerical study on the solution of the sixth-order BVPs is not too vast. In 1986, Agrawal [8] presented the existence and uniqueness of the solution of such BVPs, however, he did not discuss any numerical strategies.

In this manuscript, we have discussed the approximate solution of the following sixth-order BVPs:

$$w^{(6)}(r) = f(w, r), \quad 0 \leq r \leq 1, \tag{1}$$

with respect to the boundary conditions:

$$w^{(i)}(0) = a \quad \text{and} \quad w^{(i)}(1) = b, \quad i = 0, 1, 2, \tag{2}$$

where $f(w, r)$ is a given linear/non-linear function and a and b are given constants.

In 2001, Wazwaz [9] demonstrated the modified a domian decomposition method (MADM) for solving sixth-order BVPs with boundary conditions at two points and achieved convergent series solutions. Further, Gamel et al. [10] presented the Sinc-Galerkin technique to figure out the sixth-order BVPs and obtained better results as compared to the MADM technique. In 2006, Akram and Siddiqi [11] used the non-polynomial Spline strategy to obtain the approximate solution of sixth-order linear BVPs and proved that the method is second-order convergent. Afterward, Islam et al. [12] used the non-polynomial spline function to expand a class of numerical techniques for solving sixth-order linear and nonlinear BVPs and obtained second, fourth, and sixth-order convergence results. In 2007, Noor and Mohyud-din [13] solved higher order BVPs by using a variation iteration method (VIM). In order to solve these BVPs, they first convert the higher order BVPs into the system of integral equations and then they used VIM method to get the required solution. In 2010, Liang and Jeffrey [14] presented the homotopy analysis method (HAM) for solving parameterized sixth-order BVPs. However, for enormous parameter values, these equations cannot be clarified by other expository strategies therefore they obtain the approximate series solutions and proposed that the HAM is an analytical tool to understand the linear and nonlinear BVPs. In 2013, Akram and Rehman [15] presented the reproducing kernel method to clarify the linear and nonlinear sixth-order BVPs and provides the results in terms of convergent series.

Whereas, Agrawal et al. [5] used the monotone iterative technique and an operator spectral theorem for the presence and assortment of positive solution of sixth-order BVPs with four variable parameters. Recently, Sohaib et al. [16] proposed the Legendre-wavelet collocation method (LWCM), which is based on Legendre polynomial to get the arrangement of sixth-order BVPs. In this strategy, they used the collocation points to change the differential equation into the system of algebraic equations and then get the solution by LWCM technique. Recently, Khalid et al. [17] presented the Cubic B-Spline method to get the solution of eighth-order linear and nonlinear BVPs. In 2020, Mustafa et al. [18] introduced a technique for solving second-order singularly perturbed boundary value problems, which is based on the

basis function of a six-point interpolatory subdivision.
In 2013, Kumar and Yadav [19] gave the mathematical model and MLP ANN technique for computing the buckling load of beam column with several end conditions. They solved fourth-order BVPs by using the MLP ANN technique. Thereafter, Mall and Chakraverty [20] presented Chebyshev neural network technique to get the solution of second-order singular initial value problems. Recently, Verma and Kumar [21] presented the MLP ANN technique for solving the same problem [20] and get the better results as compared to Chebyshev neural network technique. Towards this, many researchers used the ANN technique to solve the different types of differential equations (see. [22–26]) but the solution of sixth-order two-point BVPs by using MLP ANN with the Quasi-Newton BFGS optimization technique has not been discussed by anyone.
Motivated by above, in this manuscript, we have discussed the multilayer perceptron ANN strategy to find out the solution of sixth-order two-point BVPs. This technique offers us following attractive features:
• The obtained solutions by the proposed technique are in closed analytic form whereas the other techniques such as the Euler method, Galerkin methods and finite difference method give the solutions in discrete forms.
• This method does not need any linearization procedure to solve a nonlinear problem.
• Proposed technique does not need any type of adjustment for different boundary conditions. A comparative system has followed for illuminating differential equation with a different type of boundary conditions.
• The implementation of this technique is very easy for solving the higher-order ODEs, PDEs, and system of DEs.

The arrangement of the paper is as per the following: Sect. 2 represents the architecture of multilayer perceptron neural network. In Sect. 3, we have discussed the MLP ANN technique and used it to solve the sixth-order BVPs. In Sect. 4, we have solved some numerical test problems and compared the obtained solution with exact results and other numerical results available in the literature, while Sect. 5, concluded the article.

2 Structure of MLP ANN

In this segment, we have presented the architecture and working process of multilayer perceptron neural network. The multilayer perceptron is basically a feed-forward neural network that contains one input layer r along with bias μ_j, one or more than one hidden layers and single output layer. Figure 1 depicted the framework of MLP ANN, here ξ_{ij} are the connection weights between the input layer to the hidden layer and v_i are the connection weights between the hidden layer to the output layer. This kind of network is broadly utilized in the approximation of arbitrary functions as it gives good generalization and high precision. In most cases, the multilayer

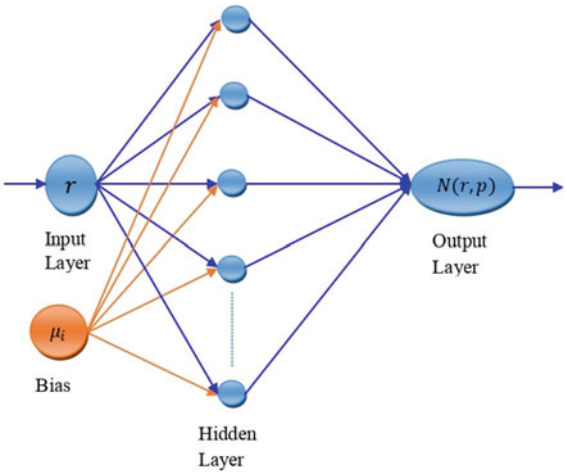

Fig. 1 Architecture of multilayer perceptron artificial neural network

perceptron with one hidden layer is enough to approximate any arbitrary function with the desired accuracy. The approximation capacity of MLP ANN is more reliant upon the number of neurons in the hidden layer rather than a number of hidden layers.

3 Description of MLP ANN Technique

To solve the second-order ODEs and PDEs, Lagaris et al. [23] presented a method based on MLP neural system. For solving the sixth-order BVPs, we have used a feed-forward neural system as a fundamental estimation component whose parameters, biases, and weights are modified to minimize the error function. For the training of the network, we have used optimization algorithms that required the computation of the gradient of the error concerning network input, weight and biases.
The proposed approach has demonstrated in terms of general sixth-order BVP:

$$G(\overrightarrow{r}, w(\overrightarrow{r}), \nabla w(\overrightarrow{r}), \nabla^2 w(\overrightarrow{r}), \nabla^3 w(\overrightarrow{r}), \nabla^4 w(\overrightarrow{r}), \nabla^5 w(\overrightarrow{r}), \nabla^6 w(\overrightarrow{r})) \quad \overrightarrow{r} \in D, \tag{3}$$

with respect to boundary points $w^{(i)}(0) = \alpha$ and $w^{(i)}(1) = \beta$ for $i = 0, 1, 2$. Here, $\overrightarrow{r} = (r_1, r_2, \ldots, r_n) \in R^n$, $D \subset R^n$ signifies the domain of definition and $w(\overrightarrow{r})$ is the answer to be calculated.

Conversion: Initially, we break the domain of definition D and its boundary S into a lot of discrete points $\hat{D}$ and $\hat{S}$, separately. Then we convert it into following

$$G(\overrightarrow{r_i}, w(\overrightarrow{r_i}), \nabla w(\overrightarrow{r_i}), \nabla^2 w(\overrightarrow{r_i}), \nabla^3 w(\overrightarrow{r_i}), \nabla^4 w(\overrightarrow{r_i}), \nabla^5 w(\overrightarrow{r_i}), \nabla^6 w(\overrightarrow{r_i})) \quad \overrightarrow{r_i} \in \hat{D}, \tag{4}$$

with respect to constraint imposed by the boundary condition.
If $w_t(\overrightarrow{r}, \overrightarrow{p})$ signifies a trial solution with the flexible parameters $\overrightarrow{p}$, then the problem is converted to an unconstrained optimization problem

$$\min_{\overrightarrow{p}} \sum_{r_i \in \hat{D}} G(\overrightarrow{r_i}, w_t(\overrightarrow{r_i}), \nabla w_t(\overrightarrow{r_i}), \nabla^2 w_t(\overrightarrow{r_i}), \nabla^3 w_t(\overrightarrow{r_i}), \nabla^4 w_t(\overrightarrow{r_i}), \nabla^5 w_t(\overrightarrow{r_i}), \nabla^6 w_t(\overrightarrow{r_i})). \tag{5}$$

Construction of Trial Solution: Assume that trial solution is

$$w_t(\overrightarrow{r}) = A(\overrightarrow{r}) + B(\overrightarrow{r})N(\overrightarrow{r}, \overrightarrow{p}), \tag{6}$$

where $A(\overrightarrow{r})$ represents the continuous ansatz function, which is created in such a manner in this way, that it fulfills boundary conditions $B(\overrightarrow{r}) = r^3(r-1)^3$ and $N(\overrightarrow{r}, \overrightarrow{p})$ represents the particular output feed-forward neural network.

Gradient Computation: The effective minimization can be considered as a cycle of preparing the neural network, where the error corresponding to each input vector is the worth that needs to get zero.
We have taken a multilayer perceptron with n input nodes, one hidden layer with h hidden nodes and a linear output node. For an input vector $\overrightarrow{r}$, the output of the network is

$$N(\overrightarrow{r}, \overrightarrow{p}) = \sum_{i=1}^{h} v_i \sigma(z_i). \tag{7}$$

Here,
σ is the activation function, which is taken as $tanh(z)$ and $(1 + exp(-z_i))^{-1}$,
$z_i = \sum_{j=1}^{n} \xi_{ij} r_j + \mu_i$,
ξ_{ij} represents the connection weight from the input node j to hidden node i,
v_i represents the connection weight from hidden node i to output node,
μ_i represents the bias of hidden node i.
Now, we have differentiate N w. r. t. r_j

$$\frac{\partial^k N}{\partial r^k} = \sum_{i=1}^{h} v_i \xi_{ij}^k \sigma_i^{(k)}, \tag{8}$$

where $\sigma_i = \sigma(z_i)$ and $\sigma^{(k)}$ signifies the kth order derivative of activation function.
Usually, the derivative of various order w. r. t. various inputs can be composed as

$$\frac{\partial^{m_1}}{\partial {r_1}^{m_1}} \frac{\partial^{m_2}}{\partial {r_2}^{m_2}} \cdots \frac{\partial^{m_n}}{\partial {r_n}^{m_n}} = \sum_{i=1}^{h} v_i P_i \sigma_i^{(\Lambda)}, \tag{9}$$

where $P_i = \prod_{k=1}^{n} \xi_{ik}^{m_k}$ and $\Lambda = \sum_{i=1}^{n} m_i$.
Gradient computation with respect to network parameters

$$\frac{\partial N}{\partial \nu_i} = P_i \sigma_i^{(\Lambda)}, \tag{10}$$

$$\frac{\partial N}{\partial \mu_i} = \nu_i P_i \sigma_i^{(\Lambda+1)}, \tag{11}$$

$$\frac{\partial N}{\partial \xi_{ij}} = r_j \nu_i P_i \sigma_i^{(\Lambda+1)} + \nu_i m_j \xi_{ij}^{(m_j-1)} \left(\prod_{k=1, k\neq j} \xi_{ik}^{m_k} \right) \sigma_j^{(\Lambda)}. \tag{12}$$

Network Parameter Updation: When the differentiation of the error function with respect to system parameters has been characterized then for updating the parameters we have used delta rule

$$\nu_i(t+1) = \nu_i(t) + \delta \frac{\partial N_g}{\partial \nu_i}, \tag{13}$$

$$\mu_i(t+1) = \mu_i(t) + \epsilon \frac{\partial N_g}{\partial \mu_i}, \tag{14}$$

$$\xi_{ij}(t+1) = \xi_{ij}(t) + \zeta \frac{\partial N_g}{\partial \xi_{ij}}, \tag{15}$$

where the learning rates have been taken as δ, ϵ, and ζ, $i = 1, 2, ..., n$ and $j = 1, 2, ..., h$.
We proceed with this iterative cycle until the error function reduces to its lowest.

4 Numerical Results

In this section, we have presented the approximate solutions of sixth-order linear and nonlinear BVPs. We have utilized a multilayer perceptron artificial neural network having one hidden layer with five hidden nodes and one output node. For each test problem, the activation function has been selected according to the accuracy of the results. To minimize the error function, we have used the Quasi-Newton BFGS optimization technique, which is quadratically convergent and shows outstanding performance. Both the test problems have been executed on MATLAB R2016a.

Problem 4.1 Consider the boundary value problem [27]

$$w^{(6)}(r) + rw(r) = -(24 + 11r + r^3)exp(r), \quad o \leq r \leq 1, \tag{16}$$

with respect to the boundary conditions
$w(0) = 0,\ w(1) = 0,\ w'(0) = 1,\ w'(1) = -e,\ w''(0) = 0, w''(1) = -4e.$

Table 1 The ideal estimations of weights and biases (Problem 4.1)

i	1	2	3	4	5
μ_i	0.53143741	−0.18649484	0.09170045	0.30018984	0.46037251
v_i	−0.39732087	−0.42266970	0.52914815	0.25034663	0.16175795
ξ_{ij}	0.57484654	0.74307111	1.11358492	0.95564375	0.95564376

Table 2 Comparison of numerical results of Problem 4.1

r	MLP ANN	Exact Solution	Cubic [27]B-Spline h=1/10	Absolute error (MLP ANN)	Absolute error [27]
0.0	0.0	0.0	–	0.0	–
0.1	0.099571	0.099465	0.099427	1.06×10^{-4}	3.79×10^{-5}
0.2	0.196024	0.195424	0.195266	5.99×10^{-4}	1.57×10^{-4}
0.3	0.284835	0.283470	0.283130	1.36×10^{-3}	3.40×10^{-4}
0.4	0.360090	0.358038	0.357505	2.05×10^{-3}	5.33×10^{-4}
0.5	0.414518	0.412180	0.411507	2.33×10^{-3}	6.74×10^{-4}
0.6	0.439393	0.437309	0.436600	2.08×10^{-3}	7.08×10^{-4}
0.7	0.424296	0.422888	0.422280	1.40×10^{-3}	6.08×10^{-4}
0.8	0.356715	0.356087	0.355696	6.28×10^{-4}	3.91×10^{-4}
0.9	0.221477	0.221364	0.221230	1.13×10^{-4}	1.35×10^{-4}
1.0	0.0	0.0	–	0.0	–

The precise solution of problem 4.1 is $r(1-r)exp(r)$ and is shown in Fig. 2. The trial solution of the problem according to the proposed technique is $r(1-r)exp(r) + r^3(1-r)^3N(r, p)$. We have prepared the system by taking 10 equidistant points in [0 1]. It has been solved in 301 epochs and the computational time is 7.455 s.
In Table 1, we have shown the ideal estimations of weights and biases. In Table 2, we compared our obtained results with the exact solution and cubic B-Spline solutions [27]. We used the first column for the inputs while the second column is used for obtained MLP ANN solution. In column 3, we have mentioned the exact solution for the problem whereas column 4 presented the approximated solution by Cubic B-Spline method with step size $\frac{1}{10}$. Columns 5 and 6 are used for the absolute error of MLP ANN solution and Cubic B-spline solution with the exact solution, respectively.

In Fig. 2, we have graphically represented the exact solution and MLP ANN solution for problem 4.1 whereas in Fig. 3, we have shown the error.

Problem 4.2 Consider the boundary value problem [27]

$$w^{(6)}(r) + exp(-r)w(r) = -720 + (r - r^2)^3 exp(r), \quad o \le r \le 1, \tag{17}$$

with respect to the boundary conditions

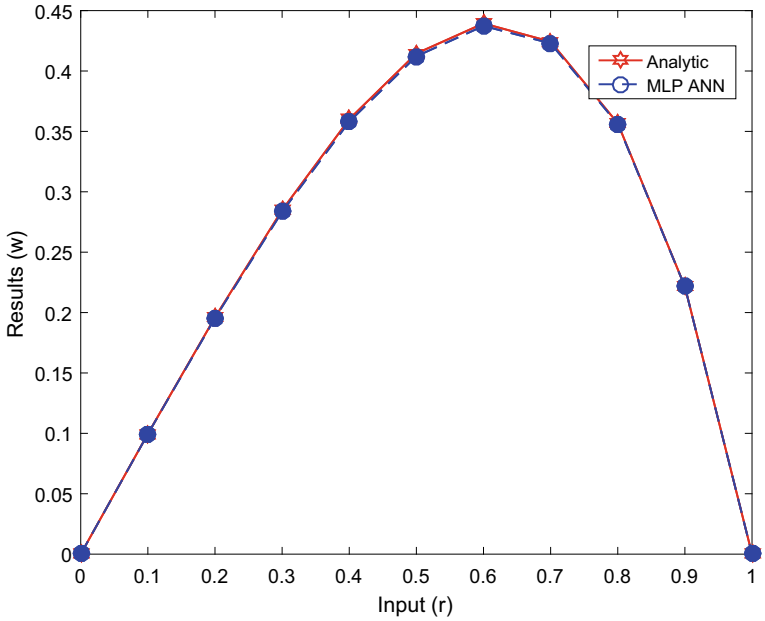

Fig. 2 Graphically comparison of MLP ANN results with Exact results (Problem 4.1)

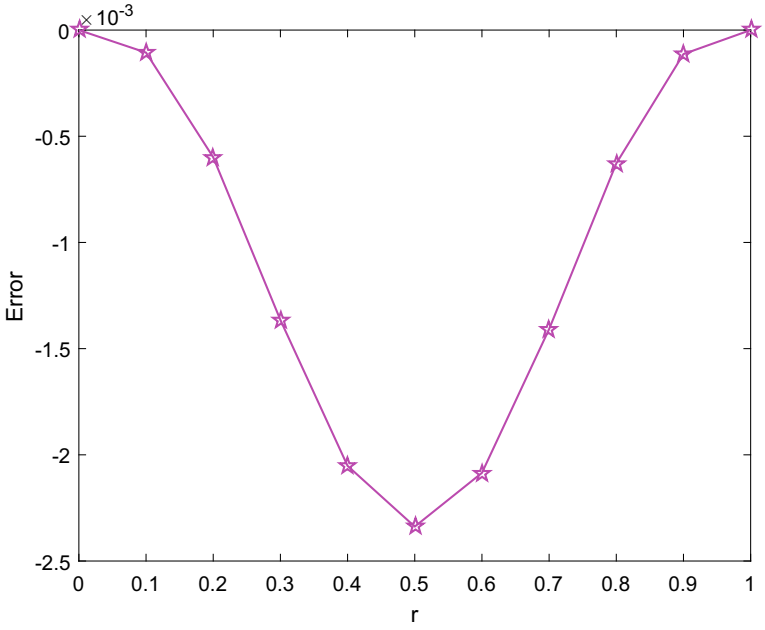

Fig. 3 Graph of the error between exact solution and MLP ANN solution (Problem 4.1)

Table 3 The ideal estimation of weights and biases (Problem 4.2)

i	1	2	3	4	5
μ_i	0.60704392	0.48918147	−9.262512E−04	0.41202518	0.00370112
v_i	−0.03415692	0.14825743	1.03624592	−0.09377157	0.50964194
ξ_{ij}	0.60996704	0.89110647	0.37717831	0.71546001	0.55369925

Table 4 Comparison of numerical results of Problem 4.2

r	MLPNN	$Exactsolution$	Cubic [27] B-Spline h=1/10	Absolute error (MLPNN)	Absolute error [27]
0.0	0.0	0.0	–	0.0	–
0.1	0.000729	0.000729	0.000504	0.0	2.25×10^{-4}
0.2	0.004096	0.004096	0.003360	0.0	7.36×10^{-4}
0.3	0.009261	0.009261	0.007980	0.0	1.28×10^{-3}
0.4	0.013824	0.013824	0.012144	0.0	1.68×10^{-3}
0.5	0.015625	0.015625	0.013800	0.0	1.83×10^{-3}
0.6	0.013824	0.013824	0.012144	0.0	1.68×10^{-3}
0.7	0.009261	0.009261	0.007980	0.0	1.28×10^{-3}
0.8	0.004096	0.004096	0.003360	0.0	7.36×10^{-4}
0.9	0.000729	0.000729	0.000504	0.0	2.25×10^{-4}
1.0	0.0	0.0	–	0.0	–

$$w(0) = 0,\ w(1) = 0,\ w'(0) = 0,\quad w'(1) = 0,\quad w''(0) = 0, w''(1) = 0.$$

The precise solution of Problem 4.2 is $r^3(1-r)^3$ and is shown in Fig. 4. According to the proposed technique, the trial solution of the problem is $r^3(1-r)^3 N(r, p)$. We have prepared the system by taking ten equidistant points in [0 1]. It has been solved in 87 epochs and the computational time is 3.346 s.

In Table 3, we have shown the ideal estimations of weights and biases. The obtained outcomes have been compared with the exact results and cubic B-Spline results [27] which is shown in Table 4. We used the first column for the inputs while the second column is used for obtained MLP ANN solution. In column 3, we have mentioned the exact solution for the problem whereas column 4 presented the approximated solution by Cubic B-Spline method with step size $\frac{1}{10}$. Columns 5 and 6 are used for the absolute error of MLP ANN solution and Cubic B-spline solution with the exact solution respectively.

In Fig. 4, we have graphically represented the exact solution and MLP ANN solution for problem 4.2 whereas in Fig. 5 we have shown the error.

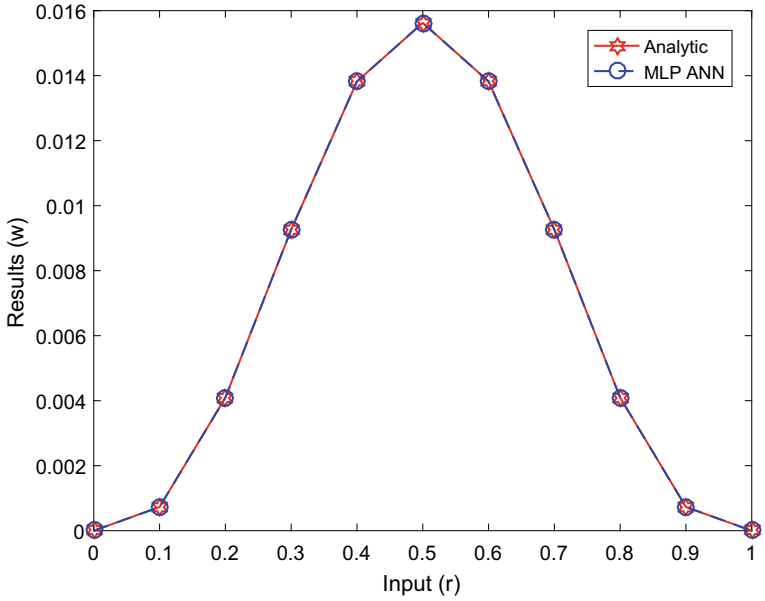

Fig. 4 Graphically comparison of MLP ANN results with exact results (Problem 4.2)

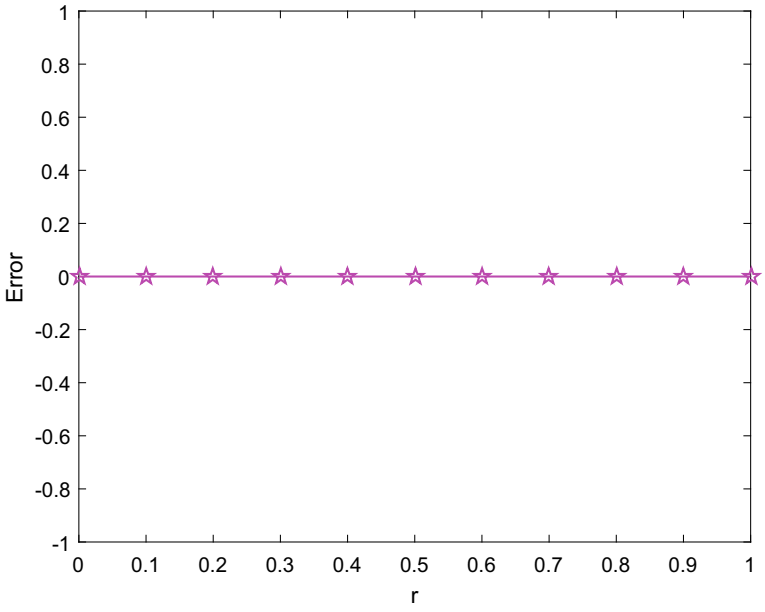

Fig. 5 Graph of error between exact solution and MLP ANN solution (Problem 4.2)

5 Conclusion

In this manuscript, we have proposed an approximation technique for solving the sixth-order BVPs, which relies on the capacity estimate abilities of feed-forward neural network. We have shown that our obtained results are in closed analytic form and are very close to the exact solution. Moreover, in Problem 4.2 from Fig. 5 and table 4, it can be seen that the obtained results are equal to the exact results. So we can say that the proposed technique combines accuracy, effectiveness and does not need any special lattice discretization for tackling the problems. Also, this technique has been considered as a mesh free numerical technique.

Acknowledgements This work is supported by the National Board of Higher Mathematics (NBHM) grant funded by the Government of India. Its project sanctioned Order No. 02011/-25/2019/R & D-II/3889. We express our sincere thanks to editor in chief, editor and reviewers for their valuable suggestions to revise this manuscript.

References

1. Chandrasekhar S (1981) Hydrodynamic and hydromagnetic stability. Dover, New York
2. Boutayeb A, Twizell EH (1992) Numerical methods for the solution of special sixth-order boundary-value problems. Int J Comput Math 45(3–4):207–223
3. Toomre J, Zahn JP, Latour J Spiegel EA (1976) Stellar convection theory. ii—single-mode study of the second convection zone in an a-type star. Astrophys J 207:545–563
4. Glatzmaier GA (1985) Numerical simulations of stellar convective dynamos iii. at the base of the convection zone. Geophys Astrophys Fluid Dyn 31(1–2):137–150
5. Kovacs B, Agarwal RP, O'Regan D (2013) Positive solutions for a sixth-order boundary value problem with four parameters. Bound Value Prob 184:1–22
6. Khalid M, Sultana M, Zaidi F (2014) Numerical solution of sixth-order differential equations arising in astrophysics by neural network. Int J Comput Appl 107(6):1–6
7. Ullah I, Khan H, Rahim MT (2014) Numerical solutions of fifth and sixth order nonlinear boundary value problems by Daftardar Jafari method. J Comput Eng 1:1–9
8. Agarwal RP (1986) Boundary value problems from higher order differential equations
9. Wazwaz AM (2001) The numerical solution of sixth-order boundary value problems by the modified decomposition method. Appl Math Comput 118:311–325
10. El-gamel M, Cannon JR, Zayed AI (2003) Sinc-Galerkin method for solving linear sixth order boundary-value problem. Mathe Comput 73(247):1325–1343
11. Akram G, Siddiqi SS (2006) Solution of sixth order boundary value problems using non-polynomial spline technique. Appl Math Comput 181:708–720
12. Islam S, Tirmizi IA, Haq F, Khan MA (2008) Non-polynomial splines approach to the solution of sixth-order boundary-value problems. Appl Math Comput 195:270–284
13. Noor MA, Mohyud-din ST (2007) Variational iteration technique for solving higher order boundary value problems. Appl Math Comput 189:1929–1942
14. Liang S, Jeffrey DJ (2010) Approximate solutions to a parameterized sixth order boundary value problem. Comput Math Appl 59(1):247–253
15. Akram G, Rehman HU (2013) Solutions of a class of sixth order boundary value problems. In: Hindawi publishing corporation abstract and applied analysis, pp 1–8
16. Sohaib M, Haq S, Mukhtar S, Khan I (2018) Numerical solution of sixth-order boundary-value problems using Legendre wavelet collocation method. Results Phys 8:1204–1208

17. Ullah Z, Ghaffar A, Baleanu D, Nisar KS, Khalid A, Naeem MN, Al-Qurashi MM (2019) Numerical solution of the boundary value problems arising in magnetic fields and cylindrical shells. Mathematics 508(7(6)):1–20
18. Baleanu D, Gaffar A, Mustafa G, Ejaz ST, Nisar KS (2020) A subdivision-based approach for singularly perturbed boundary value problem. Adv Differ Equ 282:1–20
19. Kumar M, Yadav N (2013) Buckling analysis of a beam-column using multilayer perceptron neural network technique. J Franklin Inst 350(10):3188–3204
20. Mall S, Chakraverty S (2015) Numerical solution of non-linear singular initial value problems of Emden fowler type using Chebyshev neural network method. Neurocomputing 149:975–982
21. Verma A, Kumar M (2019) Numerical solution of lane-Emden type equations using multilayer perceptron neural network method. Int J Appl Comput Math 5(5):1–14
22. Kumar M, Yadav N (2011) Multilayer perceptrons and radial basis function neural network methods for the solution of differential equations: a survey. Comput Math Appl 62:3796–3811
23. Lagaris IE, Likas A, Fotiadis DI (1998) Artificial neural network for solving ordinary and partial differential equation. IEEE Trans Neural Netw 9(17):1–26
24. Lee H, Kang IS (1990) Neural algorithm for solving differential equations. J Comput Phys 91:110–131
25. Mcfall KS, Mahan JR (2009) Boundary value problems with exact satisfaction of arbitrary boundary conditions. IEEE Trans Neural Network 20(8):1221–1233
26. Verma A, Kumar M (2020) Numerical solution of third-order Emden-fowler type equations using artificial neural network technique. Eur Phys J Plus 135(751):1–14
27. Agarwal P, Ghaffar A, Ullah Z, Khalid A, Naeem MN, Jain S (2009) Numerical approximation for the solution of linear sixth order boundary value problems by cubic b-spline. Adv Diff Equ 9:1–16

Wavelet Transform on Generalized Quotient Spaces and Its Applications

Abhishek Singh, Aparna Rawat, and Jagdev Singh

Abstract The concept of Schwartz distributions presents a unique area of mathematical research, which contributed to the development of several mathematical disciplines. In this chapter, we discuss the theory of generalized quotients which is a generalization of Schwartz distributions. The general construction of generalized quotients is discussed, which is applied to various function spaces in order to obtain several generalized quotient spaces. Consequently, wavelet transform is extended to these spaces to obtain some generalized results. The concept of convolution related to wavelet is applied to obtain operational properties for quotient of sequences. Further, wavelet transform of periodic quotient of sequences is presented and a uniqueness theorem is defined for the wavelet transform of analytic functions. Moreover, we discuss some fundamental concepts of the theory of generalized quotients and then explain some of its applications such as extending the wavelet transform on a space of generalized quotients on the torus $\mathcal{B}_{\mathcal{S}'}(T^d)$.

Keywords Fourier transform · Wavelet transform · Schwartz distributions · Tempered Boehmians

Mathematics Subject Classification (2010) 44A15 · 46F12 · 54B15 · 46F99

1 Introduction

Wavelets are the latest area in the frontiers of mathematics, signal processing, image processing and scientific computing. It is a versatile tool in every aspect of mathematical context and possesses great potential for applications, as wavelets can be viewed as a unique basis for representing functions for time-frequency analysis. The theory

A. Singh (✉) · A. Rawat
Department of Mathematics and Statistics, Banasthali Vidyapith, Banasthali, India
e-mail: mathdras@gmail.com

J. Singh
Department of Mathematics, JECRC University, Jaipur, India

J. Singh et al. (eds.), *Advances in Mathematical Modelling, Applied Analysis and Computation*, Lecture Notes in Networks and Systems 415,
https://doi.org/10.1007/978-981-19-0179-9_6

of Fourier analysis is well established and popular subject at the core of pure and applied mathematical analysis. The basic building blocks of the Fourier transform (complex exponentials: $e^{i2\pi tu}$) oscillate over all of the time ($-\infty < t < \infty$). As a result, it is difficult for the Fourier transform to represent signals that are localized in time. Thus, it fails to accumulate information that varies with time. As it does not provide the time at which frequency exists hence, it is only ideal for stationary signals. Hence, Fourier methods are not very effective in recapturing the non-smooth signal. In these cases, wavelet analysis is often very efficient, as it presents a simple approach for dealing with the local aspects of a signal. For the last two decades, the advancement of wavelet transform in the field of signal analysis is expanding making it an important mathematical tool. The main reason is wavelet transform, which can represent a function of the time domain in a time-frequency plane. Therefore, it works as a frequency and time localization operator. Also, wavelets can change according to time intervals to obtain high and low-frequency components. Hence, enhancing the study of signal analysis with localized impulses and oscillations. In particular, wavelet analysis is efficient in extracting noise from signals that complement the classical methods of Fourier analysis. Wavelet analysis has been one of the major research directions in both pure and applied mathematics and is still undergoing rapid growth.

The wavelets were developed mostly during the last two decades and are associated with the classical theories of different disciplines, including pure and applied mathematics and engineering. The concept of wavelets started to emerge in the literature in the late 1980s. The theory of wavelets can be seen as syntheses of different ideas that started from various areas, including physics (coherent states formalism in quantum mechanics), mathematics (Caldern Zygmund operators and Littlewood–Paley theory) and engineering (in signal and image processing). The mathematical interpretation of the wavelet transform started in the year 1985 when Meyer discovered the results given by Morlet and the Marseille group. He noticed a link of Morlets algorithm to the resolution of identity in the harmonic analysis due to Caldern in 1964. Therefore, Meyer built the mathematical foundation of wavelet analysis and hence may be regarded as the founder of it. He still actively promotes the field of wavelet analysis as an interdisciplinary area of research. Recently, applications of wavelet analysis have been extended across various fields of mathematics, physics, computer science and engineering.

Based on the idea of wavelets as a family of functions, the mother wavelet $\psi_{b,a}(t)$ is constructed from translation and dilation of a single function $\psi \in L^2(\mathbb{R})$ and is defined by

$$\psi_{b,a}(t) = (\sqrt{a})^{-1}\psi\left(\frac{t-b}{a}\right), \quad t, b \in \mathbb{R}, \quad a > 0, \tag{1}$$

where a and b act as the dilation and translation parameter that measures the level of compression and finds the location of the wavelet. Further, if $|a| < 1$, then (1) is the compressed version of the mother wavelet and represents higher frequencies.

The wavelet transform of $\phi \in L^2(\mathbb{R})$, with respect to (1), is defined by [18]

$$(W\phi)(b,a) = \int_{\mathbb{R}} \phi(t)\overline{\psi_{b,a}}(t)dt, \quad t, b \in \mathbb{R}, \quad a > 0 \tag{2}$$

and the inversion for (2) is given by

$$\phi(x) = \frac{2}{C_\psi} \int_0^\infty \left[\int_{-\infty}^\infty \frac{1}{\sqrt{a}} (W\phi)(b,a)\psi\left(\frac{x-b}{a}\right) db \right] \frac{da}{a^2}, \quad x \in \mathbb{R}, \tag{3}$$

where

$$\frac{C_\psi}{2} = \int_0^\infty \frac{|\hat{\psi}(v)|^2}{|v|} dv = \int_0^\infty \frac{|\hat{\psi}(-v)|^2}{|v|} dv < \infty \quad [3;\ p.64]. \tag{4}$$

If (2) exists, then $(W\phi)(b,a)$ maps each square integrable function ϕ on $\mathbb{R}$ to wavelet transform function W on $\mathbb{R} \times \mathbb{R}_+$. Therefore, from (2),

$$(W\phi)(b,a) = (\phi * h_{a,0})(b), \tag{5}$$

where $h(t) = \bar{\psi}(-t)$.
If $\phi \in L^p(\mathbb{R})$ and $\psi \in L^q(\mathbb{R})$, then

$$\phi * h_{a,0}(b) \in L^r(\mathbb{R}), \quad \frac{1}{p} + \frac{1}{q} = \frac{1}{r} + 1. \tag{6}$$

Now, applying Fourier transform to (5), we get

$$\begin{aligned}(W\phi)(b,a) &= \frac{|a|^{1/2}}{(2\pi)} \int_{\mathbb{R}} e^{i\omega b}\overline{\hat{\psi}(a\omega)}\hat{\phi}(\omega)d\omega \\ &= \frac{|a|^{1/2}}{(2\pi)} \mathcal{F}^{-1}\left[\hat{\phi}(\omega)\overline{\hat{\psi}(a\omega)}\right](b,a).\end{aligned} \tag{7}$$

Hence,

$$\mathcal{F}\left[(W\phi)(b,a)\right](\omega) = |a|^{1/2}\hat{\phi}(\omega)\overline{\hat{\psi}(a\omega)}. \tag{8}$$

This relation holds in general, for $\phi \in L^p(\mathbb{R})$ and $\psi \in L^q(\mathbb{R})$, where $\frac{1}{p} + \frac{1}{q} = \frac{1}{r} + 1;\ 1 \le p, q, r \le 2$.

The theory of Distribution or generalized function was first proposed by Sergei Sobolev in the year 1935 while exploring the uniqueness of the solution for the Cauchy problem of linear hyperbolic equations. Later, Schwartz expanded the area of mathematical research by extending the theory of generalized function in the well-

known hand graph Theories des Distributions which provided a detailed basis for the numerical concept of generalized function spaces [23]. The theory of wavelet analysis provides fundamental characterizations of function and distribution spaces. Using the representation of wavelet transform given by (7), $(W\phi)(b, a)$ is expanded to Schwartz tempered distributions and inversion formulae are also obtained in the distribution setting [12–18, 20, 26, 27, 30].

In recent years, the theory of distributions or generalized functions is at its peak bringing a great revolution in mathematical analysis. In 1935, Sergei L. Sobolev derived the theory of generalized functions while working on the second-order hyperbolic partial differential equations. But in the 1950s, L. Schwartz introduced the concept of distributions that opened a new area of mathematical research. This concept supported the development of several mathematical disciplines, such as transformation theory, operational calculus, ordinary and partial differential equations, and functional analysis. Another approach for this theory was given by S. Bochner around 1930s, to generalize the Fourier transformation for functions $f(t)$ that grow as t approaches infinity [1]. The concept of distribution gives a better mechanism for analysing various entities, such as the delta function, which arise naturally in several mathematical sciences and which can be corrected using distributions. The idea behind distribution is assigning a function not by its values but by its behaviour as a functional on some space of testing functions. Here the space of testing functions is represented by $\mathcal{D}$ which contains all complex-valued functions that are infinitely smooth and have compact support. A continuous linear functional on the space $\mathcal{D}$ is called a distribution and space of all distributions is dual of the space $\mathcal{D}$, denoted by $\mathcal{D}'$.

In the theory of distributional analysis, differentiation is a continuous operation as every distribution has derivatives of all orders. Consequently, distributional differentiation commutes with different limiting processes such as integration and infinite summation. This is the contrast to classical analysis wherein either such operations cannot be interchanged or the inversion of the order must be justified by an additional argument. Though not very recently, yet during the last five decades the theory of generalized functions and integral transforms has been combined, which gave rise to fruitful results in the theory of integral transforms associated with distributions, known as distributional transform analysis. Recently, there were many applications of wavelet and other transforms in distribution spaces [14, 16]. Further, the investigation of the wavelet transform of distributions, tempered distributions and ultra-distributions has extended the applications of the wavelet transform.

There are various other approaches to the theory of generalized functions. One of them is Mikusiński's algebraic approach or the sequential approach, used to define generalized quotient spaces also known as the Boehmian spaces. Here, distributions are defined as a class of equivalent sequences. The construction of generalized quotient space with its brief introduction is presented in Sect. 2. In Sect. 3, we study the wavelet transform of periodic generalized quotients to obtain a uniqueness property. Sections 4 and 5 examine the wavelet transform on generalized quotients in Lebesgue space and in tempered distribution space. The last section is dedicated to presenting the applications of generalized quotient spaces.

2 Generalized Quotient Spaces

The theory of quotient of sequences (Boehmians) in 1973 by Boehme [2] brought a new change in the theory of applicable functional analysis, whereas the generalized quotients are considered to be a generalization of Schwartz distribution theory (see [23]). The use of an algebraic approach, quite similar to the construction of Mikusiński operators, advented a new class of generalized function $\mathcal{B}$, called generalized quotients. This is constructed by Piotr Mikusiński. Motivation for the development of the theory of generalized quotients lies in the core of regular operators, given by Mikusiński and Mikusiński in [6], since these operators form a subalgebra of Mikusinski operators and contain the distributions whose supports are bounded from the left, which does not allow them to contain all continuous functions. Strictly speaking, the space of generalized quotients contains all regular operators, all distributions, and few objects which are neither distributions nor operators. Mikusiński introduced and studied the convergence of generalized quotients, where the space provided with the induced convergence [7, 8]. Further, there always exists a corresponding field of quotients for a ring without zero divisors.

The theory of convolution quotients is inclusive of operators of differentiation, integration and related operators of differentiation and integration. This is the theory that provides a satisfactory answer to Heaviside's calculus, particularly when applied to partial differential equations. This generalization of the Schwartz distribution theory together with their integral transforms is further generalized, came to be known as Boehmianian transform analysis, that is the theory of generalized quotients and their integral transforms, which prompted several authors to study several such integral transforms on various generalized quotient spaces along with their specific properties.

A natural extension of tempered distribution is tempered generalized quotients hence the wavelet transform can be extended for this class of generalized quotients. In [21], Roopkumar defined convolution theorems for the wavelet transform of tempered distributions and hence constructed space of tempered generalized quotient for the wavelet transform. Application of generalized quotients to different spaces with the convolution product gives numerous generalized spaces. Therefore, different integral transforms have been studied in the space of generalized quotients [4, 5, 11, 24, 25].

Let us denote a linear space by G and its subspace by S. For each pair of elements $\phi \in G$ and $\varphi \in S$, let the product $f * g$ be assigned ($*$ is a map from $G \times S$ to G) such that

(i) if $\psi, \varphi \in S$, then $\psi * \varphi \in S$ and $\psi * \varphi = \varphi * \psi$

(ii) if $\phi \in G$ and $\psi, \varphi \in S$, then $(\phi * \varphi) * \psi = \phi * (\varphi * \psi)$

(iii) if $\phi, f \in G, \varphi \in S$, and $k \in \mathbb{R}$, then $(\phi + f) * \varphi = (\phi * \varphi) + (f * \varphi)$ and $k(\phi * \varphi) = (k\phi) * \varphi$.

Let the set of delta sequences denoted by Δ satisfies

(iv) if $\phi, f \in G, (\delta_n) \in \Delta$ and $\phi * \delta_n = f * \delta_n$ $(n = 1, 2, \ldots)$, then $\phi = f$.

(v) if $(\varphi_n), (\delta_n) \in \Delta$, then $(\varphi_n * \delta_n) \in \Delta$.

Let $\mathcal{A}$ denotes the class for which the pair of sequences are defined by $\mathcal{A} = \{(\phi_n), (\varphi_n) : (\phi_n) \subseteq G^{\mathbb{N}}, (\varphi_n) \in \Delta\}$, for each $n \in \mathbb{N}$. An element $((\phi_n), (\varphi_n)) \in \mathcal{A}$ is called quotient of sequences, denoted by ϕ_n/φ_n, if

$$\phi_i * \varphi_j = \phi_j * \varphi_i, \qquad \forall i, j \in \mathbb{N}.$$

Let ϕ_m/φ_m and f_n/ψ_n be two quotients of sequences, then these two are equivalent, if

$$\phi_m * \psi_n = f_n * \varphi_m, \qquad \forall m, n \in \mathbb{N},$$

which divides $\mathcal{A}$ into equivalence classes, denoted by $[\phi_n/\varphi_n]$. These are called generalized quotients and their space is given by $\mathcal{B} = \mathcal{B}(G, \Delta)$. Following illustrates the behaviour of generalized quotients for the algebraic properties.
(i) Addition of two generalized quotients and multiplication by a scalar are defined by

$$[\phi_n/\varphi_n] + [f_n/\psi_n] = [(\phi_n * \psi_n) + (f_n * \varphi_n)/(\varphi_n * \psi_n)]$$

and

$$\alpha[\phi_n/\varphi_n] = [\alpha\phi_n/\varphi_n], \qquad \alpha \in \mathbb{C}.$$

(ii) The differentiation and the operation $*$ are, respectively, defined by

$$[\phi_n/\varphi_n] * [f_n/\psi_n] = [(\phi_n * f_n)/(\varphi_n * \psi_n)]$$

and

$$D^{\alpha}[\phi_n/\varphi_n] = [D^{\alpha}\phi_n/\varphi_n].$$

In particular, if $[\phi_n/\varphi_n] \in \mathcal{B}$ and $\delta \in S$ is any fixed element, then the product $*$ is defined by

$$[\phi_n/\varphi_n] * \delta = [(\phi_n * \delta)/\varphi_n],$$

which is said to be in $\mathcal{B}(G, \Delta)$.

3 Uniqueness Theorem for Wavelet Transform for Generalized Quotients of Analytic Functions

Let $\mathbb{T}$ be a unit circle of the complex plane and $C^{\infty}(\mathbb{T})$ be the space of smooth periodic functions of period 2π. In [22], Roopkumar defined wavelet transform for periodic generalized quotients and showed that it is uniform with the wavelet transform on $C^{\infty}(\mathbb{T})$. An analytic function $\phi(z)$ is bounded in the unit disc D satisfies the uniqueness property, i.e. if the radial limit $\lim_{r\to 1} \phi(re^{i\theta}) = 0$ on $\mathbb{T}$ then $\phi(z) \equiv 0$, almost everywhere on $\mathbb{T}$. Let $C(\mathbb{T})$ represents the set of all continuous complex-

valued function on $\mathbb{T}$ and $C^N(\mathbb{T})$ represents collection of such sequences. A function on the real line with period 2π and a function on $\mathbb{T}$ are treated the same. Let $\phi, \eta \in C(\mathbb{T})$, then their convolution is given by

$$(\phi * \eta)(t) = \frac{1}{2\pi} \int_{-\pi}^{\pi} \phi(t-u)\eta(u)du, \qquad t \in [-\pi, \pi]. \tag{9}$$

Let ϕ be a $2\pi-$periodic function which is L^p integrable over the interval $[-\pi, \pi]$, then by (8) the kth coefficient of the wavelet transform in terms of Fourier coefficient can also be defined by

$$c_k\{(W\phi_n)\}(k) = |a|^{1/2}\hat{\phi}_n(k)\overline{\hat{\psi}(ak)}. \tag{10}$$

Theorem 1 *Let* $F = \left[\frac{\phi_n}{\varphi_n}\right] \in \mathcal{B}_{\mathbb{T}}$. *For each* k, *the sequence* $\{c_k\{(W\phi_n)\}\}_{n=1}^{\infty}$ *converges.*

Proof For $F = \left[\frac{\phi_n}{\varphi_n}\right] \in \mathcal{B}_{\mathbb{T}}$, we have $\phi_n \in C^N(\mathbb{T})$ and $\{\varphi_p\}_{p=1}^{\infty} \in \Delta$, then there exist a natural number p such that $\varphi_p \neq 0$ and $\hat{\varphi}_p \to 1$ as $p \to \infty$.

Let $k \in \mathbb{Z}$ and $a > 0$. Consider

$$\begin{aligned} c_k\{(W\phi_n)\}(k) &= \lim_{n\to\infty} a^{1/2}\hat{\phi}_n(k)\overline{\hat{\psi}(ak)} \\ &= \frac{a^{1/2}\hat{\phi}_n(k)\overline{\hat{\psi}(ak)}\hat{\varphi_m}(k)}{\hat{\varphi_m}(k)} \\ &= \frac{a^{1/2}\,(\phi_n * \varphi_m)\hat{}(k)\overline{\hat{\psi}(ak)}}{\hat{\varphi_m}(k)} \\ &= \frac{a^{1/2}\hat{\phi}_m(k)\overline{\hat{\psi}(ak)}\hat{\varphi_n}(k)}{\hat{\varphi_m}(k)}. \end{aligned} \tag{11}$$

Since, $\hat{\varphi}_n \to 1$ as $n \to \infty$, therefore from (11), we have

$$\lim_{n\to\infty} c_k\{(W\phi_n)\}(k) = \frac{a^{1/2}\hat{\phi}_m(k)\overline{\hat{\psi}}(a\omega)}{\hat{\varphi_m}(k)}. \tag{12}$$

□

Definition 1 For $F = \left[\frac{\phi_n}{\delta_n}\right] \in \mathcal{B}_{\mathbb{T}}$, the wavelet coefficient of the generalized quotient F is defined by

$$c_k((W\phi)) = \lim_{n\to\infty} c_k((W\phi_n)).$$

Definition 2 Let $F = \left[\frac{\phi_n}{\varphi_n}\right] \in \mathcal{B}_{\mathbb{T}}$, then $F = 0$ on an open set Ω, if there exists a delta sequence $\{\varphi_n\}$ such that $F * \varphi_n \in C(\mathbb{T}),\ \forall n \in \mathbb{N}$ and $F * \varphi_n \to 0$ uniformly on compact subset of Ω as $n \to \infty$.

Definition 3 A generalized quotient $F = \left[\frac{\phi_n}{\varphi_n}\right] \in \mathcal{B}_{\mathbb{T}}$ is of analytic type if the wavelet transform of the generalized quotient F is zero.

Theorem 2 *If $F = \left[\frac{\phi_n}{\varphi_n}\right] \in \mathcal{B}_{\mathbb{T}}$ is of analytic type and its wavelet transform be given by $(WF)(b, a)$ such that F is zero on some open arc Ω, then F is equivalent to zero.*

Proof Let $F \in \mathcal{B}_{\mathbb{T}}$ be of analytic type with $F = 0$ on Ω. As $(WF)(n, a) = 0$ for $n = -1, -2, \ldots$. Therefore, for each n

$$(W\phi_n)(b, a) = (WF)(b, a)\varphi_n(b) = 0 \text{ for } b = -1, -2, \cdots . \tag{13}$$

Thus, ϕ_n is identically zero on $\mathbb{T}$.
By definition of generalized quotients, $\phi_n * \varphi_k = \phi_k * \varphi,\ \ \forall n, k \in \mathbb{N}$, then we have

$$\phi_n = \phi_n - (\phi_n * \varphi_k) + (\phi_n * \varphi_k),\ \ \forall n, k \in \mathbb{N}. \tag{14}$$

As $\{\varphi_n\} \in \Delta$, then for each k, $(\phi_n * \varphi_k) \to \phi_n$ as $k \to \infty$ on $\mathbb{T}$ .We consider a closed subinterval I_2 on Ω. Then there is another closed interval I_1, such that for any $h > 0$, $I_2 \subset I_1 \subset \Omega$, and $(-h, h) + I_2 \subseteq I_1$. Also, supp $\varphi_n \subseteq (-h, h)$, for $n \geq m \in \mathbb{N}$. Let for fixed m and for $k \geq k_0$, let $\epsilon > 0$. As $k \to \infty$, we have $\phi_k \to 0$ uniformly on I_1. Then there exist a natural number k_0 such that for all $x \in I_1$, $|\phi_k(x)| < \epsilon$ for all $k \geq k_0$. Hence

$$\begin{aligned} |\,(\phi_n * \varphi_k)\,(t)| &= |(\phi_k * \varphi_n)(t)| \\ &\leq \frac{1}{2\pi} \int_{-h}^{h} |\phi_k(t-u)|\varphi_n(u)du \\ &\leq \frac{\epsilon}{2\pi} \int_{-h}^{h} \varphi_n(u)du = \epsilon,\ \forall t \in I_2. \end{aligned} \tag{15}$$

Therefore, $(\phi_n * \varphi_k) \to 0$ uniformly on I_2 as $k \to \infty$, for each $n \geq m$. By combining (13), (14) and (15), we see that for each $n \geq m$, ϕ_n vanishes on I_2.
This completes the proof of the theorem. □

Let $\mathcal{B}_{\mathbb{T}}$ denote the space of generalized quotients that contains the analytic functions of the complex plane in the open unit disc D. A generalized quotient is an analytic element of $\mathcal{B}_{\mathbb{T}}$, and is defined as follows:

$$\mathscr{A} = \left\{ \phi(z) = \sum_{k=0}^{\infty} s_k z^k : |s_k| \leq Ce^{-l\omega(k)},\ \forall k \in \mathbb{N},\ \text{and for each } l > 0 \right\}. \quad (16)$$

Let $\phi_n(t)$ be the sequence of trigonometric polynomial, given by

$$\phi_n(t) = \sum_{m=1}^{n} s_m e^{l_m t_i}, \quad (17)$$

then the wavelet transform of an periodic function $\phi(t)$ which is the uniform limit of the $\{\phi_n(t)\}$ is defined by

$$(W\phi) = \lim_{n\to\infty} (W\phi_n) = \sum_{m=1}^{\infty} s_m |a|^{1/2} \overline{\hat{\psi}(a\omega)} e^{l_m \omega i}, \quad (18)$$

provided the limit exists.

Definition 4 Let $F = \left[\frac{\phi_n}{\varphi_n}\right] \in \mathcal{B}_{\mathbb{T}}$. The wavelet coefficient of F, is defined as $c_k((WF)) = \lim_{n\to\infty} a^{1/2} \hat{\phi}_n(k) \overline{\hat{\psi}(ak)}$.

Definition 5 A sequence $\{F_n\} \in \mathcal{B}_{\mathbb{T}}$ is said to $\delta-$converge to some $F \in \mathcal{B}_{\mathbb{T}}$ as $n \to \infty$ if there exists $\{\varphi_m\} \in \Delta$, such that $F_n * \varphi_m, F * \varphi_m \in L^1(\mathbb{T})$ and $F_n * \varphi_m \to F * \varphi_m \in L^1(\mathbb{T})$ as $n \to \infty$ for each fixed m.

Theorem 3 *Let S be a Schwartz distribution and the pth order distribution S is given by $D^p S = \sum_{n=1}^{m} s_n (l_n i)^p e^{l_n t i}$, then the trigonometric series given by $\sum_{n=1}^{m} s_n e^{l_n t i}$ converges to S in weak sense. Also, let ϕ belongs to the class of analytic functions in open unit disc D, then there exists a sequence $\{T_m\} \in \mathscr{A}$ and $F \in \mathcal{B}_{\mathbb{T}}$ such that $T_m \to \phi$ and $D^k S \xrightarrow{\delta} F$ as $m \to \infty$.*

Proof Let $\phi(z)$ be an analytic function in the open unit disc D, given by

$$\phi(z) = \sum_{n=0}^{m} s_n z^n, \quad (19)$$

where

$$\sum_{n=0}^{m} |s_m| < \infty. \quad (20)$$

Now, for each $m \in \mathbb{N}$, let

$$T_m(z) = \sum_{n=0}^{m} s_m z^n, \quad z \in \mathcal{D}. \quad (21)$$

Then by (16), $T_m \in \mathscr{A}$ and $T_m \to \phi$ as $m \to \infty$. Also, for some $l_n > 0$, we have

$$S = \sum_{n=0}^{m} s_n e^{l_n t i}. \tag{22}$$

By taking convolution of two functions S and ϕ_k, we get

$$\begin{aligned}
(S * \phi_k)(\omega) &= \frac{1}{2\pi} \int_{-\pi}^{\pi} S(\omega - x)\phi_k(x)dx \\
&= \frac{1}{2\pi} \int_{-\pi}^{\pi} \sum_{n=0}^{m} s_n e^{l_n(\omega - x)i} \phi_k(x)dx \\
&= \frac{1}{2\pi} \int_{-\pi}^{\pi} \sum_{n=0}^{m} s_n e^{il_n\omega} e^{-il_n x} \phi_k(x)dx \\
&= \sum_{n=0}^{m} s_n e^{il_n\omega} \hat{\phi}_k(l_m) \\
&= \lim_{n\to\infty} \frac{(W\phi_n)}{\overline{\hat{\psi}(a\omega)}} |a|^{1/2} \hat{\phi}_k.
\end{aligned}$$

Taking $\eta_k(t) = \sum_{n=0}^{m} s_n e^{il_n\omega} \hat{\phi}_k(l_n) \in L^1(\mathbb{T})$ and choosing

$$\hat{\phi}_k(l_n) = \begin{cases} \left(1 + \dfrac{|l_n|}{k+1}\right), & |l_n| \le k \\ 0, & \text{otherwise,} \end{cases}$$

then for each k, we have $S * \phi_k \to \sum_{n=0}^{m} s_n e^{il_n\omega} \in L^1(\mathbb{T})$ as $m \to \infty$ and $(\{\eta_k\}, \{\phi_k\}) \in \mathscr{A}$. Hence, for $F = (\{\eta_k\}, \{\phi_k\}) \in \mathcal{B}_{\mathbb{T}}$, by definition we get $T_m \xrightarrow{\delta} F \in \mathcal{B}_{\mathbb{T}}$ as $m \to \infty$. This completes the proof. □

4 Wavelet Transform on Generalized Quotients in Lebesgue Space

The convolution related to wavelet transform is given by

$$(W(\phi \# f))(b, a) = (W\phi)(b, a)(Wf)(b, a). \tag{23}$$

The association among the wavelet convolution # and Fourier convolution $*$ is defined by [18, p. 131]

$$\overline{\hat{\psi}(a\omega)}(\phi\# f)^{\wedge}(\omega) = (2\pi)^{-1}[\overline{\hat{\psi}(a\cdot)}\hat{\phi}(\cdot) * \overline{\hat{\psi}(a\cdot)}\,\hat{f}(\cdot)](\omega). \tag{24}$$

Uniqueness: If $\frac{1}{p} + \frac{1}{q} = 1$ then $\overline{\hat{\psi}(a\omega)}\hat{\phi}(a\omega) \in L^1(\mathbb{R})$, $\overline{\hat{\psi}(a\omega)}\,\hat{f}(\omega) \in L^1(\mathbb{R})$ and $\hat{\psi}(a\omega) \neq 0$ for $a \in \mathbb{R}_+$. Let $(W\phi)(b, a) = (Wf)(b, a)$, $\forall (b, a) \in \mathbb{R} \times \mathbb{R}_+$. Then $\phi = f$, a.e.

Now, dividing (24) by $\overline{\hat{\psi}(a\omega)} \neq 0$ and then applying inverse Fourier transform [18, p. 131], we obtain

$$(\phi\# f)(z) = \int_{\mathbb{R}} \int_{\mathbb{R}} \phi(x) f(y) D_a(x, y, z) dx dy,$$

where

$$D_a(x, y, z) = (2\pi)^{-2n} \int_{\mathbb{R}} \left\{ \int_{\mathbb{R}} e^{-i(y-z)\omega - i(x-y)\eta} + \psi(a\omega, a\eta) d\omega \right\} d\eta$$

with

$$\chi(\omega, \eta) = \overline{\hat{\psi}(\eta)} \frac{\overline{\hat{\psi}(\omega - \eta)}}{\overline{\hat{\psi}(\omega)}}.$$

The wavelet convolution # in terms of the basic function is given by [18, p. 119]:

$$\begin{aligned} D(x, y, z) =& \frac{1}{C_\psi} \int_0^\infty \int_{\mathbb{R}} \overline{\psi_{b,a}(x)}\ \ \overline{\psi_{b,a}(y)} \psi_{b,a}(z) db \frac{da}{a} \\ =& W_\psi^{-1}[\overline{\psi_{b,a}(x)}\ \ \overline{\psi_{b,a}(y)}](z). \end{aligned} \tag{25}$$

Hence

$$\int_{-\infty}^{\infty} D(x, y, z) \overline{\psi_{b,a}(z)} db da = \overline{\psi_{b,a}(x)} \cdot \overline{\psi_{b,a}(y)}. \tag{26}$$

Multiplying both sides of (24) by $\frac{\hat{\psi}(a\omega)}{a}$ and integrating with respect to a from 0 to ∞, we get

$$\int_0^\infty |\hat{\psi}(a\omega)|^2 \frac{da}{a} (\phi \# f)^\wedge(\omega)$$

$$= (2\pi)^{-n} \int_0^\infty \frac{\hat{\psi}(a\omega)}{a} da[\overline{\hat{\psi}(a\cdot)}\hat{\phi}(\cdot) * \overline{\hat{\psi}(a\cdot)}\hat{f}(\cdot)](\omega). \tag{27}$$

By using inverse Fourier transform and (4), we get

$$C_\psi(\phi \# f)(z) = (2\pi)^{-2n} \int_{\mathbb{R}} e^{i\omega z} d\omega$$

$$\int_0^\infty e^{-i\omega a v} \psi(u) du[\overline{\hat{\psi}(a\cdot)}\hat{\phi}(\cdot) * \overline{\hat{\psi}(a\cdot)}\hat{f}(\cdot)](\omega)$$

$$(\phi \# f)(z) = \int_{\mathbb{R}} \int_{\mathbb{R}} \phi(x) f(y) D(x, y, z) dx dy.$$

Translation, denoted by τ, is given by

$$(\tau_y \phi)(x) = \phi * (x, y) = \int_{\mathbb{R}} D(x, y, z) \phi(z) dz.$$

Therefore, the wavelet convolution of ϕ and f is given by

$$(\phi \# f)(z) = \int_{\mathbb{R}} \int_{\mathbb{R}} D(x, y, z) \phi(x) f(y) dx dy.$$

Lemma 1 *If $\phi \in L^p$ and $\varphi \in S$, then $(\phi \# \varphi) \in L^p$.*

In view of Lemma 1, the mapping of convolution product # is given by

$$\# : L^p \times S \to L^p. \tag{28}$$

Let,

$$A = \{((\phi_n), (\varphi_n)) : \phi_n \in L^p, (\varphi_n) \in \Delta\}. \tag{29}$$

Then $((\phi_n), (\varphi_n)) \in A$ is said to be a quotient of sequence, if

$$\phi_m \# \varphi_n = \phi_n \# \varphi_m, \quad \forall \ m, n \in \mathbb{N}. \tag{30}$$

If two quotients of sequence ϕ_n/φ_n and f_n/σ_n are equivalent, i.e.

$$\phi_n \# \sigma_n = f_n \# \varphi_n, \quad \forall \ n \in \mathbb{N} \tag{31}$$

then such quotient of sequences or generalized quotient is known as L^p—generalized quotient and the space of such L^p—generalized quotients is represented by $\mathcal{B}(L^p, \Delta)$. Let C^∞ be the set of infinitely differentiable function on the real line, then the equivalence class $F = [\phi_n/\varphi_n]$, where $\phi_n \in C^\infty$ and $\varphi_n \in \Delta$, is known as C^∞—generalized quotient. Its space is given by $\mathcal{B}(C^\infty, \Delta)$.

A function $\phi \in L^p$ is identified with L^1-generalized quotient $[(\phi \# \varphi_n)/\varphi_n]$, where $(\varphi_n) \in \Delta$. Likewise, let f be a C^∞—function identified with C^∞—generalized quotient $[(f \# \epsilon_n)/\epsilon_n]$, where $(\epsilon_n) \in \Delta$ is another delta sequence.

Let under the identification $u = [(u \# \delta_n)/\delta_n]$, the space $\mathcal{D}'$ be identified with C^∞—generalized quotient. Then, these identifications possess the aspired algebraic and topological properties [8].

Lemma 2 *If $\phi \in L^p$, $1 \leq p \leq \infty$ and $\psi \in L^q(\mathbb{R})$ with $a > 0$ and $\rho = 1$ also $\delta \in S$, then $(W[\phi \# \delta]) = (W[\phi]) \cdot \psi[\delta]$.*

Definition 6 A L^p generalized quotient $[\phi_n/\varphi_n]$ is wavelet transformable if there exists a C^∞-generalized quotient y and a representative $[f_n/\psi_n]$ for y with $f_n = (W[\phi_n])$. The space $\mathcal{B}_W(L^r, \Delta)$ represents the set of all wavelet transform of generalized quotients.

Lemma 3 *If $[\phi_n/\varphi_n]$ is a quotient in $\mathcal{B}_W(L^r, \Delta)$, then $(W[\phi_n])/(W[\varphi_n])$ is also a quotient in $\mathcal{B}(C^\infty, \Delta)$.*

Proposition 1 *Let $F = [\phi_n/\varphi_n]$ be a wavelet transformable L^p-generalized quotient. Then the wavelet transform of F is a C^∞-generalized quotient y, given by*

$$y = (WF) = \frac{(W[\phi_n])}{(W[\varphi_n])}. \tag{32}$$

Theorem 4 *If $\phi \in L^p$, $\psi \in L^q$ and wavelet transform is in L^r and, also if $F = [(\phi \# \delta_n)/\delta_n]$ and $y = [(W\phi).(W\delta_n)/(W\delta_n)]$, then $F \in \mathcal{B}_W(L^1, \Delta)$ for $p, q = 1$ such that $(WF) = y \in \mathcal{B}(C^\infty, \Delta)$.*

Proof A L^p function ϕ can be identified with the generalized quotient $F = [(\phi \# \delta_n)/\delta_n]$, where $(\delta_n) \in \Delta$. As $\phi \in L^p$ (by Lemma 1), therefore, $(\phi \# \delta_n) \in L^p$, which asserts that $(W(\phi \# \delta_n)) = (W[\phi]).(W[\delta_n])$, (by Lemma 3). Also, $(W[f]).(W[\delta_n]) \in C^\infty$ shows that $F = [(\phi \# \delta_n)/\delta_n] \in \mathcal{B}_W(L^1, \Delta)$ for $p, q = 1$. Then

$$(WF) = \left[\frac{\phi \# \delta_n}{\delta_n}\right] = \frac{(W[f])(W[\delta_n])}{(W[\delta_n])} = y. \tag{33}$$

□

Theorem 5 *Let $F \in \mathcal{B}_W(L^r, \Delta)$ and α be a constant. Then $\alpha x \in \mathcal{B}_W(L^r, \Delta)$ and $(W(\alpha F)) = \alpha(WF)$.*

Proof Let $x = [f_n/\varphi_n]$, then we have $\alpha x = [\alpha f_n/\varphi_n]$. Also, $(W[(\alpha f_n)]) = \alpha(Wf_n) \in C^\infty$ as $(Wf_n) \in C^\infty$. Hence $[(W(\alpha f_n))/\varphi_n] \in B(C^\infty, \Delta)$.

This shows that $[(\alpha f_n)/\varphi_n] = \alpha x \in B_W(L^r, \Delta)$, and that

$$\begin{aligned}(W(\alpha x)) &= [(W(\alpha f_n))/(W\varphi_n)] \\ &= \alpha[(W(f_n)/(W\varphi_n)] \\ &= \alpha(Wx).\end{aligned}$$

□

Theorem 6 *If $x \in B_W(L^r, \Delta)$, and $\delta \in S$, then $(x\#\delta) \in B_W(L^1, \Delta)$ and $(Wx)\#\delta$.*

Proof If $x = \left[\frac{f_n}{\varphi_n}\right] \in B_W(L^1, \Delta)$ for $p, q = 1$, then $(Wx) = \left[\frac{(Wf_n)}{(W\varphi_n)}\right] \in B(C^\infty, \Delta)$. From Lemma 1

$$x\#\delta = \left[\frac{f_n\#\delta}{\delta}\right] \in B_W(L^1, \Delta).$$

Here

$$(W(f_n\#\delta)) = (W[f_n]).(W[\delta]) \in C^\infty. \tag{34}$$

Therefore, $[(W(f_n\#\delta))/\varphi_n] \in B(C^\infty, \Delta)$ and hence, $[(f_n\#\delta)/\varphi_n] = (x\#\delta) \in B_W(L^1, \Delta)$ for both $p = 1$ and $q = 1$. Also,

$$\begin{aligned}(W[x\#\delta]) &= \left[\frac{(W(f_n\#\delta))}{(W\varphi_n)}\right] = \left[\frac{(Wf_n)\cdot(W\delta)}{(W\varphi_n)}\right] \\ &= \frac{(Wf_n)\cdot\delta}{(W\varphi_n)} = (Wx)\#\delta.\end{aligned}$$

□

Lemma 4 *If $f, f_n \in L^1$ and $f_n \to f$ as $n \to \infty$, then f and f_n, are elements of $B(C^\infty, \Delta)$, satisfying $f_n \to f$ in $B(C^\infty, \Delta)$.*

Theorem 7 *The wavelet transform for generalized quotient is a continuous linear map from $B_W(L^1, \Delta)$ to $B(C^\infty, \Delta)$.*

Proof As x_n converges to x in $B_W(L^1, \Delta)$, there exists a sequence $(\delta_k) \in \Delta$ such that $(x\#\delta_k), (x_n\#\delta_k) \in L^1$, and as $n \to \infty$

$$(x_n\#\delta_k) \to (x\#\delta_k) \text{ in } L^1, \forall k \in \mathbb{N}$$

i.e.

$$(W(x_n\#\delta_k)) \to (W(x\#\delta_k)) \text{ in } L^1 \text{ for } p,\ q = 1 \text{ as } n \to \infty, \forall\ k \in \mathbb{N}.$$

Let $f_n = (W(x_n\#\delta_k))$, $f = (W(x\#\delta_k))$ as C^∞—generalized quotients, then

$$f_n \to f \text{ in } B(C^\infty, \Delta). \tag{35}$$

By the definition of generalized quotients, we get

$$\begin{aligned}(W(x_n\#\delta_k)) &= (W(x\#\delta_k)) \\ &= (W[x_n]) \cdot (W[\delta_k]) \\ &= (Wx_n)\#\delta_k. \quad \text{(by Theorem 6)}\end{aligned}$$

Similarly,

$$(W(x_n\#\delta_k)) = (Wx)\#\delta_k, \tag{36}$$

and (30) can be written as

$$(Wx_n)\#\delta_k \to (Wx)\#\delta_k \text{ in } B(C^\infty, \Delta). \tag{37}$$

Therefore, for $((Wx_n)\#\delta_k)\#\delta_k$ and $((Wx)\#\delta_k)\#\delta_k$ in C^∞, we have

$$(W(x_n\#\delta_k))\#\delta_k \to (W(x\#\delta_k))\#\delta_k, \text{ as } n \to \infty \text{ in } C^\infty.$$

Hence,

$$(Wx_n) \to (Wx), \text{ as } n \to \infty \text{ in } B(C^\infty, \Delta).$$

□

Theorem 8 *Let $y \in B(C^\infty, \Delta)$. Then there exists $x \in B_W(L^1, \Delta)$ such that $(Wx) = y$ iff y is a quotient g_n/ψ_n such that $g_n \in L^1 \cap C^\infty$.*

Proof Let us consider a generalized quotient $x = [f_n/\varphi_n] \in B_W(L^1, \Delta)$ and $f_n \in L^1$. Then $(Wf_n) \in L^1$. From Proposition 1, we can define, $y = (Wx) = W[f_n/\varphi_n] \in B(C^\infty, \Delta)$ and from Definition 1, we get $(Wf_n) \in C^\infty$. Hence $y = (Wx) = W[f_n/\varphi_n]$ satisfies $(Wf_n) \in L^1 \cap C^\infty$.

Conversely, let $y = [g_n/\psi_n] \in B(C^\infty, \Delta)$, for $g_n \in L^1 \cap C^\infty$. Let $x = [f_n/\varphi_n]$ such that $f_n = (W[g_n])$. As, $g_n \in L^1$, we have $f_n \in L^1$ and $f_i\#\psi_j = f_j\#\psi_i, \forall i, j \in \mathbb{N}$ and $g_i\#\psi_j = g_j\#\psi_i, \forall i, j \in \mathbb{N}$. This shows that $x = [f_n/\psi_n] \in B_W(L^1, \Delta)$ and $(W[f_n]) = g_n \in C^\infty$. Hence $x = [f_n/\psi_n] \in B_W(L^1, \Delta)$ and $(Wx) = y$.
Therefore, the image of the wavelet transformable generalized quotient, under the classical wavelet transform, is given from the L^p space to C^∞ space. □

Example 1 Let the Mexican hat wavelet (MHW), which is considered as an even wavelet and is derived by taking the second derivative of the Gaussian function is defined by

$$\psi(t) = e^{\frac{-t^2}{2}}(1 - t^2) = -\frac{d^2}{dt^2}e^{\frac{-t^2}{2}}. \tag{38}$$

The Fourier transform of MHW is as follows:

$$\hat{\psi}(w) = \sqrt{2\pi} w^2 e^{\frac{-w^2}{2}} \tag{39}$$

and the jth derivative of MHW is given by

$$D^j \psi(t) = \sum_{r=0}^{j} \binom{j}{r} D^{(r)}(1-t^2) D^{(j-r)} e^{\frac{-t^2}{2}}. \tag{40}$$

Using Hermite polynomial's property in (40), we have

$$D^j \psi(t) = \sum_{r=0}^{j} \binom{j}{r} D^{(r)}(1-t^2) e^{\frac{-t^2}{2}} H_{j-r}(t)$$

$$= j(1-t^2) e^{\frac{-t^2}{2}} H_j(t) + \binom{j}{r} (-2t) e^{\frac{-t^2}{2}} H_{k-1}(t), \tag{41}$$

where $H_k(t)$ denotes the Hermite polynomial. Therefore, $\psi(t) \in L^p(\mathbb{R})$ and the Mexican hat wavelet transform of $f \in L^q(\mathbb{R})$ is given by (2), [19].

5 Wavelet Transform on $\mathcal{B}_{\mathcal{S}'}(T^d)$

In the next section, we discuss the space of tempered distribution and tempered generalized quotients for the wavelet transform on the torus $\mathcal{B}_{\mathcal{S}'}(T^d)$. Further, convergence structure for the wavelet transform on $\mathcal{B}_{\mathcal{S}'}(T^d)$ is discussed and an inversion formula is obtained for the same.

Let $\mathcal{S}(\mathbb{R})$ and $\mathcal{S}(\mathbb{R} \times \mathbb{R}_+)$ be the Schwartz testing function spaces. The space consists of rapidly decreasing smooth functions on $\mathbb{R}$ and $\mathbb{R} \times \mathbb{R}_+$ with compact support and hence, their dual is the space of tempered distributions denoted by $\mathcal{S}'(\mathbb{R})$ and $\mathcal{S}'(\mathbb{R} \times \mathbb{R}_+)$.

Lemma 5 *Let $W : \mathcal{S}'(\mathbb{R}) \to \mathcal{S}'(\mathbb{R} \times \mathbb{R}_+)$ be a continuous, linear map such that for $f \in \mathcal{S}'(\mathbb{R})$ its wavelet transform is defined by*

$$\langle (Wf), \phi \rangle = \left\langle f, W^* \phi \right\rangle, \quad \forall \phi \in \mathcal{S}(\mathbb{R} \times \mathbb{R}_+). \tag{42}$$

The space of tempered generalized quotients is denoted by $\mathcal{B}_{\mathcal{S}'(\mathbb{R})}$ and let $\alpha = (\alpha_1, \cdots, \alpha_d)$, where α_j is a non-negative integer. Then,

$$|\alpha| = \alpha_1 + \alpha_2 + \cdots + \alpha_d \text{ and } D^\alpha = \left(\frac{\partial}{\partial x_1}\right)^{\alpha_1} \cdots \left(\frac{\partial}{\partial x_d}\right)^{\alpha_d}.$$

Let $x = (x_1, \cdots, x_d) \in \mathbb{R}^d$ and $y = (y_1, \cdots, y_d) \in \mathbb{R}^d$, such that

$$x \cdot y = x_1 y_1 + \cdots + x_d y_d, \qquad \text{and} \qquad \|x\| = \sqrt{x \cdot x}.$$

Now, a complex-valued infinitely differentiable function is rapidly decreasing if

$$\sup_{|\alpha| \le m} \sup_{x \in \mathbb{R}^d} \left(1 + x_1^2 + \cdots + x_d^2\right)^m |D^\alpha f(x)| < \infty \tag{43}$$

for every non-negative integer m. Further, let $\mathcal{S}(\mathbb{R}^d)$ be the space of all rapidly decreasing functions on $\mathbb{R}^d$.

Let $\mathcal{A}$ be the class of pair of sequences defined by

$$\mathcal{A} = \{((f_i), (\eta_i)) : (f_i) \subset \Gamma,\ (\eta_i) \in \Delta\}.$$

An element $((f_i), (\eta_i)) \in \mathcal{A}$, is said to be a quotient of sequences also denoted by $\dfrac{f_i}{\eta_i}$, if

$$f_i \star \eta_j = f_j \star \eta_i, \quad \forall i, j \in \mathbb{N}. \tag{44}$$

Two quotient of sequences $\dfrac{f_i}{\eta_i}$ and $\dfrac{g_i}{\xi_i}$ are said to be equivalent if

$$f_i \star \xi_j = g_j \star \eta_i, \quad \forall i, j \in \mathbb{N}. \tag{45}$$

The equivalence class including $\dfrac{f_i}{\eta_i}$ is represented by $\left[\dfrac{f_i}{\eta_i}\right]$ and are called generalized quotients. The collection of all generalized quotients is given by $\mathcal{B}(\Gamma, (S, *), \star, \Delta)$. A function $f \in \Gamma$ can be identified as a generalized quotient $\left[\dfrac{f_i \star \eta_i}{\eta_i}\right]$, where $(\eta_i) \in \Delta$ is arbitrary. The space of generalized quotients has two convergences which are defined as follows.

Definition 7 (Δ-convergence) A sequence $\{X_i\}_{i=1}^{\infty}$ in $\mathcal{B}(\mathcal{S}'(\mathbb{R}))$ is said to Δ-converge to $X \in \mathcal{B}(\mathcal{S}'(\mathbb{R}))$, represented by $X_i \xrightarrow{\Delta} X$, if there exist $(\eta_j) \in \Delta$ such that $(X_i - X) \star \eta_i \in \Gamma$ for all $i \in \mathbb{N}$ and $(X_i - X) \star \eta_i \to 0$ in Γ as $i \to \infty$.

Definition 8 (δ-convergence) A sequence $\{X_i\}_{i=1}^{\infty}$ in $\mathcal{B}(\mathcal{S}'(\mathbb{R}))$ is said to δ-converge to $X \in \mathcal{B}(\mathcal{S}'(\mathbb{R}))$, represented by $X_i \xrightarrow{\delta} X$, if there exist $(\eta_j) \in \Delta$ such that $X_i \star \eta_j \in \Gamma$ and $X \star \eta_j \in \Gamma$, $\forall\, i, j \in \mathbb{N}$ and $X_i \star \eta_j \to X \star \eta_j$ in Γ as $i \to \infty$.

Mikusiński [9] introduced the space of tempered generalized quotients denoted by $\mathcal{B}(\mathbb{R}) = \mathcal{B}(\mathcal{S}'(\mathbb{R}), (\mathcal{D}(\mathbb{R}), *), *, \Delta_0)$ and the family of sequences (φ_n) from $\mathcal{D}(\mathbb{R})$ such that

1. $\int_{\mathbb{R}} \varphi_n(x)dx = 1$, for all $n \in \mathbb{N}$,
2. $\int_{\mathbb{R}} |\varphi_n(x)|dx \le M$, for some constant $M \ge 0$ and all $n \in \mathbb{N}$,

3. The support of φ_n, decreases to 0 as $n \to \infty$.
3. $S(\varphi_n) \to 0$ as $n \to \infty$, where $S(\varphi_n) = \sup\{|x| : \varphi_n(x) \neq 0\}$.

The generalized quotients space $\mathcal{B}(\mathbb{R} \times \mathbb{R}_+) = \mathcal{B}(\mathcal{S}'(\mathbb{R} \times \mathbb{R}_+), (\mathcal{D}(\mathbb{R}), \star), \otimes, \Delta_0)$ or simply $\mathcal{B}$ has been constructed by Roopkumar [21]. Every generalized quotient in $\mathcal{B}(\mathbb{R} \times \mathbb{R}_+)$ is of the form $\left[\frac{F_i}{\eta_i}\right]$, where $F_i \in \mathcal{B}(\mathbb{R} \times \mathbb{R}_+),\ \forall i \in \mathbb{N},\ (\eta_i) \in \Delta_0$ and $F_i \otimes \delta_j = F_j \otimes \delta_i,\ \forall i, j \in \mathbb{N}$.

The space $\mathcal{D}(\mathbb{R}^d)$ consists of smooth functions with compact support which are rapidly decreasing on $\mathbb{R}^d$. The dual space of $\mathcal{D}(\mathbb{R}^d)$ is the space of distributions denoted by $\mathcal{D}'(\mathbb{R}^d)$.

The wavelet transform (Wf) of $f \in \mathcal{S}'(\mathbb{R}^d)$ is the tempered distribution defined by

$$\langle (Wf), \phi \rangle = \left\langle f, W^*\phi \right\rangle, \quad \forall \phi \in \mathcal{S}(\mathbb{R}^d \times \mathbb{R}_+). \tag{46}$$

In this section, we introduce the space of generalized quotients on the torus given by Nemzer[10]. The space of torus is defined by

$$T^d = \left\{ \left(e^{ix_1}, \cdots, e^{ix_d}\right) : x_j \text{ real} \right\}.$$

A function on T^d and on $\mathbb{R}^d$ will be treated same, which is 2π-periodic in each variable. For $f \in \mathcal{T}$, define

$$\tau_{2\pi} f(x) = f(x_1 + 2\pi, \cdots, x_d + 2\pi).$$

The translation operator $\tau_{2\pi}$ can be extended to $\mathcal{B}_{\mathcal{T}}$ as follows:

$$\text{For } F = \left[\frac{f_n}{\varphi_n}\right], \text{ we have } \tau_{2\pi} F = \left[\frac{\tau_{2\pi} f_n}{\varphi_n}\right].$$

Thus, $\tau_{2\pi} F$ is a tempered generalized quotient.
The space of generalized quotients on the torus $\mathcal{B}_{\mathcal{S}'}(T^d)$ is defined by

$$\mathcal{B}_{\mathcal{S}'}(T^d) = \{F \in \mathcal{B} : \tau_{2\pi} F = F\}. \tag{47}$$

Lemma 6 *Let $F = \left[\frac{f_n}{\varphi_n}\right] \in \mathcal{B}$. Then $F \in \mathcal{B}_{\mathcal{S}'}(T^d)$ if and only if for all $n \in \mathbb{N}$, f_n is 2π-periodic in each variable.*

Definition 9 Let $F = \left[\frac{f_n}{\delta_n}\right] \in \mathcal{B}$. Then $F \in \mathcal{B}_{\mathcal{S}'}(T^d)$ if and only if for all $n \in \mathbb{N}$, f_n is 2π periodic in each variable.

The wavelet coefficient of ϕ on T^d is defined by

$$C_{j,k}(\phi) = \int_{T^d} \phi(x)\psi_{j,k}(t)dt, \tag{48}$$

where $j \in \mathbb{Z}$ and $k \in J = \{0, \ldots, 2^j - 1\}^d$.

Theorem 9 *Let* $F = \left[\frac{\phi_n}{\varphi_n}\right] \in \mathcal{B}_{\mathcal{S}'}(T^d)$, *then for each* $j \in \mathbb{Z}$ *and* $k \in J$ *the sequence* $\left\{C_{j,k}(\phi_n)\right\}_{n=1}^{\infty}$ *converges.*

Proof For $F = \left[\frac{\phi_n}{\varphi_n}\right] \in \mathcal{B}_{\mathcal{S}'}(T)^d$ and $\left\{\varphi_p\right\}_{p=1}^{\infty}$ be a delta sequence, then there exist a natural number p such that $\varphi_p \neq 0$ and $\varphi_p \to 1$ as $p \to \infty$.
For $j \in \mathbb{Z}$ and $k \in J$, consider

$$\begin{aligned} C_{j,k}(\phi_n) &= C_{j,k}\left(\left[\frac{(\phi_n * \varphi_p)}{\varphi_p}\right]\right) \\ &= \left[\frac{C_{j,k}(\phi_n * \varphi_p)}{\varphi_p}\right] \\ &= \left[\frac{C_{j,k}(\phi_p * \varphi_n)}{\varphi_p}\right] \\ &= \left[\frac{C_{j,k}(\phi_p) \otimes \varphi_n}{\varphi_p}\right]. \end{aligned} \tag{49}$$

Therefore, (49) converges to $\left[\frac{C_{j,k}(\phi_p)}{\varphi_p}\right]$ as $n \to \infty$. Hence, the theorem is proved. □

Definition 10 For $F = \left[\frac{\phi_n}{\delta_n}\right] \in \mathcal{B}_{\mathcal{S}'}(T^d)$, the wavelet coefficient of the generalized quotient F is defined by

$$C_{j,k}(F) = \lim_{n\to\infty} C_{j,k}(\phi_n).$$

Theorem 10 *Let* $F \in \mathcal{B}_{\mathcal{S}'}(T^d)$. *Then*

$$(WF) = \sum_{j\in\mathbb{Z}} \sum_{k\in J} C_{j,k}(F)\delta(x-k, y-j).$$

Proof The proof of this theorem is given in [29]. □

The next theorem shows that the wavelet transform maps $\mathcal{B}_{\mathcal{S}'}(T^d)$ onto $\mathcal{S}'(\mathbb{R}^d \times \mathbb{R}_+)$ such that the space of hyperfunctions on T^d can be identified with a proper subspace of $\mathcal{B}_{\mathcal{S}'}(T^d)$.

Theorem 11 *The wavelet transform is a bijection from* $\mathcal{B}_{S'}(T^d)$ *onto* $\mathcal{S}'_\delta(\mathbb{R}^d \times \mathbb{R}_+)$, *where* $\mathcal{S}'_\delta(\mathbb{R}^d \times \mathbb{R}_+)$ *is the collection of all distributions of the form* $\sum_j \sum_k \alpha_{j,k}\delta(x - k, y - j)$.

Proof The proof of this theorem is given in [29]. □

6 Conclusions

In recent years, the theory of generalized quotients and their integral transforms has become an active and important part of the theory of generalized integral transforms. The study of generalized quotients and its spaces has given substantial support to the study of applied functional analysis. Mikusiński and his associates described different classes of generalized quotients on transform, viz., Fourier, Laplace, Radon, and Zak. Kalpakam and later extended this theory of generalized quotients on Fourier transform, Hilbert transform and Weierstrass transform. In this chapter, a uniqueness theorem is proved for the wavelet transform for the quotient space of analytic functions. Further, the wavelet transform is studied on the space of generalized quotients on the torus. This generalized space contains the space of periodic hyperfunctions and space of distributions. We have successfully derived the corresponding wavelet inversion formula by involving wavelet coefficients on the torus. It may be concluded here that the employed wavelet transform method in this chapter is a very efficient technique and could lead to a promising approach to function spaces on other domains, like locally compact groups and manifolds. The wavelet theory has been applied widely in many fields, such as signal analysis and processing, image compression, pattern recognition, detecting the mutation signal and so on.

Acknowledgements This work is supported by Major Research Project by SERB-DST, Government of India, through sanction No. ECR/2017/000394.

References

1. Bochner S (1932) Vorlesungen über Fourierische. Integrale Akademie-Verlag, Berlin
2. Boehme TK (1973) The support of Mikusiński operators. Trans Am Math Soc 176:319–334
3. Chui CK (1992) An introduction to wavelets. San Diego Academic press
4. Loonker D, Banerji PK, Debnath L (2004) Wavelet transforms for integrable Boehmians. J Math Anal Appl 296:473–478
5. Loonker D, Banerji PK, Debnath L (2010) On the Hankel transform for Boehmians. Integr Transforms Special Funct 21(7):479–486
6. Mikusiński J (1981) Quotients de suites et leurs applications dans l'analyse fonctionelle. CR Acad Sci Paris 293:463–464
7. Mikusiński P (1995) Tempered Boehmians and ultradistributions. Proc Am Math Soc 123(3):813–817
8. Mikusiński P (1983) Convergence of Boehmains. Jpn J Math 9(1):159–179

9. Mikusiński P (1994) The Fourier transform of tempered Boehmians. In: Fourier analysis. Lecture notes in pure and applied mathematics (Marcel Dekker), pp 303–309
10. Nemzer D (2006) Boehmians on the torus. Bull Korean Math Soc 43(4):831–839
11. Nemzer D (2010) S-asymptotic properties of Boehmians. Integr Transforms Spec Funct 21(7):503–513
12. Pathak RS (2004) The Wavelet transform of distributions. Tohoku Math J 56:411421
13. Pathak RS, Singh A (2016) Distributional wavelet transform. Proc Natl Acad Sci India Sect A: Phys Sci 86(2):273–277
14. Pathak RS, Abhishek Singh (2016) Wavelet transform of generalized functions in $K'\{M_p\}$ spaces. Proc Math Sci 126(2):213–226
15. Pathak RS, Abhishek Singh (2017) Wavelet transform of Beurling-Bjrck type ultradistributions. Rendiconti del Seminario Matematico della Universita di Padova 137(1):211–222
16. Pathak RS, Abhishek Singh (2019) Paley-Wiener-Schwartz type theorem for the wavelet transform. Appl Anal 98(7):1324–1332
17. Pathak RS (2017) Integral transforms of generalized functions and their applications. Routledge
18. Pathak RS (2009) The wavelet transform, vol 4. Springer Science & Business Media
19. Pathak RS, Abhishek Singh (2016) Mexican hat wavelet transform of distributions. Integral Transforms Special Funct 27(6):468–483
20. Rawat A, Abhishek Singh (2021) Mexican hat wavelet transform of generalized functions in $\mathcal{G}'$ spaces. Proc Math Sci 131(2):1–13
21. Roopkumar R (2009) Convolution theorems for wavelet transform on tempered distributions and their extension to tempered Boehmians. Asian-Eur J Math 2(01):117–127
22. Roopkumar R (2003) Wavelet analysis on a boehmian space. Int J Math Math Sci 2003(15):917926
23. Schwartz L (1957, 1959) Théorie des distributions, vol 2, Hermann,Paris (1950, 1951), vol I and II are republished by Actualitées Scientifiques et Industrilles, Herman & Cie, Paris
24. Abhishek S, Banerji PK, Kalla SL (2012) A uniqueness theorem for Mellin transform for quotient space. Sci Ser A Math Sci (N. S.) 23:25–30
25. Abhishek Singh, Banerji PK (2018) Fractional integrals of fractional Fourier transform for integrable Boehmians. Proc Natl Acad Sci India Sect A: Phys Sci 88(1):49–53
26. Abhishek Singh, Raghuthaman N, Rawat A, Singh J (2020) Representation theorems for the Mexican hat wavelet transform. Math Methods Appl Sci 43(7):3914–3924
27. Abhishek Singh, Raghuthaman N, Rawat A (2021) Paley-Wiener-Schwartz type theorem for ultra distributional wavelet transform. Complex Anal Oper Theory 15(4):1–11
28. Abhishek S, Rawat A, Singh S, Banerji PK (2021) On the wavelet transform of Boehmians. Proc Natl Acad Sci India Sect A Phys Sci. https://doi.org/10.1007/s40010-021-00733-0
29. Abhishek S, Rawat A (2022) Generalized quotient space on the torus associated with wavelet transform. Preprint
30. Srivastava HM, Abhishek Singh, Rawat A, Singh S (2021) A family of Mexican hat wavelet transforms associated with an isometry in the heat equation. Math Methods Appl Sci 44(14):11340–11349

Certain Image Formulae of the Incomplete I-Function Under the Conformable and Pathway Fractional Integral and Derivative Operators

Manish Kumar Bansal, Devendra Kumar, and Junesang Choi

Abstract In this paper, we establish several interesting image formulae of the incomplete I-function under the conformable and pathway fractional integral and derivative operators. Since both the incomplete I-function and the conformable fractional integral and derivative operators are very general among special functions as well as fractional integral and derivative operators, the main results presented here can give a number of specific identities, some of which are explicitly demonstrated in the corollaries.

Keywords Incomplete I-functions · Mellin-Barnes-type contour · Fractional integral operator · Fractional differential operator · Pathway fractional integral

2010 Mathematics Subject Classification: Primary 26A33 · 30E20 Secondary 33E20 · 33C60

1 Introduction and Preliminaries

Numerous scholars have studied and developed various special functions over the years, including incomplete ℵ-functions [1], incomplete I-functions [2], incomplete H-functions [3], Fox's H-function [4–6], Mittag-Leffler function and its extended variants [7–12], and others. Numerous researchers have investigated the aforemen-

M. K. Bansal (✉)
Department of Mathematics, Jaypee Institute of Information Technology, Noida 201309, Uttar Pradesh, India
e-mail: bansalmanish443@gmail.com; manish.bansal@mail.jiit.ac.in

D. Kumar
Department of Mathematics, University of Rajasthan, Jaipur 302004, Rajasthan, India
e-mail: devendra.maths@gmail.com

J. Choi
Department of Mathematics, Dongguk University, Gyeongju 38066, Republic of Korea
e-mail: junesang@dongguk.ac.kr

J. Singh et al. (eds.), *Advances in Mathematical Modelling, Applied Analysis and Computation*, Lecture Notes in Networks and Systems 415,
https://doi.org/10.1007/978-981-19-0179-9_7

tioned functions and given a number of their properties (see, for example, [13–16]), and they have been extensively used in the areas of engineering and applied sciences (see, for example, [17–23]). Bansal and Kumar [2] recently introduced the ${}^{(\Gamma)}I^{\mathsf{m},\mathsf{n}}_{\mathsf{p}_\ell,\mathsf{q}_\ell;\mathsf{s}}(w)$ and ${}^{(\gamma)}I^{\mathsf{m},\mathsf{n}}_{\mathsf{p}_\ell,\mathsf{q}_\ell;\mathsf{s}}(w)$ families of incomplete I-functions. Incomplete I-functions are an extension of Saxena's I-functions [24]. Several special functions may be produced by specializing the parameters of the incomplete I-functions (for example, incomplete H-function, H-function, Mittag-Leffler function, etc.).
The following Mellin-Barnes-type contour integral is used to define the incomplete I-function:

$$
\begin{aligned}
{}^{(\Gamma)}I^{\mathsf{m},\mathsf{n}}_{\mathsf{p}_\ell,\mathsf{q}_\ell;\mathsf{s}}(w) &= {}^{(\Gamma)}I^{\mathsf{m},\mathsf{n}}_{\mathsf{p}_\ell,\mathsf{q}_\ell;\mathsf{s}}\left[w \,\middle|\, \begin{matrix}(a_1,\alpha_1,\mathfrak{u}),(a_i,\alpha_i)_{2,\mathsf{n}},(a_{i\ell},\alpha_{i\ell})_{\mathsf{n}+1,\mathsf{p}_\ell}\\ (b_j,\beta_j)_{1,\mathsf{m}},(b_{j\ell},\beta_{j\ell})_{\mathsf{m}+1,\mathsf{q}_\ell}\end{matrix}\right] \\
&= \frac{1}{2\pi\iota}\int_{\mathfrak{L}} \chi(\xi,\mathfrak{u})w^{-\xi}\,d\xi,
\end{aligned}
\tag{1}
$$

where

$$
\chi(\xi,\mathfrak{u}) = \frac{\Gamma(1-a_1-\alpha_1\xi,\mathfrak{u})\prod_{i=2}^{\mathsf{n}}\Gamma(1-a_i-\alpha_i\xi)\prod_{j=1}^{\mathsf{m}}\Gamma(b_j+\beta_j\xi)}{\sum_{\ell=1}^{\mathfrak{s}}\left[\prod_{i=\mathsf{n}+1}^{\mathsf{p}_\ell}\Gamma(a_{i\ell}+\alpha_{i\ell}\xi)\prod_{j=\mathsf{m}+1}^{\mathsf{q}_\ell}\Gamma(1-b_{j\ell}-\beta_{j\ell}\xi)\right]}. \tag{2}
$$

Here, the following conditions are satisfied:

(i) $\iota=\sqrt{-1}$, $w\in\mathbb{C}\setminus\{0\}$, the multiple valued function $w^{-\xi}$ is taken as the principal branch.

(ii) $\mathfrak{u}$ is a non-negative real number, m, n, p_ℓ, q_ℓ are non-negative integers such that

$$
0\le\mathsf{n}\le\mathsf{p}_\ell,\quad 0\le\mathsf{m}\le\mathsf{q}_\ell\quad\left(\ell\in\overline{1,\mathfrak{s}}:=\{k\in\mathbb{N}:\,1\le k\le\mathfrak{s}\}\right).
$$

(iii) $\alpha_i,\beta_j,\alpha_{i\ell},\beta_{j\ell}$ are positive real numbers, and $a_i,b_j,a_{i\ell},b_{j\ell}\in\mathbb{C}$.

(iv) The contour $\mathfrak{L}$ of integration in the complex ξ-plane is an infinite vertical line which runs from $\gamma-\iota\infty$ to $\gamma+\iota\infty$, for some $\gamma\in\mathbb{R}$, (if necessary, it is indented) so that singularities of $\Gamma(1-a_i-\alpha_i\xi)\ \left(i\in\overline{1,\mathsf{n}}\right)$ lie entirely to the right of the contour and the singularities of $\Gamma(b_j+\beta_j\xi)\ \left(j\in\overline{1,\mathsf{m}}\right)$ lie entirely to the left of the contour.

(v) The integrand $\chi(\xi,\mathfrak{u})$ has simple poles. An empty product is interpreted to be unity.

(vi) Here and elsewhere, let $\mathbb{N}$, $\mathbb{Z}_0^-$, $\mathbb{R}$, $\mathbb{R}^+$, and $\mathbb{C}$ denote the sets of positive integers, non-positive integers, real numbers, positive real numbers, and complex numbers, respectively, and also let $\mathbb{N}_0:=\mathbb{N}\cup\{0\}$.

The following are the convergence criteria for the integral in (1) (see [2]): Let

$$\Omega_\ell := \sum_{i=1}^{\mathsf{n}} \alpha_i + \sum_{j=1}^{\mathsf{m}} \beta_j - \sum_{i=\mathsf{n}+1}^{\mathsf{p}_\ell} \alpha_{i\ell} - \sum_{j=\mathsf{m}+1}^{\mathsf{q}_\ell} \beta_{j\ell} \tag{3}$$

and

$$\mathcal{E}_\ell := \sum_{j=1}^{\mathsf{m}} b_j - \sum_{i=1}^{\mathsf{n}} a_i + \sum_{j=\mathsf{m}+1}^{\mathsf{q}_\ell} b_{j\ell} - \sum_{i=\mathsf{n}+1}^{\mathsf{p}_\ell} a_{i\ell} + \frac{1}{2}(\mathsf{p}_\ell - \mathsf{q}_\ell) \quad \left(\ell \in \overline{1, \mathfrak{s}}\right). \tag{4}$$

Then, under one of the following conditions, the integral in (1) converges:

$$\Omega_\ell > 0, \quad |\arg(w)| < \frac{\pi}{2}\Omega_\ell \quad \left(\ell \in \overline{1, \mathfrak{s}}\right) \tag{5}$$

and

$$\Omega_\ell \geq 0, \quad |\arg(w)| < \frac{\pi}{2}\Omega_\ell, \quad \Re(\mathcal{E}_\ell) + 1 < 0 \quad \left(\ell \in \overline{1, \mathfrak{s}}\right). \tag{6}$$

Numerous special functions can be obtained by specializing the parameters of the incomplete I-function. Several of them are listed below:

1. Setting $\mathfrak{u} = 0$ in (1) yields Saxena's I-function (see [25]):

$$I^{\mathsf{m},\mathsf{n}}_{\mathsf{p}_\ell,\mathsf{q}_\ell,\mathsf{s}}\left[w \,\middle|\, \begin{matrix}(a_i, \alpha_i)_{1,\mathsf{n}}, (a_{i\ell}, \alpha_{i\ell})_{\mathsf{n}+1,\mathsf{p}_\ell} \\ (b_j, \beta_j)_{1,\mathsf{m}}, (b_{j\ell}, \beta_{j\ell})_{\mathsf{m}+1,\mathsf{q}_\ell}\end{matrix}\right]. \tag{7}$$

2. Putting $\mathfrak{s} = 1$ in (1) gives the incomplete H-functions (see [3]; see also [26]):

$$\Gamma^{\mathsf{m},\mathsf{n}}_{\mathsf{p},\mathsf{q}}\left[w \,\middle|\, \begin{matrix}(a_1, \alpha_1, \mathfrak{u}), (a_i, \alpha_i)_{2,\mathsf{p}} \\ (b_j, \beta_j)_{1,\mathsf{q}}\end{matrix}\right]. \tag{8}$$

3. Taking $\mathfrak{u} = 0$ and $\mathfrak{s} = 1$ in (1) produces the familiar Fox's H-function (see, for example, [4, p. 10]):

$$\begin{aligned} {}^{(\Gamma)}I^{\mathsf{m},\mathsf{n}}_{\mathsf{p}_\ell,\mathsf{q}_\ell,1}\left[w \,\middle|\, \begin{matrix}(a_1, \alpha_1, 0), (a_i, \alpha_i)_{2,\mathsf{n}}, (a_{i\ell}, \alpha_{i\ell})_{\mathsf{n}+1,\mathsf{p}_\ell} \\ (b_j, \beta_j)_{1,\mathsf{m}}, (b_{j\ell}, \beta_{j\ell})_{\mathsf{m}+1,\mathsf{q}_\ell}\end{matrix}\right] \\ = H^{\mathsf{m},\mathsf{n}}_{\mathsf{p},\mathsf{q}}\left[w \,\middle|\, \begin{matrix}(a_1, \alpha_1), \cdots, (a_\mathsf{p}, \alpha_\mathsf{p}) \\ (b_1, \beta_1), \cdots, (b_\mathsf{q}, \beta_\mathsf{q})\end{matrix}\right]. \end{aligned} \tag{9}$$

4. Setting $\mathfrak{s} = 1$, $\mathsf{m} = 1$, $\mathsf{n} = \mathsf{p}$, q being replaced by $\mathsf{q} + 1$, and modifying some parameters in (1) offers the incomplete Fox-Wright Ψ-function ${}_\mathsf{p}\Psi^{(\Gamma)}_\mathsf{q}$ (see [3, Eq. (6.4)]):

$$ {}^{(\Gamma)}I^{1,\mathfrak{p}}_{\mathfrak{p},\mathfrak{q}+1}\left[-w\,\middle|\,\begin{matrix}(1-a_1,\alpha_1,\mathfrak{u}),(1-a_j,\alpha_j)_{2,\mathfrak{p}}\\(0,1),(1-b_j,\beta_j)_{1,\mathfrak{q}}\end{matrix}\right]={}_{\mathfrak{p}}\Psi^{(\Gamma)}_{\mathfrak{q}}\left[\begin{matrix}(a_1,\alpha_1,\mathfrak{u}),(a_j,\alpha_j)_{2,\mathfrak{p}};\\(b_j,\beta_j)_{1,\mathfrak{q}};\end{matrix}w\right]. \tag{10} $$

Numerous researchers have been engaged in research on fractional calculus and its applications. They introduced and investigated many different types of fractional derivatives and integrals. Also, they explored many features and applications of fractional calculus. The most widely used schemes, Riemann-Liouville and Caputo derivatives, are utilized in engineering, mathematical physics, image processing, biology, applied sciences, medical and health sciences, control systems, and bio-engineering, among others [27–36].

The Riemann-Liouville left and right fractional integral operators designated ${}_{\mathfrak{a}}J^{\kappa}$ and $J^{\kappa}_{\mathfrak{b}}$ and the corresponding Riemann-Liouville fractional derivative operators ${}_{\mathfrak{a}}D^{\kappa}$ and $D^{\kappa}_{\mathfrak{b}}$ of arbitrary order are defined as follows: (see [37–39]):

$$ {}_{\mathfrak{a}}J^{\kappa}f(\mathsf{w})=\frac{1}{\Gamma(\kappa)}\int_{\mathfrak{a}}^{\mathsf{w}}(\mathsf{w}-\rho)^{\kappa-1}f(\rho)d\rho\quad(\Re(\kappa)>0,\ \mathsf{w}>\mathfrak{a}); \tag{11} $$

$$ J^{\kappa}_{\mathfrak{b}}f(\mathsf{w})=\frac{1}{\Gamma(\kappa)}\int_{\mathsf{w}}^{\mathfrak{b}}(\rho-\mathsf{w})^{\kappa-1}f(\rho)d\rho\quad(\Re(\kappa)>0,\ \mathfrak{b}>\mathfrak{a}); \tag{12} $$

$$ {}_{\mathfrak{a}}D^{\kappa}f(\mathsf{w})=D^{n}{}_{\mathfrak{a}}J^{n-\kappa}f(\mathsf{w})=\frac{1}{\Gamma(n-\kappa)}\left(\frac{d}{dt}\right)^{n}\int_{\mathfrak{a}}^{\mathsf{w}}(\mathsf{w}-\rho)^{n-\kappa-1}f(\rho)d\rho \quad (\Re(\kappa)\geq 0,\ n=[\Re(\kappa)]+1); \tag{13} $$

$$ D^{\kappa}_{\mathfrak{b}}f(\mathsf{w})=(-D)^{n}J^{n-\kappa}_{\mathfrak{b}}f(\mathsf{w})=\frac{1}{\Gamma(n-\kappa)}\left(-\frac{d}{dt}\right)^{n}\int_{\mathsf{w}}^{\mathfrak{b}}(\rho-\mathsf{w})^{n-\kappa-1}f(\rho)d\rho \quad (\Re(\kappa)\geq 0,\ n=[\Re(\kappa)]+1). \tag{14} $$

The left-sided and right-sided Caputo fractional derivative operators of order κ are defined, respectively, by (see [37–39]):

$$ {}^{C}_{\mathfrak{a}}D^{\kappa}f(\mathsf{w})={}_{\mathfrak{a}}J^{n-\kappa}_{\mathsf{w}}f^{(n)}(\mathsf{w})=\frac{1}{\Gamma(n-\kappa)}\int_{\mathfrak{a}}^{\mathsf{w}}(\mathsf{w}-\rho)^{n-\kappa-1}f^{n}(\rho)d\rho \quad (\Re(\kappa)\geq 0,\ n=[\Re(\kappa)]+1) \tag{15} $$

and

$$ {}^{C}D^{\kappa}_{\mathfrak{b}}f(\mathsf{w})=J^{n-\kappa}_{\mathfrak{b}}(-1)^{n}f^{(n)}(\mathsf{w})=\frac{(-1)^{n}}{\Gamma(n-\kappa)}\int_{\mathsf{w}}^{\mathfrak{b}}(\rho-\mathsf{w})^{n-\kappa-1}f^{n}(\rho)d\rho \quad (\Re(\kappa)\geq 0,\ n=[\Re(\kappa)]+1). \tag{16} $$

The left-sided and right-sided Hadamard fractional integral operators designated ${}_{\mathfrak{a}}\mathfrak{J}^{\kappa}$ and $\mathfrak{J}^{\kappa}_{\mathfrak{b}}$ and the corresponding Hadamard fractional derivative operators ${}_{\mathfrak{a}}\mathfrak{D}^{\kappa}$ and $\mathfrak{D}^{\kappa}_{\mathfrak{b}}$ are defined as follows (see [40]):

$$ {}_{\mathfrak{a}}\mathfrak{J}^{\kappa} f(\mathsf{w}) = \frac{1}{\Gamma(\kappa)} \int_{\mathfrak{a}}^{\mathsf{w}} (\ln \mathsf{w} - \ln \rho)^{\kappa-1} f(\rho) \frac{d\rho}{\rho} \qquad (\Re(\kappa) > 0, \mathsf{w} > \mathfrak{a}); \quad (17) $$

$$ \mathfrak{J}_{\mathfrak{b}}^{\kappa} f(\mathsf{w}) = \frac{1}{\Gamma(\kappa)} \int_{\mathsf{w}}^{\mathfrak{b}} (\ln \rho - \ln \mathsf{w})^{\kappa-1} f(\rho) \frac{d\rho}{\rho} \qquad (\Re(\kappa) > 0, \mathfrak{b} > \mathfrak{a}); \quad (18) $$

$$ {}_{\mathfrak{a}}\mathfrak{D}^{\kappa} f(\mathsf{w}) = \left(\mathsf{w}\frac{d}{d\mathsf{w}}\right)^{n} {}_{\mathfrak{a}}\mathfrak{J}^{n-\kappa} f(\mathsf{w}) \qquad (\Re(\kappa) > 0, n = [\kappa] + 1); \quad (19) $$

$$ \mathfrak{D}_{\mathfrak{b}}^{\kappa} f(\mathsf{w}) = \left(-\mathsf{w}\frac{d}{d\mathsf{w}}\right)^{n} \mathfrak{J}_{\mathfrak{b}}^{n-\kappa} f(\mathsf{w}) \qquad (\Re(\kappa) > 0, n = [\kappa] + 1, \mathfrak{b} > \mathfrak{a}). \quad (20) $$

The left-sided and right-sided Katugampola fractional integral operators designated ${}_{\mathfrak{a}}\mathcal{I}^{\sigma,\kappa}$ and $\mathcal{I}_{\mathfrak{b}}^{\sigma,\kappa}$ and the corresponding Katugampola fractional derivative operators ${}_{\mathfrak{a}}\mathscr{D}^{\sigma,\kappa}$ and $\mathscr{D}_{\mathfrak{b}}^{\sigma,\kappa}$ are defined as follows (see [41, 42]):

$$ \left({}_{\mathfrak{a}}\mathcal{I}^{\sigma,\kappa} f\right)(\mathsf{w}) = \frac{1}{\Gamma(\sigma)} \int_{\mathfrak{a}}^{\mathsf{w}} \left(\frac{\mathsf{w}^{\kappa} - \rho^{\kappa}}{\kappa}\right)^{\sigma-1} f(\rho) \frac{d\rho}{\rho^{1-\kappa}} \qquad (\Re(\sigma) > 0); \quad (21) $$

$$ \left(\mathcal{I}_{\mathfrak{b}}^{\sigma,\kappa} f\right)(\mathsf{w}) = \frac{1}{\Gamma(\sigma)} \int_{\mathsf{w}}^{\mathfrak{b}} \left(\frac{\rho^{\kappa} - \mathsf{w}^{\kappa}}{\kappa}\right)^{\sigma-1} f(\rho) \frac{d\rho}{\rho^{1-\kappa}} \qquad (\Re(\sigma) > 0); \quad (22) $$

$$ \begin{aligned} \left({}_{\mathfrak{a}}\mathscr{D}^{\sigma,\kappa} f\right)(\mathsf{w}) &= \left(\mathsf{w}^{1-\kappa}\frac{d}{d\mathsf{w}}\right)^{n} \left({}_{\mathfrak{a}}\mathcal{I}^{n-\sigma,\kappa} f\right)(\mathsf{w}) \\ &= \frac{1}{\Gamma(n-\sigma)} \left(\mathsf{w}^{1-\kappa}\frac{d}{d\mathsf{w}}\right)^{n} \int_{\mathfrak{a}}^{\mathsf{w}} \left(\frac{\mathsf{w}^{\kappa} - \rho^{\kappa}}{\kappa}\right)^{n-\sigma-1} f(\rho) \frac{d\rho}{\rho^{1-\kappa}}; \end{aligned} \quad (23) $$

$$ \begin{aligned} \left(\mathscr{D}_{\mathfrak{b}}^{\sigma,\kappa} f\right)(\mathsf{w}) &= \left(-\mathsf{w}^{1-\kappa}\frac{d}{d\mathsf{w}}\right)^{n} \left({}_{\mathfrak{a}}\mathcal{I}^{n-\sigma,\kappa} f\right)(\mathsf{w}) \\ &= \frac{1}{\Gamma(n-\sigma)} \left(-\mathsf{w}^{1-\kappa}\frac{d}{d\mathsf{w}}\right)^{n} \int_{\mathsf{w}}^{\mathfrak{b}} \left(\frac{\rho^{\kappa} - \mathsf{w}^{\kappa}}{\kappa}\right)^{n-\sigma-1} f(\rho) \frac{d\rho}{\rho^{1-\kappa}}. \end{aligned} \quad (24) $$

The left-sided and right-sided fractional conformable integral operators ${}^{\sigma}_{\mathfrak{a}}\mathfrak{J}^{\kappa}$ and ${}^{\sigma}\mathfrak{J}_{\mathfrak{b}}^{\kappa}$ and the corresponding fractional conformable derivative operators ${}^{\sigma}_{\mathfrak{a}}\mathcal{D}^{\kappa}$ and ${}^{\sigma}\mathcal{D}_{\mathfrak{b}}^{\kappa}$ are defined as follows (see [43]):

$$ {}^{\sigma}_{\mathfrak{a}}\mathfrak{J}^{\kappa} f(\mathsf{w}) = \frac{1}{\Gamma(\sigma)} \int_{\mathfrak{a}}^{\mathsf{w}} \left(\frac{(\mathsf{w}-\mathfrak{a})^{\kappa} - (\rho-\mathfrak{a})^{\kappa}}{\kappa}\right)^{\sigma-1} f(\rho) \frac{d\rho}{(\rho-\mathfrak{a})^{1-\kappa}} \qquad (\Re(\sigma) > 0); \quad (25) $$

$$ {}^{\sigma}\mathfrak{J}_{\mathfrak{b}}^{\kappa} f(\mathsf{w}) = \frac{1}{\Gamma(\sigma)} \int_{\mathsf{w}}^{\mathfrak{b}} \left(\frac{(\mathfrak{b}-\mathsf{w})^{\kappa} - (\mathfrak{b}-\rho)^{\kappa}}{\kappa}\right)^{\sigma-1} f(\rho) \frac{d\rho}{(\mathfrak{b}-\rho)^{1-\kappa}} \qquad (\Re(\sigma) > 0); \quad (26) $$

$$
\begin{aligned}
{}^{\sigma}_{\mathfrak{a}}\mathcal{D}^{\kappa} f(\mathsf{w}) &= {}^{n}_{\mathfrak{a}}T^{\kappa}\left({}^{n-\sigma}_{\mathfrak{a}}\mathfrak{I}^{\kappa}\right) f(\mathsf{w}) \\
&= \frac{{}^{n}_{\mathfrak{a}}T^{\kappa}}{\Gamma(n-\sigma)} \int_{\mathfrak{a}}^{\mathsf{w}} \left(\frac{(\mathsf{w}-\mathfrak{a})^{\kappa} - (\rho-\mathfrak{a})^{\kappa}}{\kappa}\right)^{n-\sigma-1} f(\rho) \frac{d\rho}{(\rho-\mathfrak{a})^{1-\kappa}} \qquad (\Re(\sigma) \geq 0);
\end{aligned} \tag{27}
$$

$$
\begin{aligned}
{}^{\sigma}\mathcal{D}^{\kappa}_{\mathfrak{b}} f(\mathsf{w}) &= {}^{n}T^{\kappa}_{\mathfrak{b}}\left({}^{n-\sigma}\mathfrak{I}^{\kappa}_{\mathfrak{b}}\right) f(\mathsf{w}) \\
&= \frac{(-1)^{n}\,{}^{n}T^{\kappa}_{\mathfrak{b}}}{\Gamma(n-\sigma)} \int_{\mathsf{w}}^{\mathfrak{b}} \left(\frac{(\mathfrak{b}-\mathsf{w})^{\kappa} - (\mathfrak{b}-\rho)^{\kappa}}{\kappa}\right)^{n-\sigma-1} f(\rho) \frac{d\rho}{(\mathfrak{b}-\rho)^{1-\kappa}} \qquad (\Re(\sigma) \geq 0).
\end{aligned} \tag{28}
$$

Here

$$
n = [\Re(\sigma)] + 1, \qquad {}^{n}_{\mathfrak{a}}T^{\kappa} = \underbrace{{}_{\mathfrak{a}}T^{\kappa}\,{}_{\mathfrak{a}}T^{\kappa} \cdots {}_{\mathfrak{a}}T^{\kappa}}_{n-\text{times}}, \qquad {}^{n}T^{\kappa}_{\mathfrak{b}} = \underbrace{T^{\kappa}_{\mathfrak{b}} T^{\kappa}_{\mathfrak{b}} \cdots T^{\kappa}_{\mathfrak{b}}}_{n-\text{times}}, \tag{29}
$$

and

$$
{}_{\mathfrak{a}}T^{\kappa} f(\mathsf{w}) = (\mathsf{w}-\mathfrak{a})^{1-\kappa} f'(\mathsf{w}), \qquad T^{\kappa}_{\mathfrak{b}} f(\mathsf{w}) = (\mathfrak{b}-\mathsf{w})^{1-\kappa} f'(\mathsf{w}). \tag{30}
$$

Remark 1 The fractional conformable integral and derivative operators may be reduced to yield the aforementioned fractional integral and derivative operators as follows:

(i) Taking $\mathfrak{a} = 0, \kappa = 1$ in (25) yields the left-sided Riemann-Liouville fractional integral operator (11);
Setting $\mathfrak{a} = 0, \kappa \to 0$ in (25) gives the left-sided Hadamard fractional integral operator (17);
Putting $\mathfrak{a} = 0$ in (25) produces the left-sided Katugampola fractional integral operator (21).

(ii) Setting $\mathfrak{b} = 0, \kappa = 1$ in (26) yields the right-sided Riemann-Liouville fractional integral operator (12);
Taking $\mathfrak{b} = 0, \kappa \to 0$ in (26) gives the right-sided Hadamard fractional integral operator (18);
Putting $\mathfrak{b} = 0$ in (26) offers the right-sided Katugampola fractional integral operator (22).

(iii) Taking $\mathfrak{a} = 0, \kappa = 1$ in (27) yields the left-sided Riemann-Liouville fractional derivative operator (13);
Setting $\mathfrak{a} = 0, \kappa \to 0$ in (27) gives the left-sided Hadamard fractional integral operator (19);
Putting $\mathfrak{a} = 0$ in (27) produces the left-sided Katugampola fractional integral operator (23).

(iv) Setting $\mathfrak{b} = 0, \kappa = 1$ in (28) yields the right-sided Riemann-Liouville fractional integral operator (14);

Putting $\mathfrak{b} = 0, \kappa \to 0$ in (28) gives the right-sided Hadamard fractional integral operator (20);
Taking $\mathfrak{b} = 0$ in (28) produces the right-sided Katugampola fractional integral operator (24).

In this paper, we aim to establish several intriguing image formulae related with the incomplete I-function under the fractional conformable integral operators. For our purpose, we begin by presenting some image formulae of power functions under the conformable fractional operators, asserted in the following theorem.

Theorem 1.1 *Let* $\Re(\lambda) > 0$, $\Re(\kappa) > 0$, $\Re(\sigma) > 0$, *and* $\mathfrak{a} \in \mathbb{R}$. *Then*

$$ {}^{\sigma}_{\mathfrak{a}}\mathcal{I}^{\kappa}(\mathsf{w}-\mathfrak{a})^{\lambda} = \frac{1}{\kappa^{\sigma}} \frac{\Gamma\left(\frac{\lambda}{\kappa}+1\right)}{\Gamma\left(\frac{\lambda}{\kappa}+\sigma+1\right)} (\mathsf{w}-\mathfrak{a})^{\kappa\sigma+\lambda}; \tag{31} $$

$$ {}^{\sigma}\mathcal{I}^{\kappa}_{\mathfrak{b}}(\mathfrak{b}-\mathsf{w})^{\lambda} = \frac{1}{\kappa^{\sigma}} \frac{\Gamma\left(\frac{\lambda}{\kappa}+1\right)}{\Gamma\left(\frac{\lambda}{\kappa}+\sigma+1\right)} (\mathfrak{b}-\mathsf{w})^{\kappa\sigma+\lambda}; \tag{32} $$

$$ {}^{\sigma}_{\mathfrak{a}}\mathcal{D}^{\kappa}(\mathsf{w}-\mathfrak{a})^{\lambda} = \kappa^{\sigma} \frac{\Gamma\left(\frac{\lambda}{\kappa}+1\right)}{\Gamma\left(\frac{\lambda}{\kappa}-\sigma+1\right)} (\mathsf{w}-\mathfrak{a})^{\lambda-\kappa\sigma}; \tag{33} $$

$$ {}^{\sigma}\mathcal{D}^{\kappa}_{\mathfrak{b}}(\mathfrak{b}-\mathsf{w})^{\lambda} = \kappa^{\sigma} \frac{\Gamma\left(\frac{\lambda}{\kappa}+1\right)}{\Gamma\left(\frac{\lambda}{\kappa}-\sigma+1\right)} (\mathfrak{b}-\mathsf{w})^{\lambda-\kappa\sigma}. \tag{34} $$

Proof We find

$$ {}^{\sigma}_{\mathfrak{a}}\mathcal{I}^{\kappa}(\mathsf{w}-\mathfrak{a})^{\lambda} = \frac{1}{\Gamma(\sigma)} \int_{\mathfrak{a}}^{\mathsf{w}} \left(\frac{(\mathsf{w}-\mathfrak{a})^{\kappa} - (\rho-\mathfrak{a})^{\kappa}}{\kappa} \right)^{\sigma-1} (\rho-\mathfrak{a})^{\lambda} \frac{d\rho}{(\rho-\mathfrak{a})^{1-\kappa}}, $$

which, upon setting $\mathsf{u} = \left(\frac{\rho-\mathfrak{a}}{\mathsf{w}-\mathfrak{a}}\right)^{\kappa}$, yields

$$ {}^{\sigma}_{\mathfrak{a}}\mathcal{I}^{\kappa}(\mathsf{w}-\mathfrak{a})^{\lambda} = \frac{(\mathsf{w}-\mathfrak{a})^{\kappa\sigma+\lambda}}{\kappa^{\sigma}\Gamma(\sigma)} \int_{0}^{1} (1-\mathsf{u})^{\sigma-1} \mathsf{u}^{\frac{\lambda}{\kappa}} d\mathsf{u}. $$

Now, applying the well-known beta function (see, e.g., [44, p. 8])

$$ B(\alpha,\ \beta) = \begin{cases} \int_0^1 u^{\alpha-1}(1-u)^{\beta-1}\, du & (\Re(\alpha) > 0,\ \Re(\beta) > 0) \\ \frac{\Gamma(\alpha)\,\Gamma(\beta)}{\Gamma(\alpha+\beta)} & \left(\alpha,\ \beta \in \mathbb{C} \setminus \mathbb{Z}_0^-\right) \end{cases} \tag{35} $$

to the last integral, we obtain the desired identity (31).

Similarly, the other ones can be proved. We omit the details. □

Let $\phi \in \mathsf{L}(\mathsf{c}, \mathsf{d})$, which denotes the set of Lebesgue measurable functions defined on the interval (c, d). Then the pathway fractional integral operator $\mathcal{P}_{0^+}^{(\eta,\alpha,\mathfrak{a})}\phi$ with

a pathway parameter $\alpha < 1$ is defined as follows (see [45, p. 239]; see also [26, Eq. (24)]):

$$\left(\mathcal{P}_{0+}^{(\eta,\alpha,\mathfrak{a})}\phi\right)(t) := t^{\eta}\int_0^{\frac{t}{\mathfrak{a}(1-\alpha)}}\left[1-\frac{\mathfrak{a}(1-\alpha)w}{t}\right]^{\frac{\eta}{1-\alpha}}\phi(w)\,dw \tag{36}$$

$$\left(\Re(\eta)>0,\ \ \mathfrak{a}\in\mathbb{R}^{+},\ \ \phi\in L(0,\infty)\right).$$

It is easy to find the following relationship between the pathway fractional integral operator and the left-sided Katugampola fractional integral operator:

$$\left(\mathcal{P}_{0+}^{(\eta-1,0,1)}\phi\right)(w) = \int_0^{w}\frac{\phi(u)}{(w-u)^{1-\eta}}du = \Gamma(\eta)\left({}_0\mathcal{I}^{\eta,1}\phi\right)(w). \tag{37}$$

We also recall a known formula (see [45, Eq. (12)])

$$\mathcal{P}_{0+}^{(\eta,\alpha,\mathfrak{a})}(t^{\beta-1}) = \frac{t^{\eta+\beta}}{[\mathfrak{a}(1-\alpha)]^{\beta}}\frac{\Gamma(\beta)\,\Gamma(1+\frac{\eta}{1-\alpha})}{\Gamma(1+\beta+\frac{\eta}{1-\alpha})} \tag{38}$$

$$\left(\mathfrak{a}\in\mathbb{R}^{+},\ \ \alpha<1,\ \ \Re(\eta)>0,\ \ \Re(\beta)>0,\ \ \Re\left(1+\frac{\eta}{1-\alpha}\right)>0\right).$$

2 Main Results

In this section, under the fractional conformable integral and derivative operators, we establish the image formulae of incomplete I-functions.

Theorem 2.1 *Let* $u \geq 0$, $\Re(\lambda)>0$, $\Re(\mu)>1$, $\Re(\kappa)>0$, $\Re(\sigma)>0$, *and* $\mathfrak{a}\in\mathbb{R}$. *Then*

$$\begin{aligned}
&{}_{\mathfrak{a}}^{\sigma}\mathfrak{I}^{\kappa}(w-\mathfrak{a})^{\mu-1}(\Gamma)\,I_{p_\ell,q_\ell;s}^{m,n}\left[(w-\mathfrak{a})^{\lambda}\right]\\
&={}_{\mathfrak{a}}^{\sigma}\mathfrak{I}^{\kappa}(w-\mathfrak{a})^{\mu-1}(\Gamma)\,I_{p_\ell,q_\ell;s}^{m,n}\left[(w-\mathfrak{a})^{\lambda}\,\middle|\,\begin{matrix}(a_1,\alpha_1,u),(a_i,\alpha_i)_{2,n},(a_{i\ell},\alpha_{i\ell})_{n+1,p_\ell}\\ (b_j,\beta_j)_{1,m},(b_{j\ell},\beta_{j\ell})_{m+1,q_\ell}\end{matrix}\right]\\
&=\frac{(w-\mathfrak{a})^{\kappa\sigma+\mu-1}}{\kappa^{\sigma}}(\Gamma)\,I_{p_\ell+1,q_\ell+1;s}^{m,n+1}\left[(w-\mathfrak{a})^{\lambda}\,\middle|\,\begin{matrix}(a_1,\alpha_1,u),\left(\frac{1}{\kappa}-\frac{\mu}{\kappa},\frac{\lambda}{\kappa}\right),(a_i,\alpha_i)_{2,n},(a_{i\ell},\alpha_{i\ell})_{n+1,p_\ell}\\ (b_j,\beta_j)_{1,m},(b_{j\ell},\beta_{j\ell})_{m+1,q_\ell},\left(\frac{1}{\kappa}-\frac{\mu}{\kappa}-\sigma,\frac{\lambda}{\kappa}\right)\end{matrix}\right].
\end{aligned} \tag{39}$$

Proof Let $\mathcal{L}$ be the left member of (39). Using (25) and (1), we get

$$\mathcal{L} = {}_{\mathfrak{a}}^{\sigma}\mathfrak{I}^{\kappa}\left\{(w-\mathfrak{a})^{\mu-1}\frac{1}{2\pi i}\int_{\mathfrak{L}}\chi(\xi,u)(w-\mathfrak{a})^{-\lambda\xi}d\xi\right\}, \tag{40}$$

where $\chi(\xi, u)$ is given as in (2). Then, interchanging the order of the integrals in (40), which can be verified under the given restrictions, we derive

$$\mathcal{L} = \frac{1}{2\pi\iota}\int_{\mathfrak{L}} \chi(\xi, u)\, {}_{a}^{\sigma}\mathcal{J}^{\kappa}\left\{(w-a)^{\mu-\lambda\xi-1}\right\} d\xi. \tag{41}$$

Using (31) to evaluate the left conformable fractional integral in (41), we obtain

$$\mathcal{L} = \frac{1}{2\pi\iota}\int_{\mathfrak{L}} \chi(\xi, u)\frac{1}{\kappa^{\sigma}}\frac{\Gamma\left(\frac{\mu-\lambda\xi-1}{\kappa}+1\right)}{\Gamma\left(\frac{\mu-\lambda\xi-1}{\kappa}+\sigma+1\right)}(w-a)^{\kappa\sigma+\mu-\lambda\xi-1}\, d\xi.$$

Finally, with the help of (2), we get the right-hand side of (39). □

Theorem 2.2 *Let* $u \geq 0$, $\Re(\lambda) > 0$, $\Re(\mu) > 1$, $\Re(\kappa) > 0$, $\Re(\sigma) > 0$, *and* $b \in \mathbb{R}$. *Then*

$$\begin{aligned}
&{}_{b}^{\sigma}\mathcal{J}^{\kappa}(b-w)^{\mu-1}(\Gamma) I^{m,n}_{p_\ell,q_\ell;s}\left[(b-w)^{\lambda}\right]\\
&= {}_{b}^{\sigma}\mathcal{J}^{\kappa}(b-w)^{\mu-1}(\Gamma) I^{m,n}_{p_\ell,q_\ell;s}\left[(b-w)^{\lambda}\left|\begin{matrix}(a_1,\alpha_1,u),(a_i,\alpha_i)_{2,n},(a_{i\ell},\alpha_{i\ell})_{n+1,p_\ell}\\ (b_j,\beta_j)_{1,m},(b_{j\ell},\beta_{j\ell})_{m+1,q_\ell}\end{matrix}\right.\right]\\
&= \frac{(b-w)^{\kappa\sigma+\mu-1}}{\kappa^{\sigma}}(\Gamma) I^{m,n+1}_{p_\ell+1,q_\ell+1;s}\left[(b-w)^{\lambda}\left|\begin{matrix}(a_1,\alpha_1,u),\left(\frac{1}{\kappa}-\frac{\mu}{\kappa},\frac{\lambda}{\kappa}\right),(a_i,\alpha_i)_{2,n},(a_{i\ell},\alpha_{i\ell})_{n+1,p_\ell}\\ (b_j,\beta_j)_{1,m},(b_{j\ell},\beta_{j\ell})_{m+1,q_\ell},\left(\frac{1}{\kappa}-\frac{\mu}{\kappa}-\sigma,\frac{\lambda}{\kappa}\right)\end{matrix}\right.\right].
\end{aligned} \tag{42}$$

Proof The proof would run parallel to that of Theorem 2.1. We omit the details. □

Theorem 2.3 *Let* $u \geq 0$, $\Re(\lambda) > 0$, $\Re(\mu) > 1$, $\Re(\kappa) > 0$, $\Re(\sigma) \geq 0$, *and* $a \in \mathbb{R}$. *Then*

$$\begin{aligned}
&{}_{a}^{\sigma}\mathcal{D}^{\kappa}(w-a)^{\mu-1}(\Gamma) I^{m,n}_{p_\ell,q_\ell;s}\left[(w-a)^{\lambda}\right]\\
&= {}_{a}^{\sigma}\mathcal{D}^{\kappa}(w-a)^{\mu-1}(\Gamma) I^{m,n}_{p_\ell,q_\ell;s}\left[(w-a)^{\lambda}\left|\begin{matrix}(a_1,\alpha_1,u),(a_i,\alpha_i)_{2,n},(a_{i\ell},\alpha_{i\ell})_{n+1,p_\ell}\\ (b_j,\beta_j)_{1,m},(b_{j\ell},\beta_{j\ell})_{m+1,q_\ell}\end{matrix}\right.\right]\\
&= \kappa^{\sigma}(w-a)^{\mu-\kappa\sigma-1}(\Gamma) I^{m,n+1}_{p_\ell+1,q_\ell+1;s}\left[(w-a)^{\lambda}\left|\begin{matrix}(a_1,\alpha_1,u),\left(\frac{1}{\kappa}-\frac{\mu}{\kappa},\frac{\lambda}{\kappa}\right),(a_i,\alpha_i)_{2,n},(a_{i\ell},\alpha_{i\ell})_{n+1,p_\ell}\\ (b_j,\beta_j)_{1,m},(b_{j\ell},\beta_{j\ell})_{m+1,q_\ell},\left(\frac{1}{\kappa}-\frac{\mu}{\kappa}+\sigma,\frac{\lambda}{\kappa}\right)\end{matrix}\right.\right].
\end{aligned} \tag{43}$$

Proof Let Δ be the left member of (43). Using (27) and (1), we obtain

$$\Delta = {}_{a}^{\sigma}\mathcal{D}^{\kappa}\left\{(w-a)^{\mu-1}\frac{1}{2\pi\iota}\int_{\mathfrak{L}}\chi(\xi,u)(w-a)^{-\lambda\xi}d\xi\right\},$$

where $\chi(\xi, u)$ is given as in (2). Then, interchanging the order of the integrals, which can be justified under the given constraints, we find

$$\Delta = \frac{1}{2\pi\iota}\int_{\mathfrak{L}} \chi(\xi,\mathfrak{u})\,{}^{\sigma}_{\mathfrak{a}}\mathcal{D}^{\kappa}\left\{(\mathsf{w}-\mathfrak{a})^{\mu-\lambda\xi-1}\right\} d\xi. \tag{44}$$

Using t (33) to evaluate the left conformable fractional derivative in (44) gives

$$\Delta = \frac{1}{2\pi\iota}\int_{\mathfrak{L}} \chi(\xi,\mathfrak{u})\kappa^{\sigma}\frac{\Gamma\left(\frac{\mu-\lambda\xi-1}{\kappa}+1\right)}{\Gamma\left(\frac{\mu-\lambda\xi-1}{\kappa}-\sigma+1\right)}(\mathsf{w}-\mathfrak{a})^{\mu-\lambda\xi-1-\kappa\sigma} d\xi. \tag{45}$$

Finally, upon employing (2) in (45), we get the last equality of (43). □

Theorem 2.4 *Let* $\mathfrak{u} \geq 0$, $\Re(\lambda) > 0$, $\Re(\mu) > 1$, $\Re(\kappa) > 0$, $\Re(\sigma) \geq 0$, *and* $\mathfrak{a} \in \mathbb{R}$. *Then*

$$\begin{aligned}
&{}^{\sigma}\mathcal{D}^{\kappa}_{\mathfrak{b}}(\mathfrak{b}-\mathsf{w})^{\mu-1}\,{}^{(\Gamma)}I^{\mathsf{m},\mathsf{n}}_{\mathsf{p}_\ell,\mathsf{q}_\ell;\mathfrak{s}}\left[(\mathfrak{b}-\mathsf{w})^{\lambda}\right]\\
&\quad = {}^{\sigma}\mathcal{D}^{\kappa}_{\mathfrak{b}}(\mathfrak{b}-\mathsf{w})^{\mu-1}\,{}^{(\Gamma)}I^{\mathsf{m},\mathsf{n}}_{\mathsf{p}_\ell,\mathsf{q}_\ell;\mathfrak{s}}\left[(\mathfrak{b}-\mathsf{w})^{\lambda}\left|\begin{matrix}(a_1,\alpha_1,\mathfrak{u}),(a_i,\alpha_i)_{2,\mathsf{n}},(a_{i\ell},\alpha_{i\ell})_{\mathsf{n}+1,\mathsf{p}_\ell}\\ (b_j,\beta_j)_{1,\mathsf{m}},(b_{j\ell},\beta_{j\ell})_{\mathsf{m}+1,\mathsf{q}_\ell}\end{matrix}\right.\right]\\
&\quad = \kappa^{\sigma}(\mathfrak{b}-\mathsf{w})^{\mu-\kappa\sigma-1}\,{}^{(\Gamma)}I^{\mathsf{m},\mathsf{n}+1}_{\mathsf{p}_\ell+1,\mathsf{q}_\ell+1;\mathfrak{s}}\left[(\mathfrak{b}-\mathsf{w})^{\lambda}\left|\begin{matrix}(a_1,\alpha_1,\mathfrak{u}),\left(\frac{1}{\kappa}-\frac{\mu}{\kappa},\frac{\lambda}{\kappa}\right),(a_i,\alpha_i)_{2,\mathsf{n}},(a_{i\ell},\alpha_{i\ell})_{\mathsf{n}+1,\mathsf{p}_\ell}\\ (b_j,\beta_j)_{1,\mathsf{m}},(b_{j\ell},\beta_{j\ell})_{\mathsf{m}+1,\mathsf{q}_\ell},\left(\frac{1}{\kappa}-\frac{\mu}{\kappa}+\sigma,\frac{\lambda}{\kappa}\right)\end{matrix}\right.\right].
\end{aligned} \tag{46}$$

Proof The proof would run parallel to that of Theorem 2.3. We omit the details. □

3 Pathway Fractional Integral Formula

Here, we establish a pathway fractional integral formula for the incomplete I-function.

Theorem 3.1 *Let* $\mathfrak{a} \in \mathbb{R}^{+}$, $\alpha < 1$, $\mu \in \mathbb{R}^{+}$, $\Re(\lambda) > 0$, $\Re\left(1+\frac{\eta}{1-\alpha}\right) > 0$, $\mathfrak{u} \geqq 0$, *and* $k \in \mathbb{R}$. *Also let* $a_i \in \mathbb{C}$, $\alpha_i \in \mathbb{R}^{+}$ $(i = 1,\ldots,\mathsf{p})$ *and* $b_j \in \mathbb{C}$, $\beta_j \in \mathbb{R}^{+}$ $(j = 1,\ldots,\mathsf{q})$ *be the same as in* (2). *Then*

$$\begin{aligned}
&\mathcal{P}^{(\eta,\alpha,\mathfrak{a})}_{0+}\left\{\mathsf{w}^{\lambda-1}\,{}^{(\Gamma)}I^{\mathsf{m},\mathsf{n}}_{\mathsf{p}_\ell,\mathsf{q}_\ell;\mathfrak{s}}(k\mathsf{w}^{\mu})\right\} = \frac{\mathsf{w}^{\eta+\lambda}\Gamma(\frac{\eta}{1-\alpha}+1)}{[\mathfrak{a}(1-\alpha)]^{\lambda}}\\
&\quad \times {}^{(\Gamma)}I^{\mathsf{m},\mathsf{n}+1}_{\mathsf{p}_\ell+1,\mathsf{q}_\ell+1;\mathfrak{s}}\left[\frac{k\mathsf{w}^{\mu}}{[\mathfrak{a}(1-\alpha)]^{\mu}}\left|\begin{matrix}(a_1,\alpha_1,\mathfrak{u}),(1-\lambda,\mu),(a_i,\alpha_i)_{2,\mathsf{n}},(a_{i\ell},\alpha_{i\ell})_{\mathsf{n}+1,\mathsf{p}_\ell}\\ (b_j,\beta_j)_{1,\mathsf{m}},(-\lambda-\frac{\eta}{1-\alpha},\mu),(b_{j\ell},\beta_{j\ell})_{\mathsf{m}+1,\mathsf{q}_\ell}\end{matrix}\right.\right].
\end{aligned} \tag{47}$$

Proof Let $\mathcal{L}_1$ be the left member of (47). Using (36) and (1), we obtain

$$\mathcal{L} = \mathcal{P}^{(\eta,\alpha,\mathfrak{a})}_{0+}\left\{\mathsf{w}^{\lambda-1}\frac{1}{2\pi\iota}\int_{\mathfrak{L}}\chi(\xi,\mathfrak{u})(k\mathsf{w}^{\mu})^{-\xi}d\xi\right\}, \tag{48}$$

where $\chi(\xi, u)$ is given as in (2). Then, in the double integral of the right member of (48), we interchange the order of the integrals, which can be verified under the given conditions, to find

$$\mathcal{L}_1 = \frac{1}{2\pi\iota}\int_{\mathfrak{L}} \chi(\xi, u)\, k^{-\xi}\mathcal{P}_{0+}^{(\eta,\alpha,\mathfrak{a})}\left\{w^{\lambda-\mu\xi-1}\right\} d\xi. \tag{49}$$

Using (38) to evaluate the pathway fractional integral in (49), we get

$$\mathcal{L}_1 = \frac{w^{\eta+\lambda}}{[\mathfrak{a}(1-\alpha)]^{\lambda}}\frac{1}{2\pi\iota}\int_{\mathfrak{L}} \chi(\xi, u)\, k^{-\xi}\left(\frac{w}{\mathfrak{a}(1-\alpha)}\right)^{-\mu\xi}\frac{\Gamma(\lambda-\mu\xi)\Gamma\left(1+\frac{\eta}{1-\alpha}\right)}{\Gamma\left(\lambda-\mu\xi+\frac{\eta}{1-\alpha}+1\right)} d\xi.$$

Finally, with the help of (1) and (2), interpreting the right member of the last identity, we get the desired result (47). □

4 Particular Cases

Since the main identities in Sects. 2 and 3 are very generalized ones, they may produce a large number of particular identities. Here we consider several of them as in the following corollaries.

Corollary 4.1 *Let* $\Re(\lambda) > 0$, $\Re(\mu) > 1$, $\Re(\kappa) > 0$, $\Re(\sigma) > 0$, *and* $\mathfrak{a}, \mathfrak{b} \in \mathbb{R}$. *Then*

$$\begin{aligned}
&{}_{\mathfrak{a}}^{\sigma}\mathfrak{I}^{\kappa}(w-\mathfrak{a})^{\mu-1} I^{m,n}_{p_\ell,q_\ell;s}\left[(w-\mathfrak{a})^{\lambda}\right] \\
&\quad = {}_{\mathfrak{a}}^{\sigma}\mathfrak{I}^{\kappa}(w-\mathfrak{a})^{\mu-1} I^{m,n}_{p_\ell,q_\ell;s}\left[(w-\mathfrak{a})^{\lambda}\left|\begin{matrix}(a_i,\alpha_i)_{1,n},(a_{i\ell},\alpha_{i\ell})_{n+1,p_\ell}\\ (b_j,\beta_j)_{1,m},(b_{j\ell},\beta_{j\ell})_{m+1,q_\ell}\end{matrix}\right.\right] \\
&\quad = \frac{(w-\mathfrak{a})^{\kappa\sigma+\mu-1}}{\kappa^{\sigma}} I^{m,n+1}_{p_\ell+1,q_\ell+1;s}\left[(w-\mathfrak{a})^{\lambda}\left|\begin{matrix}\left(\frac{1}{\kappa}-\frac{\mu}{\kappa},\frac{\lambda}{\kappa}\right),(a_i,\alpha_i)_{1,n},(a_{i\ell},\alpha_{i\ell})_{n+1,p_\ell}\\ (b_j,\beta_j)_{1,m},(b_{j\ell},\beta_{j\ell})_{m+1,q_\ell},\left(\frac{1}{\kappa}-\frac{\mu}{\kappa}-\sigma,\frac{\lambda}{\kappa}\right)\end{matrix}\right.\right]
\end{aligned} \tag{50}$$

and

$$\begin{aligned}
&{}^{\sigma}\mathfrak{I}_{\mathfrak{b}}^{\kappa}(\mathfrak{b}-w)^{\mu-1} I^{m,n}_{p_\ell,q_\ell;s}\left[(\mathfrak{b}-w)^{\lambda}\right] \\
&\quad = {}_{\mathfrak{a}}^{\sigma}\mathfrak{I}^{\kappa}(\mathfrak{b}-w)^{\mu-1} I^{m,n}_{p_\ell,q_\ell;s}\left[(\mathfrak{b}-w)^{\lambda}\left|\begin{matrix}(a_i,\alpha_i)_{1,n},(a_{i\ell},\alpha_{i\ell})_{n+1,p_\ell}\\ (b_j,\beta_j)_{1,m},(b_{j\ell},\beta_{j\ell})_{m+1,q_\ell}\end{matrix}\right.\right] \\
&\quad = \frac{(\mathfrak{b}-w)^{\kappa\sigma+\mu-1}}{\kappa^{\sigma}} I^{m,n+1}_{p_\ell+1,q_\ell+1;s}\left[(\mathfrak{b}-w)^{\lambda}\left|\begin{matrix}\left(\frac{1}{\kappa}-\frac{\mu}{\kappa},\frac{\lambda}{\kappa}\right),(a_i,\alpha_i)_{1,n},(a_{i\ell},\alpha_{i\ell})_{n+1,p_\ell}\\ (b_j,\beta_j)_{1,m},(b_{j\ell},\beta_{j\ell})_{m+1,q_\ell},\left(\frac{1}{\kappa}-\frac{\mu}{\kappa}-\sigma,\frac{\lambda}{\kappa}\right)\end{matrix}\right.\right].
\end{aligned} \tag{51}$$

Proof Taking $u = 0$ in the identities in Theorems 2.1 and 2.2 yields the results here. □

Corollary 4.2 *Let* $\Re(\lambda) > 0$, $\Re(\mu) > 1$, $\Re(\kappa) > 0$, $\Re(\sigma) \geq 0$, *and* $\mathfrak{a}, \mathfrak{b} \in \mathbb{R}$. *Then*

$$
\begin{aligned}
&{}_{\mathfrak{a}}^{\sigma}\mathcal{D}^{\kappa}(\mathsf{w}-\mathfrak{a})^{\mu-1}I^{\mathsf{m},\mathsf{n}}_{\mathsf{p}_\ell,\mathsf{q}_\ell;\mathsf{s}}\left[(\mathsf{w}-\mathfrak{a})^{\lambda}\right]\\
&\quad={}_{\mathfrak{a}}^{\sigma}\mathcal{D}^{\kappa}(\mathsf{w}-\mathfrak{a})^{\mu-1}I^{\mathsf{m},\mathsf{n}}_{\mathsf{p}_\ell,\mathsf{q}_\ell;\mathsf{s}}\left[(\mathsf{w}-\mathfrak{a})^{\lambda}\left|\begin{matrix}(a_i,\alpha_i)_{1,\mathsf{n}},(a_{i\ell},\alpha_{i\ell})_{\mathsf{n}+1,\mathsf{p}_\ell}\\(b_j,\beta_j)_{1,\mathsf{m}},(b_{j\ell},\beta_{j\ell})_{\mathsf{m}+1,\mathsf{q}_\ell}\end{matrix}\right.\right]\\
&\quad=\kappa^{\sigma}(\mathsf{w}-\mathfrak{a})^{\mu-\kappa\sigma-1}I^{\mathsf{m},\mathsf{n}+1}_{\mathsf{p}_\ell+1,\mathsf{q}_\ell+1;\mathsf{s}}\left[(\mathsf{w}-\mathfrak{a})^{\lambda}\left|\begin{matrix}\left(\frac{1}{\kappa}-\frac{\mu}{\kappa},\frac{\lambda}{\kappa}\right),(a_i,\alpha_i)_{1,\mathsf{n}},(a_{i\ell},\alpha_{i\ell})_{\mathsf{n}+1,\mathsf{p}_\ell}\\(b_j,\beta_j)_{1,\mathsf{m}},(b_{j\ell},\beta_{j\ell})_{\mathsf{m}+1,\mathsf{q}_\ell},\left(\frac{1}{\kappa}-\frac{\mu}{\kappa}+\sigma,\frac{\lambda}{\kappa}\right)\end{matrix}\right.\right]
\end{aligned}
\tag{52}
$$

and

$$
\begin{aligned}
&{}^{\sigma}\mathcal{D}_{\mathfrak{b}}^{\kappa}(\mathfrak{b}-\mathsf{w})^{\mu-1}I^{\mathsf{m},\mathsf{n}}_{\mathsf{p}_\ell,\mathsf{q}_\ell;\mathsf{s}}\left[(\mathfrak{b}-\mathsf{w})^{\lambda}\right]\\
&\quad={}^{\sigma}\mathcal{D}_{\mathfrak{b}}^{\kappa}(\mathfrak{b}-\mathsf{w})^{\mu-1}I^{\mathsf{m},\mathsf{n}}_{\mathsf{p}_\ell,\mathsf{q}_\ell;\mathsf{s}}\left[(\mathfrak{b}-\mathsf{w})^{\lambda}\left|\begin{matrix}(a_i,\alpha_i)_{1,\mathsf{n}},(a_{i\ell},\alpha_{i\ell})_{\mathsf{n}+1,\mathsf{p}_\ell}\\(b_j,\beta_j)_{1,\mathsf{m}},(b_{j\ell},\beta_{j\ell})_{\mathsf{m}+1,\mathsf{q}_\ell}\end{matrix}\right.\right]\\
&\quad=\kappa^{\sigma}(\mathfrak{b}-\mathsf{w})^{\mu-\kappa\sigma-1}I^{\mathsf{m},\mathsf{n}+1}_{\mathsf{p}_\ell+1,\mathsf{q}_\ell+1;\mathsf{s}}\left[(\mathfrak{b}-\mathsf{w})^{\lambda}\left|\begin{matrix}\left(\frac{1}{\kappa}-\frac{\mu}{\kappa},\frac{\lambda}{\kappa}\right),(a_i,\alpha_i)_{1,\mathsf{n}},(a_{i\ell},\alpha_{i\ell})_{\mathsf{n}+1,\mathsf{p}_\ell}\\(b_j,\beta_j)_{1,\mathsf{m}},(b_{j\ell},\beta_{j\ell})_{\mathsf{m}+1,\mathsf{q}_\ell},\left(\frac{1}{\kappa}-\frac{\mu}{\kappa}+\sigma,\frac{\lambda}{\kappa}\right)\end{matrix}\right.\right].
\end{aligned}
\tag{53}
$$

Proof Setting $\mathfrak{u}=0$ in the identities Theorems 2.3 and 2.4 produce the formulae here. □

Corollary 4.3 *Let* $\mathfrak{u}\geq 0$, $\Re(\lambda)>0$, $\Re(\mu)>1$, $\Re(\kappa)>0$, $\Re(\sigma)>0$, *and* $\mathfrak{a},\mathfrak{b}\in\mathbb{R}$. *Then*

$$
\begin{aligned}
&{}_{\mathfrak{a}}^{\sigma}\mathfrak{I}^{\kappa}(\mathsf{w}-\mathfrak{a})^{\mu-1}\Gamma^{\mathsf{m},\mathsf{n}}_{\mathsf{p},\mathsf{q}}\left[(\mathsf{w}-\mathfrak{a})^{\lambda}\right]\\
&\quad={}_{\mathfrak{a}}^{\sigma}\mathfrak{I}^{\kappa}(\mathsf{w}-\mathfrak{a})^{\mu-1}\Gamma^{\mathsf{m},\mathsf{n}}_{\mathsf{p},\mathsf{q}}\left[(\mathsf{w}-\mathfrak{a})^{\lambda}\left|\begin{matrix}(a_1,\alpha_1,\mathfrak{u}),(a_i,\alpha_i)_{2,\mathsf{p}}\\(b_j,\beta_j)_{1,\mathsf{q}}\end{matrix}\right.\right]\\
&\quad=\frac{(\mathsf{w}-\mathfrak{a})^{\kappa\sigma+\mu-1}}{\kappa^{\sigma}}\Gamma^{\mathsf{m},\mathsf{n}+1}_{\mathsf{p}+1,\mathsf{q}+1}\left[(\mathsf{w}-\mathfrak{a})^{\lambda}\left|\begin{matrix}(a_1,\alpha_1,\mathfrak{u}),\left(\frac{1}{\kappa}-\frac{\mu}{\kappa},\frac{\lambda}{\kappa}\right),(a_i,\alpha_i)_{2,\mathsf{p}}\\(b_j,\beta_j)_{1,\mathsf{q}},\left(\frac{1}{\kappa}-\frac{\mu}{\kappa}-\sigma,\frac{\lambda}{\kappa}\right)\end{matrix}\right.\right]
\end{aligned}
\tag{54}
$$

and

$$
\begin{aligned}
&{}^{\sigma}\mathfrak{I}_{\mathfrak{b}}^{\kappa}(\mathfrak{b}-\mathsf{w})^{\mu-1}\Gamma^{\mathsf{m},\mathsf{n}}_{\mathsf{p},\mathsf{q}}\left[(\mathfrak{b}-\mathsf{w})^{\lambda}\right]\\
&\quad={}^{\sigma}\mathfrak{I}_{\mathfrak{b}}^{\kappa}(\mathfrak{b}-\mathsf{w})^{\mu-1}\Gamma^{\mathsf{m},\mathsf{n}}_{\mathsf{p},\mathsf{q}}\left[(\mathfrak{b}-\mathsf{w})^{\lambda}\left|\begin{matrix}(a_1,\alpha_1,\mathfrak{u}),(a_i,\alpha_i)_{2,\mathsf{p}}\\(b_j,\beta_j)_{1,\mathsf{q}}\end{matrix}\right.\right]\\
&\quad=\frac{(\mathfrak{b}-\mathsf{w})^{\kappa\sigma+\mu-1}}{\kappa^{\sigma}}\Gamma^{\mathsf{m},\mathsf{n}+1}_{\mathsf{p}+1,\mathsf{q}+1}\left[(\mathfrak{b}-\mathsf{w})^{\lambda}\left|\begin{matrix}(a_1,\alpha_1,\mathfrak{u}),\left(\frac{1}{\kappa}-\frac{\mu}{\kappa},\frac{\lambda}{\kappa}\right),(a_i,\alpha_i)_{2,\mathsf{p}}\\(b_j,\beta_j)_{1,\mathsf{q}},\left(\frac{1}{\kappa}-\frac{\mu}{\kappa}-\sigma,\frac{\lambda}{\kappa}\right)\end{matrix}\right.\right].
\end{aligned}
\tag{55}
$$

Proof Using the identity (8), we can get the desired results directly from Theorems 2.1 and 2.2. □

Corollary 4.4 *Let* $\Re(\lambda)>0$, $\Re(\mu)>1$, $\Re(\kappa)>0$, $\Re(\sigma)\geq 0$, *and* $\mathfrak{a},\mathfrak{b}\in\mathbb{R}$. *Then*

$$
\begin{aligned}
&{}_{\mathfrak{a}}^{\sigma}\mathcal{D}^{\kappa}(\mathsf{w}-\mathfrak{a})^{\mu-1}\Gamma_{\mathsf{p},\mathsf{q}}^{\mathsf{m},\mathsf{n}}\left[(\mathsf{w}-\mathfrak{a})^{\lambda}\right]\\
&\quad={}_{\mathfrak{a}}^{\sigma}\mathcal{D}^{\kappa}(\mathsf{w}-\mathfrak{a})^{\mu-1}\Gamma_{\mathsf{p},\mathsf{q}}^{\mathsf{m},\mathsf{n}}\left[(\mathsf{w}-\mathfrak{a})^{\lambda}\left|\begin{matrix}(a_1,\alpha_1,\mathsf{u}),(a_i,\alpha_i)_{2,\mathsf{p}}\\ \\ (b_j,\beta_j)_{1,\mathsf{q}}\end{matrix}\right.\right]\\
&\quad=\kappa^{\sigma}(\mathsf{w}-\mathfrak{a})^{\mu-\kappa\sigma-1}\Gamma_{\mathsf{p}+1,\mathsf{q}+1}^{\mathsf{m},\mathsf{n}+1}\left[(\mathsf{w}-\mathfrak{a})^{\lambda}\left|\begin{matrix}(a_1,\alpha_1,\mathsf{u}),\left(\frac{1}{\kappa}-\frac{\mu}{\kappa},\frac{\lambda}{\kappa}\right),(a_i,\alpha_i)_{2,\mathsf{p}}\\ \\ (b_j,\beta_j)_{1,\mathsf{q}},\left(\frac{1}{\kappa}-\frac{\mu}{\kappa}+\sigma,\frac{\lambda}{\kappa}\right)\end{matrix}\right.\right]
\end{aligned}
\tag{56}
$$

and

$$
\begin{aligned}
&{}^{\sigma}\mathcal{D}_{\mathfrak{b}}^{\kappa}(\mathfrak{b}-\mathsf{w})^{\mu-1}\Gamma_{\mathsf{p},\mathsf{q}}^{\mathsf{m},\mathsf{n}}\left[(\mathfrak{b}-\mathsf{w})^{\lambda}\right]\\
&\quad={}_{\mathfrak{a}}^{\sigma}\mathcal{D}^{\kappa}(\mathfrak{b}-\mathsf{w})^{\mu-1}\Gamma_{\mathsf{p},\mathsf{q}}^{\mathsf{m},\mathsf{n}}\left[(\mathfrak{b}-\mathsf{w})^{\lambda}\left|\begin{matrix}(a_1,\alpha_1,\mathsf{u}),(a_i,\alpha_i)_{2,\mathsf{p}}\\ \\ (b_j,\beta_j)_{1,\mathsf{q}}\end{matrix}\right.\right]\\
&\quad=\kappa^{\sigma}(\mathfrak{b}-\mathsf{w})^{\mu-\kappa\sigma-1}\Gamma_{\mathsf{p}+1,\mathsf{q}+1}^{\mathsf{m},\mathsf{n}+1}\left[(\mathfrak{b}-\mathsf{w})^{\lambda}\left|\begin{matrix}(a_1,\alpha_1,\mathsf{u}),\left(\frac{1}{\kappa}-\frac{\mu}{\kappa},\frac{\lambda}{\kappa}\right),(a_i,\alpha_i)_{2,\mathsf{p}}\\ \\ (b_j,\beta_j)_{1,\mathsf{q}},\left(\frac{1}{\kappa}-\frac{\mu}{\kappa}+\sigma,\frac{\lambda}{\kappa}\right)\end{matrix}\right.\right].
\end{aligned}
\tag{57}
$$

Proof With the aid of (8), we can derive the desired results directly from Theorems 2.3 and 2.4. □

Corollary 4.5 *Let* $\Re(\lambda)>0$, $\Re(\mu)>1$, $\Re(\kappa)>0$, $\Re(\sigma)>0$, *and* $\mathfrak{a},\mathfrak{b}\in\mathbb{R}$. *Then*

$$
\begin{aligned}
&{}_{\mathfrak{a}}^{\sigma}\mathfrak{I}^{\kappa}(\mathsf{w}-\mathfrak{a})^{\mu-1}H_{\mathsf{p},\mathsf{q}}^{\mathsf{m},\mathsf{n}}\left[(\mathsf{w}-\mathfrak{a})^{\lambda}\right]\\
&\quad={}_{\mathfrak{a}}^{\sigma}\mathfrak{I}^{\kappa}(\mathsf{w}-\mathfrak{a})^{\mu-1}H_{\mathsf{p},\mathsf{q}}^{\mathsf{m},\mathsf{n}}\left[(\mathsf{w}-\mathfrak{a})^{\lambda}\left|\begin{matrix}(a_i,\alpha_i)_{1,\mathsf{p}}\\ \\ (b_j,\beta_j)_{1,\mathsf{q}}\end{matrix}\right.\right]\\
&\quad=\frac{(\mathsf{w}-\mathfrak{a})^{\kappa\sigma+\mu-1}}{\kappa^{\sigma}}H_{\mathsf{p}+1,\mathsf{q}+1}^{\mathsf{m},\mathsf{n}+1}\left[(\mathsf{w}-\mathfrak{a})^{\lambda}\left|\begin{matrix}\left(\frac{1}{\kappa}-\frac{\mu}{\kappa},\frac{\lambda}{\kappa}\right),(a_i,\alpha_i)_{1,\mathsf{p}}\\ \\ (b_j,\beta_j)_{1,\mathsf{q}},\left(\frac{1}{\kappa}-\frac{\mu}{\kappa}-\sigma,\frac{\lambda}{\kappa}\right)\end{matrix}\right.\right]
\end{aligned}
\tag{58}
$$

and

$$
\begin{aligned}
&{}^{\sigma}\mathfrak{I}_{\mathfrak{b}}^{\kappa}(\mathfrak{b}-\mathsf{w})^{\mu-1}H_{\mathsf{p},\mathsf{q}}^{\mathsf{m},\mathsf{n}}\left[(\mathfrak{b}-\mathsf{w})^{\lambda}\right]\\
&\quad={}^{\sigma}\mathfrak{I}_{\mathfrak{b}}^{\kappa}(\mathfrak{b}-\mathsf{w})^{\mu-1}H_{\mathsf{p},\mathsf{q}}^{\mathsf{m},\mathsf{n}}\left[(\mathfrak{b}-\mathsf{w})^{\lambda}\left|\begin{matrix}(a_i,\alpha_i)_{1,\mathsf{p}}\\ \\ (b_j,\beta_j)_{1,\mathsf{q}}\end{matrix}\right.\right]\\
&\quad=\frac{(\mathfrak{b}-\mathsf{w})^{\kappa\sigma+\mu-1}}{\kappa^{\sigma}}H_{\mathsf{p}+1,\mathsf{q}+1}^{\mathsf{m},\mathsf{n}+1}\left[(\mathfrak{b}-\mathsf{w})^{\lambda}\left|\begin{matrix}\left(\frac{1}{\kappa}-\frac{\mu}{\kappa},\frac{\lambda}{\kappa}\right),(a_i,\alpha_i)_{1,\mathsf{p}}\\ \\ (b_j,\beta_j)_{1,\mathsf{q}},\left(\frac{1}{\kappa}-\frac{\mu}{\kappa}-\sigma,\frac{\lambda}{\kappa}\right)\end{matrix}\right.\right].
\end{aligned}
\tag{59}
$$

Proof Setting $\mathfrak{u} = 0$ and $\mathfrak{s} = 1$ in the results in Theorems 2.1 and 2.2 yields the desired identities here. □

Corollary 4.6 *Let* $\Re(\lambda) > 0$, $\Re(\mu) > 1$, $\Re(\kappa) > 0$, $\Re(\sigma) \geq 0$, *and* $\mathfrak{a}, \mathfrak{b} \in \mathbb{R}$. *Then*

$$
\begin{aligned}
&{}_{\mathfrak{a}}^{\sigma}\mathcal{D}^{\kappa}(\mathsf{w}-\mathfrak{a})^{\mu-1}H_{\mathsf{p},\mathsf{q}}^{\mathsf{m},\mathsf{n}}\left[(\mathsf{w}-\mathfrak{a})^{\lambda}\right]\\
&\quad={}_{\mathfrak{a}}^{\sigma}\mathcal{D}^{\kappa}(\mathsf{w}-\mathfrak{a})^{\mu-1}H_{\mathsf{p},\mathsf{q}}^{\mathsf{m},\mathsf{n}}\left[(\mathsf{w}-\mathfrak{a})^{\lambda}\left|\begin{matrix}(a_i,\alpha_i)_{1,\mathsf{p}}\\(b_j,\beta_j)_{1,\mathsf{q}}\end{matrix}\right.\right]\\
&\quad=\kappa^{\sigma}(\mathsf{w}-\mathfrak{a})^{\mu-\kappa\sigma-1}H_{\mathsf{p}+1,\mathsf{q}+1}^{\mathsf{m},\mathsf{n}+1}\left[(\mathsf{w}-\mathfrak{a})^{\lambda}\left|\begin{matrix}\left(\frac{1}{\kappa}-\frac{\mu}{\kappa},\frac{\lambda}{\kappa}\right),(a_i,\alpha_i)_{1,\mathsf{p}}\\(b_j,\beta_j)_{1,\mathsf{q}},\left(\frac{1}{\kappa}-\frac{\mu}{\kappa}+\sigma,\frac{\lambda}{\kappa}\right)\end{matrix}\right.\right]
\end{aligned}
\tag{60}
$$

and

$$
\begin{aligned}
&{}^{\sigma}\mathcal{D}_{\mathfrak{b}}^{\kappa}(\mathfrak{b}-\mathsf{w})^{\mu-1}H_{\mathsf{p},\mathsf{q}}^{\mathsf{m},\mathsf{n}}\left[(\mathfrak{b}-\mathsf{w})^{\lambda}\right]\\
&\quad={}^{\sigma}\mathcal{D}_{\mathfrak{b}}^{\kappa}(\mathfrak{b}-\mathsf{w})^{\mu-1}H_{\mathsf{p},\mathsf{q}}^{\mathsf{m},\mathsf{n}}\left[(\mathfrak{b}-\mathsf{w})^{\lambda}\left|\begin{matrix}(a_i,\alpha_i)_{1,\mathsf{p}}\\(b_j,\beta_j)_{1,\mathsf{q}}\end{matrix}\right.\right]\\
&\quad=\kappa^{\sigma}(\mathfrak{b}-\mathsf{w})^{\mu-\kappa\sigma-1}H_{\mathsf{p}+1,\mathsf{q}+1}^{\mathsf{m},\mathsf{n}+1}\left[(\mathfrak{b}-\mathsf{w})^{\lambda}\left|\begin{matrix}\left(\frac{1}{\kappa}-\frac{\mu}{\kappa},\frac{\lambda}{\kappa}\right),(a_i,\alpha_i)_{1,\mathsf{p}}\\(b_j,\beta_j)_{1,\mathsf{q}},\left(\frac{1}{\kappa}-\frac{\mu}{\kappa}+\sigma,\frac{\lambda}{\kappa}\right)\end{matrix}\right.\right].
\end{aligned}
\tag{61}
$$

Proof Taking $\mathfrak{u} = 0$ and $\mathfrak{s} = 1$ in the identities in Theorems 2.3 and 2.4 gives the desired results here. □

Corollary 4.7 *Let* $\mathfrak{a} \in \mathbb{R}^{+}$, $\alpha < 1$, $\mu \in \mathbb{R}^{+}$, $\Re(\lambda) > 0$, $\Re\left(1+\frac{\eta}{1-\alpha}\right) > 0$, $\mathfrak{u} \geqq 0$, *and* $k \in \mathbb{R}$. *Also let* $a_i \in \mathbb{C}$, $\alpha_i \in \mathbb{R}^{+}$ $(i = 1, \ldots, \mathsf{p})$, *and* $b_j \in \mathbb{C}$, $\beta_j \in \mathbb{R}^{+}$ $(j = 1, \ldots, \mathsf{q})$ *be the same as in* (2). *Then*

$$
\begin{aligned}
\mathcal{P}_{0^{+}}^{(\eta,\alpha,\mathfrak{a})}\left\{\mathsf{w}^{\lambda-1}I_{\mathsf{p}_\ell,\mathsf{q}_\ell;\mathfrak{s}}^{\mathsf{m},\mathsf{n}}(k\mathsf{w}^{\mu})\right\}&=\frac{\mathsf{w}^{\eta+\lambda}\Gamma(\frac{\eta}{1-\alpha}+1)}{[\mathfrak{a}(1-\alpha)]^{\lambda}}\\
&\times I_{\mathsf{p}_\ell+1,\mathsf{q}_\ell+1;\mathfrak{s}}^{\mathsf{m},\mathsf{n}+1}\left[\frac{k\mathsf{w}^{\mu}}{[\mathfrak{a}(1-\alpha)]^{\mu}}\left|\begin{matrix}(a_i,\alpha_i)_{1,\mathsf{n}},(1-\lambda,\mu),(a_{i\ell},\alpha_{i\ell})_{\mathsf{n}+1,\mathsf{p}_\ell}\\(b_j,\beta_j)_{1,\mathsf{m}},(-\lambda-\frac{\eta}{1-\alpha},\mu),(b_{j\ell},\beta_{j\ell})_{\mathsf{m}+1,\mathsf{q}_\ell}\end{matrix}\right.\right].
\end{aligned}
\tag{62}
$$

Proof Putting $\mathfrak{u} = 0$ in Theorem 3.1 produces the desired identity here. □

Corollary 4.8 *Let* $\mathfrak{u} \geq 0$, $\Re(\lambda) > 0$, $\Re(\mu) > 1$, $\Re(\kappa) > 0$, $\Re(\sigma) > 0$, *and* $\mathfrak{a} \in \mathbb{R}$. *Then*

$$
\begin{aligned}
{}_0\mathcal{I}^{\sigma,\kappa}\,\mathsf{w}^{\mu-1}(\Gamma)\,I^{\mathsf{m},\mathsf{n}}_{\mathsf{p}_\ell,\mathsf{q}_\ell;\mathfrak{s}}\left[\mathsf{w}^{\lambda}\right] &= {}_0\mathcal{I}^{\sigma,\kappa}\,\mathsf{w}^{\mu-1}(\Gamma)\,I^{\mathsf{m},\mathsf{n}}_{\mathsf{p}_\ell,\mathsf{q}_\ell;\mathfrak{s}}\left[\mathsf{w}^{\lambda}\,\middle|\,\begin{matrix}(a_1,\alpha_1,\mathfrak{u}),(a_i,\alpha_i)_{2,\mathsf{n}},(a_{i\ell},\alpha_{i\ell})_{\mathsf{n}+1,\mathsf{p}_\ell}\\ (b_j,\beta_j)_{1,\mathsf{m}},(b_{j\ell},\beta_{j\ell})_{\mathsf{m}+1,\mathsf{q}_\ell}\end{matrix}\right]\\
&= \frac{\mathsf{w}^{\kappa\sigma+\mu-1}}{\kappa^{\sigma}}(\Gamma)\,I^{\mathsf{m},\mathsf{n}+1}_{\mathsf{p}_\ell+1,\mathsf{q}_\ell+1;\mathfrak{s}}\left[\mathsf{w}^{\lambda}\,\middle|\,\begin{matrix}(a_1,\alpha_1,\mathfrak{u}),\left(\frac{1}{\kappa}-\frac{\mu}{\kappa},\frac{\lambda}{\kappa}\right),(a_i,\alpha_i)_{2,\mathsf{n}},(a_{i\ell},\alpha_{i\ell})_{\mathsf{n}+1,\mathsf{p}_\ell}\\ (b_j,\beta_j)_{1,\mathsf{m}},(b_{j\ell},\beta_{j\ell})_{\mathsf{m}+1,\mathsf{q}_\ell},\left(\frac{1}{\kappa}-\frac{\mu}{\kappa}-\sigma,\frac{\lambda}{\kappa}\right)\end{matrix}\right]
\end{aligned}
\tag{63}
$$

and

$$
\begin{aligned}
&\mathcal{I}_0^{\sigma,\kappa}(-\mathsf{w})^{\mu-1}(\Gamma)\,I^{\mathsf{m},\mathsf{n}}_{\mathsf{p}_\ell,\mathsf{q}_\ell;\mathfrak{s}}\left[(-\mathsf{w})^{\lambda}\right]\\
&\quad= \mathcal{I}_0^{\sigma,\kappa}(-\mathsf{w})^{\mu-1}(\Gamma)\,I^{\mathsf{m},\mathsf{n}}_{\mathsf{p}_\ell,\mathsf{q}_\ell;\mathfrak{s}}\left[(-\mathsf{w})^{\lambda}\,\middle|\,\begin{matrix}(a_1,\alpha_1,\mathfrak{u}),(a_i,\alpha_i)_{2,\mathsf{n}},(a_{i\ell},\alpha_{i\ell})_{\mathsf{n}+1,\mathsf{p}_\ell}\\ (b_j,\beta_j)_{1,\mathsf{m}},(b_{j\ell},\beta_{j\ell})_{\mathsf{m}+1,\mathsf{q}_\ell}\end{matrix}\right]\\
&\quad= \frac{(-\mathsf{w})^{\kappa\sigma+\mu-1}}{\kappa^{\sigma}}(\Gamma)\,I^{\mathsf{m},\mathsf{n}+1}_{\mathsf{p}_\ell+1,\mathsf{q}_\ell+1;\mathfrak{s}}\left[(-\mathsf{w})^{\lambda}\,\middle|\,\begin{matrix}(a_1,\alpha_1,\mathfrak{u}),\left(\frac{1}{\kappa}-\frac{\mu}{\kappa},\frac{\lambda}{\kappa}\right),(a_i,\alpha_i)_{2,\mathsf{n}},(a_{i\ell},\alpha_{i\ell})_{\mathsf{n}+1,\mathsf{p}_\ell}\\ (b_j,\beta_j)_{1,\mathsf{m}},(b_{j\ell},\beta_{j\ell})_{\mathsf{m}+1,\mathsf{q}_\ell},\left(\frac{1}{\kappa}-\frac{\mu}{\kappa}-\sigma,\frac{\lambda}{\kappa}\right)\end{matrix}\right].
\end{aligned}
\tag{64}
$$

Proof Taking $\mathfrak{a}=0$ and $\mathfrak{b}=0$ in the results in Theorems 2.1 and 2.2 gives the desired identities here. □

Corollary 4.9 *Let* $\mathfrak{u}\geq 0$, $\Re(\lambda)>0$, $\Re(\mu)>1$, $\Re(\kappa)>0$, $\Re(\sigma)>0$, *and* $\mathfrak{a}\in\mathbb{R}$. *Then*

$$
\begin{aligned}
J^{\sigma}\mathsf{w}^{\mu-1}(\Gamma)\,I^{\mathsf{m},\mathsf{n}}_{\mathsf{p}_\ell,\mathsf{q}_\ell;\mathfrak{s}}\left[\mathsf{w}^{\lambda}\right] &= J^{\sigma}\mathsf{w}^{\mu-1}(\Gamma)\,I^{\mathsf{m},\mathsf{n}}_{\mathsf{p}_\ell,\mathsf{q}_\ell;\mathfrak{s}}\left[\mathsf{w}^{\lambda}\,\middle|\,\begin{matrix}(a_1,\alpha_1,\mathfrak{u}),(a_i,\alpha_i)_{2,\mathsf{n}},(a_{i\ell},\alpha_{i\ell})_{\mathsf{n}+1,\mathsf{p}_\ell}\\ (b_j,\beta_j)_{1,\mathsf{m}},(b_{j\ell},\beta_{j\ell})_{\mathsf{m}+1,\mathsf{q}_\ell}\end{matrix}\right]\\
&= \mathsf{w}^{\sigma+\mu-1}(\Gamma)\,I^{\mathsf{m},\mathsf{n}+1}_{\mathsf{p}_\ell+1,\mathsf{q}_\ell+1;\mathfrak{s}}\left[\mathsf{w}^{\lambda}\,\middle|\,\begin{matrix}(a_1,\alpha_1,\mathfrak{u}),(1-\mu,\lambda),(a_i,\alpha_i)_{2,\mathsf{n}},(a_{i\ell},\alpha_{i\ell})_{\mathsf{n}+1,\mathsf{p}_\ell}\\ (b_j,\beta_j)_{1,\mathsf{m}},(b_{j\ell},\beta_{j\ell})_{\mathsf{m}+1,\mathsf{q}_\ell},(1-\mu-\sigma,\lambda)\end{matrix}\right].
\end{aligned}
\tag{65}
$$

Proof Putting $\mathfrak{a}=0$ and $\kappa=1$ in the result in Theorem 2.1 yields the desired identity here. □

5 Concluding Remarks

Classical special functions and polynomials, their numerous generalizations and variations have acquired great reputation and significance owing in particular to their proven applicability in diverse and broad areas of science and engineering. In this paper, we established several interesting image formulae of the incomplete I-function under the conformable and pathway fractional integral and derivative operators. As shown in Sect. 1, since both the incomplete I-function and the conformable fractional integral and derivative operators are very general amid special functions as well as

fractional integral and derivative operators, the main results presented here can give a number of particular identities, some of which were explicitly demonstrated in the corollaries. More particular formulae of our main identities can be provided.

References

1. Bansal MK, Kumar D, Nisar KS, Singh J (2020) Certain fractional calculus and integral transform results of incomplete $\aleph$-functions with applications. Math Meth Appl Sci 43(8):5602–5614. https://doi.org/10.1002/mma.6299
2. Bansal MK, Kumar D (2020) On the integral operators pertaining to a family of incomplete I-functions. AIMS Math 5(2):1247–1259. https://doi.org/10.3934/math.2020085
3. Srivastava HM, Saxena RK, Parmar RK (2018) Some families of the incomplete H-functions and the incomplete $\bar{H}$-functions and associated integral transforms and operators of fractional calculus with applications. Russ J Math Phys 25(1):116–138. https://doi.org/10.1134/S1061920818010119
4. Srivastava HM, Gupta KC, Goyal SP (1982) The H-functions of one and two variables with applications. South Asian Publishers, Chennai, New Delhi
5. Mathai AM, Saxena RK (1978) The H-function with applications in statistics and other disciplines. Halsted Press (John Wiley & Sons), New York, London, Sydney, Toronto
6. Mathai AM, Saxena RK, Haubold HJ (2010) The H-function: theory and applications. Springer, New York
7. Srivastava HM, Tomovski Ž (2009) Fractional calculus with an integral operator containing a generalized Mittag-Leffler function in the kernel. Appl Math Comput 211(1):198–210. https://doi.org/10.1016/j.amc.2009.01.055
8. Srivastava HM, Bansal MK, Harjule P (2018) A study of fractional integral operators involving a certain generalized multi-index Mittag-Leffler function. Math Meth Appl Sci 41(16):6108–6121. https://doi.org/10.1002/mma.5122
9. Bansal MK, Jolly N, Jain R, Kumar D (2019) An integral operator involving generalized Mittag-Leffler function and associated fractional calculus results. J Anal 27(3):727–740. https://doi.org/10.1007/s41478-018-0119-0
10. Prabhakar TR (1971) A singular integral equation with a generalized Mittag-Leffler function in the kernel. Yokohama Math J 19:7–15
11. Shukla AK, Prajapati JC (2007) On a generalization of Mittag Leffler function and its properties. J Math Anal Appl 336(2):797–811. https://doi.org/10.1016/j.jmaa.2007.03.018
12. Tomovski Ž, Hilfer R, Srivastava HM (2010) Fractional and operational calculus with generalized fractional derivative operators and Mittag-Leffler type functions. Integr Transforms Spec Funct 21(11):797–814. https://doi.org/10.1080/10652461003675737
13. Baleanu1 D, Jangid NK, Joshi S, Purohit SD (2020) The pathway fractional integrals of incomplete I-functions. Int J Appl Comput Math 6(5). Article ID 151. https://doi.org/10.1007/s40819-020-00902-6
14. Jangid K, Bhatter S, Meena S, Baleanu D, Qurashi MI, Purohit SD (2020) Some fractional calculus findings associated with the incomplete I-functions. Adv Differ Equ 2020. Article ID 265. https://doi.org/10.1186/s13662-020-02725-7
15. Bansal MK, Kumar D (2021) On a family of the incomplete H-functions and associated integral transforms. J Appl Anal 27(1):143–152. https://doi.org/10.1515/jaa-2020-2040
16. Singh J, Kumar D, Bansal MK (2020) Solution of nonlinear differential equation and special functions. Math Meth Appl Sci 43(5):2106–2116. https://doi.org/10.1002/mma.5918
17. Mainardi F, Pagnini G, Saxena RK (2005) Fox H functions in fractional diffusion. J Comput Appl Math 178(1–2):321–331. https://doi.org/10.1016/j.cam.2004.08.006

18. Gorenflo R, Luchko Y, Mainardi F (2000) Wright functions as scale-invariant solutions of the diffusion-wave equation. J Comput Appl Math 118(1–2):175–191. https://doi.org/10.1016/S0377-0427(00)00288-0
19. Srivastava HM, Saxena RK (2005) Some Voterra-type fractional integro-differential equations with a multivariable confluent hypergeometric function as their kernel. J Integr Equations Appl 17(2):199–217. https://doi.org/10.1216/jiea/1181075324
20. Kumar D, Singh J, Tanwar K, Baleanu D (2019) A new fractional exothermic reactions model having constant heat source in porous media with power, exponential and Mittag-Leffler laws. Int J Heat Mass Transf 138:1222–1227. https://doi.org/10.1016/j.ijheatmasstransfer.2019.04.094
21. Singh J, Kumar D, Baleanu D (2019) New aspects of fractional Biswas-Milovic model with Mittag-Leffler law. Math Model Nat Phenom 14(3). Article ID 303. https://doi.org/10.1051/mmnp/2018068
22. Suthar DL, Purohit SD, Khan AM, Dave S (2021) Impacts of environmental pollution on the growth and conception of biological populations involving incomplete I-function. In: Sharma H, Saraswat M, Kumar S, Bansal JC (eds) Intelligent learning for computer vision. CIS 2020. Lecture notes on data engineering and communications technologies, vol 61. Springer, Singapore. https://doi.org/10.1007/978-981-33-4582-9-44
23. Jangid K, Mathur M, Purohit SD, Suthar DL (2021) Certain expansion formulae for incomplete I-functions and I-functions involving bessel function. In: Kumar S, Purohit SD, Hiranwal S, Prasad M (eds) Proceedings of International conference on communication and computational technologies. Algorithms for intelligent systems. Springer, Singapore. https://doi.org/10.1007/978-981-16-3246-4-11
24. Saxena VP (2008) The I-function. Anamaya Publishers, New Delhi, pp 18–36
25. Saxena VP (1982) Formal solution of certain new pair of dual integral equations involving H-function. Proc Natl Acad Sci India Sect A 52:366–375
26. Bansal MK, Choi J (2019) A note on pathway fractional integral formulas associated with the incomplete H-functions. Int J Appl Comput Math 5(5). Article ID 133. https://doi.org/10.1007/s40819-019-0718-8
27. Atangana A, Baleanu D (2016) New fractional derivatives with non-local and non-singular kernel: theory and application to heat transfer model. Therm Sci 20(2):763–769. https://doi.org/10.2298/TSCI160111018A
28. Caputo M, Fabrizio M (2015) A new definition of fractional derivative without singular kernel. Prog Fract Differ Appl 1(2):73–85. https://doi.org/10.12785/pfda/010201
29. Hilfer R (2000) Applications of fractional calculus in physics. Word Scientific, Singapore
30. Magin RL (2006) Fractional calculus in bioengineering. Begell House Publishers, Redding
31. Srivastava HM, Saxena RK (2001) Operators of fractional integration and their applications. Appl Math Comput 118(1):1–52. https://doi.org/10.3390/math6090157
32. Bansal MK, Shivlal Kumar D, Kumar S, Singh J (in press) Fractional differential equation pertaining to an integral operator involving the family of incomplete H-functions in the kernel. Math Meth Appl Sci. https://doi.org/10.1002/mma.6670
33. Harjule P, Bansal MK (2020) Fractional order models for viscoelasticity in lung tissues with power, exponential and Mittag Leffler memories. Int J Appl Comput Math 6(4). Article ID 119. https://doi.org/10.1007/s40819-020-00872-9
34. Srivastava HM, Saad KM (2020) New approximate solution of the time-fractional Nagumo equation involving fractional integrals without singular kernel. Appl Math Inform Sci 14:1–8. https://doi.org/10.18576/amis/140101
35. Nisar KS, Eata AF, Al-Dhaifallah M, Choi J (2016) Fractional calculus of generalized k-Mittag-Leffler function and its applications to statistical distribution. Adv Differ Equ. Article ID 304. https://doi.org/10.1186/s13662-016-1029-6
36. Baleanu D, Rezapour S, Saberpour Z (2019) On fractional integro-differential inclusions via the extended fractional Caputo Fabrizio derivation. Bound Value Probl Article ID 79. https://doi.org/10.1186/s13661-019-1194-0

37. Kilbas AA, Srivastava HM, Trujillo JJ (2006) Theory and applications of fractional differential equations. North-Holland mathematical studies, vol 204. Elsevier (North-Holland) Science Publishers, Amsterdam, London and New York
38. Podlubny I (1999) Fractional differential equations. Academic Press, California, USA
39. Samko SG, Kilbas AA, Marichev OI (1993) Fractional integrals and derivatives: theory and applications. Gordon and Breach Science Publishers, Reading, Tokyo, Paris, Berlin and Langhorne (Pennsylvania)
40. Kilbas AA (2001) Hadamard type fractional calculus. J Korean Math Soc 38(6):1191–1204
41. Katugampola UN (2011) New approach to a generalized fractional integral. Appl Math Comput 218(3):860–865. https://doi.org/10.1016/j.amc.2011.03.062
42. Katugampola UN (2014) New approach to generalized fractional derivatives. Bull Math Anal Appl 6(4):1–15
43. Jarad F, Uğurlu E, Abdeljawad T, Baleanu D (2017) On a new class of fractional operators. Adv Differ Equ. Article ID 247. https://doi.org/10.1186/s13662-017-1306-z
44. Srivastava HM, Choi J (2012) Zeta and q-zeta functions and associated series and integrals. Elsevier Science Publishers, Amsterdam, London and New York
45. Nair SS (2009) Pathway fractional integration operator. Fract Calc Appl Anal 12(3):237–252

Explicit Exact Solutions and Conservation Laws of Modified α Equation

Sachin Kumar and Divya Jyoti

Abstract The invariant solutions of generalised modified α equation are obtained by using the Lie classical symmetry method. The obtained solutions are in terms of trigonometric functions and hyperbolic functions. This equation can be used in solidifying and nucleation problem. The conservation laws are obtained by using the multiplier approach. The graphical representations are also shown for some of the obtained solutions. Some new solutions of those equations are found that have been considered earlier in literature, as well as some of the previous solutions can also be recovered by taking particular values.

Keywords Modified α equation · Lie classical method · Infinitesimals · Invariant solutions · Solitons · Conservation laws

Mathematics Subject Classification (2010) 35B06 · 35B10 · 35C07 · 35C09 · 35C11 · 35G20

PACS 02.30.Jr · 04.20.Jb · 11.30.-j

1 Introduction

Nonlinear science is important for studying the various nonlinear physical phenomena [10, 16]. It possesses both scientific and practical significance in various fields like engineering, finance and many other. The analysis of solutions of nonlinear differential equations is very significant to solve numerous problems. Sumudu transform method, Homotopy perturbation method [6], fractional natural decomposition method [20], Lie symmetry method [4, 9, 15, 19] can be used to solve these nonlinear

S. Kumar · D. Jyoti (✉)
Department of Mathematics and Statistics, School of Basic and Applied Sciences, Central University of Punjab, Bathinda 151 001, Punjab, India
e-mail: divya.jyoti1995@gmail.com

S. Kumar
e-mail: sachin1jan@yahoo.com

J. Singh et al. (eds.), *Advances in Mathematical Modelling, Applied Analysis and Computation*, Lecture Notes in Networks and Systems 415,
https://doi.org/10.1007/978-981-19-0179-9_8

differential equations [7, 11, 12]. The Lie symmetry method is the more powerful method. This method has been used by Kumar [14] to find invariant solutions of Biswas–Milovic equation.

One of the most important equation, named, shallow water equation, is extensively applied to represent the environmental science, fluid dynamics and some other fields. Tsunami is also a sort of shallow water [5]. Thus, finding the exact solutions of these equations has become an important task.

A class of nonlinear shallow water wave equations

$$u_t - u_{xxt} + (\alpha + 1)uu_x - \alpha u_x u_{xx} - uu_{xxx} = 0, \tag{1}$$

is known as α equation. Here, the unnamed function $u(x, t)$, denoting the dimension of the relevant wave mode, is a function of two independent variables x and t that specify the space variables in the flank of wave publicity and time, respectively [2]. Also, the term u_{xxt} represents disbandment wave effects, uu_x and uu_{xxx} represent the nonlinear wave steepening and α is any real constant. Chang et al. [5] performed Lie symmetry analysis and bifurcation analysis for this class of equations. In 2006, Wazwaz [21] studied this important family of physical equations by changing the nonlinear convection term uu_x into u^2u_x, i.e.

$$u_t - u_{xxt} + (\alpha + 1)u^2u_x - \alpha u_x u_{xx} - uu_{xxx} = 0, \tag{2}$$

which is known as modified α equation. For $\alpha = 2$, it reduces to modified Camassa–Holm (CH) equation and for $\alpha = 3$, it reduces to Degasperis–Procesi (DP) equation. The modification cause changes in the physical characteristics of the solutions from multi-peakon solutions into bell-shaped solitary wave solutions [3]. Wazwaz [21] obtained the soliton solutions of (2) using tanh method and sine-cosine method. Baskonus et al. [2] also obtained mixed dark-bright soliton solutions as well as complex soliton solutions of (2) by using sine-Gordon expansion method.

In this paper, the generalised modified α equation is considered as

$$u_t - bu_{xxt} + (\alpha + 1)u^2u_x - \alpha u_x u_{xx} - cuu_{xxx} = 0. \tag{3}$$

This equation is a tactical application for outlining the method of phase dissociation in cold steel alloy and is generally used in solidifying and nucleation problem [2]. The exact explicit solutions of (3) are obtained by using the Lie symmetry method. The solutions are obtained in terms of trigonometric functions and hyperbolic functions. The graphical representations are also shown for some obtained solutions. The conservation laws [1, 13] of (3) are also obtained by using the multiplier approach.

2 Symmetry Analysis

The Lie classical method [19] is used in this section for symmetry analysis in order to solve the above nonlinear PDE (3). Consider the Lie group of point transformations

$$\begin{aligned} x^* &= x + \epsilon\xi(x,t,u) + O(\epsilon^2), \\ t^* &= t + \epsilon\tau(x,t,u) + O(\epsilon^2), \\ u^* &= u + \epsilon\eta(x,t,u) + O(\epsilon^2), \end{aligned} \tag{4}$$

such that if u satisfies (3), then u^* also satisfies (3). The invariance condition is

$$\eta^t - b\eta^{xxt} + (\alpha+1)(2uu_x\eta + u^2\eta^x) - \alpha(u_x\eta^{xx} + u_{xx}\eta^x) - c(u\eta^{xxx} + u_{xxx}\eta) = 0. \tag{5}$$

By substituting the values of extended infinitesimals, a set of determining equations were obtained. The infinitesimals $\xi,\ \tau,\ \eta$ obtained by solving the determining equations [4] are found as

$$\xi = C_2, \qquad \tau = C_1, \qquad \eta = 0, \tag{6}$$

where $C_1,\ C_2$ are arbitrary constants. The corresponding vector fields are

$$V_1 = \partial_t, \qquad V_2 = \partial_x. \tag{7}$$

Corresponding to the vector field $V_1 + \epsilon V_2$, the similarity variables [14] are

$$r = x - \epsilon t, \quad u = g(r), \tag{8}$$

where r is new independent variable and g is new dependent function. Back substituting these variables in Eq. (3), the reduced ODE is obtained as

$$(\alpha+1)g^2 g' - \alpha g' g'' - \epsilon g' + b\epsilon g''' - cgg''' = 0, \tag{9}$$

where $'$ denotes the differentiation with respect to r.

3 Exact Solutions

In this part, the exact solutions of ODE (9) are obtained in the form of hyperbolic and trigonometric functions by using Maple.

Equation (9) possesses travelling wave solutions as

$$g(r) = C_4 \csc^2(C_2 r + C_1),$$
$$\text{with} \quad b = -\frac{1}{4C_2^2}, \quad c = \frac{-6C_2^2\alpha + C_4\alpha + C_4}{12C_2^2}, \quad \epsilon = \frac{1}{9}(6\alpha C_4 C_2^2 + \alpha C_4^2 + C_4^2), \tag{10}$$

where C_1, C_2 and C_4 are arbitrary constants. Thus, the exact solutions of generalised modified α Eq. (3) are

$$(i) \quad u(x,t) = C_4 \csc^2(C_2(x - \epsilon t) + C_1), \quad \text{with}$$
$$b = -\frac{1}{4C_2^2}, \quad c = \frac{-6C_2^2\alpha + C_4\alpha + C_4}{12C_2^2}, \quad \epsilon = \frac{C_4}{9}(6\alpha C_2^2 + \alpha C_4 + C_4). \tag{11}$$

Similarly, the other exact solutions can be obtained as

$$(ii) \quad u(x,t) = C_4 \sec^2(C_2(x - \epsilon t) + C_1), \quad \text{with}$$
$$b = -\frac{1}{4C_2^2}, \quad c = \frac{-6C_2^2\alpha + C_4\alpha + C_4}{12C_2^2}, \quad \epsilon = \frac{C_4}{9}(6\alpha C_2^2 + \alpha C_4 + C_4), \tag{12}$$

$$(iii) \quad u(x,t) = C_4 \cot^2(C_2(x - \epsilon t) + C_1), \quad \text{with}$$
$$b = \frac{6C_2^2\alpha + C_4\alpha + C_4}{2C_2^2(6C_2^2\alpha + 4C_4\alpha + 4C_4)}, \quad c = \frac{-6C_2^2\alpha + C_4\alpha + C_4}{12C_2^2}, \tag{13}$$
$$\epsilon = \frac{C_4}{9}(6\alpha C_2^2 + 4\alpha C_4 + 4C_4),$$

$$(iv) \quad u(x,t) = C_4 \operatorname{csch}^2(C_2(x - \epsilon t) + C_1), \quad \text{with}$$
$$b = \frac{1}{4C_2^2}, \quad c = \frac{-6C_2^2\alpha + C_4\alpha + C_4}{12C_2^2}, \quad \epsilon = \frac{C_4}{9}(6\alpha C_2^2 + \alpha C_4 + C_4), \tag{14}$$

$$(v) \quad u(x,t) = C_4 \operatorname{sech}^2(C_2(x - \epsilon t) + C_1), \quad \text{with}$$
$$b = \frac{1}{4C_2^2}, \quad c = -\frac{6C_2^2\alpha + C_4\alpha + C_4}{12C_2^2}, \quad \epsilon = \frac{C_4}{9}(-6\alpha C_2^2 + \alpha C_4 + C_4), \tag{15}$$

$$(vi) \quad u(x,t) = C_4 \coth^2(C_2(x - \epsilon t) + C_1), \quad \text{with}$$
$$b = -\frac{6C_2^2\alpha + C_4\alpha + C_4}{2C_2^2(6C_2^2\alpha + 4C_4\alpha + 4C_4)}, \quad c = \frac{-6C_2^2\alpha + C_4\alpha + C_4}{12C_2^2}, \tag{16}$$
$$\epsilon = \frac{C_4}{9}(6\alpha C_2^2 + 4\alpha C_4 + 4C_4),$$

where C_1, C_2 and C_4 are arbitrary constants.

3.1 Special Case: $b = 1,\ c = 1$

For $b = 1,\ c = 1$, the ODE system (9) reduces to

$$(\alpha + 1)g^2 g' - \alpha g' g'' - \epsilon g' + \epsilon g''' - g g''' = 0. \tag{17}$$

Equation (17) possesses solutions in terms of doubly periodic Jacobi elliptic sine function. Thus, the corresponding solutions to modified α Eq. (2) are

$$\begin{aligned} u(x,t) =& \frac{1}{2\alpha+2}\Bigg(M - \alpha - 1 + 4(\alpha+2)C_3^2\Bigg(-1 - C_1^2 + 3C_1^2 \\ & \times \mathrm{sn}^2\left(\frac{C_3}{2}tM + \frac{C_3}{2}(2x - \alpha t - t) + C_2, C_1\right)\Bigg)\Bigg), \\ \text{with} \quad & \epsilon = \frac{1}{4}(\alpha M - 2M + 2\alpha + 4), \\ \text{where} \quad & M = \sqrt{(\alpha+1)^2 - 16\alpha C_3^4(\alpha+2)(C_1^4 - C_1^2 + 1)}, \end{aligned} \tag{18}$$

where C_1, C_2 and C_3 are arbitrary constants.

4 Conservation Laws

In this part, the local conservation laws [8] of generalised modified α equation (3) are obtained by using the multiplier approach [18]. Consider a multiplier of the form $\Lambda(x, t, u, u_x, u_{xx})$. The simplified determining equations to be solved are

$$\Lambda_x = 0, \quad \Lambda_t = 0, \quad \Lambda_u = 0, \quad \Lambda_{u_x} = 0, \quad \Lambda_{u_{xx}} = 0. \tag{19}$$

The solution of above determining equations (19) yields $\Lambda = C_1$. Thus, the conserved fluxes [17] in accordance to this multiplier are

$$\begin{aligned} T_t &= u - b u_{xx}, \\ T_x &= -cuu_{xx} - \frac{1}{2}(\alpha - c)u_x^2 + \frac{1}{3}(\alpha+1)u^3. \end{aligned} \tag{20}$$

5 Results and Discussions

The graphical representations of solution (15) are shown by considering particular values of arbitrary constants. These graphical representations depict the 3D and

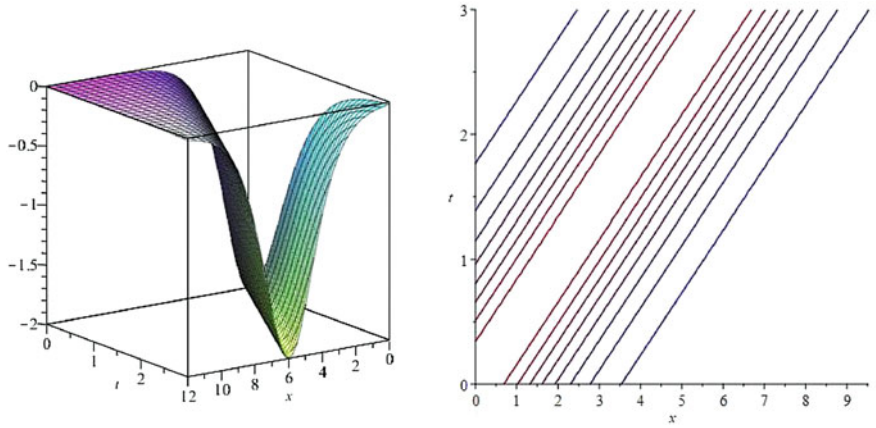

(a) 3D plot (b) Contour plot

Fig. 1 3D plot and contour plot of solution (15) with $C_1 = 0,\ C_2 = \frac{1}{2},\ C_4 = 2,\ \alpha = 2$

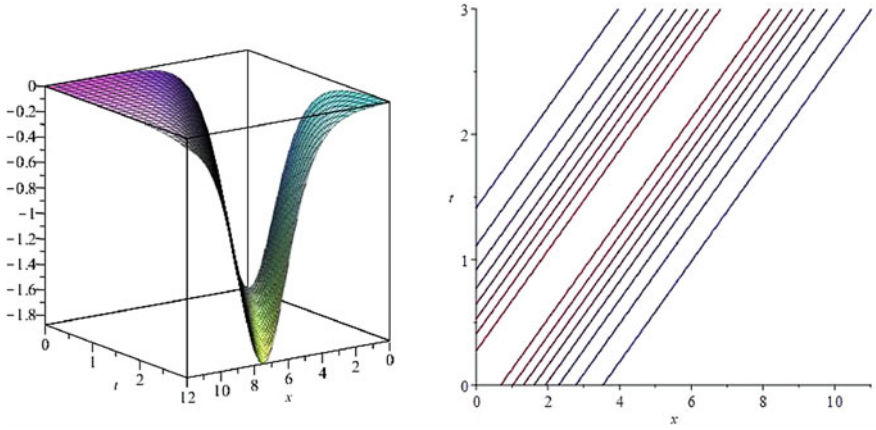

(a) 3D plot (b) Contour plot

Fig. 2 3D plot and contour plot of solution (15) with $C_1 = 0,\ C_2 = \frac{1}{2},\ C_4 = \frac{15}{8}\ \alpha = 3$

contour plots of (15) for different values of α. For $\alpha = 2$, Fig. 1 represent the graph of solution of generalised modified α Eq. (3) and of modified CH equation. For $\alpha = 3$, Fig. 2 represent the graph of solution of equation (3) and of modified DP equation. Figure 3 represent the graph of solution of Eq. (3) for $\alpha = 4$. These graphs represent the soliton solutions for different values of α.

Remarks:

1. On taking $C_1 = 0, C_2 = \frac{1}{2}, C_4 = \frac{3(\alpha+2)}{2(\alpha+1)}$ in solution (14), the solution reduces to one of the solutions of general modified DP-CH equation, as obtained by Wazwaz

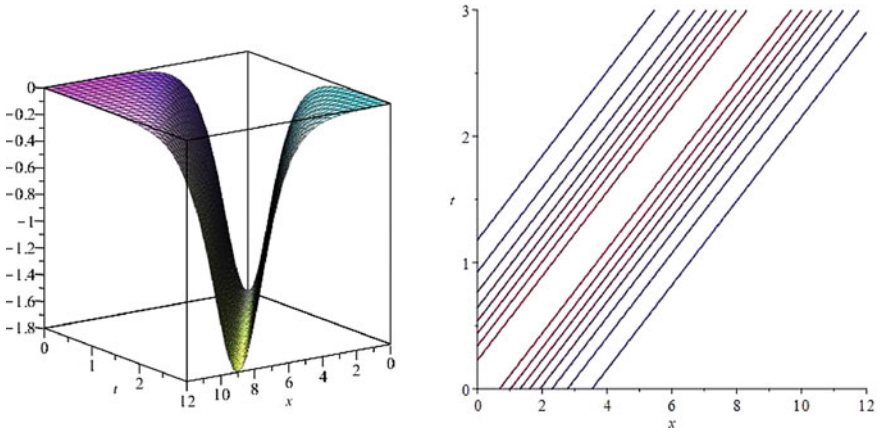

(a) 3D plot (b) Contour plot

Fig. 3 3D plot and contour plot of solution (15) with $C_1 = 0,\ C_2 = \frac{1}{2},\ C_4 = -\frac{9}{5},\ \alpha = 4$

[21]. For $\alpha = 2$, it reduces to the solution of modified CH equation and for $\alpha = 3$, it reduces to the solution of modified DP equation.

2. On considering $C_1 = 0, C_2 = \frac{1}{2}, C_4 = -\frac{3(\alpha+2)}{2(\alpha+1)}$ in solution (15), the solution reduces to one of the solutions of general modified DP-CH equation, as obtained by Wazwaz [21]. For $\alpha = 2$, it reduces to the solution of modified CH equation and for $\alpha = 3$, it reduces to the solution of modified DP equation.
3. On letting $C_1 = 0, C_2 = \frac{1}{2}, C_4 = -\frac{3(\alpha+2)}{2(\alpha+1)},\ \alpha = 4$, in solution (15), the solution reduces to one of the dark soliton solutions of modified α equation, as obtained by Baskonus [2].
4. Solution (18) represents the new doubly periodic solution of equation (2) considered by Wazwaz [21].

6 Conclusion

The explicit exact solutions of generalised modified α Eq. (3) have been obtained by using the Lie classical symmetry method. The solutions (11)–(16), (18) have been obtained in terms of trigonometric functions and hyperbolic functions. Also, some new solutions of equations, considered in literature (2), have been obtained in terms of doubly periodic Jacobi elliptic functions. The general form of equation considered here (3) is useful to obtain new solutions of the existing equations in literature (2), as well as to obtain solutions of some new equations, for different values of b and c in (3). The conservation laws (20) have also been obtained by using the multiplier approach. The graphical representations of some of the obtained solutions depict the solitary wave solutions.

Conflict of Interest:

The authors declare that they have no conflict of interest.

Acknowledgements Second author (Divya Jyoti) is very much thankful to CSIR for providing financial assistance in terms of JRF fellowship via letter Sr. No. 1061841352 and Ref. No. 17/06/2018(i)EU-V.

References

1. Anco S, Bluman G (2002) Direct construction method for conservation laws of partial differential equations. Part I: examples of conservation law classifications. Eur J Appl Math 13(5):545–566
2. Baskonus H, Guirao J, Kumar A, Causanilles F, Bermudez G (2020) Complex mixed dark-bright wave patterns to the modified α and modified Vakhnenko-Parkes equations. Alexandria Eng J 59(4):2149–2160
3. Biswas A (2009) Solitary wave solution for KdV equation with power-law nonlinearity and time-dependent coefficients. Nonlinear Dyn 58(1–2):345
4. Bluman G, Anco S (2002) Symmetry and integration methods for differential equations, vol 154. Springer
5. Chang L, Liu H, Zhang L (2020) Symmetry reductions, dynamical behavior and exact explicit solutions to a class of nonlinear shallow water wave equation. Qual Theory Dyn Syst 19(1):35
6. Goswami A, Singh J, Kumar D (2019) An efficient analytical approach for fractional equal width equations describing hydro-magnetic waves in cold plasma. Phys A: Stat Mech its Appl 524:563–575
7. Gupta R, Jain R, Kumar S, Jyoti D (2021) On new symmetries and exact solutions of Einstein's field equation for perfect fluid distribution. Pramana 95(3):1–4
8. Ibragimov NH (2007) A new conservation theorem. J Math Anal Appl 333(1):311–328
9. Jyoti D, Kumar S (2020) Exact non-static solutions of Einstein vacuum field equations. Chin J Phys 68:735–744
10. Jyoti D, Kumar S (2020) Modified Vakhnenko-Parkes equation with power law nonlinearity: Painlevé analysis, analytic solutions and conservation laws. Eur Phys J Plus 135:762
11. Jyoti D, Kumar S (2021) Invariant solutions and conservation laws of Einstein field equations in non-comoving radiation fields. Chin J Phys 70:37–43
12. Jyoti D, Kumar S, Gupta RK (2020) Exact solutions of Einstein field equations in perfect fluid distribution using Lie symmetry method. Eur Phys J Plus 135:604
13. Kara A, Mahomed F (2002) A basis of conservation laws for partial differential equations. J Nonlinear Math Phys 9(2):60–72
14. Kumar S (2016) Invariant solutions of Biswas-Milovic equation. Nonlinear Dyn 87(2):1153–1157
15. Kumar S, Jyoti D (2021) Invariant solutions of Einstein field equations in pure radiation fields. Ind J Phys 1–6
16. Kumar S, Jyoti D, Nisar KS, Zakarya M (2021) New exact static solutions of Einstein-Maxwell field equations with a magnetic dipole. Results Phys 24:104136
17. Naz R (2012) Conservation laws for some systems of nonlinear partial differential equations via multiplier approach. J Appl Math 2012:871253
18. Naz R, Naeem I, Khan M (2013) Conservation laws of some physical models via symbolic package GeM. Math Probl Eng 2013:897912
19. Olver PJ (1986) Applications of Lie groups to differential equations, vol 107. Springer

20. Veeresha P, Prakasha D, Kumar D, Baleanu D, Singh J (2020) An efficient computational technique for fractional model of generalized Hirota-Satsuma-coupled Korteweg-de Vries and coupled modified Korteweg-de Vries equations. J Comput Nonlinear Dyn 15(7):071003
21. Wazwaz A (2006) Solitary wave solutions for modified forms of Degasperis-Procesi and Camassa-Holm equations. Phys Lett A 352(6):500–504

Some Approximation Results on Durrmeyer Modification of Generalized Szász–Mirakjan Operators

Rishikesh Yadav, Ramakanta Meher, and Vishnu Narayan Mishra

Abstract This paper deals with the approximation properties of the summation-integral type operators defined by Mishra et al. (Boll Unione Mat Ital 8:297–305, 2016). It consists of the local results and convergence theorem of the defined operators. Here, we discuss the asymptotic behaviour of the operators and the quantitative means of Voronovskaja type theorem is obtained. In this direction, we determine the Grüss Voronovskaya type theorem. Graphical representation is given to support the approximation results of the operators and, at last, conclusions are given.

Keywords Szász–Mirakjan operators · Rate of convergence · Voronovskaya type theorem · Lipschitz space

1 Introduction

In 2016, Mishra et al. [12] carried out their works on approximation properties for the operators defined by

$$S_n^*(g;x) = u_n \sum_{j=0}^{\infty} s_{u_n,j}(x) \int_0^{\infty} s_{u_n,j}(t) g(t) dt, \tag{1}$$

R. Yadav (✉) · R. Meher
Department of Mathematics and Humanites, Sardar Vallabhbhai National Institute of Technology Surat, Surat 395007, Gujarat, India
e-mail: rishikesh2506@gmail.com; rishikesh.yadav@unamur.be
URL: https://sites.google.com/view/yadavrishi/home

R. Yadav
Namur Institute for Complex Systems (naXys) and Department of Mathematics, University of Namur, 5000 Namur, Belgium

V. N. Mishra
Department of Mathematics, Indira Gandhi National Tribal University, Lalpur, Amarkantak, Anuppur 484887, Madhya Pradesh, India

J. Singh et al. (eds.), *Advances in Mathematical Modelling, Applied Analysis and Computation*, Lecture Notes in Networks and Systems 415,
https://doi.org/10.1007/978-981-19-0179-9_9

where $s_{u_n,j}(x) = e^{-u_n x}\frac{(u_n x)^j}{j!}$ and $u_n \to \infty$ as $n \to \infty$ with condition $u_1 = 1$, here the functions are considered to be Lebesgue integrable. By simple calculation, if we take $u_n = n$, then the above operators (1), reduced into Szász–Mirakjan Durremeyr operators defined by Mazhar and Totik [8]. The important properties of the defined operators are studied by Mishra et al., which can be applied to the operators defined by Mazhar and Totik. Regarding the approximation of the function by Durrmeyer type operators, as well as with the other approximation properties, many works have been done in this direction [10, 11, 13, 18].

Also, the discussion regarding Durrmeyer-type modification of Szász–Mirakjan operators is seen in [8] where the authors gave a vital result for the Durrmeyer type operators, which are defined on $[0, \infty)$ as

$$A_n(g; x) = g(0)s_{n,0}(x) + n\sum_{j=1}^{\infty} s_{n,j}(x)\int_0^{\infty} s_{n,j-1}(t)g(t)dt. \tag{2}$$

All the above operators (1, 2) are generalized form of the Szász–Mirakjan operators [9, 15] defined by

$$SM_n(g; x) = \sum_{j=0}^{\infty} s_{n,j}(x)g\left(\frac{j}{n}\right), \tag{3}$$

where $s_{n,j} = e^{-nx}\frac{(nx)^j}{j!}$ is the Szász–Mirakjan basis function. Also, a natural generalization of the Szász–Mirakjan operators can be seen (presented in [3]) in the form of strictly increasing sequence as a simple replacement of n by u_n such that $u_1 = 1$ and $u_n \to \infty$ as $n \to \infty$ in the above operators (3), and hence the modification can be seen in the form of

$$S_n^*(g; x) = \sum_{j=0}^{\infty} s_{u_n,j}(x)g\left(\frac{j}{u_n}\right). \tag{4}$$

Thus, the works have been done by Mishra et al. [12] for the above operators (1) on the natural modification of the operators defined in [8] called as Szász–Mirakjan Durremeyr operators which put a crucial impact in the theory of approximation. For further proceeding to study the approximations properties of the operators (1), we need some basic lemma.

Lemma 1 *Consider the function g is integrable, continuous and bounded on the given interval $[0, \infty)$. Then the central moments are as*

$$\Theta_{n,m} = u_n\sum_{j=0}^{\infty} s_{u_n,j}(x)\int_0^{\infty} s_{u_n,j}(t)(t-x)^m dt, \tag{5}$$

where $m = 0, 1, 2, \ldots$. *So for* $m = 0, 1$, *we can get the the central moments as follows:*

$$\Theta_{n,0} = 1, \Theta_{n,1} = \frac{1}{u_n}, \tag{6}$$

in general, we have

$$u_n \Theta_{n,m+1} = x\left(\Theta'_{n,m} + 2m\Theta_{n,m-1} + (1+m)\Theta_{n,m}\right), \tag{7}$$

this lead us to

$$\Theta_{n,m} = O\left(u_n^{-\left[\frac{m+1}{2}\right]}\right). \tag{8}$$

Remark 1 For all $n \in \mathbb{N}$, we have

$$\lim_{n\to\infty} u_n \Theta_{n,2} = \lim_{n\to\infty} \frac{2(1+u_n x)}{u_n} = 2x. \tag{9}$$

2 Local Approximation Properties

Next, we estimate the approximation of the defined operators (1), by a new type of Lipschitz maximal function with order $r \in (0, 1]$, defined by Lenze [7] as

$$\kappa_r(g, x) = \sup_{x,s\geq 0} \frac{|g(u) - g(v)|}{|u - v|^r}, \quad u \neq v. \tag{10}$$

Using the definition of Lipschitz maximal function, we have the following theorem.

Theorem 1 *For any* $g \in C_B[0, \infty)$ *with* $r \in (0, 1]$, *then one can obtain*

$$\left|S_n^*(g; x)(g; x) - g(x)\right| \leq \kappa_r(g, x)\left(\Theta_{n,2}\right)^{\frac{r}{2}}.$$

Proof By Eq. (10), we can write

$$\left|S_n^*(g; x) - g(x)\right| \leq \kappa_r(g, x) S_n^*(|u - v|^r; x).$$

Using, Hölder's inequality with $j = \frac{2}{r}, l = \frac{2}{2-r}$, one can get

$$\left|S_n^*(g; x)(g; x) - g(x)\right| \leq \kappa_r(g, x)\left(S_n^*(g; x)((u - v)^2; x)\right)^{\frac{r}{2}} = \kappa_r(g, x)\left(\Theta_{n,2}\right)^{\frac{r}{2}}.$$

Next theorem is based on modified Lipschitz type spaces [14] and this spaces is defined by

$$Lip_M^{a_1,a_2}(s) = \left\{ g \in C_B[0,\infty) : |g(u) - g(v)| \le M \frac{|u-v|^s}{\left(u + v^2 a_1 + v a_2\right)^{\frac{s}{2}}}, \right.$$
$$\left. \text{where } u, v \ge 0 \text{ are variables, } s \in (0,1] \right\},$$

here, a_1, a_2 are the fixed numbers and $M > 0$ is a constant.

Theorem 2 *For $g \in Lip_M^{a_1,a_2}(s)$ and $0 < s \le 1$, an inequality holds*

$$\left|S_n^*(g;x) - g(x)\right| \le M \left(\frac{\Theta_{n,2}}{x(xa_1 + a_2)}\right)^{\frac{s}{2}}, \quad M > 0.$$

Proof Since $s \in (0,1]$, so we have two cases on s.
Case 1. For $s = 1$, it can be observed that $\frac{1}{t+x^2a_1+xa_2)} \le \frac{1}{x(xa_1+a_2)}$ and it implies

$$\begin{aligned}
\left|S_n^*(g;x) - g(x)\right| &\le S_n^*(|g(t) - g(x)|; x) \\
&\le M S_n^* \left(\frac{|t-x|}{\left(t + x^2 a_1 + x a_2\right)^{\frac{1}{2}}}; x \right) \\
&\le \frac{M}{(x(xa_1 + a_2))^{\frac{1}{2}}} S_n^*(|t-x|; x) \\
&\le \frac{M}{(x(xa_1 + a_2))^{\frac{1}{2}}} \left(\Theta_{n,2}\right)^{\frac{1}{2}} \le M \left(\frac{\Theta_{n,2}}{x(xa_1 + a_2)}\right)^{\frac{1}{2}}.
\end{aligned}$$

Case 2. For $s \in (0,1)$ and using Hölder inequality with $l = \frac{2}{s}$, $m = \frac{2}{2-s}$, we get

$$\begin{aligned}
\left|S_n^*(g;x) - g(x)\right| &\le \left(S_n^*(|g(t) - g(x)|^{\frac{2}{s}}; x)\right)^{\frac{s}{2}} \le M S_n^* \left(\frac{|t-x|^2}{\left(t + x^2 a_1 + x a_2\right)}; x \right)^{\frac{s}{2}} \\
&\le M S_n^* \left(\frac{|t-x|^2}{(x(xa_1 + a_2))}; x \right)^{\frac{s}{2}} \le M \left(\frac{\Theta_{n,2}}{x(xa_1 + a_2)}\right)^{\frac{s}{2}}.
\end{aligned}$$

Thus, the proof is completed.

Theorem 3 *For the continuous and bounded function g defined on $[0,\infty)$, the convergence of the operators can be obtained as*

$$\lim_{n\to\infty} S_n^*(g;x) = g(x), \tag{11}$$

uniformly on any compact interval of $[0,\infty)$.

Proof Using Bohman–Korovkin theorem, we can get our required result. Since $\lim_{n\to\infty} S_n^*(1;x) \to 1$, $\lim_{n\to\infty} S_n^*(t;x) \to x$, $\lim_{n\to\infty} S_n^*(t^2;x) \to x^2$, and hence the proposed

operators $S_n^*(g;x)$ converge uniformly to the function $g(x)$ on any compact interval of $[0,\infty)$.

3 Asymptotic Behaviour of the Operators

To check the asymptotic behaviour of the operators, we shall prove the Voronovskaaya type theorem.

Theorem 4 *Let us consider the function g is integrable, continuous and bounded on* $[0,\infty)$*, as well as the second derivative of the function, exists at a point* $x \in [0,\infty)$*. Then the convergence of the operators can be obtained as*

$$\lim_{n\to\infty} u_n \left(S_n^*(g;x) - g(x)\right) = g'(x) + xg''(x). \tag{12}$$

Proof Using the Taylor's series expansion, one can write

$$g(t) - g(x) = (t-x)g'(x) + \frac{1}{2}(t-x)^2 g''(x) + \zeta(t,x)(t-x)^2, \tag{13}$$

where $\zeta(t,x)$ be such that $\lim_{t\to x}\zeta(t,x) = 0$. Applying the proposed operators to the above Eq. (13), we get

$$S_n^*(g;x)g(t) - g(x) = g'(x)S_n^*(t-x;x) + \frac{g''(x)}{2}S_n^*((t-x)^2;x) + S_n^*\left(\zeta(t,x)(t-x)^2\right) \tag{14}$$

Here

$$S_n^*\left(\zeta(t,x)(t-x)^2\right) \le \sqrt{S_n^*\left(\zeta^2(t,x)\right) S_n^*\left((t-x)^4\right)} \tag{15}$$

Using Theorem 3, we get

$$\lim_{n\to\infty} S_n^*\left(\zeta^2(t,x)\right) = \zeta^2(x,x) = 0. \tag{16}$$

And using Lemma 1, we have

$$S_n^*\left((t-x)^4\right) = O\left(u_n^{-2}\right), \tag{17}$$

thus

$$\lim_{n\to\infty} S_n^*\left(\zeta(t,x)(t-x)^2\right) = 0 \tag{18}$$

Therefore, from Eq. (14) and Lemma 1, one can write

$$\lim_{n\to\infty} u_n \left(S_n^*(g;x)g(t) - g(x)\right) = g'(x) + xg''(x). \tag{19}$$

Hence, the required result is obtained.

4 Quantitative Approximation

Since we have already discussed the Voronovskaya type theorem and here we shall determine quantitative means of the Voronovskaya type theorem for the proposed operators. Before, proceeding on the main results, we need some functions classes, which are defined below

$B_w[0,\infty) = \{g : [0,\infty) \to \mathbb{R}| \quad |g(x)| \le Mw(x)$ with the supremum norm $\|g\|_w = \sup_{x\in[0,\infty)} \frac{g(x)}{w(x)} < +\infty\}$, where $M > 0$ is a constant depending on g and the spaces

$$C_w[0,\infty) = \{g \in B_w[0,\infty),\ g \text{ is contiuous}\},$$

$$C_w^k[0,\infty) = \{g \in C_w[0,\infty),\ \lim_{x\to\infty} \frac{|g(x)|}{w(x)} = k_g < +\infty\},$$

where $w(x) = 1 + x^2$ is a weight function. Here, the weighted modulus of smoothness is defined in [6] and is denoted by $\Delta(g;\xi)$, given as

$$\Delta(g;\xi) = \sup_{0\le h\le\xi,\ 0\le x\le\infty} \frac{|g(x+h) - g(x)|}{(1+h^2)(1+x^2)}, \qquad g \in C_w^k[0,\infty), \quad \xi > 0. \tag{20}$$

The properties of the weighted modulus of smoothness are as

$$\lim_{\xi\to 0} \Delta(g;\xi) = 0, \tag{21}$$

and

$$\Delta(g;\eta\xi) \le 2(1+\eta)(1+\xi^2)\Delta(g;\xi), \quad \eta > 0. \tag{22}$$

Remark 2 By above relations (22) and (20), one can write

$$\begin{aligned} |g(t) - g(x)| &\le (1 + (t-x)^2)(1+x^2)\Delta(g;|t-x|) \\ &\le 2\left(1 + \frac{|t-x|}{\xi}\right)(1+\xi^2)\Delta(g;\xi)(1+(t-x)^2)(1+x^2). \end{aligned}$$

Theorem 5 *For the function $g \in C_w^k[0,\infty)$ and assuming $g''(x)$ exists at a point x, the following inequality holds:*

$$u_n\left|S_n^*(g;x)-g(x)-\frac{g'(x)}{u_n}-\frac{g''(x)}{u_n}\left(x+\frac{1}{u_n}\right)\right|=O(1)\Delta\left(g'',\sqrt{\frac{1}{u_n}}\right). \quad (23)$$

Proof By Taylor's series expansion, one can obtain

$$g(t)-g(x)=g'(x)(t-x)+\frac{g''(x)}{2}(t-x)^2+\zeta(t,x), \quad (24)$$

where $\zeta(t,x)=\frac{g''(\theta)-g''(x)}{2!}(\theta-x)^2$ and $\theta\in(t,x)$. Applying operators (1) and multiplying by u_n on both sides to above expansion, we obtain

$$u_n\left|S_n^*(g;x)-g(x)-g'(x)S_n^*(t-x;x)-\frac{g''(x)}{2}S_n^*((t-x)^2;x)\right|\le u_nS_n^*(|\zeta(t,x)|;x)$$

$$u_n\left|S_n^*(g;x)-g(x)-\frac{g'(x)}{u_n}-\frac{g''(x)}{u_n}\left(x+\frac{1}{u_n}\right)\right|\le u_nS_n^*(|\zeta(t,x)|;x).$$

On the other hand,

$$\begin{aligned}\frac{g''(\theta)-g''(x)}{2}&\le\frac{1}{2}(1+(\theta-x)^2)(1+x^2)\Delta(g'',|\theta-x|)\\&\le\frac{1}{2}(1+(t-x)^2)(1+x^2)\Delta(g'',|t-x|)\\&\le\left(1+\frac{|t-x|}{\delta}\right)(1+\delta^2)(1+(t-x)^2)(1+x^2)\Delta(g'',\delta),\end{aligned}$$

and it can be written as

$$\left|\frac{g''(\theta)-g''(x)}{2}\right|\le\begin{cases}2(1+\delta^2)^2(1+x^2)\Delta(g'',\delta), & |t-x|<\delta,\\ 2(1+\delta^2)^2(1+x^2)\frac{(t-x)^4}{\delta^4}\Delta(g'',\delta), & |t-x|\ge\delta.\end{cases} \quad (25)$$

So, for $\delta\in(0,1)$, we get

$$\left|\frac{g''(\theta)-g''(x)}{2}\right|\le 8(1+x^2)\left(1+\frac{(t-x)^4}{\delta^4}\right)\Delta(g'',\delta). \quad (26)$$

Hence,

$$(|\zeta(t,x)|;x)\le 8(1+x^2)\left((t-x)^2+\frac{(t-x)^6}{\delta^4}\right)\Delta(g'',\delta).$$

Thus, applying the proposed operators (1) to the both sides and using the Lemma 1, we get

$$S_n^*(|\zeta(t,x)|;x) \le 8(1+x^2)\Delta(g'',\delta)\left(S_n^*((t-x)^2;x)+\frac{S_n^*((t-x)^6;x)}{\delta^4}\right)$$
$$\le 8(1+x^2)\Delta(g'',\delta)\left(O\left(\frac{1}{u_n}\right)+\frac{1}{\delta^4}O\left(\frac{1}{u_n^3}\right)\right), \quad \text{as } u_n\to\infty.$$

Choose, $\delta=\sqrt{\frac{1}{u_n}}$, then

$$S_n^*(|\zeta(t,x)|;x) \le 8O\left(\frac{1}{u_n}\right)(1+x^2)\Delta\left(g'',\sqrt{\frac{1}{u_n}}\right). \tag{27}$$

Thus, it yields as

$$u_n S_n^*(|\eta(t,x)|;x) = O(1)\Delta\left(g'',\sqrt{\frac{1}{u_n}}\right). \tag{28}$$

By (25) and (28), we obtain the required result.

4.1 Grüss Voronovskaya Type Theorem

In 1935, Grüss [5], developed an inequality known as Grüss inequality after his name, which has vital importance in the theory of approximation. It estimates with a relation of integral of a product and product of integrals of the two function. First of all, Gal and Gonska [2] applied this inequality on the Bernstein's operators to discuss the Grüss Voronovskaya type theorem, and after this significant contribution in this direction, many researchers put their efforts to develop interesting ideas using the Grüss inequality. In a note [4], the authors obtained a new approach with the help of the least concave majorant by using Grüss inequality to the operators on a compact interval. Some research regarding Grüss Voronovskaya can be seen in [1, 16, 17, 19].

Theorem 6 *If $f, g \in C_w^k[0,\infty)$ for which $f', f'', g', g'' \in C_w^k[0,\infty)$, then for each $x \ge 0$, an expression can be obtained, which is*

$$\lim_{n\to\infty} u_n\left(S_n^*(fg;x)-S_n^*(f;x)S_n^*(g;x)\right)=2xf'(x)g'(x). \tag{29}$$

Proof For the function $f, g \in C_w^k[0,\infty)$ with $f', f'', g', g'' \in C_w^k[0,\infty)$, we can write

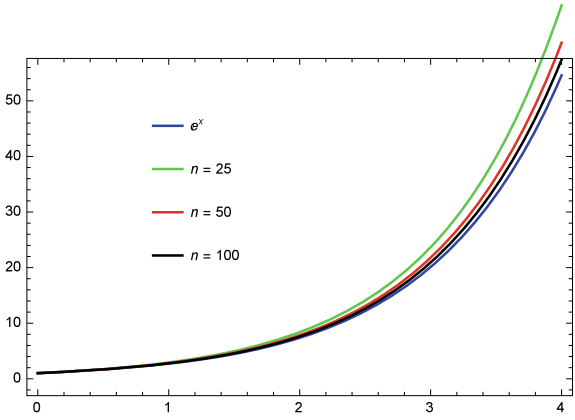

Fig. 1 Convergence of operators $S_n^*(g;x)$ to the function $g(x)$ $(blue)$

$$
\begin{aligned}
n\left(S_n^*(fg;x) - S_n^*(f;x)S_n^*(g;x)\right) = n\Bigg\{&\left(S_n^*(fg;x) - f(x)g(x) - (fg)'\Theta_{n,1} - \frac{(fg)''}{2!}\Theta_{n,2}\right)\\
&-g(x)\left(S_n^*(f;x) - f(x) - f'(x)\Theta_{n,1} - \frac{f''(x)}{2!}\Theta_{n,2}\right)\\
&-S_n^*(f;x)\left(S_n^*(g;x) - g(x) - g'(x)\Theta_{n,1} - \frac{g''(x)}{2!}\Theta_{n,2}\right)\\
&+\frac{g''(x)}{2!}S_n^*((t-x)^2;x)\left(f - S_n^*(f;x)\right) + f'(x)g'(x)\Theta_{n,2}\\
&+g'(x)\Theta_{n,1}\left(f - S_n^*(f;x)\right)\Bigg\}.
\end{aligned}
$$

Applying Theorem 3 for each $x \in [0,\infty)$, $n \to \infty$, as well as using Remark 1, then with the help of Theorem 5, we get our desired result.

$$\lim_{n\to\infty} u_n\left(S_n^*(fg;x) - \mathcal{U}_n^{[\alpha]}(f;x)S_n^*(g;x)\right) = 2xf'(x)g'(x).$$

Example 1 For the approximation by the operators defined by (1) to the given function, here, we consider the function $g : [0,4] \to [0,\infty)$ such that $g(x) = e^x$ (blue), for all $x \in [0,4]$. Choosing $n = 25, 50, 100$ and corresponding operators are as S_{25}^* (green), S_{50}^* (red), S_{100}^* (black), shown in Fig. 1. Here, the approach of the operators can be seen in given Fig. 1. As the value of n is increased, the operators approach towards the function. For large value of n, the approximation is good.

Example 2 Let the function $g = x^2 \sin 2\pi x$ (blue). For the values of $n = 50$, 100, 150, 200, 300, the approach of the corresponding operators S_{50}^*, S_{100}^*, S_{150}^*, S_{200}^*, S_{300}^*, represented by pink, red, magenta, black, green colours, respectively in Fig. 2, to the function is good for large value of n.

Conclusions and applications: Here we have determined the approximation properties for the functions belonging to different spaces and the order of approxima-

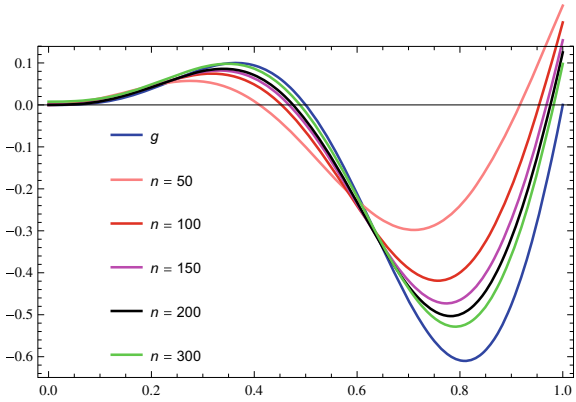

Fig. 2 Convergence of operators $S_n^*(g;x)$ to the function $g(x)$ $(blue)$

tion of the operators has been estimated. The asymptotic behaviour of the operators is discussed and we determined the quantitative means of the asymptotic formula, as well as proved the Grüss Voronovskaya type theorem. Finally, we have justified the approximation results by graphical representations. Derived results are all beneficial and these can be applied in mathematical analysis, mathematical physics and quantum calculus with q and (p,q) analogues of the proposed operators. Concerning the proposed operators as for the applications, one can apply these in the integral equations to solve the Volterra and Fredholm equations of the first and second kind for the numerical approximate solutions. Also, some specific differential equations with boundary conditions can be solved.

References

1. Deniz EM (2016) Quantitative estimates for Jain-Kantorovich operators. Commun Fac Sci Univ Ank Sér A1 Math Stat 65(2):121–132
2. Gal S, Gonska H (2014) Grüss and Grüss-Voronovskaya-type estimates for some Bernstein-type polynomials of real and complex variables. arXiv:1401.6824
3. Gandhi RB, Deepmala, Mishra VN (2017) Local and global results for modified Szász-Mirakjan operators. Math Methods Appl Sci 40(7):2491–2504
4. Gonska H, Tachev G (2011) Grüss-type inequalities for positive linear operators with second order moduli. Matematiçki vesnik 63(4):247–252
5. Grüss G (1935) Über das Maximum des absoluten Betrages von $\frac{1}{b-a}\int_a^b f(x)g(x)dx - \frac{1}{(b-a)^2}\int_a^b f(x)dx \int_a^b g(x)dx$. (German) Math Z 39(1):215–226
6. Ispir N (2007) Rate of convergence of generalized rational type Baskakov operators. Math Comput Model 46(5–6):625–631
7. Lenze B (1988) On Lipschitz-type maximal functions and their smoothness spaces. Indagationes Mathematicae (Proc) 91(1):53–63
8. Mazhar S, Totik V (1985) Approximation by modified Szász-operators. Acta Scientiarum Mathematicarum 49(1–4):257–269

9. Mirakjan GM (1941) Approximation of continuous functions with the aid of polynomials. Dokl Acad Nauk SSSR 31:201–205
10. Mishra VN, Gandhi RB (2017) A summation-integral type modification of Szász-Mirakjan operators. Math Methods Appl Sci 40(1):175–82
11. Mishra VN, Yadav R (2018) Some estimations of summation-integral-type operators. Tbilisi Math J 11(3):175–91 Sep
12. Mishra VN, Gandhi RB, Nasaireh F (2016) Simultaneous approximation by Szász-Mirakjan-Durrmeyer-type operators. Bollettino dell'Unione Matematica Italiana 8(4):297–305
13. Mishra VN, Gandhi RB, Mohapatra RN (2016) A summation-integral type modification of Szász-Mirakjan-Stancu operators. J Numer Anal Approx Theory 45(1):27–36 Sep 19
14. Özarslan MA, Actuğlu H (2013) Local approximation properties for certain King type operators. Filomat 27(1):173–181
15. Szász O (1950) Generalization of S. Bernstein's polynomials to the infinite interval. J Res Nat Bur Standards 45:239–245
16. Tariboon J, Ntouyas SK (2014) Quantum integral inequalities on finite intervals. J Inequal Appl 2014(1):121 Dec 1
17. Ulusoy G, Acar T (2016) q-Voronovskaya type theorems for q-Baskakov operators. Math Methods Appl Sci 39(12):3391–401 Aug
18. Yadav R, Meher R, Mishra VN (2020) Further approximations on Durrmeyer modification of Szász-Mirakjan operators. Eur J Pure Appl Math 13(5):1306–1324
19. Yadav R, Meher R, Mishra VN (2019) Approximations on Stancu variant of Szász-Mirakjan-Kantorovich type operators. arXiv:1911.11479

Fuzzy Approach to Solve General De-Novo Programming Problem

Sayanta Chakraborty and Debasish Bhattacharya

Abstract A General De-Novo Programming Problem (GDNPP) is a multi-objective De-Novo Programming Problem (MODNPP) involving both maximizing and minimizing type of objectives. In this paper, a modified fuzzy approach is adopted to solve GDNPP by means of reflection of decision-maker's choice. It is seen that flexibility in decision-maker's choice to some extent could be reflected in multi-objective linear programming problem (MOLPP) using Meta-Goal Programming (GP) technique. This flexibility in decision process can also be efficiently incorporated using fuzzy technique to solve GDNPP, which is achieved by introducing new constraints as per requirement of the problem. Moreover, these constraints could be so chosen that the highest possible number of objectives could attain their ideal values. This is a new type of flexibility introduced in the decision process. The proposed method of solution has been illustrated by a numerical example. Finally, the solutions obtained have been compared with those of other existing method of solving GDNPP.

Keywords Multi-objective De-Novo Programming · Non-compensatory operator · Ideal values · Meta-GP

1 Introduction

The De-Novo Programming Problem (DNPP) introduced by Zeleny [17] is popularly used to design an optimal system by extending existed resources (if necessary) instead of finding an optimum in a given system with fixed resources. The main advantage of De-Novo Programming is that through this approach a decision-maker can obtain trade-off free solution for its objectives. In his papers [13–23], Zeleny considered only maximizing type of objective functions. Now there was no general method to solve MODNPP containing both maximizing and minimizing type of objectives. But to apply the DNPP technique for the solution of real-life problems, DNPP having both maximizing and minimizing type of objectives, also known as General De-Novo

S. Chakraborty (✉) · D. Bhattacharya
NIT Agartala, Jirania 799046, India
e-mail: sayantasmailbox@gmail.com

J. Singh et al. (eds.), *Advances in Mathematical Modelling, Applied Analysis and Computation*, Lecture Notes in Networks and Systems 415,
https://doi.org/10.1007/978-981-19-0179-9_10

Programming Problem (GDNPP), has to be considered. Later on some researchers, e.g., Li and Lee [7], Chen [4], Nurullah [12] solved GDNPP. The first two authors utilized fuzzy techniques for the solution of the problem by replacing the objectives by their membership functions. While Nurullah employed min–max Goal Programming (GP) technique for its solution, which is akin to fuzzy method. In [1, 2], authors solved GDNPP using compensatory and non-compensatory operators under fuzzy environment.

In fuzzy method of solution of MOLPP, the overall performance of the system is maximized, i.e., overall satisfaction of the decision-maker is maximized. But it is beyond the scope of fuzzy MOLPP techniques to maximize the level of satisfaction of all the objectives separately or paying attention to a particular set of objectives for their attainment of highest level of membership values. Also due to the conflicting nature of the objectives, it is impossible to optimize all the conflicting objectives simultaneously. Thus fuzzy methods of solution of GDNPP elicit solution giving moderate values of the objectives. But decision-maker's choice of attaining some targeted values to a specified set of objectives could not be taken into account. This is a drawback of fuzzy methods in solving DNPP in its true spirit.

To overcome this weakness of fuzzy method, Rodriguez et al. [9] introduced meta-GP in 2002, based on some variants of GP, to solve MOLPP by incorporating flexibility. Through this approach a decision-maker can set some additional goals (which are not real goals), called meta-goals [2], to offer more flexibility for preference expression. One of the advantages of meta-GP is that the decision-maker can use any one of the GP variants for the solution process. The decision-maker can set an aspiration level for each goal in the chosen GP variant. The meta-goals can be thought of as a "secondary/derived goals" from the original set of explicit goals. So through meta-GP approach, flexibility can be incorporated in the solution of any MOLPP. In [9], the authors proposed three types of meta-goals for reflecting decision-maker's choice, which are given as follows:

Type 1 meta-goal: The pro-rata-based sum of unwanted deviations (represented by deviation variables) should not exceed a certain bound.

Type 2 meta-goal: The maximum percentage of deviation of some goals in concern (i.e., some of the goals) should not exceed a certain bound.

Type 3 meta-goal: Among some specifically watched explicit goals, the percentage of (the number of) unachieved goals should not exceed a certain bound.

Finally, the authors minimized the deviations of the achievement of the meta-goals from their targeted values using lexicographic, min–max, and weighted GP techniques.

But in this meta-GP method too it has been seen that if a large number of constraints are used in the problem formulation, then the solution may render to infeasibility [9]. So a limited number of constraints were used in the problem formulation. Due to such constraints it has been seen that few objectives could reach to their ideal values (as per the choice of the decision-maker), whereas the others could not and in fact they assume worst possible values (negative ideal values).

In 2017, Zhuang et al. [25] used meta-GP technique to solve GDNPP. Here also the authors considered three types of meta-goals as explained above. Meta-GP approach

of solving GDNPP also suffers from the similar limitations as mentioned above. So it would be very much pertinent and appreciable if the highest number of objectives in a GDNPP could get to their respective ideal values and at the same time the overall performance of the system could be maximized. With this motivation, by annexing some additional constraints (like the secondary goals in meta-GP) to the fuzzy method [1–3], a new method of solving GDNPP is introduced. The introduced method inherits the merits of both of the fuzzy method and meta-GP technique to solve GDNPP.

In literature [1, 2, 7], it has been seen that when a GDNPP is solved by fuzzy method, then the solution yields overall satisfaction of the decision-maker in the form of moderate objective values. However, there is no space of reflecting decision-maker's choice in the solution process. But generally decision-maker wants to incorporate flexibility in choosing certain objectives of his/her interest which he/she intends to get to their respective ideal values [9, 25]. This is based on the ground reality of the problem.

1.1 Research Gap

So far our knowledge is concern, as in GDNPP, the objectives are conflicting in nature, so there exists no method available in the literature through which maximum number of objectives could reach their ideal values and at the same time, the overall performance of the decision-making process could be maximized. Also the decision-maker's choice could not be reflected in the decision-making process through the existing approaches of solving GDNPP.

1.2 Novelty

In the present treatise, it has been seen that flexibility in the decision process could also be embedded to fuzzy technique [1, 2, 7] of solving GDNPP by incorporating some additional constraints as per the requirement of the problem or choice of the decision-maker. The benefit of the proposed fuzzy method is that it maximizes the overall performance of the system as well as satisfies the additional constraints. Also by judicious choice of the additional constraints, the highest possible number of objectives could attain their ideal values. The number of such objectives could be determined and possible combinations of such objectives could also be ascertained. This is a new type of flexibility in the decision process. The novelty of the proposed method is threefold.

i. First of all, it provides a way in ascertaining the highest possible number of objectives which could attain their ideal values and their possible combinations.

ii. Secondly, it elicits solution with highest number of objectives attaining their ideal values.
iii. Thirdly, overall performance of the system is maximized.

The method has been discussed with the help of a real-life example and the results obtained by the proposed approach have also been compared with the existing methods.

With this aim the paper has been organized as follows:

In Sect. 1, a brief introduction of the previous works related to the proposed approach is given. Section 2 consists of three sub-sections, namely, Sects. 2.1, 2.2, and 2.3 where, respectively, the Zimmermann's technique, the proposed method, and the algorithm of the solution procedure of the proposed method have been discussed. In Sect. 3, a numerical problem is solved using the proposed method and the results are compared with that obtained by the existing methods. Finally, Sect. 4 includes conclusion and the proposed future works.

2 Proposed Approach for Solving GDNPP

Before describing the proposed approach it is necessary to know briefly the process of solution of GDNPP under fuzzy environment using Zimmermann's non-compensatory operator λ introduced by the authors in [1–3].

2.1 Solution of MODNPP Using Zimmermann's Non-compensatory Operator λ

To describe this method, let us first consider a GDNPP [7] as follows:

$$\left.\begin{array}{c} \text{Max } \mathbf{Z_k} = \sum_{\mathbf{j}=1}^{\mathbf{n}} \mathbf{c_{kj}x_j}, \mathbf{k} = 1, 2, \ldots, \mathbf{l} \\ \text{Min } \mathbf{W_s} = \sum_{\mathbf{j}=1}^{\mathbf{n}} \mathbf{c_{sj}x_j}, s = 1, 2, \ldots, r \\ subject\ to \sum_{\mathbf{j}=1}^{\mathbf{n}} \mathbf{a_{ij}x_j} - \mathbf{b_i} \leq 0, \mathbf{i} = 1, 2, \ldots, \mathbf{m} \\ \sum_{\mathbf{i}=1}^{\mathbf{m}} \mathbf{p_i b_i} \leq B \\ \mathbf{x_j} \geq 0, j = 1, 2, \ldots, n \end{array}\right\} \quad (1)$$

Now $\sum_{i=1}^{n} p_i a_{ij}$ represents per unit cost of the product j. Let us denote it by a variable v_j. Then $\sum_{i=1}^{n} p_i a_{ij} = v_j$, j = 1, 2, ..., m. The constraints of system (1) can be rewritten as $\sum_{i=1}^{n} p_i \sum_{j=1}^{n} a_{ij} x_j \leq \sum_{i=1}^{m} p_i b_i$ or, $\sum_{j=1}^{n} (\sum_{i=1}^{m} p_i a_{ij}) x_j \leq B$, that is, $\sum_{j=1}^{n} v_j x_j \leq B$. Thus using v_j, system (1) can be reframed as

$$\left.\begin{array}{c} \text{Max } Z_k = \sum_{j=1}^{n} c_{kj}x_j,\ k = 1, 2, \ldots, l \\ \text{Min } W_s = \sum_{j=1}^{n} c_{sj}x_j,\ s = 1, 2, \ldots, r \\ \text{subject to } \sum_{j=1}^{n} v_j x_j \le B \\ x_j \ge 0,\ j = 1, 2, \ldots, n \end{array}\right\} \tag{2}$$

In fact, systems (1) and (2) are equivalent [7].

There are n basic feasible solutions (BFSs) of system (2) which are given by $(\frac{B}{v_1}, 0, \ldots, 0)$, $(0, \frac{B}{v_2}, 0, \ldots, 0), \ldots, (0, 0, \ldots 0, \frac{B}{v_n})$. Substituting each of these n BFSs to all the objectives one by one, the ideal values, that is, max (respectively, min) values of the maximizing (respectively, minimizing) objectives could be easily determined. These are

Let $Z_k^* = \text{Max}Z_k(x) = \text{Max}(c_{k1}\frac{B}{v_1}, c_{k2}\frac{B}{v_2}, \ldots, c_{kn}\frac{B}{v_n})$ and

$W_s^* = \text{Min}W_s(x) = \text{Min}(c_{s1}\frac{B}{v_1}, c_{s2}\frac{B}{v_2}, \ldots, c_{sn}\frac{B}{v_n})$. Thus, the ideal point α^* of the system for the present state is given by $\alpha^* = (Z_1^*, Z_2^*, \ldots, Z_l^*, W_1^*, W_2^*, \ldots, W_r^*)$.

Alternatively solving (l + r) single-objective Linear Programming Problems (LPPs) independently subject to the single constraint $\sum_{j=1}^{n} v_j x_j \le B$, the decision-maker maximizes each of the objectives $Z_1, Z_2, \ldots, Z_l$ and minimizes each of the objectives $W_1, W_2, \ldots, W_r$ to find the ideal point α^* based on the present configuration and available resources.

Further, let the pessimistic values of the objective functions obtained by Luhandjula's technique [8] be, respectively, given by $\widehat{Z}_1, \widehat{Z}_2, \ldots, \widehat{Z}_l, \widehat{W}_1, \widehat{W}_2, \ldots, \widehat{W}_r$. The linear membership functions [7] for the objectives of (2) are constructed as follows:

$$\mu_{Z_k} = \begin{cases} 0, & Z_k \le \widehat{Z}_k \\ \frac{Z_k - \widehat{Z}_k}{Z_k^* - \widehat{Z}_k}, & \widehat{Z}_k < Z_k < Z_k^*,\ k = 1, 2, .., l \\ 1, & Z_k \ge Z_k^* \end{cases} \tag{3}$$

$$\mu_{W_s} = \begin{cases} 0, & W_s \ge \widehat{W}_s \\ \frac{\widehat{W}_s - W_s}{\widehat{W}_s - W_s^*}, & W_s^* < W_s < \widehat{W}_s,\ s = 1, 2, .., r \\ 1, & W_s \le W_s^* \end{cases} \tag{4}$$

These membership functions indicate the degree of satisfaction of the decision-maker for the attainment of the aspiration levels (here the ideal values) of the corresponding objectives.

Zimmermann's operator $\lambda = \min\{\mu_{Z_k}, \mu_{W_s}\}$ is a non-compensatory operator because it is used to represent "logical and" or "fuzzy and". It does not take the maximum possible values of the individual membership functions into consideration. Using the non-compensatory operator λ for the solution of the GDNPP (2) under fuzzy environment, the authors in [1, 2] proposed the following model:

$$\left.\begin{array}{c} Max\lambda \\ \text{subject to } \lambda \leq \frac{Z_k - \widehat{Z}_k}{Z_k^* - \widehat{Z}_k}, k = 1, 2, \ldots, l \\ \lambda \leq \frac{\widehat{W}_s - W_s}{\widehat{W}_s - W_s^*}, s = 1, 2, \ldots, r \\ \sum_{j=1}^{n} v_j x_j \leq B \\ x_j \geq 0, j = 1, 2, \ldots, n \\ \lambda \in [0, 1] \end{array}\right\} \quad (5)$$

It has been seen that system (5) yields a solution which maximizes the overall performance of the system, that is, yielding intermediate objective values lying between their optimistic (here ideal values) and pessimistic values (obtained by Luhandjula's technique). As mentioned earlier, there is no scope of reflecting decision-maker's choice regarding the attainment of specific objective values. Also the spirit of De-Novo Programming [4–7, 10–12, 17–19, 21–26] for the attainment of as many objectives as possible to their respective ideal values under the given budgetary provision is also not fulfilled.

2.2 Proposed Method

The method proposed here takes care of the flexibility in decision-maker's choice along with maximizing the overall performance of the system. This is achieved by incorporating some additional constraints in system (5) for solving a GDNPP under fuzzy environment.

The additional constraints are constructed as follows:

Type-I Constraint

The first set of constraints is the goal constraints representing the aspiration levels (ideal values) of each objective. For maximizing and minimizing objectives, they are, respectively, $Z_k + n_k = Z_k^*$ and $W_s - p_s = W_s^*$. In [25], both positive and negative deviation variables n_k, p_k (respectively, n_s, p_s) in each of the goal constraints were used. But here only negative and positive deviation variables, respectively, have been used for maximizing and minimizing objectives. This is because of the simple reason that a maximizing objective can never exceed its ideal value and minimizing objective cannot be less than its ideal values. This will reduce the number of deviation variables.

Type-II Constraint

The second set of constraints are formed introducing some binary variables y_i, one for each goal constraint of Type-I. The binary variable y_i assuming the value 1 reflects that the corresponding objective must not attain its ideal value, whereas $y_i = 0$ indicates that the objective attains its ideal value. To achieve this the binary variables

are multiplied with a large positive integer (say 10 times of the corresponding ideal value Z_k^* *or* W_s^*) and are subtracted from the corresponding deviation variable n_k or p_s. The difference is constrained to be non-positive. Thus, the second set of constraints could be represented as $n_k - 10Z_k^* y_k \leq 0$, for kth maximizing objective and $p_s - 10W_s^* y_s \leq 0$, for sth minimizing objective.

Also if the decision-maker considers that the maximum number of unachieved goals should not exceed a certain bound (a positive integer I) then the binary variables introduced in Type-II goal constraints must satisfy $\sum_{i=1}^{l+r} y_i \leq I$, where l, r, respectively, denote the number of maximizing and minimizing objectives of the problem. Introducing one negative deviation variable β, the corresponding goal constraint takes the form $\sum_{i=1}^{l+r} y_i + \beta = I$ and it states that I is the maximum number of objectives that do not attain their ideal values.

To embed the decision-maker's choice in system (5), we annex the Type-I and Type-II goal constraints to the system and also try to maximize λ and minimize β simultaneously after converting I to a dimensionless quantity. This is done by dividing β by I. Thus, introducing the additional constraints as explained in Sect. 2.2, the proposed method of solution can be described by the following system:

$$\left.\begin{array}{c} Max\lambda - \frac{\beta}{I} \\ subject\,to\,\lambda \leq \frac{Z_k - \widehat{Z}_k}{Z_k^* - \widehat{Z}_k}, k = 1, 2, \ldots, l \\ \lambda \leq \frac{\widehat{W}_s - W_s}{\widehat{W}_s - W_s^*}, s = 1, 2, \ldots, r \\ \sum_{\mathrm{j}=1}^{\mathrm{n}} \mathrm{v_j x_j} \leq \mathrm{B} \\ Z_k + n_k = Z_k^* \\ W_s - p_s = W_s^* \\ n_k - 10 \times Z_k^* \times y_k \leq 0 \\ p_s - 10 \times W_s^* \times y_s \leq 0 \\ \sum_{i=1}^{l+r} y_i + \beta = I \\ \mathrm{x_j} \geq 0, j = 1, 2, \ldots, n \\ n_k \geq 0, k = 1, 2, \ldots, l \\ p_s \geq 0, s = 1, 2, \ldots, r \\ \lambda, \beta \in [0, 1] \\ y_i \in \{0, 1\}, i = 1, 2, \ldots, l + r \end{array}\right\} \quad (6)$$

Again the maximization of λ, the confluence of the membership functions of the objectives tries to maintain the overall satisfaction of the decision process. So that, the other objectives which could not have reached to their ideal values is not very far from their targets. The algorithm based on system (6) of the proposed method is as follows:

2.3 Algorithm

Step 1: Evaluate ideal values Z_k^*, $k = 1, 2, \ldots, l$ and W_s^*, $s = 1, 2, \ldots, r$, respectively, for the maximizing and minimizing objectives and calculate the corresponding BFSs using the process as explained in Sect. 2.1.

Step 2: Place the results obtained in Step 1 in a tabular form. From the table, check the number of objectives who have attained their optimal values for each BFS. From this the maximum number of objectives (Λ say) which could reach to their ideal values corresponding to a particular BFS is found, $\Lambda = l + r - I$.

Step 3: Construct Type-I goal constraints $Z_k + n_k = Z_k^*$ and $W_s - p_s = W_s^*$, where n_k and p_s are, respectively, the negative and positive deviation variables, $k = 1, 2, \ldots, l$; $s = 1, 2, \ldots, r$.

Step 4: Introduce $(l + r)$ number of binary variables y_i, one for each of the $(l + r)$ number of objectives and then formulate corresponding goal constraint $\sum_{i=1}^{l+r} y_i + \beta = I$.

Step 5: The deviation variables introduced in Step 3 are constrained as $n_k - 10Z_k^* y_k \leq 0$ and $p_s - 10W_s^* y_s \leq 0$.

Step 6: Annexing the introduced goal constraints in system (5) formulate system (6) where instead of maximizing λ, $\lambda - \frac{\beta}{I}$ is maximized. Here at the same time λ is maximized and β is minimized.

Step 7: Finally, solve system (6) by using LINGO 18.0 software.

The applicability of the proposed method has been discussed with the help of a real-life example.

3 Numerical Example

Let us consider a numerical problem from example from [25]. In the problem, there are three maximizing objectives Z_1, Z_2, and Z_3 and two minimizing objectives W_1 and W_2 in three decision variables x_1, x_2, and x_3 with $x_i \geq 60$, $i = 1, 2, 3$. So the system has $\binom{3}{1} = 3$ BFSs, given by (as explained in Sect. 2) $x_1 = 98.7$, $x_2 = 60$, $x_3 = 60$; $x_1 = 60$, $x_2 = 60$, $x_3 = 60$ and $x_1 = 98.74189$, $x_2 = 60$, $x_3 = 109.1$.

Next is to find the optimistic and pessimistic values of the objectives. We calculate the value of each objective at each of the BFSs. The calculations are shown in Table 1. The optimistic values are shown in bold face and the pessimistic values are bold and underlined.

From the table, it is clear that the ideal values of the objectives are given by

$$Z_1^* = 6812.192,\ W_1^* = 8.376,\ Z_2^* = 11630184885,\ W_2^* = 900,$$
$$Z_3^* = 8753585.276,\ Z_4^* = 1518.896$$

The pessimistic values of the objectives are determined using Luhandjula's technique [11] and are given by

Table 1 Calculation of optimistic (ideal) and pessimistic values of the objectives

Basic feasible solutions			Optimal values of the objectives					
x_1	x_2	x_3	Z_1	Z_2	Z_3	Z_4	W_1	W_2
98.7	60	60	6812.2	11,630,184,993.1	8,753,585.3	1471.2	9.6	1047.2
60	60	60	5340	8,680,929,660	6,871,620	1200	8.4	900
60	60	109.1	6370.3	9,648,039,659	8,222,953.4	1518.9	11.6	1243.4

$$(\widehat{Z}_k = 5340, \widehat{W}_1 = 11.5993, \widehat{Z}_2 = 8680929660, \widehat{W}_2 = 1243.426,$$
$$\widehat{Z}_3 = 6871620, \widehat{Z}_4 = 1200).$$

From the table, it is clear that for the given problem the maximum number of objectives which could attain their respective ideal values is 3, since for the solution $x_1 = 98.7419$, $x_2 = 60$, $x_3 = 60$, three objectives, namely, Z_1, Z_2, and Z_3 achieved their respective ideal values. Thus, maximum number of unachieved goals, $I = (4 + 2) - 3 = 3$, $\Lambda = l + r - I = 3$.

Thus, for the given problem the proposed method yields the following model:

$$\left.\begin{array}{c} \text{Max}\lambda - \frac{\beta}{3} \\ subject\ to\ \lambda \le \frac{Z_1 - 5340}{6812.192 - 5340} \\ \lambda \le \frac{11.5993 - W_1}{11.5993 - 8.376} \\ \lambda \le \frac{Z_2 - 8680929660}{11630184885 - 8680929660} \\ \lambda \le \frac{1243.426 - W_2}{1243.426 - 900} \\ \lambda \le \frac{Z_3 - 6871620}{8753585.276 - 6871620} \\ \lambda \le \frac{Z_4 - 1200}{1518.896 - 1200} \end{array}\right\} \text{Fuzzy Goal Constraint}$$

$47806358.75x_1 + 42740622.5x_2 + 37751198.75x_3 \le 9550000000$ Budget Constraint

$$\left.\begin{array}{c} Z_1 + n_1 = 6812.192 \\ W_1 - n_2 = 8.376 \\ Z_2 + n_3 = 11630184885 \\ W_2 - n_4 = 900 \\ Z_3 + n_5 = 8753585.276 \\ Z_4 + n_6 = 1518.896 \end{array}\right\} \text{Type-I Constraint}$$

$$\left.\begin{array}{c} n_1 - 68120y_1 \leq 0 \\ n_2 - 80y_2 \leq 0 \\ n_3 - 116301849330y_3 \leq 0 \\ n_4 - 9000y_4 \leq 0 \\ n_5 - 87535850y_5 \leq 0 \\ n_6 - 15180y_6 \leq 0 \\ \sum_{i=1}^{6} y_i + \beta = 3 \end{array}\right\} \text{Type-II Constraint}$$

$$\left.\begin{array}{c} x_1 \geq 60 \\ x_2 \geq 60 \\ x_3 \geq 60 \end{array}\right\} \text{Hard Constraint}$$

$$n_i \geq 0, i = 1, 2, \ldots, 6$$

$$\lambda \in [0, 1]$$

$$y_i \in \{0, 1\}, i = 1, 2, \ldots, 6$$

Solution

By LINGO 18.0 software the solution of the above model is given as follows:

$\lambda = 0.571$, $\beta = 0$, $Z_1 = 6812.192$, $W_1 = 9.573$, $Z_2 = 11630184885$, $W_2 = 1047.219$, $Z_3 = 8753585.276$, $Z_4 = 1471.193$, $n_1 = 0$, $n_2 = 1.197125$, $n_3 = 384.2183$, $n_4 = 147.2192$, $n_5 = 0.255$, $n_6 = 47.70274$, $y_1 = y_3 = y_5 = 0$, $y_2 = y_4 = y_6 = 1$, $x_1 = 98.74189$, $x_2 = 60$, $x_3 = 60$.

It has been seen that three objectives Z_1, Z_2, and Z_3 have reached to their respective ideal values and the other objectives assumed moderate values as reflected by overall satisfaction $(\lambda - \frac{\beta}{3}) = 0.571$. A comparison of the solution obtained by the proposed method and that by Zhuang et al. [25] is furnished in Table 2. It clearly shows that the proposed method yields better solution.

From the comparison table, it is clear that both meta-GP approach and the proposed approach yield same optimal objective values for the given example.

Table 2 Comparison of solution obtained by different methods

Objectives	Ideal values	Meta-GP approach	Proposed approach
Z_1	6812.1922	6812.1922	6812.1922
Z_2	11,630,184,993.06	11,630,184,993.06	11,630,184,993.06
Z_3	8,753,585.31	8,753,585.31	8,753,585.31
Z_4	1518.896	1471.1933	1471.219
W_1	8.3760	9.5731	9.573
W_2	900.00	1083.2192	1047.219

But through the meta-GP approach, neither the overall performance of the decision-making process could not maximized, nor the number of objectives which could reach to their ideal values could be identified. On the other hand, as the proposed approach is a fuzzy approach, so the value of $\lambda = 0.571$ indicates that the overall satisfaction of the decision-making process is fulfilled. At the same time, $y_1 = y_3 = y_5 = 0$ are indicating that their corresponding objectives, that is, Z_1, Z_2, and Z_3 have reached to their ideal values. Also through the proposed model, it could be identified that total number of unachieved goals will be 3.

4 Conclusion

A fuzzy method of solving GDNPP was proposed by the authors in [1–3]. To incorporate flexibility in decision-maker's choice, the said fuzzy method of solving GDNPP has been modified in this paper. Here, by incorporating some additional constraints, decision-maker's choice regarding the objectives and their attainment to the respective ideal values has been achieved. In the process, maximum number of such objectives could also attain their ideal values. To validate the applicability of the proposed method, a numerical example has been solved and compared with meta-GP approach. It has been seen that the proposed method yields same solution as that of meta-GP approach. Also, the proposed approach indicates that the maximum number of unachieved goals is three and the value of $\boldsymbol{\lambda} = 0.571$ indicates that half of the total number of objectives, that is, three objectives could reach to their ideal values. The most promising advantage of this approach is that apart from the desired flexibility to reflect the decision-maker's preference, the overall satisfaction of the decision process could also be maintained. It has been seen that for each GDNPP, all the objectives may not attain their ideal values. Only a certain number of objectives could reach to their ideal values. But the very essence of DNPP is to lead all the objectives to their respective ideal values. In future, this could be investigated either by sensitivity analysis or by investing more resources in terms of investment of more budgets. This approach could be applied to solve any real-life problem which could be modeled as multi-objective optimization problem, like resource allocation, academic planning, budget allocation, etc. In this regard, the parameters could be chosen as triangular or trapezoidal fuzzy numbers.

References

1. Bhattacharya D, Chakraborty S (2015) A new approach to solve general multi-objective De-Novo Programming Problem under fuzzy environment. CGCMS. https://doi.org/10.5176/2251-1911_CMCGS15.06
2. Bhattacharya D, Chakraborty S (2018) Solution of the general MODNPP using compensatory operator under fuzzy environment. J Phys: Conf Ser 1039 012012: 1–8

3. Chakraborty S, Bhattacharya D (2012) A new approach of solution of multi-stage and multi-objective decision-making problem using De-Novo Programming. Eur J Sci Res 79(3):393–417
4. Chen YW, Hsieh HE (2006) Fuzzy multi-stage De-Novo Programming problem. Appl Math Comput 181:1139–1147
5. Fiala P (2011) Multi-objective De-Novo linear programming. Acta Univ Palacki Olomuc Fac Rer Nat Math 5092:29–36
6. Hessel M, Zeleny M (1987) Optimal system designs: towards new interpretation of shadow prices in linear programming. Comput Oper Res 14(4):265–271
7. Li RJ, Lee ES (1990) Fuzzy approaches to multi-criteria De-Novo programs. J Math Anal Appl 153:97–111
8. Luhandjula MK (1982) Compensatory operators in fuzzy linear programming with multiple objectives. Fuzzy Sets Syst 8:24
9. Rodriguez M, Caballero R, Ruiz F, Romero C (2002) Meta goal programming. Eur J Oper Res 136:422–429
10. Sasaki M, Gen M, Yamashiro M (1995) A method for solving Fuzzy De-Novo Programming problem by genetic algorithms. Comput Ind Eng 29(1–40):507–511
11. Saeedia S, Mohammadia M, Torabib SA (2014) A De-Novo Programming approach for a robust closed-loop supply chain design under uncertainty: an M/M/1 queuing model. Int J Ind Eng Comput 6:211–228
12. Umarusman N (2013) Min-Max goal programming approach for solving multi-objective De Novo programming problems. Int J Oper Res 10(2):92–99
13. Zeleny M (1974) A concept of compromise solutions and the method of the displaced ideal. Comput Oper Res 1:479–496
14. Zeleny M (1976) Multi-objective design of high-productivity systems. In: Proceedings of the joint automatic control conference, paper APPL94, New York
15. Zeleny M (1980) Mathematical programming with multiple objectives (Special issue). Comput Ops Res 7:101–107
16. Zeleny M (1981) On the squandering of resources and profits via linear programming. Interfaces 11(S):101–107
17. Zeleny M (1981) A case study in multi-objective design: De-Novo Programming, in multiple criteria analysis. In: Nijkamp P, Spronk J (eds) Operational methods. Lexington Books, Lexington, MA
18. Zeleny M (1982) Multiple criteria decision making. McGraw-Hill, New York
19. Zeleny M (1986) Optimal system design with multiple criteria: De-Novo Programming approach. Eng Costs Product Econ 10:89–94
20. Zeleny M (1998) Multiple criteria decision making: eight concepts of optimality. Hum Syst Manag 17(2):97–107
21. Zeleny M. The evolution of optimality: De-Novo Programming. EMO, LNC, vol 3410, pp 1–13
22. Zeleny M (2005) Optimization, optimal design and De-Novo Programming: discussion notes. Fordham University, New York
23. Zeleny M (2009) On the essential multidimensionality of an economic problem: towards tradeoffs-free Economics. Acta Univ Carolinae Oeconomica 3:154–175
24. Zhang YM, Huang GB, Zhang XD (2009) Inexact De-Novo Programming for water resources system planning. Eur J Oper Res 199:531–541
25. Zhuang Z, Hocine A (2017) Meta goal programming approach for solving multi-criteria de Novo programming problem. Eur J Oper Res 1–11
26. Zimmermann HJ (1978) Fuzzy programming and linear programming with several objective functions. Fuzzy Sets Syst 1:45–55

Comparative Study of Eight Classification Models for Diagnosis and Prediction of Breast Cancer

Hemangini Mohanty and Santilata Champati

Abstract Nowadays, breast cancer is creating wea big problem for women all over the world. Correct and early prediction of disease is very much important for the treatment of curing the disease. Women identified at the stage of benign have high chances of getting curable but identifying at the stage of malignant is regarded as a dangerous state of cancer. Many machine learning algorithms are used for the diagnosis of breast cancer effectively. In this article, eight classification models such as Logistic Regression (LR), K-Nearest Neighborhood (K-NN), Decision Tree (DT), Random Forest (RF), Artificial Neural Network (ANN), Gaussian Naïve Bayes (NB), Support Vector Machine (SVM), and AdaBoost classifier are used for predicting two classes, i.e., benign and malignant. To choose the best fit classification model for prediction, a confusion matrix is used to evaluate the performance of each model. Also, parameters such as accuracy, precision, recall, specificity, F-measure, and Matthews correlation coefficient (MCC) are discussed for each model. For experimental results, the Wisconsin Breast Cancer Diagnosis dataset and Coimbra Breast cancer datasets are used, and at last, a comparison is being done for all of these models.

Keywords Decision Tree (DT) · K-Nearest Neighborhood (K-NN) · Logistic Regression (LR) · Random Forest (RF) · Support Vector Machine (SVM) · Artificial Neural Network (ANN) · Gaussian Naïve Bayes (NB) · AdaBoost Classifier

H. Mohanty (✉)
Department of Centre for Applied Mathematics and Computing, Siksha 'O' Anusandhandhan (Deemed to Be University), Bhubaneswar, India
e-mail: hemangini.newindia@gmail.com

S. Champati
Department of Mathematics, Siksha 'O' Anusandhandhan (Deemed to Be University), Bhubaneswar, India
e-mail: santilatachampati@soa.ac.in

J. Singh et al. (eds.), *Advances in Mathematical Modelling, Applied Analysis and Computation*, Lecture Notes in Networks and Systems 415,
https://doi.org/10.1007/978-981-19-0179-9_11

1 Introduction

Breast cancer is the most commonly occurring cancer disease among women worldwide [1, 2], and about 10% of women is getting affected by breast cancer disease at some stage in their life [3]. Among all types of cancer, it is the second most common cancer overall and in countries like Belgium, Luxembourg, Netherlands, etc., the number of affected women by breast cancer is very high [4]. Approximately, 2 million women are diagnosed in 2018 around the world and 140 out of 148 countries worldwide are frequently diagnosed with this cancer [5]. In the last few years, the rate of increase of this disease is found to be 0.5% per year [5]. The chance of women will die is about 1 in 39 in breast cancer disease. This disease can be curable if detected early. If a woman is diagnosed at the benign stage, then she must be curable and the death rate by this disease can be reduced [6]. So, early diagnosis of this disease is very much important. Data Mining (DM) methods can be helpful to classify a patient as benign or malignant. In many health databases, these DM techniques are proved to be predicting accurate class labels of many diseases [1, 7, 8]. Many researchers are using these techniques to improve the correct prediction of the disease and also to reduce the false-positive and false-negative rates [1].

Supervised learning is a machine learning process that has labeled data. That means you have to train the machine using existing classified data which is well labeled. This will help you to predict the class labels of unknown data [9, 10]. In medical fields, all datasets are well labeled. Hence, a supervised learning algorithm helps to develop predictive models to give accurate prediction results [8]. Classification is a supervised learning process of analysis of datasets by constructing models which describe important data labels [2]. It helps to predict the class labels of new data. It has many applications like medical diagnosis, fraud detection, performance prediction, and target achieving in the market, etc. [8, 10, 11]. In predicting the class labels of a woman affected by breast cancer as benign or malignant classification is the most suitable technique as the dataset is labeled. There are many classifiers used to predict class labels such as Decision Tree classifiers, Random Forest, Bayesian classifiers, Support Vector Machine, K-Nearest Neighborhood, Artificial Neural Network, Logistic Regression Model, and AdaBoost classifier [8, 12].

In this article, the authors discussed eight classification models to predict the class labels of breast cancer by analyzing the dataset collected from the UCI machine learning repository [13]. In the next sections, related works of these techniques, the working methods of these techniques have been described. Then, to choose the best model confusion matrix is used to evaluate the performance measure of all the models. One least-studied classification method named AdaBoost classifier is used to build a model. At last, the comparison of all these eight models is done. In the last section, a conclusion is made.

2 Literature Review

Nowadays, many researchers are applying machine learning techniques to the health database to predict the accurate class labels of disease diagnosis. Many classification algorithms such as DT, Logistic Regression, Random Forest, SVM, and ANN are used to develop a model for prediction of disease diagnosis and to select the best classifier for breast cancer prediction a comparison is also made by their model performance. Ahmad et al. [1] proposed three classification models such as DT, ANN, and SVM for predicting breast cancer disease and comparing their performance on the Iranian Centre for breast cancer program from 1997 to 2008. The authors have shown that SVM is the best classifier among all three models and it gives the highest accuracy 97.1%. Bazazeh et al. [3] made a comparison of three popular ML techniques such as SVM, RF, and BN to Wisconsin original breast cancer dataset, and their results have shown that RF classifier performs better to classify between benign and malignant. They have compared the value of precision, recall, and ROC area of these three techniques to choose the best classifier. Scientific Committee [8] showed that the voting classifier gives 98.90% accuracy to predict the class as benign and malignant. They have also made a comparison of other classifiers such as Gaussian naïve Bayes, logistic regression, neural network, and SVM which gives 93.61%, 97.80%, 98.40%, and 98.50% accuracy, respectively.

3 Data Mining Techniques

Supervised learning and unsupervised learning are two types of learning mechanisms in machine learning. In supervised learning, all data are labeled and so it is easy to classify some new datasets into labeled data. But in unsupervised learning, no labeled data are present, and classifying some new data is a difficult task. In supervised learning, the classification task is mostly found. Mainly, classification is the task of predicting new data into existing labeled data.

Here, we have discussed different steps involved in eight classification models in classifying datasets.

3.1 Logistic Regression (LR)

To predict a data value based on prior observations of a dataset, logistic regression is mainly used which is a kind of statistical analysis method [8]. This is mainly used for classification problems. It helps to find a relationship between a dependent variable (target) and one or more independent variables (predictors) where the dependent variable is categorical/nominal. The logistic regression model makes a model which predicts the probability of a given data entity belongs to the class label. This model

uses the sigmoid function, which takes any real value between zero and one, i.e., $\sigma(t) = \frac{e^t}{e^t+1} = \frac{1}{1+e^{-t}}$ [14].

3.2 Decision Tree Classifier (DT)

A Decision Tree is a supervised learning method which is in the tree form that maps instances to their target value beginning from the root to leaf [1, 12]. It uses a top-down approach which starts from the root as training tuples and the nodes represented associated class labels of training tuples. Mainly it is a graphical representation for predicting class labels by using a solution to a decision based on certain conditions [11]. This algorithm performs the following steps:

- The tree starts with a root node that represents the entire dataset.
- Then using attribute selection measure (ASM) it selects the best attribute in the dataset for splitting. It tells the best way to split the dataset into individual classes.
- Using the splitting attribute, the nodes are labeled and generate the decision tree node.
- Using the subsets of the dataset, make new decision trees. Continue the process until the tree cannot further classify the nodes and the final node gives the class labels which is called a leaf node.

3.3 Random Forest (RF)

Random forest is one of the ensemble techniques that bag decision trees from multiple subsets of a given dataset [1, 3, 8]. This method aims to reduce overfitting to the training dataset. The algorithm consists of two parts:

- Split the dataset into many subsets based on its features and then build a decision tree classifier.
- Bag all the classifiers obtained from every subset and classify the test data. Based on voting or average method classify the data.

3.4 Support Vector Machine (SVM)

SVM is a discriminative classifier that intakes training data. The algorithm results an optimal hyperplane that classifies the data points [1, 7]. The advantage of this method is that it classifies both linear and nonlinear data [3]. This method works in following steps.

- If the data are linearly separable, then using support vectors are used to define a margin. Support vectors are those vectors that are equal distances from both sides of the margin.
- Now, it finds a linear optimal hyperplane that acts as a decision boundary separating all the tuples from one class label to another class label. This hyperplane is the linear separating plane with maximum distances between the nearest support vectors.
- In case of data which are not linearly separable, then a nonlinear mapping is used to transform the original training data into a higher dimension. After data are converted to linear separable form, similarly using support vectors a maximum margin hyperplane can be found. This hyperplane is corresponding to the nonlinear separating hypersurface in the original space.

3.5 K-Nearest Neighborhood (K-NN)

K-NN is a supervised learning algorithm used for classification. It is instance-based learning which uses specific training instances for the prediction of class labels without having a model formed by using the dataset [11]. It uses lazy learners who don't require any model for prediction and the classifier makes a prediction based on the local information [15]. K-NN classification algorithm is performed using the following steps:

- To classify a new sample to a class label, calculate the distance from the sample point to all other sample points in the data. You can use any distance metric like Euclidean distance or Manhattan distance for calculation.
- Choose the number of K-neighbors you want to take into consideration.
- Now, find the K-neighbors of the new sample point and rank the points by increasing order.
- Take the majority of these K-neighbor's sample points and assign the new sample point into the majority class label.

3.6 Artificial Neural Network (ANN)

The artificial neural network is a classification algorithm that assigns weights to each input nodes to predict the output class labels [8]. It is designed as a human brain. All the nodes in the network are called artificial neurons that are connected by edges. Each node is assigned some initial weight. This model computes the output value by using a weighted sum of its inputs nodes and subtracting a bias factor from the sum. These artificial neurons have specified threshold values such that if the output value crosses the threshold value, then the output value will be calculated [1]. This algorithm works as follows:

- In the input layer, all the input nodes are connected to the hidden layer through an edge. All input nodes are assigned some weight randomly.
- Then, calculate net input y_{in} by adding a bias "b" to all input nodes after weights are multiplied with them individually.

$$y_{in} = x_1 w_1 + x_2 w_2 + b$$

- The output of the network is given by $y = f(y_{in})$, where $f(y_{in})$ is the activation function defined as $f(y_{in}) = \begin{cases} 1 & if\ y_{in} > \theta \\ 0 & if\ -\theta \leq y_{in} \leq \theta \\ -1 & if\ y_{in} < -\theta \end{cases}$
- Here, θ is the fixed threshold.
- If the calculated output is equal to the actual output, then the process stops.
- Otherwise, the weights of the input nodes will be adjusted based on the learning rate if an error has occurred for a particular training sample. The updated weight is

$$w_i(new) = w_i(old) + \alpha.t.x_i$$

$$b(new) = b(old) + \alpha.t,$$

where t is the target output value and α is the learning rate defined by the user.
- Continue the process till the calculated output is equal to the actual output.

3.7 Gaussian Naïve Bayes (NB)

Gaussian Naive Bayes is a variant of Naïve Bayes classifier which works on continuous data and data are distributed to a normal (or Gaussian) distribution [8]. Naïve Bayes classifier is a supervised machine learning algorithm based on the Bayes theorem. Gaussian distribution depends on two parameters such as the mean and the standard deviation and there is no covariance between dimensions [8]. The algorithm works as follows:

- First, determine the prior probability of given class labels.
- Then calculate the mean and standard deviation of each attribute. Determine likelihood probability with each attribute for each class.
- The likelihood of the attribute is $P(x_i|c) = \frac{1}{\sqrt{2\pi\sigma^2{}_c}} exp\left(-\frac{(x_i-\mu_c)^2}{2\sigma^2{}_c}\right)$.
- Find posterior probability using the Bayes formula.
  $P(c|x) = \frac{P(x_i|c)P(c)}{P(x)}$.
- Here, $P(c|x)$ is the posterior probability of class (c) at a given attribute (x).
  $P(x_i|c)$ is the likelihood probability of a given class.
  $P(c)$ is the prior probability of class.

$P(x)$ is the prior probability of attribute.

- Assign the input to the higher probability class.

3.8 AdaBoost Classifier

Adaptive Boosting or AdaBoost classifier is an ensemble technique that combines multiple weak classifiers to create a strong classifier to increase the accuracy of the model [11]. It is an iterative process that follows a decision tree model with a depth of one single node. AdaBoost works like the forest of stumps by putting less weight on those who give correct predictions and more weight on those who incorrectly classify instances [16, 17]. This algorithm will be working as follows:

- Initially, each sample is assigned identical weights in the dataset and the initial weight is calculated by 1 divided by the total number of samples.
- The AdaBoost classifier used a decision tree as its base learners. Each decision tree is created with one node and two leaves referred to as stumps. Then random samples are used to fit in the model and predict the class labels for each sample in the original data.
- Now the total error is calculated. The sum of weights of incorrectly classified records is the total error and the value will always lie between 0 and 1.
- Calculate the significance of the base learner by using the following formula:

$$\text{Significance} = \frac{1}{2}\log\left(\frac{1 - total\,error}{total\,error}\right)$$

- Using the value of significance update the weights of each sample. The weights of the sample which classifies correctly decrease their weights and increase the weights of the sample which misclassifies the sample by the following formula:
- For correctly classified samples: $new\,weight = weight \times e^{significance}$.
- For misclassified samples: $new\,weight = weight \times e^{-significance}$.
- Normalize the new sample weight so that their sum is equal to 1. To normalize weight, divide the new weight by the sum of the updated weights.
- Now make the second stump in the forest by using normalized weight. A new dataset was created based on the newly updated sample weight. Hence, the misclassified samples have a higher probability of getting selected. Repeat steps (ii) to (vi) and update the weights for a specified number of iterations.
- In the last step, use the forest of decision trees to make final predictions on data outsides of training data.

After applying all these classification models in the Breast Cancer Diagnosis dataset, a comparison of performance measures of these models plays a very significant role. To find out the best classification model accuracy is a measure to be calculated and it is determined by the number of correct predictions divided by the total number of sample size. A confusion matrix is another most popular method

Table 1 Confusion matrix for a binary classification

		Predicted class label	
		Benign	Malignant
Accurate class label	Benign	True positives (TP)	False negatives (FN)
	Malignant	False positives (FP)	True negative (TN)

used for calculating various performance measures of a classification model [8, 11, 18]. It is a specific table that is used to estimate the performance of an algorithm. Mainly, it is used to summarize the performance of a classification algorithm. Here, each sample can be classified into two classes: benign and malignant. The matrix is consisting of four elements (Table 1).

TP (True Positive)—Patients who are sick correctly predicted as sick.

TN (True Negative)—Patients who are healthy correctly predicted as healthy.

FP (False Positive)—Patients who are healthy incorrectly predicted as sick.

FN (False Negative)—Patients who are sick are incorrectly classified as healthy.

Using these four basic factors other evaluation measures can be evaluated to measure the goodness of the classification model.

1. Accuracy: Accuracy is a measurement of how well a model can correctly predict the class label of their actual class label [3, 8, 18]. It is calculated by the number of correct predictions divided by the total number of samples.

$$\text{Accuracy} = \frac{TP + TN}{N} \tag{1}$$

2. Precision: Precision is the rate of correctly predicted positive class labels from the total number of predicted positive classes [3, 8, 18].

$$\text{Precision} = \frac{TP}{TP + FP} \tag{2}$$

3. Recall/sensitivity: It is the effectiveness of a model how well it predicts the positive class labels from the total number of actual positive classes [3, 18]. It is also known as the true positive rate.

$$\text{Recall} = \frac{TP}{TP + FN} \tag{3}$$

4. Specificity: It is the rate of the correctly predicted negative class label from the total number of the actual negative class label [1, 8, 18]. It is also known as selectivity or true negative rate.

$$\text{Specificity} = \frac{TN}{FP + TN} \tag{4}$$

5. Misclassification error rate: Error is classifying a sample belonging to a positive class into predicted as a negative class label or belong to negative class into predicted as positive class label [11]. The error rate is the percent of misclassified samples out of the total samples in the dataset.

$$\text{Error rate} = 1 - \text{Accuracy} \tag{5}$$

6. F-measure: It is a metric that takes into account both precision and recall. Mainly, it is the harmonic mean of precision and recall [8, 18, 19].

$$\text{F-measure} = 2 \times \frac{precision \times recall}{precision + recall} \tag{6}$$

7. Matthews correlation coefficient (MCC): Biochemist Brian W. Matthews has introduced this correlation coefficient in 1975 [19]. This coefficient is used as a measurement of the quality of binary classification and the coefficient is considered as a balance measure where the classes are of very different sizes. The MCC is a correlation coefficient that lies between −1 and 1 from the actual and predicted binary classifications. −1 represents total disagreement of actual and predicted class, 0 represents no better than random prediction, and +1 indicates a perfect prediction. The coefficient can be determined by using the following formula [19]:

$$MCC = \frac{TP \times TN - FP \times FN}{\sqrt{(TP + FP)(TP + FN)(TN + FP)(TN + FN)}} \tag{7}$$

4 Results and Discussion

In this section, we have shown the experimental results of these eight classification techniques incorporated in the proposed datasets.

4.1 Data Pre-processing

In this article, we have used the most popular dataset Wisconsin Diagnostic Breast Cancer (WDBC) from the machine learning repository of the University of California, Irvine [13]. WDBC data was taken from the University of Wisconsin, Dr. William H. Wolberg, W. Nick Street, and Olvi L. Mangasarian. In this dataset, a total of 569 instances and ten real value attributes, and one outcome variable are present. This dataset represents two types of cancer patients, i.e., benign and malignant can be diagnosis by ten input features. There is no missing attribute value contained in the dataset. From 569 instances, 357 instances are benign and 212 instances are

malignant. Also, three indicators are measured which are presented in the dataset: mean, standard error, and maximum value. So, there is a 569×32 matrix from which we remove two attributes that represent ID and Diagnosis. Now the present matrix has 569×30. To reduce the dimensionality of the dataset, we used Principal Component Analysis (PCA). Using PCA we found that only two principal components retained approximately 99.8% of information from the original dataset. After that, we split the dataset into training data (455 instances) and testing data (114 instances). Then, the eight classification models were performed to the training data and testing data. All the algorithms are successfully run in Python 3.3 and using the confusion matrix model performance was measured. Then, we consider another breast cancer dataset from the Faculty of Medicine of the University of Coimbra (CBC) to test our result validation. This dataset contains 116 instances and 10 attributes. There are no missing values found in the dataset. The same procedure has been applied for data pre-processing. All the results are described below.

4.2 Results and Discussion

To evaluate the performance measure of each classification model, a confusion matrix is used. From the matrix, parameters such as accuracy, precision, recall, specificity, and F-measure are evaluated and shown in Table 2. From the above table, one can observe that the AdaBoost classifier gives the highest accuracy (98.6%) and least error rate (1.39%) among all the eight models. Then RF gives 97.2%, both K-NN and ANN have 96.5%, and LR and SVM both have 95.8% accuracy. DT classifier showed the lowest accuracy 95.1%. After the AdaBoost classifier, the RF classifier

Table 2 Performance analysis for WDBC dataset

Parameters	Method							
	LR	DT	RF	SVC	K-NN	ANN	GAUSSIAN NB	AdaBoost
Accuracy (%)	95.8	95.1	97.2	95.8	96.5	96.5	95.8	**98.6**
Precision (%)	95.6	96.59	96.7	95.6	95.65	94.68	96.62	**98.87**
Recall (%)	97.75	93.54	98.87	97.75	98.87	1	96.62	98.87
Error rate (%)	4.19	4.89	2.79	4.19	3.49	3.49	4.19	**1.39**
Specificity (%)	92.59	94.44	94.44	92.59	92.59	90.74	94.44	**98.14**
F-measure (%)	96.66	95.04	97.77	96.66	97.23	96.62	97.26	**98.87**
MCC	0.9109	0.8963	0.9404	0.9104	0.9257	0.9268	0.9107	**0.9702**

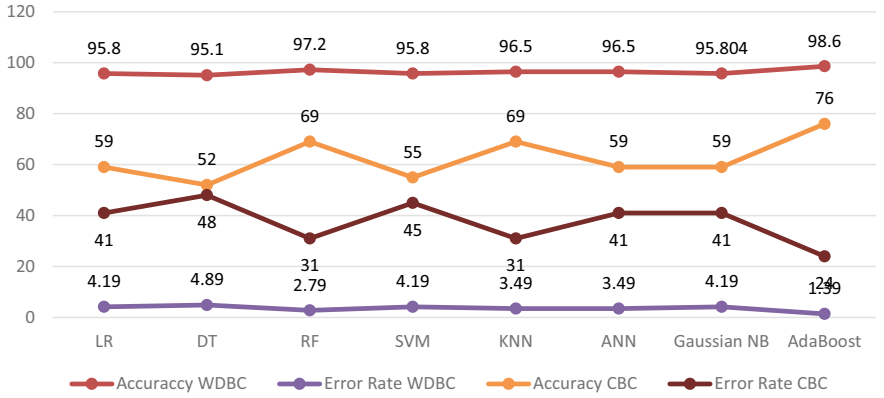

Fig. 1 Accuracy and error rate of WDBC and CBC dataset

gives the second highest accuracy with the second lowermost error rate (2.79%). From all other classifiers, both K-NN and ANN give an equal error (3.49%) and LR and Gaussian NB give 4.19% error. DT classifier gives the highest error rate, i.e., 4.89%. Graph of accuracy and error rate of each classifier have been shown in Fig. 1.

Also, from Table 2, it has been observed that the AdaBoost classifier gives the highest value, i.e., 98.87% for F-Measure. It shows that the average rate of precision and recall for predicting the actual positive class is approximately high. Hence, AdaBoost classifier is considered the best classifier for predicting the actual positive class. Again, it is observed that from the specificity value AdaBoost classifier is considered as the best classifier among all these classifiers because it is used to predict correctly the actual negative class, i.e., 98.14%. It gives the highest correlation coefficient, i.e., 0.9702. According to all these parameter considerations, it can be concluded that AdaBoost is the best classifier among all these eight classifiers. After that RF, ANN, K-NN, Gaussian NB, SVM, LR, and DT classifiers performed well to predict the class label for each sample sequentially.

Next, we have applied all the eight classification algorithm on Breast Cancer dataset from University of Coimbra. Since the dataset is very small dimension as it has only 116 instances and 10 attributes, the classification models are underfitted. But apart from that among all the classifiers AdaBoost classifier has performed well for classifying the patients. This model gives the highest accuracy of approximately 76% with precision 0.72, recall value 0.67, and Matthew's correlation coefficient is 0.4976. Then RF and K-NN model gives the second highest accuracy of 69%. Then, LR, Gaussian NB, and ANN-based classification model have approximately same accuracy score of 59%. In Table 3, all the parameters are shown below. Therefore, AdaBoost-based classification model has performed well both on small dataset and large volume of dataset.

Table 3 Performance measure of CBC dataset

Parameters	Methods							
	LR	DT	RF	SVC	K-NN	Gaussian NB	ANN	AdaBoost
Accuracy (%)	59	52	69	55	69	59	59	**76**
Precision	0.50	0.44	0.60	0.45	0.67	0.50	0	**0.72**
Recall	0.42	0.58	0.75	0.42	0.50	0.58	0.0	**0.67**
Error rate (%)	41	48	31	45	31	41	41	**24**
Specificity	0.70	0.47	0.64	0.64	0.82	0.77	1	0.82
F-measure	0.45	0.50	0.67	0.43	0.57	0.54	0.0	**0.69**
MCC	0.1269	0.0534	0.3913	0.0646	0.0001	0.2163	0.0000	**0.4976**

5 Conclusion

Data mining techniques have been broadly used in the medical field and proved to be one of the best ways to predict the desired results about the disease and analyze the dataset as well as design a predictive model. In this article, eight classification models are used for diagnosis of breast cancer disease, namely, Logistic regression (LR), Decision Tree (DT), Random Forest (RF), Support Vector Machine (SVM), Artificial Neural Network (ANN), K-Nearest Neighborhood (K-NN), Gaussian Naïve Bayes (NB), and AdaBoost classifier. The principle and the methodology of each classifier were described. To compare the performance measure of each classification model, we use the Wisconsin Diagnosis Breast Cancer dataset and Coimbra Breast Cancer dataset from UCI Machine learning repository.

Using the confusion matrix some evaluation measures such as Accuracy, Precision, Recall, Error rate, Specificity, and F-measure are calculated for each model. Based on the results obtained it shows that the AdaBoost classifier is the best fit model for classifying the cancer patient into benign and malignant class labels. It gives the highest performance in terms of accuracy (98.6%), precision (98.87%), recall (98.87%), and specificity (98.14%). In literature [16, 17], it is being found that the decision tree is used as a base classifier for the AdaBoost classification model. Although the CBC dataset was small in dimension, AdaBoost classifier gives the highest accuracy rate among all the classification models. But, one can study other classifiers such as SVM, RF as base classifiers to understand how they perform. Also, this classification model can be applied to different datasets having missing values or some noisy data and study the result. Also, by taking different training and testing ratio classification models can be compared to validate the test results.

References

1. Ahmad LG, Eshlaghy AT, Poorebrahimi A, Ebrahimi M, Razavi AR (2013) Using three machine learning techniques for predicting breast cancer recurrence. J Health med inform 4:124. https://doi.org/10.4172/2157-7420.1000124
2. Nilashi M, Ibrahim O, Ahmadi H, Shahmoradi L (2017) A knowledge-based system for breast cancer classification using fuzzy logic method. Telematics Inform 34:133–144
3. Bazazeh D, Shubair R (2016) Comparative study of machine learning algorithms for breast cancer detection and diagnosis. In: 5th International conference on electronic devices, systems and applications (ICEDSA), pp 1–4
4. World Cancer Research Fund. American Institute for Cancer Research. https://www.wcrf.org/dietandcancer/cancer-trends/breast-cancer-statistics
5. Breast Cancer Statistics: World Cancer Research Fund International. https://www.wcrf.org/int/cancer-facts-figures/data-specific-cancers/breast-cancer-statistics%20
6. Scheidhauer K, Walter C, Seemann MD (2004) FDG PET and other imaging modalities in the primary diagnosis of suspicious breast lesions. Eur J Nucl Med Mol Imaging 31(suppl. 1):70–90
7. Delen D, Walker G, Kadam A (2005) Predicting breast cancer survivability: a comparison of three data mining methods. Artif Intell Med 34:113–127
8. Scientific Committee (2019) Application of data mining techniques to predict breast cancer. In: 16th international learning and technology conference. Procedia computer science
9. Dhankhad S, Mohammed E, Far B (2018) Supervised machine learning algorithms for credit card fraudulent transaction detection: a comparative study. In: IEEE International conference on information reuse and integration (IRI), pp 122–125
10. Chaurasia V, Pal S (2017) Data mining techniques: to predict and resolve breast cancer survivability
11. Han J, Kamber M, Pei J (2019) Data mining concepts and techniques, 3rd edn. Elsevier
12. Kourou K, Exarchos TP, Exarchos KP, Karamouzis MV, Fotiadis DL (2015) Machine learning applications in cancer prognosis and prediction. Comput Struct Biotechnol J 13:8–17
13. Bache K, Lichman M (2013) UCI machine learning repository
14. Dayton CM (1992) Logistic regression analysis, statistics, and evaluation. University of Maryland, Department of Measurement
15. Li C, Zhang S, Zhang H, Pang L, Lam K, Hui C, Zhang S (2012) Using the K-nearest neighbor algorithm for the classification of Lymph node metastasis in gastric cancer. Comput Math Methods Med Article ID 876545
16. Wang R (2012) AdaBoost for feature selection, classification and it's relation with SVM, a review. Phys Procedia 25:800–807
17. Chengsheng TU, Huacheng L, Bing XU (2017) AdaBoost typical algorithm and its application research. In: MATEC web of conference. ICMITE 2017,vol 139, p 00222
18. Powers D (2011) Evaluation: from precision, recall and F-measure to ROC, informedness, markedness, and correlation. J Mach Learn Technol 2(1):37–63
19. Chicco D, Jurman G (2020) The advantages of the Matthews correlation coefficient (MCC) over F1 score and accuracy in binary classification evaluation. BMC Genomics 21:6
20. Polat K, Günes S (2007) Breast cancer diagnosis using least square support vector machine. Digital Signal Process 17(4):694–701
21. Setiono R (2000) Generating concise and accurate classification rules for breast cancer diagnosis. Artif Intell Med 18(3):205–219

Mathematical Model for Demonetization

Amidu Yusuf and Ebenezer Bonyah

Abstract Mathematical models have over the years been used to examine most of the present economic challenging problems. In this paper, demonetization effect on a population is examined using a compartmental mathematical model. Mathematical analysis of the model reveals that there is an existence of demonetization free equilibrium and demonetization existence equilibrium. The two equilibria are locally and globally asymptotically stable when $\mathcal{R}_0 < 1$ and $\mathcal{R}_0 > 1$, respectively. Moreover, numerical simulation of the model is carried out and the results show that demonetization effect persists in the system.

Keywords Demonetization · Basic reproduction number · Stability

1 Introduction

Demonetization is a fundamental regulatory act of banning or stripping a currency unit of its original status so that it ceases to be a legal tender [1]. The government of a country can decide to invalidate certain banknotes or coins totally from circulation or replace specific currency with new ones. There are numerous essential reasons why the government of a country resorts to demonetization; some of these reasons include to curb corruption, tackle black money, withdraw fake currency, and to stabilize the economy [2]. Demonetization has a lot of impact on the individuals living in a country. While some of these impacts are positive, others tend to be negative.

Demonetization effect is a long-term or short-term experience basically felt by the lower and middle income class of a country [3]. Besides, the demonetization

A. Yusuf (✉)
African Institute for Mathematical Sciences, Accra, Ghana
e-mail: yusuf@aims.edu.gh

E. Bonyah
Department of Mathematics Education, Akenten Appiah Menka University of Skills Training and Entrepreneurial Development, Kumasi, Ghana

J. Singh et al. (eds.), *Advances in Mathematical Modelling, Applied Analysis and Computation*, Lecture Notes in Networks and Systems 415,
https://doi.org/10.1007/978-981-19-0179-9_12

effect targeted at one percent of the affluence consequently affects 99 percent of the masses.

Demonetization effect is a long-term or short-term experience basically felt by the lower and middle income class of a country [3]. Besides, the demonetization effect targeted at one percent of the affluence consequently affects 99 percent of the masses. History shows that several countries worldwide have practised demonetization due to one reason or the other. In 1873, the United States withdrew silver from circulation and replaced it with gold. The move was a successful effort in controlling black money in circulation [1]. In 1923, the government of Germany under the Weimar Republic withdrew the old currency and replaced it with a new note called Rentenmark. Accordingly, all old cash ceased to be legally tendered. Moreover, the aim of such move was to combat hyperinflation in the economy [4]. India in 1946 had its first demonetization of high denominations of Rs. 1000 and Rs. 10,000. After 32 years, it was followed by a new reform which was the withdrawal of Rs. 1000, Rs. 5000, and Rs. 10,000 from circulation. Subsequently, another demonetization was announced in 2016 where the Prime Minister of India Narendra Modi banned high denominations which include Rs. 500 and Rs. 1000 and were replaced with new Rs. 500 and Rs. 2000; a move targeted at controlling black money in circulation [5].

Ghana in 1982, invalidated 50 Cedi note, an effort made toward curbing corruption, tax evasion, and to eradicate excessive liquidity in the country [6]. In 1984, the Nigerian government led by Muhammadu Buhari was forced to initiate an anti-corruption crackdown which replaced the old currency with new notes. However, the new reform failed to yield positive result on Nigeria's economy since debt-burdened and inflation ridden economy were not fixed [1]. Myanmar in 1987 banned about 80 percent of its currency in circulation. The reform was directed toward the then-existing black market. Consequently, the move triggered mass protest across the country after 1 year of economic hardship. Early 1990s, Zaire made a move to withdraw obsolescent currency from circulation by establishing new bank reforms. However, the plan was not successful due to surge in inflation and a breakdown in the exchange rate against dollar. Russia in 1991 retired large bubble bills from circulation. The effort was directed toward curtailing black money in the economy [6]. Europe in 2002 carried out a successful currency changeover operation. Prior to the execution of the new reform, the European central bank had for 3 years prepared while disseminating information about the demonetization which would take effect in the nearest future [7]. In 2010, North Korea government mounted a reform which knocked off two zeros in the face value of the old currency. Moreover, the drastic step was taken in order to tighten control of the economy and to eradicate black market [6]. Demonetization actually worked for some countries while in others, it resulted into a total failure. However, some key factors behind successful demonetization include proper conceptualization, adequate planning, and implementation.

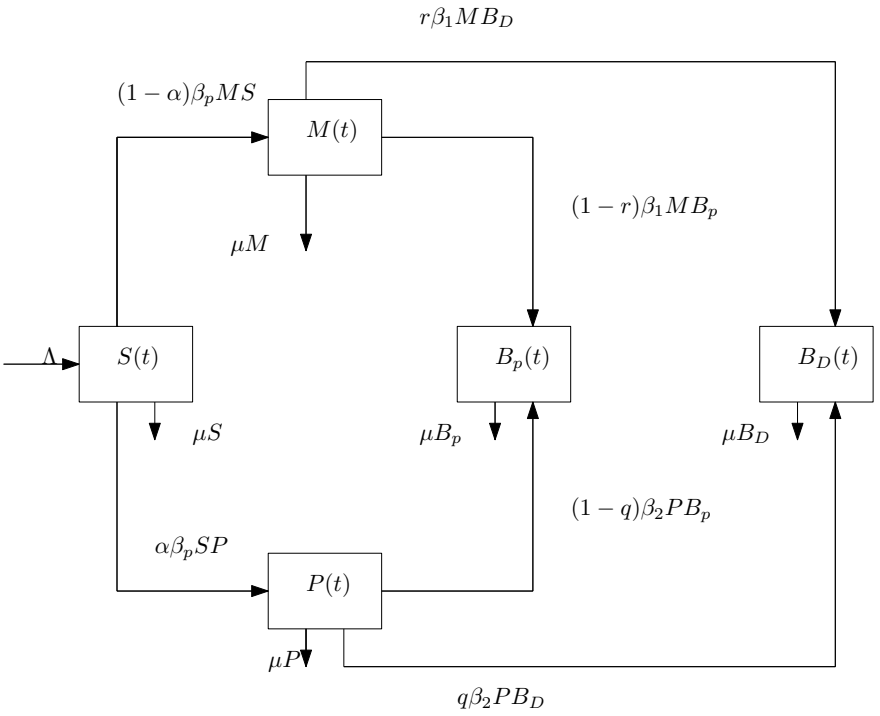

Fig. 1 Schematic diagram of demonetization effects on a population

2 Model Formulation

At a given time t, a population $N(t)$ is subpartitioned into five different compartments. The class of individuals yet to experience demonetization is represented by $S(t)$ and those that are partially affected are denoted by $M(t)$. Similarly, the individuals that are potentially affected are denoted by $P(t)$ and the class that deposited their money partially in a bank is represented by $B_p(t)$. Moreover, those that deposited their money fully in a bank are denoted by $B_D(t)$. The total population is given by

$$N(t) = S(t) + M(t) + P(t) + B_p(t) + B_D(t).$$

An appropriate diagram below is used to illustrate the dynamics of the total population (Fig. 1).

Table 1 shows a clear description of each variable and parameter used in the Model (1).

From Model (1), we derived a system of non-linear differential equations which are

Table 1 Variables and parameters of the model

Variables	Description
N	Total number of individuals in a population
S	Individuals that are yet to experience demonetization effects
M	Individuals that are partially affected with demonetization
P	Individuals that are fully affected with demonetization
B_p	Individuals that partially deposited their old currency into a bank
B_D	Individuals that fully deposited their old currency into a bank
Parameters	Description
Λ	Remitted rate into the population
μ	Rate at which individuals opt for digital payment
α	fraction of susceptible class that are fully affected
$1-\alpha$	fraction of susceptible class that are partially affected
r	fraction of mildly affected class that fully deposited their old currency in a bank
$1-r$	fraction of mildly affected class that partially deposited their old currency into a bank
q	fraction of fully affected class that deposited their old currency fully into a bank
$1-q$	fraction of fully affected class that partially deposited their old currency into a bank
β_p	The rate at which susceptible individuals move into partially and mildly affected classes
β_1	rate at which mildly affected class move into depositors class
β_2	rate at which fully affected class move into depositors class

$$\left.\begin{aligned}
\frac{dS(t)}{dt} &= \Lambda - (1-\alpha)\beta_p MS - \alpha\beta_p SP - \mu S,\\
\frac{dM(t)}{dt} &= (1-\alpha)\beta_p MS - r\beta_1 MB_D - (1-r)\beta_1 MB_p - \mu M,\\
\frac{dP(t)}{dt} &= \alpha\beta_p SP - (1-q)\beta_2 PB_p - q\beta_2 PB_D - \mu P,\\
\frac{dB_p(t)}{dt} &= (1-r)\beta_1 MB_p + (1-q)\beta_2 PB_p - \mu B_p,\\
\frac{dB_D}{dt} &= r\beta_1 MB_D + q\beta_2 PB_D - \mu B_D.
\end{aligned}\right\} \quad (1)$$

For the above system to be mathematically equipped, we subject it to the following initial conditions:

$$S(0) = S_0 > 0,\ M(0) = M_0 > 0,\ P(0) = P_0 > 0,\ B_p(0) = B_{p_0} > 0$$
$$B_D(0) = B_{D_0} > 0.$$

The total population at a definite time t is given as follows:

$$N(t) = S(t) + M(t) + P(t) + B_p(t) + B_D(t)$$

and

$$\frac{dN(t)}{dt} = \frac{dS(t)}{dt} + \frac{dM(t)}{dt} + \frac{dP(t)}{dt} + \frac{dB_p(t)}{dt} + \frac{dB_D(t)}{dt},$$

which simplifies to

$$\frac{dN(t)}{dt} = \Lambda - \mu(S + M + P + B_p + B_D),$$

$$\frac{dN(t)}{dt} = \Lambda - \mu N. \tag{2}$$

2.1 The Positivity of Solutions

It is essential that we investigate the solutions of each variables in Eq. (1) to make sure that they are all positive at any given time $t \geq 0$. To accomplish this task, we apply the following theorem.

Theorem 1 *The solutions of equation (1) with non-negative initial conditions will always be non-negative for any time $t > 0$ [8].*

Proof Let $t_1 = \sup\{t > 0 : S > 0,\ M > 0,\ P > 0,\ B_p > 0,\ B_D > 0 \in [0, t)\}$.

We now consider each of the equations in Eq. (1).

For the first equation in Eq. (1), we have

$$\frac{dS(t)}{dt} = \Lambda - (1-\alpha)\beta_p MS - \alpha\beta_p SP - \mu S.$$

Since at any given time $t \geq 0$, the parameter $\Lambda \geq 0$ so we have

$$\frac{dS(t)}{dt} \geq -[(1-\alpha)\beta_p M + \alpha\beta_p P + \mu]S,$$

$$\int_0^{t_1} \frac{dS(t)}{S(t)} \geq -\int_0^{t_1} [(1-\alpha)\beta_p M + \alpha\beta_p P + \mu]dt,$$

$$ln\left\{\frac{S(t_1)}{S(0)}\right\} \geq -\int_0^{t_1} [(1-\alpha)\beta_p M + \alpha\beta_p P + \mu]dt,$$

$$S(t_1) \geq S(0)\exp\left\{-\int_0^{t_1} [(1-\alpha)\beta_p M + \alpha\beta_p P + \mu]dt\right\},$$

therefore,

$$S(t) \geq S(0) \exp\left\{-\int_0^t [(1-\alpha)\beta_p M + \alpha\beta_p P + \mu]dt\right\} \geq 0.$$

Similarly, we prove positivity for other variables $M(t)$, $P(t)$, $B_p(t)$, $B_D(t)$. □

2.2 The Boundedness of Solutions

Theorem 2 *The closed set of all solutions* $\xi = \left(S(t), M(t), P(t), B_p(t), B_D(t), \mid N \leq \frac{\Lambda}{\mu}\right)$ *with respect to Eq. (1) is uniformly bounded [8].*

Proof Suppose the set $\{S(t), M(t), P(t), B_p(t), B_D(t)\} \in \mathbb{R}_+^5$ at any given time $t > 0$.

We consider the rate of change of the total population N with respect to time t. This is represented by Eq. (2): The integrating factor of Eq. (2) is $e^{\mu t}$.

$$N(t)e^{\mu t} = \int \Lambda e^{\mu t} dt,$$
$$N(t) = \frac{\Lambda}{\mu} + ce^{-\mu t},$$

where c is a real constant of integration. At initial time $t = 0$, the total population $N(t) = N(0)$, such that

$$N(t) = \frac{\Lambda}{\mu} + \left(N(0) - \frac{\Lambda}{\mu}\right)e^{-\mu t},$$

$$N(t) = N(0)e^{-\mu t} + (1 - e^{-\mu t})\frac{\Lambda}{\mu}.$$

Model (1) represents a population which varies over time, hence $\frac{dN}{dt} \neq 0$ so we expect feasible solutions. If $N > \frac{\Lambda}{\mu}$, we have $\frac{dN}{dt} < 0$.

The rate of change of total population $\frac{dN}{dt}$ is bounded by $\Lambda - \mu N$. We now consider using the standard comparison theorem by Birkoff and Rota (1989) so that we have

$$0 \leq N(t) \leq N(0)e^{-\mu t} + (1 - e^{-\mu t})\frac{\Lambda}{\mu}.$$

But, as

$$t \to \infty, \quad 0 \leq N(t) \leq \frac{\Lambda}{\mu}.$$

Therefore, $N(t) \leq \frac{\Lambda}{\mu}$ whenever, $N(0) \leq \frac{\Lambda}{\mu}$. This implies that $N(t)$ is bounded and all the feasible solutions representing human component of the Model (1) begin and remain in the closed set ξ [9]. □

3 Equilibrium Points

3.1 Demonetization Free Equilibrium (DFE)

The DFE point is determined by setting all equations in Eq. (1) to zero and solving for each variables. At this equilibrium point, there is no existence of demonetization and hence the entire population are susceptible. This means that

$$M(t) = P(t) = B_p(t) = B_D(t) = 0.$$

Considering first equation in Eq. (1),

$$\frac{dS(t)}{dt} = \Lambda - (1-\alpha)\beta_p MS - \alpha\beta_p SP - \mu S = 0.$$

Since

$$M = P = 0,$$

therefore,

$$S(t) = \frac{\Lambda}{\mu}.$$

The demonetization free equilibrium point of (1) is $H_0 = \left(\frac{\Lambda}{\mu}, 0, 0, 0, 0\right)$.

3.2 Demonetization Existence Equilibrium (DEE)

The DEE is obtained by setting each equation in Eq. (1) to zero and evaluating each variable. At this equilibrium point, demonetization persists in the economy. This is obtained from Eq. (1) when $S(t)$, $M(t)$, $P(t)$, $B_p(t)$, and $B_D(t)$ are all non-zeros

and it is represented by

$$H^\star = \left[S^\star,\ M^\star,\ P^\star,\ B_p^\star,\ B_D^\star\right],$$

where

$$\begin{aligned}
S^\star &= \frac{\Lambda\beta_1\beta_2(r-q)}{(1-\alpha)\beta_p\beta_2\mu(1-2q)+\alpha\beta_p\beta_1\mu(2r-1)+\mu\beta_1\beta_2(r-q)},\\
M^\star &= \frac{\mu(1-2q)}{\beta_1(r-q)},\\
P^\star &= \frac{\mu(2r-1)}{\beta_2(r-q)},\\
B_p^\star &= \frac{\mu(2\alpha-1)-B_D^\star[(1-\alpha)\beta_2-r\alpha\beta_1]}{(1-q)(1-\alpha)\beta_2-\alpha(1-r)\beta_1},\\
B_D^\star &= \frac{\mu(2\alpha-1)-B_p^\star[(1-q)(1-\alpha)\beta_2-\alpha(1-r)\beta_1]}{(1-\alpha)\beta_2-r\alpha\beta_1}.
\end{aligned}$$

4 The Basic Reproduction Number ($\mathcal{R}_0$)

The basic reproduction number ($\mathcal{R}_0$) is the average number of secondary effects of demonetization caused by an affected individual who has been introduced into the susceptible class throughout the lifetime of the affected individual [10, 11]. It is also a threshold parameter for dissemination of demonetization effect into a completely susceptible population. To calculate ($\mathcal{R}_0$), we consider the equations in Eq. (1) that show the existence of demonetization and changes within the affected compartments. Next, we construct a next-generation matrix K which relates the number of newly affected individuals with demonetization in various compartments of Eq. (1). Suppose that there are n compartments and $H = (H_1, ..., H_n)^T$ are the number of individuals in each compartment, let the first $m < n$ compartments contain individuals affected with demonetization [12]. Suppose that the linearized equations for $H_1, ..., H_m$ at H_0 decoupled from the other equations and we consider the decoupled equations as $\dfrac{dH_j}{dt} = \mathcal{F}_j(H) - \mathcal{V}_j(H)$ For $j = 1, ..., m$.

Let $\mathcal{F}_j$ represent the rate of appearance of new effects of demonetization in compartment j. And $\mathcal{V}_j$ represents the rate of other transitions between compartment j and other affected compartments. Similarly, we defined the entrywise non-negative matrix F and the non-singular M-matrix V

where $F = \left[\dfrac{\partial\mathcal{F}_j(H_0)}{\partial H_k}\right]$ and $V = \left[\dfrac{\partial\mathcal{V}_j(H_0)}{\partial H_k}\right]$ for $j, k = 1, ..., m$.

The next-generation matrix is determined by $K = FV^{-1}$, this gives the rate at which the affected individuals in H_k compartment becomes potentially affected in

H_j compartment. $\mathcal{R}_0$ is determined as $\mathcal{R}_0 = \rho(K)$, where ρ denotes the spectral radius of the next-generation matrix [13].

Assume that $H' = \left(M,\ P,\ B_p,\ B_D,\ S\right)'$, $\qquad H' = \dfrac{dH}{dt} = \mathcal{F}(H) - \mathcal{V}(H)$.

Considering the compartments that disseminate demonetization from Eq. (1). We decompose the equations into two parts where the first part shows appearance terms and the second part shows transition terms of demonetization effects. From Eq. 1, we have equations which reveal effect of demonetization. These are

$$\frac{dM(t)}{dt} = (1-\alpha)\beta_p MS - r\beta_1 MB_D - (1-r)\beta_1 MB_p - \mu M.$$

$$\frac{dP(t)}{dt} = \alpha\beta_p SP - (1-q)\beta_2 PB_p - q\beta_2 PB_D - \mu P.$$

Decomposing the two equations into two parts gives

$$\mathcal{F} = \begin{bmatrix} \mathcal{F}_1 \\ \mathcal{F}_2, \end{bmatrix} = \begin{bmatrix} (1-\alpha)\beta_p MS \\ \alpha\beta_p SP \end{bmatrix}$$

$$\mathcal{V} = \begin{bmatrix} \mathcal{V}_1 \\ \mathcal{V}_2 \end{bmatrix} = \begin{bmatrix} r\beta_1 MB_D + (1-r)\beta_1 MB_p + \mu M \\ (1-q)\beta_2 PB_p + q\beta_2 PB_D + \mu P \end{bmatrix}.$$

The Jacobian matrices are obtained as

$$F = \begin{bmatrix} \dfrac{\partial \mathcal{F}_1}{\partial M} & \dfrac{\partial \mathcal{F}_1}{\partial P} \\ \dfrac{\partial \mathcal{F}_2}{\partial M} & \dfrac{\partial \mathcal{F}_2}{\partial P} \end{bmatrix} \text{ and } V = \begin{bmatrix} \dfrac{\partial \mathcal{V}_1}{\partial M} & \dfrac{\partial \mathcal{V}_1}{\partial P} \\ \dfrac{\partial \mathcal{V}_2}{\partial M} & \dfrac{\partial \mathcal{V}_2}{\partial P} \end{bmatrix}.$$

$$F = \begin{bmatrix} (1-\alpha)\beta_p S & 0 \\ 0 & \alpha_p S \end{bmatrix} \text{ and } V = \begin{bmatrix} r\beta_1 B_D + (1-r)\beta_1 B_p + \mu & 0 \\ 0 & q\beta_2 B_D + \mu \end{bmatrix}.$$

We then evaluate F and V at DEF point $H_0 = \left(\dfrac{\Lambda}{\mu}, 0, 0, 0, 0\right)$. So F and V become

$$F = \begin{bmatrix} \dfrac{(1-\alpha)\beta_p \Lambda}{\mu} & 0 \\ 0 & \dfrac{\alpha\beta_p \Lambda}{\mu} \end{bmatrix},$$

and

$$V = \begin{bmatrix} \mu & 0 \\ 0 & \mu \end{bmatrix}.$$

Finding the inverse of the matrix V, we have

$$V^{-1} = \begin{bmatrix} \frac{1}{\mu} & 0 \\ 0 & \frac{1}{\mu} \end{bmatrix}.$$

Determining the next-generation matrix $K = FV^{-1}$ which is obtained as

$$K = \begin{bmatrix} \frac{(1-\alpha)\beta_p \Lambda}{\mu^2} & 0 \\ 0 & \frac{\alpha\beta_p \Lambda}{\mu^2} \end{bmatrix}.$$

The reproduction number is calculated as

$$\begin{aligned} \mathcal{R}_0 &= \rho(K), \\ &= \max\left\{ \left| \frac{(1-\alpha)\beta_p \Lambda}{\mu^2} \right|, \left| \frac{\alpha\beta_p \Lambda}{\mu^2} \right| \right\}. \end{aligned}$$

The reproduction number accounts for the effect caused by partially affected and potentially affected individuals in a completely susceptible class.

Here $\mathcal{R}_{0_M} = \frac{(1-\alpha)\beta_p \Lambda}{\mu^2}$ and $\mathcal{R}_{0_P} = \frac{\alpha\beta_p \Lambda}{\mu^2}$.

5 Stability Analysis

5.1 The Local Stability of the System

The equilibrium points of a system are said to be *locally stable* if by slight alteration of the initial condition of the system the system remains in the neighborhood of that equilibrium point [14].

5.2 Local Stability of the DFE

Theorem 3 *If the reproduction number $\mathcal{R}_0 < 1$ then demonetization free equilibrium point H_0 is locally asymptotically stable but if $\mathcal{R}_0 > 1$ then H_0 is unstable [1].*

Proof We consider the Jacobian matrix of Eq. (1) at H_0 which gives

$$J(H_0) = \begin{pmatrix} -\mu & -(1-\alpha)\beta_p\frac{\Lambda}{\mu} & -\alpha\beta_p\frac{\Lambda}{\mu} & 0 & 0 \\ 0 & (1-\alpha)\beta_p\frac{\Lambda}{\mu} - \mu & 0 & 0 & 0 \\ 0 & 0 & \alpha\beta_p\frac{\Lambda}{\mu} - \mu & 0 & 0 \\ 0 & 0 & 0 & -\mu & 0 \\ 0 & 0 & 0 & 0 & -\mu \end{pmatrix}.$$

The eigenvalues are obtained from the characteristic equations of $|J(H_0) - I\lambda| = 0$.

$$\begin{vmatrix} -\mu-\lambda & -(1-\alpha)\beta_p\frac{\Lambda}{\mu} & -\alpha\beta_p\frac{\Lambda}{\mu} & 0 & 0 \\ 0 & \left((1-\alpha)\beta_p\frac{\Lambda}{\mu} - \mu\right) - \lambda & 0 & 0 & 0 \\ 0 & 0 & \left(\alpha\beta_p\frac{\Lambda}{\mu} - \mu\right) - \lambda & 0 & 0 \\ 0 & 0 & 0 & -\mu-\lambda & 0 \\ 0 & 0 & 0 & 0 & -\mu-\lambda \end{vmatrix} = 0.$$

Therefore, the obtained eigenvalues are

$$\begin{aligned}
\lambda_1 &= -\mu,\\
\lambda_2 &= -\left(\mu - (1-\alpha)\beta_p \frac{\Lambda}{\mu}\right),\\
\lambda_3 &= -\left(\mu - \alpha\beta_p \frac{\Lambda}{\mu}\right),\\
\lambda_4 &= -\mu,\\
\lambda_5 &= -\mu.
\end{aligned}$$

From λ_2, we have

$$\begin{aligned}
\lambda_2 &= -\left(\mu - (1-\alpha)\beta_p \frac{\Lambda}{\mu}\right),\\
&= -\mu\left(1 - (1-\alpha)\beta_p \frac{\Lambda}{\mu^2}\right),\\
&= -\mu(1-\mathcal{R}_{0_M}).
\end{aligned}$$

From λ_3, we have

$$\begin{aligned}
\lambda_3 &= -\left(\mu - \alpha\beta_p \frac{\Lambda}{\mu}\right),\\
&= -\mu\left(1 - \alpha\beta_p \frac{\Lambda}{\mu^2}\right),\\
&= -\mu(1-\mathcal{R}_{0_P}).
\end{aligned}$$

Considering

$$K_1\left(1-\frac{S^\star}{S}\right)\frac{dS}{dt} = K_1\left(1-\frac{S^\star}{S}\right)(\Lambda - (1-\alpha)\beta_p MS - \alpha\beta_p SP - \mu S).$$

At endemic equilibrium equation, $\Lambda = (1-\alpha)\beta_p M^\star S^\star + \alpha\beta_p S^\star P^\star + \mu S^\star$

$$\begin{aligned}
K_1\left(1-\frac{S^\star}{S}\right)\frac{dS}{dt} &= K_1\left(1-\frac{S^\star}{S}\right)((1-\alpha)\beta_p M^\star S^\star + \alpha\beta_p S^\star P^\star + \mu S^\star - (1-\alpha)\beta_p MS - \alpha\beta_p SP - \mu S)\\
&= K_1(1-\alpha)\beta_p\left(M^\star S^\star - \frac{M^\star S^{\star^2}}{S} - MS + MS^\star\right)\\
&\quad + K_1\alpha\beta_p\left(S^\star P^\star + S^\star P - SP - \frac{S^{\star^2}}{S}\right) + K_1\mu\left(2S^\star - \frac{S^{\star^2}}{S} - S\right).
\end{aligned}$$

Similarly,

$$K_2\left(1-\frac{M^\star}{M}\right)\frac{dM}{dt} = K_2\left(1-\frac{M^\star}{M}\right)((1-\alpha)\beta_p MS - r\beta_1 MB_D - (1-r)\beta_1 MB_p - \mu M)$$
$$= K_2(1-\alpha)\beta_p S(M-M^\star) + K_2 r\beta_1 B_D(M^\star - M) + K_2(1-r)\beta_1 B_p(M^\star - M)$$
$$+ K_2(M^\star - M)\mu.$$

Also,

$$K_3\left(1-\frac{P^\star}{P}\right)\frac{dP}{dt} = K_3\left(1-\frac{P^\star}{P}\right)(\alpha\beta_p SP - (1-q)\beta_2 PB_p - q\beta_2 PB_D - \mu P)$$
$$= K_3\alpha\beta_p(SP - SP^\star) + K_3(1-q)\beta_2 B_p(P^\star - P) + K_3 q\beta_2 B_D(P^\star - P)$$
$$+ K_3\mu(P^\star - P).$$

Furthermore,

$$K_4\left(1-\frac{B_p^\star}{B_p}\right)\frac{dB_p}{dt} = K_4\left(1-\frac{B_p^\star}{B_p}\right)((1-r)\beta_1 MB_p + (1-q)\beta_2 PB_p - \mu B_p)$$
$$= K_4(1-r)\beta_1(MB_p - MB_p^\star) + K_4(1-q)\beta_2(PB_p - PB_p^\star)$$
$$+ K_4\mu(B_p^\star - B_p).$$

Finally,

$$K_5\left(1-\frac{B_D^\star}{B_D}\right)\frac{dB_D}{dt} = K_5\left(1-\frac{B_D^\star}{B_D}\right)(r\beta_1 MB_D + q\beta_2 PB_D - \mu B_D)$$
$$= K_5(MB_D - MB_D^\star) + K_5 q\beta_2(PB_D - PB_\star) + K_5\mu(B_D^\star - B_D).$$

$$\frac{dV}{dt} = ((1-\alpha)\beta_p M^\star S^\star + \alpha\beta_p S^\star P^\star)\left(1-\frac{S^\star}{S}\right) + (1-\alpha)\beta_p S^\star M\left(1-\frac{S}{S^\star}\right) + \alpha\beta_p S^\star\left(1-\frac{S}{S^\star}\right)$$
$$+ \mu S^\star\left(2-\frac{S}{S^\star}-\frac{S^\star}{S}\right) + (1-\alpha)\beta_p MS\left(1-\frac{M^\star}{M}\right) + r\beta_1 B_D M^\star\left(1-\frac{M}{M^\star}\right)$$
$$+ r\beta_1 B_p M^\star\left(1-\frac{M}{M^\star}\right) + \mu M^\star\left(1-\frac{M}{M^\star}\right) + \alpha\beta_p\left(1-\frac{P^\star}{P}\right) + (1-q)\beta_2 P^\star\left(1-\frac{P}{P^\star}\right)$$
$$+ q\beta_2 B_D P^\star\left(1-\frac{P^\star}{P}\right) + \mu P^\star\left(1-\frac{P^\star}{P}\right) + (1-r)\beta_1 MB_p\left(1-\frac{B_p^\star}{B_p}\right) + (1-q)\beta_2 PB_p\left(1-\frac{B_p^\star}{B_p}\right)$$
$$+ \mu B_p^\star\left(1-\frac{B_p}{B_p^\star}\right) + r\beta_1 MB_D\left(1-\frac{B_D^\star}{B_D}\right) + q\beta_2 PB_D\left(1-\frac{B_D^\star}{B_D}\right) + \mu B_D^\star\left(1-\frac{B_D}{B_D^\star}\right)$$

$K_i = 1$ for $i = 1, 2, 3, 4, 5$. Since the arithmetic mean is greater than or equal to the geometric mean, then the terms between the brackets are less or equal to zero.

Table 2 Variable and parameter values of the model

Variables	Initial condition	Source
$N(t)$	1000	[15]
$S(t)$	618	Estimate
$M(t)$	130	Estimate
$P(t)$	120	Estimate
$B_p(t)$	70	Estimate
$B_D(t)$	62	Estimate
Parameters	Value when $\mathcal{R}_0 < 1$	Value when $\mathcal{R}_0 > 1$
Λ	100	100
β_p	0.000006	0.0990
β_1	0.50005	0.0010
β_2	0.00003	0.0200
α	0.88890	0.7005
q	0.00550	0.5900
r	0.00333	0.0090
μ	0.09300	0.09300

Therefore, $\frac{dV}{dt} = 0$ holds provided $(S,\ M,\ P, B_p,\ B_D) = (S^\star,\ M^\star,\ P^\star,\ B_p^\star,\ B_D^\star)$. The singleton set $\{(S,\ M,\ P, B_p,\ B_D) = (S^\star,\ M^\star,\ P^\star,\ B_p^\star,\ B_D^\star)\}$ which is a subset of the set where $\frac{dV}{dt} = 0$ is the largest compact invariant set. Therefore, by Lasalle's invariance principle, it follows that as time t approaches infinity, $(S,\ M,\ P,\ B_p,\ B_D) \to (S^\star,\ M^\star,\ P^\star,\ B_p^\star,\ B_D^\star)$. We therefore conclude that the endemic equilibrium is globally asymptotically stable [8]. □

Numerical simulations are carried out in order to appropriately analyze the behavior of Eq. (1). The parameter values were estimated from the existing literature. Due to unavailability of data, we considered using some estimated parameter values and assumed variable values. The table of variable and parameter values is shown in Table 2.

From Fig. 2a, it is observed that at $\mathcal{R}_0 = 0.08$ the susceptible population increases toward the carrying capacity of the system $\left(\frac{\Lambda}{\mu}\right)$, as time increases. However, at $\mathcal{R}_0 = 0.08$, the populations in Fig. 2b–e gradually decrease to zero over a period of time. This confirms the demonetization equilibrium of the system. Also, it means that the total number of individuals in the population before declaration of demonetization are susceptible.

In Fig. 3a, one can observe that while the transmission rate is increasing, the number of individuals moving into mildly affected class decreases gradually when $\beta_p = 0.000006$ and rapidly for other values of β_p. This decreases and settles at zero as time increases.

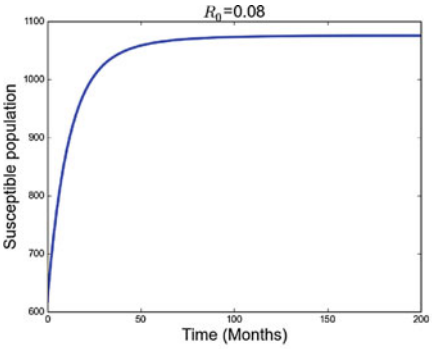

(a) A plot of susceptible population against time

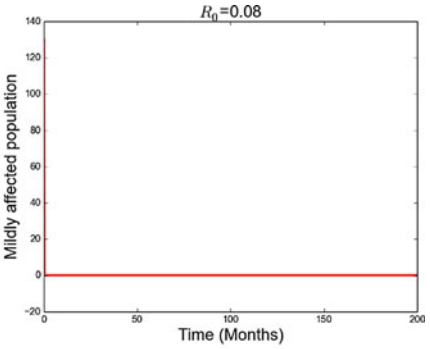

(b) A plot of mildly affected population against time

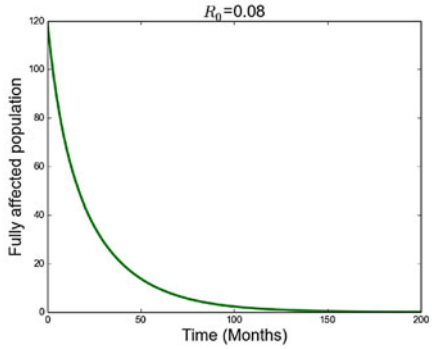

(c) A plot of fully affected population against time

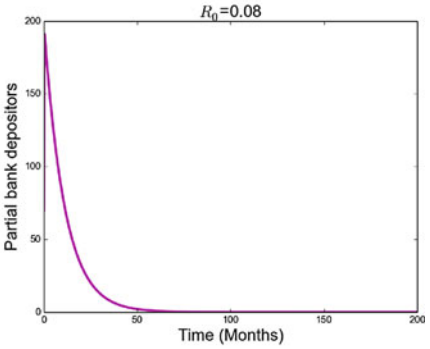

(d) A plot of partial bank depositors against time.

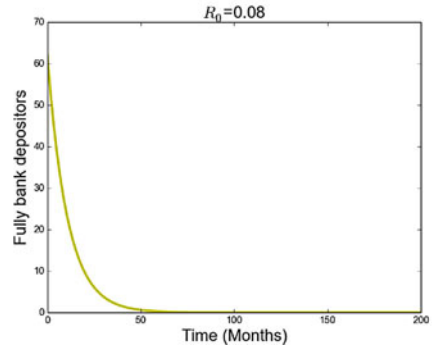

(e) A plot of fully bank depositors against time

Fig. 2 Simulation results of individual population when $\mathcal{R}_0 < 1$

From Fig. 4a, one observed that there is a little increase and decrease in the number of individuals remaining in the susceptible class when demonetization occurred. This explains the fact that once demonetization is declared, most of the susceptible

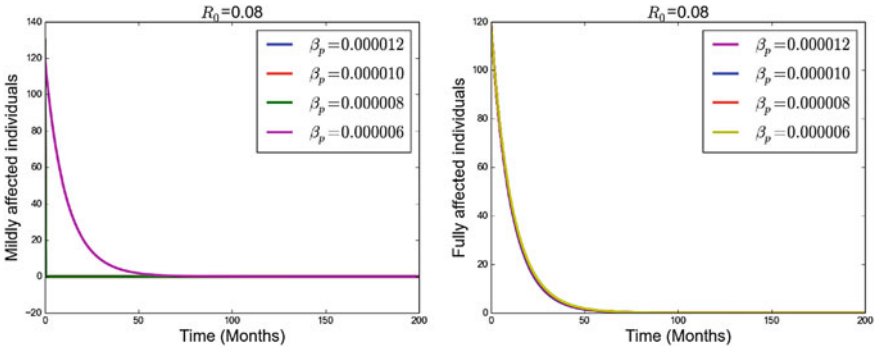

(a) A plot of mildly affected population against time at varying rate of (β_p)

(b) A plot of fully affected population against time at varying rate of (β_p)

Fig. 3 Simulation results of mildly and fully affected individuals at varying transmission rate (β_p)

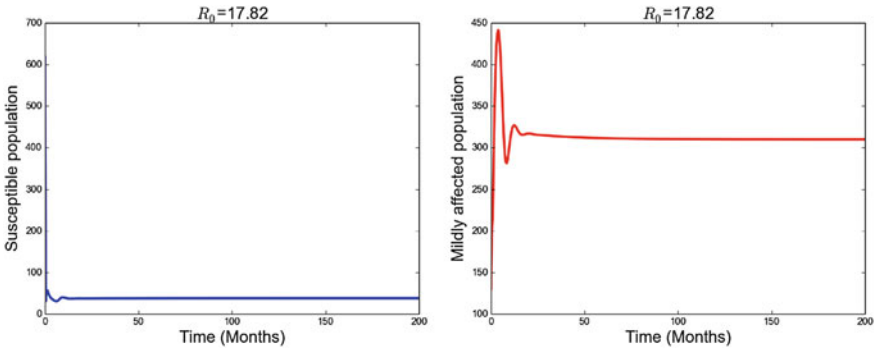

(a) A plot of suceptible population against time

(b) A plot of mildly affected population against time

Fig. 4 Simulation results of susceptible and mildly affected population at $(\mathcal{R}_0 = 17.82)$

individuals move into affected classes while the remaining few unaffected settle and exchange their old cash for new currency in form of digital payment. Figure 4b shows sharp increase and gradual decrease in the number of mildly affected population who later settle at a higher number within the population as time increases. This means that demonetization always force majority of the susceptible individuals to become partially affected and only few could return into the susceptible class within a short period. In Fig. 5a, there is a rapid increase but a gradual decrease in the number of fully affected individuals who settle within the population. This means that susceptible individuals increasingly move into potentially affected class and remain in within the population as time increases. In Fig. 5b, the number of partial bank depositors decreases at first and then increases to a constant level. The sudden decrease could be that affected individuals are receding from cash exchange policy on illegal, black and counterfeit currency in order to evade tax and prosecution. While the increase could be a decision to exchange illegal cash for new currency by affected individuals.

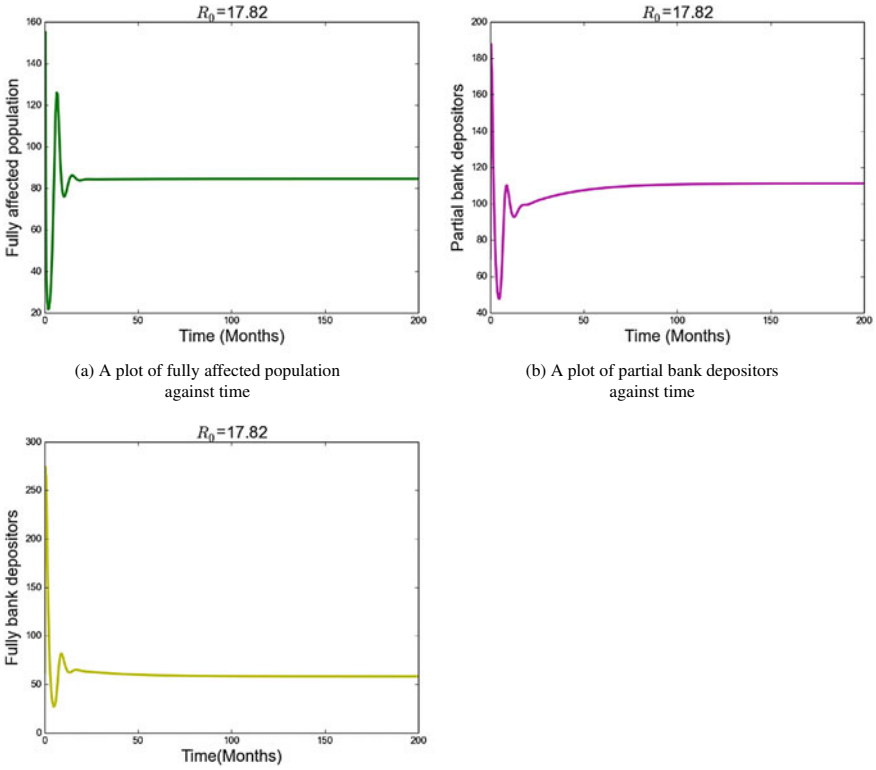

(a) A plot of fully affected population against time

(b) A plot of partial bank depositors against time

(c) A plot of fully bank depositors against time

Fig. 5 Simulation results of individual population when $\mathcal{R}_0 > 1$

In Fig. 5c, there is a rapid decrease of fully bank depositors who later settle at a lower level. The rapid decrease could be a result of few affected individuals successfully exchange old cash for new currency while other individuals' cash exchange was unsuccessful. Also, only the poor and hard income earners exchanged their old cash fully for new currency.

From Fig. 6a, it is seen that as the rate of transmission increases, the number of mildly affected individuals increases and decreases at equal pace and stabilizes after 10 months. The interpretation of this graph is that the transmission rate has little influence on the number of individuals who eventually become mildly affected. From Fig. 6b, one noticed that the number of fully affected individuals increases in accordance to transmission rate but maintains a stable state after 12 months. This explains the fact that the transmission rate has a limited effect on the number of mildly affected population.

From Fig. 7a, we noticed the significant effects of the basic reproduction number ($\mathcal{R}_0$) on the total population. When $\mathcal{R}_0$ is less than unity, the susceptible population

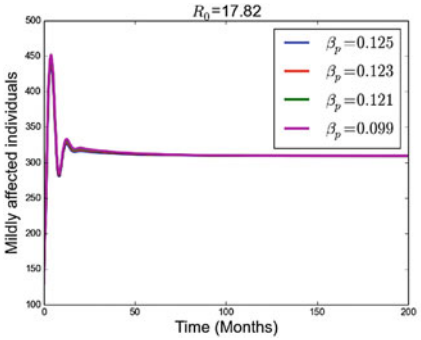

(a) A plot of mildly affected population against time at varying rate of β_p

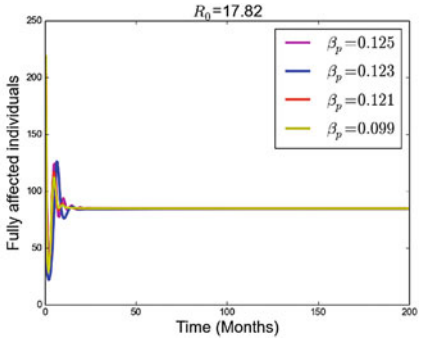

(b) A plot of fully affected population against time at varying rate of β_p

Fig. 6 Simulation results of mildly and fully affected individuals at varying transmission rate (β_p)

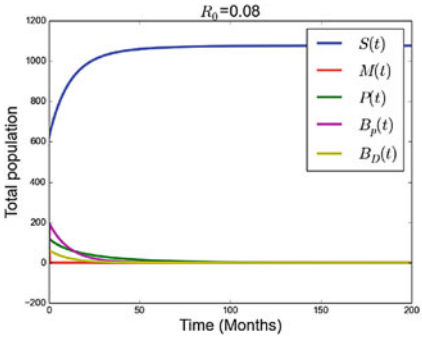

(a) A plot of total population against time

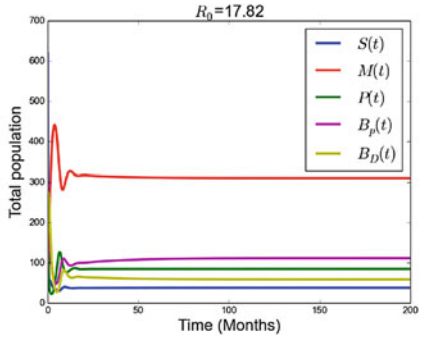

(b) A plot of total population against time

Fig. 7 Simulation results of total population when $\mathcal{R}_0 < 1$ and $\mathcal{R}_0 > 1$

increase to equilibrium point $\frac{\Lambda}{\mu}$ which is about 1200 while other demonetization-affected populations converge to zero over a period of time. This confirms the demonetization free equilibrium point which is stable when $\mathcal{R}_0 < 1$. From Fig. 7b, one can observe that when $\mathcal{R}_0 > 1$, majority of the susceptible population are mildly affected and few are potentially affected. Due to demonetization drive, few of these affected individuals deposited their old cash partially into the bank while the remaining fewer deposited their old cash completely into the bank in exchange of new currency. This confirms the demonetization existence equilibrium which is stable when $\mathcal{R}_0 > 1$.

6 Conclusion

In this work, we consider the effects of demonetization on a population over a given period of time. We formulated a mathematical model diagram which incorporates five different classes of sub-populations. The basic reproduction number $\mathcal{R}_0$ was calculated using the next-generation matrix method. Moreover, we determined the demonetization free equilibrium (DFE) and demonetization existence equilibrium (DEE). The stability analysis of the demonetization free equilibrium (DFE) had been examined. Moreover, we carried out numerical simulations of the stable states when $\mathcal{R}_0 < 1$ and $\mathcal{R}_0 > 1$. The simulation results of the model system (1) suggested that demonetization had a lifetime effect on individuals particularly those on the middle class suffering the most. Hence, for a successful demonetization to hold, the government needs proper planning and implementation. Therefore, we implore the government to enlighten individuals on the benefits of digital banking and online transaction.

References

1. Bijal MY (2017) Stability analysis of transmission of social issues. Unpublished PhD thesis
2. What is demonetization? What are some simple examples of it? Sushant Puri (2014). https://www.quora.com/What-is-demonetization-What-are-some-simple-examples-of-it/answer/Sushant-Puri-3. Accessed April 2018
3. Impact of demonetization on economy, businesses and people. Prog Harmony Dev (1995). http://phdcci.in/image/data/ResearchBureau-2014/EconomicDevelopments, Accessed April 2018
4. 1 Demonetization: lessons from the international experience. http://www.jagannathuniversityncr.ac.in/wp-content/uploads/2017/09/V-1-I-4/Demonetization-Lessons-from-International-Experience-Ms-Chandni-Tyagi-and-Dr-Vani-Narula.pdf. Accessed April 2018
5. India's history with demonetization: from 1946 to 2016. Free Press J (2016). http://www.freepressjournal.in/featured-blog/indias-history-with-demonetisation-from-1946-to-2016/988212. Accessed April 2018
6. Singh A (2017) Impact of demonetization on Indian economy. Int J Eng Manag Res (IJEMR) 785–788
7. Europe's successful currency changeover highlights everything India did wrong. https://thewire.in/economy/europe-currency-changeover-demonetisation. Accessed April 2018
8. Safi MA, Garba SM (2012) Global stability analysis of SEIR model with holling type II incidence function. Comput Math Methods Med
9. Okongo MO (2015) The local and global stability of the disease free equilibrium in a co infection model of HIV/AIDS, Tuberculosis and malaria. IOSR J Math 11:33–43
10. Ugwa KA, Agwu I (2013) A mathematical analysis of the endemic equilibrium of the transmission dynamics of tuberculosis. Int J Sci Technol Res 263–269
11. Diekmann O, Heesterbeek JAP, Metz JAJ (1990) On the definition and the computation of the basic reproduction ratio R_0 in models for infectious diseases in heterogeneous populations. J Math Biol 365–382
12. Pauline VD, Watmough J (2002) Reproduction numbers and sub-threshold endemic equilibria for compartmental models of disease transmission. Math Biosci 29–48

13. Pauline VD, Watmough J (2008) Further notes on the basic reproduction number. Math Epidemiol (Springer) 159–178
14. Stability and performance, Lecture note. https://www.cds.caltech.edu/~murray/courses/cds101/fa03/caltech/am03_ch3-13oct03.pdf. Accessed April 2018
15. Shah NH, Thakkar FA, Yeolekar BM (2016) Mathematical analysis of optimal control theory on underweight. Adv Res 8(5)
16. Diekmann O, Heesterbeek JAP, Roberts MG (2009) The construction of next-generation matrices for compartmental epidemic models. J R Soc Interface

An Inflationary Demand Scheme with Pareto Deterioration in Two Warehouses

Sunita and Ganesh Kumar

Abstract Inventory management is one of the biggest issues in any business federation. There are many instances when storage space is no longer adequate, and a new warehouse is needed. This article deals with a two storage inventory model (one of them is Own Warehouse (OW) and another is Rented Warehouse (RW)) with exponentially time-varying demand considering partial backlogging. The capacity of own warehouse is fixed (U units), to store more units than the limited range of OW, the supplier has to rent another warehouse (RW) at higher holding cost. We study two warehouse policies with linear holding cost and Pareto type decay in an inflationary environment. We have worked out a model for determining costs and they are much lower than previous estimates. Ultimately, sensitivity investigation has been executed to demonstrate the effects of diverse parameters of the inventory system. We have also calculated the economic order quantity Q with the help of MATLAB software.

Keywords Two storage inventory system · Pareto type decay rate · Inflation · Partial backlogging

1 Introduction

The two warehouse inventory model was first brought to the world by Hartley [10]. Afterward several researchers attempted to make the field more transparent. In this field, Pakkala and Achary [24], Sharma and Choudhary [34], and Gothi et al. [9] analyzed two storage inventory systems for depreciating products. Zhou and Yang [41] proposed a dual storage system for depreciating commodities without allowing any shortages with stock-dependent demand. Yang [39] flourished a dual storage inventory system for partially backlogged depreciating commodities with persistent demand under an inflationary surrounding. Saxena et al. [30] established a dual storage production inventory system for declining products with exponential demand under trade credit period policy in an inflationary environment. Khanna et al. [13]

Sunita · G. Kumar (✉)
Department of Mathematics, University of Rajasthan, Jaipur, Rajasthan 302004, India
e-mail: ganeshmandha1988@gmail.com

J. Singh et al. (eds.), *Advances in Mathematical Modelling, Applied Analysis and Computation*, Lecture Notes in Networks and Systems 415,
https://doi.org/10.1007/978-981-19-0179-9_13

established an inventory system for fully backlogged declining imprecise standard artifacts with price-sensitive demand under trade credit period policy. Shaikh et al. [33] explored a dual storage system for declining products with stock-dependent demand and interval-value-based costs under an inflationary environment. Shah et al. [32] established a pricing inventory system for declining artifacts with dynamic demand without allowing any shortages. Aastha et al. [1] established a dual storage system for completely backlogged depreciating imperfect quality commodities with continuous demand. Agrawal et al. [3] proposed a dual storage system for partially backlogged declining products with ramp-type demand. Kumar and Chanda [15] established a dual storage system for depreciating products with demand taken as innovation criterion based. Rong et al. [29] proposed a dual storage system for a declining commodity with demand as selling price-dependent using fuzzy lead time. They were the first who introduced fuzzy lead time.

Singh and Rathore [35] explored a dual storage system for depreciating commodities with linearly stock reliant demand using preservation technology in inflationary environment. Agarwal et al. [2] addressed the repetitive resupply rate and time delays. Pradhan and Tripathy [27] explored a production inventory system for three parameter Weibull distributed depreciating artifacts with persistent demand and production under conditionally price discount. Panda et al. [26] proposed a solo vendor numerous retailer dual storage system for declining products having price and stock-sensitive demand in fuzzy circumstances. Palanivel and Uthayakumar [25] proposed a dual storage system for declining commodities with credit period reliant demand under trade credit period policy in inflationary surroundings. Öztürk [21] applied in industrial scenarios. Various models for the process of input performance have been developed by Xu et al. (2016) and Yang [40]. Sett et al. [31], Indrajitsingha et al. [11], Alawneh and Zhang [4], Bhunia et al. [5], Jaggi et al. [12], and Lee and Hsu [16] implemented dual storage system with time-varying requirement.

Liang and Zhou [17] established a dual storage system for declining artifacts with persistent demand under conditionally trade credit period policy. Ghiami and Beullens [8] established a dual storage system for declining commodities with stock-sensitive demand. They focused on consecutive resupply policy between OW and RW. Singh and Pattnayak [36] proposed a dual storage system for depreciating commodities with linearly time-reliant demand and admissible delay in payments. Khurana [14] presented a two storage inventory system for declining products with diverse type of deterioration in both warehouses in inflationary surrounding. Pakhira et al. [22] studied memory effect on an inventory system with time-variant demand. Pakhira et al. [23] evaluated memory effect on an inventory system having constant depreciation rate. Vandana et al. [37] explored a new method using duality relations in multi-objective fractional programming. Dubey et al. [7] established higher order duality methods for arbitrary cones in fractional programming. Dubey et al. [7] established some new duality relations using generalized assumptions. Masud et al. (2021) explored a dual storage system for partially backlogged declining commodities with price-sensitive demand under admissible credit period policy. Nath and Sen [20] developed a two storage inventory system for completely backlogged depreciating products with time variable and selling price-sensitive demand. Manna et al. [18]

established a dual storage system for partially backlogged declining products with time-sensitive demand using all unit discount policy. Rana et al. [28] investigated a two storage inventory system for partially backlogged depreciating commodities with freshness and price-sensitive demand in inflationary circumstances.

This paper demonstrates a model with two reservoirs and a demand that has an exponential decrease, Pareto type decay, shortages allowed, partly backlogged, and inflation. Formation of the paper: Sect. 2 furnishes notations and assumptions. The mathematical formulation with solution procedure is provided in Sects. 3 and 4. Section 5 illustrates a numerical study by allocating values to parameters. Section 6 impersonates a sensitivity investigation of this model by adjusting parameters. Consequences of this paper have been provided in Sect. 7 (Table 1).

2 Assumptions and Notations

The notations as shown in Table 2 and the following are the assumptions for developing this inventory model:

2.1 Assumptions

- The replenishment has been kept unlimited and immediate while keeping the lead time zero.
- Inventory planning horizon is finite.
- Demand exponentially depends on time, defined as $D(t) = r\, e^{st}$, where r and s are positive constant ($r > s$).
- Decay of the products is Pareto type. Deterioration rate $\theta(t) = \left(\frac{\theta_1\theta_2}{1+\theta_2 t}\right)$, where $\theta_1 > 0$ and $0 < \theta_2 < 1$ (for OW) and deterioration rate $\theta(t) = \left(\frac{\theta_3\theta_4}{1+\theta_4 t}\right)$, where $\theta_3 > 0$ and $0 < \theta_4 < 1$ (for RW).
- Decay rates are different in both warehouses.
- OW has limited storage space (say U) and RW has unlimited storage space.
- The holding cost (HC) of RW is more than the holding cost (HC) in OW.
- Inflation is considered.
- T_1 is inventory holding time in RW, $(T_1 + T_2)$ is inventory holding time in OW, and shortages occur in OW at time T_2.
- Supplier has provided no return or replacement policy.
- Shortages are allowed and partially backlogged, shortage rate is defined as $B(t) = e^{-\delta t}$, where $0 < \delta << 1$ is backlogging parameter.

Table 1 List of relevant disquisition on two storage model for depreciating products

Authors	Demand	Holding cost	Deterioration rate	Shortage	Inflation
Aastha et al. [1]	Continuous	Constant	Uniform	Complete	No
Agarwal et al. [2]	Exponential	linear	Two parameter Weibull	Partial	Yes
Agrawal et al. [3]	Ramp	Constant	Constant	Partial	No
Alawneh and Zhang [4]	Stochastic	Constant	Constant	Allowed	No
Bhunia et al. [5]	Constant	Constant	Constant	Partial	No
Ghiami and Beullens [8]	Stock sensitive	Constant	Constant	Allowed	No
Gothi et al. [9]	Quadratic	Linear	Constant	Not allowed	Yes
Indrajitsingha et al. [11]	Price sensitive	Constant	Constant	Partial	No
Jaggi et al. [12]	Price sensitive	Constant	Constant	Complete	No
Khanna et al. [13]	Price sensitive	Constant	Constant	Complete	No
Khurana [14]	Time	Constant	Time/Two parameter Weibull	Not allowed	Yes
Kumar and Chanda [15]	Innovation	Constant	Constant	Not allowed	No
Lee and Hsu [16]	Time	Constant	Constant	Not allowed	No
Liang and Zhou [17]	Constant	Constant	Constant	Not allowed	No
Manna et al. [18]	Linear	Constant	Constant	Partial	No
Mashud et al. (2021)	Price sensitive	Constant	Constant	Partial	No
Nath and Sen [20]	Time and Selling Price sensitive	Constant	Constant	Complete	No
Öztürk [21]	Constant	Constant	Constant	Not allowed	No
Pakkala and Achary [24]	Constant	Constant	Constant	Allowed	No
Palanivel and Uthayakumar [25]	Exponential function of credit period	Constant	Constant	Partial	Yes
Panda et al. [26]	Price and Stock sensitive	Constant	Constant	Not allowed	No
Pradhan and Tripathy [27]	Constant	Constant	Three parameter Weibull	Not allowed	No

(continued)

Table 1 (continued)

Authors	Demand	Holding cost	Deterioration rate	Shortage	Inflation
Rana et al. [28]	Freshness and Price sensitive	Constant	Constant	Partial	Yes
Rong et al. [29]	Price sensitive	Constant	Constant	Partially/fully	No
Saxena et al. [30]	Exponential function of time	Constant	Time/Weibull	Not allowed	Yes
Sett et al. [31]	Quadratic	Constant	Time sensitive	Not allowed	No
Shah et al. [32]	Linear	Constant	Constant	Not allowed	No
Shaikh et al. [33]	Stock sensitive	Constant	Constant	Partial	Yes
Sharma and Chaudhary [34]	Ramp	Constant	Time sensitive	Partial	Yes
Singh and Rathore [35]	Stock sensitive	Constant	Constant	Partial	Yes
Singh and Pattnayak [36]	Linear	Constant	Constant	Not allowed	No
Xu et al. (2016)	Constant	Constant	Constant	Not allowed	No
Yang [39]	Constant	Constant	Constant	Partial	Yes
Yang [40]	Constant	Constant	Three parameter Weibull	Partial	Yes
Zhou and Yang [41]	Stock sensitive	Constant	Constant	Not allowed	No
Present paper	Exponentially time sensitive	Constant	Pareto type	Partial	Yes

Table 2 Notations

U	Maximal extent of OW
I_r	Maximal inventory level in RW
T_1	Inventory holding time in RW
T_2	Time to exhaust stock within a replenishment cycle, $0 < T_2 < T$
T	Total length of a replenishment cycle
A	Fixed ordering cost/order
v	Inflation parameter
p	Purchasing cost/item
C_s	Unit shortage cost of an item
C_{oh}	HC per item per unit time in OW
C_{rh}	HC per item per unit time in RW
C_l	Unit lost sale cost/item/unit time
TAC	Total average cost

3 Mathematical Formulation

Since OW has limited space, the supplier must store the first U units in OW and the remaining in RW. Here we know that the carrying cost is higher in RW. Hence, RW is used when space of OW is completely used. But RW inventory is used first because of higher rent. Till time T_1 supply in OW declines due to decay alone, but in RW it downgrades due to the combined impact of decay and demand. OW exhausts store due to the mixed impact of degradation and demand between T_1 and T_2. Shortages occur in OW between T_1 and T_2. As shown in (Fig. 1).

Governing differential equations of OW are

$$\frac{dI_1(t)}{dt} + \frac{\theta_1\theta_2}{1+\theta_2 t} I_1(t) = 0, 0 \le t \le T_1 \tag{1}$$

$$\frac{dI_2(t)}{dt} + \left(\frac{\theta_1\theta_2}{1+\theta_2 t}\right) I_2(t) = -re^{st}, T_1 \le t \le T_2 \tag{2}$$

$$\frac{dI_3(t)}{dt} = -re^{st}e^{-\delta t} = -re^{(s-\delta)t}, T_2 \le t \le T. \tag{3}$$

Using $I_1(0) = U$, $I_2(T_2) = 0$, and $I_3(T_2) = 0$, solutions are

$$I_1(t) = U(1 - \theta_1\theta_2 t), 0 \le t \le T_1. \tag{4}$$

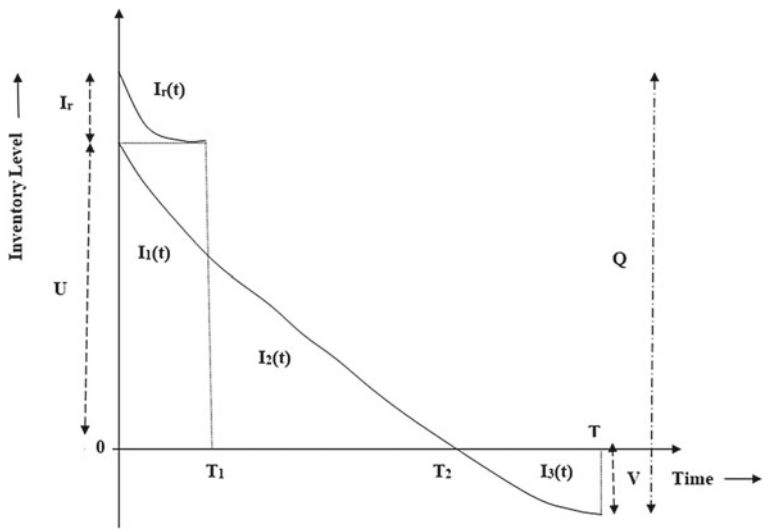

Fig. 1 Two storage inventory system

$$\mathrm{I}_2(\mathrm{t}) = \mathrm{r}\left\{(T_2 - t) + \frac{s}{2}(T_2 - t)^2 + \frac{\theta_1\theta_2}{2}\left(T_2^2 - t^2\right) + \frac{s\theta_1\theta_2}{2}(2T_2 - t)(T_2 - t)^2\right\},$$

$\mathrm{T}_1 \le \mathrm{t} \le \mathrm{T}_2.$ (5)

$$I_3(t) = r\left\{T_2 - t + \frac{s - \delta}{2}\left({T_2}^2 - t^2\right)\right\}, T_2 \le t \le T. \quad (6)$$

Using $\mathrm{I}_3\,(\mathrm{T}) = -\mathrm{V}$,

$$V = -r\left\{(T_2 - T) + \frac{(s - \delta)}{2}\left({T_2}^2 - T^2\right)\right\}. \quad (7)$$

Governing differential equation of RW is

$$\frac{dI_r(t)}{dt} + \left(\frac{\theta_3\theta_4}{1 + \theta_4 t}\right)I_r(t) = -\mathrm{r}e^{st}, 0 \le \mathrm{t} \le \mathrm{T}_1. \quad (8)$$

Using $\mathrm{I_r}(\mathrm{T}_1) = 0$, solution is

$$\mathrm{I_r(t)} = \mathrm{r}\left\{(T_1 - t) + \frac{s}{2}(T_1 - t)^2 + \frac{\theta_3\theta_4}{2}\left({T_1}^2 - t^2\right) + \frac{s\theta_3\theta_4}{2}(2T_1 - t)(T_1 - t)^2\right\}, 0 \le \mathrm{t} \le \mathrm{T}_1. \quad (9)$$

Using $\mathrm{I_r}(0) = \mathrm{I_r}$, we get

$$\mathrm{I_r} = \mathrm{r}\left\{T_1 + \frac{s}{2}T_1^2 + \frac{\theta_3\theta_4}{2}T_1^2 + \frac{s\theta_3\theta_4}{3}T_1^3\right\}. \quad (10)$$

Total inventory $\mathrm{Q} = \mathrm{U} + \mathrm{V} + \mathrm{I_r}$ is

$$\mathrm{Q} = U - r\left\{(T_2 - T) + \frac{(s - \delta)}{2}\left({T_2}^2 - T^2\right)\right\} + \mathrm{r}\left\{T_1 + \frac{s}{2}{T_1}^2 + \frac{\theta_3\theta_4}{2}{T_1}^2 + \frac{s\theta_3\theta_4}{3}{T_1}^3\right\}. \quad (11)$$

We have used the following costs in this model:

I. Ordering cost

$$OC = \frac{A}{T} \quad (12)$$

II. OW shortage cost

$$
\begin{aligned}
SC &= \frac{C_s}{T}\int_{T_2}^{T}[-I_3(t)]e^{-v(T_1+T_2+t)}dt \\
&= -\frac{rC_s}{T}\left\{\left(TT_2 - \frac{T^2}{2} - \frac{T_2^2}{2} - \frac{vT_2^2}{2} + \frac{vT^3}{2} + \frac{5vT_2^3}{6} - vT_2^2T - vT_1T_2T + \frac{vT_1T_2^2}{2} + \frac{vT_1T^2}{2}\right)\right. \\
&+\frac{(s-)}{2}\left(TT_2^2 - \frac{T^3}{3} - \frac{2T_2^3}{3} - vT_2^3T + \frac{vT^4}{4} + \frac{11vT_2^4}{12}\right. \\
&\left.\left. -vT_1T_2^2T + \frac{vT_1T^3}{3} - \frac{vT_2^2T^2}{2} + \frac{2vT_1T_2^3}{3} + \frac{vT_2T^3}{3}\right)\right\}
\end{aligned}
\tag{13}
$$

III. OW holding cost

$$
\begin{aligned}
HC_o &= \frac{C_{oh}}{T}\left[\int_0^{T_1} I_1(t)e^{-vt}dt + \int_{T_1}^{T_2} I_2(t)e^{-v(T_1+t)}dt\right] \\
&= \frac{C_{oh}}{T}U\left[\left\{\left(1 - \frac{v}{2} - \frac{\theta_1\theta_2}{2}\right)T_1^2 + \frac{v\theta_1\theta_2T_1^3}{3}\right\}+\right. \\
&r\left\{\frac{1}{2}\left((T_2-T_1)^2 - vT_1T_2^2 + 3vT_1^2T_2 - \frac{5vT_1^3}{3} - \frac{vT_2^3}{3}\right)\right. \\
&+\frac{s}{6}\left((T_2-T_1)^3 + \frac{9vT_1^2T_2^2}{2} - vT_1T_2^3 - 5vT_1^3T_2 + \frac{7vT_1^4}{4} - \frac{vT_2^4}{4}\right) \\
&+\frac{\theta_1\theta_2}{2}\left(\frac{2T_2^3}{3} + \frac{T_1^3}{3} - T_1T_2^2 - \frac{2vT_1T_2^3}{3} + \frac{3vT_1^2T_2^2}{2} - \frac{7vT_1^4}{12} - \frac{vT_2^4}{4}\right)+ \\
&\frac{s\theta_1\theta_2}{6}\left(\frac{5T_2^4}{4} - \frac{T_1^4}{4} - 2T_1T_2^3 + T_1^3T_2 - \frac{5vT_1T_2^4}{4}\right. \\
&\left.\left.\left.+3vT_1^2T_2^3 - \frac{7vT_1^4T_2}{4} + \frac{2vT_1^5}{5} - \frac{9vT_2^5}{20}\right)\right\}\right]
\end{aligned}
\tag{14}
$$

IV. OW lost sales cost

$$
\begin{aligned}
LSC &= \frac{C_l}{T}\int_{T_2}^{T} re^{st}(1-e^{-t})e^{-v(T_1+T_2+t)}dt \\
&= \frac{rC_l}{2T}(1 - vT_1 - vT_2)\left(T^2 - T_2^2\right).
\end{aligned}
\tag{15}
$$

V. OW item cost

$$
\begin{aligned}
IT_o &= \frac{p}{T}\left\{U - I_3(T)e^{-v(T_1+T_2+T)}\right\} \\
&= \frac{p}{T}\left[U - r(1 - v(T_1+T_2+T))\left\{T_2 - T + \frac{(s-)}{2}\left(T_2^2 - T^2\right)\right\}\right]
\end{aligned}
\tag{16}
$$

VI. RW holding cost

$$\begin{aligned} HC_r &= \frac{C_{rh}}{T}\int_0^{T_1} I_r(t)e^{-vt}dt \\ &= \frac{rC_{rh}}{T}\left\{\left(\frac{T_1^2}{2}-\frac{vT_1^3}{6}\right)+\frac{s}{2}\left(\frac{T_1^3}{3}-\frac{vT_1^4}{12}\right)\right. \\ &\left.+\frac{\theta_3\theta_4}{2}\left(\frac{2T_1^3}{3}-\frac{vT_1^4}{4}\right)+\frac{s\theta_3\theta_4}{6}\left(\frac{5T_1^4}{4}-\frac{9vT_1^5}{20}\right)\right\} \end{aligned} \tag{17}$$

VII. RW item cost

$$IT_r = \frac{pI_r}{T} = \frac{pr}{T}\left\{T_1+\frac{s}{2}T_1^2+\frac{\theta_3\theta_4}{2}T_1^2+\frac{s\theta_3\theta_4}{3}T_1^3\right\} \tag{18}$$

Total average cost is given by

$$TAC(T_1,T_2) = OC + HC_o + HC + LSC + IT_o + HC_r + IT_r \tag{19}$$

4 Solution Procedure of the Model

Necessary condition for minima of TAC per unit time is

$$\frac{\partial TAC(T_1,T_2)}{\partial T_1} = 0, \text{and} \frac{\partial TAC(T_1,T_2)}{\partial T_2} = 0. \tag{20}$$

After solving above equations by MATLAB software, we acquired the optimal esteem of T_1 and T_2 (mentioned as T_1^* and T_2^*) which satisfies the following sufficient conditions:

$$\begin{aligned} &\frac{\partial^2 \mathrm{TAC}(T_1,T_2)}{\partial T_1^2} > 0, \frac{\partial^2 \mathrm{TAC}(T_1,T_2)}{\partial T_2^2} > 0, \\ &\left(\frac{\partial^2 \mathrm{TAC}(T_1,T_2)}{\partial T_1^2}\right)\left(\frac{\partial^2 \mathrm{TAC}(T_1,T_2)}{\partial T_2^2}\right) - \left(\frac{\partial^2 \mathrm{TAC}(T_1,T_2)}{\partial T_1 \partial T_2}\right)^2 > 0. \end{aligned} \tag{21}$$

From Eqs. (11) and (19), the optimal values of Q^* and TAC^* are obtained assuming suitable values for A, T, r, s, p, v, U, C_{oh}, C_{rh}, δ, θ_1, θ_2, θ_3, θ_4, C_l, and C_s with appropriate units.

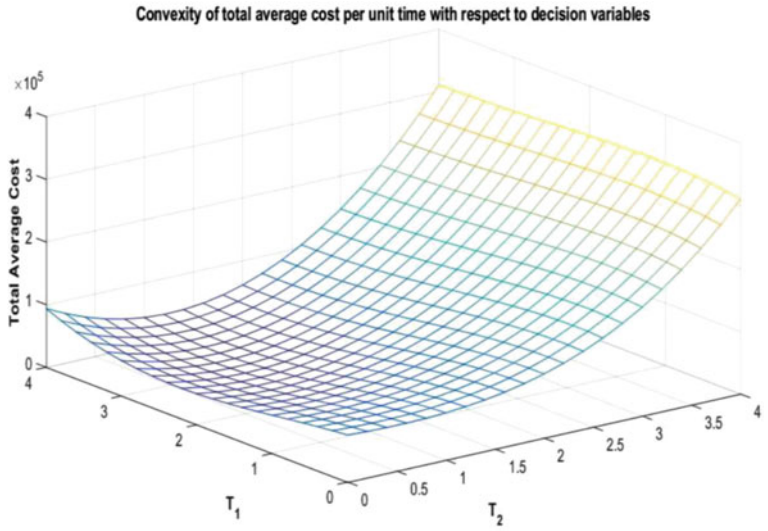

Fig. 2 Convexity of TAC per unit time in regard to the verdict variables

5 Numerical Example

Using data A = 1000, r = 100, s = 15, p = 20, v = 0.08, U = 170, C_l = 12, C_s = 10, C_{oh} = 24, C_{rh} = 60, δ = 0.05, θ_1 = 0.008, θ_2 = 0.007, θ_3 = 0.004, θ_4 = 0.005 and T = 4. After solving Eqs. (20) and (21), we get T_1^* = 0.9484, T_2^* = 2.9869, Q^* = 6331.7 and TAC^* = 33,277 (Fig. 2).

6 Sensitivity Analysis

Sensitivity investigation has been performed by using the data given in the above example and changing the values of the parameters U, v, δ, θ_1, θ_2, θ_3, and θ_4 by −50%, −25%, 0, +25%, and +50%. The remaining parameters are kept at their original value (Figs. 3, 4, 5, 6, 7, 8, and 9).

Effects of different parameters on optimal values of this inventory system are as follows:

1. From Table 3, we can see that as values of parameter U range from 85 to 255 then T_1^* decreases from 0.9712 to 0.9264, T_2^* decreases from 3.0032 to 2.9711, TAC^* increases from 32,401 to 34,132, and Q^* increases from 6207.3 to 6455.7.
2. From Table 3, we can see that as values of parameter v range from 0.04 to 0.12 then T_1^* decreases from 1.0852 to 0.8687, T_2^* decreases from 3.4299 to 2.5957, TAC^* decreases from 43,630 to19922, and Q^* increases from 4384.9 to 7886.7.

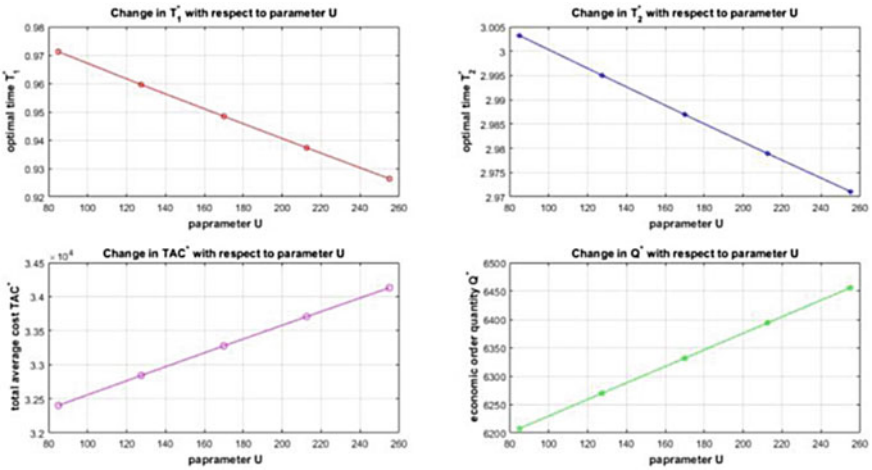

Fig. 3 Percentage change in optimum time, total average cost, and economic order quantity with respect to parameter U

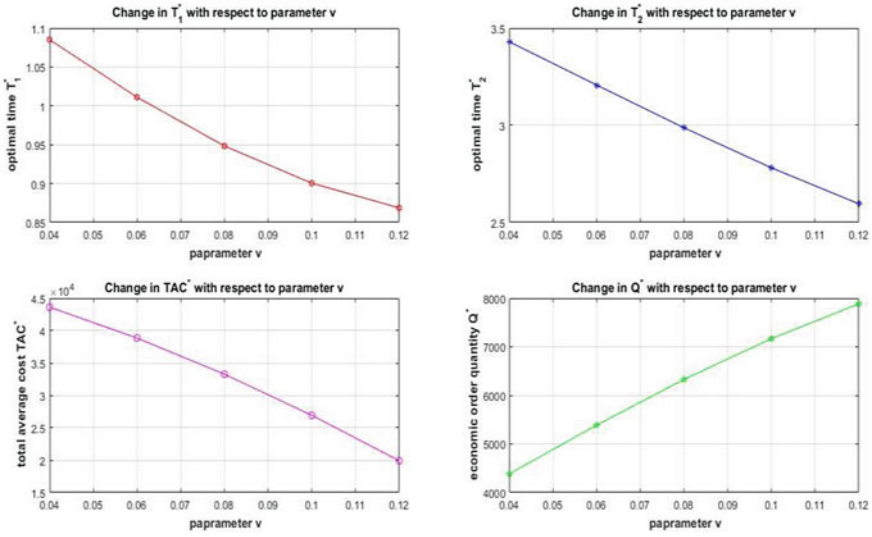

Fig. 4 Percentage change in optimum time, total average cost, and economic order quantity with respect to parameter v

3. From Table 3, we can see that as values of parameter δ range from 0.0250 to 0.0750, T_1^* decreases from 0.9486 to 0.9482, T_2^* decreases from 2.9874 to 2.9864, TAC^* decreases from 33,279 to 33,275, and Q^* decreases from 6338.5 to 6325.7.

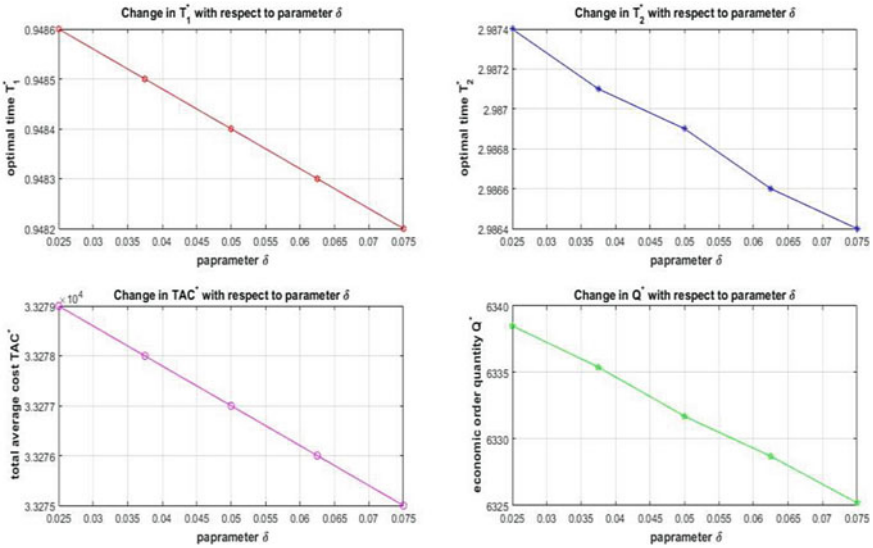

Fig. 5 Percentage change in optimum time, total average cost, and economic order quantity with respect to parameter δ

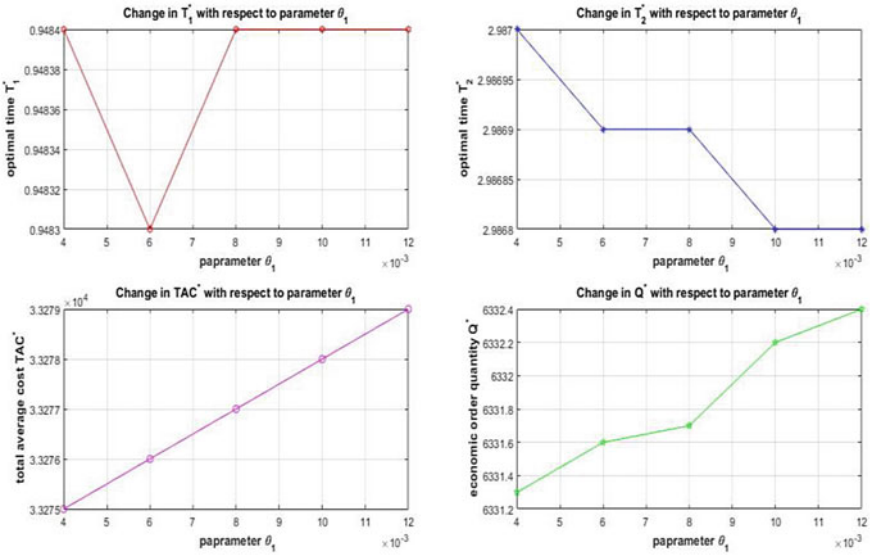

Fig. 6 Percentage change in optimum time, total average cost, and economic order quantity with respect to parameter θ_1

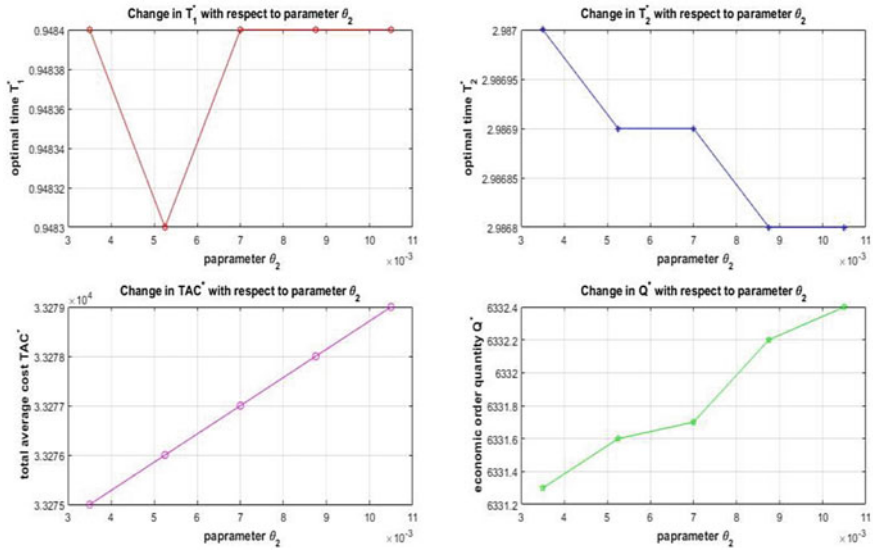

Fig. 7 Percentage change in optimum time, total average cost, and economic order quantity with respect to parameter θ_2

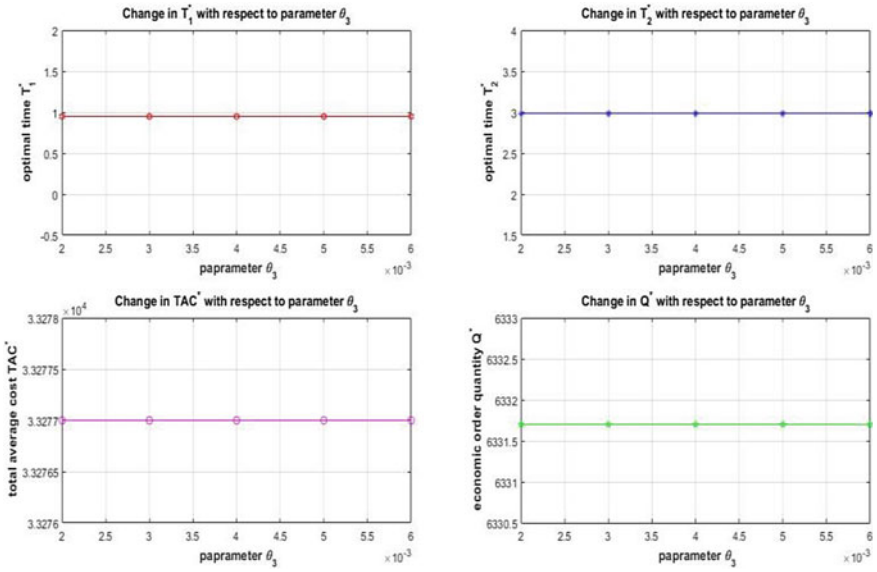

Fig. 8 Percentage change in optimum time, total average cost, and economic order quantity with respect to parameter θ_3

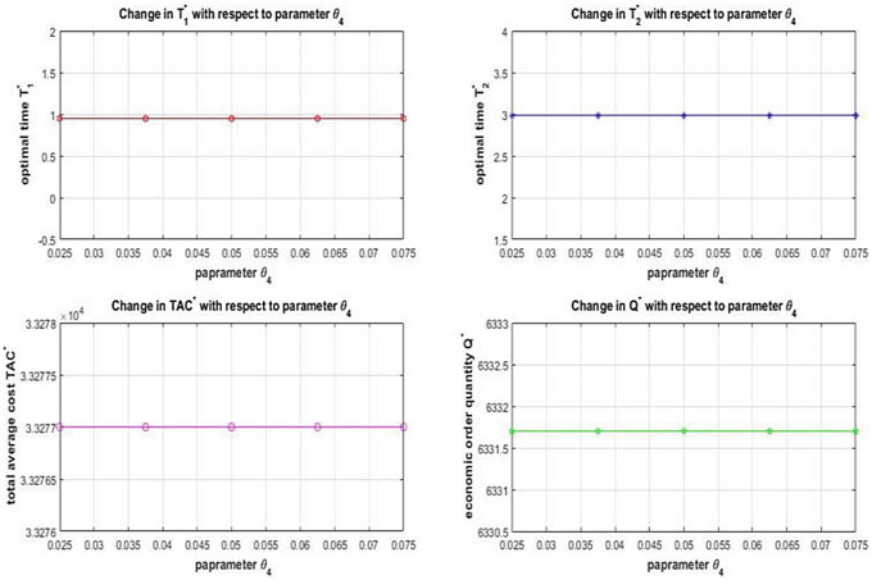

Fig. 9 Percentage change in optimum time, total average cost, and economic order quantity with respect to parameter θ_4

4. From Table 3, we can see that as values of parameter θ_1 range from 0.004 to 0.012, T_1^* decreases from 0.9484 to 0.9483 and after that it remains constant at 0.9484, T_2^* decreases from 2.9870 to 2.9868, TAC^* increases from 33,275 to 33,279, and Q^* increases from 6331.3 to 6332.4.
5. From Table 3, we can see that as values of parameter θ_2 range from 0.00350 to 0.01050, T_1^* decreases from 0.9484 to 0.9483 and after that it remains constant at 0.9484, T_2^* decreases from 2.9870 to 2.9868, TAC^* increases from 33,275 to 33,279, and Q^* increases from 6331.3 to 6332.4.
6. From Table 3, we can see that as values of parameter θ_3 range from 0.002 to 0.006, T_1^*, T_2^*, TAC^*, and Q^* remain constant at their optimal values.
7. From Table 3, we can see that as values of parameter θ_4 range from 0.00250 to 0.00750, T_1^*, T_2^*, TAC^*, and Q^* remain constant at their optimal values.

7 Conclusion

We have established the model using deterioration under-inflation when rented warehouses have higher holding costs than own warehouse. We have proposed an optimal policy to minimize the TAC and verified this inventory system by employing a numerical example through the medium of MATLAB, and obtained the optimal esteems of T_1, T_2, Q, and TAC. The convexity of TAC concerning the ruling variables has also been manifested graphically. Sensitivity investigation is accomplished by modifying

Table 3 Sensitivity investigation for diverse inventory parameters

Parameter	Percentage change	Value of the parameter	Optimal values						
			T_1^*	T_2^*	TAC*	HD*	SC*	LSC*	**Q***
U	−50%	85	0.9712	3.0032	32,401	15,620	−2420.9	571.3412	6207.3
	−25%	127.5	0.9596	2.9950	32,842	15,778	−2469.4	576.7214	6269.7
	0%	170	0.9484	2.9869	33,277	15,930	−2517.3	581.9803	6331.7
	+25%	212.5	0.9373	2.9789	33,707	16,075	−2565.5	587.2217	6393.9
	+50%	255	0.9264	2.9711	34,132	16,215	−2613.0	592.3364	6455.7
v	−50%	0.04	1.0852	3.4299	43,630	25,453	−1465.1	416.4600	4384.9
	−25%	0.06	1.0112	3.2072	38,867	20,228	−2140.4	512.1253	5388.5
	0%	0.08	0.9484	2.9869	33,277	15,930	−2517.3	581.9803	6331.7
	+25%	0.10	0.9005	2.7809	26,928	12,566	−2426.0	626.7836	7169.4
	+50%	0.12	0.8687	2.5957	19,922	10,028	−1806.6	649.3790	7886.7
δ	−50%	0.0250	0.9486	2.9874	33,279	15,938	−2518.7	290.8391	6338.5
	−25%	0.0375	0.9485	2.9871	33,278	15,933	−2518.3	436.3983	6335.4
	0%	0.0500	0.9484	2.9869	33,277	15,930	−2517.3	581.9803	6331.7
	+25%	0.0625	0.9483	2.9866	33,276	15,926	−2517.1	727.7222	6328.7
	+50%	0.0750	0.9482	2.9864	33,275	15,922	−2516.2	873.4626	6325.2
θ_1	−50%	0.004	0.9484	2.9870	33,275	15,930	−2516.9	581.9337	6331.3
	−25%	0.006	0.9483	2.9869	33,276	15,930	−2517.3	581.9777	6331.6
	0%	0.008	0.9484	2.9869	33,277	15,930	−2517.3	581.9803	6331.7
	+25%	0.010	0.9484	2.9868	33,278	15,930	−2518.0	582.0479	6332.2
	+50%	0.012	0.9484	2.9868	33,279	15,930	−2518.1	582.0567	6332.4

(continued)

Table 3 (continued)

Parameter	Percentage change	Value of the parameter	Optimal values						
			T_1^*	T_2^*	TAC^*	HD^*	SC^*	LSC^*	$\mathbf{Q}^*$
θ_2	−50%	0.00350	0.9484	2.9870	33,275	15,930	−2516.9	581.9337	6331.3
	−25%	0.00525	0.9483	2.9869	33,276	15,930	−2517.3	581.9777	6331.6
	0%	0.00700	0.9484	2.9869	33,277	15,930	−2517.3	581.9803	6331.7
	+25%	0.00875	0.9484	2.9868	33,278	15,930	−2518.0	582.0479	6332.2
	+50%	0.01050	0.9484	2.9868	33,279	15,930	−2518.1	582.0567	6332.4
θ_3	−50%	0.002	0.9484	2.9869	33,277	15,930	−2517.3	581.9803	6331.7
	−25%	0.004	0.9484	2.9869	33,277	15,930	−2517.3	581.9803	6331.7
	0%	0.006	0.9484	2.9869	33,277	15,930	−2517.3	581.9803	6331.7
	+25%	0.008	0.9484	2.9869	33,277	15,930	−2517.3	581.9803	6331.7
	+50%	0.010	0.9484	2.9869	33,277	15,930	−2517.3	581.9803	6331.7
θ_4	−50%	0.00250	0.9484	2.9869	33,277	15,930	−2517.3	581.9803	6331.7
	−25%	0.00375	0.9484	2.9869	33,277	15,930	−2517.3	581.9803	6331.7
	0%	0.00500	0.9484	2.9869	33,277	15,930	−2517.3	581.9803	6331.7
	+25%	0.00625	0.9484	2.9869	33,277	15,930	−2517.3	581.9803	6331.7
	+50%	0.00750	0.9484	2.9869	33,277	15,930	−2517.3	581.9803	6331.7

various parameters to see this parameter's effect on the system's optimal values. Someone can further extend the model by adding reliability, admissible delay in payments, advertisement, stock, and price-sensitive demand. Someone can also apply fuzzy mathematics to the model to get optimal solutions of real-world models under uncertainty.

References

1. Aastha PS, Mittal M, Cárdenas-Barrón L (2020) Impact of imperfect quality items on inventory management for two warehouses with shortages. Int J Math Eng Manag Sci 5(5):869–885
2. Agarwal A, Sangal I, Singh SR, Rani S (2018) Two-warehouse inventory model for life time deterioration and inflation with exponential demand and partial lost sales. Int J Pure Appl Math 118(22):1253–1265
3. Agrawal S, Banerjee S, Papachristos S (2013) Inventory model with deteriorating items, ramp-type demand and partially backlogged shortages for a two warehouse system. Appl Math Model 37(20–21):8912–8929. https://doi.org/10.1016/j.apm.2013.04.026
4. Alawneh F, Zhang G (2018) Dual-channel warehouse and inventory management with stochastic demand. Transp Res Part E: Logist Transp Rev 112:84–106
5. Bhunia AK, Jaggi CK, Sharma A, Sharma R (2014) A two-warehouse inventory model for deteriorating items under permissible delay in payment with partial backlogging. Appl Math Comput 232:1125–1137. https://doi.org/10.1016/j.amc.2014.01.115
6. Dubey RD, Mishra VN (2020) Higher-order symmetric duality in nondifferentiable multi-objective fractional programming problem over cone contraints. Stat Optim Inf Comput 8(1):187–205
7. Dubey RV, Mishra VN, Karateke S (2020) A class of second order nondifferentiable symmetric duality relations under generalized assumptions. J Math Comput SCI-JM 21(2):120–126
8. Ghiami Y, Beullens P (2020) The continuous resupply policy for deteriorating items with stock-dependent observable demand in a two-warehouse and two-echelon supply chain. Appl Math Model 82:271–292
9. Gothi UB, Saxena P, Parmar K (2016) An inventory model for two warehouses with constant deterioration and quadratic demand rate under inflation and permissible delay in payments. Am J Eng Res (AJER) 5(6):62–73
10. Hartley RV (1976) Operation research-a managerial emphasis. Good Year Publishing Company, Santa Monica California, pp 315–317
11. Indrajitsingha SK, Samanta P, Raju LK, Misra U (2019) Two-storage inventory model for deteriorating items with price dependent demand and shortages under partial backlogged in fuzzy approach. LogForum 15(4):487–499. https://doi.org/10.17270/J.LOG.2019.344
12. Jaggi CK, Pareek S, Khanna A, Sharma R (2014) Credit financing in a two-warehouse environment for deteriorating items with price-sensitive demand and fully backlogged shortages. Appl Math Model 38(21–22):5315–5333
13. Khanna A, Gautam P, Jaggi CK (2017) Inventory modeling for deteriorating imperfect quality items with selling price dependent demand and shortage backordering under credit financing. Int J Math Eng Manag Sci 2(2):110–124
14. Khurana D (2015) Two warehouse inventory model for deteriorating items with time dependent demand under inflation. Int J Comput Appl 114(7):34–38
15. Kumar A, Chanda U (2018) Two-warehouse inventory model for deteriorating items with demand influenced by innovation criterion in growing technology market. J Manag Anal 5(3):198–212
16. Lee CC, Hsu SL (2009) A two-warehouse production model for deteriorating inventory items with time-dependent demands. Eur J Oper Res 194(3):700–710. https://doi.org/10.1016/j.ejor.2007.12.034

17. Liang Y, Zhou F (2011) A two-warehouse inventory model for deteriorating items under conditionally permissible delay in payment. Appl Math Model 35(5):2221–2231
18. Manna AK, Akhtar M, Shaikh AA, Bhunia AK (2021) Optimization of a deteriorated two-warehouse inventory problem with all-unit discount and shortages via tournament differential evolution. Appl Soft Comput 107:107388
19. Mashud AHM, Wee HM, Sarkar B, Li YHC (2020) A sustainable inventory system with the advanced payment policy and trade-credit strategy for a two-warehouse inventory system. Kybernetes. https://doi.org/10.1108/K-01-2020-0052
20. Nath BK, Sen N (2021) A Completely backlogged two-warehouse inventory model for non-instantaneous deteriorating items with time and selling price dependent demand. Int J Appl Comput Math 7(4):1–22. https://doi.org/10.1007/s40819-021-01070-x
21. Öztürk H (2018) Optimization of fuzzy production inventory models for crisp or fuzzy production time. Pak J Stat Oper Res 661–695
22. Pakhira R, Ghosh U, Sarkar S (2019) Study of memory effect in an economic order quantity model with quadratic type demand rate. Comput Methods Sci Technol 25(2):71–80
23. Pakhira R, Ghosh U, Sarkar S, Mishra V (2021) Study of memory effect in an inventory model with constant deterioration rate. J Appl Nonlinear Dyn 10(2):229–243. https://doi.org/10.5890/JAND.2021.06.004
24. Pakkala TPM, Achary KK (1992) A deterministic inventory model for deteriorating items with two warehouses and finite replenishment rate. Eur J Oper Res 57(1):71–76
25. Palanivel M, Uthayakumar R (2016) Two-warehouse inventory model for non–instantaneous deteriorating items with optimal credit period and partial backlogging under inflation. J Control Decis 3(2):132–150. https://doi.org/10.1080/23307706.2015.1092099
26. Panda D, Maiti MK, Maiti M (2010) Two warehouse inventory models for single vendor multiple retailers with price and stock dependent demand. Appl Math Model 34(11):3571–3585
27. Pradhan LM, Tripathy CK (2012) A production inventory model for an item with three parameter weibull deterioration and price discount. LogForum 8(3):257–266
28. Rana RS, Kumar D, Prasad K (2021) Two warehouse dispatching policies for perishable items with freshness efforts, inflationary conditions and partial backlogging. Operat Manag Res 1–18
29. Rong M, Mahapatra NK, Maiti M (2008) A two warehouse inventory model for a deteriorating item with partially/fully backlogged shortage and fuzzy lead time. Eur J Oper Res 189(1):59–75
30. Saxena P, Singh S, Sangal I (2016) A two-warehouse production inventory model with trade credit under reliability consideration. Uncertain Supply Chain Manag 4(4):319–330
31. Sett BK, Sarkar B, Goswami A (2012) A two-warehouse inventory model with increasing demand and time varying deterioration. Sci Iran 19(6):1969–1977
32. Shah NH, Rabari K, Patel E (2021) Dynamic demand and pricing inventory model for non-instantaneous deteriorating items. Int J Math Eng Manag Sci 6(2):510–521. https://doi.org/10.33889/IJMEMS.2021.6.2.031
33. Shaikh AA, Cárdenas-Barrón LE, Tiwari S (2019) A two-warehouse inventory model for non-instantaneous deteriorating items with interval-valued inventory costs and stock-dependent demand under inflationary conditions. Neural Comput Appl 31(6):1931–1948. https://doi.org/10.1007/s00521-017-3168-4
34. Sharma V, Chaudhary R (2016) Two-warehouse optimized inventory model for time dependent decaying items with ramp type demand rate under inflation. Uncertain Supply Chain Manag 4(4):287–306
35. Singh SR, Rathore H (2016) A two warehouse inventory model with preservation technology investment and partial backlogging. Sci Iran 23(4):1952–1958
36. Singh T, Pattnayak H (2014) A two-warehouse inventory model for deteriorating items with linear demand under conditionally permissible delay in payment. Int J Manag Sci Eng Manag 9(2):104–113
37. Vandana, Dubey R, Deepmala, Mishra L, Mishra V (2018) Duality relations for a class of a multiobjective fractional programming problem involving support functions. Am J Operat Res 8:294–311. https://doi.org/10.4236/ajor.2018.84017

38. Xu X, Bai Q, Chen M (2017) A comparison of different dispatching policies in two-warehouse inventory systems for deteriorating items over a finite time horizon. Appl Math Model 41:359–374
39. Yang HL (2006) Two-warehouse partial backlogging inventory models for deteriorating items under inflation. Int J Prod Econ 103(1):362–370
40. Yang HL (2012) Two-warehouse partial backlogging inventory models with three-parameter Weibull distribution deterioration under inflation. Int J Prod Econ 138(1):107–116
41. Zhou YW, Yang SL (2005) A two-warehouse inventory model for items with stock-level-dependent demand rate. Int J Prod Econ 95(2):215–228

Exact Solitary Wave Solutions of the (3+1)-Dimensional Generalised Kadomtsev–Petviashvili Benjamin–Bona–Mahony Equation

Biswajit Mallick and Prakash Kumar Sahu

Abstract In this paper, the authors studied the (3+1)-dimensional generalised Kadomtsev–Petviashvili Benjamin–Bona–Mahony (KP-BBM) equation. The exact solitary wave solutions of the nonlinear partial differential equation have been obtained by using the modified hyperbolic function expansion method. The required preliminaries for the method of modified hyperbolic expansion have been given. Two numerical examples have been illustrated and the exact solutions obtained are explained with the help of two-dimensional and three-dimensional graphs. The solutions have different physical structures depending on the involved parameters. This technique can also be employed to compute the new exact solution of higher order nonlinear partial differential equations.

Keywords KP equation · BBM equation · Nonlinear pdes · Hyperbolic function expansion method

1 Introduction

The nonlinear partial differential equations (NPDEs) arise in a wide variety of problems in mathematics and physics. In recent years, most of the scientific phenomena are designed via nonlinear partial differential equations. Apart from the traditional physical problems like fluid dynamics, plasma physics, quantum physics, solid physics, and meteorology, the nonlinear partial differential equations have also important applications in the development of marine dynamics [1], in biology and population genetics [2], in aerospace industry [3], in mathematical finance [4], and so on. Due to their enormous applications, many researchers have devoted their attention towards investigating the solutions of nonlinear partial differential equations using various methods. The exact solutions of nonlinear partial differential equations pro-

B. Mallick (✉) · P. K. Sahu
Department of Mathematics, School of Applied Sciences, KIIT Deemed to be University, Bhubaneswar 751024, Odisha, India
e-mail: biswajitmallick610@gmail.com

J. Singh et al. (eds.), *Advances in Mathematical Modelling, Applied Analysis and Computation*, Lecture Notes in Networks and Systems 415,
https://doi.org/10.1007/978-981-19-0179-9_14

vide a better understanding for the development, analysis, and verification of the mechanisms of nonlinear physical phenomena, as well as for the testing of the validity, reliability, and acceptability of the solutions which are obtained by approximate analytical and numerical methods. Some of the recent methods used for solving the nonlinear partial differential equations are optimal perturbation iteration technique [2], the Riccati–Bernoulli Sub-ODE approach [5], generalised exponential rational function method [6], the Tarig projected differential transform method [8], and much more.

In 1970, Boris Kadomtsev (1928–1998) together with Vladimir Petviashvili (1936–1993) [7] introduced a model in the form of a nonlinear partial differential equation in two spatial and one temporal coordinate to describe the nonlinear waves of small amplitude propagating in a dispersive medium, which is known as the Kadomtsev–Petviashvili equation (or simply the KP equation) and it came as a natural generalisation of the KdV equation [9] (derived by Korteweg and De Vries in 1895). The Kadomtsev–Petviashvili (KP) equation is written in the form

$$(v_t + 6vv_x + v_{xxx})_x + 3\sigma v_{yy} = 0. \tag{1}$$

Since the Kadomtsev–Petviashvili (KP) equation is one of the most universal models in nonlinear wave theory, it has been extensively studied in the mathematical community in the last fifty years. Some recent study includes the $\exp(-\varphi(\eta))$-expansion technique and the adaptive moving mesh method for obtaining the analytical and numerical solutions of the Kadomtsev–Petviashvili (KP) equation arising in plasma physics [10]; construction of multi-wave complexion solutions [11]; and the study of the compatibility conditions by the Painleve analysis and the WTC–Kruskal method [12], lump solutions by Hirota bilinear method [13], the novel explicit wave solutions by using the modified Khater method [14], multiple-order line rogue wave solutions [15], etc.

In 1972, Benjamin, Bona, and Mahony [16] derived a model to study the dynamical properties of long waves in nonlinear dispersive systems, known as the Benjamin–Bona–Mahony (BBM) equation or regularised long-wave (RLW) equation which was considered as an improvement of the KdV equation [9] of the form

$$v_t + v_x + vv_x - v_{xxt} = 0. \tag{2}$$

The Benjamin–Bona–Mahony (BBM) equation is used to describe different physical models that arise in the fields of mathematical physics, fluid dynamics, and in other scientific applications like in the optical illusions field [19]. Recent study on the BBM equation includes the modified Khater method and B-spline collection schemes [19], the iterative analysis [17], the geometrical demonstration for continuation of solutions [18], the solitary wave solutions [20], etc. Wazwaz [21] proposed BBM equation formulated in KP sense and named it as the KP-BBM equation

$$(v_t + v_x - a(v^2)_x - bv_{xxt})_x + rv_{yy} = 0, \tag{3}$$

a generalised form of KP-BBM equation

$$(v_t + v_x - a(v^n)_x - bv_{xxt})_x + rv_{yy} = 0, \quad n > 1, \tag{4}$$

and a variant of KP-BBM equation

$$(v_t + v_x - a(v^2{-}n)_x - bv_{xxt})_x + rv_{yy} = 0, \quad n > 1, \tag{5}$$

where a, b, and r are real parameters and n is positive integer. This equation has been studied by many researchers with various methods, and Wazwaz constructed a variety of exact travelling wave solutions of compact and noncompact structures using the tanh method and the sine–cosine method [21]; Mekki et al. used finite difference method to obtain the approximate solutions [22]; Abdou used the extended mapping method to obtain exact periodic wave solutions [23]; Bifurcation method of dynamical systems has been used to obtain exact solitary wave solutions [24, 25]; Hoque et al. used the Hirota bilinear approach to obtain higher order rogue wave solutions [26].

In this work, the authors use the modified hyperbolic function expanding method to solve the (3+1)-dimensional generalised KP-BBM equation [27, 28],

$$v_{tx} + \mu_1 v_{xx} + \mu_2 (vv_x)_x - \mu_3 v_{xxtx} + \mu_4 v_{yy} + \mu_5 v_{zz} = 0, \tag{6}$$

which describes the fluid flow in the case of an offshore structure [29]. Here, $v(x, y, z, t)$ is an analytic function of space coordinates, x, y, z, and time coordinate, t, and the coefficients μ_i, $(i = 1, 2, 3, 4, 5)$ are all constants. Recently, many researchers worked on this (3+1)-dimensional KP-BBM equation as follows: in [27], Tariq et al. obtained the soliton solutions of (3 + 1)-dimensional KP-BBM equation with some other similar type of equations and their applications in water waves; in [28], Yin et al. derived the lump-wave and breather-wave solutions for a (3 + 1)-dimensional generalised KP-BBM equation for an offshore structure; in [30], Liu et al. derived multiple rogue wave solutions through symbolic calculation approach, etc. Different approaches for solving nonlinear PDEs motivate us to find solitary wave solutions of (3 + 1)-dimensional generalised KP-BBM equation in a very simplified form.

This article has been structured as follows. In the first section, the detailed introduction of the considered problem has been discussed which is followed by the preliminary section where the general solutions of an equation which are satisfied by the hyperbolic function have been defined. Section 3 has been devoted to the description of the modified hyperbolic function expanding method. The exact solitary wave solution of (3 + 1)-dimensional generalised KP-BBM equation, using the modified hyperbolic function expanding method, is presented in Sect. 4. Some numerical results and the graphical interpretation of the exact solutions to (3 + 1)-dimensional generalised KP-BBM equations with help of 3D and 2D figures are illustrated in Sect. 5. Finally, discussion and conclusions about the work are presented in Sect. 6, followed by the references.

2 Preliminaries

Given the hyperbolic function $\psi(\xi)$ satisfying the equation

$$\psi'(\xi) = \gamma + \psi^2(\xi), \tag{7}$$

where γ is an arbitrary real number.
Depending on the value of γ, the general solutions of Eq. (7) are defined as follows:

1. if $\gamma > 0$,
$$\psi_1(\xi) = \sqrt{\gamma}\tan\left(\sqrt{\gamma}(\xi + \rho)\right), \tag{8}$$
2. if $\gamma = 0$,
$$\psi_2(\xi) = -\frac{1}{\xi + \rho}, \tag{9}$$
3. if $\gamma < 0$,
$$\psi_3(\xi) = -\sqrt{-\gamma}\tan\left(\sqrt{-\gamma}(\xi + \rho)\right), \tag{10}$$

where ρ is any arbitrary real number.

3 Description of Modified Hyperbolic Function Expanding Method

In this part, the basic steps involved in the modified hyperbolic function expanding method have been described.
Consider the general nonlinear partial differential equation having independent spatial variables $x_1, x_2, \cdots, x_n$ and time variable t in closed form as

$$\mathtt{P}(v, v_t, v_{x_1}, \cdots, v_{x_n}, v_{tt}, v_{tx_1}, \cdots) = 0, \tag{11}$$

where $v = v(x_1, x_2, \cdots, x_n, t)$ is an unknown function and $\mathtt{P}$ denotes a polynomial function of its arguments.
Assume that the exact solution of Eq. (11) is

$$v(x_1, x_2, \cdots, x_n, t) = v(\kappa_1 x_1 + \kappa_2 x_2 + \cdots + \kappa_n x_n + ct) = v(\xi), \tag{12}$$

where $\xi = \kappa_1 x_1 + \kappa_2 x_2 + \cdots + \kappa_n x_n + ct$, and the coefficients $\kappa_1, \kappa_2, \cdots, \kappa_n, c$ are real constants to be determined with the restriction that the product $\kappa_1\kappa_2\cdots\kappa_n \neq 0$.
Substituting Eq. (12) into Eq. (11), it reduces to an ordinary differential equation of the form

$$\mathtt{P}(v, v', v'', v''' \cdots) = 0, \tag{13}$$

where the derivatives are with respect to ξ.
Equation (13) is then integrated as long as all the terms contain derivatives and the integration constants are considered as zeros.
Assume that the solution $v(\xi)$ of Eq. (13) can be expressed as a finite series of the form

$$v(\xi) = a_0 + \sum_{i=1}^{M} \left(a_i \psi^{-i}(\xi) + b_i \psi^{i}(\xi) + c_i \psi^{i}(\xi)\psi'(\xi) + d_i \psi^{-i}(\xi)\psi'(\xi)\right), \quad (14)$$

where $\psi(\xi)$ satisfies Eq. (7) and $a_0, a_i, b_i, c_i, d_i, 1 \leq i \leq M$ are constants to be determined later. The parameter M in Eq. (14) can be found by balancing the linear term of the highest order with the nonlinear term of highest degree of Eq. (13) using homogeneous balance method [31].
Inserting Eqs. (14) and (7) into the ordinary differential equation (13) and collecting the coefficients of ψ^i, then setting the coefficients equal to zero, a system of nonlinear algebraic equations involving the parameters $a_0, a_i, b_i, c_i, d_i, \kappa_i, 1 \leq i \leq M$, and c have been obtained. Solving the system, the values of the parameters are obtained . Substituting these parameters $a_0, a_i, b_i, c_i, d_i, \kappa_i, 1 \leq i \leq M$, and c into Eq. (14), the exact solitary wave solution of Eq. (11) has been obtained.

4 Solutions of the (3+1)-Dimensional Generalised Kadomtsev–Petviashvili Benjamin–Bona–Mahony (KP-BBM) Equation

Consider Eq. (6). For simplicity, we assume the coefficients which are real constant as unity reduce Eq. (6) to the form

$$v_{tx} + v_{xx} + (vv_x)_x - v_{xxtx} + v_{yy} + v_{zz} = 0. \quad (15)$$

For Eq. (15), let us set

$$v(x, y, z, t) = v(\xi), \quad \xi = \kappa_1 x + \kappa_2 y + \kappa_3 z + ct, \quad (16)$$

where κ_1, κ_2, κ_3, and c are any real numbers to be determine, and $\kappa_1 \cdot \kappa_2 \cdot \kappa_3 \neq 0$. By substituting Eqs. (16) in (15), it reduces to an ordinary differential equation of the form

$$(c\kappa_1 + \kappa_1^2 + \kappa_2^2 + \kappa_3^2)v'' + \kappa_1^2(vv'' + v'^2) - \kappa_1^3 c v^{(iv)} = 0. \quad (17)$$

Integrating Eq. (17) with respect to ξ from 0 to ξ, we get

$$(c\kappa_1 + \kappa_1^2 + \kappa_2^2 + \kappa_3^2)v' + \kappa_1^2 vv' - \kappa_1^3 c v''' = 0. \quad (18)$$

Integrating once more, it gives

$$(c\kappa_1 + \kappa_1^2 + \kappa_2^2 + \kappa_3^2)v + \frac{1}{2}\kappa_1^2 v^2 - \kappa_1^3 c v'' = 0. \tag{19}$$

By considering the balance coefficient method [31] for balancing the nonlinear term v^2, that has the exponent $2M$, with the highest order derivative v'', that has the exponent $M+2$, in Eq. (19), we get $M = 2$.
Therefore, $v(\xi)$ can be expressed as

$$\begin{aligned} v(\xi) &= a_0 + \sum_{i=1}^{2} \left(a_i \psi^{-i}(\xi) + b_i \psi^{i}(\xi) + c_i \psi^{i}(\xi)\psi'(\xi) + d_i \psi^{-i}(\xi)\psi'(\xi)\right) \\ &= a_0 + a_1\psi^{-1}(\xi) + a_2\psi^{-2}(\xi) + b_1\psi^{1}(\xi) + b_2\psi^{2}(\xi) + c_1\psi^{1}(\xi)\psi'(\xi) \\ &+ c_2\psi^{2}(\xi)\psi'(\xi) + d_1\psi^{-1}(\xi)\psi'(\xi) + d_2\psi^{-2}(\xi)\psi'(\xi). \end{aligned} \tag{20}$$

Substituting Eqs. (7) and (20) into Eq. (19) and collecting all terms with the same powers of $\psi(\xi)$ to obtain a system of algebraic equations for the coefficients a_0, a_1, a_2, b_1, b_2, c_1, c_2, d_1, d_2, κ_1, κ_2, κ_3, and c. Solving this system, the following set of values for the unknown parameters are obtained:

Set-1: $a_0 = -d_2 + 12c\kappa_1\gamma, a_1 = -d_1\gamma, a_2 = \gamma(-d_2 + 12c\kappa_1\gamma), b_1 = -d_1, b_2 = 0, c_1 = 0, c_2 = 0, d_1 = d_1, d_2 = d_2, \kappa_1 = \kappa_1,$
$\kappa_2 = \kappa_2, \kappa_3 = \pm(-c\kappa_1 - \kappa_1^2 - \kappa_2^2 - 4c\kappa_1^3\gamma)^{1/2}, c = c, \gamma = \gamma.$
Set-2: $a_0 = -d_2 + 4c\kappa_1\gamma, a_1 = -d_1\gamma, a_2 = \gamma(-d_2 + 12c\kappa_1\gamma), b_1 = -d_1, b_2 = 0, c_1 = 0, c_2 = 0, d_1 = d_1, d_2 = d_2, \kappa_1 = \kappa_1,$
$\kappa_2 = \kappa_2, \kappa_3 = \pm(-c\kappa_1 - \kappa_1^2 - \kappa_2^2 + 4c\kappa_1^3\gamma)^{1/2}, c = c, \gamma = \gamma.$
Set-3: $a_0 = -d_2 + 24c\kappa_1\gamma, a_1 = -d_1\gamma, a_2 = \gamma(-d_2 + 12c\kappa_1\gamma), b_1 = -d_1, b_2 = 12c\kappa_1, c_1 = 0, c_2 = 0, d_1 = d_1, d_2 = d_2,$
$\kappa_1 = \kappa_1, \kappa_2 = \kappa_2, \kappa_3 = \pm(-c\kappa_1 - \kappa_1^2 - \kappa_2^2 - 16c\kappa_1^3\gamma)^{1/2}, c = c, \gamma = \gamma.$
Set-4: $a_0 = -d_2 + 12c\kappa_1\gamma, a_1 = -d_1\gamma, a_2 = -d_2\gamma, b_1 = -d_1, b_2 = 12c\kappa_1, c_1 = 0, c_2 = 0, d_1 = d_1, d_2 = d_2, \kappa_1 = \kappa_1, \kappa_2 = \kappa_2,$
$\kappa_3 = \pm(-c\kappa_1 - \kappa_1^2 - \kappa_2^2 - 4c\kappa_1^3\gamma)^{1/2}, c = c, \gamma = \gamma.$
Set-5: $a_0 = -d_2 + 4c\kappa_1\gamma, a_1 = -d_1\gamma, a_2 = -d_2\gamma, b_1 = -d_1, b_2 = 12c\kappa_1, c_1 = 0, c_2 = 0, d_1 = d_1, d_2 = d_2, \kappa_1 = \kappa_1, \kappa_2 = \kappa_2,$
$\kappa_3 = \pm(-c\kappa_1 - \kappa_1^2 - \kappa_2^2 + 4c\kappa_1^3\gamma)^{1/2}, c = c, \gamma = \gamma.$
Set-6: $a_0 = -d_2 + 8c\kappa_1\gamma, a_1 = -d_1\gamma, a_2 = \gamma(-d_2 + 12c\kappa_1\gamma), b_1 = -d_1, b_2 = 12c\kappa_1, c_1 = 0, c_2 = 0, d_1 = d_1, d_2 = d_2, \kappa_1 = \kappa_1,$
$\kappa_2 = \kappa_2, \kappa_3 = \pm(-c\kappa_1 - \kappa_1^2 - \kappa_2^2 + 16c\kappa_1^3\gamma)^{1/2}, c = c, \gamma = \gamma.$

Now, these solution sets together with the solutions of Eq. (7) will be substituted in Eq. (20) and simplified to obtain the solutions for Eq. (15).

Consider the solution set-1. The solutions for Eq. (15) are obtained as follows.
For $\gamma > 0$, the solution of Eq. (15) is

$$v_{11}(\xi) = 12c\gamma \csc\left[(\rho + \xi)\sqrt{\gamma}\right]^2 \kappa_1, \tag{21}$$

where $\xi = \kappa_1 x + \kappa_2 y \pm (-c\kappa_1 - \kappa_1^2 - \kappa_2^2 - 4c\kappa_1^3\gamma)^{1/2} z + ct$ and c, κ_1, κ_2, ρ, and γ are any real numbers.
For $\gamma < 0$, the solution of Eq. (15) is

$$v_{12}(\xi) = -12c\gamma \operatorname{csch}\left[(\rho + \xi)\sqrt{-\gamma}\right]^2 \kappa_1, \tag{22}$$

where $\xi = \kappa_1 x + \kappa_2 y \pm (-c\kappa_1 - \kappa_1^2 - \kappa_2^2 - 4c\kappa_1^3\gamma)^{1/2} z + ct$ and c, κ_1, κ_2, ρ, and γ are any real numbers.
For $\gamma = 0$, there does not exist any trivial solution for Eq. (15).

Similarly, for solution set-2, the solutions for Eq. (15) are obtained as follows.
For $\gamma > 0$, the solution of Eq. (15) is

$$v_{21}(\xi) = 4c\gamma \left(2 + \cos\left[2(\rho+\xi)\sqrt{\gamma}\right]\right) \operatorname{csc}\left[(\rho+\xi)\sqrt{\gamma}\right]^2 \kappa_1, \tag{23}$$

where $\xi = \kappa_1 x + \kappa_2 y \pm (-c\kappa_1 - \kappa_1^2 - \kappa_2^2 + 4c\kappa_1^3\gamma)^{1/2} z + ct$ and c, κ_1, κ_2, ρ, and γ are any real numbers.
For $\gamma < 0$, the solution of Eq. (15) is

$$v_{22}(\xi) = -4c\gamma \left(2 + \cosh\left[2(\rho+\xi)\sqrt{-\gamma}\right]\right) \operatorname{csch}\left[(\rho+\xi)\sqrt{-\gamma}\right]^2 \kappa_1, \tag{24}$$

where $\xi = \kappa_1 x + \kappa_2 y \pm (-c\kappa_1 - \kappa_1^2 - \kappa_2^2 + 4c\kappa_1^3\gamma)^{1/2} z + ct$ and c, κ_1, κ_2, ρ, and γ are any real numbers.
For $\gamma = 0$, there does not exist any trivial solution for Eq. (15).

For solution set-3, the solutions for Eq. (15) are obtained as below.
For $\gamma > 0$, the solution of Eq. (15) is

$$v_{31}(\xi) = 48c\gamma \operatorname{csc}\left[2(\rho+\xi)\sqrt{\gamma}\right]^2 \kappa_1, \tag{25}$$

where $\xi = \kappa_1 x + \kappa_2 y \pm (-c\kappa_1 - \kappa_1^2 - \kappa_2^2 - 16c\kappa_1^3\gamma)^{1/2} z + ct$ and c, κ_1, κ_2, ρ, and γ are any real numbers.
For $\gamma < 0$, the solution of Eq. (15) is

$$v_{32}(\xi) = -48c\gamma \operatorname{csc} h\left[2(\rho+\xi)\sqrt{-\gamma}\right]^2 \kappa_1, \tag{26}$$

where $\xi = \kappa_1 x + \kappa_2 y \pm (-c\kappa_1 - \kappa_1^2 - \kappa_2^2 - 16c\kappa_1^3\gamma)^{1/2} z + ct$ and c, κ_1, κ_2, ρ, and γ are any real numbers.
For $\gamma = 0$, the solution for Eq. (15) is

$$v_{33}(\xi) = \frac{12c\kappa_1}{(\rho+\xi)^2}, \tag{27}$$

where $\xi = \kappa_1 x + \kappa_2 y \pm (-c\kappa_1 - \kappa_1^2 - \kappa_2^2)^{1/2} z + ct$ and c, κ_1, κ_2, and ρ are any real numbers.

For solution set-4, the solutions for Eq. (15) are obtained as follows.
For $\gamma > 0$, the solution of Eq. (15) is

$$v_{41}(\xi) = 12c\gamma\kappa_1 \sec\left[(\rho+\xi)\sqrt{\gamma}\right]^2, \tag{28}$$

where $\xi = \kappa_1 x + \kappa_2 y \pm (-c\kappa_1 - \kappa_1^2 - \kappa_2^2 - 4c\kappa_1^3\gamma)^{1/2} z + ct$ and c, κ_1, κ_2, ρ, and γ are any real numbers.
For $\gamma < 0$, the solution of Eq. (15) is

$$v_{42}(\xi) = 12c\gamma\kappa_1 \operatorname{sech}\left[(\rho+\xi)\sqrt{-\gamma}\right]^2, \tag{29}$$

where $\xi = \kappa_1 x + \kappa_2 y \pm (-c\kappa_1 - \kappa_1^2 - \kappa_2^2 - 4c\kappa_1^3\gamma)^{1/2} z + ct$ and c, κ_1, κ_2, ρ, and γ are any real numbers.

Now consider the solution set-5. The solutions for Eq. (15) are obtained as follows. For $\gamma > 0$, the solution of Eq. (15) is

$$v_{51}(\xi) = -4c\gamma \left(-2 + \cos\left[2(\rho+\xi)\sqrt{\gamma}\right]\right) \sec\left[(\rho+\xi)\sqrt{\gamma}\right]^2 \kappa_1, \tag{30}$$

where $\xi = \kappa_1 x + \kappa_2 y \pm (-c\kappa_1 - \kappa_1^2 - \kappa_2^2 + 4c\kappa_1^3\gamma)^{1/2} z + ct$ and c, κ_1, κ_2, ρ, and γ are any real numbers.
For $\gamma < 0$, the solution of Eq. (15) is

$$v_{52}(\xi) = -4c\gamma \left(-2 + \cosh\left[2(\rho+\xi)\sqrt{\gamma}\right]\right) \operatorname{sech}\left[(\rho+\xi)\sqrt{\gamma}\right]^2 \kappa_1, \tag{31}$$

where $\xi = \kappa_1 x + \kappa_2 y \pm (-c\kappa_1 - \kappa_1^2 - \kappa_2^2 + 4c\kappa_1^3\gamma)^{1/2} z + ct$ and c, κ_1, κ_2, ρ, and γ are any real numbers.

Lastly, for solution set-6, the solutions for Eq. (15) are obtained as follows.
For $\gamma > 0$, the solution of Eq. (15) is

$$v_{61}(\xi) = 16c\gamma \left(2 + \cos\left[4(\rho+\xi)\sqrt{\gamma}\right]\right) \csc\left[2(\rho+\xi)\sqrt{\gamma}\right]^2 \kappa_1, \tag{32}$$

where $\xi = \kappa_1 x + \kappa_2 y \pm (-c\kappa_1 - \kappa_1^2 - \kappa_2^2 + 16c\kappa_1^3\gamma)^{1/2} z + ct$ and c, κ_1, κ_2, ρ, and γ are any real numbers.
For $\gamma < 0$, the solution of Eq. (15) is

$$v_{62}(\xi) = -16c\gamma \left(2 + \cos\left[4(\rho+\xi)\sqrt{-\gamma}\right]\right) \csc\left[2(\rho+\xi)\sqrt{-\gamma}\right]^2 \kappa_1, \tag{33}$$

where $\xi = \kappa_1 x + \kappa_2 y \pm (-c\kappa_1 - \kappa_1^2 - \kappa_2^2 + 16c\kappa_1^3\gamma)^{1/2} z + ct$ and c, κ_1, κ_2, ρ, and γ are any real numbers.
For the solution sets 4, 5, and 6, the solution for $\gamma = 0$, for Eq. (15), coincides with the solution set of 3 which is defined in Eq. (27).

5 Numerical Results and Graphical Interpretation

In this part of the work, we will discuss some numerical examples for the (3+1)-dimensional generalised Kadomtsev–Petviashvili Benjamin–Bona–Mahony (KP-BBM) equation to validate our obtained result and interpret the exact solitary wave solutions in graphs.

Example 1 In this example, for the solutions of Eq. (15), by using Set-3, we assume the following parameters:

$$k_1 = -1 \ (1 \ for \ \gamma < 0), \ k_2 = -1, \ c = 1, \ \rho = 0.$$

For any real number $\gamma > 0$, let $\gamma = 4$, the solution (25) becomes

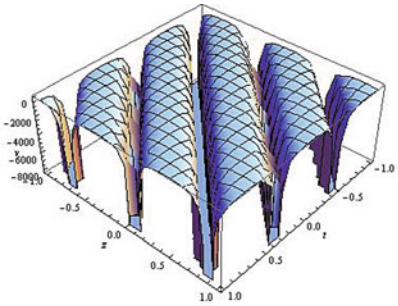

(a) 3-D figure of solution v_{31}

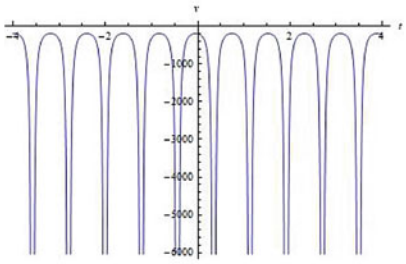

(b) 2-D figure of solution v_{31}

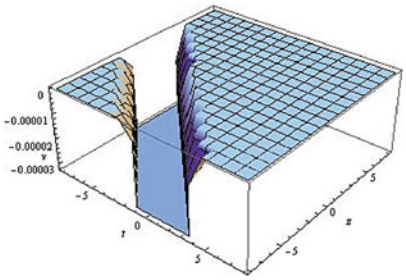

(c) 3-D figure of solution v_{32}

Fig. 1 Behaviour of solutions for example 1

$$v_{31}(\xi) = -192 \csc(4\xi)^2, \tag{34}$$

where $\xi = t - x - y + 3\sqrt{7}z$. The three-dimensional $x - t - v$ space and two-dimensional $\xi - v$ plane are figures (a) and (b), respectively, in Fig. 1.

For any real number $\gamma < 0$, let $\gamma = -4$, the solution (26) becomes

$$v_{32}(\xi) = -192 \operatorname{csch}(4\xi)^2, \tag{35}$$

where $\xi = x - y + \sqrt{61}z + t$. The three-dimensional $x - t - v$ space is shown in fiure (c) of Fig. 1.

Example 2 In this example, for the solutions of Eq. (15), by using Set-5, we assume the following parameters:

$$k_1 = 1\ (-1\ for\ \gamma < 0),\ k_2 = -1,\ c = 1,\ \rho = 0.$$

For any real number $\gamma > 0$, let $\gamma = 4$, the solution (30) becomes

$$v_{51}(\xi) = -16\,[-2 + \cos(4\xi)] \csc(2\xi)^2, \tag{36}$$

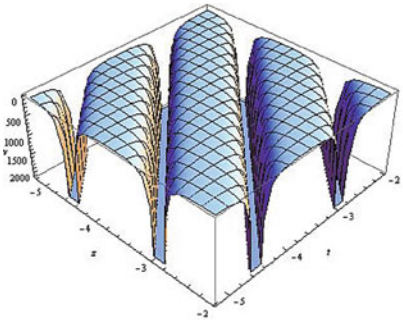

(a) 3-D figure of solution v_{51}

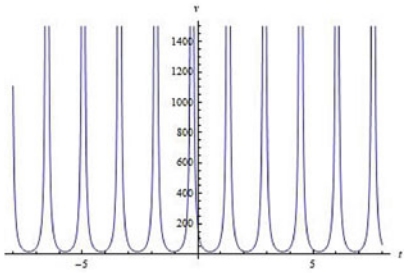

(b) 2-D figure of solution v_{51}

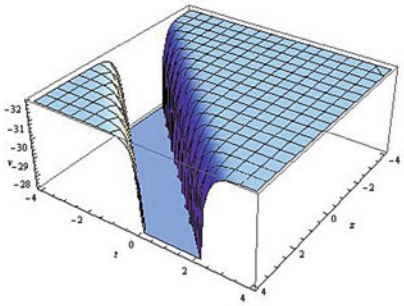

(c) 3-D figure of solution v_{52}

Fig. 2 Behaviour of solutions for example 2

where $\xi = x - y + \sqrt{13}z + t$. The three-dimensional $x - t - v$ space and two-dimensional $\xi - v$ plane are figures (a) and (b), respectively, in Fig. 2.

For any real number $\gamma < 0$, let $\gamma = -4$, the solution (31) becomes

$$v_{52}(\xi) = -16\left[-2 + \cosh(4\xi)\right]\operatorname{sech}(2\xi)^2, \tag{37}$$

where $\xi = t - x - y + \sqrt{15}z$. The three-dimensional $x - t - v$ space is shown in figure (c) of Fig. 2.

6 Conclusion

In this work, the authors discussed about the nonlinear partial differential equation, (3+1)-dimensional generalised Kadomtsev–Petviashvili Benjamin–Bona–Mahony (KP-BBM) equation. The modified hyperbolic function expanding method has been used to obtain the exact solution of the (3+1)-dimensional generalised KP-BBM equation. This particular method can also be used to solve higher order partial dif-

ferential equations. Using this method, a system of nonlinear algebraic equations has been obtained and solved by using MATHEMATICA software. Two numerical examples are included with respective figures to demonstrate the validity, reliability, and efficiency of the discussed method.

References

1. Yang C (2020) Nonlinear partial differential equations in marine dynamics. J Coast Res 112(SI):356–358. https://doi.org/10.2112/JCR-SI112-094.1
2. Agarwal P, Deniz S, Jain S, Alderremy AA, Aly S (2020) A new analysis of a partial differential equation arising in biology and population genetics via semi analytical techniques. Phys A: Stat Mech Appl 542:122769. https://doi.org/10.1016/j.physa.2019.122769
3. Yano M (2020) Goal-oriented model reduction of parametrized nonlinear partial differential equations: application to aerodynamics. Int J Numer Methods Eng 121(23):5200–5226. https://doi.org/10.1002/nme.6395
4. Gobet E, Pimentel I, Warin X (2020) Option valuation and hedging using an asymmetric risk function: asymptotic optimality through fully nonlinear partial differential equations. Finance Stoch 24(3):633–675. https://doi.org/10.1007/s00780-020-00428-1
5. Alharbi AR, Almatrafi MB (2020) Riccati-Bernoulli sub-ODE approach on the partial differential equations and applications. Int J Math Comput Sci 15(1):367–388
6. Gao W, Ghanbari B, Günerhan H, Baskonus HM (2020) Some mixed trigonometric complex soliton solutions to the perturbed nonlinear Schrödinger equation. Mod Phys Lett B 34(03):2050034. https://doi.org/10.1142/S0217984920500347
7. Kadomtsev BB, Petviashvili VI (1970) On the stability of solitary waves in weakly dispersing media. In Sov Phys Dokl 15(6):539–541
8. Bagyalakshmi M, SaiSundarakrishnan G (2020) Tarig projected differential transform method to solve fractional nonlinear partial differential equations. Boletim da Sociedade Paranaense de Matemática 38(3):23–46. https://doi.org/10.5269/bspm.v38i3.34432
9. Korteweg DJ, De Vries G (1895) XLI. On the change of form of long waves advancing in a rectangular canal, and on a new type of long stationary waves. Lond Edinb Dublin Philos Mag J Sci 39(240):422–443 (1895). https://doi.org/10.1080/14786449508620739
10. Alharbi AR, Almatrafi MB, Abdelrahman MA (2020) Analytical and numerical investigation for Kadomtsev-Petviashvili equation arising in plasma physics. Phys Scripta 95(4):045215. https://doi.org/10.1088/1402-4896/ab6ce4
11. Yusuf A, Sulaiman TA, Khalil EM, Bayram M, Ahmad H (2021) Construction of multi-wave complexiton solutions of the Kadomtsev-Petviashvili equation via two efficient analyzing techniques. Results Phys 21:103775. https://doi.org/10.1016/j.rinp.2020.103775
12. Wazwaz AM, Xu GQ (2020) Kadomtsev–Petviashvili hierarchy: two integrable equations with time-dependent coefficients. Nonlinear Dyn 100:3711–3716. https://doi.org/10.1007/s11071-020-05708-1
13. Guan X, Liu W, Zhou Q, Biswas A (2020) Some lump solutions for a generalized (3+ 1)-dimensional Kadomtsev–Petviashvili equation. Appl Math Comput 366. https://doi.org/10.1016/j.amc.2019.124757
14. Yue C, Khater MM, Attia RA, Lu D (2020) Computational simulations of the couple Boiti–Leon–Pempinelli (BLP) system and the (3+ 1)-dimensional Kadomtsev–Petviashvili (KP) equation. AIP Adv 10(4). https://doi.org/10.1063/1.5142796
15. Guo J, He J, Li M, Mihalache D (2021) Multiple-order line rogue wave solutions of extended Kadomtsev–Petviashvili equation. Math Comput Simul 180:251–257. https://doi.org/10.1016/j.matcom.2020.09.007

16. Benjamin TB, Bona JL, Mahony JJ (1972) Model equations for long waves in nonlinear dispersive systems. Philos Trans R Soc London Ser A, Math Phys Sci 272(1220):47–78. https://doi.org/10.1098/rsta.1972.0032
17. Ali G, Ahmad I, Shah K, Abdeljawad T (2020) Iterative analysis of nonlinear BBM equations under nonsingular fractional order derivative. Adv Math Phys. https://doi.org/10.1155/2020/3131856
18. da Silva PL, Freire IL (2021) A geometrical demonstration for continuation of solutions of the generalised BBM equation. Monatshefte für Mathematik 194(3):495–502. https://doi.org/10.1007/s00605-020-01453-0
19. Khater MM, Nofal TA, Abu-Zinadah H, Lotayif MS, Lu D (2021) Novel computational and accurate numerical solutions of the modified Benjamin–Bona–Mahony (BBM) equation arising in the optical illusions field. Alex Eng J 60(1):1797–1806. https://doi.org/10.1016/j.aej.2020.11.028
20. Gupta AK, Hazarika J (2021) On the solitary wave solutions of modified Benjamin–Bona–Mahony equation for unidirectional propagation of long waves. Pramana 94(1):1–8. https://doi.org/10.1007/s12043-020-01998-7
21. Wazwaz AM (2005) Exact solutions of compact and noncompact structures for the KP-BBM equation. Appl Math Comput 169(1):700–712. https://doi.org/10.1016/j.amc.2004.09.061
22. Mekki A, Ali MM (2013) Numerical simulation of Kadomtsev–Petviashvili–Benjamin–Bona–Mahony equations using finite difference method. Appl Math Comput 219(24):11214–11222. https://doi.org/10.1016/j.amc.2013.04.039
23. Abdou MA (2008) Exact periodic wave solutions to some nonlinear evolution equations. Int J Nonlinear Sci 6(2):145–153
24. Song M, Yang C, Zhang B (2010) Exact solitary wave solutions of the Kadomtsov–Petviashvili-Benjamin–Bona–Mahony equation. Appl Math Comput 217(4):1334–1339. https://doi.org/10.1016/j.amc.2009.05.007
25. Tang S, Huang X, Huang W (2010) Bifurcations of travelling wave solutions for the generalized KP-BBM equation. Appl Math Comput 216(10):2881–2890. https://doi.org/10.1016/j.amc.2010.03.139
26. Hoque MF, Alshammari FS (2020) Higher-order rogue wave solutions of the Kadomtsev Petviashvili-Benjanim Bona Mahony (KP-BBM) model via the Hirota-bilinear approach. Phys Scripta 95(11). https://doi.org/10.1088/1402-4896/abbf6f
27. Tariq KUH, Seadawy AR (2017) Bistable Bright-Dark solitary wave solutions of the (3+1)-dimensional Breaking soliton, Boussinesq equation with dual dispersion and modified Korteweg-de Vries-Kadomtsev–Petviashvili equations and their applications. Results Phys 7:1143–1149. https://doi.org/10.1016/j.rinp.2017.03.001
28. Yin Y, Tian B, Wu XY, Yin HM, Zhang CR (2018) Lump waves and breather waves for a (3+ 1)-dimensional generalized Kadomtsev–Petviashvili Benjamin–Bona–Mahony equation for an offshore structure. Mod Phys Lett B 32(10):1850031. https://doi.org/10.1142/S0217984918500318
29. Xie Y, Li L (2022) Multiple-order breathers for a generalized (3+ 1)-dimensional Kadomtsev–Petviashvili Benjamin–Bona–Mahony equation near the offshore structure. Math Comput Simul 193:19–31. https://doi.org/10.1016/j.matcom.2021.08.021
30. Liu S (2020) Multiple rogue wave solutions for the (3+ 1)-dimensional generalized Kadomtsev–Petviashvili Benjamin–Bona–Mahony equation. Chin J Phys 68:961–970. https://doi.org/10.1016/j.cjph.2020.10.024
31. Wazwaz AM (2010) Partial differential equations and solitary waves theory. Springer Science & Business Media (2010)

Effect of Oblique Magnetic and Electric Fields on the Kelvin-Helmholtz Instability at the Interface Between Porous and Fluid Layers

Guruva Reddy Chandra Shekara

Abstract The effect of inclined magnetic and electric field on the growth rate of the Kelvin-Helmholtz instability of a flow in the porous layer is presented. The base flow is assumed to be fully developed and the linear theories along with normal modes are used to understand the stability of the flow over the interface between the fluid saturated porous layer and the clear fluid layer to a large extent. The effect of inclined magnetic and electric fields on the growth rate of instability is studied in terms of non-dimensional parameters like the Darcy number, Electric and Magnetic parameters. It is observed that the inclined magnetic field has a stabilizing impact when the angle of orientation is 90° and whereas the horizontal magnetic field with a zero angle of inclination has a neutral impact on the stability of the system. For the large Darcy numbers, that is a porous medium with small porosity, the system will be stable whereas for smaller values of Darcy number, the system is marginally stable. The numerical and graphical results were presented and validated for a wide range of non-dimensional parameters.

Keywords Shear-instability · Inclined-magnetic-field · Hartmann-number · Electric-number · Growth-rate · Dispersion-relation

1 Introduction

The Kelvin-Helmholtz instability(KHI) will be set up at the interface between two fluid layers with different velocities flowing one over the other at the interface between these fluids. This instability occurs at the interface due to shear between fluid layers; hence, some authors refer to it as shear instability. This kind of instability will be crucial in understanding phenomena like the formation of clouds, waves and

BMS College of Engineering.

G. R. Chandra Shekara (✉)
Assistant Professor, Department of Mathematics, BMS College of Engineering, Bull Temple Road, Basavagudi, Bangalore 560019, India
e-mail: chandrashekarag.maths@bmsce.ac.in

J. Singh et al. (eds.), *Advances in Mathematical Modelling, Applied Analysis and Computation*, Lecture Notes in Networks and Systems 415,
https://doi.org/10.1007/978-981-19-0179-9_15

flow through sand beds. The industrial applications similar to the melting process, processing of polymers and the mixing of paints can be made well understood by analyzing this instability. Using analysis of this instability, it is possible to understand the onset of instability and transitions nature of fluid flow with dissimilar densities with different flow velocities. This type of instability was first studied by Helmholtz [3] by introducing a small wave-like disturbance over the interface of fluid layers flowing with dissimilar speeds. In the year 1871, [4] experimentally proved that if two layers flow with different velocities, they will be unstable even for small velocities.

The Kelvin-Helmholtz instability has been studied by authors like Shore [2] and Chandrasekhar [1] because of its significance in astrophysical, geophysical and industrial applications. Chandrasekhar [1] presented the impact of physical quantities like surface tension, variable density, rotation and magnetic field on the KH instability. Sharma and Srivastava [5] show that the effect of rotation and an inclined magnetic field will suppress the growth rate of KHI. The electro-hydrodynamic KHI influenced by an electric field with surface charges and separating two dielectric fluid layers has been discussed by El-Sayed [6]. Elhefnawy [7] presented a multiple scales method to study nonlinear KH instability with an influence of an electric field. KHI at the interface between two viscous, rotating and conducting fluids layers was investigated by Mehta and Bhatia [8]. Benjamin and Bridges [9] have shown the significance of KH instability and they have a good reappraisal of the classic KH instability in hydrodynamics. KHI of superposed fluids with heat and mass transfer was investigated by Allah [10] by considering an applied magnetic field. The effect of magnetic fields on the natural convection in vertical cylindrical annulus was studied by Sankar et al. [21]. Jayalakshmamma et al. [22] presented the creeping flow past composite sphere by considering porous shell in the presence of magnetic field effect.

Further, it is noticed that the flow through the porous layer is very significant mainly among geophysical fluid dynamic researchers and petroleum engineers. Theories of Babchin et al. [11] and Chandra Shekara et al. [12] along with Beavers and Joseph [13] slip conditions are utilized with the main focus of using magnetic and electric fields along with porous layer to reduce the instability. El-Sayed [14] investigated the electro-hydrodynamic KH instability at the interface between two superposed Rivlin-Ericksen visco-elastic dielectric fluid-particle mixtures in the porous medium. Electro-rheological KH instability of a fluid sheet was studied by El-Dib and Matoog [15]. Chandra Shekara et al. [12] have shown that if electric and magnetic fields are applied together, the growth rate of Kelvin-Helmholtz instability can be reduced effectively compared to that of individual effects. Chandra Shekara and Rudraiah [16] have shown that the effect of nanostructure porous layer will reduce KH instability and they also proved that the couple stress effect will suppress KH instability. Krishna Chavaraddi et al. [18] studied the Kelvin-Helmholtz instability in a rectangular channel with a couple stress fluid layer bounded above by a porous layer and below by a rigid surface. The effect of magnetic field on the Kelvin-Helmholtz instability in a couple stress fluid layer bounded above by a porous layer and below by a rigid surface is studied by Krishna B. Chavaraddi et al. [19]. More recently,

Krishna B Chavaraddi et al. [20] analyzed the influence of boundary roughness on the Rayleigh-Taylor instability at the interface of the superposed couple stress fluids. To our knowledge, KHI at the interface between two fluids of very small conductivity in the presence of an oblique magnetic and electric field with an impact of porous layer thickness is not been given much attention. In the present work, the effects of electric and magnetic fields applied in the direction inclined at an angle with fluid flow through the porous channel are examined. It is noticed that the inclined field is having a stabilizing impact on the dispersion rate if the angle of inclination is orthogonal to the fluid flow through the porous medium. Further, if these fields are applied in the horizontal direction to the flow of the fluid in the porous medium, they will have a negligible impact on the dispersion relation of KHI compared to the vertical fields.

2 Mathematical Formulation

The flow configuration of the present work consists of region-1 with a fluid layer of composed small thickness h with incompressible viscous fluid with very small conductivity and this region is bounded below by an inflexible surface. The upper side of region-1 consists porous layer of large thickness $H > h$ with small porosity and a viscous incompressible fluid saturated in it called region-2 as shown in Fig. 1. The inclined magnetic field is applied with an angle of inclination θ with the lower surface of region-1. Further, an electric field is applied by embedding electrodes at the lower surface and over the interface of region-1 and region-2. The instability will be set up over interface due to shear formed by flows in region-1 and 2 and also the opposition of flow in the porous layer. The cartesian coordinate system (x, y) is used to study the instability considered in the present work with $\eta(x, y)$ and is the disturbed interface between region-1 and 2 as shown in Fig. 1.

The governing equations of fluid flow in region-1 and 2 are derived by following Chandra Shekara and Rudraiah [12, 16] and they are conservation of mass, momentum, energy and charges as given below:

$$\nabla.\mathbf{q} = 0 \tag{1}$$

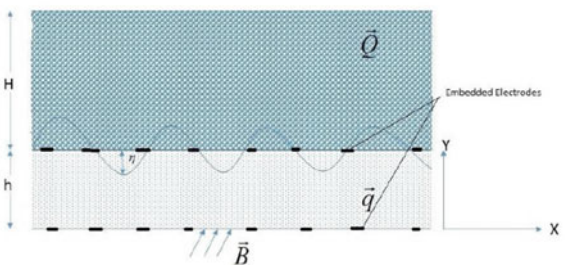

Fig. 1 Schematic representation of flow configuration

Region-1:

$$\rho_f \left[\frac{\partial \mathbf{q}}{\partial t} + (\mathbf{q}.\nabla)\mathbf{q} \right] = -\nabla p + \mu_f \nabla^2 \mathbf{q} + \rho_e \mathbf{E} + \mathbf{J} \times B \tag{2}$$

Region-2:

$$\nabla p = -\frac{\mu}{k}\mathbf{Q} + \rho_e \mathbf{E} + \mathbf{J} \times B \tag{3}$$

$$\left[\frac{\partial T}{\partial t} + (\mathbf{q}.\nabla)T \right] = \kappa \nabla^2 T \tag{4}$$

$$\frac{\partial \rho_e}{\partial t} + (\mathbf{q}.\nabla)\rho_e + \nabla.\mathbf{J} = 0 \tag{5}$$

In the above equations, $\mathbf{q}$ and $\mathbf{Q}$ are velocities of the fluid in region-1 and 2, respectively. ρ_b be the density, μ_r the coefficient of viscosity, $\mathbf{E}$ the electric field, P the pressure, k the permeability of a porous layer, ρ_e is the density of charge distribution and $\mathbf{J} = \sigma \mathbf{E}$ is the conduction current density. The fluid considered in the present study is of very small conductivity and hence Eqs. (1) to (5) are supplemented with the Maxwell equations like the Gauss law and Faraday's law, respectively, given by

$$\nabla.\mathbf{E} = \frac{\rho_e}{\varepsilon_0} \tag{6}$$

$$\nabla \times \mathbf{E} = 0 \tag{7}$$

$$\mathbf{E} = -\nabla\phi \tag{8}$$

Here in the above equations, ε_0 be the dielectric constant and ϕ be the electric potential. The fluid with conductivity $\sigma << 1$ depends only on the conduction temperature, T_b, such that

$$\sigma_b = \sigma_0 \left[1 + \alpha_h (T_b - T_0)\right] \tag{9}$$

where T_0 is the wall temperature, and at $T = T_0$, $\sigma_0 = \sigma_b$ and α_h is the expansion coefficient of conductivity.

3 Problem Solution

3.1 Basic State Solutions

The fluid considered in this study is highly viscous and electrically poorly conducting, so that diffusion terms dominate. Further, to understand flow, the fluid is set to be in

quiescent state initially with an applied uniform electric field $\mathbf{E_0}$ and magnetic field $\mathbf{H_0}$ inclined at an angle θ with xy- plane. The fluid under the basic state is assumed to be at static state, that is

$$\mathbf{q} = (0, 0) \tag{10}$$

and

$$\mathbf{E} = \mathbf{E_0} = (E_{0x}, E_{0y}) \tag{11}$$

$$\mathbf{H} = \mathbf{H_0} = (H_{0x}, H_{0y}) \tag{12}$$

where $H_{0x} = H_0 \cos\theta$ and $H_{0y} = H_0 \sin\theta$, θ being an angle of inclination of an electric field E_0, $\mathbf{Q} = (0, 0)$, $\phi = \phi_b$, $p = p_b$, $\rho_e = \rho_{eb}$ and $\sigma = \sigma_b$. Under these basic states, Eqs. (2) to (7), respectively, become

$$0 = -\frac{\partial p_b}{\partial x} + \rho_{eb} E_{0x} \tag{13}$$

$$0 = -\frac{\partial p_b}{\partial y} + \rho_{eb} E_{0y} \tag{14}$$

$$\nabla.(\sigma_b \mathbf{E_0}) = 0 \tag{15}$$

$$\nabla \mathbf{E_0} = \frac{\rho_{eb}}{\epsilon_0} \tag{16}$$

and

$$\nabla \times \mathbf{E_0} = 0 \tag{17}$$

$$\frac{d^2 T_b}{dy^2} = 0 \tag{18}$$

Solving Eq. (18)using boundary conditions $T_b = T_0$ at $y = 0$ and $T = T_1$ at $y = 1$ and using Eq. (9), we get

$$\sigma_b = \sigma_0 [1 + \alpha_h \Delta T y] \cong \sigma_0 e^{\alpha y} \tag{19}$$

where $\alpha = \alpha_h \Delta T$ and $\Delta T = T_1 - T_0$. We assume that initially for poorly conducting fluids, convection term and time derivative of charge density are dominated by divergence of current density in Eq. (14), which leads to

$$\frac{\partial^2 \phi_b}{\partial x^2} + \frac{\partial^2 \phi_b}{\partial y^2} + \alpha \frac{\partial \phi_b}{\partial y} = 0 \tag{20}$$

On solving Eq. (20) using embedded conditions at the lower boundary and at the interface, respectively, given by $\phi_b = \frac{Vx}{h}$ at $y = 0$ and $\phi_b = \frac{V(x-x_0)}{h}$ at $y = 1$, we

get

$$\phi_b = x - x_0\left(\frac{1-e^{-\alpha y}}{1-e^{-\alpha}}\right) \tag{21}$$

$$E_{0x} = -\frac{\partial \phi}{\partial x} = -1 \tag{22}$$

$$E_{0y} = -\frac{\partial \phi}{\partial y} = \frac{x_0 \alpha e^{-\alpha y}}{1-e^{-\alpha}} \tag{23}$$

$$\rho_{eb} = -\varepsilon_0 \frac{\partial^2 \phi_b}{\partial y^2} = -\frac{x_0 \varepsilon_0 \alpha^2 e^{-\alpha y}}{1-e^{-\alpha}} \tag{24}$$

3.2 Perturbed Sate Equation

In this section, we super impose a very small perturbation on the basic state given in previous section as $\mathbf{q} = (u, v)$, $\mathbf{E} = \mathbf{E_0} + \mathbf{E'}$, $E_x = E_{0x} + E'_x$, $E_y = E_{0y} + E'_y$, $\mathbf{Q} = (Q_x, Q_y), \phi = \phi_b + \phi', p = p_b + p'$ and $\rho_e = \rho_{eb} + \rho'_e$. Using these perturbed quantities in Eqs. (1) to (5) applying linear theory and making dimensionless using scales h for length, δh for pressure, $\mu \delta h^2$ for velocity, $\mu \delta^{-2} h^{-3}$ for time, Vh^{-1} for electric field, $\epsilon V h^{-1}$ for charge density and V for electric potential and also using the basic state discussed in previous section, we get

$$\frac{\partial u}{\partial x} + \frac{\partial v}{\partial y} = 0 \tag{25}$$

$$\frac{\partial p}{\partial x} = \left(\frac{\partial^2 u}{\partial x^2} + \frac{\partial^2 u}{\partial y^2}\right) + W_e(\rho_e E_{0x} + \rho_{eb} E_x) + M^2 u \cos\theta \tag{26}$$

$$\frac{\partial p}{\partial y} = \left(\frac{\partial^2 v}{\partial x^2} + \frac{\partial^2 v}{\partial y^2}\right) + W_e(\rho_e E_{0y} + \rho_{eb} E_y) + M^2 v \sin\theta \tag{27}$$

$$\frac{\partial p}{\partial x} = -\frac{1}{D_a^2} Q_x + W_e(\rho_e E_{0x} + \rho_{eb} E_x) + M^2 Q_x \cos\theta \tag{28}$$

$$\frac{\partial p}{\partial y} = -\frac{1}{D_a^2} Q_y + W_e(\rho_e E_{0y} + \rho_{eb} E_y) + M^2 Q_y \sin\theta \tag{29}$$

$$\frac{\partial \rho_e}{\partial t} + v\frac{\partial \rho_{eb}}{\partial y} + \sigma_b\left(\frac{\partial E_x}{\partial x} + \frac{\partial E_y}{\partial y}\right) = 0 \tag{30}$$

$$\frac{\partial E_x}{\partial x} + \frac{\partial E_y}{\partial y} = \Gamma \rho_e \tag{31}$$

$$\frac{\partial E_y}{\partial x} - \frac{\partial E_x}{\partial y} = 0 \tag{32}$$

where W_e is an electric number, M is magnetic number and D_a be a porous parameter and $\Gamma = \epsilon^{-1}$.

4 Dispersion Relation

The main objective of the present study is to find the dispersion relation of a small periodic perturbations at the interface. To derive this relation, all physical fields are expressed in waveform given by

$$\left[\mathbf{q}, \mathbf{Q}, \mathbf{E}, \rho_e\right](x, y, t) = (q(y), Q(y), E(y), \rho_e(y))e^{ilx+nt} \tag{33}$$

here l denotes the wavenumber and n is the growth rate. Using Eq. (33) in Eqs. (25) to (32) takes the form

$$Dv + ilu = 0 \tag{34}$$

$$ilp = (D^2 - l^2)u + W_e(\rho_e E_{0x} + \rho_{eb} E_x) + M^2 u \cos\theta \tag{35}$$

$$Dp = (D^2 - l^2)v + E_e(\rho_e E_{0y} + \rho_{eb} E_y) + M^2 v \sin\theta \tag{36}$$

$$ilp = -\frac{1}{D_a^2} Q_x + W_e(\rho_e E_{0x} + \rho_{eb} E_x) + M^2 Q_x \cos\theta \tag{37}$$

$$Dp = -\frac{1}{D_a^2} Q_y + W_e(\rho_e E_{0y} + \rho_{eb} E_y) + M^2 Q_y \sin\theta \tag{38}$$

$$n\rho_e + vD\rho_{eb} + \sigma_b(ilE_x + DE_y) = 0 \tag{39}$$

$$ilE_x + DE_y = \frac{\rho_e}{\epsilon_0} \tag{40}$$

$$ilE_y - DE_x = 0 \tag{41}$$

Eliminating pressure terms in Eqs. (35) and (36) and using Eq. (24) give

$$(D^2 - l^2)^2 v - ilW_e \cos\theta(D\rho_e E_{0x} + D\rho_{eb} E_x) = 0 \tag{42}$$

Similarly, eliminating pressure terms in Eqs. (37) and (38) and using Eq. (24), we get

$$(D^2 - l^2)Q_y - ilW_e D_a \cos\theta (D\rho_e E_{0x} + D\rho_{eb} E_x) = 0 \tag{43}$$

Further, using $\mathbf{E} = -\nabla\phi$, Eqs. (30) to (32) take the form

$$n\rho_e + vD\rho_{eb} - D_a(D^2 - l^2)\phi = 0 \tag{44}$$

These equations are solved using the boundary condition mentioned below:
At lower rigid boundary:

$$v = Dv = 0 \quad at \quad y = 0 \tag{45}$$

$$v = Qy = v_0 \quad at \quad y = 1 \tag{46}$$

The BJ-slip condition:

$$\frac{\partial v}{\partial y} = -\alpha\sigma(v_0 - Q_y) \quad at \quad y = 1 \tag{47}$$

The interface elevation equation is given by

$$y = h + \eta(x, t) \tag{48}$$

where η represents the perturbed interface from the equilibrium state and α and v_0 are, respectively, slip parameter and the slip velocity at $y = 1$.
The interface conditions are dynamic surface and kinematic conditions are, respectively, given by

$$p = -\delta\eta - \gamma\frac{\partial^2\eta}{\partial x^2} + \mu_f\frac{\partial v}{\partial y} \quad at \quad y = 1 \tag{49}$$

where δ and γ are, respectively, stress gradient and surface tension.

$$v = \frac{\partial\eta}{\partial t} + u\frac{\partial\eta}{\partial x} \quad at \quad y = 1 \tag{50}$$

4.1 Effect of Transverse Fields

The dispersion relation in case of applied magnetic field in the direction perpendicular to the flow with an applied electric field is derived in this section. In this case, angle of inclination $\theta = \frac{\pi}{2}$; hence, Eqs. (42) and (43), respectively, become

$$(D^2 - l^2)^2 v = 0 \tag{51}$$

$$(D^2 - l^2)Q_y = 0 \tag{52}$$

The solution of Eqs. (51) and (52) satisfying the boundary conditions Eqs. (45) to (47) is of the form

$$v = (A_1 + A_2 y)\cosh ly + (A_3 + A_4 y)\sinh ly \tag{53}$$

and

$$Q_y = B_1 \cosh ly + B_2 \sinh ly \tag{54}$$

where

$A_1 = 0,$

$$A_2 = \frac{lV_0 \cosh l + lV_0 \sinh l - K\alpha\sigma_p \sinh l + V_0\alpha\sigma_p \sinh l}{l(\cosh^2 l - 2\sinh^2 l)},$$

$$A_3 = -\frac{lV_0 \cosh l + lV_0 \sinh l - K\alpha\sigma_p \sinh l + V_0\alpha\sigma_p \sinh l}{l(\cosh^2 l - 2\sinh^2 l)},$$

$$A_4 = -\frac{lV_0 \sinh l - \alpha\sigma_p(V_0 - K)(\sinh l - \cosh l)}{l(\cosh^2 l - 2\sinh^2 l)},$$

$$B_1 = -\frac{V_0 \sinh 2l}{\cosh 2l \sinh l - \sinh 2l}$$

and

$$B_2 = \frac{V_0 \cosh 2l}{\cosh 2l \sinh l - \sinh 2l}.$$

From Eq. (44), it can be solved for n, which is the growth rate at the interface and it is called the dispersion relation, as follows:

$$n = -\frac{vD\rho_{eb} + \sigma_b(D^2 - l^2)\phi}{\epsilon_0(D^2 - l^2)\phi} \tag{55}$$

The growth rate given in Eq. (55) refers to a linear case of KHI of a viscous incompressible fluid layer bounded below by an inflexible surface and above by a porous layer with very small conductivity. This dispersion relation coincides with the one derived by Brown [17].

4.2 Effect of Horizontal Fields

The dispersion relation derived under the influence of horizontal magnetic field which is parallel to the flow (i.e.angle $\theta = 0$) with an applied electric field. This horizontal magnetic field (i.e. parallel to x axis) offers a rigidity to the flow and hence produces a tension. The impact of this tension will elongate the force lines and causes oscillations. In this case, Eqs. (42) and (43) become

$$(D^2 - l^2)^2 v - ilw_1(D\rho_e E_{0x} + D\rho_{eb} E_x) = 0 \tag{56}$$

$$(D^2 - l^2)Q_y - ilw_1\sigma_p^2(D\rho_e E_{0x} + D\rho_{eb}E_x) = 0 \tag{57}$$

Solving Eqs. (56) and (57) using the boundary conditions Eqs. (45) to (47) gives

$$v = (A_1 + A_2 y)\cosh ly + (A_3 + A_4 y)\sinh ly + f(y) \tag{58}$$

and

$$Q_y = B_1 \cosh ly + B_2 \sinh ly + g(y) \tag{59}$$

where $f(y) = \dfrac{ilw_1 e^{-\alpha y}}{(\alpha^2 - l^2)^2}$ and $g(y) = \dfrac{ilw_1 e^{-\alpha y}}{(\alpha^2 - l^2)}$. From Eq. (44) the frequency of the growth rate n is obtained as:

$$n = \frac{D\phi D\sigma_b - vD\rho_{eb} + \sigma_b(D^2 - l^2)\phi}{\epsilon(D^2 - l^2)\phi} \tag{60}$$

Equation (60) represents the dispersion relation with respect to the linear case of KHI of a fluid in the form of a thin film as shown in Fig. 1. The direct impact of an electric and magnetic field is clearly seen in Eq.(60), besides there is a roundabout effect from the adjustment of velocity and the Darcy velocity at the interface.

5 Results and Discussions

The growth rate of KHI of fluid in the presence of an electric and magnetic field with an angle of inclination θ to the x-axis is derived in terms of dispersion relation Eq. (60). When both H_{0x} and H_{0y} are zero along with $\mathbf{E} = 0$, this dispersion relation coincides with the form derived by Brown [17] in the case of hydrodynamic as follows:

$$n = \frac{(\delta - \gamma\lambda^2)V\lambda^2}{\mu_f(2\lambda^2 DV - D^2 V)} \tag{61}$$

If $H_{0y} = 0$, the dispersion relation is obtained in the form of Eq. (61) for the case of a magnetic field parallel to flow. In this case, the velocities given in Eqs. (53) and (54) represent hyperbolic and trigonometric functions and exhibit oscillations depending on the strength of an electric field. The growth rate n is evaluated for different values of W_e and l and graphically the results are depicted in Fig. 2. It is noticed and found that the growth rate increases for short period and then becomes stable for all values of λ and W_e=2,20,200 and 2000. For $\theta = 0°$, the horizontal magnetic field and high-strength electric fields, the stability criteria for the velocity difference between the layers are derived. This condition in case of long wave perturbations will be inversely proportional to the angular frequency cube and also surface tension, and the applied electric fields are found to have no effect on the stability. Whereas in the case of

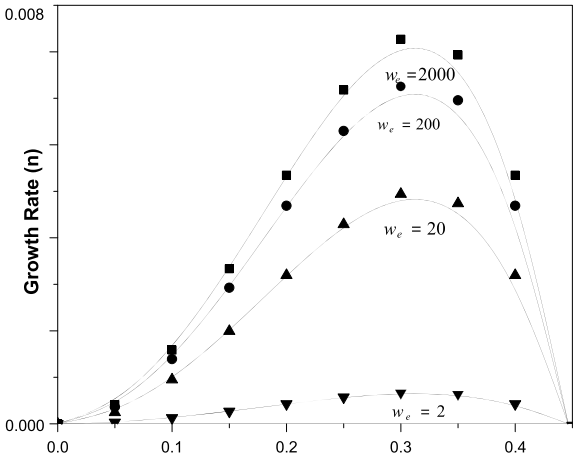

Fig. 2 Graph of dispersion relation n versus wavenumber l for different values of electric number W_e with angle of inclination $\theta = 0°$

shorter wave disturbances, the surface tension with an applied electric and magnetic field shows a stabilizing effect.

If $H_{0x} = 0$, the dispersion relation obtained as in Eq. (60) for the transverse magnetic and applied electric field and corresponding flow velocities are given by Eqs. (58) and (59) and it is a function of hyperbolic similar to the hydrodynamic case. The dispersion relation n is found with respect to different values of W_e and l, and the results are presented graphically in Fig. 3. It is noticed that the interface becomes more stable for all values of α and $W_e > 1$ on contrary to the hydrodynamic case. For $\theta = 90°$, the long wave disturbances are similar to those for horizontal magnetic and electric fields. For short wave disturbances, it is noticed that the magnetic and electric fields have a destabilizing impact and stabilizing impact by the surface tension. It is found also that the transverse fields will destabilize the interface when compared to the horizontal fields.

In general, it was observed that the inclined magnetic field will reduce the growth rate of instability of a thin layer with $h < 1$ for fields with small strength. The increase in the magnetic field strength leads to a growth rate to take both negative and positive values if the layer is of small thickness. Physically, this is due to the fact that the high electric field and shear by the fluid saturated porous layer will amplify the disturbance such that there is an inflectional profile which is the interesting character of this instability. It is fascinating to note that electric force balances the viscous force ($We = 1$) at the interface in the case of transverse magnetic field and electric field for all layer thickness but this is true for the aligned electric field only for $h < 10$. It is noticed that the peaks of growth rate n in Figs. 2 and 3 are due to the balance of shear and applied electric field. Further, it is also observed for the limiting case when the angle of inclination of both fields is perpendicular to flow direction, the growth rate coincides with Chandra Shekara et al. [15]. In the case of a transverse magnetic field as shown in Fig. 3, the increasing the values of the electric number We, the value of n decreases. Hence, it is noteworthy that the growth rate of KHI decreases with an

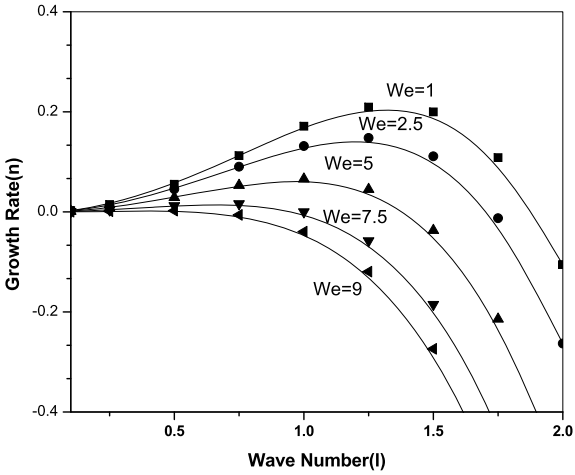

Fig. 3 Graph of dispersion relation n versus wavenumber l for different values of electric number W_e with angle of inclination $\theta = 90°$

increase in electric field effect. Particularly, for $We = 9$, the growth rate decreases considerably and hence stabilizes the interface. On the contrary to this, in the case of the aligned magnetic field, the interface will be unstable even for larger values of electric number We which can be observed in Fig. 2.

6 Conclusions

The impact of inclined magnetic and electric fields on KH instability is studied and it is observed that the transverse or aligned fields tend to reduce the dispersion of instability in case of a thin layer under small strength fields. The high-strength electric field causes the dispersion relation to exhibit both negative and positive values for very small layer thickness. Practically, this observation is due to the high field strength and shear offered by the porous layer may amplify the dispersion. It is exciting to note that Electric force negates viscous force at the interface and makes it stable in the case of transverse electric field for all layer thicknesses. Further, it is noted that the inclined magnetic field has a stabilizing impact when the angle of inclination is 90° degrees whereas the aligned magnetic field with a zero angle of inclination has a neutral impact on the stability of the system. For the large Darcy numbers, that is a porous medium with small porosity, the system will be stable whereas for smaller values of the Darcy number, the system is marginally stable. Finally, from the present study, it is concluded that it is possible to suppress the instability at the interface by

using a suitable combination of inclined magnetic and electric fields and porous layer thickness. Also, the nonlinear stability analysis is required to understand how exactly an electric field reduced KH instability.

Acknowledgements The author Chandra Shekara G. would be greatful to BMS College of Engineering, Bengaluru-19, India, for their support to conduct this research work.

References

1. Chandrasekhar S (1961) Hydrodynamic and hydromagnetic stability. Dover Publications, New York
2. Shore SN (1992) An introduction to astrophysical hydro-dynamics. Academic Press, New York
3. Helmholtz HV (1868) On the discontinuous movements of fluids. Philos Mag Ser 4(36):337–346
4. Kelvin L (1871) Hydrokinetic solutions and observations. Philos Mag 42:362–377
5. Sharma RC, Srivastava KM (1968) Effect of horizontal and vertical magenetic fields on Rayleigh-Taylor instability. Aust J Phys 21(6):923–930
6. El-Sayed MF (1998) Electrohydrodynamic Kelvin-Helmholtz instability of two rotating dielectric fluids. Zeitschrift für Naturforschung A 53(1–2):17–26
7. Elhefnawy ARF (1992) Nonlinear electrohydrodynamics Kelvin-Helmholtz instability under the influence of an oblique electric field. Physica A 182(3):419–435
8. Mehta V, Bhatia PK (1998) Kelvin-Helmholtz instability of two viscous superposed rotating and conducting fluids. Astrophys Space Sci 141(1):151–158
9. Benjamin TB, Bridges TJ (1997) Reappraisal of the Kelvin-Helmholtz problem. Part-2: interaction of the Kelvin-Helmholtz superharmonic and Benjamin-Feir instabilities. J Fluid Mech 333:327–373
10. Allah MHO (1998) The effects of magnetic field and mass and heat transfer on Kelvin-Helmholtz stability. Proc Natl Acad Sci 68(2):163–173
11. Babchin AJ, Frenkel AL, Levich BG, Sivashinsky GI (1983) Nonlinear saturation of Rayleigh-Taylor instability in thin films. Phys Fluids 26(11):3159–3161
12. Chandra Shekara G, Gayathri MS, Sujatha N (2019) Effect of electric and magnetic field on the growth rate of Kelvin-Helmholtz instability. STRPM: An Int J 10(2):143–154
13. Beavers GS, Joseph DD (1967) Boundary conditions at naturally permeable wall. J Fluid Mech 30(part-1):197–207
14. El-Sayed MF (2002) Effect of variable magnetic field on the stability of a stratified rotating fluid layer in porous medium. Czechoslovak J Phys 50:607
15. El-dib Y, Matoog RT (2005) Electrorheological Kelvin-Helmholtz instability of a fluid sheet. J Colloid Interface Sci 289(1):223–241
16. Rudraiah N, Chandrashekara G (2011) Electrorheological Kelvin-Helmholtz instability at the interface between a nano structured porous layer and thin shell with poorly conducting couple stress fluid. Fusion Sci Tech 60(1T):56–63
17. Brown K, Choudhury S (2002) An analytical study of the Kelvin-Helmholtz instabilities of compressible, magnetized tangential velocity discontinuities with generalized polytrope laws. Q Appl Math 60(4):601–630
18. Chavaraddi Krishna B, Awati VB, Priya M (2013) Surface instability of Kelvin-Helmholtz type in couple stress fluid layer bounded above by a porous layer and below by rigid surface. IOSR J Math 9(2):01–08
19. Chavaraddi Krishna B, Awati Vishwanath B, Katagi Nagaraj N, Gouder Priya M (2016) Effect of magnetic field on Kelvin-Helmholtz instability in a couple-stress fluid layer bounded above by a porous layer and below by a rigid surface. Appl Math 7:2021–2032

20. Chavaraddi KB, Gouder PM, Kudenatti RB (2020) The influence of boundary roughness on Rayleigh-Taylor instability at the interface of superposed couple-stress fluids. J Adv Res Fluid Mech Thermal Sci 75(2)
21. Jayalakshmamma DV, Dinesh PA, Sankar M (2011) Analytical study of creeping flow past a composite sphere: solid core with porous shell in presence of magnetic field. Mapana J Sci 10(2)
22. Sankar M, Venkatachalappa M, Shivakumara IS (2006) Effect of magnetic field on natural convection in a vertical cylindrical annulus. Int J Eng Sci 44(20):1556–1570

Heat Transfer for MHD Flow in an Inclined Channel with Heat Generation/Absorption

Pradip Kumar Gaur and Abhay Kumar Jha

Abstract The present paper deals with the motion of an incompressible viscous fluid in an inclined channel. A Uniform magnetic field is applied normal to the channel, taking heat absorption, heat generation and viscous dissipation into account. The non-dimensional partial differential equations are transferred to ordinary differential equations and the perturbation method is employed to solve basic differential equations. The velocity and temperature characteristics have been studied through graphs.

Keywords Porous medium · MHD · Heat transfer

1 Introduction

The magnetohydrodynamics flow with heat transfer in a porous medium is more significant in recent times for the reason that the magnetic field effects, boundary layer flows and with the help of electrically conducting fluids performance of various systems can be controlled, Geothermal energy extractions, nuclear reactors, plasma studies and MHD generators are such examples. The phenomena of heat transfer are the subject of wide research due to its application in the industry of chemical engineering such as the production of polymers and the processing of food. The study of flows through a porous medium is important amongst mathematicians and engineers due to its applications in biochemical, electrochemical and petroleum. Petroleum engineering and hydrology depends on the properties of porous media. The exact solution of Hartmann plane Coutte flow has been extensively [1]. Engineering problems, Geophysical and Astrophysical etc. are the applications of MHD Nigam [2], Soundalgekar and Bhat [3], Raptis [4], Vajravelue [5], and Attia et al. [6]. Studied

P. K. Gaur (✉)
Department of Mathematics, JECRC University, Jaipur, Rajasthan 303905, India
e-mail: pradeep.gaur@jecrcu.edu.in

A. K. Jha
Department of Mathematics, Motihari College of Engineering, Bihar 845401, India

J. Singh et al. (eds.), *Advances in Mathematical Modelling, Applied Analysis and Computation*, Lecture Notes in Networks and Systems 415,
https://doi.org/10.1007/978-981-19-0179-9_16

MHD flows through a channel. The motion of an MHD fluid with heat transfer between two flat plates with a heat source and heat sink has been investigated by Bodosa and Borkakti [7]. Makinde and Mhone [8] investigated MHD flow through a channel by considering a porous medium. In the presence of a heat source, MHD flow with heat transfer was studied by Choudhary and Jha [9]. Attia [10] analyzed heat transfer and MHD steady flow between two plates which are parallel and taking variations in physical variable into account. MHD motion of a fluid through two parallel plates with heat transfer was studied by Mebine [11]. Adesanya [12] and Hassan [13] taking radiation heat generation/absorption into account. Rathore et al. [14] presented a study using homotopy perturbation sumudu transform method for viscous MHD flow on a sheet which is stretching. Gaur et al. [15] analyzed MHD flow of polar fluid bounded by horizontal parallel plates. A study of C6H9NAO7 fluid by using entropy generation through an accelerated heated plate was given by Ahmed et al. [16]. A study for transient MHD Brinkman nanoliquid by using Caputo–Fabrizio fractional derivatives was given by Ali et al. [17]. Hussain et al. [18] presented conservation laws and explicit solution of a spatially Burgers–Huxley two dimensional equation. Sheikh et al. [19] introduce new model of fractional Casson fluid with heat and mass transfer based on generalized Fick's and Fourier's laws together. A study for Jeffery-Hamel flow in non-parallel walls by using hybrid computational approach was given by Singh et al. [20]. For the partial differential equations arising in physical sciences an efficient computational scheme for systems of nonlinear time fractional has been given by Dubey et al. [21]. For constant heat source through porous medium with Mittag–Leffler, exponential and power Laws a new fractional exothermic reactions model was given by Kumar et al. [22]. Hanif et al. [23] provide an entropy analysis for motion of a magneto-hybrid nanofluid with heat transfer exaggeration in a vertical cone. Recently Khan et al. [24] provide comparative study by considering two AA7072 and AA7075 and hybridized nanomaterials alloys with activation energy through binary chemical reaction comprising nonlinear MHD radiative motion through a moving thin needle.

2 Mathematical Formulation

We consider, electrically conducting, incompressible, viscous, unsteady fluid flow through an inclined channel formed by two parallel plates standing in x–y direction and making an angle θ with the horizontal. The axis of x is considered along the centre of the channel and the axis of y perpendicular to it. In the direction of y-axis, a uniform magnetic field B_0 is considered. The induced magnetic field compared with the applied magnetic field arising from induced current is negligible. The governing equations of the motion by assuming Boussinesq's approximation are given below:

$$\frac{\partial u'}{\partial t'} = -\frac{1}{\rho}\frac{\partial \rho'}{\partial x'} + \upsilon\frac{\partial^2 u'}{\partial y^2} - \frac{Ge\,\mathrm{Pr}\;B_0^2}{\rho}u' + g\,\sin\theta - \frac{\upsilon\,\mathrm{u}}{K} \tag{1}$$

$$\frac{\partial T'}{\partial t'} = \frac{k}{\rho\, C_p}\frac{\partial^2 T}{\partial y^2} + \frac{\mu}{\rho\, C_p}\left(\frac{\partial u}{\partial y}\right)^2 - \frac{Cs\,(T - T_0)}{\rho\, C_p} \tag{2}$$

And the corresponding boundary conditions are

$$u' = -h_0,\ T' = T_0\,,\ at\ y' = -h$$

$$u' = 0,\ T' = T_1\,,\ at\ y' = h \tag{3}$$

where T is temperature of the fluid, t is the time, u is the axial velocity,, g is gravitatonal acceleration, C_p is the specific heat at constant temperature, k the thermal conductivity, K is permeability of the porous medium, ρ is the density, G_e conductivity of the fluid, B_0 is the intensity of the magnetic field, P is the pressure, υ is the kinematic viscosity, Cs is the volumetric heat generation and T_0 is the wall temperature.

Non-dimensional parameters are:

$$x = \frac{x' u_0}{\upsilon},\ y = \frac{y' u_0}{\upsilon},\ t = \frac{t' u_0^2}{\rho},\ \rho = \frac{\rho\, w}{u_0^2},\ T = \frac{T' - T_0}{T_w - T_0},$$
$$\mathrm{Re} = \frac{u_0 h}{\upsilon},\ F_r = \frac{h_0^2}{gh},\ S^2 = \frac{\upsilon^2}{Ku} \tag{4}$$

Now using Eq. (4) in Eqs. (1), (2) and (3), we get dimensionless equations

$$\frac{\partial u}{\partial t} = -\frac{\partial p}{\partial x} + \frac{\partial^2 u}{\partial y^2}(H_a^2 + S^2)u + \frac{s\sin\theta}{\mathrm{F_r\,Re}} \tag{5}$$

$$\frac{\partial T}{\partial t} = \frac{1}{\mathrm{Pr}}\frac{\partial^2 T}{\partial y^2} + Ec\left(\frac{\partial u}{\partial y}\right)^2 - \alpha^2 T \tag{6}$$

where $H_a^2 = \frac{\sigma\, B_0^2 \upsilon}{u_0^2}$(Magnetic field parameter)

$$Q = \frac{Cs'\upsilon}{\rho C_p u0}\ \text{(Heat source/sink parameter)}$$

$$Ec = \frac{u_0^2}{\mu\rho C_p (T_w - T_0)^2}\ \text{(Eckert number)}$$

$u = -1,\ T = 0\,,\ at\ y = -1$The corresponding boundary conditions becomes

$$u = 0,\ T = 1\,,\ at\ y = 1 \tag{7}$$

For solving Eqs. (5) and (6) let

$$\frac{\partial P}{\partial x} = ht, \quad u = f(y)e^{-nt}, \quad T = g(y)e^{-nt}$$

Now from Eqs. (5), (6) and (7), we get

$$u = \frac{s\text{inha (y - 1)}}{\text{sinh2a}} + \frac{h_0 e^{-nt} + b}{a^2}\left[1 - \frac{\cosh ay}{\cosh a}\right] \tag{8}$$

where $R^2 = H_a^2 + S^2$, $a^2 = R^2 - n$, $b = \frac{s\text{in}\theta}{\text{F}_\text{r}\,\text{Re}}$, $h = h_0 e^{-nt}$

$$T = e^{-nt}\left[\begin{array}{l}(C_1 \cos Ay + C_2 s\text{inMy}) + K_1 \cosh 2a\,(y-1)e^{2nt} + \\ K_2 e^{2nt} + K_3\, s\text{inh2ay} - \text{K}_4 - \text{K}_5\text{sinh2a(y - 1)} - K_6\end{array}\right] \tag{9}$$

$$A^2 = (n - Q)\,\text{Pr},$$

$$K_1 = \frac{a^2}{(2s\text{inh}^2\text{2a})(4\text{a}^2 + \text{A}^2)},$$

$$K_2 = \frac{a^2}{4A^2 s\text{inh}^2\text{2a}},$$

$$K_3 = \frac{\left(h_0 e^{-nt} + b\right)}{2\text{a}(4\text{a}^2 + \text{A}^2)\cosh^2 a},$$

$$K_4 = -\frac{\left(h_0 e^{-nt} + b\right)^2}{4\text{A}^2},$$

$$K_5 = \frac{\left(h_0 e^{-nt} + b\right)^2 \text{e}^{\text{nt}}}{2\text{sinh2a sinha}},$$

$$K_6 = \frac{\left(h_0 e^{-nt} + b\right) s\text{inha}}{2\text{sinh2a sinha}}$$

3 Results and Discussions

In the preceding section, numerical solution of the velocity profile and temperature profile are obtained and shown in graphs 1–5. In order to obtain physical insight into the problem and establish the influence of different parameters on velocity profile

and temperature profile, numerical calculation are performed and presented graphically. Figure 1 displays the dimensionless velocity distribution for different values of Reynolds number. It is found that the magnitude of velocity is enhanced with the raise of the Re. This is consistent with the fact that if Reynolds number is small, in the entire flow field, viscosity will be felt down and the viscous force will be predominant. Figure 2 shows the effect of permeability parameter (S) on the velocity distribution. It is noted that thickness of the boundary layer increases as S increases. Figure 3 depict the effect of transverse magnetic field on velocity. We observe that, for the increasing value of magnetic field parameter Ha the velocity distribution decreases.

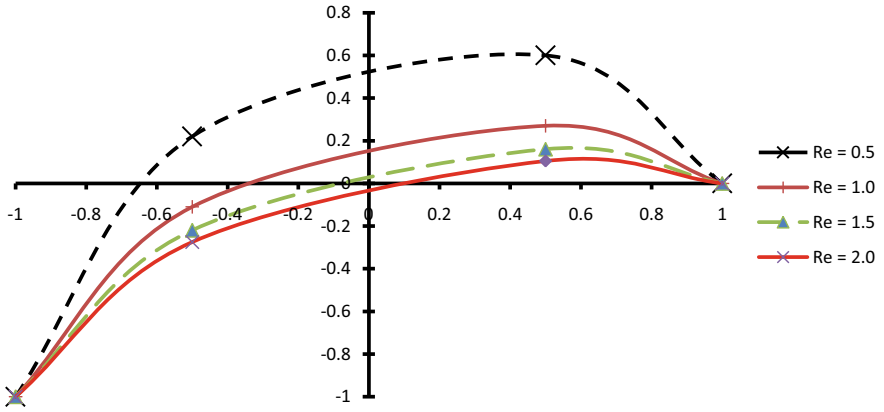

Fig. 1 Effect of Re on velocity

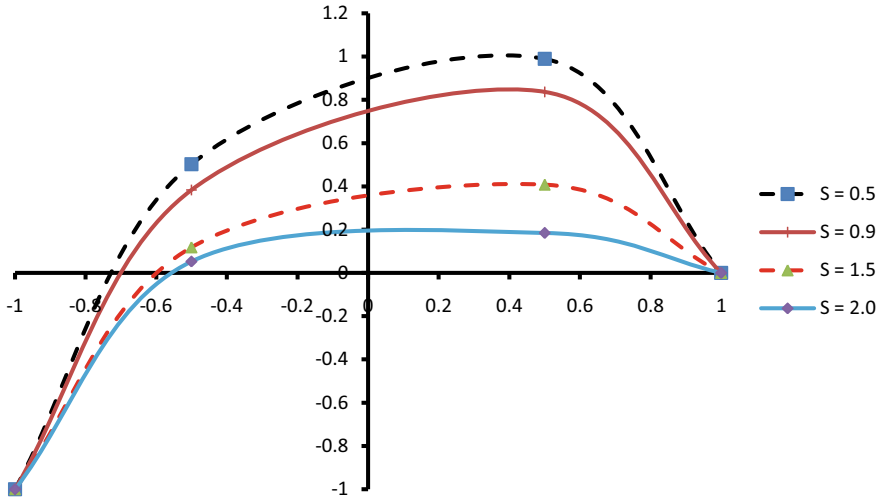

Fig. 2 Effect of S on velocity

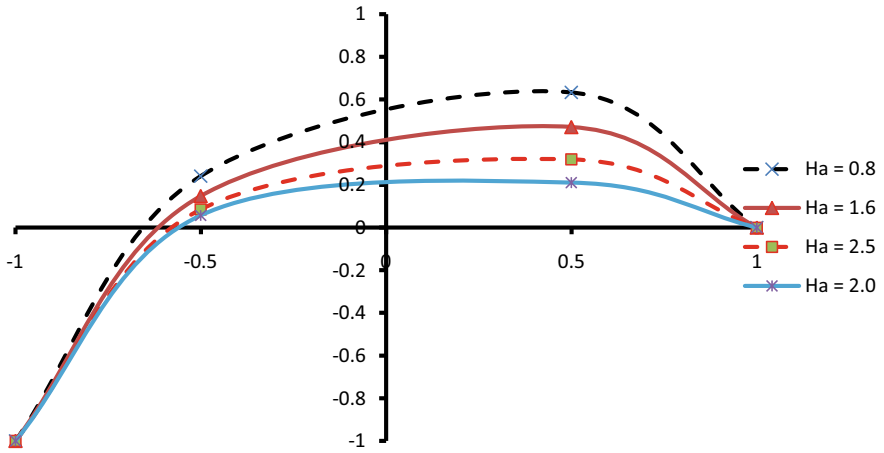

Fig. 3 Effect of Ha on velocity

That temperature plummets as the value of Prandtl number increases, (shown in Fig. 4) because the thickness of thermal boundary layer decreases as the value of Prandtl number increases. Figure 5 is for knowing the effects of heat absorption and heat generation parameter (Q) on heat transfer. We observe that temperature increases for the increasing strength of heat source ($Q > 0$) while reverse effect is noted for heat sink ($Q < 0$). Thus width of the thermal boundary layer enlarges corresponding to heat generation parameter but thickness reduces for increasing heat absorption.

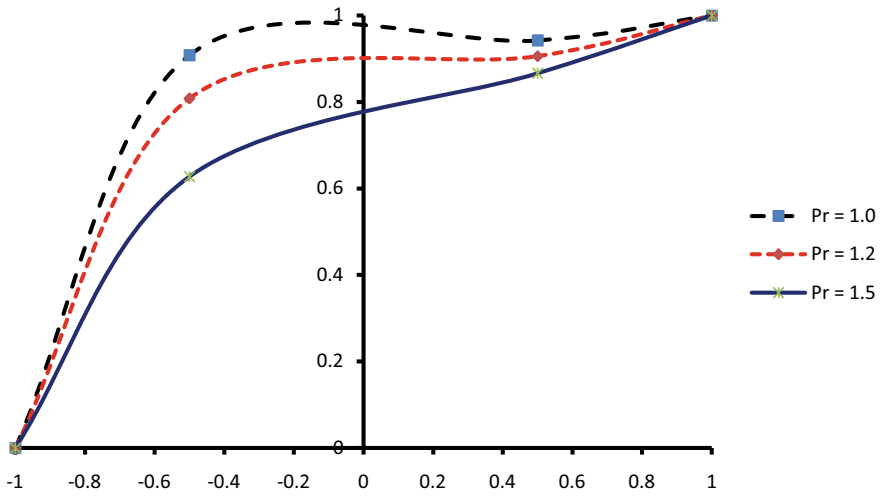

Fig. 4 Effect of Pr on temperature

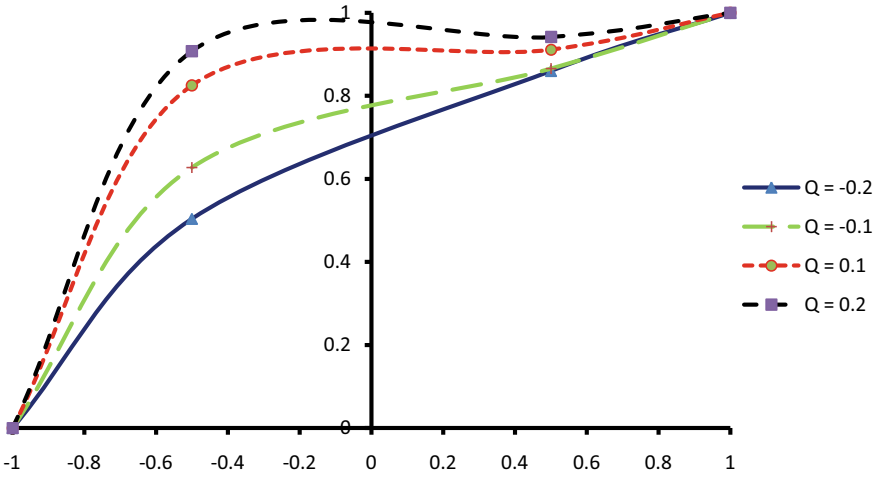

Fig. 5 Effect of Q on temperature

References

1. Cramer KR, Pai SI (1973) Magneto fluid dynamics for engineers and applied physicists. MacGraw-Hill, New York
2. Nigam SD, Singh SN (1960) Heat transfer by Laminar flow between parallel plates under the action of transverse magnetic field. Q J Mech Appl Math 13:85–87
3. Soundalgekar VM, Bhat JP (1971) Oscillatory MHD channel flow and heat transfer. Indian J Pure Appl Math 15:819–828
4. Raptis A, Massias C, Tzivanidis G (1982) Hydromagnetic free convection flow through porous medium between two parallel plates. Phys Lett 90(A):288–299
5. Vajravelu K (1988) An exact periodic solution of hydromagnetic flow in a horizontal channel. ASME J Appl Mech 55:981–983
6. Attia HA, Kotb NA (1996) MHD. Flow between two parallel plates with heat transfer. Acta Mech 117:215–220
7. Bodosa G, Borkakti AK (2003) Unsteady free convection MHD flow and heat transfer of a visco-elastic fluid past between two heated horizontal plates with heat sources or sinks. Indian Theo Phys 51(1):39–46
8. Makinde OD, Mhone PY (2005) Heat transfer to MHD oscillatory flow in a channel filled with porous medium. Rom J Phys 50:931–938
9. Attia HA (2006) On the effectiveness of variation in the physical variance on MHD steady flow between parallel plates with heat transfer. Int J Numer Methods Eng 65:224–235
10. Chaudhary RC, Jha AK, Dhayal SS (2006) Heat transfer to magneto-hydrodynamic flow in a horizontal channel with heat source. J Rajasthan Acad Phy Sci 5(2):233–238
11. Mebine P (2007) Radiation effects on MHD flow with heat transfer between two parallel plates. Glob J Pure Appl Math **3**:191–202
12. Adesanya SO (2012) Study of magneto-hydrodynamic visco-elastic heat generating/absorbing slip flow through porous medium with radiation effect. Int J Heat Technol 30:69–74
13. Rathore S, Singh J, Shishodia Y (2013) An efficient analytical approach for MHD viscous flow over a stretching sheet via homotopy perturbation sumudu transform method. Ain Shams Eng J 4:549–555. https://doi.org/10.1016/j.asej.2012.12.002
14. Hassan AR, Gbadeyan AJ (2015) A reacting hydro-magnetic internal heat generating fluid flow through channel. Int J Heat Technol 33(3):43–50

15. Gaur PK, Jha AK, Sharma RP (2017) MHD flow of a polar fluid through a porous medium of variable permeability bounded by horizontal parallel plates. Acta Tech 62(2-B):1–12
16. Ahmed TN, Khan I (2019) Entropy generation in C6H9NAO7 fluid over an accelerated heated plate. Front Phys 7:250. https://doi.org/10.3389/fphy
17. Ali F, Sheikh NA, Khan I, Nisar KS (2019) Caputo-Fabrizio fractional derivatives modeling of transient MHD Brinkman nanoliquid: applications in food technology. Chaos, Solitons Fractals 131:109489
18. Hussain A, Bano S, Khan I, Baleanu D, Nisar KS (2019) Lie symmetry analysis, explicit solutions and conservation laws of a spatially two-dimensional burgers-huxley equation. Symmetry 12(1):170
19. Sheikh NA, Ching DLC, Khan I, Kumar D, Nisar KS (2019) A new model of fractional Casson fluid based on generalized Fick's and Fourier's laws together with heat and mass transfer. Alex Eng J
20. Singh J, Rashidi MM, Rathore S, Kumar D (2019) A hybrid computational approach for Jeffery-Hamel flow in non-parallel walls. Neural Comput Appl 31:2407–2413
21. Kumar D, Singh J, Tanwar K, Baleanu D (2019) A new fractional exothermic reactions model having constant heat source in porous media with power, exponential and Mittag-Leffler Laws. Int J Heat Mass Transf 138:1222–1227
22. Dubey VP, Kumar R, Kumar D, Singh J, Khan I (2020) An efficient computational scheme for nonlinear time fractional systems of partial differential equations arising in physical sciences. Adv Differ Equ 46. https://doi.org/10.1186/s13662-020-2505-6
23. Hanif H, Khan I, Shafie S (2020) Heat transfer exaggeration and entropy analysis in magneto-hybrid nanofluid flow over a vertical cone: a numerical study. J Therm Anal Calorim 1–17
24. Khan U, Zaib A, Khan I, Baleanu D, Sherif ESM (2020) Comparative investigation on MHD nonlinear radiative flow through a moving thin needle comprising two hybridized AA7075 and AA7072 alloys nanomaterials through binary chemical reaction with activation energy. J Mater Res Technol

Volterra Equation with Constant Fractional Order and Variable Order Fractal Dimension

Abdon Atangana and Anum Shafiq

Abstract Very recently, Atangana and Anum suggested a class of differential and integral operators with a constant fractional order and variable order fractal dimension. The idea was the extension of the concept of fractal-fractional differential and integral operators that was also suggested and applied in 2016. In this chapter, we consider a general Volterra equation with the new differential and integral operators. We present the condition under which the uniqueness and existence of the exact solutions can be obtained for three cases including power law, exponential decay law and the generalized Mittag-Leffler function. For each case, we present a numerical solution and error analysis. We present some illustrative examples.

Keywords Fractal variable order · Fractional order · New Volterra equation · Numerical analysis

1 Introduction

Very recently, Atangana and Anum introduced a new class of differential and integral operators. These operators have two orders, a variable fractional order and variable fractal dimension [1]. The new operators are superior to the existing one as when the variable order and fractal dimension are constant, we recover the concept of fractal fractional differentiation and integration. When the variable order is reduced to zero and the variable fractal dimension is constant, we recover the so-called fractal

A. Shafiq (✉)
School of Mathematics and Statistics, Nanjing University of Information Science and Technology, Nanjing 210044, China
e-mail: anumshafiq@ymail.com

A. Atangana
Faculty of Natural and Agricultural Science, Institute for Groundwater Studied, University of Free State, Bloemfontein 9300, South Africa

Department of Medical Research, China Medical University Hospital, China Medical University, Taichung, Taiwan

J. Singh et al. (eds.), *Advances in Mathematical Modelling, Applied Analysis and Computation*, Lecture Notes in Networks and Systems 415,
https://doi.org/10.1007/978-981-19-0179-9_17

operators. However, if the fractal dimension is reduced to zero, then the operators provided the well-known variable fractional orders that are mainly used for modeling anomalous diffusion. If finally both are 1, we recover the classical differential and integral operators. These new operators have been applied recently in a few problems and amazing results were obtained [1]. The aim of these new differential and integral operators was to depict more complex problems faced by humankind in their daily activities. The theory and application of such are still in their genesis and more needs to be done. In this paper, we introduce a different approach that consists of combining a chaotic attractor and a fractal mapping. However before this, we provide very important fundamental theoretical results associated with these new operators. We present numerical approximation of both integral and differential operators [2–7].

2 Fundamental Properties

In this section, we present some important properties of the new operators. We start with the power law case. Let $(\alpha, \lambda) \in (0, 1)$

$$
\begin{aligned}
{}_0^{FFP}D_t^{\alpha,\beta(t)}\left[{}_0^{FFP}D_t^{\lambda,\beta(t)} f(t)\right] &= \frac{1}{\Gamma(1-\alpha)}\frac{d}{dt^{\beta(t)}}\int_0^t (t-\tau)^{-\alpha} f(\tau)\ {}_0^{FFP}D_t^{\alpha,\beta(t)} d\tau, \\
&= \frac{d}{dt}\frac{1}{\Gamma(1-\alpha)}\int_0^t (t-\tau)^{-\alpha} f(\tau)\ {}_0^{FFP}D_t^{\alpha,\beta(t)} d\tau \frac{t^{-\beta(t)}}{\beta'(t)\ln t + \frac{\beta(t)}{t}}, \\
&= \frac{d}{dt}\frac{1}{\Gamma(1-\alpha)}\int_0^t (t-\tau)^{-\alpha}\frac{1}{\Gamma(1-\lambda)}\frac{d}{d\tau}\int_0^\tau (\tau-s)^{-\lambda} f(s)\, ds \\
&\quad \frac{\tau^{-\beta(\tau)}}{\beta'(\tau)\ln\tau + \frac{\beta(\tau)}{t}} d\tau \frac{t^{-\beta(t)}}{\beta'(t)\ln t + \frac{\beta(t)}{t}},
\end{aligned} \tag{1}
$$

$$
{}_0^{FFP}D_t^{\alpha+\lambda,\beta(t)} f(t) = \frac{1}{\Gamma(1-\alpha-\lambda)}\frac{d}{dt}\int_0^t (t-\tau)^{-\alpha-\lambda} f(\tau)\, d\tau \frac{t^{-\beta(t)}}{\beta'(t)\ln t + \frac{\beta(t)}{t}}, \tag{2}
$$

$$
\begin{aligned}
{}_0^{FFP}D_t^{\lambda,\beta(t)}\left[{}_0^{FFP}D_t^{\alpha,\beta(t)} f(t)\right] &= \frac{d}{dt}\frac{1}{\Gamma(1-\lambda)}\int_0^t (t-\tau)^{-\lambda} f(\tau)\ {}_0^{FFP}D_t^{\alpha,\beta(t)} d\tau, \\
&= \frac{d}{dt}\frac{1}{\Gamma(1-\lambda)}\int_0^t (t-\tau)^{-\lambda} f(\tau)\ {}_0^{FFP}D_t^{\alpha,\beta(t)} d\tau \frac{t^{-\beta(t)}}{\beta'(t)\ln t + \frac{\beta(t)}{t}}, \\
&= \frac{d}{dt}\frac{1}{\Gamma(1-\lambda)}\int_0^t (t-\tau)^{-\lambda}\frac{1}{\Gamma(1-\alpha)}\frac{d}{d\tau}\int_0^\tau (\tau-s)^{-\alpha} f(s)\, ds \\
&\quad \frac{\tau^{-\beta(\tau)}}{\beta'(\tau)\ln\tau + \frac{\beta(\tau)}{t}} d\tau \frac{t^{-\beta(t)}}{\beta'(t)\ln t + \frac{\beta(t)}{t}}.
\end{aligned} \tag{3}
$$

This shows that

$$
{}_0^{FFP}D_t^{\alpha,\beta(t)}\left[{}_0^{FFP}D_t^{\lambda,\beta(t)} f(t)\right] + {}_0^{FFP}D_t^{\lambda,\beta(t)}\left[{}_0^{FFP}D_t^{\alpha,\beta(t)} f(t)\right] \neq {}_0^{FFP}D_t^{\alpha+\lambda,\beta(t)} f(t); \tag{4}
$$

if $\alpha = 0$, then we have

$$ {}_0^{FFP}D_t^{0,\beta(t)} f(t) = f(t) \frac{t^{-\beta(t)}}{\beta'(t)\ln t + \frac{\beta(t)}{t}}; \tag{5} $$

if $\beta(t) = 0$, then we have

$$ {}_0^{FFP}D_t^{\alpha,0} f(t) = \frac{1}{\Gamma(1-\alpha)} \frac{d}{dt} \int_0^t (t-\tau)^{-\alpha} f(\tau)\, d\tau = {}_0^R D_t^{\alpha} f(t). \tag{6} $$

If $\alpha = \beta(t) = 0$, we have

$$ {}_0^{FFP}D_t^{0,0} f(t) = f(t). \tag{7} $$

If $\alpha = 1$ and $\beta(t)$ a continuous function, we have the following if $f(t)$ is differentiable:

$$ {}_0^{FFP}D_t^{1,\beta(t)} f(t) = f'(t) \frac{t^{-\beta(t)}}{\beta'(t)\ln t + \frac{\beta(t)}{t}} = \frac{d}{dt^{\beta(t)}} f(t). \tag{8} $$

Proof

$$ \begin{aligned} \lim_{\alpha\to 1} {}_0^{FFP}D_t^{\alpha,\beta(t)} f(t) &= \lim_{\alpha\to 1} \frac{1}{\Gamma(1-\alpha)} \frac{d}{dt^{\beta(t)}} \int_0^t (t-\tau)^{-\alpha} f(\tau)\, d\tau, \\ &= \lim_{\alpha\to 1} \frac{1}{\Gamma(1-\alpha)} \frac{d}{dt} \int_0^t (t-\tau)^{-\alpha} f(\tau)\, d\tau \frac{t^{-\beta(t)}}{\beta'(t)\ln t + \frac{\beta(t)}{t}}, \\ &= \frac{d}{dt} f(t) \frac{t^{-\beta(t)}}{\beta'(t)\ln t + \frac{\beta(t)}{t}}, \\ &= \frac{d}{dt^{\beta(t)}} f(t). \end{aligned} \tag{9} $$

Let $\beta_1(t)$ and $\beta_2(t)$ be two different positive and differentiable functions, then

$$ \begin{aligned} {}_0^{FFP}D_t^{\alpha,\beta_1(t)+\beta_2(t)} f(t) &= \frac{1}{\Gamma(1-\alpha)} \frac{d}{dt^{\beta_1(t)+\beta_2(t)}} \int_0^t (t-\tau)^{-\alpha} f(\tau)\, d\tau, \\ &= \frac{1}{\Gamma(1-\alpha)} \frac{d}{dt} \int_0^t (t-\tau)^{-\alpha} f(\tau)\, d\tau \frac{t^{-\beta_1(t)+\beta_2(t)}}{(\beta_1(t)+\beta_2(t))'\ln t + \frac{\beta_1(t)+\beta_2(t)}{t}}, \end{aligned} \tag{10} $$

$$
\begin{aligned}
{}_{0}^{FFP}D_{t}^{\alpha,\beta_1(t)}\left[{}_{0}^{FFP}D_{t}^{\alpha,\beta_2(t)}f(t)\right] &= \frac{d}{dt^{\beta_1(t)}}\int_0^t \frac{1}{\Gamma(1-\alpha)}(t-\tau)^{-\alpha} f(\tau)\ {}_{0}^{FFP}D_{t}^{\alpha,\beta_2(t)}d\tau,\\
&= \frac{1}{\Gamma(1-\alpha)}\frac{1}{\Gamma(1-\alpha)}\frac{d}{dt}\int_0^t (t-\tau)^{-\alpha}\frac{d}{d\tau}\int_0^\tau (\tau-s)^{-\alpha} f(s)\,ds\\
&\quad \frac{\tau^{-\beta_2(\tau)}}{\beta_2'(\tau)\ln\tau+\frac{\beta_2(\tau)}{\tau}}d\tau\frac{t^{-\beta_1(t)}}{\beta_1'(t)\ln t+\frac{\beta_1(t)}{t}},
\end{aligned}
\tag{11}
$$

$$
\begin{aligned}
{}_{0}^{FFP}D_{t}^{\alpha,\beta_2(t)}\left[{}_{0}^{FFP}D_{t}^{\alpha,\beta_1(t)}f(t)\right] &= \frac{d}{dt^{\beta_2(t)}}\int_0^t \frac{1}{\Gamma(1-\alpha)}(t-\tau)^{-\alpha} f(\tau)\ {}_{0}^{FFP}D_{t}^{\alpha,\beta_1(t)}d\tau,\\
&= \frac{1}{\Gamma(1-\alpha)}\frac{1}{\Gamma(1-\alpha)}\frac{d}{dt}\int_0^t (t-\tau)^{-\alpha}\frac{d}{d\tau}\int_0^\tau (\tau-s)^{-\alpha} f(s)\,ds\\
&\quad \frac{\tau^{-\beta_1(\tau)}}{\beta_1'(\tau)\ln t+\frac{\beta_1(\tau)}{\tau}}d\tau\frac{t^{-\beta_2(t)}}{\beta_2'(t)\ln t+\frac{\beta_2(t)}{t}}.
\end{aligned}
\tag{12}
$$

The above proof shows that the following relations are not satisfied:

$$
{}_{0}^{FFP}D_{t}^{\alpha,\beta_1(t)}\left[{}_{0}^{FFP}D_{t}^{\alpha,\beta_2(t)}f(t)\right] \neq {}_{0}^{FFP}D_{t}^{\alpha,\beta_1(t)+\beta_2(t)}f(t),
\tag{13}
$$

and

$$
{}_{0}^{FFP}D_{t}^{\alpha,\beta_1(t)}\left[{}_{0}^{FFP}D_{t}^{\alpha,\beta_2(t)}f(t)\right] \neq {}_{0}^{FFP}D_{t}^{\alpha,\beta_2(t)}\left[{}_{0}^{FFP}D_{t}^{\alpha,\beta_1(t)}f(t)\right].
\tag{14}
$$

We next verify if the product rule of the classical derivative can be obtained or not for this new differential operator. To do this, we let f and g be two differentiable functions, and $\beta(t)$ be differentiable functions, then

$$
\begin{aligned}
{}_{0}^{FFP}D_{t}^{\alpha,\beta(t)}[f(t)\,g(t)] &= \frac{1}{\Gamma(1-\alpha)}\frac{d}{dt^{\beta(t)}}\int_0^t (t-\tau)^{-\alpha}(f.g)(\tau)\,d\tau,\\
&= \frac{1}{\Gamma(1-\alpha)}\frac{d}{dt}\int_0^t (t-\tau)^{-\alpha}(f.g)(\tau)\\
&\quad d\tau\frac{t^{-\beta(t)}}{\beta'(t)\ln t+\frac{\beta(t)}{t}},
\end{aligned}
\tag{15}
$$

using the Leibniz rule for fractional differentiation, we have

$$
\begin{aligned}
{}_{0}^{FFP}D_{t}^{\alpha,\beta(t)}[f(t)\,g(t)] &= \sum_{k=0}^{m}\binom{\alpha}{k} f^k(t)\ {}_{0}^{FFP}D_{t}^{\alpha-k}g(t)\ \frac{t^{-\beta(t)}}{\beta'(t)\ln t+\frac{\beta(t)}{t}},\\
&= \sum_{k=0}^{m}\binom{\alpha}{k} f^k(t)\ {}_{0}^{FFP}D_{t}^{\alpha-k,\beta(t)}g(t).
\end{aligned}
\tag{16}
$$

Therefore

$$
\begin{aligned}
{}_0^{FFP}D_t^{\alpha,\beta(t)}\left[f\left(t\right).g\left(t\right)\right] &= \sum_{k=0}^{m}\binom{\alpha}{k}f^k\left(t\right)\ {}_0^{FFP}D_t^{\alpha-k,\beta(t)}g\left(t\right), \\
&= \sum_{k=0}^{m}\binom{\alpha}{k}g^k\left(t\right)\ {}_0^{FFP}D_t^{\alpha-k,\beta(t)}f\left(t\right). \qquad (17)
\end{aligned}
$$

Let $\alpha, \lambda \in (0, 1]$, and also suppose $\beta\left(t\right)$ be a differentiable function, then

$$
\begin{aligned}
{}_0^{FFP}J_t^{\alpha,\beta(t)}\left[{}_0^{FFP}J_t^{\lambda,\beta(t)}f\left(t\right)\right] &= \frac{1}{\Gamma\left(\alpha\right)}\int_0^t\left(t-\tau\right)^{\alpha-1}f\left(\tau\right)\ {}_0^{FFP}J_\tau^{\lambda,\beta(\tau)} \\
&\quad \tau^{\beta(\tau)}\left(\beta'\left(\tau\right)\ln\tau+\frac{\beta\left(\tau\right)}{\tau}\right)d\tau, \\
&= \frac{1}{\Gamma\left(\alpha\right)}\frac{1}{\Gamma\left(\lambda\right)}\int_0^t\left(t-\tau\right)^{\alpha-1}\tau^{\beta(\tau)}\left(\beta'\left(\tau\right)\ln\tau+\frac{\beta\left(\tau\right)}{\tau}\right) \\
&\quad \int_0^\tau\left(\tau-s\right)^{\lambda-1}s^{\beta(s)}\left(\beta'\left(s\right)\ln s+\frac{\beta\left(s\right)}{s}\right) \\
&\quad f\left(s\right)dsd\tau, \qquad (18)
\end{aligned}
$$

while

$$
\begin{aligned}
{}_0^{FFP}J_t^{\lambda,\beta(t)}\left[{}_0^{FFP}J_t^{\alpha,\beta(t)}f\left(t\right)\right] &= \frac{1}{\Gamma\left(\alpha\right)}\int_0^t\left(t-\tau\right)^{\lambda-1}f\left(\tau\right)\ {}_0^{FFP}J_\tau^{\alpha,\beta(\tau)} \\
&\quad \tau^{\beta(\tau)}\left(\beta'\left(\tau\right)\ln\tau+\frac{\beta\left(\tau\right)}{\tau}\right)d\tau, \\
&= \frac{1}{\Gamma\left(\alpha\right)}\frac{1}{\Gamma\left(\lambda\right)}\int_0^t\left(t-\tau\right)^{\lambda-1}\tau^{\beta(\tau)}\left(\beta'\left(\tau\right)\ln\tau+\frac{\beta\left(\tau\right)}{\tau}\right) \\
&\quad \int_0^\tau\left(\tau-s\right)^{\alpha-1}s^{\beta(s)}\left(\beta'\left(s\right)\ln s+\frac{\beta\left(s\right)}{s}\right) \\
&\quad f\left(s\right)dsd\tau. \qquad (19)
\end{aligned}
$$

But

$$
{}_0^{FFP}J_t^{\alpha+\lambda,\beta(t)}f\left(t\right) = \frac{1}{\Gamma\left(\alpha+\lambda\right)}\int_0^t\left(t-\tau\right)^{\alpha+\lambda-1}f\left(\tau\right)\ \tau^{\beta(\tau)}\left(\beta'\left(\tau\right)\ln\tau+\frac{\beta\left(\tau\right)}{\tau}\right)d\tau. \qquad (20)
$$

This shows that

$$
{}_0^{FFP}J_t^{\alpha,\beta(t)}\left[{}_0^{FFP}J_t^{\lambda,\beta(t)}f\left(t\right)\right] \neq {}_0^{FFP}\ J_t^{\lambda,\beta(t)}\left[{}_0^{FFP}J_t^{\alpha,\beta(t)}f\left(t\right)\right] \neq {}_0^{FFP}\ J_t^{\alpha+\lambda,\beta(t)}f\left(t\right). \qquad (21)
$$

Let $\beta_1\left(t\right)$ and $\beta_2\left(t\right)$ be two differentiable functions, let $\alpha \in (0, 1]$ and let f be continuous, then

$$
\begin{aligned}
{}_{0}^{FFP}J_{t}^{\alpha,\beta_1(t)}\left[{}_{0}^{FFP}J_{t}^{\alpha,\beta_2(t)}f(t)\right] &= \frac{1}{\Gamma(\alpha)}\int_0^t (t-\tau)^{\alpha-1} f(\tau)\ {}_{0}^{FFP}J_{\tau}^{\alpha,\beta_2(\tau)} \\
&\quad \tau^{\beta_1(\tau)}\left(\beta_1'(\tau)\ln\tau+\frac{\beta_1(\tau)}{\tau}\right)d\tau, \\
&= \frac{1}{\Gamma(\alpha)}\frac{1}{\Gamma(\alpha)}\int_0^t (t-\tau)^{\alpha-1}\tau^{\beta_1(\tau)}\left(\beta_1'(\tau)\ln\tau+\frac{\beta_1(\tau)}{\tau}\right) \\
&\quad \int_0^{\tau}(\tau-s)^{\alpha-1}s^{\beta_2(s)}\left(\beta_2'(s)\ln s+\frac{\beta_2(s)}{s}\right)f(s)\,ds d\tau \qquad (22)
\end{aligned}
$$

while

$$
\begin{aligned}
{}_{0}^{FFP}J_{t}^{\alpha,\beta_2(t)}\left[{}_{0}^{FFP}J_{t}^{\alpha,\beta_1(t)}f(t)\right] &= \frac{1}{\Gamma(\alpha)}\int_0^t (t-\tau)^{\alpha-1} f(\tau)\ {}_{0}^{FFP}J_{\tau}^{\alpha,\beta_1(\tau)} \\
&\quad \tau^{\beta_2(\tau)}\left(\beta_2'(\tau)\ln\tau+\frac{\beta_2(\tau)}{\tau}\right)d\tau, \\
&= \frac{1}{\Gamma(\alpha)}\frac{1}{\Gamma(\alpha)}\int_0^t (t-\tau)^{\alpha-1}\tau^{\beta_2(\tau)}\left(\beta_2'(\tau)\ln\tau+\frac{\beta_2(\tau)}{\tau}\right) \\
&\quad \int_0^{\tau}(\tau-s)^{\alpha-1}s^{\beta_1(s)}\left(\beta_1'(s)\ln s+\frac{\beta_1(s)}{s}\right) \\
&\quad f(s)\,ds d\tau. \qquad (23)
\end{aligned}
$$

Also

$$
\begin{aligned}
{}_{0}^{FFP}J_{t}^{\alpha,\beta_1(t)+\beta_2(t)}f(t) &= \frac{1}{\Gamma(\alpha)}\int_0^t (t-\tau)^{\alpha-1} f(\tau)\ \tau^{\beta_1(\tau)+\beta_2(\tau)} \\
&\quad \left(\left(\beta_1'(\tau)+\beta_2'(\tau)\right)\ln\tau+\frac{\beta_1(\tau)+\beta_2(\tau)}{\tau}\right)d\tau. \qquad (24)
\end{aligned}
$$

This shows that

$$
{}_{0}^{FFP}J_{t}^{\alpha,\beta_1(t)}\left[{}_{0}^{FFP}J_{t}^{\alpha,\beta_2(t)}f(t)\right] \neq {}_{0}^{FFP}J_{t}^{\alpha,\beta_2(t)}\left[{}_{0}^{FFP}J_{t}^{\alpha,\beta_1(t)}f(t)\right] \neq {}_{0}^{FFP}J_{t}^{\alpha,\beta_1(t)+\beta_2(t)}f(t). \qquad (25)
$$

If $\alpha \to 1$, we have the following:

$$
\begin{aligned}
\lim_{\alpha\to 1}\ {}_{0}^{FFP}J_{t}^{\alpha,\beta(t)}f(t) &= \lim_{\alpha\to 1}\frac{1}{\Gamma(\alpha)}\int_0^t (t-\tau)^{\alpha-1} f(\tau)\tau^{\beta(\tau)}\left(\beta'(\tau)\ln\tau+\frac{\beta(\tau)}{\tau}\right)d\tau, \\
&= \int_0^t f(\tau)\tau^{\beta(\tau)}\left(\beta'(\tau)\ln\tau+\frac{\beta(\tau)}{\tau}\right)d\tau, \\
&= \int_0^t f(\tau)\frac{d}{d\tau}\ln\tau^{\beta(\tau)}d\tau. \qquad (26)
\end{aligned}
$$

If $\alpha \to 0$, we have the following:

$$\begin{aligned}\lim_{\alpha\to 0}\ {}_0^{FFP}J_t^{\alpha,\beta(t)} f(t) &= \lim_{\alpha\to 0}\frac{1}{\Gamma(\alpha)}\int_0^t (t-\tau)^{\alpha-1} f(\tau)\,\tau^{\beta(\tau)}\left(\beta'(\tau)\ln\tau+\frac{\beta(\tau)}{\tau}\right)d\tau,\\ &= \lim_{\alpha\to 0}\frac{1}{\Gamma(\alpha)}\int_0^t (t-\tau)^{\alpha-1} F(\tau)\,d\tau,\\ &= \int_0^t f(t-\tau)\,F(\tau)\,d\tau,\\ &= F(t),\\ &= f(t)\,t^{\beta(t)}\left(\beta'(t)\ln t+\frac{\beta(t)}{t}\right). \end{aligned} \tag{27}$$

If $\beta(t)\to 1$, then we have the following:

$$\begin{aligned}\lim_{\beta(t)\to 1}\ {}_0^{FFP}J_t^{\alpha,\beta(t)} f(t) &= \lim_{\beta(t)\to 1}\frac{1}{\Gamma(\alpha)}\int_0^t (t-\tau)^{\alpha-1} f(\tau)\,\tau^{\beta(\tau)}\left(\beta'(\tau)\ln\tau+\frac{\beta(\tau)}{\tau}\right)d\tau,\\ &= \lim_{\beta(t)\to 1}\frac{1}{\Gamma(\alpha)}\int_0^t (t-\tau)^{\alpha-1} f(\tau)\,\frac{d}{d\tau}\left(\ln\tau^{\beta(\tau)}\right)d\tau,\\ &= \frac{1}{\Gamma(\alpha)}\int_0^t (t-\tau)^{\alpha-1} f(\tau)\left(\lim_{\beta(t)\to 1}\frac{d}{d\tau}\ln\tau^{\beta(\tau)}\right)d\tau,\\ &= \frac{1}{\Gamma(\alpha)}\int_0^t (t-\tau)^{\alpha-1} f(\tau)\,d\tau. \end{aligned} \tag{28}$$

If $\beta(t)\to 0$, then we have the following:

$$\begin{aligned}\lim_{\beta(t)\to 0}\ {}_0^{FFP}J_t^{\alpha,\beta(t)} f(t) &= \lim_{\beta(t)\to 0}\frac{1}{\Gamma(\alpha)}\int_0^t (t-\tau)^{\alpha-1} f(\tau)\,\tau^{\beta(\tau)}\left(\beta'(\tau)\ln\tau+\frac{\beta(\tau)}{\tau}\right)d\tau,\\ &= \lim_{\beta(t)\to 0}\frac{1}{\Gamma(\alpha)}\int_0^t (t-\tau)^{\alpha-1} f(\tau)\,\frac{d}{d\tau}\left(\ln\tau^{\beta(\tau)}\right)d\tau,\\ &= \frac{1}{\Gamma(\alpha)}\int_0^t (t-\tau)^{\alpha-1} f(\tau)\left(\lim_{\beta(t)\to 0}\frac{d}{d\tau}\ln\tau^{\beta(\tau)}\right)d\tau,\\ &= \frac{1}{\Gamma(\alpha)}\int_0^t (t-\tau)^{\alpha-1} f(\tau)\,0\,d\tau,\\ &= 0. \end{aligned} \tag{29}$$

Therefore, $\beta(t)$ must be greater than zero.

Here, we consider a function which is analytical around a given constant c.

Thus, if $f(t)$ is analytical around the constant c, by definition, we have the following when using the new differential operator for power law case:

$$
\begin{aligned}
{}_0^{FFP}D_t^{\alpha,\beta(t)} f(t) &= \frac{1}{\Gamma(1-\alpha)} \frac{d}{dt} \int_0^t (t-\tau)^{-\alpha} f(\tau)\, d\tau \frac{t^{-\beta(t)}}{\beta'(t)\ln t + \frac{\beta(t)}{t}}, \\
&= \frac{1}{\Gamma(1-\alpha)} \frac{d}{dt} \int_0^t (t-\tau)^{-\alpha} \sum_{k=0}^{\infty} a_k (\tau - c)^r\, d\tau \frac{t^{-\beta(t)}}{\beta'(t)\ln t + \frac{\beta(t)}{t}}, \\
&= \frac{1}{\Gamma(1-\alpha)} \sum_{k=0}^{\infty} a_k \int_0^t (t-\tau)^{-\alpha} (\tau - c)^r\, d\tau \frac{t^{-\beta(t)}}{\beta'(t)\ln t + \frac{\beta(t)}{t}}, \\
&= \sum_{k=0}^{\infty} a_k\, {}_0^{Rl}D_t^{\alpha} (\tau - c)^r \frac{t^{-\beta(t)}}{\beta'(t)\ln t + \frac{\beta(t)}{t}}. \qquad (30)
\end{aligned}
$$

However

$$
{}_0^{Rl}D_t^{\alpha} (\tau - c)^j = \frac{\Gamma(j+1)}{\Gamma(j-\alpha+1)} (t-c)^{j-\alpha}. \qquad (31)
$$

Thus,

$$
{}_0^{FFP}D_t^{\alpha,\beta(t)} f(t) = \sum_{k=0}^{\infty} a_k \frac{\Gamma(j+1)}{\Gamma(j-\alpha+1)} (t-c)^{j-\alpha} \frac{t^{-\beta(t)}}{\beta'(t)\ln t + \frac{\beta(t)}{t}}. \qquad (32)
$$

2.1 Properties for the Case of Exponential Decay

We now present the same proposition for the case of exponential decay law. Let $(\alpha, \lambda) \in (0, 1]$, and let $\beta(t)$ be a positive differentiable function, thus

$$
\begin{aligned}
{}_0^{FFE}D_t^{\alpha+\lambda,\beta(t)} f(t) &= \frac{M(\alpha+\beta)}{1-(\alpha+\beta)} \frac{d}{dt^{\beta(t)}} \int_0^t \exp\left[-\frac{(\alpha+\beta)(t-\tau)}{1-(\alpha+\beta)}\right] f(\tau)\, d\tau \\
&= \frac{M(\alpha+\beta)}{1-(\alpha+\beta)} \frac{d}{dt} \int_0^t \exp\left[-\frac{(\alpha+\beta)(t-\tau)}{1-(\alpha+\beta)}\right] f(\tau)\, d\tau \frac{t^{-\beta(t)}}{\beta'(t)\ln t + \frac{\beta(t)}{t}}, \qquad (33)
\end{aligned}
$$

while

$$
\begin{aligned}
{}_0^{FFE}D_t^{\alpha,\beta(t)} \left[{}_0^{FFE}D_t^{\lambda,\beta(t)} f(t)\right] &= \frac{M(\alpha)}{1-\alpha} \frac{d}{dt^{\beta(t)}} \int_0^t f(\tau) \exp\left[-\frac{\alpha(t-\tau)}{1-\alpha}\right] {}_0^{FFE}D_\tau^{\lambda,\beta(\tau)} d\tau, \\
&= \frac{M(\alpha)}{1-\alpha} \frac{d}{dt} \int_0^t f(\tau) \exp\left[-\frac{\alpha(t-\tau)}{1-\alpha}\right] {}_0^{FFE}D_\tau^{\lambda,\beta(\tau)} d\tau \\
&\quad \frac{t^{-\beta(t)}}{\beta'(t)\ln t + \frac{\beta(t)}{t}}, \\
&= \frac{M(\alpha)}{1-\alpha} \frac{M(\lambda)}{1-\lambda} \frac{d}{dt} \int_0^t \frac{d}{d\tau} \int_0^\tau f(s) \exp\left[-\frac{\lambda(\tau-s)}{1-\lambda}\right] ds \\
&\quad \frac{\tau^{-\beta(\tau)}}{\beta'(\tau)\ln\tau + \frac{\beta(\tau)}{\tau}} d\tau \frac{t^{-\beta(t)}}{\beta'(t)\ln t + \frac{\beta(t)}{t}}. \qquad (34)
\end{aligned}
$$

And finally

$$ {}_0^{FFE}D_t^{\lambda,\beta(t)}\left[{}_0^{FFE}D_t^{\alpha,\beta(t)}f(t)\right]=\frac{M(\alpha)}{1-\alpha}\frac{M(\lambda)}{1-\lambda}\frac{d}{dt}\int_0^t\frac{d}{d\tau}\int_0^\tau f(s)\exp\left[-\frac{\alpha(\tau-s)}{1-\alpha}\right]ds \frac{\tau^{-\beta(\tau)}}{\beta'(\tau)\ln\tau+\frac{\beta(\tau)}{\tau}}d\tau\frac{t^{-\beta(t)}}{\beta'(t)\ln t+\frac{\beta(t)}{t}}. \tag{35} $$

This shows that

$$ {}_0^{FFE}D_t^{\alpha,\beta(t)}\left[{}_0^{FFE}D_t^{\lambda,\beta(t)}f(t)\right]\neq{}_0^{FFE}D_t^{\lambda,\beta(t)}\left[{}_0^{FFE}D_t^{\alpha,\beta(t)}f(t)\right]\neq{}_0^{FFE}D_t^{\alpha+\lambda,\beta(t)}f(t). \tag{36} $$

Also, we take $\alpha\in(0,1]$ and $\beta_1(t)$, $\beta_2(t)$, two positively smooth functions.

$$ {}_0^{FFE}D_t^{\lambda,\beta_1(t)+\beta_2(t)}f(t)=\frac{M(\alpha)}{1-\alpha}\frac{d}{dt}\int_0^t f(\tau)\exp\left[-\frac{\alpha(t-\tau)}{1-\alpha}\right]d\tau \frac{t^{-\beta_1(t)+\beta_2(t)}}{\left(\beta_1'(t)+\beta_2'(t)\right)\ln t+\frac{\beta_1(t)+\beta_2(t)}{t}}, \tag{37} $$

while

$$ {}_0^{FFE}D_t^{\alpha,\beta_1(t)}\left[{}_0^{FFE}D_t^{\alpha,\beta_2(t)}f(t)\right]=\left(\frac{M(\alpha)}{1-\alpha}\right)^2\frac{d}{dt}\int_0^t\frac{d}{d\tau}\int_0^\tau f(s)\exp\left[-\frac{\alpha(\tau-s)}{1-\alpha}\right]ds \frac{\tau^{-\beta_2(\tau)}}{\beta_2'(\tau)\ln\tau+\frac{\beta_2(\tau)}{\tau}}d\tau\frac{t^{-\beta_1(t)}}{\beta_1'(t)\ln t+\frac{\beta_1(t)}{t}}. \tag{38} $$

Finally

$$ {}_0^{FFE}D_t^{\alpha,\beta_2(t)}\left[{}_0^{FFE}D_t^{\alpha,\beta_1(t)}f(t)\right]=\left(\frac{M(\alpha)}{1-\alpha}\right)^2\frac{d}{dt}\int_0^t\frac{d}{d\tau}\int_0^\tau f(s)\exp\left[-\frac{\alpha(\tau-s)}{1-\alpha}\right]ds \frac{\tau^{-\beta_1(\tau)}}{\beta_1'(\tau)\ln\tau+\frac{\beta_1(\tau)}{\tau}}d\tau\frac{t^{-\beta_2(t)}}{\beta_2'(t)\ln t+\frac{\beta_2(t)}{t}}. \tag{39} $$

Case 1 : If $\alpha\to0$, we have the following:

$$ \begin{aligned} \lim_{\alpha\to0}{}_0^{FFE}D_t^{\alpha,\beta(t)}f(t)&=\lim_{\alpha\to0}\frac{M(\alpha)}{1-\alpha}\frac{d}{dt^{\beta(t)}}\int_0^t\exp\left[-\frac{\alpha(t-\tau)}{1-\alpha}\right]f(\tau)\,d\tau,\\ &=\lim_{\alpha\to0}\frac{M(\alpha)}{1-\alpha}\frac{d}{dt}\int_0^t\exp\left[-\frac{\alpha(t-\tau)}{1-\alpha}\right]f(\tau)\,d\tau\frac{t^{-\beta(t)}}{\beta'(t)\ln t+\frac{\beta(t)}{t}},\\ &=\frac{d}{dt}\int_0^t\lim_{\alpha\to0}\frac{M(\alpha)}{1-\alpha}\exp\left[-\frac{\alpha(t-\tau)}{1-\alpha}\right]f(\tau)\,d\tau\frac{t^{-\beta(t)}}{\beta'(t)\ln t+\frac{\beta(t)}{t}},\\ &=\frac{d}{dt}\int_0^t f(\tau)\,d\tau\frac{t^{-\beta(t)}}{\beta'(t)\ln t+\frac{\beta(t)}{t}},\\ &=f(t)\frac{t^{-\beta(t)}}{\beta'(t)\ln t+\frac{\beta(t)}{t}}. \end{aligned} \tag{40} $$

Case 2 : If $\alpha \to 1$, we have the following:

$$\begin{aligned}
\lim_{\alpha\to 1} {}_0^{FFE}D_t^{\alpha,\beta(t)} f(t) &= \lim_{\alpha\to 1} \frac{M(\alpha)}{1-\alpha} \frac{d}{dt^{\beta(t)}} \int_0^t \exp\left[-\frac{\alpha(t-\tau)}{1-\alpha}\right] f(\tau)\, d\tau, \\
&= \lim_{\alpha\to 1} \frac{M(\alpha)}{1-\alpha} \frac{d}{dt} \int_0^t \exp\left[-\frac{\alpha(t-\tau)}{1-\alpha}\right] f(\tau)\, d\tau \frac{t^{-\beta(t)}}{\beta'(t)\ln t + \frac{\beta(t)}{t}}, \\
&= \frac{d}{dt} \int_0^t \lim_{\alpha\to 1} \frac{M(\alpha)}{1-\alpha} \exp\left[-\frac{\alpha(t-\tau)}{1-\alpha}\right] f(\tau)\, d\tau \frac{t^{-\beta(t)}}{\beta'(t)\ln t + \frac{\beta(t)}{t}}, \\
&= \frac{d}{dt} \int_0^t \delta(t-\tau) f(\tau)\, d\tau \frac{t^{-\beta(t)}}{\beta'(t)\ln t + \frac{\beta(t)}{t}}, \\
&= f'(t) \frac{t^{-\beta(t)}}{\beta'(t)\ln t + \frac{\beta(t)}{t}}. \qquad (41)
\end{aligned}$$

Case 3 : If $\beta(t) \to 1$, we have the following:

$$\begin{aligned}
\lim_{\beta(t)\to 1} {}_0^{FFE}D_t^{\alpha,\beta(t)} f(t) &= \lim_{\beta(t)\to 1} \frac{M(\alpha)}{1-\alpha} \frac{d}{dt^{\beta(t)}} \int_0^t \exp\left[-\frac{\alpha(t-\tau)}{1-\alpha}\right] f(\tau)\, d\tau, \\
&= \lim_{\beta(t)\to 1} \frac{M(\alpha)}{1-\alpha} \frac{d}{dt} \int_0^t \exp\left[-\frac{\alpha(t-\tau)}{1-\alpha}\right] f(\tau)\, d\tau \frac{t^{-\beta(t)}}{\beta'(t)\ln t + \frac{\beta(t)}{t}}, \\
&= \frac{d}{dt} \int_0^t \frac{M(\alpha)}{1-\alpha} \exp\left[-\frac{\alpha(t-\tau)}{1-\alpha}\right] f(\tau)\, d\tau \lim_{\beta(t)\to 1} \frac{t^{-\beta(t)}}{\beta'(t)\ln t + \frac{\beta(t)}{t}}, \\
&= {}_0^{CFR}D_0^{\alpha} f(t). \qquad (42)
\end{aligned}$$

3 Existence and Uniqueness

In this section, we present the well-posedness of the newly defined differential and integral operators. Other important properties from the classical differentiation and integration will also be presented. We start our investigation by presenting the case where the function under consideration is analytical around a given constant c.

$$\begin{aligned}
{}_0^{FFP}D_t^{\alpha,\beta(t)} f(t) &= \frac{AB(\alpha)}{1-\alpha} \frac{d}{dt^{\beta(t)}} \int_0^t f(\tau) E_\alpha\left[-\frac{\alpha}{1-\alpha}(t-\tau)^{-\alpha}\right] d\tau, \\
&= \frac{AB(\alpha)}{1-\alpha} \frac{d}{dt} \int_0^t f(\tau) E_\alpha\left[-\frac{\alpha}{1-\alpha}(t-\tau)^{-\alpha}\right] d\tau \frac{t^{-\beta(t)}}{\beta'(t)\ln t + \frac{\beta(t)}{t}}, \\
&= \frac{AB(\alpha)}{1-\alpha} \frac{d}{dt} \int_0^t \sum_{j=0}^{\infty} a_j (\tau-c)^j E_\alpha\left[-\frac{\alpha}{1-\alpha}(t-\tau)^{-\alpha}\right] d\tau \frac{t^{-\beta(t)}}{\beta'(t)\ln t + \frac{\beta(t)}{t}}, \\
&= \frac{AB(\alpha)}{1-\alpha} \frac{t^{-\beta(t)}}{\beta'(t)\ln t + \frac{\beta(t)}{t}} \frac{d}{dt} \int_0^t \sum_{j=0}^{\infty} a_j (\tau-c)^j \sum_{k=0}^{\infty} \left(-\frac{\alpha}{1-\alpha}\right)^k \frac{(t-\tau)^{\alpha k}}{\Gamma(\alpha k+1)} d\tau, \\
&= \frac{AB(\alpha)}{1-\alpha} \frac{t^{-\beta(t)}}{\beta'(t)\ln t + \frac{\beta(t)}{t}} \frac{d}{dt} \sum_{j=0}^{\infty} a_j \sum_{k=0}^{\infty} \frac{\left(-\frac{\alpha}{1-\alpha}\right)^k}{\Gamma(\alpha k+1)} \int_0^t (\tau-c)^j (t-\tau)^{\alpha k} d\tau.
\end{aligned}$$

Thus, under the condition Re $(c) < 0$, then

$$ {}_0^{FFP}D_t^{\alpha,\beta(t)} f(t) = \frac{AB(\alpha)}{1-\alpha} \frac{t^{-\beta(t)}}{\beta'(t)\ln t + \frac{\beta(t)}{t}} \frac{d}{dt} \sum_{j=0}^{\infty} a_j \sum_{k=0}^{\infty} \frac{\left(-\frac{\alpha}{1-\alpha}\right)^k}{\Gamma(\alpha k+1)} \frac{(-c)^j t^{1+\alpha k}}{1+\alpha k}. \tag{43} $$

Finally for the case of exponential kernel, we have

$$ \begin{aligned} {}_0^{FFE}D_t^{\alpha,\beta(t)} f(t) &= \frac{M(\alpha)}{1-\alpha} \frac{d}{dt^{\beta(t)}} \int_0^t f(\tau) \exp\left[-\frac{\alpha}{1-\alpha}(t-\tau)\right] d\tau, \\ &= \frac{M(\alpha)}{1-\alpha} \frac{d}{dt} \int_0^t f(\tau) \exp\left[-\frac{\alpha}{1-\alpha}(t-\tau)\right] d\tau \frac{t^{-\beta(t)}}{\beta'(t)\ln t + \frac{\beta(t)}{t}}, \\ &= \frac{M(\alpha)}{1-\alpha} \frac{d}{dt} \int_0^t \sum_{j=0}^{\infty} a_j (\tau-c)^j \sum_{k=0}^{\infty} \left(-\frac{\alpha}{1-\alpha}\right)^k \frac{1}{k!} (t-\tau)^k d\tau \\ &\quad \frac{t^{-\beta(t)}}{\beta'(t)\ln t + \frac{\beta(t)}{t}}, \\ &= \frac{M(\alpha)}{1-\alpha} \frac{t^{-\beta(t)}}{\beta'(t)\ln t + \frac{\beta(t)}{t}} \frac{d}{dt} \sum_{j=0}^{\infty} a_j \sum_{k=0}^{\infty} \left(-\frac{\alpha}{1-\alpha}\right)^k \frac{1}{k!} \\ &\quad \int_0^t (\tau-c)^j (t-\tau)^k d\tau. \end{aligned} \tag{44} $$

Also when Re $(c) < 0$, then

$$ \begin{aligned} {}_0^{FFE}D_t^{\alpha,\beta(t)} f(t) &= \frac{M(\alpha)}{1-\alpha} \frac{t^{-\beta(t)}}{\beta'(t)\ln t + \frac{\beta(t)}{t}} \frac{d}{dt} \sum_{j=0}^{\infty} a_j \sum_{k=0}^{\infty} \frac{\left(-\frac{\alpha}{1-\alpha}\right)^k}{k!} \frac{(-c)^j t^{1+k}}{1+k} \\ &\quad \text{Hypergeometric } 2F_1\left[1, -j, 2+k, \frac{t}{2}\right]. \end{aligned} \tag{45} $$

On the other hand, if we consider the invariant to be inside the integral, we start with the case of power law

$$ \begin{aligned} {}_0^{FFP}D_t^{\alpha,\beta(t)} f(t) &= \frac{1}{\Gamma(1-\alpha)} \int_0^t \frac{d}{d\tau^{\beta(\tau)}} f(\tau)(t-\tau)^{\alpha} d\tau, \\ &= \frac{1}{\Gamma(1-\alpha)} \int_0^t \frac{d}{d\tau} f(\tau)(t-\tau)^{\alpha} \frac{\tau^{-\beta(\tau)}}{\beta'(\tau)\ln\tau + \frac{\beta(\tau)}{\tau}} d\tau; \end{aligned} \tag{46} $$

if the function is differentiable, then we test the condition of existence of such differential operator.

Theorem 1 *Let f be differentiable such that $\beta(t)$ is differentiable and*

$$\sup_{\tau\in[0,t]}\left|\frac{\tau^{-\beta(\tau)}}{\beta'(\tau)\ln\tau+\frac{\beta(\tau)}{\tau}}\right|<M, \tag{47}$$

then

$$\left|{}_0^{FFE}D_t^{\alpha,\beta(t)}f(t)\right|<\frac{M(\alpha)}{\alpha}\left\|\frac{df}{dt}\right\|_\infty M. \tag{48}$$

Proof Let f be differentiable, then

$$\begin{aligned}
\left|{}_0^{FFE}D_t^{\alpha,\beta(t)}f(t)\right| &= \left|\frac{M(\alpha)}{1-\alpha}\int_0^t\frac{d}{d\tau^{\beta(\tau)}}f(\tau)\exp\left[-\frac{\alpha}{1-\alpha}(t-\tau)\right]d\tau\right|,\\
&= \left|\frac{M(\alpha)}{1-\alpha}\int_0^t\frac{d}{d\tau}f(\tau)\exp\left[-\frac{\alpha}{1-\alpha}(t-\tau)\right]\frac{\tau^{-\beta(\tau)}}{\beta'(\tau)\ln\tau+\frac{\beta(\tau)}{\tau}}d\tau\right|,\\
&\le \frac{M(\alpha)}{1-\alpha}\int_0^t\left|\frac{d}{d\tau}f(\tau)\right|\left|\frac{\tau^{-\beta(\tau)}}{\beta'(\tau)\ln\tau+\frac{\beta(\tau)}{\tau}}\right|\exp\left[-\frac{\alpha}{1-\alpha}(t-\tau)\right]d\tau,\\
&< \frac{M(\alpha)}{1-\alpha}\int_0^t\sup_{\tau\in[0,t]}\left|\frac{d}{d\tau}f(\tau)\right|\sup_{\tau\in[0,t]}\left|\frac{\tau^{-\beta(\tau)}}{\beta'(\tau)\ln\tau+\frac{\beta(\tau)}{\tau}}\right|\\
&\quad\exp\left[-\frac{\alpha}{1-\alpha}(t-\tau)\right]d\tau,\\
&< \frac{M(\alpha)}{1-\alpha}\left\|\frac{d}{d\tau}f\right\|_\infty M\int_0^t\exp\left[-\frac{\alpha}{1-\alpha}(t-\tau)\right]d\tau,\\
&< \frac{M(\alpha)}{1-\alpha}\left\|\frac{d}{d\tau}f\right\|_\infty M\frac{1-\alpha}{\alpha}\left[1-\exp\left[-\frac{\alpha}{1-\alpha}t\right]\right],\\
&< \frac{M(\alpha)}{\alpha}\left\|\frac{d}{d\tau}f\right\|_\infty M.
\end{aligned} \tag{49}$$

This completes the proof.

Theorem 2 *Let f and g be differentiable such that*

$$\left\|\frac{d}{dt}f-\frac{d}{dt}g\right\|_\infty<K\|f-g\|_\infty\ , \tag{50}$$

where K is the Lipschitz constant, then if in addition $\beta(t)$ is differentiable with

$$\sup_{\tau\in[0,t]}\left|\frac{\tau^{-\beta(\tau)}}{\beta'(\tau)\ln\tau+\frac{\beta(\tau)}{\tau}}\right|<M, \tag{51}$$

then

$$\left|{}_0^{FFE}D_t^{\alpha,\beta(t)} f(t) - {}_0^{FFE}D_t^{\alpha,\beta(t)} g(t)\right| = \frac{M(\alpha)}{1-\alpha}\left|\int_0^t \frac{d}{d\tau}\left[f(\tau)-g(\tau)\right] \exp\left[-\frac{\alpha}{1-\alpha}(t-\tau)\right]\frac{\tau^{-\beta(\tau)}}{\beta'(\tau)\ln\tau+\frac{\beta(\tau)}{\tau}}d\tau\right|. \quad (52)$$

Proof

$$ {}_0^{FFE}D_t^{\alpha,\beta(t)}(f(t).g(t)) = \frac{M(\alpha)}{1-\alpha}\int_0^t\left[\frac{d}{d\tau}f(\tau)\,g(\tau)+\frac{d}{d\tau}g(\tau)\,f(\tau)\right] \frac{\tau^{-\beta(\tau)}}{\beta'(\tau)\ln\tau+\frac{\beta(\tau)}{\tau}}\exp\left[-\frac{\alpha}{1-\alpha}(t-\tau)\right]d\tau, \quad (53)$$

$$\begin{aligned}
{}_0^{FFE}D_t^{\alpha,\beta(t)}(f(t).g(t)) &= \frac{M(\alpha)}{1-\alpha}\int_0^t \frac{d}{d\tau}f(\tau)\,g(\tau)\frac{\tau^{-\beta(\tau)}}{\beta'(\tau)\ln\tau+\frac{\beta(\tau)}{\tau}}\exp\left[-\frac{\alpha}{1-\alpha}(t-\tau)\right]d\tau \\
&\quad+\frac{M(\alpha)}{1-\alpha}\int_0^t \frac{d}{d\tau}g(\tau)\,f(\tau)\frac{\tau^{-\beta(\tau)}}{\beta'(\tau)\ln\tau+\frac{\beta(\tau)}{\tau}}\exp\left[-\frac{\alpha}{1-\alpha}(t-\tau)\right]d\tau, \\
&\le \frac{M(\alpha)}{1-\alpha}\int_0^t \frac{d}{d\tau}f(\tau)\,|g(\tau)|\frac{\tau^{-\beta(\tau)}}{\beta'(\tau)\ln\tau+\frac{\beta(\tau)}{\tau}}\exp\left[-\frac{\alpha}{1-\alpha}(t-\tau)\right]d\tau \\
&\quad+\frac{M(\alpha)}{1-\alpha}\int_0^t \frac{d}{d\tau}g(\tau)\,|f(\tau)|\frac{\tau^{-\beta(\tau)}}{\beta'(\tau)\ln\tau+\frac{\beta(\tau)}{\tau}}\exp\left[-\frac{\alpha}{1-\alpha}(t-\tau)\right]d\tau, \\
&< \frac{M(\alpha)}{1-\alpha}\int_0^t \frac{d}{d\tau}f(\tau)\sup_{\tau\in[0,t]}|g(\tau)|\frac{\tau^{-\beta(\tau)}}{\beta'(\tau)\ln\tau+\frac{\beta(\tau)}{\tau}}\exp\left[-\frac{\alpha}{1-\alpha}(t-\tau)\right]d\tau \\
&\quad+\frac{M(\alpha)}{1-\alpha}\int_0^t \frac{d}{d\tau}g(\tau)\sup_{\tau\in[0,t]}|f(\tau)|\frac{\tau^{-\beta(\tau)}}{\beta'(\tau)\ln\tau+\frac{\beta(\tau)}{\tau}}\exp\left[-\frac{\alpha}{1-\alpha}(t-\tau)\right]d\tau, \\
&< \|g\|_\infty\,{}_0^{FFE}D_t^{\alpha,\beta(t)}f(t)+\|f\|_\infty\,{}_0^{FFE}D_t^{\alpha,\beta(t)}g(t), \\
&< a_1\,{}_0^{FFE}D_t^{\alpha,\beta(t)}f(t)+a_2\,{}_0^{FFE}D_t^{\alpha,\beta(t)}g(t), \qquad (54)
\end{aligned}$$

$$\begin{aligned}
{}_0^{FFE}D_t^{\alpha,\beta(t)}(f(t).g(t)) &\le \frac{M(\alpha)}{1-\alpha}\int_0^t\left|\frac{d}{d\tau}f(\tau)\,g(\tau)\right|\left|\frac{\tau^{-\beta(\tau)}}{\beta'(\tau)\ln\tau+\frac{\beta(\tau)}{\tau}}\right| \\
&\quad\exp\left[-\frac{\alpha}{1-\alpha}(t-\tau)\right]d\tau, \\
&< \frac{M(\alpha)}{1-\alpha}\int_0^t \sup_{\tau\in[0,t]}\left|\frac{d}{d\tau}f(\tau)\,g(\tau)\right|\sup_{\tau\in[0,t]}\left|\frac{\tau^{-\beta(\tau)}}{\beta'(\tau)\ln\tau+\frac{\beta(\tau)}{\tau}}\right| \\
&\quad\exp\left[-\frac{\alpha}{1-\alpha}(t-\tau)\right]d\tau, \\
&< \frac{M(\alpha)}{1-\alpha}M\left\|\frac{d}{dt}f(t)-\frac{d}{dt}g(t)\right\|_\infty\frac{1-\alpha}{\alpha}\left[1-\exp\left[-\frac{\alpha}{1-\alpha}t\right]\right], \\
&< \frac{M(\alpha)}{1-\alpha}MK\|f-g\|_\infty\left(1-\exp\left[-\frac{\alpha}{1-\alpha}t\right]\right), \\
&< \frac{M(\alpha)}{1-\alpha}MK\|g-f\|_\infty, \\
&< L\|g-f\|_\infty. \qquad (55)
\end{aligned}$$

Under the same conditions, we verify that $\|g\|_\infty, \|f\|_\infty < a_1, a_2$

$$ {}_0^{FFE}D_t^{\alpha,\beta(t)}\left(f(t).g(t)\right) < a_1\, {}_0^{FFE}D_t^{\alpha,\beta(t)} f(t) + a_2\, {}_0^{FFE}D_t^{\alpha,\beta(t)} g(t). \tag{56} $$

Now

$$ \begin{aligned}
\left|{}_0^{FFP}D_t^{\alpha,\beta(t)} f(t)\right| &= \frac{1}{\Gamma(1-\alpha)}\left|\int_0^t \frac{d}{d\tau^{\beta(\tau)}} f(\tau)(t-\tau)^{-\alpha}\, d\tau\right|, \\
&= \frac{1}{\Gamma(1-\alpha)}\left|\int_0^t \frac{d}{d\tau} f(\tau)(t-\tau)^{-\alpha}\frac{\tau^{-\beta(\tau)}}{\beta'(\tau)\ln\tau + \frac{\beta(\tau)}{\tau}} d\tau\right|, \\
&\le \frac{1}{\Gamma(1-\alpha)}\int_0^t \left|\frac{d}{d\tau} f(\tau)\right|\left|\frac{\tau^{-\beta(\tau)}}{\beta'(\tau)\ln\tau + \frac{\beta(\tau)}{\tau}}\right|(t-\tau)^{-\alpha} d\tau, \\
&< \frac{1}{\Gamma(1-\alpha)}\int_0^t \sup_{\tau\in[0,t]}\left|\frac{d}{d\tau} f(\tau)\right| \sup_{\tau\in[0,t]}\left|\frac{\tau^{-\beta(\tau)}}{\beta'(\tau)\ln\tau + \frac{\beta(\tau)}{\tau}}\right| \\
&\quad (t-\tau)^{-\alpha} d\tau, \\
&< \left\|\frac{df}{dt}\right\|_\infty M\frac{1}{\Gamma(1-\alpha)}\int_0^t (t-\tau)^{-\alpha} d\tau, \\
&< \left\|\frac{df}{dt}\right\|_\infty M\frac{t^{1-\alpha}}{\Gamma(2-\alpha)}, \\
&< \left\|\frac{df}{dt}\right\|_\infty M\frac{T_0^{1-\alpha}}{\Gamma(2-\alpha)}.
\end{aligned} \tag{57} $$

Let f, g be two differentiable functions such that ${}_0^{FFP}D_t^{\alpha,\beta(t)} f(t)$ and ${}_0^{FFP}D_t^{\alpha,\beta(t)} g(t)$ exist. Then if in addition

$$ \left\|\frac{d}{dt} f - \frac{d}{dt} g\right\|_\infty < K\|f-g\|_\infty, \tag{58} $$

then

$$ \begin{aligned}
\left|{}_0^{FFP}D_t^{\alpha,\beta(t)} f(t) - {}_0^{FFP}D_t^{\alpha,\beta(t)} g(t)\right| &= \frac{1}{\Gamma(1-\alpha)}\left|\int_0^t \frac{d}{d\tau^{\beta(\tau)}}(f-g)(t-\tau)^{-\alpha} d\tau\right|, \\
&= \frac{1}{\Gamma(1-\alpha)}\left|\int_0^t \frac{d}{d\tau}(f-g)(t-\tau)^{-\alpha}\frac{\tau^{-\beta(\tau)}}{\beta'(\tau)\ln\tau + \frac{\beta(\tau)}{\tau}} d\tau\right|, \\
&\le \frac{1}{\Gamma(1-\alpha)}\int_0^t \left|\frac{d}{d\tau}(f-g)\right|\left|\frac{\tau^{-\beta(\tau)}}{\beta'(\tau)\ln\tau + \frac{\beta(\tau)}{\tau}}\right|(t-\tau)^{-\alpha} d\tau, \\
&< \frac{1}{\Gamma(1-\alpha)}\int_0^t \sup_{\tau\in[0,t]}\left|\frac{d}{d\tau}(f-g)\right| \sup_{\tau\in[0,t]}\left|\frac{\tau^{-\beta(\tau)}}{\beta'(\tau)\ln\tau + \frac{\beta(\tau)}{\tau}}\right| \\
&\quad (t-\tau)^{-\alpha} d\tau, \\
&< \frac{1}{\Gamma(1-\alpha)}\left\|\frac{d}{dt}(f-g)\right\|_\infty M\, t^{1-\alpha}.
\end{aligned} \tag{59} $$

Since $\left\| \frac{d}{dt}(f-g) \right\|_\infty < K \|f-g\|_\infty$, then

$$\left| {}_0^{FFP}D_t^{\alpha,\beta(t)} f(t) - {}_0^{FFP}D_t^{\alpha,\beta(t)} g(t) \right| < \frac{T_0^{1-\alpha}}{\Gamma(2-\alpha)} K \|f-g\|_\infty M, \\ < L \|f-g\|_\infty$$

where $L = \frac{T_0^{1-\alpha}}{\Gamma(2-\alpha)} KM$.

Theorem 3 *Also, if g and f are differentiable and bounded then*

$${}_0^{FFP}D_t^{\alpha,\beta(t)}(f(t).g(t)) < \|f\|_\infty \, {}_0^{FFP}D_t^{\alpha,\beta(t)} g(t) + \|g\|_\infty \, {}_0^{FFP}D_t^{\alpha,\beta(t)} f(t).$$

Proof

$$\begin{aligned}
{}_0^{FFP}D_t^{\alpha,\beta(t)}(f(t).g(t)) &= \frac{1}{\Gamma(1-\alpha)} \int_0^t \frac{d}{d\tau^{\beta(\tau)}} (f.g)(t-\tau)^{-\alpha} d\tau, \\
&= \frac{1}{\Gamma(1-\alpha)} \int_0^t \frac{d}{d\tau} (f.g)(t-\tau)^{-\alpha} \frac{\tau^{-\beta(\tau)}}{\beta'(\tau)\ln\tau + \frac{\beta(\tau)}{\tau}} d\tau, \\
&= \frac{1}{\Gamma(1-\alpha)} \int_0^t \left(\frac{df}{d\tau} g + \frac{dg}{d\tau} f \right) (t-\tau)^{-\alpha} \\
&\quad \frac{\tau^{-\beta(\tau)}}{\beta'(\tau)\ln\tau + \frac{\beta(\tau)}{\tau}} d\tau, \\
&\leq \frac{1}{\Gamma(1-\alpha)} \int_0^t \left(\frac{df}{d\tau} |g| + \frac{dg}{d\tau} |f| \right) (t-\tau)^{-\alpha} \\
&< \frac{1}{\Gamma(1-\alpha)} \int_0^t \left(\frac{df}{d\tau} \sup_{\tau\in[0,t]} |g| + \frac{dg}{d\tau} \sup_{\tau\in[0,t]} |f| \right) (t-\tau)^{-\alpha} \\
&\quad \frac{\tau^{-\beta(\tau)}}{\beta'(\tau)\ln\tau + \frac{\beta(\tau)}{\tau}} d\tau, \\
&< \|g\|_\infty \, {}_0^{FFP}D_t^{\alpha,\beta(t)} f(t) + \|f\|_\infty \, {}_0^{FFP}D_t^{\alpha,\beta(t)} g(t),
\end{aligned}$$

which completes the proof.

Theorem 4 *Additionally if*

$$\sup_{\tau\in[0,t]} \left| \frac{\tau^{-\beta(\tau)}}{\beta'(\tau)\ln\tau + \frac{\beta(\tau)}{\tau}} \right| < M, \tag{60}$$

in the above theorem, then

$${}_0^{FFP}D_t^{\alpha,\beta(t)}(f(t).g(t)) < M \|g\|_\infty \, {}_0^{C}D_t^{\alpha} f(t) + M \|f\|_\infty \, {}_0^{C}D_t^{\alpha} g(t). \tag{61}$$

Proof We use a similar problem as before, then

$$
\begin{aligned}
{}_{0}^{FFP}D_{t}^{\alpha,\beta(t)}\left(f\left(t\right).g\left(t\right)\right) &< \left\|g\right\|_{\infty}\,{}_{0}^{FFP}D_{t}^{\alpha,\beta(t)}f\left(t\right)+\left\|f\right\|_{\infty}\,{}_{0}^{FFP}D_{t}^{\alpha,\beta(t)}g\left(t\right),\\
&= \left\|f\right\|_{\infty}\frac{1}{\Gamma\left(1-\alpha\right)}\int_{0}^{t}\frac{dg}{d\tau}\left(t-\tau\right)^{-\alpha}\frac{\tau^{-\beta(\tau)}}{\beta'\left(\tau\right)\ln\tau+\frac{\beta(\tau)}{\tau}}d\tau\\
&\quad+\left\|g\right\|_{\infty}\frac{1}{\Gamma\left(1-\alpha\right)}\int_{0}^{t}\frac{df}{d\tau}\left(t-\tau\right)^{-\alpha}\frac{\tau^{-\beta(\tau)}}{\beta'\left(\tau\right)\ln\tau+\frac{\beta(\tau)}{\tau}}d\tau. \quad (62)
\end{aligned}
$$

Thus

$$
\begin{aligned}
{}_{0}^{FFP}D_{t}^{\alpha,\beta(t)}\left(f\left(t\right).g\left(t\right)\right) &< \left\|f\right\|_{\infty}\frac{1}{\Gamma\left(1-\alpha\right)}\int_{0}^{t}\frac{dg}{d\tau}\left(t-\tau\right)^{-\alpha}\sup_{\tau\in[0,t]}\frac{\tau^{-\beta(\tau)}}{\beta'\left(\tau\right)\ln\tau+\frac{\beta(\tau)}{\tau}}d\tau\\
&\quad+\left\|g\right\|_{\infty}\frac{1}{\Gamma\left(1-\alpha\right)}\int_{0}^{t}\frac{df}{d\tau}\left(t-\tau\right)^{-\alpha}\sup_{\tau\in[0,t]}\frac{\tau^{-\beta(\tau)}}{\beta'\left(\tau\right)\ln\tau+\frac{\beta(\tau)}{\tau}}d\tau,\\
&< \left\|f\right\|_{\infty}\,M\,{}_{0}^{C}D_{t}^{\alpha}\,g\left(t\right)+\left\|g\right\|_{\infty}\,M\,{}_{0}^{C}D_{t}^{\alpha}\,f\left(t\right), \quad (63)
\end{aligned}
$$

which completes the proof.

We now consider the case with the Mittag-Liffler function, if f' is bounded then

$$
\begin{aligned}
{}_{0}^{FFM}D_{t}^{\alpha,\beta(t)}f\left(t\right) &= \frac{AB\left(\alpha\right)}{1-\alpha}\left|\int_{0}^{t}\frac{df\left(\tau\right)}{d\tau}E_{\alpha}\left[-\frac{\alpha}{1-\alpha}\left(t-\tau\right)^{\alpha}\right]\frac{\tau^{-\beta(\tau)}}{\beta'\left(\tau\right)\ln\tau+\frac{\beta(\tau)}{\tau}}d\tau\right|,\\
&\leq \frac{AB\left(\alpha\right)}{1-\alpha}\int_{0}^{t}\left|\frac{df\left(\tau\right)}{d\tau}\right|E_{\alpha}\left[-\frac{\alpha}{1-\alpha}\left(t-\tau\right)^{\alpha}\right]\left|\frac{\tau^{-\beta(\tau)}}{\beta'\left(\tau\right)\ln\tau+\frac{\beta(\tau)}{\tau}}\right|d\tau,\\
&< \frac{AB\left(\alpha\right)}{1-\alpha}\int_{0}^{t}\sup_{\tau\in[0,t]}\left|\frac{df\left(\tau\right)}{d\tau}\right|E_{\alpha}\left[-\frac{\alpha}{1-\alpha}\left(t-\tau\right)^{\alpha}\right]\\
&\quad\sup_{\tau\in[0,t]}\left|\frac{\tau^{-\beta(\tau)}}{\beta'\left(\tau\right)\ln\tau+\frac{\beta(\tau)}{\tau}}\right|d\tau,\\
&< \frac{AB\left(\alpha\right)}{1-\alpha}\left\|\frac{df}{d\tau}\right\|_{\infty}M\int_{0}^{t}E_{\alpha}\left[-\frac{\alpha}{1-\alpha}\left(t-\tau\right)^{\alpha}\right]d\tau, \quad (64)
\end{aligned}
$$

$$
\begin{aligned}
{}_{0}^{FFM}D_{t}^{\alpha,\beta(t)}f\left(t\right) &< \frac{AB\left(\alpha\right)}{1-\alpha}\left\|\frac{df}{d\tau}\right\|_{\infty}M\int_{0}^{t}\sum_{j=0}^{\infty}\frac{\left(-\frac{\alpha}{1-\alpha}\right)^{j}\left(t-\tau\right)^{\alpha j}}{\Gamma\left(\alpha j+1\right)}d\tau,\\
&< \frac{AB\left(\alpha\right)}{1-\alpha}\left\|\frac{df}{d\tau}\right\|_{\infty}M\sum_{j=0}^{\infty}\frac{\left(-\frac{\alpha}{1-\alpha}\right)^{j}}{\Gamma\left(\alpha j+1\right)}\int_{0}^{t}\left(t-\tau\right)^{\alpha j}d\tau,\\
&< \frac{AB\left(\alpha\right)}{1-\alpha}\left\|\frac{df}{d\tau}\right\|_{\infty}M\sum_{j=0}^{\infty}\left(-\frac{\alpha}{1-\alpha}\right)^{j}\frac{t^{\alpha j+1}}{\Gamma\left(\alpha j+2\right)}.
\end{aligned}
$$

Thus

$$\left|{}_0^{FFM}D_t^{\alpha,\beta(t)} f\,(t)\right| < \frac{AB\,(\alpha)}{1-\alpha}\left\|\frac{df}{d\tau}\right\|_\infty M\ t\ E_\alpha\left[-\frac{\alpha}{1-\alpha}t^\alpha\right]. \tag{65}$$

Theorem 5 *Also, for all f differentiable then the following relation can be obtained:*

$${}_0^{FFM}D_t^{\alpha,\beta(t)} f\,(t) \le a_1\ {}_0^{ABC}D_t^\alpha\ f\,(t)\,. \tag{66}$$

Proof

$$\begin{aligned}
{}_0^{FFM}D_t^{\alpha,\beta(t)} f\,(t) &= \frac{AB\,(\alpha)}{1-\alpha}\int_0^t \frac{df\,(\tau)}{d\tau}E_\alpha\left[-\frac{\alpha}{1-\alpha}\,(t-\tau)^\alpha\right]\\
&\quad \frac{\tau^{-\beta(\tau)}}{\beta'\,(\tau)\ln\tau+\frac{\beta(\tau)}{\tau}}d\tau,\\
&\le \frac{AB\,(\alpha)}{1-\alpha}\int_0^t \frac{df\,(\tau)}{d\tau}E_\alpha\left[-\frac{\alpha}{1-\alpha}\,(t-\tau)^\alpha\right]\\
&\quad \sup_{\tau\in[0,t]}\left|\frac{\tau^{-\beta(\tau)}}{\beta'\,(\tau)\ln\tau+\frac{\beta(\tau)}{\tau}}\right|d\tau,\\
&\le \frac{AB\,(\alpha)}{1-\alpha}\int_0^t \frac{df\,(\tau)}{d\tau}E_\alpha\left[-\frac{\alpha}{1-\alpha}\,(t-\tau)^\alpha\right]d\tau\\
&\quad \sup_{\tau\in[0,t]}\left|\frac{\tau^{-\beta(\tau)}}{\beta'\,(\tau)\ln\tau+\frac{\beta(\tau)}{\tau}}\right|,
\end{aligned} \tag{67}$$

$${}_0^{FFM}D_t^{\alpha,\beta(t)} f\,(t) \le M\ {}_0^{ABC}D_t^\alpha\ f\,(t)\,. \tag{68}$$

We now consider the general Cauchy problem

$${}_0^{FFP}D_t^{\alpha,\beta(t)} y\,(t) = f\,(t, y\,(t))\,; \tag{69}$$

we know that

$$\begin{aligned}
\frac{1}{\Gamma\,(1-\alpha)}\frac{d}{dt^{\beta(t)}}\int_0^t y\,(\tau)\,(t-\tau)^\alpha\,d\tau &= f\,(t, y\,(t))\,,\\
\frac{1}{\Gamma\,(1-\alpha)}\frac{d}{dt}\int_0^t y\,(\tau)\,(t-\tau)^\alpha\,d\tau &= t^{\beta(t)}\left(\beta'\,(t)\ln t+\frac{\beta\,(t)}{t}\right)\\
&\quad f\,(t, y\,(t))\,.
\end{aligned} \tag{70}$$

The above can be converted to

$$y\,(t) = \frac{1}{\Gamma\,(\alpha)}\int_0^t \tau^{\beta(\tau)}\left(\beta'\,(\tau)\ln\tau+\frac{\beta\,(\tau)}{\tau}\right)f\,(\tau, y\,(\tau))\,(t-\tau)^{\alpha-1}\,d\tau. \tag{71}$$

Thus at $t_n = n\Delta t$, we have

$$y\left(t_n\right) = \Delta t^{\alpha}\left[\gamma_n F\left(t_0, y\left(t,1\right)\right) + \sum_{j=0}^{n} \Phi_{nj} F\left(t_j, y\left(t_j\right)\right)\right]. \tag{72}$$

Alternatively, the equation can be discretized as, at $t_{n+1} = (n+1)\,\Delta t$,

$$y\left(t_{n+1}\right) = \frac{1}{\Gamma\left(\alpha\right)} \int_0^{t_{n+1}} \left(t_{n+1} - \tau\right)^{\alpha-1} \tau^{\beta(\tau)} \left(\beta'\left(\tau\right) \ln \tau + \frac{\beta\left(\tau\right)}{\tau}\right) f\left(\tau, y\left(\tau\right)\right) d\tau. \tag{73}$$

Let $F\left(t, y\left(t\right)\right) = t^{\beta(t)} \left(\beta'\left(t\right) \ln t + \frac{\beta(t)}{t}\right) f\left(t, y\left(t\right)\right)$. Thus,

$$\begin{aligned} y\left(t_{n+1}\right) &= \frac{1}{\Gamma\left(\alpha\right)} \int_0^{t_{n+1}} \left(t_{n+1} - \tau\right)^{\alpha-1} F\left(\tau, y\left(\tau\right)\right) d\tau, \\ &= \frac{1}{\Gamma\left(\alpha\right)} \sum_{j=0}^{n} \int_{t_j}^{t_{j+1}} \left(t_{n+1} - \tau\right)^{\alpha-1} F\left(\tau, y\left(\tau\right)\right) d\tau. \end{aligned} \tag{74}$$

Thus, following the routine presented by Atangana and Toufik, we obtain

$$F\left(\tau, y\left(\tau\right)\right) = \frac{\tau - t_{j-1}}{\Delta t} F\left(t_j, y\left(t_j\right)\right) - \frac{\tau - t_j}{\Delta t} F\left(t_{j-1}, y\left(t_{j-1}\right)\right). \tag{75}$$

Finally

$$\begin{aligned} y\left(t_{n+1}\right) = \sum_{j=0}^{n} \Bigg[& \frac{\Delta t^{\alpha}}{\Gamma\left(\alpha+2\right)} F\left(t_j, y\left(t_j\right)\right) \left\{(n+1-j)^{\alpha}\left(n-j+i+\alpha\right) - (n-j)^{\alpha}\left(n-j+i+i\alpha\right)\right\} \\ & - \frac{\Delta t^{\alpha}}{\Gamma\left(\alpha+2\right)} F\left(t_{j-1}, y\left(t_{j-1}\right)\right) \left\{(n+1-j)^{\alpha+1} - (n-j)^{\alpha}\left(n-j+1+\alpha\right)\right\}\Bigg]. \end{aligned} \tag{76}$$

Replacing $F\left(t, y\left(t\right)\right) = t^{\beta(t)} \left(\beta'\left(t\right) \ln t + \frac{\beta(t)}{t}\right) f\left(t, y\left(t\right)\right)$, we get

$$\begin{aligned} y\left(t_{n+1}\right) = \sum_{j=0}^{n} \Bigg[& \frac{\Delta t^{\alpha}}{\Gamma\left(\alpha+2\right)} \left\{t_j^{\beta(t_j)} \left(\frac{\beta\left(t_{j+1}\right) - \beta\left(t_j\right)}{\Delta t} \ln t_j + \frac{\beta\left(t_j\right)}{t_j}\right) f\left(t_j, y\left(t_j\right)\right)\right\} \\ & \left\{(n+1-j)^{\alpha}\left(n-j+i+\alpha\right) - (n-j)^{\alpha}\left(n-j+i+i\alpha\right)\right\} \\ & - \frac{\Delta t^{\alpha}}{\Gamma\left(\alpha+2\right)} \left\{t_{j-1}^{\beta(t_{j-1})} \left(\frac{\beta\left(t_j\right) - \beta\left(t_{j-1}\right)}{\Delta t} \ln t_{j-1} + \frac{\beta\left(t_{j-1}\right)}{t_{j-1}}\right) f\left(t_{j-1}, y\left(t_{j-1}\right)\right)\right\} \\ & \left\{(n+1-j)^{\alpha+1} - (n-j)^{\alpha}\left(n-j+1+\alpha\right)\right\}\Bigg]. \end{aligned} \tag{77}$$

4 Numerical Schemes

In this section, we present a new procedure suggested by Atangana and Toufiq to capture chaos unit self-similarities or fractal features; this year, Atangana and Toufiq described a new complex set called trinition, a complex set of complex number with two imaginaries numbers.

$$z = a + ib + jc. \tag{78}$$

From the above, a new mapping was into similar to the Julia set and the Mandelbrot set. They considered the following iteration:

$$Z_{n+1} = z_n^2 + c, \tag{79}$$

then obtained

$$\begin{aligned} x_{n+1} &= x_n^2 - y_n^2 + z_n^2 + c_x, \\ y_{n+1} &= 2x_n y_n + c_y, \\ z_{n+1} &= 2x_n z_n + c_z. \end{aligned} \tag{80}$$

Then the next step was to use a chaotic attractor, for example, the Lorenz attractor. Then this discretized version of the chaotic model was compared with the fractal mapping. However in this section, we present first some fractal presentations in Figs. 1, 2, 3 and 4.

The next step is to consider a general system of equation depicting a chaotic model, for instance,

$$\begin{cases} {}_0^{DBC}D_t^{\alpha,\beta(t)} x(t) = f(x, y, z, t) \\ {}_0^{DBC}D_t^{\alpha,\beta(t)} y(t) = g(x, y, z, t) \\ {}_0^{DBC}D_t^{\alpha,\beta(t)} z(t) = h(x, y, z, t) \end{cases}. \tag{81}$$

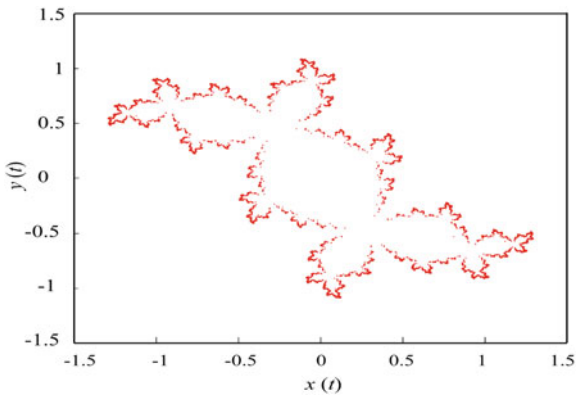

Fig. 1 Fractal within th trinition set

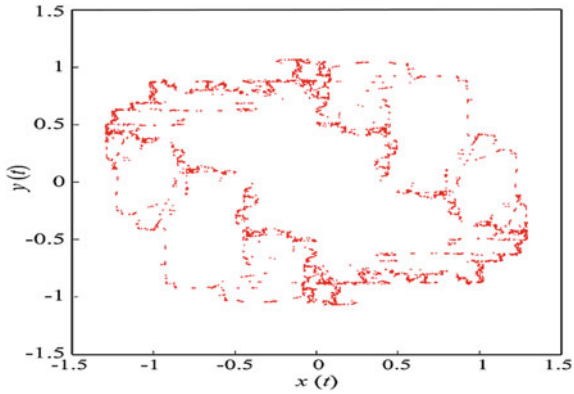

Fig. 2 Fractal within th trinition set

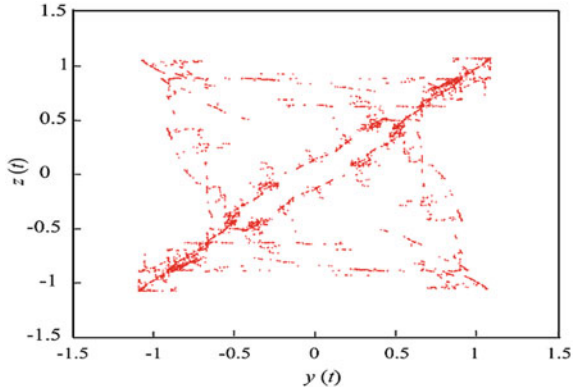

Fig. 3 Fractal within th trinition set

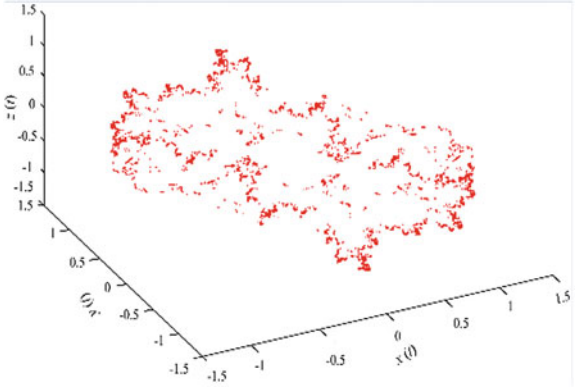

Fig. 4 Fractal within th trinition set

Using the fact that the integral is differentiable, the left-hand side of the above equations can be reformulated as

$$\frac{AB(\alpha)}{1-\alpha}\frac{d}{dt}\int_0^t x(\tau)\,E_\alpha\left[-\frac{\alpha}{1-\alpha}(t-\tau)^\alpha\right]d\tau\frac{t^{-\beta(t)}}{\beta'(t)\ln t+\frac{\beta(t)}{t}}=f(x,y,z,t), \tag{82}$$

$$\frac{AB(\alpha)}{1-\alpha}\frac{d}{dt}\int_0^t y(\tau)\,E_\alpha\left[-\frac{\alpha}{1-\alpha}(t-\tau)^\alpha\right]d\tau\frac{t^{-\beta(t)}}{\beta'(t)\ln t+\frac{\beta(t)}{t}}=g(x,y,z,t), \tag{83}$$

$$\frac{AB(\alpha)}{1-\alpha}\frac{d}{dt}\int_0^t z(\tau)\,E_\alpha\left[-\frac{\alpha}{1-\alpha}(t-\tau)^\alpha\right]d\tau\frac{t^{-\beta(t)}}{\beta'(t)\ln t+\frac{\beta(t)}{t}}=h(x,y,z,t). \tag{84}$$

Now choosing

$$F(x,y,z,t)=t^{\beta(t)}\left(\beta'(t)\ln t+\frac{\beta(t)}{t}\right)f(x,y,z,t), \tag{85}$$

$$G(x,y,z,t)=t^{\beta(t)}\left(\beta'(t)\ln t+\frac{\beta(t)}{t}\right)g(x,y,z,t), \tag{86}$$

$$H(x,y,z,t)=t^{\beta(t)}\left(\beta'(t)\ln t+\frac{\beta(t)}{t}\right)h(x,y,z,t); \tag{87}$$

after that, applying the AB integral on both sides we obtain

$$x(t)=\frac{1-\alpha}{AB(\alpha)}F(x,y,z,t)+\frac{\alpha}{\Gamma(\alpha)AB(\alpha)}\int_0^t(t-\tau)^{\alpha-1}F(x,y,z,t)\,d\tau, \tag{88}$$

$$y(t)=\frac{1-\alpha}{AB(\alpha)}G(x,y,z,t)+\frac{\alpha}{\Gamma(\alpha)AB(\alpha)}\int_0^t(t-\tau)^{\alpha-1}G(x,y,z,t)\,d\tau, \tag{89}$$

$$z(t)=\frac{1-\alpha}{AB(\alpha)}H(x,y,z,t)+\frac{\alpha}{\Gamma(\alpha)AB(\alpha)}\int_0^t(t-\tau)^{\alpha-1}H(x,y,z,t)\,d\tau. \tag{90}$$

Thus, following the routine suggested by Atangana and Toufic, we have at the point $t=t_{n+1}$

$$\begin{aligned}x(t_{n+1})=x^{n+1}=&\frac{1-\alpha}{AB(\alpha)}F\left(x^n,y^n,z^n,t_n\right)+\frac{\alpha}{\Gamma(\alpha+2)AB(\alpha)}(\Delta t)^\alpha\sum_{j=0}^{n}\Big[F\left(x^j,y^j,z^j,t_j\right)\\&\left\{(n-j+1)^\alpha(n-j+i+\alpha)-(n-j)^\alpha(n-j+2+2\alpha)\right\}\\&-F\left(x^{j-1},y^{j-1},z^{j-1},t_{j-1}\right)\left\{(n-j+1)^{\alpha+1}-(n-j)^\alpha(n-j+1+\alpha)\right\}\Big],\end{aligned} \tag{91}$$

$$y\left(t_{n+1}\right) = y^{n+1} = \frac{1-\alpha}{AB\left(\alpha\right)} G\left(x^n, y^n, z^n, t_n\right) + \frac{\alpha\left(\Delta t\right)^\alpha}{\Gamma\left(\alpha+2\right) AB\left(\alpha\right)} \sum_{j=0}^{n} \Big[G\left(x^j, y^j, z^j, t_j\right) \left\{ (n-j+1)^\alpha (n-j+i+\alpha) - (n-j)^\alpha (n-j+2+2\alpha) \right\} - G\left(x^{j-1}, y^{j-1}, z^{j-1}, t_{j-1}\right) \left\{ (n-j+1)^{\alpha+1} - (n-j)^\alpha (n-j+1+\alpha) \right\} \Big], \quad (92)$$

$$z\left(t_{n+1}\right) = z^{n+1} = \frac{1-\alpha}{AB\left(\alpha\right)} H\left(x^n, y^n, z^n, t_n\right) + \frac{\alpha\left(\Delta t\right)^\alpha}{\Gamma\left(\alpha+2\right) AB\left(\alpha\right)} \sum_{j=0}^{n} \Big[H\left(x^j, y^j, z^j, t_j\right) \left\{ (n-j+1)^\alpha (n-j+i+\alpha) - (n-j)^\alpha (n-j+2+2\alpha) \right\} - H\left(x^{j-1}, y^{j-1}, z^{j-1}, t_{j-1}\right) \left\{ (n-j+1)^{\alpha+1} - (n-j)^\alpha (n-j+1+\alpha) \right\} \Big]. \quad (93)$$

Now to combine the chaotic behavior with fractal map, the above recursive formulas are implemented up to the range N such that we have x^N, y^N, z^N. These points are now used to start the fractal mapping

$$\begin{aligned} x_{n+1} &= x_n^2 - y_n^2 + z_n^2 + c_x, \\ y_{n+1} &= 2x_n y_n + c_y, \\ z_{n+1} &= 2x_n z_n + c_z. \end{aligned} \quad (94)$$

We present an illustration in the following example where Atangana-Toufiq mapping combines with chaotic models (Figs. 5, 6, 7, 8, 9, 10, 11, 12, 13, 14, 15, 16, 17, 18, 19, 20, 21, 22, 23 and 24).

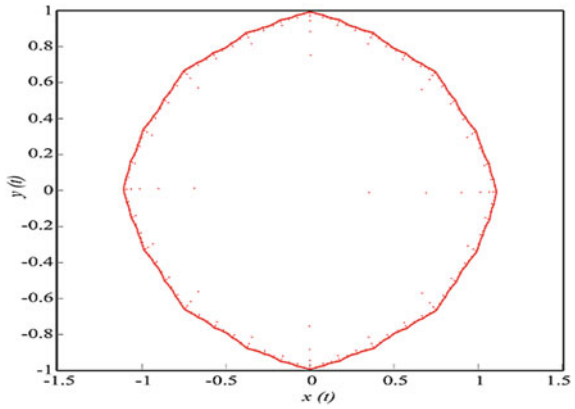

Fig. 5 Numerical simulation with combination of chaos and fractal in the trinition

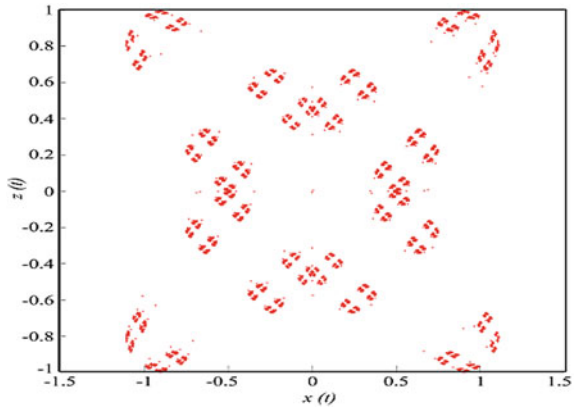

Fig. 6 Numerical simulation with combination of chaos and fractal in the trinition

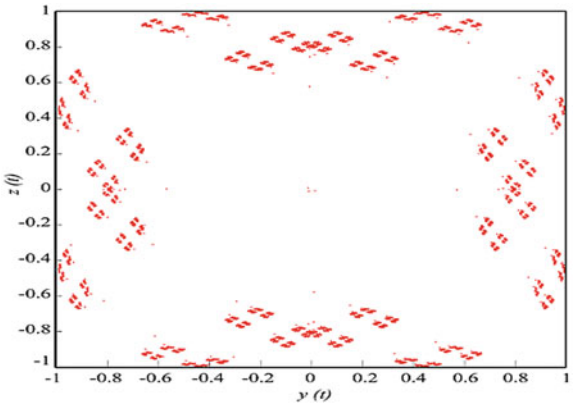

Fig. 7 Numerical simulation with combination of chaos and fractal in the trinition

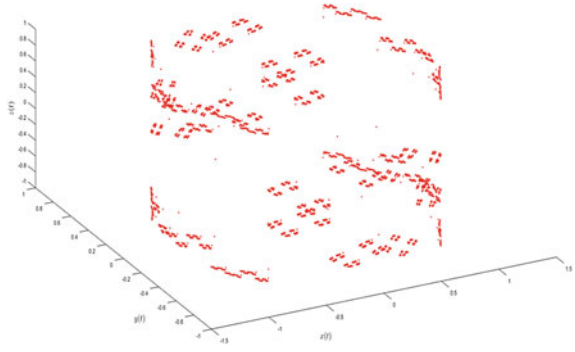

Fig. 8 Numerical simulation with combination of chaos and fractal in the trinition

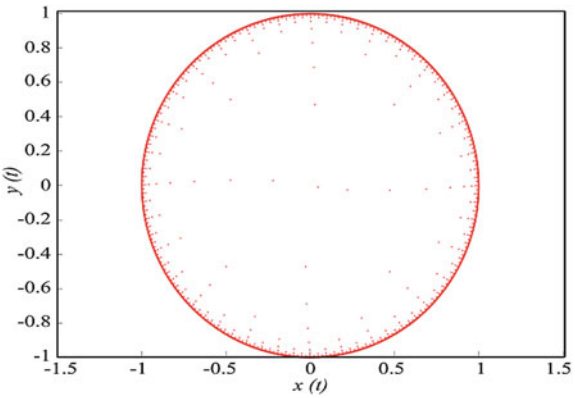

Fig. 9 Numerical simulation with combination of chaos and fractal in the trinition

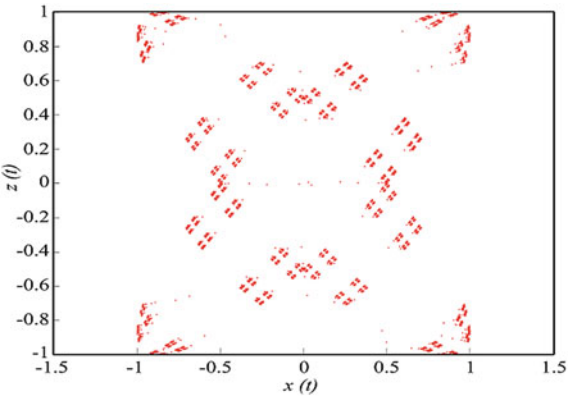

Fig. 10 Numerical simulation with combination of chaos and fractal in the trinition

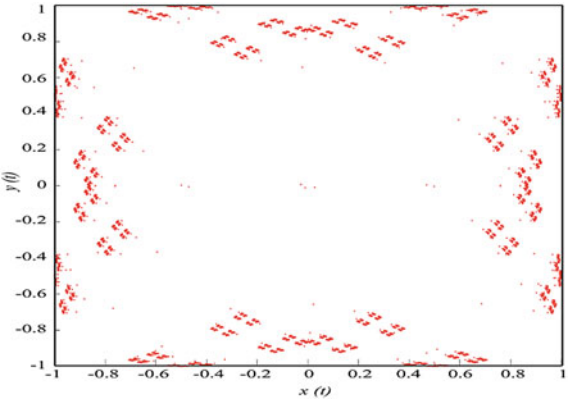

Fig. 11 Numerical simulation with combination of chaos and fractal in the trinition

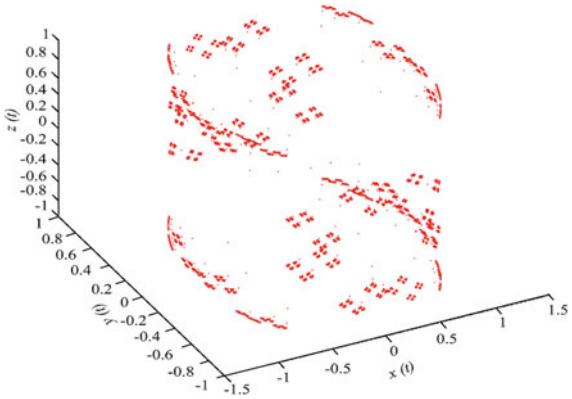

Fig. 12 Numerical simulation with combination of chaos and fractal in the trinition

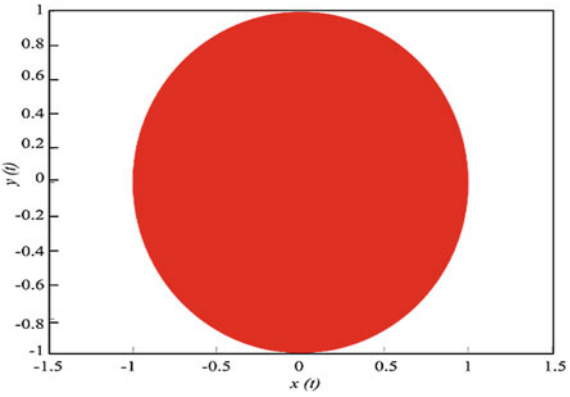

Fig. 13 Numerical simulation with combination of chaos and fractal in the trinition

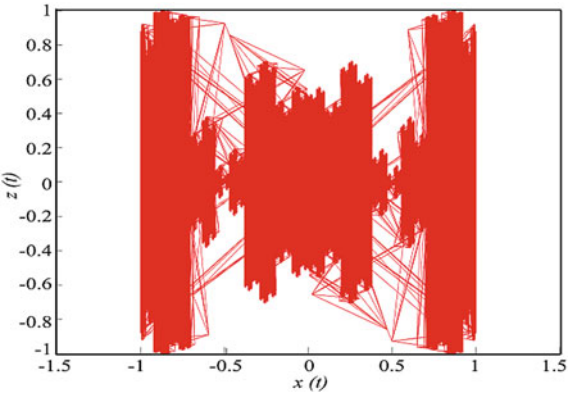

Fig. 14 Numerical simulation with combination of chaos and fractal in the trinition

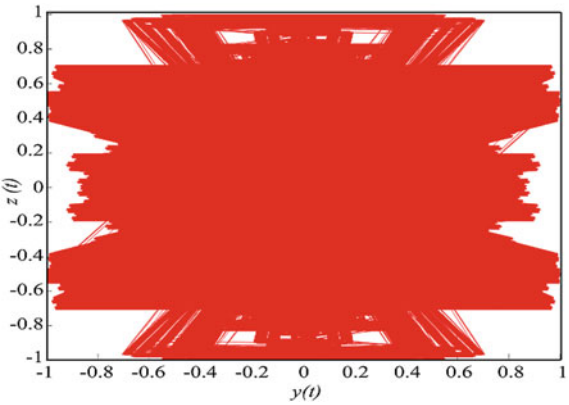

Fig. 15 Numerical simulation with combination of chaos and fractal in the trinition

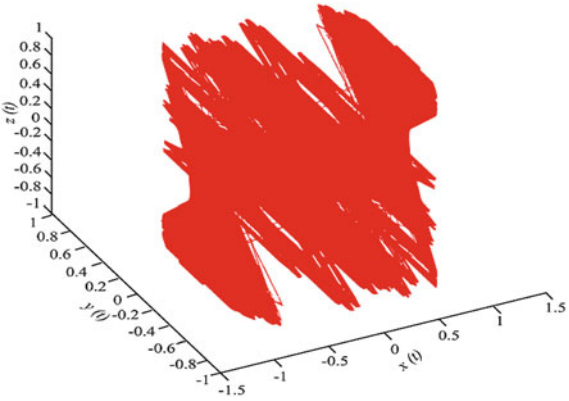

Fig. 16 Numerical simulation with combination of chaos and fractal in the trinition

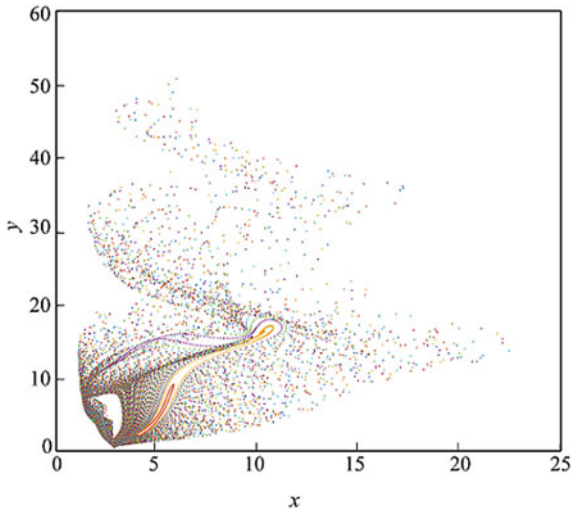

Fig. 17 Numerical simulation with combination of chaos and fractal in the trinition

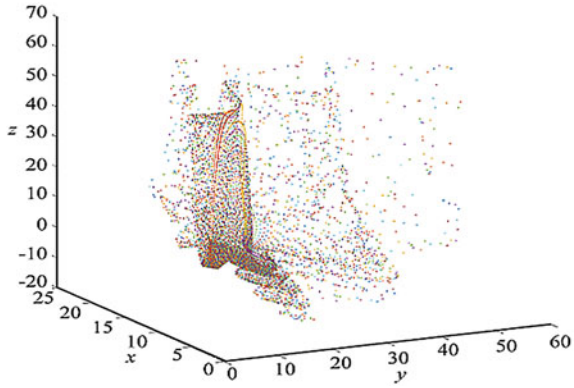

Fig. 18 Numerical simulation with combination of chaos and fractal in the trinition

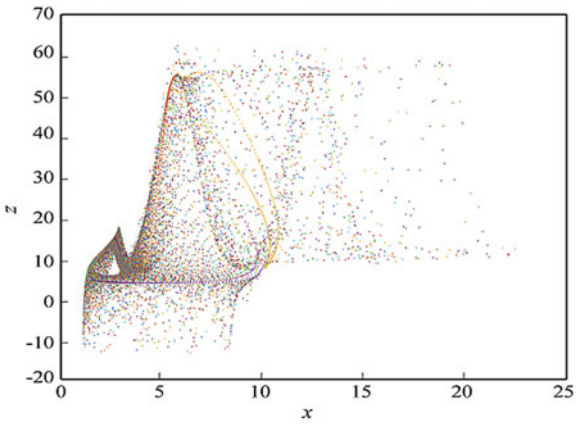

Fig. 19 Numerical simulation with combination of chaos and fractal in the trinition

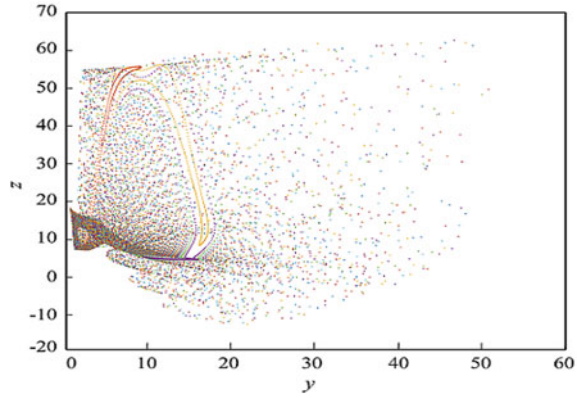

Fig. 20 Numerical simulation with combination of chaos and fractal in the trinition

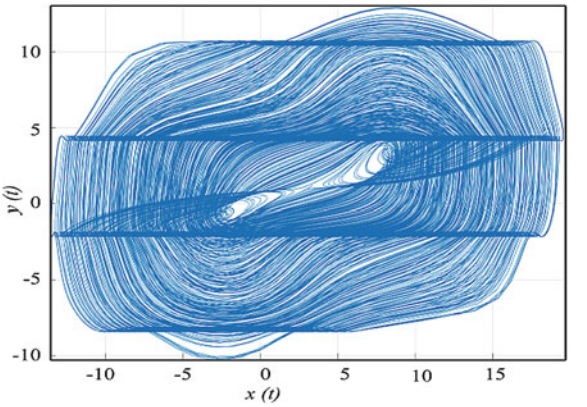

Fig. 21 Numerical simulation with combination of chaos and fractal in the trinition

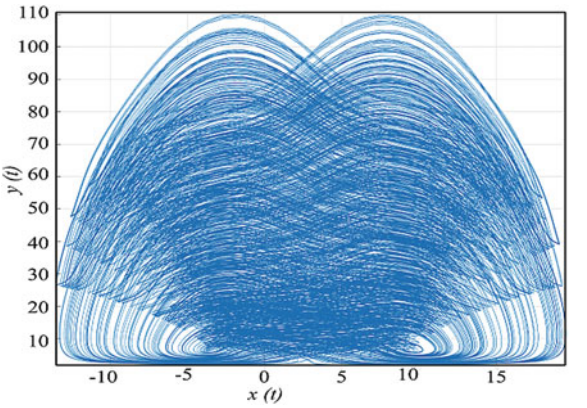

Fig. 22 Numerical simulation with combination of chaos and fractal in the trinition

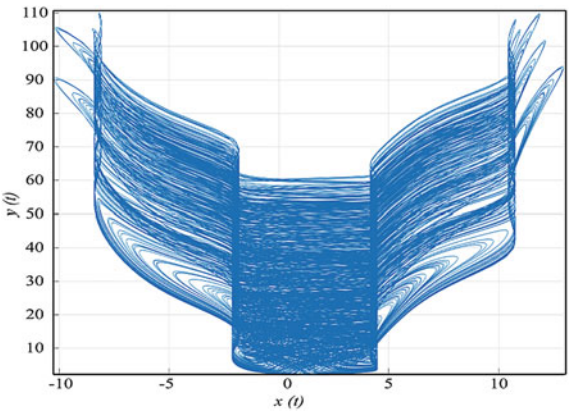

Fig. 23 Numerical simulation with combination of chaos and fractal in the trinition

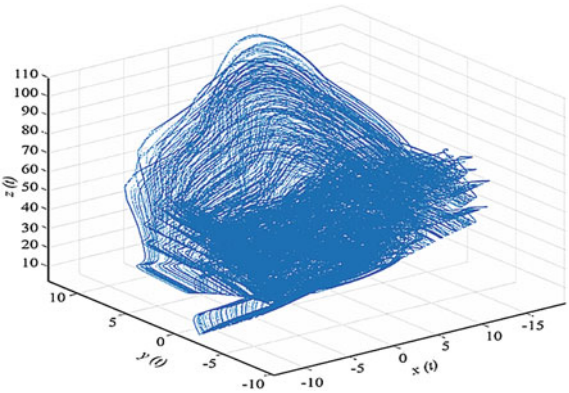

Fig. 24 Numerical simulation with combination of chaos and fractal in the trinition

5 Concluding Remarks

Fractal-Fractional differential operators with constant fractional order and variable fractal dimension have been introduced very recently and have been applied to a few problems. The theory around the new calculus has not been developed. However, they were found to be better candidates to model real- world problems ranging from anomalous diffusion to irregular spread of sickness. We have provided a comprehensive set of new theoretical results within the framework of this new calculus. We have suggested a numerical scheme that could be used to provide an approximate solution to ordinary, partial and integral equations associated with these operators. We hybridized the Julia set from the Trinition which also was introduced newly and some chaotic attractors to construct a new class of attractors. Some numerical simulations are presented.

Conflict of Interest: The authors have declared no conflict of interest.

References

1. Atangana A, Shafiq A (2019) Differential and integral operators with constant fractional order and variable fractional dimension. Chaos Solitons Fractals 127:226–243
2. Atangana A (2017) Fractal-fractional differentiation and integration: connecting fractal calculus and fractional calculus to predict complex system. Chaos Solitons Fractals 102:396–406
3. Araz SI (2020) Numerical analysis of a new volterra integro-differential equation involving fractal-fractional operators. Chaos Solitons Fractals 130:1093
4. Atangana A, Araz SI (2019) Analysis of a new partial integro-differential equation with mixed fractional operators. Chaos Solitons Fractals 127:257–271
5. Atangana A (July 2020) Modelling the spread of COVID-19 with new fractal-fractional operators: can the lockdown save mankind before vaccination? Chaos Solitons Fractals 136:109860
6. Samko SG (1995) Fractional integration and differentiation of variable order. Anal Math 21:213–236

7. Valério D, Sá da Costa J (2011) Variable-order fractional derivatives and their numerical approximations. Signal Process 91(3):470–483
8. Ross B, Samko SG (1995) Fractional integration operator of a variable order in the Holder spaces H_(x). Int J Math Math Sci 18:777–788

On the Parabolic Instability Region for Kuo Problem

S. Lavanya, V. Ganesh, and G. Venkata Ramana Reddy

Abstract We consider Kuo problem which deals with incompressible, inviscid, parallel zonal flows. For this Kuo problem, we derived a parabolic instability region without any restriction which intersects with Howard semi-circle under some conditions. Furthermore, we derived a new upper bound for the growth rate of an unstable mode.

Keywords Zonal flows · Shear flows · Incompressible fluids

1 Introduction

The study of Kuo problem is an important part of geophysical fluid dynamics. Kuo problem governs stability of incompressible, inviscid parallel zonal flows on a β-plane. This problem is the standard homogeneous stability problem that takes into account the derivative of Coriolis force (β). When $\beta = 0$, Kuo problem reduce to standard Rayleigh problem. For this problem Kuo [1] derived extension of Rayleigh inflexion point theorem namely $\left(U'' - \beta\right)$ must vanishes somewhere in the flow domain. Pedlosky [2] generalized Howard's semi-circle which includes Cariolis force. Padmini and Subbiah [3] derived two parabolic instability regions which depends on restrictions. Thenmozhy and Vijayan [4] extended their work and derived the parabolic instability region which depends on a minimum velocity greater than zero. Rana et al. [5] derived an estimate for growth rate. Kanwar and Sinha [6] derived

S. Lavanya (✉) · G. Venkata Ramana Reddy
Department of Mathematics, Koneru Lakshmaiah Education Foundation, Vaddeswaram 522502, India
e-mail: lavanya.sharmas@gmail.com

G. Venkata Ramana Reddy
e-mail: gvrr1976@kluniversity.in

V. Ganesh
Department of Engineering, University of Technology and Applied Sciences, Muscat, Sultanate of Oman

J. Singh et al. (eds.), *Advances in Mathematical Modelling, Applied Analysis and Computation*, Lecture Notes in Networks and Systems 415,
https://doi.org/10.1007/978-981-19-0179-9_18

a upper bound on the growth rate for baroclinic zonal flows. Shandil [7] obtained a sufficient condition for stability. Hickernell [8] derived growth rate of an unstable mode.
In this paper, we derived a parabolic instability region which does not depend on any condition like [3, 4]. Also, we derived the growth rate of an unstable mode.

2 Kuo Problem

Kuo eigen value problem is a second order differential equation given by [cf. [1]]

$$\phi'' - \left[\frac{U'' - \beta}{U - c} + k^2\right]\phi = 0, \tag{1}$$

with boundary conditions

$$\phi(z_1) = 0 = \phi(z_2), \tag{2}$$

where ϕ is the complex eigen function, U(z) is the basic velocity profile, k > 0 is the wave number and $c = c_r + ic_i$ is the complex phase velocity, β is the derivative of Cariolis force in the latitudinal direction.
Introducing the transformation $\phi = (U - c)^{\frac{1}{2}}\varphi$, in (1) and (2), we have

$$\left[(U - c)\varphi'\right]' - k^2(U - c)\varphi - \left(\frac{U''}{2} - \beta\right)\varphi - \frac{\frac{(U')^2}{4}}{(U - c)}\varphi = 0, \tag{3}$$

with boundary conditions

$$\varphi(z_1) = 0 = \varphi(z_2). \tag{4}$$

3 Parabolic Instability Region

Theorem 3.1 *If $c_i > 0$ then the following relations are true*

$$\int_{z_1}^{z_2}(U - c_r)\left[\left|\varphi'\right|^2 + k^2|\varphi|^2\right]dz + \int_{z_1}^{z_2}\left(\frac{U''}{2} - \beta\right)|\varphi|^2\,dz + \int_{z_1}^{z_2}\frac{\frac{(U')^2}{4}(U - c_r)}{|U - c|^2}|\varphi|^2\,dz = 0;$$

and

$$-\int_{z_1}^{z_2}\left[\left|\varphi'\right|^2+k^2\left|\varphi\right|^2\right]dz+\int_{z_1}^{z_2}\frac{\frac{\left(U'\right)^2}{4}}{\left|U-c\right|^2}\left|\varphi\right|^2dz=0.$$

Proof Multiplying (3) by complex conjugate of φ (i.e.) φ^*, integrating and applying (4),
we get

$$\int_{z_1}^{z_2}(U-c)\left[\left|\varphi'\right|^2+k^2\left|\varphi\right|^2\right]dz+\int_{z_1}^{z_2}\left(\frac{U''}{2}-\beta\right)\left|\varphi\right|^2dz$$
$$+\int_{z_1}^{z_2}\frac{\frac{\left(U'\right)^2}{4}}{(U-c)}\left|\varphi\right|^2dz=0.$$

Equating real part, we get

$$\int_{z_1}^{z_2}(U-c_r)\left[\left|\varphi'\right|^2+k^2\left|\varphi\right|^2\right]dz+\int_{z_1}^{z_2}\left(\tfrac{U''}{2}-\beta\right)\left|\varphi\right|^2dz$$
$$+\int_{z_1}^{z_2}\frac{\frac{\left(U'\right)^2}{4}(U-c_r)}{|U-c|^2}\left|\varphi\right|^2dz=0. \tag{5}$$

Equating imaginary part ($c_i>0$), we get

$$-\int_{z_1}^{z_2}\left[\left|\varphi'\right|^2+k^2\left|\varphi\right|^2\right]dz+\int_{z_1}^{z_2}\frac{\frac{\left(U'\right)^2}{4}}{\left|U-c\right|^2}\left|\varphi\right|^2dz=0. \tag{6}$$

This completes the proof of the theorem.

Theorem 3.2 *If (c,φ) is a solution of (3) and (4) then ${c_i}^2\leq\lambda\left[c_r-\frac{U_{\min}}{4}+\frac{U_{\max}}{4}\right]$, where*

$$\lambda=\frac{\left[\frac{\left(U'\right)^2}{2}\right]_{\max}}{\left|\left(\frac{3U_{\min}+U_{\max}}{2}\right)\left[\frac{\pi^2}{(z_2-z_1)^2}+k^2\right]+\left(\frac{U''}{2}-\beta\right)_{\min}\right|}.$$

Proof Multiplying (6) by (c_r+U_s) and subtracting from (5), we get

$$\int_{z_1}^{z_2}(U+U_s)\left[\left|\varphi'\right|^2+k^2\left|\varphi\right|^2\right]dz+\int_{z_1}^{z_2}\left(\frac{U''}{2}-\beta\right)\left|\varphi\right|^2dz+\int_{z_1}^{z_2}\frac{\frac{\left(U'\right)^2}{4}(U-2c_r-U_s)}{|U-c|^2}\left|\varphi\right|^2dz=0.$$

Using Rayleigh-Ritz inequality, we have

$$\int_{z_1}^{z_2}\frac{\left[(U+U_s)\left[\frac{\pi^2}{(z_2-z_1)^2}+k^2\right]+\left(\frac{U''}{2}-\beta\right)\right]|U-c|^2+\frac{\left(U'\right)^2}{4}\left[U-2c_r-U_s\right]}{|U-c|^2}\left|\varphi\right|^2dz\leq 0.$$

Since $|U-c|^2 \geq {c_i}^2$, we have

$$\int_{z_1}^{z_2} \frac{\left[(U+U_s)\left[\frac{\pi^2}{(z_2-z_1)^2}+k^2\right]+\left(\frac{U''}{2}-\beta\right)\right]c_i^2+\frac{(U')^2}{4}[U-2c_r-U_s]}{|U-c|^2}|\varphi|^2\,dz \leq 0.$$

Arbitrary number U_s is given by $U_s = \frac{U_{\min}+U_{\max}}{2}$, then we have

$${c_i}^2 \leq \left[\frac{\frac{(U')^2}{4}}{\left|(U+U_s)\left[\frac{\pi^2}{(z_2-z_1)^2}+k^2\right]+\left(\frac{U''}{2}-\beta\right)\right|}\right]_{\max}\left[2c_r-\frac{U_{\min}}{2}+\frac{U_{\max}}{2}\right];$$

i.e.,

$${c_i}^2 \leq \lambda\left[c_r-\frac{U_{\min}}{4}+\frac{U_{\max}}{4}\right], \tag{7}$$

$$where\ \lambda = \frac{\left[\frac{(U')^2}{2}\right]_{\max}}{\left|\left(\frac{3U_{\min}+U_{\max}}{2}\right)\left[\frac{\pi^2}{(z_2-z_1)^2}+k^2\right]+\left(\frac{U''}{2}-\beta\right)_{\min}\right|}.$$

This completes the proof of the theorem.

Note:

Our result is valid for $\left(U''-\beta\right)_{\min}=0$. Our instability region is valid for basic velocity changes its sign also. When $\beta=0$, this reduces a new parabolic instability region for standard Rayleigh problem (Figs. 1 and 2).

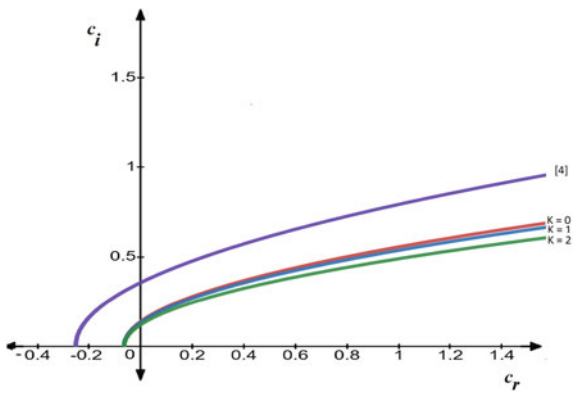

Fig. 1 c_r versus c_i (Parabolic instability region)

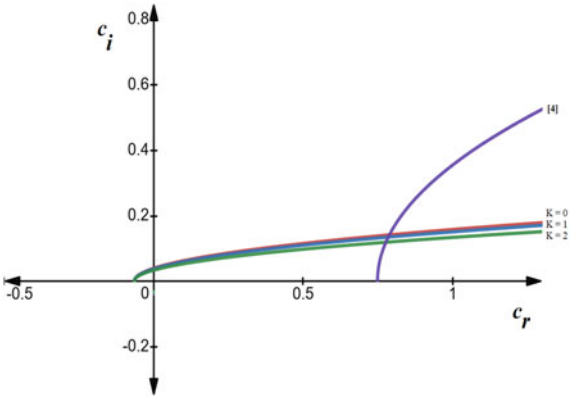

Fig. 2 c_r versus c_i (Parabolic instability region)

Below example will illustrate the reduction of parabolic instability region.

1. If $U = \left(z - \frac{1}{2}\right)^2, 0 \le z \le 1, \beta =$ constant
2. If $U = 1 + \left(z - \frac{1}{2}\right)^2, 0 \le z \le 1, \beta =$ constant

From the above two examples, it shows that as the wave number increases, the instability region is reduced.

Theorem 3.3 *If* $\lambda < \lambda_c$, *where* $\lambda_c = \frac{(U_{\min}+3U_{\max})-\sqrt{14U_{\min}U_{\max}+5{U_{\max}}^2-3{U_{\min}}^2}}{2}$ *then the parabola* $c_i^2 \le \lambda\left[c_r - \frac{U_{\min}}{4} + \frac{U_{\max}}{4}\right]$ *intersect Howard Semi Circle [cf. [9]]*

Proof Howard Semi circle [cf. [9]] is given by

$$\left[c_r - \frac{U_{\min} + U_{\max}}{2}\right]^2 + {c_i}^2 \le \left[\frac{U_{\max} - U_{\min}}{2}\right]^2. \tag{8}$$

Substituting (7) in (8), we get

$${c_r}^2 + (\lambda - U_{\min} - U_{\max})\, c_r + \left(U_{\min}U_{\max} - \frac{\lambda U_{\min}}{4} + \frac{\lambda U_{\max}}{4}\right) \le 0.$$

The discriminant part of the above equation is given by

$$\lambda^2 + (-U_{\min} - 3U_{\max})\,\lambda + (U_{\max} - U_{\min})^2 \ge 0.$$

Solving for λ, we get

$$\lambda = \frac{(U_{\min} + 3U_{\max}) \pm \sqrt{14U_{\min}U_{\max} + 5{U_{\max}}^2 - 3{U_{\min}}^2}}{2}.$$

In the above equation, the value with positive sign leads to $c_r < 0$ and hence.

If $\lambda < \lambda_c$, where $\lambda_c = \frac{(U_{\min}+3U_{\max})-\sqrt{14U_{\min}U_{\max}+5{U_{\max}}^2-3{U_{\min}}^2}}{2}$ then the parabola given in (7) intersect Howard semi-circle given in (8).

4 Growth Rate

Theorem 4.1 *The upper bound for the growth rate is given by* $k^2{c_i}^2 \leq \frac{|U''-\beta|_{\max}|U_{\max}-U_{\min}|}{\left[\frac{\pi^2}{k^2(z_2-z_1)^2}+1\right]}$.

Proof Multiply (1) by ϕ^*, integrating over $[z_1, z_2]$ and applying (2), we get.

$$\int_{z_1}^{z_2} \left|\phi'\right|^2 dz + k^2 \int_{z_1}^{z_2} |\phi|^2 dz + \int_{z_1}^{z_2} \frac{U'' - \beta}{(U-c)} |\phi|^2 dz = 0.$$

Equating the real parts, we get

$$\int_{z_1}^{z_2} \left|\phi'\right|^2 dz + k^2 \int_{z_1}^{z_2} |\phi|^2 dz + \int_{z_1}^{z_2} \frac{\left(U'' - \beta\right)(U-c_r)}{|U-c|^2} |\phi|^2 dz = 0. \quad (9)$$

We know that $|U - c_r| \leq |U_{\max} - U_{\min}|$, and $\frac{1}{|U-c|^2} \leq \frac{1}{{c_i}^2}$, using Rayleigh-Ritz inequality, we have

$$\left[\frac{\pi^2}{(z_2-z_1)^2} + k^2\right] \int_{z_1}^{z_2} |\phi|^2 dz \leq \frac{\left|U'' - \beta\right|_{\max} |U_{\max} - U_{\min}|}{{c_i}^2} \int_{z_1}^{z_2} |\phi|^2 dz;$$

i.e.,

$$k^2{c_i}^2 \leq \frac{\left|U'' - \beta\right|_{\max} |U_{\max} - U_{\min}|}{\left[\frac{\pi^2}{k^2(z_2-z_1)^2} + 1\right]}.$$

This implies that $c_i \to 0 as k \to \infty$.

5 Concluding Remarks

In this paper, we derived a new parabolic instability region for the Kuo problem which deals with inviscid, incompressible, zonal shear flows on a β-plane. Our parabolic instability region does not depend on any conditions as derived in [3] and [4]. This parabolic instability region intersects with standard Howard's semi-circle for a class of flows under condition. This is illustrated with an example. Also, we derived an upper bound for the growth rate of an unstable mode.

References

1. Kuo HL (1949) Dynamic instability of two-dimensional non-divergent flow in a barotropic atmosphere. J Meteoral 6:105–122
2. Pedlosky J (1979) Geophysical fluid dynamics. Springer, New York/Berlin
3. Padmini M, Subbiah M (1993) Note on Kuo's problem. J Math Anal Appl 173:659–665
4. Thenmozhy R, Vijayan N (2020) On the linear stability of shear flows in the β-plane. Int J Math Trends Technol 66:10–16
5. Rana SK, Goel R, Agarwal SC (2009) On the shear flow instability in the β-plane. J Int Acad Phys Sci 13:63–72
6. Kanwar V, Sinha AK (1999) A new upper bound on the growth rate of linear instability of baroclinic zonal flows in the two-layer model on a β-plane. Phys Fluids 11:2925–2927 (1999)
7. Shandil RG (2000) Linear instability of inviscid incompressible zonal flows on a β-plane. Ganita 51:165–168
8. Hickernell FJ (1985) An upper bound on the growth rate of a linear instability in a homogeneous shear flow. Stud App Math 72:87–93
9. Howard LN (1961) Note on a paper of John. W. Miles. J Fluid Mech 10:509

Font Design Through RQT Bézier Curve Using Shape Parameters

Mridula Dube and Nishi Gupta

Abstract To effectively draw the free form curves, we studied RQT (rational quintic trigonometric) Bézier curve using two shape parameters. These new curves are more adjustable because of the existence of shape parameters and geometric characteristics. To confirm whether the proposed curve fulfilled the convex hull property or not, we used limitations on shape and weight, and declared end-pointed curvatures. Local adjustments to the curve shape can be made by modifying its weights and shape parameter values. This curve is utilized for smooth curve compositions by generating piecewise rational trigonometric curves that are adjacent to parametric and geometric Hermite continuity criteria. Then, as an example in font design, piecewise curves are utilized to draw the structure of Devanagari alphabets.

Keywords Devanagari alphabets · Parametric and geometric continuity · RQT-Bézier curve · Shape parameters

1 Introduction

Designers, as well as engineers, are always fascinated by curves and surfaces. Their requirements include some superior designing strategies to define the shapes and contours of their designs and products. To fulfill their requirements, computer-aided geometric design (CAGD) methodologies were developed. In this regard, the book [4] has applications relating to the building and manipulation of CAGD free form curves and surfaces.

The two important design approaches which were first discovered in the 1950s are B-spline and Bézier curves. The Bernstein basis, which is part of curves and surfaces, drives Bézier curves and surfaces. A groundbreaking notion of curves and

M. Dube (✉) · N. Gupta
Department of Mathematics and Computer Science, R. D. University, Jabalpur, MP, India
e-mail: mdube1963@gmail.com

N. Gupta
e-mail: mah.nishi@gmail.com

J. Singh et al. (eds.), *Advances in Mathematical Modelling, Applied Analysis and Computation*, Lecture Notes in Networks and Systems 415,
https://doi.org/10.1007/978-981-19-0179-9_19

surfaces for the interactive design was proposed by a French designer, P. E. Bézier for Renault in the automobile industry. He proposed that these curves are very Intuitive, and the author [14] accomplished this by including some control points along with Bernstein's basis in his design. In his interactive design mechanism, the theory of control points and their location is the most crucial. Since then, they have been used to construct interactive curves and surfaces [12]. Polynomial parametric curves, such as B-splines and Bézier curves are both unable to represent some curves like circles and ellipses. To handle this condition, the generalization problem of B-spline curves was created, which are non-uniform rational B-spline (NURBS) curves. These curves provide more flexibility and precision when dealing with both analytic and free form shapes, but some of the problems remain the same, such as computing and regulating the weights for the curve [11, 13]. Then, instead of using B-splines, in many aspects, trigonometric splines were utilized to construct spline curves and surfaces that are much superior to B-splines. As a result, various innovative methods based on trigonometric polynomials and trigonometric and algebraic polynomials have been proposed [8, 18]. Without using rational forms, trigonometric polynomials have the advantage to represent basic trigonometric and transcendental curves.

The concept of trigonometric spline interpolation was first introduced in [6]. After that, the most difficult aspect of constructing a curve is determining how to regulate the curve's shape locally. In [1–3], the author proposes a solution based on different splines with shape parameters, allowing the user to customize the curve's shape. Since they do not require complex computations, cubic polynomials are more adjustable to construct the curve than lower degree polynomials.

In various industries, CAD/CAM programs and other graphic tools are using cubic Bézier curves to generate curves. The Bézier curve has attracted the attention of numerous designers due to its simplicity in rational and integral form. Trigonometric Bézier curves have been examined by several writers; see [5, 9, 10]. However, utilizing only one Bézier curve to define complex forms increases the degree of the curve, resulting in more intricate mathematical computations and longer processing times. To overcome this limitation of a single Bézier curve, designers link numerous curves of lesser degrees together utilizing smoothness qualities and varied continuity criteria at adjoining locations in such a way that the desired curve is a perfect match. Quartic splines with C^2 continuity for non-uniform knot vectors that are C^2 and G^3 continuous under particular cases have been proved in [17]. In this paper, the shape parameter for G^1 continuous quadratic trigonometric Bézier curve has been investigated [16]. In this study, we looked at the rational cubic trigonometric Bézier curve with two shape parameters [15]. The rational form has the benefit of being able to depict a large variety of curves and surfaces. Circles, ellipses, parabolas, and hyperbolas are examples of curves, while spheres, ellipsoids, cylinders, cones, paraboloids, hyperboloids, and hyperbolic paraboloids are examples of surfaces [4]. The sole distinction between Rational Bézier curves and their non-rational counterparts is that the coordinates that specify the curve are one dimension higher. Because of its concise and geometrical presentation, the rational form of Bézier curves is extensively employed in the CAD/CAGD field. This is referred to as a NURBS special

case. In the CAD/CAM industry, rational curves are commonly used to represent conic sections as well as circular arcs.

A newly designed RQT Bézier curve with shape parameters that achieve C^1, C^2, and G^1, G^2 continuity is provided in this study. To follow the convex hull property, the endpoint curvatures of the curve have been utilized for finding the conditions on the weight and shape parameters. The suggested curve is utilized to generate the Devanagari alphabets and obtain the geometrical attributes of the standard quintic Bézier curve. By modifying values of shape, weight, and curvature at the endpoints, the curve shape can be changed locally. In Sect. 2 of this study, Quintic trigonometric blending functions with two shape parameters are proposed. The creation of a rational quintic trigonometric (RQT) Bézier curve specified by blending functions and its geometric features is covered in Sect. 2.2. In Sect. 2.3, we'll go through the geometric significance of shape characteristics. An endpoint curvature condition in Sect. 2.4 is used to find the geometry of the curve. Piecewise rational TB (trigonometric Bézier) curves with different continuity conditions are studied in Sect. 3 and their use in the creation of font designing for Devanagari alphabets is described in Sect. 3.4. Section 4 has the conclusion.

2 Methodology

2.1 Quintic Trigonometric Blending Functions

Definition 1 QT Bézier basis functions with shape parameters λ_1 *and* λ_2, where $t \in \left[0, \pi/2\right]$ and $\lambda_1, \lambda_2 \in [-1, 1]$ defined as follows:

$$\begin{aligned} g_0(t) &= (1 - \lambda_1 \sin t)^2 (1 - \sin t)^3 \\ g_1(t) &= \cos^2 t - (1 - \lambda_1 \sin t)^2 (1 - \sin t)^3 \\ g_2(t) &= \sin^2 t - (1 - \lambda_2 \cos t)^2 (1 - \cos t)^3 \\ g_3(t) &= (1 - \lambda_2 \cos t)^2 (1 - \cos t)^3 \end{aligned} \tag{1}$$

Theorem 1 *The above definition (1) satisfies the following properties:*

i. *Non-negativity:* $g_i(t) \geq 0$ *where* $i = 0, 1, 2, 3$
ii. *Partition of unity:* $\sum_{i=0}^{3} g_i(t) = 1$
iii. *Symmetry:* $g_i(t; \lambda_1, \lambda_2) = g_{3-i}\left(\frac{\pi}{2} - t; \lambda_1, \lambda_2\right)$
iv. *Monotonicity: For certain parameter values of* λ_1 *and* λ_2, $g_3(t)$ *is monotonically increasing and* $g_0(t)$ *is monotonically decreasing.*

Proof

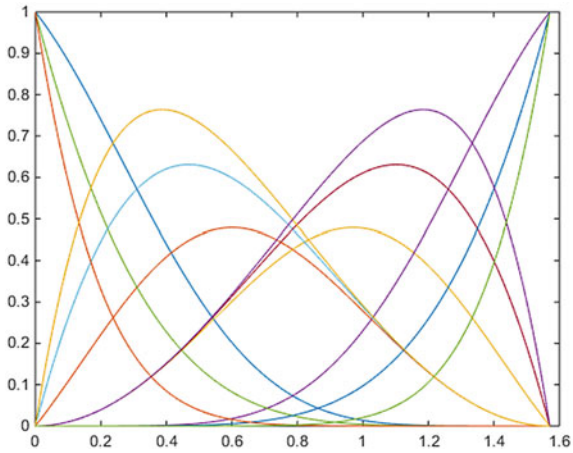

Fig. 1 Shows QT Bézier basis function for λ_1 and λ_2 = -1, 0, 1, respectively

i. $for\ t \in \left[0, \frac{\pi}{2}\right]$,
$(1 - \sin t) \geq 0,\ (1 - \cos t) \geq 0,\ \cos^2(t) \geq 0\ and\ sin^2(t) \geq 0$

ii. This implies that $g_i(t) \geq 0,\ i = 0, 1, 2, 3.$

iii. It follows a trivial solution.

iv.
$$for\ i = 1,\quad g_1(t; \lambda_1, \lambda_2) = \cos^2 t - (1 - \lambda_1 \sin t)^2 (1 - \sin t)^3$$
$$= \cos^2\left(\frac{\pi}{2} - t\right) - \left(1 - \lambda_1 \sin\left(\frac{\pi}{2} - t\right)\right)^2 \left(1 - \sin\left(\frac{\pi}{2} - t\right)\right)^3$$
$$= sin^2 t - (1 - \lambda_2 \cos t)^2 (1 - \cos t)^3$$
$$= g_2\left(\frac{\pi}{2} - t; \lambda_2, \lambda_3\right)$$

$$for\ t_1 \leq t_2, where\ t_1,\ t_2 \in \left[0, \pi/2\right],$$
$$g_0(t_1) \geq g_0(t_2)\ and\ g_3(t_1) \leq g_3(t_2)$$

which proves that $g_0(t)$ decreases, whereas $g_3(t)$ increases monotonically.

Properties (i)–(iv) show that the suggested quintic trigonometric function is analogous to the Bernstein polynomial.

In Fig. 1, quintic trigonometric blending functions are drawn for $\lambda_1 and\ \lambda_2 = -1, 0, 1$, respectively, which clearly shows the above-mentioned properties.

2.2 RQT Bézier Curve

Using Eq. (1), which uses the quintic trigonometric blending function, now we create a rational quintic TB curve (RQT-Bézier curve) with $\lambda_1 and\ \lambda_2$, where λ_1, λ_2 are shape parameters.

Definition 2 Consider the control points P_i $(i = 0, 1, 2, 3)$ $in\ \mathbb{R}^2$ $or\ \mathbb{R}^3$, then RQT-Bézier curve with two shape parameters is defined as.

$$B(t) = \sum_{i=0}^{3} g_i^*(t) P_i, \quad t \in \left[0, \tfrac{\pi}{2}\right], \quad \lambda_1, \lambda_2 \in [-1, 1] \tag{2}$$

where

$$g_i^*(t) = \frac{w_i\, g_i(t)}{\sum_{i=0}^{3} w_i\, g_i(t)}, \quad i = 0, 1, 2, 3$$

It is assumed that $w_0 = w_3 = 1\ and\ w_1, w_2 > 0$.

Properties of the RQT-Bézier curve

Properties of the RQT-Bézier curve are as follows:

i. **Properties at the endpoint**

$$\begin{aligned}
&g(0) = P_0, \quad g\left(\tfrac{\pi}{2}\right) = P_3\\
&g'(0) = (2\lambda_1 + 3)w_1(P_1 - P_0), \quad g'\left(\tfrac{\pi}{2}\right) = (2\lambda_2 + 3)w_2(P_3 - P_2)\\
&g''(0) = 2[(3\lambda_1^2 + 6\lambda_1 + 5) - w_1(2\lambda_1 + 3)^2]w_1(P_1 - P_0) + 2w_2(P_2 - P_0)\\
&g''\left(\tfrac{\pi}{2}\right) = 2[-(3\lambda_2^2 + 6\lambda_2 + 5) + w_2(2\lambda_2 + 3)^2]w_2(P_3 - P_2) + 2w_1(P_1 - P_3)
\end{aligned} \tag{3}$$

According to Eq. (3), the RQT-Bézier curve shows similar results to a normal rational quintic Bézier curve, in that, it begins at P_0 and ends at P_3, and it is tangential to P_1P_0 and P_2P_3 at P_0 and P_3, respectively.

i. **Symmetry**: The control points P_i and $P_{3\text{-}i}$, where i = 0, 1, 2, 3 describe the QT Bézier curve in altered parameterization, that is
$g(t; \lambda_1, \lambda_2, P_i) = g\left(\tfrac{\pi}{2} - t; \lambda_1, \lambda_2, P_{3-i}\right)$ for i = 0, 1, 2, 3.

ii. **Geometric invariance**: RQT-Bézier curve's shape is independent of the coordinates' choice, therefore, the following two equations are compiled using Eq. (2), i.e.

$$\begin{aligned}
&g(t; \lambda_1, \lambda_2; P_0 + r, P_1 + r, P_2 + r, P_3 + r) = g(t; \lambda_1, \lambda_2; P_0, P_1, P_2, P_3) + r,\\
&g(t; \lambda_1, \lambda_2; P_0 * q, P_1 * q, P_2 * q, P_3 * q) = g(t; \lambda_1, \lambda_2; P_0, P_1, P_2, P_3) * q,\\
&\text{where } t \in [0, 1],\ \lambda_1, \lambda_2 \in [-1, 1]
\end{aligned}$$

Here r is an arbitrary vector in $\Re^2$ or $\Re^3$, and q is an arbitrary k × k matrix, k = 2 or 3.

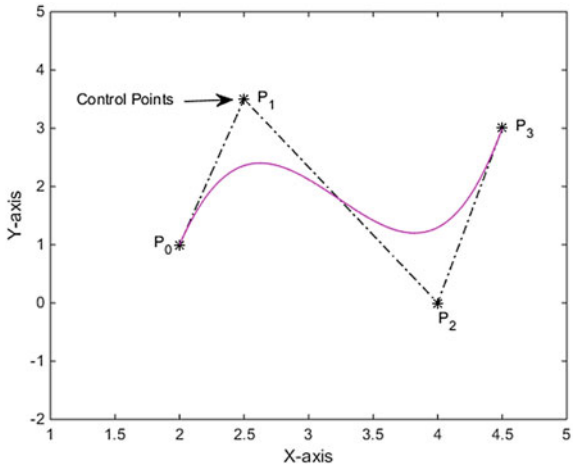

Fig. 2 Shows RQT- Bézier curve within the convex hull

i. **Convex hull Property**: Taking the positive values of weights, the entire curve will satisfy the convex hull property [Fig. 2].

i. **Affine invariance**: The RQT-Bézier curve has the property that applying an affine transformation to each control point results in the same transformation being applied to every point on the curve. For example, to rotate an RQT-Bézier curve, apply a rotation to the control points.

ii. **Endpoint curvature**: The tangent vector for the curve given in Eq. (2) is denoted by $g'(t)$, which is not equal to zero, i.e.$g'(t) \neq 0$, and the curvature κ(t) is defined in [15]

$$k(t) = \frac{\left\| g'(t) \times g''(t) \right\|}{\left\| g'(t) \right\|^3} \tag{4}$$

where '‖.‖' denotes the Euclidean norm and ' × ' shows the cross product. Also, the radius of curvature r(t) is defined by

$$r(t) = \frac{1}{k(t)}$$

Otherwise, the signed curvature of a parametric curve $B(t) = (x_1(t),\ y_1(t))$ is defined as

$$k(t) = \frac{x_1'(t)y_1''(t) - x_1''(t)y_1'(t)}{\left((x_1'(t))^2 + (y_1'(t))^2\right)^{3/2}} \tag{5}$$

Let k_0 represent the curvature of the RQT-Bézier curve at t = 0; then from Eq. (4)

$$k_0 = \frac{\left\| g'(0) \times g''(0) \right\|}{\left\| g'(0) \right\|^3} \tag{6}$$

From Eq. (3), taking the values of derivatives gives us

$$k_0 = \left(\frac{2w_2}{(2\lambda_1 + 3)^2 w_1^2} \right) \frac{\left\| \overrightarrow{p_1 p_2} \times \overrightarrow{p_0 p_1} \right\|}{\left\| \overrightarrow{p_0 p_1} \right\|^3} \tag{7}$$

Setting $\left\| \overrightarrow{p_0 p_1} \right\| = a_0 \neq 0$ *and* $\overrightarrow{p_1 p_2} \times \overrightarrow{p_0 p_1} = 2\Delta_1$ where Δ_1 is a triangle's signed area [7] measured by P_0, P_1 and P_2 control points of the RQT-Bézier curve gives

$$k_0 = \left(\frac{2w_2}{(2\lambda_1 + 3)^2 w_1^2} \right) \frac{2\Delta_1}{a_0^3} \tag{8}$$

If the distance from the line $\overrightarrow{p_0 p_1}$ to the point P_2 is denoted by m_0, then $2\Delta_1 = a_0 m_0$.

Therefore, at $t = 0$, the RQT-Bézier curve having curvature as

$$k_0 = \left(\frac{2w_2}{(2\lambda_1 + 3)^2 w_1^2} \right) \frac{m_0}{a_0^2} \tag{9}$$

Similarly, at $t = \pi/2$, the RQT-Bézier curve having curvature as

$$k_{\frac{\pi}{2}} = \left(\frac{2w_1}{(2\lambda_2 + 3)^2 w_2^2} \right) \frac{\left\| \overrightarrow{p_3 p_1} \times \overrightarrow{p_3 p_2} \right\|}{\left\| \overrightarrow{p_2 p_3} \right\|^3} \tag{10}$$

Taking $\left\| \overrightarrow{p_2 p_3} \right\| = a_1 \neq 0$ *and* $\overrightarrow{p_3 p_1} \times \overrightarrow{p_3 p_2} = 2\Delta_2$, where Δ_2 is a triangle's signed area, measured by P_0, P_1 and P_2 control points of the RQT-Bézier curve gives

$$k_{\frac{\pi}{2}} = \left(\frac{2w_1}{(2\lambda_2 + 3)^2 w_2^2} \right) \frac{2\Delta_2}{a_1^3} \tag{11}$$

If the distance from the line $\overrightarrow{p_2 p_3}$ to the point P_1 is denoted by m_1, then $2\Delta_2 = a_1 m_1$. Then

$$k_{\frac{\pi}{2}} = \left(\frac{2w_1}{(2\lambda_2 + 3)^2 w_2^2} \right) \frac{m_1}{a_1^2} \tag{12}$$

2.3 Geometric Importance of Shape Parameters

As we all know that the shape parameters λ_1 and λ_2 are key qualities for dynamic shape design. The RQT-Bézier curve has a superior ability to depict the non-rational quintic TB curve (NRQT-Bézier curve) depicted in Fig. 3a–d due to these shape parameters.

In Fig. 4a, b, the shape of the RQT-Bézier curve is varying when shape parameters λ_1 and λ_2 increase or decrease in the specified range $[-1, 1]$. Another shape control factor in the rational curve is considered as weight, which performs as other shape parameters. When we increase weight, then from where it is joined, the curve is dragged to that control point. Figure 4c shows the curve shape by varying different values of its weights.

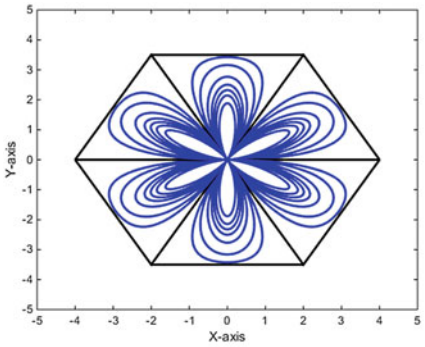

Figure3a. RQT-Bézier Curve

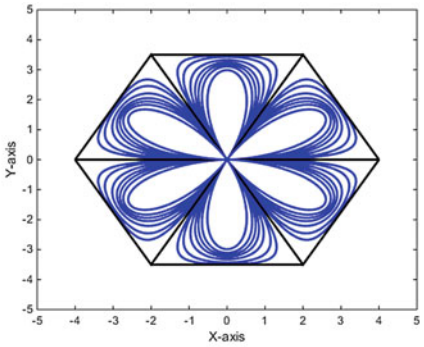

Figure3b. NRQT-Bézier Curve

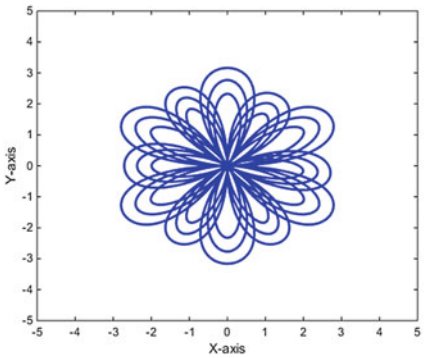

Figure3c. RQT-Bézier Curve

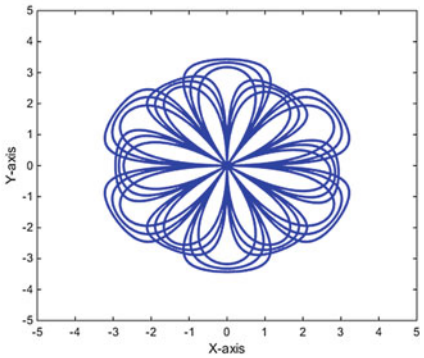

Figure3d. NRQT-Bézier Curve

Fig. 3 **a–d** Shows the comparison between the rational (left) and non-rational (right) QT Bézier curve using changed values of weight and shape parameters

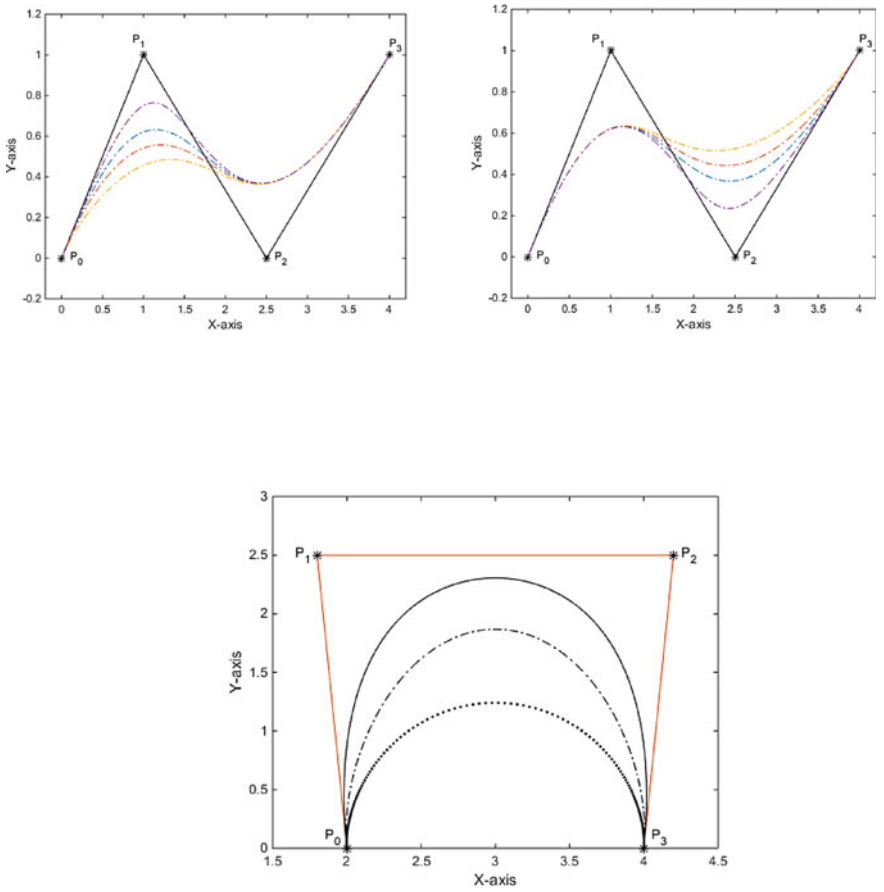

Fig. 4 **a** Shows RQT-Bézier curve for shape parameter $\lambda_1 = -1, -0.5, 0, 1$, respectively. **b** Shows RQT-Bézier curve for shape parameter $\lambda_2 = -1, -0.5, 0, 1$, respectively. **c** Shows RQT-Bézier curve for weight $w_1 = w_2 = 0.1, 0.3, 1.2$, respectively

2.4 Endpoint Curvatures Through Shape Control

The constraints on the weights and shape parameters that are obtained to limit the produced curve always in its control polygon were described in this section. By adjusting the values of weight, endpoint curvatures, and shape parameters locally, we can discover the appropriate curve shape.

Theorem 2 *The control points for the curve of RQT-Bézier are considered* P_i *(*$i = 0, 1, 2, 3$*). Let* k_0 *and* $k_{\pi/2}$ *represent the curvature at* $t = 0$ *and* $t = \pi/2$*, and* r_0 *and* $r_{\pi/2}$*, respectively, indicate the corresponding curving radii at these endpoints. For* $w_1, w_2 > 0$*, shape parameters* λ_1 *and* λ_2*, the curve will always follow the convex hull property, such that*

$$\lambda_1 = -\frac{3}{2} + \frac{1}{w_1}\sqrt{\frac{w_2 \Delta_1 r_0}{a_0^3}} \tag{13a}$$

$$\lambda_2 = -\frac{3}{2} + \frac{1}{w_2}\sqrt{\frac{w_1 \Delta_2 r_{\pi/2}}{a_1^3}} \tag{13b}$$

provided that

$$r_0 \leq \frac{w_1^2 a_0^3}{w_2 \Delta_1} \; and \; r_{\pi/2} \leq \frac{w_2^2 a_1^3}{w_1 \Delta_2} \tag{14}$$

Here, using control points P_0, P_1, P_2, and P_3, P_2, P_1, the signed area of triangles Δ_1 and Δ_2 are found, respectively. Moreover, Δ_1, r_0 and Δ_2, $r_{\pi/2}$ must have identical signs.

Proof Using Eq. (8) and Eq. (11), this can be solved directly.

The following Theorem 2 results are validated in Fig. 5. The curves are plotted by using weights, endpoint curvatures and control points. Equations (13a) and Eq. (13b) are used to calculate the value of the shape parameter.

Theorem 3 *Assume that k_0 and $k_{\pi/2}$ are as same as described in Theorem 2. For the shape parameters λ_1 and $\lambda_2 \in [-1, 1]$ and specified values of k_0 and $k_{\pi/2}$, the given curve always follows convex hull property, if the values of the weights w_1 and w_2 are given by*

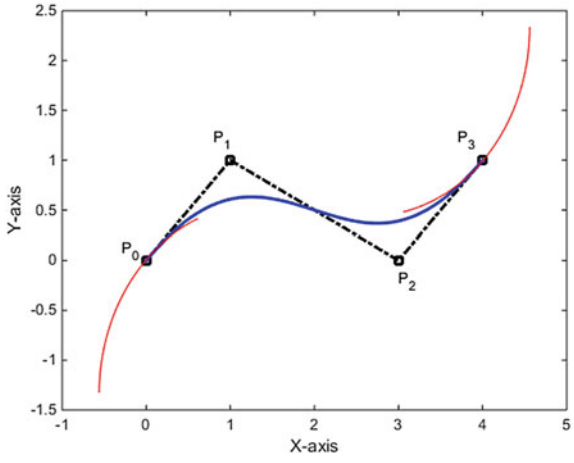

Fig. 5 Shows the curve using weights and endpoint curvatures

$$\left.\begin{aligned} w_1 &= \left(\frac{8c_1c_2^2}{\lambda_{11}^2\lambda_{21}k_0^2k_{\pi/2}}\right)^{1/3} \\ w_2 &= \left(\frac{8c_1^2c_2}{\lambda_{11}\lambda_{21}^2k_0k_{\pi/2}^2}\right)^{1/3} \end{aligned}\right\} \tag{15}$$

where $c_1 = \frac{2\Delta_1}{a_0^3}$, $c_2 = \frac{2\Delta_2}{a_1^3}$, $\lambda_{11} = (2\lambda_1 + 3)^2$ *and* $\lambda_{21} = (2\lambda_2 + 3)^2$.

Proof Using the stated values of λ_{11}, λ_{21}, c_1 and c_2, the curvatures k_0 and $k_{\pi/2}$ are.

$$k_0 = \frac{2w_2c_1}{\lambda_{11}w_1^2} \tag{16}$$

$$k_{\pi/2} = \frac{2w_1c_2}{\lambda_{21}w_2^2} \tag{17}$$

The Eq. (16) and Eq. (17) produces the value of w_1 and w_2 as given in Eq. (15).

3 Results and Discussion

3.1 Piecewise RQT-Bézier Curves

This part shows the design of a curve which is a piecewise rational quintic trigonometric Bézier curve, made by using two pieces of RQT-Bézier curves, with parametric and geometric continuities of varying order.

3.2 Two RQT-Bézier Curves Using C^1 and G^1 Continuity

Let two RQT-Bézier curves, $B_1(t)$ and $B_2(t)$ with control points P_i^1 and P_i^2 (i = 0, 1, 2, 3), respectively, are specified by

$$B_1(t) = \frac{g_0P_0^1 + g_1P_1^1w_1 + g_2P_2^1w_2 + g_3P_3^1}{g_0 + g_1w_1 + g_2w_2 + g_3} \tag{18}$$

$$B_2(t) = \frac{g_0P_0^2 + g_1P_1^2z_1 + g_2P_2^2z_2 + g_3P_3^2}{g_0 + g_1z_1 + g_2z_2 + g_3} \tag{19}$$

Here w_1, w_2, and z_1, z_2 are weights for the curves Eq. (17) and Eq. (18), respectively, and g_i, where $i = 0, 1, 2, 3$ are the basis functions indicated in Eq. (1). Moreover, for RQT-Bézier curves $B_1(t)$ and $B_2(t)$, λ_{11}, λ_{21} and λ_{12}, λ_{22} are considered as shape parameters, respectively.

With parametric continuity of order 1 (i.e. C^1 continuity), the two curve pieces are connected if

$$\begin{cases} P_3^1 = P_0^2 \\ B_1^{'}(\frac{\pi}{2}) = B_2^{'}(0) \end{cases}$$

This implies

$$P_1^2 = P_3^1 + \frac{(2\lambda_{12}+3)}{(2\lambda_{21}+3)}\frac{w_2}{z_1}\left(P_3^1 - P_2^1\right) \tag{20}$$

The curves which are specified in Eqs. (18) and (19) are geometric continuous of order 1 (i.e. G^1 continuity) if

$$\begin{cases} P_3^1 = P_0^2 \\ B_1^{'}(\frac{\pi}{2}) = \eta B_2^{'}(0), \quad \eta > 0 \end{cases}$$

Using Eq. (4), the following equation is obtained as:

$$P_1^2 - P_0^2 = \eta\frac{(2\lambda_{21}+3)}{(2\lambda_{12}+3)}\frac{w_2}{z_1}\left(P_3^1 - P_2^1\right) \tag{21}$$

Let $\xi = \eta\frac{(2\lambda_{21}+3)}{(2\lambda_{12}+3)}\frac{w_2}{z_1}$ then,

$$P_1^2 = (1+\xi)P_3^1 - \xi P_2^1, \quad \xi > 0 \tag{22}$$

In Fig. 6a and b, respectively, curves created by two connected pieces of RQT-Bézier curves with C^1 and G^1 continuity conditions are illustrated. For G^1 continuity, set $\eta = 2$.

3.3 Two RQT-Bézier Curves Using C^2 and G^2 Continuity

It is assumed that $\lambda_{11} = \lambda_{21} = \lambda_{12} = \lambda_{22} = 1$ for convenience.

A curve is parametric continuous of order 2 (i.e. C^2 continuous) if it is C^1 continuous, i.e. parametric continuous of order 1 and second-order derivative is the same at the junction, i.e.

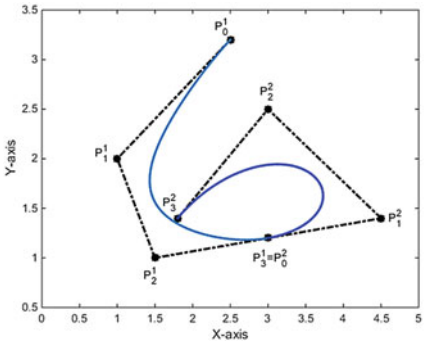

Figure 6a. Two connected pieces of RQT-Bézier curve using C^1 continuity

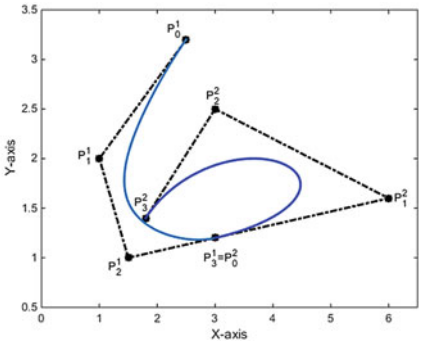

Figure 6b. Two connected pieces of RQT-Bézier curve using G^1 continuity

Fig. 6 **a** Two connected pieces of RQT-Bézier curve using C^1 continuity. **b** Two connected pieces of RQT-Bézier curve using G^1 continuity. **c** Two connected pieces of the RQT-Bézier curve using C^2 continuity. **d** Two connected pieces of the RQT-Bézier curve using G^2 continuity

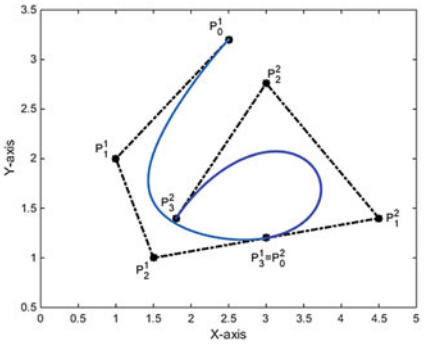

Figure 6c. Two connected pieces of the RQT-Bézier curve using C^2 continuity.

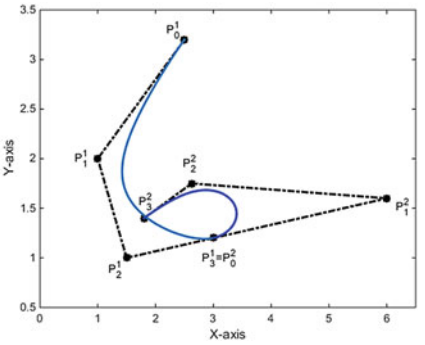

Figure 6d. Two connected pieces of the RQT-Bézier curve using G^2 continuity.

Fig. 6 (continued)

$$B_1''\left(\frac{\pi}{2}\right) = B_2''(0)$$

This gives

$$P_2^2 = P_1^1 - 28P_2^1 + 28P_3^1 \tag{23}$$

Secondly, two curves are associated by G^2 continuity if they are G^1 continuous and at the junction their curvatures are equal.

Assume that the curvature is taken as k_{B1} and k_{B2}, respectively, for two curves defined in Eqs. (18) and (19). Then, G^2 continuity is attained if

$$k_{B_1}\left(\frac{\pi}{2}\right) = k_{B_2}(0)$$

Now, from Eqs. (9) and (12), using the values of endpoint curvature in the following equation gives

$$\frac{z_2}{(2\lambda_{12}+3)^2 z_1}\frac{h_2}{\alpha_2^2} = \frac{w_1}{(2\lambda_{21}+3)^2 w_2}\frac{h_1}{\alpha_1^2} \tag{24}$$

where $\alpha_1 = \left\| P_3^1 - P_2^1 \right\|$, $\alpha_2 = \left\| P_1^2 - P_0^2 \right\|$. Also, h_1 and h_2 are the distance of P_1^1 from the line $\overrightarrow{P_2^1 P_3^1}$ and P_2^2 from the line $\overrightarrow{P_0^2 P_1^2}$, respectively.

Using Eq. (21), $\alpha_2 = \xi\alpha_1$. Thus

$$h_2 = \xi^2 \frac{w_1}{z_2} h_1 \tag{25}$$

The curves generated by the combination of two pieces of the curve RQT-Bézier employing C^2 and G^2 continuity, respectively, are shown in Fig. 6c and d.

3.4 *Font Design Using RQT-Bézier Curve*

We saw that CAGD is particularly popular for the design strategies that use rational Bézier curves. Because of its features, many designers like to utilize the Bézier curve to depict different shapes and fonts.

This section presents the proposed RQT-Bézier curve to construct Devanagari (Hindi) letters, validating the practical execution of the curve. The RQT-Bézier curve, whose five parts are used to form the Devanagari alphabet (da), is shown in Fig. 7a,

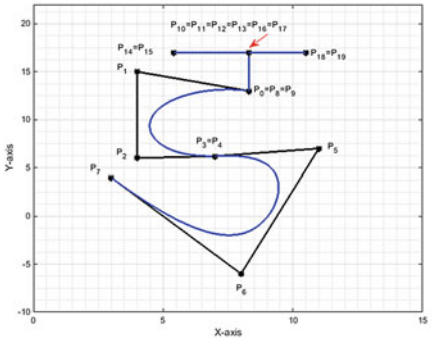

Figure 7a

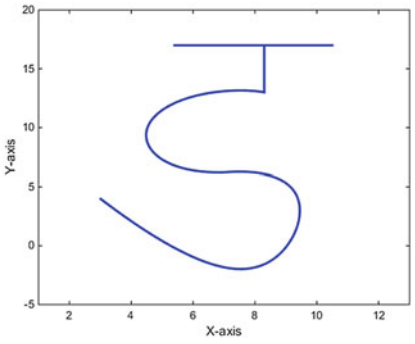

Figure 7b

Fig. 7 **a** and **b** show the construction of the Devanagari alphabet (da) with control polygon and without control polygon

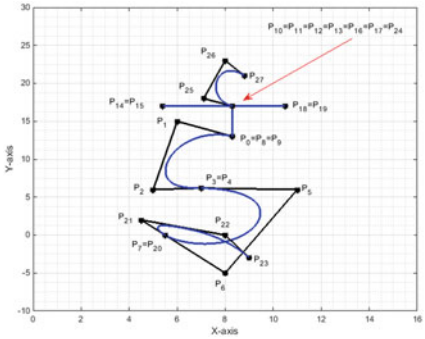

Figure 8a

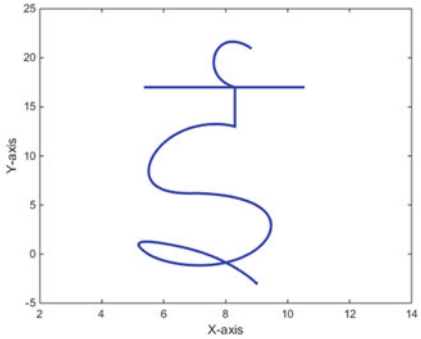

Figure 8b

Fig. 8 **a** and **b** show the construction of the Devanagari alphabet (i) with control polygon and without control polygon

Table 1 Data for Fig. 7a, b

Curve segments	Control points	Shape parameters λ_1 *and* λ_2	Weights w_1 *and* w_2
P_0-P_3	(8.3, 13), (4, 15), (4, 6), (7, 6.2)	$\lambda_1 = -0.8$, $\lambda_2 = 0.1$	$w_1 = 1$, $w_2 = 1.5$
P_4-P_7	(7, 6.2), (11, 7), (8, −6), (3, 4)	$\lambda_1 = -0.2$, $\lambda_2 = -0.5$	$w_1 = 1$, $w_2 = 1.5$
P_8-P_{11}	(8.3, 13), (8.3, 13), (8.3, 17), (8.3, 17)	$\lambda_1 = -0.2$, $\lambda_2 = -0.5$	$w_1 = 1$, $w_2 = 1.5$
P_{12}-P_{15}	(8.3, 17), (8.3, 17), (5.4, 17), (5.4, 17)	$\lambda_1 = -0.2$, $\lambda_2 = -0.5$	$w_1 = 1$, $w_2 = 1.5$
P_{16}-P_{19}	(8.3, 17), (8.3, 17), (10.5, 17), (10.5, 17)	$\lambda_1 = -0.2$, $\lambda_2 = -0.5$	$w_1 = 1$, $w_2 = 1.5$

b. The shape and weight values influence the curve pieces in this figure. Likewise in Fig. 8a, b, another form is described of the Devanagari alphabet (i) built with seven pieces of RQT-Bézier curves (Tables 1 and 2).

4 Conclusions

The Above work describes a new way to construct the shape of the curve through the RQT-Bézier curve using shape parameters. By varying the values of weight along with shape parameters, the curve shape can be regulated in desired shape. Therefore, the curve recommended in this paper is more flexible than a typical rational quintic Bézier curve. Using parametric and geometric Hermite continuity conditions, the suggested curve is utilized to build piecewise rational trigonometric curves

Table 2 Data for Fig. 8a, b

Curve segments	Control points	Shape parameters λ_1 *and* λ_2	Weights w_1 *and* w_2
P_0-P_3	(8.3, 13), (6, 15), (5, 6), (7, 6.2)	$\lambda_1 = -0.8$, $\lambda_2 = 0.1$	$w_1 = 1$, $w_2 = 1.5$
P_4-P_7	(7, 6.2), (11, 6), (8, −5), (5.5, 0)	$\lambda_1 = -0.2$, $\lambda_2 = -0.5$	$w_1 = 1$, $w_2 = 1.5$
P_8-P_{11}	(8.3, 13), (8.3, 13), (8.3, 17), (8.3, 17)	$\lambda_1 = -0.2$, $\lambda_2 = -0.5$	$w_1 = 1$, $w_2 = 1.5$
P_{12}-P_{15}	(8.3, 17), (8.3, 17), (5.4, 17), (5.4, 17)	$\lambda_1 = -0.2$, $\lambda_2 = -0.5$	$w_1 = 1$, $w_2 = 1.5$
P_{16}-P_{19}	(8.3, 17), (8.3, 17), (10.5, 17), (10.5, 17)	$\lambda_1 = -0.2$, $\lambda_2 = -0.5$	$w_1 = 1$, $w_2 = 1.5$
P_{20}-P_{23}	(5.5, 0), (4.5, 2), (8, 0), (9, −3)	$\lambda_1 = -1$, $\lambda_2 = -1$	$w_1 = 1$, $w_2 = 1.5$
P_{24}-P_{27}	(8.3, 17), (7.1, 18), (8, 23), (8.8, 21)	$\lambda_1 = -0.5$, $\lambda_2 = -1$	$w_1 = 1$, $w_2 = 1.5$

with smooth joints. An application in font design through piecewise rational quintic trigonometric curves is the justification of our curve.

References

1. Dube M, Sharma J (2018) Inflection point control by using rational cubic spline. Int J Math Appl 6(1-A):43–50
2. Dube M, Mishra U (2017) WAT rational cubic trigonometric Bezier curve and its applications. Int J Appl Math Stat Sci 6(4):115–126
3. Farin GE (2002) Curves and surfaces for CAGD: a practical guide. Morgan Kaufmann, Menlo Park
4. Dube M, Sharma R (2016) Cubic trigonometric Bézier curves with a shape parameter. Int J Innov Res Comput Commun Eng 4(4):7718–7723
5. Han XA, Ma Y, Huang X (2009) The cubic trigonometric Bézier curve with two shape parameters. Appl Math Lett 22(2):226–231
6. Schoenberg IJ (1964) On trigonometric spline interpolation. J Math Mech 13:795–825
7. Juhász I (1998) Cubic parametric curves of given tangent and curvature. Comput Aided Des 30(1):1–9
8. Khatri K, Mishra VN (2020) Generalized B\'{e}zier curves based on Bernstein-Stancu-Chlodowsky type operators. Boletim da SociedadeParanaense de Matemática 1–10. In press. https://doi.org/10.5269/bspm.52003
9. Liu H, Wang H, Li L, Zhang D (2010) Blending trigonometric curve and Bézier curve with multi-shape parameters. J Inf Comput Sci 7(12):2486–2494
10. Liu H, Li L, Zhang D (2011) Extension of cubic trigonometric polynomial Bézier curve. Adv Sci Eng Med 3(3):262–267
11. Mainar E, Peña JM, Sánchez-Reyes J (2001) Shape preserving alternatives to the rational Bézier model. Comput-Aided Geom Des 18(1):37–60
12. Mathews JH (1986) Numerical methods for computer science, engineering, and mathematics. Prentice-Hall Inc., New Jersey

13. Piegl LA, Tiller W (1997) The NURBS book. Springer, Berlin, p 123
14. Bézier P (1974) Mathematical and practical possibilities of UNISURF. Comput Aided Geom Des
15. Bashir U, Md Ali J (2014) Rational cubic trigonometric Bézier curve with two shape parameters. Comput Appl Math 35:285–300
16. Xu WX, Wang LQ, Liu XM (2011) Quadratic TC-Bézier curves with shape parameter. Adv Mater Res 179–180:1187–1192
17. Han X (2011) A class of general quartic spline curves with shape parameters. Comput-Aided Geom Des 28:151–163
18. Yan L, Liang J (2011) A class of algebraic-trigonometric blended splines. J Comput Appl Math 235(6):1713–1729

Effect of Partial Slip on Peristaltic Transport of MHD-Carreau Fluid in a Flexible Channel with Non-uniform Heat Source and Sink

S. K. Asha and Joonabi Beleri

Abstract The current work is to deliberate the effect of the magnetic field, partial slip flow, and irregular heat generation and absorption of Carreau liquid in peristaltic movement through a flexible channel. The governing equations are converted to standard non-linear partial differential equations by using suitable non-dimensional parameters. Solutions to emerging equations are found by using the Multi-Step Differential Transformation Method (Ms-DTM). The role of influential factors on velocity, concentration and temperature are shown through graphs.

Keywords Peristaltic flow · Carreau fluid · Magnetic field · Partial slip flow · Non-uniform heat source and sink · Flexible channel · Ms-DTM

2010 MSC 76XX · 76A05 · 76V05 · 76D05

Nomenclature

$\tilde{X}, \tilde{Y}$	Cartesian coordinates
$\tilde{U}, \tilde{V}$	Velocity components
T_m	Fluid mean temperature
$\tilde{\mathrm{T}}$	Temperature of the fluid
$\tilde{C}$	Concentration of fluid
B_0	Applied magnetic field
R	Reynolds number
P_r	Prandtl number
$\tilde{P}$	Pressure of fluid
M	Hartman number
E_c	Eckert number,
P_r	Prandtl number,

S. K. Asha (✉) · J. Beleri
Department of Studies and Research in Mathematics, Karnatak University, Dharwad 580003, India
e-mail: ashask@kud.ac.in

J. Singh et al. (eds.), *Advances in Mathematical Modelling, Applied Analysis and Computation*, Lecture Notes in Networks and Systems 415,
https://doi.org/10.1007/978-981-19-0179-9_20

B_r	Prandtl number,
S_c	Schmidt number,
S_r	Soret number,
C_f	Skin friction coefficient,
N_u	Nusselt number,
S_h	Sherwood number,
δ	Wave number
We	Weissenberg number
K	The thermal conductivity
β	Heat source and sink parameter
ζ	Specific heat at constant volume
K_T	Is the ratio of thermal diffusion
D	Is the mass diffusivity coefficient
$\tilde{S}_{\tilde{x}\tilde{x}}$, $\tilde{S}_{\tilde{x}\tilde{y}}$, $\tilde{S}_{\tilde{y}\tilde{y}}$	Extra stress tensor components

1 Introduction

The Carreau liquid is a generalised Newtonian liquid whose viscosity is proportional to its shear rate. Carreau fluids behave like Newtonian fluids at low shear rates. In some disciplines of biology and technology, non-Newtonian. Nowadays, Peristaltic transport is one of the most important pumping mechanisms. Peristaltic movement obstacles have significant consideration because of its wide area of pertinence. Peristaltic pumping mechanisms are embedded in plenty of biological tools including food intake through the oesophagus, chime flow in the gastrointestinal tract and urine movement from the kidney to the bladder via the ureter. In 1966 Latham [1] introduced the Peristalsis. The word "peristalsis" comes from the Greek word "Peristaltikos," which means "clasping and compression". This work was further continued by Shapiro et al. [2] and Jaffrin et al. [3]. Investigators examined the peristaltic flow of fluids is in this reference list [4, 5].

When the rate of strain is proportional to the tangential velocity component at the boundary, the phenomenon of wall slip occurs. The standard no slip requirement does not apply to non-Newtonian liquids such as foams, emulsions, suspensions, and polymer melts/solutions. Therefore, in such situations, there may be a partial slip between the fluid and the boundary. The Navier–Stokes equation using partial slip boundary constraints was possibly solved for the first time by Navier [6]. Peristalsis wall slip property is important in various biomedical applications, such as cleaning prosthetic heart valves and interior cavities. Nadeem and Akram [7] studied the partial slip effects on the peristaltic motion of the Newtonian liquid. Ali et al. [8] studied the effect of slip on the peristaltic flow. Further, Srinivas et al. [9], Akram et al. [10], Hayat et al. [11], Hina et al. [12] and Khan et al. [13] examined the effects of slip conditions.

Since peristaltic transport involves the transport of fluid by contraction and expansion, it includes kinetic energy, which results in the transfer of heat. Heat sources and sinks alter temperature distribution, which influences particle deposition rates in systems like semiconductors, nuclear reactors, and electronic chips. Rehman et al. [14] examined the impact of heat generation or absorption on the peristaltic transport of Jeffrey liquid in a symmetric channel. Sheriff et al. [15] examined peristaltic motion with heat source and sink parameters. The effect of nirregular heat generation (or absorption) on convective micropolar liquid motion in an inclined flat plate was studied by Rahman et al. [16].

It has been thought that the heat source or sink is constant, location dependent, or temperature dependent. The radiative effects of heat transmission on various flows are used in high temperature processes and space technology. Internal heat source and sink are difficult to calculate precisely, but several basic mathematical models can approximate its average behaviour in most physical settings. Further, some recent studies as a source of energy transfer. Chemical reactions are used in a variety of industries, on heat generation or absorption studied by Benazir et al. [17], Mahanthesh et al. [18], Hayat et al. [19].

Magnetohydrodynamics (MHD) offers a wide range of industrial uses, including crystal formatting, liquid metal cooling and metal casting blankets for fusion reactors. Electromagnetic pumps, electromagnetic flowmeters and hydromagnetic generators are all examples of its use. Instead of being pushed by technical advancements, MHD technology improvement should be driven by a clinical necessity. This necessity helps present and a new planned MHD tools that have a wide and real influence on the medical field. Magnetic resonance imaging (MRI), MHD micropumps for medication administration, inductive heat therapy of tumours, indicators for the quantification of biologically active elements, MHD-derived biomedical sensors, MHD micromixers, magnetorelaxometry, and actuators are just a few of the biomedical applications for magnetised fluids. Inductive heating under alternating magnetic fields is also being used to evaluate magnetic fluids for cancer therapy. Further, Hayat et al. [20], Machireddy et al. [21] and Khan et al. [22] analysed MHD Carreau fluid, Goqo et al. [23], Gupta et al. [24–26], Reddy et al. [27] and Vaidya et al. [28, 29] examined the effect of MHD in a nanofluid.

In the present paper we have used semi-analytical method known as Differential Transformation Method (DTM). Zhou first proposed the Differential Transformation Method (DTM) in 1986 [30]. A semi-analytical solution in the form of a polynomial is obtained. The Multi-Step Differential Transformation Method is a reliable semi-analytical method (Ms-DTM), which is an effective improvement to the classical differential transformation method. Odibat et al. [31] suggested the implementation of Ms-DTM in 2010 by solving the system of ordinary differential equations. Further, the use of Ms-DTM to solve nonlinear differential equations is given in the references [32–36, 37]. They compare the obtained results with other existing methods.

In view of these appliances, the purpose of this paper is to make new suggestions on the impact of the magnetic field, partial slip flow and irregular heat generation and

absorption on the peristaltic flow of carreau liquid through a flexible channel. Non-linear governingequations are obtained by using Ms-DTM and physical parameter's velocity,concentration and temperatureare are debated by drawing the graphs.

2 Construction of Governing Equations

Consider a Carreau fluid peristaltic movement propagating a sinusoidal wave towards the channel's walls in a two-dimensional flexible channel in a cartesian coordinate system $(\tilde{X}, \tilde{Y})$. The physical model of the channel wall surface is shown in Fig. 1 and is given as

$$h\left(\tilde{X}, \tilde{t}\right) = a(\tilde{X}) + b\sin\left(\frac{2\pi}{\lambda}\left(\tilde{X} - c\tilde{t}\right)\right), \tag{1}$$

here $a(\tilde{X})$ denotes channels half width, b denotes wave amplitude, λ denotes length of wave, c denotes velocity propagation and $\tilde{t}$ is time.

Let $\tilde{U}$ and $\tilde{V}$ are velocity components respectively, the velocity field Vcan be defined as

$$V = \left(\tilde{U},\ \tilde{V}, 0\right), \tag{2}$$

For an incompressible Carreau fluid, the constitutive equations are [38]

$$\frac{(\eta - \eta_\infty)}{(\eta_0 - \eta_\infty)} = \left[\left(1 + \left(\Gamma\dot{\overline{\gamma}}\right)^2\right)^{\frac{n-1}{2}}\right], \tag{3}$$

$$\overline{\tau} = -\eta_0\left[\left(1 + \frac{(n-1)}{2}\left(\Gamma\dot{\overline{\gamma}}\right)^2\right)\right]\dot{\overline{\gamma}}, \tag{4}$$

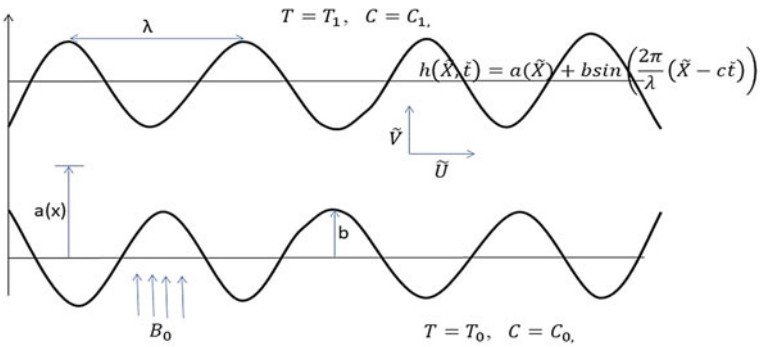

Fig. 1 Geometry of physical model

η_∞ stands for infinite shear rate viscosity, η_0 for zero shear rate viscosity, η for time constant, n for dimensionless power law index, and $\overline{\dot{\gamma}}$ is defined as.

$$\overline{\dot{\gamma}} = \sqrt{\frac{1}{2}\sum_i \sum_j \overline{\dot{\gamma}}_{ij}\overline{\dot{\gamma}}_{ji}} = \sqrt{\frac{1}{2}\Pi}, \tag{5}$$

where Π is the second invariant of strain tensor.

The governing equations of Carreau liquid are given as [39]

$$\frac{\partial \tilde{U}}{\partial \tilde{X}} + \frac{\partial \tilde{U}}{\partial \tilde{Y}} = 0\,, \tag{6}$$

$$\rho\left(\frac{\partial \tilde{U}}{\partial \tilde{t}} + \tilde{U}\frac{\partial \tilde{U}}{\partial \tilde{X}} + \tilde{V}\frac{\partial \tilde{U}}{\partial \tilde{Y}}\right) = -\frac{\partial \tilde{p}}{\partial \tilde{X}} + \frac{\partial \tilde{S}_{\tilde{x}\tilde{x}}}{\partial \tilde{X}} + \frac{\partial \tilde{S}_{\tilde{x}\tilde{y}}}{\partial \tilde{Y}} - \sigma * B_0^2 \tilde{U}\,, \tag{7}$$

$$\rho\left(\frac{\partial \tilde{V}}{\partial \tilde{t}} + \tilde{U}\frac{\partial \tilde{V}}{\partial \tilde{X}} + \tilde{V}\frac{\partial \tilde{V}}{\partial \tilde{Y}}\right) = -\frac{\partial \tilde{p}}{\partial \tilde{Y}} + \frac{\partial \tilde{S}_{\tilde{x}\tilde{x}}}{\partial \tilde{X}} + \frac{\partial \tilde{S}_{\tilde{x}\tilde{y}}}{\partial \tilde{Y}}, \tag{8}$$

$$\begin{aligned}\zeta\rho\left(\frac{\partial \tilde{T}}{\partial \tilde{t}} + \tilde{U}\frac{\partial \tilde{T}}{\partial \tilde{X}} + \tilde{V}\frac{\partial \tilde{T}}{\partial \tilde{Y}}\right) &= K\left(\frac{\partial^2 \tilde{T}}{\partial \tilde{X}^2} + \frac{\partial^2 \tilde{T}}{\partial \tilde{Y}^2}\right)\\ &\quad + \tilde{S}_{\tilde{x}\tilde{x}}\frac{\partial \tilde{U}}{\partial \tilde{X}} + \tilde{S}_{\tilde{y}\tilde{y}}\frac{\partial \tilde{V}}{\partial \tilde{Y}} + \tilde{S}_{\tilde{x}\tilde{y}}\left(\frac{\partial \tilde{V}}{\partial \tilde{X}} + \frac{\partial \tilde{U}}{\partial \tilde{Y}}\right) + Q_0,\end{aligned} \tag{9}$$

$$\frac{\partial \tilde{C}}{\partial \tilde{t}} + \tilde{U}\frac{\partial \tilde{C}}{\partial \tilde{X}} + \tilde{V}\frac{\partial \tilde{C}}{\partial \tilde{Y}} = D\left(\frac{\partial^2 \tilde{C}}{\partial \tilde{X}^2} + \frac{\partial^2 \tilde{C}}{\partial \tilde{Y}^2}\right) + \frac{DK_T}{T_m}\left(\frac{\partial^2 \tilde{T}}{\partial \tilde{X}^2} + \frac{\partial^2 \tilde{T}}{\partial \tilde{Y}^2}\right), \tag{10}$$

The relationship between the laboratory frame and wave frame is defined by

$$\tilde{x} = \tilde{X} - c\tilde{t}, \quad \tilde{y} = \tilde{Y}, \quad \tilde{u}(\tilde{x}, \tilde{y}) = \tilde{U} - c, \quad \tilde{v}(\tilde{x}, \tilde{y}) = \tilde{V}, \tag{11}$$

where $(\tilde{u}, \tilde{v})$ are velocity components, $(\tilde{x}, \tilde{y})$ are coordinates in a wave frame. B_0 denotes applied magnetic field, T_m represents fluid mean temperature, K_T is the ratio of thermal diffusion, D denotes the mass diffusivity coefficient and Q_0 denotes the non-uniform heat source and sink parameter.

Introducing, non-dimensional quantities of the following

$$\left.\begin{aligned}
&\psi = \frac{\tilde{\psi}}{ca},\ x = \frac{\tilde{x}}{\lambda},\ y = \frac{\tilde{y}}{a},\ t = \frac{c\tilde{t}}{\lambda},\ M = \sqrt{\frac{\sigma^*}{\eta_0}}B_0 a,\ p = \frac{a^2\tilde{p}}{c\lambda\eta_0},\ v = \frac{\tilde{v}}{c},\ u = \frac{\tilde{u}}{c},\ h = \frac{\tilde{h}}{a},\ \delta = \frac{a}{\lambda},\\
&R = \frac{\rho ca}{\eta_0},\ \alpha = \frac{\tilde{\alpha}}{a},\ \Omega = \frac{\tilde{C}-\tilde{C}_0}{\tilde{C}_1-\tilde{C}_0},\ \theta = \frac{\tilde{T}-\tilde{T}_0}{\tilde{T}_1-\tilde{T}_0},\ P_r = \frac{\rho\eta_0\zeta}{K},\ \dot{\Upsilon} = \frac{\tilde{\Upsilon}a}{c},\ We = \frac{\Gamma c}{a},\ m = \frac{\tilde{m}\lambda}{a},\\
&S_r = \frac{\rho DK_T\left(\tilde{T}_1-\tilde{T}_0\right)}{\eta_0 T_m\left(\tilde{C}_1-\tilde{C}_0\right)},\ S_c = \frac{\eta_0}{\rho D},\ S_{\tilde{x}\tilde{x}} = \frac{\lambda}{\eta_0 c}\tilde{S}_{\tilde{x}\tilde{x}},\ S_{\tilde{x}\tilde{y}} = \frac{a}{\eta_0 c}\tilde{S}_{\tilde{x}\tilde{y}},\ S_{\tilde{y}\tilde{y}} = \frac{a}{\eta_0 c}\tilde{S}_{\tilde{y}\tilde{y}},\ \beta = \frac{Q_0 a^2}{kT_0},\\
&E_c = \frac{c^2}{\zeta\left(\tilde{T}_1-\tilde{T}_0\right)},\ h = \frac{\tilde{h}}{a} = 1+\phi\sin 2\pi x,\ \phi = \frac{b}{a},\ f^* = \frac{q}{ca},\ u = \frac{\partial\psi}{\partial y},\ v = -\frac{\partial\psi}{\partial x},\ B_r = E_c P_r.
\end{aligned}\right\} \tag{12}$$

where θ and Ω are the dimensionless temperature and concentration respectively. R denotes Reynolds number, β is Heat source and sink parameter, M represents Hartman number, E_c is Eckert number, P_r denotes Prandtl number, B_r represents Brinkman number, S_c represents Schmidt number and S_r denotes Soret number.

The fundamental Eqs. (6)–(10) can be reduced by using the above non-dimensional variables.

$$\frac{\partial p}{\partial x} = \frac{\partial S_{xy}}{\partial y} - M^2\frac{\partial\psi}{\partial y}, \tag{13}$$

$$\frac{\partial p}{\partial y} = 0, \tag{14}$$

$$\frac{\partial^2\theta}{\partial y^2} + B_r S_{xy}\frac{\partial^2\psi}{\partial y^2} + \beta = 0, \tag{15}$$

$$\frac{1}{S_c}\frac{\partial^2\Phi}{\partial y^2} + S_r\frac{\partial^2\theta}{\partial y^2} = 0, \tag{16}$$

$$S_{XX} = 2\left(1+\frac{(n-1)}{2}We^2\dot{\gamma}^2\right)\left(\frac{\partial^2\psi}{\partial x\partial y}\right), \tag{17}$$

$$S_{XY} = S_{YX} = \left(1+\frac{(n-1)}{2}We^2\dot{\gamma}^2\right)\left(\frac{\partial^2\psi}{\partial y^2} - \delta^2\frac{\partial^2\psi}{\partial x^2}\right), \tag{18}$$

$$S_{YY} = -2\delta\left(1+\frac{(n-1)}{2}We^2\dot{\gamma}^2\right)\frac{\partial^2\psi}{\partial x\partial y}, \tag{19}$$

$$\dot{\gamma} = \left[2\delta^2\left(\frac{\partial^2\psi}{\partial x\partial y}\right)^2 + \left(\frac{\partial^2\psi}{\partial y^2} - \delta^2\frac{\partial^2\psi}{\partial x^2}\right)^2 + 2\delta^2\left(\frac{\partial^2\psi}{\partial y\partial x}\right)^2\right]^{\frac{1}{2}}, \tag{20}$$

Removing pressure from Eqs. (13) and (14), provides

$$\frac{\partial^2}{\partial y^2}\left[\frac{\partial^2 \psi}{\partial y^2}+\left(\frac{n-1}{2}\right)We^2\left(\frac{\partial^2 \psi}{\partial y^2}\right)^3\right]-M^2\frac{\partial^2 \psi}{\partial y^2}=0. \tag{21}$$

The dimensionless boundary constraints in the problem's wave frame as follows

$$\left.\begin{array}{l}\psi=0,\quad \dfrac{\partial^2 \psi}{\partial Y^2}=0,\quad \theta=0,\quad \Omega=0\quad at\quad y=0,\\ \psi=f^*,\quad \dfrac{\partial \psi}{\partial Y}+\alpha S_{xy}=-1,\quad \theta=1,\qquad \Omega=1\quad at\quad y=h=1+\phi\sin 2\pi x.\end{array}\right\}. \tag{22}$$

Here, we have considered f^* is the mean flow over a period

$$\Theta=f^*+1\,,\qquad f^*=\int_0^h \frac{\partial \psi}{\partial y}dy, \tag{23}$$

where $\Theta=\frac{Q}{ca}\quad and\quad f^*=\frac{q}{ca}$.

Using Ms-DTM with symbolic Mathematica tools, the Eqs. (19)–(21) with the boundary conditions (22) are solved.

The Skin friction coefficient (wall shear stress), Nusselt number (heat transfer rate) and Sherwood number (mass transfer rate) are presented in forms [27, 28]:

$$C_f=-\frac{\partial u}{\partial y}\Big]_{y=h}, \tag{24}$$

$$N_u=-\frac{\partial \theta}{\partial y}\Big]_{y=h}, \tag{25}$$

$$S_h=-\frac{\partial \Omega}{\partial y}\Big]_{y=h} \tag{26}$$

2.1 Multi-step Differential Transformation Method

Let us take a function $u(z)$ that is analytical in a domain T and let $_{z=z_0}$ any point denoted in T. The function $u(z)$ is then expressed by a power series with the centre placed at z_0. The differential transformation of the function $u(z)$ is written as

$$U(k)=\frac{1}{K!}\left[\frac{d^k u(z)}{dz^k}\right]_{z=z_0} \tag{27}$$

The original function $u(z)$ and the transformed function $U(k)$ are here. The conversion of the inverse is given as

$$u(z) = \sum_{k=0}^{\infty} (z - z_0)^k U(k). \tag{28}$$

From above Eqs. (27) and (28), we get

$$u(z) = \sum_{k=0}^{\infty} \frac{(z - z_0)^k}{K!} \left[\frac{d^k u(z)}{dz^k} \right]_{z=z_0} \tag{29}$$

The technique does not symbolically test the derivatives, and the concept of DTM is obtained from Taylor series expansion.

The function $u(z)$ is given by a finite series and Eq. (27) written in the form of

$$u(z) \cong \sum_{k=0}^{\infty} (z - z_0)^k U(k). \tag{30}$$

It gives that $u(z) = \sum_{k-m+1}^{\infty} (z - z_0)^k U(k)$ is neglected as it is small. Also, the convergence of the series coefficients decides the value of m.

2.2 Method of Solution

We can get the solution of the Eqs. (19–21) with the suitable boundary constraints (22) using the Multi-step DTM as follows:

$$\begin{aligned}
&(k+4)(k+3)(k+2)(k+1)\Psi(k+4) + \left(\frac{n-1}{2}\right) \\
&6We^2 \sum_{l_2=0}^{k} \sum_{l_1=0}^{l_2} \Psi(l_1+2)\Psi(l_2-l_1+3)\Psi(k-l_2+3) \\
&(l_1+1)(l_1+2)(l_2-l_1+1)(l_2-l_1+2) \\
&(l_2-l_1+3)(k-l_2+1)(k-l_2+2)(k-l_2+3) + \\
&\left(\frac{n-1}{2}\right) 3We^2 \sum_{l_2=0}^{k} \sum_{l_1=0}^{l_2} \Psi(l_1+4)\Psi(l_2-l_1+2) \\
&\Psi(k-l_2+2)(l_1+4)(l_1+3)(l_1+2)(l_1+1) \\
&(l_2-l_1+1)(l_2-l_1+2)(k-l_2+1)(k-l_2+2) \\
&-M^2(k+2)(k+1)\Psi(k+2) = 0
\end{aligned} \tag{31}$$

$$\begin{aligned}
&(k+2)(k+1)\Theta(k+2) + B_r \sum_{l=0}^{k} (l+1)(l+2)\Psi(l+2) \\
&(k-l+1)(k-l+2)\Psi(k-l+2) + \left(\frac{n-1}{2}\right) We^2 \\
&\sum_{l_3=0}^{k} \sum_{l_2=0}^{l_3} \sum_{l_1=0}^{l_2} \Psi(l_1+2)\Psi(l_2-l_1+2)\Psi(l_3-l_2+2)\Psi(k-l_3+2) \\
&(l_1+1)(l_1+2)(l_2-l_1+1)(l_2-l_1+2)(l_3-l_2+1)(l_3-l_2+2) \\
&(k-l_3+1)(k-l_3+2) + \beta\,\delta(k-0) = 0
\end{aligned} \tag{32}$$

$$\left(\frac{1}{S_c}\right)(k+2)(k+1)\Phi(k+2) + S_r(k+2)(k+1)\Theta(k+2) = 0 \tag{33}$$

where $\Psi[k]$, Θ[k] and $\Phi[k]$ and are the differential transformation functions of $\psi(y)$, $\theta(y)$ and $\Omega(y)$ respectively and given as

$$\psi(y) \cong \sum_{k=0}^{m} \Psi(k) y^k, \tag{34}$$

$$\theta(y) \cong \sum_{k=0}^{m} \Theta(k) y^k, \tag{35}$$

$$\Omega(y) \cong \sum_{k=0}^{m} \Phi(k) y^k, \tag{36}$$

The transformed form of boundary conditions areas follows

$$\begin{aligned} &\Psi(0) = 0, \quad \Psi(1) = a, \quad \Psi(2) = 0, \quad \Psi(3) = \frac{b}{6}, \\ &\Theta(0) = 0, \quad \Theta(1) = c, \quad \Phi(0) = 0, \quad \Phi(1) = d. \end{aligned} \tag{37}$$

where a, b, c, d are unknown coefficients that must be determined.

Putting Eq. (37) into Eqs. (21)–(33) and other values ofΨ[k], Θ[k] and $\Phi[k]$ can be determined by the recursive method. Hence, substitute all $\Psi[k]$, Θ[k] and $\Phi[k]$ into Eqs. (34)–(36), We have a series of solutions as

$$\psi(y) = ay + \frac{b}{6}y^3 + \left(\frac{M^2 b - 3we^2(n-1)b^3}{125}\right)y^5 + \ldots \tag{38}$$

$$\theta(y) = cy + \frac{\beta}{2}y^2 - \left(\frac{B_r b^2}{12}\right)y^4 + \ldots \tag{39}$$

$$\Omega(y) = dy - \left(\frac{S_c S_r \beta}{2}\right)y^2 + \left(\frac{S_c S_r B_r b^2}{12}\right)y^3 + \ldots \tag{40}$$

Differentiating Eq. (38) partially with respect to y we get the velocity equation as

$$U(y) = a + \frac{b}{2}y^2 + \left(\frac{M^2 b - 3we^2(n-1)b^3}{24}\right)y^4 + \ldots \tag{41}$$

Using boundary conditions of Eq. (22) we can obtain the values of a, b, c, d.

$$a \to 0, b \to -1.9231537254,$$

$$c \to 0.9813324, d \to 0.000307692.$$

3 Results and Discussion

The system of non-linear coupled partial differential equations is obtained from the above description. Exact solutions are difficult to achieve when solving explicitly. The problem in hand is approximated semi-analytically using Multi-step-Differential Transformation Method with Mathematica software and graphical results are drawn in Origin software. Here we discuss the development of velocity, temperature and concentration profiles corresponding to the variation of velocity slip α, Hartman number M, Weissenberg number We, Power law index n, heat source and sink parameter β, Brinkman number B_r, Skin friction coefficient C_f, Nusselt number N_u, Sherwood number S_h, ΔP Pressure gradient, Schmidt number S_c and Soret number S_r.

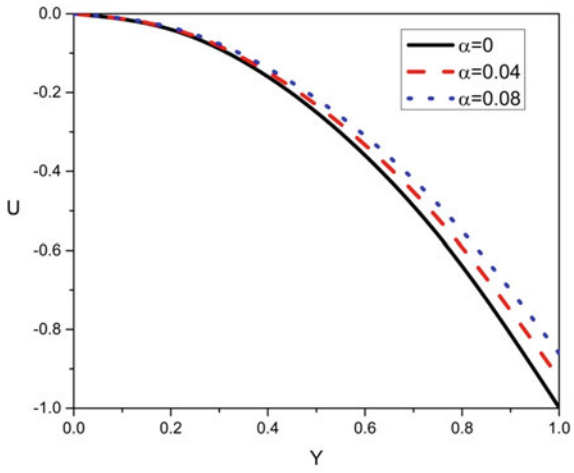

Fig. 2 Velocity distribution for various values of velocity slip parameter α with $M = 0.1,\ n = 2,\ We = 0.1,\ \beta = 0.1,\ B_r = 0.1,\ S_c = S_r = 0.1$

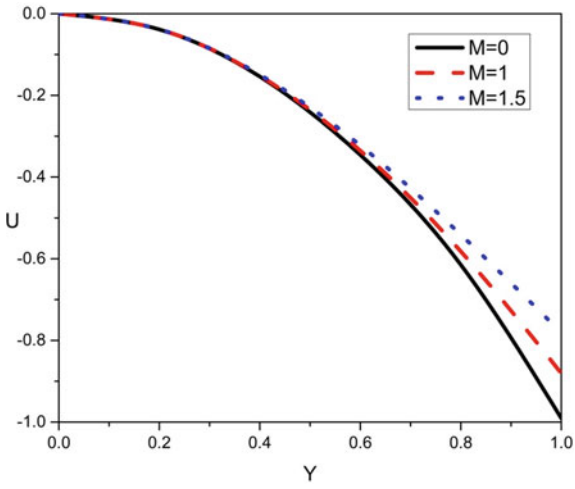

Fig. 3 Velocity profile for various values of Hartman number M with $\alpha = 0.02,\ n = 2,\ We = 0.1,\ \beta = 0.1,\ B_r = 0.1,\ S_c = S_r = 0.1$

3.1 Velocity Profile

The effects of α,M,We and n on velocity profile $u(y)$ are presented through Figs. 2 and 5. It is seen from Fig. 2 that velocity in peristaltic pumping increases with enhancing the magnitudes of velocity slip α. It is discovered that enhancing α, decreases the velocity of the fluid in the channel's central part while raising it near the channel's walls. For larger levels of the velocity slip characteristic, the momentum barrier layer is smaller. Figure 3 shows that the velocity near the centre of the channel surface diminishes by enhancing the Hartman number M. An opposite outcome is observed near the surface. The magnetic parameter is the ratio of electromagnetic force to viscous force from a physical aspect, and large magnitudes of the magnetic characteristic indicate that the Lorentz force enhances, resulting in increased resistance to transport phenomena and a decrease in fluid velocity. As a result, the thickness of the momentum barrier layer drops as the magnetic factor increases. Figures 4 and 5 shows that velocity profile decreases with enhancing the values of Weissenberg number We and Power law index n.

3.2 Temperature Profile

Figures 6 and 7 are prepared to examine the temperature via β and B_r. Figure 6 shows the increase in temperature by enhancing the values of the heat source and sink parameter β. Figure 7 demonstrates the nature of the temperature pattern for several values of the Brinkman number B_r. The heat function and irregular heat factors are inversely proportional. Heat producers are irregular heat parameters with positive values. As a result, the boundary layer discharges a significant quantity of

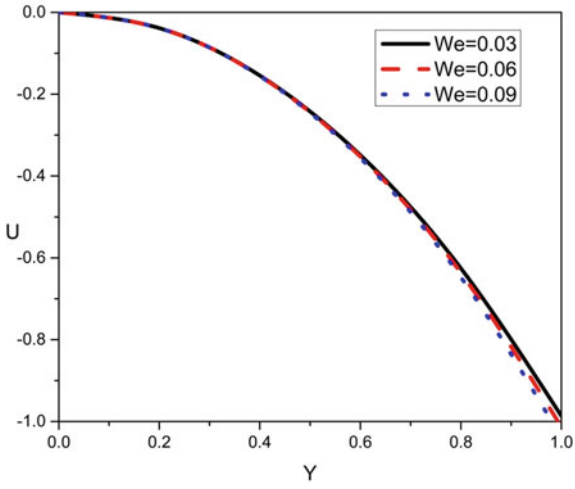

Fig. 4 Velocity distribution for various values of Weissenberg number We. $M = 0.1,\ n = 2,\ \alpha = 0.02,\ \beta = 0.1,\ B_r = 0.1,\ S_c = S_r = 0.1$

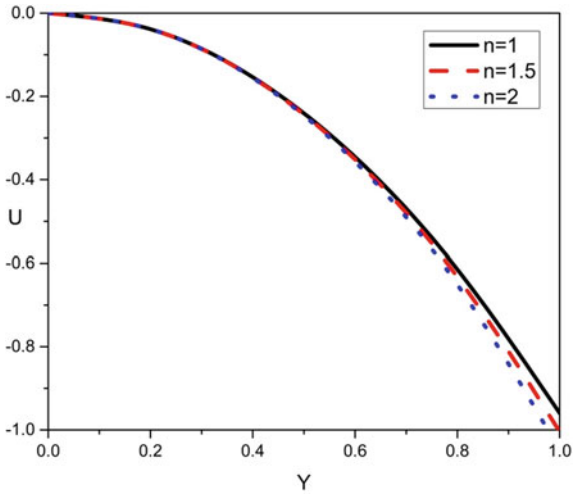

Fig. 5 Velocity distribution for various values of power law index n. $M = 0.1,\ We = 0.1,\ \alpha = 0.02,\ \beta = 0.1,\ B_r = 0.1,\ S_c = S_r = 0.1$

thermal energy into the flow, resulting in an increase in the fluid's temperature. As a result, temperature profiles are boosted by heat source/sink parameters that are temperature and space dependent.

3.3 Concentration Profile

Figures 8, 9, 10 and 11 demonstrate that the concentration profile of the nanoparticle is clarified by the effects of β, B_r,S_c and S_r. It is observed from Fig. 8 that concentration

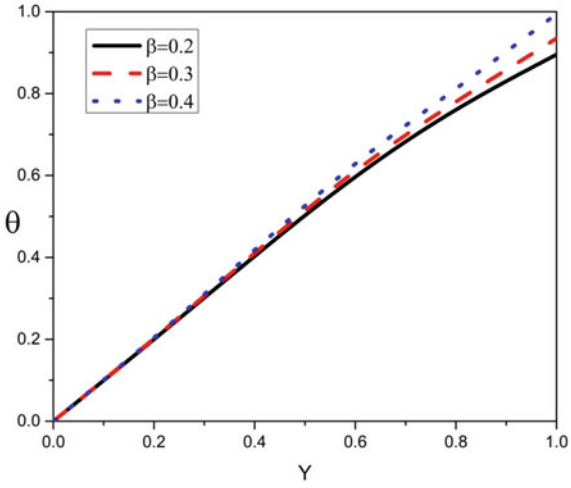

Fig. 6 Temperature distribution for various values of non-uniform heat source and sink parameter β. $M = 0.1$, $We = 0.1$, $\alpha = 0.02$, $n = 2$, $B_r = 0.8$, $S_c = S_r = 0.1$

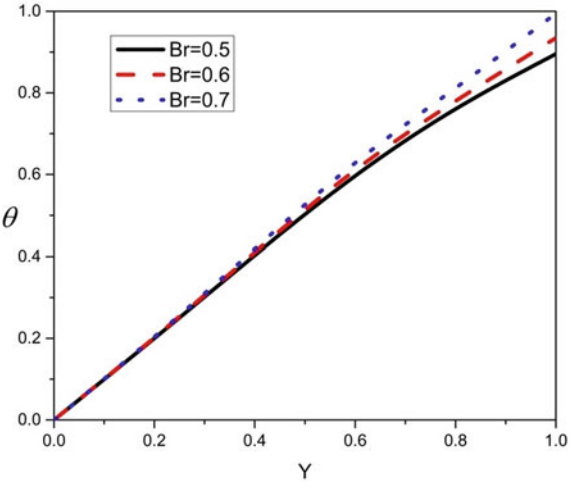

Fig. 7 Temperature distribution for various values of Brinkman number B_r. $M = 0.1$, $We = 0.1$, $\alpha = 0.02$, $n = 2$, $\beta = 0.2$, $S_c = S_r = 0.1$

in peristaltic motion lessens by enhancing the values of heat source and sink parameter β. Figure 9 demonstrates the nature of the concentration profile for different values of the Brinkman number B_r. Figure 10 shows that Schmidt number S_c have an increasing effect on concentration. Schmidt number S_c is a rate of viscous diffusion to molecular diffusion. Hence, a greater Schmidt number S_c enhances the rate of viscous diffusion. A substantial increase in concentration is seen by enhancing the Soret number S_r (see Fig. 11). The ratio of the thermodiffusion coefficient to the diffusion coefficient is known as the Soret number.

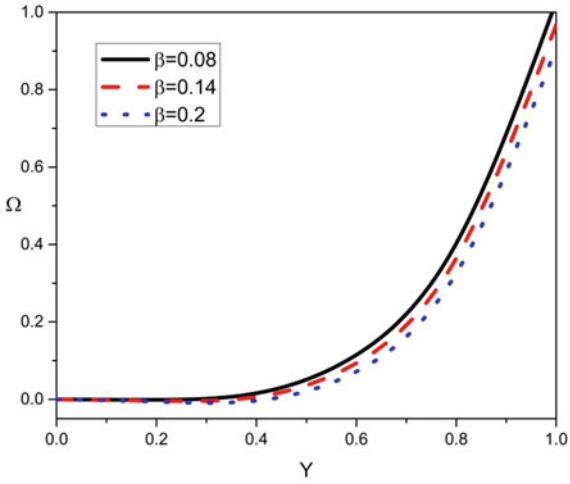

Fig. 8 Concentration distribution for various values of non-uniform heat source and sink parameter β. $M = 0.1,\ We = 0.1,\ \alpha = 0.02,\ n = 2,\ B_r = 1.8,\ S_c = 2,\ S_r = 1$

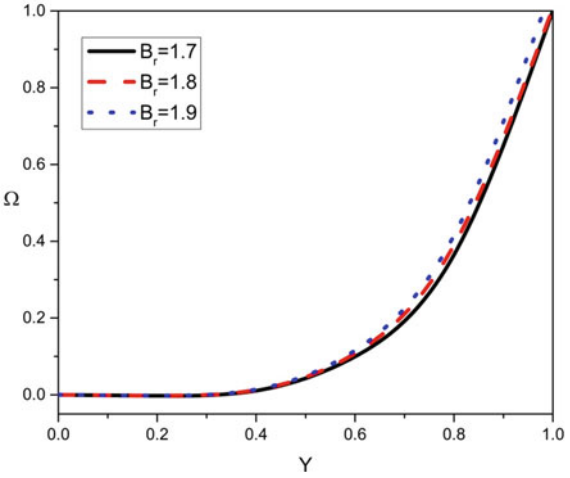

Fig. 9 Concentration distribution for various values of Brinkman number B_r. $M = 0.1,\ We = 0.1,\ \alpha = 0.02,\ n = 2,\ \beta = 0.1,\ S_c = 2,\ S_r = 1$

3.4 Impact of Phycical Parameters

Shear stress, rate of heat transfer, and rate of mass transfer on the channel walls progress as a real fluid flows through it. As a result, the distribution of the (shear stress) skin friction coefficient, (mass transfer rate) Sherwood number, and the (heat transfer rate) Nusselt number are discussed in this subsection for a wide range of physical constant values. It is observed from Fig. 12 that skin friction coefficient rises by enhancing the values of velocity slip α. Figure 13 demonstrates the nature of skin friction coefficient for different values of the Hartmann number M. Figure 14 shows the Nusselt number N_u diminishes as the heat source and sink parameter β

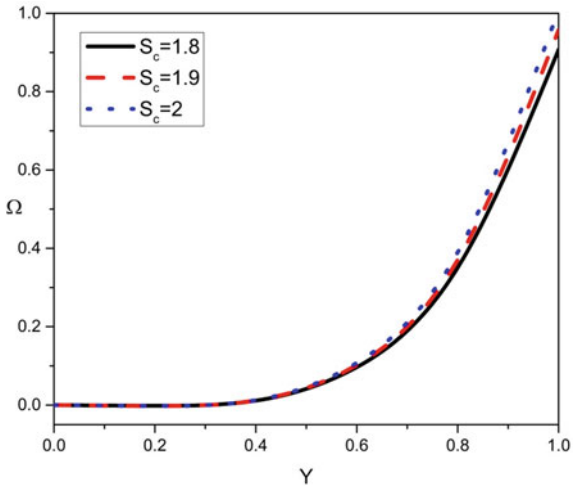

Fig. 10 Concentration distribution for various values of Schmidt number S_c. $M = 0.1,\ We = 0.1,\ \alpha = 0.02,\ n = 2,\ \beta = 0.1,\ B_r = 1.8,\ S_r = 1$

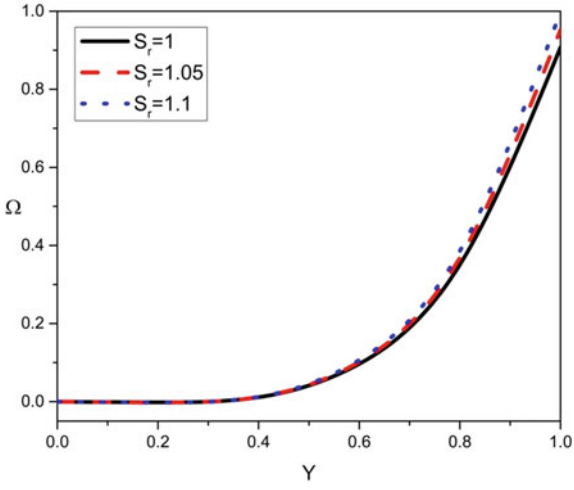

Fig. 11 Concentration profile for various values of Soret number S_r. $M = 0.1,\ We = 0.1,\ \alpha = 0.02,\ n = 2,\ \beta = 0.1,\ B_r = 1.8,\ S_c = 1.8$

fall. A substantial increase in the Nusselt number is seen by enhancing the Brinkman number B_r (see Fig. 15). Figures 16 and 17 show that the Schmidt number S_c and Soret number S_r have a decreasing effect on the Sherwood number S_h. It is seen that the relation between pressure rise in contrast to the time averaged flow rate is linear and inversely proportional to each other. The variations of pressure rise versus mean flow for different values of velocity slip α is illustrated in Fig. 18. The effect of the Hartmann number M on the streamline pattern is shown in Figs. 19 and 20. The volume of the trapped bolus decreases with increasing M. The effect of the velocity slip parameter on the streamline pattern is shown in Figs. 21 and 22. From this figure,

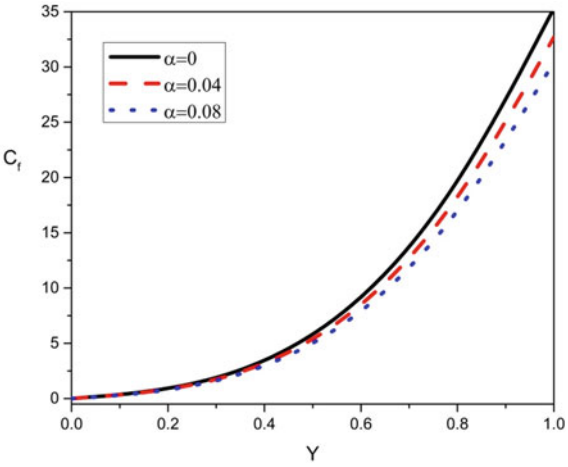

Fig. 12 Skin friction coefficient for various values of velocity slip α. $M = 0.1,\ n = 2,\ We = 0.1,\ \beta = 0.1,\ B_r = 0.1,\ S_c = S_r = 0.1$

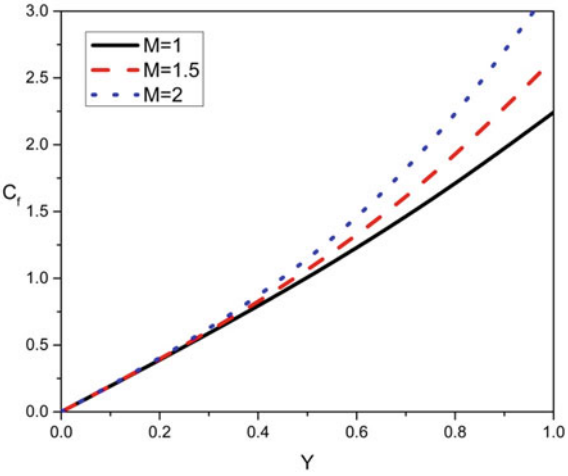

Fig. 13 Skin friction coefficient for various values of Hartman number M. $\alpha = 0.02,\ n = 2,\ We = 0.1,\ \beta = 0.1,\ B_r = 0.1,\ S_c = S_r = 0.1$

we observe that the size of the trapping bolus increases with the increasing velocity slip parameter α.

4 Conclusion

In this study, we investigated the effect of partial slip circumstances and MHD on peristaltic transport of a Carreau fluid in a flexible channel with a heat source or sink parameter under the assumptions of long wavelength and low Reynolds number. Graphs are used to examine the flow characteristics' behaviour.

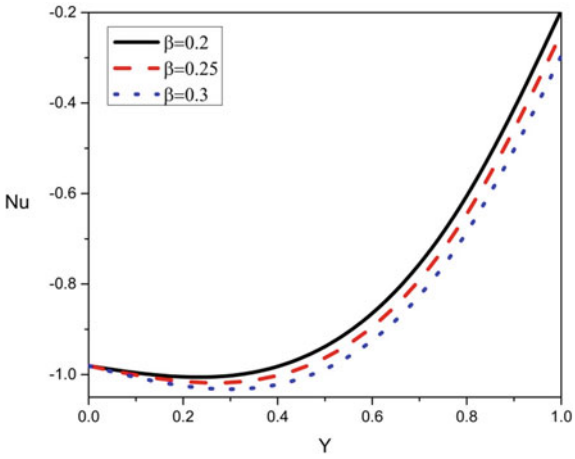

Fig. 14 Nusselt number for various values of non-uniform heat source and sink parameter β. $M = 0.1,\ We = 0.1,\ \alpha = 0.02,\ n = 2,\ B_r = 0.8,\ S_c = S_r = 0.1$

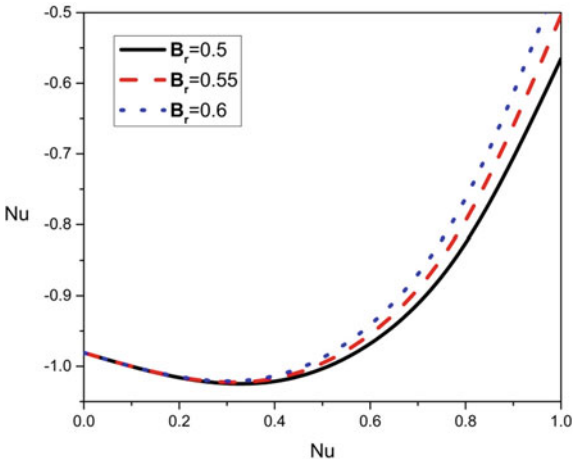

Fig. 15 Nusselt number for various values of Brinkman number B_r. $M = 0.1,\ We = 0.1,\ \alpha = 0.02,\ n = 2,\ \beta = 0.2,\ S_c = S_r = 0.1$

The following are the key findings of this study:

- The velocity appears to be increasing with enhancing the values of velocity slip α. The velocity near the centre of the channel wall diminishes by enhancing M, while opposite outcomes are observed near the wall.
- It is observed that the temperature increases with increasing the magnitudes of heat generation or absorption sink parameter β and Brinkman number B_r.
- It is observed that concentration diminishes with enhancing the magnitudes of heat source and sink parameter β. A substantial increase in concentration is seen by enhancing the Brinkman number B_r, Soret number S_r and Schmidt number S_c.
- It is observed that skin friction coefficient rises by enhancing the values of velocity slip α. The Nusselt number N_u diminishes as the heat source and sink parameter

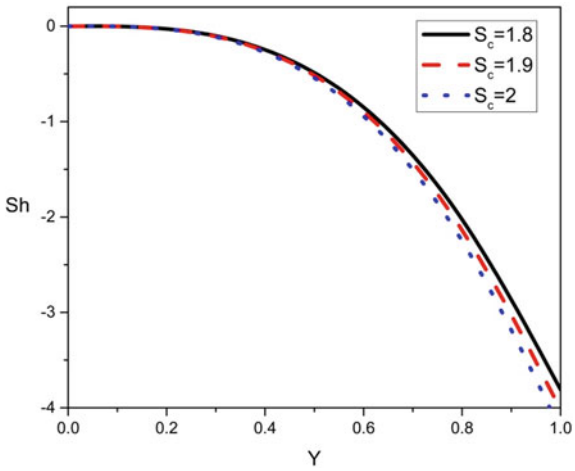

Fig. 16 Sherwood number for various values of Brinkman number S_c. $M = 0.1,\ We = 0.1,\ \alpha = 0.02,\ n = 2,\ \beta = 0.1,\ B_r = 1.8,\ S_r = 1$

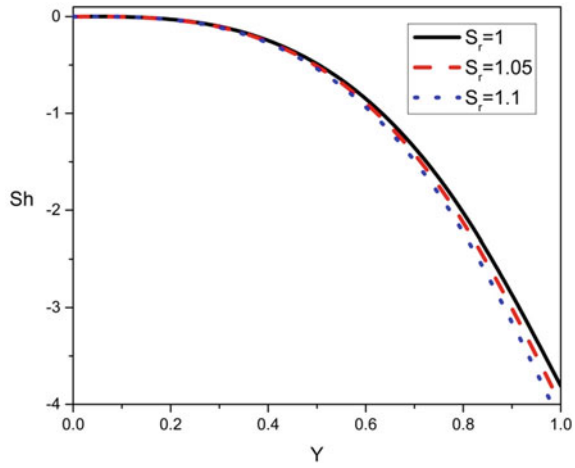

Fig. 17 Sherwood number for various values of Brinkman number S_r. $M = 0.1,\ We = 0.1,\ \alpha = 0.02,\ n = 2,\ \beta = 0.1,\ B_r = 1.8,\ S_c = 1.8$

β falls. A substantial increase in the Nusselt number is seen by enhancing the Brinkman number B_r. Schmidt number S_c and Soret number S_r have a decreasing effect on Sherwood number S_h.

- The effect of the velocity slip parameter on the streamline pattern is that the size of the trapping bolus increases with the increasing velocity slip parameter α. The effect of the Hartmann number M on the streamline pattern is that the volume of the trapped bolus decreases with increasing M.

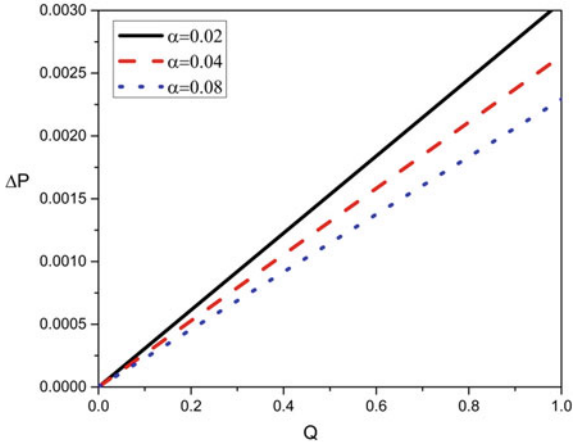

Fig. 18 Variation of ΔP for various values of velocity slip α.
$M = 0.1,\ n = 2,\ We = 0.1$

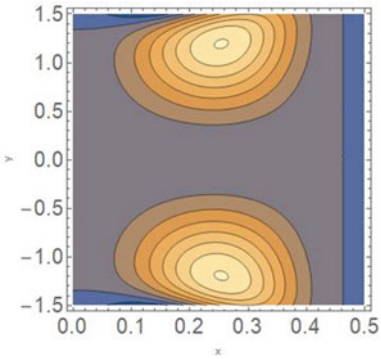

Fig. 19 Effect of M on stream lines when M = 1.5

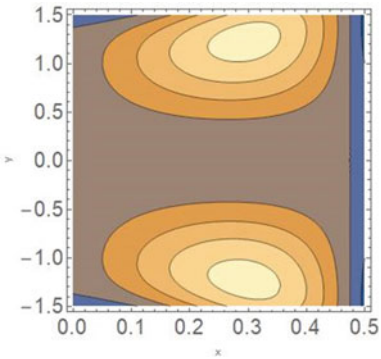

Fig. 20 Effect of M on stream lines when M = 1.6

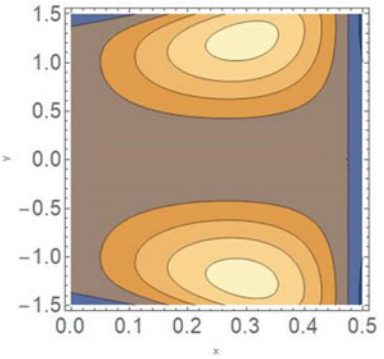

Fig. 21 Effect of velocity slip α on stream lines when $\alpha = 0.02$

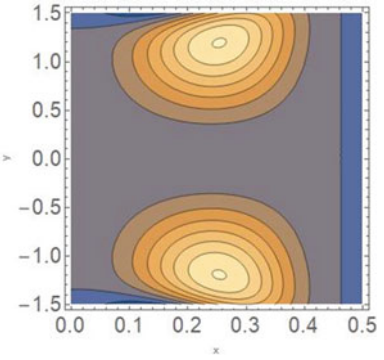

Fig. 22 Effect of velocity slip α on stream lines when $\alpha = 0.04$

Acknowledgements Author Asha S. K is thankful to the Karnataka University, Dharwad for their financial support under the Seed grant for the research programme [KU/PMEB/2021/77 dated 25/06/2021]. Author Joonabi Beleri would like to thank the Directorate of Minorities for their financial support [DOMWDD/Ph.D//FELLOWSHIP/CR-01/2019-20] Date: 15.10.2019.

Disclosure Statement We report that we have no potential conflict of interest with any other author.

References

1. Latham TW (1966) Fluid motion in a peristaltic pump. M.S. thesis. MIT, Cambridge
2. Shapiro AH, Jaffrin MY, Weinberg SL (1969) Peristaltic pumping with long wavelengths at low Reynolds number. J Fluid Mech 37(4):799–825
3. Jaffrinand MY, Shapiro AH (1971) Peristaltic pumping. Annu Rev Fluid Mech 3(1):13–37
4. Asha SK, Sunita G (2017) Effect of couple stress in peristaltic transport of blood flow by homotopy analysis method. AJST 12:6958–6964
5. Hayat T, Rafiq M, Ahmad B (2016) Soret and Dufour effects on MHD peristaltic flow of Jeffrey fluid in a rotating system with porous medium. PLoS ONE 11(1):e0145525
6. Navier CLMH (1823) Mémoire sur les lois du mouvement des fluids. Mémoires de l'Académie Royale des Sciences de l'Institut de France 6:389–440

7. Nadeem S, Akram S (2010) Heat transfer in a peristaltic flow of MHD fluid with partial slip. Comm Nonlinear Sci Numer Simulat 1:312–321
8. Ali N, Hussian Q, Hayat T, Asghar S (2008) Slip effects on the peristaltic transport of MHD fluid with variable viscosity. Phys Lett 372:1477–1489
9. Srinivas S, Gayathri R, Kothandapani M (2009) The influence of slip conditions, wall properties and heat transfer on MHD peristaltic transport. Comput Phys Commun 180:2115–2122
10. Akram S, Nadeemand S, Hussain A (2015) Partial slip consequences on peristaltic transport of Williamson fluid in an asymmetric channel. Walailak J Sci Technol (WJST) 12(10):885–908
11. Hayat T, Tanveer A, Alsaedi A (2016) Numerical analysis of partial slip on peristalsis of MHD Jeffery nanofluid in curved channel with porous space. J Mol Liq 224:944–953
12. Hina S, Yasin M (2018) Slip effects on peristaltic flow of magnetohydrodynamics second grade fluid through a flexible channel with heat/mass transfer. J Therm Sci Eng Appl 10(5)
13. Khan M (2016) Flow and heat transfer to Sisko fluid with partial slip. Can J Phys 94(8):724–730
14. Rehman M, Noreen S, Haider A, Azam H (2015) Effect of heat sink/source on peristaltic flow of Jeffrey fluid through a symmetric channel. Alex Eng J 54(3):733–743
15. Sheriff S, Mir NA, Ahmad S (2020) Numerical analysis of heat source/sink on peristalsis of MHD carbon-water nanofluid in symmetric channel with permeable space. Adv Mech Eng 12(10):1687814020967181
16. Rahman MM, Uddin MJ, Aziz A (2009) Effects of variable electric conductivity and non-uniform heat source (or sink) on convective micropolar fluid flow along an inclined flat plate with surfaceheat flux. Int J Therm Sci 48(12):2331–2340
17. Benazir AJ,Sivaraj R, Rashidi MM, Vijayaragavan R. Magnetohydrodynamic mixed convective flow of Casson fluid in a channel with non-uniform heat source/sink
18. Mahanthesh B (2020) Magnetohydrodynamic flow of Carreau liquid over a stretchable sheet with a variable thickness: the biomedical applications. Multidisc Model Mater Struct
19. Hayat T, Qayyum S, Alsaedi A, Asghar S (2017) Radiation effects on the mixed convection flow induced by an inclined stretching cylinder with non-uniform heat source/sink. PLoS ONE 12(4):e0175584
20. Hayat T, Saleem N, Asghar S, Alhothualiand MS, Alhomaidan A (2011) Influence of induced magnetic field and heat transfer on peristaltic transport of a Carreau fluid. Commun Nonlinear Sci Numer Simul 16(9):3559–3577
21. Machireddyand GR, Naramgari S (2018) Heat and mass transfer in radiative MHD Carreau fluid with cross diffusion. Ain Shams Eng J 9(4):1189–1204
22. Khan M, Azam M (2017) Unsteady heat and mass transfer mechanisms in MHD Carreau nanofluid flow. J Mol Liq 225:554–562
23. Goqo S (2020) Unsteady flow of Jeffrey nanofluid: a numerical simulation by bivariate simple iteration method
24. Gupta S, Kumar D, Singh J (2020) Analytical study for MHD flow of Williamson nanofluid with the effects of variable thickness, nonlinear thermal radiation and improved Fourier's and Fick's Laws. SN Appl Sci 2(3):1–12
25. Gupta S, Kumar D, Singh J, Gupta S (2019) Impact of generalized Fourier's law and Fick's law for MHD flow of Ag–H2O and TiO2–H2O nanomaterials. Multidisc Model Mater Struct
26. Gupta S, Kumar D, Singh J (2019) Magnetohydrodynamic three-dimensional boundary layer flow and heat transfer of water-driven copper and alumina nanoparticles induced by convective conditions. Int J Mod Phys B 33(26):1950307
27. Reddy KV, Reddy MG, Makinde OD (2021) Heat and mass transfer of a peristaltic electro-osmotic flow of a couple stress fluid through an inclined asymmetric channel with effects of thermal radiation and chemical reaction. Period Polytech Mech Eng 65(2):151–162
28. Vaidya H, Rajashekhar C, Prasad KV, Khan SU, Riaz A, Viharika JU (2021) MHD peristaltic flow of nanofluid in a vertical channel with multiple slip features: an application to chyme movement. Biomech Model Mechanobiol 20(3):1047–1067
29. Vaidya H, Rajashekhar C, Manjunatha G, Prasad KV, Makinde OD, Vajravelu K (2020) Heat and mass transfer analysis of MHD peristaltic flow through a complaint porous channel with variable thermal conductivity. Phys Scr 95(4):045219

30. Zhou JK (1986) Differential transformation and its applications for electrical circuits. Huazhong University Press, Wuhan, China, pp 1279–1289
31. Odibat ZM, Bertelle C, Aziz-Alaoui MA, Duchamp GH (2010) A multi-step differential transform method and application to non-chaotic or chaotic systems. Comput Math Appl 59(4):1462–1472
32. Nourifar M, Sani AA, Keyhani A (2017) Efficient multi-step differential transform method: theory and its application to nonlinear oscillators. Commun Nonlinear Sci Numer Simul 53:154–183
33. Keimanesh M, Rashidi MM, Chamkha AJ, Jafari R (2011) Study of a third-grade non-Newtonian fluid flow between two parallel plates using the multi-step differential transform method. Comput Math Appl 62(8):2871–2891
34. Hatami M, Sheikholeslami M, Domairry G (2014) High accuracy analysis for motion of a spherical particle in plane Couette fluid flow by multi-step differential transformation method. Powder Technol 260:59–67
35. Hatami M, Ganji DD (2014) Motion of a spherical particle on a rotating parabolausing Lagrangian and high accuracy multi-step differential transformation method. Powder Technol 258:94–98
36. Hasona WM, El-Shekhipy A, Ibrahim MG (2019) Semi-analytical solution to MHD peristaltic flow of a Jeffrey fluid in presence of Joule heat effect by using multi-step differential transforms method. New Trends Math Sci 7(2):123–137
37. Mirzaaghaian A, Ganji DD (2016) Application of differential transformation method in micropolar fluid flow and heat transfer through permeable walls. Alex Eng J 55(3):2183–2191
38. Akram S (2014) Effects of nanofluid on peristaltic flow of a Carreau fluid model in an inclined magnetic field. Heat Transf Asian Res 43(4):368–383
39. Vajravelu K, Sreenadh S, Saravana R (2013) Combined influence of velocity slip, temperature and concentration jump conditions on MHD peristaltic transport of a Carreau fluid in a non-uniform channel. Appl Math Comput 225:656–676

Invariant Preserving Schemes for Multi-symplectic Integrator of Two Long Waves' Interactions

Ram Dayal Pankaj

Abstract The concept of discrete conservation of symplecticity to discretization for two long waves' interactions is presented. This property is endemic and we express that it also leads to exact discrete conservation of momentum and energy for the propagation of two long waves' interactions. This restricted property is stronger than the global property which that synthesis over all spatial framework points leads to a distinct symplectic scheme in the time route. Multi-symplectic integrators are earned for the propagation of two long waves' interactions and investigate the conservation properties of multi-symplectic integrators. Numerical simulations are also offered.

Keywords Multi-symplectic integrators · Two long waves' interactions · Numerical simulations

1 Introduction

Physical phenomena and processes occurring in nature usually have complicated nonlinear effects. Most of the physical phenomena are described by an appropriate set of nonlinear partial differential equations. A modal which describes the two long waves' interactions through different dispersion relations is called nonlinear-coupled Korteweg-de Vries (NCKDV) system [1] as follows:

$$\begin{aligned} &\Psi_t - \alpha\Psi_{xxx} - \left[3\alpha\Psi^2 + \beta\upsilon^2\right]_x = 0 \\ &\upsilon_t + \upsilon_{xxx} + 3\Psi\upsilon_x = 0 \end{aligned} \tag{1}$$

where both α and β are nonzero positive parameters and $\Psi(x,t)$ *and* $\upsilon(x,t)$ are the function of x and t. This system is used for wave-wave interactions in different media [2–4]. Currently, many analytic methods [5–15] and numerical methods [16–26] have been applied to constructing the exact solutions of nonlinear evolution equations

R. D. Pankaj (✉)
Department of Mathematics, J.N.V. University, Jodhpur, Rajasthan, India
e-mail: drrdpankaj@yahoo.com

J. Singh et al. (eds.), *Advances in Mathematical Modelling, Applied Analysis and Computation*, Lecture Notes in Networks and Systems 415,
https://doi.org/10.1007/978-981-19-0179-9_21

(NLEEs). In this assignment, we will discretize the propagation of the CKDV system with a new six-point scheme, which is a correspondent finite difference scheme and explain the multi-symplectic structure. The benefit of this structure will be provided with evidence by numerical simulations.

2 Multi-symplectic Integrator of Two Long Waves' Interactions

We take $E(x,t)$, $\eta(x,t)$, $\theta(x,t)$ and$\phi(x,t)$ as the functions of x and t, such as $\Psi = E(x,t) + i\eta(x,y)$, $\upsilon = \theta(x,t) + i\phi(x,y)$ put in Eq. (1) and we get

$$E_t - \alpha E_{xxx} - 6\alpha\{EE_x + \eta\eta_x\} - 2\beta\{\theta\theta_x - \phi\phi_x\} = 0 \tag{2}$$

$$\eta_t - \alpha\eta_{xxx} - 6\alpha\{\eta E_x + \eta E_x\} - 2\beta\{\theta\phi_x + \phi\theta_x\} = 0 \tag{3}$$

$$\theta_t + \theta_{xxx} + 3\{E\theta_x - \eta\phi_x\} = 0 \tag{4}$$

$$\phi_t + \phi_{xxx} + 3\{\eta\theta_x + E\phi_x\} = 0 \tag{5}$$

Announcing the recognized momenta

$$E_x = p, \eta_x = r, \theta_x = \hbar, \phi_x = m, p_x = q, r_x = s, \hbar_x = I, m_x = k \tag{6}$$

The system may be transcribed as follows:

$$A\omega_t + B\omega_x = \nabla_\omega F(\omega) \tag{7}$$

where x and t are independent variables belonging to $\mathbb{R}^2$, ω is a state variable belonging to $\mathbb{R}^d$ with $d \geq 2$ and F: $\mathbb{R}^d \to \mathbb{R}$ is a scalar-valued smooth function, ∇_ω as benchmark gradient in $\mathbb{R}^d$ for $F(\omega)$, $\nabla_\omega F(\omega)$, $\omega_x = \frac{\partial\omega}{\partial x}$ and $\omega_t = \frac{\partial\omega}{\partial t}$. In the sense of a multi-symplectic integrator for the model, A is a square matrix of 12×12 order for t trend and B is the same as in x trend and F as Hamiltonian [18, 19, 21]. Eq. (7) is a multi-symplectic structure for model equation Eq. (1) with the state variables

$$\omega = (E, \eta, p, r, \theta, \phi, \hbar, m, q, s \cdot I, k)^T \in \mathbb{R}^{12}$$

Then we get the multi-symplectic structure for the model equation

$$
\begin{aligned}
E_x &= p,\\
\eta_x &= r,\\
\theta_x &= \hbar\,,\\
\phi_x &= m\,,\\
p_x &= q,\\
r_x &= s\,,\\
\hbar_x &= I,\\
m_x &= k\,,
\end{aligned}
$$

$$E_t - \alpha q_x - 6\alpha\{Ep + \eta r\} - 2\beta\{\theta\hbar - \phi m\} = 0$$

$$\eta_t - \alpha s_x - 6\alpha\{p\eta - Er\} - 2\beta\{\theta m + \phi\hbar\} = 0$$

$$\theta_t + I_x + 3\{E\hbar - \eta m\} = 0$$

$$\phi_t + k_x + 3\{\eta\hbar + Em\} = 0$$

so that $\nabla_\omega S(\xi) = (E, \eta, p, r, \theta, \phi, \hbar, m, q, s \cdot I, k)$, and the pair of skew-symmetric matrices A and B are

$$A = \begin{bmatrix}
1&0&0&0&0&0&0&0&0&0&0&0\\
0&1&0&0&0&0&0&0&0&0&0&0\\
0&0&0&0&0&0&0&0&0&0&0&0\\
0&0&0&0&0&0&0&0&0&0&0&0\\
0&0&0&0&1&0&0&0&0&0&0&0\\
0&0&0&0&0&1&0&0&0&0&0&0\\
0&0&0&0&0&0&0&0&0&0&0&0\\
0&0&0&0&0&0&0&0&0&0&0&0\\
0&0&0&0&0&0&0&0&0&0&0&0\\
0&0&0&0&0&0&0&0&0&0&0&0\\
0&0&0&0&0&0&0&0&0&0&0&0\\
0&0&0&0&0&0&0&0&0&0&0&0
\end{bmatrix}
B = \begin{bmatrix}
0&0&0&0&0&0&0&0&0&0&0&0\\
0&0&0&0&0&0&0&0&0&0&0&0\\
0&0&0&0&0&0&0&0&0&0&0&0\\
0&0&0&0&0&0&0&0&0&0&0&0\\
0&0&0&0&0&0&0&0&0&0&0&0\\
0&0&0&0&0&0&0&0&0&0&0&0\\
0&0&0&0&0&0&0&0&0&0&0&0\\
0&0&0&0&0&0&0&0&0&0&0&0\\
0&0&0&0&0&0&0&0&0&0&0&0\\
0&0&0&0&0&0&0&0&$-\alpha$&0&0&0\\
0&0&0&0&0&0&0&0&0&$-\alpha$&0&0\\
0&0&0&0&0&0&0&0&0&0&1&0\\
0&0&0&0&0&0&0&0&0&0&0&1
\end{bmatrix}$$

So as

$$A \approx \chi = \begin{bmatrix} 1&0&0&0\\ 0&1&0&0\\ 0&0&1&0\\ 0&0&0&1 \end{bmatrix}, \text{ with eigen value one (1)}$$

$$B \approx \kappa = \begin{bmatrix} -\alpha & 0 & 0 & 0 \\ 0 & -\alpha & 0 & 0 \\ 0 & 0 & 1 & 0 \\ 0 & 0 & 0 & 1 \end{bmatrix}, \text{ with eigen value one (1) and } -\alpha$$

Applying the midpoint finite difference method for discretizing multi-symplectic integrator of NCKDV systems (multi-symplectic structure for model equations) respectively, we shall be able to get

$$\frac{E_{l+1}^{n+1/2} - E_l^{n+1/2}}{\Delta x} = p_{l+1/2}^{n+1/2} = \hat{p} \tag{8}$$

$$\frac{\eta_{l+1}^{n+1/2} - \eta_l^{n+1/2}}{\Delta x} = r_{l+1/2}^{n+1/2} = \hat{r} \tag{9}$$

$$\frac{p_{l+1}^{n+1/2} - p_l^{n+1/2}}{\Delta x} = q_{l+1/2}^{n+1/2} = \hat{q} \tag{10}$$

$$\frac{r_{l+1}^{n+1/2} - r_l^{n+1/2}}{\Delta x} = s_{l+1/2}^{n+1/2} = \hat{s} \tag{11}$$

$$\frac{\theta_{l+1}^{n+1/2} - \theta_l^{n+1/2}}{\Delta x} = \hbar_{l+1/2}^{n+1/2} = \hat{\hbar} \tag{12}$$

$$\frac{\phi_{l+1}^{n+1/2} - \phi_l^{n+1/2}}{\Delta x} = m_{l+1/2}^{n+1/2} = \hat{m} \tag{13}$$

$$\frac{\hbar_{l+1}^{n+1/2} - \hbar_l^{n+1/2}}{\Delta x} = I_{l+1/2}^{n+1/2} = \hat{I} \tag{14}$$

$$\frac{m_{l+1}^{n+1/2} - m_l^{n+1/2}}{\Delta x} = k_{l+1/2}^{n+1/2} = \hat{k} \tag{15}$$

$$\frac{E_{l+1/2}^{n+1} - E_{l+1/2}^{n}}{\Delta t} - \alpha \frac{q_{l+1}^{n+1/2} - q_l^{n+1/2}}{\Delta x} = \left[6\alpha \left(\hat{E}\,\hat{p} - \hat{\eta}\hat{r} \right) + 3\beta \left(\hat{\theta}\hat{\hbar} - \hat{\phi}\hat{m} \right) \right] \tag{16}$$

$$\frac{\eta_{l+1/2}^{n+1} - \eta_{l+1/2}^{n}}{\Delta t} - \alpha \frac{s_{l+1}^{n+1/2} - s_l^{n+1/2}}{\Delta x} = \left[6\alpha \left(\hat{\eta}\hat{p} + \hat{E}\hat{r} \right) + 3\beta \left(\hat{\theta}\hat{m} + \hat{\phi}\hat{\hbar} \right) \right] \tag{17}$$

$$\frac{\theta_{l+1/2}^{n+1} - \theta_{l+1/2}^{n}}{\Delta t} + \frac{I_{l+1}^{n+1/2} - I_l^{n+1/2}}{\Delta x} = 3\left(\hat{\eta}\hat{m} - \hat{E}\hat{\hbar} \right) \tag{18}$$

$$\frac{\phi_{l+1/2}^{n+1}-\phi_{l+1/2}^{n}}{\Delta t}+\frac{k_{l+1}^{n+1/2}-k_{l}^{n+1/2}}{\Delta x}=-3\left(\hat{E}\hat{m}+\hat{\eta}\hat{\hbar}\right) \tag{19}$$

where $\hat{E}=E_{l+1/2}^{n+1/2},\ \hat{\eta}=\eta_{l+1/2}^{n+1/2},\ \hat{\theta}=\theta_{l+1/2}^{n+1/2},\ \hat{\phi}=\phi_{l+1/2}^{n+1/2}$.

We eliminate $p, r, \hbar, m, q, s, I$ *and* k. From the above equations, therefore, we derive from Eqs. (16), (17), (18) and (19), respectively

$$\begin{aligned}&\frac{E_{l+1/2}^{n+1}-E_{l+1/2}^{n}+E_{l+3/2}^{n+1}-E_{l+3/2}^{n}}{\Delta t}-\alpha\frac{\left(E_{l+2}^{n+1/2}-3E_{l+1}^{n+1/2}+3E_{l}^{n+1/2}-E_{l-1}^{n+1/2}\right)}{(\Delta x)^3}\\&-\frac{3\alpha}{(\Delta x)}\left(\left(E_{l+2}^{n+1/2}E_{l+2}^{n+1/2}-E_{l}^{n+1/2}E_{l}^{n+1/2}\right)-\left(\eta_{l+2}^{n+1/2}\eta_{l+2}^{n+1/2}-\eta_{l}^{n+1/2}\eta_{l}^{n+1/2}\right)\right)\\&-\frac{\beta}{(\Delta x)}\left(\left(\theta_{l+2}^{n+1/2}\theta_{l+2}^{n+1/2}-\theta_{l}^{n+1/2}\theta_{l}^{n+1/2}\right)-\left(\phi_{l+2}^{n+1/2}\phi_{l+2}^{n+1/2}-\phi_{l}^{n+1/2}\phi_{l}^{n+1/2}\right)\right)=0\end{aligned} \tag{20}$$

$$\begin{aligned}&\frac{\eta_{l+1/2}^{n+1}-\eta_{l+1/2}^{n}+\eta_{l+3/2}^{n+1}-\eta_{l+3/2}^{n}}{\Delta t}-\alpha\frac{\left(\eta_{l+2}^{n+1/2}-3\eta_{l+1}^{n+1/2}+3\eta_{l}^{n+1/2}-\eta_{l-1}^{n+1/2}\right)}{(\Delta x)^3}\\&-\frac{6\alpha}{(\Delta x)}\left(E_{l+2}^{n+1/2}\eta_{l+2}^{n+1/2}-E_{l}^{n+1/2}\eta_{l}^{n+1/2}\right)-\frac{2\beta}{(\Delta x)}\left(\theta_{l+2}^{n+1/2}\phi_{l+2}^{n+1/2}-\theta_{l}^{n+1/2}\phi_{l}^{n+1/2}\right)=0\end{aligned} \tag{21}$$

$$\begin{aligned}&\frac{\theta_{l+1/2}^{n+1}-\theta_{l+1/2}^{n}+\theta_{l+3/2}^{n+1}-\theta_{l+3/2}^{n}}{\Delta t}+\frac{\left(\theta_{l+2}^{n+1/2}-3\theta_{l+1}^{n+1/2}+3\theta_{l}^{n+1/2}-\theta_{l-1}^{n+1/2}\right)}{(\Delta x)^3}\\&+\frac{3}{2(\Delta x)}\left\{\begin{array}{l}\left(E_{l+2}^{n+1/2}\theta_{l+2}^{n+1/2}-E_{l+2}^{n+1/2}\theta_{l+1}^{n+1/2}+E_{l+1}^{n+1/2}\theta_{l+2}^{n+1/2}-E_{l+1}^{n+1/2}\theta_{l}^{n+1/2}+E_{l}^{n+1/2}\theta_{l+1}^{n+1/2}-E_{l}^{n+1/2}\theta_{l}^{n+1/2}\right)\\-\left(\eta_{l+2}^{n+1/2}\phi_{l+2}^{n+1/2}-\eta_{l+2}^{n+1/2}\phi_{l+1}^{n+1/2}+\eta_{l+1}^{n+1/2}\phi_{l+2}^{n+1/2}-\eta_{l+1}^{n+1/2}\phi_{l}^{n+1/2}+\eta_{l}^{n+1/2}\phi_{l+1}^{n+1/2}-\eta_{l}^{n+1/2}\phi_{l}^{n+1/2}\right)\end{array}\right\}=0\end{aligned} \tag{22}$$

$$\begin{aligned}&\frac{\phi_{l+1/2}^{n+1}-\phi_{l+1/2}^{n}+\phi_{l+3/2}^{n+1}-\phi_{l+3/2}^{n}}{\Delta t}+\frac{\left(\phi_{l+2}^{n+1/2}-3\phi_{l+1}^{n+1/2}+3\phi_{l}^{n+1/2}-\phi_{l-1}^{n+1/2}\right)}{(\Delta x)^3}\\&+\frac{3}{2(\Delta x)}\left\{\begin{array}{l}\left(E_{l+2}^{n+1/2}\phi_{l+2}^{n+1/2}-E_{l+2}^{n+1/2}\phi_{l+1}^{n+1/2}+E_{l+1}^{n+1/2}\phi_{l+2}^{n+1/2}-E_{l+1}^{n+1/2}\phi_{l}^{n+1/2}+E_{l}^{n+1/2}\phi_{l+1}^{n+1/2}-E_{l}^{n+1/2}\phi_{l}^{n+1/2}\right)\\+\left(\eta_{l+2}^{n+1/2}\theta_{l+2}^{n+1/2}-\eta_{l+2}^{n+1/2}\theta_{l+1}^{n+1/2}+\eta_{l+1}^{n+1/2}\theta_{l+2}^{n+1/2}-\eta_{l+1}^{n+1/2}\theta_{l}^{n+1/2}+\eta_{l}^{n+1/2}\theta_{l+1}^{n+1/2}-\eta_{l}^{n+1/2}\theta_{l}^{n+1/2}\right)\end{array}\right\}=0\end{aligned} \tag{23}$$

The multi-symplectic integrators container be rewritten in this discretization shape

$$\begin{aligned}&\phi_{n+1}^{m+1/2}=\frac{\left(\phi_{n+1}^{m+1}+\phi_{n+1}^{m}\right)}{2},\ \phi_{n+1}^{m+1}+\phi_{n}^{m+1}-2\phi_{n+1/2}^{m+1}=0\\&\phi_{n+1}^{m}+\phi_{n}^{m}+\phi_{n+1}^{m+1}+\phi_{n}^{m+1}-4\phi_{n+1/2}^{m+1/2}=0\end{aligned}$$

where ϕ_n^m is an estimate of $\phi(m\Delta t, n\Delta x)$.

Then we apply (20) + i (iota) (21) and (22) + i (iota) (23). We can get respectively

$$\begin{aligned}&\frac{\left(\Psi_{l-1}^{n+1}+2\Psi_{l}^{n+1}+\Psi_{l-1}^{n+1}\right)-\left(\Psi_{l+1}^{n}+2\Psi_{l}^{n}+\Psi_{l-1}^{n}\right)}{2\Delta t}\\&-\alpha\frac{\left(\Psi_{l+2}^{n+1}-\Psi_{l+2}^{n}\right)-2\left(\Psi_{l+1}^{n+1}-\Psi_{l+1}^{n}\right)+2\left(\Psi_{l-1}^{n+1}-\Psi_{l-1}^{n}\right)+\left(\Psi_{l-2}^{n+1}-\Psi_{l-2}^{n}\right)}{2(\Delta x)^3}\end{aligned}$$

$$-\frac{3\alpha}{(\Delta x)}\left(\Psi_{l+2}^{n+1/2}\Psi_{l+2}^{n+1/2}-\Psi_{l}^{n+1/2}\Psi_{l}^{n+1/2}\right)-\frac{\beta}{(\Delta x)}\left(\upsilon_{l+2}^{n+1/2}\upsilon_{l+2}^{n+1/2}-\upsilon_{l}^{n+1/2}\upsilon_{l}^{n+1/2}\right)=0 \tag{24}$$

$$\begin{aligned}&\frac{\left(\upsilon_{l-1}^{n+1}+2\upsilon_{l}^{n+1}+\upsilon_{l-1}^{n+1}\right)-\left(\upsilon_{l+1}^{n}+2\upsilon_{l}^{n}+\upsilon_{l-1}^{n}\right)}{2\Delta t}\\&+\frac{\left(\upsilon_{l+2}^{n+1}-\upsilon_{l+2}^{n}\right)-2\left(\upsilon_{l+1}^{n+1}-\upsilon_{l+1}^{n}\right)+2\left(\upsilon_{l-1}^{n+1}-\upsilon_{l-1}^{n}\right)+\left(\upsilon_{l-2}^{n+1}-\upsilon_{l-2}^{n}\right)}{2(\Delta x)^{3}}\\&-\frac{3}{2(\Delta x)}\left(\Psi_{l+2}^{n+1/2}\upsilon_{l+2}^{n+1/2}-\Psi_{l+2}^{n+1/2}\upsilon_{l+1}^{n+1/2}+\Psi_{l+1}^{n+1/2}\upsilon_{l+2}^{n+1/2}-\Psi_{l+1}^{n+1/2}\upsilon_{l}^{n+1/2}+\Psi_{l}^{n+1/2}\upsilon_{l+1}^{n+1/2}-\Psi_{l}^{n+1/2}\upsilon_{l}^{n+1/2}\right)=0\end{aligned} \tag{25}$$

And we get

$$\begin{aligned}&\frac{\left(\Psi_{l-1}^{n+1}+2\Psi_{l}^{n+1}+\Psi_{l-1}^{n+1}\right)-\left(\Psi_{l+1}^{n}+2\Psi_{l}^{n}+\Psi_{l-1}^{n}\right)}{2\Delta t}\\&-\alpha\frac{\left(\Psi_{l+2}^{n+1}-\Psi_{l+2}^{n}\right)-2\left(\Psi_{l+1}^{n+1}-\Psi_{l+1}^{n}\right)+2\left(\Psi_{l-1}^{n+1}-\Psi_{l-1}^{n}\right)+\left(\Psi_{l-2}^{n+1}-\Psi_{l-2}^{n}\right)}{2(\Delta x)^{3}}\\&-\frac{3\alpha}{(\Delta x)}\left\{\left(\Psi_{l+1}^{n+1/2}+\Psi_{l-1}^{n+1/2}\right)\left(\Psi_{l+1}^{n+1/2}-\Psi_{l-1}^{n+1/2}\right)\right\}-\frac{\beta}{(\Delta x)}\left\{\left(\upsilon_{l+1}^{n+1/2}+\upsilon_{l-1}^{n+1/2}\right)\left(\upsilon_{l+1}^{n+1/2}-\upsilon_{l-1}^{n+1/2}\right)\right\}=0\end{aligned} \tag{26}$$

$$\begin{aligned}&\frac{\left(\upsilon_{l-1}^{n+1}+2\upsilon_{l}^{n+1}+\upsilon_{l-1}^{n+1}\right)-\left(\upsilon_{l+1}^{n}+2\upsilon_{l}^{n}+\upsilon_{l-1}^{n}\right)}{2\Delta t}\\&+\frac{\left(\upsilon_{l+2}^{n+1}-\upsilon_{l+2}^{n}\right)-2\left(\upsilon_{l+1}^{n+1}-\upsilon_{l+1}^{n}\right)+2\left(\upsilon_{l-1}^{n+1}-\upsilon_{l-1}^{n}\right)+\left(\upsilon_{l-2}^{n+1}-\upsilon_{l-2}^{n}\right)}{2(\Delta x)^{3}}\\&-\frac{3}{2(\Delta x)}\left(\Psi_{l+1}^{n+1/2}\upsilon_{l+1}^{n+1/2}-\Psi_{l+1}^{n+1/2}\upsilon_{l}^{n+1/2}+\Psi_{l}^{n+1/2}\upsilon_{l+1}^{n+1/2}-\Psi_{l}^{n+1/2}\upsilon_{l-1}^{n+1/2}+\Psi_{l-1}^{n+1/2}\upsilon_{l}^{n+1/2}-\Psi_{l-1}^{n+1/2}\upsilon_{l-1}^{n+1/2}\right)=0\end{aligned} \tag{27}$$

So, in (26) and (27), we get a six-point difference scheme for Ψ and υ, and this can be treated as a multi-symplectic integrator.

3 Conservation Property for Multi-symplectic Integrators

For conservation properties investigation and verify the average norm conservation property of two long waves' interactions, we rewrite Eq. (26) with the help of discretization

$$\begin{aligned}&\frac{1}{2\Delta t}\left(\Psi_{l-1/2}^{n+1}-\Psi_{l-1/2}^{n}\right)+\left(\Psi_{l+1/2}^{n+1}-\Psi_{l+1/2}^{n}\right)\\&-\frac{\alpha}{(\Delta x)^{3}}\left(\Psi_{l+2}^{n+1/2}-3\Psi_{l+1}^{n+1/2}+3\Psi_{l}^{n+1/2}-\Psi_{l-1}^{n+1/2}\right)\\&-\frac{3\alpha}{(\Delta x)}\left\{\left(\Psi_{l+1}^{n+1/2}\right)^{2}-\left(\Psi_{l-1}^{n+1/2}\right)^{2}\right\}-\frac{\beta}{(\Delta x)}\left\{\left(\upsilon_{l+1}^{n+1/2}\right)^{2}-\left(\upsilon_{l-1}^{n+1/2}\right)^{2}\right\}=0\end{aligned} \tag{28}$$

Taking complex conjugate

$$\frac{1}{2\Delta t}\overline{\left(\Psi_{l-1/2}^{n+1}-u_{l-1/2}^{n}\right)}+\overline{\left(\Psi_{l+1/2}^{n+1}-\Psi_{l+1/2}^{n}\right)}-\frac{\alpha}{(\Delta x)^3}\overline{\left(\Psi_{l+2}^{n+1/2}-3\Psi_{l+1}^{n+1/2}+3\Psi_{l}^{n+1/2}-\Psi_{l-1}^{n+1/2}\right)}$$
$$-\frac{3\alpha}{(\Delta x)}\left\{\overline{\left(\Psi_{l+1}^{n+1/2}\right)^2-\left(\Psi_{l-1}^{n+1/2}\right)^2}\right\}-\frac{\beta}{(\Delta x)}\left\{\overline{\left(\upsilon_{l+1}^{n+1/2}\right)^2-\left(\upsilon_{l-1}^{n+1/2}\right)^2}\right\}=0 \tag{29}$$

For Eq. (28), take $l=1,2,3\ldots N$ and multiple $\overline{\Psi_l^{n+1/2}}$ we can get

$$\frac{1}{2\Delta t}\sum_{l=1}^{N}\left\{\left(\Psi_{l-1/2}^{n+1}-\Psi_{l-1/2}^{n}\right)+\left(\Psi_{l+1/2}^{n+1}-\Psi_{l+1/2}^{n}\right)\right\}\overline{\Psi_l^{n+1/2}}$$
$$-\frac{\alpha}{(\Delta x)^3}\sum_{l=1}^{N}\left(\Psi_{l+2}^{n+1/2}-3\Psi_{l+1}^{n+1/2}+3\Psi_{l}^{n+1/2}-\Psi_{l-1}^{n+1/2}\right)\overline{\Psi_l^{n+1/2}}$$
$$-\frac{3\alpha}{(\Delta x)}\sum_{l=1}^{N}\left\{\left(\Psi_{l+1}^{n+1/2}\right)^2-\left(\Psi_{l-1}^{n+1/2}\right)^2\right\}\overline{\Psi_l^{n+1/2}}-\frac{\beta}{(\Delta x)}\sum_{l=1}^{N}\left\{\left(\upsilon_{l+1}^{n+1/2}\right)^2-\left(\upsilon_{l-1}^{n+1/2}\right)^2\right\}\overline{\Psi_l^{n+1/2}}=0 \tag{30}$$

In Eq. (29), take $l=1,2,3,\ldots N$ and multiply $\Psi_l^{n+1/2}$ we can get

$$\frac{1}{2\Delta t}\sum_{l=1}^{N}\overline{\left(\Psi_{l-1/2}^{n+1}-\Psi_{l-1/2}^{n}\right)}+\overline{\left(\Psi_{l+1/2}^{n+1}-\Psi_{l+1/2}^{n}\right)}\Psi_l^{n+1/2}-\frac{\alpha}{(\Delta x)^3}\sum_{l=1}^{N}\overline{\left(\Psi_{l+2}^{n+1/2}-3\Psi_{l+1}^{n+1/2}+3\Psi_{l}^{n+1/2}-\Psi_{l-1}^{n+1/2}\right)}\Psi_l^{n+1/2}$$
$$-\frac{3\alpha}{(\Delta x)}\sum_{l=1}^{N}\left\{\overline{\left(\Psi_{l+1}^{n+1/2}\right)^2-\left(\Psi_{l-1}^{n+1/2}\right)^2}\right\}\Psi_l^{n+1/2}-\frac{\beta}{(\Delta x)}\sum_{l=1}^{N}\left\{\overline{\left(\upsilon_{l+1}^{n+1/2}\right)^2-\left(\upsilon_{l-1}^{n+1/2}\right)^2}\right\}\Psi_l^{n+1/2}=0 \tag{31}$$

In Eq. (30), we have

$$\sum_{l=1}^{N}\left(\Psi_{l-1/2}^{n+1}-\Psi_{l-1/2}^{n}\right)\overline{\Psi_l^{n+1/2}}=\sum_{l=1}^{N}\left(\Psi_{l+1/2}^{n+1}-\Psi_{l+1/2}^{n}\right)\overline{\Psi_l^{n+1/2}}+\left(\Psi_{1/2}^{n+1}-\Psi_{1/2}^{n}\right)\overline{\Psi_l^{n+1/2}}-\left(\Psi_{N+1/2}^{n+1}-\Psi_{N+1/2}^{n}\right)\overline{\Psi_{N+1}^{n+1/2}} \tag{32}$$

$$\sum_{l=1}^{N}\left(\Psi_{l+2}^{n+1/2}-3\Psi_{l+1}^{n+1/2}+3\Psi_{l}^{n+1/2}-\Psi_{l-1}^{n+1/2}\right)\overline{\Psi_l^{n+1/2}}$$
$$=\sum_{l=1}^{N}\left(\Psi_{l+2}^{n+1/2}\overline{\Psi_l^{n+1/2}}-3\Psi_{l+1}^{n+1/2}\overline{\Psi_l^{n+1/2}}-\Psi_{l}^{n+1/2}\overline{\Psi_{l+1}^{n+1/2}}\right)$$
$$+\sum_{l=1}^{N}\left|\Psi_l^{n+1}+\Psi_{l+1}^{n}\right|^2-3\Psi_0^{n+1/2}\overline{\Psi_l^{n+1/2}}+3\Psi_{N+1}^{n+1/2}\overline{\Psi_{N+1}^{n+1/2}} \tag{33}$$

$$\sum_{l=1}^{N}\left(\Psi_{l-1}^{n+1/2}\right)^2\overline{\Psi_l^{n+1/2}}=\sum_{l=1}^{N}\left(\Psi_{l}^{n+1/2}\right)^2\overline{\Psi_{l+1}^{n+1/2}}+\left(\Psi_{0}^{n+1/2}\right)^2\overline{\Psi_{1}^{n+1/2}}-\left(\Psi_{N}^{n+1/2}\right)^2\overline{\Psi_{N+1}^{n+1/2}} \tag{34}$$

$$\sum_{l=1}^{N}\upsilon_{l-1}^{n+1/2}\overline{\Psi_l^{n+1/2}}=\sum_{l=1}^{N}\left(\upsilon_{l}^{n+1/2}\overline{\Psi_{l+1}^{n+1/2}}\right)+\upsilon_{0}^{n+1/2}\overline{\Psi_{1}^{n+1/2}}-\upsilon_{N}^{n+1/2}\overline{\Psi_{N+1}^{n+1/2}} \tag{35}$$

Put these values from Eqs. (32) to (35) in Eq. (30). Similarly, we apply it for Eq. (31) and use the zero-boundary points situation for Eqs. (30) and (31), we can get the following conservation formula:

$$\sum_{l=1}^{N}\left(\left|\Psi_l^n+\Psi_{l+1}^n\right|^2\right)=\sum_{l=1}^{N}\left(\left|\Psi_l^{n+1}+\Psi_{l+1}^{n+1}\right|^2\right)$$

Similarly, with the average norm conservation property for Eq. (27), we can get the conservation formula

$$\sum_{l=1}^{N}\left(\left|\upsilon_l^n+\upsilon_{l+1}^n\right|^2\right)=\sum_{l=1}^{N}\left(\left|\upsilon_l^{n+1}+\upsilon_{l+1}^{n+1}\right|^2\right)$$

4 Numerical Simulations

For numerical results, we will focus on the screening of energy conservation properties for multi-symplectic integrators of the NCKDV system from Eq. (1)

$$\begin{aligned}&\Psi_t-\alpha\Psi_{xxx}-\left[3\alpha\,\Psi^2+\beta\upsilon^2\right]_x=0\\&\upsilon_t+\upsilon_{xxx}+3\Psi\,\upsilon_x=0\end{aligned}\tag{36}$$

with the initial value

$$\Psi(x,o)=\left(\frac{\hbar_1\left(1+\beta k^2\right)}{3\alpha}-4\beta k^2 sn^2\left(\hbar_1 x+\frac{\hat{\lambda}_0}{2}\right)\right)e^{i\theta x/4}$$

$$\upsilon(x,o)=2k^2\sqrt{\frac{-6\alpha}{\beta}}\hbar_2 sn^2\left(\hbar_2 x+\frac{1}{2}\hat{\lambda}_0\right)e^{-i\theta x/4}$$

where k^2 is the modulus of Jacobi elliptic function $sn\left(\hbar_1 x+\dfrac{\hat{\lambda}_0}{2};k\right)$.

5 Results and Discussion

The multi-symplectic scheme is embellished to locate a solitary wave solution of two long waves' interactions for the NCKDV system. The solitary wave solutions Figs. 1 and 2 and their interaction in Fig. 3 of this system exist for eigenvalue less than zero, which are similar to [22]. We learn that this method well emulates the development of soliton and energy conservation properties for the system. This scheme has shown the way for a long-playing computing truthfulness and preserves conservation property.

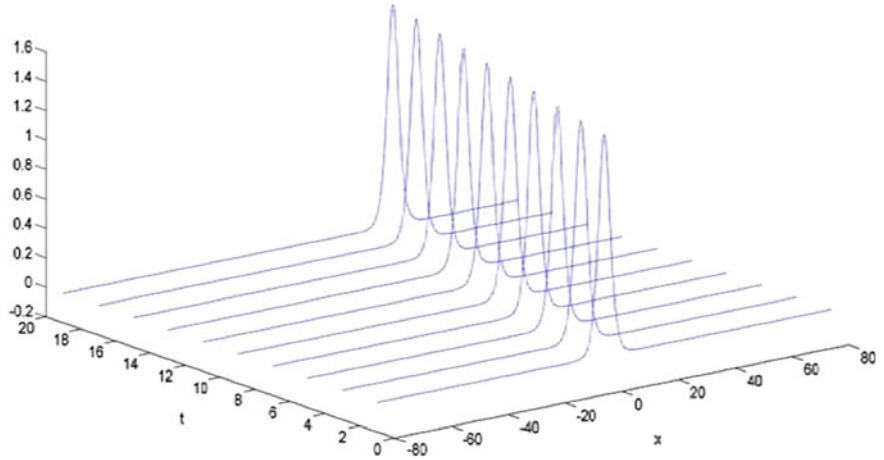

Fig. 1 Solitary wave motion of $\Psi(x, t)$ with $\Delta t = 0.1$ for $0 \leq t \leq 20$, $\Delta x = 0.2$ for $-80 \leq x \leq 80$, $\beta = 1$ and $\alpha = 1/3$

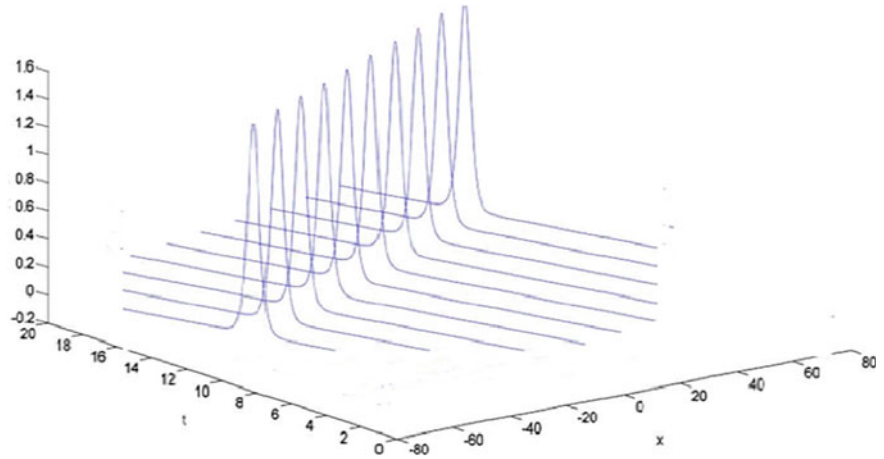

Fig. 2 Solitary wave motion of $|\upsilon(x, t)|$ with $\Delta t = 0.1$ for $0 \leq t \leq 20$ and $\Delta x = 0.2$ for $-80 \leq x \leq 80$, $\beta = 1$ and $\alpha = 1/3$

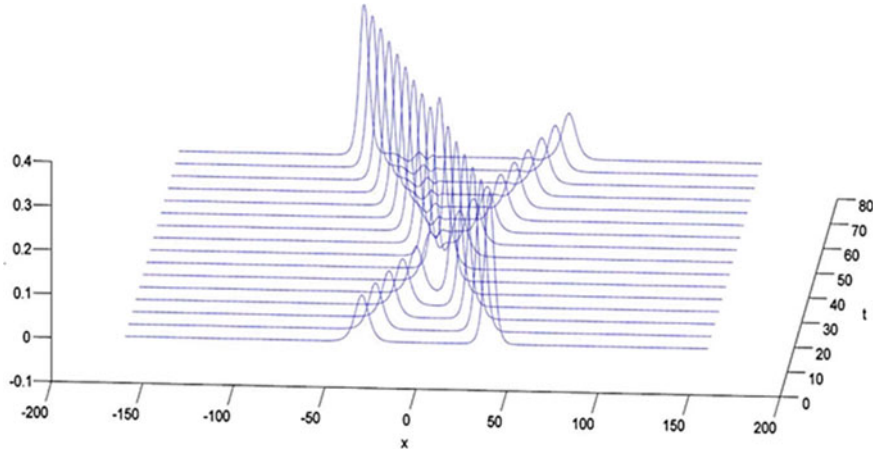

Fig. 3 Simulation results $\{\Psi^2 + \upsilon^2\}$ of two solitary wave interactions with $\hat{\lambda}_0 = 25, \theta = \pi/2$, $\hbar_1 = \hbar_2 = 1$, $\beta = 1$, $\alpha = 1/3$, $\Delta t = 0.1$ for $0 \leq t \leq 80$ and $\Delta x = 0.2$ for $-200 \leq x \leq 200$

References

1. Hirota R, Satsuma J (1981) Soliton solutions of a coupled Korteweg-de Vries equation. Phys Lett A 85(8–9):407–408
2. Halim AA, Kshevetskii SP, Leble SB (2003) Numerical integration of a coupled Korteweg-de-Vries system. Comput Math Appl 45(4–5):581–591
3. Halim AA, Leble SB (2004) Analytical and numerical solution of a coupled KdV-MKdV system. Chaos, Solitons Fractals 19(1):99–108
4. Sanz-Serna JM, Christie I (1981) Petrov-Galerkin methods for nonlinear dispersive waves. J Comput Phys 39(1):94–102
5. Zayed EME, Al-Joudi S (2009) The traveling wave solutions for nonlinear partial differential equations using the expansion method. Int J Nonlinear Sci 8(4):435–447
6. Wu Y, Geng X, Hu X, Zhu S (2009) A generalized Hiroota-Satauma coupled Kortewegde Vries equation and Miura transformations. Phys Lett A 255:259–264
7. Yepeng S, Bi J, Chen D (2005) N solitons solutions and double Wronskian solution of the non isospectral AKNS equation. Chaos Solitons Fractals 26(3):905–912
8. Sakka A (2002) Backland transformations for Painleve I and II equations to Painleve type equations of second order and higher degree. Phys Lett A 300(23):228–232
9. Kumar A, Pankaj RD (2014) Tanh-coth scheme for traveling wave solutions for Nonlinear Wave Interaction model. J Egyptian Math Soc 23(2):282–285. ISSN 1110-256X
10. Pankaj RD, Kumar A, Singh B (2020) Evolution of modulational instability in non-linear Hirota types equation. Sci Tech Asia 25(1):123–127
11. Liu Z, Chen C (2004) Compactons in a general compressible hyper elastic rod. Chaos Solitons Fractals 22(3):627–640
12. Kaya D, El Sayed SM (2003) An application of the decomposition method for the generalized KdV and RLW equations. Chaos Solitons Fractals 17(5):869–877
13. Kumar A, Pankaj RD (2015) Laplace-modified decomposition method for the generalized Hiroota-Satauma coupled Kdv equation. CJBAS 3(4):126–133
14. Kumar A, Pankaj RD (2013) Solitary Wave Solutions of Schrödinger Equation by Laplace Adomian Decomposition Method. Phys Rev Res Int 3(4):702–712

15. Pankaj RD (2021) A novel narration for propagation of wave in relaxing medium by expansion scheme. Adv Appl Math Sci 20(8):1517–1523
16. Ghoreishi M, Ismail AIB, Rashid A (2012) Numerical solution of Klein Gordon Zakharov equations using Chebyshev cardinal functions. J Comput Anal Appl 14(1):574–582
17. Xiaofei Z, Li Z (2013) Numerical methods and simulations for the dynamics of one dimensional Zakharov Rubenchik equations. J Sci Comput 59(2):412–438
18. Kumar A. Pankaj RD, Gaur M (2011) Finite difference scheme of a model for nonlinear wave-wave interaction in ionic media. Comput Math Model 22(3):255–265
19. Kumar A. Pankaj RD (2014) Finite difference scheme for the Zakharov equation as a model for nonlinear wave-wave interaction in ionic media. Int J Sci Eng Res 5(2): 759–762
20. Al-khaled K (2015) Numerical wave solutions for nonlinear coupled equations using Sinc-collocation method. Squ J Sci 20(2):19–30 (2015)
21. Pankaj RD, Kumar A, Singh B (2018) Multi-symplectic integrator for complex nonlinear system. J Chem Biol Phys Sci C 7(3):631–637
22. Ismail MS, Ashi HA (2014) A numerical solution for Hirota-Satsuma coupled KdV equation. Hindawi Publishing Corporation Abstract and Applied Analysis, vol 2014. Article ID 819367, 9 pp. https://doi.org/10.1155/2014/819367
23. Goswami A, Singh J, Kumar D (2018) Numerical simulation of fifth order KdV equations occurring in magneto-acoustic waves. Ain Shams Eng J 9(4):2265–2273
24. Goswami A, Singh J, Kumar D, Gupta S, Rathore S (2019) An efficient analytical technique for fractional partial differential equations occurring in ion acoustic waves in plasma. J Ocean Eng Sci 4(2):85–99. https://doi.org/10.1016/j.joes.2019.01.003
25. Goswami A, Singh J, Kumar D, Gupta S, Rathore S (2020) Numerical computation of fractional Kersten-Krasil'shchik coupled KdV-mKdV system occurring in multi-component plasmas. AIMS Math 5(3):2346–2368. https://doi.org/10.3934/math.2020155
26. Pankaj RD, Lal C (2021) Numerical elucidation of Klein-Gordon-Zakharov system. Jñānābha 51(1):207–212 (2021). Print ISSN 0304-9892, Online ISSN 2455-7463

Study of Effect of Overlapping Stenosis on Flow Field Considering Non-Newtonian Reiner Rivlin Blood Flow in Artery

Nibedita Dash and Sarita Singh

Abstract Stenosis, the abnormal narrowing of blood vessels resist blood flow significantly altering the flow field. The change is observed in blood flow velocity, pressure distribution, wall shear stress and resistance impedence parameters. The present paper aims to find the impact of overlapping stenosis relative to symmetric stenosis for different shape parameters on parameters of flow field. Governing conservation equations are formulated by incorporating Reiner Rivlin stress and strain constitutive relations suitable for blood rheology. From the literature the suitability of generalized Reiner Rivlin constitutive relation is reported to explain shear thinning, shear thickening and dilatancy effect. The solution for flow field is obtained for steady axi-symmetric case for both overlapping stenosis and axially symmetric for different shape parameters. The flow fields for symmetric and overlapping stenosis are compared to study the effect of overlapping stenosis relative to symmetric stenosis.

Keywords Arterial stenosis · Cross viscosity · Overlapping stenosis · Perturbation · Reiner-Rivlin · Symmetric stenosis

1 Introduction

The narrowing of blood vessels due to the deposition of the cholesterol and other fatty substances leads to a medical condition called stenosis. The etiological studies on stenosis suggests that deposition of calcium, fats and cholesterol on the inner walls of the artery resists blood flow significantly changing the flow field [1–3]. The change is observed in blood flow velocity, pressure distribution, wall shear stress and resistance impedance parameters. Therefore, it is imperative to understand the impact of overlapping stenosis on parameters of flow field.

N. Dash (✉) · S. Singh
Department of Mathematics, School of Physical Sciences, Doon University, Dehradun, India
e-mail: dashnibedita@yahoo.co.in

J. Singh et al. (eds.), *Advances in Mathematical Modelling, Applied Analysis and Computation*, Lecture Notes in Networks and Systems 415,
https://doi.org/10.1007/978-981-19-0179-9_22

Conventionally, Navier Stokes conservation equations are used as the boundary valued governing equations to develop mathematical model for flow field by incorporating stress and strain constitutive relations suitable for blood rheology. Shear stress–strain and viscosity of blood is greatly influenced by rate of shear, viscosity of plasma, blood composition, arterial diameter [1–3], aggregation, deformability and hardening of erythrocytes [4] and high shear rate induced dilatancy [5]. Conventional viscous inelastic models reported in literature suitably explains shear thinning viscosity, and yield stress, but fails to explain dilatancy effect. From the literature the suitability of generalized Reiner Rivlin constitutive relation [6] is observed to explain dilatancy effect. Since blood shows shear thinning and shear thickening properties along with dilatancy, it is appropriate to use Reiner Rivlin constitutive stress and strain relation in conservation equations to develop differential type model.

Therefore, in the present paper, conservation equations are formulated considering Reiner-Rivlin constitutive relation. The solution for flow field is obtained for steady axi-symmetric case for both axially symmetric and overlapping stenosis. The flow fields for symmetric and overlapping stenosis are compared to study the effect of overlapping stenosis relative to symmetric stenosis.

2 Formulation of Problem

A differential type Reiner Rivlin model has been developed in this paper by solving Navier–Stokes conservation equations for steady axis-symmetric case by considering following conditions.

1. If (r, θ, z) be the cylindrical-polar coordinate system with $r = 0$ is the axis of symmetry of artery, the cylindrical co-ordinate (r, z) is considered where, $\frac{\partial}{\partial\theta} = 0$.
2. Flow of blood in artery is considered as incompressible Reiner-Rivlin fluid, i.e. $\left(\frac{\partial\rho}{\partial t}\right) = \left(\frac{\partial\rho}{\partial r}\right) = \left(\frac{\partial\rho}{\partial z}\right) = 0$.
3. Steady flow of blood is considered. Thus, $\frac{\partial}{\partial t} = 0$. Viscosity is considered to be constant.
4. No slip boundary condition is considered ie. $\frac{\partial w}{\partial r} = 0$ at $r = 0$; $w = 0$ at $r = h_z$.

Considering above conditions, the conservation equations are:

$$\frac{\partial\overline{u}}{\partial\overline{r}} + \frac{\overline{u}}{\overline{r}} + \frac{\partial\overline{w}}{\partial\overline{z}} = 0 \tag{1}$$

$$\rho\left(\overline{u}\frac{\partial\overline{u}}{\partial\overline{r}} + \overline{w}\frac{\partial\overline{u}}{\partial\overline{z}}\right) = -\frac{\partial\overline{p}}{\partial\overline{r}} + \frac{1}{\overline{r}}\frac{\partial}{\partial\overline{r}}(\overline{r}\,\overline{\tau}_{\overline{r}\overline{r}}) + \frac{\partial\overline{\tau}_{\overline{z}\overline{r}}}{\partial\overline{z}} \tag{2}$$

$$\rho\left(\overline{u}\frac{\partial\overline{w}}{\partial\overline{r}} + \overline{w}\frac{\partial\overline{w}}{\partial\overline{z}}\right) = -\frac{\partial\overline{p}}{\partial\overline{z}} + \frac{1}{\overline{r}}\frac{\partial}{\partial\overline{r}}(\overline{r}\,\overline{\tau}_{\overline{z}\overline{r}}) + \frac{\partial\overline{\tau}_{\overline{z}\overline{z}}}{\partial\overline{z}} \tag{3}$$

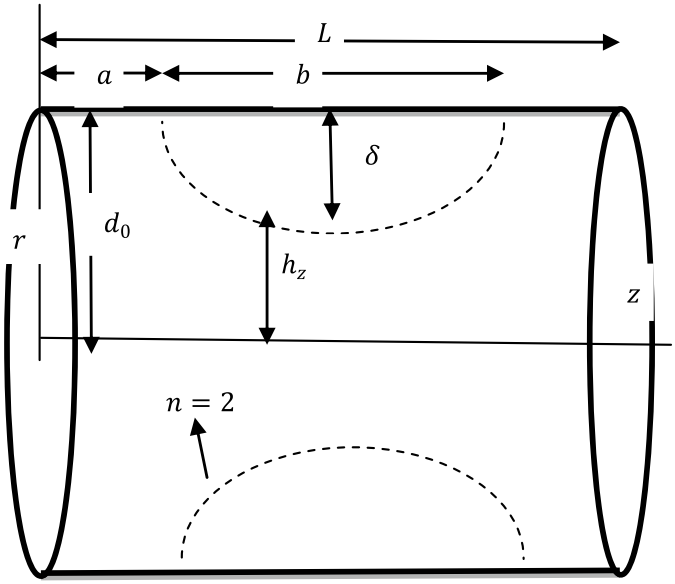

Fig. 1 Schematic diagram of stenotic artery with co-ordinate system

The schematic diagram of stenotic artery with co-ordinate system is shown below in Fig. 1.

The geometry of symmetric stenosis in non-dimensional form is described as [7]:

$$h_z = \begin{cases} d_z\left[1 - \omega\left\{(z-s) - (z-s)^n\right\}\right], & s \le z \le 1+s \\ d_z, & \text{otherwise} \end{cases} \tag{4}$$

where,

$$\omega = \frac{\delta(n)^{\frac{n}{n-1}}}{(n-1)d_0 b^n}, = \frac{a}{b},\ \varphi = \tan\tilde{\theta} \text{ and } d_z = 1 + \varphi z$$

For non-tapered artery, $\tilde{\theta} = 0$, divergent artery, $\tilde{\theta} \ge 0$ and convergent artery, $\tilde{\theta} \le 0$.

The geometry of overlapping stenosis in non-dimensional form is described as [8–11]:

$$h_z = \begin{cases} \left[d_z - 1.5\omega_1 \left\{ \begin{array}{l} 11(z-s) - 47(z-s)^2 + \\ 72(z-s)^3 - 36(z-s)^4 \end{array} \right\}\right], & s \le z \le 1+s \\ d_z, & \text{otherwise} \end{cases} \tag{5}$$

where, $\omega_1 = \frac{\delta}{d_0 b^4}$.

For isotropic Reiner and Rivlin fluid, the relation between stress tensor τ_{ij} and rate of deformation tensor $\in_{ij}$ is given as [12, 13]:

$$\tau_{ij} = -p\delta_{ij} + \mu \in_{ij} + \mu_c \varepsilon_{ij} \tag{6}$$

where,

$$\varepsilon_{ij} = \in_{ik} \in_{kj},\ \in_{ij} = \left(\nabla u + \nabla u^T\right),\ \left(\delta_{ij}\right) \text{ and}$$

Kronecker delta, $\delta_{ij} = 0$, when $i = j$; $\delta_{ij} = 0$, $for\ i, j$

μ and μ_c in Eq. 6, are viscosity and cross viscosity respectively.

The stress tensors in cylindrical coordinates (r, z) are:

$$\tau_{\overline{rr}} = -\overline{p} + 2\mu \frac{\partial \overline{u}}{\partial \overline{r}} + 4\mu_c \left(\frac{\partial \overline{u}}{\partial \overline{r}}\right)^2$$

$$\tau_{\overline{\theta\theta}} = -\overline{p} + 2\mu \frac{\overline{u}}{\overline{r}} + 4\mu_c \left(\frac{\overline{u}}{\overline{r}}\right)^2$$

$$\tau_{\overline{zz}} = -\overline{p} + 2\mu \frac{\partial \overline{w}}{\partial \overline{z}} + \mu_c \left[4\left(\frac{\partial \overline{w}}{\partial \overline{z}}\right)^2 + \left(\frac{\partial \overline{u}}{\partial \overline{z}} + \frac{\partial \overline{w}}{\partial \overline{r}}\right)^2\right]$$

$$\tau_{\overline{rz}} = \mu\left(\frac{\partial u}{\partial z} + \frac{\partial w}{\partial r}\right) + 2\mu_c \left[\left(\frac{\partial \overline{u}}{\partial \overline{r}}\right)\left(\frac{\partial \overline{u}}{\partial \overline{z}} + \frac{\partial \overline{w}}{\partial \overline{r}}\right) + \left(\frac{\partial \overline{u}}{\partial \overline{z}} + \frac{\partial \overline{w}}{\partial \overline{r}}\right)\left(\frac{\partial \overline{w}}{\partial \overline{z}}\right)\right]$$

Let the following non-dimensional variables are introduced.

$$\overline{r} = r d_0;\ \overline{z} = bz;\ \overline{w} = u_0 w;\ \overline{u} = \left(\frac{u_0 \delta}{b}\right) u;\ \overline{p} = \left(\frac{u_0 b \mu}{d_0^2}\right) p;\ \overline{h} = d_0 h;$$

$$Re = \frac{\rho b u_0}{\mu};\ \gamma = \frac{\mu_c u_0}{\mu b};\ \overline{\tau}_{\overline{rr}} = \left(\frac{b}{u_0 \mu}\right)\tau_{\overline{rr}};\ \overline{\tau}_{\overline{zr}} = \left(\frac{d_0}{u_0 \mu}\right)\tau_{\overline{zr}};$$

$$\overline{\tau}_{\overline{zz}} = \left(\frac{b}{u_0 \mu}\right)\tau_{\overline{zz}};\ \overline{\tau}_{\overline{\theta\theta}} = \left(\frac{b}{u_0 \mu}\right)\tau_{\overline{\theta\theta}}$$

Further, following conditions are also used to consider mild stenosis [9–11].

$$\frac{\delta}{d_0} \ll 1;\ \frac{Re \delta n^{\left(\frac{1}{n-1}\right)}}{b} \ll 1;\ \frac{d_0 n^{\left(\frac{1}{n-1}\right)}}{b} \sim 0$$

The non-dimensional form of Eqs. 1, 2 and 3 becomes:

$$\frac{\partial u}{\partial r} + \frac{u}{r} + \frac{\partial w}{\partial z} = 0 \tag{7}$$

$$\frac{\partial p}{\partial r} = 0 \tag{8}$$

$$\frac{\partial p}{\partial z} = \frac{1}{r}\frac{\partial}{\partial r}\left[r\frac{\partial w}{\partial r} + 2\beta r\frac{\partial w}{\partial r}\frac{\partial w}{\partial z}\right] \tag{9}$$

Equation 9 is a nonlinear partial differential equation. Therefore, method Perturbation is employed to obtain the solution.

3 Solution of Reiner Rivlin Model by Perturbation Method

To get the Perturbation solution, let axial velocity (w), Pressure (p) and Flowrate (Q) are expanded considering β as the Perturbation parameter. The expanded expressions are:

$$w = w_0 + \beta w_1 + \beta^2 w_2 + \ldots$$

$$p = p_0 + \beta p_1 + \beta^2 p_2 + \ldots$$

$$Q = Q_0 + \beta Q_1 + \beta^2 Q_2 + \ldots$$

Using above expansions in Eq. (9), Eq. (9) becomes:

$$r\frac{1}{2}\left(\frac{\partial p_0}{\partial z} + \beta\frac{\partial p_1}{\partial z} + \beta^2\frac{\partial p_2}{\partial z} + \ldots\right) = \left(\frac{\partial w_0}{\partial r} + \beta\frac{\partial w_1}{\partial r} + \beta^2\frac{\partial w_2}{\partial r} + \ldots\right) + 2\beta\left(\frac{\partial w_0}{\partial r} + \beta\frac{\partial w_1}{\partial r} + \beta^2\frac{\partial w_2}{\partial r} + \ldots\right)\left(\frac{\partial w_0}{\partial z} + \beta\frac{\partial w_1}{\partial z} + \beta^2\frac{\partial w_2}{\partial z} + \ldots\right)$$

Ignoring higher order of β, above equation becomes:

$$r\frac{1}{2}\left(\frac{\partial p_0}{\partial z} + \beta\frac{\partial p_1}{\partial z}\right) = \left(\frac{\partial w_0}{\partial r} + \beta\frac{\partial w_1}{\partial r}\right) + 2\beta\left[\left(\frac{\partial w_0}{\partial r}\frac{\partial w_0}{\partial z} + \beta^2\frac{\partial w_1}{\partial r}\frac{\partial w_1}{\partial z}\right)\right] \tag{10}$$

The zeroth order system becomes:

$$r\frac{1}{2}\left(\frac{\partial p_0}{\partial z}\right) = \left(\frac{\partial w_0}{\partial r}\right) \tag{11}$$

Integrating above equation with respect to r and using boundary condition, it becomes:

$$w_0 = \frac{\partial p_0}{\partial z}\left[\frac{r^2 - h_z^2}{4}\right] \tag{12}$$

The final expression of w becomes:

$$w = \left(\frac{\partial p}{\partial z}\right)\left[\frac{r^2 - h_z^2}{4}\right] + \beta\left\{\left(\frac{\partial p}{\partial z}\right)^2\left(h_z\frac{\partial h_z}{\partial z}\right)\left(\frac{r^2}{4} - \frac{h_z^2}{4}\right) + \left(\frac{\partial p}{\partial z}\right)\left(\frac{\partial^2 p}{\partial z^2}\right)\left(\frac{r^2 h_z^2}{8} - \frac{r^4}{16} - \frac{h_z^4}{16}\right)\right\} \tag{13}$$

From volume flow rate, pressure gradient ($\frac{\partial p}{\partial z}$) is determined as:

$$\frac{\partial p}{\partial z} = 16\left(Q/2\pi\right)\left(-\frac{1}{h_z^4}\right) - \beta\left[\left(\frac{512}{3}\right)\left(Q/2\pi\right)^2\left(\frac{-1}{h_z^7}\right) + 256\left(Q/2\pi\right)^2\left(\frac{1}{h_z^7}\right)\left(\frac{\partial h_z}{\partial z}\right)\right] \tag{14}$$

Above result is utilised to compute wall shear stress and resistance impedence. The wall shear stress,

$$\tau_w = \left(\frac{\partial p}{\partial z}\right)\left(\frac{r}{2}\right) \tag{15}$$

The Resistance impedence,

$$\gamma = \frac{\Delta p}{Q} \tag{16}$$

where $\Delta p = \int_s^{s+1}\left(-\frac{\partial p}{\partial z}\right)dz$.

Axial velocity, wall shear stress and resistance impedence are computed using Eqs. 13, 15 and 16 respectively. For symmetric stenosis Eq. 4 is substituted for h_z and similarly for overlapping stenosis Eq. 5 is considered. The results obtained for symmetric stenosis and overlapping stenosis are compared to understand the effect of overlapping stenosis relative to symmetric stenosis.

4 Numerical Results and Discussion

MATLAB codes are written in to compute axial velocity (w), wall shear stress (τ_w) and resistance impedence (γ) substituting values of ratio of cross viscosity

to viscosity (β), flow rate (Q) and stenotic wall radius (h_z). Stenotic wall radius (h_z) is computed using values of taper angle of artery (θ) and maximum height of stenosis (δ) for overlapping symmetric stenosis and additionally shape parameter (n) for symmetric stenosis. Variation of axial velocity with respect to radial distance for symmetric and overlapping stenosis at different plane normal to longitudinal axis are plotted in Fig. 2. The results are plotted at 0.2 and 0.5 axial distance from the commencement of stenosis. At 0.2 axial distance, the lumen radius is smaller in case of overlapping stenosis whereas at 0.5 axial distance lumen radius in case of symmetric stenosis is smaller. It is observed that the magnitude of axial velocity developed at the central axis at 0.2 axial distance in case of overlapping stenosis is higher than that of symmetric stenosis and the fall towards wall is also relatively steeper. The reverse is observed at 0.5 axial distance. Further, it is observed that the axial velocity profile is dependent on lumen radius. Lower the lumen radius higher is the axial velocity. Since, lumen radius changes with respect to axial distance (z)

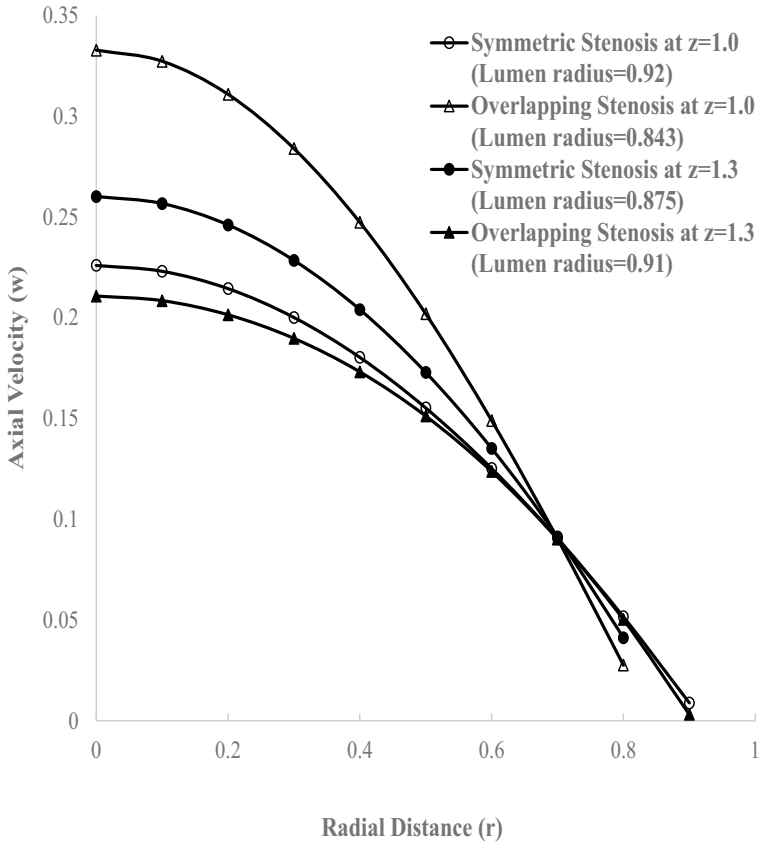

Fig. 2 Variation of axial velocity with respect to radial distance at 0.2 and 0.5 axial distances from the commencement of stenosis. $n = 2,\ \delta = 0.125, s = 0.8, r = 0,\ Q = 0.3$ and $\beta = 0.3$

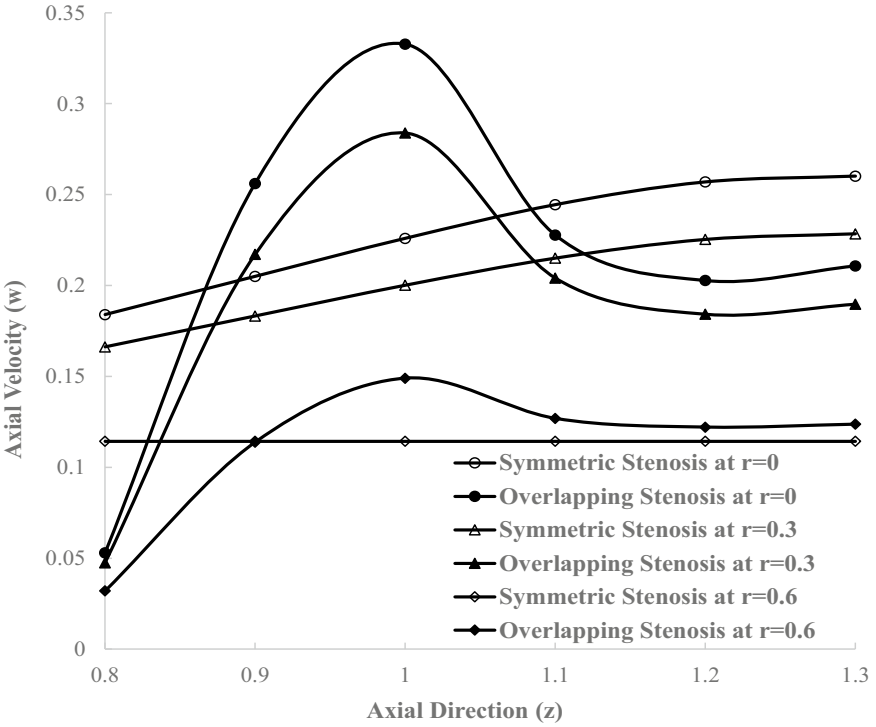

Fig. 3 Axial velocity profile with respect to axial distance under stenotic region. $n = 2$, $\delta = 0.125$, $s = 0.8$, $Q = 0.3$ and $\beta = 0.3$

as per Eqs. 4 and 5 for symmetric and overlapping stenosis respectively, in Fig. 3 axial velocity profile with respect to axial distance at different radii for symmetric and overlapping stenosis are plotted.

From Fig. 3, it is observed that nearing wall, the axial velocity profile is relatively flatter as compared to the axial velocity profile at center line. Further, throughout the length of stenosis, the magnitude of axial velocity at corresponding r for overlapping stenosis is higher than the axial velocity profile for symmetric stenosis corresponding radial positions. The axial velocity profile under the full length of stenotic region is shown in Fig. 4. The profile is the inverted profile of the geometry of overlapping stenosis. As it approaches wall the magnitude of axial velocity reduces and at wall it satisfies no slip boundary condition. Figure 5 shows the axial velocity profile for different shape parameter (n) under the full length of stenotic region for symmetric stenosis. As shape parameter increases, the location of the maximum height of stenosis shifts towards right and the transverse symmetry is lost. From Fig. 5, it is observed that the magnitude of axial velocity reaches a maximum value at the axial location corresponding to the maximum height of stenosis. In case of symmetric stenosis, the axial velocity profile exhibits to be laterally inversion of stenosis profile.

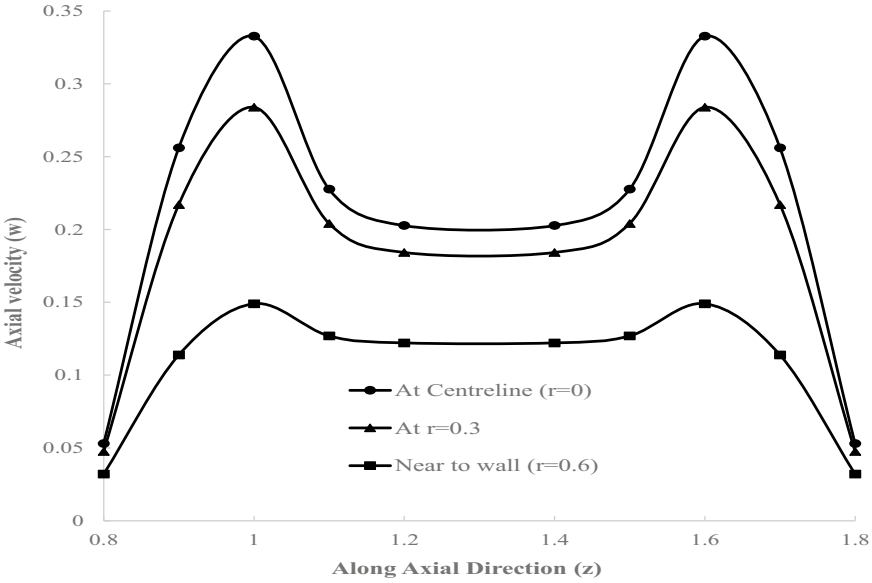

Fig. 4 Axial velocity profile with respect to axial distance under overlapping stenotic region. $\delta = 0.125$, $s = 0.8$, $Q = 0.3$ and $\beta = 0.3$

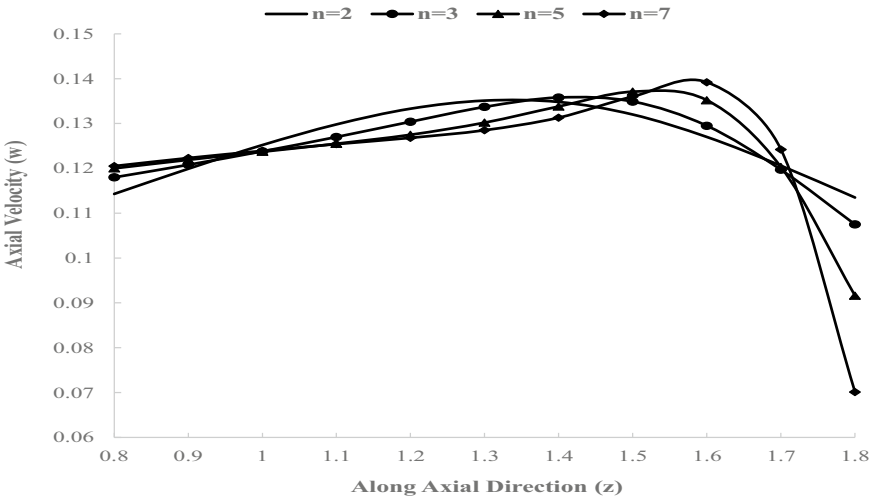

Fig. 5 Axial velocity profile with respect to axial distance under symmetric stenotic region. $\delta = 0.125$, $s = 0.8$, $Q = 0.3$ and $\beta = 0.3$

Figure 6 shows the variation of wall shear stress with respect to axial distance under the length of stenosis. The profile of shear stress for different shape parameter in case of symmetric stenosis and overlapping stenosis are shown. It is observed that evolution of wall shear stress is relatively acute in case of overlapping stenosis. Similarly, as shape parameter increases higher wall shear stress is developed compared to the stenosis for $n = 2$. Figure 7 shows the variation of resistance impedence with respect to maximum height of stenosis (δ). It is observed that as the shape parameter increase the resistance impedence shows a decreasing trend. Mathematically, resistance impedence is the area under $\left(\frac{\partial p}{\partial z}\right)/Q$ curve and is affected by the location of the maximum height of stenosis. Further, as the maximum height of stenosis increases there is an increasing trend of resistance impedence.

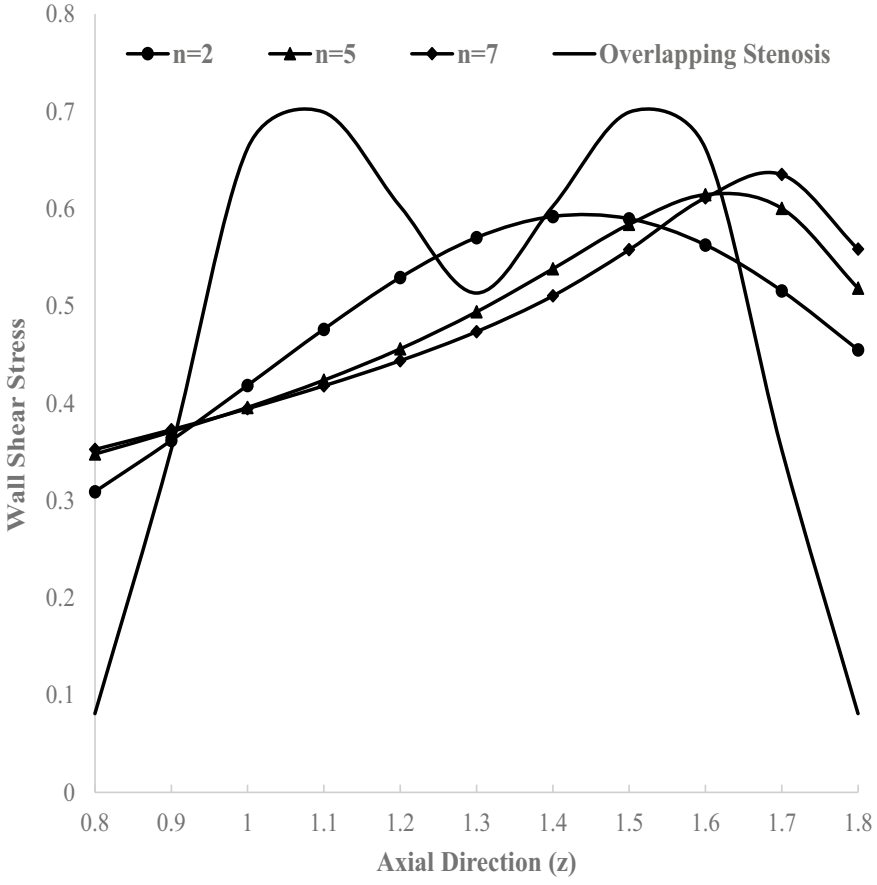

Fig. 6 Variation of wall shear stress with respect to axial distance under stenotic region. $\delta = 0.125$, $s = 0.8$, $Q = 0.3$ and $\beta = 0.3$

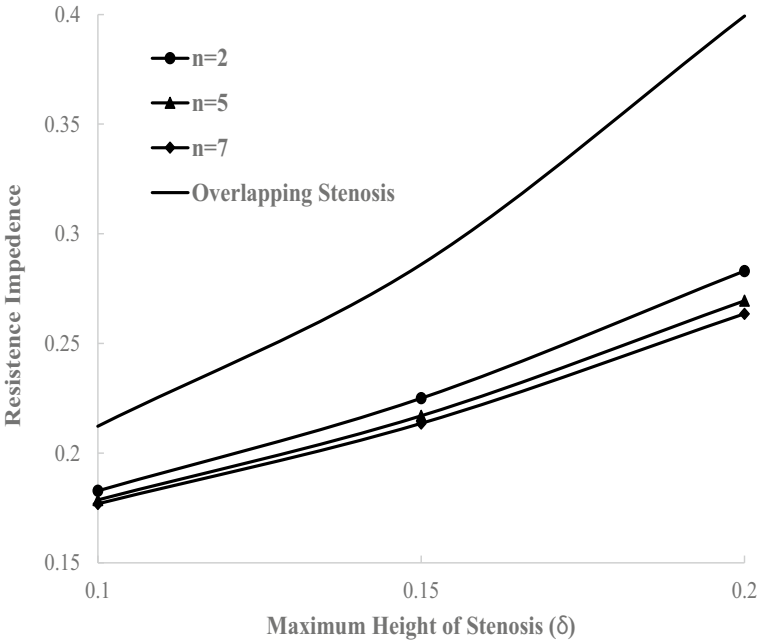

Fig. 7 Variation of resistance impedence with respect to maximum height of stenosis (δ) for different shape parameters and for overlapping stenosis.$s = 0$, $Q = 0.3$ and $\beta = 0.3$

Finally, the magnitude of resistance impedence in case of overlapping stenosis is significantly higher than the symmetric stenosis for all shape parameters and for all values of maximum height of stenosis. From the trend discussed above, it is concluded that higher axial velocity, higher wall shear stress and higher resistance impedence are developed in case of overlapping stenosis relative to symmetric stenosis for different shape parameters.

5 Conclusions

Mathematical models for axisymmetric blood flow through a symmetric mild stenosis and overlapping stenosis are worked out by semi-analytical Perturbation method. Blood flow is considered to obey Reiner-Rivlin fluid having an additional cross viscosity parameter. The Perturbation solution is obtained from z-momentum equation in non-dimensional form considering mild stenosis conditions. The expressions for the axial velocity, wall shear stress and resistance impedence distribution for the stenotic region are derived. The nature of variation of axial velocity, wall shear stress and resistance impedence are studied by plotting graphs of the results obtained for

overlapping stenosis and symmetric stenosis at different shape parameters. The main findings can be summarized as follows:

1. The axial velocity profile is dependent on lumen radius. Lower the lumen radius higher is the axial velocity.
2. In case of overlapping stenosis, the axial velocity profile along the length of stenosis is relatively higher than the symmetric stenosis for different shape parameters.
3. As shape parameters increases, higher axial velocity is obtained along the length of the stenosis.
4. Higher wall shear stress is developed in case of overlapping stenosis relative to symmetric stenosis for different shape parameters.
5. As shape parameters increases, higher wall shear stress is obtained along the length of the stenosis.
6. As shape parameters increases, lower values of resistance impedence with respect to maximum height of stenosis are is obtained.
7. The magnitude of resistance impedence in case of overlapping stenosis is significantly higher than the symmetric stenosis for all shape parameters and for all values of maximum height of stenosis.

From the above conclusions, it is possible to diagnose the overlapping stenosis condition and its acuteness by observing the deviations in flow field. From the results and trend line a significant deviations in flow field is observed not only for overlapping stenosis relative to symmetric stenosis but also for different shape parameters.

Nomenclature

u: Non-dimensional radial component of velocity of flow
$\overline{u}$: Radial component of velocity of flow [ms^{-1}]
u_0 Averaged velocity on cross section of artery [ms^{-1}]
w Non-dimensional axial component of velocity of flow
$\overline{w}$: Axial component of velocity of flow [ms^{-1}]
p: Non-dimensional pressure
$\overline{p}$: Pressure [Nm^{-2}]
β: Ratio of cross-viscosity to viscosity
Re: Reynold number
a: Length of artery before the commencement of stenosis [m]
b: Length of artery in stenotic region [m]
L: Total length of artery [m]
δ: Maximum height of stenosis [m]
d_z: Radius of the tapered arterial segment [m]
d_0: Radius of non-tapered artery in non-stenotic region [m]
$\tilde{\theta}$: Tapered angle of artery, [rad]
ρ: Density of blood [kg m^{-3}]

t: Non-dimensional time
r: Non-dimensional radial distance
z: Non-dimensional axial distance
θ: Non-dimensional angular distance
μ: Coefficient of Newtonian viscosity [kg m^{-1} s^{-1}]
μ_c: Coefficient of cross viscosity [ms^{-1}]
τ_{ij}: Stress tensor in non-dimensional form
$\overline{\tau}_{ij}$: Stress tensor [Nm^{-2}]

References

1. Yilmaz F, Gundogdu MY (2008) A critical review on blood flow in large arteries; relevance to blood rheology, viscosity models, and physiologic conditions. Korea-Australia Rheol J 20(4):197–211
2. Antonova N (2012) On some mathematical models in hemorheology. Biotechnol Biotechnol Equip 26(5):3286–3291
3. Thomas B, Suman KS (2016) Blood flow in human arterial system—a review. Proc Technol 24:339–346
4. Thurston GB (2000) Erythrocyte rigidity as a factor in blood rheology: viscoelastic dilatancy. J Rheol 23(6):703–707
5. Thurston GB, Henderson NM (2006) Effects of flow geometry on blood viscoelasticity. Biorheology 43(6):729–46
6. Massoudi M (2011) A generalization of Reiner's mathematical model for wet sand. Mech Res Commun 38:378–381
7. Mekheimer KhS, El Kot MA (2008) The micropolar fluid model for blood flow through a tapered artery with a stenosis. Acta Mech Sin 24:637–644
8. Chakraborty S, Mandal PK (1994) Mathematical modelling of blood flow through an overlapping arterial stenosis. Math Comput Model 19(1):59–70
9. Ismail Z, Abdullah I, Mustapha N, Amin N (2008) A power-law model of blood flow through a tapered overlapping stenosed artery. Appl Math Comput 195:669–680
10. Riahi DN, Roy R, Cavazos S (2011) On arterial blood flow in the presence of an overlapping stenosis. Math Comput Model 54:2999–3006
11. Srikanth D, Reddy JVR, Jain S, Kale A (2015) Unsteady polar fluid model of blood flow through tapered w-shape stenosed artery: effects of catheter and velocity slip. Ain Shams Eng J 6:1093–1104
12. Narasimham MNL (1956) On steady laminar flow of certain non-Newtonian liquids through an elastic tube. Proc Indian Acad Sci Sec A 43(4):237–246
13. Rathna SL, Bhatnagar PL (1962) Weissenberg and Merrington effects in non-Newtonian fluids. J Indian Inst Sci 45(3):57–82

Pathway Fractional Integral Formulae Involving Extended Bessel-Maitland Function in the Kernel

D. L. Suthar, Hafte Amsalu, M. Bohra, K. A. Selvakumaran, and S. D. Purohit

Abstract The aim of this paper is to present two composition formulae of pathway fractional integral (PFI) operators connected with altered extensions of the Bessel-Maitland function. We point out pertinent connections of certain particular cases of our main results with known results.

Keywords Extended Bessel-Maitland function · Pathway fractional integral operator · Gamma function · Beta function

Mathematics Subject Classification 33E12 · 05C38 · 26A33

1 Introduction and Preliminaries

The Bessel-Maitland function $J_{\vartheta}^{\varsigma}(.)$ is a generalization of Bessel function introduced by Ed. Maitland Wright [8] through a series representation as

$$J_{\vartheta}^{\varsigma}(z) = \sum_{m=0}^{\infty} \frac{(-z)^m}{\Gamma(\varsigma m + \vartheta + 1)\, m!} \quad (z, \vartheta \in \mathbb{C}, \varsigma > 0)\,. \tag{1}$$

D. L. Suthar
Department of Mathematics, Wollo University, P.O. Box: 1145, Dessie, Ethiopia

H. Amsalu
Department of Physics, Wollo University, P.O. Box: 1145, Dessie, Ethiopia

M. Bohra (✉)
Department of Mathematics, Government Mahila Engineering College, Ajmer 305001, India
e-mail: maheshkbohra@gmail.com

K. A. Selvakumaran
Department of Mathematics, R.M.K. College of Engineering and Technology, Puduvoyal 601206, Tamil Nadu, India

S. D. Purohit
Department of HEAS (Mathematics), Rajasthan Technical University, Kota 324010, India

J. Singh et al. (eds.), *Advances in Mathematical Modelling, Applied Analysis and Computation*, Lecture Notes in Networks and Systems 415,
https://doi.org/10.1007/978-981-19-0179-9_23

In fact, the application of Bessel-Maitland function is found in the diverse field of mathematical physics, engineering, biological and chemical sciences in the book of Watson [30].

Further, Pathak [17] defined generalization of the Bessel-Maitland function $J_{\vartheta,q}^{\varsigma,\delta}(.)$ in the form as

$$J_{\vartheta,q}^{\varsigma,\delta}(z) = \sum_{m=0}^{\infty} \frac{(\delta)_{qm}(-z)^m}{\Gamma(\varsigma m + \vartheta + 1)\, m!}, \tag{2}$$

where $z \in \mathbb{C}\backslash(-\infty, 0]$; $\varsigma, \vartheta, \delta \in \mathbb{C}, \Re(\varsigma) \geq 0, \Re(\vartheta) \geq -1, \Re(\delta) \geq 0$ and $q \in (0, 1) \cup \mathbb{N}$, and $(\delta)_{qm}$ is known as generalized Pochhammer symbol defined as

$$(\delta)_0 = 1, \quad (\delta)_{qm} = \frac{\Gamma(\delta + qm)}{\Gamma(\delta)}.$$

Since the Bessel-Maitland function was introduced in 1983, a variety of extensions and generalizations with diverse applications have been presented and investigated (see details [3, 7, 18, 22, 24, 25, 27–29]). By motivating these investigations and applications of Bessel-Maitland function, Suthar et al. [26] extended the generalized Bessel-Maitland function (2) in the following manner:

$$J_{\vartheta,q}^{\varsigma,\delta;c}(z;\, p) = \sum_{m=0}^{\infty} \frac{\mathcal{B}_p(\delta + qm, c - \delta)\,(c)_{qm}(-z)^m}{\mathrm{B}(\delta, c - \delta)\Gamma(\varsigma m + \vartheta + 1)\, m!} \tag{3}$$

$$(p > 0, q \in \mathbb{N}, \Re(c) > \Re(\delta) > 0),$$

which is known as extended generalized Bessel-Maitland function and where $\mathcal{B}_p(s, t)$ is the extended beta function (see [4]).

$$\mathcal{B}_p(s, t) = \int_0^1 z^{s-1}(1 - z)^{t-1} e^{\frac{-p}{z(1-z)}} dz \quad (\Re(p) > 0, \Re(s) > 0, \Re(t) > 0). \tag{4}$$

For $p = 0$, (4) reduces to the well-known beta function (see, e.g., [23], Sect. 1.1)

$$\mathrm{B}(s, t) = \int_0^1 z^{s-1}(1 - z)^{t-1} dz = \frac{\Gamma(s)\,\Gamma(t)}{\Gamma(s + t)} \tag{5}$$

$$\left(s, t \in \mathbb{C}\backslash\mathbb{Z}_0^-; (\min(\Re(s) > 0, \Re(t) > 0)\right).$$

Remark 1.1

(i) In a particular case of Eq. (3), when $p = 0$ it reduces to (2) and for $p = q = 0$ reduces to (1).

(ii) When $q = 1$, $\vartheta = \vartheta - 1$ and $z = -z$ in (3), the equation reduces to the extended Mittag–Leffler function defined by Özarslan and Yilmaz ([16], Eq. (4)).

Recently, an expending PFI operator introduced by Nair [12], which was earlier defined by Mathai [12] and Mathai and Haubold [10, 11], is defined as follows:

$$\left(\mathcal{P}_{0+}^{\varepsilon,\upsilon} f\right)(x) = x^{\varepsilon} \int_0^{\left[\frac{x}{\alpha(1-\upsilon)}\right]} \left(1 - \frac{\alpha(1-\upsilon)\xi}{x}\right)^{\frac{\varepsilon}{(1-\upsilon)}} f(\xi) d\xi, \tag{6}$$

where Lebesgue measurable function $f \in L(a, b)$ for real or complex term valued function, $\varepsilon \in \mathbb{C}$, $\Re(\varepsilon) > 0$, $\alpha > 0$ and $\upsilon < 1$ (υ is a pathway parameter).

Remark 1.2 The pathway model for a real scalar υ and scalar random variables is represented by the probability density function (p.d.f.) in the following manner:

$$f(x) = \frac{c}{|x|^{1-\upsilon}} \left[1 - \alpha(1-\upsilon)|x|^{\rho}\right]^{\frac{\varepsilon}{(1-\upsilon)}} \tag{7}$$

where $x \in (-\infty, \infty)$; $\varepsilon > 0$; $\rho > 0$; $[1 - \alpha(1-\upsilon)|x|^{\rho}]^{\frac{\varepsilon}{(1-\upsilon)}} > 0$; $\upsilon > 0$ and where υ and c denote the pathway parameter and normalizing constant, respectively.

Additionally, for $\upsilon \in \mathbb{R}$, the normalizing constants are expressed in the following way:

$$c = \begin{cases} \frac{1}{2} \frac{\rho[\alpha(1-\upsilon)]^{\frac{\upsilon}{\rho}} \Gamma\left(\frac{\upsilon}{\rho} + \frac{\varepsilon}{1-\upsilon} + 1\right)}{\Gamma\left(\frac{\upsilon}{\rho}\right)\Gamma\left(\frac{\varepsilon}{1-\upsilon} + 1\right)} & (\upsilon < 1), \\ \frac{1}{2} \frac{\rho[\alpha(1-\upsilon)]^{\frac{\upsilon}{\rho}} \Gamma\left(\frac{\varepsilon}{\upsilon-1}\right)}{\Gamma\left(\frac{\upsilon}{\rho}\right)\Gamma\left(\frac{\varepsilon}{\upsilon-1} - \frac{\upsilon}{\rho}\right)} & \left(\frac{1}{\upsilon-1} - \frac{\upsilon}{\rho} > 0, \upsilon > 1\right), \\ \frac{1}{2} \frac{[\alpha\varepsilon]^{\frac{\upsilon}{\rho}}}{\Gamma\left(\frac{\upsilon}{\rho}\right)}, & (\upsilon \to 1). \end{cases}$$

Here, it is noted that if $\upsilon < 1$, then finite range density with $[1 - \alpha(1-\upsilon)|x|^{\rho}]^{\frac{\varepsilon}{(1-\upsilon)}} > 0$, and (7) may be a part of the extended generalized type-1 beta family. Also, the triangular density, the uniform density, the extended type-1 beta density and various other probability density functions are precise special cases of the pathway density function defined in (7) for $\upsilon < 1$.

For example, if $\upsilon > 1$ and by setting $(1 - \upsilon) = -(\upsilon - 1)$ in (6) then yields

$$\left(\mathcal{P}_{0+}^{\varepsilon,\upsilon} f\right)(x) = x^{\varepsilon} \int_0^{\left[\frac{x}{-\alpha(\upsilon-1)}\right]} \left(1 + \frac{\alpha(\upsilon-1)\xi}{x}\right)^{\frac{\varepsilon}{-(\upsilon-1)}} f(\xi) d\xi \tag{8}$$

and

$$f(x) = \frac{c}{|x|^{1-\upsilon}} \left[1 + \alpha(\upsilon-1)|x|^{\rho}\right]^{\frac{\varepsilon}{-(\upsilon-1)}} \tag{9}$$

provided that $x \in (-\infty, \infty)$; $\rho > 0$; $\varepsilon > 0$; $\upsilon > 1$ characterizes the extended generalized type-2 beta model for real x. The specific cases of the density function (9)

include the type-2 beta density function, the p density function and the student t density function. For $\upsilon \to 1$, (6) diminishes to the Laplace integral transform.

In a similar way, if $\upsilon = 0$, $\alpha = 1$ and ε takes the place of $\varepsilon - 1$, then (6) diminishes to the familiar Riemann-Liouville (R-L) fractional integral operator $I_{0+}^{\varepsilon} f$ (e.g., [2]).

$$\left(\mathcal{P}_{0+}^{\varepsilon-1,0} f\right)(x) = x^{1-\varepsilon}\Gamma(\varepsilon)\left(I_{0+}^{\varepsilon} f\right)(x) \quad (\Re(\varepsilon) > 1). \tag{10}$$

The PFI operator (6) leads to numerous interesting illustrations such as fractional calculus associated with probability density functions and their significance in statistical theory. Nowadays, many researchers working on PFI formulae are associated with various special functions (see [1, 5, 6, 13–15, 20, 21]). Motivated by these researchers, we aim to extend the generalized Bessel-Maitland function, which is connected with the PFI operator (6) to present their integral formulae. Suitable connections of some particular cases are also pointed out.

2 Pathway Fractional Integral Operator of an Extended Generalized Bessel-Maitland Function

In this section, we establish the PFI formula involving the extended generalized Bessel-Maitland function, which is stated in Theorems 2.1 and 2.6.

Theorem 2.1 *Suppose* $\varsigma, \delta, \vartheta, \varepsilon, c \in \mathbb{C}$ *such that* $\Re(\delta) \geq 0, \Re(\varsigma) \geq 0, \Re(c) > \Re(\delta) > 0, \Re(\vartheta) \geq -1, \Re(\varepsilon) > 0, \Re\left(\frac{\varepsilon}{1-\upsilon}\right) > -1$; $p > 0, \upsilon < 1, q \in N$ *and* $\omega \in \Re$. *Then the following formula holds true:*

$$\mathcal{P}_{0+}^{\varepsilon,\upsilon}\left[\xi^{\vartheta} J_{\vartheta,q}^{\varsigma,\delta;c}\left(\omega\xi^{\varsigma}; p\right)\right](x) = \frac{x^{\varepsilon+\vartheta+1}\Gamma\left(\frac{\varepsilon}{1-\upsilon}+1\right)}{(\alpha(1-\upsilon))^{\vartheta+1}} J_{\vartheta+\frac{\varepsilon}{1-\upsilon}+1,q}^{\varsigma,\delta;c}\left(\omega\left(\frac{x}{\alpha(1-\upsilon)}\right)^{\varsigma}; p\right). \tag{1}$$

Proof We indicate the RHS of Eq. (1) by $\Im_1$, and invoking Eqs. (3) and (6), we have

$$\Im_1 = x^{\varepsilon}\int_0^{\left[\frac{x}{\alpha(1-\upsilon)}\right]}\left(1-\frac{\alpha(1-\upsilon)\xi}{x}\right)^{\frac{\varepsilon}{(1-\upsilon)}}\xi^{\vartheta}$$

$$\times\sum_{m=0}^{\infty}\frac{\mathcal{B}_p(\delta+qm, c-\delta)\,(c)_{qm}\,(-\omega\xi^{\varsigma})^m}{\mathrm{B}(\delta, c-\delta)\Gamma(\varsigma m+\vartheta+1)\,m!}d\xi. \tag{2}$$

Now for changing the order of integration and summation, we obtain

$$\Im_1 = x^{\varepsilon}\sum_{m=0}^{\infty}\frac{\mathcal{B}_p(\delta+qm, c-\delta)\,(c)_{qm}\,(-\omega)^m}{\mathrm{B}(\delta, c-\delta)\Gamma(\varsigma m+\vartheta+1)\,m!}$$

$$\times \int_0^{\left[\frac{x}{\alpha(1-\upsilon)}\right]} \left(1-\frac{\alpha(1-\upsilon)\xi}{x}\right)^{\frac{\varepsilon}{(1-\upsilon)}} \xi^{\vartheta+\varsigma m} d\xi.$$

Taking the substitution $u = \frac{\alpha(1-\upsilon)\xi}{x}$, we can change the limit of integration into the following:

$$\Im_1 = x^{\varepsilon} \sum_{m=0}^{\infty} \frac{\mathcal{B}_p(\delta+qm, c-\delta)\,(c)_{qm}\,(-\omega)^m}{\mathrm{B}(\delta, c-\delta)\Gamma\left(\varsigma m+\vartheta+1\right) m!} \left(\frac{x}{\alpha\,(1-\upsilon)}\right)^{\vartheta+\varsigma m+1}$$

$$\times \int_0^1 (1-u)^{\frac{\varepsilon}{(1-\upsilon)}}\, u^{\vartheta+\varsigma m} du. \tag{3}$$

Using (5) in (3), this reduces to

$$\Im_1 = x^{\varepsilon} \sum_{m=0}^{\infty} \frac{\mathcal{B}_p(\delta+qm, c-\delta)\,(c)_{qm}\,(-\omega)^m}{\mathrm{B}(\delta, c-\delta)\Gamma\left(\varsigma m+\vartheta+1\right) m!} \left(\frac{x}{\alpha\,(1-\upsilon)}\right)^{\vartheta+\varsigma m+1}$$

$$\times \mathrm{B}\left(\vartheta+\varsigma m+1, \frac{\varepsilon}{(1-\upsilon)}+1\right)$$

$$= \frac{x^{\varepsilon+\vartheta+1}\Gamma\left(\frac{\varepsilon}{(1-\upsilon)}+1\right)}{(\alpha\,(1-\upsilon))^{\vartheta+1}} \sum_{m=0}^{\infty} \frac{\mathcal{B}_p(\delta+qm, c-\delta)\,(c)_{qm}}{\mathrm{B}(\delta, c-\delta)m!}$$

$$\times \frac{(-\omega)^m}{\Gamma\left(\vartheta+\varsigma m+1+\frac{\varepsilon}{(1-\upsilon)}+1\right)} \left(\frac{x}{\alpha\,(1-\upsilon)}\right)^{\varsigma m}$$

$$= \frac{x^{\varepsilon+\vartheta+1}\Gamma\left(\frac{\varepsilon}{(1-\upsilon)}+1\right)}{(\alpha\,(1-\upsilon))^{\vartheta+1}} J^{\varsigma,\delta;c}_{\vartheta+\frac{\varepsilon}{1-\upsilon}+1,q}\left(\omega\left(\frac{x}{\alpha\,(1-\upsilon)}\right)^{\varsigma}; p\right),$$

which completes the desired proof. □

Corollary 2.2 *If we put* $p = 0$*, then* (1) *leads to the subsequent result of Bessel-Maitland function:*

$$\mathcal{P}^{\varepsilon,\upsilon}_{0+}\left[\xi^{\vartheta} J^{\varsigma,\delta;c}_{\vartheta,q}\left(\omega\xi^{\varsigma}\right)\right](x) = \frac{x^{\varepsilon+\vartheta+1}\Gamma\left(\frac{\varepsilon}{1-\upsilon}+1\right)}{(\alpha(1-\upsilon))^{\vartheta+1}} J^{\varsigma,\delta}_{\vartheta+\frac{\varepsilon}{1-\upsilon}+1,q}\left(\omega\left(\frac{x}{\alpha(1-\upsilon)}\right)^{\varsigma}\right). \tag{4}$$

Corollary 2.3 *If* $p = q = 0$*,* (1) *gives the subsequent result in terms of Bessel-Maitland function as*

$$\mathcal{P}_{0+}^{\varepsilon,\upsilon}\left[\xi^{\vartheta}J_{\vartheta}^{\varsigma}\left(\omega\xi^{\varsigma}\right)\right](x)=\frac{x^{\varepsilon+\vartheta+1}\Gamma\left(\frac{\varepsilon}{1-\upsilon}+1\right)}{(\alpha(1-\upsilon))^{\vartheta+1}}J_{\vartheta+\frac{\varepsilon}{1-\upsilon}+1}^{\varsigma}\left(\omega\left(\frac{x}{\alpha(1-\upsilon)}\right)^{\varsigma}\right). \quad (5)$$

Corollary 2.4 *If we set* $\upsilon=0,\alpha=1$ *and* $\varepsilon=\varepsilon-1$ *in* (1)*, then the following formula holds true:*

$$\mathcal{P}_{0+}^{\varepsilon-1,0}\left[\xi^{\vartheta}J_{\vartheta,q}^{\varsigma,\delta;c}\left(\omega\xi^{\varsigma};p\right)\right](x)=x^{\varepsilon+\vartheta}\Gamma\left(\varepsilon\right)J_{\vartheta+\varepsilon,q}^{\varsigma,\delta;c}\left(\omega x^{\varsigma};p\right). \quad (6)$$

Corollary 2.5 *If* $\delta=1$, $c=2$ *and* $q=1$, *then* (1) *holds the following formula:*

$$\mathcal{P}_{0+}^{\varepsilon,\upsilon}\left[\xi^{\vartheta}J_{\vartheta,1}^{\varsigma,1;2}\left(\omega\xi^{\varsigma};p\right)\right](x)=\frac{x^{\varepsilon+\vartheta+1}\Gamma\left(\frac{\varepsilon}{1-\upsilon}+1\right)}{(\alpha(1-\upsilon))^{\vartheta+1}}J_{\vartheta+\frac{\varepsilon}{1-\upsilon}+1,1}^{\varsigma,1;2}\left(\omega\left(\frac{x}{\alpha(1-\upsilon)}\right)^{\varsigma};p\right). \quad (7)$$

Theorem 2.6 *Let* $\vartheta,\varepsilon,\varsigma,\delta,c\in\mathbb{C}$ *such that* $\Re(\varsigma)\geq 0,\Re(\delta)\geq 0,\Re(c)>\Re(\delta)>0,\Re(\vartheta)\geq -1,\ \Re(\varepsilon)>0,\ \Re\left(\frac{\varepsilon}{1-\upsilon}\right)>-1;\ p>0,\ \upsilon>1,\ q\in\mathbb{N}$ *and* $\omega\in\Re$. *Then the following formula holds true:*

$$\mathcal{P}_{0+}^{\varepsilon,\upsilon}\left[\xi^{\vartheta}J_{\vartheta,q}^{\varsigma,\delta;c}\left(\omega\xi^{\varsigma};p\right)\right](x)=\frac{x^{\varepsilon+\vartheta+1}\Gamma\left(1-\frac{\varepsilon}{\upsilon-1}\right)}{(-\alpha(\upsilon-1))^{\vartheta+1}}J_{\vartheta+1-\frac{\varepsilon}{\upsilon-1},q}^{\varsigma,\delta;c}\left(\omega\left(\frac{x}{-\alpha(\upsilon-1)}\right)^{\varsigma};p\right). \quad (8)$$

Proof Denote the right-hand side of (8) by $\Im_2$. By using (3) and (6) and changing the order of integration and summation, which is confirmed under the provided conditions in Theorem 2.6, we obtain

$$\Im_2=x^{\varepsilon}\sum_{m=0}^{\infty}\frac{\mathcal{B}_p(\delta+qm,c-\delta)\,(c)_{qm}\,(-\omega)^m}{\mathrm{B}(\delta,c-\delta)\Gamma\left(\varsigma m+\vartheta+1\right)m!}$$

$$\times\int_0^{\left[\frac{x}{-\alpha(\upsilon-1)}\right]}\left(1+\frac{\alpha(\upsilon-1)\xi}{x}\right)^{\frac{\varepsilon}{-(\upsilon-1)}}\xi^{\vartheta+\varsigma m}d\xi. \quad (9)$$

By setting $v=-\frac{\alpha(\upsilon-1)\xi}{x}$ and using (5), we obtain

$$\Im_2=x^{\varepsilon}\sum_{m=0}^{\infty}\frac{\mathcal{B}_p(\delta+qm,c-\delta)\,(c)_{qm}\,(-\omega)^m}{\mathrm{B}(\delta,c-\delta)\Gamma\left(\varsigma m+\vartheta+1\right)m!}\left(\frac{x}{-\alpha\left(\upsilon-1\right)}\right)^{\vartheta+\varsigma m+1}$$

$$\times\int_0^1(1-v)^{1-\frac{\varepsilon}{(\upsilon-1)}-1}v^{\vartheta+\varsigma m+1-1}dv,$$

$$=x^{\varepsilon}\sum_{m=0}^{\infty}\frac{\mathcal{B}_p(\delta+qm,c-\delta)\,(c)_{qm}\,(-\omega)^m}{\mathrm{B}(\delta,c-\delta)\Gamma\left(\varsigma m+\vartheta+1\right)m!}\left(\frac{x}{-\alpha\left(\upsilon-1\right)}\right)^{\vartheta+\varsigma m+1}$$

$$\times \frac{\Gamma\left(\vartheta+\varsigma m+1\right)\Gamma\left(1-\frac{\varepsilon}{(\upsilon-1)}\right)}{\Gamma\left(\vartheta+\varsigma m+2-\frac{\varepsilon}{(\upsilon-1)}\right)}$$

$$= \frac{x^{\varepsilon+\vartheta+1}\Gamma\left(1-\frac{\varepsilon}{(\upsilon-1)}\right)}{\left(-\alpha\left(\upsilon-1\right)\right)^{\vartheta+1}} \sum_{m=0}^{\infty} \frac{\mathcal{B}_p(\delta+qm, c-\delta)\,(c)_{qm}}{\mathrm{B}(\delta, c-\delta)m!}$$

$$\times \frac{1}{\Gamma\left(\vartheta+\varsigma m+2-\frac{\varepsilon}{(\upsilon-1)}\right)} \left(-\omega\left(\frac{x}{-\alpha\left(\upsilon-1\right)}\right)^{\varsigma}\right)^{m}$$

$$= \frac{x^{\varepsilon+\vartheta+1}\Gamma\left(1-\frac{\varepsilon}{(\upsilon-1)}\right)}{\left(-\alpha\left(\upsilon-1\right)\right)^{\vartheta+1}} J^{\varsigma,\delta;c}_{\vartheta+1-\frac{\varepsilon}{\upsilon-1},q}\left(\omega\left(\frac{x}{-\alpha\left(\upsilon-1\right)}\right)^{\varsigma}; p\right),$$

we arrive at the desired result (8).

Corollary 2.7 *If we put $p = 0$, then (8) gives the result in terms of Bessel-Maitland function as follows:*

$$\mathcal{P}^{\varepsilon,\upsilon}_{0+}\left[\xi^{\vartheta} J^{\varsigma,\delta;c}_{\vartheta,q}\left(\omega\xi^{\varsigma}\right)\right](x) = \frac{x^{\varepsilon+\vartheta+1}\Gamma\left(1-\frac{\varepsilon}{\upsilon-1}\right)}{\left(-\alpha(\upsilon-1)\right)^{\vartheta+1}} J^{\varsigma,\delta}_{\vartheta+1-\frac{\varepsilon}{\upsilon-1},q}\left(\omega\left(\frac{x}{-\alpha(\upsilon-1)}\right)^{\varsigma}\right). \quad (10)$$

Corollary 2.8 *If we set $p = q = 0$, then (8) provides the result as*

$$\mathcal{P}^{\varepsilon,\upsilon}_{0+}\left[\xi^{\vartheta} J^{\varsigma}_{\vartheta}\left(\omega\xi^{k}\right)\right](x) = \frac{x^{\varepsilon+\vartheta+1}\Gamma\left(1-\frac{\varepsilon}{\upsilon-1}\right)}{\left(-\alpha(\upsilon-1)\right)^{\vartheta+1}} J^{\varsigma}_{\vartheta+1-\frac{\varepsilon}{\upsilon-1}}\left(\omega\left(\frac{x}{-\alpha(\upsilon-1)}\right)^{\varsigma}\right). \quad (11)$$

Corollary 2.9 *$\alpha = 1$, $\upsilon = 2$ and $\varepsilon = \varepsilon - 1$, then (8) holds the following formula:*

$$\mathcal{P}^{\varepsilon-1,2}_{0+}\left[\xi^{\vartheta} J^{\varsigma,\delta;c}_{\vartheta,q}\left(\omega\xi^{\varsigma}; p\right)\right](x) = x^{\varepsilon+\vartheta}\,(-1)^{\vartheta+1}\,\Gamma\left(2-\varepsilon\right) J^{\varsigma,\delta;c}_{\vartheta+2-\varepsilon,q}\left(\omega\,(-x)^{\varsigma}; p\right). \quad (12)$$

Corollary 2.10 *If $\delta = 1$, $c = 2$ and $q = 1$, then resulting formula of (8) holds true:*

$$\mathcal{P}^{\varepsilon,\upsilon}_{0+}\left[\xi^{\vartheta} J^{\xi,1;2}_{\vartheta,1}\left(\omega\xi^{\varsigma}; p\right)\right](x) = \frac{x^{\varepsilon+\vartheta+1}\Gamma\left(1-\frac{\varepsilon}{\upsilon-1}\right)}{\left(-\alpha(\upsilon-1)\right)^{\vartheta+1}} J^{\varsigma,1;2}_{\vartheta+1-\frac{\varepsilon}{\upsilon-1},1}\left(\omega\left(\frac{x}{-\alpha(\upsilon-1)}\right)^{\varsigma}; p\right). \quad (13)$$

3 Concluding Remarks

We have established two pathway fractional integral formulae associated with the extended generalized Bessel-Maitland function. The results are the extended forms of the known results which are earlier proved by [12, 19].

References

1. Agarwal P, Purohit SD (2013) The unified pathway fractional integral formulae. J Fract Calc Appl 4(1):105–112
2. Baleanu D, Diethelm K, Scalas E, Trujillo JJ (2012) Fractional calculus. Models and numerical methods, series on complexity, nonlinearity and chaos 3. World Scientific Publishing Co. Pte. Ltd., Hackensack, NJ
3. Bhatter S, Mathur A, Kumar D, Nisar KS, Singh J (2020) Fractional modified Kawahara equation with Mittag-Leffler law. Chaos Solitons Fractals 131:109508
4. Chaudhry MA, Qadir A, Srivastava HM, Paris RB (2004) Extended hypergeometric and confluent hypergeometric functions. Appl Math Comput 159:589–602
5. Khan WA, Nisar KS (2016) Unified integral operator involving generalized Bessel-Maitland function. Proc Jangjeon Math Soc 21(3):339–346
6. Kumar D, Saxena RK, Daiya J (2017) Pathway fractional integral operators of generalized k-Wright function and k_4-function. Bol Soc Paran Mat 35(2):235–246
7. Kumar D, Singh J, Baleanu D (2020) On the analysis of vibration equation involving a fractional derivative with Mittag-Leffler law. Math Methods Appl Sci 43:443–457
8. Marichev OI (1983) Handbook of integral transform and Higher transcendental functions. Ellis, Harwood, Chichester, Wiley, New York
9. Mathai AM (2005) A pathway to matrix-variate gamma and normal densities. Linear Algebra Appl 396:317–328
10. Mathai AM, Haubold HJ (2007) Pathway model, superstatistics, Tsallis statistics and a generalized measure of entropy. Phys A 375:110–122
11. Mathai AM, Haubold HJ (2008) On generalized distributions and pathways. Phys Lett A 372:2109–2113
12. Nair SS (2009) Pathway fractional integration operator. Fract Calc Appl Anal 12:237–252
13. Nisar KS, Mondal SR, Agarwal P (2016) Pathway fractional integral operator associated with Struve function of first kind. Adv Stud Contemp Math 26:63–70
14. Nisar KS, Mondal SR, Wang G (2019) Pathway fractional integral operators involving k-Struve function. Afr Mat 30:1267–1274
15. Nisar KS, Purohit SD, Abouzaid MS, Qurashi MA, Baleanu D (2016) Generalized k-Mittag-Leffler function and its composition with pathway integral operators. J Nonlinear Sci Appl 9:3519–3526
16. Özarslan MA, Yilmaz B (2014) The extended Mittag-Leffler function and its properties. J Inequal Appl 2014:85, 10 p
17. Pathak RS (1966) Certain convergence theorems and asymptotic properties of a generalization of Lommel and Maitland transform. Proc Natl Acad Sci India Sect A 36:81–86
18. Purohit SD, Suthar DL, Kalla SL (2012) Marichev-Saigo-Maeda fractional integration operators of the Bessel functions. Matematiche (Catania) 67(1):12–32
19. Rahman G, Ghaffar A, Mubeen S, Arshad M, Khan SU (2017) The composition of extended Mittag-Leffler functions with pathway integral operator. Adv Differ Equ 2017:176. https://doi.org/10.1186/s13662-017-1237-8
20. Rahman G, Nisar KS, Choi J, Mubeen S, Arshad M (2019) Pathway fractional integral formulas involving extended Mittag-Leffler functions in the kernel. Kyungpook Math J 59:125–134

21. Saxena RK, Ram J, Daiya J (2012) Fractional integration of the Aleph functions via pathway operator. Inter J Phys Math Sci 2(1):163–172
22. Singh J, Kumar D, Baleanu D (2019) New aspects of fractional Biswas-Milovic model with Mittag-Leffler law. Math Model Nat Phenom 14. https://doi.org/10.1051/mmnp/2018068
23. Srivastava HM, Choi J (2012) Zeta and q-Zeta functions and associated series and integrals. Elsevier Science Publishers, Amsterdam, London and New York
24. Suthar DL, Amsalu H (2017) Certain integrals associated with the generalized Bessel-Maitland function. Appl Appl Math 12(2):1002–1016
25. Suthar DL, Habenom H (2016) Integrals involving generalized Bessel-Maitland function. J Sci Arts 37(4):357–362
26. Suthar DL, Khan AM, Alaria A, Purohit SD, Singh J (2020) Extended Bessel-Maitland function and its properties pertaining to integral transforms and fractional calculus. AIMS Math 5(2):1400–1410
27. Suthar DL, Purohit SD, Parmar RK (2017) Generalized fractional calculus of the multiindex Bessel function. Math Nat Sci 1:26–32
28. Suthar DL, Reddy GV, Abeye N (2017) Integral formulas involving product of Srivastava's polynomial and generalized Bessel Maitland functions. Int J Sci Res 11(6):343–351
29. Suthar DL, Tsegaye T (2017) Riemann-Liouville fractional integrals and differential formula involving Multiindex Bessel-function. Math Sci Lett 6(3):1–5
30. Watson GN (1965) A treatise on the theory of Bessel functions. Cambridge Mathematical Library edition, Cambridge University Press. Reprinted 1996

Analytical Approximate Approach to the Helmholtz-Duffing Oscillator

B. Ghanbari

Abstract In this paper, a novel analytical approximation for the period and periodic solutions for the Helmholtz-Duffing oscillator is presented. The main idea of present work is to approximate the integration in exact analytical period of equation using a well-known quadrature rules. This approach gives us not only the accurate period of motion but also a truly periodic solution in a rational form as a function of the amplitude of oscillation. Comparison of the result obtained using this approach with the exact one and existing results reveals that the high accurate, simplicity, and efficiency of the proposed procedure for the whole range of initial amplitudes and the equation parameter in a variety of cases. The method can be easily extended to other strongly nonlinear oscillators.

Keywords Highly nonlinear oscillators · Analytical approximate solutions · Periodic solution · Numerical integration · Helmholtz-Duffing oscillator

1 Introduction

The topic of nonlinear oscillators has received lots of attention especially in the last decade. Though it is still very difficult to solve governing nonlinear problems either numerically or analytically, various analytic, and numerical techniques have been employed to search numerical solutions of nonlinear oscillators [1–13].
The intention of this paper is to develop a novel solving procedure for conservative Helmholtz-Duffing oscillator giving by [9–13]:

$$\ddot{u} + u + (1 - \sigma)u^2 + \sigma u^3 = 0, \tag{1}$$

with the following given information

B. Ghanbari (✉)
Department of Basic Science, Kermanshah University of Technology, Kermanshah, Iran
e-mail: b.ghanbary@yahoo.com

J. Singh et al. (eds.), *Advances in Mathematical Modelling, Applied Analysis and Computation*, Lecture Notes in Networks and Systems 415,
https://doi.org/10.1007/978-981-19-0179-9_24

$$x(0) = a, \quad \dot{x}(0) = 0. \tag{2}$$

where $\sigma \in \mathcal{R}$. For $\sigma = 1$, the Helmholtz-Duffing oscillator (1) is reduced to the classical Duffing oscillator. It also degenerates to the Helmholtz oscillator with a single-well potential by letting $\sigma = 0$.
Since Eq. (1) has no exact solution, researchers have been used many approximate techniques tp obtain the numerical solutions. For instance, Leung and Guo [11] used the homotopy perturbation method to obtain the period of the Helmholtz-Duffing oscillator (1). Guo and Leung [12] examined the approximate period of the oscillator using the iterative homotopy harmonic balance method. In [13], the authors have adopted He's Energy Balance Method (HEBM) and He's Frequency Amplitude Formulation (HFAF) as the solution methods to approximate periodic solutions for the Helmholtz-Duffing oscillator. Recently, in [14] the exact and explicit homoclinic solution of the undamped Helmholtz-Dufng oscillator is derived by a presented hyperbolic function balance procedure.

In the paper, we give an explicit formula for the analytical period and approximate solutions of the Helmholtz-Duffing oscillator.

2 Conservative Helmholtz-Duffing Oscillator

Due to the fact that the behavior of an asymmetric nonlinear oscillator is different in positive and negative directions, the equation can be conveniently studied in two parts [9–13]:

$$\ddot{u} + u + (1-\sigma)u^2 sgn(u) + \sigma u^3 = 0, \quad for \quad u \geq 0, \tag{3}$$

$$\ddot{u} + u - (1-\sigma)u^2 sgn(u) + \sigma u^3 = 0, \quad for \quad u \leq 0, \tag{4}$$

in which

$$sgn(x) = \begin{cases} 1 & x > 0 \\ 0 & x = 0 \\ -1 & x < 0 \end{cases}.$$

To proceed further, we multiply u' on both sides Eq. (1)

$$u''u' + uu' + (1-\sigma)u^2u' + \sigma u^3u' = 0, \tag{5}$$

Now we integrate (5) as

$$\frac{1}{2}u'^2 + \frac{1}{2}u^2 + \frac{1}{3}(1-\sigma)u^3 + \frac{1}{4}\sigma u^4 = C, \tag{6}$$

where C is an integration constant.

Imposing $u' = 0$ at $u = a$ and $u = -b$, it reads

$$\frac{1}{2}a^2 + \frac{1}{3}(1-\sigma)a^3 + \frac{1}{4}\sigma a^4 = \frac{1}{2}b^2 - \frac{1}{3}(1-\sigma)b^3 + \frac{1}{4}\sigma b^4. \tag{7}$$

Now, solving (7) for b yields

$$b = \frac{1}{9a}(3a\alpha + 4 - 4a) + \frac{1}{9a}\Delta^{1/3} - \frac{2}{9a}(9a^2\alpha^2 + 6a\alpha - 6a\alpha^2 + 43\alpha - 8 - 8\alpha^2)\Delta^{-1/3} \tag{8}$$

where

$$\begin{aligned}\Delta \;=\; & 270a^2\alpha^2(1 - a\alpha - \alpha) - 72a(1+\alpha^2) - 516\alpha(1-\alpha) + 64(1-\alpha^3) \\ & + 54\alpha[-12(1+\alpha^2) + 16a(a + 1 + a\alpha^4 - \alpha^3) + 78a(1 + a^3\alpha - a^3\alpha^2) \\ & - 8a^3\alpha(1-\alpha^3) - 172a^2\alpha(1+\alpha^2) - 120a\alpha(1-\alpha) \\ & + 9a^4\alpha^2(1 + 5a\alpha + 10\alpha + 3a^2\alpha^2 - 5a\alpha^2 + \alpha^2) + 447a^2\alpha^2]^{1/2}.\end{aligned}$$

Therefore, the two auxiliary equations with initial conditions become

$$u'' + u + (1-\sigma)u^2 sgn(u) + \sigma u^3 = 0, \quad for \quad u \geq 0, \quad u(0) = a, u'(0) = 0, \tag{9}$$

$$u'' + u - (1-\sigma)u^2 sgn(u) + \sigma u^3 = 0, \quad for \quad u \leq 0, \quad u(0) = b, u'(0) = 0. \tag{10}$$

3 Solution Method

Multiply u' on both sides of equations in (9) and (10), then integrating once using the initial conditions, the following relations is obtained

$$\frac{1}{2}u'^2 + \frac{1}{2}u^2 + \frac{1}{3}(1-\sigma)u^3 + \frac{1}{4}\sigma u^4 = \frac{1}{2}a^2 + \frac{1}{3}(1-\sigma)a^3 + \frac{1}{4}\sigma a^4, \tag{11}$$

$$\frac{1}{2}u'^2 + \frac{1}{2}u^2 - \frac{1}{3}(1-\sigma)u^3 + \frac{1}{4}\sigma u^4 = \frac{1}{2}b^2 - \frac{1}{3}(1-\sigma)b^3 + \frac{1}{4}\sigma b^4, \tag{12}$$

After some mathematical simplification in (11) and (12), we get

$$u' = \sqrt{a^2 - u^2 + \frac{2}{3}(1-\sigma)\left(a^3 - u^3\right) + \frac{1}{2}\sigma\left(a^4 - u^4\right)}, \tag{13}$$

$$u' = \sqrt{b^2 - u^2 - \frac{2}{3}(1-\sigma)\left(b^3 - u^3\right) + \frac{1}{2}\sigma\left(b^4 - u^4\right)}. \tag{14}$$

Table 1 A comparison between the approximate natural frequencies for $\sigma = 0$

a	b	T_{HPM} [11] (Error%)	T_{IHHBM} [12] (Error%)	$T_{EBM(C)}$ [13] (Error%)	T_{QBM} (Error%)	T_{excat}
0.1	0.1071797	6.311687 (0.0014)	6.311627 (0.000443)	6.311970 (0.00587806)	6.3116000 (0.0000158)	6.311599
0.2	0.2315342	6.411861 (0.007315)	6.411541 (0.002324)	6.4129012 (0.02353934)	6.4113931 (0.0000171)	6.411392
0.3	0.3803848	6.631084 (0.02605)	6.629894 (0.00810)	6.6322974 (0.04435422)	6.6293591 (0.0000316)	6.629357
0.4	0.5725083	7.131872 (0.1025)	7.126674 (0.029574)	7.1232178 (0.01893729)	7.1245696 (0.0000364)	7.124567
0.49	0.8728321	9.283958 (0.8249)	9.2084853 (0.005303)	8.9467250 (2.83744662)	9.2080165 (0.0002117)	9.207997

Thus for $u \geq 0$, the following relation is satisfied

$$\frac{du}{\sqrt{a^2 - u^2 + \frac{2}{3}(1-\sigma)(a^3 - u^3) + \frac{1}{2}\sigma(a^4 - u^4)}} = dt. \tag{15}$$

Further, in negative directions we obtain

$$\frac{du}{\sqrt{b^2 - u^2 - \frac{2}{3}(1-\sigma)(b^3 - u^3) + \frac{1}{2}\sigma(b^4 - u^4)}} = dt. \tag{16}$$

Integrating of (15) from $t = 0$ to $t = a$ yields

$$\int_0^a \frac{du}{\sqrt{a^2 - u^2 + \frac{2}{3}(1-\sigma)(a^3 - u^3) + \frac{1}{2}\sigma(a^4 - u^4)}} = \int_0^{\frac{T_a}{4}} dt = \frac{T_a}{4}, \tag{17}$$

Similarly, integrating of (16) from $t = 0$ to $t = b$, one gets

$$\int_0^b \frac{du}{\sqrt{b^2 - u^2 - \frac{2}{3}(1-\sigma)(b^3 - u^3) + \frac{1}{2}\sigma(b^4 - u^4)}} = \int_0^{\frac{T_b}{4}} dt = \frac{T_b}{4}, \tag{18}$$

Thus, the periods of oscillatory solutions of (9) and (10) can be consequently obtained in the form of

$$T_a = \int_0^a \frac{4du}{\sqrt{a^2 - u^2 + \frac{2}{3}(1-\sigma)(a^3 - u^3) + \frac{1}{2}\sigma(a^4 - u^4)}}. \tag{19}$$

Table 2 A comparison between the approximate natural frequencies for $\sigma = 0.5$

a	b	T_{HPM} [11] (Error%)	T_{IHHBM} [12] (Error%)	T_{QBM} (Error%)	T_{excat}
0.01	0.0100334	6.283133 (0.00000031018)	6.2831328 (0.000000318)	6.2831334 (0.00000636)	6.283133
0.02	0.0201342	6.282975 (0.000001592)	6.2829746 (0.00000095496)	6.2829749 (0.00001432)	6.282974
0.05	0.0508466	6.281856 (0.00007959)	6.2818528 (0.000002865)	6.2818519 (0.00001432)	6.281851
0.10	0.1034340	6.2777408 (0.000315)	6.2777277 (0.00001067)	6.2777222 (0.00001911)	6.277721
0.20	0.2140335	6.260044 (0.00118)	6.2599943 (0.0000388)	6.2599706 (0.00000958)	6.259970
0.40	0.4567433	6.174871 (0.0032066)	6.1747439 (0.001148)	6.1746744 (0.00002267)	6.174673
0.60	0.7224905	5.999168 (0.00120018)	5.9991487 (0.0000878)	5.9990972 (0.00002000)	5.999096
0.80	0.9981976	5.727689 (0.008449)	5.7280820 (0.001589)	5.7281740 (0.00001745)	5.728173
1.0	1.2709626	5.393792 (0.022798)	5.3947130 (0.0057275)	5.3950234 (0.00002594)	5.395022
2.0	2.4901645	3.8385182 (0.067735)	3.8400367 (0.0282)	3.8411204 (0.00001041)	3.841120
5.0	5.6270290	1.8926895 (0.086968)	1.8932562 (0.057054)	1.8943360 (0.00005278)	1.894337
10	10.655726	1.0032703 (0.089795)	1.0035198 (0.06495)	1.0041722 (0.00001991)	1.004172
20	20.663811	0.51387692 (0.090578)	0.51399634 (0.06736)	0.51434260 (0.00003888)	0.5143428
50	50.666199	0.20808755 (0.0907687)	0.20813487 (0.068049)	0.20827654 (0.00002880)	0.2082766
100	100.66655	0.1044264 (0.090795)	0.1044501 (0.06812)	0.10452128 (0.00001913)	0.1045213

$$T_b = \int_0^b \frac{4du}{\sqrt{b^2 - u^2 - \frac{2}{3}(1-\sigma)(b^3 - u^3) + \frac{1}{2}\sigma(b^4 - u^4)}}. \tag{20}$$

The relations (19) and (20) give us the exact period of vibration in the in elliptic integral form as:

$$T_{ex} = \frac{T_a + T_b}{2} = \int_0^a \frac{2du}{\sqrt{a^2 - u^2 + \frac{2}{3}(1-\sigma)(a^3 - u^3) + \frac{1}{2}\sigma(a^4 - u^4)}} + \int_0^b \frac{2du}{\sqrt{b^2 - u^2 - \frac{2}{3}(1-\sigma)(b^3 - u^3) + \frac{1}{2}\sigma(b^4 - u^4)}}. \tag{21}$$

Table 3 A comparison between the approximate natural frequencies for $\sigma = 0.9$

a	b	T_{HPM} [11] (Error%)	T_{IHHBM} [12] (Error%)	$T_{EBM(C)}$ [13] (Error%)	T_{QBM} (Error%)	T_{excat}
0.01	0.0100067	6.2829757 (0.000000013)	6.2829757 (0.000000013)	6.2829756 (0.0000015916)	6.2829762 (0.000007958)	6.2829757
0.1	0.1006651	6.2622098 (0.000011178)	6.2622093 (0.000000319)	6.2622070 (0.0000335344)	6.2622098 (0.000011178)	6.2622091
0.5	0.5139226	5.8065145 (0.00005511)	5.8065164 (0.0000022389)	5.8039852 (0.043614781)	5.8065182 (0.000008611)	5.8065177
1.0	1.0357708	4.8411819 (0.003038)	4.8412347 (0.001948)	4.8242738 (0.3522834329)	4.8413300 (0.000020655)	4.841329
5.0	5.0709716	1.5043714 (0.072025)	1.5046447 (0.05387)	1.4763900 (1.930691152)	1.5054552 (0.000033212)	1.5054557
10	10.073268	0.77207482 (0.08555)	0.7722400 (0.06417)	0.75645192 (2.107315061)	0.77273560 (0.000038823)	0.7727359
50	50.074041	0.15604183 (0.090579)	0.1560771 (0.06800)	0.15279481 (2.169559742)	0.15618326 (0.000025610)	0.1561833
100	100.07407	0.07806849 (0.090748)	0.07808616 (0.06813)	0.0764425 (2.17163172)	0.078139385 (0.000019196)	0.0781394

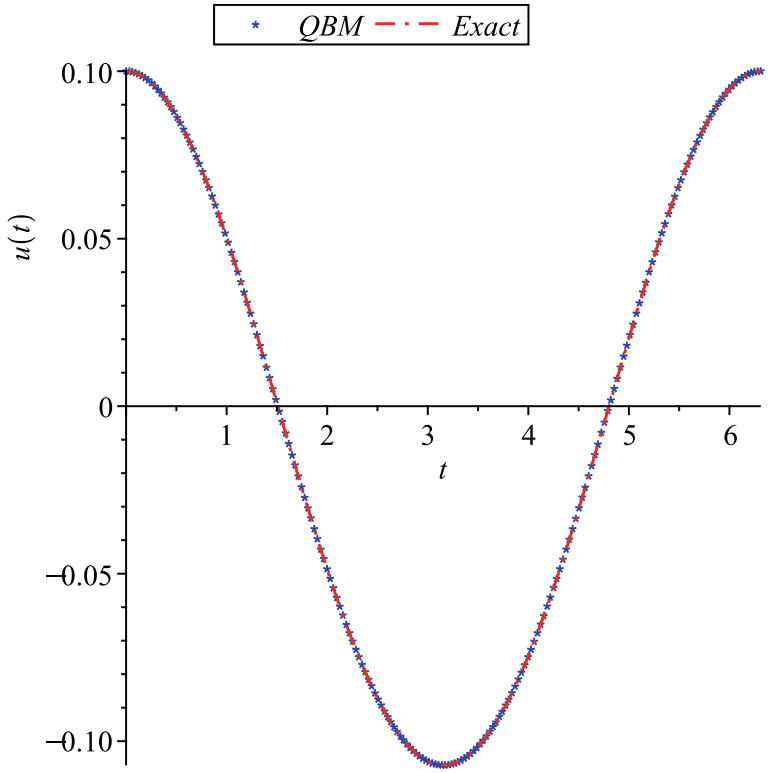

Fig. 1 A comparison between exact and approximate solutions of Eq. (1) for $a = 0.1$ and $\sigma = 0$

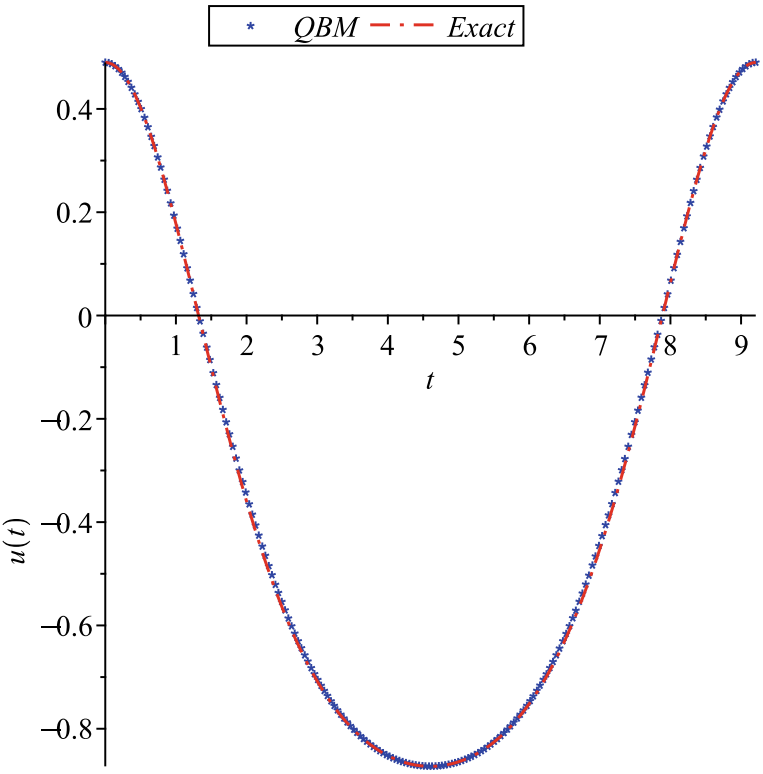

Fig. 2 A comparison between exact and approximate solutions of Eq. (1) for $a = 0.49$ and $\sigma = 0$

In framework of the proposed method, based on a numerical integration quadrature rule, we first present a closed-form formula for T_a and T_b , then B_a and B_b will be obtained afterward. One can easily check that both integrals in (19) and (20) have singularities at the upper bound of integrals, which can be easily removed as follows. By applying change of variable $u = a - at^2$ and $u = b - bt^2$ in the integrals (19) and (20) and after some manipulations, we respectively get

$$T_a = \frac{8}{k_{1a}} \int_0^1 f_a(t)dt. \tag{22}$$

$$T_b = \frac{8}{k_{1b}} \int_0^1 f_b(t)dt. \tag{23}$$

where

$$f_a(t) = \left(1 + k_{2a}t^2 + k_{3a}t^4 + k_{4a}t^6\right)^{-1/2}, \tag{24}$$

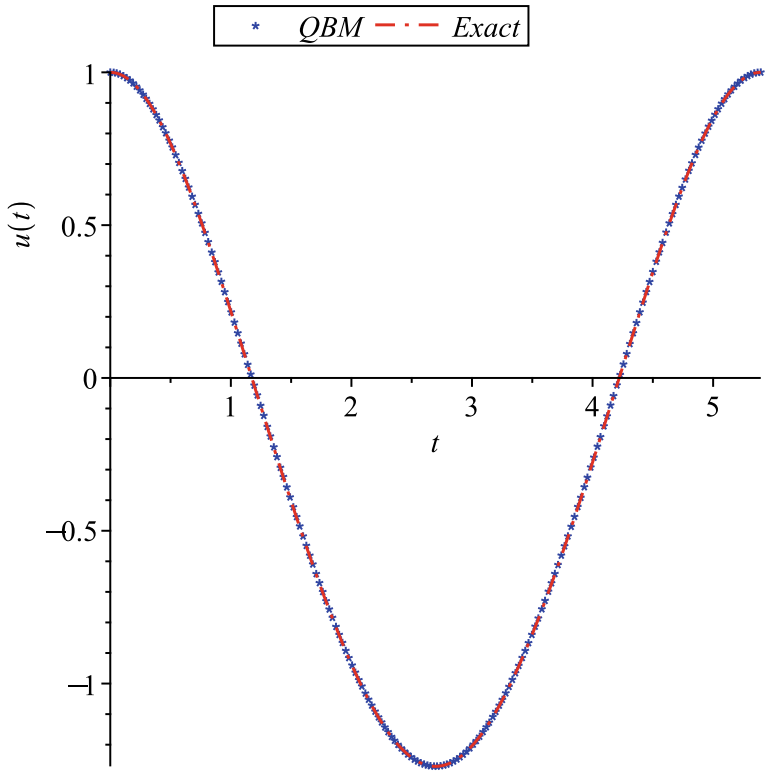

Fig. 3 A comparison between exact and approximate solutions of Eq. (1) for $a = 1$ and $\sigma = 0.5$

$$f_b(t) = \left(1 + k_{2b}t^2 + k_{3b}t^4 + k_{4b}t^6\right)^{-1/2}, \tag{25}$$

and

$$k_{1a} = \left(2\,\sigma\,a^2 + (2 - 2\,\sigma)\,a + 2\right)^{-1/2}, \quad k_{2a} = \frac{-3\,\sigma\,a^2 + 2\,(-1+\sigma)\,a - 1}{2\,\sigma\,a^2 - 2\,(-1+\sigma)\,a + 2},$$

$$k_{3a} = \frac{a\,(3\,\sigma\,a - \sigma + 1)}{3\,\sigma\,a^2 + (3 - 3\,\sigma)\,a + 3}, \quad k_{4a} = -\frac{\sigma\,a^2}{4\,\sigma\,a^2 - (4\,\sigma - 4)\,a + 4},$$

and also,

$$k_{1b} = \left(2\,\sigma\,b^2 + (2\sigma - 2)\,b + 2\right)^{-1/2}, \quad k_{2b} = \frac{-3\,\sigma\,b^2 - 2\,(\sigma - 1)\,b - 1}{2\,\sigma\,b^2 + 2\,(\sigma - 1)\,b + 2},$$

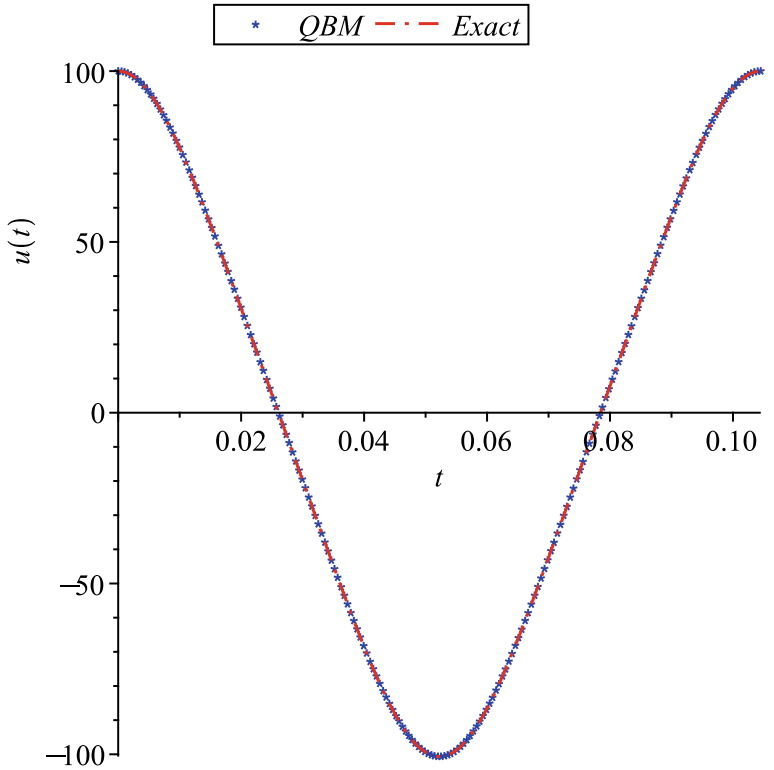

Fig. 4 A comparison between exact and approximate solutions of Eq. (1) for $a = 100$ and $\sigma = 0.5$

$$k_{3b} = \frac{b\,(3\,\sigma\,b + \sigma - 1)}{3\,\sigma\,b^2 + (3\,\sigma\, - 3)\,b + 3}, \quad k_{4b} = -\frac{\sigma\,b^2}{4\,\sigma\,b^2 + (4\,\sigma - 4)\,b + 4}.$$

It is noted that to investigate Gauss quadrature formulas for approximating integrals the linear mapping $t = \frac{b+a+x(b-a)}{2}$ is used to map integrals on finite intervals $[a, b]$ over $[-1, 1]$, as follows:

$$\int_a^b f(t)dt = \frac{b-a}{2}\int_{-1}^{1} g\,(x)\,dx. \tag{26}$$

where

$$g\,(x) = f\left(\frac{b+a+x(b-a)}{2}\right). \tag{27}$$

Consequently, by using (26) and (27) Eqs. (22) and (23) may be viewed as

$$T_a = \frac{4}{k_{1a}}\int_{-1}^{1} g_a(x)dx. \tag{28}$$

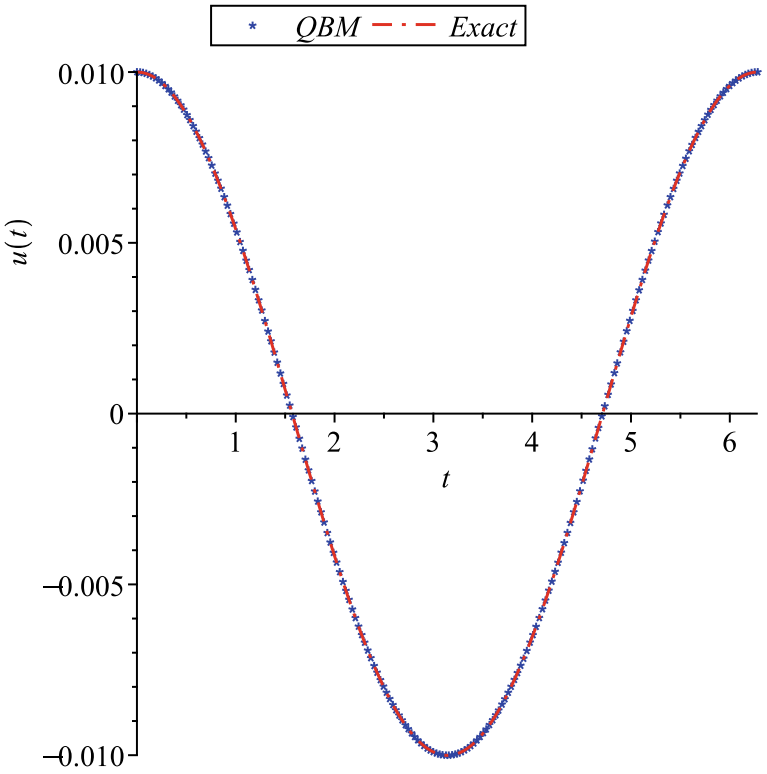

Fig. 5 A comparison between exact and approximate solutions of Eq. (1) for $a = 0.01$ and $\sigma = 0.9$

$$T_b = \frac{4}{k_{1b}} \int_{-1}^{1} g_b(x)dx. \tag{29}$$

where $g_a(x) = f_a\left(\frac{1+x}{2}\right)$ and $g_b(x) = f_b\left(\frac{1+x}{2}\right)$.

Now, to approximate the values of integrals (28) and (29), we can try the well-known Lobatto quadrature rules on $[-1, 1]$ as:

$$\int_{-1}^{1} g(x)dx \approx \frac{2}{n(n-1)}g(-1) + \frac{2}{n(n-1)}g(1) + \frac{2}{n(n-1)} \sum_{i=1}^{n-2} \frac{1}{[P_{n-1}(x_i)]^2} g(x_i). \tag{30}$$

where x_i is the $(i-1)$ st root of $P'_{n-1}(x)$ and $P_n(x)$ is Legendre polynomials of degree n. This rule yields an exact result for polynomials of degree $2n-3$ or less [16].

For $n = 7$ in (30), we have:

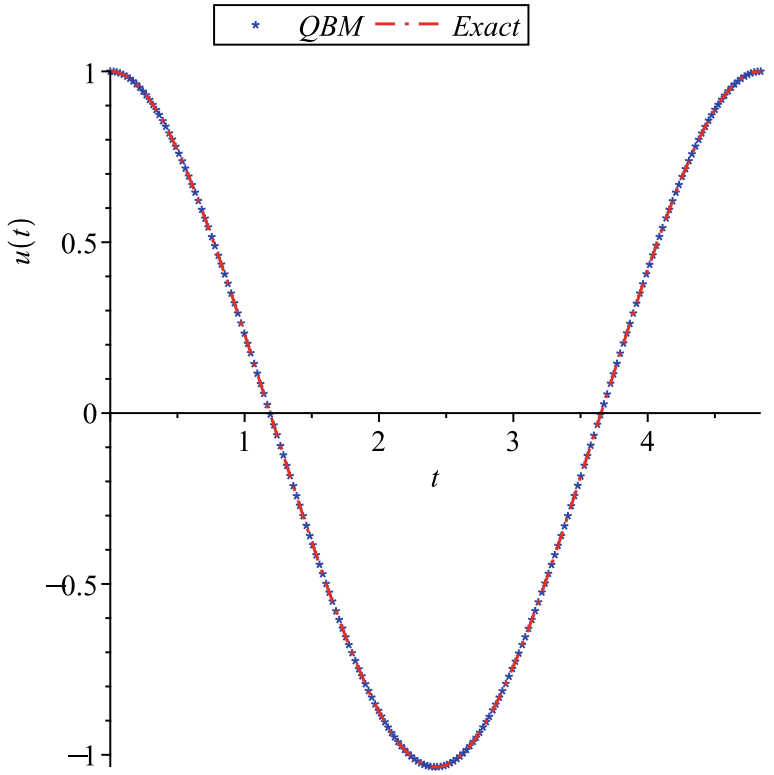

Fig. 6 A comparison between exact and approximate solutions of Eq. (1) for $a = 1$ and $\sigma = 0.9$

$$\begin{aligned}\int_{-1}^{1} g(x)dx \approx\ & 0.4876190476\, g(0) + 0.0476190476\, (g(1) + g(-1)) \\ & + 0.4317453812\, (g(0.4688487934) + g(-0.4688487934)) \\ & + 0.2768260473\, (g(0.8302238962) + g(-0.8302238962))\,.\end{aligned} \tag{31}$$

Using Eq. (31) in (28)–(29), we obtain the analytical approximations for T_a and T_b, as:

$$\begin{aligned}\hat{T}_a = \frac{1}{k_{1a}}[&1.950476190\, g_a(0) + 0.1904761904\, (g_a(1) + g_a(-1)) \\ & + 1.726981525\, (g_a(0.4688487934) + g_a(-0.4688487934)) \\ & + 1.107304189\, (g_a(0.8302238962) + g_a(-0.8302238962))].\end{aligned} \tag{32}$$

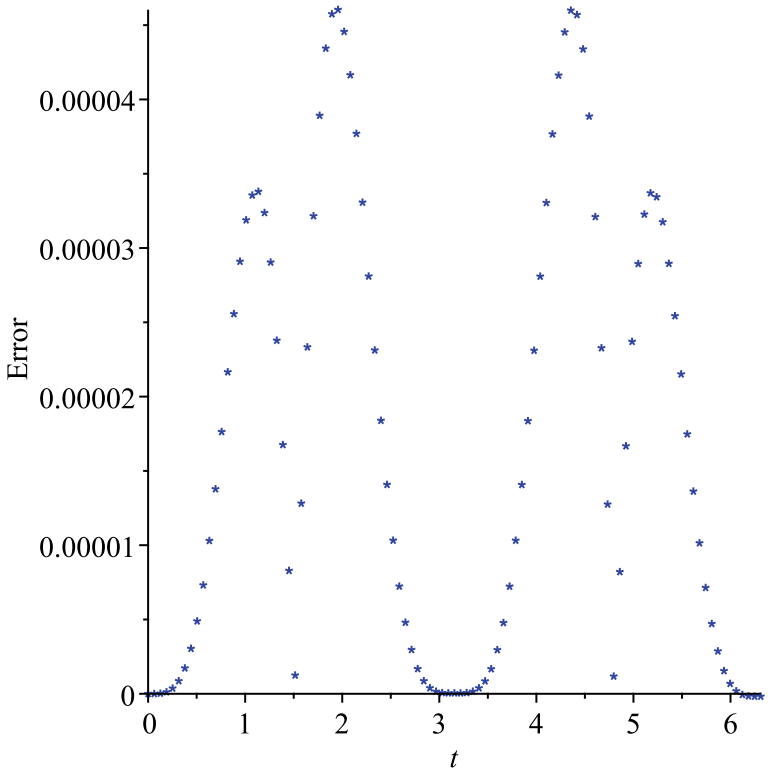

Fig. 7 Difference between the exact and approximate solutions of Eq. (1) for $a = 0.1$ and $\sigma = 0$

$$\begin{aligned}\hat{T}_b = \frac{1}{k_{1b}}[&1.950476190\, g_b(0) + 0.1904761904\, (g_b(1) + g_b(-1)) \\ &+ 1.726981525\, (g_b(0.4688487934) + g_b(-0.4688487934)) \\ &+ 1.107304189\, (g_b(0.8302238962) + g_b(-0.8302238962))].\end{aligned} \tag{33}$$

Moreover, we utilize a generalized rational form of solution given by [8]:

$$u(t) = \begin{cases} \frac{a(1+B_a)\cos\omega_a t}{1+B_a\cos 2\omega_a t}, & 0 \le t \le \frac{\hat{T}_a}{4} \\ \frac{b(1+B_b)\cos\omega_b(t-\frac{\hat{T}_a}{4}+\frac{\hat{T}_b}{2})}{1+B_b\cos 2\omega_b(t-\frac{\hat{T}_a}{4}+\frac{\hat{T}_b}{2})}, & \frac{\hat{T}_a}{4} \le t \le \frac{\hat{T}_a}{4}+\frac{\hat{T}_b}{2} \\ \frac{a(1+B_a)\cos\omega_a(t+\frac{\hat{T}_a}{4}-\frac{\hat{T}_b}{2})}{1+B_a\cos 2\omega_a(t+\frac{\hat{T}_a}{4}-\frac{\hat{T}_b}{2})}, & \frac{\hat{T}_a}{4}+\frac{\hat{T}_b}{2} \le t \le T \end{cases} \tag{34}$$

where $\omega_a = 2\pi/\hat{T}_a$, $\omega_b = 2\pi/\hat{T}_b$ and B_a, B_b are functions of the constant parameters σ and the initial amplitudes a, b.
To determine the values of B_a and B_b, first, from Eqs. (1) we have

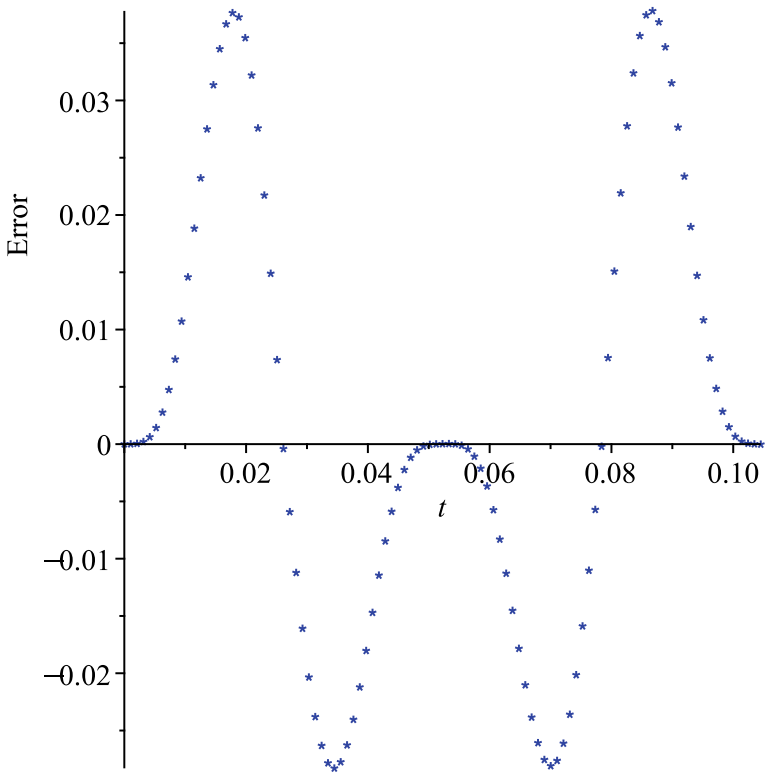

Fig. 8 Difference between the exact and approximate solutions of Eq. (1) for $a = 100$ and $\sigma = 0.5$

$$\ddot{x}(0) = -a - (1-\sigma)a^2 - \sigma a^3. \tag{35}$$

$$\ddot{x}\left(\frac{T_a}{4} + \frac{T_b}{4}\right) = b - (1-\sigma)b^2 + \sigma b^3. \tag{36}$$

On the other hand, after doing some algebra in (34) we get

$$\ddot{x}(0) = \frac{a\omega_a^2(-1+3B_a)}{1+B_a} \tag{37}$$

$$\ddot{x}\left(\frac{T_a}{4} + \frac{T_b}{4}\right) = -\frac{b\omega_b^2(-1+3B_b)}{1+B_b} \tag{38}$$

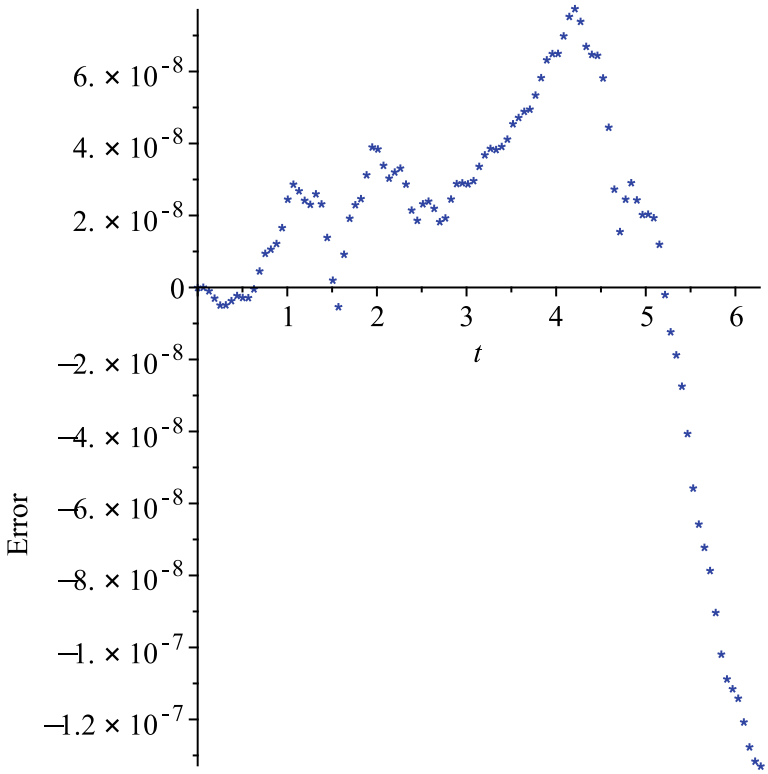

Fig. 9 Difference between the exact and approximate solutions of Eq. (1) for $a = 0.01$ and $\sigma = 0.9$

Equating (35)–(37) and (36)–(38), we obtain the explicit formulae for B_a and B_b, as follows

$$B_a = -\frac{a^2\sigma - a\sigma - \omega_a^2 + a + 1}{a^2\sigma - a\sigma + 3\,\omega_a^2 + a + 1}. \tag{39}$$

$$B_b = -\frac{\sigma\, b^2 + b\sigma - {w_b}^2 - b + 1}{\sigma\, b^2 + b\sigma + 3\,{w_b}^2 - b + 1}, \tag{40}$$

where ω_a and ω_b are obtained from Eqs. (32) and (33), respectively.

4 Results and Discussions

In order to verify the accuracy of the proposed method, numerical simulations are carried out in this section.

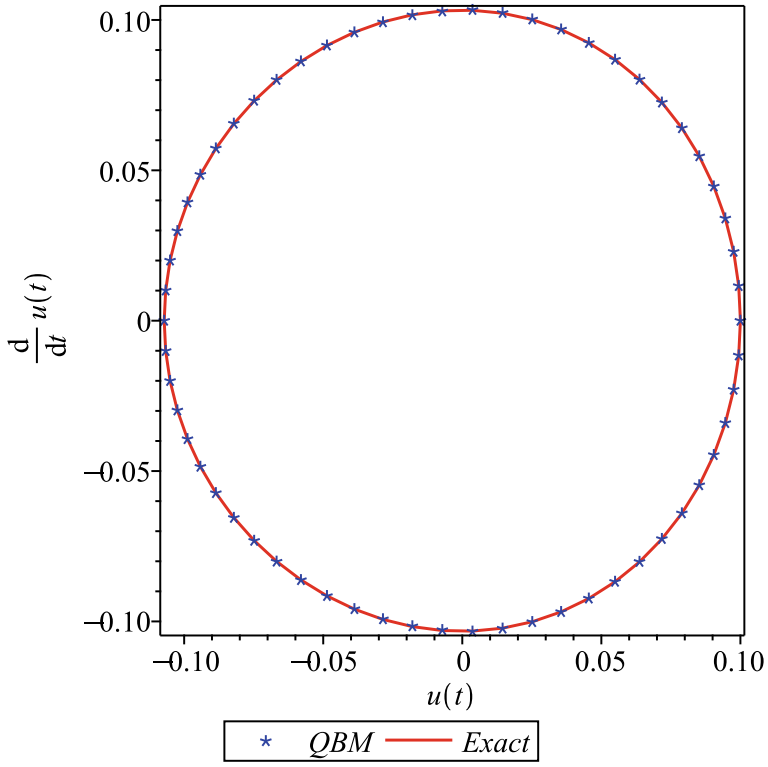

Fig. 10 Phase plane trajectories of Eq. (1) for $a = 0.1$ and $\sigma = 0$

Comparisons between the exact periods (21) and corresponding approximate ones of the periods as well as their relative error of different methods are listed in Tables 1, 2 and 3, where the relative error of the analytical approximation, T_{Method}, is giving by:

$$Error(\%) = \frac{|T_{ex} - T_{Method}|}{T_{ex}} \times 100. \tag{41}$$

It can be observed that the proposed T_{QBM} has a smaller relative error and provide excellent approximations to the exact frequency regardless of the oscillation amplitude a and parameter σ.

As can be seen, the presented approximation for periods in this contribution T_{QBM} (QBM stands for the present quadature-based method in this paper) is more efficient than the other compared methods for solving Eq. (1) for small as well as large values of oscillation amplitude a and parameter σ as compared with other existing approximations.

For graphical comparison, we have plotted the comparison of $u(t)$ for different approximate periodic solutions with the exact solution in Figs. 1, 2, 3, 4, 5, 6, 7, 8,

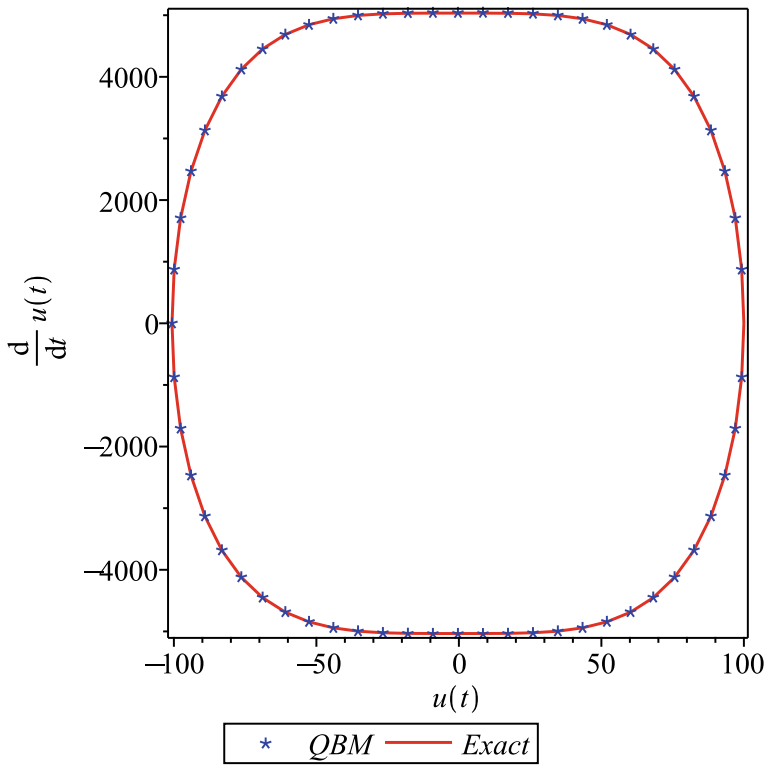

Fig. 11 Phase plane trajectories of Eq. (1) for $a = 100$ and $\sigma = 0.5$

and 9, respectively. It is obvious that the results obtained in this paper are in excellent agreement with exact solutions and the difference between exact and appriximate solutions is negligible.

Furthermore, corresponding phase plane trajectories of the time responses of the compared approximate solutions for three different cases are depicted in Figs. 10, 11, and 12. It is readily apparent that the proposed method here is not only able to predict accurate approximations for frequency even for very large oscillation amplitude but also to maintain very good agreement with exact periodic solutions of a nonlinear oscillators as time goes on.

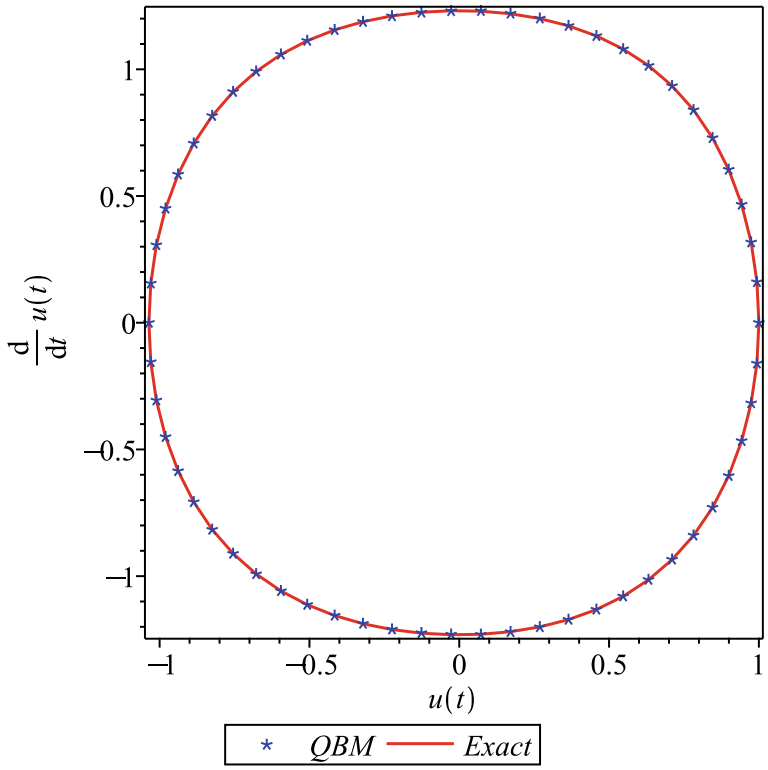

Fig. 12 Phase plane trajectories of Eq. (1) for $a = 1$ and $\sigma = 0.9$

References

1. Goswami A, Rathore S, Singh J, Kumar D (2021) Analytical study of fractional nonlinear Schrödinger equation with harmonic oscillator. Discret Continuous Dyn Syst Ser S 14(10):3589–3610
2. Goswami A, Sushila, Singh J, Kumar D (2020) Numerical computation of fractional Kersten-Krasil'shchik coupled KdV-mKdV system arising in multi-component plasmas. AIMS Math 5(3):2346–2368
3. Goswami A, Singh J, Kumar D, Sushila (2019) An analytical approach to fractional EW equations describing hydro-magnetic waves in cold plasma. Phys A Stat Mech Appl 524:563–575
4. Goswami A, Singh J, Kumar D, Gupta S, Sushila (2019) An efficient analytical technique for fractional partial differential equations occurring in ion acoustic waves in plasma. J Ocean Eng Sci 4:85–99
5. Goswami A, Singh J, Kumar D (2018) Numerical simulation of fifth order KdV equations occurring in magneto-acoustic waves. Ain Shams Eng J 9:2265–2273
6. Kovacic I, Brennan MJ (2011) The Duffing equation: nonlinear oscillators and their behaviour. Wiley, New York
7. Nayfeh AH, Mook DT (1978) Nonlinear oscillations. Wiley, New York
8. Mickens RE (1996) Oscillations in planar dynamics systems. World Scientific, Singapore

9. He JH (2003) Homotopy perturbation method: a new nonlinear analytical technique. Appl Math Comput 135(1):73–79
10. He JH (2004) The homotopy perturbation method for nonlinear oscillators with discontinuities. Appl Math Comput 151(1):287–292
11. Guo Z, Leung AYT (2009) Homotopy perturbation for conservative Helmholtz-Duffing oscillators. J Sound Vib 325:287–296
12. Leung AYT, Guo Z (2010) The iterative homotopy harmonic balance method for conservative Helmholtz-Duffing oscillators. Appl Math Comput 215:3163–3169
13. Askari H, Saadatnia Z, Younesian D, Yildirim A, Kalami-Yazdi M (2011) Approximate periodic solutions for the Helmholtz-Duffing equation. Comput Math Appl 62:3894–3901
14. Chen YY, Chen SH, Wang WW (2016) Novel hyperbolic homoclinic solutions of the Helmholtz-Duffing oscillators. Shock Vib 2016. Article ID 9471423
15. Mickens RE (1998) Periodic solutions of the relativistic harmonic oscillator. J Sound Vib 212: 905–908
16. Zwillinger D (2010) Standard mathematical tables and formulae, 32nd edn. CRC Press, New York

Haar Wavelet Series Method for Solving Simultaneous Proportional Delay Differential Equations

Basharat Hussain and Afroz Afroz

Abstract A new numerical approach is presented to obtain the approximate solution of simultaneous proportional delay differential equations (SPDDEs). The method utilizes delayed Haar wavelet series and collocation points to transform the SPDDEs into a system of algebraic matrix equations with unknown coefficient matrices. The values of these unknown row matrices can be obtained by using a suitable solver. Using these coefficients, the solution in terms of collocated Haar wavelet series is obtained. Also, a numerical experiment is conducted on linear/non-linear systems to examine the applicability, appropriateness, and efficacy of the method.

Keywords Simultaneous delay differential equations · Pantograph equations · Collocation points · Haar wavelets

2020 Mathematics Subject Classification 34Kxx · 65L03 · 65L05 · 65L60

1 Introduction

The proportional delay differential equation is a particular class of functional differential equations known as the pantograph equation. Pantograph is a device first used in 1851 for the construction of the electric locomotive. A mathematical model for the pantograph was first introduced in 1971 [22]. These equations have applications in the scientific, industrial, and engineering domains. For further details on theory and applications of pantograph equation, one may refer to [8–11, 15, 28, 30] and the references therein.

Many scientific models require high consistency and real-time accuracy, mathematical modeling of such phenomena involves systems of delay differential equa-

B. Hussain (✉) · A. Afroz
MANUU, Hyderabad 500032, India
e-mail: basharathussain_rs@manuu.edu.in

A. Afroz
e-mail: afroz.ahmad@manuu.edu.in

J. Singh et al. (eds.), *Advances in Mathematical Modelling, Applied Analysis and Computation*, Lecture Notes in Networks and Systems 415,
https://doi.org/10.1007/978-981-19-0179-9_25

tions. In most cases, we are unable to find the exact solutions for the system of delay differential equations via analytical methods. Hence, a numerical method is required to tackle such problems.

Many mathematicians have contributed various efficient numerical methods concerning the solution of the proportional delay differential equation. For instance, in [18], authors used the rational approximation method for solving proportional delay differential equations, Ali et al. [4] considered spectral collocation points method for the numerical solution of proportional delay differential equations. Chen and Wang [6] investigated the solution of neutral proportional delay differential equations using variational iteration method(VIM) and [5] provides Legendre–Gauss collocation technique to obtain the solution of proportional delay differential equations. Some recent methods are as follows: Doha et al. [12] solved generalized pantograph equations using the spectral collocation method. Reutskiy [26] solved higher order functional–differential equation with proportional delay using semi-analytic collocation points method. Akyuz-Dascioglu and Sezer [3] solved higher order pantograph equations using Bernoulli collocation method. Cheng et al. [7] used the optimal residual method to solve Neutral proportional delay differential equations. Jafari et al. [19] presented a transferred Legendre pseudo-spectral method to tackle pantograph equations. Recently, Faheem et al.[13, 14] obtained numerical solutions of neutral delay differential equations using Legendre wavelet, Hermite wavelet, Chebyshev wavelet, Laguerre wavelet, Gegenbauer wavelet, and Bernoulli wavelet.

In this study, we apply the Haar wavelet series method to solve the following simultaneous proportional delay differential equations:

$$\begin{aligned}
&\chi_1'(t) = t_1(t, \chi_1(t), \chi_2(t), \ldots, \chi_n(t), \chi_1(q_1 t), \chi_2(q_2 t), \ldots, \chi_n(q_\lambda t))\\
&\chi_2'(t) = t_2(t, \chi_1(t), \chi_2(t), \ldots, \chi_n(t), \chi_1(q_1 t), \chi_2(q_2 t), \ldots, \chi_n(q_\lambda t))\\
&\vdots\\
&\chi_n'(t) = t_n(t, \chi_1(t), \chi_2(t), \ldots, \chi_n(t), \chi_1(q_1 t), \chi_2(q_2 t), \ldots, \chi_n(q_\lambda t))\\
&\chi_\sigma(0) = \chi_{\sigma 0}, \quad \sigma = 1, 2, \ldots, n
\end{aligned} \tag{1}$$

where t_σ's are analytical functions, and q_σ's $\in (0, 1)$, $\sigma = 1, 2, \ldots, n$.

These equations have been noticed widely in several models such as biological models, aerospace systems, control theory, disease spread model, tumor growth models, etc. Therefore, this study is an important contribution in the field of Applied mathematical modeling and Numerical analysis.

The article is organized in the following outline: Definition of Haar wavelet is given in Sect. 2. The method is described in Sect. 3. A step-wise algorithm is provided in Sect. 4. In Sect. 5 the method is applied to some test problems to check its efficiency and correctness. The last Section is devoted to conclusion.

2 Basic Definitions

2.1 Wavelet

In 1982, Jean Morlet, a French geophysical engineer, first introduced the concept of wavelets as a family of functions generated by shifting and stretching of a single function known as the "mother wavelet":$\psi(t)$. When the stretch a and shift b varies continuously, we get the family of continuous wavelet as

$$\psi_{a,b}(t) = \frac{1}{\sqrt{a}}\psi\frac{(t-b)}{a}, a \neq 0, b \in \mathbb{R}. \tag{2}$$

If we restrict a and b to discrete values as $a = a_0^{-j}$, $b = kb_0a^{-j}$, where $a_0 \geq 1$, $b_0 \geq 0$ and $j, k \in \mathbb{N}$. We have the following family of discrete wavelets as

$$\psi_{j,k}(t) = \frac{1}{\sqrt{a_0^{-j}}}\psi(a_0^j t - kb_0),$$

where $\{\psi_{j,k}(t)\}_{j,k\in\mathbb{N}}$ forms a wavelet basis for $L^2(\mathbb{R}) - space$. In particular, the choices $a_0 = 2$ and $b_0 = 1$ produced an orthonormal basis [2, 20, 21].

2.2 Haar Wavelet

To construct the Haar wavelet system $\{\mathfrak{h}_i(t)\}_{i=1}^{\infty}$ on $[\Gamma_1, \Gamma_2]$ two basic functions are required, namely:
(a) The Haar scaling function (father wavelet):

$$\mathfrak{h}_1(t) = \mathbb{I}_{[\Gamma_1,\Gamma_2)}(t); \tag{3}$$

(b) The mother wavelet:

$$\mathfrak{h}_2(t) = \mathbb{I}_{[\Gamma_1,(\Gamma_1+\Gamma_2)/2)}(t) - \mathbb{I}_{[(\Gamma_1+\Gamma_2)/2,\Gamma_2)}(t), \tag{4}$$

where $\mathbb{I}_{[a,b]}(t)$ is characteristic/indicator function. Now for generating the Haar wavelet series, let j be dilation and k be translation parameter.

Then ith Haar Wavelet is defined as

$$\mathfrak{h}_i(t) = \begin{cases} 1 & \text{for } t \in [\vartheta_1(i), \vartheta_2(i)) \\ -1 & \text{for } t \in [\vartheta_2(i), \vartheta_3(i)) \\ 0 & otherwise, \end{cases} \tag{5}$$

where

$\vartheta_1(i) = \Gamma_1 + (\Gamma_2 - \Gamma_1)k/2^j, \vartheta_2(i) = \Gamma_1 + (\Gamma_2 - \Gamma_1)(k + 0.5)/2^j, \vartheta_3(i) = \Gamma_1 + (\Gamma_2 - \Gamma_1)(k + 1)/2^j$. The index $i = 2^j + k + 1$, $j = 0, 1, \ldots, J$ where J is maximum level of wavelet and $k = 0, 1, \ldots, 2^j - 1$.

(c) Define scaling function space and wavelet space as follows:

$$\begin{aligned} V_j &= span\{2^{j/2}\mathfrak{h}_1(2^j t - k), t \in [\Gamma_1, \Gamma_2]\}_{k=0}^{2^j-1}, \\ W_j &= span\{2^{j/2}\mathfrak{h}_2(2^j t - k), t \in [\Gamma_1, \Gamma_2]\}_{k=0}^{2^j-1}. \end{aligned} \tag{6}$$

Suppose $0 \leq J_0 < J$, then following relation holds:

$$V_J = V_{J_0} \otimes W_{J_0} \otimes W_{J_0+1} \cdots \otimes W_{J-1}. \tag{7}$$

The spaces V_j are such that $V_0 \subset V_1 \subset V_2 \cdots \subset L^2([\Gamma_1, \Gamma_2])$ and $\overline{\cup_{j=0}^{\infty} V_j} = L^2([\Gamma_1, \Gamma_2])$. Hence, $L^2([\Gamma_1, \Gamma_2]) = V_0 \bigotimes(\bigotimes_{j_0}^{\infty} W_j)$ holds. It allows us to approximate any $f \in L^2([\Gamma_1, \Gamma_2])$ with following truncated Haar wavelet series:

$$f_{approx}(t) = \sum_{i=1}^{2^{J+1}} a_i \mathfrak{h}_i(t). \tag{8}$$

To apply the Haar wavelet, following integral is required:

$$\mathcal{P}_i(t) = \int_{\Gamma_1}^{t} \mathfrak{h}_i(t)dt.$$

The analytic integration of (5) yields

$$\mathcal{P}_i(t) = \begin{cases} t - \vartheta_1(i) & \text{for } t \in [\vartheta_1(i), \vartheta_2(i)) \\ \vartheta_3(i) - t & \text{for } t \in [\vartheta_2(i), \vartheta_3(i)) \\ 0 & otherwise \end{cases} \tag{9}$$

Haar wavelet is considered an efficient tool in numerical analysis, image processing, signal processing, and has numerous other applications in mathematics and engineering. For details, readers may refer to [1, 16, 17, 23–25, 27] and their further references.

3 Description of Method

In this section, We apply the Haar wavelet series method for solving simultaneous proportional delay differential equation (1).

Let

$$\begin{aligned}
\chi_1'(t) &= \sum_{i=1}^{2^{J+1}} a_i \mathfrak{h}_i(t), \\
\chi_2'(t) &= \sum_{i=1}^{2^{J+1}} b_i \mathfrak{h}_i(t), \\
&\vdots \\
\chi_n'(t) &= \sum_{i=1}^{2^{J+1}} c_i \mathfrak{h}_i(t),
\end{aligned} \tag{10}$$

where a_i's, b_i's $\ldots$ c_i's are the Haar wavelet coefficients.

Now, by integrating equation (10), we have

$$\begin{aligned}
\chi_1(t) &= \sum_{i=1}^{2^{J+1}} a_i \mathcal{P}_i(t) + \chi_1(0), \\
\chi_2(t) &= \sum_{i=1}^{2^{J+1}} b_i \mathcal{P}_i(t) + \chi_2(0), \\
&\vdots \\
\chi_n(t) &= \sum_{i=1}^{2^{J+1}} c_i \mathcal{P}_i(t) + \chi_n(0).
\end{aligned} \tag{11}$$

Also,

$$\begin{aligned}
\chi_1(q_1 t) &= \sum_{i=1}^{2^{J+1}} a_i \mathcal{P}_i(q_1 t) + \chi_1(0), \\
\chi_2(q_2 t) &= \sum_{i=1}^{2^{J+1}} b_i \mathcal{P}_i(q_2 t) + \chi_2(0), \\
&\vdots \\
\chi_n(q_n t) &= \sum_{i=1}^{2^{J+1}} c_i \mathcal{P}_i(q_n t) + \chi_n(0),
\end{aligned} \tag{12}$$

where $\chi_\sigma(0)$'s are the given initial conditions and q_σ'$s \in (0, 1)$, $\sigma = 1, 2, \ldots, n$.

Now, upon plugging equations (10), (11), and (12) in the governing equation (1) along with the collocation points we get a system of an algebraic equations. After solving the system, we obtain the unknown Haar wavelet coefficients, and finally

using these coefficients in (11), approximate solution at collocation points can be obtained.

4 Algorithm

Input: Level of resolution J.

Step-1: Set collocation points $t_l = \frac{(l-0.5)}{2^{J+1}}$, $l = 1, 2, 3 \ldots 2^{J+1}$.

Step-2: Compute Haar wavelets $\mathfrak{h}_i$ and integral of Haar wavelets $\mathcal{P}_i$ from Eqs. (5) and (9), respectively.

Step-3: Assume $\chi'_\sigma(t) = \sum_{i=1}^{2^{J+1}} (a_i)_\sigma \mathfrak{h}_i(t)$, where $\sigma = 1, 2, \ldots n$ and i is wavelet index.

Step-4: Integration of Step-3 within the limits 0 to t yields,

$$\chi_\sigma(t) = \sum_{i=1}^{2^{J+1}} (a_i)_\sigma \mathcal{P}_i(t) + \chi_\sigma(0), \quad \sigma = 1, 2, \ldots, n.$$

Step-5: Upon using the expressions for $\chi'_\sigma(t)$'s, $\chi_\sigma(t)$'s , $\ldots$, $\chi_\sigma(q_\sigma t)$'s along with collocation points in equation (1), we get an algebraic system in unknown vectors $(a_i)_1, (a_i)_2, \ldots, (a_i)_n$.

Step-6: Solve the algebraic system for the unknown vectors $(a_i)_1, (a_i)_2, \ldots, (a_i)_n$.

Step-5: Utilize the values of the vectors $(a_i)_1, (a_i)_2, \ldots, (a_i)_n$ in Step-4 to obtained the unknown functions
$\chi_1(t), \chi_2(t), \ldots, \chi_n(t)$.

Output: Approximate solution $\chi_1(t_l), \chi_2(t_l), \ldots, \chi_n(t_l)$ is obtained.

5 Implementation of Method on Test Problems

The efficiency and numerical validation of the method are demonstrated with the help of the following test problems.

Case-1: Consider the system

$$\begin{cases} \chi'_1(t) = \chi_1(t/2) + \chi_1(t) - \chi_2(t) + exp(-t) - exp(t/2) \\ \chi'_2(t) = -\chi_1(t/2) - \chi_1(t) - \chi_2(t) + exp(t) + exp(t/2) \\ with \;\; \chi_1(0) = \chi_2(0) = 1, \quad 0 \le t \le 1. \end{cases} \tag{13}$$

The system has exact solution $\chi_1(t) = \exp(t)$, $\chi_2(t) = \exp(-t)$.

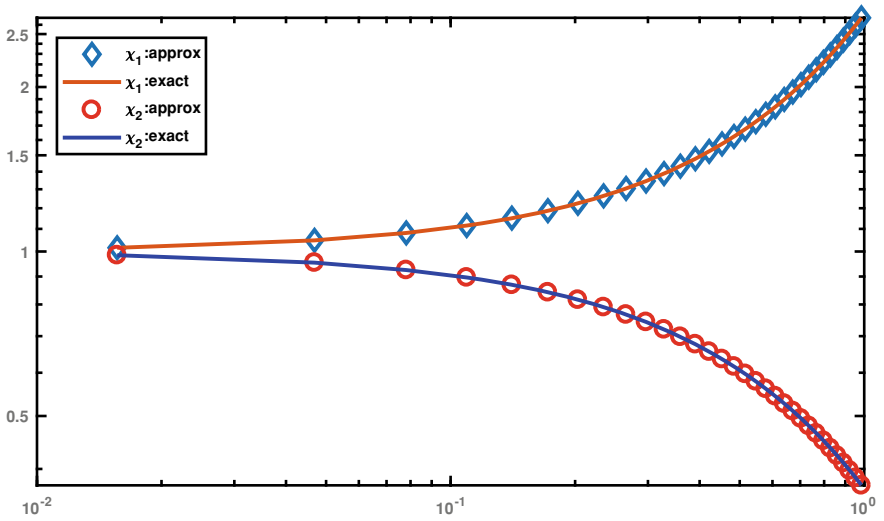

Fig. 1 Exact and approximate solution of case-1

Table 1 Maximum Absolute Error (MAE) at different levels of J

Case-1			Case-2	
J	MAE:$\chi_1(t)$	MAE:$\chi_2(t)$	MAE:$\chi_1(t)$	MAE:$\chi_2(t)$
2.0	$1.3000e-02$	$5.4000e-03$	$7.3000e-03$	$7.3000e-03$
3.0	$3.4187e-03$	$1.4267e-03$	$1.9007e-03$	$1.9007e-03$
4.0	$8.7870e-04$	$3.6790e-04$	$4.8190e-04$	$4.8190e-04$
5.0	$2.2290e-04$	$9.3500e-05$	$1.2170e-04$	$1.2170e-04$
6.0	$5.6150e-05$	$2.3570e-05$	$3.0580e-05$	$3.0570e-05$
7.0	$1.4090e-05$	$5.9200e-06$	$7.6620e-06$	$7.6620e-06$
8.0	$3.5290e-06$	$1.4820e-06$	$1.9180e-06$	$1.9180e-06$
9.0	$8.8310e-07$	$3.7090e-07$	$4.7980e-07$	$4.7980e-07$

We have solved the above system of differential equation using the Haar wavelet series method. The maximum absolute error (MAE) at a different level of resolution is given in Table 1. It can be observed from Table 1 that error decreases from $O(10^{-2})$ to $O(10^{-7})$, which ensures the convergence of the method. Also, Fig. 1 shows that approximate and exact curves match closely.

Case-2: Consider the system

$$\begin{cases} \chi_1'(t) = \exp(t/2)\chi_2(t/2) + \chi_1(t) \\ \chi_2'(t) = \exp(t/2)\chi_1(t/2) + \chi_2(t) \\ with \;\; \chi_1(0) = \chi_2(0) = 1, \quad 0 \le t \le 1. \end{cases} \tag{14}$$

The system has exact solution $\chi_1(t) = \exp(t)$, $\chi_2(t) = \exp(t)$.

Approximate solution of the above system obtained using the Haar wavelet series method are satisfactory. Computer simulation is carried out and numerical results are presented in Table 1. The exact and approximate solution of case 2 is plotted in Fig. 2 for J = 4. Also, the convergence of method can be observed in Fig. 3.

Case-3: Consider the following non-linear proportional delay system:

$$\begin{cases} \chi_1'(t) = 2\chi_2(t/2) + \chi_3(t) + t\cos(t/2) \\ \chi_2'(t) = -2\chi_3^2(t) + 1 - t\sin(t) \\ \chi_3'(t) = \chi_2(t) - \chi_1(t) - t\cos(t) \\ with \;\; \chi_1(0) = -1, \chi_2(0) = \chi_3(0) = 0, \quad 0 \le t \le 1. \end{cases} \tag{15}$$

Exact solution is $\chi_1(t) = -\cos(t)$, $\chi_2(t) = t\cos(t)$, $\chi_1, (t) = \sin(t)$

In this case, we have solved a non-linear system with three equations using the Haar wavelet series method. The exact and approximate solution for case-3 is plotted in Fig. 4. It is observed that both curves match closely. Absolute errors at different levels of resolution are depicted in Table 2 which shows that computed numerical solution is satisfactory. Also, it is evident from Fig. 5 that the accuracy of the solution is directly proportional to the values of J. Moreover, the error in each case was reduced from $O(10^{-2})$ to $O(10^{-7})$.

6 Conclusion

In this article, we have applied the Haar wavelet series method, to solve the simultaneous proportional delay differential equations. These equations play a vital role in the study of several mathematical models such as the disease spread model, drug delivery model, population growth model, etc.; therefore, this research is a significant development in the field of applied mathematical modeling. The present numerical scheme used a well-known real-valued Haar function (compactly supported, symmetric, and orthogonal) and is fast, simple, and computationally efficient. This method is computer-oriented and does not involve manual solving and simplification of sophisticated expressions. In order to ensure the consistency, correctness, and efficacy of the method, we provide the approximate solution of the three illustrations at different counts of collocation points. Also, the MAEs for case 1 and case 2 using

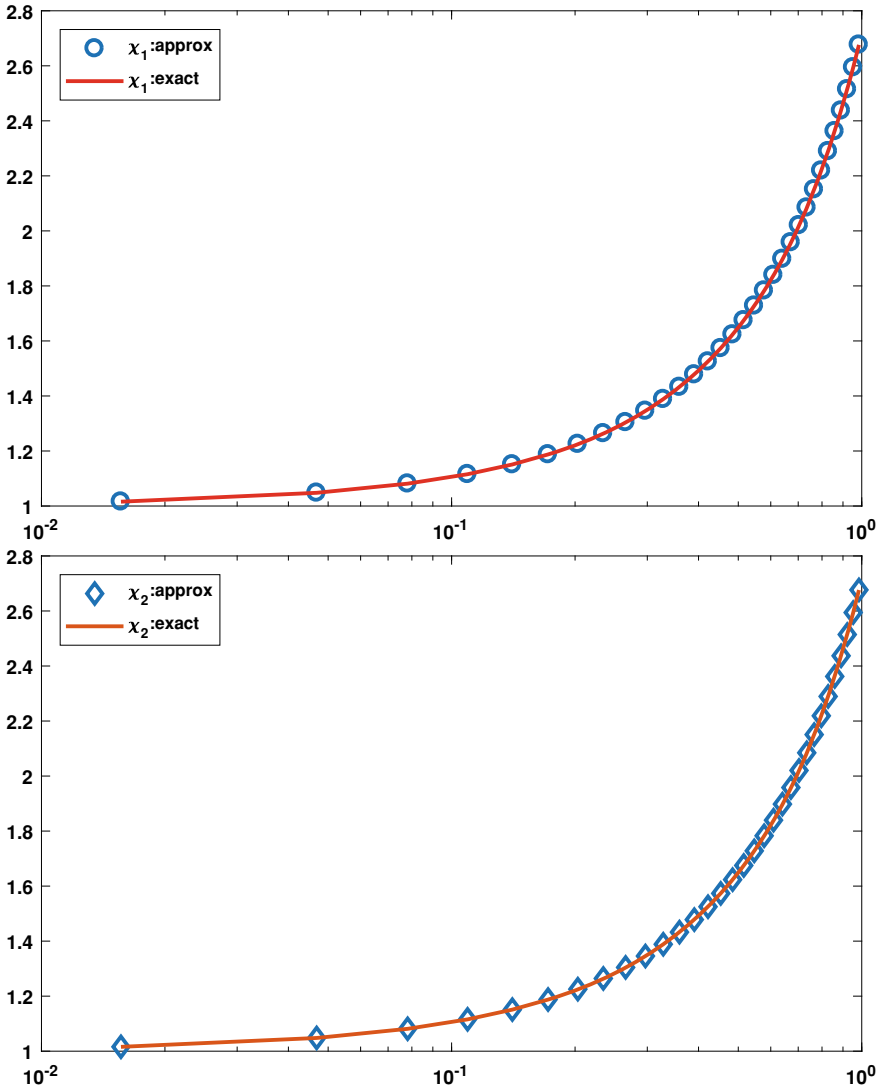

Fig. 2 Exact and approximate solution of case-2

the Laplace decomposition algorithm are $O(10^{-3})$ at $n = 6$ and $O(10^{-2})$ at $n = 3$, respectively [29]. It can be observed from the aforementioned tables and figures that the performance of the Haar wavelet series method is good. Moreover, this method can be extended to solve several other types of linear and non-linear simultaneous delay differential equations.

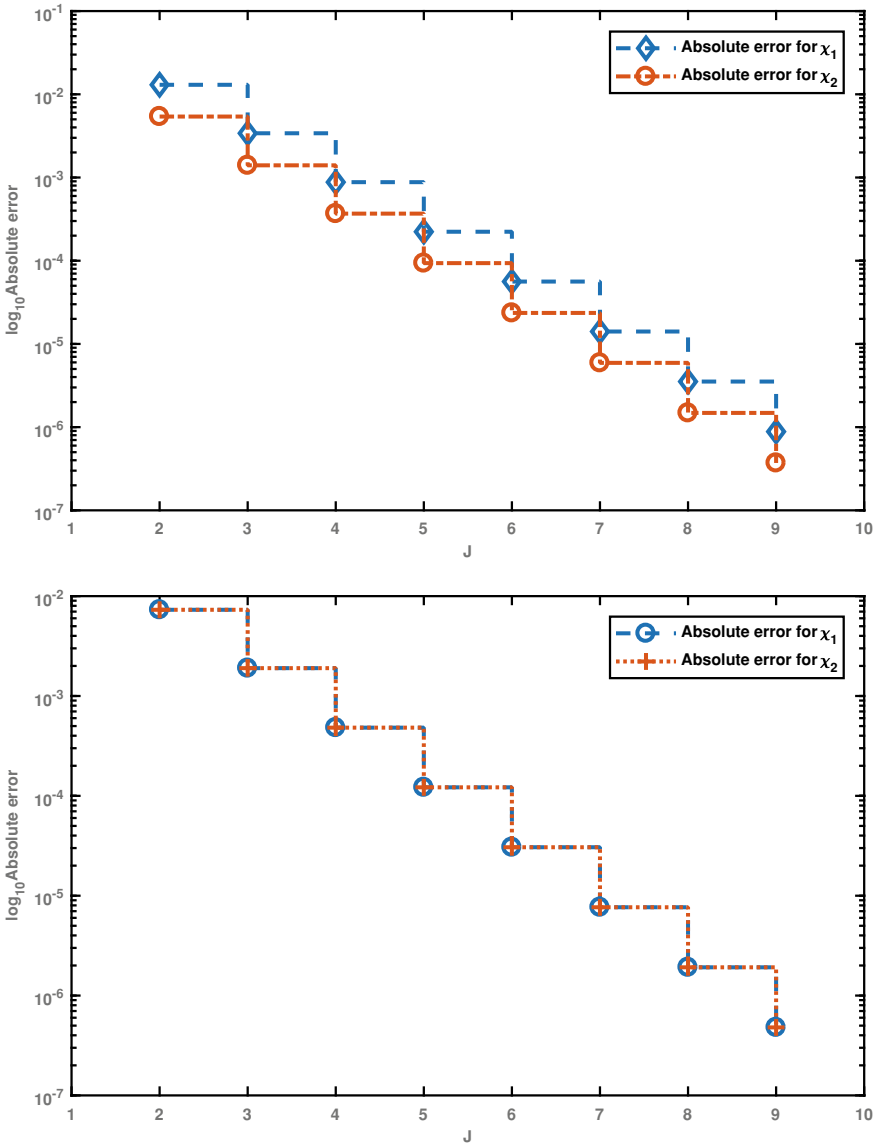

Fig. 3 Absolute error versus J

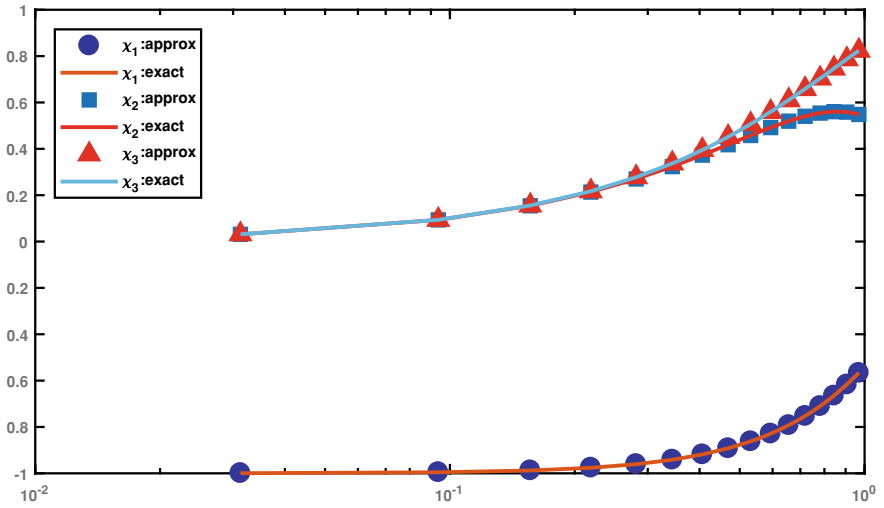

Fig. 4 Exact and approximate solution of case-3

Table 2 Maximum Absolute Error (MAE) at different levels of J for Case-3

J	MAE:$\chi_1(t)$	MAE:$\chi_2(t)$	MAE:$\chi_3(t)$
2.0	$1.9167e-03$	$2.0504e-03$	$3.1668e-03$
3.0	$4.8600e-04$	$5.1360e-04$	$8.0760e-04$
4.0	$1.2190e-04$	$1.2850e-04$	$2.0340e-04$
5.0	$3.0510e-05$	$3.2120e-05$	$5.1000e-05$
6.0	$7.6300e-06$	$8.0300e-06$	$1.2770e-05$
7.0	$1.9070e-06$	$2.0070e-06$	$3.1930e-06$
8.0	$4.7680e-07$	$5.0190e-07$	$7.9860e-07$
9.0	$1.1920e-07$	$1.2550e-07$	$1.9970e-07$

Acknowledgements The authors are indebted to the referees for their careful review of this manuscript and their insightful suggestions which led to an improved version.

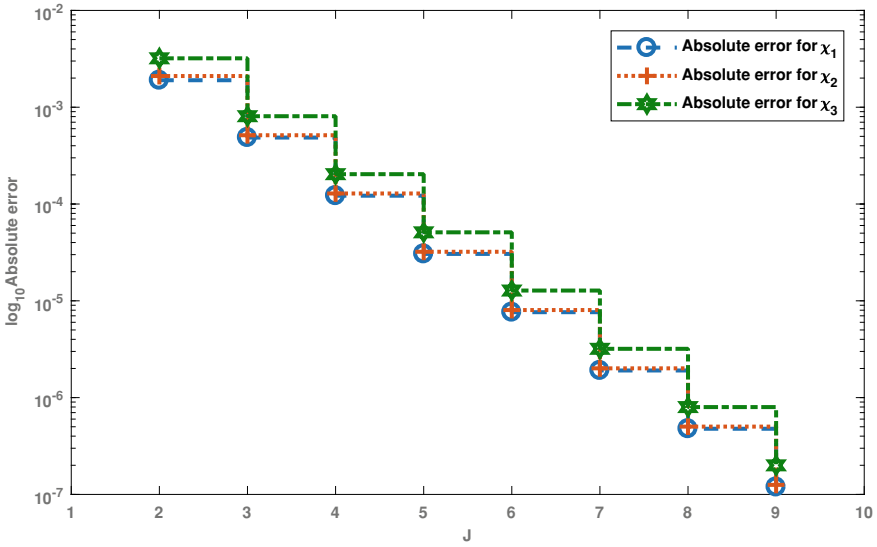

Fig. 5 Absolute error versus J (Case-3)

References

1. Abdullah A, Rafiq M (2021) A new numerical scheme based on Haar wavelets for the numerical solution of the Chen-Lee-Liu equation. Optik 226:165847
2. Ahmad K, Shah FA (2013) Introduction to wavelets with applications. Real World Education Publishers, New Delhi
3. Akyuz-Dascioglu A, Sezer M (2015) Bernoulli collocation method for high-order generalized pantograph equations. New Trends Math Sci 3(2):96–109
4. Ali I, Brunner H, Tang T (2009) Spectral methods for pantograph-type differential and integral equations with multiple delays. Front Math China 4:49–61
5. Bhrawy AH, Assas LM, Tohidi E, Alghamdi MA (2013) A Legendre-Gauss collocation method for neutral functional-differential equations with proportional delays. Adv Differ Equ 2013:63
6. Chen X, Wang L (2010) The variational iteration method for solving a neutral functional-differential equation with proportional delays. Comput Math Appl 59(8):2696–2702
7. Cheng X, Chen Z, Zhang Q (2015) An approximate solution for a neutral functional-differential equation with proportional delays. Appl Math Comput 260:27–34
8. Derfel G (1980) On compactly supported solutions of a class of functional-differential equations. Modern problems of function theory and functional analysis. Karaganda University Press, Kazakhstan
9. Derfel GA (1982) On the behaviour of the solutions of functional and functional-differential equations with several deviating arguments. Ukr Math J 34:286–291
10. Derfel GA (1990) Kato problem for functional-differential equations and difference Schrödinger operator. Oper Theory Adv Appl 46:319–321 (1990)
11. Driver RD (1977) Introduction to delay differential equations. In: ordinary and delay differential equations. Applied mathematical sciences, vol 20. Springer, New York, NY
12. Doha EH, Bhrawy AH, Baleanu D, Hafez RM (2014) A new Jacobi rational-Gauss collocation method for numerical solution of generalized pantograph equations. Appl Numer Math 77:43–54

13. Faheem M, Raza A, Khan A (2021) Wavelet collocation methods for solving neutral delay differential equations. Int J Nonlinear Sci Numer Simul
14. Faheem M, Raza A, Khan A (2021) Collocation methods based on Gegenbauer and Bernoulli wavelets for solving neutral delay differential equations. Math. Comput. Simul. 180:72–92
15. Fox L, Ockendon DF, Tayler AB (1971) On a functional-differential equations. J Inst Math Appl 8(3):271–307
16. Lepik Ü, Hein H (2014) Haar wavelets. In: Haar wavelets. Mathematical engineering. Springer, Cham
17. Hariharan G, Kannan K (2014) Review of wavelet methods for the solution of reaction-diffusion problems in science and engineering. Appl Math Model 38(3):799–813
18. Ishiwata E, Muroya Y (2007) Rational approximation method for delay differential equations with proportional delay. Appl Math Comput 187(2):741–747
19. Jafari H, Mahmoudi M, Noori Skandari MH (2021) A new numerical method to solve pantograph delay differential equations with convergence analysis. Adv Differ Equ 2021:129
20. Mehra M, Mehra W, Ahmad M (2018) Wavelets theory and its applications. Springer Singapore
21. Nievergelt Y (1999) Wavelets made easy, vol 174. Birkhäuser, Boston
22. Ockendon JR, Tayler AB (1971) The dynamics of a current collection system for an electric locomotive. Proc R Soc Lond Ser A 322:447–468
23. Raza A, Khan A (2019) Haar wavelet series solution for solving neutral delay differential equations. J King Saud Univ Sci 31(4):1070–1076
24. Raza A, Khan A (2018) Approximate solution of higher order two point boundary value problems using uniform Haar wavelet collocation method. In: International workshop of mathematical modelling, applied analysis and computation, pp 209–220. Springer, Singapore
25. Reisenhofer R, Bosse S, Kutyniok G, Wiegand T (2018) A Haar wavelet-based perceptual similarity index for image quality assessment. Sig Process Image Commun 61:33–43
26. Reutskiy SY (2015) A new collocation method for approximate solution of the pantograph functional differential equations with proportional delay. Appl Math Comput 266:642–655
27. Ray SS, Gupta AK (2018) Wavelet methods for solving partial differential equations and fractional differential equations. CRC Press
28. Song XL, Zhao P, Xing ZW, Peng JG (2016) Global asymptotic stability of CNNs with impulses and multi-proportional delays. Math Methods Appl Sci 39(4):722–733
29. Widatalla S, Koroma MA (2012) Approximation algorithm for a system of pantograph equations. J Appl Math
30. Xu C, Li P, Yuan S (2019) New findings on exponential convergence of a Nicholson's blowflies model with proportional delay. Adv Diff Equ 2019(1):1–7

Fractional Reaction–Diffusion Model: An Efficient Computational Technique for Nonlinear Time-Fractional Schnakenberg Model

Naveen S. Malagi, D. G. Prakasha, P. Veeresha, and B. C. Prasannakumara

Abstract In this article, the q-homotopy analysis transform method (q-HATM) is committed to finding the solutions and analyzing the gathered results for the nonlinear fractional-order reaction–diffusion systems such as the fractional Schnakenberg model. These models are well known for the modelling of morphogen in developmental biology. The efficiency and reliability of the q-HATM, which is the proper mixture of Laplace transform and q-HAM, always keep it in a better position in comparison with many other analytical techniques. By choosing a precise value for the auxiliary parameter $\hbar$, one can modify the region of convergence of the series solution. In the current framework, the investigation of the Schnakenberg models is implemented with exciting results. The acquired results guarantee that the considered method is very satisfying and scrutinizes the complex nonlinear issues that arise in the arena of science and technology.

Keywords Schnakenberg model · Liouville–Caputo derivative · Laplace transform · Homotopy analysis method

N. S. Malagi · D. G. Prakasha (✉) · B. C. Prasannakumara
Department of Studies in Mathematics, Davangere University, Shivagangothri Davangere-577007, India
e-mail: prakashadg@gmail.com

N. S. Malagi
e-mail: naveen2018m@gmail.com

B. C. Prasannakumara
e-mail: dr.bcprasanna@gmail.com

P. Veeresha
Center for Mathematical Needs, Department of Mathematics, CHRIST (Deemed to Be University), Bengaluru-560029, India
e-mail: pundikala.veeresha@christuniversity.in

J. Singh et al. (eds.), *Advances in Mathematical Modelling, Applied Analysis and Computation*, Lecture Notes in Networks and Systems 415,
https://doi.org/10.1007/978-981-19-0179-9_26

1 Introduction

The fractional calculus (FC) is a well-known notion in multiple areas of science and technology, which is defined as the generalization of the classical calculus, where we study the integral and differential operators of fractional order, even can be lengthened to complex sets. In the past few decades, many mathematical minds have strengthened this concept and designed various fractional differential and integral operators [1, 2]. Many young mathematical minds have demonstrated that fractional operators may effectively describe complex memory and a wide range of things in a traditional mathematical fashion, such as classical differential calculus. However, we are still at the initial stage of implementing the concept of FC in various areas of research. Nowadays, FC is a very promising tool due to its larger applications in the dynamics of complex nonlinear phenomena.

Leibnitz appreciated the concept of fractional derivatives. Additionally, it was demonstrated that FC is far preferable to traditional calculus for negotiating the majority of complicated real-world situations. Fractional calculus has grown exponentially in applied research. A large number of researches have already revealed its capacity to solve a variety of issues, notably in science disciplines such as robotics [3], continuum mechanics [4], optics [5], biological population models [6], and many other [7–15]. Compared to the integer-order differential equations, fractional counterparts are unhooked to get the precise exact solutions for highly nonlinear problems. For this purpose, many numerical and analytical techniques are developed to solve this category of problems.

Distinct analytical techniques are hired to get adequate analytical solutions such as the variational iteration method (VIM) [16–18], Adomian decomposition method (ADM) [19], etc. A semi-analytical technique known as the homotopy analysis technique (HAM) is a very efficient strategy suggested and shown by Liao [20–22] to tackle linear and non-linear problems. El-Tavil and Hussain [23, 24] presented the q-homotopy analysis technique (q-HAM) as a new notion of HAM for handling nonlinear situations. Latterly, the combination of the semi-analytical schemes with the Laplace transform is hired to scrutinize the nonlinear equations such as Volterra integrodifferential equations [25], nonlinear fractional diffusion wave equation [26], nonlinear boundary value problem on the semi-infinite domain [27], two-dimensional Burger's equation [28], class of nonlinear differential equations [29], nonlinear fractional Zakharov-Kuznetsov equation [30], fractional Klein–Gordon–Schrödinger equations [31], and so on.

In the present paper, the q-homotopy analysis transform method is imposed to examine the fractional-order Schnakenberg model. In the present work, we investigate the reliability and effectiveness of the q-homotopy analysis transform method (q-HATM) [32] for solving the time-fractional Schnakenberg model. The strategy presented is a blend of the Laplace transform (LT) technique and the q-homotopy analysis method (q-HAM). The availability of the term $\left(\frac{1}{n}\right)$ in the q-HATM solution ensures that it converges faster than the conventional HAM. The efficacy and positivity of the investigated algorithm are demonstrated by its capacity to provide

highly accurate precision, a large convergence zone, and a straightforward solution technique.

In developmental biology, the mathematical simulations of various systems have brought out diverse models, which lead to space–time patterning phenomena. In 1952, Turing introduced the possible association between the patterns that could have a quick formation in chemical reaction–diffusion systems and those that arise in the biological systems. The research work on the mathematical models concerning the pattern formation was encouraged by Turing's analysis, but until 1990, the Turing-type patterns are not detected in the controlled laboratory experiments [33]. This theory is based on the concept that the two substances, one is having the "large-range inhibition" capacity and the other is "locally activated" in the homogeneously distributed space to yield novel gradients and shapes.

Reaction–diffusion systems are mathematical models, which describe the way of concentration distribution of one or more substances in a region that changes under two mechanisms: The transformation of the substances into each other under the local chemical reactions, and diffusion by the influence of which the substances dissipated over the surface in space. The following equations give the class of nonlinear reaction–diffusion system:

$$\frac{\partial u}{\partial t} = d_1 \nabla^2 u + a_1 u + b_1 v + f(u, v) + g_1(x),$$

$$\frac{\partial v}{\partial t} = d_2 \nabla^2 v + a_2 u + b_2 v - f(u, v) + g_2(x),$$

where $\nabla^2 = \frac{\partial^2}{\partial x^2} + \frac{\partial^2}{\partial y^2}$, d_1, d_1 represents the diffusion coefficients and a_1, a_2, b_1, b_2 are the constants, known as control parameters of the system. u and v are the two chemical concentrations under examination.g_1, g_2 are the source terms. The nonlinear reaction term $f(u, v)$ is responsible for the biochemical reaction. The modelling of physical problems that arises in the real world, such as earthquake, measurement of viscoelastic material properties and the fractional fluid dynamic traffic model, etc. are effectively carried out with help of fractional differential equations. We have many bio-mathematical models of fractional order [34–40]. Numerous publications have been published on the research of integer-order bio-mathematical models, however, in this study, we focused on non-integer-order bio-mathematical models.

Schnakenberg proposed the most investigated reaction–diffusion system in 1979, known as the Schnakenberg system [41] which is hired to investigate the morphogen distribution. That is, in Acetabularia, the calcium distribution in whorl hairs [42]. The precise distribution of each cell to its site is essential for the efficient functioning of embryos, tissues, and organs. The appropriate cell differentiation is ensured by morphogen concentration gradients. The assignment of the morphogens is to signal

the molecules spread over tissues and to deputize various cell fates at distinct concentrations [43, 44]. Over the past half century, the morphogens are extensively introduced for tissue patterning, but as per the recent research, and works allow us to understand the interaction of morphogens with patterns that come forth [45–54].

Consider the simplest fractional reaction–diffusion system, known as the fractional Schnakenberg model, which is as follows:

$$D_t^{\alpha} u = d_1 \nabla^2 u + k\big(a - u + u^2 v\big),$$

$$D_t^{\alpha} v = d_2 \nabla^2 v + k\big(b - u^2 v\big).$$

The activator and inhibitor concentrations are represented by u and v, respectively. The rate constants of biological processes are k, a, and b. The diffusion coefficients are represented by d_1 and d_2.

The following is how the rest of the work is organized: Prefaces to the fractional integral in the Reimann–Liouville sense, LT, and Liouville–Caputo fractional derivative are covered in Sect. 2. The basic notion of the considered methodology is explained in Sect. 3, and the solutions for the time-fractional Schnakenberg model are discussed in Sect. 4. Plots are used to explain the reaction and nature of the acquired fractional-order findings. The last part contains comments on the acquired outcomes.

2 Preliminaries

Here, we present some basic notions of fractional operators and Laplace transform:

Definition 1 The fractional Riemann–Liouville integral of a function $f(t) \in C_{\mu}(\mu \geq -1)$ is presented [1, 2] as

$$\begin{aligned} J^{\alpha} f(t) &= \frac{1}{\Gamma(\alpha)} \int_0^t (t - \vartheta)^{\alpha - 1} f(\vartheta) d\vartheta, \\ J^0 f(t) &= f(t). \end{aligned} \tag{1}$$

Definition 2 The derivative with fractional order α of $f \in C_{-1}^n$ in the Liouville–Caputo sense [1, 2] is

$$D_t^{\alpha} f(t) = \begin{cases} \frac{d^n f(t)}{dt^n}, \alpha = n \in N, \\ \frac{1}{\Gamma(n-\alpha)} \int_0^t (t - \vartheta)^{n-\alpha-1} f^{(n)}(\vartheta) d\vartheta, \alpha \in (n-1, n), n \in \mathbb{N}. \end{cases} \tag{2}$$

Definition 3 The Laplace transform (LT) of a derivative in Eq. (2) is presented as [2, 47]

$$L\left[D_t^{\alpha} f(t)\right] = s^{\alpha} F(s) - \sum_{r=0}^{n-1} s^{\alpha-r-1} f^{(r)}\left(0^{+}\right), (n-1 < \alpha \leq n), \tag{3}$$

where $F(s)$ is represent the Laplace transform of $f(t)$.

3 The Solution Procedure for the q-Homotopy Analysis Transform Method (q-HATM)

Consider the following non-linear fractional PDE involving linear (N) and nonlinear (R) operators to illustrate the basic principle of the considered method [32]:

$$D_t^{\alpha} \mathcal{U}(x,t) + N\mathcal{U}(x,t) + R\mathcal{U}(x,t) = f(x,t), 0 < \alpha \leq 1, \tag{4}$$

where $D_t^{\alpha}\mathcal{U}(x,t)$ is the Liouville–Caputo fractional derivative of $\mathcal{U}(x,t), f(x,t)$, which is the source term. Currently, hiring the LT on Eq. (4) leads to

$$s^{\alpha} L[\mathcal{U}(x,t)] - \sum_{k=0}^{n-1} s^{\alpha-k-1} \mathcal{U}^{(k)}(x,0) + L[N\mathcal{U}(x,t)] + R[N\mathcal{U}(x,t)] = L[f(x,t)]. \tag{5}$$

By reducing Eq. (4), we get

$$\begin{aligned} &L[\mathcal{U}(x,t)] - \frac{1}{s^{\alpha}} \sum_{k=0}^{n-1} s^{\alpha-k-1} \mathcal{U}^{k}(x,0) \\ &+ \frac{1}{s^{\alpha}} \{L[N\mathcal{U}(x,t)] + L[R\mathcal{U}(x,t)] - L[f(x,t)]\} = 0. \end{aligned} \tag{6}$$

The non-linear operator N is defined as in accordance with the homotopy analysis approach as follows:

$$\begin{aligned} N[\varphi(x,t;q)] &= L[\varphi(x,t;q)] - \frac{1}{s^{\alpha}} \sum_{k=0}^{n-1} s^{\alpha-k-1} \varphi^{(k)}(x,t;q)\left(0^{+}\right) \\ &+ \frac{1}{s^{\alpha}} \{L[N\varphi(x,t;q)] + L[R\varphi(x,t;q)] - L[f(x,t)]\}, \end{aligned} \tag{7}$$

where L is the Laplace transform and $\varphi(x,t;q)$ is a real function of x, t and q(embeddingparameter) $\in \left[0, \frac{1}{\backslash}\right](n \geq 1)$.

The homotopy is defined as

$$(1 - nq)L[\varphi(x,t;q) - \mathcal{U}_0(x,t)] = \hbar q H(x,t)N[\varphi(x,t;q)], \tag{8}$$

where $\mathcal{U}_0(x,t)$ is an initial guess of $\mathcal{U}(x,t)$,$\hbar \neq 0$, which is an auxiliary parameter. For $q = 0$ and $q = 1/n$, respectively, we have

$$\varphi(x,t;0) = \mathcal{U}_0(x,t), \varphi\left(x,t;\frac{1}{n}\right) = \mathcal{U}(x,t). \tag{9}$$

As a result, by changing q from 0 to $\frac{1}{n}$, the solution $\varphi(x,t;q)$ converges from $\mathcal{U}_0(x,t)$ to $\mathcal{U}(x,t)$. The function $\varphi(x,t;q)$ can then be enlarged with the utilization of the Taylor theorem across q.

$$\varphi(x,t;q) = \mathcal{U}_0(x,t) + \sum_{m=1}^{\infty} \mathcal{U}_m(x,t)q^m, \tag{10}$$

with

$$\mathcal{U}_m(x,t) = \frac{1}{m!}\frac{\partial^m \varphi(x,t;q)}{\partial q^m}|_{q=0}. \tag{11}$$

The series (10) joins at $q = \frac{1}{n}$, resulting in the fundamental nonlinear equation, and it is one of the solutions of the type, by selecting the n and $\hbar$ (auxiliary parameter) and the initial guess $\mathcal{U}_0(x,t)$ and $H(x,t)$ properly.

$$\mathcal{U}(x,t) = \mathcal{U}_0(x,t) + \sum_{m=1}^{\infty} \mathcal{U}_m(x,t)\left(\frac{1}{n}\right)^m. \tag{12}$$

Then divide by $m!$ by differentiating Eq. (8) m times with respect to q. Finally, we derive the deformation equation of order m as follows for $q = 0$.

$$L\left[\mathcal{U}_m(x,t) - K_m\mathcal{U}_{m-1}(x,t)\right] = \hbar H(x,t)\Re_m\left(\vec{\mathcal{U}}_{m-1}\right), \tag{13}$$

and the vectors are presented as

$$\vec{\mathcal{U}}_m = \{\mathcal{U}_0(x,t), \mathcal{U}_1(x,t), \ldots, \mathcal{U}_m(x,t)\}. \tag{14}$$

Equration (13) is the recursive equation that may be represented by the effect of the inverse Laplace transform equation

$$\mathcal{U}_m(x,t) = K_m\mathcal{U}_{m-1}(x,t) + \hbar L^{-1}\left[H(x,t)\Re_m\left(\vec{\mathcal{U}}_{m-1}\right)\right], \tag{15}$$

where

$$\Re_m\left(\overrightarrow{U}_{m-1}\right) = \frac{1}{(m-1)!}\frac{\partial^{m-1}N[\varphi(x,t;q)]}{\partial q^{m-1}}|_{q=0}, \tag{16}$$

and

$$K_m = \begin{cases} 0, m \leq 1, \\ n, m > 1. \end{cases} \tag{17}$$

Finally, we find the component-wise q-HATM series solution using Eq. (15).

3.1 Solution for Non-linear Fractional Schnakenberg Model:

To check the projected scheme's resolution and correctness, the fractional Schnakenberg model is admitted.

Example 4 Consider the nonlinear fractional Schnakenberg model

$$\begin{aligned} D_t^{\alpha}u(x,y,t) &= d_1\left(\frac{\partial^2}{\partial x^2}+\frac{\partial^2}{\partial y^2}\right)u + k\left(a-u+u^2v\right), \\ D_t^{\alpha}v(x,y,t) &= d_2\left(\frac{\partial^2}{\partial x^2}+\frac{\partial^2}{\partial y^2}\right)v + k\left(b-u^2v\right), \end{aligned} \tag{18}$$

with the starting solution

$$\begin{aligned} u(x,y,0) &= a+b+10^{-3}e^{-100\left(\left(x-\frac{1}{3}\right)^2+\left(y-\frac{1}{2}\right)^2\right)}, \\ v(x,y,0) &= \frac{b}{(a+b)^2}. \end{aligned} \tag{19}$$

By making use of LT on Eq. (18) and using Eq. (19), we get

$$\begin{aligned} &L[u(x,y,t)] - \frac{1}{s}\left\{a+b+10^{-3}e^{-100\left(\left(x-\frac{1}{3}\right)^2+\left(y-\frac{1}{2}\right)^2\right)}\right\} \\ &-\frac{1}{s^{\alpha}}L\left\{d_1\left(\frac{\partial^2}{\partial x^2}+\frac{\partial^2}{\partial y^2}\right)u + k\left(a-u+u^2v\right)\right\} = 0, \\ &L[v(x,y,t)] - \frac{1}{s}\left\{\frac{b}{(a+b)^2}\right\} - \frac{1}{s^{\alpha}}L\left\{d_2\left(\frac{\partial^2}{\partial x^2}+\frac{\partial^2}{\partial y^2}\right)v + k\left(b-u^2v\right)\right\} = 0. \end{aligned} \tag{20}$$

The non-linear operator N is defined as the use of a future methodology.

$$
\begin{aligned}
&N^1[\varphi_1(x,y,t;q),\varphi_2(x,y,t;q)]\\
&=L[\varphi_1(x,y,t;q)]\\
&-\frac{1}{s}\left\{a+b+10^{-3}e^{-100\left((x-\frac{1}{3})^2+(y-\frac{1}{2})^2\right)}\right\}\\
&-\frac{1}{s^\alpha}L\left\{d_1\left(\frac{\partial^2}{\partial x^2}+\frac{\partial^2}{\partial y^2}\right)\varphi_1(x,y,t;q)\right.\\
&+k(a-\varphi_1(x,y,t;q)\\
&\left.+\varphi_1(x,y,t;q)^2\varphi_1(x,y,t;q)\right)\Big\},\\
&N^2[\varphi_2(x,y,t;q),\varphi_2(x,y,t;q)]\\
&=L[\varphi_2(x,y,t;q)]-\frac{1}{s}\left\{\frac{b}{(a+b)^2}\right\}\\
&-\frac{1}{s^\alpha}L\left\{d_2\left(\frac{\partial^2}{\partial x^2}+\frac{\partial^2}{\partial y^2}\right)\varphi_2(x,y,t;q)\right.\\
&\left.+k\big(b-\varphi_2(x,y,t;q)^2\varphi_2(x,y,t;q)\big)\right\}.
\end{aligned}
\tag{21}
$$

Following the aforementioned scheme, the mth-order deformation equation as

$$
\begin{aligned}
L\big[K_m u_{m-1}(x,y,t)\big]+\hbar\Re_{1,m}\Big[\overrightarrow{u_{m-1}},\overrightarrow{v_{m-1}}\Big]&=L[u_m(x,y,t)],\\
L\big[K_m v_{m-1}(x,y,t)\big]+\hbar\Re_{1,m}\Big[\overrightarrow{u_{m-1}},\overrightarrow{v_{m-1}}\Big]&=L[v_m(x,y,t)],
\end{aligned}
\tag{22}
$$

where

$$
\begin{aligned}
&\Re_{1,m}\Big[\overrightarrow{u_{m-1}},\overrightarrow{v_{m-1}}\Big]\\
&=L[u(x,y,t)]\\
&-\left(1-\frac{K_m}{n}\right)\frac{1}{s}\left\{a+b+10^{-3}e^{-100\left((x-\frac{1}{3})^2+(y-\frac{1}{2})^2\right)}\right\}\\
&-\frac{1}{s^\alpha}L\left\{d_1\left(\frac{\partial^2}{\partial x^2}+\frac{\partial^2}{\partial y^2}\right)u_{m-i}+k(a-u_{m-i})\right.\\
&\left.+\sum_{i=0}^{m-1}\sum_{j=0}^{i}u_i u_{i-j}v_{m-i-1}\right\},
\end{aligned}
\tag{23}
$$

$$\begin{aligned}
&\Re_{2,m}\left[\vec{u_{m-1}}, \vec{v_{m-1}}\right] \\
&= L[v(x,y,t)] - \left(1 - \frac{K_m}{n}\right)\frac{1}{s}\left\{\frac{b}{(a+b)^2}\right\} \\
&-\frac{1}{s^\alpha}L\left\{d_2\left(\frac{\partial^2}{\partial x^2} + \frac{\partial^2}{\partial y^2}\right)v_{m-i} + k(b\right. \\
&\left.-\sum_{i=0}^{m-1}\sum_{j=0}^{i} u_i u_{i-j} v_{m-i-1}\right\}.
\end{aligned}$$

We derive Eq. (24) using the inverse Laplace transform on Eq. (22) as follows.

$$\begin{aligned}
u_m(x,y,t) &= K_m u_{m-1}(x,y,t) + \hbar L^{-1}\left\{\Re_{1,m}\left[\vec{u_{m-1}}, \vec{v_{m-1}}\right]\right\}, \\
v_m(x,y,t) &= K_m v_{m-1}(x,y,t) + \hbar L^{-1}\left\{\Re_{2,m}\left[\vec{u_{m-1}}, \vec{v_{m-1}}\right]\right\}.
\end{aligned} \tag{24}$$

Solving Eq. (24), we get

$$u_0(x,y,t) = a + b + \frac{\mathrm{e}^{-100\left(\left(x-\frac{1}{3}\right)^2+\left(y-\frac{1}{2}\right)^2\right)}}{1000},$$

$$v_0(x,y,t) = \frac{b}{(a+b)^2},$$

$$\begin{aligned}
u_1(x,y,t) = &-\frac{1}{\Gamma(\alpha+1)}\hbar t^\alpha \\
&\left(k\left(\frac{b\left(a+b+\frac{\mathrm{e}^{-100\left(\left(x-\frac{1}{3}\right)^2+\left(y-\frac{1}{2}\right)^2\right)}}{1000}\right)^2}{(a+b)^2} - b - \frac{\mathrm{e}^{-100\left(\left(x-\frac{1}{3}\right)^2+\left(y-\frac{1}{2}\right)^2\right)}}{1000}\right)\right. \\
&\left.+\frac{8}{45}d_1\mathrm{e}^{-100\left(\left(x-\frac{1}{3}\right)^2+\left(y-\frac{1}{2}\right)^2\right)}\left(225x^2 - 150x + 225y^2 - 225y + 79\right)\right),
\end{aligned}$$

$$v_1(x,y,t) = -\frac{k\hbar t^\alpha\left(b - \frac{b\left(a+b+\frac{\mathrm{e}^{-100\left(\left(x-\frac{1}{3}\right)^2+\left(y-\frac{1}{2}\right)^2\right)}}{1000}\right)^2}{(a+b)^2}\right)}{\Gamma(\alpha+1)},$$

$$u_2(x,y,t) = -\frac{1}{\Gamma(\alpha+1)}\hbar(n+\hbar)$$
$$\left(\left(\frac{b\left(a+\frac{e^{-100\left(\left(x-\frac{1}{3}\right)^2+\left(y-\frac{1}{2}\right)^2\right)}}{1000}+b\right)^2}{(a+b)^2}-b-\frac{e^{-100\left(\left(x-\frac{1}{3}\right)^2+\left(y-\frac{1}{2}\right)^2\right)}}{1000}\right)\right.$$
$$k+\frac{8}{45}e^{-100\left(\left(x-\frac{1}{3}\right)^2+\left(y-\frac{1}{2}\right)^2\right)}(225x^2-150x+225y^2-225y+79)d_1)t^{\alpha}$$
$$-\frac{1}{\Gamma(2\alpha+1)}k\hbar^2\left(\left(\frac{b\left(a+\frac{e^{-100\left(\left(x-\frac{1}{3}\right)^2+\left(y-\frac{1}{2}\right)^2\right)}}{1000}+b\right)^2}{(a+b)^2}-b-\frac{e^{-100\left(\left(x-\frac{1}{3}\right)^2+\left(y-\frac{1}{2}\right)^2\right)}}{1000}\right)\right.$$
$$k+\frac{8}{45}e^{-100\left(\left(x-\frac{1}{3}\right)^2+\left(y-\frac{1}{2}\right)^2\right)}(225x^2-150x+225y^2-225y+79)d_1)t^{2\alpha}$$
$$+\frac{1}{(a+b)^2\Gamma(2\alpha+1)}\left(a+\frac{e^{-100\left(\left(x-\frac{1}{3}\right)^2+\left(y-\frac{1}{2}\right)^2\right)}}{1000}+b\right)bk\hbar^2$$
$$\left(\left(\frac{b\left(a+\frac{e^{-100\left(\left(x-\frac{1}{3}\right)^2+\left(y-\frac{1}{2}\right)^2\right)}}{1000}+b\right)^2}{(a+b)^2}-b-\frac{e^{-100\left(\left(x-\frac{1}{3}\right)^2+\left(y-\frac{1}{2}\right)^2\right)}}{1000}\right)\right.$$
$$k+\frac{8}{45}e^{-100\left(\left(x-\frac{1}{3}\right)^2+\left(y-\frac{1}{2}\right)^2\right)}\left(225x^2-150x+225y^2-225y+79\right)d_1)t^{2\alpha}$$
$$+\frac{1}{\Gamma(2\alpha+1)}\hbar^2d_1(-\frac{1}{9}32000e^{-100\left(\left(x-\frac{1}{3}\right)^2+\left(y-\frac{1}{2}\right)^2\right)}d_1(1-3x)^2-$$
$$\frac{1}{45}e^{-100\left(\left(x-\frac{1}{3}\right)^2+\left(y-\frac{1}{2}\right)^2\right)}k\left(1800x^2-1200x+191\right)$$
$$+\frac{1}{22500(a+b)^2}be^{-200\left(\left(x-\frac{1}{3}\right)^2+\left(y-\frac{1}{2}\right)^2\right)}k(3600x^2-2400x+$$
$$1000ae^{100\left(\left(x-\frac{1}{3}\right)^2+\left(y-\frac{1}{2}\right)^2\right)}\left(1800x^2-1200x+191\right)$$
$$+1000be^{100\left(\left(x-\frac{1}{3}\right)^2+\left(y-\frac{1}{2}\right)^2\right)}\left(1800x^2-1200x+191\right)+391)+$$

$$80\mathrm{e}^{-100\left(\left(x-\frac{1}{3}\right)^2+\left(y-\frac{1}{2}\right)^2\right)}d_1+\frac{320}{81}\mathrm{e}^{-100\left(\left(x-\frac{1}{3}\right)^2+\left(y-\frac{1}{2}\right)^2\right)}$$
$$\left(1800x^2-1200x+191\right)\left(225x^2-150x+225y^2-225y+79\right)d_1)t^{2\alpha}+$$
$$\frac{1}{\Gamma(2\alpha+1)}\hbar^2d_1(-8000\mathrm{e}^{-100\left(\left(x-\frac{1}{3}\right)^2+\left(y-\frac{1}{2}\right)^2\right)}d_1(1-2y)^2$$
$$-\frac{1}{5}\mathrm{e}^{-100\left(\left(x-\frac{1}{3}\right)^2+\left(y-\frac{1}{2}\right)^2\right)}k\left(200y^2-200y+49\right)+$$
$$\frac{1}{2500(a+b)^2}b\mathrm{e}^{-200\left(\left(x-\frac{1}{3}\right)^2+\left(y-\frac{1}{2}\right)^2\right)}k(400y^2-400y+1000a\mathrm{e}^{100\left(\left(x-\frac{1}{3}\right)^2+\left(y-\frac{1}{2}\right)^2\right)}$$
$$\left(200y^2-200y+49\right)+1000b\mathrm{e}^{100\left(\left(x-\frac{1}{3}\right)^2+\left(y-\frac{1}{2}\right)^2\right)}(200y^2-200y+49)+99\Bigg)$$
$$+80\mathrm{e}^{-100\left(\left(x-\frac{1}{3}\right)^2+\left(y-\frac{1}{2}\right)^2\right)}d_1+\frac{320}{9}\mathrm{e}^{-100\left(\left(x-\frac{1}{3}\right)^2+\left(y-\frac{1}{2}\right)^2\right)}\left(200y^2-200y+49\right)$$
$$(225x^2-150x+225y^2-225y+79)d_1)t^{2\alpha}$$
$$\left(a+\frac{\mathrm{e}^{-100\left(\left(x-\frac{1}{3}\right)^2+\left(y-\frac{1}{2}\right)^2\right)}}{1000}+b\right)^2\left(b-\frac{b\left(a+\frac{\mathrm{e}^{-100\left(\left(x-\frac{1}{3}\right)^2+\left(y-\frac{1}{2}\right)^2\right)}}{1000}+b\right)^2}{(a+b)^2}\right)k^2\hbar^2t^{2\alpha}$$
$$+\frac{}{\Gamma(2\alpha+1)}-$$
$$\left(bkt^{2\alpha}\hbar^2\right)\left(\frac{b\left(a+\frac{\mathrm{e}^{-100\left(\left(x-\frac{1}{3}\right)^2+\left(y-\frac{1}{2}\right)^2\right)}}{1000}+b\right)^2}{(a+b)^2}\right)/\left((a+b)^2\Gamma(\alpha+1)\Gamma(2\alpha+1)\right),$$

$$v_2(x,y,t) = -\frac{1}{(a+b)^2\Gamma(\alpha+1)^2\Gamma(3\alpha+1)} bk\hbar^3\Gamma(2\alpha+1)t^{3\alpha}$$
$$\left(k\left(\frac{b\left(a+b+\frac{e^{-100\left(\left(x-\frac{1}{3}\right)^2+\left(y-\frac{1}{2}\right)^2\right)}}{1000}\right)^2}{(a+b)^2} - b - \frac{e^{-100\left(\left(x-\frac{1}{3}\right)^2+\left(y-\frac{1}{2}\right)^2\right)}}{1000}\right)+\right.$$
$$\left.\frac{8}{45}d_1 e^{-100\left(\left(x-\frac{1}{3}\right)^2+\left(y-\frac{1}{2}\right)^2\right)}\left(225x^2-150x+225y^2-225y+79\right)\right)^2$$
$$+\frac{1}{(a+b)^2\Gamma(2\alpha+1)} bk\hbar^2t^{2\alpha}\left(a+b+\frac{e^{-100\left(\left(x-\frac{1}{3}\right)^2+\left(y-\frac{1}{2}\right)^2\right)}}{1000}\right)$$
$$\left(k\left(\frac{b\left(a+b+\frac{e^{-100\left(\left(x-\frac{1}{3}\right)^2+\left(y-\frac{1}{2}\right)^2\right)}}{1000}\right)^2}{(a+b)^2} - b - \frac{e^{-100\left(\left(x-\frac{1}{3}\right)^2+\left(y-\frac{1}{2}\right)^2\right)}}{1000}\right)\right.$$
$$\left.+\frac{8}{45}d_1 e^{-100\left(\left(x-\frac{1}{3}\right)^2+\left(y-\frac{1}{2}\right)^2\right)}\left(225x^2-150x+225y^2-225y+79\right)\right)$$
$$-\frac{1}{11250(a+b)^2\Gamma(2\alpha+1)} bd_2k\hbar^2t^{2\alpha}e^{-200\left(\left(x-\frac{1}{3}\right)^2+\left(y-\frac{1}{2}\right)^2\right)}$$
$$\left(4000ae^{100\left(\left(x-\frac{1}{3}\right)^2+\left(y-\frac{1}{2}\right)^2\right)}\left(225x^2-150x+225y^2-225y+79\right)+\right.$$
$$4000be^{100\left(\left(x-\frac{1}{3}\right)^2+\left(y-\frac{1}{2}\right)^2\right)}\left(225x^2-150x+225y^2-225y+79\right)$$
$$\left.+1800x^2-1200x+1800y^2-1800y+641\right)+$$
$$\frac{k^2\hbar^2t^{2\alpha}\left(a+b+\frac{e^{-100\left(\left(x-\frac{1}{3}\right)^2+\left(y-\frac{1}{2}\right)^2\right)}}{1000}\right)^2\left(b-\frac{b\left(a+b+\frac{e^{-100\left(\left(x-\frac{1}{3}\right)^2+\left(y-\frac{1}{2}\right)^2\right)}}{1000}\right)^2}{(a+b)^2}\right)}{\Gamma(2\alpha+1)}$$
$$-\frac{k\hbar(n+\hbar)t^{\alpha}\left(b-\frac{b\left(a+b+\frac{e^{-100\left(\left(x-\frac{1}{3}\right)^2+\left(y-\frac{1}{2}\right)^2\right)}}{1000}\right)^2}{(a+b)^2}\right)}{\Gamma(\alpha+1)},$$

Finally, after getting further iterative terms, the essential series solution of the Eq. (18) is presented by

$$\begin{aligned} u(x,y,t) &= u_0(x,y,t) + \sum_{m=1}^{\infty} u_m(x,y,t)\left(\frac{1}{n}\right)^m, \\ v(x,y,t) &= v_0(x,y,t) + \sum_{m=1}^{\infty} v_m(x,y,t)\left(\frac{1}{n}\right)^m. \end{aligned} \tag{25}$$

By taking $n = 1$, $\alpha = 1$ and $\hbar = -1$, we acquire the approximated solution fractional Schnakenberg model as $\sum_{m=1}^{N} u_m(x,y,t)\left(\frac{1}{\backslash}\right)^m$, $\sum_{m=1}^{N} v_m(x,y,t)\left(\frac{1}{\backslash}\right)^m$, for $u(x,y,t)$ and $v(x,y,t)$ respectively and tends to exact solution as $N \to \infty$.

Example 5 Contemplate the fractional Schnakenberg model:

$$\begin{aligned} D_t^{\alpha} u(x,t) &= d_1 \frac{\partial^2 u}{\partial x^2} + k\big(a - u + u^2 v\big), \\ D_t^{\alpha} v(x,t) &= d_2 \frac{\partial^2 v}{\partial x^2} + k\big(b - u^2 v\big), \end{aligned} \tag{26}$$

with initial conditions

$$\begin{aligned} u(x,0) &= 0.8 + \frac{1}{10}\cos(x), \\ v(x,0) &= 1.03 + \frac{1}{10}\cos(x). \end{aligned} \tag{27}$$

We get Eq. (26) by assuming LT on mutually and considering the starting solutions stated in Eq. (27)

$$\begin{aligned} &L[u(x,t)] - \frac{1}{s}\left\{0.8 + \frac{1}{10}\cos(x)\right\} - \frac{1}{s^{\alpha}} L\left\{d_1 \frac{\partial^2 u}{\partial x^2} + k\big(a - u + u^2 v\big)\right\} = 0, \\ &L[v(x,t)] - \frac{1}{s}\left\{1.03 + \frac{1}{10}\cos(x)\right\} - \frac{1}{s^{\alpha}} L\left\{d_2 \frac{\partial^2 v}{\partial x^2} + k\big(b - u^2 v\big)\right\} = 0. \end{aligned} \tag{28}$$

N is defined by using the projected methodology as

$$\begin{aligned} &N^1[\varphi_1(x,t;q), \varphi_2(x,t;q)] \\ &= L[\varphi_1(x,t;q)] - \frac{1}{s}\left\{0.8 + \frac{1}{10}\cos(x)\right\} \\ &- \frac{1}{s^{\alpha}} L\left\{d_1 \frac{\partial^2 \varphi_1(x,t;q)}{\partial x^2}\right. \\ &\left. + k\big(a - \varphi_1(x,t;q) + \varphi_1(x,t;q)^2 \varphi_2(x,t;q)\big)\right\}, \end{aligned}$$

$$
\begin{aligned}
&N^2[\varphi_1(x,t;q),\varphi_2(x,t;q)]\\
&= L[\varphi_2(x,t;q)] - \frac{1}{s}\left\{1.03 + \frac{1}{10}\cos(x)\right\}\\
&-\frac{1}{s^\alpha}L\left\{d_2\frac{\partial^2\varphi_2(x,t;q)}{\partial x^2}\right.\\
&\left.+k\big(b-\varphi_1(x,t;q)^2\varphi_2(x,t;q)\big)\right\}.
\end{aligned}
\tag{29}
$$

With the aid of the projected technique, the mth-order deformation expression is written as follows:

$$
\begin{aligned}
L\big[K_m u_{m-1}(x,t)\big] + \hbar\Re_{1,m}\Big[\overrightarrow{u_{m-1}},\overrightarrow{v_{m-1}}\Big] &= L[u_m(x,t)],\\
L\big[K_m v_{m-1}(x,t)\big] + \hbar\Re_{1,m}\Big[\overrightarrow{u_{m-1}},\overrightarrow{v_{m-1}}\Big] &= L[v_m(x,t)],
\end{aligned}
\tag{30}
$$

where

$$
\begin{aligned}
&\Re_{1,m}\Big[\overrightarrow{u_{m-1}},\overrightarrow{v_{m-1}}\Big] = L[u(x,t)]-\\
&\left(1-\frac{K_m}{n}\right)\frac{1}{s}\left\{0.8+\frac{1}{10}\cos(x)\right\}-\\
&\frac{1}{s^\alpha}L\left\{d_1\left(\frac{\partial^2}{\partial x^2}+\frac{\partial^2}{\partial y^2}\right)u_{m-i}\right.\\
&\left.+k(a-u_{m-i}+\sum_{i=0}^{m-1}\sum_{j=0}^{i}u_i u_{i-j}v_{m-i-1}\right\},\\
&\Re_{2,m}\Big[\overrightarrow{u_{m-1}},\overrightarrow{v_{m-1}}\Big] = L[v(x,t)]-\\
&\left(1-\frac{K_m}{n}\right)\frac{1}{s}\left\{1.03+\frac{1}{10}\cos(x)\right\}-\\
&\frac{1}{s^\alpha}L\left\{d_2\left(\frac{\partial^2}{\partial x^2}+\frac{\partial^2}{\partial y^2}\right)v_{m-i}\right.\\
&\left.+k(b-\sum_{i=0}^{m-1}\sum_{j=0}^{i}u_i u_{i-j}v_{m-i-1}\right\}.
\end{aligned}
\tag{31}
$$

When we apply the inverse Laplace transform to Eq. (30), we get

$$
\begin{aligned}
u_m(x,t) &= K_m u_{m-1}(x,t) + \hbar L^{-1}\left\{\Re_{1,m}\Big[\overrightarrow{u_{m-1}},\overrightarrow{v_{m-1}}\Big]\right\},\\
v_m(x,t) &= K_m v_{m-1}(x,t) + \hbar L^{-1}\left\{\Re_{2,m}\Big[\overrightarrow{u_{m-1}},\overrightarrow{v_{m-1}}\Big]\right\}.
\end{aligned}
\tag{32}
$$

On solving Eq. (32), we obtain

$$u_0(x,t) = 0.1\cos(x) + 0.8,$$

$$v_0(x,t) = 0.1\cos(x) + 1.03,$$

$$u_1(x,t) = \frac{\hbar t^{\alpha}\left(-0.001\cos^3(x) - 0.0263\cos^2(x) - 0.1088\cos(x) + 0.0008\right)}{\Gamma(\alpha+1)},$$

$$v_1(x,t) = \frac{\hbar t^{\alpha}\left((0.1\cos(x) + 1.03)(0.1\cos(x) + 0.8)^2 + 0.01\cos(x) - 0.66\right)}{\Gamma(\alpha+1)},$$

$$u_2(x,t) = \frac{\hbar^3\Gamma(2\alpha+1)t^{3\alpha}(0.1\cos(x)+1.03)}{\Gamma(\alpha+1)^2\Gamma(3\alpha+1)}$$
$$\left(-0.001\cos^3(x) - 0.0263\cos^2(x) - 0.1088\cos(x) + 0.0008\right)^2$$
$$+\frac{1}{\Gamma(2\alpha+1)}\hbar^2 t^{2\alpha}((0.1\cos(x)+0.8)$$
$$(0.1\cos(x)+1.03)\left(-0.001\cos^3(x) - 0.0263\cos^2(x) - 0.1088\cos(x) + 0.0008\right)$$
$$+1.(0.001\cos^3(x) + 0.0263\cos^2(x) + 0.1088\cos(x) - 0.0008)$$
$$+0.02(-1.0955\cos(x) - 0.526\cos(2x) - 0.0225\cos(3x)))+$$
$$\frac{\hbar^2 t^{2\alpha}\left((0.1\cos(x)+1.03)(0.1\cos(x)+0.8)^2 + 0.01\cos(x) - 0.66\right)(0.1\cos(x)+0.8)^2}{\Gamma(2\alpha+1)}$$
$$-\frac{0.14\hbar t^{\alpha}}{\Gamma(\alpha+1)} + \frac{1}{\Gamma(\alpha+1)}\hbar(\hbar+1)t^{\alpha}(-0.001\cos^3(x) - 0.0263\cos^2(x) -$$
$$0.1088\cos(x) + 0.0008),$$
$$v_2(x,t) =$$
$$\frac{\hbar^3\Gamma(2\alpha+1)t^{3\alpha}(0.1\cos(x)+1.03)\left(-0.001\cos^3(x) - 0.0263\cos^2(x) - 0.1088\cos(x) + 0.0008\right)^2}{\Gamma(\alpha+1)^2\Gamma(3\alpha+1)}$$
$$+\frac{1}{\Gamma(2\alpha+1)}\hbar^2 t^{2\alpha}((0.1\cos(x)+0.8)(0.1\cos(x)+$$
$$1.03)\left(-0.001\cos^3(x) - 0.0263\cos^2(x) - 0.1088\cos(x) + 0.0008\right)$$
$$+1.\left(0.001\cos^3(x) + 0.0263\cos^2(x) + 0.1088\cos(x) - 0.0008\right)+$$
$$0.02(-1.0955\cos(x) - 0.526\cos(2x) - 0.0225\cos(3x)))$$
$$+\frac{\hbar^2 t^{2\alpha}\left((0.1\cos(x)+1.03)(0.1\cos(x)+0.8)^2 + 0.01\cos(x) - 0.66\right)(0.1\cos(x)+0.8)^2}{\Gamma(2\alpha+1)}$$
$$-\frac{0.14\hbar t^{\alpha}}{\Gamma(\alpha+1)}+$$
$$\frac{\hbar(\hbar+1)t^{\alpha}\left(-0.001\cos^3(x) - 0.0263\cos^2(x) - 0.1088\cos(x) + 0.0008\right)}{\Gamma(\alpha+1)}$$

$$v_2(x,t) =$$
$$\frac{\hbar^3\Gamma(2\alpha+1)t^{3\alpha}(0.1\cos(x)+1.03)\left(-0.001\cos^3(x)-0.0263\cos^2(x)-0.11\cos(x)+0.0008\right)^2}{\Gamma(\alpha+1)^2\Gamma(3\alpha+1)}$$
$$+\frac{1}{\Gamma(2\alpha+1)}\hbar^2t^{2\alpha}((0.1\cos(x)+0.8)(0.1\cos(x)+1.03)(-0.001\cos^3(x)-$$
$$0.0263\cos^2(x)-0.1088\cos(x)+0.00078)+1.(0.001\cos^3(x)+$$
$$0.0263\cos^2(x)+0.1088\cos(x)-0.00078)+0.02(-1.0956\cos(x)-$$
$$0.526\cos(2x)-0.0225\cos(3x)))+$$
$$\frac{\hbar^2t^{2\alpha}\left((0.1\cos(x)+1.03)(0.1\cos(x)+0.8)^2+0.01\cos(x)-0.66\right)(0.1\cos(x)+0.8)^2}{\Gamma(2\alpha+1)}$$
$$-\frac{0.14\hbar t^{\alpha}}{\Gamma(\alpha+1)}+$$
$$\frac{\hbar(\hbar+1)t^{\alpha}\left(-0.001\cos^3(x)-0.0263\cos^2(x)-0.11\cos(x)+0.0008\right)}{\Gamma(\alpha+1)},$$

Excess re-iterative expressions can be produced by continuing in the same manner. The requisite $\boldsymbol{q}$-HATM solutions of Eq. (26) are thus provided by

$$\begin{aligned} u(x,t) &= u_0(x,t)+\sum_{m=1}^{\infty}u_m(x,t)\left(\frac{1}{n}\right)^m, \\ v(x,t) &= v_0(x,t)+\sum_{m=1}^{\infty}v_m(x,t)\left(\frac{1}{n}\right)^m. \end{aligned} \tag{33}$$

If we make $n = 1$, $\alpha = 1$ and $\hbar = -1$, then the secured solution $\sum_{m=1}^{N}u_m(x,t)\left(\frac{1}{n}\right)^m$,$\sum_{m=1}^{N}v_m(x,t)\left(\frac{1}{n}\right)^m$, of Schnakenberg model converges to exact solution as $N \to \infty$.

4 Numerical Results and Discussion

During the present work, we investigated the analytical behaviour of the time-fractional non-linear Schnakenberg model with the aid of an analytical scheme, called the q-homotopy analysis transform method. The 3D plots correspond to the variation of two chemical concentrations $u(x,t)$ and $v(x,t)$ and their respective 2D plots are cited in Fig. 1 and the same for $u(y,t)$ and $v(y,t)$ are depicted in Fig. 2. Figures 3 and 4 represent the behaviour of activator and inhibitor concentrations, respectively, by taking $y = 0.2, 0.3, 0.4, 0.5$. Furthermore, the variation in the plots shows that the nature of u and v also depends on the fractional order. Figure 5 quotes the performance of obtained solution of Eq. (20) attained by the presented scheme versus t. The action of n with auxiliary parameter in an acquired result of q-HATM is depicted in Fig. 6. Figure 7 shows the surface plots of the obtained approximated

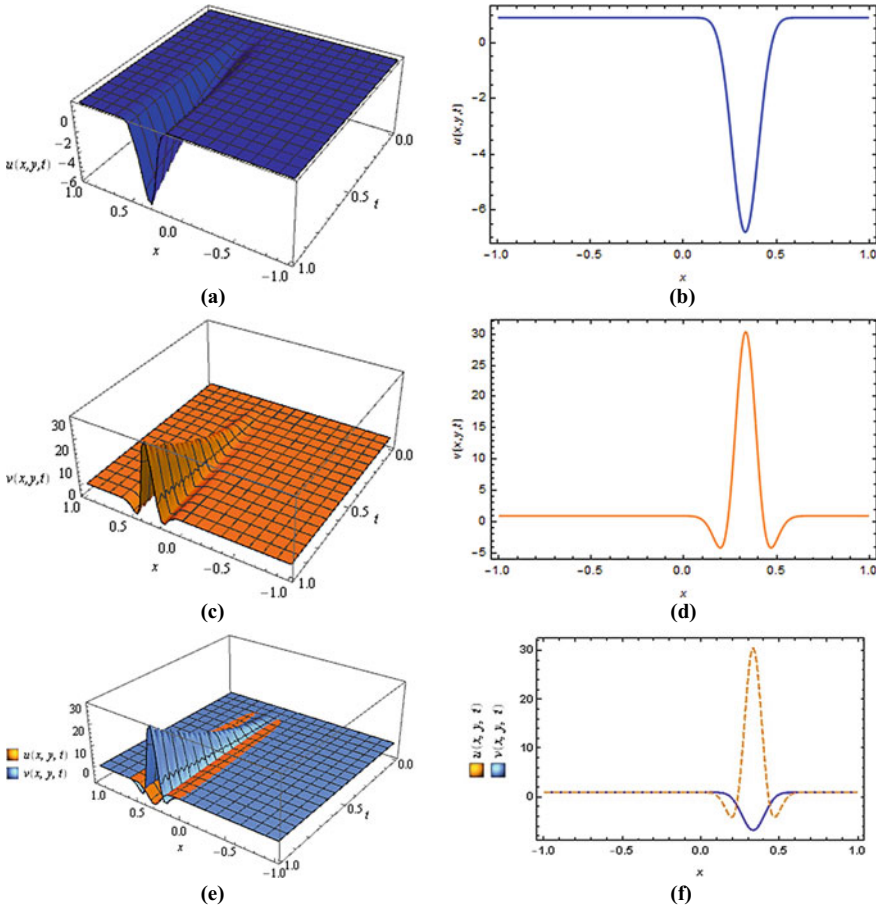

Fig. 1 **a** 3D plot for activator $u(x, y, t)$, **b** curve of $u(x, y, t)$ at $t = 1$, **c** approximated solution surface for $v(x, y, t)$, **d** 2D plot for $v(x, y, t)$ at $t = 1$, **e** coupled behaviour of the solution of Eq. 20, **f** coupled 2D plot for activator and inhibitor concentrations at $t = 1$ by taking $y = 0.5$, $k = 100$, $b = 0.7695$, $a = 0.1305$, $d_1 = 0.05$, $d_2 = 1$, $n = 1$, $\alpha = 1$, $\hbar = -1$

solutions of Ex. 4.2 with their respective 2D plots and projected views. In Fig. 8, black line represents the nature of u for $\alpha = 1$, the blue dotted line for $\alpha = 0.75$ and the orange dashed line for $\alpha = 0.50$. It shows the dependence of the results on the various fractional-order α. In Fig. 9, the behaviour of acquired solution v for various fractional orders α when $t = 2, 3, 5, 7.5, 10$ is cited. Figure 10 is decorated with the variation of attained solutions $u(x, t)$ and $v(x, t)$ with time t. Figure 11 cites the execution of n with respect to $\hbar$ in the secured result by the considered method.

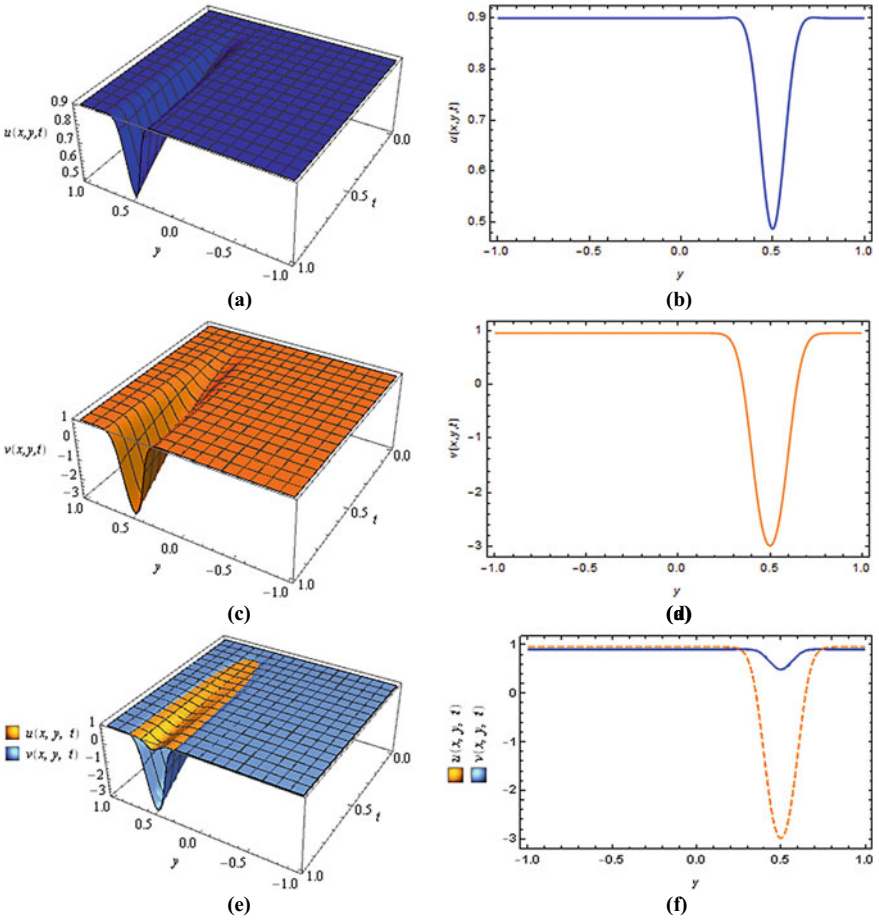

Fig. 2 **a** 3D plot for activator $u(x, y, t)$, **b** curve of $u(x, y, t)$ at $t = 1$, **c** approximated solution surface for $v(x, y, t)$, **d** 2D plot for $v(x, y, t)$ at $t = 1$, **e** coupled behaviour of the solution of Eq. 20, **f** coupled 2D plot for activator and inhibitor concentrations at $t = 1$ by taking $x = 0.5, k = 100, b = 0.7695, a = 0.1305, d_1 = 0.05, d_2 = 1, n = 1, \alpha = 1, \hbar = -1$

5 Conclusion

In the current work, we have hired the strong analytical scheme known as q-HATM to examine the nonlinear fractional reaction–diffusion systems (fractional Schnakenberg systems). To check the reliability of the considered technique, we have investigated the considered model with two different initial conditions. The secured outputs indicate that a future method can be used to generate a standardized analytical answer. Furthermore, the secured results are corresponding to the mechanisms with memory which can be seen in many biological networks, also to fractals that occur in biological systems. The considered strategy is effective in providing a simple solution, a

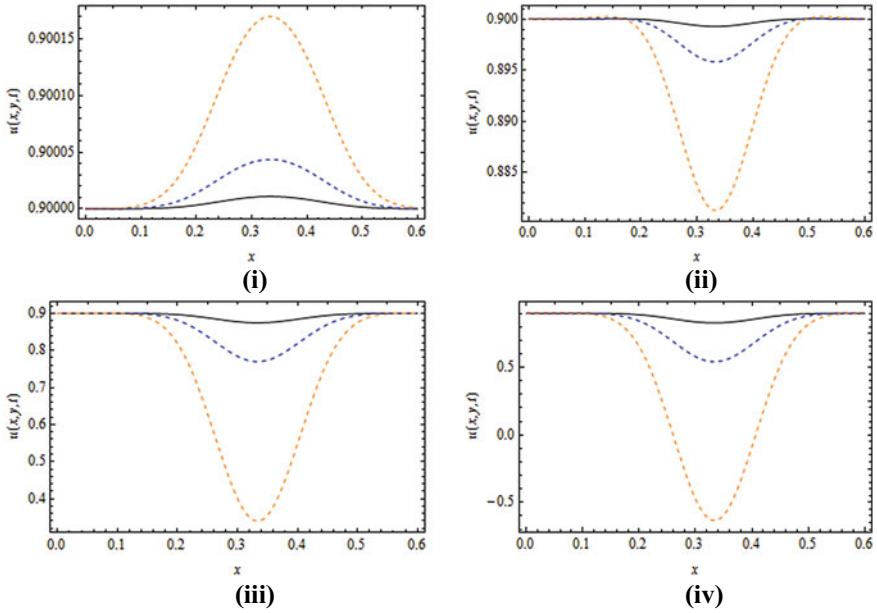

Fig. 3 Curves for activator $u(x, y, t)$ at (i)$y = 0.2$, (ii)$y = 0.3$, (iii)$y = 0.4$, (iv)$y = 0.5$ by taking $k = 100, b = 0.7695, a = 0.1305, d_1 = 0.05, d_2 = 1, n = 1, t = 0.1$, and $\hbar = -1$ for distinct values of α

critical convergence zone, and a non-local influence. Finally, we conclude that our projected technique is exceptionally serviceable and can be applied to large research categories linked to fractional-order non-linear mathematical models, which aid us in better understanding the non-linear compound phenomena.

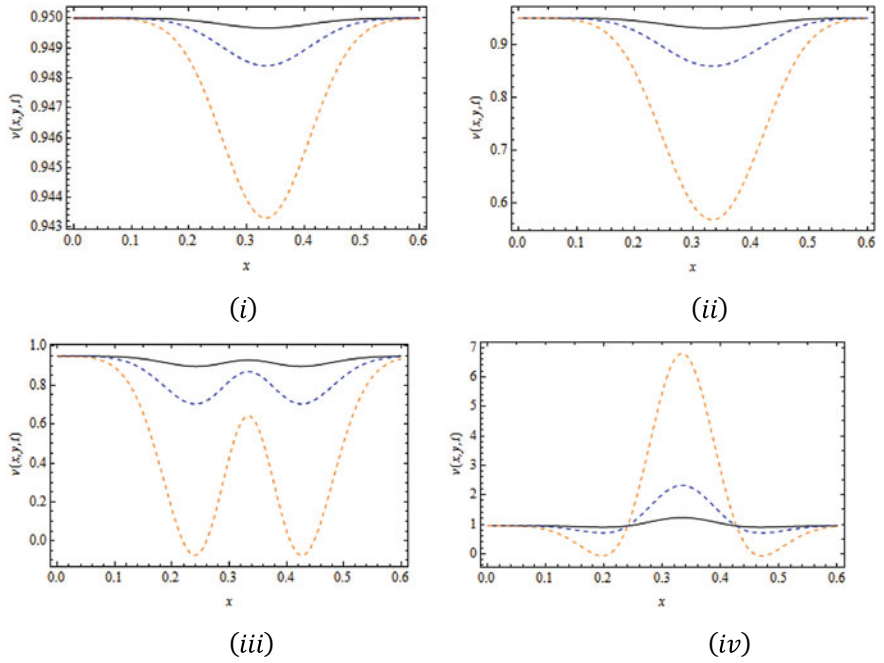

Fig. 4 Curves for inhibitor $v(x, y, t)$ at (i)$y = 0.2$, (ii)$y = 0.3$, (iii)$y = 0.4$, (iv)$y = 0.5$ by taking $k = 100, b = 0.7695, a = 0.1305, d_1 = 0.05, d_2 = 1, n = 1, t = 0.1$, and $\hbar = -1$ for distinct values of α

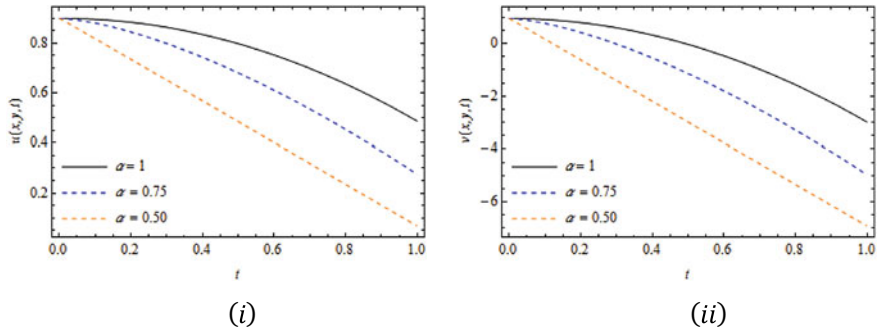

Fig. 5 (i) $u(x, y, t)$, (ii) $v(x, y, t)$ versus t for Ex. 4.1. when $x = 0.5, y = 0.5, a = 0.1305, b = 0.7695, k = 100, d_1 = 0.05, d_2 = 1, n = 1, \hbar = -1$ and $n = 1$ for diverse α

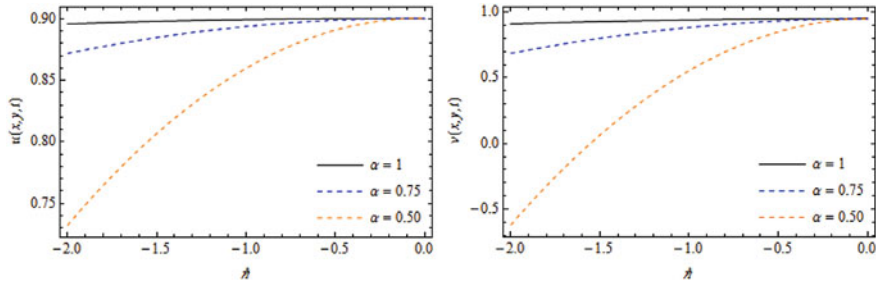

(*i*) (*ii*)

Fig. 6 The $\hbar$-curve for $u(x, y, t)$ and $v(x, y, t)$ `for foreseen Ex. 4.1.` when $n = 1, x = 0.5, y = 0.5, a = 0.1305, b = 0.7695, k = 100, d_1 = 0.05, d_2 = 1, t = 0.05$ `for various` α

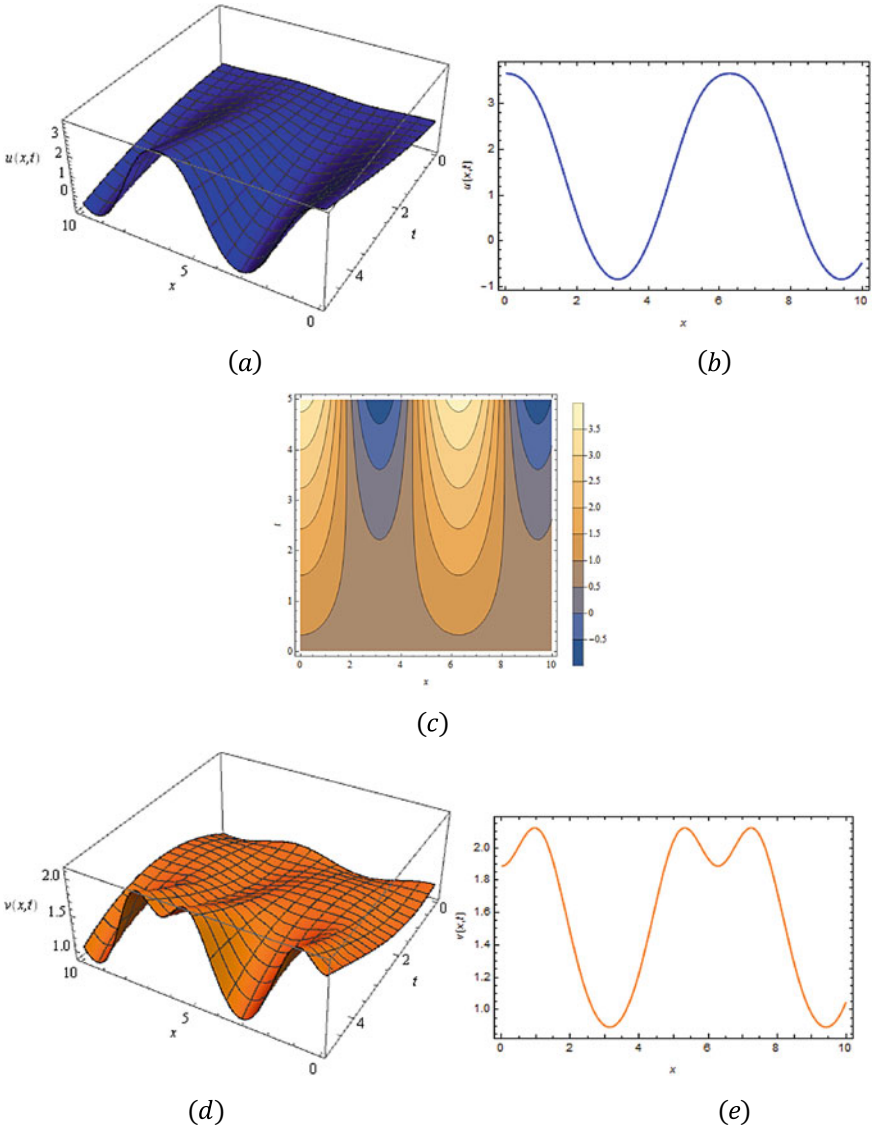

Fig. 7 **a** Surface plot for u, **b** curve of u at t = 1, **c** contour plot of u, **d** surface for $v(x, t)$, **e** 2D plot for v at $t = 1$, **f** contour plot of v, **g** coupled behaviour of the solution of Eq. 20, **h** coupled 2D plot for u and v at $t = 1$ when $k = 1, a = 0.14, b = 0.66, d_1 = 0.2, d_2 = 0.1, n = 1, \alpha = 1, \hbar = -1$

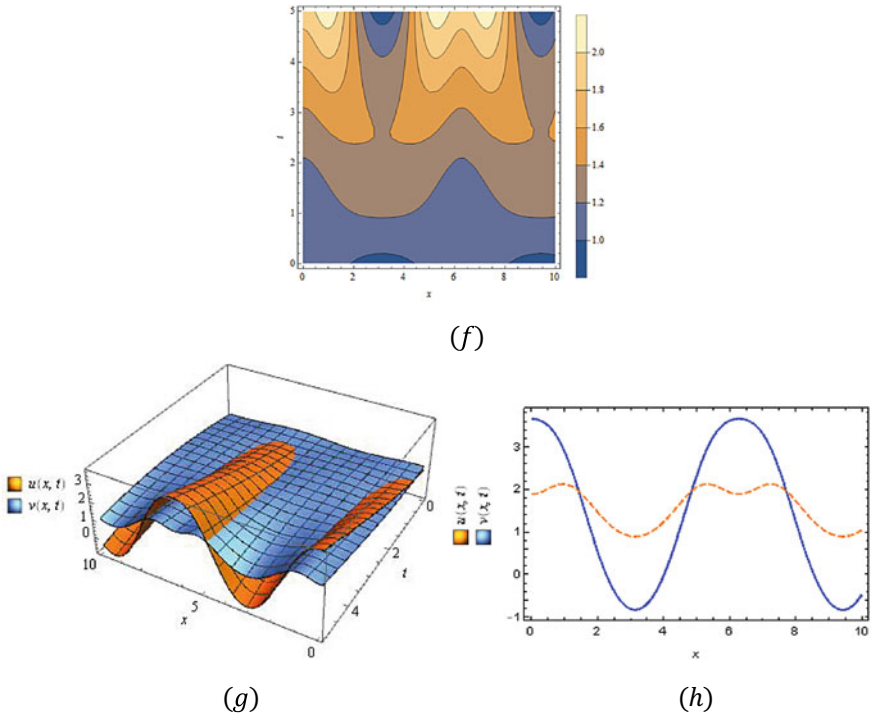

(*f*)

(*g*) (*h*)

Fig. 7 (continued)

References

1. Kilbas AA, Srivastava HM, Trujillo JJ (2006) Theory and applications of fractional differential equations. North-Holland Mathematics Studies
2. Podlubny I (1999) Fractional differential equations. Academic Press, San Diego, CA
3. Lazarevic MP (2006) Finite time stability analysis of PDα fractional control of robotic time-delay systems. Mech Res Commun 33(2):269–279
4. Drapaca CS, Sivaloganathan S (2012) A fractional model of continuum mechanics. J Elast 107:105–123
5. Lohmann AW, Mendlovic D, Zalevsky Z (1998) IV: fractional transformations in optics. Prog Opt 38:263–342
6. Veeresha P, Prakasha DG (2020) An efficient technique for two-dimensional fractional order biological population model. Int J Model Simul Sci Comput 11(1)
7. Prakasha DG, Veeresha P, Singh J (2019) Fractional approach for equation describing the water transport in unsaturated porous media with Mittag-Leffler kernel. Front Phys 7(193)
8. Akinyemi L et al (2021) Novel approach to the analysis of fifth-order weakly nonlocal fractional Schrodinger equation with Caputo derivative. Results Phys 31
9. Gao W, Veeresha P, Prakasha DG, Senel B, Baskonus HM (2020) Iterative method applied to the fractional nonlinear systems arising in thermo elasticity with Mittag-Leffler kernel. Fractals 28(8):2040040

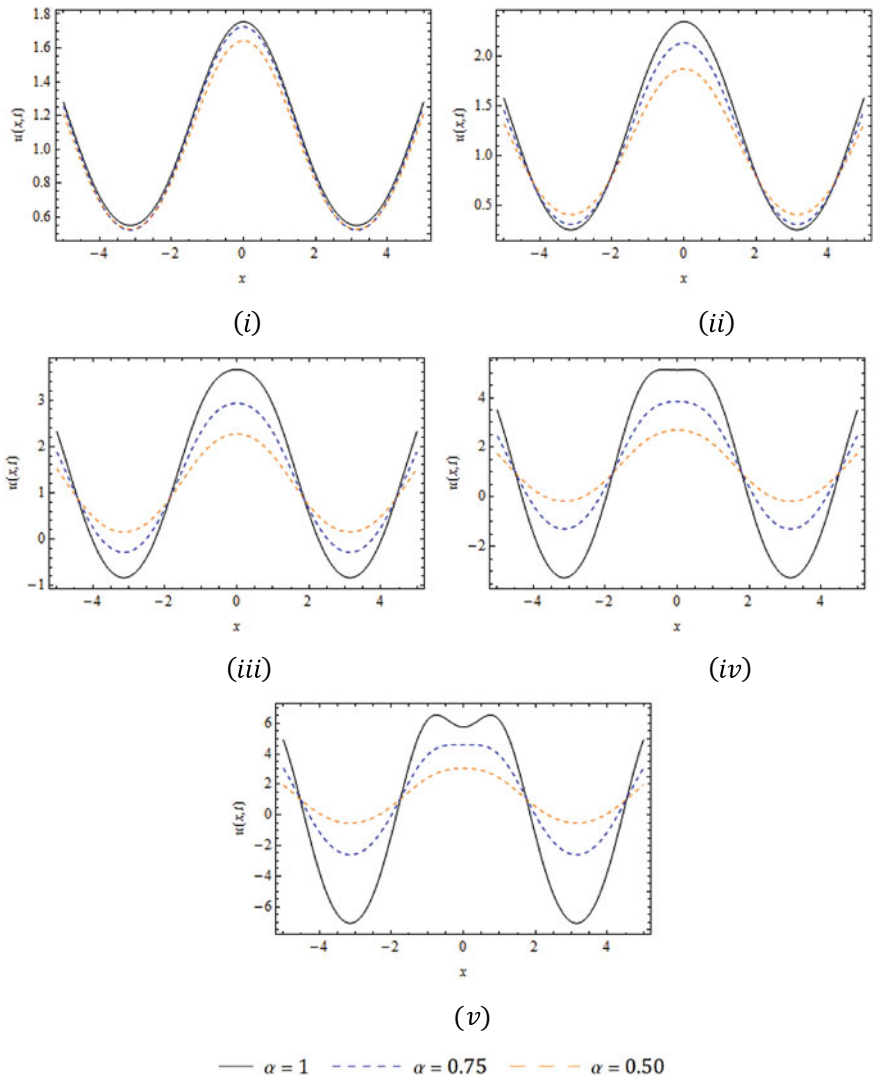

Fig. 8 Curves for activator $u(x, t)$ for Ex. 4.2 at (i)$t = 2$, (ii)$t = 3$, (iii)$t = 5$, (iv)$t = 7.5$, and (v) $t = 10$ by taking $k = 1, a = 0.14, b = 0.66, d_1 = 0.2, d_2 = 0.1, n = 1$ and $\hbar = -1$ for distinct values of α

10. Veeresha P, Prakasha DG, Hammouch Z (2020) An efficient approach for the model of thrombin receptor activation mechanism with Mittag-Leffler function. Nonlinear Anal: Probl Appl Comput Methods 44–60
11. Prakasha DG, Malagi NS, Veeresha P (2020) New approach for fractional Schrödinger-Boussinesq equations with Mittag-Leffler kernel. Math Meth Appl Sci 32(12):1519–1540
12. Prakasha DG, Malagi NS, Veeresha P, Prasannakumara BC (2020) An efficient computational technique for time-fractional Kaup-Kupershmidt equation. Numer Meth Partial Diff Eq

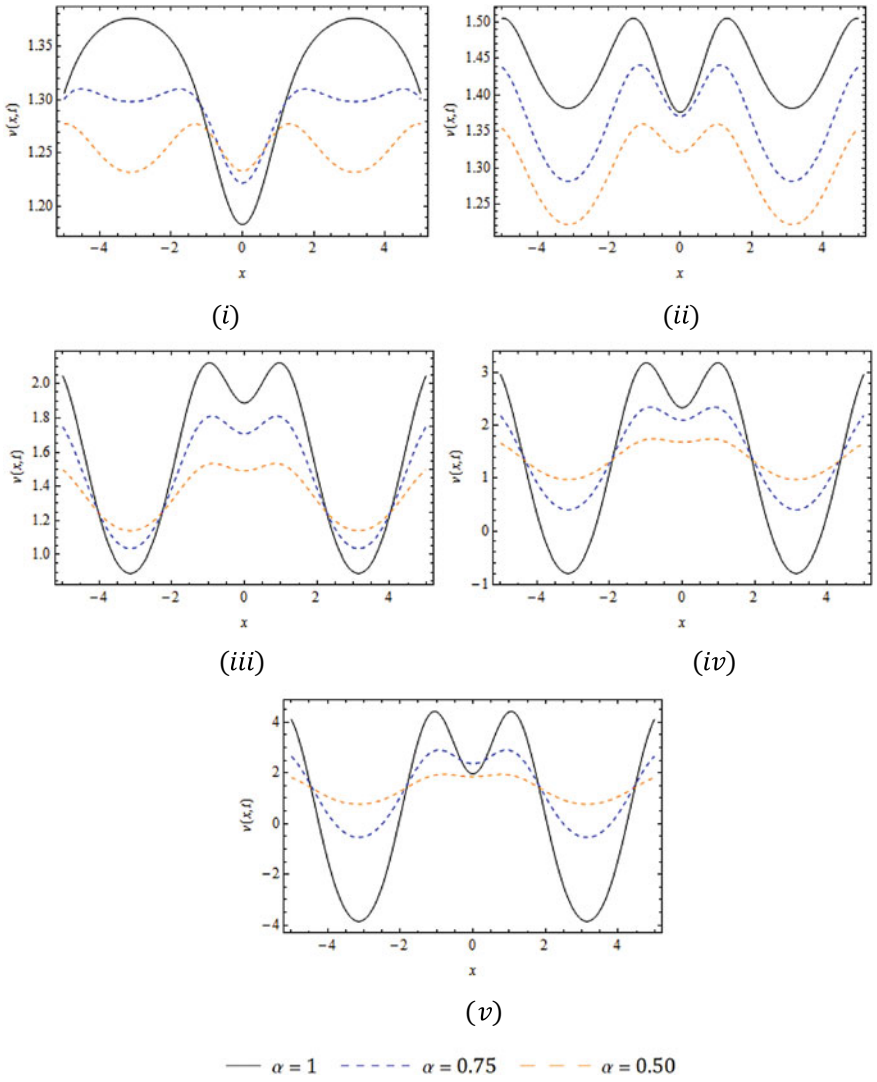

Fig. 9 Curves for inhibitor $v(x, t)$ for Ex. 4.2 at (i)$t = 2$, (ii)$t = 3$, (iii)$t = 5$, (iv)$t = 7.5$, and (v) $t = 10$ by taking $k = 1, a = 0.14, b = 0.66, d_1 = 0.2, d_2 = 0.1, n = 1$ and $\hbar = -1$ for distinct values of α

37(2):1299–1316
13. Bulut H, Kumar D, Singh J, Swroop R, Baskonus HM (2018) Analytic study for a fractional model of HIV infection of CD4+T lymphocyte cells. Math Nat Sci 2(1):33–43
14. Safare KM, Betageri VS, Prakasha DG, Veeresha P, Kumar S (2021) A mathematical analysis of ongoing outbreak COVID-19 in India through nonsingular derivative. Numer Meth Partial Diff Eq 37(2):1282–1298

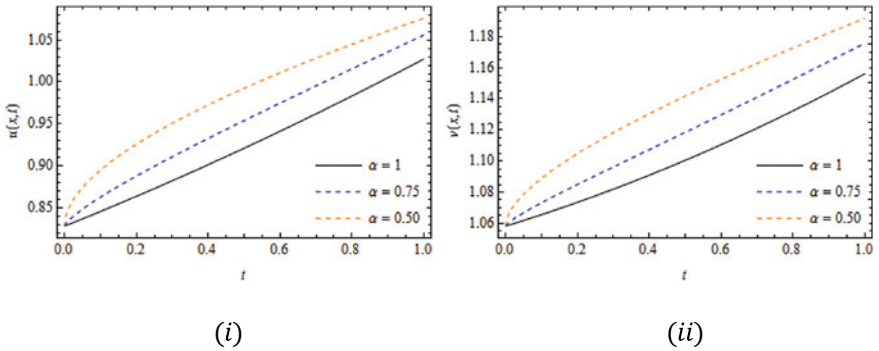

Fig. 10 (i) $u(x,t)$, (ii) $v(x,t)$ with respect to t for Ex. 4.2. when $x = 5, a = 0.14, b = 0.66, k = 1, d_1 = 0.2, d_2 = 0.1, \hbar = -1$ and $n = 1$ for diverse values of α

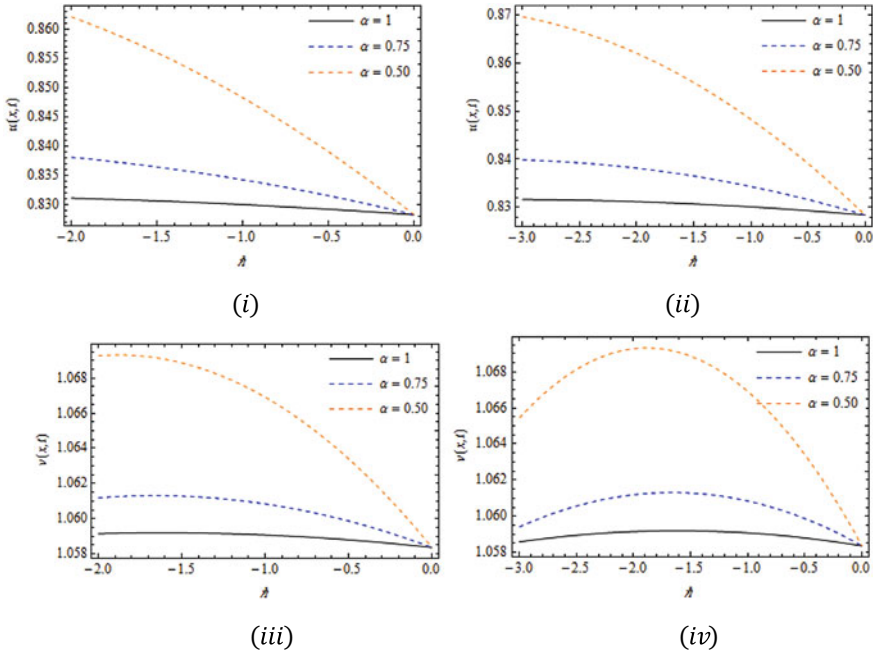

Fig. 11 The $\hbar$-curve for $u(x,t)$ and $v(x,t)$ for Ex. 4.2. at (i) & (iii) $n = 1$ and (ii) & (iv) $n = 2$ when $x = 5, a = 0.14, b = 0.66, k = 1, d_1 = 0.2, d_2 = 0.1, t = 0.01$ for diverse values of α

15. Malagi NS, Veeresha P, Prasannakumara BC, Prasanna GD, Prakasha DG (2021) A new computational technique for the analytic treatment of time-fractional Emden-Fowler equations. Math Comput Simul 190:362–376
16. He J-H (1999) Variational iteration method—a kind of nonlinear analytical technique: some examples. Int J NonLinear Mech 34(4):699–708
17. Wazawz AM (2019) A variety of optical solitons for nonlinear schrodinger equation with detuning term by the variational iteration method. Optik 196:163–169
18. Batiha B, Noorani MSM, Hashim I (2007) Applications of variational iteration method to heat and wave-like equations. Phys Lett A 369:55–61
19. El-Tawil MA, Bahnasawi AA, Abdel-Naby A (2004) Solving Riccati differential equation using Adomian's decomposition method. Appl Math Comput 157:503–514
20. Liao SJ (2003) Beyond perturbation: introduction to homotopy analysis method. Chapman and Hall/CRC Press, Boca Raton
21. Liao SJ (1995) An approximate solution technique not depending on small parameters: a special example. Int J Nonlinear Mech 30(3):371–380
22. Liao SJ (2012) Homotopy analysis method in nonlinear differential equations. Springer and Higher Education Press, Berlin and Beijing
23. El-Tawil MA, Huseen SN (2012) The q-Homotopy analysis method (q- HAM). Int J Appl Math Mech 8:51–75
24. El-Tawil MA, Huseen SN (2013) On convergence of the q-homotopy analysis method. Int J Contemp Math Sci 8:481–497
25. Wazawz AM (2010) The combined Laplace transform–adomian decomposition method for handling nonlinear Volterra integro–differential equations. Appl Math Comput 216(4):1304–1309
26. Jafari H, Khalique CM, Nazari M (2010) Application of the Laplace decomposition method for solving linear and nonlinear fractional diffusion–wave equations. Appl Math Lett 24(11):1799–1805
27. Khan M, Gondal MA, Hussain I, Vanani SK (2012) A new comparative study between homotopy analysis transform method and homotopy perturbation transform method on semi infinite domain. Math Comput Model 55:1143–1150
28. Khan M (2014) A novel solution technique for two dimensional Burger's equation. Alex Eng J 53:485–490
29. Khuri SA (2001) A Laplace decomposition algorithm applied to a class of nonlinear differential equations. J Appl Math 1:141–155
30. Kumar D, Singh J, Kumar S (2014) Numerical computation of nonlinear fractional Zakharov-Kuznetsov equation arising in ion-acoustic waves. J Egyptian Math Soc 22:373–378
31. Veeresha P, Prakasha DG, Singh J, Kumar D, Baleanu D (2020) Fractional Klein-Gordon-Schrödinger equations with Mittag-Leffler memory. Chinese J Phys 68:65–78
32. Singh J, Kumar D, Swroop R (2016) Numerical solution of time- and space-fractional coupled Burger's equations via homotopy algorithm. Alex Eng J 55(2):1753–1763
33. Turing AM (1990) The chemical basis of morphogenesis. Bull Math Biol 52:153–197
34. Rida SZ, El-Sayed AMA, Arafa AAM (2010) Effect of bacterial memory dependent growth by using fractional derivatives reaction-diffusion chemotactic model. J Stat Phys 140:797–811
35. El-Sayed AMA, Rida SZ, Arafa AAM (2010) On the solutions of the generalized reaction-diffusion model for bacteria growth. Acta Appl Math 110:1501–1511
36. Rida SZ, El-Sayed AMA, Arafa AAM (2010) On the solutions of time-fractional reaction-diffusion equations. Commun Nonlinear Sci Numer Simul 15:3847–3854
37. Veeresha P, Gao W, Prakasha DG, Malagi NS, Ilhan E, Baskonus HM (2021) New dynamical behaviour of the coronavirus (COVID-19) infection system with nonlocal operator from reservoirs to people. Inf Sci Lett 10(2):205–212
38. Magin RL (2004) Fractional calculus in bioengineering. Crit Rev Biomed Eng 32(1):1–104
39. Magin RL (2004) Fractional calculus in bioengineering-Part 2. Crit Rev Biomed Eng 32(2):105–193

40. Magin RL (2004) Fractional calculus in bioengineering-Part 3. Crit Rev Biomed Eng 32(3/4):194–377
41. Schnakenberg J (1979) Simple chemical reaction systems with limit cycle behavior. J Theor Biol 81:389–400
42. Goodwin BC, Trainor LEH (1985) Tip and whorl morphogenesis in Acetabularia by calcium-regulated strain fields. J Theor Biol 117:79–106
43. Teleman AA, Strigini M, Cohen SM (2001) Shaping morphogen gradients. Cell 105:559–562
44. Hairer E, Wanner G (1999) Stiff differential equations solved by Radau methods. J Comput Appl Math 111:93–111
45. Gurdon JB, Bourillot PY (2001) Morphogen gradient interpretation. Nature 413:797–803
46. Lander A, Nie Q, Wan F (2002) Domorphogen gradients arise by diffusion. Dev Cell 2(6):785–796
47. Miller KS, Ross B (1993) An introduction to fractional calculus and fractional differential equations. Wiley, New York
48. Singh J et al (2021) An efficient numerical approach for fractional multi-dimensional diffusion equations with exponential memory. Numer Methods Part Differ Equ 37(2):1631–1651
49. Baishya C, Veeresha P (2021) Laguerre polynomial-based operational matrix of integration for solving fractional differential equations with non-singular kernel. Proc R Soc A 477(2253)
50. Okposo NI, Veeresha P, Okposo EN (2021) Solutions for time-fractional coupled nonlinear Schrödinger equations arising in optical solitons. Chinese J Phys
51. Goswami A, Singh J, Kumar D (2019) Sushila, an efficient analytical approach for fractional equal width equations describing hydro-magnetic waves in cold plasma. Phys A 524:563–575
52. Ilhan E, Veeresha P, Baskonus HM (2021) Fractional approach for a mathematical model of atmospheric dynamics of CO2 gas with an efficient method. Chaos, Solitons and Fractals 152
53. Veeresha P, Prakasha DG, Kumar D (2020) Fractional SIR epidemic model of childhood disease with Mittag-Leffler memory. Fract Calc Med Health Sci 229–248
54. Singh J, Ganbari B, Kumar D, Baleanu D (2021) Analysis of fractional model of guava for biological pest control with memory effect. J Adv Res 32:99–108

Existence of Salvage Value in a Memory Dependent EOQ Model in Absence of Deteriorating Items

Rituparna Pakhira, Laxmi Rathour, Vishnu Narayan Mishra, Lakshmi Narayan Mishra, and Sunita

Abstract In this article, an inventory model has been developed by incorporating the effect of the past experience. This paper wants to incorporate memory effects that are based on the fact that economic agents remember the history of changes in exogenous and endogenous variables. Memory or past experiences have a great impact on the real inventory system to maintain the business. The inclusion of the memory effect in the inventory system has been done by using fractional calculus. We have also established the existence of salvage value in the memory-dependent inventory system in absence of deteriorating items. Finally, sensitivity analysis is done to determine the most important parameters of the system for the market studies so that it would be taken care seriously. Our considered numerical example is able to crack the practical situation. In practice, if the rate of change of the initial demand is more compared to the initial demand that means the selling rate is increasing for the businessman's good business policy or good product quality. By considering the rate of change of initial demand > initial demand, profit is more compared to the opposite case. From

R. Pakhira
Department of Engineering Science and Humanities, Academy Of Technology, Adisaptagram, West Bengal 712502, India
e-mail: rituparna.pakhira@gmail.com

L. Rathour
Ward number—16, Bhagatbandh, Anuppur, Madhya Pradesh 484224, India
e-mail: rathourlaxmi562@gmail.com

V. N. Mishra
Department of Mathematics, Indira Gandhi National Tribal University, Lalpur, Amarkantak, Anuppur, Madhya Pradesh, India
e-mail: vnm@igntu.ac.in

L. N. Mishra (✉)
Department of Mathematics, School of Advanced Sciences, Vellore Institute of Technology, Tamil Nadu, Vellore 632 014, India
e-mail: lakshminarayan.mishra@vit.ac.in; lakshminarayanmishra04@gmail.com

Sunita
Department of Mathematics, University of Rajasthan, Jaipur, Rajasthan 302004, India

J. Singh et al. (eds.), *Advances in Mathematical Modelling, Applied Analysis and Computation*, Lecture Notes in Networks and Systems 415,
https://doi.org/10.1007/978-981-19-0179-9_27

the numerical example, it is clear that business policy was not good for that inventory system.

Keywords Fractional-order derivative · Fractional Laplace transform method · Time-dependent holding cost with fractional effect · Salvage value

1 Introduction

Inventories are stock of goods, work-in-progress goods, and completely finished goods that are considered to be the portion of a business's assets that are ready or will be ready for sale. Formulation of a suitable inventory model is one of the major concerns for an industry. Model formulation of inventory system is one of the important research topics of operation research. It is known that a management model creates a difference in the nature of the available information on the properties of the simulated system. When the value of the model parameters is well-defined, the nature of the corresponding mathematical model is deterministic. In contrast, if the parameters of the system are considered random values with a known probability, distribution models are stochastic (probabilistic).

In real-life situations for some products, the demand rate is once constant, then increases, and finally decreases. Nowadays, the demand of the inventory system is totally market oriented, where the demand rate is time dependent. The demand rate for such inventory items as electronic goods and fashionable clothes are time or season dependent. Ghare and Schraderis [1] established the existence of time dependency in demand rate mathematically. Salvage value has another role in the inventory system. The salvage value of an item is the value of a leftover item when no further inventory is desired. The salvage value represents the disposal value of the item to the firm, perhaps through a discounted sale. Mishra et al. [2] developed an inventory model with salvage value and they also established that increases in salvage value decrease the number of units to be procured. Mishra et al. in [3] also established the existence of time dependency in holding cost of the inventory system by considering the effects of deterioration with salvage value as well as shortages. This model is more practical compared to [3] because practically holding cost depends upon the time. Many more classical inventory models with the deteriorating items and salvage value were developed with numerical examples by different researchers.

Some researchers started to apply FC to scientific and engineering problems and gave a new dimension to the calculus. We want to recall some pioneer researchers, who gave their valuable attention to developing fractional calculus. Some of them are illustrated below very shortly. De L'Hopital, Guillaume Francois Antoine (1661–1704), who may be called as the father of the fractional calculus because the first question was raised in 1695 by L'Hospital to Gottfried Leibnitz about the derivative of order ½. This question actually helps to think of a new subject, named fractional calculus. Euler, Niels Henrik (1802–1829) was a great mathematician, who developed

Euler's fractional-order derivative, which helped to continue the work on fractional-order derivative. Grunwald, Antonk (1838–1983) was one of the pioneers in the world to think about the development of fractional calculus. Grunwald fractional-order derivative was developed by him, which is a great contribution to fractional calculus. Lacroix, Sylvestre Francois was a French mathematician. His connection to fractional calculus started by studying fractional-order derivative. Mittag-Leffler, Magnus Gustaf (1846–1927) was a great Swedish mathematician, who developed Mittag–Leffler function of one parameter which is the generalization of the exponential function. Like ordinary calculus, the Mitagg-Leffler function plays an important role in fractional calculus. His contribution helped to move forward the future research of fractional calculus.

Riemann, Georg Friedrich Bernhard (1826–1866) was a German Mathematician, who developed the fractional-order derivative, which is famous as Riemann–Liouville fractional-order derivative. Weyl, Hermann Klaus Hugo (1885–1955) was German Mathematicians, who developed the Weyl fractional integral. Ross, Bertram (1886–1969) was a Hungarian Mathematician, FC pioneers. He wrote a book with K.S. Miller about fractional calculus, where fractional calculus was studied clearly. NielsAbel (1802–1829) was a Norwegian mathematician. His linking to fractional calculus originates from an application of fractional integrals. He completed the problem in physics, which is finding a tautochrone curve. Oliver-Heaviside (1850–1925) was a mathematician and engineer. He defined the fractional powers of p and established a connection between operational calculus and fractional calculus. Paulle'vy (1886–1971) was a French mathematician. His connection was started to fractional calculus through the study of a stochastic process. Kenneth Cole (1900–1984) and Robert Cole (1914–1990) were the pioneers to study the application of fractional calculus. The paper [4] was one of the first applications of fractional calculus and it shows nowadays an important role in many different scientific areas. More evidence of the Cole brothers and their contributions can be seen in [5, 6]. Andrew-Gemant (1895–1983) established the concept of a complex viscoelasticity [7]. The relationship between deformation and stress is dynamic, so that the deformation depends on the history of the previously applied stress has been clearly written. He verified that the experimental data for the dynamic viscosity of a cellulose ester supported that it varies frequency

$$\eta' = \frac{\eta}{\left(1 + (w\tau_0)^{\frac{3}{4}}\right)}$$

where η is the stationary viscosity[8]. This fractional transfer function, first published in a series of papers in 1941–1943, was the first viscoelastic relationship proposed, see [9]. Rashid Shakirovich Nigmatullin (1923–1991) was the first Russian scientist and one of the great pioneers in the world, who thought about practical applications of the operators of fractional differentiation in 1960. He suggested that the electrochemical

device performs with the fractional integration/differentiation operation of order one-half. Recently, Valentina V. Tarasova and V. E. Tarasov developed various economic models with power-law memory. Some of them are given below as follows.

(i) The logistic growth model with memory [10].
(ii) The natural growth model [11, 12].
(iii) The growth model with constant pace [13, 14].
(iv) The Keynes model [15–17].
(v) The dynamic Leontief (intersectoral) model [18–21].
(vi) The time-dependent dynamic intersectoral model with memory [18, 21].
(vii) The Phillips model with memory and lag [22].
(viii) The dynamic Keynesian model with memory and lag [23].

On the other hand, in the inventory system, the business policy has a great impact to increase or decrease of the profit. Since, the profit of the inventory system depends on its business policy like the attitude of the staff or shopkeeper, the position of the company or shop, environment or social situation near the shop or company. If any customer gets rough behavior from any shop or poor quality of the product, then they will not go further in that shop. Due to the above fact, the inclusion of past experiences in the inventory system has an important impact on the business. It is also known that the theory of derivatives and integrals of non-integer (fractional) orders has a long history. Fractional calculus plays an important role in the modeling of real problems with memory effects in the different areas of scientific and engineering processes. Memory means it depends on the past state of the process not only the current state of the process [24, 25]. The order of the fractional-order derivative and fractional order integration is established as an index of memory [25]. This concept has been used in different biological [26], economical [24, 27] models to show the memory dependency of the system. It is known that inventory models are governed by the first-order ordinary differential equations. The integer-order derivative is not able to include the memory effect or past experience effect of the system. Hence, the classical inventory model suffers from amnesia because it is governed by the ordinary differential equation. Due to the fact that to incorporate the memory effect into the inventory system, we have used fractional-order derivatives and integrals to develop the model. It is established that the strength of memory is controlled by the order of the fractional-order derivative and fractional-order integration [26, 28, 29].

Here, we have defined and applied two type of memories indexes: (i) differential memory index which comes from the fractional-order rate of change of the inventory level and (ii) integral memory index which arise from the fractional-order holding cost. Here, we have established a memory-dependent inventory model with salvage value, where deterioration and shortage are not considered, mainly significant with considering the fractional rate of change of inventory level has been shown. It is observed that for the long memory effect, the numerical value of the minimized total average cost is high compared to the short memory effect. Hence, in the long memory effect, profit is low compared to the short memory effect. Salvage value has appeared for the fractional rate of change of inventory level but salvage value

is generally considered for deteriorating item-related integer-order inventory model, where the deteriorating effect has been included.

The rest part of the paper is arranged as follows, review of fractional calculus has been presented in this section, Classical inventory model has been formulated in Sect. 2, Memory-dependent inventory model or fractional-order inventory model is given in Sect. 3, numerical example has been presented in Sect. 4, the graphical presentation of minimized total average cost and optimal ordering interval with respect to differential memory index and integral memory index have been done in Sect. 5 and finally, the article is ended with some conclusions of the work in Sect. 6.

1.1 A Subsection Sample

Please note that the first paragraph of a section or subsection is not indented. The first paragraphs that follow a table, figure, equation, etc. do not have an indent, either.

Subsequent paragraphs, however, are indented.

2 Classical Inventory Model

To develop the inventory models, the following assumptions and notations have been used. The assumptions are: (i) Lead time is zero. (ii) Time horizon is infinite. (iii) There is no shortage. (iv) Demand rate is assumed as cubic type, defined as $D(t) = (a + bt + ct^2 + et^3), a \neq 0$.(v) Holding cost is a function of time t as $C_1 t$ per unit (Table 1).

2.1 Classical Model Formulation

As per the considered assumptions, the inventory level depletes due to cubic-type demand rate $(a + bt + ct^2 + et^3)$ during the time interval $[0, T]$, where shortage is not allowed. The rate of change of inventory level during the ordering interval $[0, T]$ is governed by the following first-order differential equation as follows:

$$\frac{d(I(t))}{dt} = -(a + bt + ct^2 + et^3) \qquad for \;\; 0 \leq t \leq T \tag{1}$$

With the boundary condition $I(T) = 0$. Here, we are not interested to analyze the classical inventory model, we are only interested in the corresponding fractional-order model to incorporate the memory effect. For that reason, we have discussed the fractional order inventory model in the next section.

Table 1 Used symbols and items

Symbols	Items	Symbols	Items
(i) C_3	Ordering cost per order	(ix) γ	Salvage value per unit which is constant $\gamma < 1.0$
(ii) $C_1 t$	Holding cost or carrying cost per unit	(x) Q	Total optimal order quantity
(iii) $HC_{\alpha,\beta}$	Total Inventory holding cost with fractional effect	(xi) $TC_{\alpha,\beta}$	Total cost with fractional effect
(iv) $SL_{\alpha,\beta}$	Total salvage value with fractional effect	(xii) $T^*_{\alpha,\beta}$	Optimal ordering interval with fractional effect
(v) $PC_{\alpha,\beta}$	Total purchasing cost with fractional effect	(xiii) $TC^{av}_{\alpha,\beta}$	Total average cost with fractional effect
(vi) $I(t)$	Inventory level at time t	(xiv) $B(,.)$	Beta function
(vii) T	Length of each ordering cycle	(xv) $TC^*_{\alpha,\beta}$	Minimized total average cost with fractional effect
(viii) P	Purchasing cost per unit	(xvi) $\Gamma(,.)$	Gamma function

3 Fractional-Order Inventory Model

To study the influence of memory effects, first, the differential Eq. (1) is written using the memory kernel function in the following form [24, 28, 30]:

$$\frac{dI(t)}{dt} = -\int k\big(t-t'\big)(a+bt'+c(t')^2+e(t')^3)dt' \tag{2}$$

where $k(t-t')$ plays the role of a time-dependent kernel. This type of kernel promises the existence of scaling features as it is often intrinsic in most natural phenomena. Thus, to generate the fractional-order model, we consider $k(t-t') = \frac{1}{\Gamma(1-\alpha)}(t-t')^{\alpha-2}$, where $0 < \alpha \leq 1.0$. Using the definition of fractional derivative [31], the differential Eq. (2) can be written in the form of fractional differential equations with the Caputo-type fractional-order derivative in the following form:,

$$\frac{dI(t)}{dt} = -{}_0D_t^{-(\alpha-1)}\big(a+bt+ct^2+et^3\big) \tag{3}$$

Using the fractional Caputo-type derivative of order $(\alpha-1)$ on both sides of (3), and using inverse operators, the following fractional differential equations can be obtained for the inventory model.

$$\begin{aligned} &{}^C_0D_t^{\alpha}(I(t)) = -(a+bt+ct^2+et^3) \quad \text{Or equivalently} \\ &\frac{d^{\alpha}(\mathrm{I(t)})}{dt^{\alpha}} = -\big(a+bt+ct^2+et^3\big), 0<\alpha\leq 1.0, \quad 0\leq t\leq T \end{aligned} \tag{4}$$

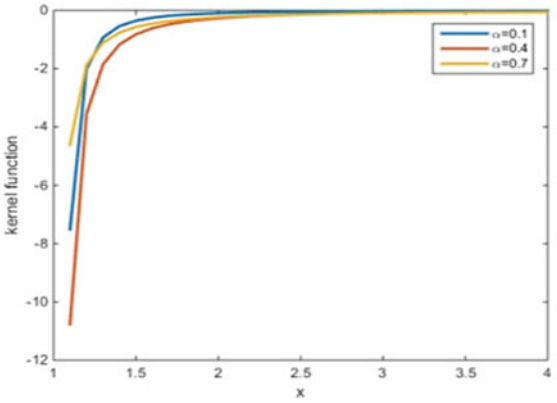

Fig. 1 Plot of memory kernel function $\left(k(x-\xi)=\frac{(x-\xi)^{(\alpha-2)}}{\Gamma(1-\alpha)},\ \text{for}\,\xi=3\right)$ for different values of α

With boundary conditions $I(T) = 0, I(0) = Q$(here, α is considered as the differential memory index).

It is clear from the Fig. 1 that the pick of the curve gradually decreases depending on α. Hence, memory strongly depends on the fractional order α.

Long and Short Memory Effect: The strength of memory is controlled by the order of the fractional-order derivative and fractional-order integration. If the fractional-order index α is in (0, 0.5], then we define the system as the long memory affected system and for short memory effected system α it is in (0.5, 1].

3.1 Solution of the Fractional-Order Inventory Model

Here, we are going to solve the formulated fractional-order differential equation by accepting the differential Eq. (4) as a differential equation of fractional order instead of the linear order, i.e., we here consider that demand rate $\left(a+bt+ct^2+et^3\right)$ varies in fractional order say α. The solution is discussed below

$$\frac{d^{\alpha}(\mathrm{I(t)})}{dt^{\alpha}} = -\left(a+bt+ct^2+et^3\right) \quad , \quad 0<\alpha\leq 1.0, \quad 0\leq t\leq T \text{ with } I(T)=0 \tag{5}$$

where a is defined as the initial demand rate and b is the rate of change of the demand rate, and α is defined as the differential memory index.

The solution to Eq. (5) is

$$I(t) = \left(\frac{a(T^{\alpha}-t^{\alpha})}{\Gamma(1+\alpha)} + \frac{b\left(T^{\alpha+1}-t^{\alpha+1}\right)}{\Gamma(2+\alpha)} + \frac{2c\left(T^{\alpha+2}-t^{\alpha+2}\right)}{\Gamma(3+\alpha)} + \frac{6e\left(T^{3+\alpha}-t^{3+\alpha}\right)}{\Gamma(4+\alpha)}\right) \tag{6}$$

The optimal order quantity Q is derived by putting $t = 0$ in Eq. (6) as follows:

$$I(0) = \left(\frac{aT^{\alpha}}{\Gamma(1+\alpha)} + \frac{bT^{\alpha+1}}{\Gamma(2+\alpha)} + \frac{2cT^{\alpha+2}}{\Gamma(3+\alpha)} + \frac{6eT^{3+\alpha}}{\Gamma(4+\alpha)} \right) = Q \tag{7}$$

In reality, the holding cost of the inventory system increases gradually with respect to time. In this regard, the holding cost is assumed to be time dependent. If $C_1 t$ is assumed as the holding cost per unit time, then the total fractional-order inventory holding cost is denoted by $HC_{\alpha,\beta}$ and it is defined and developed in the following form as

$$\begin{aligned}
&HC_{\alpha,\beta}(T) = C_1 D^{-\beta}(tI(t)) \\
&= \frac{C_1}{\Gamma(\beta)} \int_0^T (T-t)^{\beta-1} tI(t)dt \\
&= \frac{C_1}{\Gamma(\beta)} \int_0^T (T-t)^{\beta-1} t \left(\left(\frac{a\left(T^{\alpha} - t^{\alpha}\right)}{\Gamma(1+\alpha)} + \frac{b\left(T^{\alpha+1} - t^{\alpha+1}\right)}{\Gamma(2+\alpha)} + \frac{2c\left(T^{\alpha+2} - t^{\alpha+2}\right)}{\Gamma(3+\alpha)} + \frac{6e\left(T^{3+\alpha} - t^{3+\alpha}\right)}{\Gamma(4+\alpha)} \right) \right) dt \\
&= \left(\begin{array}{l} \frac{aC_1 T^{\alpha+\beta+1}}{\Gamma(\beta)\Gamma(1+\alpha)} (B(2,\beta) - B(\alpha+2,\beta)) + \frac{bC_1 T^{\alpha+\beta+2}}{\Gamma(\beta)\Gamma(2+\alpha)} (B(2,\beta) - B(\alpha+3,\beta)) \\ + \frac{2cC_1 T^{\alpha+\beta+3}}{\Gamma(\beta)\Gamma(3+\alpha)} (B(2,\beta) - B(\alpha+4,\beta)) + \frac{6eC_1 T^{\alpha+\beta+4}}{\Gamma(\beta)\Gamma(4+\alpha)} (B(2,\beta) - B(\alpha+5,\beta)) \end{array} \right)
\end{aligned} \tag{8}$$

where β is considered as the integral memory index.

We denote the total salvage value with fractional effect by $SL_{\alpha,\beta}$ and derived in the following form as

$$\begin{aligned}
SL_{\alpha,\beta} &= \gamma \left(Q - D^{-\beta} \left(a + bt + ct^2 + et^3 \right) \right) \\
&= \gamma \left(Q - \frac{1}{\Gamma(\beta)} \int_0^T (T-t)^{\beta-1} \left(a + bt + ct^2 + et^3 \right) dt \right) \\
&= \gamma \left(\begin{array}{l} \left(\frac{aT^{\alpha}}{\Gamma(1+\alpha)} + \frac{bT^{\alpha+1}}{\Gamma(2+\alpha)} + \frac{2cT^{\alpha+2}}{\Gamma(3+\alpha)} + \frac{6eT^{3+\alpha}}{\Gamma(4+\alpha)} \right) \\ - \left(\frac{aT^{\beta}}{\Gamma(\beta+1)} + \frac{bT^{\beta+1}B(2,\beta)}{\Gamma(\beta)} + \frac{cT^{\beta+2}B(3,\beta)}{\Gamma(\beta)} + \frac{eT^{\beta+3}B(4,\beta)}{\Gamma(\beta)} \right) \end{array} \right)
\end{aligned} \tag{9}$$

where γ is the salvage value per unit.

(when, $\alpha = \beta = 1$, there is no salvage value, i.e.,
$SL_{1,1} = 0$, but $SL_{\alpha,\beta} \neq 0$ when $0 < \alpha, \beta < 1$.)
For the fractional rate of change of inventory level, salvage value exists.
Purchasing cost is

$$PC_{\alpha,\beta} = \text{Perchasing cost per unit} \times \text{Total order quantity}$$
$$= P\left(\frac{aT^{\alpha}}{\Gamma(1+\alpha)} + \frac{bT^{\alpha+1}}{\Gamma(2+\alpha)} + \frac{2cT^{\alpha+2}}{\Gamma(3+\alpha)} + \frac{6eT^{3+\alpha}}{\Gamma(4+\alpha)}\right) \tag{10}$$

Here, the total cost is denoted by $TC_{\alpha,\beta}(T)$ and derived as follows:

$$TC_{\alpha,\beta}(T) = \left(HC_{\alpha,\beta} + PC_{\alpha,\beta} + C_3 - SL_{\alpha,\beta}\right)$$

(here, $HC_{\alpha,\beta}$ comes from (8) and $PC_{\alpha,\beta}$ is substituted from the Eq. (10), and $SL_{\alpha,\beta}$ comes from the Eq. (9)).

Now, the total average cost is denoted as $TC^{av}_{\alpha,\beta}(T)$ and derived as

$$TC^{av}_{\alpha,\beta}(T) = \frac{\left(HC_{\alpha,\beta} + PC_{\alpha,\beta} + C_3 - SL_{\alpha,\beta}\right)}{T}$$
$$= \begin{pmatrix} AT^{\alpha+\beta} + B_1T^{\alpha+\beta+1} + CT^{\alpha+\beta+2} + DT^{\alpha+\beta+3} + ET^{\alpha-1} + FT^{\alpha} + GT^{\alpha+1} \\ +HT^{\alpha+2} + IT^{\beta-1} + JT^{\beta} + KT^{\beta+1} + LT^{\beta+2} + MT^{-1} \end{pmatrix} \tag{11}$$

where

$$A = \frac{aC_1}{\Gamma(\beta)\Gamma(\alpha+1)}(B(2,\beta) - B(\alpha+2,\beta)),$$
$$B_1 = \frac{bC_1}{\Gamma(\beta)\Gamma(\alpha+2)}(B(2,\beta) - B(\alpha+3,\beta)),$$
$$C = \frac{2cC_1}{\Gamma(\beta)\Gamma(\alpha+3)}(B(2,\beta) - B(\alpha+4,\beta)),$$
$$D = \frac{6eC_1}{\Gamma(\beta)\Gamma(\alpha+4)}(B(2,\beta) - B(\alpha+5,\beta)),$$
$$E = \frac{a(P-\gamma)}{\Gamma(\alpha+1)}, F = \frac{b(P-\gamma)}{\Gamma(\alpha+2)}, G = \frac{2c(P-\gamma)}{\Gamma(\alpha+3)},$$
$$H = \frac{6e(P-\gamma)}{\Gamma(\alpha+4)}, I = \frac{a\gamma}{\Gamma(\beta+1)}, J = \frac{b\gamma B(2,\beta)}{\Gamma(\beta)},$$
$$K = \frac{c\gamma B(3,\beta)}{\Gamma(\beta)}, L = \frac{e\gamma B(4,\beta)}{\Gamma(\beta)}, M = C_3.$$

Now, we consider four cases depending on the particular values of the memory indexes α, β :

(i) $0 < \alpha \leq 1.0, 0 < \beta \leq 1.0$, (ii)$0 < \alpha \leq 1.0, \beta = 1.0$, (iii)$0 < \beta \leq 1, \alpha = 1.0$.

(i) **Case-1**: First, we consider the case when both memory exist i.e. rate of change of inventory level is fractional type and holding cost, salvage value is also of fractional order i.e., $0 < \alpha \leq 1.0, 0 < \beta \leq 1.0$.

In this case, the inventory model can be written as follows:

$$\begin{cases} \text{Min} TC^{av}_{\alpha,\beta}(T) = \begin{pmatrix} AT^{\alpha+\beta} + B_1T^{\alpha+\beta+1} + CT^{\alpha+\beta+2} + DT^{\alpha+\beta+3} + ET^{\alpha-1} + FT^{\alpha} + GT^{\alpha+1} \\ +HT^{\alpha+2} + IT^{\beta-1} + JT^{\beta} + KT^{\beta+1} + LT^{\beta+2} + MT^{-1} \end{pmatrix} \\ \text{Subject to } T \geq 0 \end{cases} \tag{12}$$

(a) **Primal Geometric Programming Method**

To solve (12), the primal geometric programming method has been used [24, 32, 33]. The dual form of (12) has been introduced using the dual variable (w) for the corresponding primal geometric programming problem and it has been constructed in the following form. The dual form of the primal (12) can be written in the following form:

$$\begin{aligned} \text{Max}\, d(w) = &\left(\frac{A}{w_1}\right)^{w_1}\left(\frac{B_1}{w_2}\right)^{w_2}\left(\frac{C}{w_3}\right)^{w_3}\left(\frac{D}{w_4}\right)^{w_4}\left(\frac{E}{w_5}\right)^{w_5}\left(\frac{F}{w_6}\right)^{w_6}\left(\frac{G}{w_7}\right)^{w_7} \\ &\left(\frac{H}{w_8}\right)^{w_8}\left(\frac{I}{w_9}\right)^{w_9}\left(\frac{J}{w_{10}}\right)^{w_{10}}\left(\frac{K}{w_{11}}\right)^{w_{11}}\left(\frac{L}{w_{12}}\right)^{w_{12}}\left(\frac{M}{w_{13}}\right)^{w_{13}} \end{aligned} \tag{13}$$

(where dual variables are $w_i \geq 0, i = 1, \ldots, 13$).

Normalized condition is

$$w_1 + w_2 + w_3 + w_4 + w_5 + w_6 + w_7 + w_8 + w_9 + w_{10} + w_{11} + w_{12} + w_{13} = 1 \tag{14}$$

Orthogonal condition is

$$\begin{pmatrix} (\alpha+\beta)w_1 + (\alpha+\beta+1)w_2 + (\alpha+\beta+2)w_3 \\ +(\alpha+\beta+3)w_4 + (\alpha-1)w_5 \\ +(\alpha)w_6 + (\alpha+1)w_7 + (\alpha+2)w_8 + (\beta-1)w_9 \\ +\beta w_{10} + (\beta+1)w_{11} + (\beta+2)w_{12} - w_{13} \end{pmatrix} = 0 \tag{15}$$

and the primal–dual relations are

$$\left.\begin{aligned} &AT^{(\alpha+\beta)} = w_1 d(w),\ B_1T^{(\alpha+\beta+1)} = w_2 d(w), \\ &CT^{(\alpha+\beta+2)} = w_3 d(w),\ MT^{-1} = w_{13} d(w), \\ &DT^{(\alpha+\beta+3)} = w_4 d(w),\ ET^{\alpha-1} = w_5 d(w), \\ &FT^{\alpha} = w_6 d(w),\ GT^{\alpha+1} = w_7 d(w), \\ &HT^{\alpha+2} = w_8 d(w),\ IT^{\beta-1} = w_9 d(w),\ JT^{\beta} = w_{10} d(w), \\ &KT^{\beta+1} = w_{11} d(w),\ LT^{\beta+2} = w_{12} d(w) \end{aligned}\right\} \tag{16}$$

From the above primal–dual relations (16), we have derived the following equations:

$$\left.\begin{array}{l} \dfrac{Aw_2}{B_1w_1} = \left(\dfrac{B_1w_3}{Cw_2}\right), \dfrac{Cw_4}{Dw_3} = \dfrac{Aw_2}{B_1w_1}, \dfrac{Ew_4}{Dw_5} = \left(\dfrac{Aw_2}{B_1w_1}\right)^{(\beta+4)}, \\ \left(\dfrac{Ew_6}{Fw_5}\right) = \dfrac{Aw_2}{B_1w_1}, \left(\dfrac{Fw_7}{Gw_6}\right) = \left(\dfrac{Aw_2}{B_1w_1}\right), \\ \left(\dfrac{Gw_8}{Hw_7}\right) = \left(\dfrac{Aw_2}{B_1w_1}\right), \left(\dfrac{Iw_8}{Hw_9}\right) = \left(\dfrac{Aw_2}{B_1w_1}\right)^{(\alpha+\beta+3)}, \\ \left(\dfrac{Iw_{11}}{kw_{10}}\right) = \left(\dfrac{Aw_2}{B_1w_1}\right), \left(\dfrac{Iw_{10}}{Jw_9}\right) = \left(\dfrac{Aw_2}{B_1w_1}\right), \\ \left(\dfrac{Kw_{12}}{Lw_{11}}\right) = \left(\dfrac{Aw_2}{B_1w_1}\right), \left(\dfrac{Mw_{12}}{Lw_{13}}\right) = \left(\dfrac{Aw_2}{B_1w_1}\right)^{(\beta+3)} \end{array}\right\} \quad (17)$$

Along with

$$T = \frac{Aw_2}{B_1w_1} \quad (18)$$

Solving the nonlinear Eqs. (14), (15) and (11) relations of (17), the critical values $w_i^*,\ \ i = 1, 2, 3, \ldots 13$ of the dual variable $w_i,\ \ i = 1, 2, 3, \ldots 13$ can be obtained. The optimum value T^* of T has been calculated from Eq. (18). Now, the minimized total average cost $TC^*_{\alpha,\beta}$ has been calculated by substituting $T^*_{\alpha,\beta}$ in (18) analytically. The minimized total average cost and optimal ordering interval are evaluated from (12) numerically using the MATLAB minimization process.

(ii) **Case-2**: Next, we consider the rate of change of inventory level is fractional type and integration associated holding cost, salvage value are of integer order i.e.,$0 < \alpha \leq 1.0, \beta = 1.0$.

The total average cost is derived from (11) as

$$TC^{av}_{\alpha,1}(T) = \begin{pmatrix} AT^{\alpha+1} + B_1T^{\alpha+2} + CT^{\alpha+3} + DT^{\alpha+4} + ET^{\alpha-1} + FT^{\alpha} + GT^{0} \\ +HT + IT^2 + JT^3 + KT^{-1} \end{pmatrix} \quad (19)$$

In this case, the inventory model can be written in the following form:

$$\begin{cases} \text{Min} TC^{av}_{\alpha,1}(T) = \begin{pmatrix} AT^{\alpha+1} + B_1T^{\alpha+2} + CT^{\alpha+3} + DT^{\alpha+4} + ET^{\alpha-1} + FT^{\alpha} \\ +GT^{0} + HT + IT^2 + JT^3 + KT^{-1} \end{pmatrix} \\ \text{Subject to } T \geq 0 \end{cases} \quad (20)$$

$$\text{where, } A = \frac{aC_1}{\Gamma(1)\Gamma(\alpha+1)}(B(2,1) - B(\alpha+2,1)) + \frac{2c(P-\gamma)}{\Gamma(\alpha+3)},$$
$$J = \frac{eB(4,1)\gamma}{\Gamma(1)}, I = \frac{cB(3,1)\gamma}{\Gamma(1)}, K = C_3$$
$$B_1 = \frac{bC_1}{\Gamma(1)\Gamma(\alpha+2)}(B(2,1) - B(\alpha+3,1)) + \frac{6e(P-\gamma)}{\Gamma(\alpha+4)},$$
$$C = \frac{2cC_1}{\Gamma(1)\Gamma(\alpha+3)}(B(2,1) - B(\alpha+4,1)),$$
$$D = \frac{6eC_1}{\Gamma(1)\Gamma(\alpha+4)}(B(2,1) - B(\alpha+5,1)),$$
$$E = \frac{(P-\gamma)a}{\Gamma(\alpha+1)}, F = \frac{(P-\gamma)b}{\Gamma(\alpha+2)}, G = \frac{a\gamma}{\Gamma(2)}, H = b\gamma B(2,1).$$

In a similar way to Case-1, the minimized total average cost and the optimal ordering interval have been calculated from (20).

(iii) **Case-3**: Now, we consider rate of change of inventory level is integer type but integral memory index is fractional type i.e., $0 < \beta \leq 1, \alpha = 1.0$.

Hence, the total average cost becomes as follows:

$$TC^{av}_{1,\beta}(T) = \begin{pmatrix} AT^{\beta+1} + B_1T^{\beta+2} + CT^{\beta+3} + DT^{\beta+4} + ET^0 + FT + GT^2 \\ +HT^3 + IT^{\beta-1} + JT^{\beta} + KT^{-1} \end{pmatrix} \tag{21}$$

where

$$A = \frac{aC_1}{\Gamma(\beta)\Gamma(2)}(B(2,\beta) - B(3,\beta)) + \frac{cB(3,\beta)\gamma}{\Gamma(\beta)},$$
$$B_1 = \frac{bC_1}{\Gamma(\beta)\Gamma(3)}(B(2,\beta) - B(4,\beta)) + \frac{eB(4,\beta)\gamma}{\Gamma(\beta)}$$
$$C = \frac{2cC_1}{\Gamma(\beta)\Gamma(4)}(B(2,\beta) - B(5,\beta)),$$
$$D = \frac{6eC_1}{\Gamma(\beta)\Gamma(5)}(B(2,\beta) - B(6,\beta)), H = \frac{6e(P-\gamma)}{\Gamma(5)},$$
$$I = \frac{a\gamma}{\Gamma(\beta+1)}, E = \frac{(P-\gamma)a}{\Gamma(2)}, F = \frac{(P-\gamma)b}{\Gamma(3)},$$
$$G = \frac{2c(P-\gamma)}{\Gamma(4)}, J = \frac{bB(2,\beta)\gamma}{\Gamma(\beta)}, K = C_3$$

Therefore, the inventory model is

$$\begin{cases} \text{Min} TC^{av}_{1,\beta}(T) = \begin{pmatrix} AT^{\beta+1} + B_1T^{\beta+2} + CT^{\beta+3} + DT^{\beta+4} + ET^0 + FT + GT^2 \\ +HT^3 + IT^{\beta-1} + JT^{\beta} + MT^{-1} \end{pmatrix} \\ \text{Subject to } T \geq 0 \end{cases} \tag{22}$$

In a similar way as case-1, the minimized total average cost and optimal ordering interval have been calculated from (22).

4 Numerical Example

To investigate the memory effect on the total average cost and the optimal ordering interval, we consider the parameters as given in Table 2 in proper units.

In Table 3, we have presented the optimal ordering interval ($T^*_{\alpha,\beta}$) and the minimized total average cost $TC^*_{\alpha,\beta}$ for α is in the range of (0, 1] and $\beta = 1.0$.

It is clear from Table 3 that, for gradually increasing differential memory effect, the minimized total average cost and the optimal ordering interval are gradually increasing. Hence, when the system has long past experiences, profit is low compared to the short memory effect or memory less system. Hence, here business policy was not good for the businessman.

Table 2 The numerical values of the parameters

a	b	c	e	C_1	C_3	P	γ
40	20	10	5	15	100	100	0.1

Table 3 Minimized total average cost and optimal ordering interval for $0 < \alpha \leq 1.0$, $\beta = 1.0$, $a > b$, $\gamma = 0.1$

α	β	$T^*_{\alpha,\beta}$	$TC^*_{\alpha,\beta}$
0.1	1.0	1.1967	7.5513×10^3
0.2	1.0	1.1510	7.5369×10^3
0.3	1.0	1.0945	7.4652×10^3
0.4	1.0	1.0259	7.3290×10^3
0.5	1.0	0.9435	7.1209×10^3
0.6	1.0	0.8448	6.8324×10^3
0.7	1.0	0.7269	6.4543×10^3
0.8 ↑(growing memory effect)	1.0	0.5868	5.9749×10^3
0.9	1.0	0.4275	5.3814×10^3 ↑(increasing)
1.0	1.0	0.2793 ↑(increasing)	4.6748×10^3

Table 4 Minimized total average cost and the optimal ordering interval for $0 < \alpha \leq 1.0, \beta = 1.0, \gamma = 0.5, a > b$

α	β	$T^*_{\alpha,\beta}$	$TC^*_{\alpha,\beta}$
0.1	1.0	1.1950	7.5458×10^3
0.2	1.0	1.1493	7.5310×10^3
0.3	1.0	1.0928	7.4590×10^3
0.4	1.0	1.0243	7.3228×10^3
0.5	1.0	0.9420	7.1147×10^3
0.6	1.0	0.8434	6.8266×10^3
0.7	1.0	0.7256	6.4491×10^3
0.8 ↑ (growing memory effect)	1.0	0.5858	5.9708×10^3
0.9	1.0	0.4269 ↑ (increasing)	5.3789×10^3 ↑ (increasing)
1.0	1.0	0.2793	4.6748×10^3

(b) Now, increase the salvage value per unit from $\gamma = 0.1$ to $\gamma = 0.5$, and rests of the parameters are remaining same. The optimal ordering interval $T^*_{\alpha,\beta}$ and minimized total average cost $TC^*_{\alpha,\beta}$ for these values of the parameter are presented in the Table 4.

It is found in Table 4 that for considering high salvage value (here $\gamma = 0.5$), the minimized total average cost is low compared to the low salvage value system. Hence, for high salvage value, profit is more compared to the low salvage value.

(c) Next, we consider the case when the quality of the product is high, high acceptance by the customer then demand rate at any time will be greater than the initial demand. For numerical testing purpose we consider $a = 20, b = 40, b > a$ and rests of the parameters are remaining same as the numerical example in the Table 2.

In comparison of Tables 4 and 5, we observe that if the rate of change of initial demand > initial demand, profit is high compared to the case initial demand > rate of change of the initial demand. These mathematical results conclude the practical situation of the market. In practice, if the rate of change of the initial demand is more compared to the initial demand that means the selling rate is increasing due to the businessman's good business policy or good product quality.

From Fig. 2, we see that rate of change of inventory level is different and with memory effect gives a qualitatively different result from without a memory effect.

Now, we shall draw the scatter diagram, bar diagram, pie diagram of the optimal ordering interval $T^*_{\alpha,\beta}$ and minimized total average cost $TC^*_{\alpha,\beta}$ with respect to differential memory index for (i) initial demand > rate of change of initial demand and opposite case and (ii) for different salvage values, here we consider $\gamma = 0.1$, $\gamma = 0.5$.

It is clear from Fig. 3a that if the initial demand rate(a) is greater than the initial rate of change of initial demand rate (i.e., $a > b$) then the minimized total average

Table 5 Minimized total average cost and the optimal ordering interval for $0 < \alpha \leq 1.0, \beta = 1.0, b > a$, $\gamma = 0.1$

α	β	$T^*_{\alpha,\beta}$	$TC^*_{\alpha,\beta}$
0.1	1.0	0.8779	7.4899×10^3
0.2	1.0	0.8003	7.162×10^3
0.3	1.0	0.7186	6.7685×10^3
0.4	1.0	0.6335	6.3111×10^3
0.5	1.0	0.5466	5.7967×10^3
0.6	1.0	0.4604	5.2353×10^3
0.7	1.0	0.3787	4.6418×10^3
0.8 ↑ (growing memory effect)	1.0	0.3067	4.0376×10^3
0.9	1.0	0.2507	3.4515×10^3 ↑ (increasing)
1.0	1.0	0.2136	2.9148×10^3

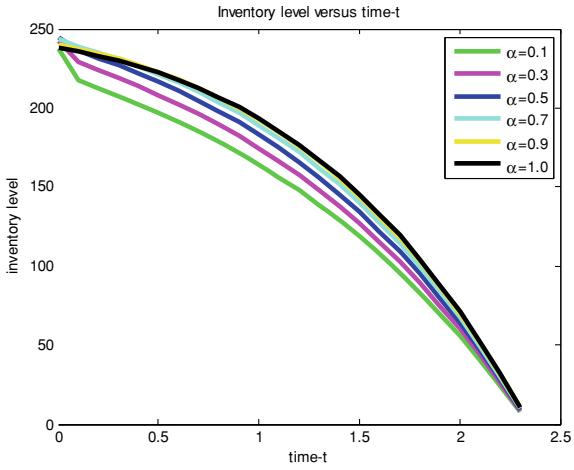

Fig. 2 Inventory level versus time-t for different values of differential memory index

cost values are higher compared to the opposite case (i.e., $b > a$) and this difference increases with the decreasing memory effect.

From the bar diagram Fig. 3b, it is clear that the length of the optimal ordering interval is much high for the case $a > b$, i.e., (initial demand rate > rate of change of the initial demand rate) compared to the case of $b > a$. Hence, when $a > b$, the business takes a long time to reach the minimum value of the total average cost. The difference in the length of the optimal ordering interval for $a > b$ and $b > a$ gradually decreases with the gradually decreasing value of the memory effect.

From Fig. 4a, it is clear that for high salvage ($\gamma = 0.5$) value minimized total average cost value is low compared to the low salvage value (here $\gamma = 0.1$).

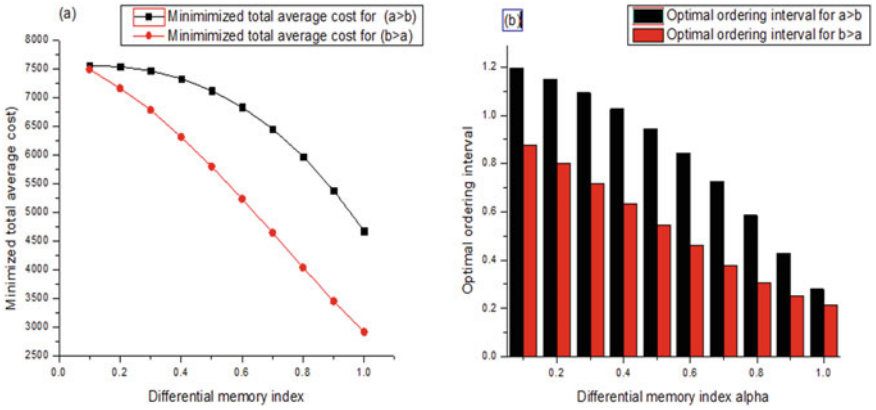

Fig. 3 Scatter diagram and bar diagram for the minimized total average cost for **a** $a > b$ and $b > a$ and **b** optimal ordering interval with respect to the differential memory index (α)

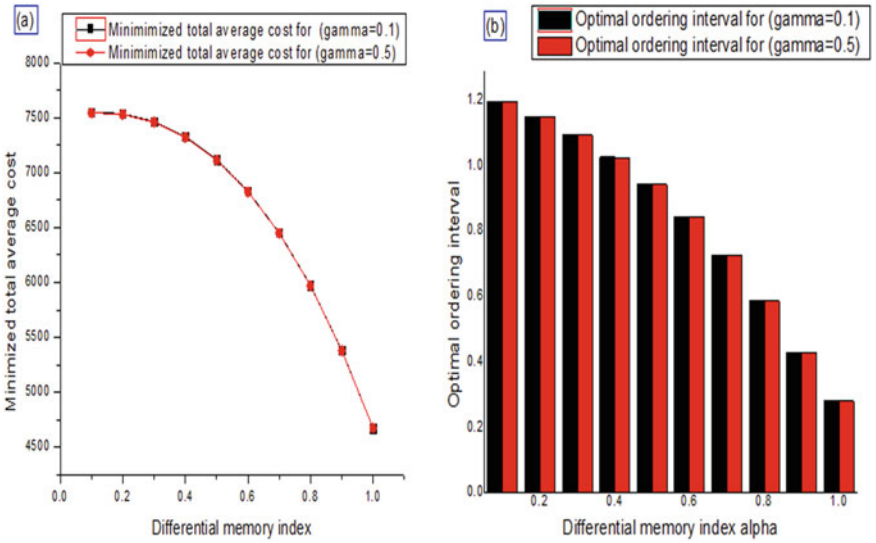

Fig. 4 **a** Scatter diagram of the minimized total average cost for $\gamma = 0.5$, $\gamma = 0.1$. **b** Bar diagram of the optimal ordering interval $\gamma = 0.5$, $\gamma = 0.1$

From Fig. 4b, it is clear that the difference in the optimal ordering interval for $\gamma = 0.5$, and $\gamma = 0.1$ gradually increases with a gradually decreasing memory effect.

From Fig. 5a–d, it is clear that the inventory holding cost is gradually decreasing for the gradually increasing memory effect.

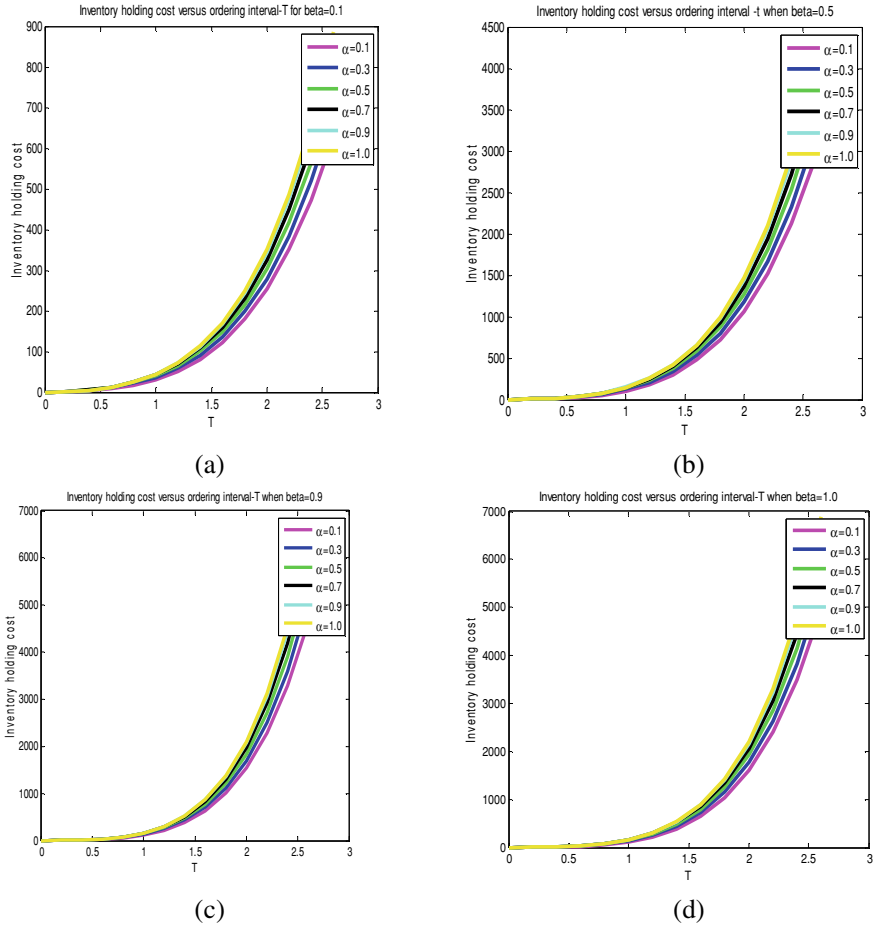

Fig. 5 **a**–**d** ordering interval versus Inventory holding cost versus for different values of α, β

5 Sensitivity Analysis

In this section, we present the sensitivity analysis of the optimal ordering interval and the minimized total average cost with respect to increase or decrease of the values of the parameters $a, b, c, e, C_1, C_3, P, \gamma$ as $+50\%$, $+25\%$, $+20\%$, $+10\%$, -10%, -20%, -25%, -50% using the numerical example as defined in the Table 2.

In our considered problem, there are a large number of parameters (Table 6). From the sensitivity analysis, it is clear that two parameters P, a are the critical parameters for the market studies because changes in the minimized total average cost and optimal ordering interval have significant differences corresponding to changes in the parameters P, a.

Table 6 Effects of changing parameters on the optimal ordering interval and the minimized total average cost where ($\alpha = 0.1$, $\beta = 1.0$)

Parameter	Percentage (%)	$T^*_{\alpha,\beta}$	$TC^*_{\alpha,\beta}$	Parameter	Percentage (%)	$T^*_{\alpha,\beta}$	$TC^*_{\alpha,\beta}$
a	+50(60)	1.3993	9.3745×10^3	C_1	+50(22.5)	1.1843	7.8156×10^3
	+25(50)	1.3155	8.5709×10^3		+25(18.75)	1.2009 ↑	7.7672×10^3
	+20(48)	1.2974	8.4046×10^3		+20(18)	1.2044	7.7573×10^3
	+10(44)	1.2594	8.0655×10^3		+10(16.5)	1.2116	7.7373×10^3
	−10(36)	1.1757	7.3575×10^3		−10(13.5)	1.2267	7.6962×10^3
	−20(32)	1.1291	6.9857×10^3		−20(12)	1.2347	7.6751×10^3
	−25(30)	1.1043	7.8156×10^3		−25(11.25)	1.2388	7.6644×10^3
	−50(20)	0.9610	7.8156×10^3		−50(7.5)	1.2607	7.6093×10^3
b	+50(30)	1.1956	8.7280×10^3	C_3	+50(150)	1.2024	7.5930×10^3
	+25(25)	1.2072	8.2229×10^3		+ 25(125)	1.1996 ↓	7.5722×10^3
	+20(24)	1.2095	8.1218×10^3		+20(120)	1.1990	7.5680×10^3
	+10(22)	1.2142	7.9194×10^3		+10(110)	1.1979	7.5597×10^3
	−10(18)	1.2237	7.5143×10^3		−10(90)	1.1956	7.5430×10^3
	−20(16)	1.2286	7.3115×10^3		−20(80)	1.1945	7.5346×10^3
	−25(15)	1.2310	7.2100×10^3		−25(75)	1.1939	7.5304×10^3
	−50(10)	1.2432	6.7023×10^3		−50(50)	1.910	7.5094×10^3
c	+50(1.139)	1.1319	8.2883×10^3	P	+50(150)	1.2188	1.1186×10^4
	+25(1.1733)	1.1733	8.0089×10^3		+25(125)	1.2096 ↓	9.3692×10^3
	+20(1.1821)	1.1821	7.9516×10^3		+20(120)	1.2074	9.0057×10^3
	+10(1.2002)	1.2002	7.8353×10^3		+10(110)	1.2025	8.2786×10^3

(continued)

Table 6 (continued)

	−10(1.2386)	1.2386	7.5962×10^3		−10(90)	1.1900	6.8238×10^3
	−20(1.2590)	1.2590	7.4731×10^3		−20(80)	1.1820	6.0960×10^3
	−25(1.2696)	1.2696	7.4106×10^3		−25(75)	1.1773	5.732×10^3
	−50(1.3259)	1.3259	7.0883×10^3		−50(50)	1.1444	3.9094×10^3
e	+50(7.5)	1.1302	8.0435×10^3	γ	+50(0.15)	1.1965	7.5506×10^3
	+25(6.25)	1.1709	7.8870×10^3		+25(0.125)	1.1966	7.5510×10^3
	+20(6)	1.1798 ↑	7.8542×10^3		+20(0.12)	1.1967	7.5511×10^3
	+10(5.5)	1.1987	7.7868×10^3		+10(0.11)	1.1967	7.5512×10^3
	−10(4.5)	1.2409	7.6443×10^3		−10(0.09)	1.1968	7.5515×10^3
	−20(4)	1.2648	7.5686×10^3		−20(0.08)	1.1968	7.5516×10^3
	−25(3.75)	1.2775	7.5295×10^3		−25(0.075)	1.1939	7.5423×10^3
	−50(2.5)	1.3517	7.3191×10^3		−50(0.05)	1.1970	7.5520×10^3

6 Conclusion

In the real markets, the salvage value of the inventory system has another impact. In this article, a memory-dependent inventory model has been developed with salvage value where shortages are not allowed. The model is developed analytically with the help of Caputo fractional-order derivative and Riemann–Liouville (R–L) fractional-order integration. The numerical example shows that corresponding to the differential memory index (α), the minimized total average cost gradually increases with the gradually increasing memory effect. Corresponding to the differential memory index α, the minimized total average cost is high compared to the short memory effect. Hence, in the long memory effect, the profit of the business is low compared to the short memory effect. A numerical example shows that profit becomes high corresponding to the high salvage value compared to a low salvage value. Hence, we were able to establish the memory dependency in this model using fractional calculus. Actually, salvage value is considered when deteriorating items are included in the classical inventory model. Salvage value has appeared for the fractional rate of change of inventory level but salvage value generally is considered for deteriorating item-related integer-order inventory model, where the deteriorating effect has been

included. For considering fractional effect in the inventory model with no deteriorating items, salvage value becomes nonzero. An important observation has been found which cracks the real market studies. It is found that the system (where the rate of change of initial demand rate > initial demand rate), gains more profit compared to the opposite case for long memory effect as well as the low memory effect. For future research work, the model may be extended within cooperating deterioration, stock-dependent consumption rate, inflation, and time value of money.

Acknowledgements The authors would also like to thank the Department of Science and Technology, Government of India, New Delhi, for the financial assistance under the AORC, Inspire fellowship Scheme for this research work.

References

1. Ghare PM, Schrader GF (1963) A model for an exponentially decaying inventory. J Ind Eng 14:238–243
2. Mishra P, Shah NH (2008) Inventory management of time dependent deteriorating items with salvage value. Appl Math Sci 2(16):793–798
3. Mishra VK (2012) Inventory model for time dependent holding cost and deterioration holding cost and deterioration with salvage value and shortages. J Math Comput Sci 4(1):37–47
4. Pakhira R, Ghosh U, Sarkar S (2019) Study of memory effect in an inventory model with quadratic type demand rate and salvage value. Appl Math Sci 13(5):209–223
5. Capelas de Oliveira E, Mainardi F, Vaz Jr J (2011) Models based on Mittag-Leffler functions for anomalous relaxation in dielectrics. Eur Phys J 193(1):161–171. Revised version, at http://arxiv.org/abs/1106.1761
6. Greene EF, Berberian GJ (1985) Symposium on dielectric phenomenain honor of the 70th birthday of Professor Robert H. Cole. IEEE Trans Electr Insul 20(6):897
7. Mopsik FI, Hoffman JD (1985) In honor of Professor Robert H. Cole's seventieth birthday. IEEE Trans Electr Insul 20(6):899–924
8. Gemant A (1935) The conception of a complex viscosity and its application to dielectrics. Trans Faraday Soc 31:1582–1590
9. Gemant A (1950) Frictional phenomena. Chemical Publishing Company, Brooklin
10. Tarasova VV, Tarasov VE (2017) Logistic map with memory from economic model. Chaos Solitons Fract 95:84–91
11. Tarasova VV, Tarasov VE (2016) Fractional dynamics of natural growth and memory effect in economics. Eur Res 12:30–37
12. Tarasova VV, Tarasov VE (2017) Economic model of natural growth with dynamic memory. Actual Probl Humanit Nat Sci 4:51–58 (in Russian)
13. Tarasova VV, Tarasov VE (2017) Model of economic growth with constant rate and dynamic memory. Econ Sociol Law 8:18–24 (in Russian)
14. Tarasova VV, Tarasov VE (2017) Economic growth model with constant pace and dynamic memory. Probl Mod Sci Educ 2:40–45
15. Tarasova VV, Tarasov VE (2016) Keynesian model of economic growth with memory. Econ Manag Probl Solut 10:21–29 (in Russian)
16. Tarasova VV, Tarasov VE (2016) Memory effects in hereditary Keynes model. Probl Mod Sci Educ 38:56–61 (in Russian)
17. Tarasova VV, Tarasov VE (2016) Influence of memory effects on world economics and business. Azimuth Sci Res Econ Manag 5:369–372 (in Russian)

18. Tarasov VE, Tarasova VV (2017) Time-dependent fractional dynamics with memory in quantum and economic physics. Ann Phys 383:579–599
19. Tarasova VV, Tarasov VE (2017) Dynamic intersectoral models with memory that generalize Leontief model. J Econ Entrep 2:913–924 (in Russian)
20. Tarasova VV, Tarasov VE (2018) Dynamic intersectoral models with power-law memory. Commun Nonlinear Sci Numer Simul 54:100–117
21. Tarasova VV, Tarasov VE (2017) Chronological exponent for processes with memory and dynamic intersectoral economic models. Sci Educ Today 4:29–39 (in Russian)
22. Tarasov VE, Tarasova VV (2019) Phillips model with exponentially distributed lag and power-law memory. Comput Appl Math 38:13
23. Tarasov VE, Tarasova VV (2019) Dynamic Keynesian model of economic growth with memory and lag. Mathematics 7:178
24. Pakhira R, Ghosh U, Sarkar S (2018) Study of memory effect in an inventory model with linear demand and salvage value. Int J Appl Eng Res 13(20):14741–14751
25. Tarasova VV, Tarasov VE (2016) Long and short memory in economics: fractional-order difference and differentiation. IRA-Int J Manage Soc Sci 5(2):327–334. https://doi.org/10.21013/jmss.v5.n2.p10
26. Saeedian M, Khalighi M, Azimi-Tafreshi N, Jafari GR, Ausloos M (2017) Memory effects on epidemic evolution: the susceptible-infected-recovered epidemic model. Phys Rev E95:022409
27. Tarasova VV, Tarasov VE (2016) Fractional dynamics of natural growth and memory effect in economics. Eur Res 12(23):30–37
28. Das T, Ghosh U, Sarkar S, Das S (2018) Time independent fractional Schrodinger equation for generalized Mie-type potential in higher dimension framed with Jumarie type fractional derivative. J Math Phys 59:022111. https://doi.org/10.1063/1.4999262
29. Tenreiro Machado J, Durate FB, Duarte GM (2012) Fractional dynamics in financial indices. Int J Bifurcation Chaos 22:12. https://doi.org/10.1142/S0218127412502495
30. Pakhira R, Ghosh U, Sarkar S (2018) Study of memory effects in an inventory model using fractional calculus. Appl Math Sci 12(17):797–824
31. Das AK, Roy TK (2015) Fractional order Eoq model with linear trend of time dependent demand. I.J Intell Syst Appl 03
32. Pakhira R, Ghosh U, Sarkar S (2018) Application of memory effects in an inventory model with linear demand and no shortage. Int J Res Advent Technol 6(8)
33. Tarasova VV, Tarasov VE (2016) Memory effects in hereditary Keynesian model. Prob Modern Sci Educ 38(80):38–44. https://doi.org/10.20861/2304-2338-2016-80-001. (in Russian)
34. Tarasova VV, Tarasov VE (2016) A generalization of the concepts of the accelerator and multiplier to take into account of memory effects in macroeconomics. Ekonomika I Predprinmatelstvo [J Econ Entrepreneurship] 10(10–3):1121–1129. (in Russian)
35. Tarasova,V.V., Tarasov,V.E.Marginal utility for economic processes with memory. AlmanahSovremennojNauki I Obrazovaniya [Almanac of Modern Sci Educ] 7(109):108–113. (in Russian)
36. Tarasova VV, Tarasov VE (2017) Economic interpretation of fractional derivatives. Progress Fract Diff Appl 3(1):1–6
37. Miller KS, Ross B (1993) An introduction to the fractional calculus and fractional differential equations. Wiley, New York, NY, USA
38. Caputo M (1967) Linear models of dissipation whose frequency independent. Geophys J Roy Astron Soc 13(5):529–539
39. Das S (2008) Functional fractional calculus for system identification and controls. Springer Berlin Heidelberg, New York
40. Ghosh U, Sengupta S, Sarkar S, Das S (2015) Analytic Solution of linear fractional differential equation with Jumarie derivative in term of Mittag-Leffler function. Am J Math Anal 3(2):32–38
41. Butzer PL, Westphal U, Douglas J, Schneider WR, Zaslavsky G, Nonnemacher T, Blumen A, West B (2000) Applications of fractional calculus in physics. World Scientific, Singapore
42. Rotundo G (2005) Logistic function in large financial crashes. In: Ausloos M, Dirickx M (eds) The logistic map and the route to chaos: from the beginning to modern applications. Springer-Verlag, Berlin/Heidelberg, pp 239–258

43. Podubly I (1999) Fractional differential equations, mathematics in science and engineering. Academic Press, San Diego, CA, USA, p 198
44. Mainardi F (2012) An historical perspective on fractional calculus in linear visco elasticity. Fract Calc Appl Anal 15
45. Pakhira R, Ghosh U, Sarkar S, Mishra VN (2019) Study of memory effect in an Economic order quantity model for completely during backlogged demand during shortage. Progr Fract Differ Appl
46. Pakhira R, Ghosh U, Sarkar S (2020) Study of memory effect in an inventory model for deteriorating items with partial backlogging. Comput Indus Eng 148
47. Pakhira R, Ghosh U, Sarkar S, Mishra VN (2019) Study of memory effect in an inventory model with constant deterioration rate. J Appl Non-linear Dyn

A Fuzzy Decomposable Approach for Posfust Reliability Evaluation of a Repairable Substation Automation System

M. K. Sharma, Harendra Yadav, Lakshmi Narayan Mishra, and Vishnu Narayan Mishra

Abstract In this research paper, we developed a new method to investigate the posfust reliability of a substation automated system. Failure rates and repair rates of the system are key elements of an automated system. In our method, we considered the fuzzy failure and fuzzy repair rates in the context of possibility. In this approach, a decomposition method is applied to a normal and convex fuzzy set. The decomposed fuzzy number gives a more efficient result in the context of possibility. Decomposition of membership grade generates the nested intervals for failure as well as repair rate and plays an efficient role in the estimation of posfust reliability in the automated systems. A reduced state space is used for the computation of availability with the concept of an equivalent transition rate. The whole process is compared with the existing technique and proposed technique with the help of a numerical example.

Keywords Fuzzy set · Fuzzy decomposable sets · Posfust reliability · Repairable system · Automation

1 Introduction

Substation automated engineering product faces many problems in operation with the use of classical theories. There is a lack of accuracy in the evaluation of posfust reliability. On the one hand, to achieve reliable results for the integrated solution of the model, exact values for the parameters of the model should be grown in the current uncertain environment. But, in practice, however, these values can often not

M. K. Sharma · H. Yadav
Department of Mathematics, C.C.S. University, Meerut 250004, India

L. N. Mishra
Department of Mathematics, School of Advanced Sciences, Vellore Institute of Technology, Vellore 632014, Tamil Nadu, India

V. N. Mishra (✉)
Department of Mathematics, Indira Gandhi National Tribal University, Lalpur, Amarkantak, Anuppur 484887, Madhya Pradesh, India
e-mail: vishnunarayanmishra@gmail.com

J. Singh et al. (eds.), *Advances in Mathematical Modelling, Applied Analysis and Computation*, Lecture Notes in Networks and Systems 415,
https://doi.org/10.1007/978-981-19-0179-9_28

be attained and the system reflects unusual behaviour due to a high degree of uncertainty. On the other hand, from a computational aspect, some of the parameters or the variables do not follow to take the deterministic or exact value and may deal in the haziness environment. So, we have to take into account fuzzy uncertainty in the measurement. The reliability has extensively been dealt with the probability and fuzzy set theory in various cases. It is a well-known and acceptable fact that a fuzzy perspective provides a variety of advantages concerning reliability issues. There are some variations, doubts and uncertainties associated with parameters or incorrect data values, which creates the difficulties in prediction and evaluation of reliability. The need for reliability came into effect in real-life problems at the time of World War second, thereafter concepts and theories on reliability were developed [1]. The study of reliability was a beginning in the form of a separate subject having multi-level components [2] and further this theory was extended. Mathematical models for reliability estimation were discussed [3] in the engineering discipline. The concepts of human reliability based on human nature/facts were presented by Dhillon [4] and the study of probabilistic reliability was given by Gnedenko et al. [5]. To remove the uncertainties, that exist in the data or parameters, fuzzy set theory was used and made the results free from existing errors. Zadeh [6] was the first man, who gave the concept of fuzzy logic. Fuzzy logic includes a function representing uncertainty. This function is known as the membership function. The idea given by Zadeh enlightens the fact that membership function is the key element in decision-making. Researchers have extended the concept in reliability theory and its applications were given [7–9]. Fuzzy reliability was discussed by Singer [10], which is based on the fault tree method. Cai [11] provided the fuzzy reliability theory, which is the combination of traditional and fuzzy probability set theory to present different forms of reliability. Possibility theory is a good alternative to get the goal of reliability in various complex systems. Zadeh [12] suggested the possibility in the context of fuzzy sets, which are based on the bodies of evidence. Possibility theory is able to control the vagueness, uncertainty, and variation in data due to its belief measure and necessity measure. Decision-making processes are based on a single objective, such as minimizing cost, maximizing profit, or minimizing the run time. However, a decision must be made in an environment where the problem including more than one objective and the relative value of each objective in different modes of possibility. Inuiguchi et al. [13] proposed an efficient method and decision-making under the uncertainty investigated using belief measures and necessity measures based on utility function with a set of axioms [14]. Using fuzzy state and probability assumptions, Pandey and Tyagi [15] investigated the posfust reliability of a gracefully degraded system. Chen et al. [16] gave new possibility measures and necessity measures and also discussed the coincidence of universal integrals for these measures. In the context of networking, substation automation systems (SASs) dealing with smart grids (SGs) have been taken into account under consideration [17, 18]. The concept of reliability has been used widely in various problems. The evaluation of reliability using a non-normal t-norm triangular fuzzy number was done [19]. The reliability of SAS is primarily considered and many related aspects such as reliability, availability of SASs were discussed from an architectural point of view [20–22]. A new method was used to

obtain the reliability based on the fuzzy Markov model [23, 24]. The secure operation of power systems was discussed in [25]. For a repairable SAS, the failure rate/repair rate of contributing components make a set of quantitative variables, which is known as reliability data. Structuring of a system and construction of its objective function based on the Markov process, reliability block diagram, and universal generating functions have been discussed in [26–28]. Methods based on fuzzy logic are getting more importance in the reliability investigation due to their ability for working in haziness environment and providing accurate results. A mathematical structure in the context of probability was given [29] to get fuzzy reliability and an analysis of fuzzy reliability with censored data was discussed [30]. In absence of rich data, the accuracy is replaced by uncertainty automatically. Modelling of reliability based on a fuzzy set of PMUs was investigated [31]. Focusing on the ageing factor, reliability and maintainability improvements were done [32]. Fuzzy reliability investigating the transmission of power systems using a hybrid Monte Carlo method was presented in [33]. In the context of failure rate merit, a model was provided to find the fuzzy reliability [34] and a qualitative investigation based on the fault tree approach was done by Purba et al. [35] to find the fuzzy reliability. The reliability of an automation system with fuzzy data was investigated [36]. To solve the computational problems and get straightforward results, standard fuzzy arithmetic helps in finding the overestimated results, which have no more significance [37, 38]. Uncertainties with multicomponent systems were discussed from the reliability point of view using fuzzy arithmetic [39, 40]. Fuzzy transformation method in the substation protection method was used to investigate the reliability [41].

The work done in this article is arranged into eight sections. Related definitions, the part of this research work is given in Section two. The mathematical formulation of decomposed fuzzy numbers is presented in Section three. Section four describes the mathematical formulation of equivalent transition rate in terms of possibility. Possibility measure and necessity measure are used as the lower and upper range of failure/repair rate for the possible interval of uncertainty and formulation is given in Sect. 5. We described the algorithm for the availability and reliability estimation using the possibilistic approach for failure/repair rate estimation. In Sect. 6, the diagram of the substation automation system with reliability block diagram is given and Sect. 7 presents the numerical computation and interpretation of the results are discussed. Section 8 contains the conclusion of the work done in this article.

2 Basic Definitions

2.1 Fuzzy Set

A fuzzy set $\tilde{A}$ subset of a universal set U is important due to its membership function. Fuzzy set deals with the help of its membership function, which maps every member of the universal set into the unit interval [0,1]. Mathematically, a fuzzy set can be

written as

$$\tilde{A} = \{(x, \mu_{\tilde{A}}(x)) : x \in U\}$$

and membership function is given as

$\mu_{\tilde{A}}(x) : U \rightarrow [0, 1]$.

2.2 Reliability

Reliability $R(t)$ of a product or a system is the measure of its life without failure from the goal for which it is developed/invented. Such a system, which gives satisfactory performance for a specified time t with some already fix conditions, is said to be reliable and this property is called reliability or probability of successful operation. Mathematically, it can be written as

$$R(t) = \Pr\{T > t\} = \int_t^{\infty} f(x)dx$$

And $f(x)$ is the probability density function.

2.3 Availability

Availability $A(t)$ is the function of time. It describes the behaviour of the system or equipment. Availability is also known as the probability of the system that it is performing at time t on its availability during operation. Failure rate and repair rate are the main factors affecting it. The long-term availability for a single component given by the relation

$$A(t) = A(\infty) = \frac{\mu}{\mu + \lambda}$$

where μ and λ are the repair rate and failure rate of the system, respectively.

3 Decomposed Fuzzy Number

In this method, a fuzzy number is divided into α-cuts. The concept of decomposed fuzzy number [39] is based on the decomposition theorem for regular, one-dimensional fuzzy sets and says that each fuzzy set $\tilde{A}$ can uniquely be expressed by its sequence of $cut_\alpha\left(\tilde{A}\right)$ as given below.

$$\mu_{\tilde{A}}(x) = sup_{\alpha\in[0,1]}\alpha\mu_{cut_\alpha\tilde{A}}(x)$$

where $\mu_{\tilde{A}}(x)$ is the membership function and for a fuzzy number $\tilde{t}$ it can be written as;

$$\mu_{\tilde{t}}(x) = sup_{\alpha\in[0,1]}\alpha\mu_{cut_\alpha\tilde{t}}(x)$$

3.1 Methodology

For its procedural aspect, we divide the interval [0, 1] (membership axis) into r intervals of length.

$\Delta\mu = \frac{1}{r}$,

And $\mu_k = \frac{k}{r}, k = 0, 1, \ldots .r$

With the condition $\mu_0 = 0, \mu_r = 1$,

$\mu_{k+1} = \mu_k + \Delta\mu, k = 0, 1, \ldots .r - 1$.

And r is called the decomposition number, which defines the degree of refinement of decomposition. Fuzzy number $\tilde{t}$ in its decomposed form can be written as

$$D = \left\{Y^{(0)}, Y^{(1)} \ldots Y^{(r)}\right\}$$

where $Y^{(k)} = \left[a^{(k)}, b^{(k)}\right] = cut_\mu\left(\tilde{t}\right), a^{(k)} \leq b^{(k)}, k = 0, 1, \ldots .r$.

Let a triangular fuzzy number $\tilde{t}$ be decomposed into $r = K$ intervals as shown in Fig. 1. It means the membership axis has K intervals and another axis represents the failure rate or repair rate of a system. Then corresponding to these intervals, we get nested intervals for failure/repair rate and in such conditions, it is convenient to use possibility theory.

Here $Y^{(0)}, Y^{(1)}, Y^{(2)}, Y^{(3)}$ and $Y^{(4)} \in \tilde{t}$ are the nested intervals.

Focal elements or α—cuts for this triangular fuzzy number can be written as

$$Y^{(0)} = \{F\} = [F]$$

$$Y^{(1)} = \{E, F, G\} = [E, G]$$

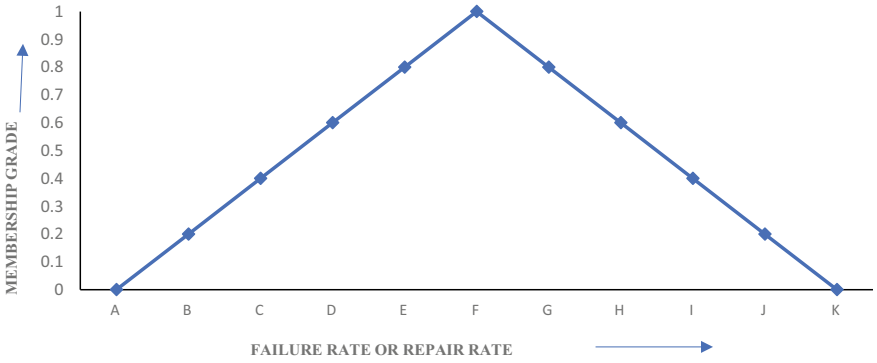

Fig. 1 Triangular fuzzy number

$$Y^{(2)} = \{D, E, F, G, H\} = [D, H]$$

$$Y^{(3)} = \{C, D, E, F, G, H, I\} = [C, I]$$

$$Y^{(4)} = \{B, C, D, E, F, G, H, I, J\} = [B, J]$$

And membership function for the above figure is as follows

$$\mu_{\tilde{t}}(x) = \begin{cases} \frac{x-A}{F-A} \; A < x \leq F \\ \frac{K-x}{K-F} \; F \leq x < K \\ 0 \; x \leq A, x \geq K \end{cases}$$

To find the possibility measure and necessity measure, the membership grades will be used corresponding to $\{A, B, \ldots, J, K\}$, which is used for failure/repair rate values and let grades be given by $\{x_0, x_1, \ldots\ldots\ldots\ldots x_9, x_{10}\}$.

Now the possibility measure is calculated as follows:

$$poss(Y^{(0)}) = max\{x_5\}$$

$$poss(Y^{(1)}) = \max\{x_4, x_5, x_6\}$$

$$poss(Y^{(2)}) = \max\{x_3, x_4, x_5, x_6, x_7\}$$

$$poss(Y^{(3)}) = \max\{x_2, x_3, x_4, x_5, x_6, x_7, x_8\}$$

$$poss(Y^{(4)}) = \max\{x_1, x_2, x_3, x_4, x_5, x_6, x_7, x_8, x_9\}$$

Now, let the compliment of above possibility measures be given by $poss(\overline{Y}^{(0)})$, $poss(\overline{Y}^{(1)})$, $poss(\overline{Y}^{(2)})$, $poss(\overline{Y}^{(3)})$and, $poss(\overline{Y}^{(4)})$.

$$poss\left(\overline{Y}^{(0)}\right) = \max\{x_0, x_1, x_2, x_3, x_4, x_6, x_7, x_8, x_9, x_{10}\}$$

$$poss(\overline{Y}^{(1)}) = \max\{x_0, x_1, x_2, x_3, x_7, x_8, x_9, x_{10}\}$$

$$poss(\overline{Y}^{(2)}) = \max\{x_0, x_1, x_2, x_8, x_9, x_{10}\}$$

$$poss(\overline{Y}^{(3)}) = \max\{x_0, x_1, x_9, x_{10}\}$$

$$poss(\overline{Y}^{(4)}) = \max\{x_0, x_{10}\}$$

Now, we need to evaluate the necessity measure using the relation as follows:
$nec(Y^{(0)}) = 1 - poss(\overline{Y}^{(0)})$
$nec(Y^{(1)}) = 1 - poss(\overline{Y}^{(1)})$
$nec(Y^{(2)}) = 1 - poss(\overline{Y}^{(2)})$
$nec(Y^{(3)}) = 1 - poss\left(\overline{Y}^{(3)}\right)$
$nec(Y^{(4)}) = 1 - poss\left(\overline{Y}^{(4)}\right)$

4 Mathematical Formulation for Fuzzy Reliability and Availability

The mathematical formulation of reliability and availability is discussed in this section.

4.1 Equivalent Transition Rate

It is assumed that components are independent and components of the same type have the same reliability. Failure rate and repair rate are considered fuzzy. A system having N components connected in series, then failure rate, repair rate, and possibility of successful operation is given as [21]

$$\lambda_{ETFR}^{poss} = \lambda_1 + \lambda_2 + \ldots\ldots\ldots\lambda_N,$$

$$\mu_{ETRR}^{poss} = \frac{\mu_1\mu_2 \ldots\ldots\ldots \mu_N(\lambda_1 + \lambda_2 + \ldots\ldots\ldots \lambda_N)}{(\mu_1 + \lambda_1) \ldots\ldots\ldots (\mu_N + \lambda_N) - \mu_1\mu_2 \ldots\ldots\ldots \mu_N}$$

$$Poss_S = \frac{\mu_1\mu_2 \ldots\ldots\ldots \mu_N}{(\mu_1 + \lambda_1) \ldots\ldots\ldots (\mu_N + \lambda_N)}$$

And for parallel connection it can be given as

$$\mu_{ETRR}^{poss} = \mu_1 + \mu_2 + \ldots\ldots\ldots C_N$$

$$\lambda_{ETFR}^{poss} = \frac{\lambda_1\lambda_2 \ldots\ldots\ldots \lambda_N(\mu_1 + \mu_2 + \ldots\ldots\ldots \mu_N)}{(\mu_1 + \lambda_1) \ldots\ldots\ldots (\mu_N + \lambda_N) - \lambda_1\lambda_2 \ldots\ldots\ldots \lambda_N}$$

$$Poss_S = 1 - \frac{\lambda_1\lambda_2 \ldots\ldots\ldots \lambda_N}{(\mu_1 + \lambda_1) \ldots\ldots\ldots (\mu_N + \lambda_N)}$$

4.2 Fuzzy Reliability

In this research work, the failure rate data fetched is exponentially distributed. Then the possibilistic reliability of the substation automated system is given by the relation $poss^L = e^{-\lambda^U t}$ and $poss^U = e^{-\lambda^L t}$.

5 Proposed Algorithm for the Automated System

Step1: First of all, failure/repair rate data is collected and then fuzzified into triangular fuzzy numbers. This value of failure/repair rate is taken to each component of the SAS system.

Step 2: The triangular fuzzy numbers obtained in step first of each component are decomposed by dividing the μ axis into $r = K$ intervals of equal length, $K = 1, 2, \ldots . N$.

Step 3: After decomposing the μ axis, we have $K + 1$ points, corresponding to these points (membership grades), we get the interval range for failure/repair rate.

Step 4: The interval ranges of each component obtained in step 3 are used as nested intervals for each $\alpha-$cuts and it is suitable to apply a possibilistic approach at this step.

Step 5: Possibility and necessity measures are calculated from the information provided in the previous step.

Step 6: Taking the mean value of the both of the measures (in the form of membership) of step 5, we again get interval ranges for each of the component

for failure/repair rate and this range presents the lower range (L) and upper range (U) for every individual rate.

Step 7:L and U ranges of failure/repair rates are used to get an equivalent transition rate for steady-state availability (possibility of successfully operating the system) of the SAS system (subsystem).

Step 8:Thus, the possibility of successfully working (availability) is obtained.

Step 9:Posfust reliability of the whole system is investigated according to the arrangement of the system's components using an exponential distribution.

6 Diagram of Automated System

Various components used in our diagram of a substation automated system and that are connected in a certain manner are presented in Fig. 2. The arrangement of components is a matter of interest and it is important to get better reliable systems.

Notations used for components of the automation substation system are given below.

BCU	Bay control unit
DCP	DC Power
EI	Ethernet interface
IPC	Industrial personal computer

(continued)

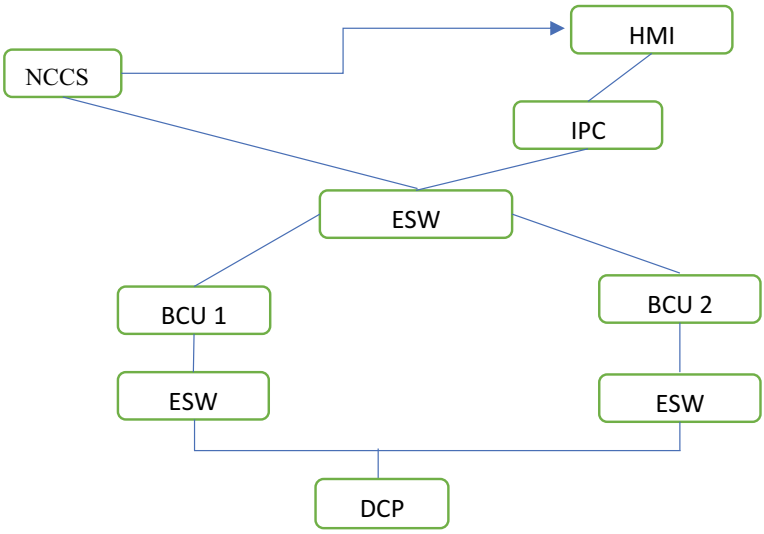

Fig. 2 Arrangement of the components of a substation automation system

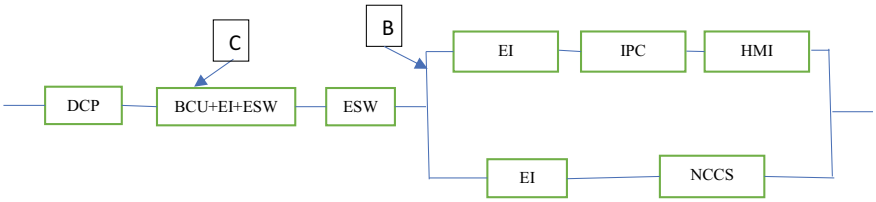

Fig. 3 Reliability block diagram for the structure of substation automation system

(continued)

BCU	Bay control unit
NCCS	Network control centre server
EWS	Ethernet switch
HMI	Human–machine interface

The reliability block diagram of the substation automation system is given in Fig. 3. Reliability evaluation is based on the minimal path set method of this block diagram.

7 Numerical Computations

The numerical data used in the proposed work is given in Table 1, which is showing the failure/repair rates of various components of the automation system [21].

Table 1 Failure rate and repair rate of system components

Name of component	Failure rate per year	Repair rate per year
BCU	0.00966	52.14
DCP	0.00912	52.14
EI	0.00333	182.5
IPC	0.06993	52.14
NCCS	0.06993	52.14
EWS	0.08696	52.14
HMI	0.1	52.14

7.1 Failure/Repair Rate Estimation

A triangular fuzzy number for the component DCP is presented in Fig. 4 for failure rate and for repair rate in Fig. 5 using the data from Table 1.

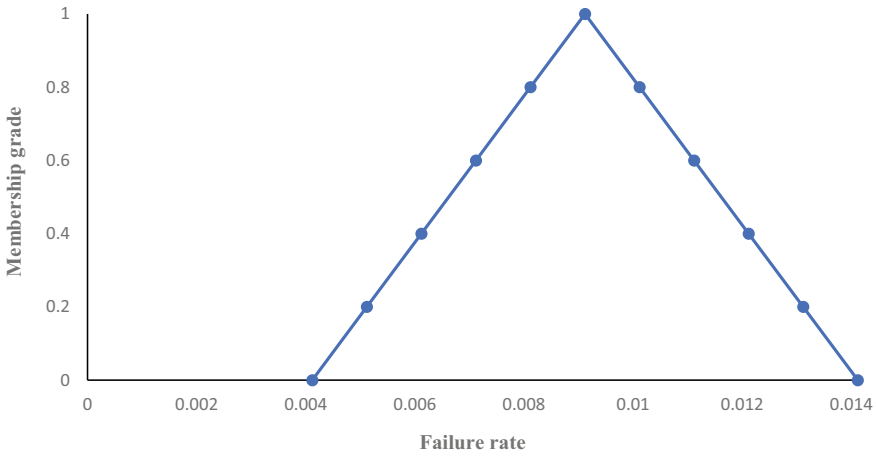

Fig. 4 Presentation of fuzzy failure rate for DCP

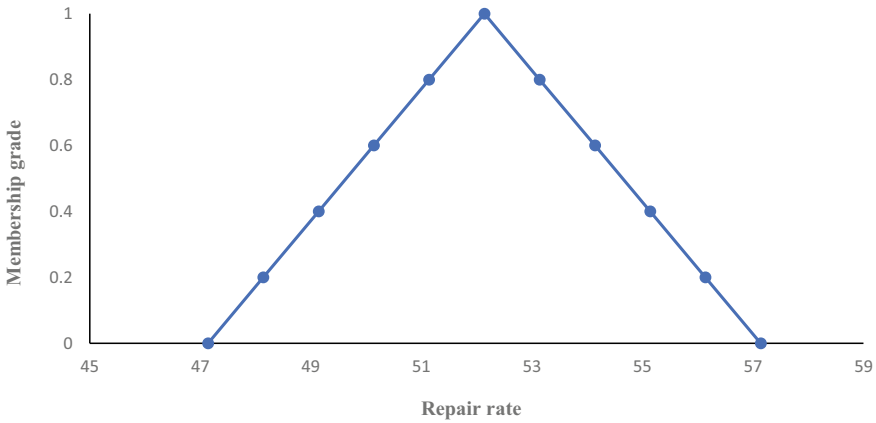

Fig. 5 Presentation of fuzzy repair rate for DCP

7.2 Evaluation of Possibility Measure and Necessity Measure

To decompose the triangular fuzzy number, $r = 5$ is taken and it results in five intervals of equal length ($1/5 = 0.2$) of the membership axis.

For the failure rate of the component DCP,

$$poss(Y^{(0)}) = 1$$

$$poss(Y^{(1)}) = 1$$

$$poss(Y^{(2)}) = 1$$

$$poss(Y^{(3)}) = 1$$

$$poss(Y^{(4)}) = 1$$

Compliments are given as

$$poss(\overline{Y}^{(0)}) = 4/5$$

$$poss(\overline{Y}^{(1)}) = 3/5$$

$$poss(\overline{Y}^{(2)}) = 2/5$$

$$poss(\overline{Y}^{(3)}) = 1/5$$

$$poss(\overline{Y}^{(4)}) = 0$$

Now, necessity measure is calculated as

$nec(Y^{(0)}) = 1 - poss(\overline{Y}^{(0)}) = 1/5$

$nec(Y^{(1)}) = 1 - poss(\overline{Y}^{(1)}) = 2/5$

$nec(Y^{(2)}) = 1 - poss(\overline{Y}^{(2)}) = 3/5$

$nec(Y^{(3)}) = 1 - poss\left(\overline{Y}^{(3)}\right) = 4/5$

To combine the possibility measure and necessity measure, the following expression is used.

The possible range of failure rate

$$= \frac{Max\{poss(Y^{(0)}), poss(Y^{(1)}), poss(Y^{(2)}), poss(Y^{(3)}), poss(Y^{(4)})\} + Min\{nec(Y^0), nec(Y^1), nec(Y^2), nec(Y^3), nec(Y^4)\}}{2}$$

Table 2 Presenting the interval for failure rate and repair rate

Name of the component	Interval for failure rate	Interval for repair rate
BCU	(0.00766,0.01766)	(50.14,60.14)
DCP	(0.00712,0.001712)	(50.14,60.14)
EI	(0.00233,0.00733)	(180.5,190.5)
IPC	(0.04996,0.14996)	(50.14,60.14)
NCCS	(0.04996,0.14996)	(50.14,60.14)
EWS	(0.06696,0.16696)	(50.14,60.14)
HMI	(0.08,0.18)	(50.14,60.14)

$$= \frac{1+0.2}{2} = 0.6$$

Corresponding to the value of membership, we get an interval of the possibility of failure of the system. The possible interval of failure rate is (0.00712, 0.001712). Similarly, the possible interval of repair rate is (50.14, 60.14). The possible range of components of the system is given in Table 2.

Block B is divided into two blocks B_1 and B_2. Block B_1 contains the components EI, IPC and HMI while B_2 contains EI and NCCS. Failure rate estimation for series components B_1

$$\lambda_{B_1}^L = \lambda_{EI}^L + \lambda_{IPC}^L + \lambda_{HMI}^L = 0.00233 + 0.04993 + 0.08 = 0.13226$$

and

$$\lambda_{B_1}^U = \lambda_{EI}^U + \lambda_{IPC}^U + \lambda_{HMI}^U = 0.00733 + 0.14993 + 0.18 = 0.40323$$

Repair rate estimation for series components B_1

$$\mu_{B1}^L = \frac{\mu_{EI}^L \mu_{IPC}^L \mu_{HMI}^L \left(\lambda_{EI}^L + \lambda_{IPC}^L + \lambda_{HMI}^L\right)}{\left(\lambda_{EI}^L + \mu_{EI}^L\right)\left(\lambda_{IPC}^L + \mu_{IPC}^L\right)\left(\lambda_{HMI}^L + \mu_{HMI}^L\right) - \mu_{EI}^L \mu_{IPC}^L \mu_{HMI}^L} = 50.7694$$

$$\mu_{B1}^U = \frac{\mu_{EI}^U \mu_{IPC}^U \mu_{HMI}^U \left(\lambda_{EI}^U + \lambda_{IPC}^U + \lambda_{HMI}^U\right)}{\left(\lambda_{EI}^U + \mu_{EI}^U\right)\left(\lambda_{IPC}^U + \mu_{IPC}^U\right)\left(\lambda_{HMI}^U + \mu_{HMI}^U\right) - \mu_{EI}^U \mu_{IPC}^U \mu_{HMI}^U} = 54.2315$$

Failure rate for B_2

$$\lambda_{B_2}^L = \lambda_{EI}^L + \lambda_{NCCS}^L = 0.00233 + 0.04993 = 0.05226$$

$$\lambda_{B_2}^U = \lambda_{EI}^U + \lambda_{NCCS}^U = 0.15726$$

Repair rate for B_2

$$\mu_{B2}^{L} = \frac{\mu_{EI}^{L}\mu_{NCCS}^{L}\left(\lambda_{EI}^{L} + \lambda_{NCCS}^{L}\right)}{\left(\lambda_{EI}^{L} + \mu_{EI}^{L}\right)\left(\lambda_{NCCS}^{L} + \mu_{INCCS}^{L}\right) - \mu_{EI}^{L}\mu_{NCCS}^{L}} = 51.9019$$

$$\mu_{B2}^{U} = \frac{\mu_{EI}^{U}\mu_{NCCS}^{U}\left(\lambda_{EI}^{U} + \lambda_{NCCS}^{U}\right)}{\left(\lambda_{EI}^{U} + \mu_{EI}^{U}\right)\left(\lambda_{NCCS}^{U} + \mu_{NCCS}^{U}\right) - \mu_{EI}^{U}\mu_{NCCS}^{U}} = 62.1353$$

Failure rate for C

$$\lambda_{C}^{L} = 2\left(\lambda_{BCU}^{L} + \lambda_{EI}^{L} + \lambda_{ESW}^{L}\right) = 2(0.00766 + 0.00233 + 0.06696) = 0.1539$$

$$\lambda_{C}^{U} = 2\left(\lambda_{BCU}^{U} + \lambda_{EI}^{U} + \lambda_{ESW}^{U}\right) = 2(0.01766 + 0.00733 + 0.16696) = 0.51584$$

Repair rate for C

$$\mu_{C}^{L} = \frac{\left(\mu_{BCU}^{L}\right)^{2}\left(\mu_{EI}^{L}\right)^{2}\left(\mu_{ESW}^{L}\right)^{2}2\left(\lambda_{BCU}^{L} + \lambda_{EI}^{L} + \lambda_{ESW}^{L}\right)}{\left(\lambda_{BCU}^{L} + \mu_{BCU}^{L}\right)^{2}\left(\lambda_{EI}^{L} + \mu_{EI}^{L}\right)^{2}\left(\lambda_{ESW}^{L} + \mu_{ESW}^{L}\right)^{2} - \left(\mu_{BCU}^{L}\right)^{2}\left(\mu_{EI}^{L}\right)^{2}\left(\mu_{ESW}^{L}\right)^{2}} = 51.2141$$

$$\mu_{C}^{U} = \frac{\left(\mu_{BCU}^{U}\right)^{2}\left(\mu_{EI}^{U}\right)^{2}\left(\mu_{ESW}^{U}\right)^{2}2\left(\lambda_{BCU}^{U} + \lambda_{EI}^{U} + \lambda_{ESW}^{U}\right)}{\left(\lambda_{BCU}^{U} + \mu_{BCU}^{U}\right)^{2}\left(\lambda_{EI}^{U} + \mu_{EI}^{U}\right)^{2}\left(\lambda_{ESW}^{U} + \mu_{ESW}^{U}\right)^{2} - \left(\mu_{BCU}^{U}\right)^{2}\left(\mu_{EI}^{U}\right)^{2}\left(\mu_{ESW}^{U}\right)^{2}} = 82.8348$$

Failure for B

$$\lambda_{B}^{L} = \frac{\lambda_{B_1}^{L}\lambda_{B_2}^{L}\left(\mu_{B1}^{L} + \mu_{B2}^{L}\right)}{\left(\lambda_{B_1}^{L} + \mu_{B1}^{L}\right)\left(\lambda_{B_2}^{L} + \mu_{B2}^{L}\right) - \lambda_{B_1}^{L}\lambda_{B_2}^{L}} = 0.0002683$$

$$\lambda_{B}^{U} = \frac{\lambda_{B_1}^{U}\lambda_{B_2}^{U}\left(\mu_{B1}^{U} + \mu_{B2}^{U}\right)}{\left(\lambda_{B_1}^{U} + \mu_{B1}^{U}\right)\left(\lambda_{B_2}^{U} + \mu_{B2}^{U}\right) - \lambda_{B_1}^{U}\lambda_{B_2}^{U}} = 0.002168$$

Repair rate for B

$$\mu_{B}^{L} = \mu_{B1}^{L} + \mu_{B2}^{L} = 102.6713$$

$$\mu_{B}^{U} = \mu_{B1}^{U} + \mu_{B2}^{U} = 116.3668$$

Now the possibility of successful operation of the entire system

$$Poss_{S}^{U} = \frac{\mu_{DCP}^{L}\mu_{C}^{L}\mu_{ESW}^{L}\mu_{B}^{L}}{\left(\lambda_{DCP}^{L} + \mu_{DCP}^{L}\right)(\lambda_{C}^{L} + \mu_{C}^{L})(\lambda_{ESW+}^{L}\mu_{ESW}^{L})(\lambda_{B}^{L} + \mu_{B}^{L})} = 0.9908$$

Table 3 Presenting the lower range R^L and upper range R^U offuzzyreliability

Time (years)	R^L	R^U
0	1	1
1	0.8601	0.8867
2	0.6858	0.7654
3	0.5287	0.6485
4	0.409	0.5366
5	0.3094	0.4452
6	0.2258	0.3521
7	0.1669	0.2541
8	0.1136	0.1758
9	0.0925	0.1154
10	0.0726	0.0713

$$Poss_S{}^L = \frac{\mu_{DCP}^U \mu_C^U \mu_{ESW}^U \mu_B^U}{\left(\lambda_{DCP}^U + \mu_{DCP}^U\right)(\lambda_C^U + \mu_C^U)(\lambda_{ESW+}^U \mu_{ESW}^U)(\lambda_B^U + \mu_B^U)} = 0.9955$$

Possible interval of availability is (0.9908, 0.9955) while the probabilistic value is 0.9944.

7.3 Calculation and Interpretation of Fuzzy Reliability

The fuzzy reliability of the automation system has been calculated using the reliability block diagram of Fig. 3 based on the minimal path set approach and obtained numerical values are given in Table 3.

$$R = P_{DCP} P_{BCU}^2 P_{ESW}^3 P_{EI}^3 \{P_{IPC} P_{HMI}(1 - P_{EI} P_{NCCS}) + P_{NCCS}\}$$

8 Conclusion

In this scientific edge, man has developed many devices that can control the power systems at fingertips. The automation system is an advanced step in this direction, it has taken the place of human functioning like decision-making, physical action, and observations. In this research work, we have focused on availability and fuzzy reliability. A flexible approach, equivalent transition rate of the Markov process is applied in this work. Interval-valued approach sufficiently covers the uncertainty present in the data. So, a possibilistic way is used to handle uncertainty with the

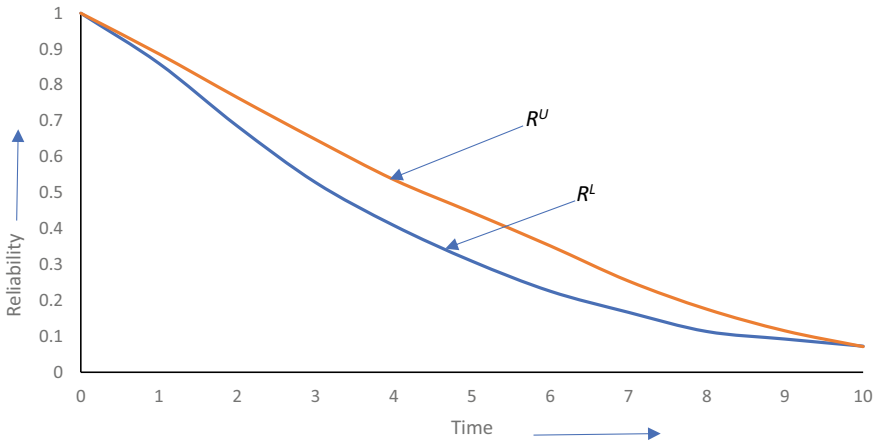

Fig. 6 Showing the variation in the results of fuzzy reliability

help of possibility measure and necessity measure. The upper and lower range of the fuzzy reliability is observed by performing necessary numerical calculations. The difference between the fuzzy reliability and classical reliability can be clearly seen in Fig. 6, which shows that this proposed technique is proving its ability over the classical methods. So, we can say that this method is dominating other methods. With the help of this method, it is easy to detect the range of accuracy of results.

9 Data Availability Statement

We are sharing the source that includes the data that support the findings of our results and the conclusion of the manuscripts. The technique which we have given can be verified on the data, which is available on the following hyperlinks:

https://ieeexplore.ieee.org/document/6175975

http://www.dl.edi-info.ir/Composite%20automated%20distribution%20system%20reliability%20model%20considering.pdf

Acknowledgements The second author extends his thanks to CSIR, India, for economical support.

Funding The work has been carried out under the government order number -47/2021/606/sattar-4-2021-4(56)/2020 and the financial support from the University Grants Commission (UGC-India).

References

1. Lloyd DK, Lipow M (1952) Reliability, management and mathematics. Prentice-Hall, Englewood Cliffs
2. Bazovsky I (1961) Reliability theory and practice. Prentice-Hall, Englewood Cliffs
3. Roberts NH (1964) Mathematical methods in reliability engineering. McGraw-Hill, New York
4. Dhillon BS (1981) Human reliability with human factors. Proc Press Inc, New York
5. Gnedenko B, Ushakov I (1995) Probabilistic reliability engineering. Wiley, NY, Chichester, Brisbane
6. Zadeh LA (1965) Fuzzy sets. Inf Control 8(3):338–353
7. Zimmermann HJ (1991) Fuzzy set theory and its application. Kluwer Academic Publishers, Dordrecht
8. Zadeh LA (1995) Fuzzy sets and fuzzy logic, theory and applications. Prentice hall PTR
9. Atanassov K (1986) Intuitionistic fuzzy sets. Fuzzy Sets Syst 20(1):87–96
10. Singer D (1990) A fuzzy set approach to fault tree and reliability analysis. Fuzzy Sets Syst 34:145–155
11. Cai KY (1996) Introduction to fuzzy reliability. Kluwer Academic Publishers, Dordrecht
12. Zadeh LA (1978) Fuzzy sets as a basis for a theory of Possibility. Fuzzy Sets Syst 1:3–28
13. Inuiguchi M, Kume Y (1992) Fuzzy reasoning based on uncertainty generation rules using necessity measures. Jpn J Fuzzy Theory Syst 4(3):329–344
14. Dubois D, Prade H (1991) Fuzzy sets in approximate reasoning, part 1: inference with possibility distributions. Fuzzy Sets Syst 40:143–202
15. Pandey D, Tyagi SK (2007) Profust reliability of a gracefully degradable system. Fuzzy Sets Syst 158:794–803
16. Chen T, Mesiar R (2017) Jun Lia and Andrea, possibility and necessity measures and integral equivalence. Int J Appro Reason 86:62–72
17. Lee B et al (2015) Role-based access control for substation automation systems using *XACML*. Info Syst 53:237–249
18. Lei H, Singh C (2015) Power system reliability evaluation considering cybermall functions in substations. Electr Power Syst Res 129:160–169
19. Verma M et al (2013) Application of non-normal p-norm trapezoidal fuzzy number in reliability evaluation of electrical substations. Neural Comput Appl 23(2):531–539
20. Hajian-Hoseinabadi H et al (2014) Composite automated distribution system reliability model considering various automated substations. Int J Electr Power Energy Syst 54:211–220
21. Hajian-Hoseinabadi H, Hamedani Golshan ME (2012) Availability, reliability and component importance evaluation of various repairable substation automation systems. IEEE Trans Power Del 27(3):1358–1367
22. Hajian-Hoseinabadi H (2011) Impacts of automated control systems on substation reliability. IEEE Trans Power Del 26(3):1681–1691
23. Tanrioven M et al (2004) A new approach to real-time reliability analysis of transmission system using fuzzy Markov model. Int J Electr Power Energy Syst 26(10):821–832
24. Ge H, Asgarpoor S (2010) Reliability evaluation of equipment and substations with fuzzy Markov processes. IEEE Trans Power Syst 25(3):1319–1328
25. Anderson PM (1999) Power system protection. Wiley – IEEE Press, New York
26. Lisnianski A, Frenkel I (2012) Recent advances in system reliability. Springer
27. Rubino G, Sericola B (2014) Markov chains and dependability theory. Cambridge University Press
28. Marshall AW, Olkin I (2007) Life distributions; structure of non-parametric, semiparametric and parametric families. Springer
29. Li G et al (2015) A fuzzy reliability approach for structures based on probability perspective. Struct Safety 54:10–18
30. Gonzalez D et al (2014) Fuzzy reliability analysis with only censored data. Eng Appl Artif Intel 32:151–159

31. Aminifar F et al (2010) Reliability modeling of PMUs using fuzzy sets. IEEE Trans Power Del 25(4):2384–2391
32. Ge H, Asgarpoor S (2011) Reliability and maintainability improvement of substations with aging infrastructure. IEEE Trans Power Del 27(4):1868–1876
33. Canizes B et al (2012) Hybrid fuzzy Monte Carlo technique for reliability assessment in transmission power systems. Energy 45(1):1007–1017
34. Chandna R, Ram M (2014) Fuzzy reliability modelling in the system failure rates merit context. Int J Syst Assur Eng Manage 5(3):245–251
35. Purba JH et al (2014) A fuzzy reliability assessment of basic events of fault trees through qualitative data processing. Fuzzy Sets Syst 243:250–269
36. Bai X, Asgaroor S (2004) Fuzzy based approaches to substation reliability evaluation. Electr Power Syst Res 69:197–204
37. El-Hawary ME (1998) Electric power application of fuzzy systems. Wiley IEEE Press, New York
38. Hanss M (2005) Applied fuzzy arithmetic an introduction with engineering applications. Springer, Berlin
39. Mordeson JN, Nair PS (2001) Fuzzy mathematics: an introduction for engineers and scientist. Springer, New York
40. Walz NP, Hanss M (2013) Fuzzy arithmetical analysis of multibody systems with uncertainties. Arch Mech Eng
41. Aghili SJ, Hajian-Hoseinabadi H (2014) The reliability investigation considering data uncertainty; an application of fuzzy transformation method in substation protection. Int J Electr Power Energy Syst 63:988–999

Solution of Fingering Phenomenon Arising in Porous Media in Horizontal Direction by Combination of Elzaki Transform and Adomian Decomposition Method

Archana Varsoliwala and Twinkle Singh

Abstract The concerned paper discusses the solution of fingering phenomenon occurring in fluid flow through porous media in horizontal direction. Nowadays, majority of oil firms focus on maximizing the recovery factor from their oil fields. Therefore, this concept has a very important role in oil recovery process. Mathematical structure of the fingering phenomenon has been derived and it is given by non-linear partial differential equation (NPDE). Elzaki Adomian Decomposition Method (EADM) can be used to obtain the solution for the considered model along with its convergence analysis. EADM gives the solution in a convergent series without any linearization or perturbation. Comparisons are built between the results obtained by EADM and Variational Iteration Method (VIM) to examine the accuracy of the proposed method. Numerical and graphical presentations are derived by MATHEMATICA and MATLAB.

Keywords Fingering phenomenon · Homogeneous porous media · Elzaki Adomian decomposition method

1 Introduction

The displacement of single fluid by another immiscible fluid in porous medium is known as imbibitions and this development plays a crucial role in several engineering fields like soil mechanics, agriculture engineering, water, geophysical science, etc. However, the particular interest of this paper is connected with oil recovery. The practice of oil extraction is done traditionally by primary and secondary method. The method of extracting oil via the natural rise of hydrocarbons to the surface of the world or via pump jacks and different artificial lift devices is known as primary oil recovery. A recovery of 5–15% of the well's potential is possible through primary

A. Varsoliwala (✉) · T. Singh
Applied Mathematics and Humanities Department, Sardar Vallabhbhai National Institute of Technology, Gujarat 395 007, India
e-mail: archanavarsoliwala@gmail.com

J. Singh et al. (eds.), *Advances in Mathematical Modelling, Applied Analysis and Computation*, Lecture Notes in Networks and Systems 415,
https://doi.org/10.1007/978-981-19-0179-9_29

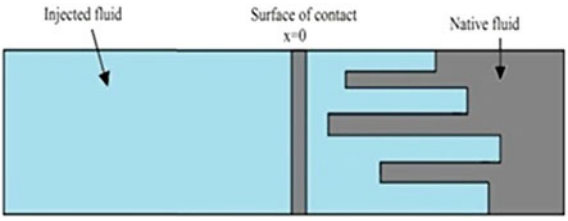

Fig. 1 Representation of fingering phenomenon

method. The injection of gas or water which can transfer the oil and compel it to move from its resting place and produce it to the surface is possible through secondary oil recovery. During the secondary oil recovery if a fluid (oil) contained in a porous matrix of an oil formatted region in an oil reservoir is displaced by another fluid of lesser consistency, i.e., water, rather than regular displacement of the full front, protuberances (fingers) may occur that shoot through the porous medium at fair speed. Such protuberances are called fingers. This phenomenon is called fingering [14]. In petroleum technology, oil production is the main significance of this phenomenon.
The present paper expresses the fingering phenomenon. In the statistical processing of fingers as depicted in Fig. 1, only the mean behavior of the two fluids is considered. The main aim is to find fluid's saturation (S_w). Therefore, the saturation of the displacement fluid in porous medium represents the average cross-sectional area occupied by fingers. In present work, some assumptions are taken as there are maximum size distribution and penetration length of fingers. This kind of occurrence has been considered by various researchers with various techniques and different perspectives [11, 12, 15, 22]. The external sources and sink in the mass conservation equations have been ignored by above researchers. Recently, many researchers have also worked on different kinds of fractional differential equations to study the behavior of various mathematical models [2–6, 17, 18].
The primary goal of this paper is to apply Elzaki Adomian decomposition method [23] to the considered model. Elzaki transform [8] is well known for solving various equations [1, 7, 10, 19–21].

2 Mathematical Structure

In the mathematical structure of fingering phenomenon, here we assumed that uniform injection of oil-saturated homogeneous and isotropic media with good finger flow. By Darcy's law, the seepage velocities of water and oil are given by

$$V_w = -\frac{k_w}{\mu_w} K \left(\frac{\partial P_w}{\partial x} \right), \tag{1}$$

$$V_n = -\frac{k_n}{\mu_n} K \left(\frac{\partial P_n}{\partial x} \right), \tag{2}$$

where the permeability is given by K; k_n and k_w are the relative permeabilities of oil and water, respectively; the pressure of oil and water are given by P_n and P_w, respectively; and viscosity of oil and water are μ_n and μ_w, respectively.

Continuity equations of two phases are given as [11]

$$\frac{\partial (m\rho_w S_w)}{\partial t} + \frac{\partial (\rho_w V_w)}{\partial x} = 0, \tag{3}$$

$$\frac{\partial (m\rho_n S_n)}{\partial t} + \frac{\partial (\rho_n V_n)}{\partial x} = 0. \tag{4}$$

The porosity m will be constant because medium is homogeneous. S_n and S_w are saturation of oil and water, respectively. Also we assumed that two fluids are not compressible. Therefore, densities of both the fluids are constants.
From Eqs. (3) and (4),

$$m\frac{\partial S_w}{\partial t} + \frac{\partial V_w}{\partial x} = 0, \tag{5}$$

$$m\frac{\partial S_n}{\partial t} + \frac{\partial V_n}{\partial x} = 0, \tag{6}$$

By the phase saturation concept,

$$S_w + S_n = 1. \tag{7}$$

Capillary pressure P_C is obtained as the pressure discontinuity between the flowing phase yields

$$P_C = P_n - P_w. \tag{8}$$

The connection between P_C and S_w is given by [13]

$$P_C = -\beta S_w, \tag{9}$$

β is constant and negative sign represents the direction of capillary pressure P_C opposite to S_w [16].

$$k_w = S_w \tag{10}$$

and

$$k_n = S_n = 1 - S_w. \tag{11}$$

Substituting Eqs. (1) and (2) into Eqs. (5) and (6), respectively.

$$m\frac{\partial S_w}{\partial t} = \frac{\partial}{\partial x}\left[K\frac{k_w}{\mu_w}\left(\frac{\partial P_w}{\partial x}\right)\right], \tag{12}$$

$$m\frac{\partial S_n}{\partial t} = \frac{\partial}{\partial x}\left[K\frac{k_n}{\mu_n}\left(\frac{\partial P_n}{\partial x}\right)\right], \tag{13}$$

Now, eliminate $\frac{\partial P_w}{\partial x}$ from Eqs. (8) and (12),

$$m\frac{\partial S_w}{\partial t} = \frac{\partial}{\partial x}\left[K\frac{k_w}{\mu_w}\left(\frac{\partial P_n}{\partial x} - \frac{\partial P_C}{\partial x}\right)\right]. \tag{14}$$

Merging both Eqs. (13) and (14) and then using Eq. (7),

$$0 = \frac{\partial}{\partial x}\left[\left(K\frac{k_w}{\mu_w} + K\frac{k_n}{\mu_n}\right)\frac{\partial P_n}{\partial x} - K\frac{k_w}{\mu_w}\frac{\partial P_C}{\partial x}\right]. \tag{15}$$

Integrate Eq. (15) w.r.t x ,

$$A = \left(K\frac{k_w}{\mu_w} + K\frac{k_n}{\mu_n}\right)\frac{\partial P_n}{\partial x} - K\frac{k_w}{\mu_w}\frac{\partial P_C}{\partial x}, \tag{16}$$

(A is a constant).
Simplifying Eq. (16), we have

$$\frac{\partial P_n}{\partial x} = \frac{A}{\left(K\frac{k_w}{\mu_w} + K\frac{k_n}{\mu_n}\right)} + \frac{K\frac{k_w}{\mu_w}}{\left(K\frac{k_w}{\mu_w} + K\frac{k_n}{\mu_n}\right)}\frac{\partial P_C}{\partial x}. \tag{17}$$

Substituting the value of $\frac{\partial P_n}{\partial x}$ in Eq. (14)

$$m\frac{\partial S_w}{\partial t} = \frac{\partial}{\partial x}\left[K\frac{k_w}{\mu_w}\left(\frac{A}{\left(K\frac{k_w}{\mu_w} + K\frac{k_n}{\mu_n}\right)} + \frac{K\frac{k_w}{\mu_w}}{\left(K\frac{k_w}{\mu_w} + K\frac{k_n}{\mu_n}\right)}\frac{\partial P_C}{\partial x} - \frac{\partial P_C}{\partial x}\right)\right]. \tag{18}$$

P_n is defined as $P_n = \frac{P_n+P_w}{2} + \frac{P_n-P_w}{2} = \bar{P} + \frac{1}{2}P_C$, where the mean pressure is given by $\bar{P}$ and it is constant, we have

$$\frac{\partial P_n}{\partial t} = \frac{1}{2}\frac{\partial P_C}{\partial x}. \tag{19}$$

Thus from Eqs. (16) and (19), we get

$$A = \left(K\frac{k_w}{\mu_w} + K\frac{k_n}{\mu_n}\right)\frac{1}{2}\frac{\partial P_C}{\partial x} - K\frac{k_w}{\mu_w}\frac{\partial P_C}{\partial x}. \tag{20}$$

In Eq. (18), replacement of A is given by Eq. (20),

$$m\frac{\partial S_w}{\partial t} = \frac{\partial}{\partial x}\left[-\frac{K}{2}\frac{k_w}{\mu_w}\frac{\partial P_C}{\partial x}\right]. \tag{21}$$

Using Eqs. (9) and (10) in Eq. (21),

$$\frac{\partial S_w}{\partial t} = \left(\frac{K\beta}{2m\mu_w}\right)\frac{\partial}{\partial x}\left[S_w\frac{\partial S_w}{\partial x}\right]. \tag{22}$$

To make Eq. (22) dimensionless, defining the variables

$$X = \frac{x}{L},\ T = \frac{K\beta}{2m\mu_w L^2}t. \tag{23}$$

So that Eq. (22) reduces to

$$\frac{\partial S_w}{\partial T} = \frac{\partial}{\partial X}\left[S_w\frac{\partial S_w}{\partial X}\right]. \tag{24}$$

Governing non-linear PDE is given by Eq. (24) which describes the fingering phenomenon.
The specific conditions at initial and boundary levels are [11]

$$S_w(X,0) = \frac{\xi}{(\sigma_p)^2}f(X),\quad 0 \le X \le 1, \tag{25}$$

$$S_w(0,T) = 1,\quad T \ge 0, \tag{26}$$

$$S_w(1,T) = 0,\quad T \ge 0. \tag{27}$$

Here $f(X)$ denotes arbitrary reaction of the primary saturation pattern. σ_p and ξ denote size of variance and disturbances in X-direction, respectively. It can be presumed over here that the whole oil has been displaced for every time by the impact of the injected water. Also $X = x/L$ and boundary condition (26) offer that fluid's saturation S_w is one (100%) for $T \ge 0$. This means that the value of k_n is always zero at the common interface. At the second end $x = L$ it's presumed that the water isn't attending to the boundary. Hence $S_w(1,T) = 0,\quad T \ge 0$. An approximate solution of governing Eq. (24) is defined by Elzaki Adomian decomposition approach within these conditions.

3 Solution of Problem by Elzaki Adomian Decomposition Method

In the present area, the effectiveness of proposed method is illustrated by obtaining the solution of non-linear equation.
Applying Elzaki transform of Eq. (24) subject to the specified conditions,

$$\therefore E\left[S_w(X,T)\right] = v^2 \frac{\xi}{\left(\sigma_p\right)^2} f(X) + vE\left[S_w\left(S_{wXX}\right) + \left(S_{wX}\right)^2\right].$$

We choose the initial approximation [11]

$$S_{w0} = \frac{\xi}{\left(\sigma_p\right)^2}(X-1)^2,$$

Considering $\xi = 100$ and $\sigma_p = 10$, we have $S_{w0} = (X-1)^2$,

$$E\left[S_w(X,T)\right] = v^2(X-1)^2 + vE\left[S_w\left(S_{wXX}\right) + \left(S_{wX}\right)^2\right]. \tag{28}$$

On applying an inverse of Elzaki transform,

$$S_w(X,T) = (X-1)^2 + E^{-1}\left\{vE\left[S_w\left(S_{wXX}\right) + \left(S_{wX}\right)^2\right]\right\}. \tag{29}$$

Using Adomian decomposition approach,

$$\sum_{n=0}^{\infty} S_{wn}(X,T) = (X-1)^2 + E^{-1}\left\{vE\left[\sum_{n=0}^{\infty} A_n(X,T) + \sum_{n=0}^{\infty} B_n(X,T)\right]\right\}. \tag{30}$$

Comparing the results on two sides of Eq. (30),

$$\begin{aligned}
S_{w0}(X,T) &= (X-1)^2,\\
S_{w1}(X,T) &= E^{-1}\left\{vE\left[A_0(X,T) + B_0(X,T)\right]\right\},\\
S_{w2}(X,T) &= E^{-1}\left\{vE\left[A_1(X,T) + B_1(X,T)\right]\right\},\\
S_{w3}(X,T) &= E^{-1}\left\{vE\left[A_2(X,T) + B_2(X,T)\right]\right\},\\
S_{w4}(X,T) &= E^{-1}\left\{vE\left[A_3(X,T) + B_3(X,T)\right]\right\},\\
&\vdots
\end{aligned} \tag{31}$$

Here A_n and B_n are Adomian polynomials which represent the non-linear term $S_w\,(S_{wXX})$ and $(S_{wX})^2$, respectively, and can be computed using the formula given in [1].
Few of the Adomian polynomials are given as

$$\begin{aligned}
A_0 &= S_{w0}\,(S_{w0})_{XX} = 2 - 4X + 2X^2,\\
A_1 &= S_{w0}\,(S_{w1})_{XX} + (S_{w0})_{XX}\,S_{w1} = 24T - 48XT + 24X^2\,T,\\
A_2 &= S_{w1}\,(S_{w1})_{XX} + (S_{w2})_{XX}\,S_{w0} + S_{w2}\,(S_{w0})_{XX}\\
&= 216X^2\,T^2 - 432XT^2 + 216T^2,\\
A_3 &= \frac{1}{6}\left[\begin{matrix}4S_{w2}\,(S_{w1})_{XX} + 4S_{w1}\,(S_{w2})_{XX} + S_{w0}\,(6S_{w3})_{XX} +\\ 6S_{w3}\,(S_{w0})_{XX} + 2S_{w2}\,(S_{w1})_{XX} + S_{w1}\,(2S_{w2})_{XX}\end{matrix}\right]\\
&= 192\,T^3(X-1)^2(5+2X),\\
&\quad\vdots\\
B_0 &= ((S_{w0})_X)^2 = 4 - 8X + 4X^2,\\
B_1 &= 2\,(S_{w0})_X\,(S_{w1})_X = 48T - 96XT + 48X^2\,T,\\
B_2 &= 2S_{w0}\,(S_{w2})_X + ((S_{w1})_X)^2 = 144\,(X-1)^2\,XT^2,\\
B_3 &= \frac{1}{6}\left[8\,(S_{w1})_X\,(S_{w2})_X + 12\,(S_{w0})_X\,(S_{w3})_X + 4\,(S_{w2})_X\,(S_{w1})_X\right]\\
&= 192\,T^3(X-1)^2(11+3X),\\
&\quad\vdots
\end{aligned} \tag{32}$$

Using Adomian polynomials (32) and the iteration formulas (31),

$$\begin{aligned}
S_{w0}(X,T) &= (X-1)^2\,,\\
S_{w1}(X,T) &= 6\,T\,(X-1)^2\,,\\
S_{w2}(X,T) &= 36\,T^2\,(X-1)^2\,,\\
S_{w3}(X,T) &= 24\,T^3\,(X-1)^2\,(3+2X),\\
S_{w4}(X,T) &= 48\,T^4\,(X-1)^2\,(16+5X),\\
&\quad\vdots
\end{aligned} \tag{33}$$

Thus, an approximate solution is

$$S_w(X,T) = S_{w0}(X,T) + S_{w1}(X,T) + S_{w2}(X,T) + S_{w3}(X,T) + S_{w4}(X,T) + \ldots$$

$$\therefore S_w(X,T) = (X-1)^2 + 6T\,(X-1)^2 + 36T^2\,(X-1)^2 + 24T^3\,(X-1)^2\,(3+2X) + 48T^4\,(X-1)^2\,(16+5X) + \ldots \quad (34)$$

Equation (34) is an approximate solution of Eq. (24). Numerical solution and its graphical representations can be found out with the help of MATHEMATICA and MATLAB.

4 Convergence Analysis

Using Theorem 1 and Corollary 1 [9],

$$\begin{aligned} \psi_0 &= \frac{\|S_{w1}\|}{\|S_{w0}\|} = 0.60 < 1, \\ \psi_1 &= \frac{\|S_{w2}\|}{\|S_{w1}\|} = 0.60 < 1, \\ \psi_2 &= \frac{\|S_{w3}\|}{\|S_{w2}\|} = 0.32 < 1, \\ \psi_3 &= \frac{\|S_{w4}\|}{\|S_{w3}\|} = 0.854167 < 1, \\ &\vdots \end{aligned} \quad (35)$$

Hence, it said that $\sum_{i=0}^{\infty} S_{wi}$ is convergent. Therefore, the approximate solution given by (34) is convergent.

5 Results and Discussion

Using the following parameter values [11], we obtain the numerical solution of Eq. (34).

Porosity (m) is given by 0.1, permeability (K) is taken as $1 \times 10^{-13} m^2$, length (L) is 10 m, viscosity of water (μ_w), and density of water (ρ_w) are 1 cP (at 20 °C) (0.001 N.s/m^2), and 1000 Kg/m^3, respectively. Here maximum distribution size (ξ) is 100 and penetration length (σ_p) is 10. Now we are finding the value of $S_w(X,T)$ for different $T = 0.01, 0.02, 0.03, \ldots 0.07$. So from Table 1, we notice that value of

Table 1 Saturation of injected fluid for different distance and time

X	$T = 0.01$	$T = 0.02$	$T = 0.03$	$T = 0.04$	$T = 0.05$	$T = 0.06$	$T = 0.07$
0.1	0.861585	0.919464	0.984243	1.05668	1.13769	1.22833	1.32982
0.2	0.680761	0.726517	0.777769	0.835143	0.899392	0.971393	1.05215
0.3	0.52121	0.556261	0.595552	0.639587	0.688965	0.744383	0.80664
0.4	0.382932	0.408696	0.437602	0.470034	0.506448	0.547379	0.593433
0.5	0.265926	0.283828	0.303928	0.326504	0.351888	0.380461	0.412662
0.6	0.170194	0.181656	0.194538	0.209022	0.225328	0.243711	0.264459
0.7	0.095734	0.102186	0.109441	0.117608	0.126815	0.137209	0.148958
0.8	0.042549	0.045418	0.048646	0.052285	0.056392	0.061036	0.066293
0.9	0.010637	0.011355	0.012163	0.013075	0.014106	0.015272	0.016595
1	0	0	0	0	0	0	0

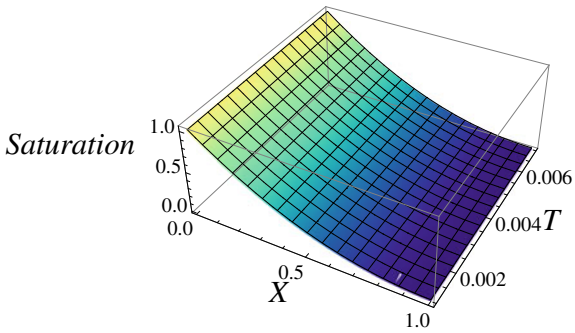

Fig. 2 Graphical representation of solution (34)

$S_w(X, T)$ decreases with X and increases with T. Table 2 shows the numerical values of saturation of injected fluid for different values of X and T. That is, from a physical point of view, we say that as T increases the fingers will extend and the oil will move in direction of the production well. Also notice that after long time ($T = 0.007$) the saturation of injected water doesn't simulate together with the phenomenon. So fingers will not be any more after a specific time frame. So it matches with real-world phenomenon. Graphical representations are given in Figs. 2, 3, 4, and 5.

6 Concluding Remarks

In the present study, Elzaki Adomian decomposition method has been successfully employed to find the solution of governing equation which can be derived from fingering phenomenon. From Tables 1 and 2, we can concluded that the saturation of injected fluid reduces with distance and slightly grows with time which is perfect with physical phenomenon. From Table 2 and Fig. 4, it is observed that there is an

Table 2 Comparison of saturation of injected fluid by EADM and Variational Iteration Method (VIM) (Mistry and Pradhan, 2015)

X	$T = 0.001$		$T = 0.002$		$T = 0.003$		$T = 0.004$	
	EADM	VIM	EADM	VIM	EADM	VIM	EADM	VIM
0.1	0.814887	0.814889	0.819829	0.819837	0.824824	0.824844	0.829874	0.82991
0.2	0.643861	0.643863	0.647764	0.647773	0.651709	0.651729	0.655695	0.655732
0.3	0.492955	0.492958	0.495942	0.495951	0.498959	0.49898	0.502007	0.502044
0.4	0.362171	0.362173	0.364363	0.364372	0.366576	0.366597	0.36881	0.368849
0.5	0.251507	0.251509	0.253026	0.253036	0.254559	0.254581	0.256104	0.256145
0.6	0.160963	0.160966	0.161932	0.161943	0.162907	0.162932	0.163889	0.163933
0.7	0.09054	0.090543	0.091081	0.091093	0.091622	0.091649	0.092164	0.092212
0.8	0.040238	0.040241	0.040473	0.040485	0.040703	0.040733	0.040931	0.040983
0.9	0.010057	0.01006	0.010057	0.010121	0.010151	0.010183	0.010188	0.010245
X	$T = 0.005$		$T = 0.006$		$T = 0.007$			
	EADM	VIM	EADM	VIM	EADM	VIM		
0.1	0.834979	0.835036	0.840137	0.84022	0.84535	0.845469		
0.2	0.659724	0.659782	0.667907	0.66388	0.667907	0.668025		
0.3	0.505086	0.505145	0.511338	0.50828	0.511338	0.511456		
0.4	0.371066	0.371127	0.375641	0.37343	0.375641	0.375764		
0.5	0.257663	0.257727	0.259234	0.25933	0.260819	0.260947		
0.6	0.164876	0.164945	0.165869	0.16597	0.166869	0.167006		
0.7	0.092707	0.092781	0.09325	0.09336	0.093792	0.093941		
0.8	0.041154	0.041236	0.041373	0.04149	0.04159	0.041751		
0.9	0.010219	0.010309	0.010242	0.01037	0.01026	0.010437		

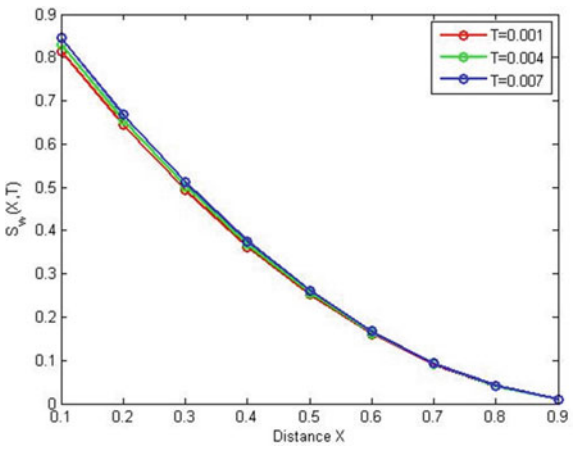

Fig. 3 Saturation of injected fluid versus distance for $T = 0.001, 0.004, 0.007$

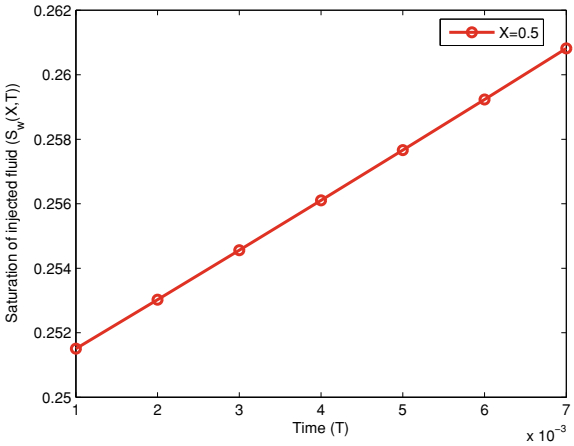

Fig. 4 Comparison of solutions by EADM and VIM

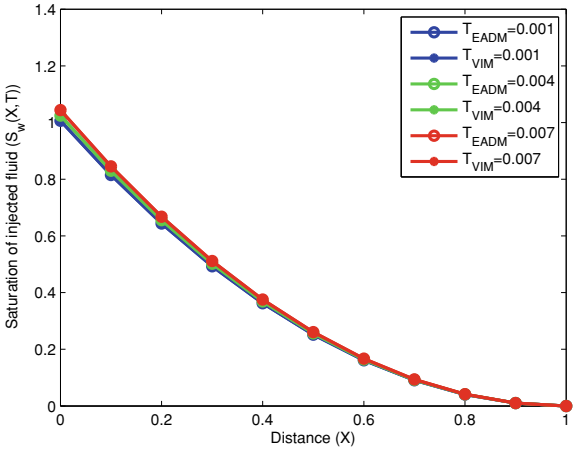

Fig. 5 Saturation of injected fluid versus T for $X = 0.5$

excellent agreement between the results obtained using EADM and VIM. Thus, from the numerical comparison and its convergence analysis, we can say that the proposed methodology is extremely reliable, powerful, and also provides precise and careful arrangement. Fractional model can be used in future to study the behavior of proposed phenomenon.

Acknowledgements The authors, Archana C. Varsoliwala, and Dr. Twinkle R. Singh, are very much thankful to S. V. National Institute of Technology, Surat-395007 for providing great opportunity for research work.

References

1. Adomian G (1994) Solution of physical problems by decomposition. Comput Math Appl 27(9–10):145–154
2. Dubey VP, Kumar R, Kumar D (2019) Approximate analytical solution of fractional order biochemical reaction model and its stability analysis. Int J Biomath 12(05):1950059
3. Dubey VP, Kumar R, Kumar D (2020) Numerical solution of time-fractional three-species food chain model arising in the realm of mathematical ecology. Int J Biomath 13(02):2050011
4. Dubey VP, Kumar R, Singh J, Kumar D (2021) An efficient computational technique for time-fractional modified Degasperis-Procesi equation arising in propagation of nonlinear dispersive waves. J Ocean Eng Sci 6(1):30–39
5. Dubey VP, Kumar R, Kumar D (2019) A reliable treatment of residual power series method for time-fractional Black-Scholes European option pricing equations. Phys A: Stat Mech Appl 533:122040
6. Dubey VP, Kumar R, Kumar D (2020) A hybrid analytical scheme for the numerical computation of time fractional computer virus propagation model and its stability analysis. Chaos, Solitons Fract 133:109626
7. Elzaki TM (2011) The new integral transform "Elzaki transform". Global J Pure Appl Math 7(1):57–64
8. Elzaki TM (2012) On the new integral transform "ELzaki Transform" fundamental properties investigations and applications. Global J Math Sci Theory Pract 4(1):1–13
9. Hosseini MM, Nasabzadeh H (2006) On the convergence of Adomian decomposition method. Appl Math Comput 182(1):536–543
10. Kumar D, Singh J, Baleanu D (2016) Numerical computation of a fractional model of differential-difference equation. J Comput Nonlinear Dyn 11(6):061004
11. Mistry PR, Pradhan VH (2015) Approximate analytical solution of non-linear equation in one dimensional instability phenomenon in homogeneous porous media in horizontal direction by variational iteration method. Procedia Eng 127:970–977
12. Meher R, Meher SK (2013) Analytical treatment and convergence of the Adomian decomposition method for instability phenomena arising during oil recovery process. Int J Eng Math
13. Mehta MN (1977) Asymptotic expansion of fluid flow through porous media. PhD Thesis, South Gujarat University, Surat, India
14. Muskat M (1937) The flow of fluids through porous media. J Appl Phys 8(4):274–282
15. Pradhan VH, Mehta MN, Patel T (2011) A numerical solution of nonlinear equation representing one-dimensional instability phenomena in porous media by finite element technique. Int J Adv Eng Technol 2(1):221–227
16. Scheidegger AE, Johnson EF (1961) The statistical behavior of instabilities in displacement processes in porous media. Can J Phys 39(2):326–334
17. Singh H, Srivastava HM, Kumar D (2018) A reliable algorithm for the approximate solution of the nonlinear Lane-Emden type equations arising in astrophysics. Numer Methods Partial Differ Equ 34(5):1524–1555
18. Singh H, Srivastava HM (2020) Numerical investigation of the fractional-order Liénard and Duffing equations arising in oscillating circuit theory. Front Phys 8:120
19. Varsoliwala A, Singh T (2019) Analysis of fish farm model by differential transform method. In: 2019 international conference on sustainable computing in science, technology and management. Jaipur, India, pp. 1043–1048
20. Varsoliwala AC, Singh TR (2021) Mathematical modeling of tsunami wave propagation at mid ocean and its amplification and run-up on shore. J Ocean Eng Sci 6(4):367–375
21. Varsoliwala AC, Singh TR (2021) Mathematical modelling of atmospheric internal waves phenomenon and its solution by Elzaki Adomian decomposition method. J Ocean Eng Sci
22. Verma AP (1969) Statistical behavior of fingering in a displacement process in heterogeneous porous medium with capillary pressure. Can J Phys 47(3):319–324
23. Ziane D, Cherif MH (2015) Resolution of nonlinear partial differential equations by Elzaki transform decomposition method. J Approx Theory Appl Math 5:17–30

Numerical Study of Melting Impact on MHD Non-Newtonian Casson Fluid Flow Ran on a Stretching Sheet in a Porous Medium with Radiation and Dissipation Effect

Sanju Jangid, Ruchika Mehta, Tripti Mehta, and Devendra Kumar

Abstract The present work is enclosing the features of melting heat transference in the porous medium of MHD Casson fluid influenced by thermal radiation and viscous dissipation also with the heat source/sink effect. This paper formulation is explained by the Runge–Kutta–Fehlberg technique by converting the governing equations (PDEs) into ordinary differential equations. After that, the graph is found using MATLAB software with the shooting technique. The impacts of skin-friction coefficient and Nusselt number are also illustrated. The effects of Rayleigh number Ra, Eckert number Ec and heat source/sink parameter Q along with various persistent parameters are derived for velocity and temperature profile. The outcomes of the existing investigation are associated with the accessible works in specific conditions and more contracts have been detected.

Keywords Casson fluid · Porous media · Viscous dissipation

1 Introduction

Given the stipulated trait of definitive product stooping based on the rate of heat transfer via stretching, sheets find several praxes, namely paper production, aerodynamic extrusion of polymer, augmentation incapacity of paints, and lubricants, plastic modelling, and so on. Crane [2] connected the boundary layer flow and heat transfer over a stretching sheet conducting with electrically viscous fluid. Bachok et al. [1] studied the analysis of the time-independent 2D stagnation point fluid flow from a torrid, laminar fluid flow to a decay shrinking/stretching plate. Nadeem et al.

S. Jangid · R. Mehta (✉)
Department of Mathematics & Statistics, Manipal University Jaipur, Jaipur, Rajasthan, India
e-mail: ruchika.mehta1981@gmail.com

T. Mehta
Department of Mathematics, S. S. Jain Subodh P. G. College, Jaipur, Rajasthan, India

D. Kumar
Department of Mathematics, University of Rajasthan, Jaipur, Rajasthan, India

J. Singh et al. (eds.), *Advances in Mathematical Modelling, Applied Analysis and Computation*, Lecture Notes in Networks and Systems 415,
https://doi.org/10.1007/978-981-19-0179-9_30

[25] inspected a Casson fluid over an exponentially erect shrinking plate with an MHD effect. Kirubhashankar et al. [13] investigated the stipulated plate temperature of unsteady 2D flow over a stretching stratum in the non-Newtonian fluid. The effects of viscous dissipation and second-order slip on the MHD boundary layer flow of an incompressible, electrically conducting water-based nanofluid across a stretched sheet were examined by Mabood and Mastroberardino [22]. Gireesha et al. [6] examined numerically a constant 2D hydromagnetic stagnation point flow of an electrically conducting nanofluid across a stretched surface with the generated magnetic field, melting effect, and heat generation/absorption. Mabood and Das [21] addressed an examination of MHD flow and melting heat transfer of a nanofluid across a stretched surface using a second-order slip model and thermal radiation.

Mabood et al. [24] investigated alterable fluid possessions on heat transference in MHD Casson fluid in a porous medium on a moving surface in the existence of the radiation. Pushpalatha et al. [26] considered the unsteady (time-dependent) free convection fluid flow of a Casson fluid restricted by a dynamic erect plane plate in a rotating tract with convective limitations. Fetecau et al. [3] found interesting new features of Stoke's second problem with the new solutions of Stoke's first problem in the recap of oscillating plates, which tends to zero under the consideration of porous and magnetic impacts. Ijaz et al. [8] presented the interaction of liquid and solid elements in a finite symmetrical wavy network in electro-osmotic flow with magnetohydrodynamics impacts. Khan et al. [11] broadcasted the mass transfer on chemicalized fourth-grade unsolidified model suckled and peristaltically passed by a curved riffle in the largest amount of magnetic field. Mahdy [23] examined the time-independent MHD free and forced convection in non-Newtonian Casson nanofluid of a ragingly rotating sphere with an alterable enclosure temperature of an electrically conducting fluid flow. Zeeshan et al. [30] presented the impact of magnetohydrodynamics bio-bi-phase in a rectangular conduit with peristaltic transport of non-Newtonian Jeffery fluid with homogeneously issued alike stiff particles.

The delinquent of melting heat transference has been skilled pointedly by investigators due to its extensive variety of scientific and engineering that created bids in the research of semiconductor device melting of frozen lands, solidifying of molten rock movements, etc. Melting is a phase change process that is accompanied by thermal energy absorption. Melting heat transfer in non-Newtonian fluids has a wide range of thermal engineering applications, including permafrost melting, magma solidification, geothermal energy recovery, oil extraction, and semiconductor material preparation. Qayyum et al. [27] analysed the time-dependent squeezing flow of an MHD Casson fluid in the porous medium. Kumar et al. [14] communicated with unsteady and steady Magnetohydrodynamic flow in Williamson fluid given the curved surface in the existence of thermal radiation and a chemical reaction. Lakshmi et al. [15] inspected the heat and mass transference features of 2D nonlinear convective non-Newtonian nanofluids (Walters-B and Casson) that pass through a thick surface with steady and laminar flow in the presence of thermophoresis and Brownian motion. Li et al. [16] found the result of Darcy and Richardson numbers by creating 2-phase mixed convection of non-Newtonian nanofluid (copper oxide nanofluids and H_2O + 0.5% CMC) in an H-shaped porous hole with the help of Boussinesq approximation

inside the four rotating cylinders. Lund et al. [17] found the non-Newtonian heating equation in time-independent incompressible MHD mixed convective boundary layer current of Casson fluid on an exponentially erect shrinking plate. Mabood et al. [20] found the delay with thermal radiation in the porous system in the framing of melting heat transference in MHD (magnetohydrodynamic) Casson fluid.

Many industrial building strides embrace non-Newtonian fluids, for example, lubricants, biological fluids, liquid crystals with rigid molecules, lubricants, polymeric suspensions, paints, and animal blood. Also, many uses of magnetohydrodynamics in different areas such as MHD sidestep energy generators, fluid metallic production forms, MHD tube flows occur in ionized hurrying agents, bubble levitation, bubble floating, and so on. Kirubhashankar et al. [12] considered the thermal influence of fleeting MHD Casson fluid tide between two equivalent plates. Lund et al. [18, 19] developed a tract of the magnetohydrodynamic Casson nanofluid in the presence of electric current on exponential stretching and shrinking scale. Lund et al. [18, 19] focus their attention on heat transfer and Brownian and thermophoresis impacts of micropolar nanofluid on an accessible stretching/shrinking biased surface. Salahuddin et al. [28] considered the steady-state motion heat and mass transference in Casson fluid flow in the attendance of pre-exponential components. Shah et al. [29] analysed the radiative electrically conducting Casson nanofluid flow over a nonlinearly stretching sheet by applying the Second Law of Thermodynamics to detect entropy generation rate.

There are many applications of heat transport resolute by thermal radiation including missiles, satellites, diverse technological procedures, space vehicles, which generate thrust instrument for aircraft engines, nuclear power plant, and gas turbines. Gbadeyan et al. [4] examined an MHD Casson nanofluid flow over a perpendicular plane plate with a convective heating system and speed slip boundary limitations with impacts of assorted alterable viscosity and also with non-Darcian porous medium, non-linear radiation, and thermal conductivity. Idowu et al. [7] examined the Cattaneo–Christov heat flux replacement paradox of MHD Casson fluid flow with dissipative impacts, heat generation, and buoyancy impact for natural convection. Gireesha et al. [5] studied the characteristics of dusty Casson fluid MHD flow, and melting heat transfer across a stretched sheet have been revealed. Through the Cattaneo–Christov heat flux, a modified form of Fourier's law is used. Jabeen et al. [9] investigated the comparative study of MHD boundary layer fluid flow nearby a linearly stretching surface in the impendence of heat generation/absorption, radiative heat flux, chemical reaction, and thermophoresis velocity impacts on an accessible surface. Kala et al. [10] studied an MHD Casson fluid movement with speed slip over an engaged non-linearly stretching surface in a non-Darcy porous medium.

Because of its vital applications in permafrost melting, frozen ground thawing, liquid polymer extrusion, casting, and welding processes, as well as phase change material, heat transmission followed by melting effect has garnered a lot of attention in recent years. Metals, polymers, ceramics, and other materials are pushed or dragged through a die with the required cross-section to manufacture various sorts of objects in manufacturing techniques such as hot extrusion. Because hot extrusion or hot working is done above the material's recrystallization temperature to prevent work

hardening and make it simpler to push the material through the die, the melting effect is crucial. In permafrost research, the melting effect plays a significant role in permafrost melting and frozen ground thawing difficulties. In the present case, there are many researchers who did a lot of work to inspect the features of heat transfer given the melting process in different types of fluid flows. The experience of melting heat transport is not studied yet with dissipation effect along with radiation in the porous surface on the stretching surface. The main aim of this work is to fill up this gap with Mabood and Das [20]. After formulation, the outcome is shown by figures and a table of various parameters, Nusselt number, and skin-friction coefficient.

2 Formulation

In this work, the condition of 2D Casson fluid flow over a horizontally linear stretching surface in the existence of a porous medium is analysed. The porous medium is discussed with permeability K and a steady rate of melting with constant properties.

In this flow, uniform transverse magnetic field B_0 is conducted with electrically fluid flow. Here we neglect the magnetic field. Contemplate exterior flow is $u_e(x) = ax$ and the speed of the stretching plate is $u_w(x) = cx$, where a and c are real positive constants and x is the coordinate along with the stretching plate as shown in (Fig. 1).

Here T_m and T_∞ are the melting and temperature for a free stream of the fluid flow, respectively, with the condition $T_\infty > T_m$.

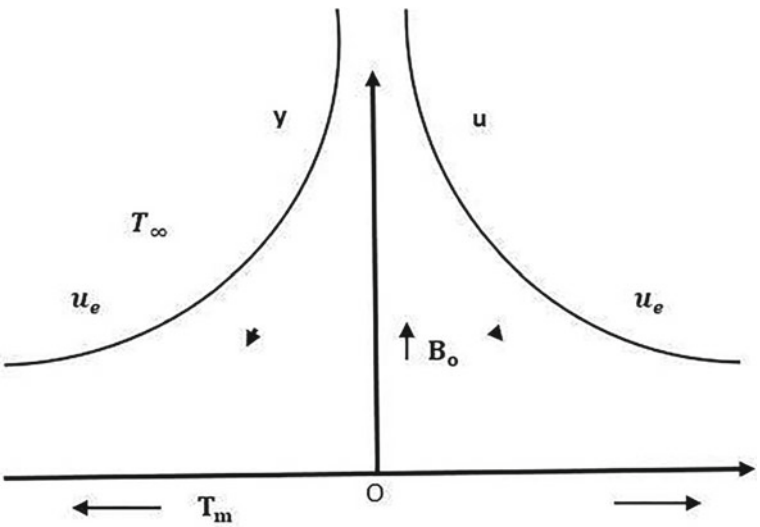

Fig. 1 Physical model of present work

The rheologic governing equation of a non-Newtonian Casson fluid (Refs. [4, 7, 13]) is written by

$$\tau_{ij} = \begin{cases} 2\left(\mu_B + P_y/\sqrt{2\pi}\right)e_{ij}, \pi > \pi_c, \\ 2\left(\mu_B + P_y/\sqrt{2\pi_c}\right)e_{ij}, \pi > \pi_c, \end{cases} \tag{1}$$

where μ_B = plastic dynamic viscosity,
$\pi = e_{ij}e_{ij}$ and $e_{ij} = (i, j)$th the component of deformation rate,
π = deformation rate,
π_c = critical value of the non-Newtonian model,
P_y = yield stress of fluid.
The governing equations (Refs. [13, 20]) are given by

$$\frac{\partial u}{\partial x} + \frac{\partial v}{\partial y} = 0 \tag{2}$$

$$u\frac{\partial u}{\partial y} + v\frac{\partial u}{\partial y} = u_e\frac{du_e}{dx} + \nu\left(1 + \frac{1}{\beta}\right)\frac{\partial^2 u}{\partial y^2} - \frac{\sigma B_0^2(u - u_e)}{\rho} - \frac{\nu}{K}(u - u_e) + g_0\beta_T^*(T - T_m) \tag{3}$$

$$u\frac{\partial T}{\partial x} + v\frac{\partial T}{\partial y} = \alpha\frac{\partial^2 T}{\partial y^2} - \frac{1}{\rho C_p}\frac{\partial q_r}{\partial y} + \frac{\sigma B_0^2 u^2}{\rho C_p} + \frac{\mu}{\rho C_p}\left(1 + \frac{1}{\beta}\right)\left(\frac{\partial u}{\partial y}\right)^2 + \frac{Q_0}{\rho C_p}(T - T_m) \tag{4}$$

with limitations

$$\begin{aligned} u = u_w(x) = cx,\ \ T = T_m,\ \ at\ \ y = 0 \\ u \to u_e(x) = ax,\ T \to T_\infty,\ at\ y = \infty \end{aligned} \tag{5}$$

and

$$k\left(\frac{\partial T}{\partial y}\right)_{y=0} = \rho[\lambda + c_s(T_m - T_0)]v(x, 0), \tag{6}$$

where α is the thermal radiation, K is the permeability of the medium, (u, v) denotes the velocity components along axes, k is the thermal conductivity, β is the Casson fluid parameter, σ exhibits the electrical conductivity of fluid, λ conveys the latent heat of the fluid, ν expresses the kinematic viscosity of the fluid, c_s indicates the heat capacity of the solid surface, ρ indicates the density of the fluid, q_r exhibits radiative heat flux, c_p conveys the specific heat at constant pressure, Q expresses the temperature Gradient dependent heat sink/source parameter.

Again Eq. (4) becomes a new form by taking Rosseland approximation for radiations, and we have

$$q_r = \frac{-4\sigma^*}{3k^*}\frac{\partial T^4}{\partial y} \tag{7}$$

where σ^* is the Stefan–Boltzmann constant, k^* = absorption coefficient and $T^4 \approx T_2^3 - T_2^4$

$$u\frac{\partial T}{\partial x} + v\frac{\partial T}{\partial y} = \alpha\frac{\partial^2 T}{\partial y^2} + \frac{16\sigma^* T_\infty^3}{3\rho c_p k^*}\frac{\partial^2 T}{\partial y^2} \tag{8}$$

All the above equations (dimension form) are changed into non-dimension form by taking some similarities which are given below:

$$\psi = x\sqrt{av}f(\eta), \quad \theta(\eta) = \frac{T - T_m}{T_\infty - T_m}, \quad \eta = y\sqrt{\frac{a}{v}} \tag{9}$$

where ψ = stream function and explain as $u = \frac{\partial \psi}{\partial y}$ and $v = -\frac{\partial \psi}{\partial x}$.

So that

$$u = axf'(\eta), \quad v = -\sqrt{av}f(\eta) \tag{10}$$

The new forms of Eqs. (2) to (5) are written as

$$\left(1 + \frac{1}{\beta}\right)f''' = f'^2 - ff'' - (Mn + \Omega)\left(1 - f'\right) - Ra\theta + 1 \tag{11}$$

$$\theta''(1 + R) + Mn^2 \text{Ec Pr}\left(f'\right)^2 + \left(1 + \frac{1}{\beta}\right)\text{Ec Pr}\left(f''\right)^2 + Q\,\text{Pr}\,\theta + \text{Pr}\, f\theta' = 0 \tag{12}$$

The boundary status is

$$f'(0) = \varepsilon, \text{Pr}\, f(0) + Me\theta'(0) = 0, \theta(0) = 0, f'(\infty) = 1, \theta(\infty) = 1. \tag{13}$$

where Mn^2 (magnetic parameter) $= \frac{\sigma B_0^2}{a\rho}$, Ω (permeability parameter) $= \frac{v}{aK}$, Ra (Rayleigh number) $= \frac{g_0\beta_T^*(T - T_m)}{a^2 x}$, R (radiation parameter) $= \frac{16\sigma^* T_\infty^3}{3\rho c_p k^*}$, Pr (Prandtl number) $= \frac{v}{\alpha}$, Ec (Eckert number) $= \frac{a^2 x^2}{C_p(T_\infty - T_m)}$, Q (Temperature gradient dependent heat sink/source parameter) $= \frac{Q_0}{\rho a C_p}$, β (non-Newtonian Casson fluid parameter) $= \frac{\mu_B\sqrt{2\pi_C}}{P_y}$, Me (melting parameter) $= \frac{C_p(T_\infty - T_m)}{\lambda + C_S(T_m - T_\infty)}$, ε (Stretching parameter) $= \frac{c}{a}$. And

here prime ($'$) represents the differential with respect to η. Also, the melting number (Me) is the combination of the Stefan numbers $\frac{C_p(T_\infty - T_m)}{\lambda}$ and $\frac{C_S(T_m - T_0)}{\lambda}$ for the liquid and solid phases, respectively.

The physical quantities are

$$\text{Skin friction coefficient } \left(C_f\right) = \frac{\tau_w}{\rho u_e^2} \Rightarrow \text{Re}_x^{1/2} C_f = \left(1 + \frac{1}{\beta}\right) f''(0), \tag{14}$$

where $\tau_w = \left(1 + \frac{1}{\beta}\right)\left(\frac{\partial u}{\partial y}\right)_0$ (shear stress).

$$\text{Local Nusselt number } (Nu_x) = \frac{x q_w}{k(T_\infty - T_m)} \Rightarrow \text{Re}_x^{1/2} Nu_x = (1 + R)\theta'(0), \tag{15}$$

where $q_w = -k\left(\frac{\partial u}{\partial y}\right)_{y=0} + q_r$ = (surface heat flux) and $\text{Re}_x = \frac{u_e x}{\nu}$ = (local Reynolds number).

If Ec = Q = Ra = 0, as $\beta \to \infty$ in Eqs. (11) and (12), then this present work reduces to the work of Mabood and Das [20].

3 Result and Discussion

The outcomes of different parameters are represented in table and graph with a pervasive mathematical study. Results of Eckert number Ec, Rayleigh number Ra, radiation number R, permeability number Ω, melting number Me, non-Newtonian Casson number β, magnetic field number Mn, and temperature gradient number Q are discussed for the stretching number $\varepsilon = 1.5$ and 0.5.

Figure 2 depicts that the growing values of β diminishes the values of velocity at $\varepsilon = 1.5$ due to reduction in boundary layer thickness but reverse impact at $\varepsilon = 0.5$. Figure 3 shows the velocity conclusion of the rising magnetic parameter Mn. Velocity increases at $\varepsilon = 0.5$ and decreases at $\varepsilon = 1.5$ due to Lorentz force that has the properties to slow down the flow of conducting fluid flow. The increasing impact of Ω (permeability parameter) on velocity is shown in Fig. 4 with $\varepsilon = 1.5$ and the reverse effect is with $\varepsilon = 0.5$. The influence of velocity with increasing Prandtl number Pr is depicted in Fig. 5 at $\varepsilon = 1.5$ and the converse effect at $\varepsilon = 0.5$. One may consider that when β surges indeterminately, the existing experience clearly diminish to a Newtonian fluid. In Fig. 6, the impact of radiation parameter R increases the velocity effect. Since the growing Radiation parameter, R increases in the thermal boundary layer. The different values of the temperature gradient heat source/sink Q parameter in Fig. 7 rises the velocity profile due to the width of the boundary layer. Also, velocity increases with increasing Rayleigh number Ra at ε

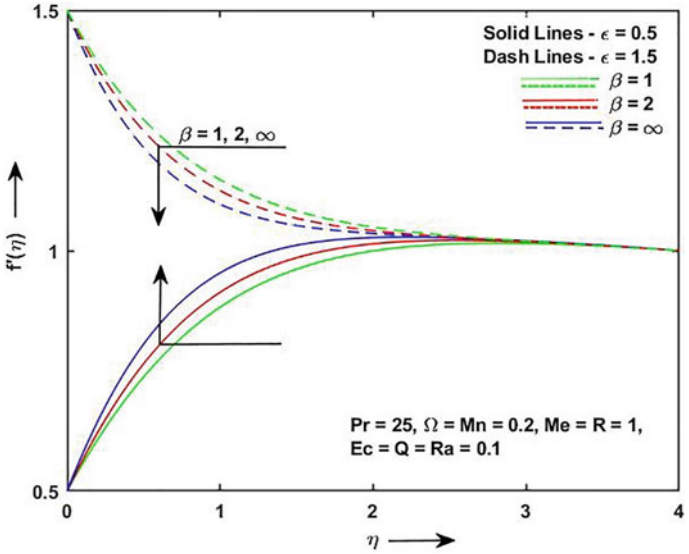

Fig. 2 Casson parameter β impact on velocity

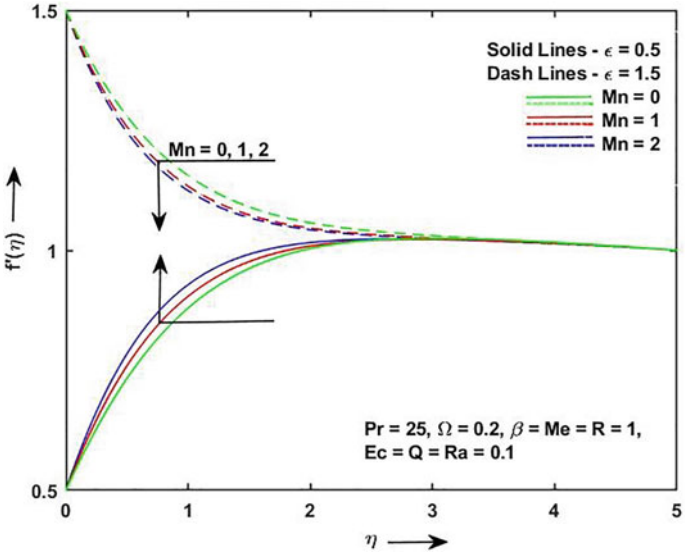

Fig. 3 Magnetic parameter Mn impact on velocity

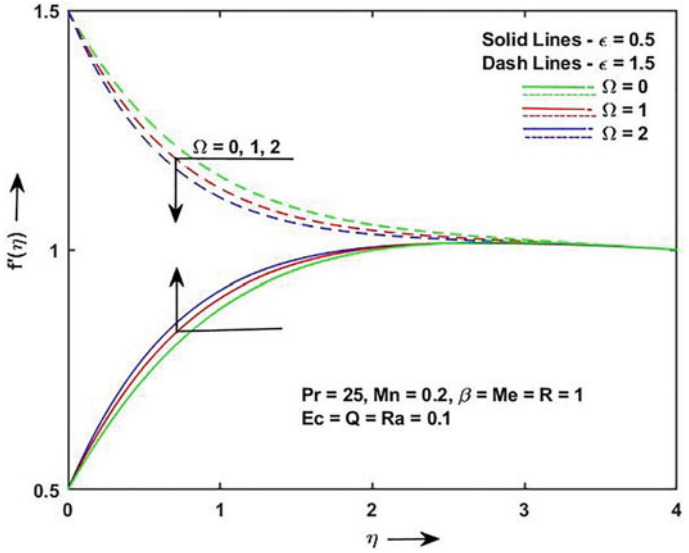

Fig. 4 Permeability parameter Ω impact on velocity

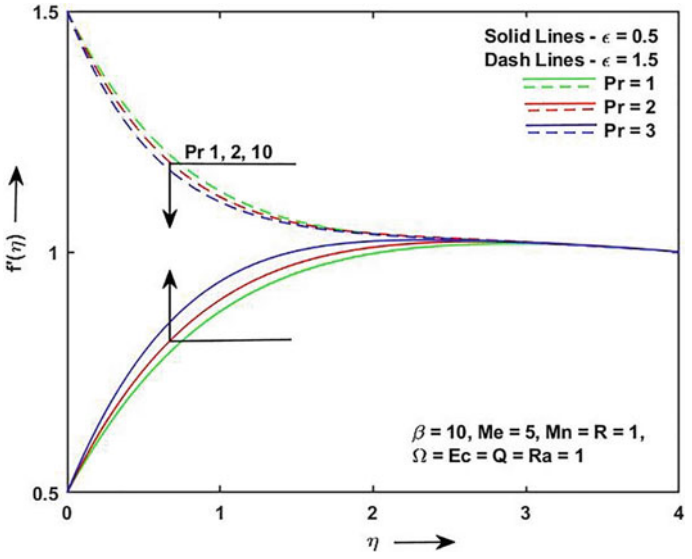

Fig. 5 Prandtl number Pr impact on velocity

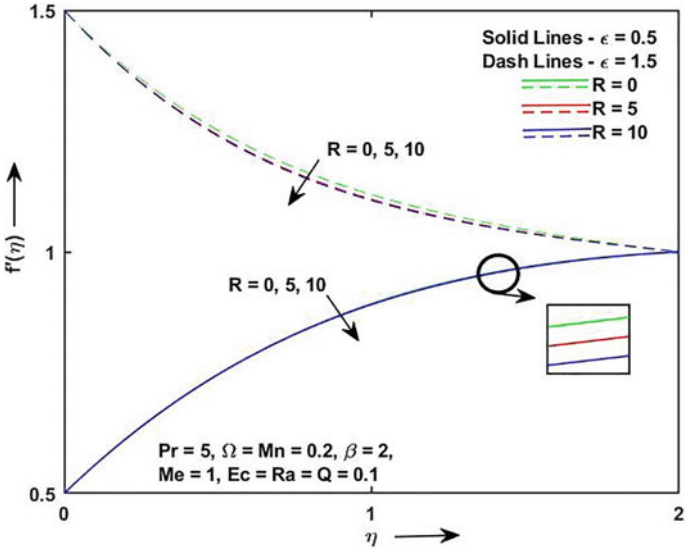

Fig. 6 Radiation parameter R impact on velocity

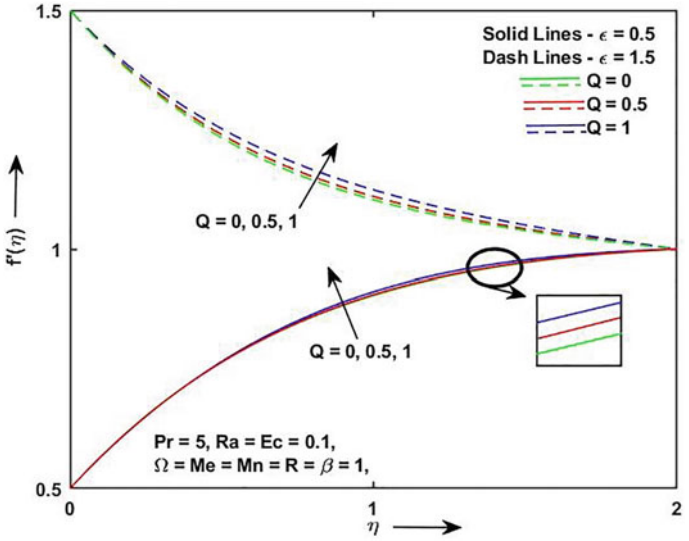

Fig. 7 Temperature gradient dependent heat sink/source parameter Q impact on velocity

$= 0.5$ and at $\varepsilon = 1.5$ in Fig. 8. Figure 9 displays the rising Eckert number Ec that decreases the velocity effect at $\varepsilon = 0.5$ and increases the velocity effect at $\varepsilon = 1.5$.

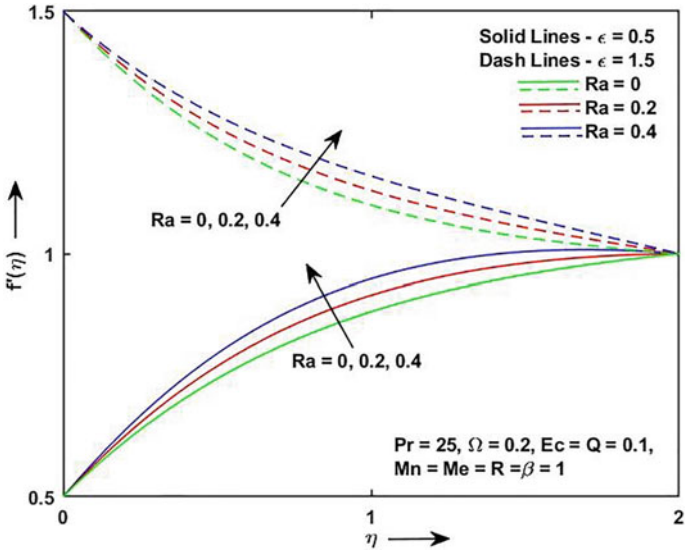

Fig. 8 Rayleigh number Ra impact on velocity

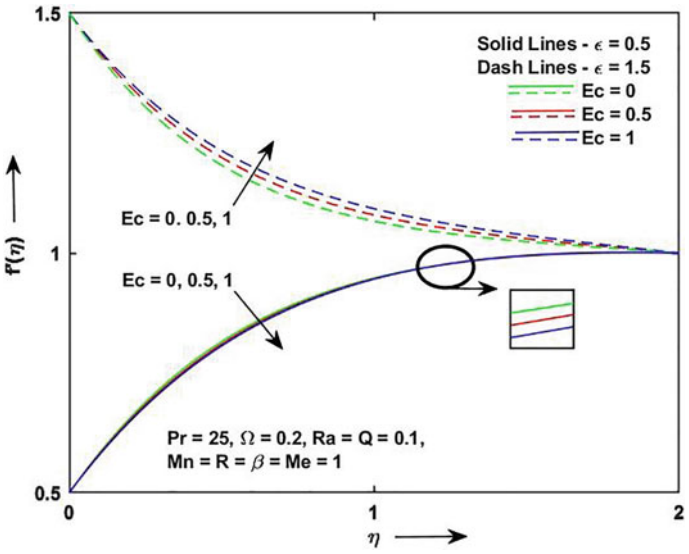

Fig. 9 Eckert number Ec impact on velocity

Clearly, Fig. 10 shows the temperature effect on the Casson parameter β with magnetic effect. Temperature increases with β due to slight increases in the thermal boundary layer thickness with $\varepsilon = 0.5$ and reverse effect with $\varepsilon = 1.5$. Figure 11 presents the conclusion of the increasing magnetic parameter Mn on temperature

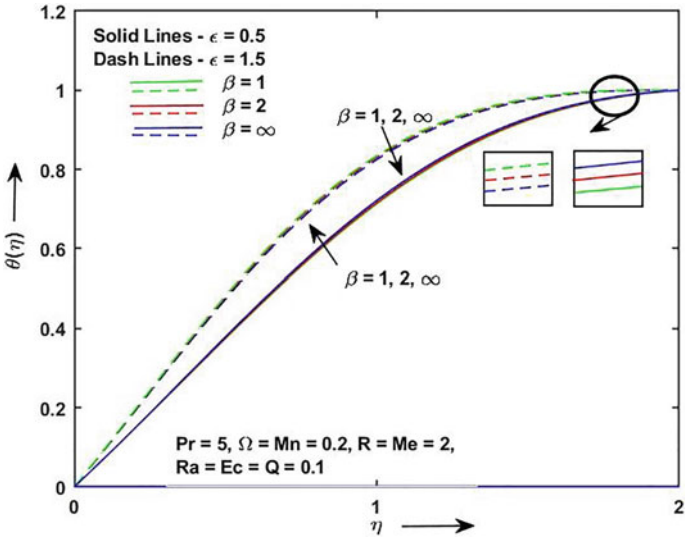

Fig. 10 Casson parameter β impact on temperature

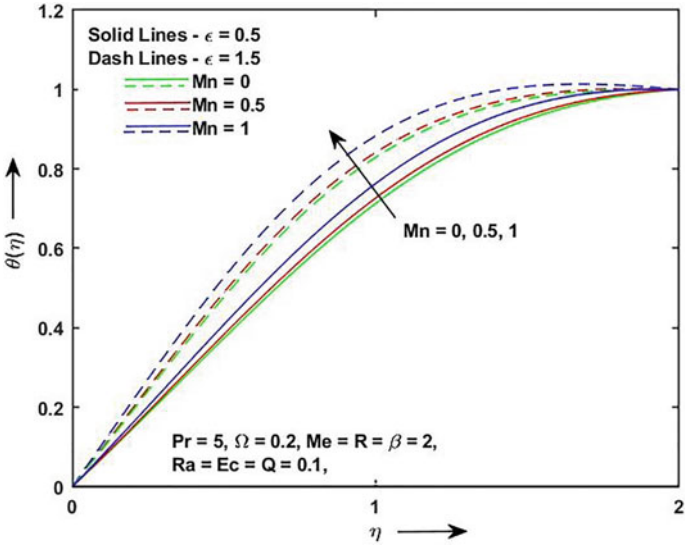

Fig. 11 Magnetic parameter Mn impact on temperature

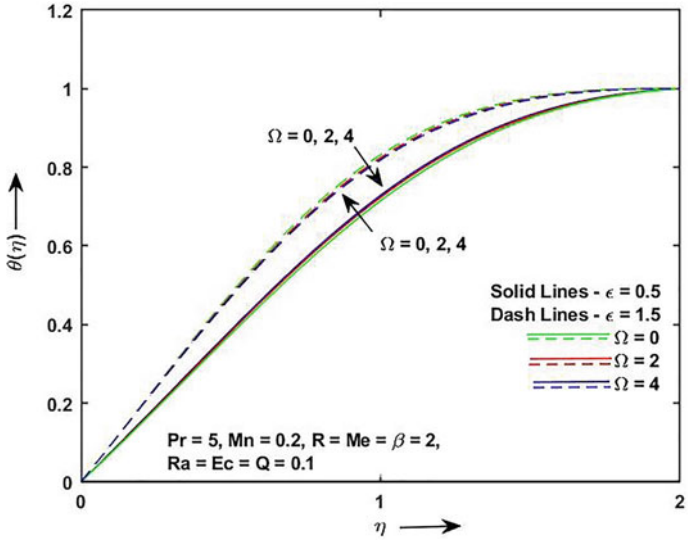

Fig. 12 Permeability parameter Ω impact on temperature

over a radiating plane stretching plane for $\varepsilon = 0.5$ and $\varepsilon = 1.5$. From Fig. 12, it is inferred that the temperature improves due to the permeability parameter Ω with stretching parameter $\varepsilon = 0.5$ but reverses with $\varepsilon = 1.5$. The outcome of the permeability parameter Ω over non-dimensional temperature outlines is exposed by the diagram. It is detected that a rise of Ω rises the temperature a little within the section. Prandtl number Pr signifies the ratio to momentum and thermal diffusivities. Developed Prandtl number is linked to lower thermal diffusivity. Hence, a negligible amount of heat is transported from heated fluid to the melting surface and as an outcome, the temperature remains developed with Fig. 13. Temperature gradient heat source/sink parameter Q impacts on temperature is exposed in Fig. 14, i.e., temperature increases with $\varepsilon = 0.5$ and $\varepsilon = 1.5$ when Q rises. The result of thermal radiation number R on temperature is inspected in Fig. 15 for $\varepsilon = 0.5$ and 1.5. It is detected that the temperature retards reliably with growing thermal radiation number R. Also, in Fig. 16, temperature increases when Ra Rayleigh's number increases. Figure 17 depicts the temperature rises with the rising Eckert number Ec. Eckert number is the ratio of kinetic energy to heat content. Here kinetic energy grows into internal energy by fluid flow compared to the viscous fluid stresses.

The skin-friction coefficient result of various dimensionless physical parameters alongside $\varepsilon = 0.5$ and $\varepsilon = 1.5$ is discussed in Table 1.

Table 2 shows the Nusselt number for various dimensionless physical parameters with $\varepsilon = 0.5$ and $\varepsilon = 1.5$.

The current work's validation of skin-friction and Nusselt number impressions is compared to Mabood and Das [20] when non-dimensional physical parameters Ra, Ec, and Q are zero, as shown in Table 3.

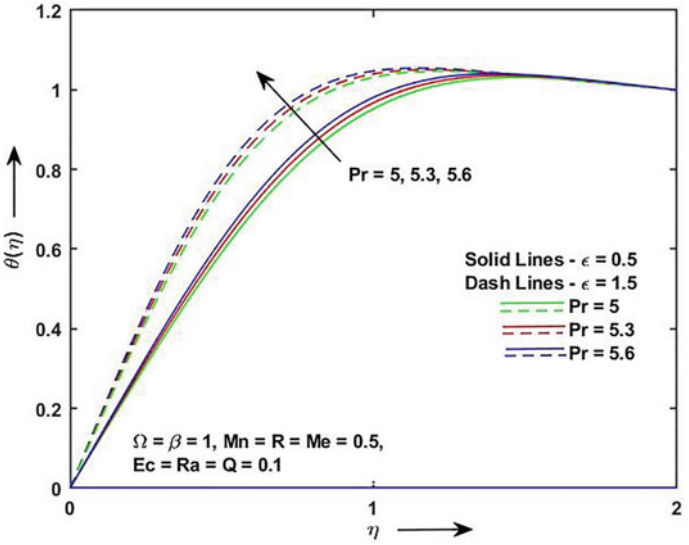

Fig. 13 Prandtl number Pr impact on temperature

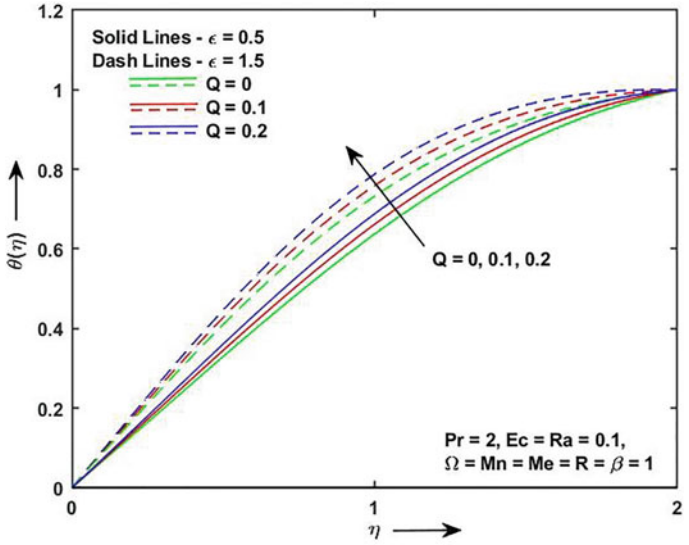

Fig. 14 Temperature gradient dependent heat sink/source parameter Q impact on temperature

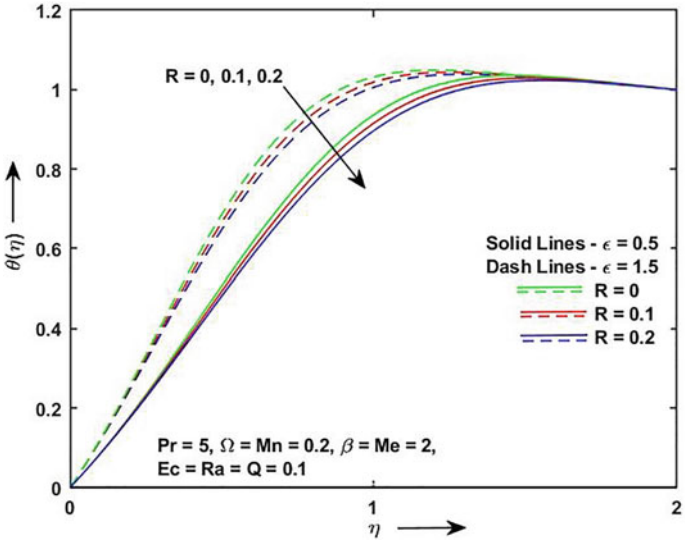

Fig. 15 Radiation parameter R impact on temperature

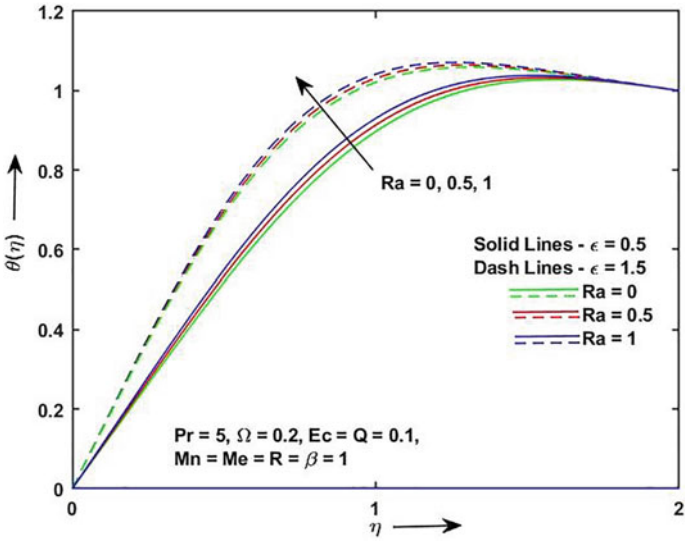

Fig. 16 Rayleigh number Ra impact on temperature

4 Conclusion

The existing work gives the mathematical resolutions for steady (time-independent) boundary layer fluid flow and heat transference of MHD Casson fluid happening

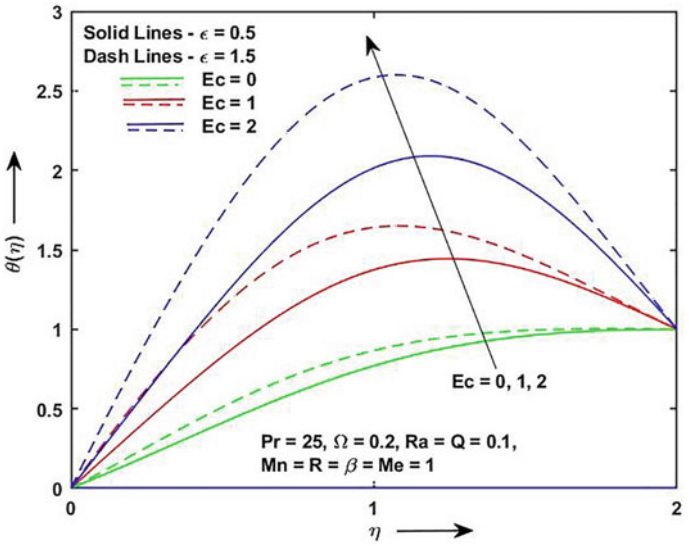

Fig. 17 Eckert number Ec impact on temperature

through the melting procedure due to stretching plate with radiation and diffusion effect fixed in a porous medium. In this work, the dimensional governing equations are converted into non-dimensional equations with the help of some parallel transformation. The ordinary differential equation solved using the Runge–Kutta–Fehlberg technique with the shooting procedure is described. The weighty outcomes of the effort are as follows:

- Velocity reduction with non-Newtonian Casson fluid parameter, magnetic field, permeability parameter, Prandtl number decrease when stretching parameter is 1.5 and increase when the stretching parameter is 0.5. and the temperature gradient heat source/sink parameter, radiation parameter, and Rayleigh number increase when the stretching parameter is 1.5 and 0.5 both. Velocity increases when the Eckert number along with stretching parameter is 1.5 and reverses the effect when 0.5.
- Temperature declines with non-Newtonian Casson fluid parameter and permeability parameter when the stretching parameter is 1.5 but conversely when the stretching parameter is 0.5 and the radiation parameter declines when the stretching parameters are 1.5 and 0.5. Also, temperature increases with Prandtl number, temperature gradient heat source/sink parameter, Rayleigh number, Eckert number, and the magnetic parameter when the stretching parameter is 1.5 and 0.5.
- The skin-friction coefficient improves with non-Newtonian Casson fluid parameter, magnetic parameter, permeability parameter, Prandtl number, and radiation parameter when the stretching parameter is 0.5 but reverse effect when the

Table 1 The outcomes of skin-friction coefficient and for the different values of parameters with velocity result on $\varepsilon = 0.5$ and $\varepsilon = 1.5$

									$\varepsilon = 0.5$	$\varepsilon = 1.5$
β	Mn	Ω	Pr	R	Q	Ra	Ec	Me	f″(0)	f″(0)
1 **2** ∞	0.2	0.2	25	1	0.1	0.1	0.1	1	0.58156 0.6685 0.8117925	−0.599575 −0.68954 −0.839785
1	**0** **1** **2**	0.2	25	1	0.1	0.1	0.1	1	0.56318 0.663384 0.757903	−0.576781 −0.663702 −0.7217585
1	0.2	**0** **1** **2**	25	1	0.1	0.1	0.1	1	0.56091 0.658085 0.74332	−0.57905 −0.675875 −0.76101
10	1	0.1	**1** **2** **10**	1	0.1	0.1	0.1	5	0.57987511 0.6509119 0.772362	−0.6356165 −0.701524 −0.800739
2	0.2	0.2	5	**0** **5** **10**	0.1	0.1	0.1	1	0.6077 0.61343 0.61593	−0.66177 −0.6924 −0.70135
1	1	1	5	1	**0** **0.5** **1**	0.1	0.1	1	0.70179 0.6951 0.68475	−0.7435 −0.72252 −0.68396
1	1	0.2	25	1	0.1	**0** **0.2** **0.4**	0.1	1	0.62745 0.68683 0.74651	−0.71182 −0.65255 −0.5934
1	1	0.2	25	1	0.1	0.1	**0** **0.5** **1**	1	0.912 0.8793 0.853255	−0.9761 −0.90304 −0.84485

stretching parameter is 1.5. Skin-friction coefficient diminishes with temperature gradient heat source/sink parameter and Eckert number when the stretching parameter is 0.5 but reverse effect when the stretching parameter is 1.5. Also, the skin-friction coefficient increases when increasing the Rayleigh number for stretching parameters 0.5 and 1.5.

- The local Nusselt number grows with non-Newtonian Casson fluid parameter, and permeability parameter for a stretching parameter value of 0.5 but reverse effect when the stretching parameter is 1.5. Local Nusselt number increases with magnetic parameter, Prandtl number, Rayleigh number, temperature gradient heat source/sink parameter, and Eckert number for stretching parameter values 0.5 and 1.5. Also, the local Nusselt number decreases with increasing radiation parameters for stretching parameters 0.5 and 1.5.

Table 2 The outcomes of Nusselt number for the different values of parameters with temperature effect on $\varepsilon = 0.5$ and $\varepsilon = 1.5$

									$\varepsilon = 0.5$	$\varepsilon = 1.5$
β	Mn	Ω	Pr	R	Q	Ra	Ec	Me	$\theta'(0)$	$\theta'(0)$
1 **2** ∞	0.2	0.2	5	2	0.1	0.1	0.1	2	0.71409 0.71615 0.7209	0.94209 0.93385 0.92255
2	**0** **0.5** **1**	0.2	5	2	0.1	0.1	0.1	2	0.71125 0.73298 0.78655	0.92799 0.96569 1.07745
2	0.2	**0** **2** **4**	5	2	0.1	0.1	0.1	2	0.7137 0.73465 0.75015	0.9342 0.93185 0.9313
1	0.5	1	**5** **5.3** **5.6**	0.5	0.1	0.1	0.1	0.5	1.232 1.272 1.3111	1.6981 1.7377 1.7752
2	0.2	0.2	5	**0** **0.1** **0.2**	0.1	0.1	0.1	2	0.81677 0.81339 0.80913	1.1258 1.1185 1.10942
1	1	1	2	1	**0** **0.1** **0.2**	0.1	0.1	1	0.64797 0.677 0.70785	0.84755 0.88115 0.9166
1	1	0.2	5	1	0.1	**0** **0.5** **1**	0.1	1	1.03155 1.06909 1.1099	1.49415 1.503 1.5151
1	1	0.2	25	1	0.1	0.1	**0** **1** **2**	1	0.76795 1.728765 2.43932	0.98225 2.68425 3.89372

Table 3 Justification of present work with Mabood and Das [20] of $f''(0)$ and $\theta'(0)$ for different parameters of ε and Me when $Pr = 1$, $Ra = Q = Ec = 0$ and $\beta \to \infty$

Parameters		Mabood et al.		Current results	
ε	Me	$f''(0)$	$\theta'(0)$	$f''(0)$	$\theta'(0)$
0.0	0	1.232588	−0.570465	1.232588	−0.570465
	1	1.037003	−0.361961	1.037003	−0.361961
0.5	0	0.713295	−0.692064	0.713295	−0.692064
	1	0.599090	−0.438971	0.599090	−0.438971
2.0	0	−1.887307	−0.979271	−1.887307	−0.979271
	1	−1.580484	−0.621187	−1.580484	−0.621187
5.0	0	−10.264749	−1.396355	−10.264749	−1.396355
	1	−8.5746752	−0.886425	−8.5746752	−0.886425
6.0	0	−13.774813	−1.511165	−13.774813	−1.511165
	1	−11.501531	−0.959514	−11.501531	−0.959514

References

1. Bachok N, Ishak A, Pop I (2010) Melting heat transfer in boundary layer stagnation-point flow towards a stretching/shrinking sheet. Phys Lett A 374(40):4075–4079
2. Crane LJ (1970) Flow past a stretching sheet. J Appl Math Phys 21:645–647
3. Fetecau C, Ellahi R, Khan M, Shah NA (2018) Combined porous and magnetic effects on some fundamental motions of newtonian fluids over an infinite plate. J Porous Media 21(7):589–605
4. Gbadeyan JA, Titiloye EO, Adeosun AT (2020) Effect of variable thermal conductivity and viscosity on Casson nanofluid flow with convective heating and velocity slip. Heliyon 6:1–10
5. Gireesha BJ, Shankaralingappa BM, Prasannakumar BC, Nagaraja B (2020) MHD flow and melting heat transfer of dusty Casson fluid over a stretching sheet with Cattaneo–Christov heat flux model. Int J Ambient Energy 1–9
6. Gireesha BJ, Mahanthesh B, Shivakumara IS, Eshwarappa KM (2016) Melting heat transfer in boundary layer stagnation-point flow of nanofluid toward a stretching sheet with induced magnetic field. Eng Sci Technol Int J 19(1):313–321
7. Idowu AS, Akolade MT, Abubakar JU, Falodun BO (2020) MHD free convective heat and mass transfer flow of dissipative Casson fluid with variable viscosity and thermal conductivity effects. J Taibah Univ Sci 14(1):851–862
8. Ijaz N, Zeeshan A, Bhatti MM, Ellahi R (2018) Analytical study on liquid-solid particles interaction in the presence of heat and mass transfer through a wavy channel. J Mol Liq 250:80–87
9. Jabeen K, Mushtaq M, Muntazir RMA (2020) Analysis of MHD fluids around a linearly stretching sheet in porous media with thermophoresis, radiation, and chemical reaction. Math Probl Eng 2020:1–14
10. Kala BS, Rawat MS, Kuumar A (2020) Numerical analysis of the flow of a Casson fluid in magnetic field over an inclined nonlinearly stretching surface with velocity slip in a Forchheimer porous medium. Asian Res J Math 16(7):34–58
11. Khan AA, Masood F, Ellahi R, Bhatti MM (2018) Mass transport on chemicalized fourth-grade fluid propagating peristaltically through a curved channel with magnetic effects. J Mol Liq 258:186–195
12. Kirubhashankar CK, Vaithyasubramanian S, Immanuel Y, Muniappan P (2020) Thermal effects on magneto hydrodynamic Casson liquid stream between electrically conducting plates. Int J Innov Technol Explor Eng (IJITEE) 9(4):213–217
13. Kirubhashankar CK, Ganesh S, Ismail AM (2015) Casson fluid flow and heat transfer over an unsteady porous stretching surface. Appl Math Sci 9:345–351
14. Kumar KA, Reddy JVR, Sugunamma V, Sandeep N (2019) Simultaneous solutions for mhd flow of Williamson fluid over a curved sheet with nonuniform heat source/sink. Heat Transfer Res 50(6):581–603
15. Lakshmi KB, Kumar KA, Reddy JVR, Sugunamma V (2019) Influence of nonlinear radiation and cross diffusion on MHD flow of Casson and Walters-B nanofluids past a variable thickness sheet. J Nanofluids 8:1–11
16. Li Z, Barnoon P, Toghraie D, Dehkordi RB, Afrand M (2019) Mixed convection of non-Newtonian nanofluid in an H-shaped cavity with cooler and heater cylinders filled by a porous material: two phase approach. Adv Powder Technol 30:2666–2685
17. Lund LA, Omar Z, Khan I (2019) Steady incompressible magnetohydrodynamics Casson boundary layer flow past a permeable vertical and exponentially shrinking sheet: a stability analysis. Heat Transfer—Asian Res 48(8):3538–3556
18. Lund LA, Omar Z, Khan I, Sherif ESM, Abdo HS (2020) Stability analysis of the magnetized Casson nanofluid propagating through an exponentially shrinking/stretching plate: dual solutions. Symmetry 12(7):1–19
19. Lund LA, Omar Z, Khan U, Khan I, Baleanu D, Nisar KS (2020) Stability analysis and dual solutions of micropolar nanofluid over the inclined stretching/shrinking surface with convective boundary condition. Symmetry 12:2–20

20. Mabood F, Das K (2019) Outlining the impact of melting on MHD Casson fluid flow past a stretching sheet in a porous medium with radiation. Heliyon 5(2):1–17
21. Mabood F, Das K (2016) Melting heat transfer on hydromagnetic flow of a nanofluid over a stretching sheet with radiation and second-order slip. European Phys J Plus 131(1):1–12
22. Mabood F, Mastroberardino A (2015) Melting heat transfer on MHD convective flow of a nanofluid over a stretching sheet with viscous dissipation and second order slip. J Taiwan Inst Chem Eng 57:62–68
23. Mahdy A (2018) Simultaneous impacts of MHD and variable wall temperature on transient mixed Casson nanofluid flow in the stagnation point of rotating sphere. Appl Math Mech 39(9):1327–1340
24. Mabood F, Abdel-Rahman RG, Lorenzini G (2016) Effect of melting heat transfer and thermal radiation on Casson fluid flow in porous medium over moving surface with magnetohydrodynamics. J Eng Thermophys 25(4):536–547
25. Nadeem S, Haq RU, Lee C (2012) MHD flow of a Casson fluid over an exponentially shrinking sheet. Scientia Iranica 19(6):1550–1553
26. Pushpalatha K, Sugunamma V, Reddy JR, Sandeep N (2016) Heat and mass transfer in unsteady MHD Casson fluid flow with convective boundary conditions. Int J Adv Sci Technol 91(2016):19–38
27. Qayyum M, Khan H, Khan O (2017) Slip analysis at fluid-solid interface in MHD squeezing flow of Casson fluid through porous medium. Results Phys 7:732–750
28. Salahuddin T, Siddique N, Arshad M, Tlili I (2020) Internal energy change and activation energy effects on Casson fluid. AIP Adv 10:1–11
29. Shah Z, Kumam P, Deebani W (2020) Radiative MHD Casson nanofluid flow with activation energy and chemical reaction over past nonlinearly stretching surface through entropy generation. Sci Rep 10:1–14
30. Zeeshan A, Ijaz N, Abbas T, Ellahi R (2018) The sustainable characteristic of bio-bi-phase flow of peristaltic transport of MHD Jeffrey fluid in the human body. Sustainability 10:1–17

Impact of Hall Current and Rotation on Unsteady MHD Oscillatory Dusty Fluid Flow Through Horizontal Porous Plates

R. Vijayalakshmi, A. Govindarajan, and B. Thiripura Sundari

Abstract In this paper, an attempt has been taken to study the impact of Hall current on unsteady Magnetohydrodynamics (MHD) oscillatory dusty fluid flow through horizontal rotating porous plates. On the basis of certain conditions, the momentum and energy equations are derived. The governing equations are non-dimensionalized, simplified, and solved analytically. The closed analytical form solutions for velocity and temperature are obtained. The numerical computations are presented graphically to show the salient features of various physical parameters on the fluid flow. The effect of skin friction and Nusselt number is also analysed qualitatively. Also the results obtained in this paper are compared and validated with the previous literatures.

Keywords Hall current · Rotation · Unsteady flow · MHD · Oscillatory · Dusty fluid · Porous plates

1 Introduction

In nature, the availability of pure air and water is scarce, since both are contaminated with impurities like carbon dioxide, NH, oxygen and salts, and this leads to the study of physical properties of dusty fluid. This dusty concept is used in nuclear reactor cooling, acoustics, rain erosion of guided missiles, aerosol, paint spraying, etc. Generally, the Hall current term was ignored in many physical problems, as

R. Vijayalakshmi (✉) · B. Thiripura Sundari
Department of Mathematics, SRM Institute of Science and Technology, Ramapuram, Chennai, India
e-mail: vijayalr1@srmist.edu.in

B. Thiripura Sundari
e-mail: tb6934@srmist.edu.in

A. Govindarajan
Department of Mathematics, SRM Institute of Science and Technology, Kattankulathur, Chennai, India
e-mail: govindaa@srmist.edu.in

J. Singh et al. (eds.), *Advances in Mathematical Modelling, Applied Analysis and Computation*, Lecture Notes in Networks and Systems 415,
https://doi.org/10.1007/978-981-19-0179-9_31

it marks less effect for small and moderate values of magnetic field. However, the current trend of MHD is towards a strong magnetic field, and hence the Hall current term makes a remarkable effect on the magnitude and direction of current density and consequently on the magnetic force term.

Saffman [1] studied the nature of dusty laminar flow in the absence of volume fraction. Nandkeolyar [2] made a detailed study on the unsteady convective flow of a dusty fluid moving through a vertical plate. Makinde et al. [3] studied the heat transfer of dusty fluid with Navier slip condition through a channel with variable physical properties.

Recently, the importance of MHD fluid in real-life applications was investigated by Devendra Kumar et al. [24] and Jagdev Singh et al. [25].

Tani [5] discussed the Hall effect for steady-state motion of conducting fluids. Soundalgekar et al. [6] investigated the impact of Hall and ion slip in hydromagnetic Couette flow. He [7] also extended his research with heat transfer for the same geometry.

Hazem Attia [8] analysed the impact of Hall current for an unsteady Hartmann flow. Hazem Attia [9, 10] also extended his research by varying physical properties and uniform suction/injection for the same physical configuration.

Olajuwon et al. [11] considered the impact of thermal radiation, Hall current, and heat and mass transfer on an unsteady hydromagnetic viscoelastic micropolar fluid flow through a porous channel. Singh et al. [12] studied the impact of thermal radiation and Hall current effect on mixed convection hydromagnetic flow through a vertical porous channel.

Khem Chand et al. [13] made an analysis on the influence of Hall effect and heat and mass transfer for an oscillating viscoelastic fluid with Navier slip conditions. Khem Chand [14] also worked on the impact of radiation, Hall current and chemical reaction effects on rotating hydromagnetic oscillatory dusty viscoelastic flow.

Khan et al. [15] studied the impact of Hall current for a generalized Oldroyd-B fluid. For a non-grey gas, the differential approximation for radiative transfer was given by Cogley et al. [4]. Hazem Attia [16] studied the Hall effect and heat transfer for a dusty Couette flow under exponential decaying pressure gradient.

Das et al. [17] worked on the free convective flow of nanofluid through an oscillating porous plate with Hall effects. Makinde et al. [18, 19] observed Hall effects on unsteady MHD flow with Arrhenius reaction rate through a porous channel.

Many investigations were carried out by Govindarajan et al. [20–23] to study the nature and physical properties of dusty fluid flow through various porous channels.

Also Khem Chand et al. [26] made a detailed analysis on the effect of Hall current and heat transfer on MHD oscillating dusty fluid flow through a rotating channel with porous medium.

Inspired by all works, it is found that no researcher has discussed the topic impact of Hall current and rotation on unsteady hydromagnetic dusty fluid flow through horizontal plates with porous medium. The current paper discusses this problem.

2 Mathematical Formulation

Let the fluid moves between horizontal porous plates located at $z^* = \left(-\frac{d}{2}, \frac{d}{2}\right)$ as shown in Fig. 1. The fluid is injected with velocity w_0 through the lower porous plate and simultaneously removed with the suction velocity w_0 through the upper porous plate.

The particles of dust are round in shape, non-conducting, and spread uniformly throughout the fluid. They are enough large, so that they are not coming out through the porous plates. The lower porous plate is kept at temperature T_0^* and the upper porous plate is kept at temperature T_w^* with $T_w^* > T_0^*$.

The velocities of fluid and dust particles are $\mathbf{u}\,(u, v, w)$, $\mathbf{u_d}\,(u_d, v_d, w_d)$. The magnetic field and angular velocity are $\mathbf{B}\,(0, 0, B_0)$ and $\Omega\,(0, 0, \Omega_0)$. The impact of viscous and Joule's dissipation is not considered in the energy equation. A pressure gradient changing with time and a magnetic field of strength B_0 are considered in the x^*-direction and z^*-direction, respectively. Let the magnetic Reynolds number be very small, so that the induced magnetic field is neglected.

Let the whole system be rotated with constant angular velocity Ω_0 about z^*-axis. It is necessary to obtain the velocity and temperature of fluid as well as temperature of dust particles. As the plates are long in x^*- and y^*-directions, all physical quantities are dependent only on z^* and t^* except the pressure.

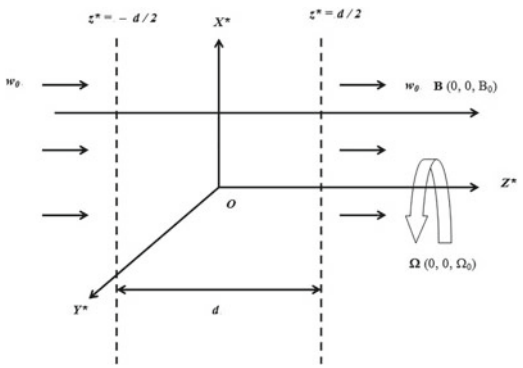

Fig. 1 Geometry of flow

Governing Equations

Fluid Phase
Momentum Equation

$$\frac{\partial u^*}{\partial t^*} + w_0 \frac{\partial u^*}{\partial z^*} - 2\,\Omega^*\,v^* = -\frac{1}{\rho}\frac{\partial P^*}{\partial x^*} + \nu \frac{\partial^2 u^*}{\partial z^{*2}} - \frac{\nu}{K^*}u^* + \frac{\sigma_e\, B_0^2\,(m\,v^* - u^*)}{\rho\,(1+m^2)} + g\,\beta_T\,(T^* - T_0^*) + \frac{K_0\,N_0\,(u_d^* - u^*)}{\rho} \tag{1}$$

$$\frac{\partial v^*}{\partial t^*} + w_0 \frac{\partial v^*}{\partial z^*} + 2\,\Omega^*\,u^* = -\frac{1}{\rho}\frac{\partial P^*}{\partial y^*} + \nu \frac{\partial^2 v^*}{\partial z^{*2}} - \frac{\nu}{K^*}\,v^* - \frac{\sigma_e\,B_0^2\,(m\,u^* + v^*)}{\rho\,(1+m^2)} + \frac{K_0\,N_0\,(v_d^* - v^*)}{\rho} \tag{2}$$

$$-\frac{1}{\rho}\frac{\partial P^*}{\partial z^*} = 0 \tag{3}$$

Energy Equation

$$\frac{\partial T^*}{\partial t^*} + w_0 \frac{\partial T^*}{\partial z^*} = \frac{k}{\rho\,C_p}\frac{\partial^2 T^*}{\partial z^{*2}} + \frac{1}{\rho\,C_p}\frac{\partial q^*}{\partial z^*} + \frac{\mu}{\rho\,C_p}\left(\frac{\partial u^*}{\partial z^*}\right)^2 + \frac{\sigma_e\,B_0^2\,(u^*)^2}{\rho} + \frac{\rho_d\,C_d\,(T_d{}^* - T^*)}{\rho\,C_p\,\gamma_T} \tag{4}$$

Here the term $\frac{\mu}{\rho\,C_p}\left(\frac{\partial u^*}{\partial z^*}\right)^2$ represents viscous dissipation, $\frac{\sigma_e\,B_0^2\,(u^*)^2}{\rho}$ represents Joule dissipation, and $\frac{\rho_d\,C_d\,(T_d{}^* - T^*)}{\rho\,C_p\,\gamma_T}$ represents the heat conduction between the fluid and dust particles.

Particle Phase
Momentum Equation

$$m_d\left[\frac{\partial u_d^*}{\partial t^*} - 2\,\Omega^*\,v_d^*\right] = K_0\,(u^* - u_d^*) \tag{5}$$

$$m_d\left[\frac{\partial v_d^*}{\partial t^*} + 2\,\Omega^*\,u_d^*\right] = K_0\,(v^* - v_d^*) \tag{6}$$

Energy Equation

$$\frac{\partial T_d^*}{\partial t^*} = -\frac{1}{\gamma_T}\,(T_d^* - T^*) \tag{7}$$

Boundary Conditions

$$u^* = v^* = {u_d}^* = v_d^* = 0,\ T^* = {T_0}^*,\ {T_d}^* = {T_0}^* \text{ at } z^* = -\frac{d}{2} \tag{8}$$

$$\left.\begin{aligned} u^* = v^* = {u_d}^* = v_d^* = 0,\ T^* &= {T_0}^* + \left({T_w}^* - {T_0}^*\right) cos\ (\omega^*\, t^*) \\ {T_d}^* &= {T_0}^* + \left({T_w}^* - {T_0}^*\right) cos\ (\omega^*\, t^*) \end{aligned}\right\}$$

$$\text{at } z^* = \frac{d}{2} \tag{9}$$

According to Cogley [4],

$$\frac{\partial q^*}{\partial z^*} = 4\ \alpha^2 \left(T^* - {T_0}^*\right) \tag{10}$$

The above set of governing equations are altered into non-dimensional form by the dimensionless parameters.

Dimensionless Parameters

$$\begin{aligned}
&x = \frac{x^*}{d},\ y = \frac{y^*}{d},\ z = \frac{z^*}{d},\ t = \frac{t^*\, w_0}{d}, \\
&\omega = \frac{\omega^*\, d}{w_0},\ u = \frac{u^*}{w_0}, v = \frac{v^*}{w_0}, \\
&u_d = \frac{{u_d}^*}{w_0},\ v_d = \frac{{v_d}^*}{w_0}, \\
&\theta = \frac{T^* - {T_0}^*}{{T_w}^* - {T_0}^*}, \theta_d = \frac{{T_d}^* - {T_0}^*}{{T_w}^* - {T_0}^*}, Da = \frac{K^*}{d^2}, \\
&s^2 = \frac{1}{Da}, M^2 = \frac{\sigma_e\ B_0^2\ d^2}{\rho\ \nu},\ P = \frac{P^*}{\rho\ w_0^2}, \\
&Pr = \frac{\nu\ \rho\ C_p}{k}, N^2 = \frac{4\ \alpha^2\ d^2}{k},\ Gr = \frac{g\ \beta_T\ ({T_w}^* - {T_0}^*)\ d^2}{\nu\ w_0}, \\
&R = \frac{K_0\ N_0\ d^2}{\rho\,\nu}, G = \frac{m_d\ \nu}{K_0\ d^2}, \\
&L_0 = \frac{d}{w_0\ \gamma_T},\ \gamma_T = \frac{3\ Pr\ \gamma_p\ C_d}{2\ C_p},\ \gamma_p = \frac{2\ \rho_s\ D^2}{9\ \mu}, \\
&\rho_s = \frac{3\ \rho_d}{4\,\pi\ D^3\ N_0},\ \Omega = \frac{\Omega^*\ d^2}{\nu},\ S = \frac{w_0\ d}{\nu}
\end{aligned} \tag{11}$$

where ρ is density of the fluid, ρ_d is mass of dust particles per unit volume of the fluid, ρ_s is density of material in the dust particles, γ_T is temperature relaxation time, γ_p is velocity relaxation time, C_d is specific heat capacity of dust particles, C_p is specific heat capacity of fluid at constant pressure, m_d is average mass of dust particles, R is particle concentration parameter, G is particle mass parameter,

$K_0 = 6\pi\rho\nu D$ Stokes' drag constant, θ is dimensionless fluid temperature function, θ_d is dimensionless dust particles temperature function, Da is Darcy number, s is porous medium shape factor term, P is pressure term, Pr is Prandtl number, N is thermal radiation parameter, Gr is Grashof number for heat transfer, S is suction parameter, and Ω is rotation parameter.

3 Solution of the Problem

Equations (1–9) are solved using Eqs. (10) and (11).

Fluid Phase

$$\frac{\partial u}{\partial t} + \frac{\partial u}{\partial z} - \frac{2\,\Omega\,v}{S} = -\frac{\partial P}{\partial x} + \frac{1}{S}\frac{\partial^2 u}{\partial z^2} - \frac{s^2}{S}\,u + \frac{M^2}{S}\frac{(m\,v-u)}{1+m^2} + \frac{Gr\,\theta}{S} + \frac{R}{S}\,(u_d-u) \tag{12}$$

$$\frac{\partial v}{\partial t} + \frac{\partial v}{\partial z} + \frac{2\,\Omega\,u}{S} = -\frac{\partial P}{\partial y} + \frac{1}{S}\frac{\partial^2 v}{\partial z^2} - \frac{s^2}{S}\,v - \frac{M^2}{S}\frac{(m\,u+v)}{1+m^2} + \frac{R}{S}\,(v_d-v) \tag{13}$$

$$\frac{\partial \theta}{\partial t} + \frac{\partial \theta}{\partial z} = \frac{1}{S\,Pr}\frac{\partial^2 \theta}{\partial z^2} + \frac{N^2}{S\,Pr}\,\theta + \frac{2\,R}{3\,S\,Pr}\,(\theta_d-\theta) \tag{14}$$

Particle Phase

$$\frac{\partial u_d}{\partial t} - \frac{2\,\Omega}{S}\,v_d = \frac{1}{G\,S}\,(u-u_d) \tag{15}$$

$$\frac{\partial v_d}{\partial t} + \frac{2\,\Omega}{S}\,u_d = \frac{1}{G\,S}\,(v-v_d) \tag{16}$$

$$\frac{\partial \theta_d}{\partial t} = -L_0\,(\theta_d-\theta) \tag{17}$$

Boundary Conditions

$$u=0,\ v=0,\ u_d=0,\ v_d=0,\ \theta=0,\ \theta_d=0 \text{ at } z=-\frac{1}{2} \tag{18}$$

$$u=0,\ v=0,\ u_d=0,\ v_d=0,\ \theta=\cos(\omega\,t),\ \theta_d=\cos(\omega\,t) \text{ at } z=\frac{1}{2} \tag{19}$$

Since the fluid flows under the pressure gradient varying with time along the x^*-axis, let $-\frac{\partial P^*}{\partial x^*} = A\, e^{i\,\omega\, t}$; $\frac{\partial P^*}{\partial y^*} = 0$, where A is the amplitude of pressure gradient. Since $\frac{\partial P^*}{\partial z^*} = 0$, the fluid pressure is constant along the axis of rotation.
Introduce the complex velocities for fluid and dust particles of the form $F = u + i\ v$ and $F_d = u_d + i\ v_d$ where $i = \sqrt{-1}$.
Equations (12) & (13) and (15) & (16) can be combined into following equations:

Fluid Phase

$$\frac{\partial F}{\partial t} + \frac{\partial F}{\partial z} + \frac{2\ \Omega\ i\ F}{S} = -\frac{\partial P}{\partial x} + \frac{1}{S}\ \frac{\partial^2 F}{\partial z^2} - \frac{s^2}{S}\ F - \frac{M^2\ F}{S\ (1+m^2)}\ (1 + i\ m) + \frac{Gr\ \theta}{S} + \frac{R}{S}\ (F_d - F) \tag{20}$$

$$\frac{\partial \theta}{\partial t} + \frac{\partial \theta}{\partial z} = \frac{1}{S\ Pr}\ \frac{\partial^2 \theta}{\partial z^2} + \frac{N^2}{S\ Pr}\ \theta + \frac{2\ R}{3\ S\ Pr}\ (\theta_d - \theta) \tag{21}$$

Particle Phase

$$\frac{\partial F_d}{\partial t} + \frac{2\ \Omega\ i\ F_d}{S} = \frac{1}{G\ S}\ (F - F_d) \tag{22}$$

$$\frac{\partial \theta_d}{\partial t} = -L_0\ (\theta_d - \theta) \tag{23}$$

Boundary Conditions

$$F = 0,\ F_d = 0,\ \theta = 0,\ \theta_d = 0,\ \text{ at } z = -\frac{1}{2} \tag{24}$$

$$F = 0,\ F_d = 0,\ \theta = cos\ (\omega\ t)\ ,\ \theta_d = cos\ (\omega\ t)\ \text{ at } z = \frac{1}{2} \tag{25}$$

For an oscillatory flow, let

$$F(z,t) = F_0\,(z)\ e^{i\,\omega\, t};\ \ F_d\,(z,t) = F_{d_0}(z)\ e^{i\,\omega\, t};$$
$$\theta\,(z,t) = \theta_0\,(z)\ e^{i\,\omega\, t};\ \ \theta_d\,(z,t) = \theta_{d_0}(z)\ e^{i\,\omega\, t} \tag{26}$$

Equations (20–25) are solved using Eq. (26).

Fluid Phase

$$\frac{d^2F_0}{dz^2} - S\,\frac{dF_0}{dz} - m_2^2\,F_0 = -A\,S - Gr\,\theta_0 \tag{27}$$

$$\frac{d^2\theta_0}{dz^2} - S\,Pr\,\frac{d\theta_0}{dz} + m_1^2\,\theta_0 = 0 \tag{28}$$

Particle Phase

$$F_{d_0} = \left(\frac{1}{1 + 2\,i\,\Omega\,G + i\,\omega\,G\,S}\right)\,F_0 \tag{29}$$

$$\theta_{d_0} = \left(\frac{L_0}{L_0 + i\,\omega}\right)\,\theta_0 \tag{30}$$

Boundary Conditions

$$F_0 = 0,\, F_{d_0} = 0,\, \theta_0 = 0,\, \theta_{d_0} = 0,\ \text{at } z = -\frac{1}{2} \tag{31}$$

$$F_0 = 0,\, F_{d_0} = 0,\, \theta_0 = 1,\, \theta_{d_0} = 1 \text{ at } z = \frac{1}{2} \tag{32}$$

where the constants are given by

$$m_1^2 = N^2 - \frac{2\,R}{3} + \frac{2\,R}{3}\left(\frac{L_0}{L_0 + i\,\omega}\right) - i\,\omega\,S\,Pr \tag{33}$$

$$m_2^2 = s^2 + \frac{M^2\,(1 + i\,m)}{1 + m^2} + R + i\,\omega\,S + 2\,\Omega\,i - \frac{1}{1 + 2\,i\,\Omega\,G + i\,\omega\,G\,S} \tag{34}$$

Equations (27–30) are solved using Eqs. (31) and (32) to get the temperature and velocity of fluid as well as dust particles, respectively.

Temperature

Fluid Phase

$$\theta\,(z, t) = \left(\frac{e^{-\frac{t_2}{2}}\,e^{t_1\,z} - e^{-\frac{t_1}{2}}\,e^{t_2\,z}}{2\,\sin h\left(\frac{t_1 - t_2}{2}\right)}\right)e^{i\,\omega\,t} \tag{35}$$

Particle Phase

$$\theta_d\,(z,t) = \left(\frac{L_0}{L_0 + i\ \omega}\right)\theta\,(z,t) \tag{36}$$

Velocity

Fluid Phase

$$F\,(z,t) = C_1\ e^{t_3\ z} + C_2\ e^{t_4\ z} + \frac{A\ S}{m_2^2} - \frac{Gr}{2\ \sin h\left(\dfrac{t_1 - t_2}{2}\right)}\left[\frac{e^{-\frac{t_2}{2}}\ e^{t_1\ z}}{t_1^2 - S\ t_1 - m_2^2} - \frac{e^{-\frac{t_1}{2}}\ e^{t_2\ z}}{t_2^2 - S\ t_2 - m_2^2}\right] e^{i\ \omega\ t} \tag{37}$$

Particle Phase

$$F_d\,(z,t) = \left(\frac{1}{1 + 2\ i\ \Omega\ G + i\ \omega\ G\ S}\right)\ F\,(z,t) \tag{38}$$

where

$$t_1 = \frac{S\ Pr + \sqrt{(S\ Pr)^2 - 4\ m_1^2}}{2},$$

$$t_2 = \frac{S\ Pr - \sqrt{(S\ Pr)^2 - 4\ m_1^2}}{2},$$

$$t_3 = \frac{S + \sqrt{S^2 + 4\ m_2^2}}{2},\ t_4 = \frac{S - \sqrt{S^2 + 4\ m_2^2}}{2},$$

$$t_5 = -\frac{A\ S}{m_2^2},\ t_6 = \frac{Gr}{2\ \sin h\left(\dfrac{t_1 - t_2}{2}\right)},$$

$$t_7 = e^{-\left(\frac{t_1 + t_2}{2}\right)},\ t_8 = e^{\left(\frac{t_1 - t_2}{2}\right)},\ t_9 = e^{-\left(\frac{t_1 - t_2}{2}\right)},$$

$$t_{10} = \frac{1}{t_1^2 - S\ t_1 - m_2^2},\ t_{11} = \frac{1}{t_2^2 - S\ t_2 - m_2^2},$$

$$C_1 = \frac{(t_5 + t_6\ t_7\ t_{10} - t_6\ t_7\ t_{11})\ e^{\frac{t_4}{2}} - (t_5 + t_6\ t_8\ t_{10} - t_6\ t_9\ t_{11})\ e^{-\frac{t_4}{2}}}{e^{-\frac{t_3}{2}}\ e^{\frac{t_4}{2}} - e^{-\frac{t_4}{2}}\ e^{\frac{t_3}{2}}}$$

$$C_2 = \frac{(t_5 + t_6\ t_8\ t_{10} - t_6\ t_9\ t_{11})\ e^{-\frac{t_3}{2}} - (t_5 + t_6\ t_7\ t_{10} - t_6\ t_7\ t_{11})\ e^{\frac{t_3}{2}}}{e^{-\frac{t_3}{2}} e^{\frac{t_4}{2}} - e^{-\frac{t_4}{2}}\ e^{\frac{t_3}{2}}}$$

Skin Friction

Fluid Phase

$$\tau = \left[\mu \frac{\partial F}{\partial z}\right] \quad \text{at} \quad z = \left(-\frac{1}{2}, \frac{1}{2}\right). \tag{39}$$

$$\tau = \mu \left(C_1\, t_3\, e^{t_3\, z} + C_2\, t_4\, e^{t_4\, z} - \frac{Gr}{2\, \sin h\left(\frac{t_1 - t_2}{2}\right)} \left[\frac{t_1\, e^{-\frac{t_2}{2}}\, e^{t_1\, z}}{t_1^2 - S\, t_1 - m_2^2} - \frac{t_2\, e^{-\frac{t_1}{2}}\, e^{t_2\, z}}{t_2^2 - S\, t_2 - m_2^2}\right]\right) e^{i\, \omega\, t} \tag{40}$$

Particle Phase

$$\tau_d = \left[\mu \frac{\partial F_d}{\partial z}\right] \quad \text{at} \quad z = \left(-\frac{1}{2}, \frac{1}{2}\right). \tag{41}$$

$$\tau_d = \mu \left(\frac{1}{1 + 2\, i\, \Omega\, G + i\, \omega\, G\, S}\right) \left(C_1\, t_3\, e^{t_3\, z} + C_2\, t_4\, e^{t_4\, z} - \frac{Gr}{2\, \sin h\left(\frac{t_1 - t_2}{2}\right)} \left[\frac{t_1\, e^{-\frac{t_2}{2}}\, e^{t_1\, z}}{t_1^2 - S\, t_1 - m_2^2} - \frac{t_2\, e^{-\frac{t_1}{2}}\, e^{t_2\, z}}{t_2^2 - S\, t_2 - m_2^2}\right]\right) e^{i\, \omega\, t} \tag{42}$$

Nusselt Number

Fluid Phase

$$Nu = -\left[\frac{\partial \theta}{\partial z}\right] \quad \text{at} \quad z = \left(-\frac{1}{2}, \frac{1}{2}\right). \tag{43}$$

$$Nu = -\left(\frac{t_1\, e^{-\frac{t_2}{2}}\, e^{t_1\, z} - t_2\, e^{-\frac{t_1}{2}}\, e^{t_2\, z}}{2\, \sin h\left(\frac{t_1 - t_2}{2}\right)} \right) e^{i\, \omega\, t} \quad \text{at} \quad z = \left(-\frac{1}{2}, \frac{1}{2}\right) \tag{44}$$

Particle Phase

$$Nu = -\left[\frac{\partial \theta_d}{\partial z}\right] \quad \text{at} \quad z = \left(-\frac{1}{2}, \frac{1}{2}\right). \tag{45}$$

$$Nu = -\left(\frac{L_0}{L_0 + i\ \omega}\right)\left(\frac{t_1\ e^{-\frac{t_2}{2}}\ e^{t_1\ z} - t_2\ e^{-\frac{t_1}{2}}\ e^{t_2\ z}}{2\ \sin h\left(\frac{t_1 - t_2}{2}\right)}\right) e^{i\ \omega\ t} \quad \text{at} \quad z = \left(-\frac{1}{2}, \frac{1}{2}\right) \tag{46}$$

4 Graphical Results and Discussions

The results derived by the analytical method are graphically plotted using the software MATLAB R2021b. The following parameter values are used to plot all graphs in this paper as the fluid under consideration is mixed convective laminar dusty fluid flow: $1 \leq \mathrm{Gr} \leq 5, 1 \leq \mathrm{M} \leq 5, 2.7 \leq \mathrm{N} \leq 3.1, 5 \leq \mathrm{G} \leq 25, 5 \leq \mathrm{R} \leq 25, 0 \leq \mathrm{L}_0 \leq 20, 1 \leq \mathrm{s} \leq 5, -3 \leq \mathrm{S} \leq 3, 0.5 \leq \mathrm{A} \leq 2.5, 1 \leq \omega \leq 5, 0.5 \leq \mathrm{t} \leq 2.5, 5 \leq \mathrm{m} \leq 25, 5 \leq \Omega \leq 25$. Prandtl number is taken as Pr = 0.71 that corresponds to air at 20° C. For each parameter, the graphs are drawn to show the effect of non-linear terms.

Figures 2, 3, 4, 5, 6, 7, 8, 9, 10, 11, 12, 13, 14 demonstrate the impact of different parameters on velocity of fluid as well as velocity of dust particles. The nature of the partial differential equation related to velocity is parabolic. Also the velocity profiles of fluid and dust particles attain utmost value in the centre of the plate and attain least value near the walls of the plate, satisfying the prescribed boundary conditions.

Figures 15, 16, 17, 18, 19, 20 show the impact of various physical parameters on temperature of fluid as well as temperature of dust particles. It is also noted that the nature of the curve showing temperature profiles is also parabolic. Moreover, the temperature profiles of fluid and temperature profiles of dust particles reach its maximum value in the centre of the plate ($z = 0$).

The skin friction coefficient (SFC) and the rate of heat transfer for fluid and dust particles by varying various pertinent parameters are tabulated. Tables 1, 2, 3, 4.

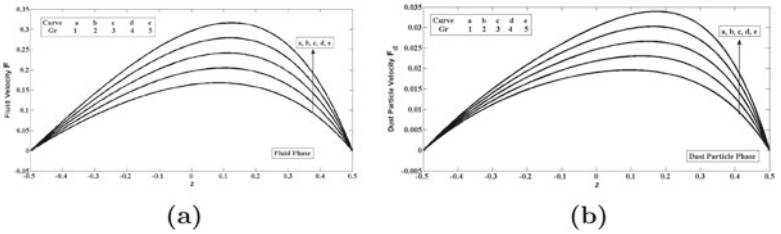

Fig. 2 Impact of Gr on **a** Velocity of fluid (F), **b** Velocity of dust particles (F_d), with $Pr = 0.71$; $M = 1$; $N = 1$; $G = 1$; $R = 1.5$; $L_0 = 1$; $s = 1$; $S = 1.5$; $m = 1$; $\Omega = 5$; $A = 1$; $\omega = 1$; $t = 0.5$ While enhancing the value of Grashof number for heat transfer (Gr), the velocity of fluid and velocity of dust particles increase gradually. It is clear that Gr has significant effect on velocity of fluid as well as velocity of dust particles. This is due to buoyancy force

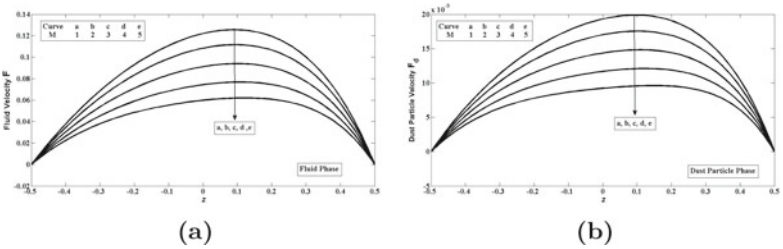

Fig. 3 Impact of M on **a** F, **b** F_d, with $Pr = 0.71$; $Gr = 1$; $N = 1$; $G = 1$; $R = 1.5$; $L_0 = 1$; $s = 1$; $S = 1.5$; $m = 1$; $\Omega = 5$; $A = 1$; $\omega = 1$; $t = 0.5$ Increase in the value of Hartmann number (M) decreases the velocity of fluid as well as velocity of dust particles evenly. This is due to the transverse magnetic field intensity, which gives rise to a resistive force called Lorentz force. This force slows down the motion. It is clear that M has significant effect on velocity of fluid as well as velocity of dust particles. This result coincides with the result obtained by Khem Chand et al. [26] for the same flow geometry without porous medium parameter and heat transfer effects

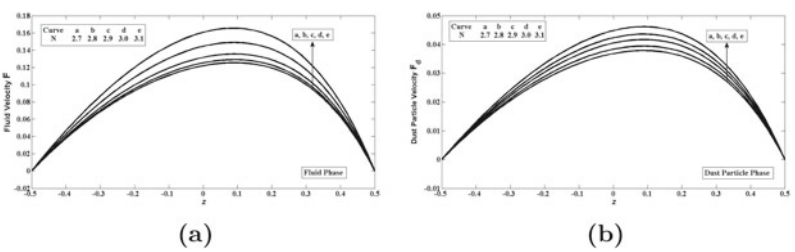

Fig. 4 Impact of N on **a** F, **b** F_d, with $Pr = 0.71$; $Gr = 1$; $M = 1$; $G = 1$; $R = 1.5$; $L_0 = 1$; $s = 1$; $S = 1.5$; $m = 1$; $\Omega = 5$; $A = 1$; $\omega = 1$; $t = 0.5$. Increase in the value of radiation parameter (N) increases the velocity of fluid as well as velocity of dust particles. It is observed from the figures that N shows significant effect on velocity of fluid as well as velocity of dust particles

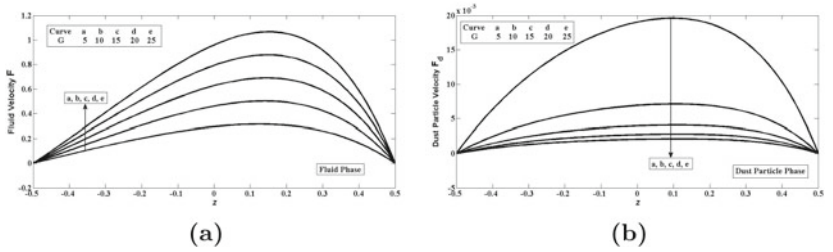

Fig. 5 Impact of G on **a** F, **b** F_d, with $Pr = 0.71$; $Gr = 1$; $M = 1$; $N = 1$; $R = 1.5$; $L_0 = 1$; $s = 1$; $S = 1.5$; $m = 1$; $\Omega = 5$; $A = 1$; $\omega = 1$; $t = 0.5$. While augmenting the value of particle mass parameter (G), it is found that the velocity of fluid increases uniformly. But, the velocity of dust particles decreases rapidly. G has remarkable effect on velocity of fluid as well as velocity of dust particles

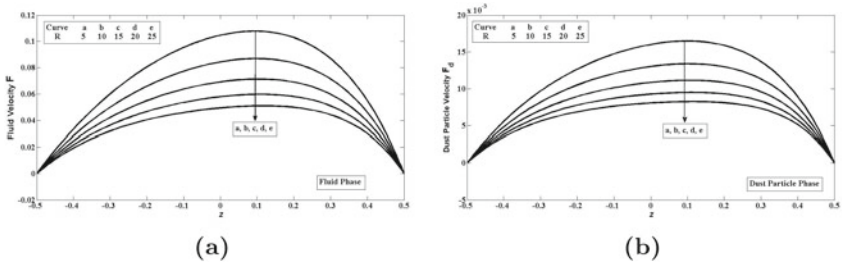

Fig. 6 Impact of R on **a** F, **b** F_d, with $Pr = 0.71$; $Gr = 1$; $M = 1$; $N = 1$; $G = 1$; $L_0 = 1$; $s = 1$; $S = 1.5$; $m = 1$; $\Omega = 5$; $A = 1$; $\omega = 1$; $t = 0.5$. Rise in the value of particle concentration parameter (R) decreases the velocity of fluid as well as velocity of dust particles gently. R has major impact on velocity of fluid as well as velocity of dust particles. This fact coincides with the result of Khem Chand et al. [26] for the same flow geometry without porous medium parameter and heat transfer effects

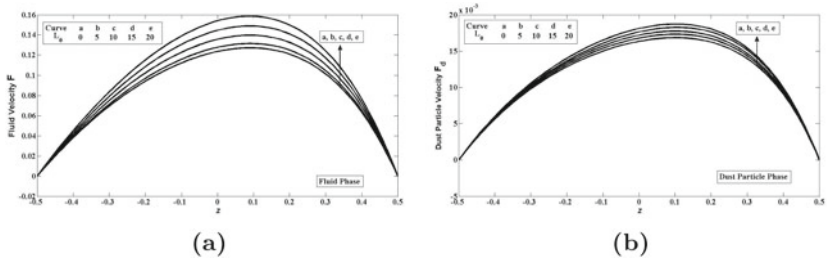

Fig. 7 Impact of L_0 on **a** F, **b** F_d, with $Pr = 0.71$; $Gr = 1$; $M = 1$; $N = 1$; $G = 1$; $R = 1.5$; $s = 1$; $S = 1.5$; $m = 1$; $\Omega = 5$; $A = 1$; $\omega = 1$; $t = 0.5$. It is noteworthy to mention that an increase in the value of temperature relaxation time parameter (L_0) increases the velocity of fluid as well as velocity of dust particles. L_0 has major impact on velocity of fluid as well as velocity of dust particles. This result coincides with the observation done by Khem Chand et al. [26] for the same flow geometry without porous medium parameter and heat transfer effects

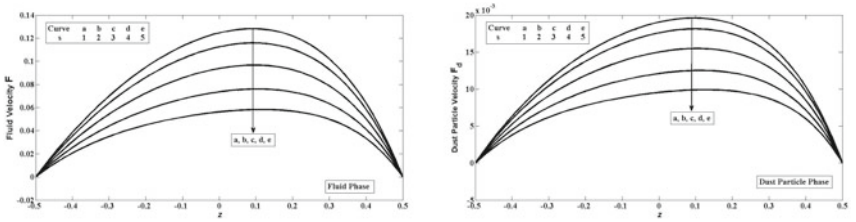

Fig. 8 Impact of s on **a** F, **b** F_d, with $Pr = 0.71$; $Gr = 1$; $M = 1$; $N = 1$; $G = 1$; $R = 1.5$; $L_0 = 1$; $S = 1.5$; $m = 1$; $\Omega = 5$; $A = 1$; $\omega = 1$; $t = 0.5$. It is noted that the velocity of fluid and velocity of dust particles decrease steadily for an increase in the value of porous medium shape factor (s). s has considerable impact on velocity of fluid as well as velocity of dust particles

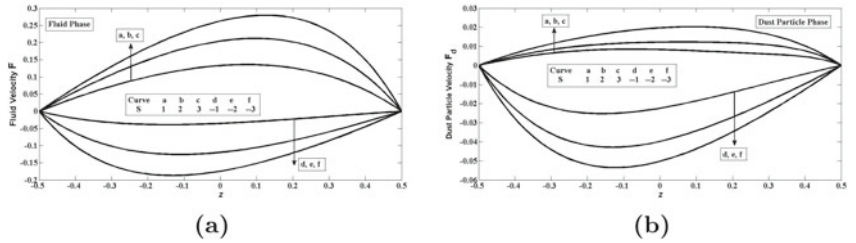

Fig. 9 Impact of S on **a** F, **b** F_d, with $Pr = 0.71$; $Gr = 1$; $M = 1$; $N = 1$; $G = 1$; $R = 1.5$; $L_0 = 1$; $s = 1$; $m = 1$; $\Omega = 5$; $A = 1$; $\omega = 1$; $t = 0.5$. It is evident that the velocity of fluid and velocity of dust particles increase for positive values of suction/injection parameter (S), decrease for negative values. S has remarkable impact on velocity of fluid as well as velocity of dust particles

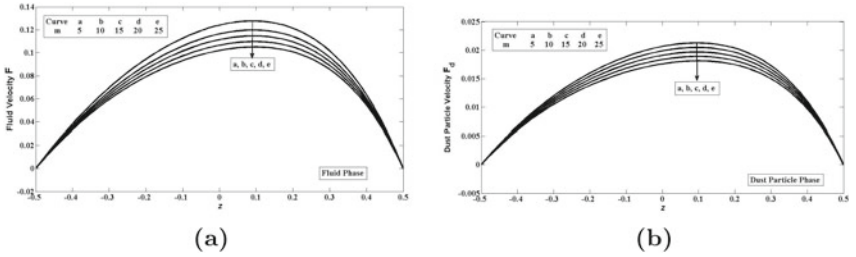

Fig. 10 Impact of m on **a** F, **b** F_d, with $Pr = 0.71$; $Gr = 1$; $M = 1$; $N = 1$; $G = 1$; $R = 1.5$; $L_0 = 1$; $s = 1$; $S = 1.5$; $\Omega = 5$; $A = 1$; $\omega = 1$; $t = 0.5$. Rise in the value of Hall parameter (m) decreases the velocity of fluid as well as velocity of dust particles uniformly. m has significant influence on velocity of fluid as well as velocity of dust particles. This result agrees with Khem Chand et al. [26] for the same flow geometry without porous medium parameter and heat transfer effects

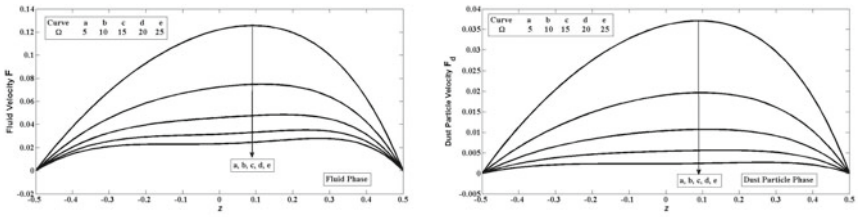

Fig. 11 Impact of Ω on **a** F, **b** F_d, with $Pr = 0.71$; $Gr = 1$; $M = 1$; $N = 1$; $G = 1$; $R = 1.5$; $L_0 = 1$; $s = 1$; $S = 1.5$; $m = 1$; $A = 1$; $\omega = 1$; $t = 0.5$. Increase in the value of rotation parameter (Ω) decreases the velocity of fluid as well as velocity of dust particles. Ω makes notable change on velocity of fluid as well as velocity of dust particles

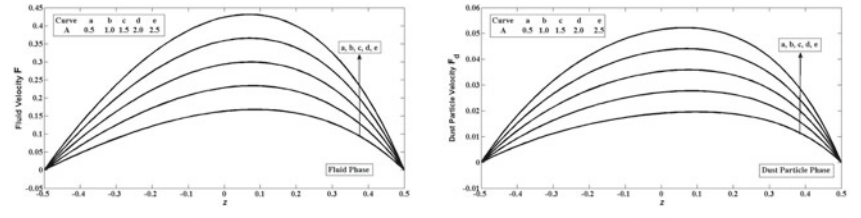

Fig. 12 Impact of A on **a** F, **b** F_d, with $Pr = 0.71$; $Gr = 1$; $M = 1$; $N = 1$; $G = 1$; $R = 1.5$; $L_0 = 1$; $s = 1$; $S = 1.5$; $m = 1$; $\Omega = 5$; $\omega = 1$; $t = 0.5$. The rise in the value of amplitude of pressure gradient (A) increases the velocity of fluid as well as velocity of dust particles gradually. A has major impact on the velocity of fluid as well as velocity of dust particles. This observation adapts with the earlier results of Khem Chand et al. [26] for the same flow geometry without porous medium parameter and heat transfer effects

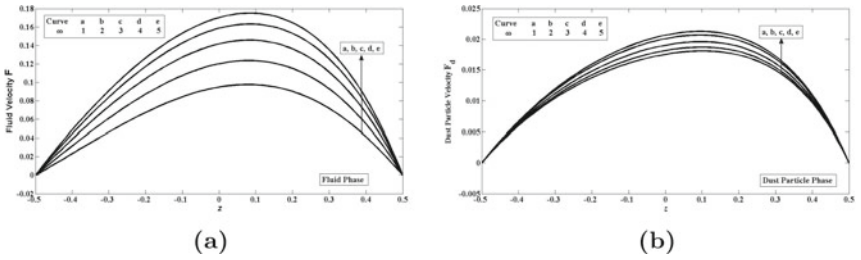

Fig. 13 Impact of ω on **a** F, **b** F_d, with $Pr = 0.71$; $Gr = 1$; $M = 1$; $N = 1$; $G = 1$; $R = 1.5$; $L_0 = 1$; $s = 1$; $S = 1.5$; $m = 1$; $\Omega = 5$; $A = 1$; $t = 0.5$. Increase in the value of frequency of oscillation parameter (ω) rises the velocity of fluid rapidly when compared to that of dust particles. ω has major impact on the velocity of fluid as well as velocity of dust particles

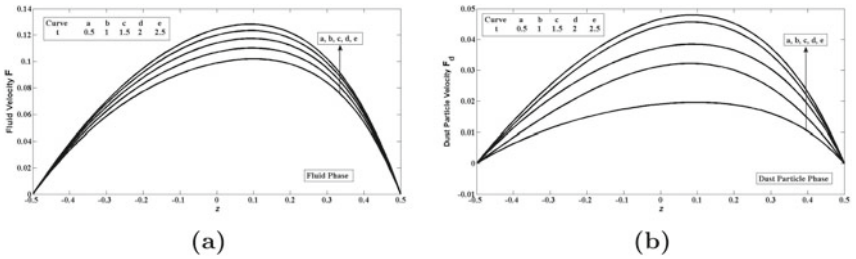

Fig. 14 Impact of t on **a** F, **b** F_d, with $Pr = 0.71$; $Gr = 1$; $M = 1$; $N = 1$; $G = 1$; $R = 1.5$; $L_0 = 1$; $s = 1$; $S = 1.5$; $m = 1$; $\Omega = 5$; $A = 1$; $\omega = 1$. Increase in the value of time (t) uniformly increases the velocity of fluid than that of dust particles. t has remarkable impact on the velocity of fluid as well as velocity of dust particles

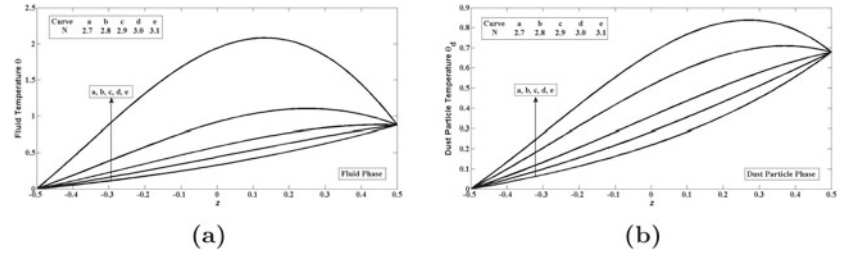

Fig. 15 Impact of N on **a** Temperature of fluid (θ), **b** Temperature of dust particles (θ_d), with $Pr = 0.71$; $R = 1.5$; $L_0 = 1$; $S = 1.5$; $\omega = 1$; $t = 0.5$. It is obvious that for an increase in the value of radiation parameter (N), the temperature of fluid increases rapidly compared to that of dust particles. N has major impact on temperature of fluid as well as temperature of dust particles

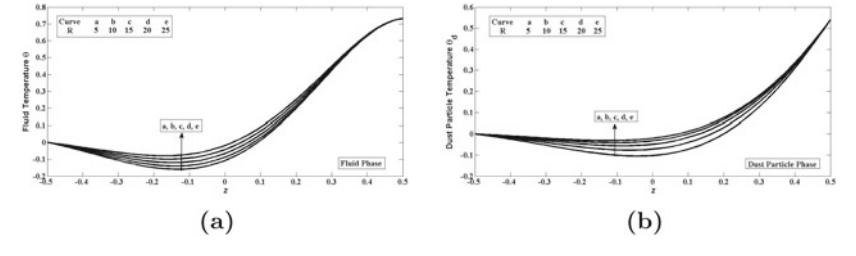

Fig. 16 Impact of R on **a** θ, **b** θ_d, with $Pr = 0.71$; $N = 1$; $L_0 = 1$; $S = 1.5$; $\omega = 1$; $t = 0.5$ It is evident that the temperature of fluid and temperature of dust particles increase for an increase in the value of particle concentration parameter (R). R has significant effect on temperature of fluid as well as temperature of dust particles. This fact coincides with the result of Khem Chand et al. [26] for the same flow geometry without porous medium parameter and heat transfer effects

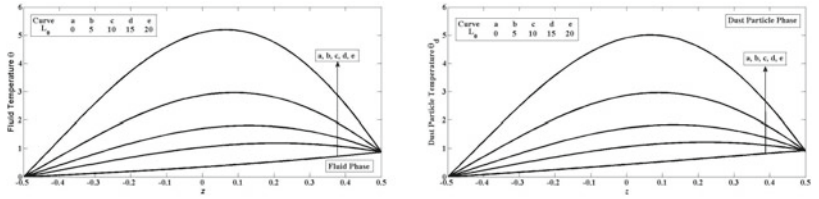

Fig. 17 Impact of L_0 on **a** θ, **b** θ_d, with $Pr = 0.71$; $N = 1$; $R = 1.5$; $S = 1.5$; $\omega = 1$; $t = 0.5$. It is noted that the temperature of fluid and temperature of dust particles increase gradually for an increase in the value of temperature relaxation time parameter (L_0). L_0 has similar influence on temperature of fluid as well as temperature of dust particles. This result consents with Khem Chand et al. [26] for the same flow geometry without porous medium parameter and heat transfer effects

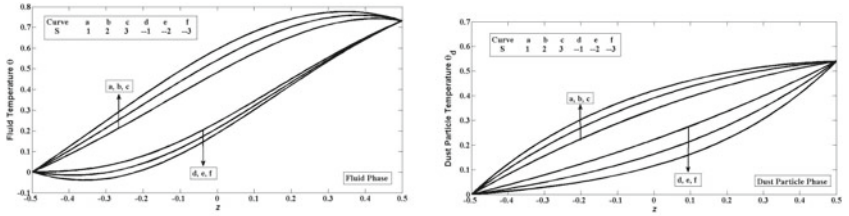

Fig. 18 Impact of S on **a** θ, **b** θ_d, with $Pr = 0.71$; $N = 1$; $R = 1.5$; $L_0 = 1$; $\omega = 1$; $t = 0.5$. It is known that the temperature of fluid and temperature of dust particles increase for positive values of suction/injection parameter (S), decrease for negative values. S plays a vital role on temperature of fluid as well as temperature of dust particles

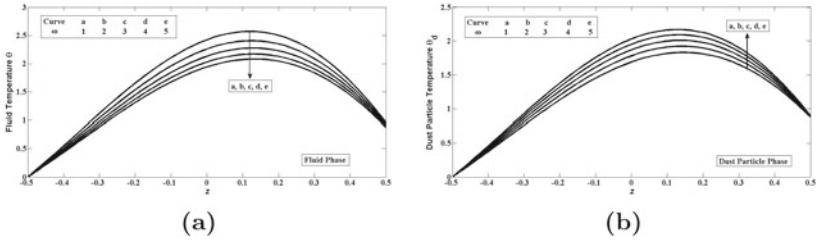

Fig. 19 Impact of ω on **a** θ, **b** θ_d, with $Pr = 0.71$; $N = 1$; $R = 1.5$; $L_0 = 1$; $S = 1.5$; $t = 0.5$. It is noted that rise in the value of frequency of oscillation parameter (ω) decreases the temperature of fluid, whereas an opposite effect is seen for the temperature of dust particles. ω has major effect on temperature of fluid as well as temperature of dust particles

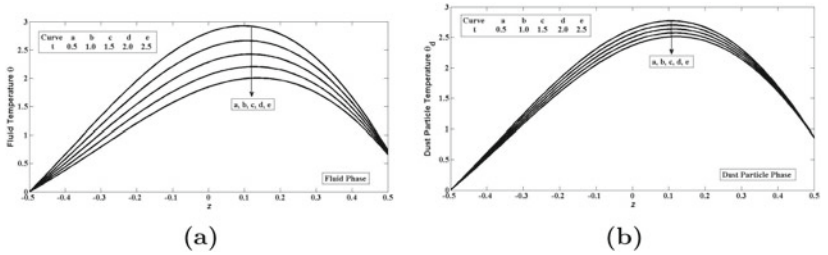

Fig. 20 Impact of t on **a** θ, **b** θ_d, with $Pr = 0.71$; $N = 1$; $R = 1.5$; $L_0 = 1$; $S = 1.5$; $\omega = 1$. As time (t) increases, the temperature of fluid decreases gradually compared to that of dust particles. t plays a significant role on temperature of fluid as well as temperature of dust particles

5 Tables and Discussions

It is clear from Table 1 that as time (t) increases, the SFC for fluid and dust particles decreases at all positions across the plates, maximum at the lower plate ($z = -0.5$) and minimum at the upper plate ($z = 0.5$) and increases along the lower plate ($z = -0.5$) up to the middle plate ($z = 0$) and then decreases along the upper plate ($z = 0.5$).

It is notable* from Table 2 that by varying particle concentration parameter (R) and particle mass parameter (G), the SFC for fluid and dust particles decreases at all positions across the plates, maximum at the lower plate ($z = -0.5$) and minimum at the upper plate ($z = 0.5$) and decreases along the lower plate ($z = -0.5$) up to the middle plate ($z = 0$) and then increases along the upper plate ($z = 0.5$).

It is seen from Table 3 that as time (t) increases, the rate of heat transfer for fluid and dust particles increases at all positions across the plates, minimum at the lower plate ($z = -0.5$) and maximum at the upper plate ($z = 0.5$) and decreases along the lower plate ($z = -0.5$) up to the middle plate ($z = 0$) and then increases along the upper plate ($z = 0.5$).

Table 1 SFC for fluid phase (τ) and dust particle phase (τ_d) by varying t with $Pr = 0.71$; $Gr = 1$; $M = 1$; $N = 1$; $G = 1$; $R = 1.5$; $L_0 = 1$; $s = 1$; $S = 1.5$; $m = 1$; $\Omega = 5$; $A = 1$; $\omega = 1$

t	Fluid phase			Dust particle phase		
	τ at $z = -0.5$	τ at $z = 0$	τ at $z = 0.5$	τ_d at $z = -0.5$	τ_d at $z = 0$	τ_d at $z = 0.5$
0.1	0.4190	0.0764	−0.7482	0.0209	0.0026	−0.0403
0.2	0.4239	0.0777	−0.7560	0.0341	0.0050	−0.0636
0.3	0.4246	0.0780	−0.7562	0.0469	0.0074	−0.0863
0.4	0.4270	0.0783	−0.7579	0.0592	0.0098	−0.1082
0.5	0.4332	0.0790	−0.7589	0.0710	0.0120	−0.1290

Table 2 SFC for fluid phase (τ) and dust particle phase (τ_d) by varying R and G with $Pr = 0.71$; $Gr = 1$; $M = 1$; $N = 1$; $L_0 = 1$; $s = 1$; $S = 1.5$; $m = 1$; $\Omega = 5$; $A = 1$; $\omega = 1$, $t = 0.6$

R	G	Fluid phase			Dust particle phase		
		τ at $z = -0.5$	τ at $z = 0$	τ at $z = 0.5$	τ_d at $z = -0.5$	τ_d at $z = 0$	τ_d at $z = 0.5$
1	1	0.4132	0.0770	−0.7341	0.0710	0.0120	−0.1290
2	1	0.3853	0.0709	−0.6868	0.0679	0.0112	−0.1235
3	1	0.3610	0.0656	−0.6457	0.0652	0.0105	−0.1185
3	2	0.3597	0.0654	−0.6434	0.0259	0.0040	−0.0473
3	3	0.3594	0.0653	−0.6430	0.0154	0.0023	−0.0283

Table 3 Nusselt number (Nu) for fluid phase and dust particle phase by varying t with $Pr = 0.71$; $N = 1$; $R = 1.5$; $L_0 = 1$; $S = 1.5$; $\omega = 1$

t	Fluid phase			Dust particle phase		
	Nu at $z = -0.5$	Nu at $z = 0$	Nu at $z = 0.5$	Nu at $z = -0.5$	Nu at $z = 0$	Nu at $z = 0.5$
0.1	−1.0202	−1.0117	−0.1974	−0.3864	−0.2828	−0.2531
0.2	−1.0398	−1.0284	−0.1057	− 0.4478	−0.4407	−0.2149
0.3	−1.0477	−1.0332	−0.0179	−0.5046	−0.4921	−0.1714
0.4	−1.0490	−1.0463	−0.0170	−0.5564	−0.5367	−0.0823
0.5	−1.0589	−1.0579	−0.0152	−0.6027	−0.5739	−0.0079

Table 4 Nusselt number (Nu) for fluid phase and dust particle phase by varying L_0 and Pr with $N = 1$; $R = 1.5$; $S = 1.5$; $\omega = 1$, $t = 0.6$

L_0	Pr	Fluid phase			Dust particle phase		
		Nu at $z = -0.5$	Nu at $z = 0$	Nu at $z = 0.5$	Nu at $z = -0.5$	Nu at $z = 0$	Nu at $z = -0.5$
0.1	0.71	0.9272	1.0577	1.1269	0.0336	0.0564	0.0761
0.2	0.71	0.9352	1.0622	1.1411	0.0799	0.1288	0.1575
0.3	0.71	0.9456	1.0676	1.1694	0.1368	0.1924	0.2356
0.3	1.0	1.1205	1.0755	1.3575	0.2880	0.2141	0.3534
0.3	6.7	1.1305	1.0787	1.3644	0.3000	0.3374	2.2299

It is evident from Table 4 that by varying temperature relaxation time parameter (L_0) and Prandtl number (Pr), the rate of heat transfer for fluid and dust particles increases at all positions across the plates, minimum at the lower plate ($z = -0.5$) and maximum at the upper plate ($z = 0.5$) and increases along the ends of the plate.

6 Conclusion

Based on the above findings, the following results are obtained:

- Increase in radiation parameter (N) and temperature relaxation time parameter (L_0) enhances the velocity and temperature of fluid as well as temperature of dust particles.
- Increase in Grashof number (Gr), amplitude of pressure gradient (A), frequency of oscillation (ω) and time (t) increases the velocity of fluid as well as velocity of dust particles.
- Increase in Hartmann number (M), particle concentration parameter (R), porous medium shape factor (s), Hall parameter (m) and rotation parameter (Ω) decreases the velocity of fluid and dust particles.
- Increase in particle mass parameter (G) increases the velocity of fluid whereas it shows a reverse trend for dust particles.
- Increase in frequency of oscillation (ω) decreases the temperature of fluid, but increases the temperature of dust particles.
- Increase in time (t) decreases the temperature of fluid as well as temperature of dust particles.
- Positive values of suction/injection parameter (S) increase the velocity and temperature of fluid as well as temperature of dust particles, but an opposite effect is observed for negative values.
- The skin friction (shear stress) coefficient decreases at all positions across the plates for fluid and dust particles.
- The rate of heat transfer increases at all positions across the plates for fluid and dust particles.

Limiting Case: In the absence of porous medium parameter ($K^* \to 0$) and heat transfer $\left((T^* - T_0^*) \to 0\right)$, the results obtained in this paper coincide with those of Khem Chand et al. [26] for horizontal porous plates.

References

1. Saffman PG (1962) On the stability of Laminar Fow of a dusty gas. J Fluid Mech 13:120–128
2. Nandkeolyar R, Seth GS, Makinde OD, Sibanda P, Ansari MS (2013) Unsteady hydromagnetic natural convection flow of a dusty fluid past an impulsively moving vertical plate with ramped temperature in the presence of thermal radiation. ASME J Appl Mech 80(1–9):061003
3. Makinde OD, Chinyoka T (2010) MHD transient flows and heat transfer of dusty fluid in a channel with variable physical properties and Navier slip condition. Comput Math Appl 60:660–669
4. Cogley AC, Gilles SE, Vincenti WG (1968) Differential approximation for radiative transfer in a Nongrey gas near equilibrium. Am Inst Aeronaut Astronaut 6:551–553
5. Tani I (1962) Steady motion of conducting fluids in channels under transverse magnetic fields with consideration of hall effect. J Aerospace Sci 29:287
6. Soundalgekar VM, Vighnesam NV, Takhar HS (1979) Hall and ion-slip effects in MHD Couette flow with heat transfer. IEEE Trans Plasma Sci PS 7(3)

7. Soundalgekar VM, Uplekar AG (1986) Hall effects in MHD Couette flow with heat transfer. IEEE Trans Plasma Sci PS 14(5)
8. Hazem A (1998) Hall current effects on the velocity and temperature fields of an unsteady Hartmann flow. Can J Phys 76:739–746
9. Hazem AA (2009) Effect of hall current on the velocity and temperature distributions of Couette flow with variable properties and uniform suction and injection. Comput Appl Math 28(N. 2):195–212
10. Hazem A (2001) Effect of hall current on the unsteady MHD flow due to a rotating disk with uniform suction or injection. Appl Math Modell 25:1089–1098
11. Olajuwon BI, Oahimire JI, Ferdow M (2014) Effect of thermal radiation and hall current on heat and mass transfer of unsteady MHD flow of a viscoelastic micropolar fluid through a porous medium. Eng Sci Technol 17:185–193
12. Singh KD, Kumar R (2009) Effect of rotation and hall current on mixed convection MHD flow through a porous medium filled in a vertical channel in the presence of thermal radiation. Indian J Pure Appl Phys 47:617
13. Chand Khem, Kumar Rakesh (2012) Hall effect on heat and mass transfer in the flow of oscillating viscoelastic fluid through porous medium with wall slip conditions. Indian J Pure Appl Phys 50:149–155
14. Chand Khem (2013) Effect of hall current and rotation on chemically reacting and radiating MHD oscillatory dusty viscoelastic flow through porous vertical channel. Int J Appl Math Comput 5(3):17–32
15. Khan M, Maqbool K, Hayat T (2006) Influence of hall current on the flows of a generalised oldroyd-B fluid in a porous space. Acta Mechanica 184:1–13
16. Hazem AA (2006) Hall effect on Couette flow with heat transfer of dusty conducting fluid between parallel porous plate under exponential decaying pressure gradient. J Mech Sci Technol 20:569–579
17. Das S, Jana RN, Makinde OD (2016) Magnetohydrodynamic free convective flow of nanofluid past an oscillating porous flat plate in a rotating system with thermal radiation and Hall effects. J Mech 32(2):197–210
18. Das S, Guchhait SK, Jana RN, Makinde OD (2016) Hall effects on an unsteady magneto-convection and radiative heat transfer past a porous plate. Alexandria Eng J 55(2):1321–1331
19. Das S, Patra RR, Jana RN, Makinde OD (2017) Hall effects on unsteady MHD reactive flow through a porous channel with convective heating at the Arrhenius reaction rate. J Eng Phys Thermophys 90(5):1178–1191
20. Govindarajan A, Vijayalakshmi R, Ramamurthy V (2018) Combined effects of heat and mass transfer to MHD oscillatory dusty fluid flow in a porous channel. J Phys Conf Ser 1000:1–11
21. Vijayalakshmi R, Govindarajan A (2019) Effect of partial slip on hydromagetic oscillatory dusty fluid flow in an asymmetric wavy channel. AIP Conf Proc 2112:1–9
22. Govindarajan A, Vijayalakshmi R (2019) Energy transfer effects in hydromagetic oscillatory dusty fluid flow in a vertical porous channel. AIP Conf Proc 2112:1–8
23. Vijayalakshmi R, Govindarajan A (2019) Impact of heat transfer and viscous dissipation on unsteady MHD oscillatory dusty fluid flow through a vertical porous channel. J Phys Conf Ser 1377:1–16
24. Gupta Sumit, Kumar Devendra, Singh Jagdev (2020) Analytical study for MHD flow of Williamson nanofluid with the effects of variable thickness, nonlinear thermal radiation and improved Fourier's and Fick's Laws. SN Appl Sci 2(438):1–12
25. Gupta Sumit, Kumar Devendra, Singh Jagdev (2019) Magnetohydrodynamic three-dimensional boundary layer flow and heat transfer of water-driven copper and alumina nanoparticles induced by convective conditions. Int J Modern Phys B 33(26):1950307
26. Chand K, Singh KD, Sharma S (2013) Effect of hall current and rotation on heat transfer in MHD flow of oscillating dusty fluid in a porous channel. Indian J Pure Appl Phys 51:669–682

Study of Aligned MHD Casson Fluid Past a Shrinking Sheet with Viscous Dissipation

Renu Devi, Vikas Poply, and Makkar Vinita

Abstract This manuscript examined the impact of viscous dissipation on aligned MHD flow in a Casson fluid with heat and flow transfer over the shrinking sheet. The impact of various fluid parameters like Casson fluid parameter, magnetic parameter, Prandtl number, and Eckert number has been discussed in this article. In continuation of Casson fluid, magnetic field parameter is influenced by the presence of Eckert number. The governing partial differential equations are moulded to ordinary differential equations using similarity transformations. The scientific results of the differential equations have been figured out by the Runge–Kutta–Fehlberg method with the help of the shooting technique. Emerging parameters are characterized graphically and their results have been discussed in the table.

Keywords Shrinking sheet · Aligned MHD · Viscous dissipation · Casson fluid

Nomenclature

R	Constant
β	Casson parameter
x, y	Cartesian coordinates
T	Dimensionless temperature
μ	Dynamic viscosity
σ	Electrical conductivity

R. Devi (✉)
Department of Mathematics, SOES, GD Goenka University, Gurugram 122103, Haryana, India
e-mail: renu15dahiya@gmail.com

V. Poply
Department of Mathematics, KLP College, Rewari 123401, Haryana, India
e-mail: vikaspoply@gmail.com

M. Vinita
Department of Mathematics, SoBAS, GD Goenka University, Gurugram 122103, Haryana, India
e-mail: vini252011makkar@gmail.com

J. Singh et al. (eds.), *Advances in Mathematical Modelling, Applied Analysis and Computation*, Lecture Notes in Networks and Systems 415,
https://doi.org/10.1007/978-981-19-0179-9_32

Ec	Eckert number
ρ	Fluid density
ν	Kinematic viscosity
q_m	Local heat flux
Nu_x	Local Nusselt number
M	Magnetic parameter (Chandrasekhar number)
B_0	Magnetic field strength
f_a	Normal component of flow
Pr	Prandtl number
C_P	Specific heat
Ψ	Stream function
C_f	Skin friction coefficient
K	Thermal conductivity
T_w	Temperature at surface
T	Temperature profile
T_∞	Uniform ambient temperature
u, v	Velocity component
τ_w	Wall shear stress

1 Introduction

Stretching sheet problems under the influence of boundary layer flow became a part of the attraction for many researchers due to its mathematical simplicity. Secondly, there are vital applications of stretching sheets in industries as well as in engineering fields like polymer processing, metal spinning, and drawing of plastic film. The effect of boundary layer flow over stretching sheet is shown by [1–4]. These researchers showed the impact of stagnation point on boundary layer flow and behavior of flow over a stretching sheet.

Stretching sheets have become part of study for many years ago in the research area, after that shrinking sheets become a concern for many researchers. Literature for flow towards shrinking sheet is reserved as compared to stretching sheet. Still, after this limitation, there are many applications of flow over shrinking sheets such that polymer sheets, manufacturing of filaments, glass-fibre, and paper production; whereas applications in chemical engineering and manufacturing industries are also included. Miklavcic and Wang [5] investigated the characteristics of viscous flow over the shrinking sheet with suction effects, whereas Fang and Zhong [6] analysed the effect of arbitrary velocity flow over boundary layer flow properties. Khan et al. [7] described the heat transfer concept on horizontal stretching/shrinking sheets. All of the above researchers analysed the behaviour of boundary layer flow in different scenarios.

There exists great importance of stagnation point in boundary layer flow. The concept behind the shrinking sheet came into existence after observing the pattern

of stretching and shrinking of the balloon. It is noticed that results do not exist due to boundary layer flow, so adding the presence of stagnation flow on the boundary layer makes the possibility of a similar solution that gives exact outcomes. Wang [8] described the influence of stagnation flow over shrinking sheets, whereas [9–12] were concerned with heat transfer analysis of boundary layer flow with stagnation point over the stretching/shrinking sheets. Mahapatra and Nandy [13] used unsteady stagnation point flow with slip flow, whereas Lok and Pop [14] described unsteady separated stagnation point flow over the shrinking sheet. On the other hand, Mahapatra et al. [15] described the behaviour of oblique flow with thermal radiation over the shrinking sheet. Rosali et al. [16] further investigate their study by observing the impact of stagnation point flow over the shrinking sheet in presence of a porous medium. Zaimi and Ishak [17] analysed the nature of boundary layer flow on convective boundary conditions over permeable stretching/shrinking sheets.

Magnetohydrodynamic (MHD) is generally in the existence of a magnetic field on electrically conducting moving fluid. Its concept makes this area special after having applications in electromagnetic pump, plasma studies, blood flow measurements, metallurgical process, designing of heat exchanger, accelerator and generator. The behaviour of magnetic field strength over viscous fluid flow was noticed as discussed by Abbasbandy and Ghehsareh [18]. Akyildiz and Siginer [19] analysed the numerical simulation of results regarding magnetohydrodynamic viscous flow in the existence of suction over the shrinking sheet. Study of hydromagnetic stagnation point flow with viscous fluid flow over shrinking sheet is described by [20–22]. The study of stagnation point with MHD fluid flow properties with slip effect was observed by [23]; whereas an important part of a flow which is oblique MHD flow was extended by Lok et al. [24]. Problems related to the MHD boundary layer were analysed by [25] and [26]. Bhattacharya [27] performed the heat transfer and MHD flow with radiation effect in the presence of heat source/sink and suction/injection. Chauhan and Agrawal [28] extended their study for heat flow and MHD flow by having a porous substrate plate.

Casson fluid is characterized by non-Newtonian fluid having properties of shear-thinning fluid that is known by yield stress and makes the fluid flow possible otherwise fluid seems like a solid. Sauce, jelly, soup and honey are some examples of viscous fluids that are added to Casson fluid, whereas human blood is the most appropriate example of Casson fluid which is the main part of the biomedical field. Therefore, Sheikh and Abbas [29] analysed stagnation point flow with Casson fluid to solve heterogeneous and homogeneous solutions. Qasim and Noreen [30] included the viscous dissipation with heat transfer analysis of Casson fluid passed on a porous shrinking sheet.

On the bases of the literature survey, no such research has been carried out so far; the non-orthogonal magnetic field on Casson fluid along with viscous dissipation past a shrinking sheet. The motivation of the current assessment is to analyse the effects of viscous dissipation on an aligned magnetic field with the existence of Casson fluid. Getting the desired quality of the final product in industries is found by controlling the rate of heat transfer and fluid velocity during the process.

2 Materials and Methods

Steady 2D Casson fluid flow of a non-compressible, viscous, electrical conducting fluid on a shrinking sheet is considered. Aligned magnetic fields are also assumed the impact on fluid flow. $u_W(x)$ and T_W are the linear velocity and uniform temperature on a shrinking surface, respectively (as shown in Fig. 1).

The generating equations of flow under the above assumptions are described as

$$\frac{\partial u}{\partial x} + \frac{\partial v}{\partial y} = 0 \tag{1}$$

$$u\frac{\partial u}{\partial x} + v\frac{\partial u}{\partial y} = \nu\left(1 + \frac{1}{\beta}\right)\left(\frac{\partial^2 u}{\partial x^2} + \frac{\partial^2 u}{\partial y^2}\right) - \frac{\sigma B_0^2 u \sin^2 l}{\rho} \tag{2}$$

$$\rho C_P\left(u\frac{\partial T}{\partial x} + v\frac{\partial T}{\partial y}\right) = K\frac{\partial^2 T}{\partial y^2} + \mu\left(1 + \frac{1}{\beta}\right)\left(\frac{\partial u}{\partial y}\right)^2 \tag{3}$$

where velocity along y (vertical axis) and x (horizontal axis)-axes are taken as v and u, respectively. $\nu, \sigma, C_P, T, K, \mu$ and B_0 denote the kinematic viscosity, electrical conductivity, specific heat at constant pressure, fluid temperature, thermal conductivity, dynamic viscosity and magnetic field strength of the fluid, respectively.

Restrictions on the boundary are describing the flow model as

$$\left.\begin{array}{lll} y = 0 & u = u_w(x) = -bx, \; v = 0, & T = T_w \\ y \to \infty & u = 0, & T = T_\infty \end{array}\right\} \tag{4}$$

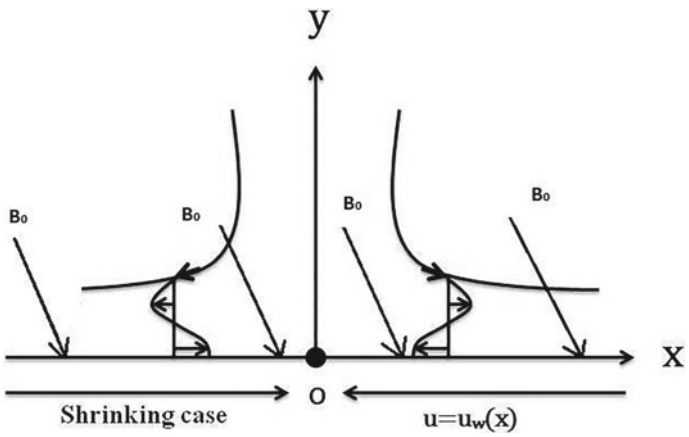

Fig. 1 Schematic diagram

where b is the non-negative invariable values of dimension ($time^{-1}$). The fluid has unvarying temperature T_∞ very far from the surface.

Introducing $\xi = \sqrt{\frac{b}{\nu}}x$, $\eta = \sqrt{\frac{b}{\nu}}y$ and $\Psi(\xi, \eta)$ (stream function) as dimensionless variables such that $u = \frac{\partial \Psi}{\partial \eta}$ and $v = -\frac{\partial \Psi}{\partial \xi}$. The boundary condition in terms of stream function $\Psi(\xi, \eta)$ is given by

$$\left.\begin{array}{lll} \xi = 0 & \frac{\partial \Psi}{\partial \eta} = -\xi, \; on & \eta = 0 \\ \frac{\partial \Psi}{\partial \eta} = 0 & as & \eta \to \infty \end{array}\right\} \tag{5}$$

We require the solution of Eq. (6) from the relation $\psi = \xi f_a(\eta)$, where $f_a(\eta)$ is referred as tangential and normal parts of the flow. Also, $v = -f_a(\eta)$ and $u = \xi f_a^{'}(\eta)$.

Equation (1) is contented by the given v and u and Eqs. (2) and (4) are transformed to Eqs. (5) and (6),

$$\left(1 + \frac{1}{\beta}\right) f_a(\eta) + f_a'''(\eta) f_a''(\eta) - \left(f_a'(\eta)\right)^2 - M \sin^2 l f_a'(\eta) = 0 \tag{6}$$

$$f_a(0) = 0, \; f_a^{'}(0) = -1, \; f_a^{'}(\infty) = 0 \tag{7}$$

Here, $M = \frac{\sigma B_0^2}{b\rho}$ is the Chandrasekhar number (magnetic parameter).

Dimensionless temperature $\theta(\eta) = (T - T_\infty)/(T_w - T_\infty)$. Substituting $\theta(\eta)$ in Eq. (3), we get

$$\theta''(\eta) + \Pr \theta'(\eta) f_a(\eta) + \Pr Ec \left(1 + \frac{1}{\beta}\right) f_a''(\eta) = 0 \tag{8}$$

where $\Pr(= \mu C_P/K)$, $Ec = u_w^2/C_P(T_w - T_\infty)$.

Corresponding boundary conditions of (4) reduce to $\theta(0) = 1, \theta(\infty) = 0$

The terms of practical importance are C_f and Nu_x are defined as follows.

The wall shear stress τ_w is described as $C_f = \frac{\tau_w}{\rho(u_w)^2}$ then $C_f \propto f_a^{''}(0)$ when $\tau_w = \mu\left(1 + \frac{1}{\beta}\right)\frac{\partial u}{\partial y}\Big|_{y=0}$.

The wall heat flux q_w is given as $Nu_x = \frac{x q_w}{K(T_w - T_\infty)}$ then $Nu_x \propto -\theta'(0)$ when $q_w = -\left(K\frac{\partial T}{\partial y}\right)\Big|_{y=0}$.

3 Results and Discussion

Here, Runge–Kutta–Fehlberg technique is applied to find out the solution to differential Eqs. (6) and (8) with the help of a shooting procedure. Dimensionless velocity and

dimensionless temperature of the model have been acquired for different entries of various fluid parameters. The value of $C_f \propto f_a''(0)$ and $Nu_x \propto -\theta'(0)$ are computed for further analysis.

Figure 2 exhibits the significance of velocity profile under influence of β. Figure 2 expresses that the fluid velocity rises with rising entries of β. This graph elaborates that enhancement in the value of β will decline yield stress that hurdles the free movement of fluid particles and hence boundary layer thickness reduces. Figure 3 discloses the behavior of β for temperature distribution. Figure 3 indicates that the fluid temperature reduces and this graph elaborates that enhancement in the value of β enhances fluid velocity that will intensify the heat transfer. We notice from Table 1 that with the increase in Casson fluid parameter β, $C_f \propto f_a''(0)$ and $Nu_x \propto -\theta'(0)$ values rise.

Figure 4 manifests the variation of fluid velocity against M on velocity. This figure shows that the existence of magnetic parameter M resist the fluid particles to move freely and the main reason behind the resistance is that M produces Lorentz force and

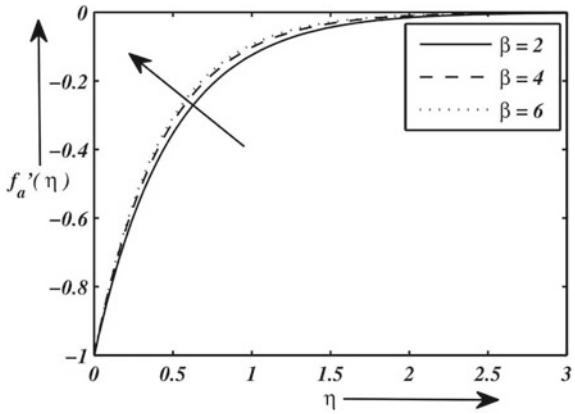

Fig. 2 Pattern of $f_a'(\eta)$ for distinct β with fixed entries $M = 10, l = \pi/3, Ec = 0.5, Pr = 1.1$

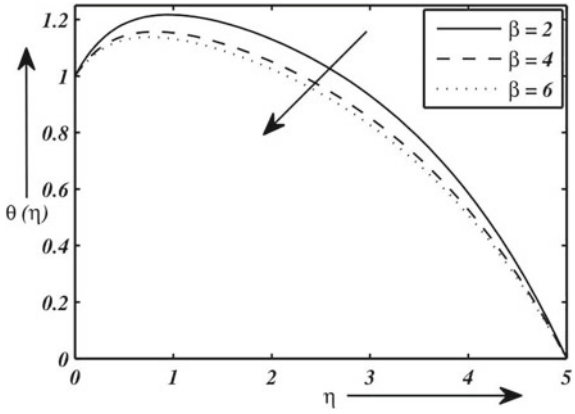

Fig. 3 Pattern of $\theta(\eta)$ for distinct β with fixed entries $M = 10, l = \pi/3, Ec = 0.5, Pr = 1.1$

Table 1 Outcomes of $f_a''(0)$ and $-\theta'(0)$ for fixed entries of $M = 10, l = \pi/3, Ec = 0.5$ and $Pr = 1.1$

β	$f_a''(0)$	$-\theta'(0)$
2	2.08166	−0.66900
4	2.28035	−0.55190
6	2.36038	−0.51181

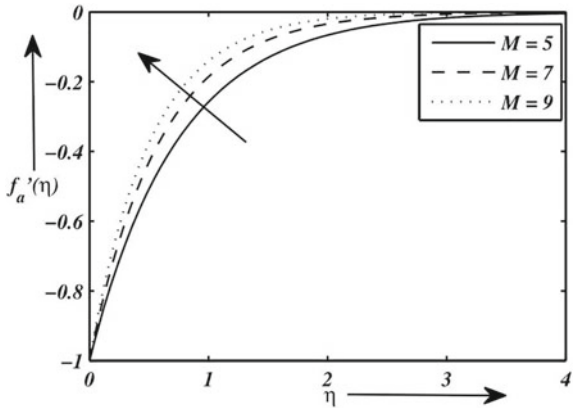

Fig. 4 Pattern of $f_a'(\eta)$ for distinct M with fixed entries $\beta = 4, l = \pi/3, Ec = 0.5, Pr = 1.1$

this magnetism behavior can be adopted for controlling the fluid movement. Thus, an enhancement in M causes the enhancement of velocity distribution as depicted in Fig. 4. Figures 5 represents that the temperature profile declines marginally with the rise in M because a slight conversion in Nu_x has been seen with rising M (shown in Table 2). As heat transfer rate can be controlled with the help of magnetism. As fluid velocity increases, the rate of heat transfer increases, and due to this fluid temperature decreases. Therefore, it can be concluded that in flow characteristics, M

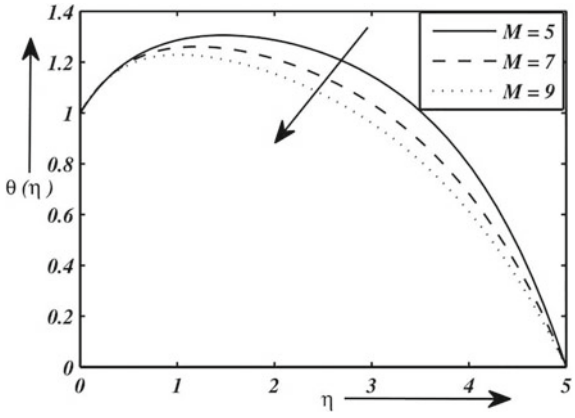

Fig. 5 Pattern of $\theta(\eta)$ for distinct M with fixed entries $\beta = 4, l = \pi/3, Ec = 0.5, Pr = 1.1$

Table 2 Outcomes of $f_a''(0)$ and $-\theta'(0)$ for fixed entries of $\beta = 2, l = \pi/3, Ec = 0.5$ and $Pr = 1.1$

M	$f_a''(0)$	$-\theta'(0)$
5	1.35400	−0.62087
7	1.68325	−0.65073
9	1.95789	−0.66474

plays a substantial role. From Table 2, we observed that with the increase in magnetic parameter M, $C_f \propto f_a''(0)$ and $Nu_x \propto -\theta'(0)$ both increase.

Figure 6 analyses the impact of l on dimensionless velocity distribution. Here, an increment in velocity profile has been noticed with the rising in value of l. This happened because of a higher value of l that reinforces the applied magnetic field and this situation creates a reverse force to flow. That reverse force reduced the velocity that is exhibited in Fig. 6. This force has the capacity to reduce boundary layer thickness. In Fig. 7, the effect of l on temperature distribution is observed. As

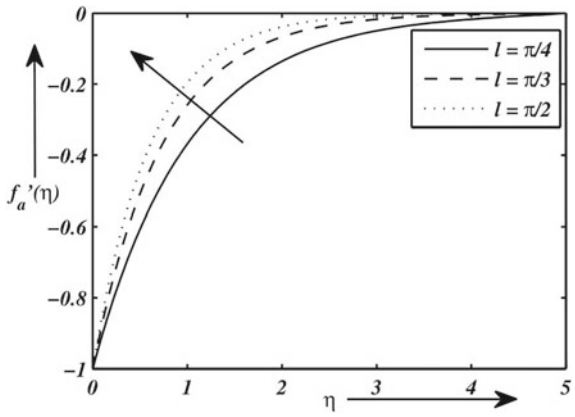

Fig. 6 Pattern of $f_a'(\eta)$ for distinct l with fixed entries $\beta = 4, M = 10, Ec = 0.5, Pr = 1.1$

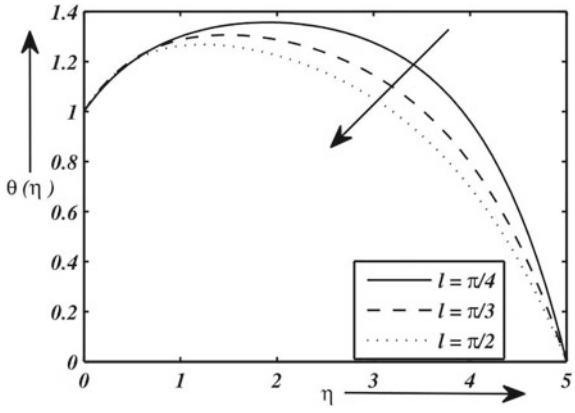

Fig. 7 Pattern of $\theta(\eta)$ for distinct l with fixed entries $\beta = 4, M = 10, Ec = 0.5, Pr = 1.1$

Table 3 Outcomes of $f_a^{''}(0)$ and $-\theta'(0)$ for fixed entries of $\beta = 2$, $M = 5$, $Ec = 0.5$ and $Pr = 1.1$

l	$f_a^{''}(0)$	$-\theta'(0)$
$\pi/4$	1.00001	−0.56022
$\pi/3$	1.35400	−0.62087
$\pi/2$	1.63299	−0.64728

l increases, the temperature of the fluid and thermal boundary thickness are both reduced. As fluid velocity increases, the rate of heat transfer increases, due to this fluid temperature decreases. From Table 3, we observed that with the increase in l then $C_f \propto f_a^{''}(0)$ and $Nu_x \propto -\theta'(0)$ both increase.

Figure 8 examines the study of the effect of Ec on temperature distribution. Here, an increment in fluid temperature has been noticed with the rising in value of Ec. This happened because kinetic energy transforms into thermal energy and thus fluid temperature as well as the width of thermal boundary increases. During this process, a huge amount of energy is released and due to this, the temperature of the fluid increases. From Table 4, we observed that with the increase in Ec $Nu_x \propto -\theta'(0)$ decreases.

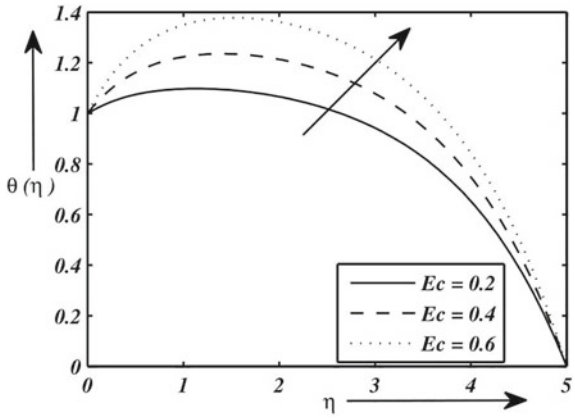

Fig. 8 Pattern of $\theta(\eta)$ for distinct Ec with fixed entries $\beta = 4$, $M = 10$, $l = \pi/3$, $Pr = 1.1$

Table 4 Outcomes of $f_a''(0)$ and $-\theta'(0)$ for fixed entries of $\beta = 2$, $M = 5$, $l = \pi/3$ and $Pr = 1.1$

Ec	$f_a''(0)$	$-\theta'(0)$
0.2	1.35400	−0.23304
0.4	1.35400	−0.49159
0.6	1.35400	−0.75015

4 Conclusions

Steady 2D Casson fluid flow of a non-compressible, viscous, orthogonally electrical conducting fluid on a shrinking sheet has been studied. Runge–Kutta–Fehlberg has been used to solve numerically the differential equations with their corresponding boundary conditions through the shooting technique. The numerical results obtained in this study include the influence of aligned magnetic field and Casson parameter on temperature and velocity profiles of the flow. This analysis revealed major recommendations of the outcomes are compiled as below:

1. The fluid velocity increases and momentum boundary layer thickness decreases, whereas fluid temperature and thermal boundary layer thickness decrease with the increase of Casson fluid parameter β.
2. On increasing magnetic parameter M, fluid velocity increases and momentum boundary layer thickness decreases, whereas fluid temperature and thermal boundary layer thickness decrease.
3. On increasing aligned angle parameter l, momentum boundary layer thickness decreases as well as fluid velocity increases, whereas fluid temperature and thermal boundary layer thickness decrease.
4. The fluid temperature and thermal boundary thickness increase with the increasing Eckert number Ec.

These results have possible technological applications in liquid-based systems involving shrinking materials. The finding of this study may serve to control the rate of heat transportation. A future study of this analysis can be done by considering a study on Casson fluid with an aligned magnetic field having an impact on viscous dissipation over shrinking cylindrical surfaces.

References

1. Mahapatra TR, Gupta AS (2008) Stagnation-point flow towards a stretching surface. Can J Chem Eng 81:258–263
2. Mustafa M, Hayat T, Ioan P, Hendi A (2012) Stagnation-point flow and heat transfer of a Casson fluid towards a stretching sheet. Zeitschrift fr Naturforschung A 67:70–76
3. Lok Y, Amin N, Pop I (2006) Non-orthogonal stagnation point flow towards a stretching sheet. Int J Non-Linear Mech 41:622–627
4. Singh P, Tomer NS, Kumar S, Sinha D (2010) MHD oblique stagnation-point flow towards a stretching sheet with heat transfer. Int J Appl Math Mech 6(13):94–111
5. Miklavi M, Wang CY (2006) Viscous flow due to a shrinking sheet. Q Appl Math 64:283–290
6. Fang T, Zhong Y (2010) Viscous flow over a shrinking sheet with an arbitrary surface velocity. Commun Nonlinear Sci Numer Simul 15:3768–3776
7. Khan Y, Faraz Q, Wu N, Yildirim A (2011) The effects of variable viscosity and thermal conductivity on a thin film flow over a shrinking/stretching sheet. Comput Math Appl 61:3391–3399
8. Wang C (2008) Stagnation flow towards a shrinking sheet. Int J Non-Linear Mech 43:377–382
9. Bachok N, Ishak A, Pop I (2010) Melting heat transfer in boundary layer stagnation-point flow towards a stretching/shrinking sheet. Phys Lett A 374:4075–4079

10. Bachok N, Ishak A, Pop I (2013) Stagnation point flow toward a stretching/shrinking sheet with a convective surface boundary condition. J Franklin Inst 350:2736–2744
11. Bhattacharyya K, Mukhopadhyay S, Layek G (2011) Slip effects on boundary layer stagnation-point flow and heat transfer towards a shrinking sheet. Int J Heat Mass Transf 54:308–313
12. Bhattacharyya K (2013) Heat transfer analysis in unsteady boundary layer stagnation-point flow towards a shrinking/stretching sheet. Ain Shams Eng J 4:259–264
13. Mahapatra TR, Nandy SK (2013) Slip effects on unsteady stagnation-point flow and heat transfer over a shrinking sheet. Meccanica 48:1599–1606
14. Lok YY, Pop I (2014) Stretching or shrinking sheet problem for unsteady separated stagnation-point flow. Meccanica 49:1479–1492
15. Mahapatra TR, Nandy SK, Gupta AS (2012) Oblique stagnation-point flow and heat transfer towards a shrinking sheet with thermal radiation. Meccanica 47:1325–1335
16. Rosali H, Ishak A, Pop I (2011) Stagnation point flow and heat transfer over a stretching/shrinking sheet in a porous medium. Int Commun Heat Mass Transfer 38:1029–1032
17. Zaimi K, Ishak A (2015) Boundary layer flow and heat transfer over a permeable stretching/shrinking sheet with a convective boundary condition. J Appl Fluid Mech 8(3):499–505
18. Abbasbandy S, Ghehsareh HR (2013) Solutions for MHD viscous flow due to a shrinking sheet by HankelPad method. Int J Numer Methods Heat Fluid Flow 23:388–400
19. Akyildiz FT, Siginer DA (2010) Existence results and numerical simulation of magnetohydrodynamic viscous flow over a shrinking sheet with suction. Math Comput Model 52:346–354
20. Van Gorder RA, Vajravelu K, Pop I (2012) Hydromagnetic stagnation point flow of a viscous fluid over a stretching or shrinking sheet. Meccanica 47:31–50
21. Noor N, Awang KS, Hashim I (2010) Simple non-perturbative solution for MHD viscous flow due to a shrinking sheet. Commun Nonlinear Sci Numer Simul 15:144–148
22. Fang T, Zhang J (2009) Closed-form exact solutions of MHD viscous flow over a shrinking sheet. Commun Nonlinear Sci Numer Simul 14:2853–2857
23. Aman F, Ishak A, Pop I (2013) Magnetohydrodynamic stagnation-point flow towards a stretching/shrinking sheet with slip effects. Int Commun Heat Mass Transfer 47:68–72
24. Lok YY, Merkin JH, Pop I (2015) MHD oblique stagnation-point flow towards a stretching/shrinking surface. Meccanica 50:2949–2961
25. Cortell R (2010) On a certain boundary value problem arising in shrinking sheet flows. Appl Math Comput 217:4086–4093
26. Merkin J, Kumaran V (2010) The unsteady MHD boundary-layer flow on a shrinking sheet. Eur J Mech B Fluids 29:357–363
27. Bhattacharyya K (2011) Effects of radiation and heat source/sink on unsteady MHD boundary layer flow and heat transfer over a shrinking sheet with suction/injection. Front Chem Sci Eng 5:376–384
28. Chauhan DS, Agrawal R (2011) MHD flow and heat transfer in a channel bounded by a shrinking sheet and a plate with a porous substrate. J Eng Phys Thermophys 84:1034–1046
29. Sheikh M, Abbas Z (2015) Homogeneous and heterogeneous reactions in stagnation point flow of Casson fluid due to a stretching/shrinking sheet with uniform suction and slip effects. Ain Shams Eng J
30. Qasim M, Noreen S (2014) Heat transfer in the boundary layer flow of a Casson fluid over. Eur Phys J Plus Heat 129:1–8. https://doi.org/10.1140/epjp/i2014-14007-5
31. Poply V, Singh P, Yadav AK (2015) A study of temperature-dependent fluid properties on MHD free stream flow and heat transfer over a non-linearly stretching sheet. Procedia Eng 127:391–397
32. Vinita V, Poply V (2019) Impact of outer velocity MHD slip flow and heat transfer of nanofluid past a stretching cylinder. Mater Today Proc 26:3429–3435. https://doi.org/10.1016/j.matpr.2019.11.304
33. Devi R, Poply V, Manimala (2019) Impact of inclined outer velocity in MHD Casson fluid over stretching sheet. Int J Adv Trends Comp Appl 1:32–38

34. Devi R, Poply V, Manimala (2019) Impact of aligned MHD flow with inclined outer velocity for casson nanofluid over a stretching sheet. Heat Transfer 49:3702–3725
35. Devi R, Poply V, Manimala (2021) Effect of aligned magnetic field and inclined outer velocity in Casson fluid flow over a stretching sheet with heat source. J Thermal Eng 7:823–844
36. Goyal R, Vinita, Sharma N, Bhargava R (2020) GFEM analysis of MHD nanofluid flow toward a power-law stretching sheet in the presence of thermodiffusive effect along with regression investigation. Heat Transfer 1–23
37. Hussanan A, Salleh MZ, Khan I, Shafie S (2017) Convection heat transfer in micropolar nanofluids with oxide nanoparticles in water, kerosene and engine oil. J Mol Liq 229:482–488
38. Aman S, Khan I, Ismail Z (2017) Heat transfer enhancement in free convection flow of CNTs Maxwell nanofluids with four different types of molecular liquids. Sci Rep 7:2445
39. Khan NS, Gul T, Islam S, Khan I, Alqahtani AM, Alshomrani AS (2017) Magnetohydrodynamic nanoliquid thin film sprayed on a stretching cylinder with heat transfer. Appl Sci 7:271
40. Gupta S, Kumar D, Singh D (2019) Magnetohydrodynamic three-dimensional boundary layer flow and heat transfer of water-driven copper and alumina nanoparticles induced by convective conditions. Int J Mod Phys B 33(26):1950307
41. Gupta S, Kumar D, Singh D (2020) Analytical study for MHD flow of Williamson nanofluid with the effects of variable thickness, nonlinear thermal radiation and improved Fourier's and Fick's Laws. SN Appl Sci 2:438
42. Sushila, Kumar D, Singh D, Baleanu D (2021) A hybrid analytical algorithm for thin film flow problem occurring in non-Newtonian fluid mechanics. Ain Shams Eng J 12(2):2297–2302

Spin Coating of Non-Newtonian Nanofluid with Silver and Copper as Nanoparticle

Swatilekha Nag and Susanta Maity

Abstract In this paper, we have discussed the behavior of the flow and film thickness variation of non-Newtonian nanofluid during spin coating process. In case of non-Newtonian fluid, the viscosity is not a constant term. For non-Newtonian fluid, the viscosity and solvent diffusivity are dependent on polymer concentration. In this article, we are taking silver and copper as a nanoparticle and sodium alginate as a non-Newtonian base fluid. Here, we investigate the behavior of the film thickness for different parameters such as initial film thickness, angular velocity of the rotating disk, volume fraction of the nanoparticle, etc.

Keywords Nanofluid · Non-Newtonian fluid · Spin coating · Volume fraction

1 Introduction

From the last few years, numerous researchers investigate on spin coating process. Covering the surface with a thin layer of liquid of a horizontal rotating disk with the help of centrifugal force is known as spin coating. We use the technology to build integrated circuits, color television screen etc. For Newtonian nanofluid, the viscosity is constant. But in case of non-Newtonian nanofluid, the viscosity is not constant, i.e. can change when more liquid or more solid is added. On a circular rotating disk, the flow of a thin fluid film was first given by Emslie et al. [1]. Meyerhofer [2] gave us a model for the portrayal of thin films prepared in spin coating process. Flack et al. [3] derived a mathematical model for non-Newtonian fluid thin film formation. In asymptotic method, the flow of unsteady fluid and film development was first considered by Higgins [4]. In 1991, a theoretical study was given for the

S. Nag (✉)
Pandit Deendayal Upadhaya Adarsha Mahavidyalaya, Behali 784184, Assam, India
e-mail: swatidkj103@gmail.com

S. Maity
National Institute of Technology, Arunachal Pradesh Yupia, Dist. Papum Pare 791112, Arunachal Pradesh, India

J. Singh et al. (eds.), *Advances in Mathematical Modelling, Applied Analysis and Computation*, Lecture Notes in Networks and Systems 415,
https://doi.org/10.1007/978-981-19-0179-9_33

unsteady non-Newtonian flow by Lawrence and Zhou [5]. Choi [6] first investigated the thermal conductivity of nanofluids. Then, Choi et al. [7] showed that the heat transfer of nanoliquids increases two times the thermal conductivity of the fluid. In 2001, Im et al. [8] give us a numerical study of thick photoresist film formation on a spin coating process. Charpin et al. [9] studied the flow of ellis fluid during spin coating process. Over a stretching sheet, Javed et al. [10]studied the flow of a non-Newtonian fluid. As far as we know, no research paper on non-Newtonian nanofluid film development during spin coating process has been given till now. In this article, we studied the film thinning rate of non-Newtonian nanofluid over a rotating disk. Here all the terms are assumed to be in terms of nanoparticle volume fraction. Here the viscosity is not constant. Viscosity is a function of r and t.

2 Mathematical Analysis

Let us consider initial the film thickness be h_0 which is very small as compared to the radius of the rotating disk. At the speed of $\Omega(t)$ the disk rotates and initially the disk rotates with a speed of Ω_0. We are doing the spin coating process with the non-Newtonian nanofluid as the coating liquid. Here, we consider the velocity components are (ψ_1, ψ_2, ψ_3) for the cylindrical coordinates (r, θ, z). The set of governing equations are given by as follows

$$\psi_{1_t} + \frac{\psi_1}{r} + \psi_{3_z} = 0 \tag{1}$$

$$\rho_{nf}(\psi_{1_t} + \psi_1\psi_{1_r} + \psi_3\psi_{1_z} - \frac{v^2}{r}) = -p_r + (\mu_{nf}\psi_{1_r})_r + \mu_{nf}(\frac{\psi_1}{r})_r + (\mu_{nf}\psi_{1_z})_z \tag{2}$$

$$\rho_{nf}(\psi_{2_t} + \psi_1\psi_{2_r} + \psi_3\psi_{2_z} + \frac{uv}{r}) = \frac{1}{r^2}(r^3\mu_{nf}(\frac{\psi_2}{r})_r)_r + (\mu_{nf}\psi_{2_z})_z \tag{3}$$

$$\rho_{nf}(\psi_{3_t} + \psi_1\psi_{3_r} + \psi_3\psi_{3_z}) = -p_z + \frac{1}{r}(\mu_{nf}r\psi_{3_r})_r + (\mu_{nf}\psi_{3_z})_z \tag{4}$$

$$(\rho c_p)_{nf}(T_t + \psi_1 T_r + \psi_3 T_z) = k_{nf}(T_{rr} + \frac{1}{r}T_r + T_{zz}) \tag{5}$$

$$\omega_t + \psi_3\omega_z = (D\omega_z)_z \tag{6}$$

Table 1 Properties of different nanoparticles and non-Newtonian base fluid

		ρ (kg/m^3)	C_p (J/kgK)	k (W/mK)
Base fluid	Sodium alginate	989	4175	0.06376
Nanoparticles	Silver	10500	235	429
	Copper	8933	385	401

where the pressure is represented by p, ρ_{nf} is the density, μ_{nf} is the dynamic viscosity, $(\rho C_p)_{nf}$ is thermal conductivity and k_{nf} is the heat capacity of the nanoliquid, which are defined as follows:

$$\rho_{nf} = (1-\phi)\rho_{bl} + \phi\rho_{SC}$$

$$\mu_{nf} = \frac{\mu_{bl}}{(1-\phi)^{\frac{5}{2}}}$$

$$\left(\rho C_p\right)_{nf} = (1-\phi)\left(\rho C_p\right)_{bl} + \phi\left(\rho C_p\right)_{SC}$$

$$k_{nf} = k_{bl}\left(\frac{(1-\phi)+\frac{2\phi k_{SC}}{k_{SC}-k_{bl}} log\left(\frac{k_{SC}+k_{bl}}{2k_{bl}}\right)}{(1-\phi)+\frac{2\phi k_{bl}}{k_{SC}-k_{bl}} log\left(\frac{k_{SC}+k_{bl}}{2k_{bl}}\right)}\right)$$

where suffixes bl and SC represent base liquid and nanoparticles respectively, ϕ is the volume fraction of the nanoparticle (Table 1).

On the surface of the disk no slip boundary condition i.e. at z = 0

$\psi_1 = 0, \psi_2 = r\Omega_0, \psi_3 = 0, T = T_0 - \frac{\lambda r^2}{2} T_1$

At the free surface z = h(t)

$p_a - p + 2\mu_{nf}\psi_{3_z} = 0$

$\mu_{nf}(\psi_{3_r} + \psi_{1_z}) = \frac{\partial\sigma}{\partial T} T_r = 0$

$\mu_{nf}\psi_{2_z} = \frac{\partial\sigma}{\partial T} T_z = 0$

$T_z = 0.$

The initial condition at time t = 0 is

$\psi_1 = \psi_2 = \psi_3 = 0, h = h_0, T = T_0$

where p_a is the atmospheric pressure. σ is the surface tension, which varies linearly with the temperature as $\sigma = \sigma_0[1 - \gamma(T - T_0) - \lambda(\omega - \omega_0)]$, σ_0 is the surface tension at initial time.

Again we considered the similarity transformations are as follows:

$\psi_1 = rf(z,t), \psi_2 = rg(z,t), \psi_3 = w(z,t), \omega = \omega(z,t), T = T_0 - \frac{r^2}{2}M - N, p = -\frac{r^2}{2}A(z,t) + B(z,t)$

New transformed equations from (2.1) to (2.6) are

$$2f + \psi_{1_z} = 0 \tag{7}$$

$$\rho_{nf}(f_t + f^2 + wf_z - g^2) = A + (\mu_{nf} f_z)_z \tag{8}$$

$$\rho_{nf}(g_t + 2fg + wg_z) = (\mu_{nf} g_z)_z \tag{9}$$

$$\rho_{nf}(w_t + ww_z) = (\mu_{nf} w_z)_z - B_z \tag{10}$$

$$(\rho C_p)_{nf}(M_t + 2FM + WM_z) = k_{nf} M_{zz} \tag{11}$$

$$(\rho C_p)_{nf}(N_t + WN_z) = k_{nf}(2M + N_{zz}) \tag{12}$$

$$\omega_t + w\omega_z = (D\omega_z)_z \tag{13}$$

At z = 0
$f = 0, g = \Omega_0, w = 0, M = T_1, N = 0$
At the free surface z = h(t)
$A = 0, B = 2\mu_{nf}\psi_{3z}, f_z = 0, g_z = 0, M_z = 0, N_z = 0$
At t = 0
$f = g = w = 0, M = N = 0$
Using the dimensionless variables
$\eta = \frac{z}{h_0}, \tau = t\Omega_0, F = \frac{f}{\Omega_0}, G = \frac{g}{\Omega_0}, W = \frac{w}{h_0\Omega_0}, \theta = \frac{T}{T_0}, H = \frac{h}{h_0}, \bar{\nu} = \frac{\nu}{\nu_0}, \bar{D} = \frac{D}{D_0}, \hat{M} = \frac{{h_0}^2 M}{\Delta T}, \hat{N} = \frac{N}{\Delta T}, \Delta T = \left|\lambda {h_0}^2 T_1\right|$

New dimensionless form of the above equations is

$$2F + W_\eta = 0 \tag{14}$$

$$F_\tau + F^2 - G^2 + WF_\eta = \frac{1}{\mathrm{Re}\phi_1}(\bar{\nu}F_\eta)_\eta \tag{15}$$

$$G_\tau + 2FG + WG_\eta = \frac{1}{\mathrm{Re}\phi_1}(\bar{\nu}G_\eta)_\eta \tag{16}$$

$$\hat{M}_\tau + 2F\hat{M} + W\hat{M}_\eta = \frac{1}{\mathrm{RePr}\phi_2}\frac{K_{nf}}{k_f}\hat{M}_{\eta\eta} \tag{17}$$

$$\hat{N}_\tau + W\hat{N}_\eta = \frac{1}{\mathrm{RePr}\phi_2}\frac{k_{nf}}{k_f}(2\hat{M} + \hat{N_{\eta\eta}}) \tag{18}$$

$$\omega_\tau + W\omega_\eta = \frac{1}{\mathrm{Re}Sc}(\bar{D}\omega_\eta)_\eta \tag{19}$$

where ω is the mass solvent fraction, D is the binary diffusivity, $\mathrm{Re} = \frac{\Omega_0 {h_0}^2}{\nu_f}$, $\mathrm{Pr} = \frac{\nu_f}{\alpha_f}$, $Sc = \frac{\nu_0}{D_0}$, $\alpha_f = \frac{k_f}{\rho C_{pf}}$, ν_f are the thermal diffusivity and kinematic viscosity of the base liquid, respectively, and $\phi_1 = (1-\phi)^{\frac{5}{2}}\left[(1-\phi) + \phi\frac{\rho_s}{\rho_f}\right]$, $\phi_2 =$

$\left[(1-\phi)+\phi\frac{(\rho C_p)_s}{(\rho C_p)_f}\right]$ are dimensionless constants.
At $\eta = 0$
$F = 0, G = 1, W = 0, \hat{M} = 1, \hat{N} = 0, \omega_\eta = 0$
At $\eta = H(\tau)$
$F_\eta = 0, G_\eta = 0, \hat{M}_\eta = 0, \hat{N}_\eta = 0$
$\frac{\partial H}{\partial \tau} = W - st.\omega$
At the boundary the conditions for solvent mass fraction are: $\frac{\partial \omega}{\partial \eta} = 0$
$\frac{1}{1-\omega}.\frac{\partial \omega}{\partial \eta} + sh.\omega = 0$
where $st = k/(h_0\Omega_0)$, $sh = kh_0/D$ here the mass transfer coefficient $k = 4 \times 10^{-5}\sqrt{\Omega}$.

3 Numerical Solution

Consider the transformation

$$\xi(\tau) = 1 - a_1 ln\left(\frac{a_2 H(\tau) - \eta}{b_2 H(\tau) + \eta}\right), 1 < c < \infty \tag{20}$$

where c is grid controlling parameter (for small values of c cluster grid points near disk surface but for large of c makes uniform grid distribution throughout the liquid film). $a_1 = [ln(a_2/b_2)]^{-}1$, $a_2 = c + 1$ and $b_2 = c - 1$. By using transformation (3.1), the equations (2.14–2.19) are transformed and solved by the Crank-Nicholson scheme. Finally, the numerical computation is carried out with the following trigonal system of algebraic equations.

$$P_1 U_{j-1}^{n+1} + Q_1 U_j^{n+1} + R_1 U_{j+1}^{n+1} = (S_1)_j^n, \tag{21}$$

$$P_1 V_{j-1}^{n+1} + Q_1 V_j^{n+1} + R_1 V_{j+1}^{n+1} = (S_2)_j^n, \tag{22}$$

$$P_2 \omega_{j-1}^{n+1} + Q_2 \omega_j^{n+1} + R_2 \omega_{j+1}^{n+1} = (S_3)_j^n \tag{23}$$

$$P_3 \Sigma_{j-1}^{n+1} + Q_3 \Sigma_j^{n+1} + R_3 \Sigma_{j+1}^{n+1} = (S_4)_j^n \tag{24}$$

$$P_3 \Pi_{j-1}^{n+1} + Q_3 \Pi_j^{n+1} + R_3 \Pi_{j+1}^{n+1} = (S_5)_j^n \tag{25}$$

where
$P_1 = \frac{C-A}{4\Delta\xi} - \frac{B}{2(\Delta\xi)^2}$, $Q_1 = \frac{1}{\Delta\tau} + \frac{B}{(\Delta\xi)^2} + 2U_j^n$, $R_1 = \frac{A-C}{4\Delta\xi} - \frac{B}{2(\Delta\xi)^2}$
$(S_1)_j^n = U_{j-1}^n\left[\frac{A-C}{4\Delta\xi} + \frac{B}{2(\Delta\xi)^2}\right] + U_j^n\left[\frac{1}{\Delta\tau} - \frac{B}{(\Delta\xi)^2} + U_j^n\right] + U_{j+1}^n\left[\frac{C-A}{4\Delta\xi} + \frac{B}{2(\Delta\xi)^2}\right] + \frac{1}{\mathrm{Re}\phi_1}(V_j^n)^2$

$$(S_2)_j^n = V_{j-1}^n\left[\frac{A-C}{4\Delta\xi} + \frac{B}{2(\Delta\xi)^2}\right] + V_j^n\left[\frac{1}{\Delta\tau} - \frac{B}{(\Delta\xi)^2}\right] + V_{j+1}^n\left[\frac{C-A}{4\Delta\xi} + \frac{B}{2(\Delta\xi)^2}\right]$$

$$P_2 = \frac{E-A}{4\Delta\xi} - \frac{D}{2(\Delta\xi)^2},\ Q_2 = \frac{1}{\Delta\tau} + \frac{D}{(\Delta\xi)^2},\ R_2 = \frac{A-E}{4\Delta\xi} - \frac{D}{2(\Delta\xi)^2}$$

$$(S_3)_j^n = \omega_{j-1}^n\left[\frac{A-E}{4\Delta\xi} + \frac{D}{2(\Delta\xi)^2}\right] + \omega_j^n\left[\frac{1}{\Delta\tau} - \frac{D}{(\Delta\xi)^2} + \omega_j^n\right] + \omega_{j+1}^n\left[\frac{E-A}{4\Delta\xi} + \frac{B}{2(\Delta\xi)^2}\right] + \frac{1}{\mathrm{Re}\phi_1}(V_j^n)^2$$

$$P_3 = \frac{I-A}{4\Delta\xi} - \frac{L}{2(\Delta\xi)^2},\ Q_3 = \frac{1}{\Delta\tau} + \frac{L}{(\Delta\xi)^2},\ R_3 = \frac{A-I}{4\Delta\xi} - \frac{L}{2(\Delta\xi)^2}$$

$$(S_4)_j^n = M_{j-1}^n\left[\frac{A-I}{4\Delta\xi} + \frac{L}{2(\Delta\xi)^2}\right] + M_j^n\left[\frac{1}{\Delta\tau} - \frac{L}{(\Delta\xi)^2} + U_j^n\right] + M_{j+1}^n\left[\frac{I-A}{4\Delta\xi} + \frac{L}{2(\Delta\xi)^2}\right] + \frac{1}{\mathrm{Re}\phi_1}(V_j^n)^2$$

$$(S_5)_j^n = N_{j-1}^n\left[\frac{A-I}{4\Delta\xi} + \frac{L}{2(\Delta\xi)^2}\right] + N_j^n\left[\frac{1}{\Delta\tau} - \frac{L}{(\Delta\xi)^2} + \right] + N_{j+1}^n\left[\frac{I-A}{4\Delta\xi} + \frac{L}{2(\Delta\xi)^2}\right]$$

$$A = \frac{a_1(a_2+b_2)(\bar{W}H(\tau)-\eta H'(\tau))}{(a_2H(\tau)-\eta)(b_2H(\tau)+\eta)}$$

$$B = \frac{1}{\mathrm{Re}\phi_1}\bar{\nu}\left[\frac{a_1(a_2+b_2)H(\tau)}{(a_2H(\tau)-\eta)(b_2H(\tau)+\eta)}\right]^2$$

$$C = \frac{1}{\mathrm{Re}\phi_1}\left[\frac{a_1(a_2+b_2)H(\tau)[a_1(a_2+b_2)H(\tau)\bar{\nu}_\xi+\bar{\nu}((b_2-a_2)H(\tau)+2\eta)]}{(a_2H(\tau)-\eta)^2(b_2H(\tau)+\eta)^2}\right]$$

$$D = \frac{1}{\mathrm{Re}Sc}\bar{D}\left[\frac{a_1(a_2+b_2)H(\tau)}{(a_2H(\tau)-\eta)(b_2H(\tau)+\eta)}\right]^2$$

$$E = \frac{1}{\mathrm{Re}Sc}\left[\frac{a_1(a_2+b_2)H(\tau)[a_1(a_2+b_2)H(\tau)\bar{D}_\xi+\bar{D}((b_2-a_2)H(\tau)+2\eta)]}{(a_2H(\tau)-\eta)^2(b_2H(\tau)+\eta)^2}\right]$$

$$I = \frac{1}{\mathrm{RePr}\phi_2}\left(\frac{k_n f}{k_f}\right)\left[\frac{a_1(a_2+b_2)H(\tau)[(b_2-a_2)H(\tau)+2\eta]}{(a_2H(\tau)-\eta)^2(b_2H(\tau)+\eta)^2}\right]$$

$$L = \frac{1}{\mathrm{RePr}\phi_2}\left(\frac{k_n f}{k_f}\right)\left[\frac{a_1(a_2+b_2)H(\tau)}{(a_2H(\tau)-\eta)(b_2H(\tau)+\eta)}\right]^2$$

The viscosity is dependent on concentration and the model was proposed by Meyerhofer [2] is used $\mu = \mu_f(1-\omega) + \mu_s$ where $\mu_f = 10000P$ and $\mu_s = 0.01P$ Here, we use the relation between diffusivity and concentration which was proposed by Flack et al. [3]: $D = D_0 exp(\frac{\omega}{a\omega+b})$ where $D_0 = 7.8 \times 10^{-12}$ cm^2/s, a = 0.04, b = 0.043.

4 Result and Discussion

In this article, we described the flow of non-Newtonian nanofluid. Here, we take the nanoparticles silver and copper with the non-Newtonian base fluid sodium alginate. In Fig. 1, we have shown the variation of film thickness for different nanoparticles. From Fig. 1, we have seen that in case of copper the thickness of the film is high as compared to silver. In Fig. 2, we have shown the variation of velocity in radial direction for different values of nanoparticles with different values of ϕ. From these

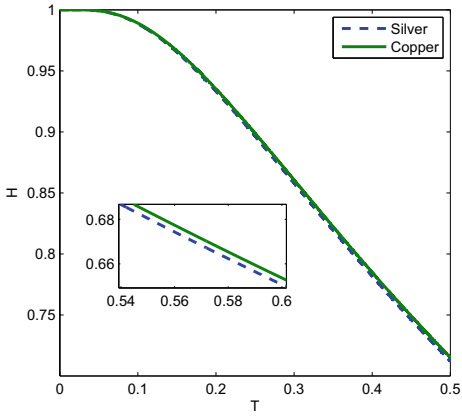

Fig. 1 Variation of film thickness H with time for different nanoparticles

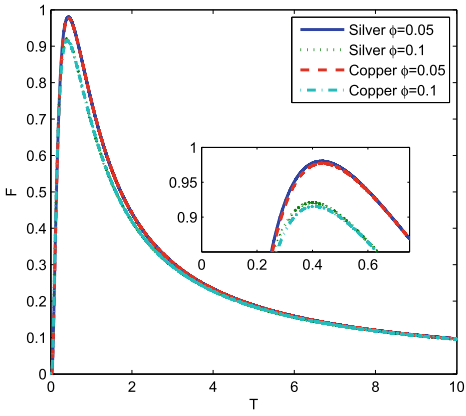

Fig. 2 Variation of radial velocity with time for different nanoparticles and different values of ϕ

figures, we conclude that the velocity is high in case of silver as compared to copper and with the increasing values of ϕ the velocity decreases. Figure 3 describes the variation of film thickness for different values of ϕ and considering the initial film thickness $h_0 = 0.1$ and the disk rotates with an angular velocity $\Omega = 2000$. From these figures, we have seen that the film thickness increases with the increasing value of ϕ. In Fig. 4, we have shown the variation of film thinning rate for different values of h_0. From Fig. 4, we have seen that the thickness of the film increases for increasing values of h_0. Figure 5 describes the variation of film thickness for different values of Ω (angular velocity of disk rotation). These figures indicate that the film thickness decreases for increasing values of Ω.

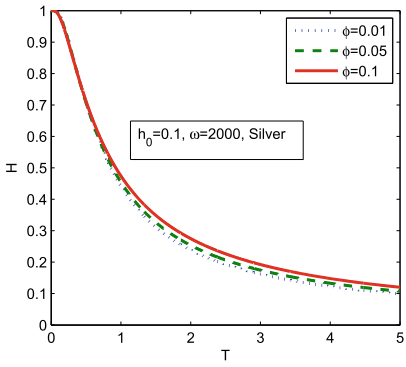

Fig. 3 Variation of film thickness H with time for different values of ϕ. Here we consider $h_0 = 0.1$, $\Omega = 2000$ rpm

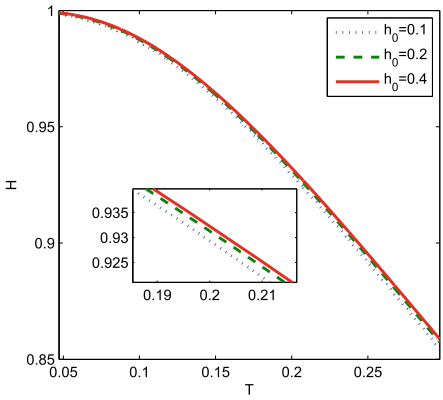

Fig. 4 Variation of film thickness H with time for different values of initial film thickness h_0

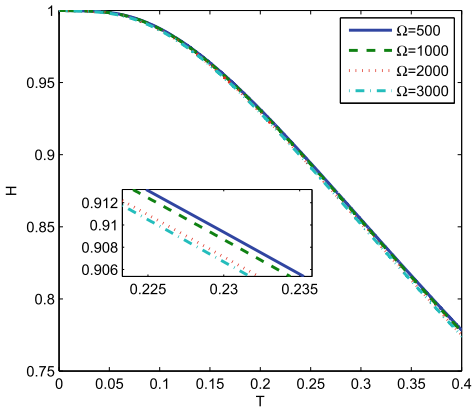

Fig. 5 Variation of film thickness H with time for different values of Ω

References

1. Emslie AC, Bonner FD, Peck LG (1958) Flow of a viscous liquid on a rotating disk. J Appl Phys 29:858–862
2. Meyerhofer D (1978) Characteristics of resist films produced by spinning. J Appl Phys 49:3993–3997
3. Flack WW, Soong DS, Bell AT, Hess DW (1985) A mathematical model for spin coating of polymer resists. J Appl Phys 56(4):1199–1206
4. Higgins BG (1986) Film flow on a rotating disk. Phys Fluids 29:3522–3529
5. Lawrence CJ, Zhou W (1991) Spin coating of non-Newtonian fluids 29:137–187
6. Choi SUS (1995) Enhancing thermal conductivity of fluids with nanoparticles. In: The proceedings of the 1995 ASME international mechanical engineering congress and exposition, San Francisco, USA, ASME, FED231/MD66, pp 99–105
7. Choi SUS, Zhang ZG, Yu W, Lockwood FE, Grulke EA (2001) Anomalously thermal conductivity enhancement in nanotube suspensions. Appl Phys Lett 79:2252–2254
8. Im IT, Kim KS, Cho JK (2001) Flow and evaporation of a thick polymer film on a rotating disk 29. 0-7803-7157-7
9. Charpin JPF, Lombe M, Myers TG (2007) Spin coating of non-Newtonian fluids with a moving front 29(76):016312 (2007)
10. Javed T, Ali N, Abbas Z (2012) Flow of an Eyring-Powell non-Newtonian fluid over a stretching sheet 29:327–336 (2012)

Analysis of Soret and Dufour Effect on MHD Fluid Flow Over a Slanted Stretching Sheet with Chemical Reaction, Heat Source and Radiation

Ruchi Jain, Ruchika Mehta, Himanshu Rathore, and Jagdev Singh

Abstract The intent of the current chapter is to scrutinize the MHD laminar flow with heat flux, mass flux and magnetic flux, buoyancy ratio, thermal conduction and radiation with convective boundary condition for suction and injection of an electromagnetic fluid. The similarity transformations are used to find the coupled ODE from coupled partial differential equation and then are solved by RK-4 method in MATLAB. The effects of different physical quantities are described numerically and presented graphically. The numerical values of Nusselt number local skin friction and Sherwood number are shown through tables. This investigation is relevant to the chapter production industry, astrophysics, polymer industry and cooling of metallic sheets.

Keywords Heat flux · Mass flux · Soret effect · Dufour effect

Abbreviations

$\lambda_T = \frac{x^{(1/3)} g\beta_T (T_W - T_\infty)}{c^2}$	Thermal buoyancy parameter
$Gc = \frac{x^{(1/3)} g\beta_c (C_W - C_\infty)}{c^2}$	Concentration buoyancy parameter
$S = \frac{-3x^{\frac{1}{3}} v_w}{2\sqrt{cv}}$	Injection/suction parameter
$Q = \frac{Q^* v}{cx^{(-2/3)} K}$	Heat source parameter
$Sr = \frac{DmK_T (T_w - T_\infty)}{Tm\gamma (C_w - C_\infty)}$	Soret number

R. Jain · R. Mehta (✉)
Department of Mathematics & Statistics, Manipal University Jaipur, Jaipur, Rajasthan, India
e-mail: ruchika.mehta1981@gmail.com

H. Rathore
Department of Mechanical Engineering, Arya College of Engineering & I.T, Jaipur, Rajasthan, India

J. Singh
Department of Mathematics, JECRC University, Jaipur, Rajasthan, India

J. Singh et al. (eds.), *Advances in Mathematical Modelling, Applied Analysis and Computation*, Lecture Notes in Networks and Systems 415,
https://doi.org/10.1007/978-981-19-0179-9_34

$\beta = \frac{K_r x^{(1/3)}}{c}$	Reaction rate parameter
$M = \frac{\sigma \beta_0^2 x^{(1/3)}}{\rho C}$	Magnetic parameter
$Du = \frac{Dm K r (C_w - C_\infty)}{C_f C_P \gamma (T_w - T_\infty)}$	Dufour number
$Bi = \frac{h_f}{K}\sqrt{\frac{\upsilon^2}{c}}$	Biot number
$Sc = \frac{\gamma}{Dm}$	Schmith number
$Da = \frac{\nu x^{(-2/3)}}{K_P C}$	Darcy parameter
$Pr = \frac{\rho C_P \nu}{K}$	Prandtl number
α	Inclination angle
$Ec = \frac{c^2}{C_P (T_f - T_\infty)}$	Eckert number
$Nr = \frac{16\sigma^* T_\infty^3}{3KK^*}$	Radiation parameter

1 Introduction

Heat and mass transfer in fluids are known as a vast importance in many fields like science and engineering. When suction and injection are applied on moving fluid temperature, difference occurs, and this phenomenon gives the rise to Soret and DuFour effect. An incompressible fluid analysed for the effect of viscosity with Soret and Dufour over an expending upstanding lamina by Bazid et al. [3]. Under Newtonian heating, the quiescent fluid is examined for the convective border line flow of electro-conductive nanofluid on a upstanding steady laminate by Mohammed et al. [19]. Border line flow over a extending plan lamina in existence of unsteady magnetic factor is examined by Ferdows et al. [11] 0.2-D MHD fluid under thermal radiation with unsteady magnetic fluid is investigated for free convective heat admass transfer by Rashidi et al. [22]. Viscous bouncy fluid with heat and mass transfer is analysed under Soret and DuFour effect over a upstanding surface by Rashidi et al. [23]. Thermo buoyancy effect on a extending permeable sheet is examined by Daniel and Daniel [6]. Nanofluid through extending layer with Soret effect along with injection is examined by Sulochana and Sandeep [28] An inclined plate is inserted in permeable medium with fluctuating temperature and concentration by Pattnaik et al. [21]. Tanwar Hayat et al. examined the effect of heat over Jeffrey liquid [14]. Glutinous bouncy fluid is studied for 2-D MHD flow over expending upstanding surface with heat and mass transfer and chemical reaction by Anuradha and Yeganmai [1]. Nanofluid is studied for MHD flow over expending lamina inserted in porous medium for chemical reaction in crosswise electromagnetic field by Daniel et al. [7]. Viscous fluid is examined for thermo diffusion over combined thermo-conductive and mass transfer of a permeable slanting lamina with chemical reaction by Mondal et al. [20]. Thumma and Shamshuddin examined the electro-transmit fluid on a slanting extending lamina in changing magnetic factor and waves with buoyancy ratio [30]. A tilted plate placed in a permeable medium along with steady porosity changing temperature is examined for the effect of magnetic field with chemical reaction by

Endalew and Nayak [10]. Nanofluid is studied for mixed effect of electromagnetic thermodiffusion for glutinous squandering and joules heating by Daniel et al. [8]. MHD fluid with microstructure flow is examined for fluctuating temperature over an extending sheet from non-Darcy permeable medium by Reddy and Krishna [27]. Glutinous fluid with micro-structure flow is studied over an extending sheet inserted in permeable medium for the effect of magnetic field on non-uniform MHD flow by Babu et al. [2]. Sisko fluid is investigated for the effect of MHD flow with steady heat source over a expending lamina by Bhagya Lakshmi et al. [18]. Nanofluid is investigated for MHD flow with electro-conducting over a slanted extending sheet by Barik et al. [4]. A non-uniform 2-D jitter boundary line stratum flow of a Jeffrey fluid over a slanted expanding lamina is examined by Tlili [29]. Water as a main fluid is examined by adding four different particles are studied for non-uniform 2-D fluid over a upstanding expandable porous plate in slanted magnetic field by Elazar [9]. Gupta et al. [12, 13] analysed the Williamson nanofluid and water-driven copper and alumina nanoparticles induced by convective conditions. A nanofluid is analysed for the Brownian Motion, Soret and Dufour effect over a curvilinear slanted extendable lamina by Rafique [24]. A viscous fluid is analysed for Brownian motion with thermo-diffusion and diffusion thermo over a slanted spreading sheet by Rafique [25]. A viscous incompressible bouncy nanofluid is investigated for the effect of heat transfer and mass transfer over a curvilinear extending lamina by Rasool and Zhang [26]. Magnetic hydrodynamic combined convective fluid with chemical reaction is examined for the impact of the thermo-diffusion and diffusion thermo effect over a extending sheet by Bhuvaneswari et al. [5]. Prandtl fluid in existence of particle adjournment of a laminar flow with heat transfer over a extending sheet studied by Kumar [17]. Magnetohydrodynamic fluid with glutinous and ohmic depletion flow over a permeable media with suction and injection explained by Jabeen et al. [15]. In a non-Darcy permeable medium, Casson fluid is investigated for the effect of heat and mass transfer over an extending plane by Kala et al. [16]. A non-Newtonian fluid with micro-structure for heat and mass transfer is examined over non-linear extending sheet by Yasmin et al. [31].

2 Mathematical Formulation of the Model

Examined the invariable, 2-D, isochoric, boundary layer and free convection stream of an electro-conducting fluid on a tilted porous non-collinear extending lamina, tilt at an angle α ($0^0 \leq \alpha \leq 90^0$) to the upstanding direction. The substantial image is shown in Fig. 1. The x-axis is along the uniform porous spreading sheet, and the y-axis is perpendicular to the *x-axis*. The expansion of the lamina is applied by same but reversed forces at the same time along the x-axis. The pole is taken firmed, the sheet is extended with nonlinear velocity $u_w(x) = c\, x^{1/3}$, c is an extending potency.

Some assumptions are made that stream takes place for $y \geq 0$ and T_f temperature is applied on the porous extending laminar face by hot fluid. While the temperature

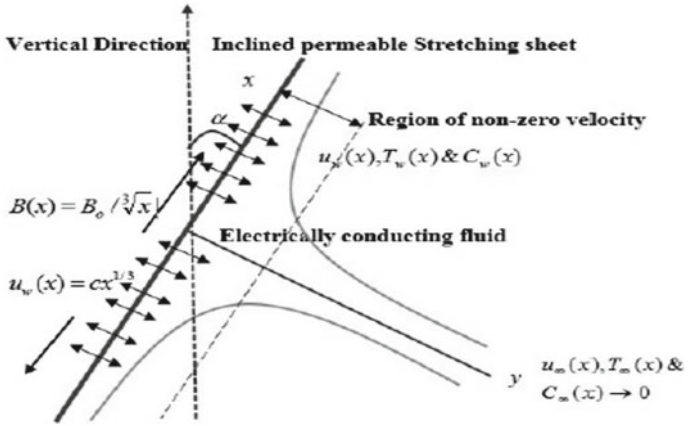

Fig. 1 Geometry and coordinate system for slanted extending lamina

of the electro-conducting encompassing fluid with the fix value T_∞ as $y \to \infty$ and also imagine that the temperature changes in the *x–axis* direction as ($T_w = T_\infty + ax$).

Using these presumptions with Boussinesq approximation, the boundary layer leading equation following Thirupathi Thumma is given below:

Equations:

$$\frac{\partial \mathrm{u}}{\partial \mathrm{x}} + \frac{\partial \mathrm{v}}{\partial \mathrm{y}} = 0, \tag{1}$$

$$\mathrm{u}\frac{\partial \mathrm{u}}{\partial \mathrm{x}} + \mathrm{v}\frac{\partial \mathrm{u}}{\partial \mathrm{y}} = \frac{\mathrm{u}}{\rho}\frac{\partial^2 \mathrm{u}}{\partial \mathrm{y}^2} + \mathrm{g}\beta_\mathrm{T}(\mathrm{T} - \mathrm{T}_\infty)\cos\alpha + \mathrm{g}\beta_\mathrm{C}(\mathrm{C} - \mathrm{C}_\infty)\cos\alpha - \frac{\sigma \mathrm{u}\mathrm{B}^2(\mathrm{x})}{\rho} - \frac{\vartheta \mathrm{u}}{\mathrm{K_P}} \tag{2}$$

$$\mathrm{u}\frac{\partial \mathrm{T}}{\partial \mathrm{x}} + \mathrm{v}\frac{\partial \mathrm{T}}{\partial \mathrm{y}} = \alpha\frac{\partial^2 \mathrm{T}}{\partial \mathrm{y}^2} - \frac{1}{\rho C_P}\frac{\partial \mathrm{q_r}}{\partial \mathrm{y}} + \frac{Q^*}{\rho C_P}(\mathrm{T} - \mathrm{T}_\infty) + \frac{\vartheta}{\mathrm{C_P}}\left(\frac{\partial \mathrm{u}}{\partial \mathrm{y}}\right)^2 + \frac{\sigma \mathrm{u}^2 \mathrm{B_0}^2}{\rho C_P} + \frac{Dm K_T}{C_S C_P}\frac{\partial^2 C}{\partial y^2}, \tag{3}$$

$$u\frac{\partial C}{\partial x} + v\frac{\partial C}{\partial y} = D_m\frac{\partial^2 C}{\partial y^2} - K_r(C - C_\infty) + \frac{Dm K_T}{T_m}\frac{\partial^2 T}{\partial y^2} \tag{4}$$

Corresponding boundary conditions are

$$\text{at y} = 0 \left\{ \begin{array}{c} u = \mathrm{u_w}, v = \mathrm{v_w} \\ -K\frac{\partial T}{\partial y} = h_f(T_\mathrm{w} - T) \\ \mathrm{C_w} = \mathrm{C}_\infty + bx \end{array} \right\} \tag{5}$$

$$at\, y \to \infty, \mathrm{u} \to 0, T \to T_\infty, C \to \mathrm{C}_\infty. \tag{6}$$

For optical broad boundary surface, we use Rosseland's dissemination approximately for the radiative heat current $q_r \left\{ q_r = \frac{-4\sigma^*}{3k^*} \frac{\partial T^4}{\partial y} \right\}$ where σ^* is the Stephan-Boltzmann ($5.6697 * 10^{-8} w_m^{-2} k^{-4}$) constant, k^* is the Rosseland's mean absorption coefficient. The expression T^4 due to emission is represented as a collinear function of temperature. Therefore, T^4 can be approximated by Taylor's series about T_∞ after neglecting the higher order terms as $T^4 = 4T_\infty^3 - 3\ T_\infty^4$. Consequently, by putting $\frac{\partial q_r}{\partial y} = \frac{-16\sigma^* T_\infty^3}{3k^*} \frac{\partial^2 T}{\partial y^2}$ in the energy Eq. (3), we get the subsequent form of the equation:

$$\mathrm{u}\frac{\partial \mathrm{T}}{\partial \mathrm{x}} + \mathrm{v}\frac{\partial \mathrm{T}}{\partial \mathrm{y}} = \alpha \frac{\partial^2 \mathrm{T}}{\partial \mathrm{y}^2} - \frac{1}{\rho C_P} \left\{ \frac{-16\sigma^* T_\infty^3}{3k^*} \frac{\partial^2 T}{\partial y^2} \right\} + \frac{Q^*}{\rho C_P} (\mathrm{T} - \mathrm{T}_\infty) + \frac{\vartheta}{\mathrm{C_P}} \left(\frac{\partial \mathrm{u}}{\partial \mathrm{y}} \right)^2 + \frac{\sigma \mathrm{u}^2 \mathrm{B}_0{}^2}{\rho C_P} + \frac{Dm K_T}{C_S C_P} \frac{\partial^2 C}{\partial y^2} \tag{7}$$

Method of solution:

Proceeding with the investigation, it is relevant to bring in the following similarity transformations:

$$\psi = x^{\frac{2}{3}} \sqrt{c\upsilon} f(\eta), \eta = \frac{c}{\sqrt[3]{x}\sqrt{\upsilon}} y,$$
$$\theta(\eta) = \frac{T - T_\infty}{T_w - T_\infty}, \phi(\eta) = \frac{C - C_\infty}{C_w - C_\infty} \tag{8}$$

where the stream function ψ is defined as

$u = \frac{\partial \psi}{\partial y}, v = -\frac{\partial \psi}{\partial x}$ that identically satisfies the continuity equations.

Again by putting Eq. (8) in Eqs. (2), (4), (7) and the resultant boundary conditions of the system given in Eqs. (5), (6), the leading border line equations change to the following problem of highly coupled nonlinear ODE, in form of an independent Variable (η), given by

$$f''' = \frac{1}{3} f'^2 + (M + Da) f' - \frac{2}{3} f f'' - \lambda_T \theta \cos\alpha - \lambda_c \theta \cos\alpha, \tag{9}$$

$$\theta'' = (1 + N_r - S_c S_r D_u P_r)^{-1} \left[P_r f' \theta - \frac{2}{3} f \theta' P_r - E_c P_r f''^2 - M E_c P_r f'^2 - Q\theta - D_u P_r \left\{ S_c \phi f' - \frac{2}{3} S_c \phi' f + S_c \phi \beta \right\} \right], \tag{10}$$

$$\phi'' = S_c \theta f' - \frac{2}{3} S_c \phi' f + S_c \phi \beta - S_c S_r \left\{ (1 + N_r - S_c S_r D_u \mathrm{P}_r)^{-1} \right\} \left[P_r f' \theta - \frac{2}{3} f \theta' P_r - E_c P_r f''^2 - M E_c P_r f'^2 - Q\theta - D_u P_r \left\{ S_c \phi f' - \frac{2}{3} S_c \phi' f + S_c \phi \beta \right\} \right] \tag{11}$$

The corresponding transformed boundary conditions are

$$at\ \eta = 0 \left\{ \begin{array}{c} f(\eta) = S,\ f'(\eta) = 1 \\ \theta'(\eta) = -Bi(1 - \theta(0)), \phi(\eta) = 1 \end{array} \right\}, \tag{12}$$

$$as\ \eta \to \infty \left\{ f'(\eta) \to 0, \theta(\eta) \to 0, \phi(\eta) \to 0 \right\} \tag{13}$$

where dash represents derivatives with respect to η.

Since Eqs. (9–11) are highly non-collinear, so it is difficult to find the closed-form solutions. These equations are transformed into system of first ODE by substituting.

$f = f_1, f^{'} = f_2, f^{''} = f_3, f^{'''} = f^{'}{}_3, \theta = f_4, \theta^{'} = f_5, \theta^{''} = f_5^{'}\phi = f_6, \phi^{'} = f_7, \phi^{''} = f_7{}'$.

We get the following equations:

$$f_3' = \frac{1}{3}f_2^2 + (M + Da)f_2 - \frac{2}{3}f_1 f_3 - \lambda_T f_4 \cos\alpha - \lambda_c f_6 \cos\alpha, \tag{14}$$

$$\begin{aligned} f_5' = {} & (1 + N_r - S_c S_r D_u P_r)^{-1} \\ & \left[P_r f_2 f_4 - \frac{2}{3} f_1 f_5 P_r - E_c P_r f_3^2 - M E_c P_r f_2^2 \right. \\ & \left. - Q f_4 - D_u P_r \left\{ S_c f_6 f_2 - \frac{2}{3} S_c f_7 f_1 + S_c f_6 \beta \right\} \right], \end{aligned} \tag{15}$$

$$\begin{aligned} f_7' = {} & S_c f_6 f_2 - \frac{2}{3} S_c f_7 f_1 + S_c f_6 \beta - S_c S_r \left\{ (1 + N_r - S_c S_r D_u P_r)^{-1} \right\} \\ & \left[P_r f_2 f_4 - \frac{2}{3} f_1 f_5 P_r - E_c P_r f_3^2 - M E_c P_r f_2^2 \right. \\ & \left. - Q f_4 - D_u P_r \left\{ S_c f_6 f_2 - \frac{2}{3} S_c f_7 f_1 + S_c f_6 \beta \right\} \right], \end{aligned} \tag{16}$$

$$at\ \eta = 0 \left\{ \begin{array}{c} f_1(\eta) = S,\ f_2(\eta) = 1 \\ f_5(\eta) = -Bi(1 - \theta(0)),\ f_6(\eta) = 1 \end{array} \right\} \tag{17}$$

$$as\ \eta \to \infty \{ f_2(\eta) \to 0,\ f_4(\eta) \to 0,\ f_6(\eta) \to 0 \} \tag{18}$$

.

3 Numerical Procedures

In this chapter, we have ordinary partial differential Eq. (1–4) and to solve these equations, firstly, we use similarity transformation and change these equations into Eqs. (9–11) and the boundary condition (5) and (6) converted into Eqs. (12) and (13), respectively. But these equations are highly coupled ordinary differential equations so to solve this equation first we must change these equations in first-order differential equation by substituting

$$\begin{aligned} f = f_1, f' = f_2, f'' = f_3, f''' = f_3', \theta = f_4, \theta' \\ = f_5, \theta'' = f_5'\phi = f_6, \phi' = f_7, \phi'' = f_7' \end{aligned}$$

Now, we get Eqs. (14–16) along with boundary conditions (17–18) then these equations are solved using MATLAB programming. For this kind of solution, we use

the shooting method for making initial values. Assume initial value at the boundary point and then the equation is solved numerically as the initial value problem and the correctness of the assumed value are revised by finding the difference between the assumed value and calculated value by repeating the same process, after that we find good agreement between the estimated value and given values of boundary condition at boundary points. Then the equations are solved using RK4 method in MATLAB and Graphs for the different parameters are plotted.

4 Result and Discussion

Mathematical computation is implied to examine the influence of different parameters on flow characteristics with convective boundary condition for both suction (s = 0.2) and injection (s = −0.2). Influence of M, Da, Bi, β, λ_C, λ_T, Ec, Du, Q, Sr, α velocity profile, the effect of M, Nr, Da, Bi, Pr, Sc, Ec, Du, Q, Sr on temperature profile and the effect of M, Da, Bi, Pr, Sc, Ec, Du, Q, Sr, β on concentration profile are presented graphically in Figs. 2, 3, 4, 5, 6, 7, 8, 9, 10, 11, 12, 13, 14, 15, 16, 17, 18, 19, 20, 21, 22, 23, 24, 25, 26, 27, 28, 29, 30 and 31.from all the figures we found that velocity, temperature and concentration distribution are less whereas all the profiles are more for injection. In the present paper physical parameters are taken into consideration for these fix values $\alpha = \pi/4$, Pr = 0.71, Bi = 0.1, Sc = 0.78, Q = 0.5, Du = 0.1 for velocity, temperature, and concentration gradient.

Figures 2, 3 and 4 enlightened the impression of increase value of Mon velocity gradient, temperature, and concentration gradient. This gives a thought that because

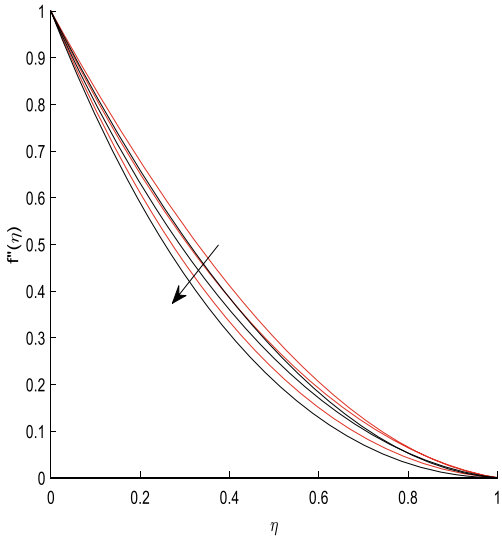

Fig. 2 Effects of M on velocity profile

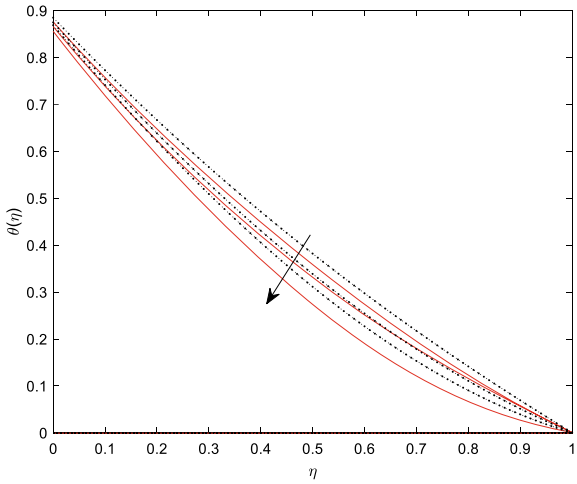

Fig. 3 Effects of M on temperature profile

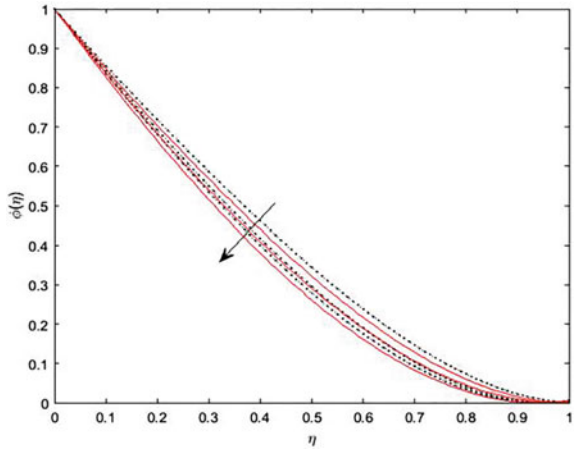

Fig. 4 Effects of M on concentration profile

of increase in magnetic factor all the three velocity, temperature and concentration gradient reduce this indicates that the effect of magnetic factor is more high up at the point of the highest value, i.e. the acme value severely decreases with an increase in the magnetic factor because the occurrence of magnetic factor in an electro-conducting fluid introduce a force called the Lorentz force. This force works in the opposite direction of the flow and hence due to rise in M, temperature of the surface increases and the boundary layer width decreases. Figures 5, 6 and 7 describes the effect of an increase in Biot number on dimensionless velocity, temperature and concentration profile. In view of Fig. 5, we find that a rise in Biot number gives growth to the velocity profile. Biot number is the fraction of resistance force that acts internally due to heat conduction to its external resistance to heat convection so as Biot number grows the resistance to convection also rises

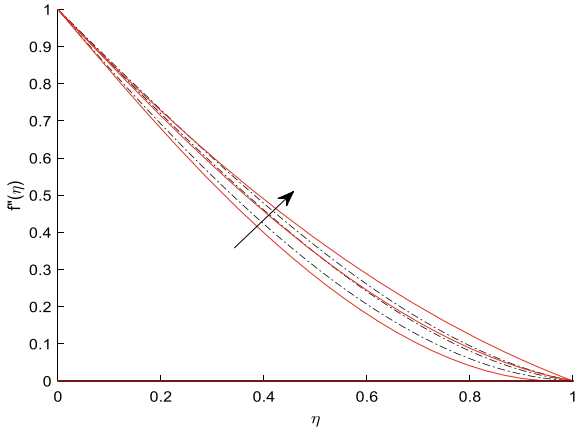

Fig. 5 Effects of Bi on velocity profile

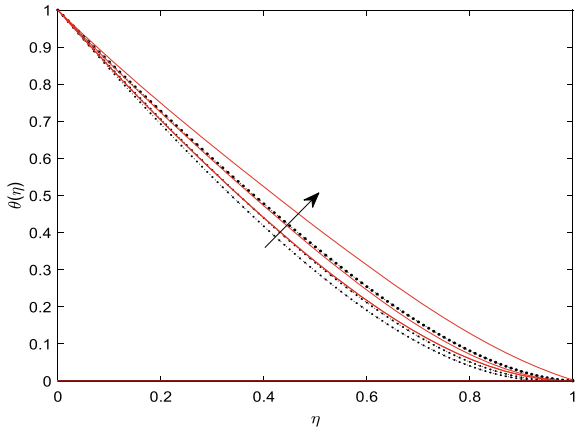

Fig. 6 Effects of Bi on temperature profile

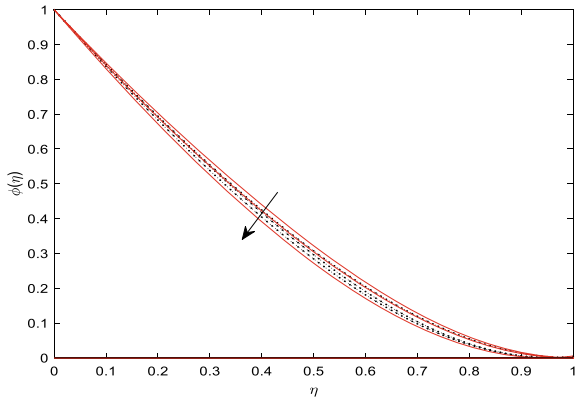

Fig. 7 Effects of Bi on concentration profile

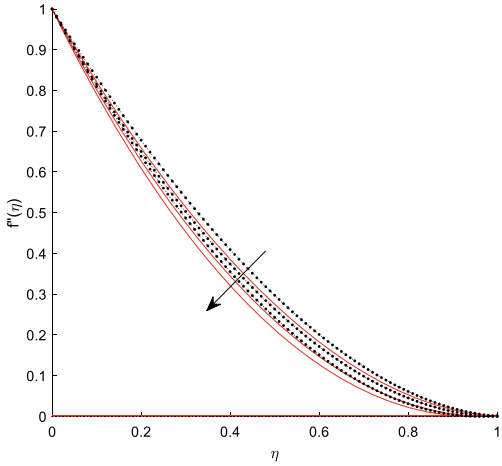

Fig. 8 Effects of Ec on velocity profile

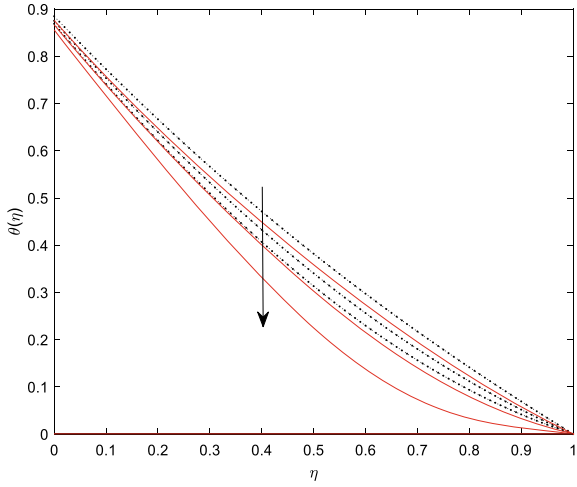

Fig. 9 Effects of on Ec temperature profile

and as result temperature gradient and concentration gradient decreases as shown in Figs. 6 and 7. Effect of Eckert number on velocity, temperature and concentration distribution is noted in Figs. 8, 9 and 10, respectively. Due to increase in Eckert number fluid velocity and temperature get decrement while concentration rises due to Eckert number. When concentration gradient results in temperature difference the DuFour effect occurs. Figures 11, 12 and 13 shows the impact of increment of DuFour number on velocity, temperature and concentration profile. Clearly, the figures show that due to the increase in DuFour effect, the velocity and temperature distribution experience a decrement while concentration profile increases that is because as Dufour number increases the buoyancy convection also increases and as

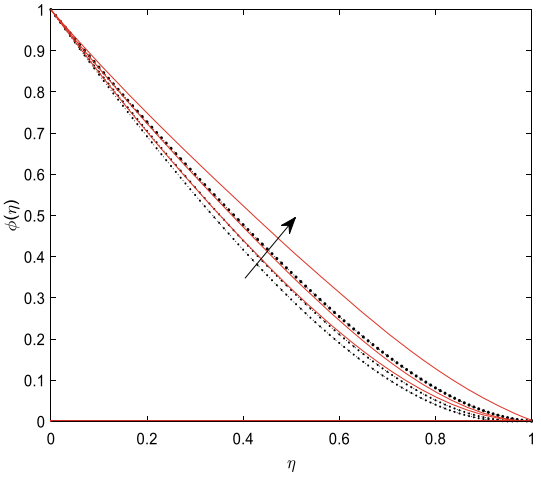

Fig. 10 Effects of Ec on concentration profile

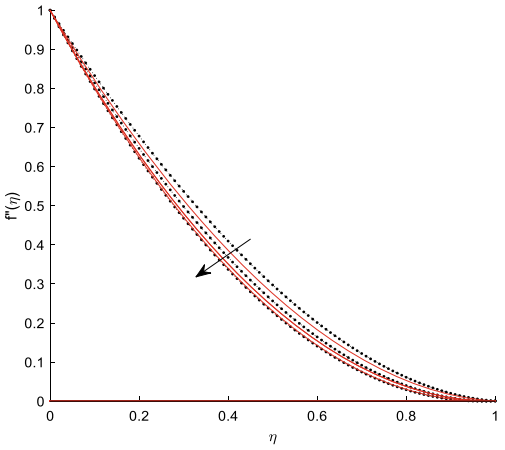

Fig. 11 Effects of Du on velocity profile

a result velocity and temperature profile reduces. The mass transfer due to temperature gradient occurs is known as Soret effect. The effect of increase in Soret number on velocity, temperature and concentration profile is described in Figures 14, 15 and 16, which shows that due to great thermal diffusion, all three-profile velocity, temperature and concentration decrease. Figures 17, 18 and 19 displays the effect of increase of Darcy number on velocity, temperature, and concentration profile. As Darcy number increases the resistance due to porous medium increases and the velocity temperature and concentration profile decreases. Figures 20 and 21 shows the effect of increasing value of heat source parameter on velocity, temperature and concentration profile. In the view as we increase heat source parameter heat convection also increases, and this gives rise to concentration and reduces the temperature profile. Figures 22 and 23 depicts the effect of increases in reaction rate parameter

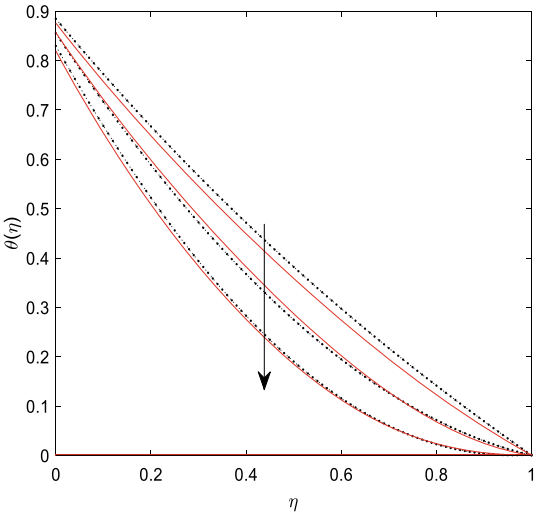

Fig. 12 Effects of Du on temperature profile

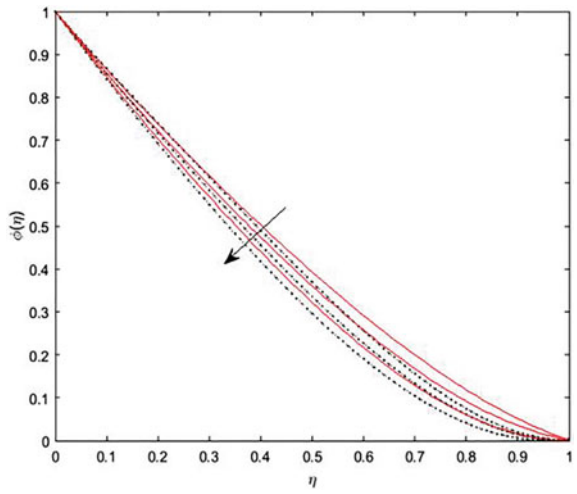

Fig. 13 Effects of Du on concentration profile

on velocity and concentration profiles as chemical reaction increases it decreases the fluid velocity and increases concentration profile. The impact of increasing value of Prandtl number over temperature and concentration gradient is given by Figs. 24 and 25 from which due to increase in Prandtl number temperature decreases where concentration increases it is because as Prandtl number increases thermal boundary layer thickness reduces thus temperature profile decreases and hydro-dynamic layer thickness reduces so that concentration increases. Figures 26 and 27 explains the influence of Schmith number on temperature distribution and concentration profile. In Fig. 26, we find that increase in smith number decreases the temperature of fluid

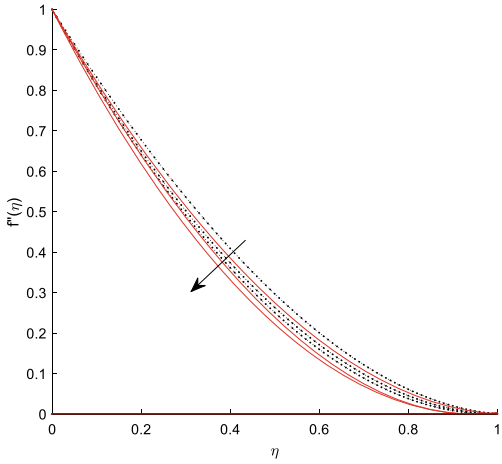

Fig. 14 Effects of Sr on velocity profile

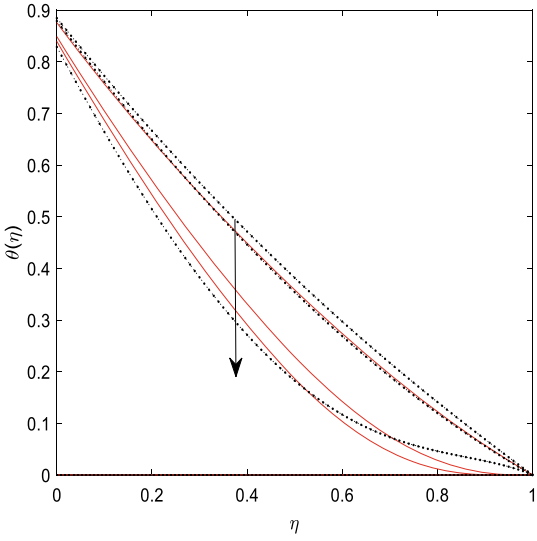

Fig. 15 Effects of Sr on temperature profile

flow where Fig. 27 shows that increase in Schmith number reduces the concentration profile. Figure 28 shows that an increase in value of angle of inclination gives increment to the velocity profile this is due to buoyancy forces. It is verified from Fig. 29 that increase in radiation parameter decreases temperature profile and from Fig. 30 it is found that concentration buoyancy parameter increases velocity profile while from Fig. 31, it is noted that thermal buoyancy parameter reduces velocity.

Table 1 describes the value of the skin-friction coefficient f”(0), Table 2 illustrates the value of the Nusselt number, and Table 3 demonstrates the Sherwood number for various values of flow parameters.

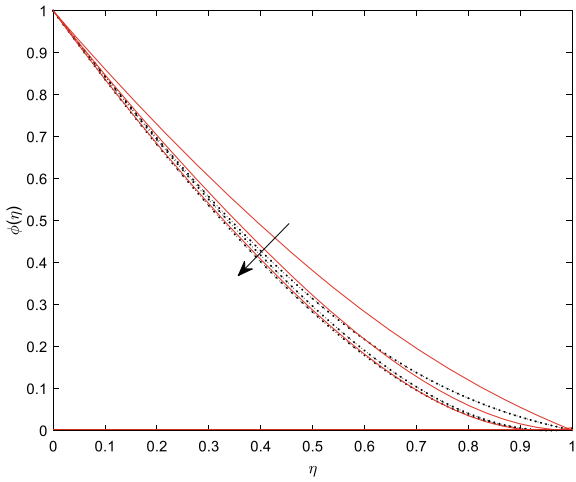

Fig. 16 Effects of Sr on concentration profile

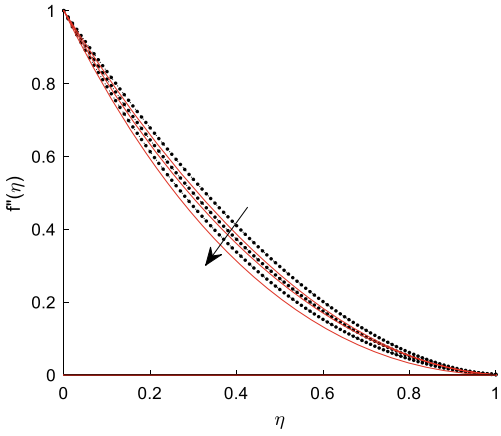

Fig. 17 Effects of Da on velocity profile

5 Conclusions

The remarkable points of this study are as follows:

- Fluid velocity rises due to increment in biot number Bi, concentration buoyancy parameter λ_C and inclination angle α where the fluid velocity reduces due to increment in magnetic parameter M, Darcy parameter Da, reaction rate parameter β, thermal buoyancy parameterλ_T, Eckert number Ec, Soret numberS_r, Dufour number Du for both suction and injection.
- Heat source parameter Q, Schmith number Sc, Prandtl number Pr, magnetic parameter M, radiation parameter Nr, Darcy number Da, Biot number Bi, Eckert number Ec for both suction and injection. Fluid temperature reduces due to increment in Dufour number Du, Soret number Sr,

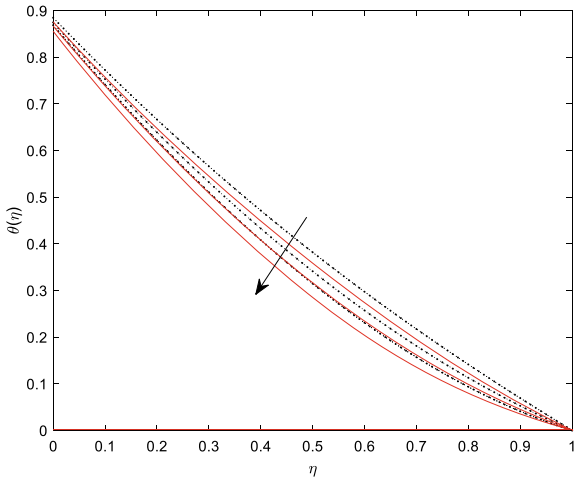

Fig. 18 Effects of Da on temperature profile

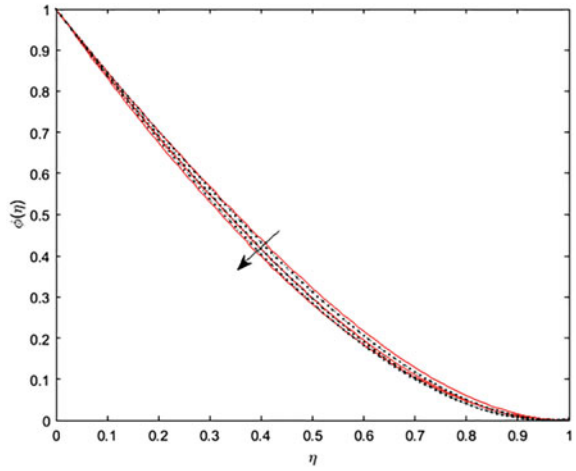

Fig. 19 Effects of Da on concentration profile

- Fluid concentration decreases due to rise in Dufour number Du, Soret number Sr, magnetic parameter M, Darcy number Du, Biot number Bi, Schmith number Sc while it rises because of increment in heat source parameter Q and Prandtl number Pr, reaction rate parameter β, Eckert number Ec for both suction and injection.

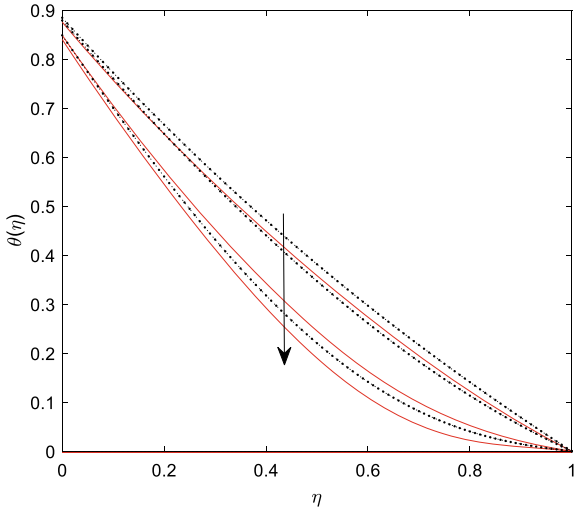

Fig. 20 Effects of Q on temperature profile

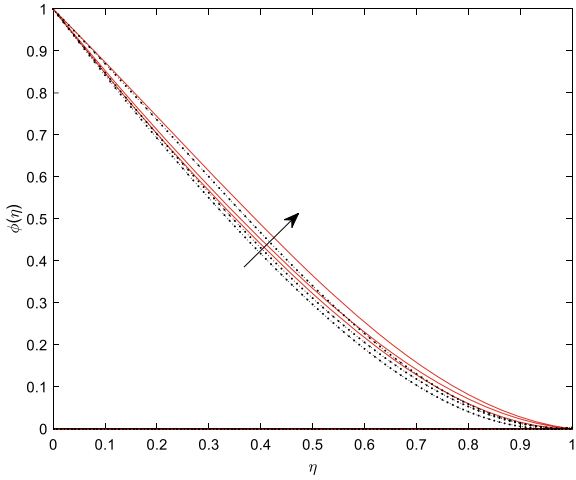

Fig. 21 Effects of Q on concentration profile

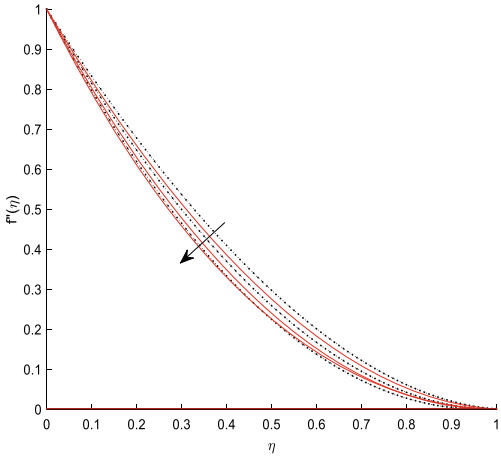

Fig. 22 Effects of β on velocity profile

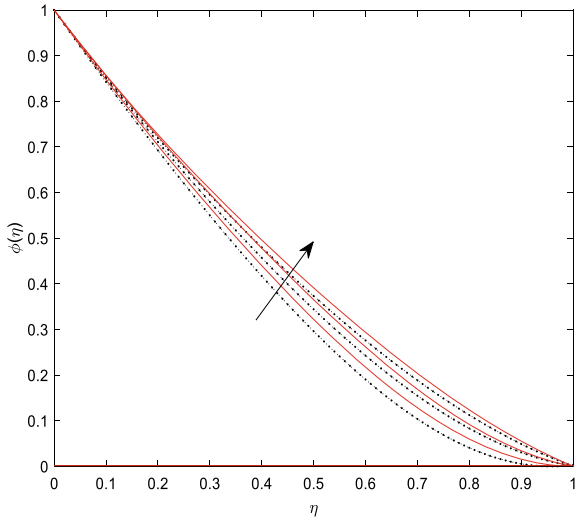

Fig. 23 Effects of β on concentration profile

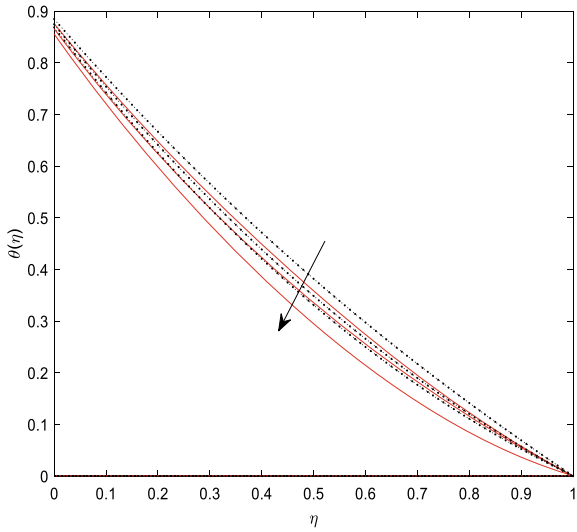

Fig. 24 Effects of Pr on temperature profile

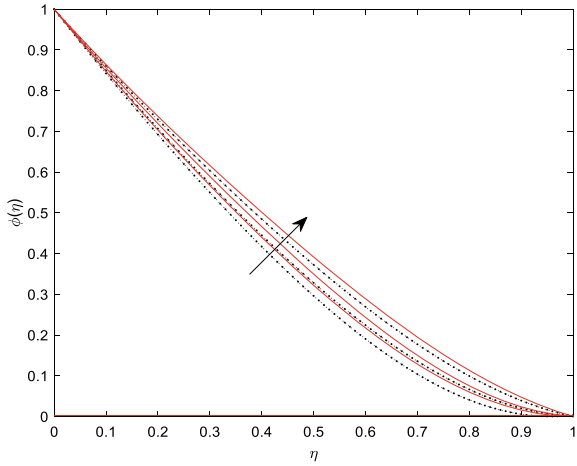

Fig. 25 Effects of Pr on concentration profile

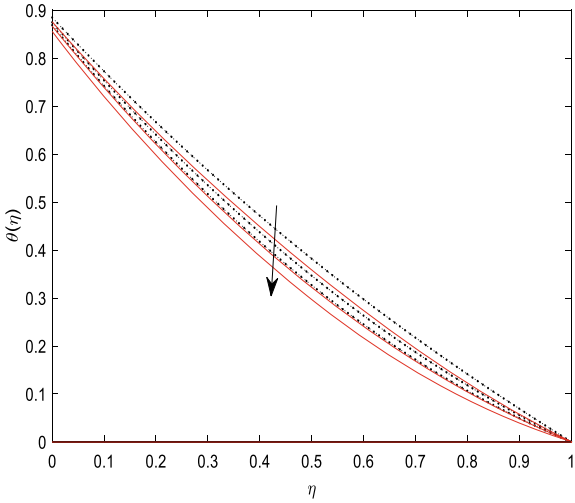

Fig. 26 Effects of Sc on temperature profile

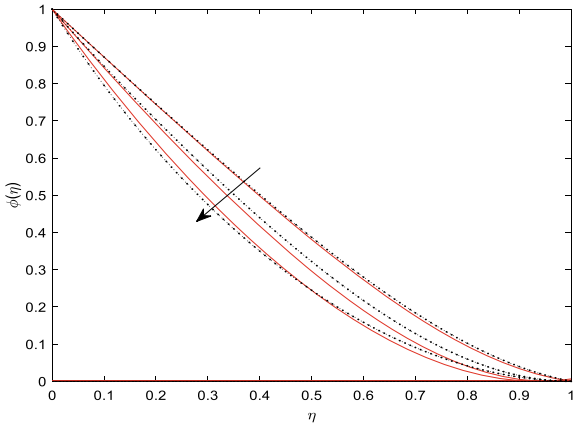

Fig. 27 Effects of Sc on concentration profile

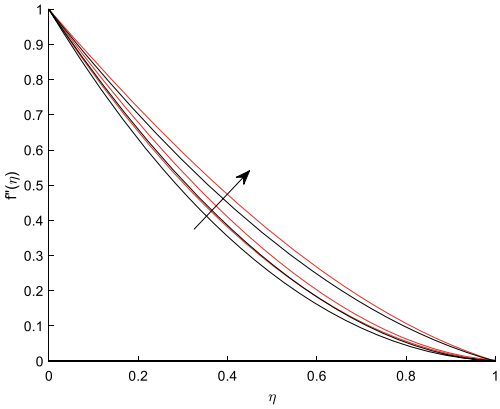

Fig. 28 Effects of α on velocity profile

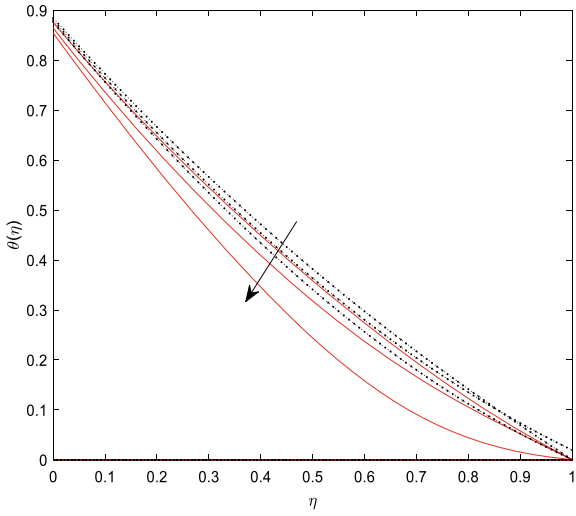

Fig. 29 Effects of Nr on temperature profile

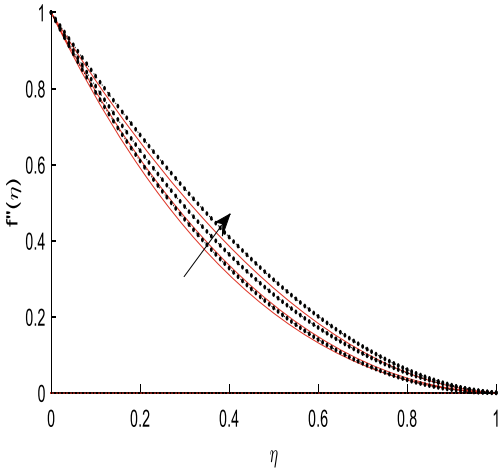

Fig. 30 Effects of λ_c on velocity profile

Table 1 For velocity profile

α	M	Bi	λ_c	λ_T	Ec	Du	Sr	Da	β	S = −0.2			S = 0.2		
										f″(0)	−θ'(0)	−ϕ'(0)	f″(0)	−θ'(0)	−ϕ'(0)
π/6	1	0.1	1	1	0.1	0.1	0.1	0.1	0.1	−1.9375	−0.2999	−1.021	−2.091	−0.2999	−1.021
π/4	1	0.1	1	1	0.1	0.1	0.1	0.1	0.1	−1.734	−0.1999	−3.121	−1.874	−0.1999	−3.121
π/3	1	0.1	1	1	0.1	0.1	0.1	0.1	0.1	−1.4765	−0.0999	−3.991	−1.6065	−0.0999	−3.991
π/4	1.5	0.1	1	1	0.1	0.1	0.1	0.1	0.1	−1.968	−0.2999	−1.111	−2.1175	−0.2999	−1.111
π/4	2	0.1	1	1	0.1	0.1	0.1	0.1	0.1	−2.277	−0.3999	−0.0021	−2.4365	−0.3999	−0.0021
π/4	1	0.5	1	1	0.1	0.1	0.1	0.1	0.1	−1.429	−0.1997	−4.9995	−1.674	−0.1997	−6.202
π/4	1	1	1	1	0.1	0.1	0.1	0.1	0.1	−1.368	−0.2997	−4.602	−1.4885	−0.2997	−4.602
π/4	1	2	1	1	0.1	0.1	0.1	0.1	0.1	−1.6151	−2.3199	−2.454	−1.451	−1.7997	−0.862
π/4	1	0.1	−1	1	0.1	0.1	0.1	0.1	0.1	−2.255	−0.2911	−1.021	−2.414	−0.3140	−1.9
π/4	1	0.1	0	1	0.1	0.1	0.1	0.1	0.1	−2.0621	−0.2999	−1.021	−2.225	−0.2999	−4.881
π /4	1	0.1	1	−1	0.1	0.1	0.1	0.1	0.1	−1.512	−0.0299	−2.121	−1.571	−0.0688	−2.6621
π/4	1	0.1	1	0	0.1	0.1	0.1	0.1	0.1	−1.551	−0.1258	−4.589	−1.5999	−0.2999	−3.821
π/4	1	0.1	1	1	0.5	0.1	0.1	0.1	0.1	−1.934	−0.2999	−1.811	−2.098	−0.2999	−1.921
π/4	1	0.1	1	1	1	0.1	0.1	0.1	0.1	−2.0026	−0.3152	−1.845	−2.230	−0.36249	−1.001
π/4	1	0.1	1	1	0.1	0.5	0.1	0.1	0.1	−1.954	−0.2999	−2.121	−2.08	−0.2999	−1.851
π/4	1	0.1	1	1	0.1	1	0.1	0.1	0.1	−2.142	−0.3999	−0.798	−2.142	−0.3999	−0.798
π/4	1	0.1	1	1	0.1	0.1	0.5	0.1	0.1	−1.934	−0.2983	−2.001	−2.151	−0.3125	−2.199
π/4	1	0.1	1	1	0.1	0.1	1	0.1	0.1	−1.992	−0.3209	−1.878	−1.976	−0.2014	−4.119
π/4	1	0.1	1	1	0.1	0.1	0.1	0.5	0.1	−1.994	−0.2999	−1.631	−2.105	−0.2999	−1.219
π/4	1	0.1	1	1	0.1	0.1	0.1	1	0.1	−2.257	−0.3999	−0.018	−2.410	−0.3968	0.048
π/4	1	0.1	1	1	0.1	0.1	0.1	0.1	0.5	−1.948	−0.2999	−2.121	−2.088	−0.2999	−2.01

(continued)

Table 1 (continued)

α	M	Bi	λ_c	λ_T	Ec	Du	Sr	Da	β	S = −0.2			S = 0.2		
										f″(0)	−θ'(0)	−ϕ'(0)	f″(0)	−θ'(0)	−ϕ'(0)
π/4	1	0.1	1	1	0.1	0.1	0.1	0.1	1	−2.1541	−0.3999	−1.107	−2.245	−0.3999	−0.411

Table 2 For temperature profile

Da	M	Bi	Pr	Nr	Ec	Du	Sr	Sc	Q	S = −0.2			S = 0.2		
										f″(0)	−θ'(0)	−ϕ'(0)	f″(0)	−θ'(0)	−ϕ'(0)
0.1	1	10	0.71	0.5	0.1	−2	0.1	0.78	0.5	−0.0181	−1.151	−1.5499	−1.581	−1.239	−3.599
0.1	1	10	0.71	1	0.1	−2	0.1	0.78	0.5	−0.0001	−1.191	−0.131	−1.799	−1.351	−11.421
0.1	1	10	0.71	2	0.1	−2	0.1	0.78	0.5	−0.00001	−1.231	−3.051	−2.849	−1.451	−17.421
0.1	2	10	0.71	0.5	0.1	−2	0.1	0.78	0.5	−0.0181	−1.251	−0.359	−1.631	−1.339	−7.5499
0.1	3	10	0.71	0.5	0.1	−2	0.1	0.78	0.5	−0.00001	−1.311	+0.3731	−2.358	−1.439	−9.1499
0.1	1	10	0.81	0.5	0.1	−2	0.1	0.78	0.5	−0.4261	−1.251	−0.359	−1.021	−1.339	−4.04999
0.1	1	10	0.91	0.5	0.1	−2	0.1	0.78	0.5	−0.479	−1.311	−0.0731	−1.579	−1.439	−5.4999
0.5	1	10	0.71	0.5	0.1	−2	0.1	0.78	0.5	−0.1361	−1.251	−0.359	−0.0001	−1.33001	−0.0001
1	1	10	0.71	0.5	0.1	−2	0.1	0.78	0.5	−0.0001	−1.311	−0.0001	−1.999	−1.439	−9.311
0.1	1	10	0.71	0.5	0.1	−2	0.1	0.88	0.5	−0.329	−1.251	−0.359	−0.2001	−1.33001	−0.00001
0.1	1	10	0.71	0.5	0.1	−2	0.1	0.98	0.5	−03,651	−1.311	−0.0001	−1.529	−1.439	−6.599
0.1	1	10	0.71	0.5	0.3	−2	0.1	0.78	0.5	−0.00001	−1.2471	−0.0001	−1.9101	−1.3308	−8.531
0.1	1	10	0.71	0.5	0.5	−2	0.1	0.78	0.5	−0.001	−1.3101	−1.2432	−2.359	−1.439	−14.799
0.1	1	10	0.71	0.5	0.1	−3	0.1	0.78	0.5	−0.0008	−1.445	−0.000001	−2.101	−1.4308	−4.421
0.1	1	10	0.71	0.5	0.1	−4	0.1	0.78	0.5	−0.221	1.701	+1.1432	−1.635	−1.801	−8.0001
0.1	1	10	0.71	0.5	0.1	−2	0.5	0.78	0.5	−0.000008	−1.207	−0.00001	−2.495	−1.508	−12.221
0.1	1	10	0.71	0.5	0.1	−2	1	0.78	0.5	+0.2521	−1.7101	+13.232	−2.893	−1.601	−18.651
0.1	1	10	0.71	0.5	0.1	−2	0.1	0.78	1	−0.00008	−1.207	−0.10001	−2.084	−1.508	−12.221
0.1	1	10	0.71	0.5	0.1	−2	0.1	0.78	2	−0.03521	−1.5101	+5.757	−2.420	−1.592	−16.481

Table 3 For concentration profile

Sc	Du	Sr	M	Bi	Da	Ec	β	Pr	Q	S = −0.2			S = 0.2		
										f″(0)	−θ'(0)	−ϕ'(0)	f″(0)	−θ'(0)	−ϕ'(0)
0.78	0.1	0.1	1	0.1	0.1	0.1	0.1	0.71	0.5	−1.137	−1.625	−1.618	−2.457	−1.8252	−1.585
0.22	0.1	0.1	1	0.1	0.1	0.1	0.1	0.71	0.5	−2.781	−2.912	−1.302	−3.021	−2.912	−1.302
2.62	0.1	0.1	1	0.1	0.1	0.1	0.1	0.71	0.5	−1.171	−0.925	−2.012	−1.721	−0.852	−2.232
0.78	−0.1	0.1	1	0.1	0.1	0.1	0.1	0.71	0.5	−3.899	−2.252	−1.368	−2.796	−1.451	−1.405
0.78	0	0.1	1	0.1	0.1	0.1	0.1	0.71	0.5	−2.545	−1.891	−1.4879	−2.607	−1.6252	−1.4879
0.78	0.1	0	1	0.1	0.1	0.1	0.1	0.71	0.5	−1.457	−4.999	−1.585	−3.457	−2.998	−1.439
0.78	0.1	0.2	1	0.1	0.1	0.1	0.1	0.71	0.5	−1.659	−1.407	−1.698	−0.079	−1.001	−1.686
0.78	0.1	0.1	1.5	0.1	0.1	0.1	0.1	0.71	0.5	−0.161	−1.362	−1.6799	−1.0059	−1.4675	−1.698
0.78	0.1	0.1	2	0.1	0.1	0.1	0.1	0.71	0.5	−1.991	−1.511	−1.4825	−0.0059	−1.3054	−1.795
0.78	0.1	0.1	1	0.2	0.1	0.1	0.1	0.71	0.5	−0.149	−2.701	−1.668	−1.457	−3.111	−1.651
0.78	0.1	0.1	1	0.5	0.1	0.1	0.1	0.71	0.5	−0.049	−5.435	−1.651	−0.259	−6.611	−1.751
0.78	0.1	0.1	1	0.1	−0.1	0.1	0.1	0.71	0.5	−0.011	−1.362	−1.671	−0.011	−1.305	−1.743
0.78	0.1	0.1	1	0.1	0.5	0.1	0.1	0.71	0.5	−1.549	−1.621	−1.568	−1.549	−1.621	−1.668
0.78	0.1	0.1	1	0.1	0.1	0.5	0.1	0.71	0.5	−1.549	−1.401	−1.548	−3.487	−1.8252	−1.485
0.78	0.1	0.1	1	0.1	0.1	1	0.1	0.71	0.5	−1.9991	−1.208	−1.444	−3.361	−1.758	−1.399
0.78	0.1	0.1	1	0.1	0.1	0.1	0.5	0.71	0.5	−1.549	−1.381	−1.548	−3.541	−1.882	−1.5058
0.78	0.1	0.1	1	0.1	0.1	0.1	1	0.71	0.5	−1.9991	−1.208	−1.537	−3.465	−1.504	−1.519
0.78	0.1	0.1	1	0.1	0.1	0.1	0.1	0.81	0.5	−1.311	−1.381	−1.548	−3.311	−1.882	−1.5058
0.78	0.1	0.1	1	0.1	0.1	0.1	0.1	0.91	0.5	−1.9991	−1.284	−1.437	−3.201	−1.504	−1.419
0.78	0.1	0.1	1	0.1	0.1	0.1	0.1	0.71	1	−0.289	−1.381	−1.548	−1.311	−1.628	−1.5058
0.78	0.1	0.1	1	0.1	0.1	0.1	0.1	0.71	2	−0.021	−1.814	−1.281	−0.751	−1.819	−1.259

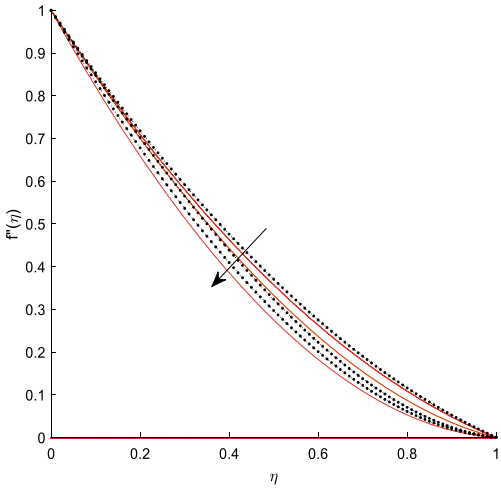

Fig. 31 Effects of λ_T on velocity profile

References

1. Anuradha S, Yegammai M (2017) MHD viscoelastic fluid flow over a vertical stretching sheet with nth order of chemical reaction. Int J Eng Tech 3(5):1–9
2. Babu SR, Venkateswarlu S, Lakshmi K (2018) Effect of magnetic field and radiation on MHD heat and mass transfer of micropolar fluid over stretching sheet with Soret and Dufour effects. Int J Appl Eng Res 13(12):10991–11000
3. Bazid MAA, Gharsseldien ZM, Seddeek MA, Alharbi M (2012) Soret and Dufour numbers effect on heat and mass transfer in stagnation point flow towards a stretching surface in the presence of Buoyancy force and variable thermal conductivity. J Comput Modell 2(4):25–50
4. Barik AK, Mishra SK, Mishra SR, Pattnaik PK (2020) Multiple slip effects on MHD nanofluid flow over an inclined, radiative, and chemically reacting stretching sheet by means of FDM. Heat Transf Asian Res 2020(49):477–501
5. Bhuvaneswari M, Sheniyappan E, Sivanandam S, Hussein AK (2019) Cross-diffusion effects on MHD mixed convection over a stretching surface in a porous medium with chemical reaction and convective condition. Eng Trans 67(1):3–19
6. Daniel YS, Daniel SK (2015) Effects of buoyancy and thermal radiation on MHD flow over a stretching porous sheet using homotopy analysis method. Alexandria Eng J pp 1–8
7. Daniel YS, Aziz ZA, Ismail Z, Salah F (2017) Double stratification effects on unsteady electrical MHD mixed convection flow of nanofluid with viscous dissipation and Joule heating. J Appl Res Technol 15:464–476
8. Daniel YS, Aziz ZA, Ismail Z, Salah F (2018) Thermal stratification effects on MHD radiative flow of nanofluid over nonlinear stretching sheet with variable thickness. J Comput Des Eng 5:232–242
9. Elazar NS (2019) Nanofluids flow over a permeable unsteady stretching surface with non-uniform heat source/sink in the presence of inclined magnetic field. J Egypt Mathe Soc 27(9):1–26
10. Endalew MF, Nayak A (2018) Thermal radiation and inclined magnetic field effects on MHD flow past a linearly accelerated inclined plate in a porous medium with variable temperature. Heat Transf—Asian Res 1–20
11. Ferdows M, Uddin MJ, Afify AA (2013) Scaling group transformation for MHD boundary layer free convective heat and mass transfer flow past a convectively heated nonlinear radiating stretching sheet. Int J Heat Mass Transf 56:181–187

12. Gupta S, Kumar D, Singh J (2020) Analytical study for MHD flow of Williamson nanofluid with the effects of variable thickness, nonlinear thermal radiation and improved Fourier's and Fick's Laws. SN Appl Sci 2:438
13. Gupta S, Kumar D, Singh J (2019) MHD three dimensional boundary layer flow and heat transfer of water driven Copper and Alumina nanoparticles induced by convective conditions. Int J Modern Phys B 33(26):1950307
14. Hayat T, Qayyum S, Alsaedi A, Asghar S (2017) Radiation effects on the mixed convection flow induced by an inclined stretching cylinder with non-uniform heat source/sink. PLoS ONE 12(4):1–23
15. Jabeen K, Mushtaq M, Akram RM (2020) Analysis of the MHD boundary layer flow over a nonlinear stretching sheet in a porous medium using semi analytical approaches. Mathe Prob Eng 2020:1–9
16. Kala BS, Rawat MS, Kumar A (2020) Numerical analysis of the flow of a Casson fluid in magnetic field over an inclined nonlinearly stretching surface with velocity slip in a Forchheimer porous Medium. Asian Res J Math 16(7):34–58
17. Kumar KG, Manjunatha S, Rudraswamy NG (2020) MHD flow and nonlinear thermal radiative heat transfer of dusty Prandtl fluid over a stretching sheet. Fluid Dyn Mater Process FDMP 16(2):131–146
18. Lakshmi BK, Sugunamma V, Reddy JVR (2018) Soret and Dufour effects on MHD flow of Sisko fluid over a stretching sheet with non-uniform heat source/sink. Int J Emerg Technol Eng Res 6(2):125–136
19. Mohammed JU, Khan WA, Ismail AI (2018) Convective boundary layer flow of a nanofluid past a flat vertical plate with Newtonian heating boundary condition. Plos One 7(11):1–8
20. Mondal H, Pal D, Chatterjee S, Sibanda P (2018) Thermophoresis and Soret-Dufour on MHD mixed convection mass transfer over an inclined plate with non-uniform heat source/sink and chemical reaction. Ain Shams Eng J 9:2111–2121
21. Pattnaik JR, Dash GC, Singh S (2017) Radiation and mass transfer effects on MHD flow through porous medium past an exponentially accelerated inclined plate with variable temperature. Ain Shams Eng J 8:67–75
22. Rashidi MM, Rostami B, Freidoonimehr N, Abbasbandy S (2014) Free convective heat and mass transfer for MHD fluid flow over a permeable vertical stretching sheet in the presence of the radiation and buoyancy effects. Ain Shams Eng J 5:901–912
23. Rashidi M, Ali M, Rostami B, Rostami P, Xie G (2015) Heat and mass transfer for MHD viscoelastic fluid flow over a vertical stretching sheet with considering Soret and Dufour effects. Mohammad, Math Prob Eng 2015:1–12
24. Rafique K, Anwar MI, Misiran M, Khan I, Seikh AH, Sherif EM, Nisar KS (2019) Brownian motion and thermophoretic diffusion effects on micropolar type nanofluid flow with Soret and Dufour impacts over an inclined sheet: Keller-box simulations. Energies 12(4191):1–22
25. Rafique K, Anwar MI, Misiran M, Khan I, Alharbi SO, Thounthong P, Nisar KS (2019) Numerical solution of Casson nanofluid flow over a non-linear inclined surface with Soret and Dufour effects by Keller-box method. Front Phys 7(139):1–13
26. Rasool G, Zhang T (2019) Darcy-Forchheimer nanofluidic flow manifested with Cattaneo-Christov theory of heat and mass flux over non-linearly stretching surface. PLoS ONE 14(8):1–23
27. Reddy GVR, Krishna YH (2018) Soret and Dufour effect on MHD micropolar fluid flow over a linearly stretching sheet through a non-darcy porous medium. Int J Appl Mech Eng 23(2):485–502
28. Sulochanaa SC, Sandeep S (2016) Thermal radiation effect on MHD nanofluid flow over a stretching sheet. Int J Eng Res 23:89–102

29. Tlili I (2019) Effects MHD and heat generation on mixed convection flow of Jeffrey fluid in microgravity environment over an inclined stretching sheet. Symmetry 438:1–11
30. Thumma T, Shamsuddin MD (2018) Buoyancy ratio and heat source effect on MHD flow over an inclined non-linearly stretching sheet. Front Heat Mass Transf (FHMT) 10(5):1–12
31. Yasmin A, Ali K, Ashraf M (2020) Study of heat and mass transfer in MHD flow of micropolar fluid over a curved stretching sheet. Sci Rep 10(4581):1–11

Entropy Generation in Fourth-Grade Fluid Flow with Variable Thermal Conductivity

Paresh Vyas and Kusum Yadav

Abstract The present paper presents a numerical study of thermo fluidic configuration confronting entropy generation in the fourth-grade fluid flow in a parallel plate channel with temperature-dependent thermal conductivity. The problem modelled as a boundary value problem has been simulated by Runge–Kutta fourth-order method coupled with the shooting scheme. Thermodynamic irreversibility analysis is conducted through quantification of entropy generation number and Bejan number. These quantities are portrayed for embedded parameters. The study would be a formidable basis to serve as a pertinent initial endeavour for future analogous systems with larger complexities.

Keywords Entropy · Fourth-grade fluid · Thermal conductivity

1 Introduction

A wide range of natural or industrial fluids such as biofluids, juices, honey, silicate melts, polymer paints, pharmaceutical suspensions, chemical pastes, etc. is non-Newtonian. Contrary to Newtonian fluids which have a linear relationship between shear stress and the shear rate, the non-Newtonian fluids exhibit a nonlinear relationship for the same and at a specified temperature and/or pressure; the apparent viscosity does not remain fixed and rather depends on flow conditions including flow history. This physical understanding underscores that the Newtonian hypothesis breaks down in addressing many real-world flow problems. In fact, one has to clearly identify the non-Newtonian characteristics of the working fluid. Working out shear stress formulation for complex nonlinear fluids is a daunting task. Some efforts have been made to put forth some empirical formulations to address the complex rheology. These include constitutive equations for the stress–tensor comprising velocity gradient (symmetric part) and higher-order gradients and other variety of rate-type and differential models. However, no single model is sufficient to portray all properties of such fluids owing to

P. Vyas · K. Yadav (✉)
Department of Mathematics, University of Rajasthan, Jaipur 302004, India
e-mail: kusum.ydv@gmail.com

J. Singh et al. (eds.), *Advances in Mathematical Modelling, Applied Analysis and Computation*, Lecture Notes in Networks and Systems 415,
https://doi.org/10.1007/978-981-19-0179-9_35

the complexities involved. A good insight into the topic can be seen in well-presented texts by Wilkinson [37], Schowalter [23], Rajagopal [20], Dunn and Rajagopal [7] and Truesdell and Noll [27]. There have been numerous theoretical studies on flow and thermal characteristics for non-Newtonian fluids. Rajagopal [19] presented a brief note on time-dependent unidirectional flows of a nonlinear fluid. In another paper, Rajagopal [21] discussed creeping second-order fluid flow. Rajagopal and Bhatnagar [17] considered Oldroyd-B fluid and derived exact solutions for some idealized cases. Rajagopal and Srinivasa [18] presented a thermodynamic analysis for differential fluid models. Siddiqui et al. [26] used the HPM solution strategy to examine third-grade fluid flow and heat transfer. Hayat et al. [10] considered magnetohydrodynamic third-grade fluid flow inside a channel. Siddiqui et al. [25] studied third-grade fluid in a parallel channel flow using the Adomian decomposition method. Keimanesh [13] employed the DTM method to investigate third-grade fluid flow trapped between parallel plates. Islam [12] examined a fourth-grade fluid flow considering partial slip. Mokarizadeh et al. [15] investigated thermal aspects of Giesekus viscoelastic Couette-Poiseuille flow. Hatami et al. [9] performed a simulation for third-grade non-Newtonian nanofluid flow in a porous cavity. Siddiqui et al. [24] used an integral method to examine second-grade fluid inside a tube. Rashidi et al. [22] studied entropy for MHD third-grade non-Newtonian fluid flow due to a stretching sheet. Rahbari et al. [16] discussed the thermodynamics of non-Newtonian Maxwell fluid flow inside a channel and solved the system analytically and numerically.

Thermal conductivity shows dependence on temperature and is well documented. Thermal conductivities of liquids and gases behave differently as it is a material property. The literature is vast to report fluid flow for variable thermal conductivities. Vyas and Rai [29, 30] studied the effects of variable thermal conductivity on stretching surface flow and point sink flow configurations. Chiam [6] examined the thermal characteristics of variable thermal conductivity over a linearly stretching sheet. Hossain [11] studied thermal conductivity effects on flow past a wedge. Lin [14] examined Marangoni convection with variable thermal conductivity in pseudo-plastic nanofluids. Asad [1] simulated a couple of stress fluid flow with nonuniform thermal conductivity. Gbadeyan et al. [8] investigated Casson nanofluid slip flow with variable thermal conductivity and subjected it to convective heating.

Every real-world thermo fluidic system encounters thermodynamic irreversibility for the simple reason that all real processes are irreversible. Quantification of thermodynamic irreversibility in thermo fluidics has received attention in recent times for possible optimization and better performance.

Bejan [3, 4] pioneered a study to enumerate entropy in fluidic systems and proposed a formulation facilitating entropy generation minimization by parametric study. The idea was well received by the investigators to report numerous pertinent studies as evident from the available literature. Aziz [2] reported entropy generation in a Couette flow with different thermal boundary conditions.

Vyas and his co-authors reported entropy in various fluidic configurations. Vyas et al. [35] reported micro polar couple stress thermo fluidics and entropy generation in Forchheimer channel. Vyas and Soni [31] reported entropy generation in

Casson MHD fluid flow in a channel experiencing hydrodynamic slip. Vyas and Srivastava [32] examined entropy analysis of generalized MHD Couette flow inside a composite duct with asymmetric convective cooling. Vyas et al. [34] discussed entropy generation analysis for oscillatory flow in a vertical channel filled with a porous medium. Vyas and Yadav [33] analysed entropy generation in mixed convection due to a vertical stretching cylinder placed in a heat-generating fluid-saturated porous medium. Vyas et al. [36] simulated entropy for boundary layer micropolar fluid flow. Vyas and Khan [28] examined entropy analysis for MHD dissipative Casson fluid flow in a porous medium due to a stretching cylinder.

In this paper an attempt has been made to quantify entropy generation for parallel plate channel flow of fourth-grade fluid with temperature-dependent thermal conductivity. The governing boundary value problem has been treated numerically by fourth-order Runge–Kutta scheme substantiated with the shooting method. The idealized setup considered here may be a launching pad for future robust explorations involving rather more complex set-ups. It is expected that the present problem would be a pertinent baby model for initial estimates.

2 The Problem

We consider a fully developed steady laminar flow of a fourth-grade non-Newtonian fluid trapped between two isothermal stationary parallel plates distant H apart and maintained at different temperatures T_1 and T_2. The flow is caused by a constant pressure gradient applied at the mouth of the channel. A Cartesian coordinate system is chosen. The governing differential equations for the setup are as follows:

$$\mu \frac{d^2u}{dy^2} + 6\beta \left(\frac{du}{dy}\right)^2 \frac{d^2u}{dy^2} = \frac{dp}{dx} \tag{1}$$

$$\frac{d}{dy}\left(\kappa \frac{dT}{dy}\right) + \delta \left(\frac{du}{dy}\right)^2 \left\{\mu + 2\beta \left(\frac{du}{dy}\right)^2\right\} - \frac{\partial q_r}{\partial y} = 0 \tag{2}$$

and the boundary conditions are as follows:

$$y = 0: \qquad u = 0, \qquad T = T_1 \tag{3}$$

$$y = H: \qquad u = 0, \qquad T = T_2 \tag{4}$$

where u and T are the fluid velocity and temperature, respectively, μ is the viscosity, β is the non-Newtonian parameter, $\frac{dP}{dx}$ is the applied pressure gradient (in x-direction), κ is the thermal conductivity and δ is the viscous heating parameter.

Using the Rooseland approximation [5] for radiation, we describe the radiative flux q_r as follows:

$$q_r = -\frac{4\gamma}{3\alpha}\frac{\partial T^4}{\partial y} \tag{5}$$

where γ and α are the Stephen–Boltzmann constant and the mean absorption coefficient, respectively. We assume that the temperature difference in the flow domain is sufficiently small enough so that T^4 may be expressed linearly by having truncated Taylor series expansion of T^4 about T_1 to give

$$T^4 \cong 4T_1^3 T - 3T_1^4 \tag{6}$$

Nondimensionalization of the governing boundary value problem is undertaken with the quantities as follows:

$$u^* = \frac{u}{u_0},\ \eta = \frac{y}{H},\ \theta = \frac{T - T_1}{T_2 - T_1} \tag{7}$$

Further, we assume that the thermal conductivity κ exhibits an inverse linear function of temperature as follows:

$$\frac{1}{\kappa} = \frac{1}{\kappa_1}\{1 + \in (T - T_1)\} \text{ or } \frac{1}{\kappa} = \lambda(T - T_k) \tag{8}$$

where κ_1 is the reference thermal conductivity, $\in$ is a constant based on the thermal property of the fluid.

The constants $T_k = T_1 - \frac{1}{\in}$ and $\lambda = \frac{\in}{\kappa_1}$ depend upon the reference state and thermal property of the fluid.

Thus the BVP in nondimensional form becomes as follows:

$$\frac{d^2u^*}{d\eta^2} + 6m\left(\frac{du^*}{d\eta}\right)^2\frac{d^2u^*}{d\eta^2} = c \tag{9}$$

$$\left\{\left(\frac{\theta_k}{\theta_k - \theta}\right) + N\right\}\frac{d^2\theta}{d\eta^2} + \frac{\theta_k}{(\theta_k - \theta)^2}\left(\frac{d\theta}{d\eta}\right)^2 + Br\left(\frac{du^*}{d\eta}\right)^2\left\{1 + 2m\left(\frac{du^*}{d\eta}\right)^2\right\} = 0 \tag{10}$$

$$\eta = 0 :\ u = 0, \theta \tag{11}$$

$$\eta = 1 :\ u = 0, \theta = 1 \tag{12}$$

where $c = \frac{H^2}{\mu u_0}\frac{\partial P}{\partial x}$, $m = \frac{\beta u_0^2}{\mu H^2}$, $Br = \frac{\mu \delta u_0^2}{\kappa_1 (T_2 - T_1)}$, $N = \frac{16\gamma T_1^3}{3\alpha\kappa_1}$,

$\theta_k = \frac{T_k - T_1}{T_2 - T_1}$ or $\theta_k = \frac{-1}{\epsilon(T_2 - T_1)}$ are the pressure gradient parameter, non-Newtonian parameter, Brinkmann number, radiation parameter and the transformed dimensionless reference temperature corresponding to thermal conductivity parameter, respectively.

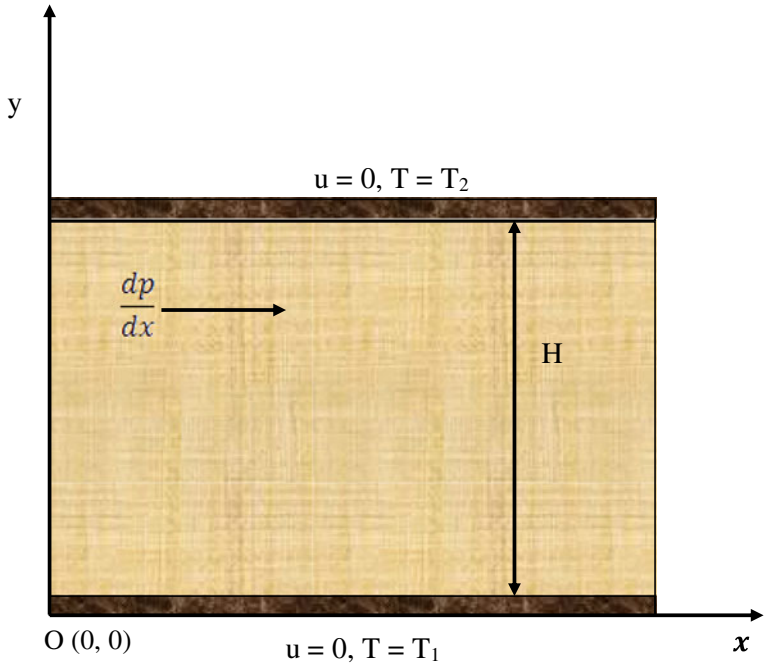

Schematic diagram

3 Solution Technique

The nonlinear BVP, given by Eqs. (9–12), has been solved by fourth-order Runge–Kutta scheme together shooting method. In this method, we first convert the BVP into a system of initial value problems (IVPs). Thereafter, we make appropriate guesses for the unknown quantities such that the given end conditions are satisfied. Estimation of unknown guesses is done on a purely hit and trial basis and their refinement is ensured to attain prescribed accuracy. In the present case, the BVP is reduced to the following system of initial value problems:

$$\frac{du^*}{d\eta} = p \tag{13}$$

$$\frac{d\theta}{d\eta} = q \tag{14}$$

$$\frac{dp}{d\eta} = \frac{c}{(1+6mp^2)} \tag{15}$$

$$\frac{dq}{d\eta} = \frac{-(\theta_k - \theta)}{\{\theta_k + N(\theta_k - \theta)\}}\left[\frac{\theta_k}{(\theta_k - \theta)^2}q^2 + Brp^2(1+2mp^2)\right] \tag{16}$$

where initial conditions are

$$u*(0) = 0, \theta(0) = 0, p(0) = a_0, q(0) = s_0 \tag{17}$$

The above system of initial value problems is solved with some guess values s_0 and a_0 for the unknown quantities $u^{*'}(0)$ and $\theta(0)$, respectively, such that the end conditions $u^*(1) = 0$ and $\theta(1) = 1$ are satisfied. If for these guess values, the end conditions are not satisfied then the system of IVPs is again solved with another guess values s_1 and a_1 for $u^{*'}(0)$ and $\theta(0)$, respectively. In order to acquire a faster refinement of estimates for unknowns $u^{*'}(0)$ and $\theta(0)$, the secant method has been applied. The process continued until the end conditions got satisfied up to the prescribed accuracy of magnitude 10^{-7}. Furthermore, a grid independence study was also conducted to a bound on computational error. It revealed that a step size = 0.0001 was sufficient for the purpose. Table 1 presents the optimized guesses for $\theta'(0)$ for different values of θ_k.

The table revealed quantitative variations in the rate of heat transfer at the lower wall with the change in values of θ_k.

Table 1 Missing values of $u^{*'}(0)$ and $\theta'(0)$ when Br = 5, N = 2, m = 3, c = −1, ω = 3

θ_k	$u^{*'}(0)$	$\theta'(0)$
1	0.495	4.00
1.2	0.495	0.88425
1.4	0.495	0.77201
1.6	0.495	0.72175
1.8	0.495	0.69228
2	0.495	0.67325
4	0.495	0.61325
6	0.495	0.59930
8	0.495	0.59307
10	0.495	0.58955

4 The Entropy Generation Analysis

The local volumetric rate of entropy generation S_G concerned with the problem is given as follows:

$$S_G = \frac{\kappa}{T_1^2}\left\{\left(\frac{dT}{dy}\right)^2 + \frac{16\gamma T_1^3}{3\alpha\kappa}\left(\frac{dT}{dy}\right)^2\right\} + \frac{1}{T_1}\left[\delta\left(\frac{du}{dy}\right)^2\left\{\mu + 2\beta\left(\frac{du}{dy}\right)^2\right\}\right] \quad (18)$$

We define the characteristic entropy generation rate S_{G_0} and the characteristic temperature ratio ω as follows:

$$S_{G_0} = \frac{\kappa(T_2 - T_1)^2}{T_1^2 H^2} \text{ and } \omega = \frac{T_1}{T_2 - T_1} \quad (19)$$

Consequently, the entropy generation number $N_S = \frac{S_G}{S_{G_0}}$ is found as follows:

$$N_S = \left\{1 + N\left(\frac{\theta_k - \theta}{\theta_k}\right)\right\}\left(\frac{d\theta}{d\eta}\right)^2 + Br\omega\left(\frac{\theta_k - \theta}{\theta_k}\right)\left(\frac{du^*}{d\eta}\right)^2\left\{1 + 2m\left(\frac{du^*}{dy}\right)^2\right\} \quad (20)$$

$$N_1 + N_2$$

$$\text{where } N_1 = \left\{1 + N\left(\frac{\theta_k - \theta}{\theta_k}\right)\right\}\left(\frac{d\theta}{d\eta}\right)^2$$

$$\text{and } N_2 = Br\,\omega\left(\frac{\theta_k - \theta}{\theta_k}\right)\left(\frac{du^*}{d}\eta\right)^2\left\{1 + 2m\left(\frac{du^*}{dy}\right)^2\right\} \quad (21)$$

The Bejan number Be which is an irreversibility parameter is defined as

$$Be = \frac{N_1}{N_S} \quad (22)$$

5 Result and Discussion

The velocity and temperature regimes are used to compute the entropy generation number N_S. The profiles of quantities of interest for different values of parameters have been portrayed in Figs. 1, 2, 3, 4, 5, 6, 7, 8, 9, 10, 11 and 12.

Before taking up the figure-wise details, we make a remark about Bejan number Be. The figures transpire that Bejan number Be = 1 at the middle of the channel for any choice of the parameter values. This stands for the situation when there is no irreversibility due to dissipation. Furthermore, the effects of parameters on Be in the rest of the channel region are well pronounced.

Figure 1 depicts the effect of the Brinkman number on entropy generation number N_S. It shows that N_S increases with the increasing values of Br. The Brinkman number that accounts for dissipation in the system has a defining impact on the entropy generation. It is in line with the expectation since the dissipation effects modify the thermal regime that is reflected in entropy also as dissipation amounts to irrecoverable energy losses. Figure 2 displays that Bejan number Be across the channel width decays with the increasing values of Br and it assumes maximum

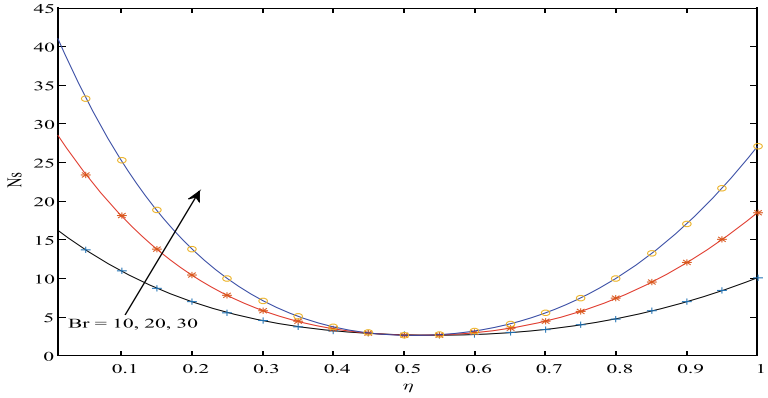

Fig. 1 Entropy generation number N_s varying with Brinkman number Br when N = 2, m = 3, c = −1, θ_k = 5, ω = 3

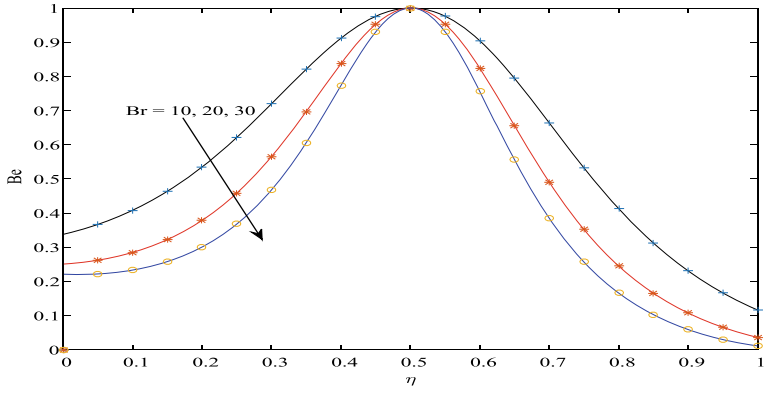

Fig. 2 Bejan number Be varying with Brinkman number Br when N = 2, m = 3, c = −1, θ_k = 5, ω = 3

value unity in the middle of the channel. Figure 3 reveals that N_S increases with an increase in pressure gradient. Figure 4 displays that Bejan number Be decreases with the increasing values of the pressure gradient. Figure 5 demonstrates that the effect of increasing non-Newtonian parameter m is to increase N_S. Figure 6 shows the effect of Newtonian parameter m on Bejan number Be. We see that Bejan number Be decays with an increase in m. Figure 7 displays that N_S registers a considerable rise with an increase in radiation parameter N; however, the effect of N on Be is opposite to the trend in the case of N_S as is evident from Fig. 8. Figure 9 exhibits that N_S increases with an increase in characteristic temperature ratio ω. Figure 10 shows the opposite trend in Be as that is seen in Fig. 9. These figures also show the quantitative changes in N_S in response to different parameters. Figure 11 reveals that the entropy number N_S decreases with an increase in θ_k in the region adjacent to the channel and then the trend is reversed at some spatial distance from the lower wall.

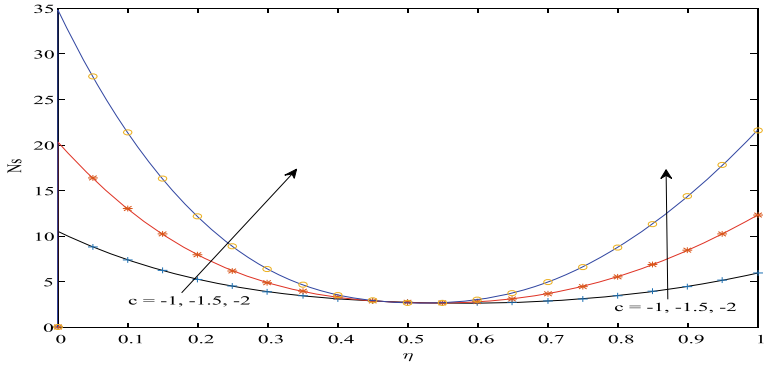

Fig. 3 Entropy generation number N_s varying with pressure c when N = 2, m = 3, Br = 5, θ_k = 5, ω = 3

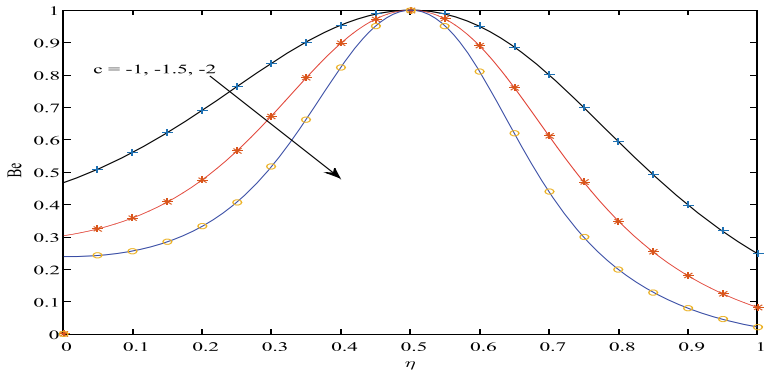

Fig. 4 Bejan number Be for varying values of pressure gradient c when N = 2, m = 3, Br = 5, θ_k = 5, ω = 3

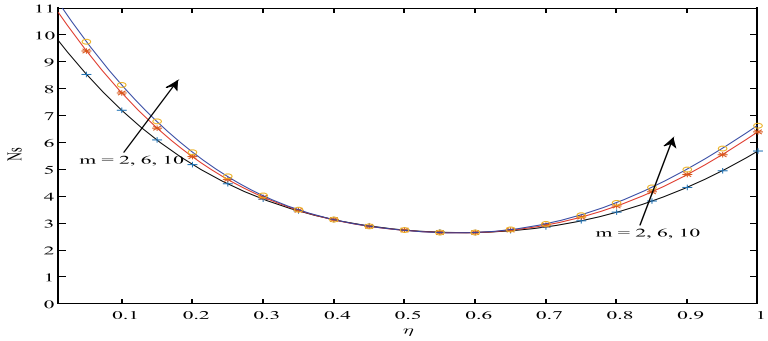

Fig. 5 Entropy generation number N_s varying with non-Newtonian parameter m when $N = 2$, $c = -1$, $Br = 5$, $\theta_k = 5$, $\omega = 3$

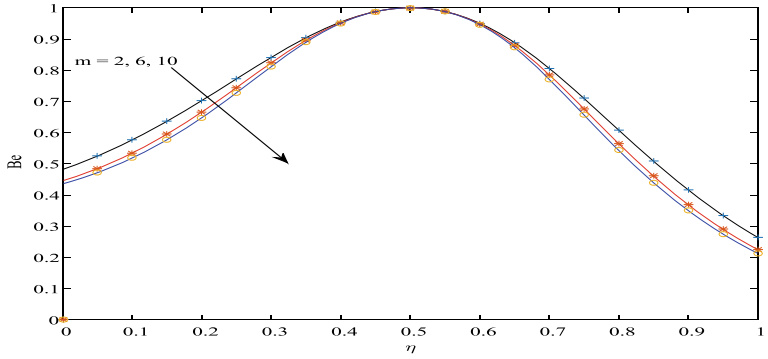

Fig. 6 Bejan number Be varying with non-Newtonian parameter m when $N = 2$, $c = -1$, $Br = 5$, $\theta_k = 5$, $\omega = 3$

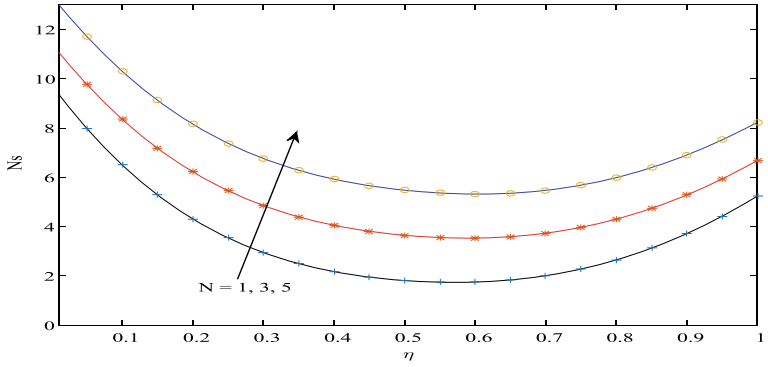

Fig. 7 Entropy generation number N_s varying with radiation parameter N when $m = 3$, $c = -1$, $Br = 5$, $\theta_k = 5$, $\omega = 3$

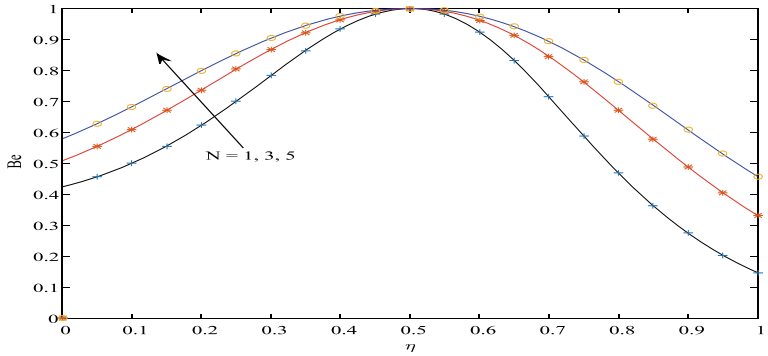

Fig. 8 Bejan number Be varying with radiation parameter N when m = 3, c = −1, Br = 5, θ_k = 5, ω = 3

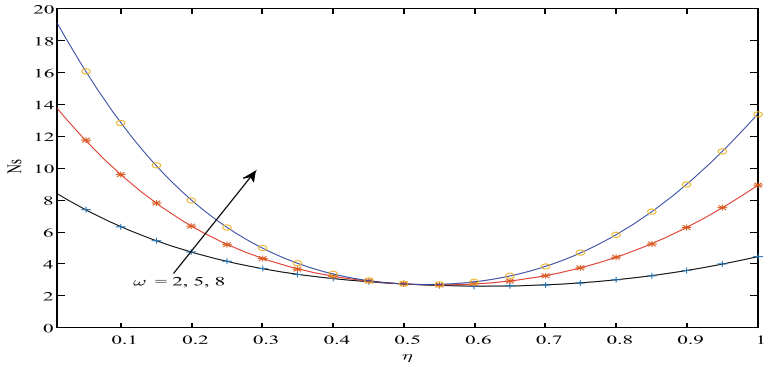

Fig. 9 Entropy generation number N_s varying with characteristic ratio ω when m = 3, c = −1, Br = 5, θ_k = 5, N = 2

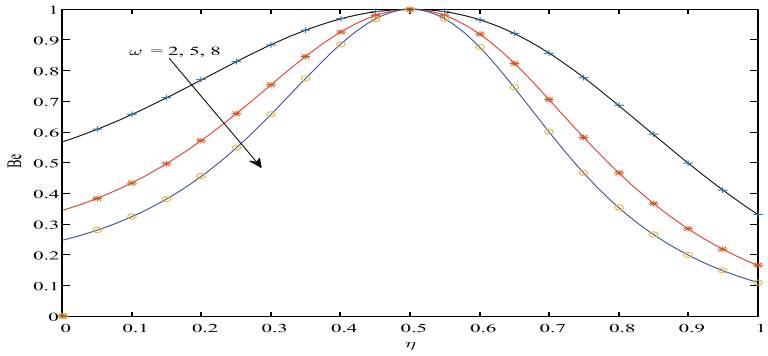

Fig. 10 Bejan number Be varying with characteristic ratio ω when m = 3, c = −1, Br = 5, θ_k = 5, N = 2

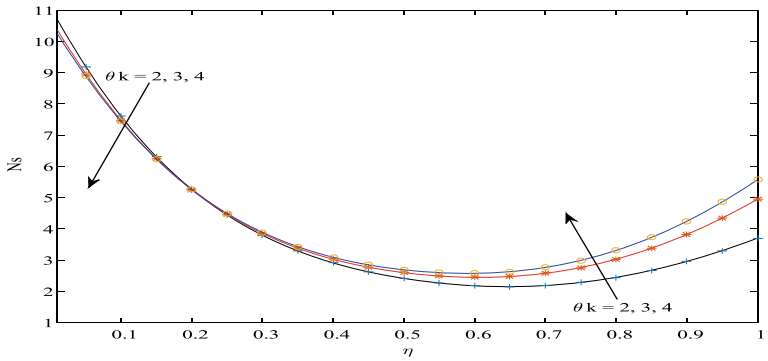

Fig. 11 Entropy generation number N_s varying with reference temperature θ_k when m = 3, c = −1, Br = 5, ω = 3, N = 2

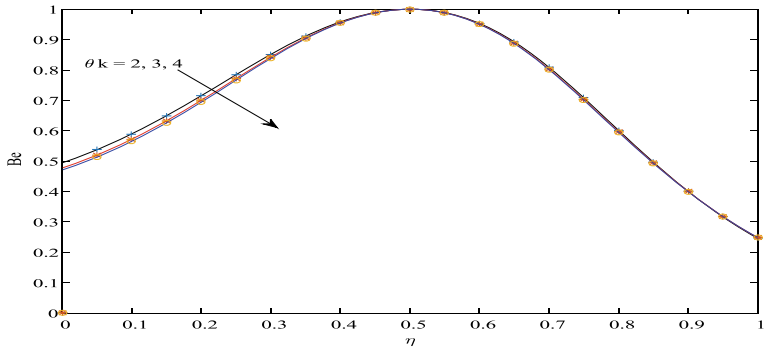

Fig. 12 Bejan number N_s varying with reference temperature θ_k when m = 3, c = −1, Br = 5, ω = 3, N = 2

It may be attributed to the rate of heat transfer at the lower wall as depicted in Table 1. Figure 12 shows qualitative variations in Be for varying values of θ_k.

6 Conclusion

A fourth-grade fluid flow with variable thermal conductivity in an isothermal parallel plate channel was considered to examine entropy generation. The thermal conductivity was assumed to have an inverse linear dependence on temperature. The BVP solved numerically provided velocity and temperature distributions which were employed to compute entropy. The main conclusions are the following:

1. The N_S value increases with the increasing values of Br, pressure gradient, non-Newtonian parameter m, radiation parameter N and the characteristic temperature ratio ω.
2. Bejan number Be attains its maximum possible value unity at the centre line of the channel for any choice of the parameter values, and the effects of parameters on Bejan number Be are well pronounced in the rest of the channel region.
3. There is a quantitative variation in the rate of heat transfer at the lower wall with the changing values of θ_k.
4. The idealized setup considered here may be a launching pad for future robust explorations involving rather more complex setups.

References

1 Asad S, Alsaedi A, Hayat T (2016) Flow of couple stress fluid with variable thermal conductivity. Appl Math Mech 37:315–324
2 Aziz A (2006) Entropy generation in pressure gradient assisted Couette flow with different thermal boundary conditions. Entropy 8:50–62
3 Bejan A (1979) A study of entropy generation in fundamental convective heat transfer. J Heat Trans 101:718–725
4 Bejan A (1980) Second law analysis in heat transfer. Energy 5:721–732
5 Brewster MQ (1992) Thermal radiative transfer properties. John Wiley & Sons, New York
6 Chiam TC (1998) Heat transfer in a fluid with variable thermal conductivity over a linearly stretching sheet. Acta Mech 129:63–72
7 Dunn JE, Rajagopal KR (1995) Fluids of differential type: critical review and thermodynamic analysis. Int J Eng Sci 33:689–729
8 Gbadeyan JA, Titiloye EO, Adeosun AT (2020) Effect of variable thermal conductivity and viscosity on Casson nanofluid flow with convective heating and velocity slip. Heliyon 6
9 Hatami M, Hatami J, Ganji DD (2014) Computer simulation of MHD blood conveying gold nanoparticles as a third grade non-Newtonian nanofluid in a hollow porous vessel. Comput Methods Programs Biomed 113(2):632–641
10 Hayat T, Momoniat E, Mahomed FM (2008) Peristaltic MHD flow of third grade fluid with an endoscope and variable viacosity. J Nonlinear Math Phy 15(1):91–104
11 Hossain MA, Munir MS, Rees DAS (2000) Flow of viscous incompressible fluid with temperature dependent viscosity and thermal conductivity past a permeable wedge with uniform surface heat flux. Int J Therm Sci 39:635–644
12 Islam S, Banoa Z, Siddique I, Siddiqui AM (2011) The optimal solution for the flow of a fourth-grade fluid with partial slip. Comput Math Appl 61:1507–1516
13 Keimanesh M, Rashidi MM, Chamkha AJ, Jafari R (2011) Study of a third grade non-Newtonian fluid flow between two parallel plates using the multi-step differential transform method. Comput Math Appl 62(8):2871–2891
14 Lin Y, Zheng L, Zhang X (2014) Radiation effects on Marangoni convection flow and heat transfer in pseudo-plastic non-Newtonian nanofluids with variable thermal conductivity. Int J Heat Mass Transfer 77:708–716
15 Mokarizadeh H, Asgharian M, Raisi A (2013) Heat transfer in Couette-Poiseuille flow between parallel plates of the Giesekus viscoelastic fluid. J Non-Newton Fluid Mech 196:95–101
16 Rahbari A, Abbasi M, Rahimipetroudi I (2018) Heat transfer and MHD flow of non-Newtonian Maxwell fluid through a parallel plate channel: analytical and numerical solution. Mech Sci 9:61–70

17 Rajagopal KR, Bhatnagar RK (1995) Exact solutions for some simple flows of an Oldroyd-B fluid. Acta Mech 113:233–239
18 Rajagopal KR, Srinivasa AR (2000) A thermodynamic frame work for rate type fluid models. J Non-Newton Fluid Mech 88:207–217
19 Rajagopal KR (1982) A note on unsteady unidirectional flows of a non-Newtonian fluid. Int J Nonlinear Mech 17(5–6):369–373
20 Rajagopal KR (1993) Mechanics of non-Newtonian fluids. In: Recent developments in theoretical fluid mechanics. Springer, Pitman Res Notes Math Ser
21 Rajagopal KR (1984) On the creeping flow of second order fluid. J Non-Newton Fluid Mech 15(2):239–246
22 Rashidi MM, Bagheri S, Momoniat E, Freidoonimehr N (2017) Entropy analysis of convective MHD flow of third grade non-Newtonian fluid over a stretching sheet. Ain Shams Eng J 8(1):77–85
23 Schowalter WR (1978) Mechanics of Non-Newton fluids. Pergamon
24 Siddiqui AM, Khan NZ, Rana MA, Haroon T (2016) Flow of a second grade fluid through constricted tube using integral method. J Appl Fluid Mech 9(6):2803–2812
25 Siddiqui A, Hameed M, Siddiqui BM, Ghori QK (2010) Use of adomian decomposition method in the study of parallel plate flow of a third grade fluid. Commun Nonlinear Sci Numer Simul 15(9):2388–2399
26 Siddiqui A, Zeb A, Ghori QK, Benharbit AM (2008) Homotopy perturbation method for heat transfer flow of a third grade fluid between parallel plates. Chaos Solitons Fract 36(1):182–192
27 Truesdell C, Noll W (2004) The non-linear field theories of mechanics. Springer, Berlin
28 Vyas P, Khan S (2016) Entropy analysis for MHD dissipative Casson fluid flow in porous medium due to stretching cylinder. Acta Tech 61:299–315
29 Vyas P, Rai A (2010) Radiative flow with variable thermal conductivity over a non-isothermal stretching sheet in a porous medium. Int J Contemp Math Sci 5(54):2685–2698
30 Vyas P, Rai A (2012) Radiative variable fluid properties flow due to a point sink inside a cone filled with porous medium. Appl Math Sci 6(87):4307–4317
31 Vyas P, Soni S (2016) Entropy analysis for MHD casson fluid flow in a channel subjected to weakly temperature dependent convection coefficient and hydrodynamic slip. J Rajasthan Acad Phys Sci 15:1–18
32 Vyas P, Srivastava N (2015) Entropy analysis of generalized MHD Couette flow inside a composite duct with asymmetric convective cooling. Arab J Sci Eng 40:603–614
33 Vyas P, Yadav K (2020) EGA for a convective regime over a vertical cylinder stretching linearly. AMNS 1–12. https://doi.org/10.2478/amns.2020.2.00058
34 Vyas P, Srivastava N, Soni S (2016) Entropy generation analysis for oscillatory flow in a vertical channel filled with porous medium. In: IEEE international conference on recent advances and innovations in engineering (ICRAIE), December 23–25, Jaipur, India
35 Vyas P, Khan S (2021) Micropolar couple stress thermofluidics and entropy in Forchheimer channel. Heat Transf 1–35. https://doi.org/10.1002/htj.22080
36 Vyas P, Kasana RK, Khan S (2020) Entropy analysis for boundary layer Micropolar fluid flow. AIMS Math 5(3):2009–2026. https://doi.org/10.3934/math.2020133
37 Wilkinson WL (1960) Non-Newtonian fluids. Pergamon Press

Solution of Nonlinear Fractional Differential Equation Using New Integral Transform Method

Gomatiben Tailor, Vinod Gill, and Ravi Shanker Dubay

Abstract In a recent study, fractional-order nonlinear partial differential equations are solved by using the Elzaki decomposition method (EDM), which is a powerful method for solving fractional differential equations. A few numerical cases are illustrated to examine the efficiency of the proposed technique. The result reveals that the required technique is systematic, clean and can be workable for linear and nonlinear problems.

Keywords Fractional differential calculus · Elzaki transform · Adomian polynomial

1 Introduction, Background and Preliminaries

At present, many researchers are working on a nonlinear differential equation. They use many methods to find the solution to it. Many analytical and numerical solutions have been found. During the development of nonlinear differential equations many reliable and efficient techniques have evolved. Nonlinear fractional differential equations have their important result in applied mathematics, chemistry, physics and are connected with engineering. Nonlinear differential equation is applied in quantum field theory, plasma physics, nonlinear optics and applied physical science [1–10].

Mathematical modeling is one of the most important tools for researchers. For scientists and researchers, mathematical modeling is the best and most useful method. It can be achieved in a different way. We follow that the modeling in some scientific situation has linear and nonlinear differential equations. Recently, many models have evolved in which fractional differential equation is used. To know more about

G. Tailor · R. S. Dubay (✉)
Department of Mathematics, AMITY School of Engineering and Technology, AMITY University, Jaipur 302002, Rajasthan, India
e-mail: ravimath13@gmail.com

V. Gill
Department of Mathematics, Government college, Nalwa(Hisar), Haryana 125037, India

J. Singh et al. (eds.), *Advances in Mathematical Modelling, Applied Analysis and Computation*, Lecture Notes in Networks and Systems 415,
https://doi.org/10.1007/978-981-19-0179-9_36

the fractional calculus, we can mention the Miller and Ross [11], Podlubny [12], Kilbas et al. [13], Hilfer [14] and others. Applications at fractional derivatives can be found in [15–22]. So many methods can be found for linear differential equation but very few methods for nonlinear differential equation, like variation iteration method [23], Laplace transform method [24], Homotopy perturbation method [25], Adomian decomposition method [26], Homotopy transform method [27], Homotopy analysis method [28, 29], q-Homotopy analysis method (q-HAM) [30], etc.

Out of them the integral transform method is found suitable. In the last two decades, using this method many problems have been solved in the field of applied mathematics, physics and engineering. Integral transformations are very valuable for the simplification they bring, very often to deal with differential equations. The result we got is, of course, the transformation of the solution of the original differential equation, and inverting this conversion is required to complete the process. An integral transform is very useful if it helps one to change a complicated problem into a simpler one. The integral transforms, in particular Laplace transform and Fourier transform are more useful. Also using it for expansion of nonlinear equation is available. Integral transform is more precious because dealing with it is easy. Transform can be chosen from the set of solutions of differential and integral equations such as Laplace transform. By using integral transform complex problems become simple [31–35]. The offered technique is a fantastic blend of homotopy analysis method (HAM) and Laplace transform (LT) operator and has been used fruitfully in the numerical computation of various fractional differential equations (FDEs) [40–44].

Elzaki transform is a very convenient technique for solving linear and nonlinear differential equations [36, 37]. It was introduced by Tarid Elzaki to facilitate the process of solving all differential equations in the time domain [38, 39].

This method is established on an infinite series that converges to an exact solution. In this thesis, we apply the method to get an accurate analytic and approximate solution to the fractional-order equation.

Let us analyze the following nonlinear fractional differential equations:

$$i D_t^{\alpha} \omega(x,t) + \beta \frac{\partial^2 \omega}{\partial x^2} + v(x)\,\omega + \gamma |\omega|^2 \omega = 0, \tag{1}$$

with

$$\omega(x,0) = \chi(x). \tag{2}$$

In Eq. (1) $v(x)$ is the trapping potential and β, γ are real constants.
The structure of this chapter is as follows:
In Sect. 2, the definition and preliminary of fractional calculus and Elzaki transform is given.
In Sect. 3, the methodology of used method is explained.
In Sect. 4, the application of Elzaki transform method is provided.
In Sect. 5, conclusion is given.

2 Definition and Preliminary of Fractional Calculus and Elzaki Transform

In this segment, we introduce the definition and theorem of fractional calculus and Elzaki transform and we will show the definition and few properties of fractional derivative [19–23].

Definition 1 The Riemann–Liouville fractional integral operator of $z(t) \in C_\mu$, $\mu \geq -1$, having order $\beta > 0$, is defined below

$$I^{\beta}[z(t)] = \frac{1}{\Gamma(\beta)} \int_0^t (t-\tau)^{\beta-1} z(\tau)\, d\tau, \qquad \beta > 0, \tag{3}$$

$$I^{0}[z(t)] = z(t). \tag{4}$$

Definition 2 The definition of fractional derivative of the function $z(t)$ in the Caputo sense is

$$\begin{aligned} D_t^{\beta} z(t) &= I^{m-\beta} D^n z(t), \\ &= \frac{1}{\Gamma(m-\beta)} \int_0^t (t-\tau)^{-\beta+m-1} z^{(m)}(\tau)\, d\tau, \qquad m-1 < \beta \leq m, \end{aligned} \tag{5}$$

where $m \in N$ *and* $t > 0$.

The property of Caputo fractional derivative operator and Riemann–Liouville fractional integral operator is

$$I_t^{\beta} D_t^{\beta} z(t) = z(t) - \sum_{k=0}^{m-1} \frac{z^k(0^+)\, t^k}{k!}. \tag{6}$$

Definition 3 [39] The Elzaki transform defined in $A = \left\{ |q(\tau)| < N e^{\frac{\tau}{k_j}}, \text{if} \tau \in (-1)^i \times [0, \infty) \right\}$ is

$$E[q(\tau)] = \rho \int_0^{\infty} q(\tau)\, e^{-\frac{\tau}{\rho}} d\tau = \mathcal{Q}(\mathrm{p}), \quad \tilde{\mathrm{n}} \geq 0, \mathrm{k}_1 \leq \rho \leq \mathrm{k}_2. \tag{7}$$

Definition 4 If $\tilde{\mathrm{n}} - 1 < \sigma \leq \tilde{\mathrm{n}}, \tilde{\mathrm{n}} \in N$ then the new integral transform (NIT) of the fractional derivative $D_*^{\sigma} q(\xi, \tau)$ is

$$E\left[D_*^{\sigma} q(\xi, \tau)\right] = \frac{\mathcal{Q}(\xi, \rho)}{\rho^{\sigma}} - \sum_{k=0}^{\tilde{\mathrm{n}}-1} \rho^{k-\sigma+2} q^{(k)}(\xi, 0), \quad \tilde{\mathrm{n}} - 1 < \sigma \leq \tilde{\mathrm{n}}, \tag{8}$$

where $\mathcal{Q}(\xi, \rho)$ be the NIT of $q(\xi, \tau)$

3 Methodology of New Integral Transform [NIT]

In this part, we introduce the methodology of new integral transform algorithm for nonlinear fractional differential equation (1).
Rewrite Eq. (1) as

$$D_t^{\alpha}\omega(x,t) = i\left[\beta\frac{\partial^2\omega}{\partial x^2} + v(x)\omega + \gamma|\omega|^2\omega\right], \quad \alpha > 0. \tag{9}$$

Applying the Elzaki transform to both parties of Eq. (9)

$$E\left(D_t^{\alpha}\omega\,(x,t)\right) = iE\left[\beta\frac{\partial^2\omega}{\partial x^2} + v(x)\omega + \gamma|\omega|^2\omega\right], \quad \alpha > 0. \tag{10}$$

Applying the property of the Elzaki transform, we get

$$\frac{W(\xi,\rho)}{\rho^{\alpha}} - \sum_{k=0}^{r-1}\rho^{-\alpha+k+2}h^{(k)}(\xi,0) = iE\left[\beta\frac{\partial^2\omega}{\partial x^2} + v(x)\omega + \gamma|\omega|^2\omega\right], \qquad \alpha > 0. \tag{11}$$

Using given initial condition in Eq. (2), we get

$$W(x,\rho) = \rho^2\chi(x) + \mathrm{i}\rho^{\alpha}\mathrm{E}\left[\beta\frac{\partial^2\omega}{\partial \mathrm{x}^2} + \mathrm{v(x)}\omega + \gamma|\omega|^2\omega\right], \qquad \alpha > 0. \tag{12}$$

The result of the new integral decomposition method gives the solution $\omega(x,t)$ in sequence [33–36]

$$\omega(x,t) = \sum_{r=0}^{\infty}\omega_r(x,t). \tag{13}$$

The nonlinear term can be written as the first Adomian polynomials, and we get [39–42]

$$\begin{aligned} E\left[\sum_{r=0}^{\infty}\omega_r(x,t)\right] &= \rho^2\chi(x) \\ &+\mathrm{i}\rho^{\alpha}\mathrm{E}\left[\beta\sum_{\mathrm{r}=0}^{\infty}\omega_{\mathrm{r_{xx}}}(\mathrm{x},t)+\mathrm{v(x)}\sum_{\mathrm{r}=0}^{\infty}\omega_{\mathrm{r}}(\mathrm{x},t)+\gamma\left|\sum_{\mathrm{r}=0}^{\infty}\omega_{\mathrm{r}}(\mathrm{x},t)^2\right|\sum_{\mathrm{r}=0}^{\infty}\omega_{\mathrm{r}}(\mathrm{x},t)\right]. \end{aligned} \tag{14}$$

Finally, we obtain the repeated algorithm as follows:

$$E\left[\omega_0(x,t)\right] = \rho^2\chi(x). \tag{15}$$

$$\begin{aligned} &E\left[\omega_{r+1}(x,t)\right] \\ &= \mathrm{i}\rho^{\alpha}\mathrm{E}\left[\beta\sum_{\mathrm{r}=0}^{\infty}\omega_{\mathrm{r_{xx}}}(\mathrm{x},t)+\mathrm{v(x)}\sum_{\mathrm{r}=0}^{\infty}\omega_{\mathrm{r}}(\mathrm{x},t)+\gamma\left|\sum_{\mathrm{r}=0}^{\infty}\omega_{\mathrm{r}}(\mathrm{x},t)^2\right|\sum_{\mathrm{r}=0}^{\infty}\omega_{\mathrm{r}}(\mathrm{x},t)\right]. \end{aligned} \tag{16}$$

Applying inverse Elzaki transform of Eqs. (15) and (16), we obtain

$$\omega_0(x,t) = E^{-1}[\rho^2 \chi(x)]. \tag{17}$$

$$\omega_{r+1}(x,t) = E^{-1}\left[\mathrm{i}\rho^{\alpha}\mathrm{E}\left[\beta\sum_{\mathrm{r}=0}^{\infty}\omega_{\mathrm{r_{xx}}}(\mathrm{x},t)+\mathrm{v}(\mathrm{x})\sum_{\mathrm{r}=0}^{\infty}\omega_{\mathrm{r}}(\mathrm{x},t)+\gamma\left|\sum_{\mathrm{r}=0}^{\infty}\omega_{\mathrm{r}}(\mathrm{x},t)\right|^2\sum_{\mathrm{r}=0}^{\infty}\omega_{\mathrm{r}}(\mathrm{x},t)\right]\right]. \tag{18}$$

Now, first applying the Elzaki transform of the term on the right-hand side of Eq. (18) and then applying inverse Elzaki transform, we get the value of $\omega_1, \omega_2, \omega_3, \ldots, \omega_n$. And from Eq. (13) we get the required solution.

4 Application of Elzaki Transform Method

In this section, we will use the new integral transform method for solving nonlinear fractional differential equation.

Example 1 Consider nonlinear differential equation as

$$i D_t^{\alpha}\omega(x,t) + \frac{1}{2}\frac{\partial^2\omega}{\partial x^2} + |\omega|^2\omega = 0, \qquad t > 0,\ 0 < \alpha \le 1. \tag{19}$$

subject to the initial condition,

$$\omega(x,0) = e^{ix}. \tag{20}$$

Equation (19) can be written in the following form:

$$D_t^{\alpha}\omega(x,t) = i\left[\frac{1}{2}\frac{\partial^2\omega}{\partial x^2} + |\omega|^2\omega\right], \qquad t > 0,\ 0 < \alpha \le 1. \tag{21}$$

Applying the Elzaki transform on both the parties in Eq. (21), we get

$$W(x,\rho) = \rho^2\omega(x,0) + \mathrm{i}\rho^{\alpha}\mathrm{E}\left[\tfrac{1}{2}\tfrac{\partial^2\omega}{\partial \mathrm{x}^2}+|\omega|^2\omega\right]. \tag{22}$$

Using the given initial condition Eq. (20) becomes

$$W(x,\rho) = \rho^2 e^{ix} + \mathrm{i}\rho^{\alpha}\mathrm{E}\left[\frac{1}{2}\frac{\partial^2\omega}{\partial \mathrm{x}^2}+|\omega|^2\omega\right]. \tag{23}$$

For the nonlinear term, in the first Adomian polynomial, we obtain

$$\sum_{r=0}^{\infty} \omega_r(x,t) = \rho^2 e^{ix} + \mathrm{i}\rho^{\alpha}\mathrm{E}\left[\frac{1}{2}\sum_{\mathrm{r}=0}^{\infty}\omega_{\mathrm{r_{xx}}}(\mathrm{x},t)+|\sum_{\mathrm{r}=0}^{\infty}\omega_{\mathrm{r}}(\mathrm{x},t)|^2\sum_{\mathrm{r}=0}^{\infty}\omega_{\mathrm{r}}(\mathrm{x},t)\right]. \tag{24}$$

Finally, using two parties of Eq. (24), we get the repeated algorithm as follows:

$$W_0(x,\rho) = \rho^2 e^{ix}. \tag{25}$$

and

$$W_{r+1}(x,\rho) = \mathrm{i}\rho^{\alpha}E\left[\frac{1}{2}\sum_{\mathrm{r}=0}^{\infty}\omega_{\mathrm{r_{xx}}}(\mathrm{x},t)+\gamma|\sum_{\mathrm{r}=0}^{\infty}\omega_{\mathrm{r}}(\mathrm{x},t)|^2\sum_{\mathrm{r}=0}^{\infty}\omega_{\mathrm{r}}(\mathrm{x},t)\right]. \tag{26}$$

Applying the inverse Elzaki transform in Eqs. (25) and (26), we obtain

$$\omega_0(x,t) = e^{ix}. \tag{27}$$

$$\omega_{r+1}(x,t) = E^{-1}\left[\mathrm{i}\rho^{\alpha}E\left[\frac{1}{2}\sum_{\mathrm{r}=0}^{\infty}\omega_{xx}(\mathrm{x},t)+\gamma|\sum_{\mathrm{r}=0}^{\infty}\omega_{\mathrm{r}}(\mathrm{x},t)|^2\sum_{\mathrm{r}=0}^{\infty}\omega_{\mathrm{r}}(\mathrm{x},t)\right]\right]. \tag{28}$$

Consequently,

$$\omega_1 = \frac{i}{2}e^{ix}\frac{t^{\alpha}}{\Gamma(\alpha+1)}, \tag{29}$$

and

$$\omega_2 = -\frac{1}{4}e^{ix}\frac{t^{2\alpha}}{\Gamma(2\alpha+1)}, \tag{30}$$

and so on. Using these results we obtain the solution of Eq. (19) as
$\omega = \omega_0 + \omega_1 + \omega_2 + \ldots$

Example 2 Consider a nonlinear differential equation:

$$D_t^{\alpha}\omega(x,t) = 0.1 - \omega(t) + 0.8\omega^2(t), \quad t > 0, 0 < \alpha \leq 1 \tag{31}$$

subject to the initial condition

$$\omega(x,0) = 0. \tag{32}$$

Applying the Elzaki transform on both the parties in Eq. (31), we get

$$W(x,\rho) = \rho^2\omega(x,0) + \rho^{\alpha}\mathrm{E}[0.1-\omega(x,t)+0.8\omega^2(x,t)] \tag{33}$$

Using the initial condition in Eq. (32), we get

$$W(x,\rho) = \rho^{\alpha}\mathrm{E}[0.1-\omega(x,t)+0.8\omega^2(x,t)]. \tag{34}$$

For the nonlinear term, in the first Adomian polynomial, we obtain

$$\sum_{r=0}^{\infty}\omega_r(x,t) = \rho^{\alpha}\mathrm{E}[0.1-\sum_{\mathrm{r}=0}^{\infty}\omega_{\mathrm{r}}(\mathrm{x},t)+0.8[\sum_{\mathrm{r}=0}^{\infty}\omega_{\mathrm{r}}(\mathrm{x},t)]^2]. \tag{35}$$

Finally using the two parties of Eq. (35), we get the repeated algorithm as follows:

$$W_0(x,\rho) = \rho^{\alpha}E\,[0.1]\,. \tag{36}$$

$$W_{r+1}(x,\rho) = \rho^{\alpha}\mathrm{E}\left[0.-\sum_{\mathrm{r}=0}^{\infty}\omega_{\mathrm{r}}(\mathrm{x},t)+0.8\left(\sum_{\mathrm{r}=0}^{\infty}\omega_{\mathrm{r}}(\mathrm{x},t)\right)^2\right]. \tag{37}$$

Applying the inverse Elzaki transform in Eqs. (38) and (39), we obtain

$$\omega_0 = 0.1\frac{t^{\alpha}}{\Gamma(\alpha+1)}, \tag{38}$$

$$\omega_{r+1}(x,t) = E^{-1}\left[\rho^{\alpha}\mathrm{E}\left[-\sum_{\mathrm{r}=0}^{\infty}\omega_{\mathrm{r}}(\mathrm{x},t)+0.8\left[\sum_{\mathrm{r}=0}^{\infty}\omega_{\mathrm{r}}(\mathrm{x},t)\right]^2\right]\right]. \tag{39}$$

Consequently,

$$\omega_0 = 0.1\frac{t^{\alpha}}{\Gamma(\alpha+1)}, \tag{40}$$

$$\omega_2 = -0.1\frac{t^{2\alpha}}{\Gamma\,(2\alpha+1)} + 0.8\frac{\Gamma(2\alpha+1)}{(\Gamma\,(\alpha+1))^2}\frac{t^{3\alpha}}{\Gamma(3\alpha+1)}, \tag{41}$$

and so on. Using these results we get the solution of Eq. (31) as

$\omega = \omega_0 + \omega_1 + \omega_2 + \cdot$

Example 3 Consider a nonlinear differential equation:

$$D_t^{\alpha}\omega(x,t) + \omega(x,t)\omega_x(x,t) = x + xt^2, \quad t > 0, 0 < \alpha \leq 1 \tag{42}$$

subject to the initial condition

$$\omega(x,0) = 0. \tag{43}$$

Equation (42) can be written in the following form:

$$D_t^{\alpha}\omega(x,t) = x + xt^2 - \omega(x,t)\omega_x(x,t), \quad t > 0, 0 < \alpha \leq 1. \tag{44}$$

Applying the Elzaki transform in Eq. (42), we get

$$W(x,\rho) = \rho^2\omega(x,0) + \rho^{\alpha}E\left(x + xt^2\right) - \rho^{\alpha}E\left[\omega(x,t)\omega_x(x,t)\right]. \tag{45}$$

By using the method of NIT, we get

$$W(x,\rho) = \rho^{\alpha}E\left(x + xt^2\right) - \rho^{\alpha}E\left[\omega(x,t)\omega_x(x,t)\right]. \tag{46}$$

For the nonlinear term, in the first Adomian polynomial, we obtain

$$\sum_{r=0}^{\infty} W_r(x,\rho) = \rho^{\alpha}E\left(x + xt^2\right) + \rho^{\alpha}\mathrm{E}\left[\sum_{\mathrm{r}=0}^{\infty}\omega_{\mathrm{r}}(\mathrm{x},t)\sum_{\mathrm{r}=0}^{\infty}\omega_{\mathrm{rx}}(\mathrm{x},t)\right]. \tag{47}$$

Finally using the two parties of Eq. (47), we get

$$W_0(x,\rho) = \rho^{\alpha}E\left(x + xt^2\right). \tag{48}$$

$$W_{r+1}(x,\rho) = \rho^{\alpha}\mathrm{E}\left[\sum_{\mathrm{r}=0}^{\infty}\omega_{\mathrm{r}}(\mathrm{x},t)\sum_{\mathrm{r}=0}^{\infty}\omega_{\mathrm{rx}}(\mathrm{x},t)\right]. \tag{49}$$

Applying the inverse Elzaki transform in Eqs. (48) and (49), we obtain

$$\omega_0(x,t) = E^{-1}\left[\rho^{\alpha}E\left(x + xt^2\right)\right]. \tag{50}$$

$$\omega_{r+1}(x,t) = E^{-1}\left(\rho^{\alpha}\mathrm{E}\left[\sum_{\mathrm{r}=0}^{\infty}\omega_{\mathrm{r}}(\mathrm{x},t)\sum_{\mathrm{r}=0}^{\infty}\omega_{\mathrm{rx}}(\mathrm{x},t)\right]\right). \tag{51}$$

Consequently,

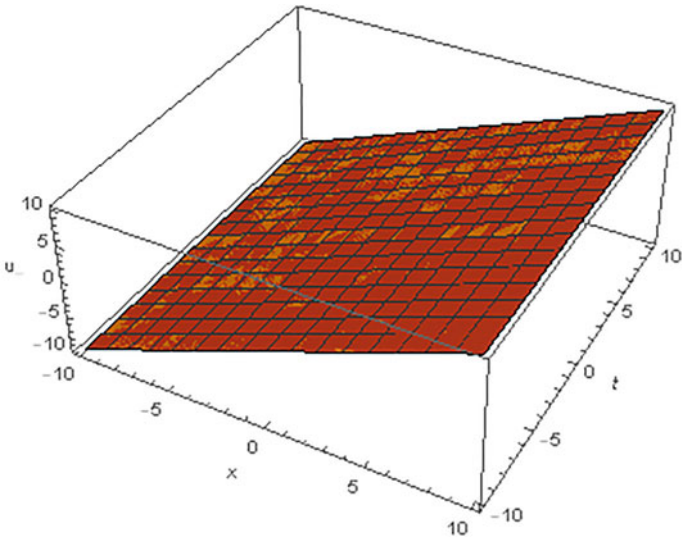

Fig. 1 The graph of $\omega(x, t)$ for example-3

$$\omega_0 = x\frac{t^{\alpha}}{\Gamma(\alpha+1)} + x\frac{2t^{\alpha+2}}{\Gamma(\alpha+3)}, \tag{52}$$

$$\omega_1 = -\left[x\frac{\Gamma(2\alpha+1)}{[\Gamma(\alpha+1)]^2}\frac{t^{3\alpha}}{\Gamma(3\alpha+1)} + 4x\frac{\Gamma(2\alpha+3)}{\Gamma(\alpha+1)\Gamma(\alpha+3)}\frac{t^{3\alpha+2}}{\Gamma(3\alpha+3)} + 4\,x\frac{\Gamma(2\alpha+5)}{[\Gamma(\alpha+3)]^2}\frac{t^{3\alpha+4}}{\Gamma(3\alpha+5)}\right], \tag{53}$$

and so on. On using the obtained results, we get the solution of Eq. (42) as the following equation. $\omega = \omega_0 + \omega_1 + \omega_2 + ...$

5 Conclusion

New integral transform method is used to find solution of fractional differential equation. This method is remarkable and very precious for the fractional differential equations which is successfully applied to find the solution of the nonlinear fractional differential equations. Also this method gives very efficient results. In conclusion, the Elzaki transformation can be seen as a proper improvement of the existing numerical techniques and may find wide applications. Graphs are also demonstrated for the solution of some examples.

References

1. Mohyud-Din ST, Noor MA, Noor KI (2009) Some relatively new techniques for nonlinear problems. Math Porb Eng. Article ID 234849. https://doi.org/10.1155/2009/234849
2. Wazwaz AM (2006) The modified decomposition method for analytic treatment of differential equations. Appl Math Comput 165–176
3. Hristov J (2017) Steady-state heat conduction in a medium with spatial non singular fading memory derivation of Caputo-Fabrizio space-fractional derivative from Cattaneo concept with Jeffrey's Kernel and analytical solutions. Therm Sci 21(2):827–839
4. Jafari H, Prasad JG, Goswami P, Dubey RS (2021) Solution of the local fractional Generalized KDV equation using homotopy analysis method. Spec Issue Sect Frac AI-Based Anal Appl Complex Syst Part I. https://doi.org/10.1142/S0218348X21400144
5. Dubey RS, Goswami P (2021) Mathematical model of diabetes and its complication involving fractional operator without singular kernel. Discrete Contin Dyn Syst S 14(7):2151–2161. https://doi.org/10.3934/dcdss.2020144
6. Alkahtani BST, Alkahtani JO, Dubey RS, Goswami P (2016) Solution of fractional oxygen diffusion problem having without singular kernel. J Nonlinear Sci Appl 11:1–9
7. Shrahili M, Dubey RS, Shafay A (2019) Inclusion of fading memory to Banister model of changes in physical condition. Discrete Contin, Dyn Syst Ser S 13(3):881–888
8. Shrivastav HM, Dubey RS, Jain M (2019) A study of the fractional-order mathematical model of diabetes and its resulting complications. Math Methods Appl Sci. https://doi.org/10.1002/mma.5681
9. Malyk I, Mykola G, Chaudhary A, Sharma S, Dubey RS (2021) Numerical solution of nonlinear fractional diffusion equation in the framework of the Yang-Abdel-Cattani derivative operator. Frac Frac 5(64). https://doi.org/10.3390/fractalfract5030064
10. Almuqrin MA, Goswami P, Sharma S, Khan I, Dubey RS, Khan A (2021) Fractional model of Ebola virus in population of bats in frame of Atangana-Baleanu fractional derivative. Res Phys 104295. https://doi.org/10.1016/j.rinp.2021.104295
11. Miller KS, Ross B (1993) An introduction to the fractional calculus and fractional differential equations. A Wiley-Inter Science Publication, John Wiley and Sons, New York, Chichester, Brisbane, Toronto and Singapore
12. Podlubny I (1999) Frac Differ Equ. Academic Press, New York
13. Kilbas AA, Srivastava HM, Trujillo JJ (2006) Theory and applications of fractional differential equations. North-Holland Mathematical Studies, vol 204. Elsevier (North-Holland) Science Publishers, Amsterdam, London and New York
14. Hilfer R (2000) Applications of fractional calculus in physics. World Scientific Publishing Company, Singapore, New Jersey, London and Hong Kong, pp 87–130
15. Atangana A, Baleanu D (2016) New fractional derivatives with nonlocal and nonsingular kernel: theory and application to heat transfer model. Therm Sci 20(2):763–769
16. Atangana A, Alqahtani RT (2018) New numerical method and application to Keller-Segel model with fractional order derivative. Chaos Solitons Fract. 116:14–21
17. Chaurasia VBL, Dubey RS (2011) Analytical solution for the differential equation containing generalized fractional derivative operators and Mittag-Leffler-type function. In: International scholarly research network ISRN applied mathematics, 9. Article ID 682381. https://doi.org/10.5402/2011/682381
18. Singh J, Kumar D, Baleanu D (2017) On the analysis of chemical kinetics system pertaining to a fractional derivative with Mittag-Leffer type kernel. Chaos 27(10):103113
19. Dubey RS, Belgacem FBM, Goswami P (2016) Homotopy perturbation approximate solutions for Bergman's Minimal Blood Glucose-Insulin Model. J Fract Geom Nonlinear Anal Med Biol (FGNAMB) 2(3):1–6
20. Alzaid SS, Alkahtani BST, Sharma S, Dubey RS (2021) Numerical solution of fractional model of HIV-1 infection in framework of different fractional derivatives. J Funct Spaces 2021. Article ID 6642957. https://doi.org/10.1155/2021/6642957

21. Yang XJ, Machado JT, Baleanu D (2017) Anomalous diffusion models with general fractional derivatives within the kernels of the extended Mittag-Leffer type functions. Rom Rep Phys 69(4):115
22. Yang XJ, Srivastava HM, Torres DFM, Debbouche A (2017) General fractional-order anomalous diffusion with non-singular power-law kernel. Therm Sci 21(1):51–59
23. Wazwaz M (2007) The variational iteration method: a powerful scheme for handling linear and nonlinear diffusion equations. Comp Math Appl 54:933–939
24. Kexue L, Jigen P (2011) Laplace transform and fractional differential equations. Appl Math Lett 24(12):2019–2023
25. He J-H (1999) Homotopy perturbation technique. Comput Methods Appl Mech Eng 178(3–4):257–262
26. Duan S, Rach R, Baleanu D, Wazwaz AM (2012) A review of the Adomian decomposition method and its application to fractional differential equations. Comm Fract Calculus 3:73–99
27. Dubey RS, Alkahtani BST, Atangana A (2015) Analytical solution of space-time fractional Fokker-Planck equation by homotopy perturbation Sumudu transform method. Math Prob Eng 7. Article ID 780929. https://doi.org/10.1155/2015/780929
28. Liao SJ (2005) Comparison between the homotopy analysis method and the homotopy perturbation method. Appl Math Comput 169(2):1186–1194
29. Liao SJ (2004) On the homotopy analysis method for non-linear problems. Appl Math Comput 147(2):499–513
30. Dubey RS, Goswami P (2018) Analytical solution of the nonlinear diffusion equation. Eur Phys J Plus 133(183). https://doi.org/10.1140/epjp/i2018-12010-6
31. Davies B (2002) Integral transforms and their applications. Springer, New York, NY
32. Kexue L, Jigen P (2011) Laplace transform and fractional differential equations. Appl Math Lett 24(12):2019–923
33. Rashid S, Hammouch Z, Kalsoom H, Ashraf R, Chu YM (2020) New investigations on the generalized K-fractional integral operators. Front Phys 8(25)
34. Yang XJ (2017) A new integral transform operator for solving the heat-diffusion problem. Appl. Mathe. Lett. 64:193–197
35. West BJ, Bologna M, Grigolini P (2003) Fractional Laplace Transforms. In: physics of fractal operators. Institute for Nonlinear Science. Springer, New York, NY
36. Elzaki TM, Elzaki SM (2011) Application of new transform Elzaki Transform to partial differential equations. Glob Pure Appl Math 7(1):65–70
37. Gill V, Dubey RS (2018) New analytical method for Klein-Gordon equations arising in quantum field theory. Eur J Adv Eng Technol 5(8):649–655
38. Elazki TM (2011) The new integral transform Elazki Transform to partial differential equations. Glob J Pure Appl Math 7(1):57–64
39. Mohamed MZ, Elazki TM (2020) Application of New Integral Transform for linear and nonlinear fractional partial differential equation. J King Soud Univ Sci 32:544–549
40. Dubey VP, Singh RJ, Kumar D (2019) A reliable treatment of residual power series method for time-fractional Black Scholes European option pricing equations. Phys A: Stat Mech Appl 533:122040
41. Dubey VP, Singh RJ, Kumar D (2020) A hybrid analytical scheme for the numerical computation of time fractional computer virus propagation model and its stability analysis. Chaos, Solitons Fractals 133:109626
42. Dubey VP, Singh RJ, Kumar D (2019) A approximate analytical solution of fractional order biochemical reaction model and its stability analysis. Int J Biomath 12(5):1–21
43. Dubey VP, Singh RJ, Kumar D (2020) Numerical solution of time fractional three-species food chain model arising in the realm of mathematical ecology. Int J Biomath 13(2):1–22
44. Dubey VP, Singh RJ, Kumar D (2021) An efficient computational technique for time-fractional modified Degasperis Procesi equation arising in propagation of nonlinear dispersive waves. J Oce Eng Sci 6(1):30–39

Author Index

J. Singh et al. (eds.), *Advances in Mathematical Modelling, Applied Analysis and Computation*, Lecture Notes in Networks and Systems 415,
https://doi.org/10.1007/978-981-19-0179-9